Yaakov Kraftmakher

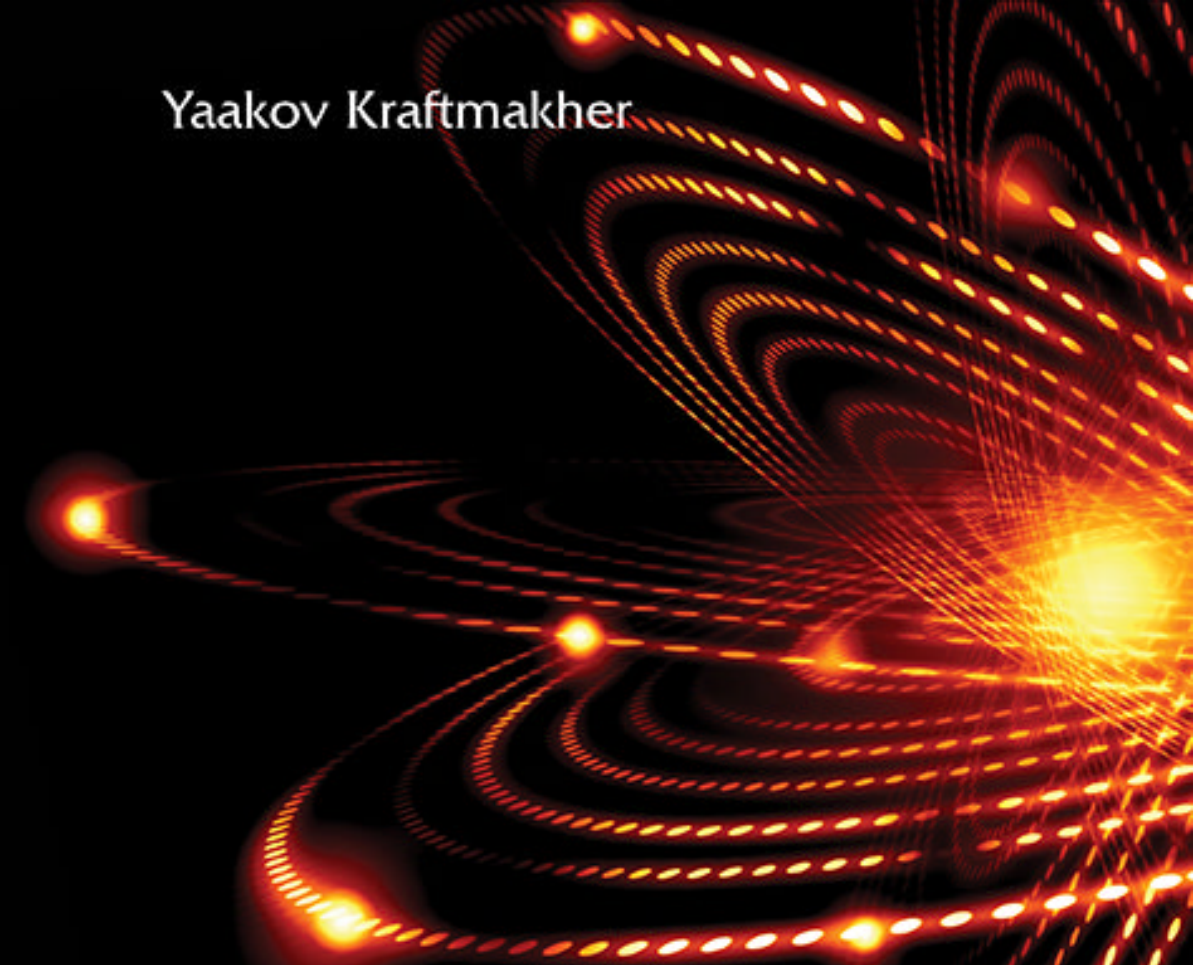

EXPERIMENTS AND DEMONSTRATIONS IN PHYSICS

Bar-Ilan Physics Laboratory

2nd Edition

World Scientific

EXPERIMENTS AND DEMONSTRATIONS IN PHYSICS

Bar-Ilan Physics Laboratory

2nd Edition

This page intentionally left blank

EXPERIMENTS AND DEMONSTRATIONS IN PHYSICS

Bar-Ilan Physics Laboratory

2nd Edition

Yaakov Kraftmakher
Bar-Ilan University, Israel

World Scientific

NEW JERSEY • LONDON • SINGAPORE • BEIJING • SHANGHAI • HONG KONG • TAIPEI • CHENNAI

Published by

World Scientific Publishing Co. Pte. Ltd.

5 Toh Tuck Link, Singapore 596224

USA office: 27 Warren Street, Suite 401-402, Hackensack, NJ 07601

UK office: 57 Shelton Street, Covent Garden, London WC2H 9HE

British Library Cataloguing-in-Publication Data
A catalogue record for this book is available from the British Library.

EXPERIMENTS AND DEMONSTRATIONS IN PHYSICS
Bar-Ilan Physics Laboratory
Second Edition

ISBN 978-981-4434-88-1
ISBN 978-981-4434-89-8 (pbk)

Printed in Singapore

Preface

The book is addressed to physicists involved in teaching physics at different levels (high school, college, and university), and to advanced students. Mainly, the book contains computer-assisted experiments and demonstrations. As a rule, such experiments may be performed in a short time, and many of the laboratory experiments may also serve as lecture demonstrations. Most of the experiments and demonstrations employ the *ScienceWorkshop 750 Interface* with *DataStudio* software or the *850 Universal Interface* with *Capstone* software from PASCO scientific. The new data-acquisition system is much more powerful than previous PASCO systems and provides new possibilities for creating or improving laboratory experiments and classroom demonstrations. It can be conveniently used in student laboratories. Additional equipment for the experiments was purchased mainly from PASCO.

The book contains 144 experiments and demonstrations. Many of them are computer-assisted versions of experiments described in laboratory manuals: Iveronova (1962, 1967, 1968); Portis (1964, 1972); Portis and Young (1971); Soloukhin (1975, 1983); Goldin (1983); Meiners *et al* (1987); Melissinos and Napolitano (2003); Mitin *et al* (2003). Some experiments and demonstrations are recommended by PASCO and PHYWE.

The first chapter, *Introductory Experiments*, describes experiments and demonstrations suitable for high schools and colleges (30 items). The subsequent chapters relate to *Mechanics* (11), *Molecular Physics* (11), *Electricity and Magnetism* (13), *Optics and Atomic Physics* (12), *Condensed Matter Physics* (11), *Semiconductors* (10), and *Applied Physics* (11). A special chapter, *Nobel Prize Experiments*, contains some milestone experiments of the twentieth century (10). The last chapter comprises *Student Projects* (25), which are addressed mainly to students of high schools and colleges.

The list of references given in the book contains about 1200 items. Nevertheless, many relevant references were not included, for which I apologize.

Many of the experiments were tested during laboratory courses for Bar-Ilan students in physics and electrical engineering. However, some of the experiments were developed especially for the book. All the illustrations pertain to actual measurements.

I am thankful to my colleagues for many useful discussions and much practical help, especially Professor Arkadii Arinstein, Professor Nathan Aviezer, Professor Moshe Deutsch, Professor Benjamin Ehrenberg, Dr. Alex Friedman, Dr. Vladimir Ginodman, Professor Moshe Gitterman, Professor Haim Halpern,

Professor Yuri Kaganovskii, Professor Eugene Kogan, Dr. Faina Kopansky, Professor Israel Laulicht, Dr. Shlomo Mansour, Professor Issai Shlimak, Professor Yehuda T. Suss, Professor Haim Taitelbaum, Dr. Leonid Wolfson, Dr. Shuki Wolfus, and Professor Yosef Yeshurun.

I wish to express my sincere thanks to Tamar Frank and Larisa Voikhansky, librarians; to Eitan Hammami, Itamar Padel, Eliezer Perel, Zeev Schmidt, Israel Tabakman, and Ronen Tirrer, electronics engineers; to Arkadii Belostotsky, Menahem Katz, and Dr. Smadar Shatz, computer experts; and to Sara Bialkovitch, Rachel Rotberg, and Hagit Tzabari, secretaries of the Department.

Many experiments developed by the author and presented in the book were published in *American Journal of Physics*, *European Journal of Physics*, *Physics Education*, and *The Physics Teacher*. I wish to thank the editors of these journals, and especially Professor Robert H. Romer, Professor Jeffrey S. Dunham, Professor Frank Wolfs, and Professor Karl C. Mamola. I am also thankful to anonymous referees of the journals for numerous useful suggestions.

I am grateful to the Nobel Foundation for permission to use photos of Nobel laureates. Personally, I wish to thank Joanna Petterson for sending me the photos. Photos of great physicists, beginning with Galilei and Newton, were obtained from the AIP Emilio Segrè Visual Archives, with the help of Heather Lindsay.

Many thanks to Lakshmi Narayanan, the editor of the book, for her help and cooperation, and to Itamar Baron for linguistic help.

Y. K.
Department of Physics
Bar-Ilan University
Ramat-Gan, Israel
April 2014

Table of contents

Introductory Experiments

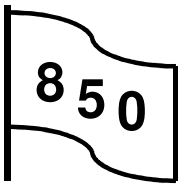

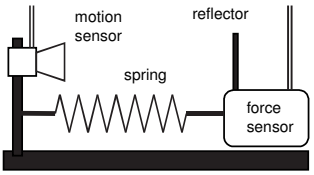

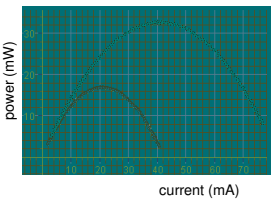

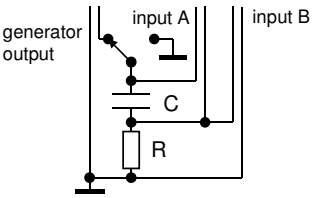

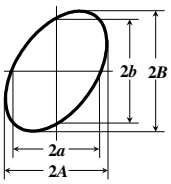

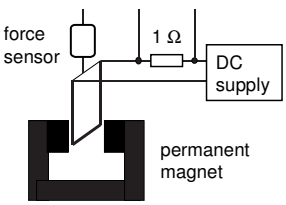

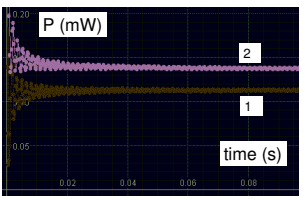

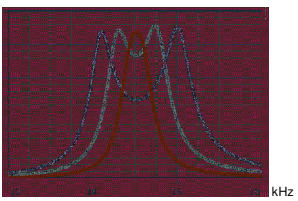

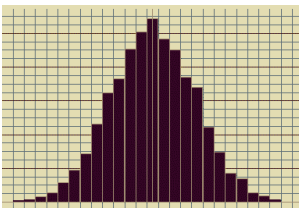

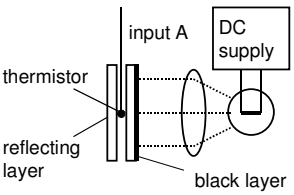

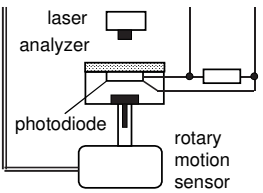

Data-acquisition systems from PASCO

In most of the experiments and demonstrations, we use the *ScienceWorkshop 750 Interface* and *DataStudio* software or *850 Universal Interface* and *Capstone* software from PASCO scientific. The following brief introduction considers some options provided by these data-acquisition systems.

ScienceWorkshop 750 Interface and *DataStudio* software

PASCO scientific provides a great number of sensors (Fig. 1).

Fig. 1. List of sensors provided by PASCO scientific.

We use only a part of the sensors available, namely: *Broad spectrum light sensor* (CI-6630), *Force sensor* (CI-6537), *High-accuracy temperature sensor* (CI-6525), *Light sensor* (CI-6504A), *Magnetic field sensor* (CI-6520A), *Motion sensor* (CI-6742), *Power amplifier II* (CI-6552A), *Radiation sensor* (TD-8553), *Rotary motion sensor* (CI-6538), *Sound sensor* (CI-6506B), *Thermistor temperature sensor* (CI-6527A), and *Voltage sensor* (CI-6503).

Displays. Many options exist for displaying results obtained by measurements or calculations: *Digits*, *Fast Fourier Transform* (*FFT*), *Graph*, *Histogram*, *Meter*, *Scope*, and *Table* (Fig. 2).

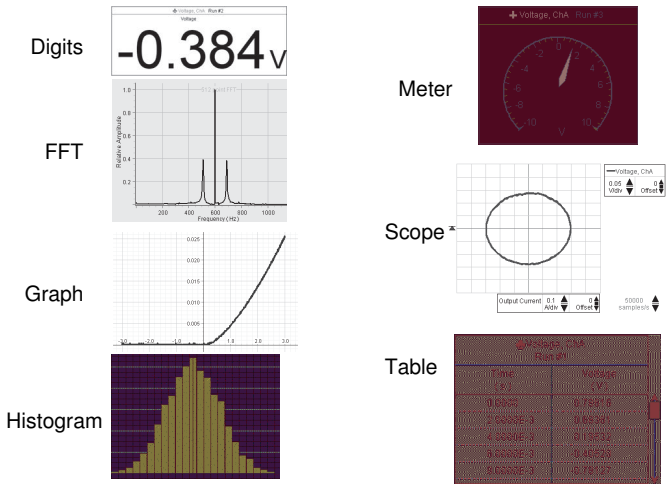

Fig. 2. *DataStudio* displays for measurement and calculation of data.

The ***Calculate* tool** is used in many experiments. To calculate new functions, one has to write down the necessary function and to define the sources of data for the calculations (Fig. 3). Along with usual polynomials, the tool provides some functions that fall into three categories, *Scientific*, *Statistical*, and *Special*.

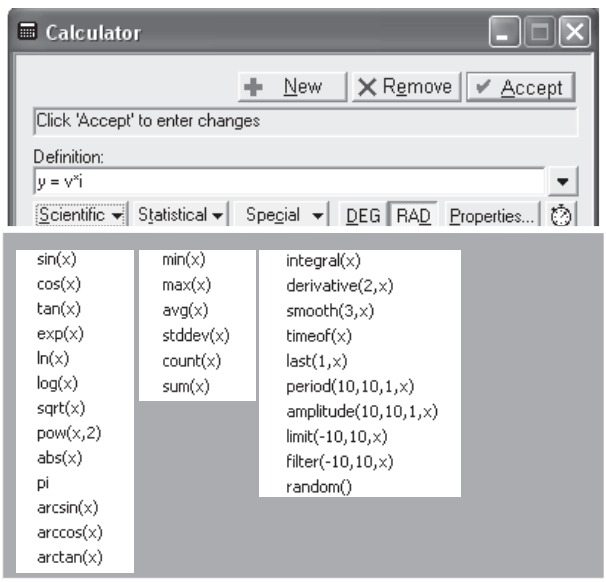

Fig. 3. Dialog box of the *Calculate* tool.

Signal generator incorporated into the *750 Interface* produces a variety of output voltages (Figs. 4 and 5). It the *Auto* regime, it builds the output voltage after pressing the *Start* button.

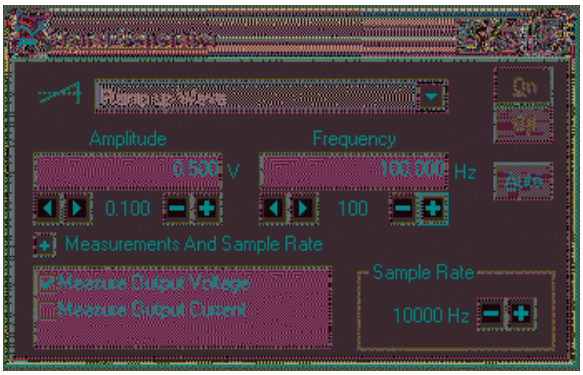

Fig. 4. Dialog box of the *Signal generator*.

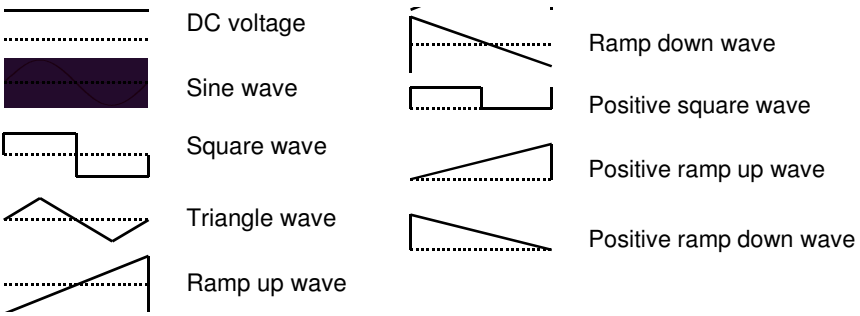

Fig. 5. List of output voltages produced by the *Signal generator*.

Fits provided by *DataStudio*. The *Fit* option includes proportional, linear, and many other functions (Fig. 6). The parameters of the fits and their standard deviations are added to the graphs.

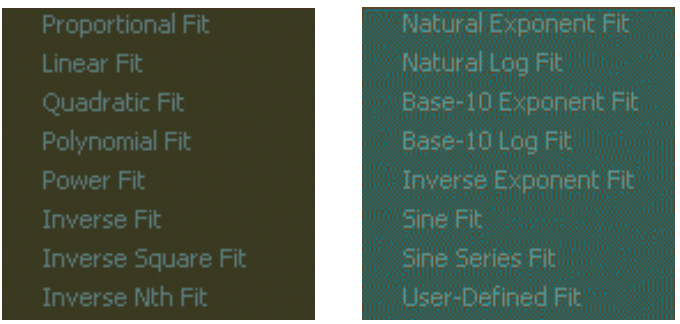

Fig. 6. *Fit* options provided by *DataStudio*.

In some experiments, a significant scatter of the data may appear. In such cases, the ***Smooth*** option solves the problem. This operation is used, for instance, when determining the heat of vaporization of nitrogen. The *Force sensor* measures the weight of a Dewar flask with liquid nitrogen. A significant scatter of the data occurs during the intensive boiling of the liquid (Fig. 7). The measurement data are smoothed by using the option *Calculate*/*Special*/ *Smooth* (30, *x*), that is, the smoothing involves 30 adjacent data points. In this example, only data from the *Force sensor* are smoothed. Both X and Y data can be smoothed when necessary.

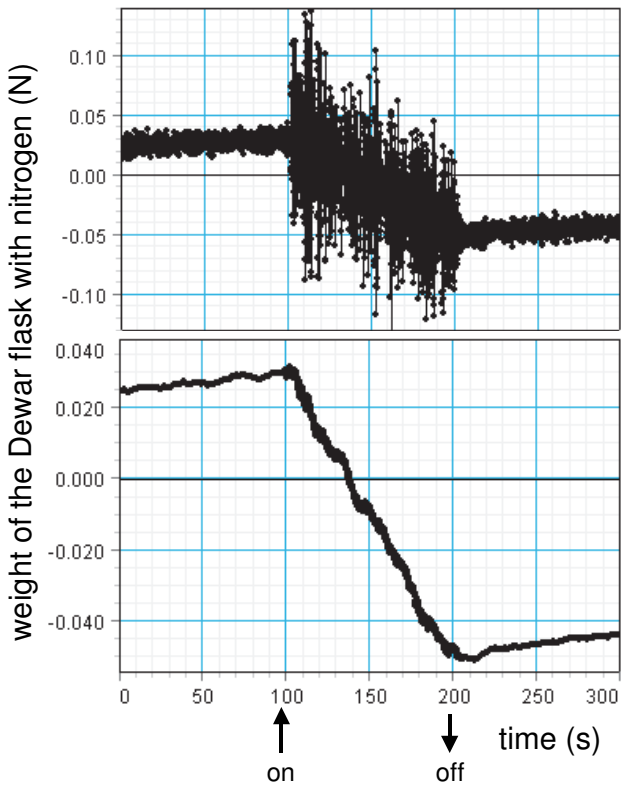

Fig. 7. Original measurement data and results after smoothing.

***Sampling*.** This option allows one to start and to stop data acquisition according to a preset time interval or definite measurement data (Fig. 8). These options are very important when the data acquisition lasts a very short time interval. Manual sampling of the data is also possible.

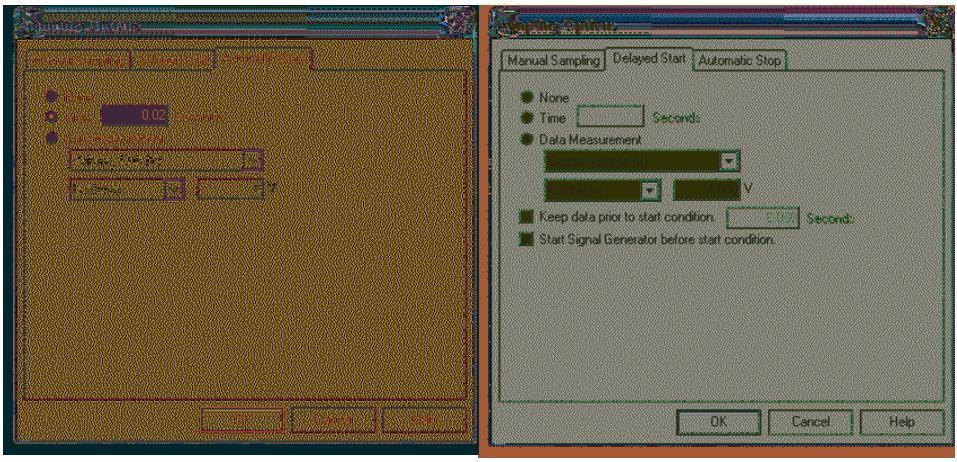

Fig. 8. Dialog box for *Sampling options*.

850 Universal Interface and *Capstone* software

The new data-acquisition system is much more powerful than previous PASCO systems and provides new possibilities for creating or improving laboratory experiments and classroom demonstrations (Kraftmakher 2013c). The version 1.1.1 of the new data-acquisition system contains many options, and it is impossible to immediately disclose all their applications. This process will last a certain time. A brief review given below is rather an introduction to the new data-acquisition system.

The new *850 Interface* (Fig. 9) supports all PASCO sensors, while the *Capstone* software is compatible with all PASCO USB interfaces and contains more options for processing experimental data. The new interface includes three built-in function generators. One of them (*Output 1*) is a power generator (±15 V, 1 A) providing voltages of various waveforms: DC, sine, square, triangle, ramp (up and down); a regulated DC offset is possible for the AC voltages. The frequency range of the generator is 1 mHz to 100 kHz, and the frequency sweep option is provided. One only needs to specify the initial and final frequencies and the sweep time. This option is very useful for determining frequency response of frequency-dependent circuits or devices. For instance, resonance curves of a pendulum or LCR circuits can be displayed without using additional function generators with VCF (voltage controlling frequency) inputs. The output voltages and currents can be recorded and processed as measurement data. The same relates to the frequency of the output voltage.

Two other built-in function generators (*Outputs 2* and *3*) provide the same waveforms in the frequency range of 1 mHz to 500 kHz. The amplitude range is ±10 V, 50 mA. The generators provide independent control of the waveform, frequency, and amplitude of the output voltages; the frequency sweep option is

also provided. The output voltages and frequencies can be stored and processed as measurement data.

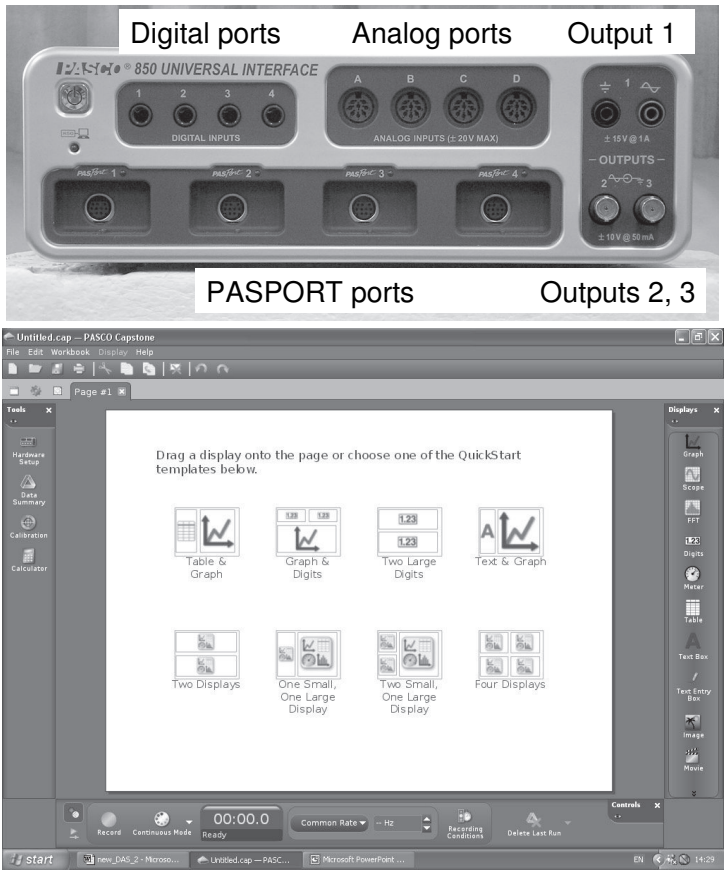

Fig. 9. Main features of the new data-acquisition system are seen immediately after opening *Capstone* software.

The *850 Universal Interface* has four differential analog ports; their input impedances are 1 MΩ. The measurement range is ±20 V, with ±250 V protection. One of four voltage scales, from 0.02 to 20 V, can be selected, and the maximum resolution is 0.01 mV. When only two channels are employed, the sampling rate can be set up to 10 MHz; with more channels used simultaneously, the maximum sampling rate is 1 MHz. Four digital ports acquire data from digital PASCO sensors, including the *Motion sensor* and *Rotary motion sensor*.

Main features of the new data-acquisition system are seen immediately after opening the *Capstone*. However, many details are important for properly designing an experiment: sensitivity of the sensors, type of recording, recording conditions, sample rate, appropriate displays, and so on. Three modes of recording data are available: *Continuous* (continuously recording data from all sensors connected to the interface), *Keep* (continuously recorded data are fixed only when commanded), and *Fast monitor* (the data are displayed continuously but only last of them can be fixed; this mode avoids restrictions posed by limited acquisition rate and memory).

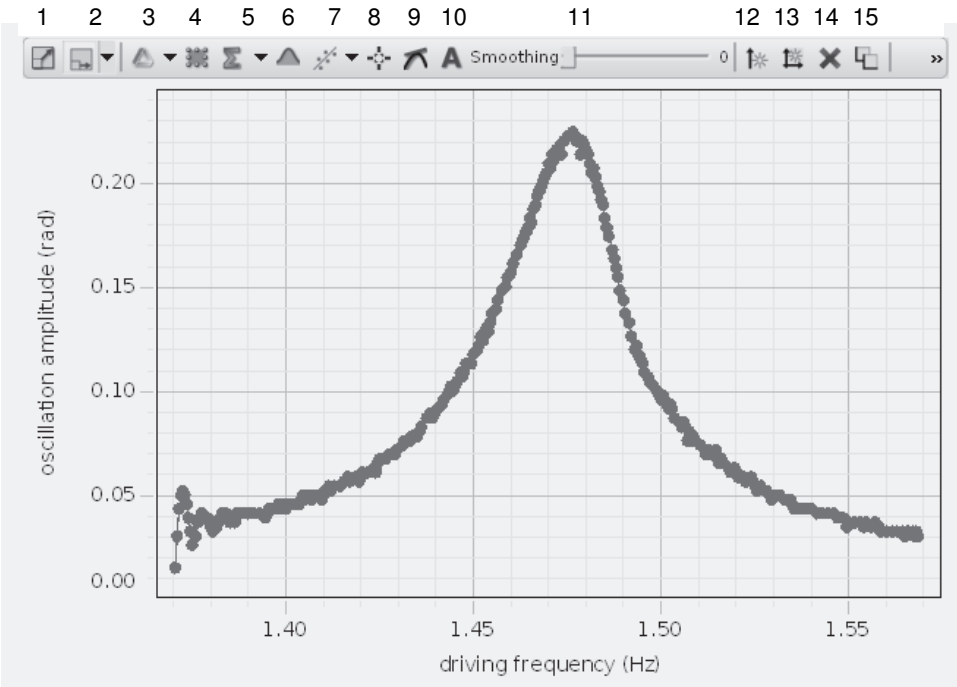

1–scale to fit, 2–automatic scaling, 3–run visibility, 4–selection for analysis, 5–statistics, 6–area, 7–curve fit, 8–coordinates tool, 9–slope tool, 10–annotation, 11–smoothing, 12–add Y axis, 13–add plot area, 14–remove, 15–rearrange

Fig. 10. The *Graph* display with the toolbar shown. Resonance curve of a pendulum is displayed as an example.

The *Calculator* tool provides numerous functions for processing measurement data, which fall into six categories: *Scientific*, *Statistics*, *Special*, *Filter*, *Logic*, and *Simple*. The experimental data or results of processing them can be displayed with a number of tools: *Graph*, *Scope*, *FFT*, *Digits*, *Meter*, *Table*, and others. Several displays can be arranged simultaneously. There are many options to make the graphs informative and easy to use: *Scale to fit*, *Run visibility*, *Selection for analysis*, *Curve fit*, *Coordinates*, *Slope*, *Smoothing*,

Annotation, and others (Fig. 10). The list of possible fit functions contains 20 items, from *Proportional fit* to *User-defined fit* (Fig. 11).

Details of the new system are given on the site http://www.pasco.com. The site includes videos demonstrating the system. It is worthless (and impossible) to reproduce all the information the site contains. Instead, many experiments that became now possible or easier to do are included in the book.

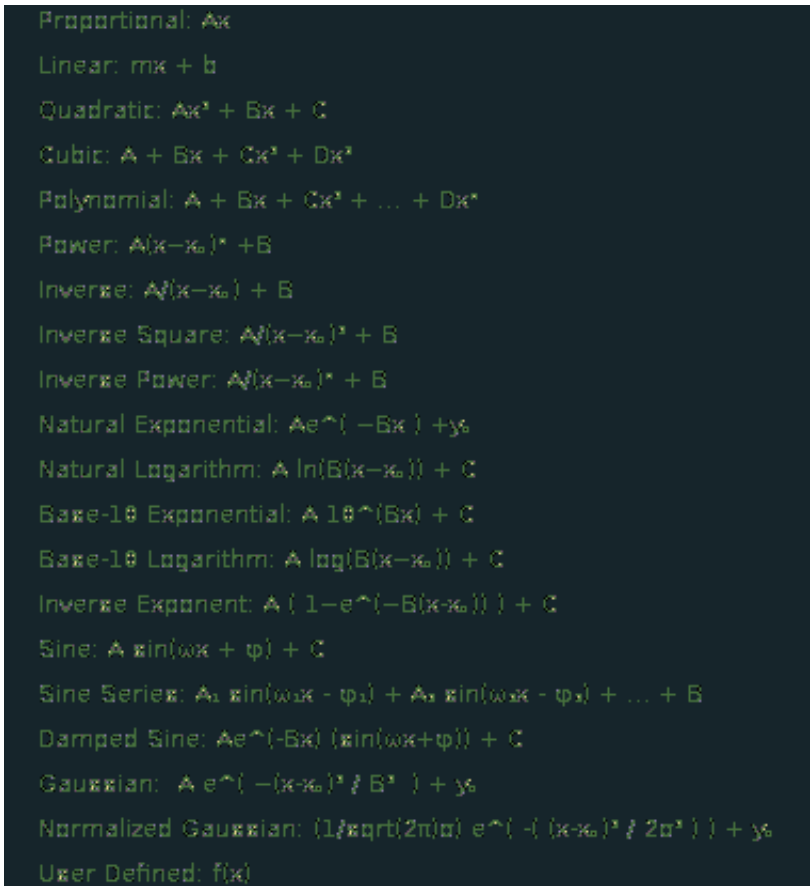

Fig. 11. List of fit functions provided by *Capstone*.

1.1. Mass on spring

Free oscillations of a mass on a spring are recorded. Varying the mass changes the period and decay of the oscillations.

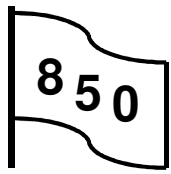

Additional equipment: *Force sensor*, spring, weights.

When a mass m is hung on a spring of a negligible mass, the spring stretches until the restoring force kx of the spring equals the weight of the mass:

$$kx = mg, \tag{1}$$

where k is the spring constant, x is the extension of the spring, and g is the free-fall acceleration.

If the mass is displaced from its equilibrium position, a restoring force tends to return it to the equilibrium. **Free oscillations** of the mass arising in this case follow the usual **motion equation**

$$mx'' = -kx, \qquad \text{or} \tag{2}$$

$$x'' + (k/m)x = 0. \tag{3}$$

The solution to this equation is

$$x = A_0\cos(\omega_0 t - \varphi), \tag{4}$$

where A_0 is the oscillation amplitude, $\omega_0 = (k/m)^{1/2}$, and φ is the initial phase. The quantity $\omega_0 = 2\pi f_0$ is called the natural angular frequency of the harmonic oscillations.

Equation (2) does not take into account **energy losses** in the system. In this case, the oscillations would occur with constant amplitude. If energy losses are caused by a friction force $\lambda x'$ proportional to the velocity of the mass, Eq. (2) should be modified to

$$mx'' = -kx - \lambda x', \qquad \text{or} \tag{5}$$

$$x'' + (\lambda/m)x' + (k/m)x = 0. \tag{6}$$

This equation describes oscillations of exponentially decaying amplitude:

$$A = A_0\exp(-\delta t), \tag{7}$$

where $\delta = \lambda/2m$. The frequency of the oscillations somewhat decreases: $\omega^2 = \omega_0^2 - \delta^2$. It was supposed that $\delta^2 << \omega^2$.

In the setup (Fig. 1), the spring is connected to the *Force sensor*. The accelerated/decelerated motion of the mass causes a force additional to the weight, so the sensor provides data on the oscillations of the mass. The aim of the experiment is to verify the expression for ω_0 using two different masses. The example presented shows the oscillations with a single and a doubled mass. The spring constant can be found under static conditions.

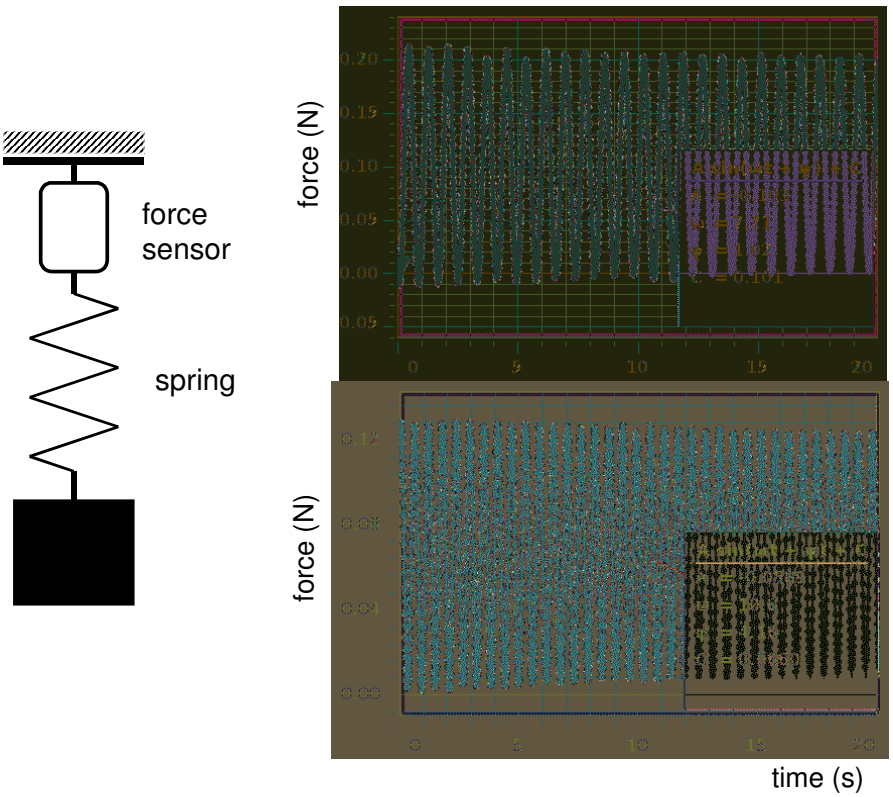

Fig. 1. Schematic of the setup and examples of free oscillations for two weights differing by factor of two.

The meter

The meter is the length of the path traveled by light in vacuum during a time interval of 1/299 792 458 of a second.

1.2. Torsional pendulum

The experiment is recommended by PASCO (see also Shanker *et al* 1985; Jiang *et al* 2007).

Additional equipment: *Voltage sensor*, wire, cylinder, permanent magnet, coil.

Sometimes, experiments with a torsional pendulum cause troubles due to an enhanced friction in the *Rotary motion sensor* when the sensor is heavily loaded. Therefore, we use another method of recording the oscillations (Fig. 1). The pendulum consists of a wire loaded by a brass cylinder, 30 mm in diameter and 50 mm in height. An opening in the cylinder is made perpendicular to its axis, and a cylindrical permanent magnet (SE-8605) is placed there. Due to the magnet, a 3200-turn coil (SF-8613) positioned under the cylinder senses the **torsional oscillations**. The *Voltage sensor* acquires the EMF induced in the coil.

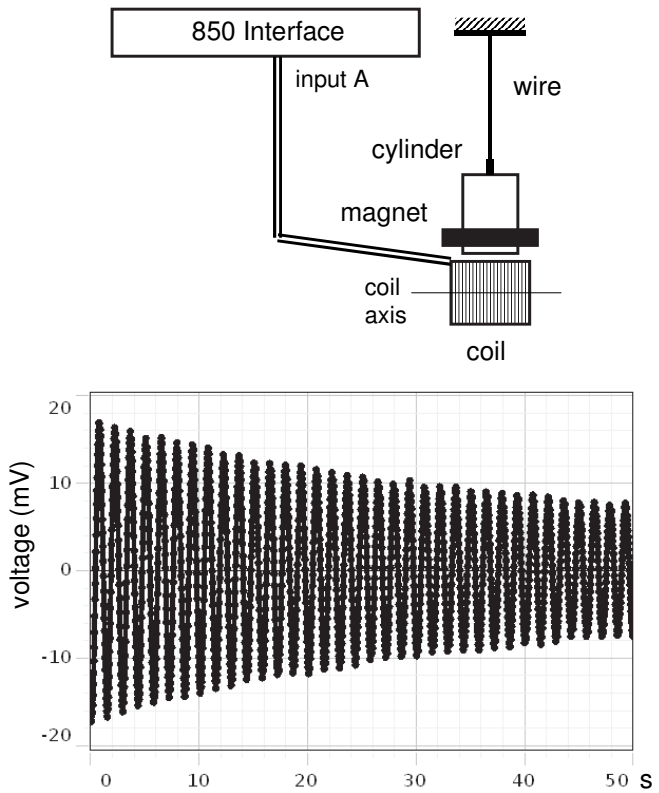

Fig. 1. Schematic of the setup and example of measurement data.

1.3. Hooke's law

The experiment is similar to that recommended by PASCO.

Additional equipment: *Force sensor*, *Motion sensor*, spring.

Hooke's law of elasticity states that strain is proportional to stress. In particular, the force $\boldsymbol{F}$ needed to extend or compress a spring by some distance $\boldsymbol{x}$ is proportional to that distance:

$$\boldsymbol{F} = -k\boldsymbol{x}, \tag{1}$$

where k is called the force constant (or spring constant). The negative sign shows that the restoring force is opposite to the displacement. The energy E of a stretched spring is

$$E = kx^2. \tag{2}$$

The simplest way to confirm Hooke's law is an experiment with a spring (Mwanje 1980a; Richards 1981; Easton 1987; Glaser 1991; Kernohan 1998; Froehle 1999; Erber 2001; De Souza Lima *et al* 2002; Struganova 2005; Euler 2008; Silva 2011).

The setup for the measurements is very simple (Fig. 1). One end of the spring is fixed, and the second is attached to the *Force sensor*, which is moved manually. The *Motion sensor* determines the extension of the spring by means of a reflector attached to the *Force sensor*. A graph of the applied force versus the extension appears during a run. For the spring used, $k = 14.5$ N.m^{-1}.

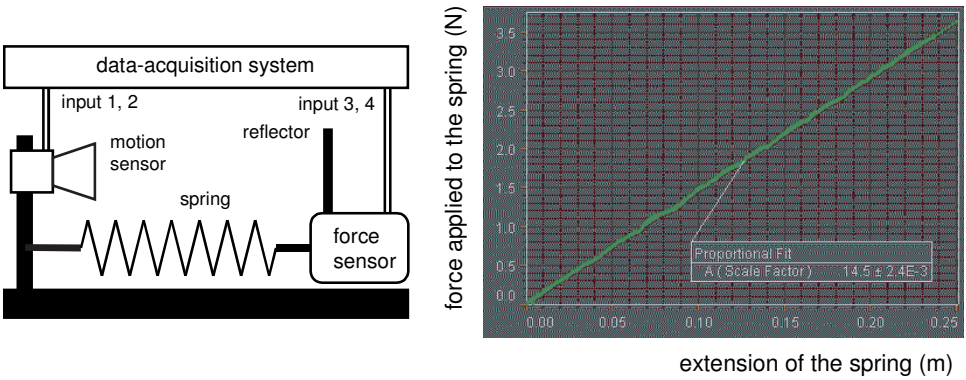

Fig. 1. Schematic of the setup and applied force versus extension of the spring.

1.4. Characteristics of DC source

V–I characteristics of a loaded DC source are displayed, and the EMF and internal resistance of the source are determined. The useful electric power and efficiency of the source are measured versus the output current.

AIP Emilio Segrè Visual Archives,
Brittle Books Collection
Alessandro Volta (1745–1827)

Additional equipment: two *Voltage sensors*, 1.5 V battery, resistors.

A variable 1 kΩ resistor and a 1 Ω resistor load a 1.5 V battery (Fig. 1). During the data acquisition, one manually changes the variable resistor R.

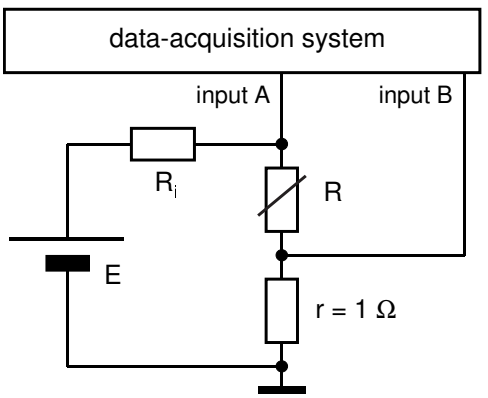

Fig. 1. Circuit for determining characteristics of a battery.

To protect the battery from shortening, a fixed resistor is added to it; it represents the **internal resistance** R_i. The voltage across the load V is displayed versus the voltage across the 1 Ω resistor, that is, versus the current. According to **Kirchhoff's loop rule**, this plot is a straight line:

$$V = E - IR_i. \quad (1)$$

The **efficiency** of the source η is a linear function of the current:

$$\eta = V/E = 1 - IR_i/E = 1 - I/I_m, \quad (2)$$

where I_m is the maximum current, E/R_i.
The full power delivered by the source dissipates on the load and internal resistance and thus equals IE. The useful electric power is

$$P = IV = I(E - IR_i) = IE - I^2R_i. \quad (3)$$

This dependence is a parabola, with two parameters, E and R_i. The maximum useful power corresponds to the condition $dP/dI = 0$, or $I = E/2R_i$. This means that the maximum useful power is achieved when the load resistance equals the internal resistance of the source; this power thus equals $E^2/4R_i$. With the *Calculate* tool, the useful power is displayed versus the current (Fig. 2).

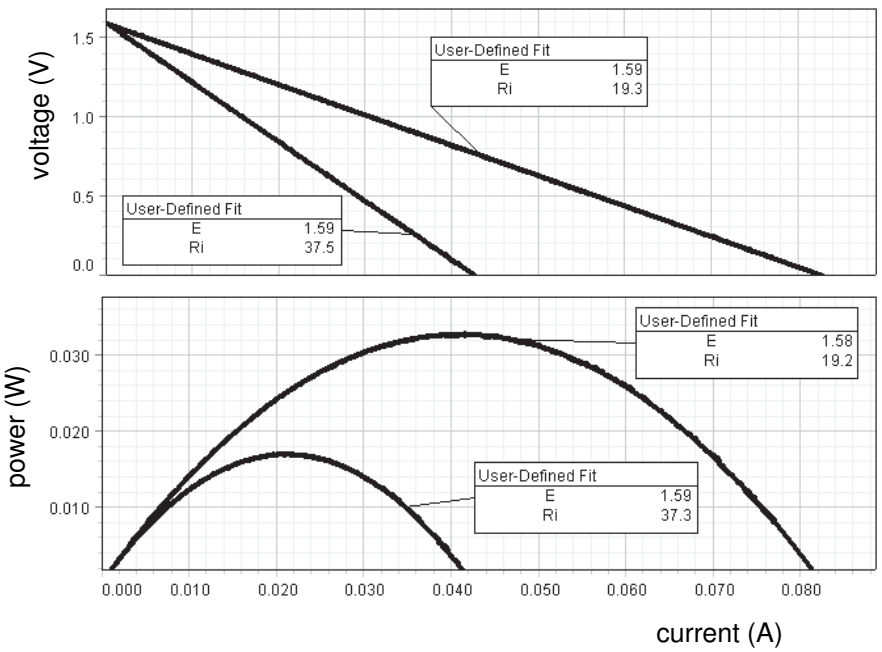

Fig. 2. *V–I* characteristics and useful power versus current, for two values of the added "internal" resistance. The minor differences between coefficients in the fits are due to the scatter of experimental points.

The **useful power** reaches a maximum when the efficiency is only 50% (Hmurcik and Micinilio 1986). Usually, the current provided by a DC source is smaller that $\frac{1}{2}I_m$. The useful power is thus less than the maximum power, but the efficiency is more than 50%.

1.5. Digital storage oscilloscope

The digital storage oscilloscope (DSO) combines features of a usual analog oscilloscope and a data-acquisition system of excellent time resolution (Kraftmakher 2012f).

Equipment: *Motion sensor*, digital storage oscilloscope, LCR circuit, photodiode, DC supply, capacitors, resistors, coil.

Nowadays, DSO becomes a device available for teaching purposes. Masters and Miers (1997) used a DSO, in conjunction with a computer, as a spectrum analyzer. The DSO served as a data-acquisition device. With a DSO, Potter (2003) demonstrated phase changes in reflected sound waves. Martínez Ricci *et al* (2007) designed a photon counting experiment; their setup included a DSO and a computer. Using a DSO, Wadhwa (2009) determined the coefficient of restitution of a ball–surface combination. De Buyl (2010) described a setup for displaying families of transistor characteristic curves. Pérez (2011) employed a DSO for measuring the speed of electromagnetic waves in a coaxial cable using the **cross-correlation function** of broadband noise (see Experiments 4.13 and 8.9).

The evident advantages of using DSOs are the following: (i) a **broad frequency band** and **high sample rate**, usually inaccessible for data-acquisition systems available in teaching laboratories; (ii) the possibility of directly observing the measurement data and obtaining hard copies of them; and (iii) the option to process the data with a computer. Many experiments are possible even with no computer involved. While computers are common devices in all teaching laboratories, software necessary for processing the data may be not readily available. We use a digital storage oscilloscope Tektronix TDS 3012B (100 MHz bandwidth and sample rates up to 1.25 GHz).

Free oscillations in LCR circuit. The input resistance of the channel is set to be 1 MΩ (the alternative is 50 Ω). For calibration purposes, the oscilloscope provides rectangular pulses of 1 kHz frequency, 5 V peak-to-peak. This voltage is used for triggering **free oscillations** in an LCR circuit (Fig. 1). The circuit is connected to the output of calibration pulses through a capacitor $C_1 = 43$ pF. This capacitor and the parallel LCR circuit form a **differentiating circuit**, so short triggering pulses are obtained. The inductance of the circuit is L = 3 mH. The DSO displays the voltage across the capacitor C = 220 pF. To estimate the total capacitance of the circuit, the capacitance of a connecting cable (in our case, it is nearly 100 pF) and of the oscilloscope's input should be added. The decay of free oscillations depends on the resistance of a variable resistor included into the LCR circuit (not shown in Fig. 1). The **persistent time** of the DSO is set to be infinity, so the pattern on the screen is seen until it is removed.

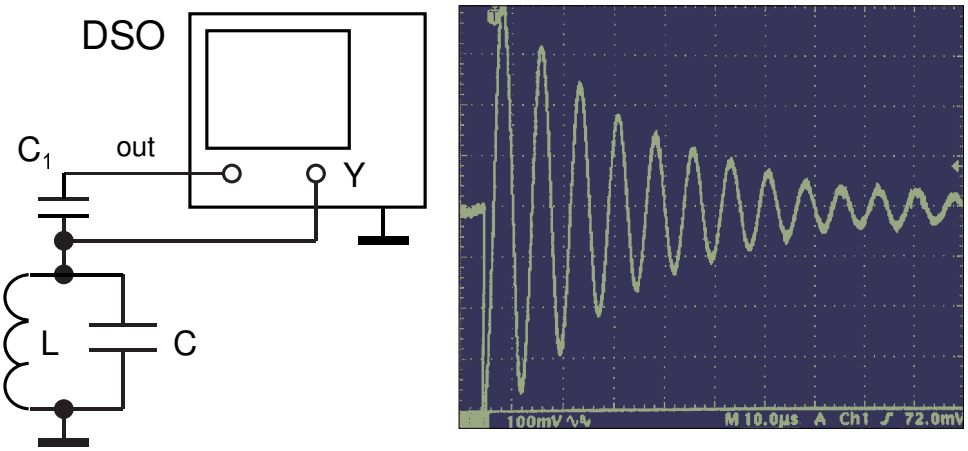

Fig. 1. Diagram of the setup and free oscillations on the DSO screen.

Displaying I–V characteristics of simple electronic devices, like a photodiod**e** or a transistor, is a usual function of common oscilloscopes. For simultaneously observing families of characteristics depending on an extra variable parameter, additional electronic circuits are employed (Barnes 1974a; Ramachandran 1993). A DSO connected to a computer equipped with suitable software may also serve for this purpose (de Buyl 2010). In many cases, however, families of *I–V* characteristics of electronic devices can be displayed during one run without involving a computer and/or additional software. The persistent time of the screen is set to be infinity, so the family of characteristics is seen until the picture is removed. Many DSO provide an option to observe the results with an extra monitor; this is useful for classroom demonstrations. Hard copies of the results are available with a common printer.

A photodiode with a 100 Ω load resistor is connected to a regulated DC supply. The voltage applied to the photodiode is fed to the X input of the DSO, while the voltage across the load of the photodiode to the Y input (Fig. 2). The AC line voltage triggers the runs. The photodiode is irradiated by a low power light bulb. The key point in this approach is that the changes of the irradiation are made while the voltage applied to the photodiode is zero. During one run, the DSO displays a family of *I–V* characteristics of the photodiode. The real *V* and *I* values are known from the sensitivities of the DSO channels, which are shown on the screen. We use a silicon photodiode of large sensitive area (United Detector Technology PIN-10D). The maximum applied voltage is nearly 18 V, and the maximum current is 2.5 mA. With a photodiode of smaller sensitive area, the current will be smaller.

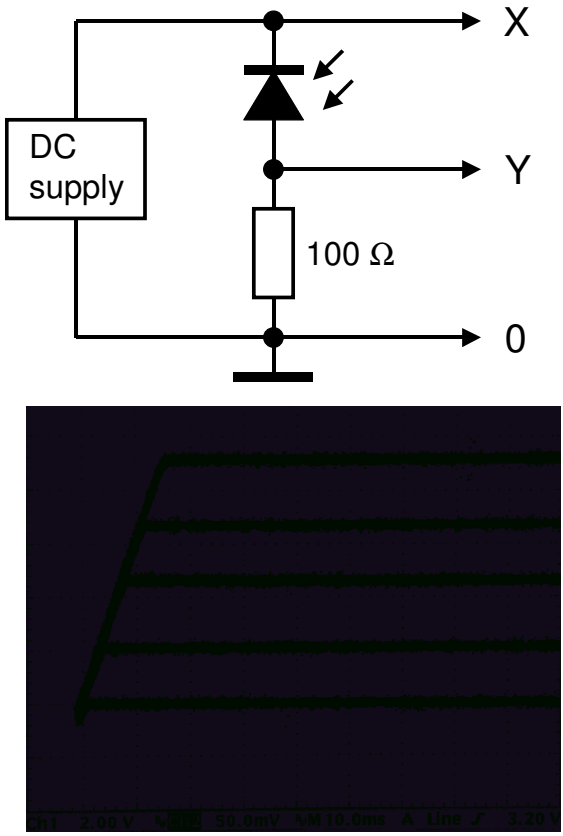

Fig. 2. Diagram of the setup and family of I–V characteristics of the photodiode.

1.6. Charging and discharging a capacitor

Charging/discharging process is displayed by a data-acquisition system. Similar experiments are described by Heinrich (1986); Wilson (1989); Fundaun *et al* (1992); Mita and Boufaida (1999); Hart (2000).

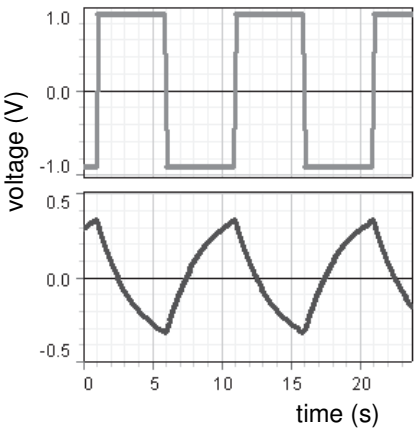

Slow charging/discharging process displayed by *DataStudio*.

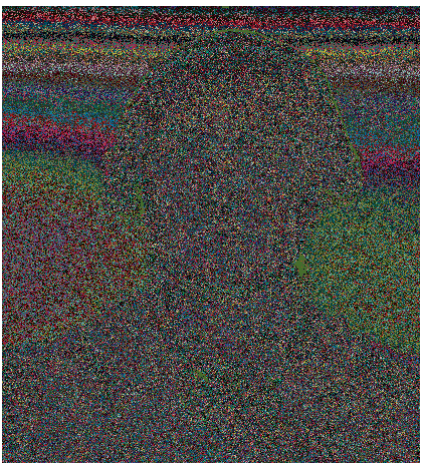

AIP Emilio Segrè Visual Archives,
Brittle Books Collection
Charles Augustin Coulomb (1736–1806)

Additional equipment: two *Voltage sensors*, resistor, capacitor.

A series RC circuit is connected to the *Signal generator* (Fig. 1), and the *Square wave* voltage is used for charging and discharging a capacitor.

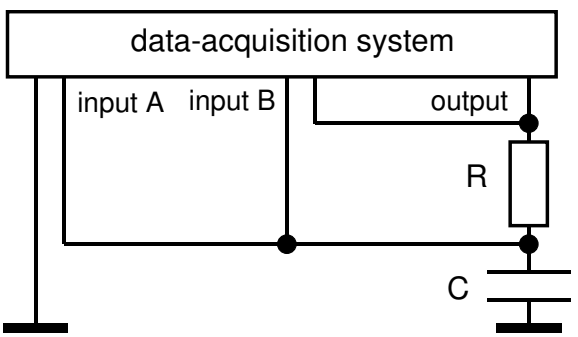

Fig. 1. Schematic of the setup.

The charging/discharging current is measured with the *Voltage sensor* as the voltage drop across the resistor R. Another *Voltage sensor* measures the voltage across the capacitor. The *Graph* tool displays the *Output voltage*, the voltage across the capacitor U_C, and the charging and discharging current I. For a demonstration, it is preferable to use an RC circuit of long time constant and observe the process on the screen of a computer. For instance, a circuit with $R = 1$ MΩ and $C = 4.7$ μF provides the time constant convenient for monitoring the process. To show how the circuit responds to input voltages of various frequencies, the frequency is set to be 10, 100, and 1000 Hz. In this case, $R = 1$ kΩ, $C = 0.47$ μF. The same equation governs all the processes, but the periodicity of the charging/discharging process is set by the frequency of applied voltage. With *Options/Automatic stop/Time* option, the measurement time is restricted by two periods of the voltage (Fig. 2).

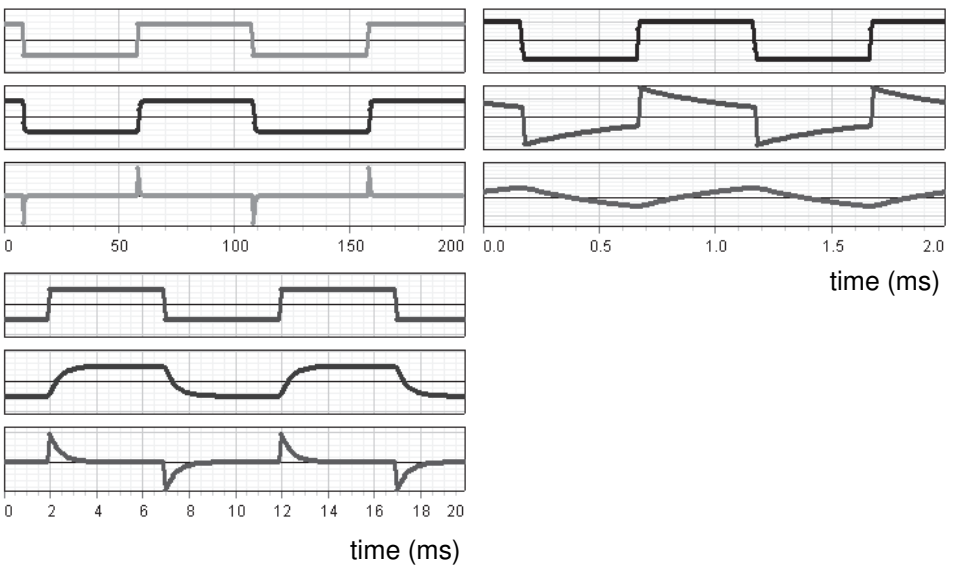

Fig. 2. Output voltage, voltage across the capacitor, and charging/discharging current for frequencies 10, 100, and 1000 Hz. $R = 1$ kΩ, $C = 0.47$ μF.

1.7. Charge and energy stored in a capacitor

The charge and energy stored in a capacitor are measured and displayed during the charging/discharging process (Kraftmakher 2012a). The experiment is similar to that described by Carvalho and Sampaio e Sousa (2008) and is usable as a laboratory work or a classroom demonstration.

Additional equipment: two *Voltage sensors*, capacitor, resistor, switch.

The charge Q and energy E stored in a capacitor depend on the voltage V applied to it: $Q = CV$, $E = \frac{1}{2}CV^2$. The energy stored can be determined with a calorimeter equipped with a heater and a thermometer (Weiss 1969; Edgar 1993). The capacitor is discharged through the heater, and the energy stored is determined from the temperature rise of the calorimeter. A calibration is therefore needed for establishing a relation between the two quantities (see Experiment 3.5).

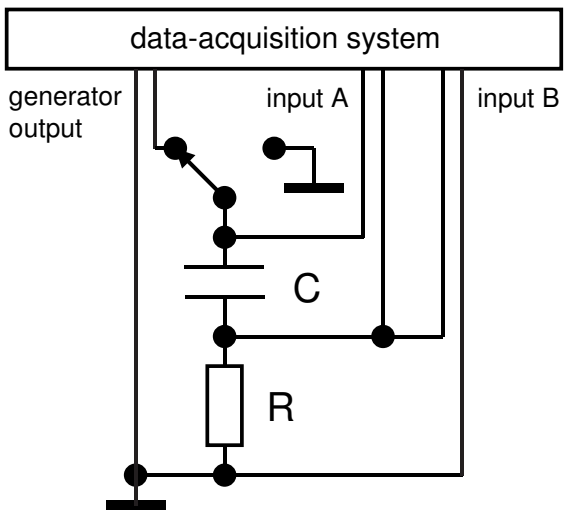

Fig. 1. Diagram of setup for observing the charging/discharging process.

In our experiment, a capacitor C, nominally 100 μF, is put in series with a resistor R = 1 kΩ (1%). With a manually operated switch, this RC circuit can be connected to a source of DC voltage and then shortened (Fig. 1). Each measurement thus includes both charging and discharging processes. The source of the DC voltage V_0 is the *Signal generator*. Two *Voltage sensors* acquire the voltage V across the capacitor and that across the resistor R. The voltage across the resistor is proportional to the charging/discharging current. With the *Automatic stop* option, each run lasts 3 s. The *Sample rate* is 1 kHz.

After starting a run, the capacitor, previously shortened, is switched to the *Signal generator* and then shortened again. During each run, the voltages across the resistor and the capacitor are displayed on the screen of a computer. The *DataStudio* software calculates and displays the charge Q and energy E stored in the capacitor. These quantities are calculated with the *Calculate/Special/integral* tool. The charge is an integral of the charging current: $Q = \int i\mathrm{d}t$. From the maximum charge Q_m, the capacitance becomes available: $C = Q_\mathrm{m}/V_0$. The energy E stored is calculated as an integral of the product of the current and the voltage across the capacitor: $E = \int Vi\mathrm{d}t$. The maximum stored energy is $E = ½CV_0^2$, so $C = 2E/V_0^2$.

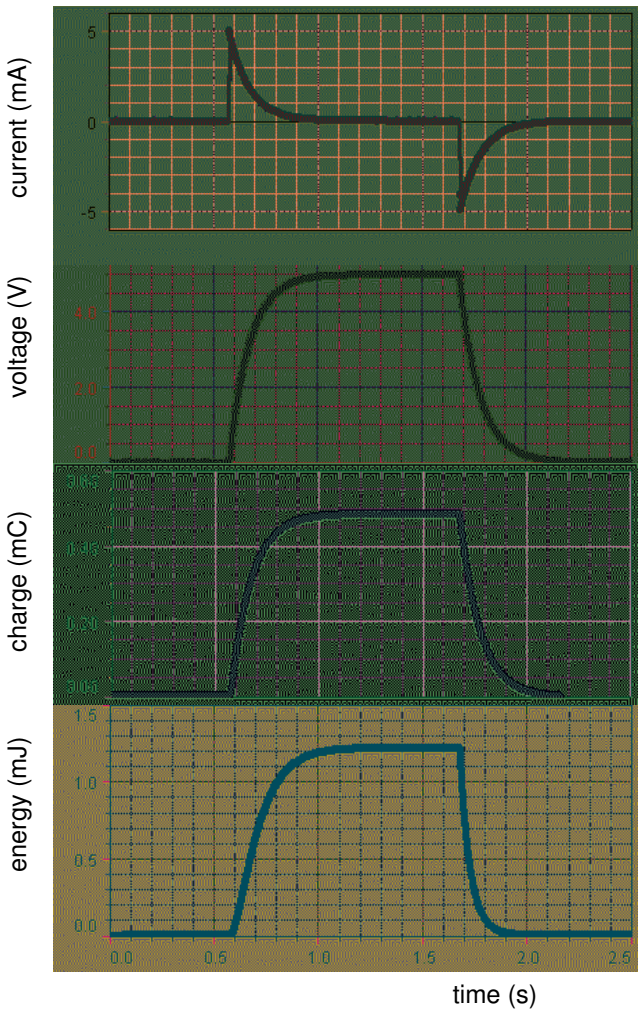

Fig. 2. Example of measurement data and calculations: charging/discharging current, voltage across the capacitor, charge, and energy stored in the capacitor.

An example of the measurement data and calculations is given here for $V_0 = 5$ V (Fig. 2). The *Smart tool* of *DataStudio* serves for determining the numerical values of V_0, Q, and E. Similar measurements are done with other values of V_0. The maximum values of Q and E are displayed versus the applied voltage V_0 (Fig. 3). The fits to the data confirm that the charge stored by the capacitor is proportional to the applied voltage, while the stored energy is proportional to the voltage squared. The fit parameters shown in the plots are close to the capacitance measured with a multimeter, 97.2 μF. The basic relations for the charge and energy stored in a capacitor thus are confirmed.

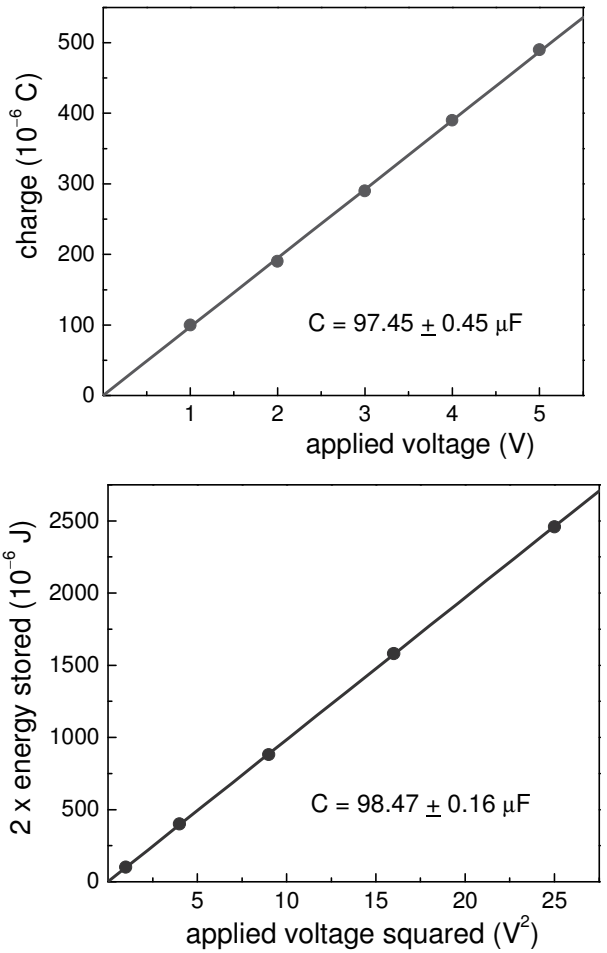

Fig. 3. The charge stored in the capacitor versus applied voltage and the energy stored versus applied voltage squared.

When a DC source charges a capacitor through a resistor, half of the energy supplied by the source is dissipated in the resistor, and half is stored in the capacitor (Newburgh 2005). This calculation can be confirmed by the present measurement data. For this aim, one has to calculate and display the quantity $E = \int i^2 R \mathrm{d}t$. The energy stored in the capacitor is nearly 1.2 mJ. The same energy is dissipated in the 1 kΩ resistor during charging and discharging the capacitor (Fig. 4).

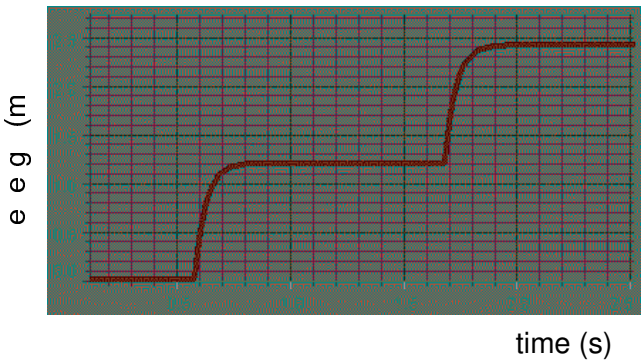

Fig. 4. Energy dissipated in the resistor during charging and discharging the capacitor.

If an external DC source is used for charging the capacitor, it should be remembered that input voltages exceeding ±10 V are dangerous for the *750 Interface*. For the *850 Universal Interface*, the measurement range is ±20 V, with ±250 V protection.

The kilogram

The kilogram is the unit of mass; it is equal to the mass of the international prototype of the kilogram.

1.8. Speed of sound in air

The speed of sound in air is evaluated by simultaneously measuring the time needed for ultrasonic pulses produced by the *Motion sensor* to return from a reflector and the displacement of the reflector determined by the *Rotary motion sensor* with the *Linear translator*.

Additional equipment: *Rotary motion sensor* with *Linear translator*, *Motion sensor*.

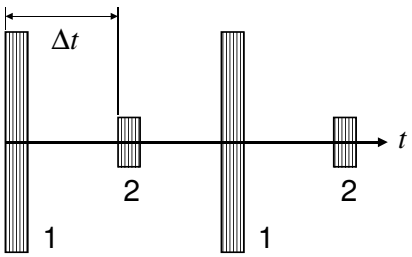

Fig. 1. Ultrasonic pulses (1) from the sensor and (2) reflected pulses; Δt is the time needed for the pulses to reach the reflector and return back.

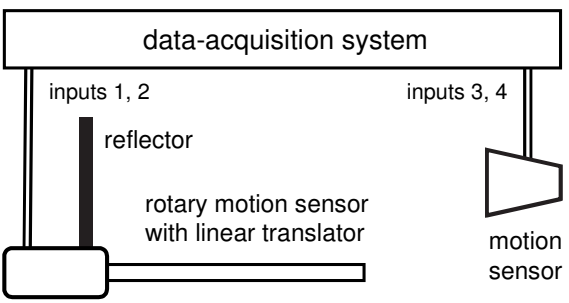

Fig. 2. Arrangement for determining the speed of sound in air using pulse method.

Determinations of the speed of sound in air are well known (Albergotti 1981; Karshner 1989; Martin 2001; Winters 1993; Carvalho *et al* 2008). Ouseph and Link (1984) and Velasco *et al* (2004) measured the speed of sound at various temperatures. In our experiment, the *Motion sensor* measures the time intervals needed for the pulses to reach the reflector and return back to the sensor (Fig. 1). The *Motion sensor* thus reproduces a technique invented by bats many years ago (Gatland *et al* 1992; MacIsaac and Hämäläinen 2002). Simultaneously, the *Rotary motion sensor* with the *Linear translator* measures the displacement of the reflector (Fig. 2). After starting the measurements, one moves the reflector toward the *Motion sensor*. Using the *Options* tool, the data acquisition starts after

a definite displacement of the reflector. The speed of sound is available from the graph of the displacement versus time: it equals two times the slope of the graph (Fig. 3).

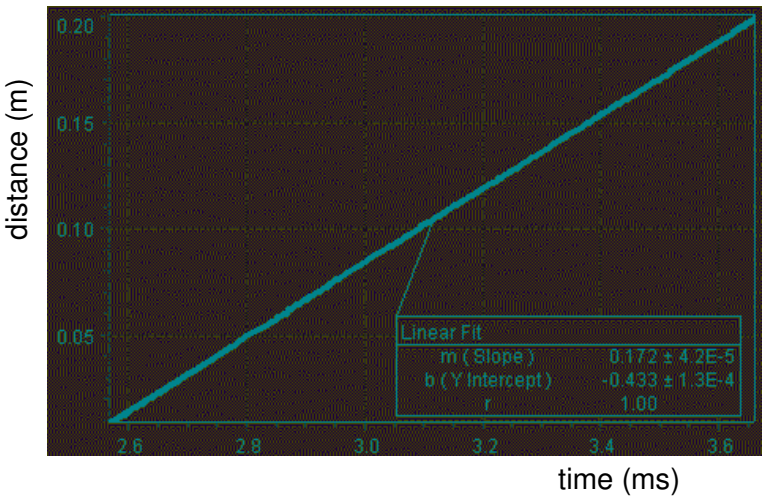

Fig. 3. From the data, the speed of sound is $344\ \mathrm{m.s^{-1}}$.

The second

The second is the duration of 9 192 631 770 periods of the radiation corresponding to the transition between the two hyperfine levels of the ground state of the cesium 133 atom.

1.9. Lissajous patterns

Lissajous patterns for different ratios of the frequencies are displayed.

Additional equipment: *Voltage sensor*, low frequency oscillator.

The *Signal generator* is one of two oscillators, and its signal is stored as the *Output voltage*. The *Voltage sensor* measures the second signal taken from an additional oscillator. The frequencies of the signals are of the order of 1 Hz. The time of the measurements set by the *Options/Automatic stop* is equal to the period of the signal of the lower frequency. The *Graph* tool displays the Lissajous patterns (Fig. 1). The patterns depend also on the phase shift between the signals (Fig. 2). A general rule for determining the frequency ratio of two signals is the following. A vertical and a horizontal line are posed on the graph, but not through its intersection points. The frequency ratio f_y:f_x equals the ratio n_x:n_y of the intersections of the straight lines with the Lissajous pattern.

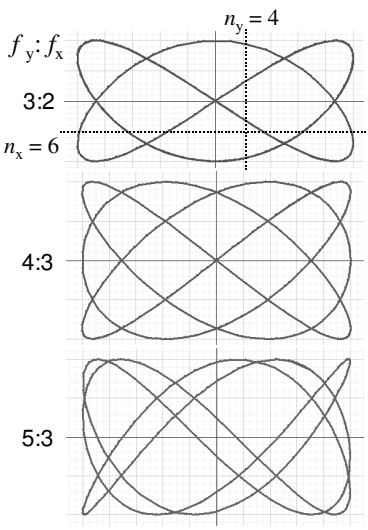

Fig. 1. Lissajous patterns for different frequency ratios.

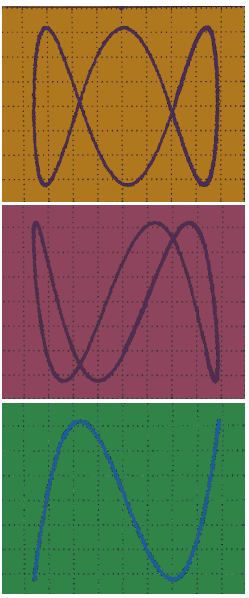

Fig. 2. Lissajous patterns for f_y:f_x = 3:1 for different phase shifts between the signals.

The *850 Universal Interface* includes three independently tuned function generators. It is possible to set the frequency of one generator close to the frequency of the second one or to its harmonics and observe the gradual change of the Lissajous pattern due to slow changes in the phase shift between the signals.

Determination of phase shifts. The phase shift between sine waves of the same frequency is available from the shape of the Lissajous pattern (Fig. 3):

$$\sin\varphi = \pm a/A = \pm b/B. \quad (1)$$

This relation is quite evident. For instance, $X = A\sin\omega t$, and $Y = B\sin(\omega t+\varphi)$. For $\omega t = 0$ or πn (n is an integer), $X = 0$, while $Y = b = \pm B\sin\varphi$. When $\omega t+\varphi = 0$ or πn, $Y = 0$, while $X = a = \pm A\sin\varphi$. The determination thus does not depend on the gain of the X and Y channels. The method is most sensitive for small phase shifts. The sensitivity decreases when the phase shift approaches 90°. The sign of the phase shift can be found by introducing a small additional phase shift of known sign or by using a usual time scale.

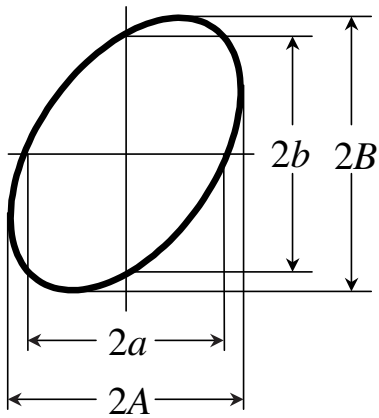

Fig. 3. Determination of phase shift between two sine waveforms from the Lissajous pattern.

Modern data-acquisition systems provide excellent tools for accurately determining frequencies of electrical signals or phase shifts between two signals of the same frequency by using the option *Sine fit*. However, the students should have an understanding of the Lissajous patterns. For demonstrations, the patterns of any frequency ratio and phase shift can be generated with software like *Origin*.

1.10. *I–V* characteristics

Families of *I–V* characteristics of a diode, a photodiode, and a light dependent resistor are displayed.

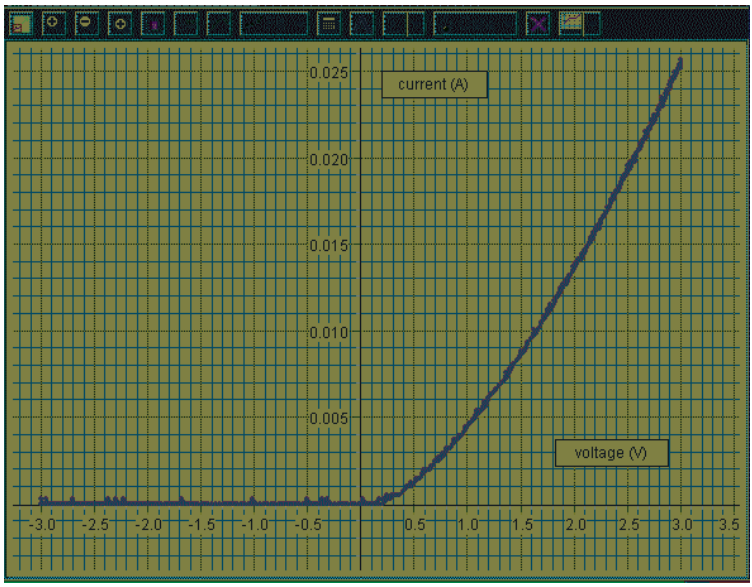

I–V characteristic of a semiconductor diode displayed by *DataStudio*.

Additional equipment: *Voltage sensor*, semiconductor diode, photodiode, light dependent resistor.

In this experiment, a semiconductor diode is connected to the output of *Signal generator* (Fig. 1). The current is measured through the voltage across a load resistor R.

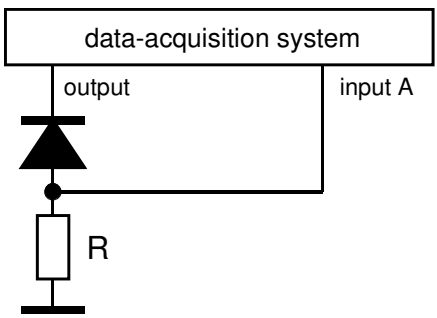

Fig. 1. Schematic of the setup.

I–V characteristics of a photodiode depend on the irradiation (Fig. 2).

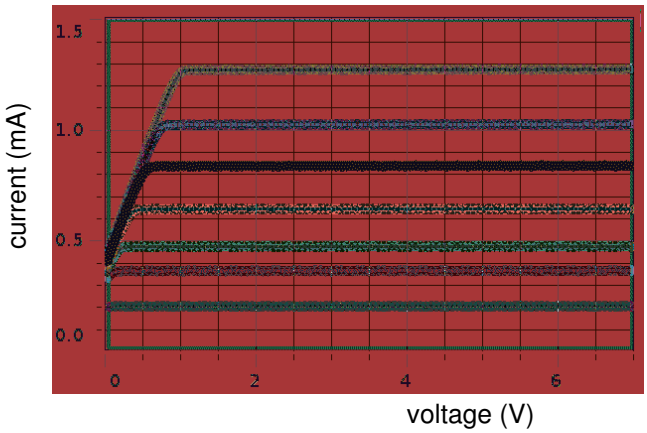

Fig. 2. *I–V* characteristics of a photodiode.

A light dependent resistor (LDR) is a semiconductor very sensitive to irradiation (see Experiment 7.6). The absorption of photons highly enhances the number of carriers, so that the resistance becomes much lower than in the dark. The resistance of the LDR does not depend on the applied voltage, so the *I–V* characteristics are linear (Fig. 3).

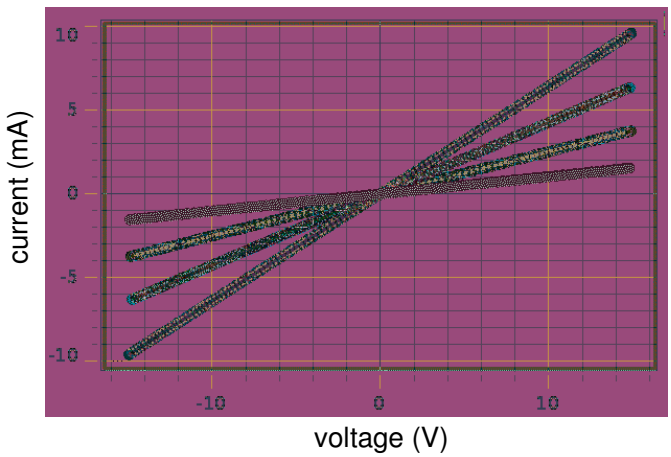

Fig. 3. *I–V* characteristics of an LDR.

1.11. Light bulb

DataStudio displays *V–I* characteristics of an incandescent light bulb at various frequencies of the heating current. The experiment is similar to that described by Clauss *et al* (2001).

Additional equipment: light bulb, digital storage oscilloscope.

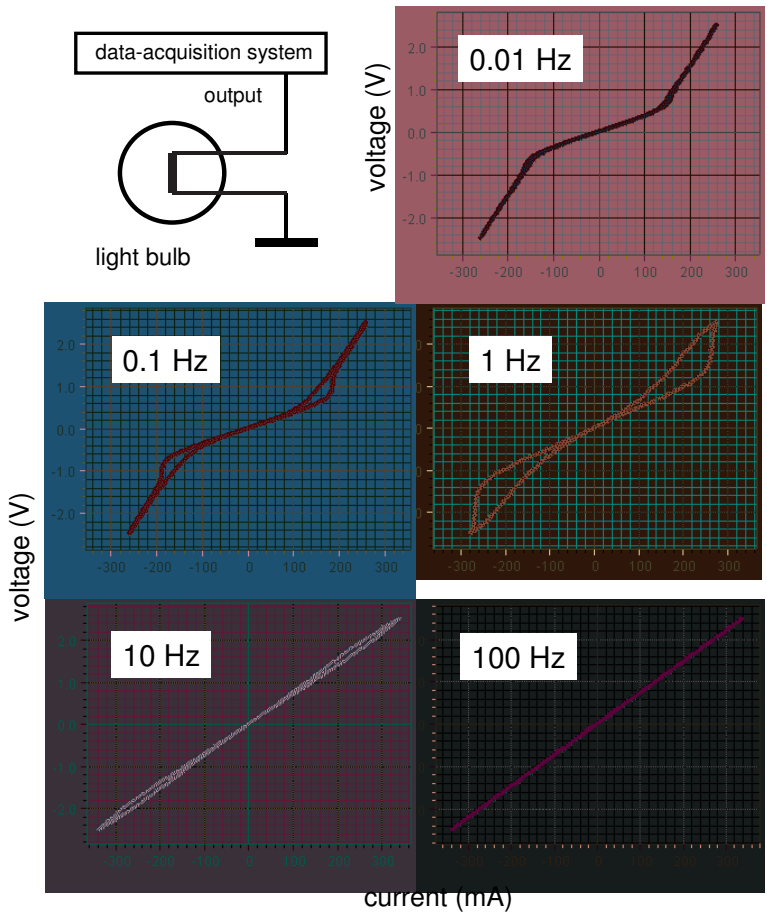

Fig. 1. Schematic of the setup and *V–I* characteristics of the light bulb for various frequencies of the heating current.

V–I characteristics and thermal inertia. An incandescent light bulb contains an electrically heated tungsten filament. The temperature of filament is in the range of 2400 to 3300 K, while the melting point of tungsten is 3695 K. The efficiency of conversion of electric power into visible light increases with increasing the

filament temperature. Above 2800 K, the evaporation of tungsten shortens the lifetime of the filament. To withstand the evaporation and achieve higher temperatures, light bulbs are filled with an inert gas, argon or krypton. Another approach is the **halogen light bulb** filled with a halogen compound, which reacts with evaporated tungsten atoms and returns them to the filament. As a rule, low power bulbs are vacuum ones, while high power bulbs are gas-filled. The highest temperatures are achieved in halogen projection light bulbs, and the price for this gain is a shortened lifetime. The temperature dependence of the resistivity of tungsten has been studied carefully, so the temperature of any tungsten filament is available from its resistance (see Experiment 3.2).

The heat capacity of the filament causes its **thermal inertia**. The heat balance equation governs this phenomenon. *V–I* characteristics of a light bulb are measured with an AC current of various frequencies, from 0.01 to 100 Hz. A *Triangle wave* voltage from the *Signal generator* feeds a low voltage, low power light bulb (Fig. 1). The *Graph* tool displays the *Output voltage* versus the *Output current*. The graphs obtained with various frequencies of the heating current manifest significant **hysteresis** depending on the frequency. At 0.01 Hz, the characteristic is close to the equilibrium one. The **relaxation time** decreases with increasing temperature of the filament due to the increase of the radiation heat exchange. At 100 Hz, the temperature oscillations become sufficiently small, so the resistance of the filament remains nearly constant.

Experiment with DSO. The *V–I* characteristics of a light bulb can be seen on the screen of a digital storage oscilloscope (Fig. 2). The current is determined through a voltage drop across a resistor put in series with the light bulb.

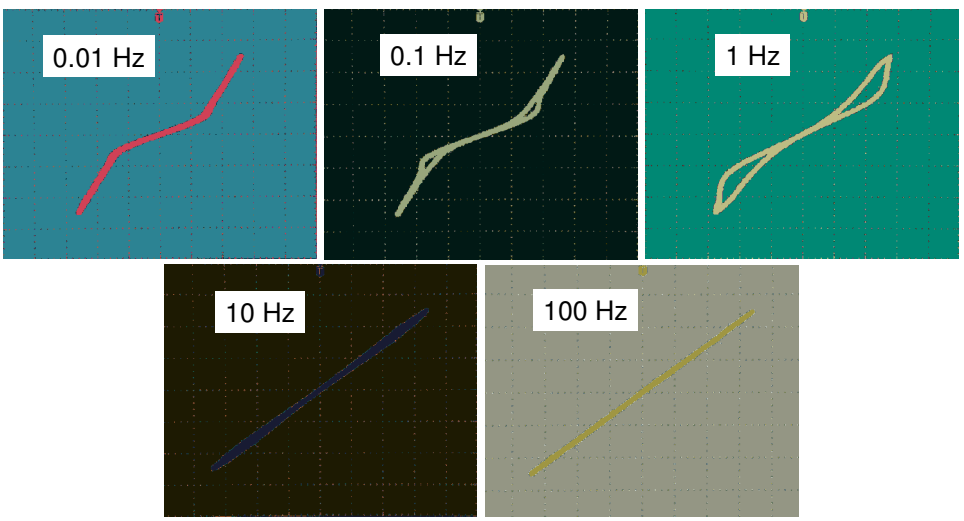

Fig. 2. *V–I* characteristics of the light bulb on the screen of DSO.

1.12. Short time intervals

Determinations of short time intervals are illustrated.

Additional equipment: *Light sensor, Voltage sensor*, light bulb, light-emitting diode (LED), light dependent resistor (LDR).

Inertia of a light bulb. Determination of short time intervals is a routine task of a common oscilloscope, and the same is true for a data-acquisition system. Two examples of such measurements are given here. The first one is the heating/cooling process of the filament of a light bulb after switching it on and off. The *Positive square wave* voltage of suitable frequency is applied to the light bulb. The *Light sensor* measures the radiation. The heating/cooling time depends on the temperature and thickness of the filament. For comparison, a light-emitting diode (LED) having a short **time constant** is used instead of the light bulb (Fig. 1).

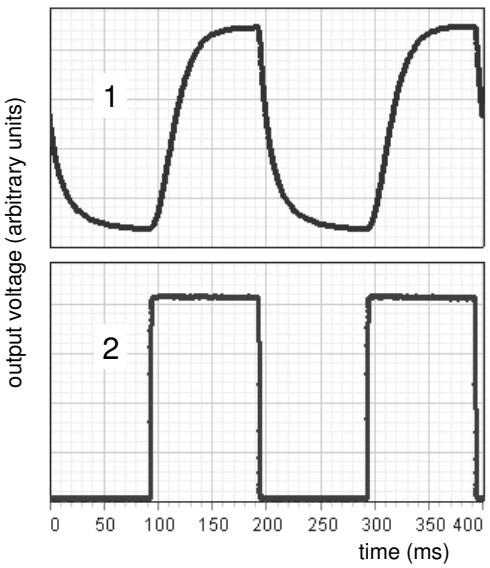

Fig. 1. Signals from *Light sensor* viewing a light bulb (1) and a LED (2).

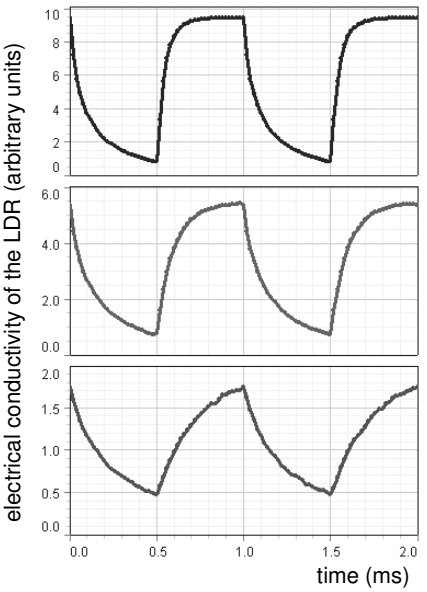

Fig. 2. Conductivity of the LDR irradiated by 1 Hz light pulses, for three light intensities.

The second example is the ***inertia of an LDR***. The *Positive square wave* voltage is fed to a LED. The rectangular light pulses irradiate the LDR loaded by a low-resistance resistor. The voltage across the load is proportional to the conductivity of the LDR (Fig. 2).

1.13. Temperature measurements

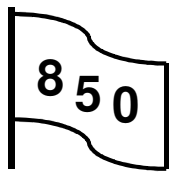

A platinum resistance thermometer is used for calibrating a thermistor and a thermocouple.

Additional equipment: *High-accuracy temperature sensor*, electrical oven, thermistor, differential thermocouple, resistor.

Brief review of temperature measurement (Kittel and Kroemer 1980; Childs *et al* 2000). The unit of **thermodynamic temperature** (absolute temperature) is **kelvin** (K) defined through the absolute temperature of the **triple point** of pure water, 273.16 K. The absolute scale was established with intention to make the value of 1 K equal to 1 C. The Celsius temperature (^{o}C) equals to the thermodynamic temperature minus 273.15. The International Temperature Scale, ITS-90, defines a scale of temperature in five overlapping ranges. These are

- 0.65 to 5 K through equilibrium **vapor pressure** of helium;
- 3 to 24.55 K using a constant volume **gas thermometer**;
- 13.80 K (triple point of hydrogen) to 273.16 K using **platinum resistance thermometers** calibrated at triple points of various materials;
- 273.15 (**freezing point** of water at normal pressure) to 1234.93 K (freezing point of silver at normal pressure) through platinum resistance thermometers calibrated at fixed freezing and melting points;
- above 1234.94 K with **Planck's law of radiation**.

The thermometers for establishing the thermodynamic temperature scale are based on fundamental physical laws related to **ideal gases** (gas pressure and velocity of sound) and **blackbody radiation** (Planck's law).

The practical temperature measurement techniques can be classified into three categories depending on the nature of contact between the measuring device and the medium of interest: (i) invasive (direct contact with the medium); (ii) semi-invasive (the medium is treated in some manner to enable remote observation, for instance, surface coating, whose color changes with temperature); and (iii) noninvasive methods, where the medium is observed remotely (Childs *et al* 2000). Among invasive techniques, the most important are gas thermometers, liquid-in-glass thermometers, thermal expansion of solids, thermoelectric devices, electrical resistance devices, junction semiconductor devices, fiber optics probes, capacitance thermometers, quartz thermometers, and **noise thermometers**. Semi-invasive techniques employ thermochromic liquid crystals, thermographic phosphors, and heat sensitive paints. The noninvasive methods include **optical pyrometers**, absorption and emission spectroscopy, Raman scattering, and laser-induced fluorescence.

In our measurements, the *High-accuracy temperature sensor* CI-6525 (a platinum resistance thermometer), a thermistor, and a junction of a copper–constantan thermocouple are put inside an electrical oven heated by a power supply. A DC current passing through the thermistor is taken from the *Output 1* of the *850 Interface*. The *Output voltage* is 10 V, and resistor R is chosen to be at least 100 times larger than the resistance of the thermistor, so the current in the circuit can be considered to be independent of the temperature. The resistance of the thermistor is determined from the voltage drop across it. The second junction of the thermocouple is put in an ice bath. The EMF produced by the thermocouple is measured using the 0.02 V range of the *Voltage sensor*.

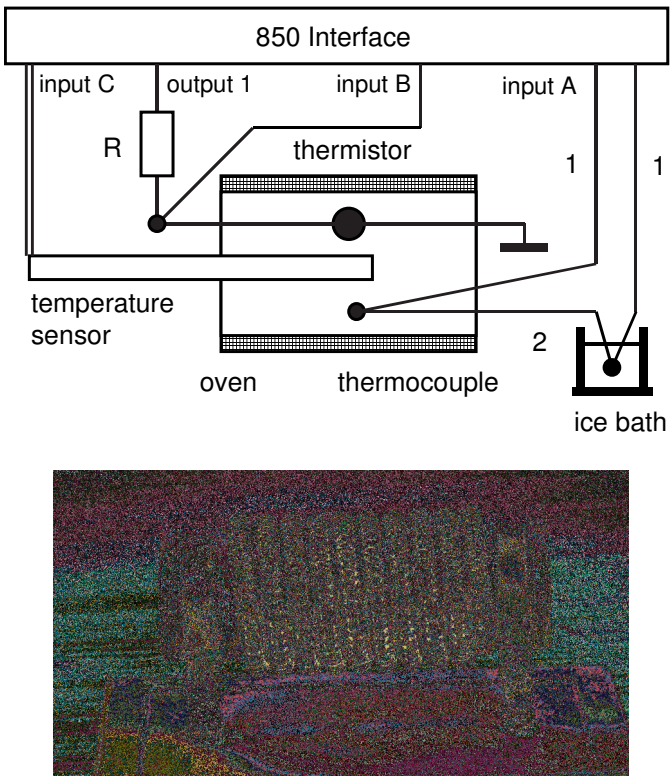

Fig. 1. Schematic of the setup and the oven. 1–copper wire, 2–constantan wire.

The oven is heated up to about 90°C, and the measurements are performed during the cooling process, which lasts nearly 30 min. *Capstone* displays the cooling curve, the EMF produced by the thermocouple, and the resistance of the thermistor versus the temperature (Fig. 2).

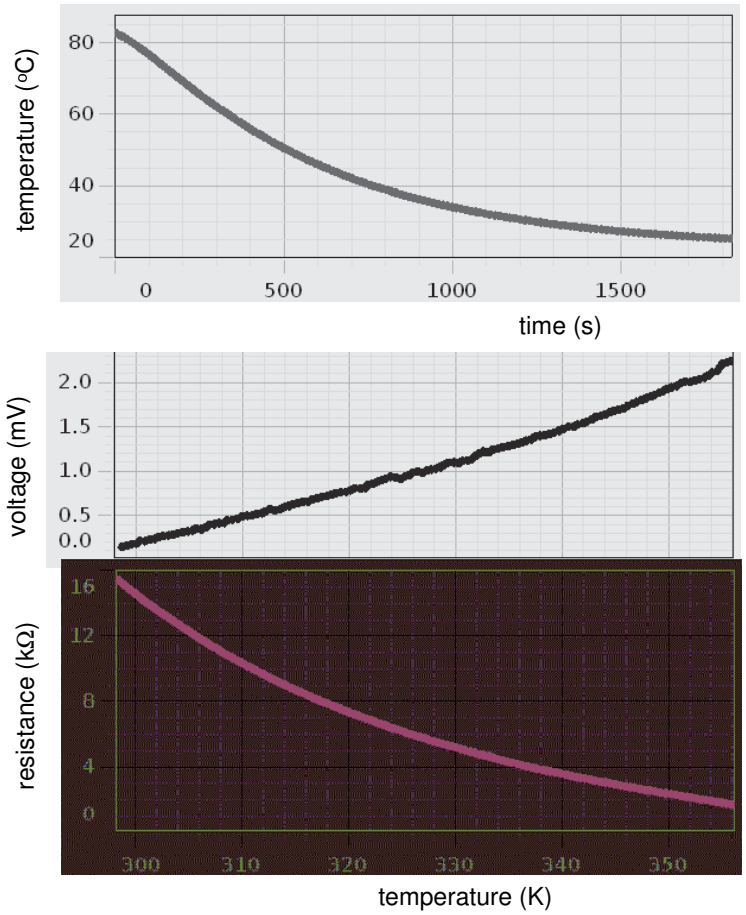

Fig. 2. The cooling curve, the EMF generated by the copper–constantan thermocouple, and resistance of the thermistor versus temperature.

The kelvin

The kelvin, unit of the thermodynamic temperature, is the fraction 1/273.16 of the thermodynamic temperature of the triple point of water.

1.14. Oersted's great discovery

The demonstration reproduces Oersted's famous experiment that revealed the connection between electricity and magnetism.

AIP Emilio Segrè Visual Archives,
Brittle Books Collection
Hans Christian Oersted
(1777–1851)

Equipment: transparent compass, overhead projector, DC supply.

We follow a story narrated by E. Whittaker (1962): "During a course of lectures, which Oersted delivered in the winter of 1819–1820 on Electricity, Galvanism and Magnetism, the idea occurred to him that the changes observed with the compass needle during a thunderstorm might give the clue to the effect of which he was in search; and this led him to think that the experiment should be tried with the galvanic circuit closed instead of open, and to inquire whether any effect is produced on a magnetic needle when an electric current is passed through a neighboring wire. At first, he placed the wire at right angles to the needle, but observed no result. After the end of a lecture, in which this negative experiment had been shown, the idea occurred to him to place the wire parallel to the needle; on trying it, a pronounced deflection was observed, and the relation between magnetism and the electric current was discovered. After confirmatory experiments with more powerful apparatus, the public announcement was made in July 1820."

Oersted's discovery was the first indication of the relation between magnetism and electricity. Exactly a weak after the news of this discovery had arrived, André-Marie Ampère (1775–1836) showed that two parallel wires carrying currents attract each other if the currents are in the same direction, and repel each other if the currents are in opposite directions. This interaction serves now for the definition of the unit of electric current, the ampere. In 1820,

Jean-Baptiste Biot and Félix Savart published the first precise analysis of the new phenomenon. According to the Biot–Savart law, a magnetic field produced by an element d$\boldsymbol{l}$ of a circuit, in which a current I is flowing, at a point whose vector distance from d$\boldsymbol{l}$ is $\boldsymbol{r}$, is (Fig. 1)

$$d\boldsymbol{H} = (I d\boldsymbol{l} \times \boldsymbol{r})/4\pi r^3. \quad (1)$$

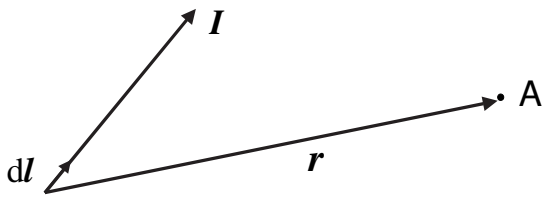

Fig. 1. Elemental magnetic field d$\boldsymbol{H}$ created by an element of electric current Id$\boldsymbol{l}$ at the point A is perpendicular to the plane containing vectors d$\boldsymbol{l}$ and $\boldsymbol{r}$.

A transparent compass is placed on the table of an overhead projector, and its needle directed to the North Pole is seen on the screen. A current-carrying wire is put over the compass at a right angle to the needle. The direction of this DC current is chosen beforehand to produce a force on the needle in the same direction as the Earth's magnetic field does. Therefore, there is no change in the position of the needle. Then the wire is brought to rotate around the center of the compass, and the needle responds to the resulting magnetic field. The deflection of the needle reaches a maximum when the wire is parallel to the magnetic meridian. When continuing the rotation, the wire comes to a right angle to the magnetic meridian, but now it produces a magnetic field opposite to the Earth's magnetic field. If the current through the wire is sufficient to overcome the Earth's field, the needle suddenly turns over and indicates the direction to the South Pole (Fig. 2).

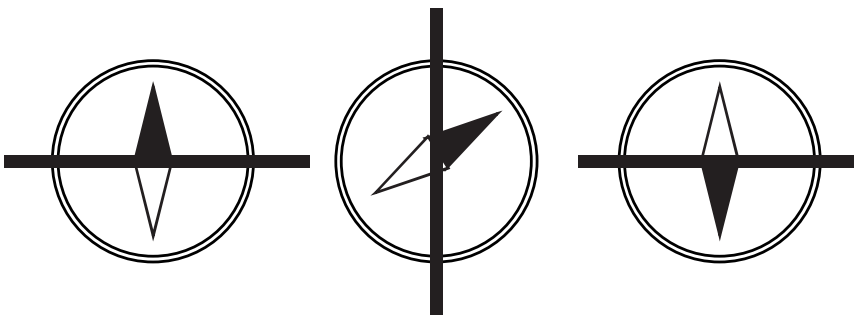

Fig. 2. Demonstration of Oersted's great discovery.

1.15. Magnetic field measurements

Magnetic field sensor based on Hall's effect measures magnetic fields.

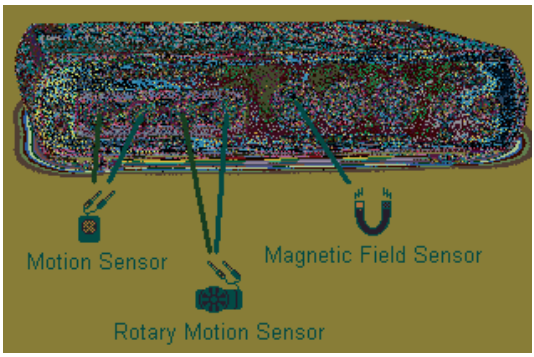

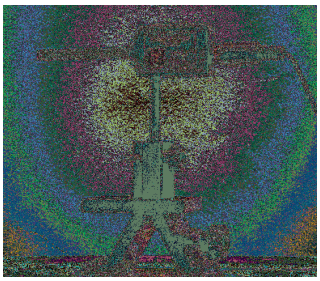

Magnetic field sensor from PASCO.

Additional equipment: *Magnetic field sensor*, *Motion sensor*, *Rotary motion sensor*, two coils, permanent bar magnet.

Measurements of magnetic fields are present in many student experiments. Gnanatilaka and Fernando (1987) investigated the magnetic field in the plane of a circular current loop. The loop is placed parallel to the magnetic meridian, and a small compass moving along the coil diameter senses the resulting magnetic field. With a Hall probe, Golden *et al* (1988) measured the axial magnetic field of a short solenoid. Leclerc (1988) used Hall's probe to verify Ampere's law. For similar measurements, Priest (1990) employed a computer. Deacon and Clarke (1993) measured the magnetic field of a plane circular coil, a solenoid, and Helmholtz's coils.

Sensor with Hall's probe. Hall's effect (Li 1993; Balkanski and Wallis 2000) is caused by the forces acting on a moving electric charge. Consider a bar of rectangular cross section, in which a DC current flows in the presence of a uniform magnetic field B (Fig. 1). The Lorentz force $\boldsymbol{F}$ on a moving charge is

$$\boldsymbol{F} = q\boldsymbol{E} + q\boldsymbol{v}\times\boldsymbol{B}, \tag{1}$$

where $\boldsymbol{E}$ is the electric field, q is the charge, and $\boldsymbol{v}$ is the charge velocity.

In the case considered, the vector $\boldsymbol{B}_z$ is perpendicular to the vector $\boldsymbol{v}_x$. The deflected carriers produce a transverse electric field $\boldsymbol{E}_y$ called the Hall field. In a steady state, this field gives rise to a force that just cancels the force due to the magnetic field:

$$qE_y = qv_xB_z. \tag{2}$$

The Hall field can be expressed as

$$E_y = j_xB_z/qn = R_Hj_xB_z, \tag{3}$$

where n is the density of carriers, j_x is the current density, and $R_H = 1/qn$ is called Hall's constant.

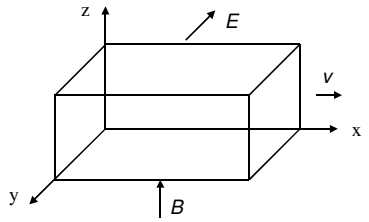

Fig. 1. Diagram for calculating Hall's effect.

Hall's effect is a popular tool for measuring magnetic fields. When an electric current passes through the probe exposed to a magnetic field perpendicular to the current, a voltage between the sides of the probe is proportional to the current and external magnetic field. PASCO provides the *Magnetic field sensor* containing two Hall's probes, for measuring magnetic fields in axial and radial directions.

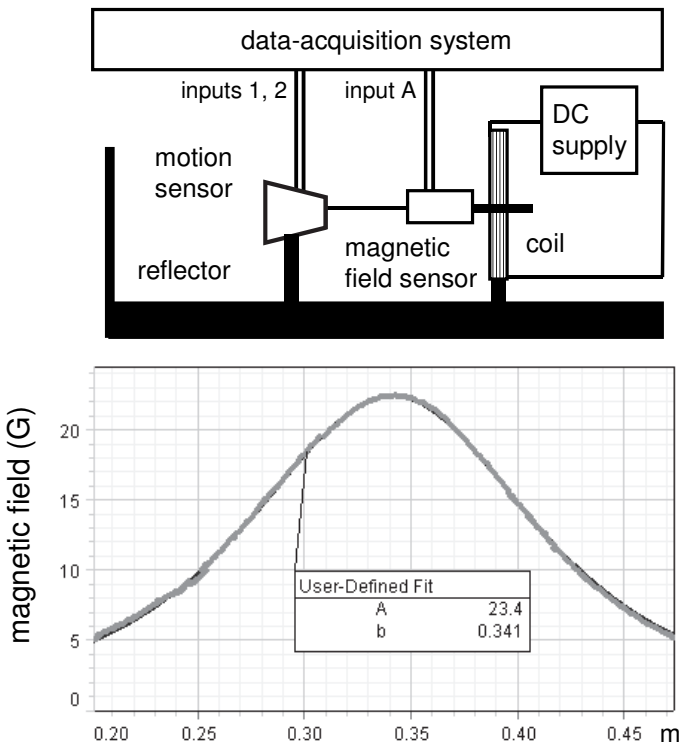

Fig. 2. Schematic of setup for measuring the axial magnetic field of a thin coil, and results obtained.

Magnetic field of a coil and a bar magnet. In this experiment, the *Magnetic field sensor* (axial) measures the axial magnetic field produced by a thin coil (EM-6711) fed by a power supply, while the *Motion sensor* determines the position of the sensor (Fig. 2). The magnetic field is displayed versus position. With the *User-defined fit*, one compares the data obtained with the theory. The axial magnetic field produced by a thin coil on its axis equals

$$B_z(z) = \mu_0 NIa^2/2(a^2 + z^2)^{3/2}, \quad (4)$$

where μ_0 is the **magnetic constant** (permeability of vacuum), N and I are the number of turns of the coil and the current in it, a is the radius of the coil, and z is the distance from the center of the coil.

The *Magnetic field sensor* (radial) is used for determining the angular dependence of the field produced by two adjacent coils. The sensor mounted on the axle of the *Rotary motion sensor* placed between the coils (Fig. 3) measures the field during rotation in the angle range from 0 to 360°. To display the angular dependence of the field in polar coordinates, one uses absolute values of the field h (*Calculate/Scientific/Abs*) and builds a function $y(x)$, where $x = h*\cos(b)$ and $y = h*\sin(b)$, where b is the rotation angle.

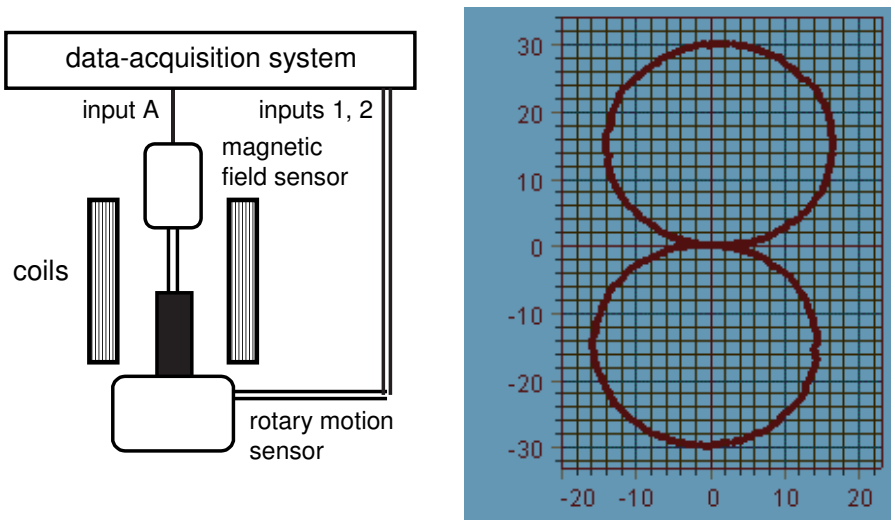

Fig. 3. Schematic of setup for measuring angular dependence of magnetic field produced by two adjacent coils, and results obtained (in gauss).

The magnetic field produced by a bar magnet is measured as a function of its orientation (Fig. 4). The magnet is mounted on the axle of the *Rotary motion sensor*. The results are similar to those for two coils. This similarity supports the concept that every magnetic field is caused by electric currents. Basano *et al* (1988) have shown, however, that the magnetic fields generated by a bar magnet and by a solenoid of the same shape and dimension are similar but not equal.

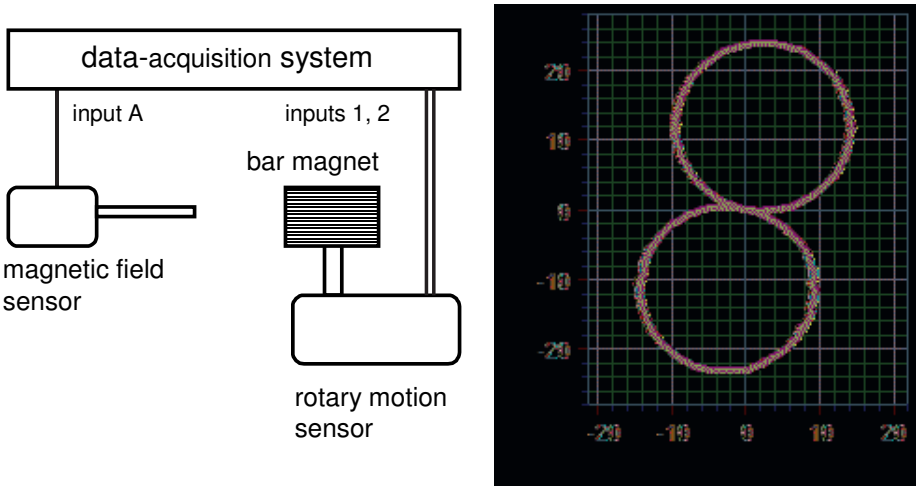

Fig. 4. Schematic of setup for measuring angular dependence of magnetic field of a bar magnet, and results obtained (in gauss).

1.16. Magnetic force

The experiment shows that (i) the magnetic force is proportional to the current flowing in the conductor, and (ii) the direction of the force depends upon the relative orientation of the field and the conductor (Kraftmakher 2004a).

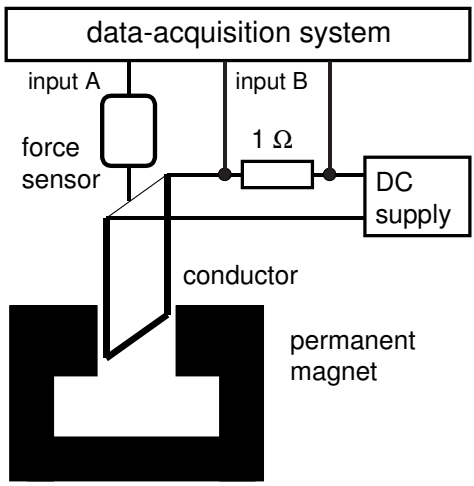

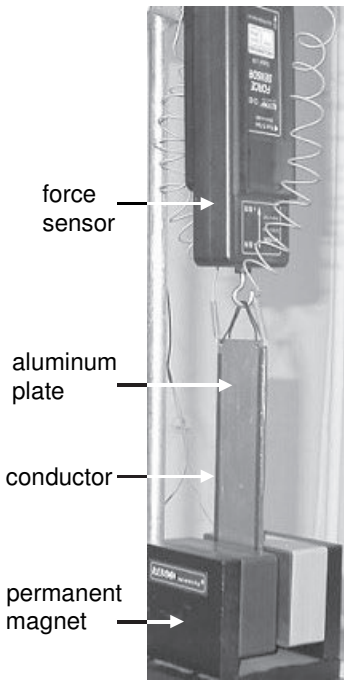

Arrangement for weighing a current-carrying conductor placed inside the gap of a permanent magnet.

Additional equipment: *Force sensor*, *Voltage sensor*, permanent magnet, variable DC supply (up to 3 A), resistor (1 Ω, 10 W), aluminum plate.

Lorentz's force acting on an electric charge contains two components, the electric force and the magnetic force. While the electric force depends only on the electric charge q and the electric field $\boldsymbol{E}$, the magnetic force depends on the charge, the magnetic field $\boldsymbol{B}$, and the velocity of the charge $\boldsymbol{v}$ (Fig. 1):

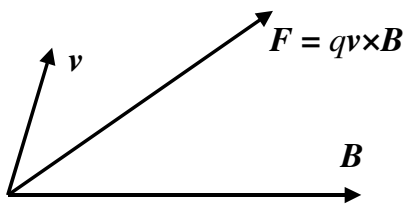

Fig. 1. Magnetic force is perpendicular to vectors $\boldsymbol{v}$ and $\boldsymbol{B}$.

$$\boldsymbol{F} = q\boldsymbol{E} + q\boldsymbol{v}\times\boldsymbol{B}. \quad (1)$$

Magnetic field measurement. The experiment consists of weighing a straight current-carrying conductor subjected to a uniform magnetic field of a permanent magnet. The *Force sensor* weighs a rectangular aluminum plate (4×15 cm), to which a flexible wire is pasted. The horizontal part of the conductor is put inside the gap of a strong permanent magnet (WA-9609A). A DC supply operating in the constant-current mode feeds the conductor, and the *Voltage sensor* measures the voltage across a 1 Ω (10 W) resistor placed in series with the conductor. The magnetic field in the gap of the magnet is horizontal, perpendicular to the conductor. Hence, the magnetic force is directed vertically, up or down. The data-acquisition system displays the data from the *Force sensor* versus the current through the conductor. The measurements with two orientations of the magnet show an increase or decrease of the weight measured. The measurements start when the current is set to its maximum. One gradually decreases the current down to zero, reverses its direction by a switch, and then increases the current up to the maximum.

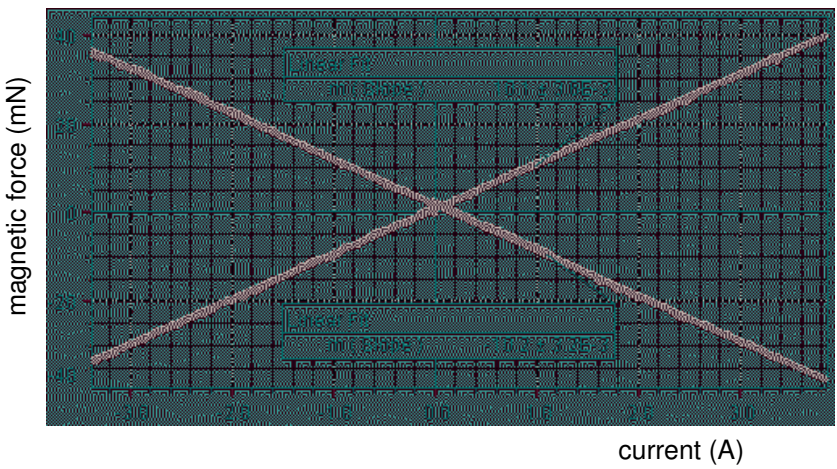

Fig. 2. Magnetic force versus current through the conductor, for two directions of the current and two orientations of the magnet.

From the graphs obtained (Fig. 2), it is easy to calculate the magnetic field in the gap of the magnet. The magnetic force equals

$$\boldsymbol{F}\ (\mathrm{N}) = l\boldsymbol{I}\times\boldsymbol{B}\ (\mathrm{m.A.T}), \quad (2)$$

where l is the length of the horizontal portion of the conductor subjected to the field, $\boldsymbol{I}$ is the vector of current flowing through the conductor, and $\boldsymbol{B}$ is the vector of magnetic field. Since the conductor is perpendicular to the magnetic field, the slope of the graph equals Bl.

The measurement lasts about 10 s, and the *Sample rate* is set to be 100 Hz. The maximum current is about 3 A. Before the measurements, it is

necessary to cancel the initial weight of the aluminum plate (the *Tare* button of the sensor). This makes it possible to use the *High sensitivity* of the *Force sensor*. The *Smooth* operation provided by *DataStudio* reduces the scatter of the data. The length of the permanent magnet is 75 mm, so that the horizontal portion of the conductor, 42 mm long, is placed in a nearly uniform magnetic field. The graphs obtained show that the magnetic force is strictly proportional to the current flowing through the conductor. The *Fit*/*Linear fit* tool serves for the determination of the slope of the graph. The force to be measured could be made stronger by using of a rectangular coil instead of a single conductor.

For experiments on the magnetic force, see Gabuzda (1987); Jones (2000); Redinz (2011).

The ampere

The ampere is that constant current which, if maintained in two straight parallel conductors of infinite length, of negligible circular cross section, and placed 1 meter apart in vacuum, would produce between these conductors a force equal to 2×10^{-7} newton per meter of length.

1.17. Magnetic braking

The experiment demonstrates the action of **eddy currents** induced in a conductor. The phenomenon is a direct consequence of **Lenz's law**.

AIP Emilio Segrè Visual Archives,
E. Scott Barr Collection
Heinrich Friedrich Emil Lenz (1804–1865)

Additional equipment: *Rotary motion sensor*, pendulum, permanent magnet.

Not long after Faraday's discovery of the magnetic induction in 1831, Lenz stated a law: when a conductor is moved in a magnetic field, the current induced in the conductor flows in such a direction that the ponderomotive forces oppose the motion. Many experiments to demonstrate Lenz's law were reported: Wiederick *et al* (1987); Heald (1988); Aguirregabiria *et al* (1997); Ochoa and Kolp (1998); LoPresto and Holody (2003); Roy *et al* (2007); Donoso *et al* (2011); Onorato and De Ambrosis (2012). A simple demonstration is presented here. A strong permanent magnet positioned close to an aluminum pendulum dramatically shortens the decay of the pendulum free oscillations.

We use a cylindrical NdFeB magnet, 18 mm in diameter and 18 mm in height. The pendulum is an aluminum-alloy disc, 150 mm in diameter and 5 mm thick. At a point close to its edge, the disc is attached to the axle of the *Rotary motion sensor* (see Experiment 2.5). The braking action of the magnet strongly depends on the distance between the magnet and the disc surface (Fig. 1). Without magnetic braking, the long decay of free oscillations does not follow the exponential law. In this case, the friction in the *Rotary motion* sensor causes the decay, and the friction force is not proportional to the angular velocity (Lapidus 1970). The decay becomes exponential when the magnetic braking dominates. With the magnet positioned close to the disc, the decay time decreases by two orders of magnitude.

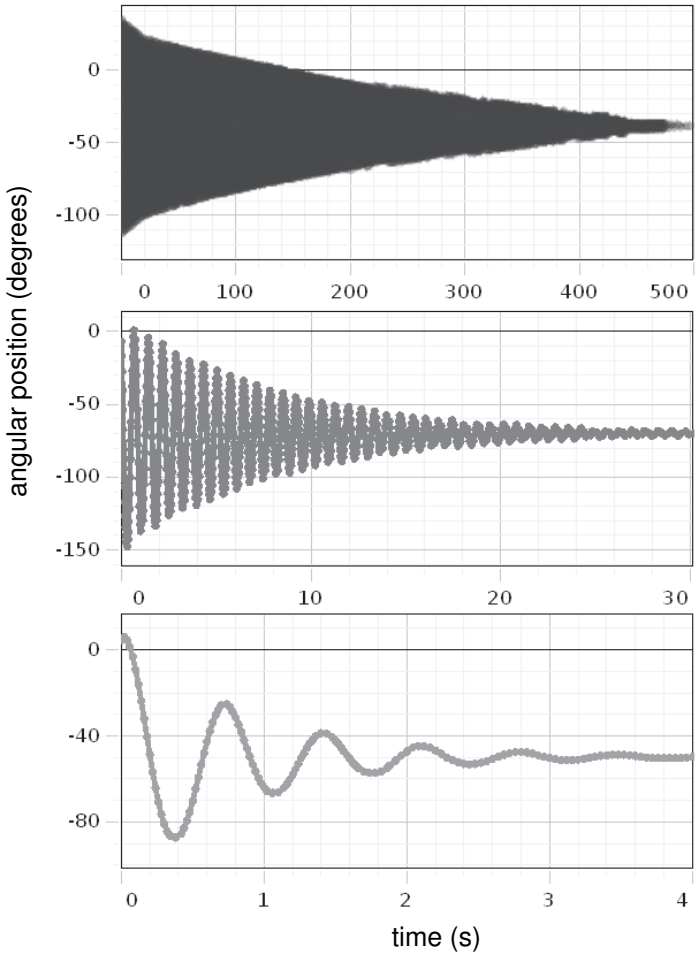

Fig. 1. Free oscillations of the pendulum without magnetic damping and for two distances between the pendulum and the magnet. Note the different time scales.

1.18. Curie's point I

A simple experiment reveals Curie's point of a ferrite sample.

Equipment: ferrite toroidal core, function generator, oscilloscope, electrical oven, thermocouple, resistor.

The crystal lattice of ferrimagnets consists of two sublattices with opposite but different magnetizations (equal magnetizations lead to antiferromagnetism), so a net magnetization arises (see Experiment 6.7). Like a **ferromagnet**, every **ferrimagnet** loses its permeability at a definite temperature, which is called Curie's temperature (Curie's point). The simplest way to determine Curie's point of a ferrite is to measure the inductance of a coil (or the mutual inductance of two coils) wrapped on a ferrite core, preferably of toroidal shape, as a function of temperature. In this case, the inductance of the coil obeys the same equation that is valid for a very long solenoid (the length is much larger than the diameter) and is proportional to the **permeability** μ of the core. The inductance L of a toroidal coil with a magnetic core of relative permeability is

$$L = \mu\mu_0 A N^2/l, \tag{1}$$

where μ_0 is the **magnetic constant** (permeability of vacuum), A is the cross sectional area of the core, l is the average length of the magnetic path, and N is the number of turns of the coil. Therefore, the temperature dependence of the inductance of the ferrite-core coil indicates its Curie's point. If two similar coils are wrapped on a toroidal ferrite core, the mutual inductance M between the coils equals

$$M = \mu\mu_0 A N_1 N_2/l. \tag{2}$$

As the sample, we use a ferrite bead taken off a power cord for a computer. Such beads protect power cords and cables connecting computers with keyboards and printers from external AC magnetic fields. The ferrite-core coil is placed in an electrical oven. The temperature is determined with a thermocouple, whose EMF is measured by a multimeter. The primary coil is connected, through a resistor R, to a function generator. The EMF created in the secondary coil is observed with an oscilloscope (Fig. 1). In our case, $N_1 = N_2 = 10$.

At room temperature, the resistance and the frequency are chosen to make the EMF in the secondary coil two orders of magnitude less than the voltage provided by the generator. This means that the current in the primary coil will be nearly independent of the permeability of the core. In our case, $R = 10$ kΩ, and the generator frequency is 1 kHz. The voltage across the coil is seen on the screen of an oscilloscope. A simple multimeter (not shown in Fig. 1) can be used to measure the AC voltage amplified by the oscilloscope. At Curie's point, this voltage vanishes. The measurements are performed during cooling process after the oven is heated above Curie's point. For a Mn-Zn ferrite, Curie's point is

nearly 135°C. Also, the inductance of the coil can be measured with a simple LCR meter, and the permeability of the sample is available from Eq. (1).

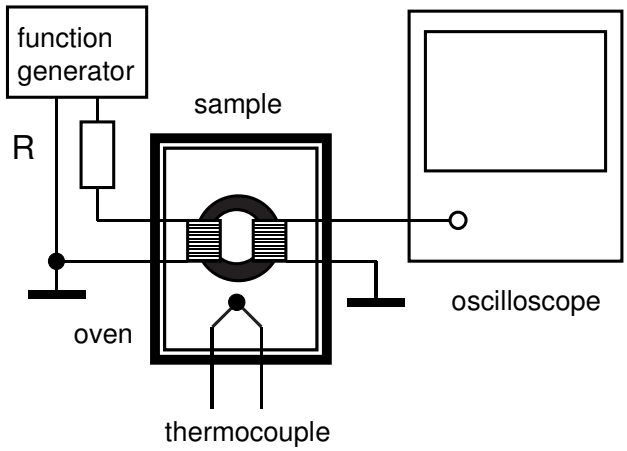

Fig. 1. Schematic of setup with ferrite-core mutual inductance.

1.19. Electric power in AC circuits

The electric power in AC circuits is determined for currents/voltages of arbitrary waveforms (Kraftmakher 2006a).

AIP Emilio Segrè Visual Archives,
Brittle Books Collection
James Prescott Joule (1818–1889)

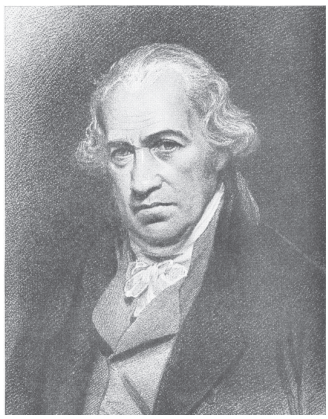

AIP Emilio Segrè Visual Archives
James Watt (1736–1819)

Additional equipment: *Voltage sensor*, light bulb, *Power amplifier II* (unnecessary when using a light bulb of low voltage and current or the *850 Interface*).

Instantaneous and mean power. The electric power developed by a DC current I equals $P = I^2R = IV$, where R is the load resistance, and V is the voltage across it. For AC currents, the energy delivered during a period of the current can be calculated by summation of energies during short intervals, where the current and the voltage are considered to remain constant. For an arbitrary waveform of the current and/or voltage of period T, the mean power equals

$$P = (1/T)\int_0^T IV\mathrm{d}t. \tag{1}$$

Power of sine waveform current and voltage equals

$$P = (1/T)\int_0^T I_\mathrm{m}V_\mathrm{m}\sin\omega t\,\sin(\omega t - \varphi)\,\mathrm{d}t, = \tfrac{1}{2}I_\mathrm{m}V_\mathrm{m}\cos\varphi = I_\mathrm{eff}V_\mathrm{eff}\cos\varphi, \tag{2}$$

where I_m and V_m are amplitude values of the current and voltage, $\omega = 2\pi/T$ is the angular frequency, φ is the phase shift between the current and the voltage; $I_\mathrm{eff} = I_\mathrm{m}/\sqrt{2}$ and $V_\mathrm{eff} = V_\mathrm{m}/\sqrt{2}$ are the so-called **effective values** of the current and voltage. For the determination of the electric power, it is thus sufficient to measure the amplitude or effective values of the current and voltage, and the phase shift φ between them. For waveforms of the current or/and voltage that are more complicated, one has to use Eq. (1).

For sine waveform currents and voltages, *DataStudio* adequately fits experimental data. By using the *Fit*/*Sine fit* option, the fits for the current and voltage measured in one run show their amplitude values and phases. The phase shift φ between two sine waves thus becomes available. This operation is demonstrated here by measurements of the power dissipated in a 400-turn coil (SF-8610) due to its inherent resistance, versus the frequency of the current passing through the coil. To make the current independent of frequency, the coil is connected to the *Signal generator* through a 500 Ω resistor. The current is stored as the *Output current*, and the *Voltage sensor* measures the voltage across the coil. The *DataStudio* also calculates the products of instantaneous values of the data and then their averaged values. The *Calculate*/*Statistical*/*Avg* tool is used to perform these operations. All the operations are observable as graphs on the screen. In the frequency range 10 to 300 Hz, the electric power dissipated in the coil remains nearly constant. The results of both determinations are in good agreement (Fig. 1), which confirms the validity of the *DataStudio* operations.

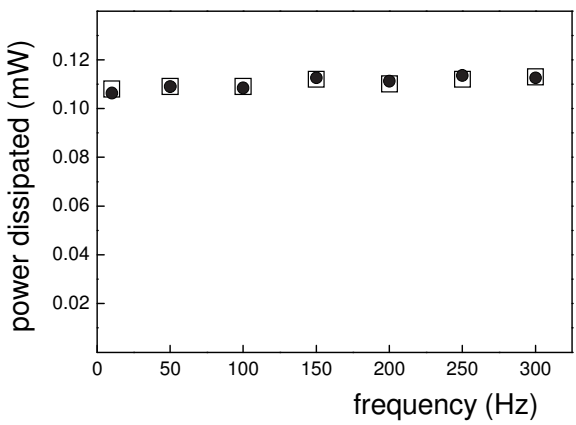

Fig. 1. Mean power dissipated in the coil determined by integration (□) and using cosφ values (●).

With this experiment, it is possible to demonstrate the effect of a conducting nonmagnetic cylinder rod, 1.5–2 cm in diameter, placed inside the coil. This causes two effects: (i) according to Lenz's law, the inductance of the coil decreases, which is seen from the change of the voltage drop across the coil, and (ii) the power consumed increases due to the eddy currents (Fig. 2). This increase is caused by the decrease of the phase shift between the current and the voltage across the coil, which can be seen by plotting the Lissajous pattern. The power dissipated in the cylinder rod depends on the resistivity and diameter of the rod and on the frequency of magnetic field (see Experiment 6.9).

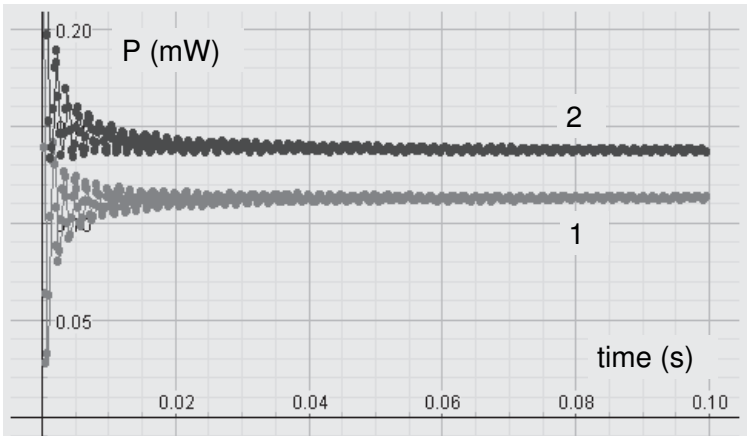

Fig. 2. Mean power dissipated in the coil, before (1) and after the conducting rod is put inside the coil (2). The frequency is 300 Hz.

Power for complicated waveforms. A low power incandescent light bulb is used to measure the dissipated power for more complicated waveforms of the current and voltage. The *Power amplifier II* connected to the *Signal generator* provides the *Positive square wave voltage* applied to the bulb. The measurements are done for two frequencies of the voltage, 1 and 100 Hz (Fig. 3). *DataStudio* stores the data and calculates the power using Eq. (1).

For the low frequency, the temperature of the filament changes in a wide range, so strong changes in the current are seen. The high current at the start of each pulse is due to a low resistance of the filament after a long cooling period, 0.5 s. For a high frequency, the temperature oscillations and thus the changes of the current are small.

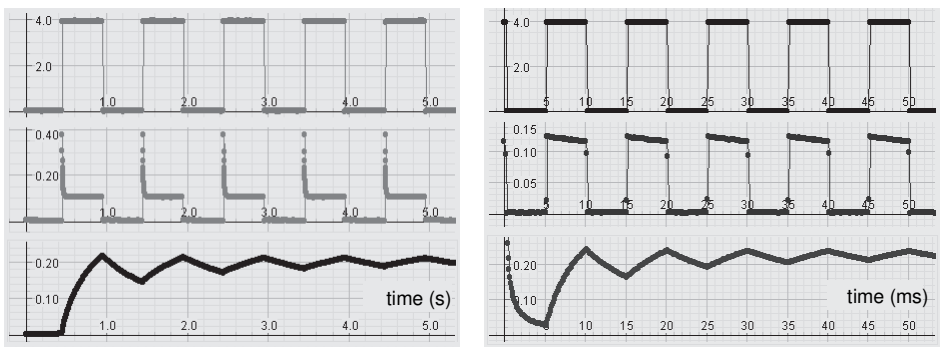

Fig. 3. Applied voltage, heating current, and mean power, for two frequencies of applied voltage, 1 and 100 Hz.

1.20. Faraday's law of induction I

The EMF generated in a coil due to the electromagnetic induction depends on the rate of changing the magnetic flux penetrating the area of the coil, but the integral of this EMF depends only on the total change in the flux.

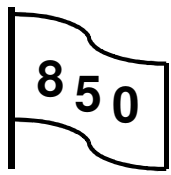

Additional equipment: *Voltage sensor*, bar magnet, coil.

For a permanent magnet placed on and oriented along the axis of a coil, a simple formula describes the **magnetic flux** Φ penetrating the area of the coil (Carpena 1997, Kingman *et al* 2002):

$$\Phi = \mu_0 m a^2/2(a^2 + z^2)^{3/2}, \quad (1)$$

where μ_0 is the magnetic constant, m is the **magnetic moment** of the magnet, a and N are the radius and number of turns of the coil, and z is the distance between the center of the magnet and the center of the coil.

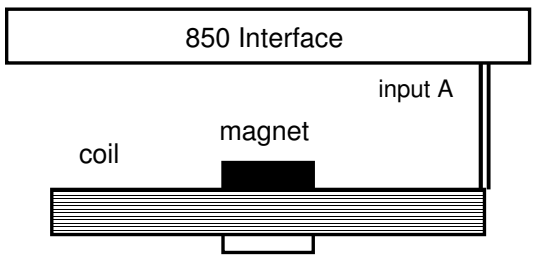

Fig. 1. Schematic of arrangement for the demonstration and determination of magnetic moment of a permanent magnet.

When the magnet is positioned at the center of the coil (z = 0), the absolute value of this flux equals

$$\Phi = \mu_0 m/2a. \quad (2)$$

In the demonstration (Fig. 1), the magnet is slowly moved from a distant point to the center of the coil (EM-6723, N = 500). The EMF induced in the coil according to Faraday's law of induction equals

$$e = -N\mathrm{d}\Phi/\mathrm{d}t \quad (3)$$

and depends on the motion of the magnet, but the integral of this EMF depends only on the total change of the magnetic flux penetrating the coil.

Then the magnet is rapidly removed from the center of the coil. Thus, the time dependences of the voltages induced in the coil are very different: the maximum induced voltages differ by one order of magnitude (Fig. 2). The software performs the integration and provides values of the magnetic flux. The

integration of the induced voltages shows that the flux returns to its initial zero value. By the use of Eq. (2), the magnetic moment of the magnet is available.

For experiments on Faraday's law of induction, see Scanlon *et al* (1969); Reed (1975); Sankovich (1985); Singh *et al* (2002).

Fig. 2. Measurement data: voltage induced in the coil and the integral of the induced voltage.

1.21. Self-inductance and mutual inductance

Self-inductance of a coil and mutual inductance of two coils are determined.

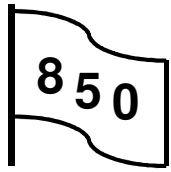

Additional equipment: *Voltage sensor*, two coils, AC-to-DC converter, resistor.

When an AC current I of angular frequency ω passes through a coil of **self-inductance** L and resistance R, the voltage drop across the coil is

$$V = I(R^2 + \omega^2 L^2)^{1/2}. \quad (1)$$

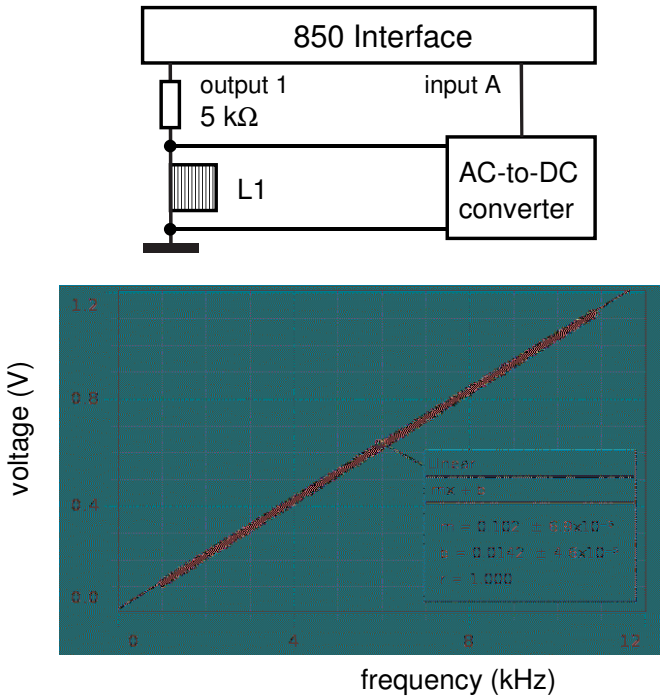

Fig. 1. Diagram of the setup and the voltage drop across the coil versus frequency.

An 800-turn coil (SF-8611) is connected to *Output 1* through a 5 kΩ resistor, so the current is almost independent of the frequency (Fig. 1). The frequency of the *Output 1* sweeps from 1 to 11 kHz in 200 s. The amplitude of the current through the coil is 2 mA. Since $R << \omega L$, the voltage drop across the coil is nearly proportional to the frequency. This voltage proceeds to an AC-to-DC converter (we use a Keithley 177 multimeter) and then to the *850 Interface*. *Capstone* displays the output voltage of the converter versus frequency and fits

the data with a *Linear fit*. The inductance of the coil is available from the slope of the graph obtained: $V = I\omega L$. It should be taken into account that the converter provides RMS values of the voltage that are $1/\sqrt{2}$ of the amplitudes. From the data, $L = 11.5$ mH.

For **magnetically coupled coils**, the EMF induced in the secondary coil is

$$e_2 = I_1 \omega M, \tag{2}$$

where I_1 is the current in the primary coil, and M is the **mutual inductance** of two coils.

The primary coil is connected to the *Output 1* through a 5 kΩ resistor (Fig. 2). The EMF induced in the secondary coil is measured versus frequency, for various distances between the coil edges. The graphs are straight lines, from which the mutual inductance is available. For instance, the maximum mutual inductance (no gap between the coil edges) is 1.3 mH: This means that the magnetic flux penetrating the secondary coil is nearly one tenth of that generated by the primary coil.

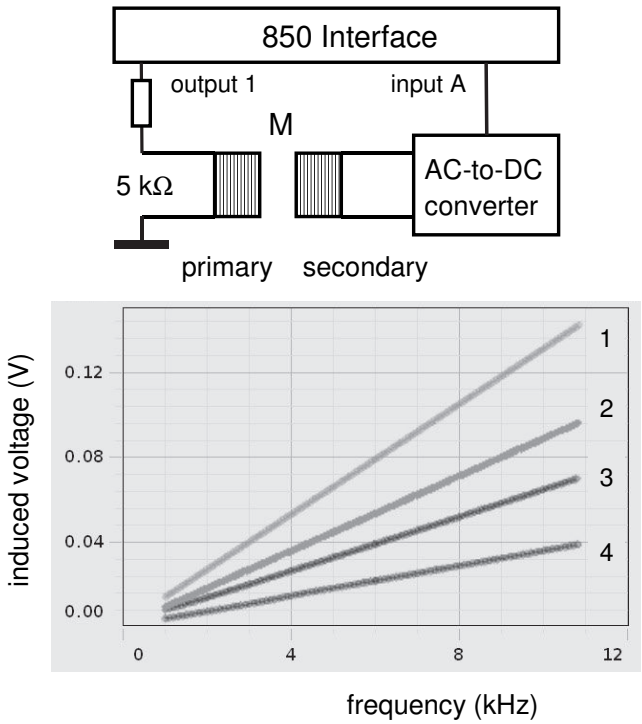

Fig. 2. Diagram of the setup and the voltage induced in the secondary coil for various gaps between the coils: 1–no gap, 2–0.5 cm, 3–1 cm, 4–2 cm.

1.22. Electromagnetic screening

The electromagnetic screening by metals is demonstrated (Kraftmakher 2014a).

Additional equipment: two *Voltage sensors*, two coils, AC-to-DC converter, aluminum-alloy sheet.

Electromagnetic screening by metals is one of manifestations of Lenz's law: electric currents induced in a conductor by the **electromagnetic induction** are in such a direction as to oppose the changes in the magnetic flux causing these currents. Electromagnetic screening by a metal is effective even when the thickness of the screen is less than the **skin depth** in the metal (Fahy *et al* 1988; Rochon and Gauthier 1990). With SI units, the skin depth for a plane surface equals

$$\delta = (2\rho/\mu_0\omega)^{1/2}, \quad (1)$$

where ρ is the resistivity of the conductor, μ_0 is the magnetic constant (permeability of vacuum), and $\omega = 2\pi f$ is the angular frequency of the magnetic field. In a form more convenient for practical use, this relation can be presented as

$$\delta = (\rho/f)^{1/2}/2\pi, \quad (2)$$

where δ is given in cm, ρ in $\mu\Omega$.cm, and f in kHz. For instance, for copper at 25°C (ρ = 1.7 $\mu\Omega$.cm) and f = 50 Hz, the skin depth equals nearly 1 cm.

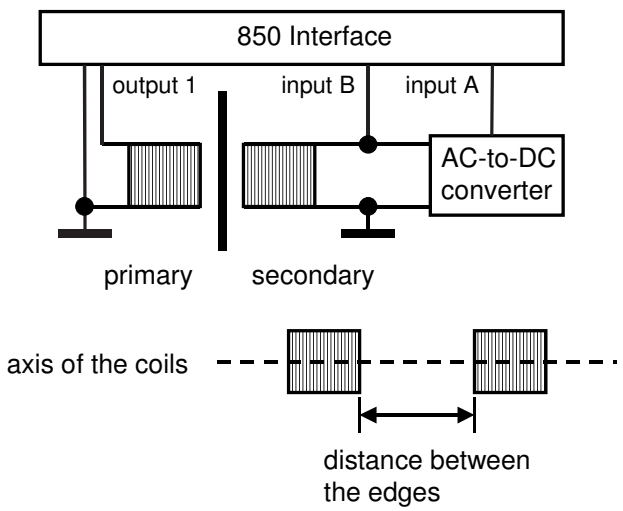

Fig. 1. Schematic of the setup.

The demonstration includes two experiments with two similar coils (SF-8611, 800 turns) and a 30×30 cm^2 aluminum-alloy sheet, 1.5 mm thick. The only relevant parameters of the sheet are its resistivity and thickness, so any sheet of metal or alloy is usable. The coils are placed coaxially, with a gap between their edges of 1 cm (Fig. 1). The *Output 1* feeding the primary coil operates in the sweep mode. The amplitude of the output voltage is set 10 V. The output frequency and current are stored during a run and used as common measurement data. An AC-to-DC converter (Keithley 177 multimeter) provides a DC voltage proportional to the EMF induced in the secondary coil, and the *Voltage sensor* acquires this voltage at input A. Another *Voltage sensor* measures the EMF at input B.

In the first experiment, the frequency of the current in the primary coil sweeps from 1 to 11 kHz in 200 s. The *Sample rate* is 10 Hz. To avoid observing transients at the start and end of a run, the *Time delay* is set to be 1 s, and the *Record time* to be 199 s. The AC-to-DC converter provides RMS values of the AC input voltage. *Capstone* displays this voltage versus the frequency of the magnetic field without and with the screen between the coils (Fig. 2).

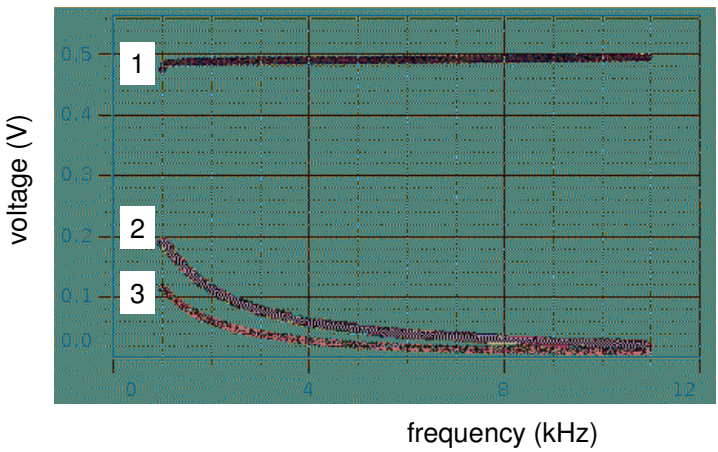

Fig. 2. Output voltage of the AC-to-DC converter versus frequency of the magnetic field: 1–no screen, 2–one screen, 3–two similar screens.

In the frequency range used, the inductive part of the impedance of the primary coil dominates, so the current amplitude is nearly inversely proportional to the frequency. On the other hand, the EMF induced in the secondary coil is proportional to the frequency of the magnetic field. The two factors lead to the result observed: without the screen, the EMF induced in the secondary coil is almost independent of frequency. With the screen between the coils, the EMF becomes much smaller and decreases with increasing frequency. As expected, the efficiency of the screening increases with the frequency of the magnetic field. It is useful to repeat the run with two similar screens between the coils.

In the second experiment, the frequency of the *Output 1* also sweeps from 1 to 11 kHz. Using the *Scope* display and the *Fast monitor* mode, the EMF in the screened secondary coil (input B) is displayed versus the current in the primary coil (that is, the *Output current*). The *Sample rate* is 1 MHz. The changes in the Lissajous pattern on the display during a run demonstrate how the EMF induced in the secondary coil and its phase lag relative to the current in the primary coil depend on the frequency. The phase lag increases from 90^o at very low frequencies to 180^o at high frequencies. Without a screen, the phase lag does not depend on frequency and equals 90^o, in accordance with Faraday's law of induction. The phase shift between the current in the primary coil and the EMF induced in the screen is also 90^o, but the phase of eddy currents in the screen is not the same as that of the EMF: the lag depends on the frequency of the magnetic field and resistivity and thickness of the screen (see Experiment 6.9).

The data can also be obtained for a set of selected fixed frequencies. The examples presented correspond to four frequencies (Fig. 3). When increasing the frequency of the magnetic field, the current in the primary coil decreases due to the inductance of the coil. If an AC-to-DC converter is not available, the second experiment is sufficient to demonstrate the electromagnetic screening.

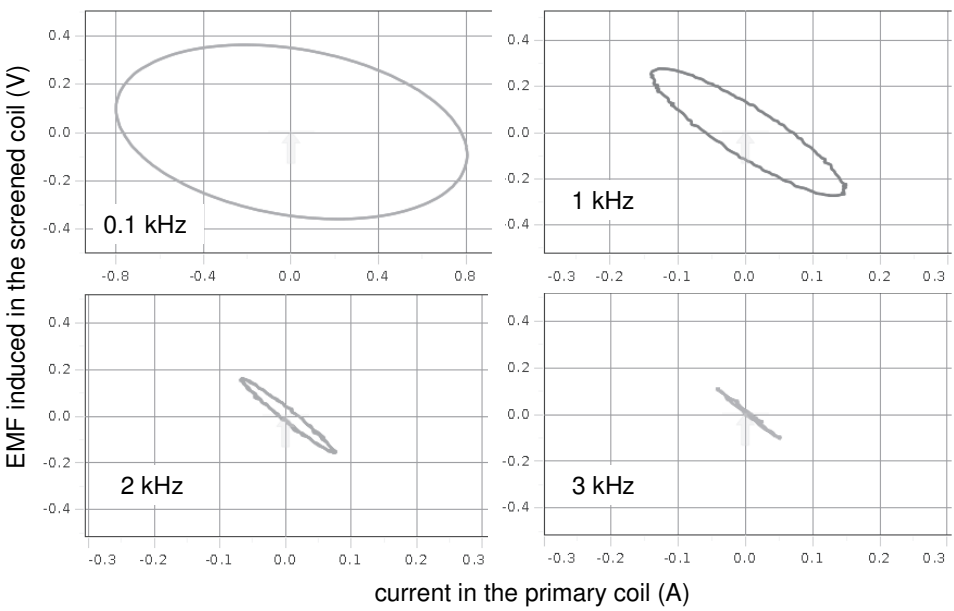

Fig. 3. EMF induced in the screened secondary coil versus current in the primary coil. Note the change in the X scale.

1.23. LCR circuit I

Resonance curves of a single LCR circuit (Kraftmakher 2014a) are displayed.

Additional equipment: two *Voltage sensors*, coil, AC-to-DC converter, capacitor, resistor.

Single LCR circuit. Resonance curves of LCR circuits were considered in many papers. Ramachandran (1991) explored free oscillations in a differently damped LCR circuit. In other papers, the main point was the determination of phase shifts between the voltages and currents (Hinton 1991; Ebert and Harvey 1992; Backman *et al* 1999).

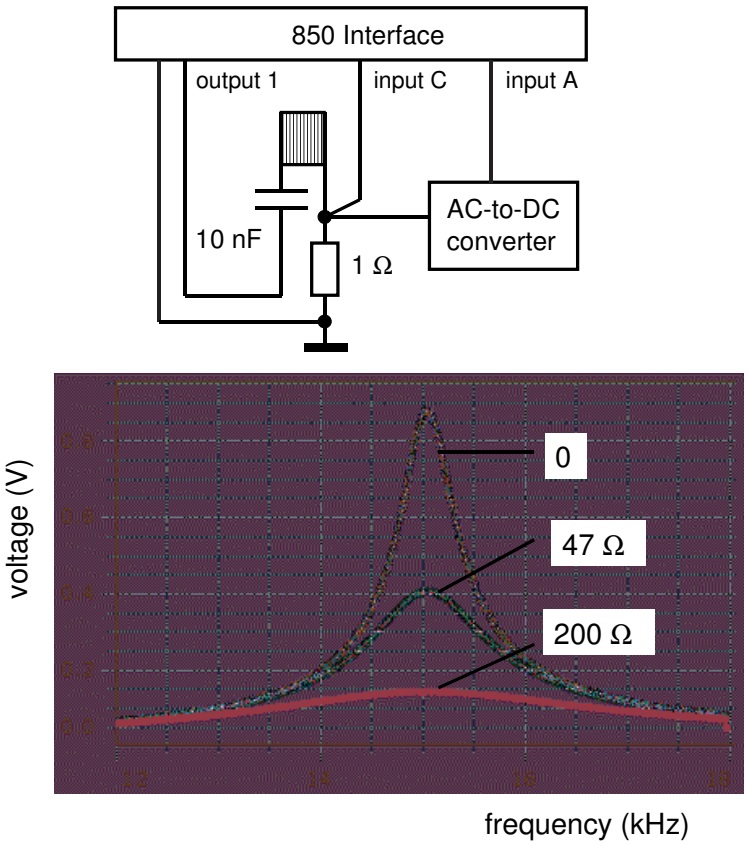

Fig. 1. Diagram of the setup, and resonance curves for various resistors added to the series LCR circuit.

To display resonance curves of a series LCR circuit, we use an 800-turn coil (SF-8611) and a 10 nF capacitor (Fig. 1). The circuit is connected to *Output 1*. A suitable resistor or a capacitor added to the circuit serves as an extra parameter. During a run lasting 200 s, the frequency of *Output 1* sweeps from 12 to 18 kHz. The current in the circuit is determined by measuring the voltage drop across a 1 Ω resistor put in series with the inductor and capacitor. This voltage is measured immediately (input C) and after converting it into a DC voltage by a Keithley 177 multimeter (input A). *Capstone* displays the output voltage of the multimeter versus the frequency. The *Sample rate* is 10 Hz. Do not forget that the voltage across the capacitor and inductor at resonance may become much larger than the input voltage.

From the resonance curves without an additional resistor and when a 47 Ω resistor is added, the inherent resistance R of the circuit becomes available. The maximum current amplitudes are inversely proportional to the total resistance values, that is, to R and $R + 47$. From the data obtained, $R = 43$ Ω. This quantity reflects all energy losses in the circuit and significantly exceeds the DC resistance, which is nearly 10 Ω.

An important parameter of an LCR circuit is the so-called **quality factor** (Q-factor). This quantity relates to the decay of free oscillations and to the sharpness of the resonance curve. The two phenomena depend on the same L, C, and R, so the definitions of the Q-factor based on the parameters of free and forced oscillations are equivalent. From the free oscillations, $Q = \omega_0/2\delta$, where δ is the decay factor of the oscillations. From the resonance curve, $Q = \omega_0/\Delta\omega$, where $\Delta\omega$ is the frequency band, in which the amplitude of the current is not less than $1/\sqrt{2}$ of its maximum value. Lastly, the Q-factor is obtainable directly from the L, C, and R values: $Q = \omega_0 L/R = 1/\omega_0 CR$. A useful exercise for the students is to derive Q values from the resonance curve and from the parameters of the circuit.

The *Fast monitor* mode and the *Scope* display allow observations of the gradually changing phase shift between the applied voltage (the *Output voltage*) and the current (input C). The data can also be obtained for several fixed frequencies (Fig. 2). At the resonance (15.17 kHz), the phase shift becomes zero. Below and above the resonance, the shift approaches $\pm 90^{\circ}$. By displaying the voltage and the current on the time scale, it is easy to see that the current leads the voltage at lower frequencies (capacitive impedance of the circuit) and follows the voltage at higher frequencies (inductive impedance).

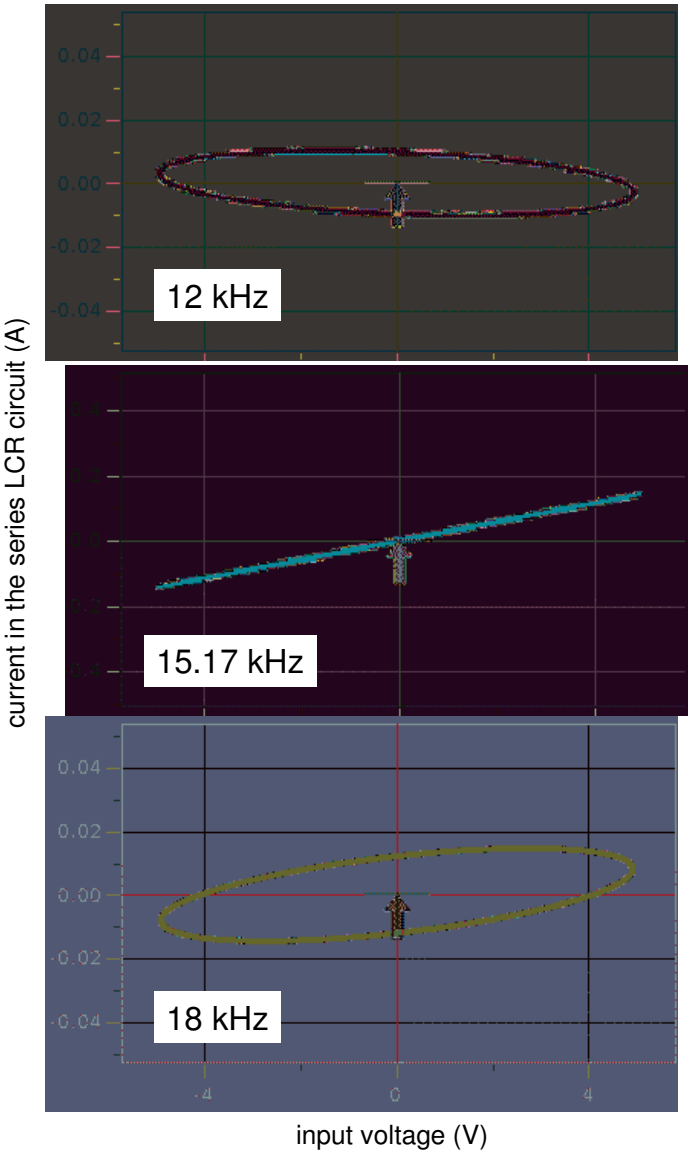

Fig. 2. Current in the series LCR circuit versus the input voltage. Note the change in the Y scale for displaying the data at resonance.

1.24. Coupled LCR circuits

Resonance curves of coupled LCR circuits are displayed. The experiment is similar to those described by Blair (1971); Gamarra *et al* (2007); Schauber *et al* (2008).

Additional equipment: three *Voltage sensors*, two coils, AC-to-DC converter, capacitors, resistors.

The setup includes two 800-turn (SF-8611) coils and 10 nF capacitors. The coils are positioned coaxially, and the primary circuit is connected to the *Output 1* (Fig. 1). The amplitude of the output voltage is 5 V.

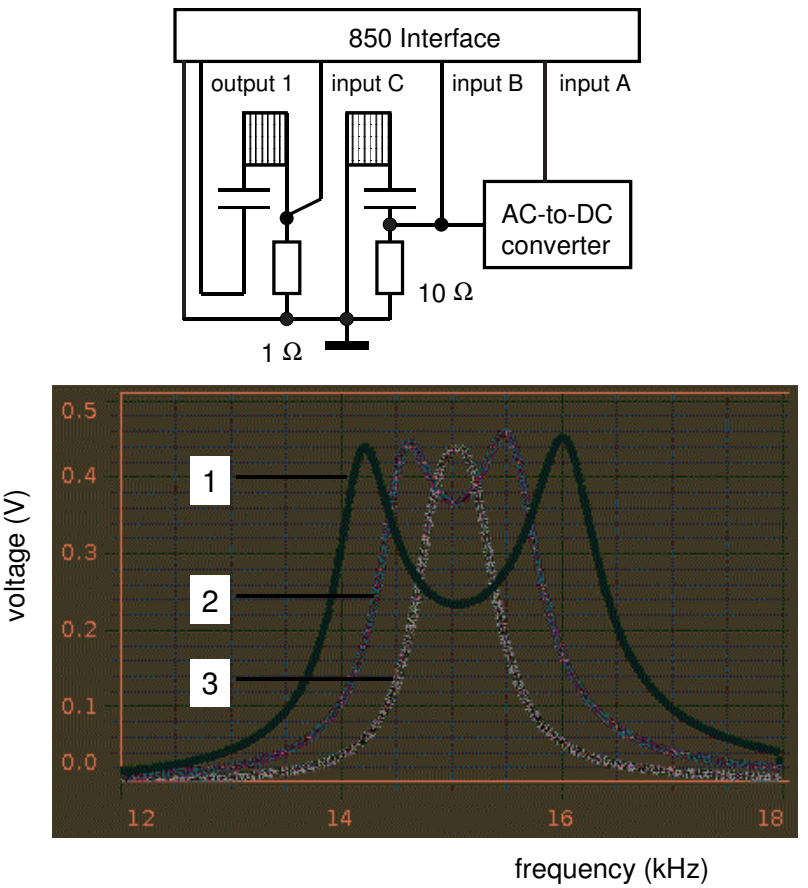

Fig. 1. Schematic of the setup and results for various gaps between the coil edges: 1–no gap, 2–1 cm, 3–3 cm.

A 1 Ω resistor included in the primary circuit serves for measuring the current in the circuit (*Voltage sensor*, input C). The current in the secondary circuit is measured through the voltage drop across a 10 Ω resistor (*Voltage sensor*, input B). This voltage also proceeds to an AC-to-DC converter (Keithley 177 multimeter) and then to the *850 Interface* (*Voltage sensor*, input A). Changing the distance between the coils controls the magnetic coupling between the circuits.

During a run lasting 200 s, the frequency of *Output 1* sweeps from 12 to 18 kHz. *Capstone* displays the output voltage of the AC-to-DC converter versus the frequency. The *Sample rate* is 10 Hz. For a weak coupling, the resonance curve is very similar to that of a single LCR circuit. However, two maxima appear when the coupling exceeds some critical level, and the band-pass frequency range can be varied. From the practical point of view, this can be considered as an advantage. The theory of coupled LCR circuits can be found elsewhere. The resonance curves are shown for three gaps between the coil edges (Fig. 3). If an AC-to-DC converter is not available, the demonstration can be performed with the *Scope* display or a common oscilloscope, by displaying the voltage across the 10 Ω resistor.

Additional measurements allow observations of phase shifts between the current in the secondary circuit (input B) and the voltage applied to the primary circuit (*Output voltage*) or the input current (input C). Using the *Scope* display and the *Fast monitor* mode, the current in the secondary coil is displayed versus the input voltage or current. The *Sample rate* is 1 MHz. During a run, the Lissajous pattern demonstrates how the phase shift changes with the frequency. The data can be displayed for some fixed frequencies.

1.25. Probability functions

Probability density functions for several waveforms generated by the *Signal generator* and for electrical noise are observed.

AIP Emilio Segrè Visual Archives,
Brittle Books Collection
Karl Friedrich Gauss (1777–1855)

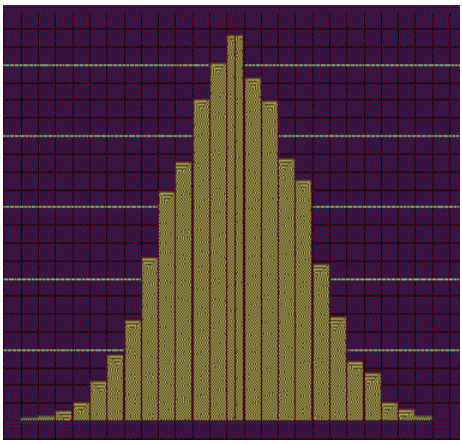

Probability density function for output noise of a high-gain amplifier.

Additional equipment: high-gain amplifier, oscilloscope.

The **probability density function** describes the probability that the data will assume a value within some defined range at any instant of time (Bendat and Piersol 1971). The probability that $x(t)$ assumes a value within the range between x and $x + \Delta x$ may be obtained by taking the ratio of T_x/T, where T_x is the total amount of time $x(t)$ falling inside the range $(x, x + \Delta x)$ during an observation time T. This ratio will approach an exact probability description as T approaches infinity:

$$\text{Prob}\,[x < x(t) < x + \Delta x] = \lim(T_x/T) \text{ when } T \to \infty. \quad (1)$$

For small Δx, a probability density function $p(x)$ can be defined:

$$\text{Prob}\,[x < x(t) < x + \Delta x] = p(x)\Delta x. \quad (2)$$

The probability density function $p(x)$ is always a real-valued, non-negative function. The probability that the instantaneous value $x(t)$ is less than or equal to some value x is defined by $P(x)$, which equals to the integral of the probability density function from minus infinity to x. This function $P(x)$ is the probability distribution function, or cumulative probability distribution function. Clearly,

$$P(x) = \text{Prob}\,[x(t) \le x] = \int_{-\infty}^{x} p(y)\,dy. \quad (3)$$

The probability that $x(t)$ falls inside a range (x_1, x_2) is given by

$$P(x_2) - P(x_1) = \int_{x_1}^{x_2} p(y)\mathrm{d}y. \quad (4)$$

For a sine wave, $x(t) = A\sin\omega t$, the probability density function is

$$p(x) = [\pi^2(A^2 - x^2)]^{-½}. \quad (5)$$

For a random noise, the probability density function is given by the **Gaussian function**

$$p(x) = (2\pi\sigma^2)^{-½} \exp(-x^2/2\sigma^2), \quad (6)$$

where σ is called the **standard deviation**. The smaller the standard deviation, the sharper the probability density function.

Arvind *et al* (2004) described measurements of instantaneous voltages across a capacitor connected to an AC source. The capacitor is randomly disconnected from the source, and a DC voltmeter with high internal resistance measures the voltage across it. This procedure takes a long time, while the *Histogram* tool immediately displays the probability density function. We use voltages generated by the *Signal generator* for determining the probability density functions of simple waveforms (Fig. 1). For a sine wave, the function obtained obeys Eq. (5), but the shape of the graph depends also on the resolution provided by the histogram. A high-gain wide-band amplifier serves as a source of noise voltage (Basano and Ottonello 1975). The *Voltage sensor* measures this voltage. The noise is also observed with an oscilloscope.

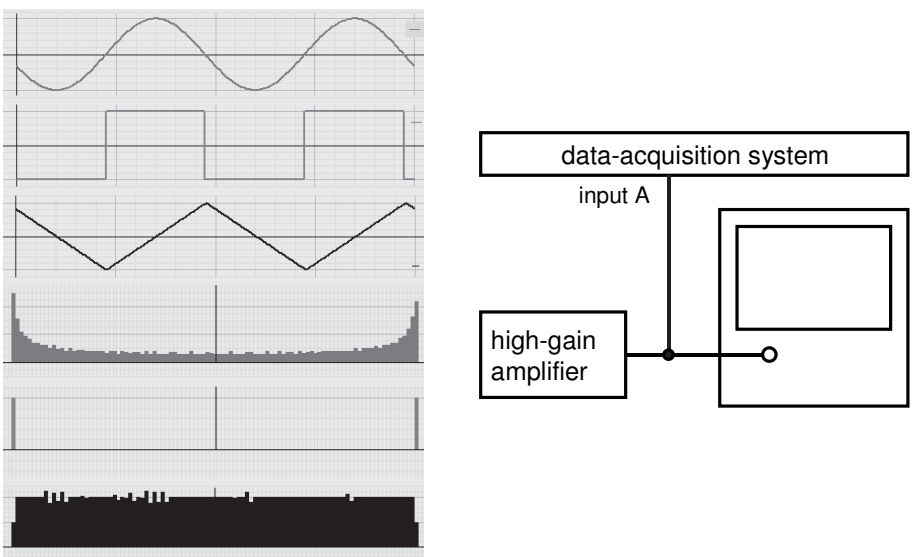

Fig. 1. Left: three waveforms and their probability density functions; right: setup for observing the probability density function of noise.

1.26. Photometric laws

Measurements of the **irradiance** versus the distance from a light source confirm the inverse squares law. The experiment is similar to that described by Kruglak (1975).

Additional equipment: *Motion sensor*, *Light sensor*, *Rotary motion sensor*, *Voltage sensor*, photodiode, light bulb.

Two fundamental laws of photometry are the following:

• The irradiance of a surface element by a point light source is inversely proportional to the square of the distance between the source and the element.

• The irradiance is proportional to the cosine of the angle between the normal to the surface and the radius vector joining the source and the surface element.

The irradiance E thus equals

$$E = I\cos\Theta/r^2, \quad (1)$$

where I is the intensity of the source. This equation is **Lambert's cosine law**, which embodies both photometric laws (Johann Heinrich Lambert, 1728–1777).

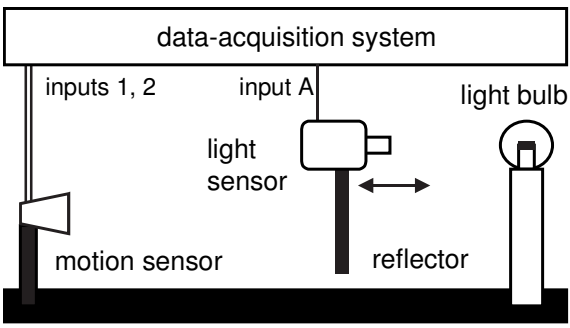

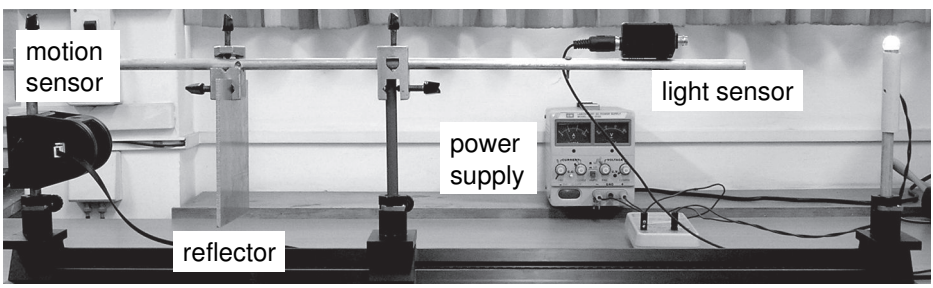

Fig. 1. Arrangement for the measurements.

The inverse squares law is confirmed by measurements, with the *Light sensor*, of the irradiance versus the distance from a light bulb measured by the *Motion sensor* (Fig. 1). The design of the light bulb should meet, as close as possible, the requirements for a point source. The *Calculate* tool calculates the distance squared, and the *Graph* tool displays the data confirming the validity of the photometric law (Fig. 2).

To determine the angular dependence of the irradiance, a photodiode is mounted on the axle of the *Rotary motion sensor*; the signal from the photodiode is displayed versus the angle of incidence.

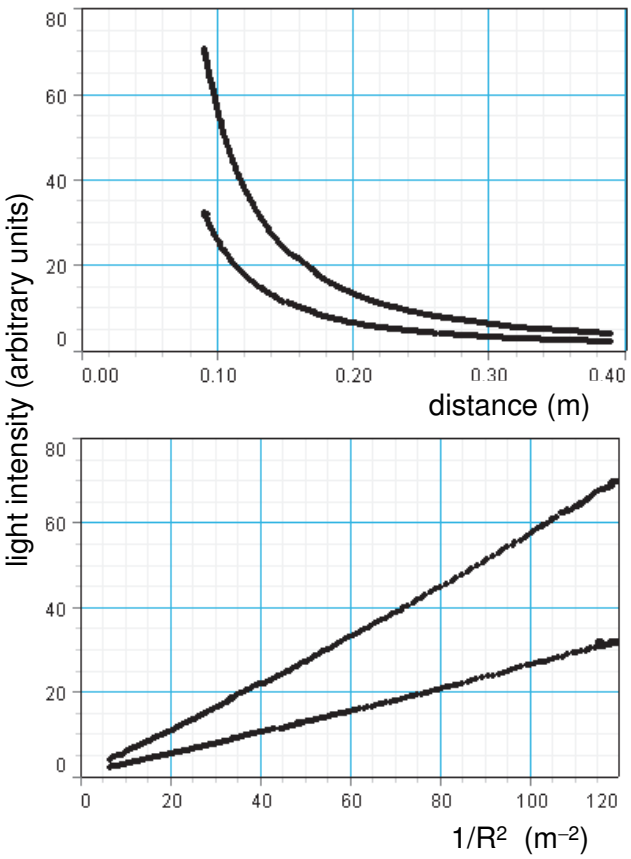

Fig. 2. Irradiance versus distance from the light bulb and versus inverse distance squared, for two voltages applied to the bulb.

1.27. Kirchhoff's rule for thermal radiation

The experiment demonstrates two phenomena related to **Kirchhoff's radiation rule:** (i) the absorption of radiation by a reflecting and a black painted surface, and (ii) the thermal radiation by different surfaces.

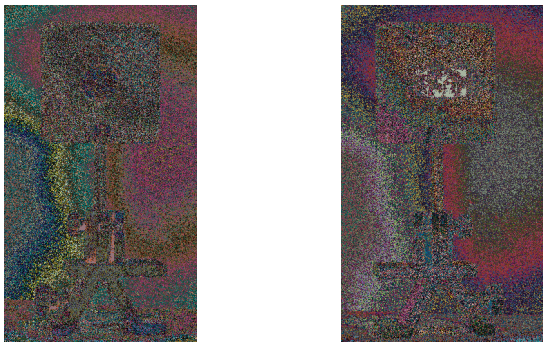

The sensor for the first demonstration: a small thermistor sandwiched between a black painted and a well reflecting metal foils.

Additional equipment: *Radiation sensor*, *Thermistor temperature sensor*, DC source, DC amplifier, lens.

When teaching thermal radiation, it is useful to consider a vacuum cavity of a certain temperature with several bodies inside (Fig. 1).

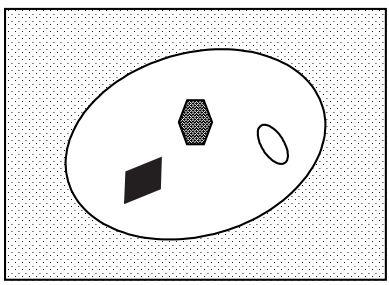

Fig. 1. Vacuum cavity with bodies inside.

The **heat exchange** between the cavity and the bodies occurs due to **thermal radiation**. Experiments show that such a system achieves a steady state, where temperatures of all the bodies are equal to that of the cavity. This means that the radiation power absorbed by each body just balances the radiation from it. From this consideration, Gustav Robert Kirchhoff (1824–1887) stated a rule bearing his name: under thermal equilibrium, the absorptance of the radiation by a body equals its emittance. The **absorptance** (dimensionless) is a

ratio of absorbed flux to incident flux. The **emittance** (dimensionless) is a ratio of flux emitted to that by a **blackbody radiator** at the same temperature and under the same spectral and geometric conditions of the measurements. Two simple experiments show the absorptance and emittance of thermal radiation by different surfaces of a body. The experiments confirm Kirchhoff's rule: the higher the absorptance, the higher the emittance. Fendley and Hutchins (1984) reported on a solar radiometer. Allen *et al* (1988) described apparatus for measuring the absorptance and emittance.

Absorptance. The first experiment shows the different absorptance of incident radiation by different surfaces of a body (Fig. 2). A small thermistor is sandwiched between two metal foils. One side of this sandwich is black painted, and its absorptance is several times higher than that of the reflecting side. A collimated light beam from an incandescent lamp irradiates the sample. The absorption of light causes an increase of the temperature of the sample, which is measured by the *Thermistor temperature sensor*. Both surfaces of the sample are exposed to the same incident radiation in turn, and the temperature rise is recorded. From the initial parts of the records, one obtains the absorptance ratio for the two surfaces. With a perfect black surface on one side, the absorptance of the other surface can be calculated.

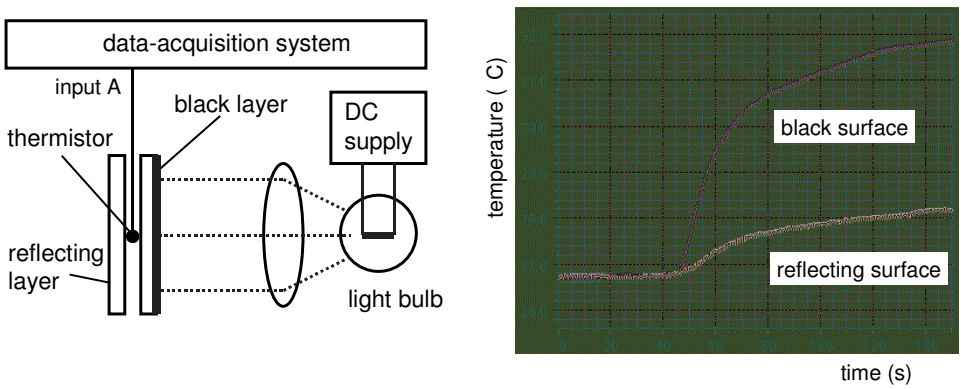

Fig. 2. Absorptance by the black surface is several times higher than that by the reflecting surface.

Radiation. The aim of the second experiment is to compare the radiation from two different surfaces of a body. A plastic can filled with hot water serves as a thermal radiator. One wall of the can is painted black, while a highly reflecting layer covers the second wall. The *Radiation sensor* (TD-8553) measures the radiation from the two different surfaces of the can (Fig. 3). A Keithley 177 multimeter amplifies the signal. The *Thermistor temperature sensor* put into an envelope measures the temperature of the water. The measurements are made during gradual cooling of the water, and the radiation is displayed as a function of the temperature.

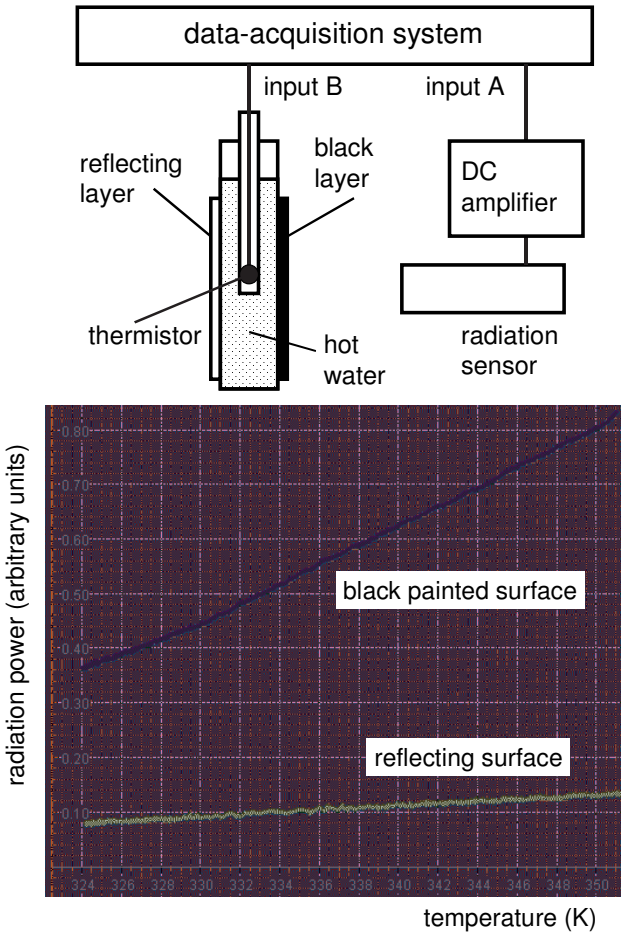

Fig. 3. The black surface radiates several times more than the reflecting surface.

The candela

The candela is the luminous intensity, in a given direction, of a source that emits monochromatic radiation of frequency 540×10^{12} hertz and that has a radiant intensity in that direction of 1/683 watt per steradian.

1.28. Malus' law

After passing two polarizers, the intensity of light depends on the relative orientation of them. The experiment follows that recommended by PASCO.

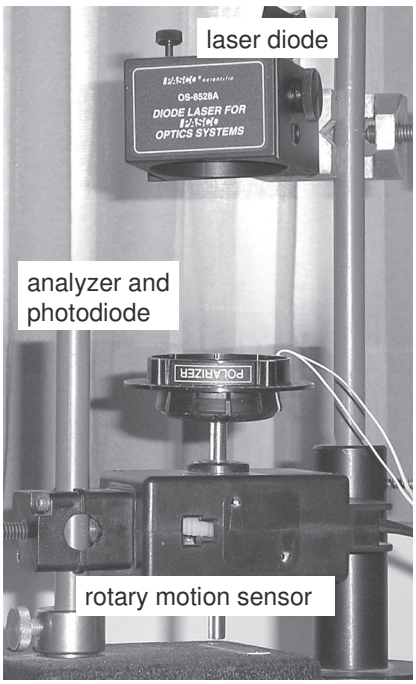

Setup for the measurements.

Additional equipment: *Rotary motion sensor*, *Voltage sensor*, laser, photodiode, analyzer.

The electromagnetic waves emitted by any common source of light, such as the Sun or a light bulb, are polarized randomly (unpolarized). This means that the electric field, being perpendicular to the direction of propagation of the wave, randomly changes its orientation. Unpolarized light becomes **polarized** when it passes a polarizer. When passing two polarizers, the intensity of light depends on the relative orientation of them. The magnitude of the electric field becomes proportional to the cosine of the angle θ between the orientations, and the light intensity I is proportional to the cosine squared:

$$I = I_0 \cos^2\theta, \tag{1}$$

where I_0 is the intensity when both polarizers have the same orientation.

This relation is known as **Malus' law** (Étienne Louis Malus, 1775–1812). Camp (1997) and Ouseph *et al* (2001) described student experiments on the polarization of light.

In our setup, the analyzer and a photodiode are placed in a cylinder box mounted on the axle of the *Rotary motion sensor* (Fig. 1). The photodiode operates in the **photovoltaic regime** (see Experiment 7.7), and a resistor of low resistance serves as a load. The voltage across this resistor, which is proportional to the short-circuit current of the photovoltaic cell, is measured by the *Voltage sensor* and displayed versus the angle of rotation. A laser diode is a source of polarized light. An incandescent light bulb could not be employed because the polarizer and analyzer used here become ineffective in the infrared region. Using the *Option/Automatic stop* tool, the data are acquired over the range of rotation angles from zero up to 360^{o} and can be displayed in polar coordinates.

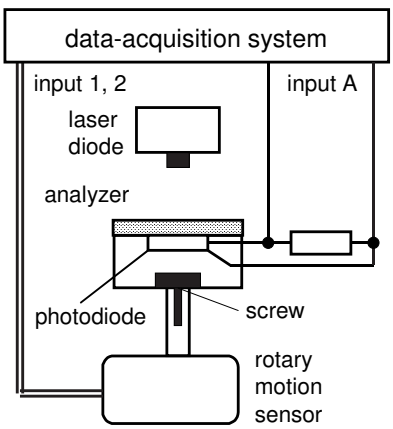

Fig. 1. Schematic of the setup.

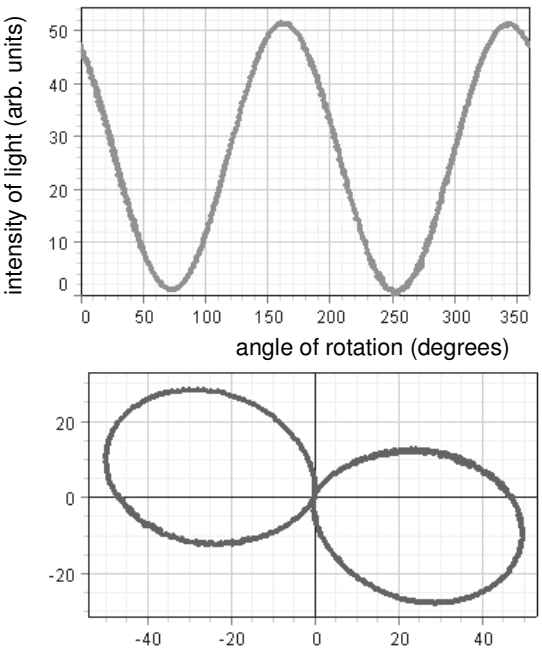

Fig. 2. Malus' law: the intensity of transmitted light is proportional to $\cos^2\theta$.

1.29. Infrared radiation

The spectrum of an incandescent light bulb is demonstrated with and without a filter blocking the infrared radiation.

Additional equipment: *Thermal radiation sensor*, *Rotary motion sensor*, *Educational spectrometer*, diffraction grating, infrared filter, incandescent light bulb, lenses.

The **infrared** part in the spectrum of an incandescent light bulb is observed using a common setup (Fig. 1) with the *Educational spectrometer* and the *Thermal radiation sensor* (TD-8553).

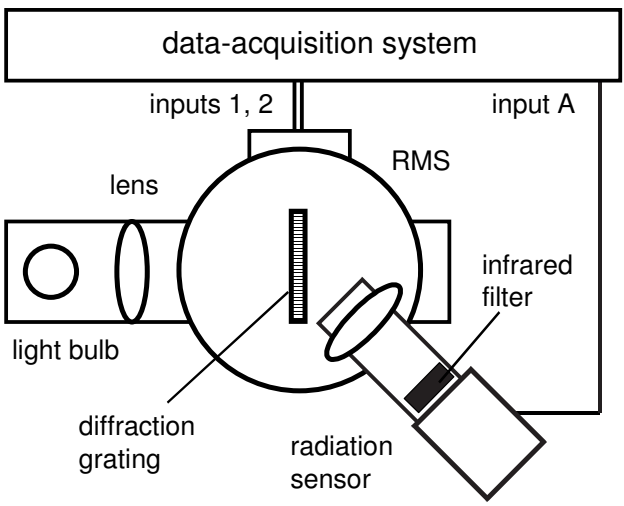

Fig. 1. Schematic of the setup. RMS–*Rotary motion sensor*.

The sensor employs a thermopile and has flat response in the range of 0.6 to 30 μm. The spectrum recorded is much broader than the visible range. An infrared filter put at the entrance of the sensor eliminates the infrared part of the spectrum, and the spectra without and with the filter can be compared (Fig. 2). The infrared part in the spectrum of a **thermal radiator** is unavoidable because the radiation obeys **Planck's law**. The spectrum of a light bulb can be compared with that of a fluorescent lamp, which is not a thermal radiator and thus free of such limitations. Fluorescent lamps are designed to produce only visible light (see Experiment 8.6). Light-emitting diodes are also free of the limitations posed by Planck's law (see Experiment 7.8).

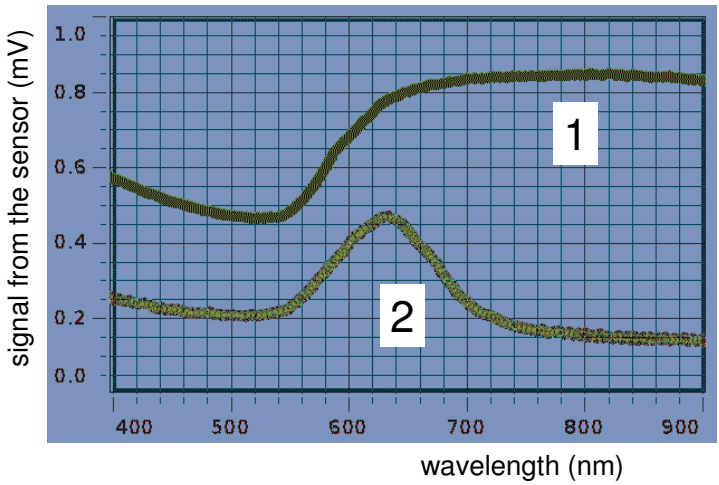

Fig. 2. Spectra of incandescent light bulb, without (1) and with (2) the infrared filter.

1.30. Irradiance and illuminance

The difference between the radiant and luminous energy is demonstrated; the latter relates to the human visual sensation.

Additional equipment: *Broad spectrum light sensor*, *Voltage sensor*, vacuum phototube, DC supply.

It is essential to distinguish between the **radiant energy** and the **luminous energy**. The first term relates to the total energy of electromagnetic radiation, while the second to the visual sensation of the human eye. The human eye is sensitive in a relatively narrow band between nearly 380 and 760 nm, and is most sensitive at 555 nm (see Experiment 8.6). Incandescent light bulbs operate at temperatures in the range 2500–3300 K, and most of the energy radiated by them is outside the response of the eye.

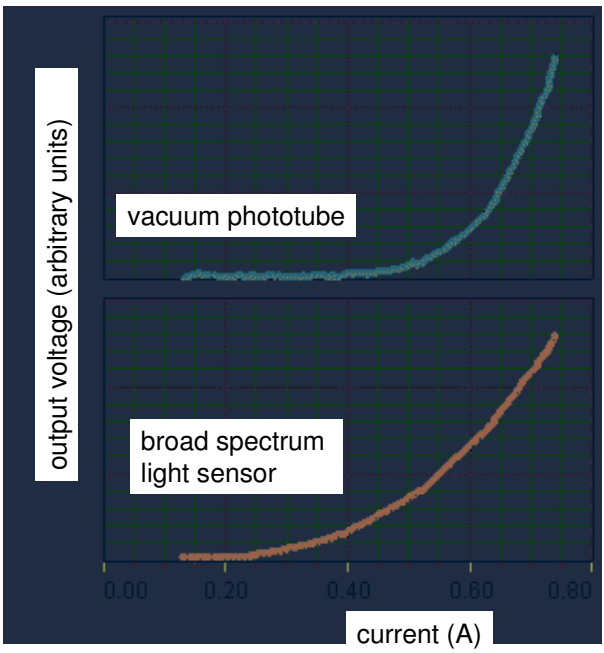

Fig. 1. Signal from a vacuum phototube and from the *Broad spectrum light sensor* viewing an incandescent light bulb, versus the heating current.

To show the difference between the radiant and luminous energy, two different light sensors measure the radiation from an incandescent light bulb connected to a DC supply. The percentage of visible light in the total radiation from the bulb increases with the filament temperature, which can be calculated

from the electrical resistance of the filament. The *Broad spectrum light sensor* is sensitive in the range of 0.3 to 10 μm and measures the total radiation, while a vacuum phototube insensitive to the infrared light serves as a sensor of visible light. The results clearly show the difference between the radiant and luminous energy (Fig. 1). While the *Broad spectrum light sensor* senses the radiation immediately after the temperature of the filament starts to increase, the phototube becomes sensitive to the radiation when the heating current becomes 0.4 A (temperature reaches nearly 1500 K).

The mole

The mole is the amount of substance of a system, which contains as many elementary entities as there are atoms in 0.012 kilogram of carbon 12; its symbol is “mol.”

When the mole is used, the elementary entities must be specified and may be atoms, molecules, ions, electrons, other particles, or specified groups of such particles.

Mechanics

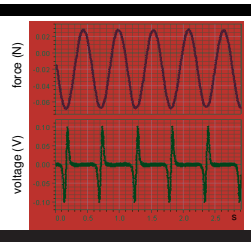
force (N)
voltage (V)
s

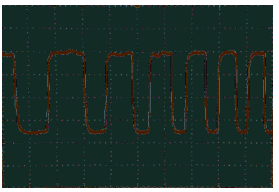

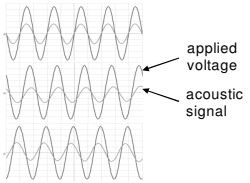
applied voltage
acoustic signal

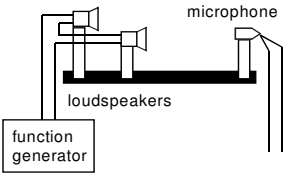
microphone
loudspeakers
function generator

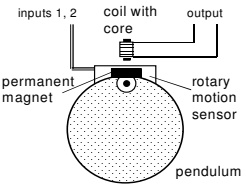
inputs 1, 2
coil with core
output
permanent magnet
rotary motion sensor
pendulum

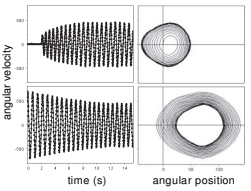
angular velocity
time (s)
angular position

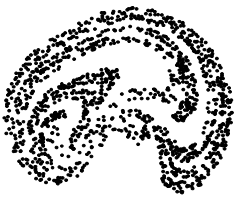

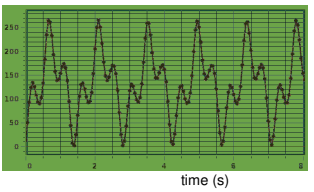
time (s)

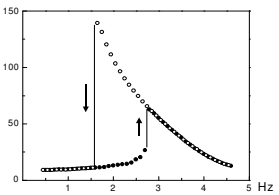
Hz

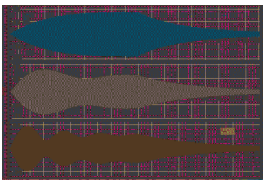

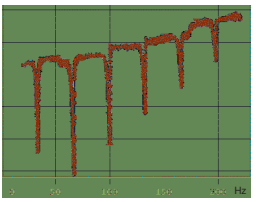
Hz

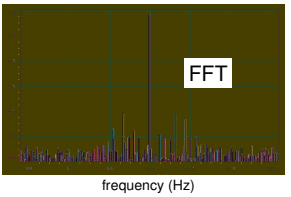
FFT
frequency (Hz)

2. Mechanics 79

2.1. Weighing a swinging pendulum

The weight of a swinging pendulum reflects the varying centripetal force due to the accelerated motion of the pendulum. The experiment follows that described by O'Connell (2002).

Additional equipment: *Force sensor*, *Voltage sensor*, simple pendulum, small magnet, coil.

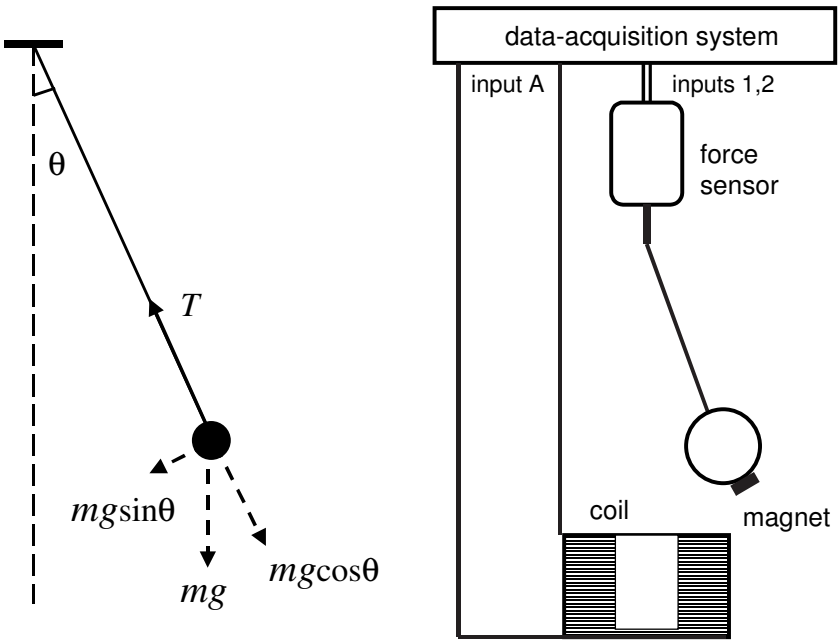

Fig. 1. Schematic of the experiment.

Weighing a swinging pendulum allows determinations of the **centripetal force** on the pendulum bob. This force reaches a maximum when the bob passes its lower position, two times a period. A steel ball and a thread form a pendulum (Fig. 1). The thread is attached to the *Force sensor*, which measures the vertical component of the tension. For small-angle oscillations, the angular position of the pendulum is

$$\theta = \theta_0 \sin\omega t, \tag{1}$$

where $\omega^2 = g/l$, l is the length of the pendulum, θ_o is the maximum angular displacement; the initial phase of the oscillations is taken zero. The angular velocity of the pendulum is $\theta' = \omega\theta_0 \cos\omega t$. The centripetal force equals

$$F = mv^2/l = ml\theta'^2, \tag{2}$$

where m is the mass of the bob, and v is its linear velocity.

The maximum kinetic energy equals the potential energy at the point of maximum deflection θ_o:

$$mv_0^2/2 = mgh = mgl\sin\theta_o. \quad (3)$$

The maximum centripetal force thus is

$$F_{max} = 2mg\sin\theta_o. \quad (4)$$

For $\theta_o = 90^o$, the maximum centripetal force is twice the weight of the bob. The tension T in the pendulum thread is the sum of the bob weight component along the thread and of the centripetal force:

$$T = ml\theta'^2 + mg\cos\theta = mg(\theta_0^2\cos^2\omega t + \cos\theta). \quad (5)$$

The vertical component of the tension equals

$$T_v = T\cos\theta = mg(\theta_0^2\cos^2\omega t\cos\theta + \cos^2\theta). \quad (6)$$

For small angles, $\cos\theta \approx 1 - \theta^2/2$. Neglecting terms involving powers of θ greater than two,

$$T_v = mg(\theta_0^2\cos^2\omega t + 1 - \theta^2). \quad (7)$$

At the lower position of the pendulum ($\theta = 0$, $\omega t = 0$),

$$T_v = mg(1 + \theta_0^2), \quad (8)$$

while at the upper position ($\theta = \theta_0$, $\omega t = \pi/2$),

$$T_v = mg(1 - \theta_0^2). \quad (9)$$

For small-angle oscillations, the weight measured by the *Force sensor* oscillates with an amplitude $\Delta T_v = mg\theta_0^2$; the frequency of the oscillations is 2ω. In our setup, m = 45 g, and l = 30 cm. The maximum displacement of the pendulum is determined with a scale positioned behind the pendulum. A small permanent magnet attached to the bob and a coil positioned under the pendulum serve for detecting the instants when the pendulum passes its lower position. The voltage induced in the coil is measured with the *Voltage sensor* and displayed by the *Graph* tool, along with the force measured by the *Force sensor* (Fig. 2). It is seen that the maximum force is reached when the bob passes its lower position. The initial weight of the pendulum is excluded using the *Tare* button of the *Force sensor*. From the measurements, the maximum kinetic energy of the pendulum, $mv_0^2/2$, is determined through $\Delta T_v = mv_0^2/l$, so that $mv_0^2/2 = l\Delta T_v/2$. This kinetic energy can be compared with the maximum potential energy of the pendulum, $mgl\sin\theta_0$.

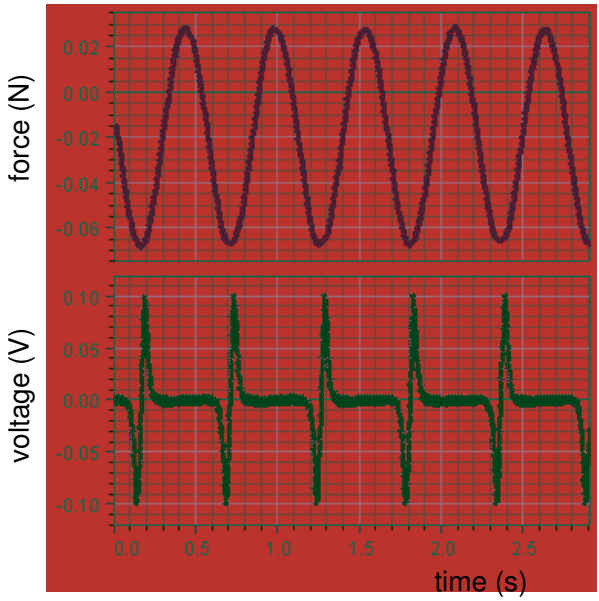

Fig. 2. Data from the *Force sensor*, and voltage induced in the coil.

2.2. Free fall

The fall of a calibrated picket fence is monitored during the initial period of the motion. The experiment follows that recommended by PASCO.

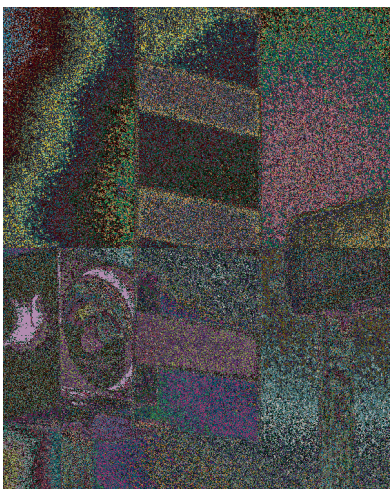

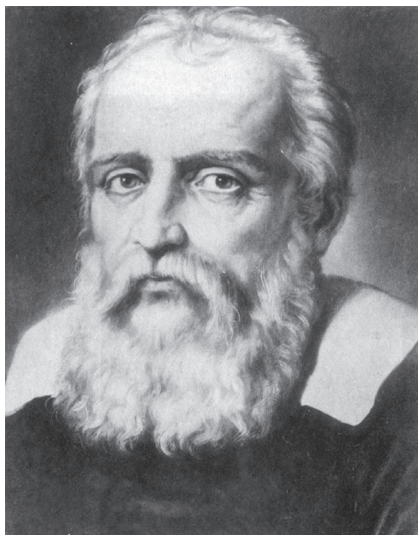

AIP Emilio Segrè Visual Archives,
E. Scott Barr Collection
Galileo Galilei (1564–1642)

Additional equipment: *Light sensor*, laser diode, calibrated picket fence.

Usually, free-fall experiments are aimed at the determination of the **acceleration of gravity**. Oliver and Pirie (1969) observed the free fall of a steel ball. Lindemuth (1971) and Walton (1974) determined the effect of air resistance on falling balls. Ferlen (1974) described a release mechanism for the free fall experiment. Blackburn and Koenig (1976) replaced optical position sensors with electrical contact switches and used an integrated-circuit timer with digital readout; the time resolution became about 0.1 ms. With an apparatus employing free fall of mercury drops, Manche (1979) achieved 0.2% accuracy of the measurements. Nelson (1981) has shown that the drag and buoyancy of air produce systematic errors that are not negligible. By taking these factors into account, the error in the measurements of g were reduced to about 0.035%. Guercio and Zanetti (1987) observed bouncing of a rubber ball. Rueckner and Titcomb (1987) described a free-fall experiment providing an overall accuracy of 0.022%. Using sphere samples, the authors have shown that the results obtained depend on the quantity ρR, the product of the density and radius of the falling sphere. The plot of the results for various spheres versus $1/\rho R$ is a straight

line intersecting the Y-axis at the correct g value. Bunker (1991) achieved accuracy better than 0.1%. Wick and Ruddick (1999) have taken into account the effects of both buoyancy and drag and reduced the error to about 0.01%. Garg *et al* (2007) took into account the contributions of buoyancy and air resistance. Terzella *et al* (2008) photographed the trace of free fall of an assembly containing a light emitting diode flashing at 30 Hz.

Fall of a picket fence. The free fall of a calibrated picket fence is monitored with a laser diode and the *Light sensor* (Fig. 1). The picket fence consists of subsequent opaque and transparent portions, 2 and 3 cm long. The measurements are made during the first 0.2 s of the fall. The influence of the air drag is therefore small.

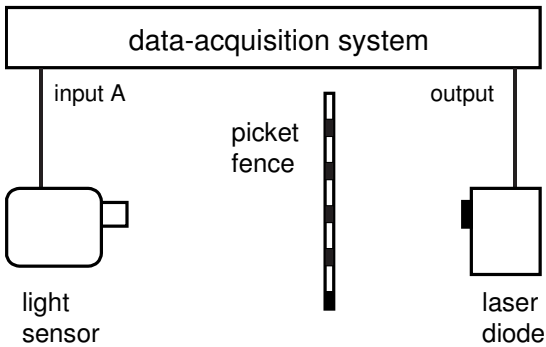

Fig. 1. Arrangement for monitoring free fall of a calibrated fence.

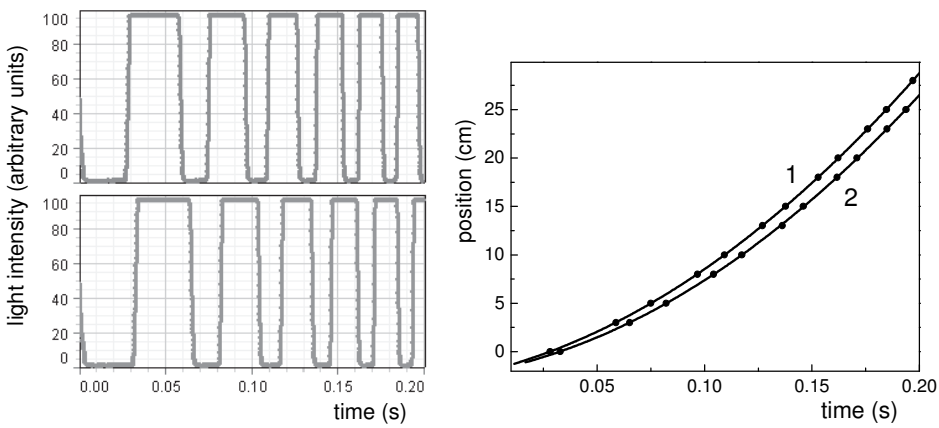

Fig. 2. Example of data and quadratic fits of the distance versus time. The data (2) are obtained with an additional weight.

The following equations govern the motion of the fence:

$$v = v_0 + gt, \tag{1}$$

$$s = v_0 t + gt^2/2, \quad (2)$$

where v_0 is the velocity at the instant the data acquisition starts.

The measurement begins automatically when the intensity of light measured by the *Light sensor* achieves a preset value. From the data (Fig. 2), the time of the subsequent 2 and 3 cm displacements of the fence are taken at the half of the amplitude of the pulses. Then one builds a graph of the distance versus time and fits it by quadratic polynomial. The quadratic term in the polynomial is $gt^2/2$, regardless of the initial velocity of the picket fence. With a weight attached to the fence, the results become closer to the correct g value.

Experiment with DSO. Similar results are available with a digital storage oscilloscope (DSO). The DSO displays the signal from the photodiode versus time (Fig. 3). The measurement reduces to determinations of instants corresponding to the vertical lines on the screen. The *V bars* tool provided by the DSO is used for this aim. The first vertical line is taken as corresponding to zeroes of the time and of the position. The position versus time is approximated by a quadratic polynomial using extra software. The accuracy of the results is nearly the same as with the PASCO data-acquisition system.

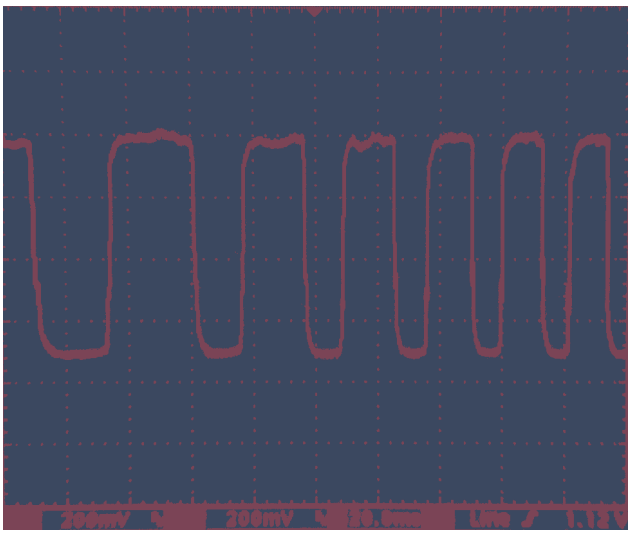

Fig. 3. Free fall experiment with DSO: example of data for calculating the acceleration of free fall.

2.3. Sound waves in gases

The speed of sound in gases and wind velocity are determined.

1. Speed of sound in air, phase measurements

The voltage applied to a loudspeaker and that from a microphone positioned at a variable distance provide two phase-shifted signals. The phase shift depends on the distance between the loudspeaker and the microphone, the velocity of sound c, and the frequency of sound f. The two signals are fed to X- and Y-inputs of an oscilloscope, and a **Lissajous pattern** is seen on its screen. The microphone is positioned to obtain a zero and an 180° phase shifts between the signals, so the Lissajous pattern becomes a straight line.

Additional equipment: *Sound sensor*, loudspeaker.

The setup is very simple (Fig. 1). A loudspeaker is connected to the output of the *Signal generator*. The *Sound sensor* can be positioned at various distances from the loudspeaker along a scale. When changing its position, the Lissajous figure is observed using the *Scope* tool. A plot of the microphone position versus the number of wavelengths is a straight line with a slope equal to the **wavelength**. The phase measurement is a very accurate technique for determining the velocity of sound. However, this is true only when reflections of sound from walls and floor cause no significant contributions to the signal from the microphone. To avoid this effect, the loudspeaker and microphone can be placed in a box with inner walls covered with a sound absorbing material. The speed of sound equals $c = f\lambda$.

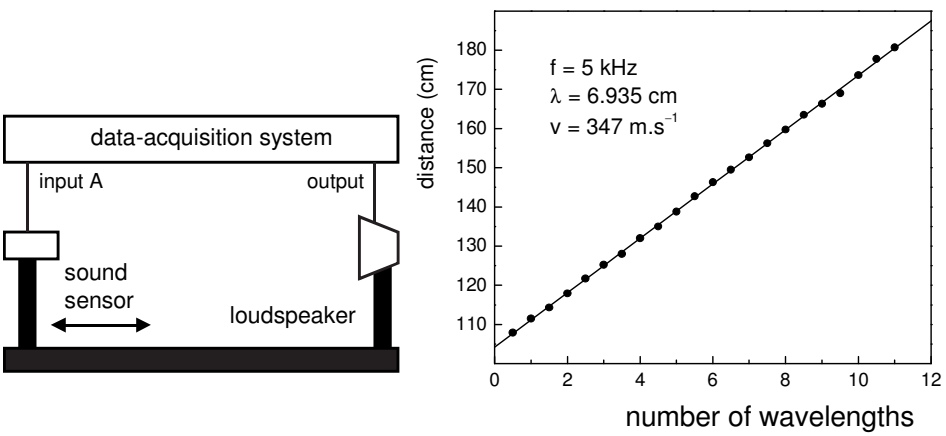

Fig. 1. Schematic of the setup, and graph for determining the sound wavelength.

Measurements of the speed of sound in gases were reported by Wintle (1963); Biehl (1989); Winters (1993); Gagne (1996); Kettler (1997); Potter (2003); Berg and Brill (2005); Tucholski (2009); Bacon (2012). By measuring the speed of sound in a binary mixture of gases, Ashkenazi and Polturak (1988) determined the mutual diffusion of one gas into another.

Wind velocity. The phase measurement technique can be used to determine the velocity of wind produced by a fan. The experiment is similar to those described by Donnelly and Bechard (1986) and Hall (1987b). The wind is directed along or opposite to the path of the sound waves. Before switching on the fan, the *Sound sensor* is positioned to obtain a zero phase shift between the voltage applied to the loudspeaker and the acoustic signal. The frequency of sound is 5 kHz. The distance between the loudspeaker and the sensor thus equals, say, $l = n\lambda = nc/f$. The *Scope* tool displays both signals.

After switching on the fan, a phase shift arises between the signals. This is due to a change of the effective velocity of sound: now it becomes $c \pm u$, where u is the velocity of the air stream. The time dependence of the signals displayed together allows one to see the sign of the phase shift (Fig. 2). To determine the velocity of wind more precisely, it is better to use the Lissajous patterns. The *Sound sensor* is positioned to obtain a straight line on the screen. After switching on the fan, the line transforms into an ellipse. To restore the straight line on the screen, it is sufficient to change the distance between the *Sound sensor* and the loudspeaker to $l_1 = n\lambda_1 = n(c \pm u)/f$. Hence,

$$\Delta l/l = u/c. \tag{1}$$

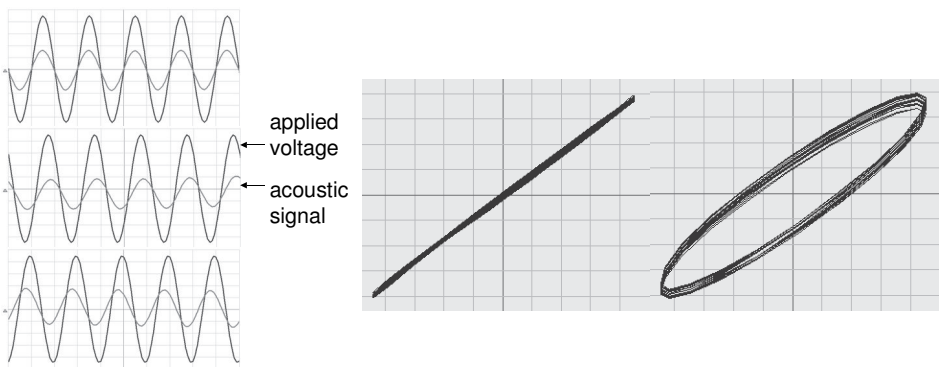

Fig. 2. The signals showing the phase shifts caused by wind directed along or opposite to the path of the sound waves, and Lissajous patterns before and after switching on the fan.

2. Speed of sound in different gases

With the *Motion sensor*, it is easy to measure the velocity of sound in different gases. The experiment follows that described by Pettersen (2002).

Additional equipment: *Motion sensor*, cardboard tube, cylinder with helium gas.

The *Motion sensor* is based on measurements of the time interval needed to ultrasonic pulses to return from the object. The sensor is positioned at the lower end of a cardboard tube (Fig. 3). A small opening near the closed upper end of the tube serves for replacing air in the tube by a gas taken from a high-pressure cylinder. When air fills the tube, the sensor measures the distance to the closed end. Along with the distance, the *Motion sensor* provides the time interval data. *DataStudio* calculates the velocity of sound of the gas in the tube and displays it versus time. The measurements are started after filling the tube by helium. Then air gradually replaces helium in the tube.

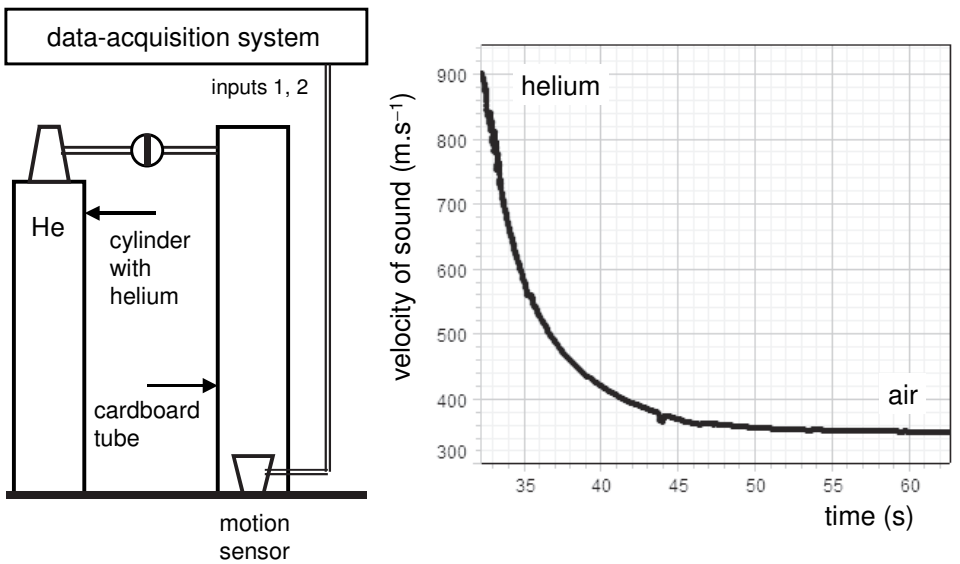

Fig. 3. Schematic of the setup and measurement data while air replaces helium in the tube.

2.4. Interference of sound waves

It is easy to demonstrate the interference of sound waves.

Equipment: function generator, oscilloscope, two loudspeakers, microphone, optics bench.

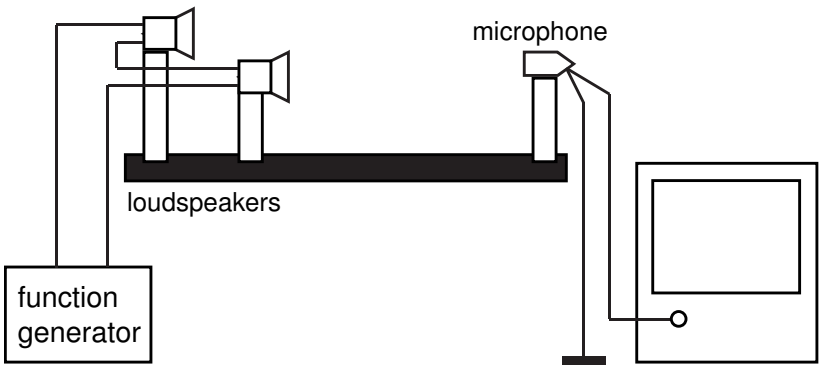

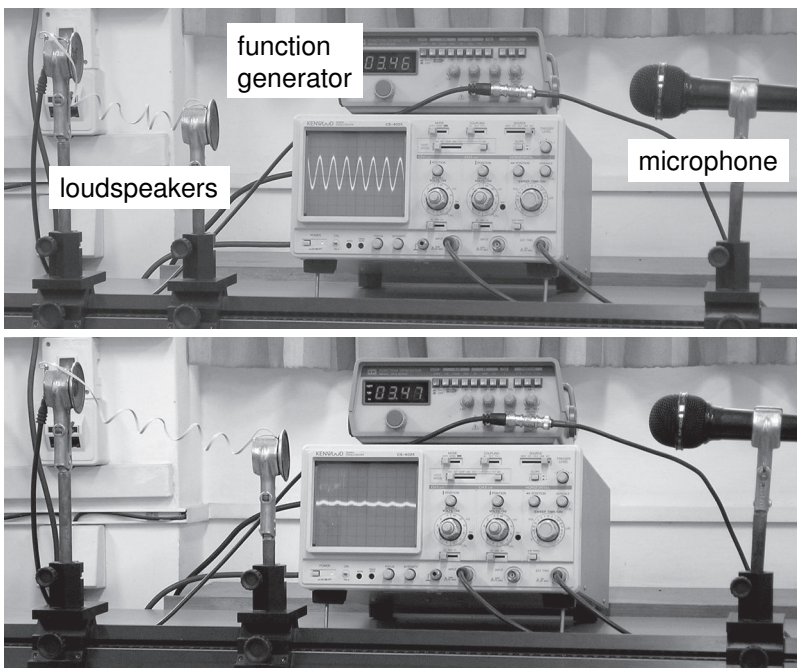

Fig. 1. Setup for demonstrating the interference of sound waves.

This demonstration is well known (Portis and Young 1971; Blum 1974). Two loudspeakers are connected in series to an audio oscillator (Fig. 1). The frequency is set in the range of 2 to 5 kHz. The loudspeakers and a microphone are positioned on an optics bench.

The microphone connected to the Y input of an oscilloscope senses the resulting amplitude of two sound waves produced by the loudspeakers. One of the loudspeakers is fixed, and the second is movable along the bench. It is easy to find a position of the second loudspeaker, where the sound waves reaching the microphone are in phase or in opposition. This is seen on the screen of the oscilloscope. The generator synchronizes the oscilloscope, so that the synchronization does not depend on the signal level. When minimum resulting amplitude is achieved, one can reduce it to about zero by slightly turning one of the loudspeakers. It is easy to determine the wavelength of sound and thus the velocity of sound in air, but such measurements are not accurate due to reflections of sound waves from the walls and equipment.

2.5. Driven physical pendulum

A simple driven physical pendulum is proposed. The magnetic braking controls the decay. With the *850 Interface* and *Capstone* software, the experiments are fully automated (Kraftmakher 2005b, 2013c).

The pendulum is a device representing many features of oscillation phenomena, and many papers are devoted to it. Fulcher and Davis (1976) studied a pendulum theoretically and experimentally. Wilkening and Hesse (1981) proposed a pendulum for demonstrating the phenomenon of magnetic induction. A coil oscillating between poles of a horseshoe permanent magnet forms the mass of the pendulum. A recorder or a galvanometer displays the EMF induced in the coil. Zilio (1982) reported on measurements and analysis of large-angle pendulum oscillations. The angle was measured with a rotary potentiometer, to which the rod of the pendulum was attached, and a plotter. Quist (1983) used a microcomputer to measure the period of a simple pendulum versus the oscillation amplitude. Nicklin and Rafert (1984) used a rigid pendulum attached to a rotary potentiometer for recording the pendulum motion by means of a computer equipped with an analog-to-digital converter. Small- and large-angle motion, and damping can be readily studied for various types of pendulum. The authors pointed out that while damping proportional to the velocity may be a good assumption for air damping at low velocities, it evidently is invalid for the more dominant damping from the potentiometer drag. Nelson and Olsson (1986) presented a discussion of the corrections needed to accurately measure the acceleration of gravity with a plane pendulum. Basano and Ottonello (1991) described a digital pendulum. Using this apparatus, Basano *et al* (1996) considered the ripples in the energy of a damped oscillator. Siahmakoun *et al* (1997) studied the dynamics of a sinusoidally driven pendulum in a repulsive magnetic field theoretically and experimentally. Amplitude jumps, hysteresis, and bistable states were observed. Fox (1971), Squire (1986) and Wang *et al* (2002) observed oscillations of a pendulum with one of three damping effects: friction not depending on the velocity (sliding friction), linear dependence on the velocity (eddy currents in a metal plate), and quadratic dependence on the velocity (air friction).

For other experiments with pendulums, see Lapidus (1970); Schery (1976); Hall and Shea (1977); Simon and Riesz (1979); Hall (1981); Yurke (1984); Eckstein and Fekete (1991); Ochoa and Kolp (1997); Peters (1999); Lewowski and Woźniak (2002); LoPresto and Holody (2003); Parwani (2004); Coullet *et al* (2005); Ng and Ang (2005); Jai and Boisgard (2007); Gintautas and Hübler (2009); Mungan and Lipscombe (2013).

Theoretical background. For a mathematical pendulum with friction, the motion equation is

$$ma = -kx - \lambda v, \qquad \text{or} \qquad (1a)$$

$$x'' + (\lambda/m)x' + (k/m)x = 0, \tag{1b}$$

where m is the mass, a is the acceleration, x is the displacement, v is the velocity, k and λ are coefficients of proportionality, $x' = v = \mathrm{d}x/\mathrm{d}t$, and $x'' = \mathrm{d}^2x/\mathrm{d}t^2$. The solution to this equation describing free oscillations is

$$x = A\exp(-\delta t)\cos(\Omega t + \varphi_1), \tag{2}$$

where A and φ_1 depend on the initial conditions. The natural frequency of the system is $\omega_0 = (k/m)^{1/2} = (g/l)^{1/2}$, the decay of free oscillations is governed by the decay constant $\delta = \lambda/2m$, and the angular frequency Ω is somewhat lower than ω_0: $\Omega^2 = \omega_0^2 - \delta^2$.

The **transient process** after application of a periodic driving force deserves special consideration. Whenever forced oscillations start, a process occurs leading to steady oscillations. This transient process is caused by the superposition of forced and free oscillations. Landau and Lifshitz (1982) and Pippard (1989) considered the problem in detail, and this analysis is partly reproduced here. For a **driven mathematical pendulum**, the motion equation is

$$ma = -kx - \lambda v + F_0\cos\omega t, \qquad \text{or} \tag{3a}$$

$$x'' + (\lambda/m)x' + (k/m)x = (F_0/m)\cos\omega t, \tag{3b}$$

where F_0 and ω are the amplitude and the frequency of the driving force.

The general solution to such an equation is the sum of any solution to the equation and of the general solution of the equation with a zero right-hand side. The solution thus consists of two terms, the first term represents the steady forced oscillations, and the second the free oscillations:

$$x = B\cos(\omega_1 t + \varphi) + A\exp(-\delta t)\cos(\Omega t + \varphi_1), \tag{4}$$

where A, B, φ and φ_1 depend on the initial conditions.

Immediately after the periodic driving force is applied, the amplitude of the oscillations, which was initially zero, grows gradually. The reason is that free oscillations also arise in the system. Initially, they have the same amplitude as the forced oscillations but an opposite phase. When the frequencies of both oscillations are equal, the amplitude of the resultant oscillation grows monotonically. When the frequencies ω and Ω differ considerably, the two terms beat rapidly, and the resultant oscillation has an amplitude changing within $x_0 \pm x_0\exp(-\delta t)$, where x_0 is the steady amplitude of the forced oscillations. Without damping ($\delta = 0$), the resultant oscillation takes the form

$$x = 2x_0\sin\omega^* t\, \sin\Delta t, \tag{5}$$

where $\omega^* = \frac{1}{2}(\omega + \Omega)$, and $\Delta = \frac{1}{2}|\omega - \Omega|$.

When the frequency of the driving force is somewhat different from the frequency of the free oscillations, many beats are observable during the transient process. The changes in the amplitude of the resultant oscillation gradually decrease, reflecting the decay of the free oscillations. Clearly, the transient process is as long as the decay of the free oscillations.

The pendulum. The pendulum is an aluminum disc, 20 cm in diameter and 3 mm thick. Its fixed point is 5 mm from the edge (Fig. 1). The pendulum is attached to the axle of the *Rotary motion sensor*. A cylindrical permanent magnet is glued to the disc at this point in a horizontal position. A 800-turn driving coil (SF-8611) with a magnetic core is placed above the magnet and connected the *Output 1*. The AC magnetic field of the coil forces the permanent magnet to oscillate and thus drives the pendulum. The *Rotary motion sensor* measures the angular position of the pendulum, and the *Graph* tool displays the oscillations. The angular resolution of the sensor is 0.25^{o}. A strong permanent magnet is used for damping the oscillations. Its magnetic field is directed perpendicular to the disc, and the interaction of the induced eddy currents with the field leads to magnetic braking, according to Lenz's law. With magnetic braking, the decay time of the pendulum can be varied over a wide range.

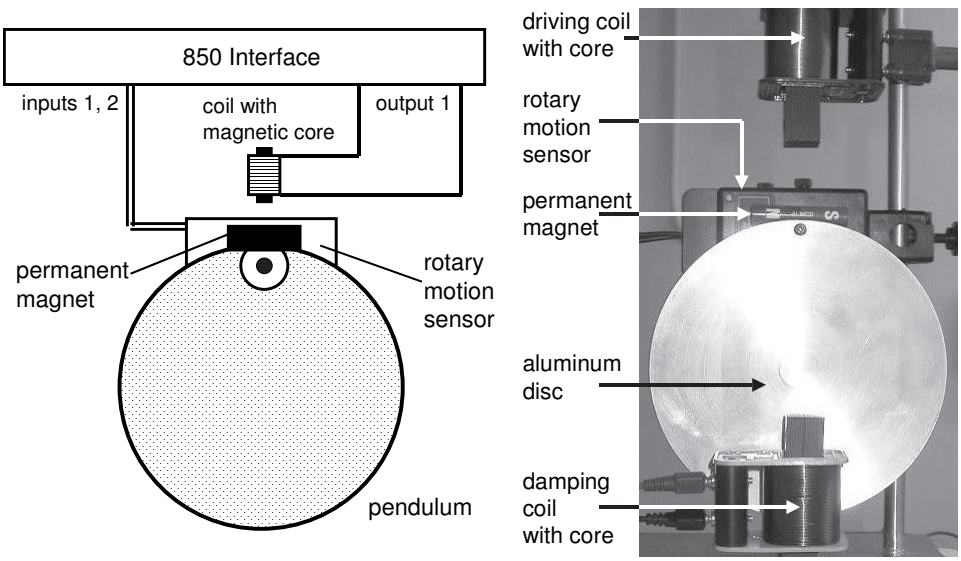

Fig. 1. The driven physical pendulum.

1. Free oscillations

The experiment includes the following items: (i) the magnetic damping; (ii) the period versus oscillation amplitude; and (iii) the phase portrait of free oscillations.

Additional equipment: *Rotary motion sensor*, driven physical pendulum, permanent magnet, magnetic core, coil.

For demonstrating **free oscillations**, it is sufficient to start the data acquisition and then to displace and release the pendulum. The decay of the oscillations depends on the magnetic damping (Fig. 2).

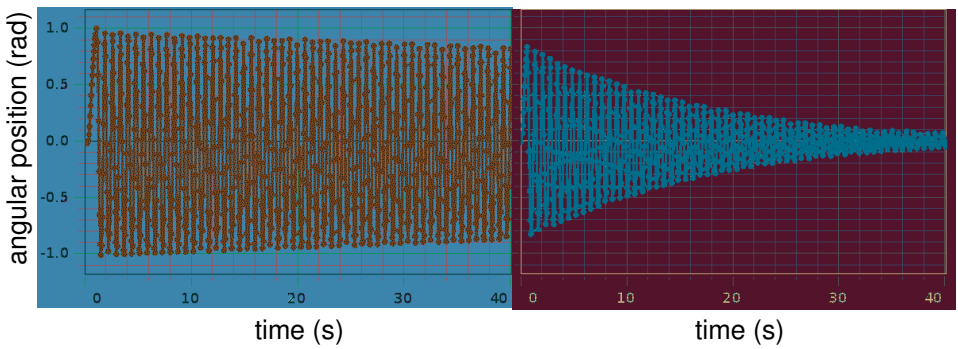

Fig. 2. Free oscillations without and with magnetic damping.

Period versus oscillation amplitude. *Capstone* calculates oscillation amplitudes in definite time intervals with the *Calculator*/*Special*/*peakamp* tool. The tool calculates half the distance between the maximum and minimum values in every time interval. An expression <peakamp(1,)> appears in the dialog box. The number (1) is the time range, over which the function is operating. Since the period of the pendulum oscillations is less than 1 s, this time (1 s) is quite acceptable. The place after the number is reserved for indicating the source of data chosen from the dialog box. Here, the source is the *Angle* measured by the *Rotary motion sensor*. The expression in the dialog box becomes *Calc1* = <peakamp(1,[Angle(rad)])>. The *Calculator*/*Special*/*period* tool calculates the oscillation period. An expression <period(10,10,1,[Angle(rad)])> appears in the dialog box. The two first numbers (10,10) are the thresholds to finding the peaks and valleys in the data source. When they are equal to 10, the function performs the searches in the top and bottom 10% of the data range; in our case, these values are quite adequate. The third number (1) is the time range, over which the function is operating; this time (1 s) is also acceptable. During the decay of free oscillations, *Capstone* calculates the oscillation amplitude, and smoothed values are displayed versus the period of free oscillations (Fig. 3).

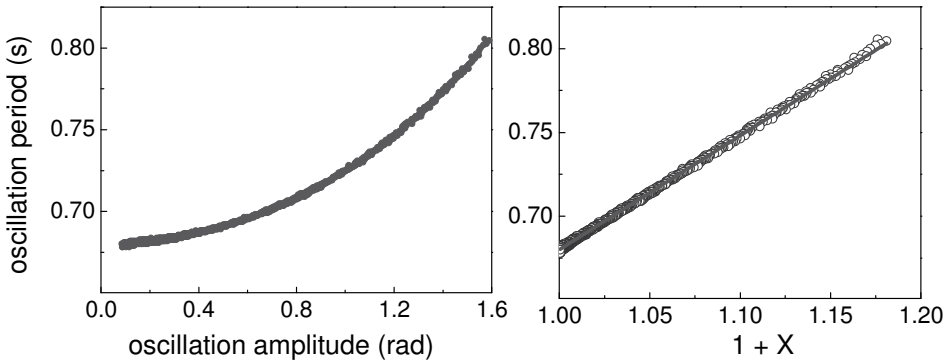

Fig 3. Period of free oscillations versus their amplitude and versus quantity $1 + X$.

The period T of free oscillations increases with the oscillation amplitude. The solution to the motion equation of a pendulum involves elliptic integral of the first kind. A series presentation for the period T can be given in terms of the oscillation amplitude θ_m or of the quantity $\alpha = \sin(\frac{1}{2}\theta_m)$ (Fulcher and Davis 1976; Thornton and Marion 2004):

$$T = T_0(1 + X), \tag{6}$$

where T_0 is the small-angle oscillation period, and X can be taken as $(1/16)\theta_m^2 + (11/3072)\theta_m^4 + \ldots$ or $(1/4)\alpha^2 + (9/64)\alpha^4 + (25/256)\alpha^6 \ldots$.

For both approximations, the plot of experimental T values versus $1 + X$ is a proportional function with $T_0 = 0.680$ s.

The *Rotary motion sensor* provides also data on the angular velocity, so the phase portrait of free oscillations is readily available (Fig. 4).

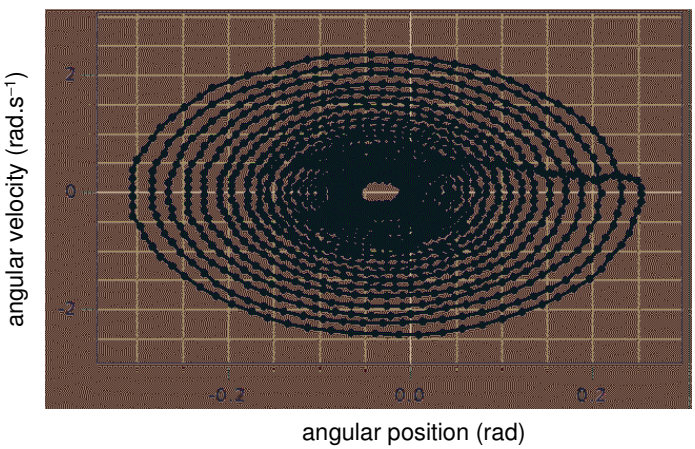

Fig. 4. Phase portrait of free oscillations with magnetic damping, smoothed data.

2. Forced oscillations and transients

During a run, *Capstone* displays the resonance curves of the pendulum. The transients and the phase shift between the driving force and pendulum position are demonstrated.

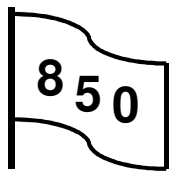

Additional equipment: the driven physical pendulum.

Resonance curves. To obtain data for graphing resonance curves of a pendulum, every measurement requires a long time until steady oscillations are established. The magnetic damping markedly shortens this time, but a real breakthrough is a completely automated recording of the resonance curves. The *Output 1* operating in the sweep mode drives the pendulum; the frequency data are stored and used to plot the resonance curves. The scan rate is chosen accordingly to the decay of the pendulum controlled by the magnetic damping; with a too fast scan, transients are seen in the resonance curve. In our case, a 0.2 Hz frequency interval, from 1.37 to 1.57 Hz, is scanned during 400 s. The *Output 1* operates in the *Auto* mode: it starts to create the output voltage of continuously varying frequency immediately after starting a run. The sample rate is 20 Hz.

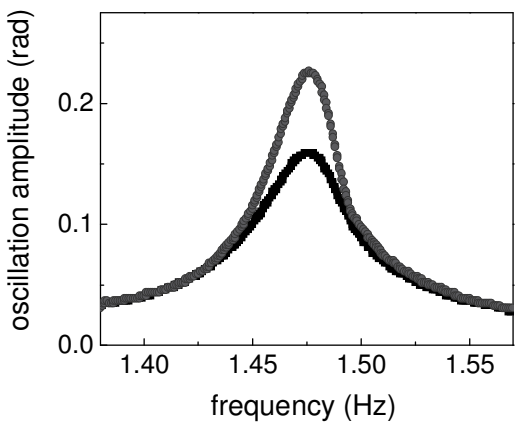

Fig. 5. Resonance curves for various decay constants.

Capstone determines the oscillation amplitude like in the preceding measurement. For small oscillations of the pendulum, the angle resolution of the *Rotary motion sensor* is insufficient; therefore, smoothed values of the oscillation amplitude are used. The software displays the amplitude of forced oscillations versus frequency, so the measurements become completely automated. Two resonance curves presented correspond to different distances between the magnet and the disc. The transient process after starting the run, which lasts nearly 20 s, is not seen in the figure because the initial 0.01 Hz

frequency range is not shown in the graph (Fig. 5). The results are quite satisfactory.

Transient processes. Demonstrations of the transient oscillations give an understanding of the process, by which the steady forced oscillations are established. The demonstration clearly shows the influence of the damping of the pendulum and of the frequency of driving force (Fig. 6).

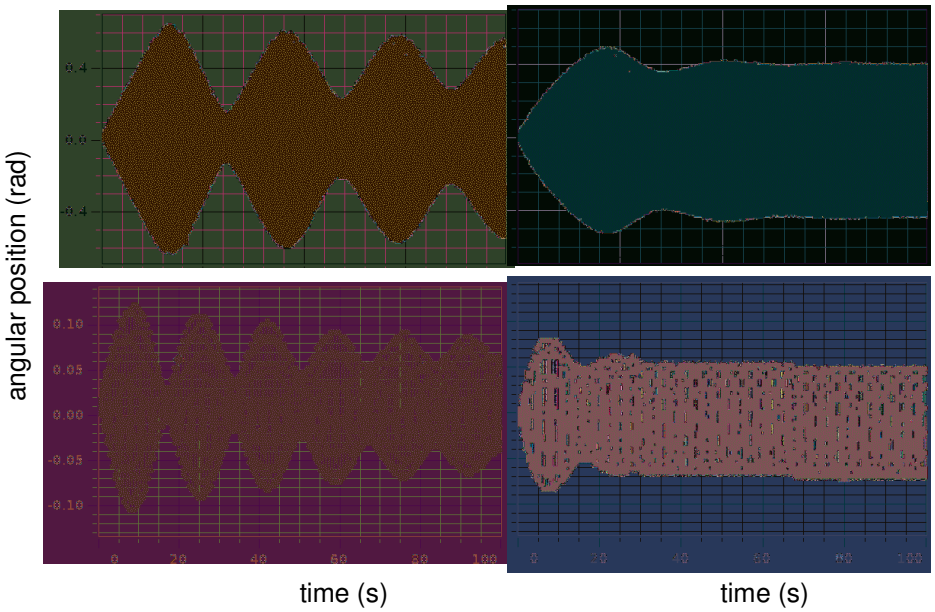

Fig. 6. The transient process for frequencies 1.46 Hz (top) and 1.41 Hz (bottom), without (left) and with (right) magnetic damping.

Phase shift between driving force and pendulum position. Another question related to the driven pendulum is the phase shift between the driving force and pendulum position. This phase shift depends on the driving frequency. It is easy to demonstrate this phenomenon by displaying the pendulum position versus the driving force. For our pendulum, the driving force is nearly proportional to the sinusoidal current in the driving coil, and this current is used to plot the graph (Fig. 7). At frequencies far below the resonance, the pendulum position should simply follow the driving force, so the oscillations are in phase with the force. With increasing the driving frequency, the oscillation lag increases up to nearly 180^{o} at frequencies far above the resonance.

The capability of automatically displaying the dependence of the period of free oscillations versus their amplitude and of resonance curves of a pendulum certainly makes the measurements more attractive. The display of the pendulum position versus the driving current can be used in classroom to demonstrate the phase shift between the two quantities.

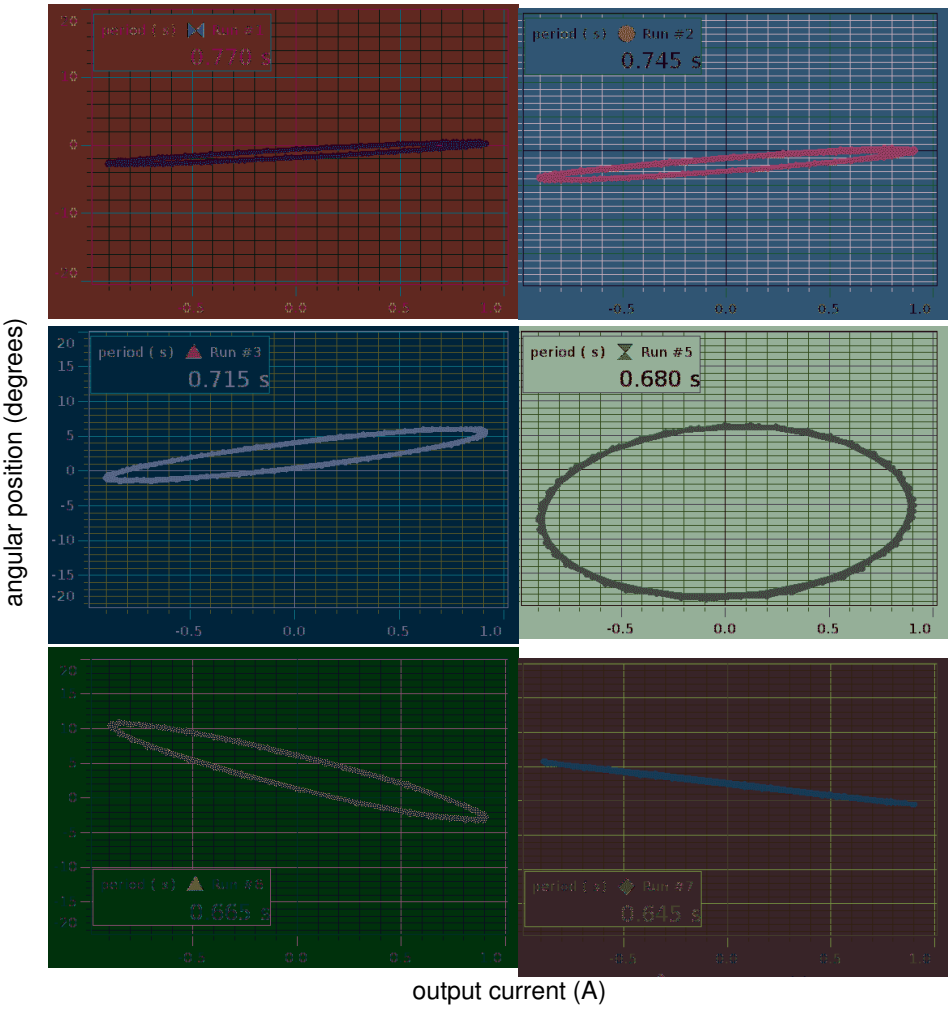

Fig. 7. Plots of pendulum position versus current in the driving coil show phase shifts between the two quantities. The oscillation periods are indicated. The maximum amplitude is seen at 0.68 s.

2.6. Nonlinear pendulum I

A magnetically controlled pendulum is used for observing nonlinear oscillations. The decay constant is modified by feedback. With high driving torques, chaotic motion is achievable (Kraftmakher 2007c).

Nonlinear oscillations and **chaos** are considered in many textbooks and papers: Moon (1987), Hilborn (1994); Baker and Gollub (1996), José and Saletan (1998). Only a small part of papers published on this subject is mentioned here. Arnold and Case (1982) considered nonlinear effects in a simple mechanical system governed by Duffing's equation. Schmidt and Childers (1984) described a magnetic pendulum for demonstrations of phase transitions. Dixon *et al* (1985) studied amplitude jumps of a nonlinear pendulum, including the motion during a jump. Grosu and Ursu (1986) described a setup for teaching linear and nonlinear oscillations, including bent tuning curves. Marega *et al* (1990) presented an electromechanical analog for Landau's theory of phase transitions. Kautz (1993) developed a classroom demonstration based on computer animation of a driven pendulum. Siahmakoun *et al* (1997) investigated the dynamics of a sinusoidally driven pendulum in a repulsive magnetic field. Regions of periodic and chaotic behavior, amplitude jumps, hysteresis and bistable states were observed. Blackburn and Baker (1998) compared commercially available chaotic pendulums. Berdahl and Vander Lugt (2001) reported on a magnetically driven chaotic pendulum. DeSerio (2003) studied nonlinear dynamics with a commercial chaotic pendulum. The pendulum was modified to determine Poincaré sections, fractal dimensions and Lyapunov exponents, and the role of the decay constant of the pendulum was shown. Laws (2004) described several experiments on linear and nonlinear oscillations, including chaotic motion. Baker (2006) considered the application of probability concepts to deterministic systems. The probability distribution of angular displacement of a pendulum was obtained for nonlinear and chaotic motion. See also Prosperetti (1976); Janssen *et al* (1983); Gatland (1991); Eckstein (1993); Ruby (1996); Sungar *et al* (2001); Sharpe and Sungar (2010).

Apparatus for teaching nonlinear oscillations should provide the following options:

- varying the **amplitude** and **frequency** of the driving force or torque;
- displaying time series of the oscillations, **phase plane** plots, **Poincaré maps**, and **Fourier spectra** and **histograms** of position and velocity;
- varying the **natural frequency** and the strength of the nonlinearity;
- changing the **decay constant** of the oscillator, preferably without changing the natural frequency;
- using low-cost components, preferably of equipment commonly available in student laboratories.

Magnetically controlled pendulum. Modifications of a magnetically controlled pendulum were described by Schmidt and Childers (1984); Marega *et al* (1990); Siahmakoun *et al* (1997); Berdahl and Vander Lugt (2001).

In our setup (Fig. 1), two similar permanent magnets are positioned on a thin aluminum rod, with a pivot attached to the axle of the *Rotary motion sensor*. Both magnets are strong ceramic magnets, 12×12×12 mm^3 in size, magnetized to about 1.2 T. The upper magnet is positioned 25 mm above the pivot, and the lower magnet is 75 mm below. The axis of the upper magnetic dipole is aligned horizontally. The lower magnet can be aligned horizontally (pendulum with feedback) or vertically (other experiments). The magnets are tightly put in plastic chutes, which makes easy to change their orientation. An 800-turn coil (SF-8611) with a magnetic core is positioned above the upper magnet. The interaction of its magnetic field with the magnet drives the pendulum. A 320-turn coil, about 14 cm in diameter, can be positioned beneath the pendulum and fed by a DC supply. The magnetic field of this coil provides attractive or repulsive action on the lower magnet aligned vertically and thus modifies the restoring torque and its angular dependence.

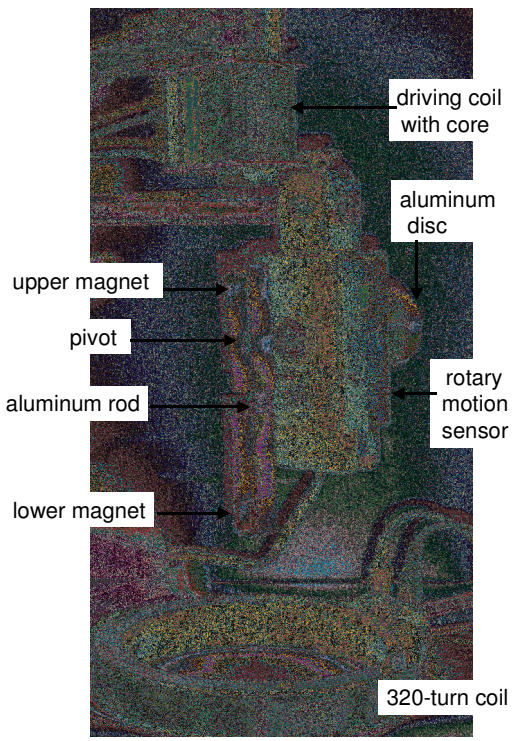

Fig. 1. The magnetically controlled pendulum.

An aluminum disc is attached to the other end of the axle of the *Rotary motion sensor* and subjected to magnetic field of another permanent magnet. The

position of this magnet controls the decay constant of the pendulum. It is worth remembering that the driving coil connected to a source of low output resistance also provides damping action on a moving magnet. Therefore, the coil should be removed or disconnected when observing free oscillations of the pendulum. It is possible to tilt the pendulum and thus to decrease the restoring torque due to gravity (the so-called variable *g* pendulum).

The external magnetic fields may serve for driving the pendulum and/or for modifying the restoring torque. Properly oriented magnets and current-carrying coils meet this purpose. The potential energy U of a magnetic dipole $\boldsymbol{m}$ in a field $\boldsymbol{B}$ equals

$$U = -\boldsymbol{mB}. \tag{1}$$

This equation shows the possibilities of controlling the pendulum. Since the magnetic fields produced by coils can be calculated or measured, the forces and torques acting on the pendulum can be determined. For qualitative determinations of the action of an external magnetic field, a magnetic dipole can be considered as two separated magnetic charges. With this approach recommended by Griffiths (1999), one can qualitatively predict the driving torque and changes in the restoring torque of the pendulum. In our case, the magnetic fields controlling the pendulum are inhomogeneous, and the properties of the pendulum strongly depend on the arrangement of the setup.

The restoring and driving torques can be made strongly dependent on the angular position of the pendulum. The nonlinearity of the driving torque depends on the gap between the magnetic core of the driving coil and the upper magnet, while the nonlinearity of the restoring torque is controlled by the DC magnetic field of the 320-turn coil. The two actions can be applied independently. In the experiments presented, only one source of nonlinearity is chosen. The motion equation for the pendulum can be presented only in a very general form reflecting the two nonlinearities:

$$\theta'' + \gamma\theta' + \omega_0^2(\theta)\theta = F(\theta)\sin\omega t, \tag{2}$$

where θ is the angular position, $\gamma\theta'$ is the damping term, $\omega_0(\theta)$ is the natural frequency, and $F(\theta)$ is a function of the angular position.

Two preliminary measurements are useful to check the apparatus. First, the angular position of the pendulum is determined versus the current in the driving coil under nearly equilibrium conditions. By increasing the gap between the upper magnet and the magnetic core of the driving coil, the nonlinearity in the driving torque can be highly reduced. Second, free oscillations of the pendulum are observed with and without magnetic damping. For determining the decay constant, the data should be fitted by an exponentially decaying sinusoid. As an alternative, we use the *User-defined fit* tool. Simply, a curve $A\exp(-Bt)$ that fits the envelope of the oscillations is added to the graph of free oscillations. The numerical values of A and B are varied for achieving an acceptable fit. The accuracy of this procedure is about 10%. Without magnetic damping, the decay

does not obey an exponential law because the dry friction in the *Rotary motion sensor* is not proportional to the angular velocity.

Changing the DC current in the 320-turn coil and the distance between the coil and the lower magnet modifies the angular dependence of the natural frequency. The nonlinear properties of the pendulum thus strongly depend on its arrangement, and additional efforts are needed for specifying the motion equation for different setups.

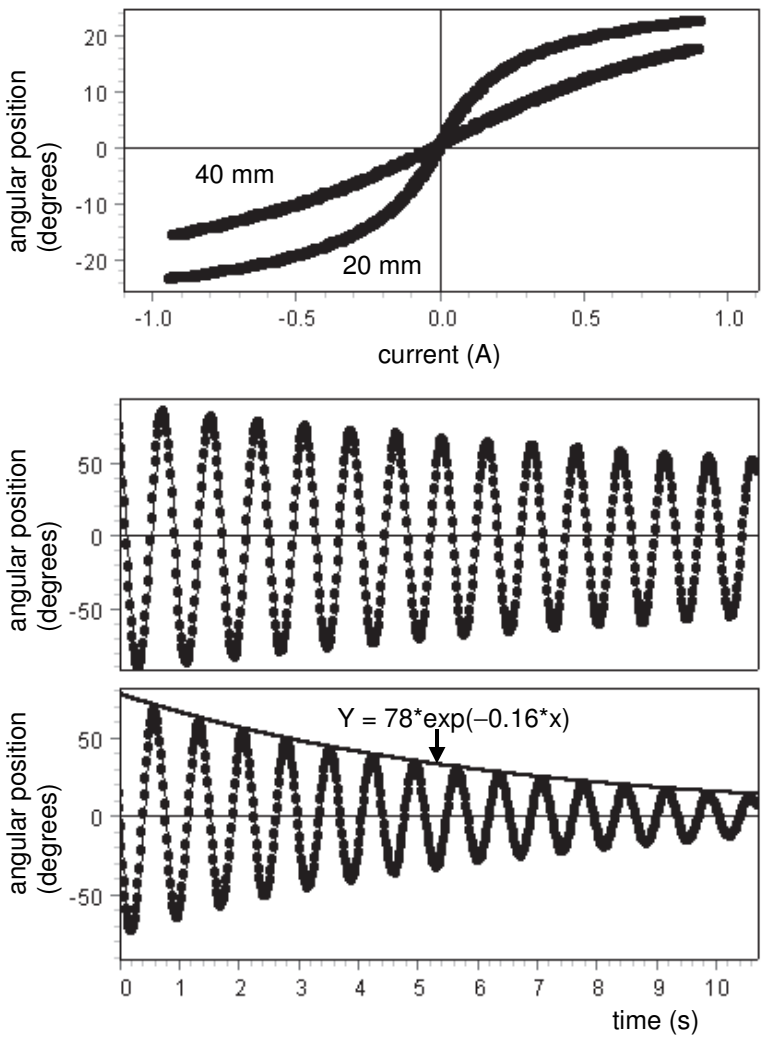

Fig. 2. Angular position versus driving current for 20 and 40 mm gap between the upper magnet and the magnetic core of the coil, and free oscillations without and with magnetic damping.

The arrangements for various experiments are shown in a general scheme (Fig. 3). The experiments include the following items:

- the amplitude dependence of the oscillation period of the pendulum with the additional nonlinearity brought in by external magnetic field;
- the **potential well** of the pendulum with the additional nonlinearity;
- the pendulum with positive or negative feedback: dependence of the decay constant on the **feedback factor**;
- **bent tuning curves** of the nonlinear pendulum: the **hysteresis** and **amplitude and phase jumps** in the vicinity of resonance;
- **nonlinear oscillations** presented as time series, phase plane plots, **Fourier spectra** and **histograms**;
- **chaotic motion** and **Poincaré sections**.

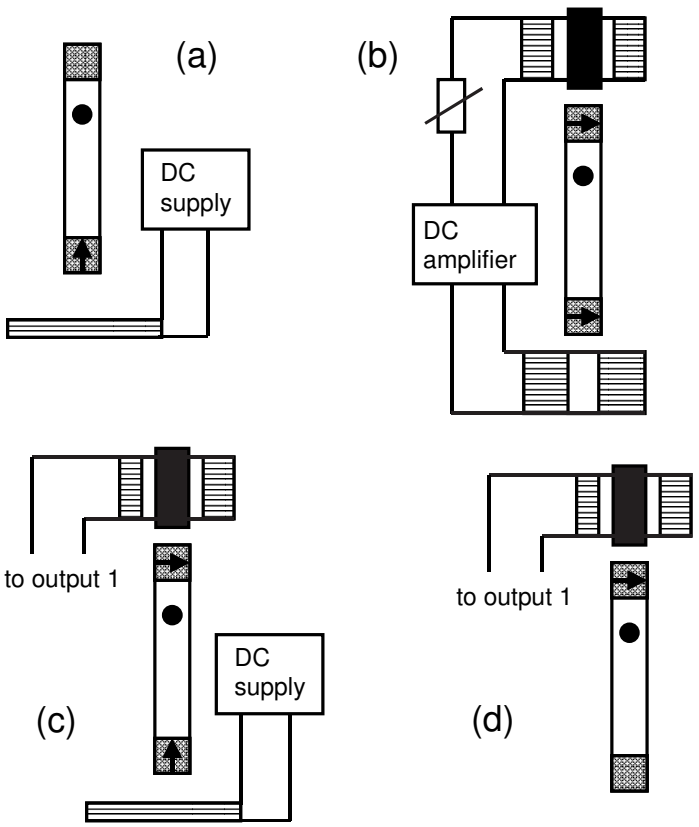

Fig. 3. Scheme of the experiments: (a) free oscillations; (b) pendulum with feedback; (c) bent tuning curves; (d) chaotic motion. The arrows show the orientation of magnetic dipoles; magnets without arrows can be excluded.

1. Free oscillations

Free oscillations are observed when the restoring torque is modified by a DC magnetic field. The decay constant depends on the feedback.

Additional equipment: DC supply, DC amplifier, variable resistor.

Period and potential well. The period of free oscillations of a usual pendulum depends on their amplitude: for amplitudes of 90°, the period becomes about 17% longer than for small-angle oscillations. For the magnetically controlled pendulum, this dependence may become significant even at small oscillation amplitudes. The lower magnet is aligned vertically, and the upper magnet is unnecessary. The interaction between the lower magnet of the pendulum and the DC magnetic field of the 320-turn coil produces a repulsive or attractive force on the pendulum, which modifies the restoring torque and thus the amplitude dependence of the period of free oscillations.

For determining the angular dependence of the oscillation period, the pendulum is displaced by an angle of 90° and released. During the decay, more than ten records of several oscillations are obtainable. Then the *Fit/Sine fit* tool of *DataStudio* is used to fit the data. The tool fits the data by the function

$$Y = A \sin[2\pi(t - C)/B] + D, \tag{3}$$

where A and B are the amplitude and period of the oscillations, D is an offset, and C shows the initial phase of the oscillations: $\varphi = \omega C = 2\pi C/B$.

The fit thus immediately provides the amplitude and the period of the oscillation. The measurements are performed with no current in the coil and with a 0.5 A DC current providing a repulsive or attractive action on the lower magnet. In these measurements, the distance between he centers of the lower magnet and of the coil is 70 mm. The additional nonlinearity is “soft” or “hard,” depending on the direction of the current in the coil (Fig. 4). The difference in the periods reaches a maximum at small-angle oscillations because in this region the attractive or repulsive action of the coil becomes stronger. Clearly, the properties of the pendulum depend on the current in the coil and on its position relative to the lower magnet. For automatically obtaining the plot of the oscillation period versus oscillation amplitude, see Experiment 2.5.

By observations of free oscillations, it is easy to evaluate the potential well of the pendulum (Pippard 1989, DeSerio 2003, Thornton and Marion 2004). For this purpose, we take data on the amplitude dependence of the oscillation period. For each oscillation, the full energy of the pendulum is proportional to the square of its maximum angular velocity. In our case, the energy is proportional to $(A/B)^2$, where A and B are the quantities in Eq. (3) evaluated by the *Fit/Sine fit* tool. A graph of the energy versus the oscillation amplitude represents the potential well. As expected, the relative changes in the potential for different strengths of nonlinearity are most significant at small oscillation amplitudes.

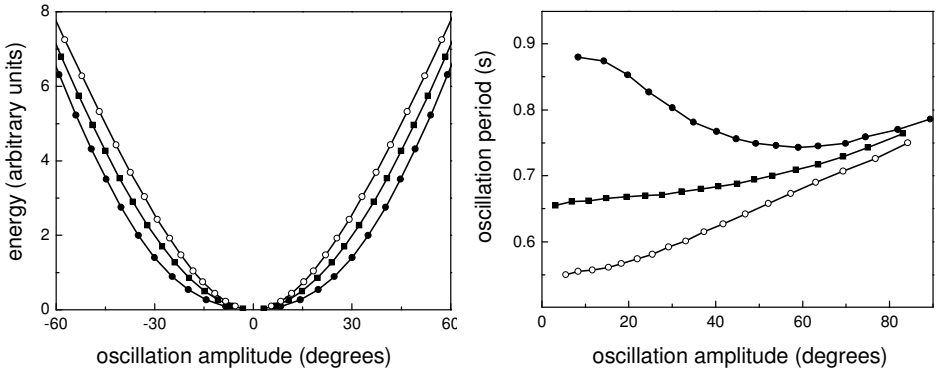

Fig. 4. Potential well of the pendulum and period of free oscillations versus their amplitude: ■ no current in the coil, • and ○ two directions of a 0.5 A current.

Rigorously speaking, the pendulum subjected to the repulsive action of the coil has two equilibrium positions on both sides of the vertical. This is insignificant in the present measurements because the wells are shallow and positioned very close to the vertical. Therefore, they are not seen in the graph.

The procedure used here for the determination of the potential well assumes a symmetrical shape of the well. This approach is inapplicable when the oscillations are asymmetrical. In such cases, data for the potential well are obtainable from the phase plane plots.

Pendulum with feedback. This experiment is useful for introducing the concept of **feedback**, which is very important in physics and modern technologies. To change the decay constant of the pendulum by feedback, both magnets are aligned horizontally. The lower magnet of the pendulum and a 3200-turn coil (SF-8613) beneath it serve for producing the feedback voltage. With the axis of the lower magnetic dipole aligned horizontally, the feedback voltage is of the same frequency as the oscillations of the pendulum, so that the voltage generated in the coil can be directly used for the feedback. This voltage is amplified and then fed to the driving coil through a variable resistor. In our setup, the amplifier is *Digital function generator-amplifier* (PI-9587C), and the variable resistor is *Decade resistance box* (PI-9588). The pulses of electric current are supplied to the driving coil every time when the angular velocity of the pendulum reaches a maximum (Fig. 5). The sign of the feedback depends on the polarity of the coils.

The motion equation for the pendulum with positive or negative feedback can be presented in a form similar to the Van der Pol equation (Moon 1987):

$$\theta'' + [\gamma \pm \beta(\theta)]\theta' + \omega_0^2\theta = 0, \qquad (4)$$

where β depends on the feedback coefficient. The plus is taken for negative feedback, and minus for positive.

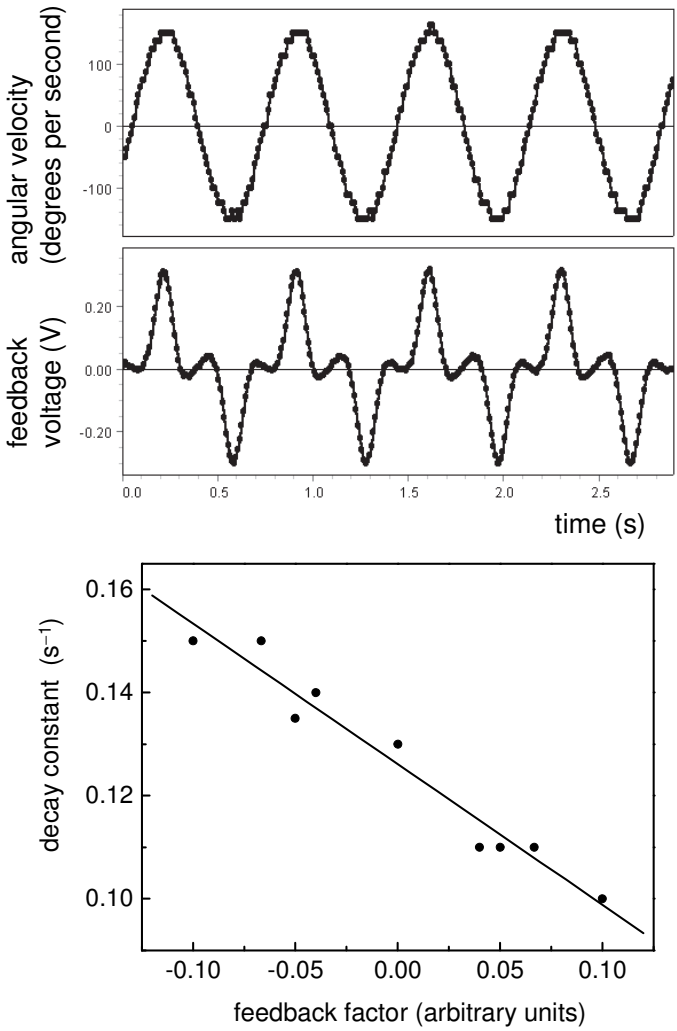

Fig. 5. Angular velocity, voltage across the feedback coil, and the decay constant versus feedback factor.

The free oscillations of the pendulum are recorded for different values of the feedback factor controllable by the variable resistor. The feedback factor is proportional to the current in the driving coil, that is, inversely proportional to the full resistance of the feedback circuit including the coil. The inverse resistance is therefore taken as a measure of the feedback factor. The decay constant is a linear function of the feedback factor. In these measurements, the gap between the upper magnet and the magnetic core of the driving coil is 40 mm, and moderate magnetic damping is used to make the decay exponential.

2. Forced oscillations

The experiments relate to (i) the hysteresis and amplitude and phase jumps, and (ii) the nonlinear oscillations. The transient processes can be observed.

Additional equipment: magnetically controlled pendulum, DC supply.

For observing forced oscillations, the driving coil is connected to the *Output 1* providing currents of ultra low frequency, so that the upper magnet aligned horizontally is subjected to a magnetic field directed in turn down and up. The interaction of the magnet with the field produces a periodic driving torque.

Bent tuning curves and hysteresis. When determining the tuning curves of the pendulum, the oscillations only slightly differ from harmonic ones due to reduced driving currents. Therefore, they can be approximated by a sinusoid. *DataStudio* stores data on the current passing through the driving coil and the angular position of the pendulum. The *Fit*/*Sine fit* tool fits both data by Eq. (3). From the two fits, one immediately obtains the amplitude of the oscillations and the phase shift between the driving torque and the angular position of the pendulum. It is necessary to confirm that at low frequencies the driving torque and the angular position of the pendulum are in phase; otherwise, it is necessary to alter the polarity of the current feeding the driving coil.

The gap between the upper magnet and the driving coil is 40 mm, and moderate magnetic damping is used. The 320-turn coil providing attractive action on the lower magnet brings in the nonlinearity. The DC current in this coil is 0.5 A. The data obtained are similar to those usually observable under similar conditions (Stockard *et al* 1967; Warden 1970; Dixon *et al* 1985; Grosu and Ursu 1986; Alessi *et al* 1992; Peters 1996). With the data-acquisition system, the phase shifts between the driving torque and the oscillation of the pendulum are available (Fig. 6). Due to the additional nonlinearity, the hysteresis and the amplitude and phase jumps in the vicinity of resonance are seen even for small-angle oscillations.

It is easy to record the transients after changing the amplitude or frequency of the driving torque. In the vicinity of the resonance, the nonlinear oscillations become very sensitive to such changes.

Regular nonlinear oscillations arise when the gap between the magnetic core of the driving coil and the upper magnet is 20 mm. The *Capstone* displays the oscillations as time series and phase plane plots, so that the nonlinear behavior of the pendulum is clearly seen. Records of the oscillations are taken when steady oscillations are well established. The *Rotary motion sensor* measures the displacement of the pendulum from the point where the run is started or when the angular position or velocity of the pendulum reaches a preset value. Examples presented show harmonic and subharmonic generation (Fig. 7). The appearance of subharmonics is one of possible routes to chaos.

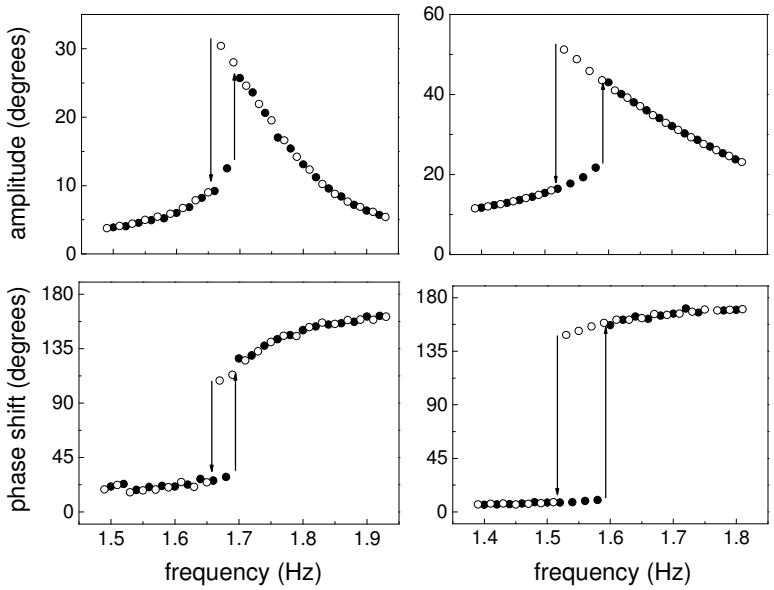

Fig. 6. Tuning curves for 0.05 A (left) and 0.2 A (right) amplitudes of the driving current: ● increasing frequency, ○ decreasing frequency.

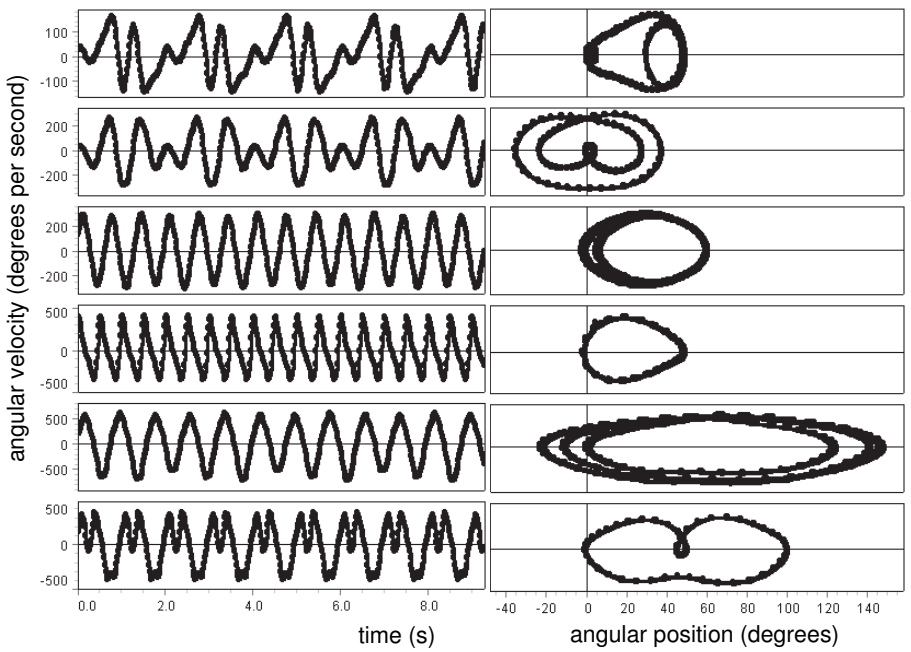

Fig. 7. Angular velocity and phase plane plots. From top to bottom: 0.5 Hz, 0.2 A; 1 Hz, 0.1 A; 1.5 Hz, 0.2 A; 2 Hz, 0.8 A; 2.5 Hz, 0.4 A; 3 Hz, 0.45 A.

In addition, the *Fast Fourier Transform* tool shows Fourier spectra of the angular position or velocity, and the *Histogram* tool displays their probability distributions (Fig. 8). These results were obtained with no magnetic damping and modifications of the restoring torque.

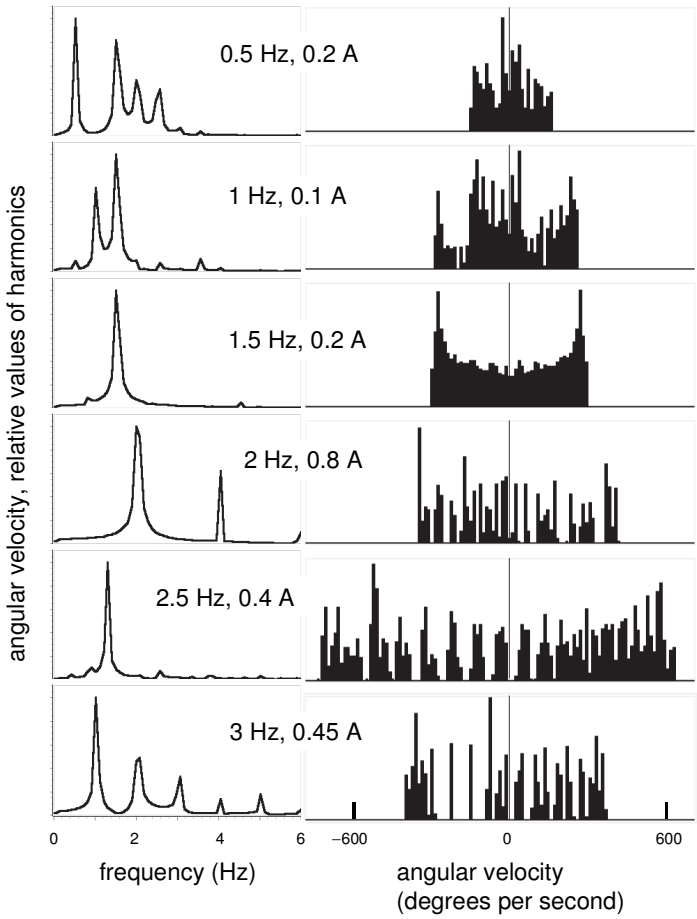

Fig. 8. Fourier spectra and histograms for the examples shown in Fig. 7.

3. Chaotic motion

Chaotic motion of the nonlinear pendulum is observed.

Poincaré maps. Many papers are devoted to the **chaotic motion** (Kautz 1993; Levien and Tan 1993; Peters 1995; Flynn and Wilson 1998; Sprott 2000; Kiers *et al* 2004; Stavrou *et al* 2013). It is a common practice to characterize chaotic motion with the so-called Poincaré sections (Poincaré maps). In our setup, the gap between the magnetic core of the driving coil and the upper magnet is reduced to 15 mm; the amplitude of the drive current is 0.8 A. The period of the driving torque is 1 s, so that the Poincaré maps could be taken with a 1 Hz sample rate. However, in this case *DataStudio* calculates the angular position and velocity as averages for 1 s intervals, which are not representative. We use a 20 Hz sample rate, so that the quantities to be measured are averages for a 1/20 part of the period. With this sample rate, 20 data points are stored during each period of the driving torque, and 20 Poincaré maps at particular phases of the period become available in one run. In a run lasting 1500 s, *DataStudio* stores 30000 data points for the angular position and velocity of the pendulum (Fig. 9).

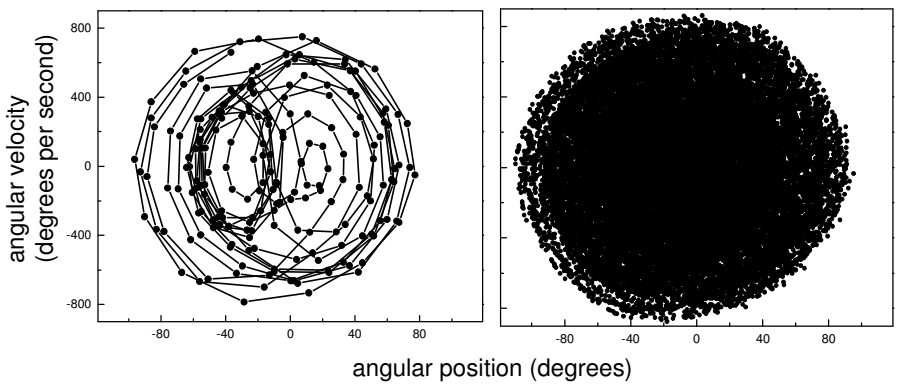

Fig. 9. Phase plane plots for the initial part of chaotic motion (10 s, 200 points) and for the whole run (1500 s, 30000 points).

To extract data necessary to plot all the Poincaré maps, simple software for *Microsoft Excel* was prepared. This easy task may be opened for student activities; therefore, the software is not given here. The program gathers data points number 1, 21, 41,… (1500 points in total) and plots the corresponding Poincaré map. The same operation is simultaneously performed for data points number 2, 22, 42,... and so on. Twenty Poincaré maps for phases separated by 1/20 part of the period of the driving torque are thus available. For obtaining sharp Poincaré maps for chaotic motion, the pendulum should be highly damped (Moon 1987, DeSerio 2003). In our setup, the damping is provided by a permanent magnet positioned close to an aluminum disc attached to the axle of

the *Rotary motion sensor*. Ten Poincaré maps for phases separated by 1/10 part of the period of the driving torque are shown here (Fig. 10). Note the symmetry in the maps separated by 180° (maps number 1 and 6, 2 and 7, and so on). For obtaining Poincaré maps for definite phases of the drive torque, we use the *Auto* mode of the *Signal generator*: the generator starts to produce the driving current after the measurements are triggered. To eliminate data stored during the transient process, it is enough to remove data for the first 10 s of the run (the first 200 data points). With this procedure, the software every time builds the Poincaré maps for the same phases of the driving torque.

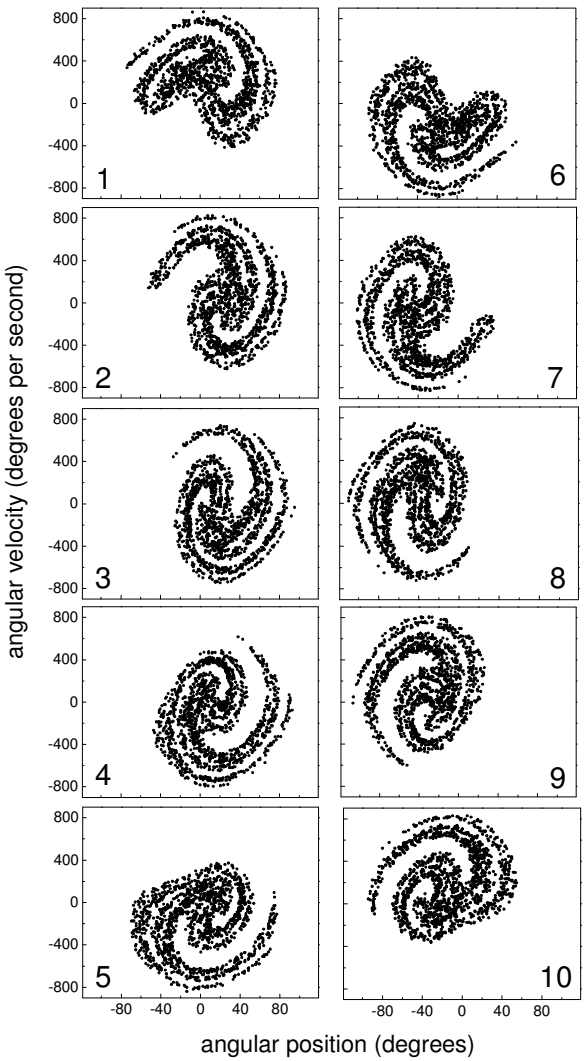

Fig. 10. Poincaré maps for chaotic motion taken at phases separated by 1/10 of the period (1500 points each).

2.7. Nonlinear pendulum II

The magnetically controlled pendulum demonstrates (i) the self-excited oscillations; (ii) the parametric excitation; and (iii) the two- and three-well potential oscillations (Kraftmakher 2010c). Schematics of the setups are shown in Fig. 1.

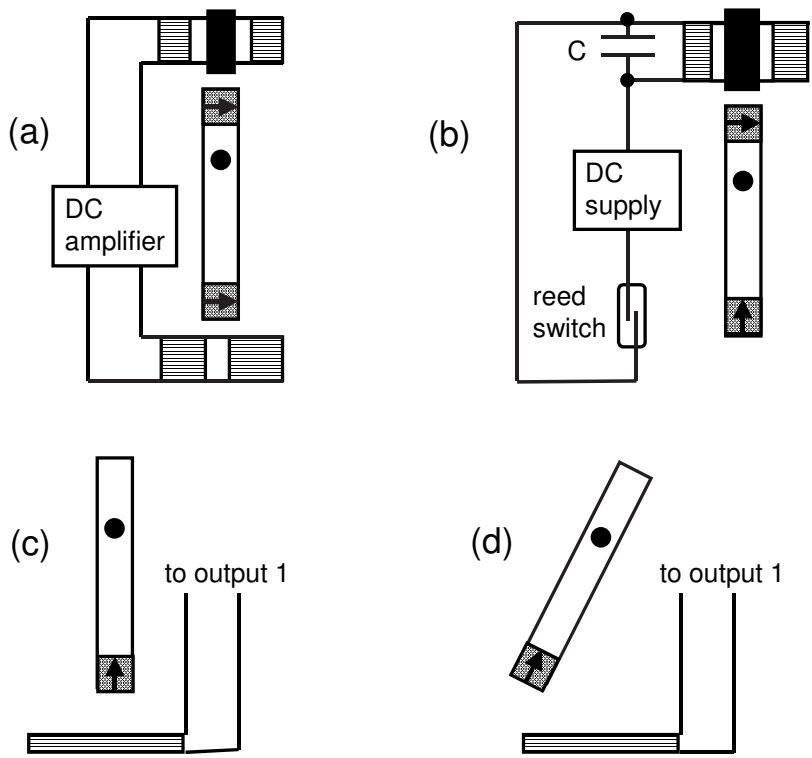

Fig. 1. General scheme of the experiments: (a) and (b) self-excited oscillations; (c) parametric excitation; (d) two- and three-well potential. The arrows indicate orientation of the magnetic dipoles.

Additional equipment: *Rotary motion sensor*, coils, reed switch, DC supply, DC amplifier.

Self-excited oscillations. With positive feedback, oscillations may become self-excited like in a pendulum clock or some toys (Pippard 1989; Moon 1987). Two methods are used to compensate the energy losses in the system and to attain self-excited oscillations. The first method relies on positive feedback provided by magnetic induction (Fig. 1a). An 800-turn driving coil (SF-8611) with a

magnetic core is positioned 2 cm above the upper magnet. Its resistance is nearly 10 Ω. The axes of both magnetic dipoles are aligned horizontally. A 3200-turn coil (SF-8613), positioned 2 cm beneath the lower magnet, provides a feedback voltage with amplitude of about 0.3 V. The feedback voltage amplified by the *Digital function generator-amplifier* (PI-9587C) is applied to the driving coil. The sign of the feedback depends on the polarity of the two coils. The motion equation of the pendulum with positive or negative feedback can be presented in a form similar to the Van der Pol equation (Moon 1987):

$$\theta'' + [\gamma \pm \beta(\theta)]\theta' + \omega_0^2\theta = 0, \quad (1)$$

where β depends on the feedback coefficient. A positive or negative sign in this equation implies negative or positive feedback, respectively. This equation is a second-order differential equation with a linear restoring force and nonlinear damping, which exhibits a limit cycle behavior. It can be solved numerically (Drish and Wild 1983). The oscillations become self-excited when

$$\gamma - \beta(\theta) = 0. \quad (2)$$

To trigger the oscillations, the pendulum is displaced slightly from its equilibrium position. After being released, the amplitude of the oscillations gradually grows and reaches a steady value. This steady-state motion is called the Poincaré limit cycle. The limit cycle depends on the energy losses to be balanced. When the pendulum is initially positioned at an angle beyond the limit cycle, its oscillations gradually decay until the same limit cycle is reached. The coefficient β decreases with increasing θ, and the system reaches the limit cycle due to this nonlinearity.

The second method used to compensate for the energy losses uses a reed switch to provide suitable current pulses for the driving coil (Fig. 1b). The switch consists of a pair of contacts on ferrous metal reeds in a sealed glass envelope. The state of the switch depends on the external magnetic field, and the lower magnet of the pendulum operates it. Now the axis of this magnetic dipole is aligned vertically. The switch is 2 cm away from the equilibrium position of the pendulum. The switch is connected in series with a DC power supply and the driving coil. Every time the pendulum reaches its lowest point, the switch is closed, and an electric current of about 0.3 A passes through the coil. The switch breaks the current when the pendulum moves away from its lowest point. A 5 μF capacitor shunting the driving coil suppresses EMF pulses in the coil when the switch opens. The limit cycles are clearly seen (Fig. 2).

To start the oscillations, the DC supply is switched on when the pendulum is in its lowest position. If the reed switch stands too far from the pendulum, one needs to push the pendulum toward the switch. The oscillation amplitude depends on the position of the reed switch and the amplitude of the current pulses passing through the driving coil. This approach is probably the simplest method to balance the energy losses. A drawback of this approach is the limited stability of the reed switch; therefore, the electrical pulses in the driving coil are not exactly reproduced. Nevertheless, the results obtained are quite satisfactory.

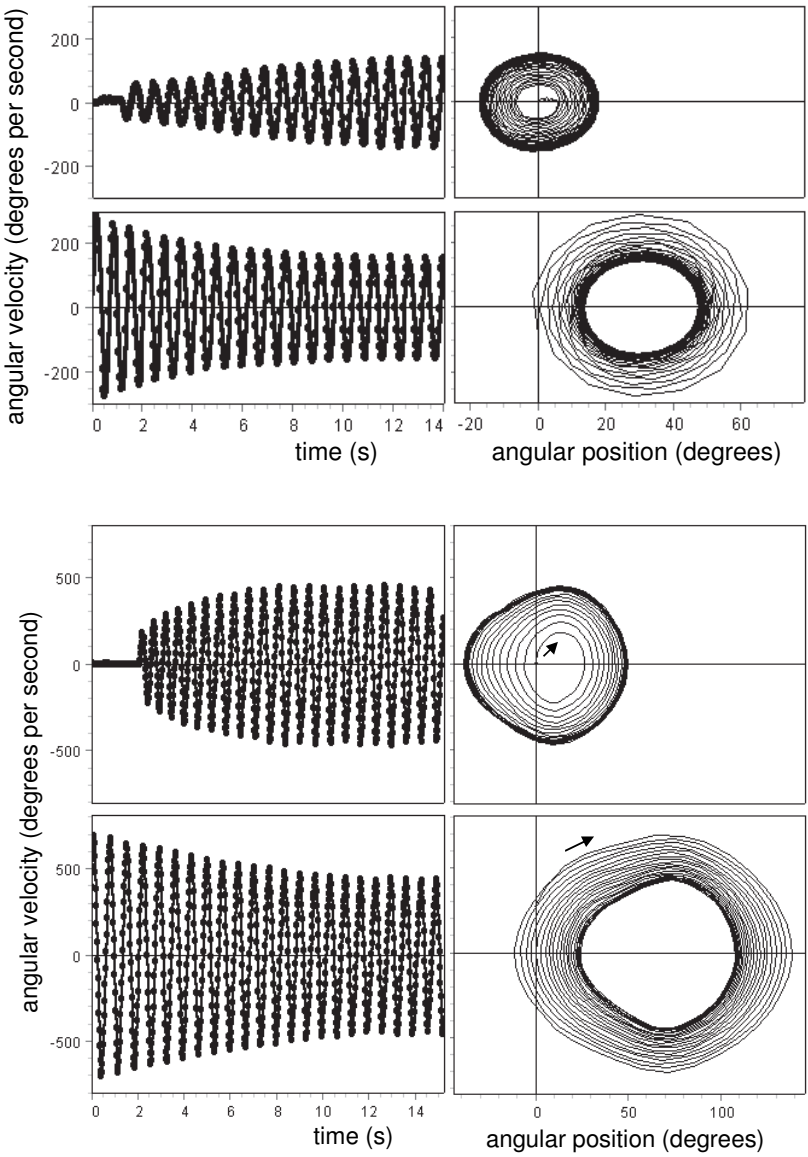

Fig. 2. Routes to limit cycles with feedback coil (top) and reed switch (bottom).

Parametric excitation. An oscillator is parametric if its motion obeys the so-called Hill's equation:

$$x'' + G(t)\, x = 0, \tag{3}$$

where $G(t)$ is a periodic function. An interesting example is a motion that satisfies the Mathieu equation:

$$x'' + \omega_0^2[1 + h\cos\Omega t\,]\,x = 0, \tag{4}$$

where ω_0 is the natural frequency of the oscillator. It is assumed that $h << 1$.

Continuous oscillations can be attained by periodically varying the natural frequency of the oscillator (Pippard 1989; Landau and Lifshitz 1982). With parametric excitation, the system acquires additional energy, and the oscillations become continuous when the gain from the parametric process outweighs the dissipative losses. Parametric oscillations are possible when the frequency of the excitation is close to

$$\Omega = 2\omega_0/n, \tag{5}$$

where n is an integer.

The frequency range $\Delta\Omega$, for which parametric excitation is possible, depends on n. For $n = 1$, this frequency range is maximized, and the necessary value of h can be minimized. Parametric oscillations occur when the system is displaced from its equilibrium position, which is quite different from the usual excitation. Experiments on parametric excitation are described in a number of papers (Adler and Breazeale 1971; Falk, 1978, 1979; Denardo *et al* 1999; Fameli *et al* 1999; Case 1980; Curzon *et al* 1995; Dittrich *et al* 2013).

In our case, it is easy to periodically change the restoring torque by an AC magnetic field. A 320-turn coil, about 14 cm in diameter, is positioned 2 cm beneath the pendulum and connected to *Output 1* (Fig. 1c).

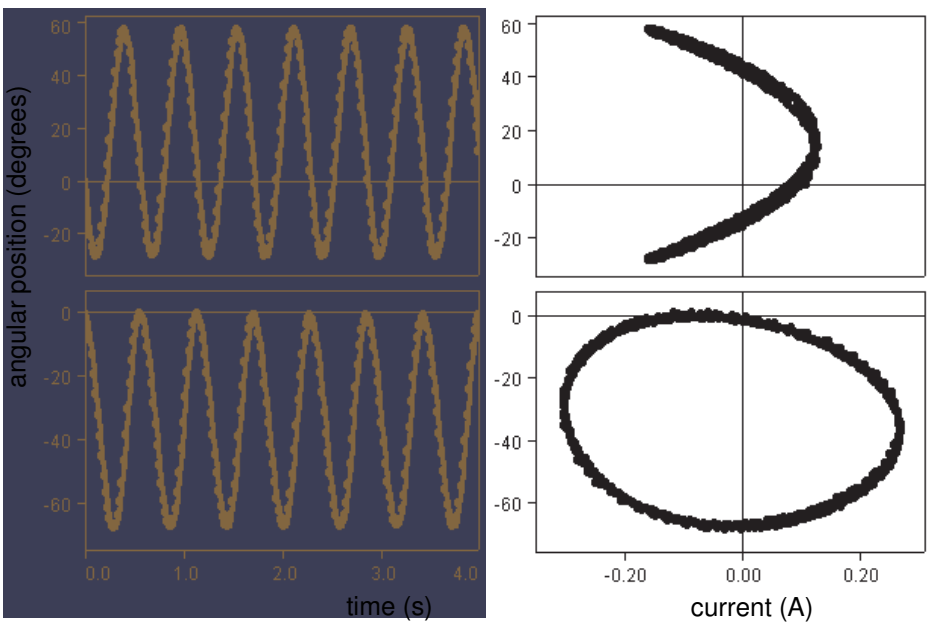

Fig. 3. Parametric oscillations of the pendulum. Lissajous patterns (angular position versus driving current) show the frequency ratios.

The lower magnet of the pendulum is directed vertically. The field produced by the lower coil modifies the restoring torque and thus the natural frequency of the pendulum. The upper magnet is not required for this experiment. With the data-acquisition system, the time series and phase plane plots are observed, as well as the phase relations between the current in the coil and the angular position of the pendulum. To trigger the parametric oscillations, the pendulum should be displaced from its equilibrium point and then released. Different frequencies obeying Eq. (5) were tried. Parametric oscillations are readily observable for n equal to 1 and 2 (Fig. 3).

Two- and three-well potential oscillators. When the lower current-carrying coil produces a repulsive action on the vertically oriented lower magnet, it is possible to create an oscillator with two or three potential wells. To make the two wells observable, it is enough to increase the DC current in the 320-turn coil up to about 1 A. The potential wells can be made dissimilar by tilting the coil or by shifting it right or left from the central position. For a specific location of the coil under the pendulum, the equilibrium positions of the pendulum depend on the DC current in this coil. Free oscillations of the pendulum decay to one of two equilibrium positions (Fig. 4). Magnetic braking increases the decay constant.

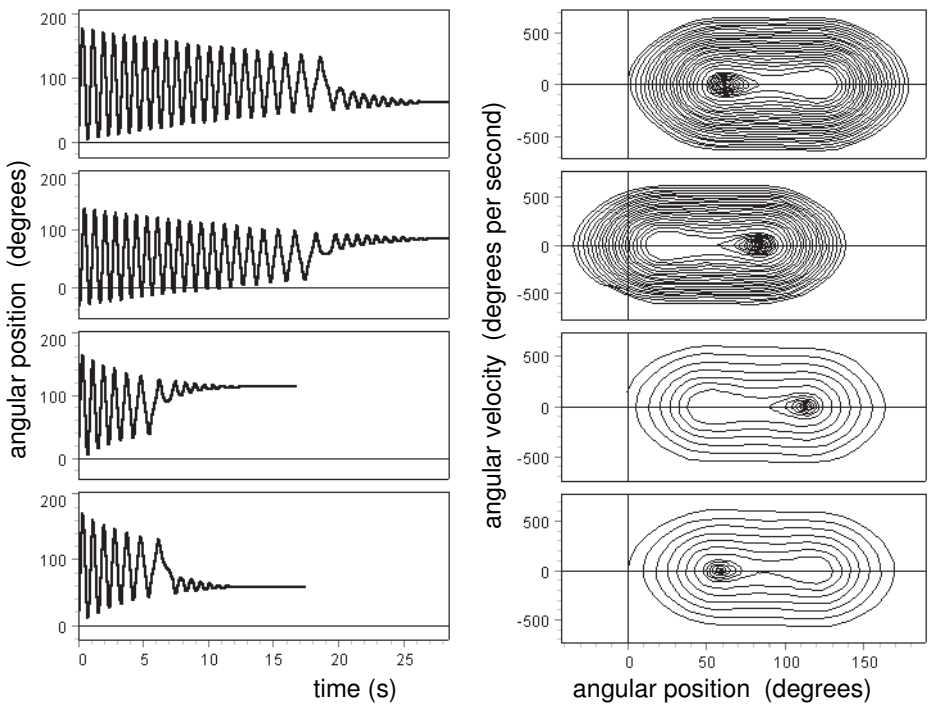

Fig. 4. Examples of free oscillations of two-well potential pendulum for two decay constants: time series and phase plane plots.

The repulsive action of the lower coil on the lower magnet depends on the gradient of the magnetic field. When the lowest position of the magnet coincides with the center of the coil, where this gradient vanishes, the vertical position of the pendulum also becomes an equilibrium position. In this case, the pendulum has three equilibrium positions: the vertical position and two positions on either side of the vertical. The pendulum thus becomes a three-well oscillator. Free oscillations of the three-well pendulum decay to one of three equilibrium positions (Fig. 5). When using the upper magnet and the driving coil above it, forced oscillations of the pendulum are also observable.

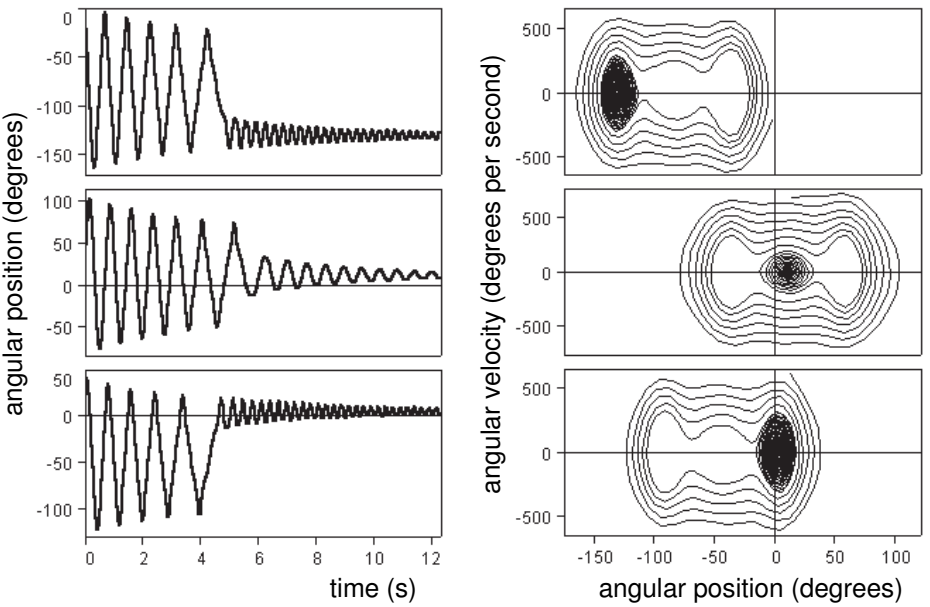

Fig. 5. Examples of free oscillations of the three-well potential pendulum. The DC current in the 320-turn coil is 0.5 A.

2.8. Nonlinear dynamics

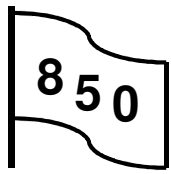

Another experiment on nonlinear dynamics is presented.

Additional equipment: *Rotary motion sensor*, Helmholtz coils, two magnets.

Many papers were published on nonlinear oscillating systems. Janssen *et al* (1983) demonstrated the resonance behavior of an anharmonic oscillator, a mass attached to a spring. Using a compass needle moving in an oscillating magnetic field, Meissner and Schmidt (1986) observed the transition from order to chaos. Briggs (1987) described several experiments in chaotic dynamics illustrating the period doubling, noisy periodicity, and continuous chaos. With a bipolar motor, Ballico *et al* (1990) demonstrated chaos in a nonlinear deterministic system. Their apparatus consisted of a permanent magnet suspended by two torsion springs and subjected to a uniform DC magnetic field. Ojha *et al* (1991) studied a nonlinear system consisting of a freely rotating compass needle placed between Helmholtz's coils. A solenoid produced an additional magnetic field. With a simple nonlinear oscillator, Khosropour and Millet (1992) demonstrated the bent tuning curve. Shinbrot *et al* (1992) observed chaotic motion of a double pendulum. Siahmakoun *et al* (1997) investigated the dynamics of a sinusoidally driven pendulum in a repulsive magnetic field. Regions of periodic and chaotic behavior, amplitude jumps, hysteresis, and bistable states were observed. Berger and Nunes (1997) designed a mechanical Duffing's oscillator (inverted pendulum) providing an introduction to nonlinear oscillations and chaotic behavior. Using an Atwood's machine and a personal computer, Pecori *et al* (1999) studied harmonic and anharmonic oscillations.

The apparatus contains a permanent magnet attached to the axle of the *Rotary motion sensor* and a pair of 200-turn Helmholtz's coils (EM-6711). An additional fixed permanent magnet provides a nonlinear restoring force (Fig. 1). The apparatus is thus similar to those described earlier (Meissner and Schmidt 1986; Briggs 1987; Ballico *et al* 1990; Marega *et al* 1991; Ojha *et al* 1991). An AC current from the *Output 1* feeds the Helmholtz coils. *Capstone* stores the angular position and angular velocity of the rotating magnet. The data are displayed as a time series and a phase space plot. The *FFT* tool provides the spectra of the oscillations. The *Histogram* tool displaying the probability function for the angular velocity of the rotating magnet provides additional information on the system. The measurements are performed for different amplitudes and frequencies of the AC magnetic field and for various separations from the fixed magnet. This simple computer-assisted apparatus is capable of demonstrating many phenomena peculiar to nonlinear oscillating systems.

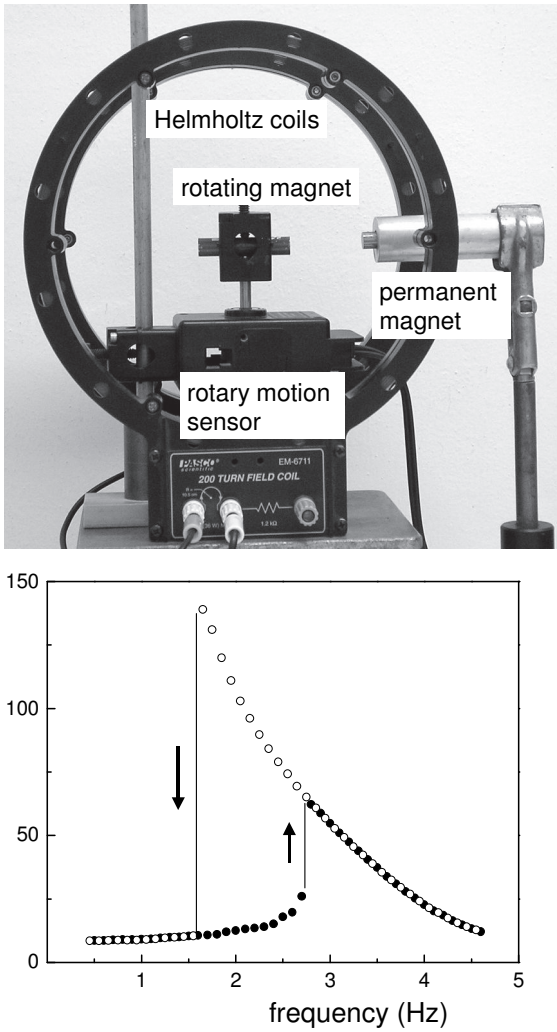

Fig. 1. The setup and the resonance curve: • increasing frequency, o decreasing frequency.

Hysteresis and amplitude jumps. One of the features of a nonlinear oscillating system is the **hysteresis** in its resonance curve accompanied by **amplitude jumps**. It is easy to see this behavior by measurements of the frequency dependence of the oscillation amplitude. The *Fit/Sine fit* tool approximates the oscillations. From the fits, one immediately obtains the data necessary to plot the resonance curve. The hysteretic behavior and amplitude jumps are clearly seen.

Route to chaos. With various frequencies of the AC magnetic field, the motion of the rotating magnet is recorded. *Capstone* displays time series of the

oscillations and their Fourier spectra. Examples presented clearly show the distortions of the oscillations, including the tripling of the frequency and period, and the route to chaotic motion (Fig. 2).

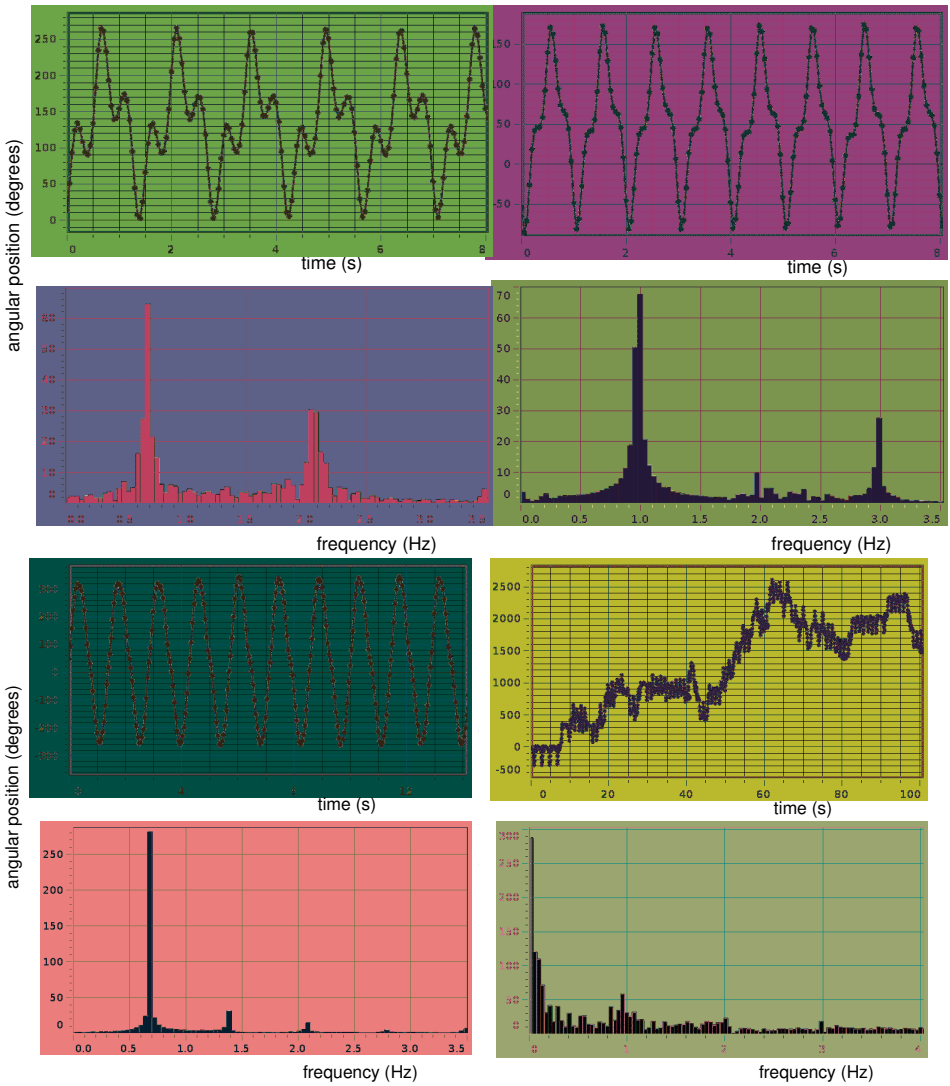

Fig. 2. Examples of time series and Fourier spectra showing frequency and period tripling, and chaotic motion. The frequency of driving force is 0.7 and 1 Hz (top), and 2.1 Hz (bottom).

2.9. Tuning fork

A tuning fork is explored (Kraftmakher 2004b).

Additional equipment: *Sound sensor*, *Voltage sensor*, tuning fork mounted to a resonance box, audio amplifier, AC-to-DC converter, microphone.

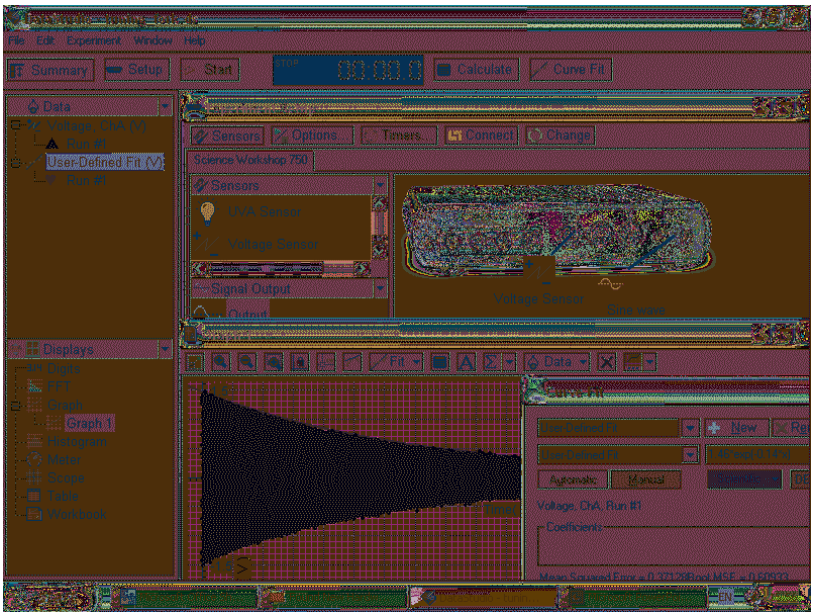

***Free oscillations*.** The tuning fork is often used for classroom demonstrations. In particular, a pair of tuning forks mounted on resonance boxes is very popular. A tuning fork is an example of high-quality resonant systems. This is seen from the long decay of free oscillations triggered in it (Rossing *et al* 1992; Russell 2000; Ong 2002). The free oscillations obey the common relation

$$x = A\exp(-\delta t)\cos(\Omega t + \varphi), \tag{1}$$

where Ω is the angular frequency of the oscillations ($\Omega = 2\pi f$), and A and φ depend on the initial conditions.

The decay of free oscillations is governed by the decay constant δ. The frequency Ω is close to the so-called **natural frequency** of the system, ω_0: $\Omega^2 = \omega_0^2 - \delta^2$. The natural frequency depends on the basic properties of the system. The quality of a resonant system is often characterized by the **quality factor** (Q-factor), which equals $Q = \omega_0/2\delta$, so it is easy to determine the Q-factor of a tuning fork. To study forced oscillations in a high-quality resonant system like a tuning fork, a source of the driving force must provide a very stable frequency and the possibility of precisely changing the frequency in the vicinity

of the resonance. The 0.001 Hz resolution provided by the *Signal generator* is quite sufficient for the determination of the **resonance curve** of a tuning fork.

A 440 Hz tuning fork is mounted on a resonance box (now PASCO offers a similar 256 Hz tuning fork, SE-7344). For our purpose, it is important that the tuning fork is made out of magnetic steel. Otherwise, a thin magnetic ribbon should be pasted to its prong. The Q-factor of the tuning fork is of the order of 10^4. A 400-turn coil (SF-8610) with a U-shaped magnetic core (SF-8614) drives the forced oscillations (Fig. 1). The coil is connected to the *Signal generator* providing a *Sine wave* voltage. The frequency of the driving force is twice the frequency of the current, which is therefore varied in the vicinity of 220 Hz. To make the frequency of the driving force equal to that of the current, a small permanent magnet should be attached to the magnetic core.

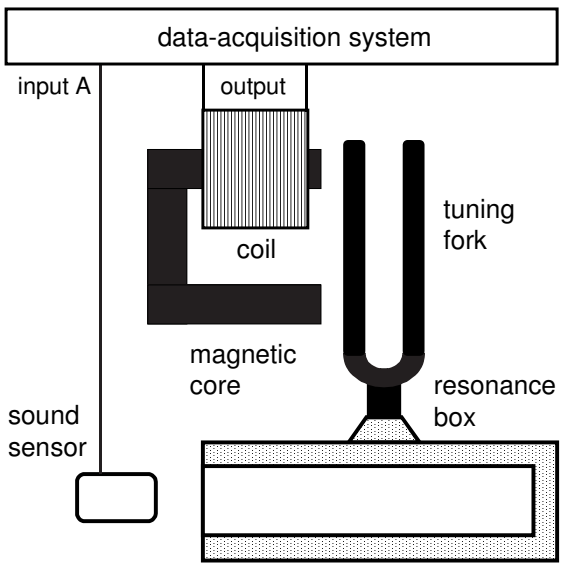

Fig. 1. Diagram of setup for observing oscillations of tuning fork.

The *Sound sensor* or a usual microphone senses the oscillations of the tuning fork, and the *Graph* tool displays the results. The *Sample rate* of the data acquisition is set to be 500 Hz, so details of the oscillations are not seen. Nevertheless, the time dependence of the amplitude of the oscillations is quite clear (Fig. 2). For determining the decay constant δ, one plots, together with the graph of the oscillations, an additional graph $A\exp(-Bt)$ to fit the envelope of the oscillations, and varies numerical values of A and B to achieve the best fit. The *User-defined fit* option is used for this purpose. The fit immediately provides the decay constant. By setting the values of B below and above the best value, one can estimate the possible error peculiar to this procedure, which does not exceed 10%.

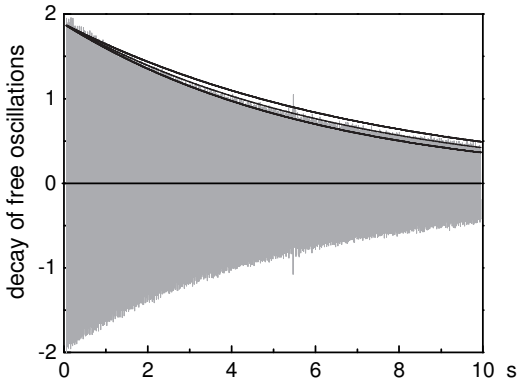

Fig. 2. Signal from *Sound sensor*. Exponential fits relate to δ equal to 0.135, 0.15 (best fit), and 0.165.

***Forced oscillations*.** Tuning forks are oscillating systems of strong nonlinearity, so the amplitude of the forced oscillations must be small. The *Sound sensor* senses even weak sound waves. With an AC-to-DC converter, the determination of the resonance curve becomes very simple. The converter provides a DC voltage proportional to the amplitude of the oscillations of the tuning fork measured with a microphone. As the AC-to-DC converter, we use a Hewlett–Packard 400E voltmeter. The *Time between measurements* is set to be sufficient for establishing steady oscillations, say, 30 s. The frequency of the *Signal generator* is changed via the dialog box. After every measurement, one changes this frequency and repeats this procedure after the next experimental point appears on the graph.

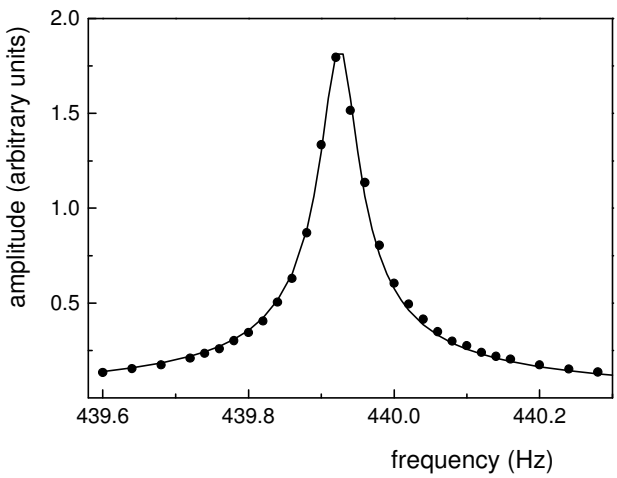

Fig. 3. The resonance curve of the 440 Hz tuning fork: • experimental points, — theoretical fit with $f_0 = 439.925$ Hz and $\delta = 0.155$.

When the scan is completed, the discrete time points should be converted into the frequency. Using this method, a detailed resonance curve (Fig. 3) is obtainable in 20 min. The resonance curve of the tuning fork is, as expected, very narrow. The amplitude of the forced oscillations follows the relation common to various resonant systems of high quality ($Q >> 1$):

$$X = X_0\delta/[(\omega - \omega_{res})^2 + \delta^2)]^{½}, \quad (2)$$

where X_0 is the amplitude of the oscillations at the resonance, $\omega - \omega_{res}$ is the difference between the driving force frequency and the resonance frequency, and δ is the decay constant.

The best way of comparing the results with the theory is fitting the data with a curve according to Eq. (2). The fit provides the resonance frequency and the decay constant. The difference between two frequencies, for which the amplitudes of forced oscillations become $\sqrt{2}$ smaller than at the resonance, is called the bandwidth of the resonant system, $\Delta\omega$. It directly relates to the Q-factor: $Q = \omega_{res}/\Delta\omega$. In the example presented, the decay constant obtained from the resonance curve ($\delta = 0.155$) agrees with that calculated from the decay of free oscillations (0.15).

The transients. Immediately after a driving force is applied, the amplitude of the oscillations starts to gradually grow. The reason is that free oscillations also arise in the system. At the first moment, they have the same initial amplitude as the forced oscillations but an opposite phase. When the frequencies of both oscillations are equal, the amplitude of the resultant oscillation grows monotonically. If the frequencies differ, the resultant oscillation amplitude changes within $x_0 \pm x_0\exp(-\delta t)$, where x_0 is the steady amplitude of the forced oscillations (Fig. 4). The beats last during the decay of the free oscillations. Pippard (1989) considered this phenomenon in detail. In a millisecond time scale, the oscillations are observable with the *Scope* tool.

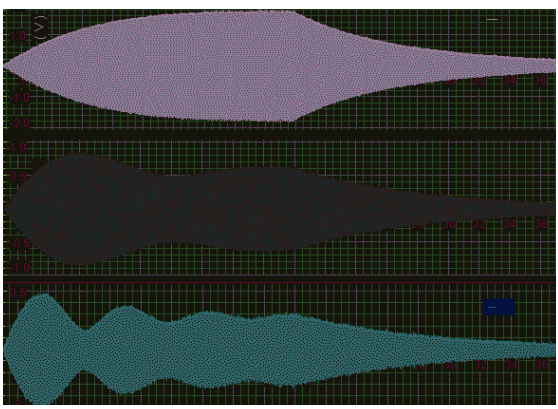

Fig. 4. Forced oscillations at the resonance and at frequencies 0.1 and 0.2 Hz lower.

Temperature dependence of resonance frequency is caused by the temperature dependence of the **dimensions** of the fork and of the **elastic modulus** of the material. Both contributions lead to a decrease of the resonance frequency with increasing temperature. The temperature coefficient of the resonance frequency is negative and expected to be of the order of 10^{-4} K^{-1}. Precise measurements with a tuning fork thus require special temperature control. Owing to the sharp resonance curve, it is easy to demonstrate the influence of temperature changes. When observing the transient process at a constant frequency of the driving force, beats of various frequencies appear when heating the tuning fork. It is enough to heat the fork by hand (Fig. 5).

With a pair of similar tuning forks, the demonstration of the temperature dependence of the frequency of free oscillations is possible without a data-acquisition system. The beats that appear after heating one of the forks are well audible and can be also shown using a microphone and an oscilloscope.

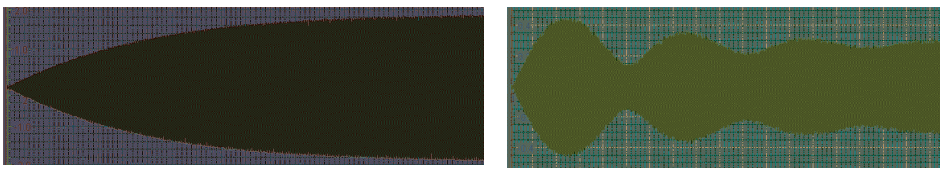

Fig. 5. The transient with the same frequency of the driving force before and after heating the tuning fork by hand.

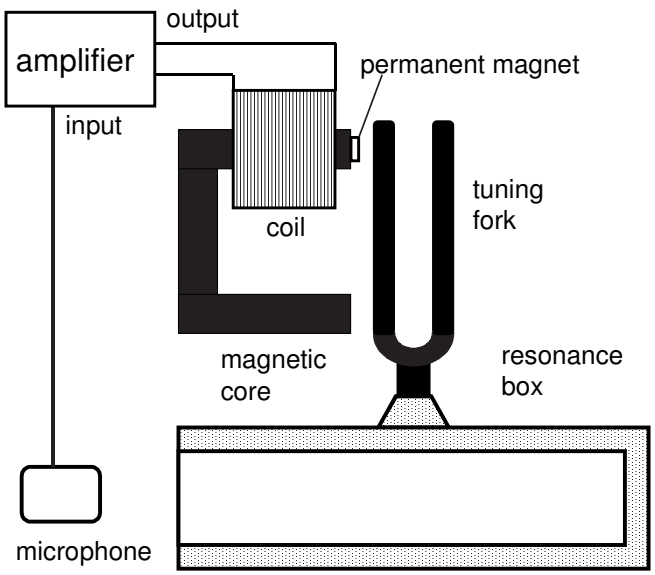

Fig. 6. Schematic of setup for generating continuous oscillations.

Continuous oscillations. For obtaining continuous oscillations of the tuning fork, a microphone sensing the oscillations is connected to the input of an audio amplifier (Fig. 6). The output current of the amplifier passes through the driving coil and provides positive feedback. To make the frequency of the driving force equal to that of the current, a small permanent magnet is attached to the magnetic core.

With an AC-to-DC converter, the decay of free oscillations (Fig. 7) and resonance curve (Fig. 8) can be recorded automatically.

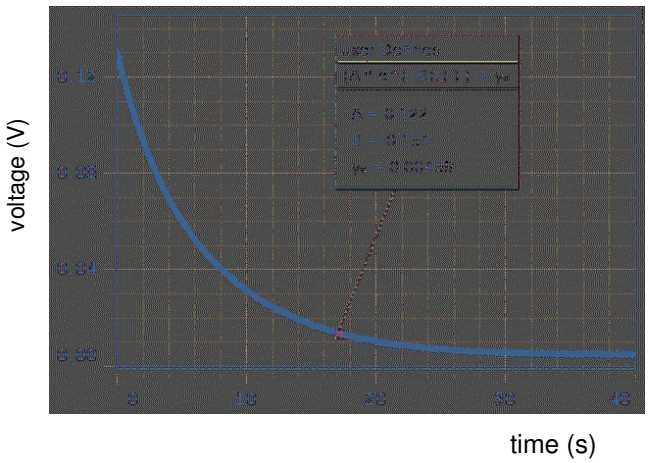

Fig. 7. Decay of free oscillations of the tuning fork.

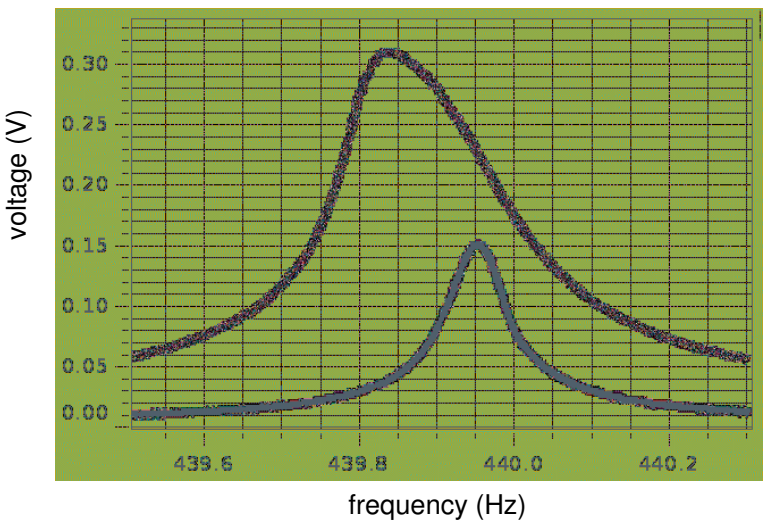

Fig. 8. Resonance curves for different driving voltages. For a higher voltage, the resonance frequency decreases, while the curve becomes distorted.

Similarly, it is easy to demonstrate the transients immediately after a periodic driving force is applied and after it is interrupted (Fig. 9), or the change in the transient after heating the tuning fork by hand (Fig. 10).

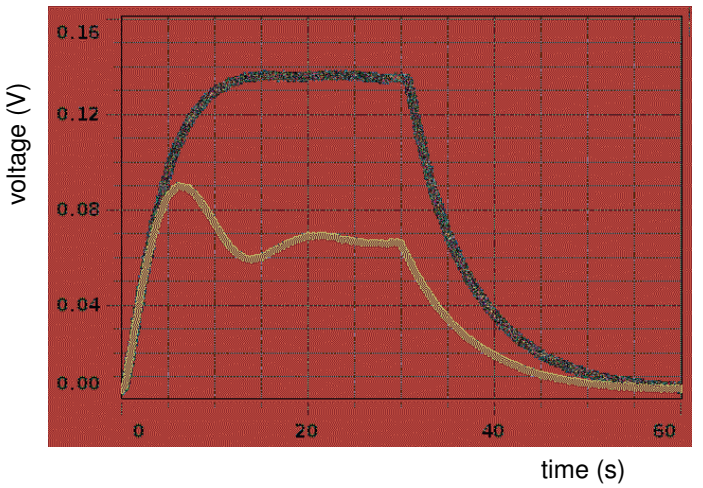

Fig. 9. Transients for frequencies close to resonance and 0.05 Hz below.

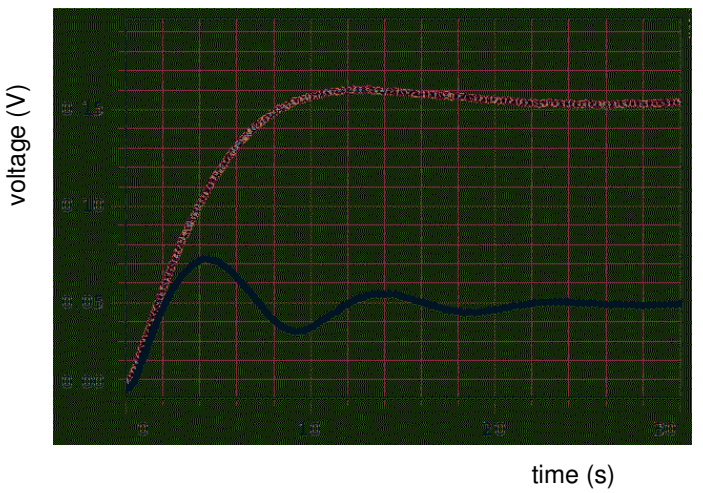

Fig. 10. Transients for a frequency close to resonance at room temperature and after heating the tuning fork by hand.

2.10. Standing waves

Three experiments are considered (Kraftmakher 2010a, 2013b).

Additional equipment: *Motion sensor*, *Voltage sensor*, *Force sensor*, *Mechanical driver*, loudspeaker, microphone, AC-to-DC converter, cardboard tube, elastic cord.

Only a part of papers devoted to standing waves is mentioned here. Using a thermistor, Hastings (1969) investigated the temperature distribution along the standing wave in a Kundt tube. With a high power loudspeaker, the temperature excursions along the tube amounted up to 20^{o}(!). Temple (1975) used a lock-in amplifier for measuring phase shifts between a voltage driving a loudspeaker and a signal from a microphone moved toward and away from the loudspeaker. May (1980) described a hollow-tube resonance experiment. Jewett (1980) observed the resonance spectrum of an air column using the frequency scanning and an oscilloscope. Eddy *et al* (1987) observed the resonance spectra in a closed tube filled with air, nitrogen, or helium. Laperre and Thys (1992) considered transient regime and transfer function for standing waves in an air column. Briggs *et al* (1993) described an apparatus for obtaining the resonance curve of an air column resonator. Santarelli *et al* (1993) observed standing sound waves in a cardboard tube. Sungar (1996) considered a demonstration with two loudspeakers facing each other. Lührs (2004) observed standing waves in tubes while the changes in the air pressure disturbed the water surface. Velasco *et al* (2004) observed resonance in a tube closed at both ends. The resonance spectrum of the tube was obtained by the use of a noise sound source. LoPresto (2005) determined end corrections for a quarter-wave tube. See also papers by Lestz (1963); El Hakeem (1965); Roemer and Koentop (1965).

Standing sound waves in air by reflection. Standing waves in air are created by reflection of sound waves from a plane reflector (Kraftmakher 2010a). Sound waves generated by a loudspeaker interfere with waves reflected by a plane reflector, which produces a standing wave (Fig. 1). The variations of sound pressure along the standing wave are determined with a cheap **electret microphone.** The positions of the loudspeaker and of the microphone are fixed, and the measurements are done while manually moving the reflector. The *Motion sensor* determines the position of the reflector. The signal from the microphone is observed with an oscilloscope and measured with an AC-to-DC converter; a Hewlett–Packard 400E voltmeter or a Keithley 177 multimeter serves for the conversion. The output voltage of the converter is proportional to the RMS of the sound pressure. The voltage is acquired by the *Voltage sensor* and displayed versus the distance between the microphone and the reflector.

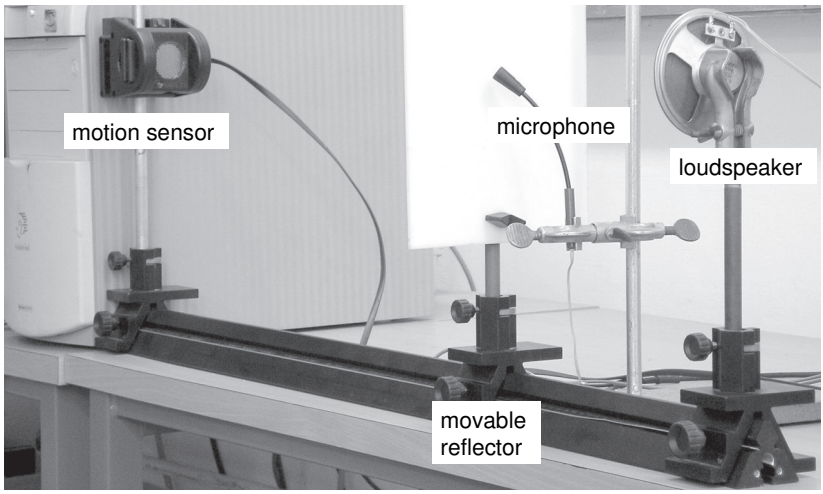

Fig. 1. Setup for observing standing sound waves in air created by reflection.

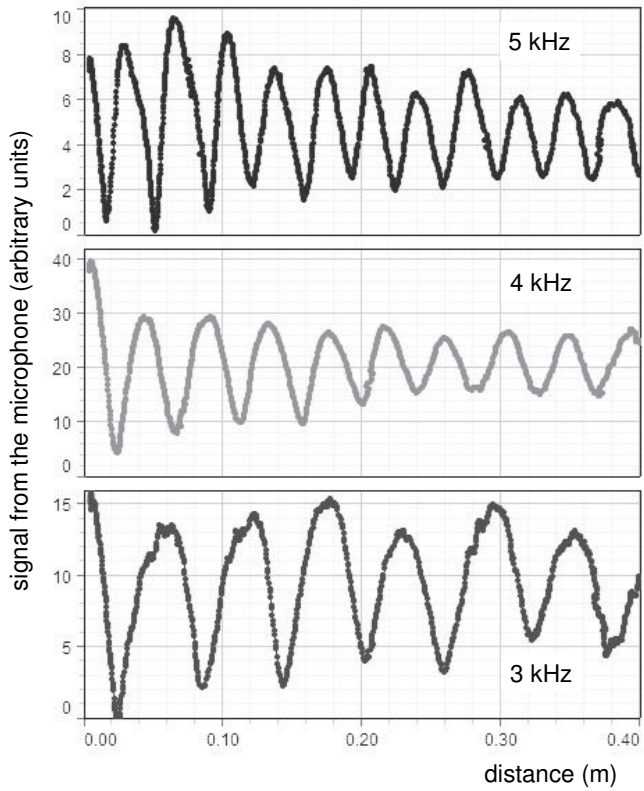

Fig. 2. Signal from the microphone versus distance from the reflector, for three sound frequencies.

The measurements are performed for several frequencies of sound. The distance between the neighboring nodes (or antinodes) in the standing wave is half the sound wavelength. The main difficulty in obtaining correct maps of sound pressure is caused by unavoidable reflections from nearest objects in the room. In the example presented (Fig. 2), the sound frequencies are 3, 4, and 5 kHz. The speed of sound obtained is sufficiently close to the correct value.

Resonance spectrum of air column. The experiment is similar to that described by Jewett (1980). The spectrum of an air column formed by an open tube is recorded using frequency scanning (Kraftmakher 2010a). A cardboard tube, 91 cm in length and 5 cm in diameter, forms an air column (Fig. 3). With a loudspeaker at one end of the open tube and a microphone at the other, the resonance spectrum is obtainable by scanning the sound frequency. The loudspeaker is connected to the *Output 1* operating in the *Auto* mode: it starts to produce the output voltage after starting a run. The frequency is swept from 100 to 2100 Hz in 200 s. The microphone signal is fed to an AC-to-DC converter and can be observed with the *Scope* display.

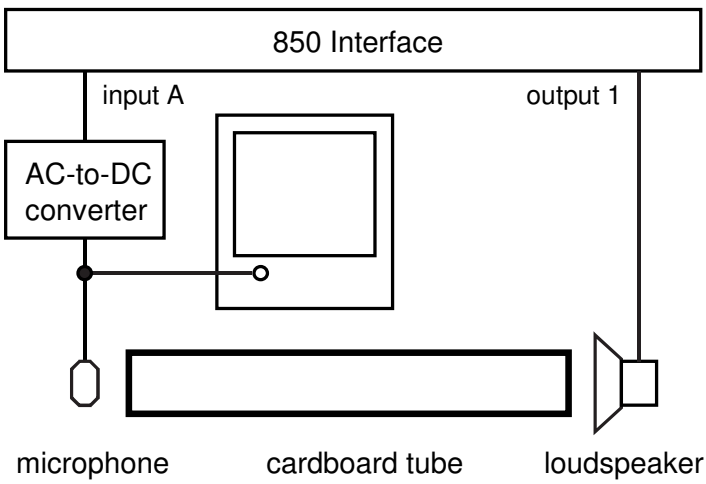

Fig. 3. Setup for recording air column resonance spectra.

DataStudio displays the air column resonance spectrum on the computer display (Fig. 4). The maxima of the spectrum are evenly spaced; in our case, the mean space equals 184.9 Hz. The harmonic frequencies are integral multiples of a fundamental frequency equal to $c/2L$, where c is the speed of sound in air, and L is the length of the column. The length should be corrected for the column radius. This correction equals 1.2 times the radius (Jewett 1980), so that the corrected length is 94 cm. The velocity of sound at 22°C thus appeared to be 347.6 m.s^{-1}.

In the spectrum obtained, an unexpected maximum is seen in the range 230–290 Hz, and the signal rapidly grows at frequencies above 1600 Hz. Both phenomena are caused by the frequency response of the loudspeaker and the microphone. To check this guess, the measurements were repeated without the tube. In these measurements, the microphone is placed close to the loudspeaker, whose power is greatly reduced. Due to this measure, the influence of reflected sound waves becomes insignificant, and one can see the frequency response of the loudspeaker–microphone combination. The sharp maximum at low frequencies is due to the loudspeaker. As the first approach, the corrected spectrum is obtainable by dividing the first graph by the second. With the correction, the maximum in the range 230–290 Hz disappears, as well as the rapid growth of signal above 1600 Hz.

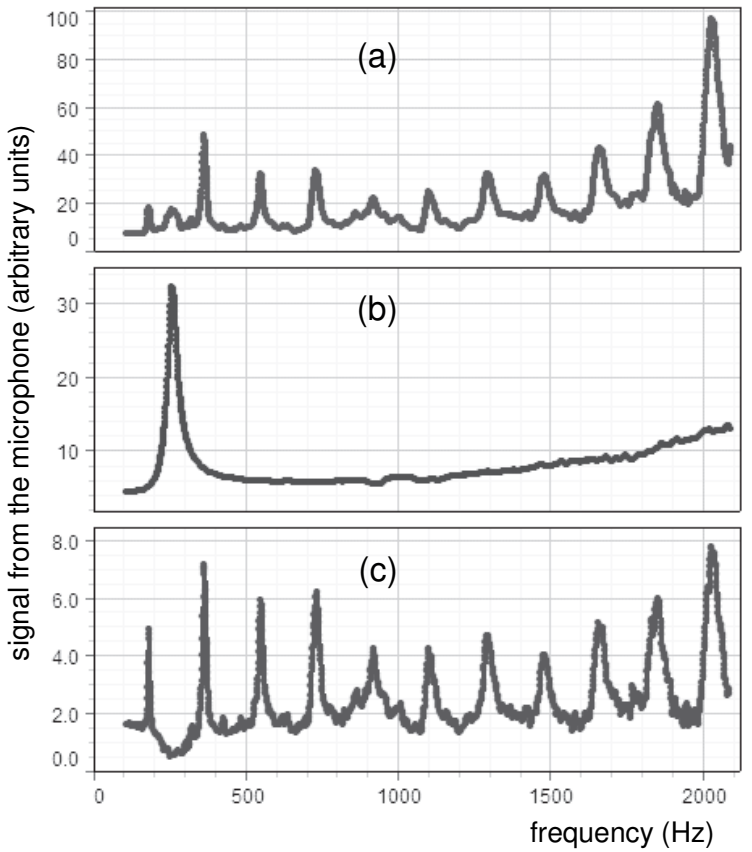

Fig. 4. Air column resonance spectrum: (a) raw measurement data; (b) frequency response of the loudspeaker–microphone combination; (c) corrected spectrum.

Standing waves in strings. Experiments on standing waves in strings were described by Pinkston (1981); Clay and Kernel (1982); Gupta (1988); Kashy *et al* (1997); Kinchin (2001); Inman (2006); Sobel (2007); Bhathal *et al* (2010). The standing waves are typically observed visually. An optical method for detecting string oscillations was reported by Sandoval and Porta (1985) and Hall (1987).

In our experiment, the *Mechanical vibrator* (SF-9324) triggers transverse oscillations of an elastic cord. The force stretching an elastic cord senses these oscillations, so the spectrum of standing waves can be seen from the *Force sensor* data (Kraftmakher 2013b). Using the frequency sweep of the driving force, *Capstone* displays the spectrum of the standing waves. The *Output 1* drives the vibrator, which triggers transverse oscillations in the cord (Fig. 5). The second end of the cord is attached to the *Force sensor* (CI-6537). The amplitude of the vibrations decreases with increasing frequency. To reduce this dependence, a capacitor (C = 100 μF) is put in series with the vibrator coil.

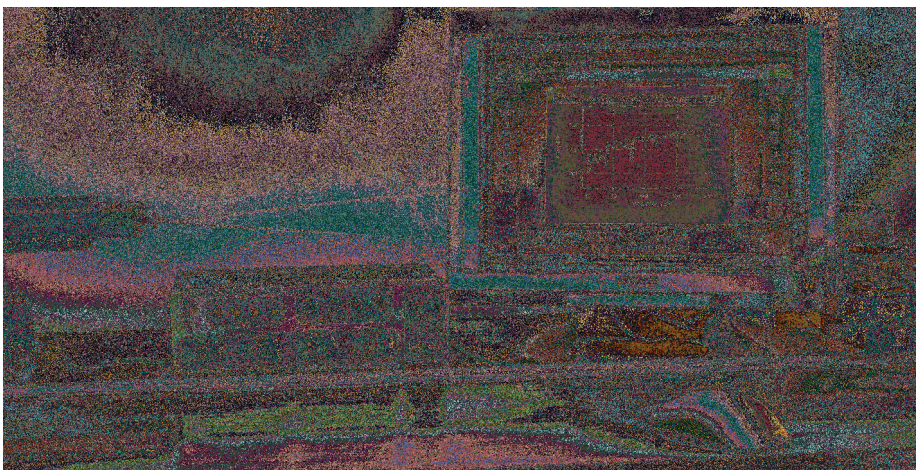

Fig. 5. The setup for observing standing waves.

The *Output 1* operates in the *Auto* mode: it begins to build the output voltage immediately after starting a run. The frequency is set to sweep from 20 to 220 Hz during 400 s, so the instant frequency is calculated by the *Capstone* software as 20+0.5*Time(s). The software displays the signal from the *Force sensor* versus the continually varying frequency of the generator. The sensor presents stretching forces with negative values. This signal shows the stretching force and its variations caused by the transverse oscillations of the cord. The oscillations increase the stretching force, and the spectrum of standing waves is clearly seen (Fig. 6). The spectrum is seen along with the stretching force, and the cord fatigue during a run is also observable. As an example, the spectrum for

an initial stretching force of nearly 2.2 N is shown. If necessary, the spectrum can be made clearer using the *Smoothing* operation.

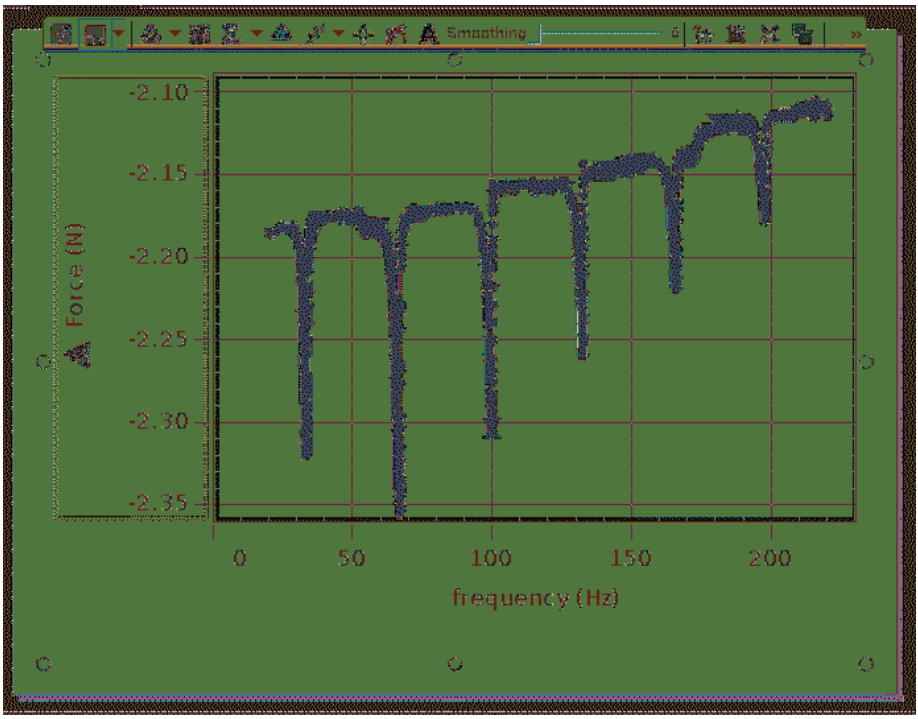

Fig. 6. Spectrum of standing waves in the elastic cord displayed by *Capstone*, raw measurement data.

2.11. Doppler's effect

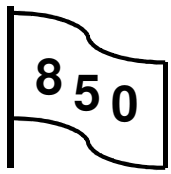

The *Sound sensor* moves toward a loudspeaker and back, and the *FFT* tool displays the spectrum of the incoming sound. The frequency conversion technique makes evident the frequency shift.

AIP Emilio Segrè Visual Archives
Christian Doppler (1803–1853)

Additional equipment: *Sound sensor*, loudspeaker.

Doppler's effect is important in many areas of physics and technology. Only a part of numerous papers devoted to this topic are listed here. Weltin (1961) described a simple and effective demonstration of Doppler's effect. A small electric buzzer and a 1.5 V battery are mounted on two ends of a meter stick. The stick is brought to rotation around its center of mass by a small hand drill. Because of a high pitch of the buzzer, the frequency variations are discernible for speeds less than one revolution per second. Barnes (1974b) used a source of sound carried by a toy car. Nerbun and Leskovec (1976) employed two ultrasonic transducers (40 kHz), the receiver stationary at the end of a linear air track, and the source mounted on a moving glider. The signal from the receiver is fed to one of the inputs of a phase detector, and the signal of the transmitter to the second input. The detector produces a frequency equal to Doppler's shift. Bates (1977) observed the effect in the microwave region. Schiel *et al* (1978) reported on measurements of the second-order Doppler's effect. For sound, Doppler's shift is somewhat different for the motion either of the observer or the emitter. Zhong (1989) used a wireless microphone fixed on the edge of a motor-driven turning disc as the receiver. Bianchetti and Ganci (1994) developed a demonstration with a moving ultrasonic source or detector. Neuhoff and McBeath (1997) considered illusions related to Doppler's effect and caused by the peculiarities of the human perception of sound. Cox and Peavy (1998)

described measurements of Doppler's shifts from a sound source carried by a walking student. The frequency of the signal received by a microphone was measured, after amplification, by a frequency meter. In another experiment, beats were produced between the moving speaker's shifted signal and the sound from a stationary speaker. Bensky and Frey (2001) used the beat technique and the spectra of signals for measuring Doppler's shift for both constant-velocity or accelerated sound sources. See also papers by Stockman (1962); Rovers and Skarsgard (1967); Muldawer and Meiners (1967); Kosiewicz (1971); Saba and da Rosa (2003).

In our demonstration, a loudspeaker is connected to the *Output 1* set at 5 kHz. *The Sound sensor* is mounted on a pendulum (Fig. 1). The *Fast Fourier Transform* displays the spectrum of the incoming signal. To enhance the sensitivity, the frequency conversion is used. The *Output 2* provides a 4.9 kHz voltage. The *Calculator* calculates the product of this voltage and the signal from the *Sound sensor*, which contains the sum and difference of the two frequencies, 9.9 and 0.1 kHz. The lower frequency is used for the detection of the Doppler shift when the sensor moves towards the loudspeaker and back. The difference in the spectra is evident. With a constant-velocity motion of the sensor, the results could be compared with the theory.

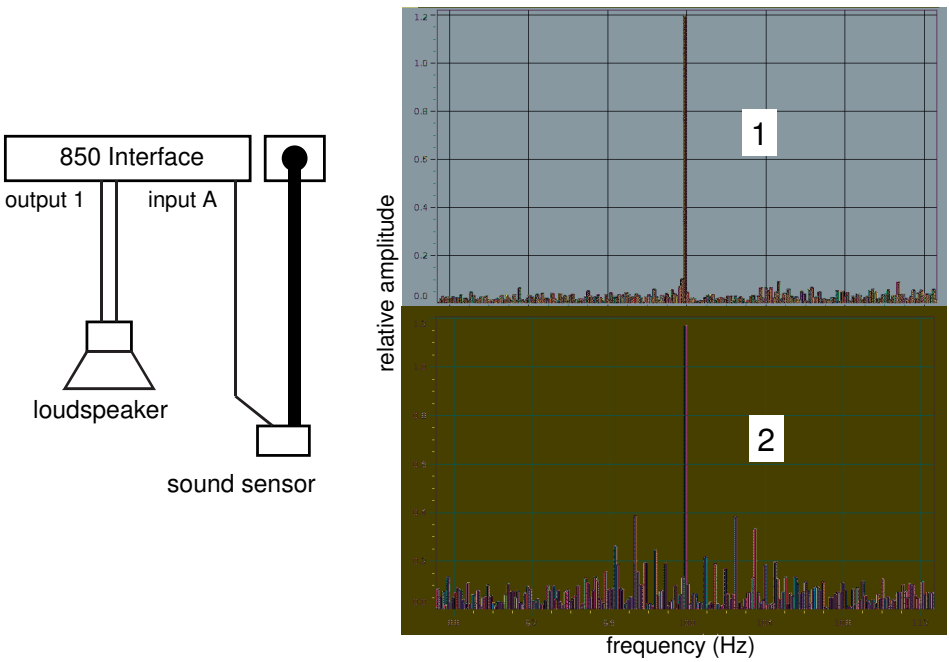

Fig. 1. The setup and spectrum of the signal after frequency conversion: 1–fixed microphone, 2–swinging microphone.

Molecular Physics

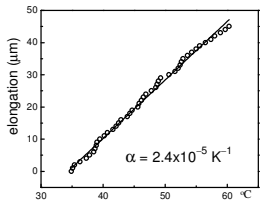

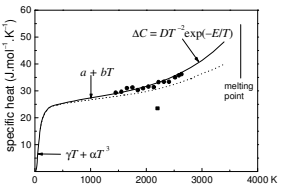

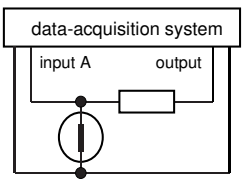

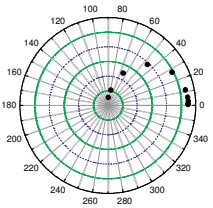

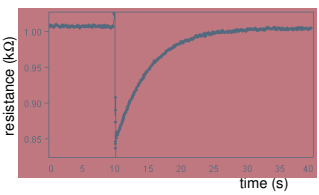

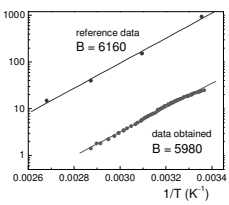

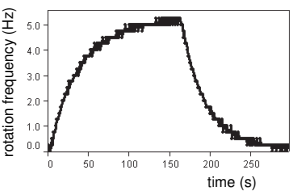

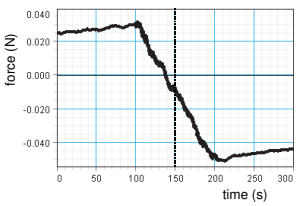

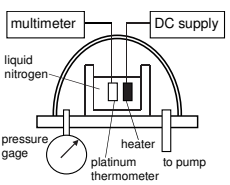

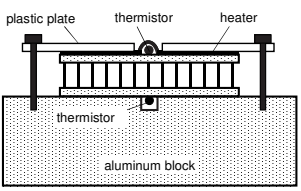

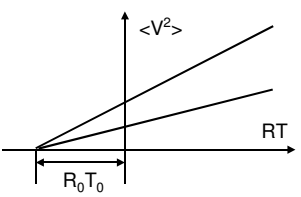

3. Molecular Physics 137

3.1. Thermal expansion of solids

The linear thermal expansivity of an aluminum-based alloy is determined using a dial gauge of 1 μm resolution (Kraftmakher 2013e)

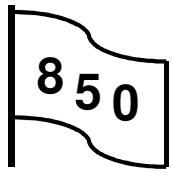

Additional equipment: *High-accuracy temperature sensor*, sample, dial gauge.

The thermal expansion of solids is due to **anharmonicity** of lattice vibrations, which increase with temperature (Pohl 1987; Kittel 2005). In addition to the general temperature dependence related to anharmonicity, the thermal expansion of solids reflects some important physical phenomena, such as **phase transitions** and formation of **equilibrium point defects** in crystal lattice. The thermal expansion of materials is very important for many technical applications.

The linear thermal expansion of a solid, ΔL, is a nonlinear function of temperature:

$$\Delta L/L_0 = f(T), \tag{1}$$

where L_0 is the length of the sample at a reference temperature, usually 293 K.

The coefficient of linear thermal expansion, or **linear expansivity**, is

$$\alpha = (1/L_0)\mathrm{d}L/\mathrm{d}T. \tag{2}$$

The expansivity usually increases with temperature. For **anisotropic** crystals, the linear expansivity depends on the orientation of the sample. At temperatures below the **Debye temperature**, the expansivity rapidly decreases when decreasing temperature. For metals, the higher the melting temperature T_m, the lower the mean expansivity. For many metals, the total linear expansion from the absolute zero to the melting point amounts to 2–3%. This simple rule may serve for estimating the mean expansivity of metals. As an example, values of the linear expansivity of copper and tungsten recommended by White and Minges (1997) are shown (Fig. 1). For both metals, the total expansion from absolute zero to melting points is nearly 2.5%. The significant nonlinear increase of the expansivity of tungsten at high temperatures is probably caused by the formation of equilibrium point defects (vacancies) in the crystal lattice. For copper, the effect is not so strong. The reason is that the maximum equilibrium vacancy concentration (at the melting point) in copper is much less than in tungsten. Similar nonlinear effects at high temperatures are seen in the specific heat of metals (Kraftmakher 2000a).

Brief review of dilatometeric techniques. Modern methods for measuring the dilatation of solids provide sensitivity of the order of 10^{-10} m and even better. Along with a significant progress in traditional **dilatometry**, two new techniques appeared, modulation dilatometry and dynamic technique.

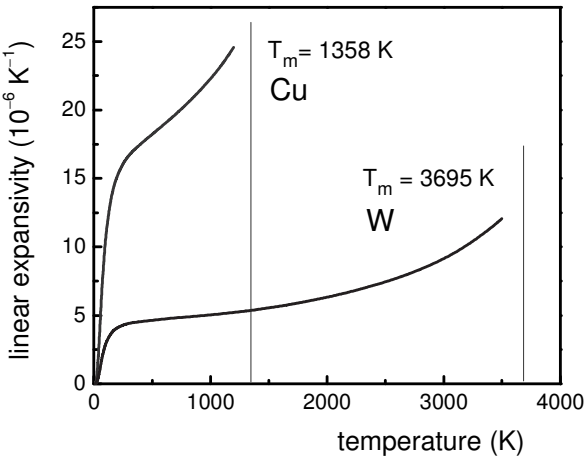

Fig. 1. Linear thermal expansivity of copper and tungsten (data recommended by White and Minges 1997). Melting points of the metals are indicated.

The traditional experimental techniques for studying the thermal expansion of solids fall into one of the following categories (Bennett 1977):

• **push-rod** dilatometers, in which the dilatation of a sample is measured with an appropriate mechanical gauge;

• **comparators** using some type of microscope;

• devices, in which the expansion of a sample causes a mirror to tilt, either directly or via a rotating rod;

• dilatometers, where the dilatation of a sample governs the **capacitance** of a specially designed capacitor;

• **X-ray diffraction** methods, where changes are measured in the spacing of a set of atomic planes in crystalline materials;

• **laser** interferometers.

Two new methods should be added to the above list:

• **dynamic dilatometry**: rapidly heating a sample over a wide temperature range and simultaneously measuring its temperature and dilatation (Miiller and Cezairliyan 1982);

• **modulation technique**: creating small temperature oscillations in a sample about a mean temperature and measuring corresponding oscillations in its length; so the linear expansivity in a narrow temperature range is directly measured (Kraftmakher and Cheremisina 1965; Johansen 1987). This technique ignores irregular external disturbances and senses only what is necessary for determining the thermal expansivity. Very sensitive methods exist to measure small periodic displacements.

The dynamic dilatometric technique developed by Miiler and Cezairliyan (1982) involves resistively heating the sample from room temperatures to above 1500 K in less than 1 s. A modified Michelson's interferometer is used to determine the dilatation of the sample. The light source is a plane-polarized He–Ne laser. The sample has the form of a tube with parallel optical flats on opposite sides. The distance between the flats, 6 mm, represents the length of the sample. The sample acts as a double reflector in the path of the laser beam. The interferometer is thus insensitive to translational motion of the sample (Fig. 2).

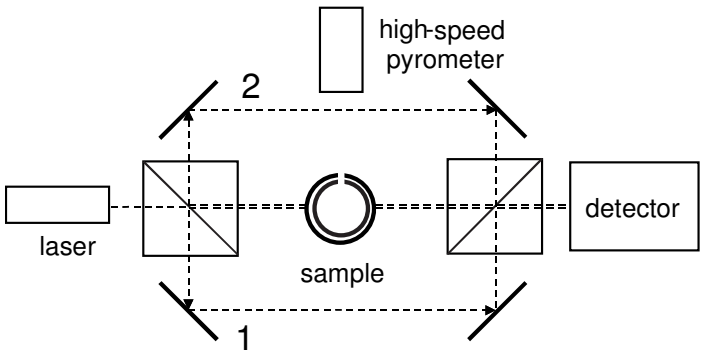

Fig. 2. Principle of dynamic dilatometry (Miiller and Cezairliyan 1982).

A small rectangular hole in the wall of the sample, 0.5×1 mm, serves as a blackbody model for temperature measurements. The temperature of the sample is measured with a high-speed photoelectric pyrometer capable of 1200 evaluations per second. The system has two important advantages: (i) the measurements relate to the blackbody temperature, and (ii) only a central portion of the sample is involved in the measurements, so that there is no need to take into account the temperature distribution along the sample. The authors investigated the high-temperature thermal expansion of Ta, Mo, Nb, and W.

Righini *et al* (1986) designed a dynamic dilatometer, which correlates the thermal expansion of the sample to its temperature profile. An interferometer measures the longitudinal expansion of a sample, while a scanning optical pyrometer with a rotating mirror determines its temperature profile (Fig. 3). A typical spacing between two consecutive measurements is 0.35 mm with a pyrometer viewing area of 0.8 mm in diameter. Two massive brass clamps maintain the ends of the sample close to room temperature and provide steep temperature gradients towards the ends. A corner cube retroreflector is attached to the lower (moving) clamp, while the beam bender to the upper clamp. Two thermocouples spot-welded at the ends of the sample measure its temperature in the regions, where pyrometric measurements are impossible. The resolution of the interferometer is about 0.15 μm, and 2000 measurements per second are feasible.

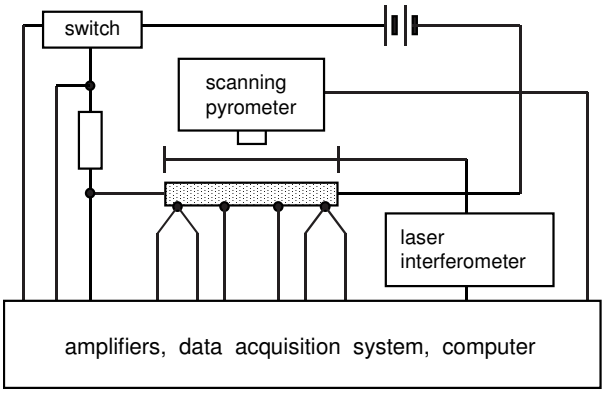

Fig. 3. Schematic of dynamic dilatometer by Righini *et al* (1986).

Direct measurements of the "true" thermal expansivity, that is, the thermal expansion coefficient within a narrow temperature interval, became possible with a modulation technique. Modulation dilatometry involves oscillating the temperature of the sample around a mean value and measuring corresponding oscillations in the length of the sample. Under such conditions, the linear expansivity is measured directly. This approach ignores the plastic deformation of the sample and irregular external disturbances: only those changes in the length are measured, which reversibly follow the temperature oscillations. This seems the best way to circumvent the main problems peculiar to the traditional dilatometry at high temperatures. To measure the oscillations in the length of the sample, most sensitive techniques are applicable.

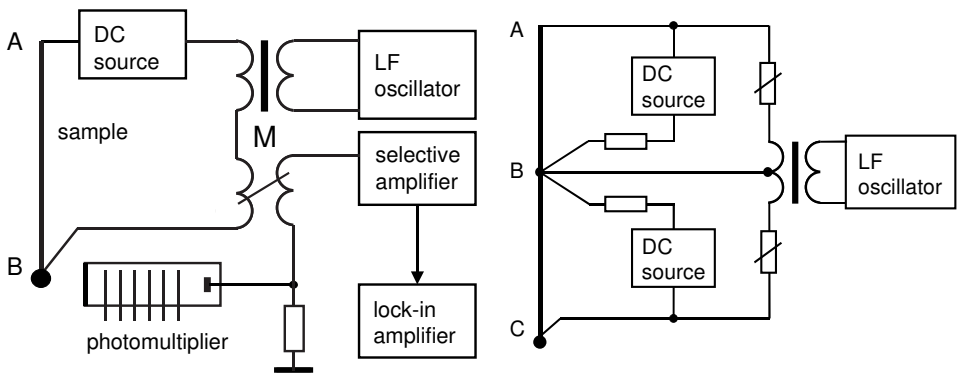

Fig. 4. Left: modulation measurements of thermal expansivity (Kraftmakher and Cheremisina 1965); right: direct comparison of thermal expansivity of two samples, AB and BC (Kraftmakher 1967b).

In the first modulation measurements, an AC current or a DC current with a small AC component heated a wire sample (Fig. 4). The upper end of the

sample is fixed, and the lower end is pulled by a load or a spring and is projected onto the entrance slit of a photomultiplier. The AC voltage at the output of the photomultiplier is proportional to the amplitude of the oscillations in the length of the sample. The temperature oscillations are determined from either the electrical resistance of the sample or the radiation from it. They can be evaluated if the specific heat of the sample is known. When a DC current I_0 with a small AC component heats the sample, the linear expansivity equals

$$\alpha = mc\omega V/2lKI_0U, \tag{3}$$

where m, c, and l are the mass, specific heat, and length of the sample, ω is the modulation frequency, U is the AC voltage across the sample, V is the AC component at the output of the photomultiplier, and K is the sensitivity of the photomultiplier to the dilatation of the sample.

The sensitivity to the dilatation is available from static measurements: $K = \mathrm{d}V_0/\mathrm{d}l$, where V_0 is the DC voltage at the output of the photomultiplier. Equation (3) is valid for an **adiabatic regime** of the modulation measurements. Determinations of the phase shift between the heating-power oscillations and the temperature oscillations are necessary for measurements in a **nonadiabatic** regime (see Experiment 3.4).

It is easy to assemble a circuit, whose balance is independent of the AC component of the heating current. In this case, the AC signal at the output of the photomultiplier is balanced by a variable mutual inductance M with the heating current passing through its primary winding. Usually, the modulation frequency in the range 10–100 Hz is sufficiently high to satisfy the criterion of adiabaticity. Otherwise, the temperature oscillations obey formulas for a nonadiabatic regime. A differential method was proposed (Kraftmakher 1967b): a wire sample consists of two portions joined together, a sample under study AB and a reference sample BC of known linear expansivity. The two portions are heated by DC currents from separate sources and by AC currents from a common LF oscillator. The temperature oscillations in the two portions are of opposite phase. By adjusting the AC components of the heating currents, the oscillations in the length of the reference portion completely balance those of the portion under study. Now the photosensor acts only as a zero indicator, and any variations in its sensitivity, as well as in the intensity of the light source, *etc*, do not contribute. To calculate the expansivity, one has to determine the temperature oscillations in the two portions. With this technique, the thermal expansion of platinum (1200–1900 K) and of tungsten (2000–2900 K) was determined. In both cases, the nonlinear increase of the thermal expansivity was attributed to the vacancy formation in crystal lattice (Kraftmakher 1967c, 1972).

Oscillations in the length of the sample are measurable by various methods, including those of highest sensitivity. The interferometric method is one of such techniques. In the interferometric modulation dilatometer (Glazkov and Kraftmakher 1983), samples are in the form of a thick wire or a rod (Fig. 5). The upper end of the sample is fixed, while a small flat mirror M1 is attached to its lower end. A DC current from a stabilized source heats the sample. A small

AC current is fed to a central portion of the sample through thin wires. The temperature oscillations thus occur only in this portion. To prevent an offshoot of the AC current to the upper and lower portions of the sample, a coil of high AC impedance is placed in series with the sample (not shown in Fig. 5).

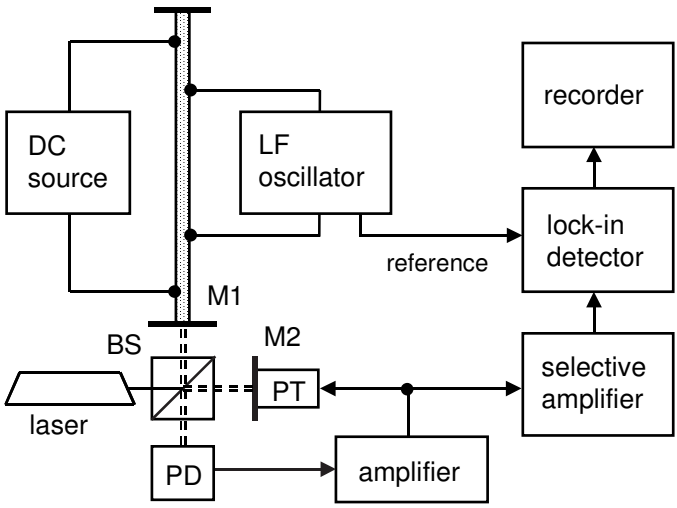

Fig. 5. Interferometric modulation dilatometer (Glazkov and Kraftmakher 1983). PT–piezoelectric transducer, BS–beam splitter, PD–photodiode, M–mirrors.

The beam of a He–Ne laser passes through a beam splitter BS and falls onto the mirror M1 and a mirror M2 attached to a piezoelectric transducer PT. A photodiode senses the intensity of the interference pattern. Its output voltage, after amplification, is applied to the transducer with such a polarity that the oscillations of both mirrors are in phase. Owing to the high gain of the amplifier, the displacements of the mirror M2 follow those of the mirror M1. The AC voltage applied to the transducer is therefore strictly proportional to the oscillations in the length of the sample. A selective amplifier tuned to the modulation frequency amplifies this voltage, and a lock-in detector measures it. The reference voltage for the detector is taken from the oscillator supplying the AC current to the central portion of the sample. The DC output voltage of the detector is proportional to the amplitude of the oscillations of the sample length. Modulation dilatometry was reviewed by the author (Kraftmakher 1973b, 1984, 1992, 2004d).

Thermal expansion of an aluminum alloy. Thermal expansion is a popular topic for student laboratory experiments and classroom demonstrations. Various measurement techniques are employed for this aim (for instance, Fox 1990; Fakhruddin 2006; Inbanathan *et al* 2007; Scholl and Liby 2009; Graf 2012; Dounas-Frazer *et al* 2013).

In our experiment, the thermal expansion of an aluminum-based alloy is determined with a common dial gauge. This simple method is well suited for undergraduate laboratories. A cylindrical sample, 38 mm in diameter and 75 mm long, is placed in a glass filled with hot water (Fig. 6). To reduce the heat exchange between the sample and the gauge, a thin glass plate is put between them. The *High-accuracy temperature sensor* (CI-6525) measures the temperature. With a dial gauge of 1 μm resolution, measurements over a limited temperature range are sufficient for determining the thermal expansivity.

The measurements are performed during the cooling process. *Capstone* displays the temperature of the sample with *Digits*. The *Keep* mode of recording data is used: commands for recording the temperature data are given whenever the length of the sample changes by 1 μm. The temperature data appear in the *Table*, and the data for corresponding changes in the length are added by hand. The *Graph* displays the dilatation of the sample versus temperature. At room temperatures, the expansivity of aluminum is 2.3×10^{-5} K^{-1} (Lide 2008). For aluminum-based alloys, this figure may be somewhat different. The linear expansivity of the sample appeared to be 2.4×10^{-5} K^{-1}.

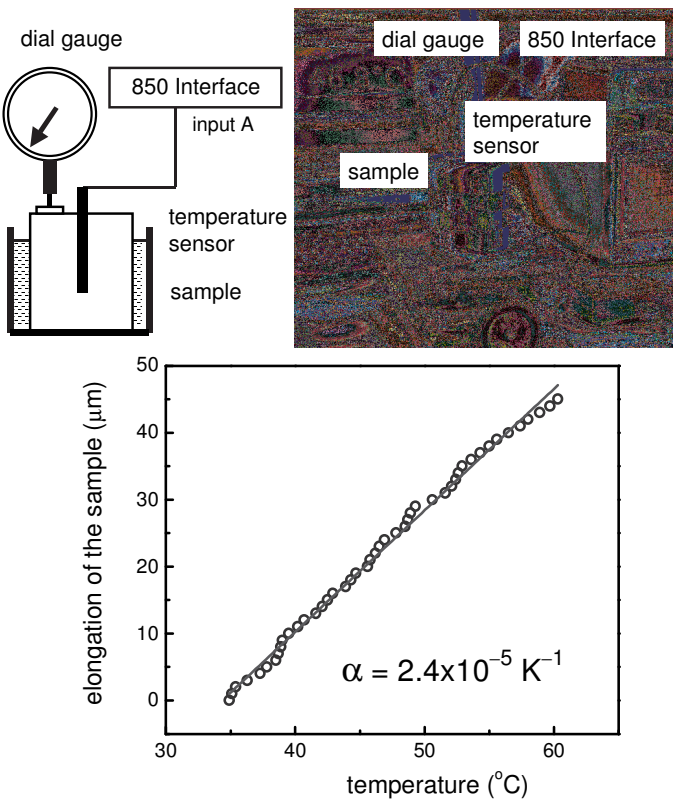

Fig. 6. The setup and thermal expansion of the sample.

3.2. Pulse calorimetry

The tungsten filament inside a low power light bulb serves as a sample, a heater, and a thermometer (Kraftmakher 2004c).

Additional equipment: *Voltage sensor*, *Power amplifier II*, decade resistance box, two resistors.

Brief review of calorimetric techniques. Calorimetric measurements seem, at first glance, to be simple and straightforward. One has to supply some heat, ΔQ, to the sample and to measure an increment in its temperature, ΔT. Clearly,

$$\Delta Q = mc\Delta T, \tag{1}$$

where m is the mass of the sample, and c is the specific heat.

The above relation is the simplest form of the **heat balance equation**, where no heat exchange occurs between the sample and its surroundings. Otherwise, the heat exchange is a problem. First, it is impossible to completely avoid uncontrollable heat exchange between the sample and its surroundings. Second, the accuracy of temperature measurements in different temperature ranges is very different. Over many years of development, the following methods have been elaborated for overcoming these difficulties (for reviews see Maglić *et al* 1984, 1992; Ho 1988).

• **Adiabatic calorimetry.** All possible precautions are undertaken to minimize the unwanted heat exchange between the sample and its surroundings. For this purpose, a shield encloses the calorimeter, and its temperature is kept equal to that of the calorimeter during the entire experiment (Fig. 1). This is the so-called

adiabatic shield. The calorimeter and the shield are placed in a vacuum chamber, so that only radiative heat exchange occurs between the calorimeter and its surroundings. An electrical heater heats the calorimeter, and a resistance thermometer or thermocouple measures its temperature. The heat supplied to the calorimeter and the temperature increment are thus accurately known. To reduce the heat flow through the electrical leads, they are thermally anchored to the adiabatic shield. Equation (1) is used for the calculations. With radiative heat exchange, the heat losses from the calorimeter are proportional to $T^3\Delta T$, where ΔT is the temperature difference between the calorimeter and the shield ($\Delta T << T$). Adiabatic calorimetry, being an excellent technique at low and intermediate temperatures, therefore fails at high temperatures.

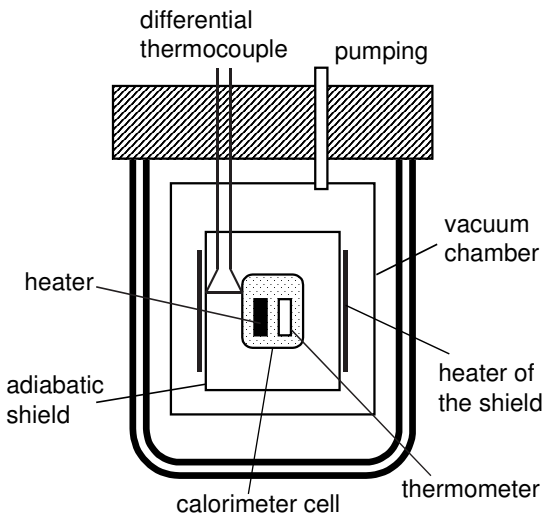

Fig. 1. Simplified diagram of adiabatic calorimeter. Temperature of the adiabatic shield is automatically kept equal to that of the calorimeter cell.

• **Drop method.** A sample under study is placed in a furnace, and its temperature is measured by a thermocouple or optical pyrometer (Fig. 2). Then the sample is dropped into a calorimeter kept at a temperature convenient for measuring the heat released from the sample, usually room temperature. A resistance thermometer measures the increment of the temperature of the calorimeter, which is proportional to the enthalpy of the sample. The calorimetric measurements are thus carried out under conditions most favorable for avoiding any unwanted heat exchange. The price for this gain is that the result of the measurements is the enthalpy, while the specific heat is obtainable as its temperature derivative. When the specific heat is weakly temperature dependent, the method is quite adequate. The situation becomes complicated when the specific heat varies in a narrow temperature range, but the corresponding changes in the enthalpy are too small to be determined precisely.

An additional problem arises if a first-order phase transition occurs at an intermediate temperature, and the thermodynamic equilibrium in the sample after cooling is doubtful. Drop calorimetry was proposed long ago when there was no alternative for measurements at high temperatures. However, it remains useful today, especially for nonconducting materials.

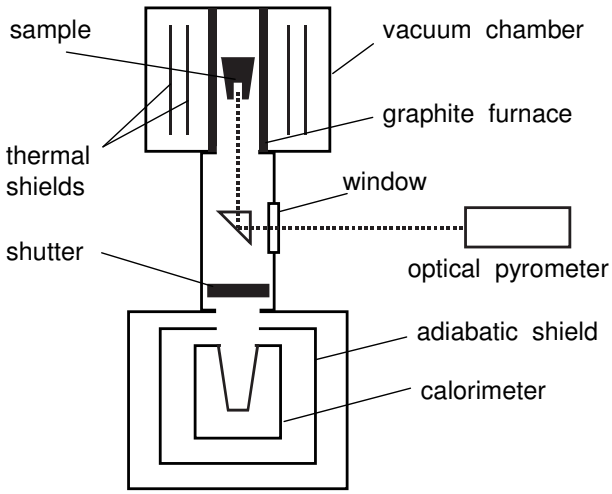

Fig. 2. Setup for drop calorimetry (Glukhikh *et al* 1966). The heat released by the sample is measured with an adiabatic calorimeter.

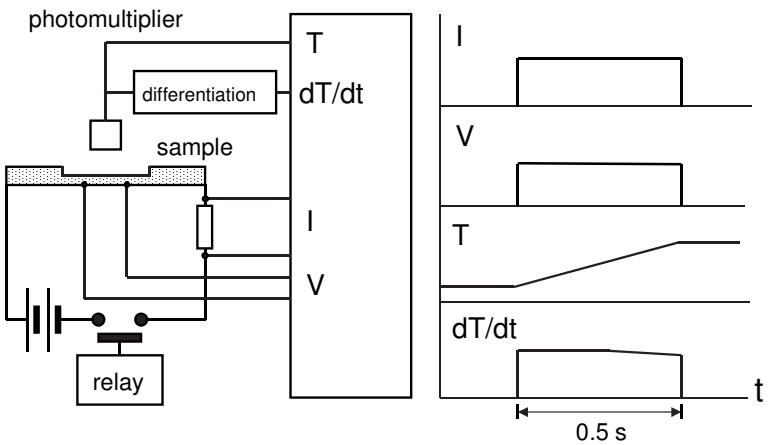

Fig. 3. Schematic of pulse calorimetry (Rasor and McClelland 1960).

• **Pulse and dynamic techniques.** Shortening the measurement time reduces the influence of any uncontrollable heat exchange between a sample and its surroundings. This approach is applicable whenever it is possible to rapidly heat the sample and measure its temperature. Conducting samples heated by an

electric current are well suited for such measurements. The temperature of the sample is measured through its electrical resistance or radiation. The results obtained can be corrected for heat losses if necessary. Pulse calorimetry employs small increments of temperature of the sample (Fig. 3), and the result of one measurement is the specific heat at a single temperature (Rasor and McClelland 1960; Kollie 1967). Dynamic calorimetry consists of rapidly heating the sample over a wide temperature range. The heating power and temperature of the sample are measured continuously during a run (Cezairliyan and McClure 1971). The heat losses from the sample are measured and taken into account. These data are sufficient to evaluate the specific heat over the whole temperature range.

• **Relaxation method.** The heat exchange between the sample and its surroundings is determined and involved in the measurements of the specific heat. This technique employs measurements of the cooling (or heating) rate of a sample, whose temperature initially differs from that of the surroundings. The calorimeter is first brought to a temperature $T = T_0 + \Delta T$, slightly higher than that of the surroundings, T_0. After the heating ends, the temperature of the calorimeter decays exponentially:

$$T = T_0 + \Delta T \exp(-t/\tau), \tag{2}$$

where $\tau = C/K$ is the relaxation time, C is the sum of the heat capacities of the sample and of the calorimeter itself, and K is the heat transfer coefficient (the temperature derivative of heat losses).

The determination of the specific heat thus includes measurement of the relaxation time and of the heat transfer coefficient. Under steady-state conditions, $P = K\Delta T$, where P is the power supplied to the calorimeter necessary to increase its temperature by ΔT. The internal time constant (inside the sample, and between the sample, the heater, and the thermometer) must be much shorter than the external relaxation time τ.

• **Modulation calorimetry.** Measurements are made in a regime of periodic oscillation of the power supplied to a sample. This causes periodic oscillations of the temperature of the sample, and their amplitude directly relates to the heat capacity of the sample. Modifications of this technique differ in the methods of modulating the heating power (direct electric heating, electron bombardment, use of separate heaters, radiation or induction heating, Peltier's effect) and of measuring the temperature oscillations (through the resistance of the sample or radiation from it, by the use of pyroelectric sensors, thermocouples, or resistance thermometers). Modulation calorimetry offers very attractive features: temperatures from 0.1 K up to melting points of refractory metals; samples as small as 1 μg; and resolution of the order of 0.01%. The temperature oscillations necessary for the measurements are of the order of 1 K at high temperatures, 1 mK at room temperatures, and 1 μK at liquid helium temperatures. Specific heat can be measured versus an external parameter, such as a magnetic field or pressure (for reviews, see Kraftmakher 1973a, 2002a, 2004d).

Student experiments on specific heat are described by Fox and McMaster (1975); Bligh *et al* (1987); Clayhold and Priest (2007).

High-temperature specific heat of tungsten. A usual incandescent light bulb provides excellent opportunities for acquaintance with pulse calorimetry at high temperatures. The tungsten filament serves simultaneously as a sample, a heater, and a thermometer. A pulse current passes through the tungsten filament and heats it. The mean temperature of the filament and the temperature increments are determined from its electrical resistance. The most reliable data on high-temperature electrical resistance of tungsten were published by Roeser and Wensel (1941) and are reproduced in Table 1.

Table 1. Resistance ratio R/R_{273} and temperature coefficient of resistance β (10^{-5} K^{-1}) for tungsten (Roeser and Wensel 1941).

T (K)	R/R_{273}	β	T (K)	R/R_{273}	β
1500	7.78	621	2600	15.08	699
1600	8.41	629	2700	15.78	704
1700	9.04	637	2800	16.48	709
1800	9.69	645	2900	17.19	713
1900	10.34	654	3000	17.90	718
2000	11.00	661	3100	18.62	723
2100	11.65	669	3200	19.35	728
2200	12.33	676	3300	20.08	733
2300	13.01	682	3400	20.82	737
2400	13.69	688	3500	21.56	739
2500	14.38	694	3600	22.30	740

A low power vacuum light bulb (5 V, 0.5 W) is included in a bridge circuit (Fig. 4). A *Positive square wave* voltage from the *Power amplifier II* feeds the bridge. The *Voltage sensor* measures the output voltage of the bridge, and the *Scope* displays it. During the heating period, the temperature of the sample increases, which is seen from the increase of its resistance. The heating period must be sufficiently short to make this increase linear with time. Due to a relatively small temperature increment, changes of heat losses from the sample during the heating period are much smaller than the heating power. Between the heating pulses, the temperature of the sample decreases but the output voltage of the bridge is zero, regardless of the resistance of the sample. The heat balance equation for the heating period Δt is

$$mc\Delta T = (P - Q)\Delta t, \tag{3}$$

where $P = IV$ is the power supplied to the sample, Q is the heat loss from it, and ΔT is the temperature increment during the heating period. This increment is supposed to be small, so that changes in the resistance of the sample and heat losses from it are also small. Therefore, if the heating current is constant during the heating, the quantity $P - Q$ is independent of time. The temperature increment ΔT is determined by the increment of the resistance of the sample ΔR:

$$\Delta T = \Delta R/R' = \Delta R/R_{273}\beta, \tag{4}$$

where $R' = \mathrm{d}R/\mathrm{d}T$ is the temperature derivative of the resistance of the sample, R_{273} is its resistance at 273 K, and $\beta = R'/R_{273}$ is the temperature coefficient of resistance.

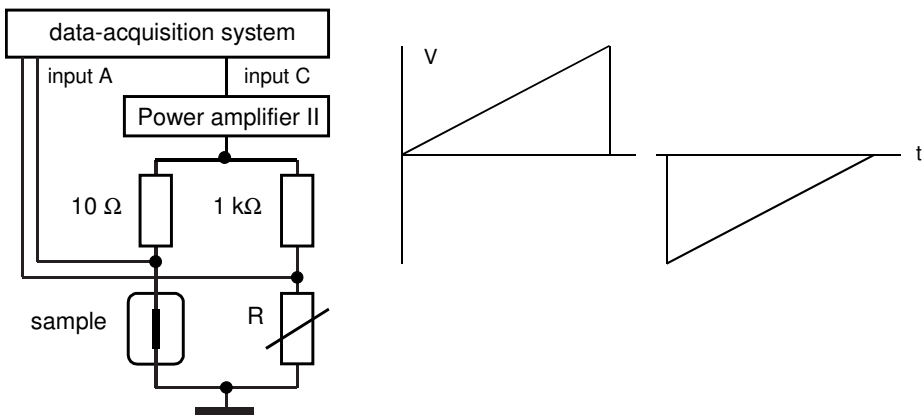

Fig. 4. Diagram explaining pulse calorimetry. The output voltage of the bridge V reflects temperature changes during the heating period.

The heat capacity of the sample thus equals

$$mc = (P - Q)R'\Delta t/\Delta R = (P - Q)R_{273}\beta\Delta t/\Delta R. \tag{5}$$

In the experiment, the amplitude of the electric pulses applied to the bridge is varied, and one balances the bridge by changing the variable resistor R. After the bridge is nearly balanced, it is easy to adjust this variable resistor to achieve the balance at the start and at the end of the heating period. From these adjustments, one determines two corresponding resistances R_1 and R_2, and calculates the increment of the resistance $\Delta R = R_2 - R_1$. In our case, the heating period Δt equals half the period of the electric pulses. In a steady-state regime, the total energy supplied to the sample during one period equals the heat loss energy. This means that $P = 2Q$, and $P - Q = Q$. The power P is calculated from values of the voltage applied to the bridge and the resistance of the sample.

The R_{273} value is obtainable from measurements taken with gradually decreasing the heating current and extrapolating the results to zero current. For tungsten, the R_{293}/R_{273} ratio equals 1.095. A correct determination of the R_{273} value for a low-resistance filament is difficult because of the contribution of

leads inside the light bulb. Therefore, it is worth remembering that vacuum light bulbs operate in the 2400 to 2500 K range. For these temperatures, the R/R_{273} ratio equals 13.69 and 14.38, respectively. With the R_{273} value, the temperature T and temperature coefficient of resistance β of a tungsten filament are available from the relations fitting the Roeser and Wensel (1941) data ($X = R/R_{273}$):

$$T = 170 + 184X - 1.8X^2 + 0.02X^3, \quad (6)$$

$$\beta = dX/dT = 0.005 + 9.6\times10^{-7}T - 7.68\times10^{-11}T^2. \quad (7)$$

In our case, $R_{273} = 3.2\pm0.1\ \Omega$. The heat capacity of the sample in a wide temperature range is determined using Eq. (5). In the measurements, the frequency of the electric pulses is in the range of 100 to 500 Hz (Table 2). The change of the frequency is necessary to restrict the temperature increments during the heating period and thus to meet the basic requirement for pulse calorimetry. Below 1500 K, cold-end effects become significant, and above 2800 K a problem arises due to the evaporation of tungsten.

Table 2. Example of experimental data and the heat capacity of the sample. R_m and T_m are the mean values of the resistance and the temperature.

f (Hz)	R_m (Ω)	ΔR (Ω)	T_m (K)	ΔT (K)	Q (mW)	mc (μJ.K^{-1})
100	23.95	0.66	1454	33.1	70	10.6
100	25.975	0.85	1556	43.1	90	10.7
200	27.99	0.52	1656	25.5	114	11.2
200	30.025	0.65	1754	31.5	142	11.3
300	33.02	0.56	1850	26.9	176	10.9
300	33.975	0.67	1945	31.8	213	11.1
300	36.02	0.80	2042	37.6	257	11.4
300	38.08	0.98	2138	45.7	310	11.3
400	39.895	0.81	2223	37.5	359	13.0
400	41.99	0.96	2319	44.0	424	13.0
400	43.965	1.13	2410	51.4	495	13.0
500	46.38	1.04	2519	46.9	592	13.6
500	47.92	1.14	2588	51.1	659	13.9
500	48.925	1.21	2634	54.0	706	13.1

A weak point of all calorimetric measurements with small samples is the determination of their mass and thus of the absolute values of the specific heat. For this purpose, it is possible to fit the data at a single temperature point to a commonly accepted value. For instance, the specific heat of tungsten at 2000 K equals 31.6±0.5 J.mol^{-1}.K^{-1} = 172±3 mJ.g^{-1}.K^{-1}. This value has been confirmed by all calorimetric methods including pulse and modulation techniques. With this procedure, the heat capacity of our sample can be transformed into the specific heat. On the other hand, it is possible to evaluate the mass of a sample

from the length of the sample l and its diameter d. In the experiment, two quantities are measured that depend on the length and the diameter of the sample: (i) the electrical resistance of the sample, and (ii) the heat losses from it (Fig. 5). The electrical resistance at 273 K equals

$$R_{273} = 4\rho_{273} l/\pi d^2, \tag{8}$$

where $\rho_{273} = 4.82$ μΩ.cm is the resistivity of tungsten at 273 K.

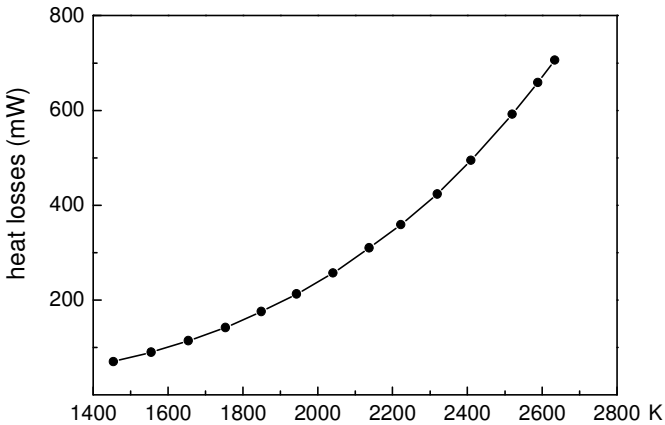

Fig. 5. Heat losses from the sample measured under equilibrium.

The radiative heat losses from the sample are proportional to its surface area $S = \pi ld$:

$$Q = \varepsilon\sigma\pi l d T^4, \tag{9}$$

where σ is Stefan–Boltzmann's constant, and ε is the hemispherical total emittance of tungsten, which depends on temperature.

Combining Eqs. (8) and (9), one obtains

$$Q/R_{273}T^4 = 2.9\times10^{-6}\varepsilon d^3. \tag{10}$$

The left-hand side of this equation contains experimentally measured quantities. At temperatures in the range 2200–2600 K, it is nearly constant and equals 4.7×10^{-15} W.Ω^{-1}.K^{-4}. In this temperature range, ε increases from 0.324 to 0.335 (Cezairliyan and McClure 1971). With its mean value, 0.329, the calculated diameter of the sample equals 17 μm, while the length of the sample is 1.5 cm. The density of tungsten is $D = 19.1$ g.cm^{-3}, so that the mass of the sample equals 65 μg. With this mass, the calculated specific heat of tungsten is in good agreement with the data recommended by White and Minges (1997).

Specific heat of solids. Calorimetric measurements provide good opportunity to consider the specific heat of solids in the whole temperature range of the solid state (Miiller 1988). One has to distinguish the specific heats at constant volume

(**isochoric, C_v**) and at constant pressure (**isobaric, C_p**). The difference between them is due to thermal expansion, which requires additional energy. The difference between the two molar specific heats is given by

$$C_p - C_v = V_m \alpha^2 T / K_T, \tag{11}$$

where V_m is the molar volume, $\alpha = V^{-1}(\partial V/\partial T)_p$ is the coefficient of volumetric thermal expansion, and $K_T = -V^{-1}(\partial V/\partial p)_T$ is the isothermal compressibility.

The main difficulty in calculating the right-hand side of Eq. (11) is the lack of reliable data on the **isothermal compressibility** of solids at high temperatures. Nevertheless, this equation remains a common method for calculating the $C_p - C_v$ value. This difference becomes significant only at high temperatures. Theoretical calculations deal mainly with C_v, but there is no way to directly measure it because it is impossible to completely exclude thermal expansion of a solid sample. However, observations of temperature fluctuations under equilibrium offer a method for determining the isochoric specific heat of solids. Temperature fluctuations in a sample and the fluctuations of the sample's volume are statistically independent (Landau and Lifshitz 1980). This was the basis of experimentally determining the C_p/C_v ratio for tungsten (Kraftmakher and Krylov 1980; Kraftmakher 2004d).

Many physical phenomena contribute to the specific heat of solids. Well below the so-called **Debye temperature** Θ_D, the main contribution is due to the vibrations of the crystal lattice (**phonon specific heat**). For temperatures well below Θ_D, the isochoric lattice specific heat is proportional to T^3 (Debye's law):

$$C_v \text{ (lattice)} = (12/5)\pi^4 R(T/\Theta_D)^3 = \alpha T^3, \tag{12}$$

where R is the universal gas constant, and Θ_D is specific for various metals. For tungsten, $\Theta_D = 380$ K.

In metals, there is an additional contribution due to conduction electrons, which is proportional to the absolute temperature:

$$C_{el} = \gamma T. \tag{13}$$

For tungsten, $\gamma = 1.3$ mJ.mol^{-1}.K^{-2}. At very low temperatures, C_{el} becomes larger than the phonon contribution.

Close to and above the Debye temperature, there exists a more or less wide temperature range, where C_v (lattice) approaches $3R = 24.9$ J.mol^{-1}.K^{-1}. This figure is often referred to as the Dulong–Petit value of specific heat. Due to anharmonicity, C_v (lattice) may weakly increase or decrease with temperature. For tungsten, the $C_p - C_v$ (lattice) difference at these temperatures is nearly linear. The electronic contribution also leads to a linear increase of the specific heat. For a long time, the linear temperature dependence of C_p was believed to continue up to the melting point. However, a **strong nonlinear increase** of the specific heat of high-melting-point metals was unexpectedly observed at temperatures above nearly two thirds of the melting temperature (Rasor and McClelland 1960; Kraftmakher and Strelkov 1962). In low-melting-point metals, the nonlinear increase of specific heat is also seen, but it is much smaller.

The origin of this phenomenon is still under debate, but many indications confirm that it is caused by the formation of equilibrium point defects in crystal lattice (Kraftmakher 1998a, 2000a). Frenkel (1926) predicted the point defect formation in solids many years ago. **Vacancies** are believed to be the predominant type of point defects. The equilibrium vacancy concentration c_{vac} obeys the relation

$$c_{vac} = \exp(S_F/k_B)\exp(-H_F/k_BT) = A\exp(-H_F/k_BT), \quad (14)$$

where H_F and S_F are the **enthalpy** and **entropy** of vacancy formation, k_B is Boltzmann's constant, and T is the absolute temperature. The entropy S_F relates to changes in vibration frequencies caused by the softening of the binding of atoms near vacancies. The excess molar enthalpy and specific heat caused by the vacancy formation are given by

$$\Delta H = NH_F c_{vac} = NH_F A\exp(-H_F/k_BT), \quad (15)$$

$$\Delta C_p = (NH_F^2 A/k_BT^2)\exp(-H_F/k_BT) = DT^{-2}\exp(-E/T), \quad (16)$$

where N is the Avogadro number. The vacancy contribution to the specific heat is due to the strong temperature dependence of the vacancy concentration.

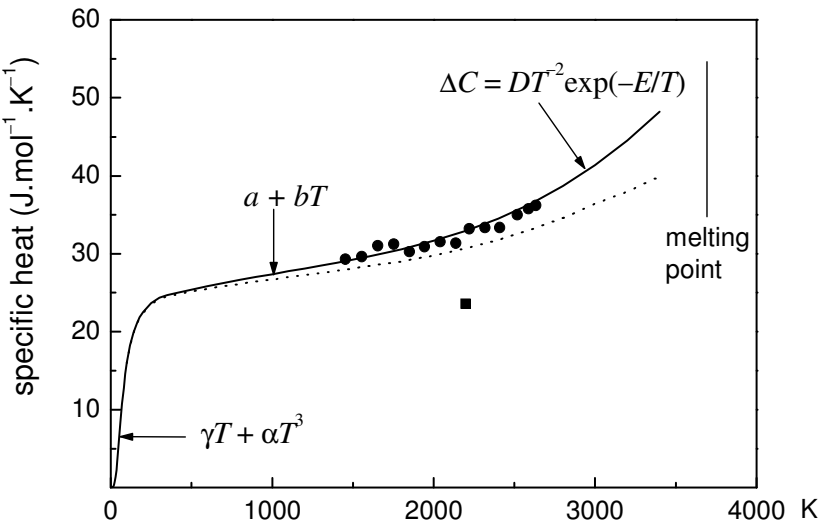

Fig. 6. Specific heat of tungsten: • results obtained; —— C_p and ····· C_v data recommended by White and Minges (1997); ■ C_v value from observations of temperature fluctuations (Kraftmakher and Krylov 1980).

Additional contributions to the specific heat of solids arise due to **phase transitions** of the first or second order. Anomalies accompanying **first-order** phase transitions are discontinuities in specific heat (for instance, Zr and Ti).

Second-order phase transitions manifest anomalies including discontinuities and singularities below and above the **transition point**. A well-known example of such anomalies is the specific heat of ferromagnets near their Curie points (for instance, Fe, Co, Ni, and Gd).

The results obtained are shown together with recommended values of C_p and C_v of tungsten in the whole temperature range and an experimental C_v value determined by observations of temperature fluctuations (Fig. 6). The C_v curve was calculated with Eq. (11). The C_v values include lattice and electronic contributions. In the linear approximation $a + bT$, the constant a is close to the Dulong–Petit value, while the coefficient b reflects the electronic contribution and the $C_p - C_v$ (lattice) difference. The significant difference between the calculations and an experimental C_v value determined by observations of temperature fluctuations (Kraftmakher and Krylov 1980) is probably caused by an exaggerated value of the isothermal compressibility of tungsten used in the calculations and/or a negative contribution of anharmonicity.

3.3. Dynamic calorimetry

In one run, the specific heat of tungsten is determined in a range encompassing more than 1000 K (Kraftmakher 2007a).

Additional equipment: *Voltage sensor*, light bulb, resistor.

Principles of dynamic calorimetry. This is a powerful technique for calorimetric studies, especially at high temperatures and pressures. In our case, a low power incandescent lamp serves as the sample. During a 15 ms heating run, the heating rate amounts to 10^5 K.s^{-1}. The experiment is a good example of measurements that are only feasible with a sufficiently fast data-acquisition system. Second, it shows how the usual heat balance equation is applicable under unusual conditions of rapid temperature changes.

One of the main difficulties of calorimetric measurements is the uncontrollable heat exchange between a sample and its surroundings. Shortening the time of the measurements reduces the role of this heat exchange. Conducting samples directly heated by an electric current are well suited for such measurements. Dynamic calorimetry consists of rapidly heating the sample over a wide temperature range. The heating power and the temperature of the sample are measured continuously during the run. When the supplied power is much greater than the power of heat losses from the sample, the instantaneous heating rate depends only on this power and the heat capacity of the sample. Otherwise, the heat losses can be taken into account. These data are sufficient for evaluating the heat capacity of the sample in the whole temperature range of the run.

Dynamic calorimetry is an invaluable technique when the samples are unstable because of evaporation or decomposition. An ultimate case of such measurements is the so-called exploding wires, where the heat capacity of the sample is measurable even for the liquid state. Dynamic measurements are limited by the possibility of rapidly heating and measuring the temperature of the samples. Cezairliyan and McClure (1971) performed dynamic measurements on tungsten up to 3600 K. The measurements confirmed the strong nonlinear increase in the specific heat of refractory metals observed earlier by pulse calorimetry (Rasor and McClelland 1960) and by modulation technique (Kraftmakher and Strelkov 1962). For reviews of dynamic calorimetry see Cezairliyan (1984, 1988); Gathers (1986); Righini *et al* (2000).

The theory of dynamic calorimetry is simple and straightforward. To heat up a sample, a power P is supplied to it. Generally, this power varies during the run. Due to the supplied power, the temperature T of the sample starts to increase. A part of this power dissipates in the environment because of heat losses Q from the sample. In vacuum, the heat losses are caused by thermal radiation. The heat balance equation has its usual form

$$P\Delta t = mc\Delta T + Q\Delta t, \tag{1}$$

where m and c are the mass and specific heat of the sample, and ΔT is the temperature increment during a short interval Δt. For a small ΔT, all the quantities involved remain constant. Hence,

$$mc = (P - Q)/T_h', \tag{2}$$

where $T_h' = (dT/dt)_h$ is the heating rate, and $P - Q$ is the net power consumed for heating the sample. When $P >> Q$,

$$mc = P/T_h'. \tag{3}$$

For a run over a wide temperature range, the above equations are valid for any short interval Δt, and the heat capacity of the sample can be determined in the whole range. All that we need is a determination of the quantities involved in the measurements during the run. Except for the mass of the sample, the quantities entering Eqs. (2) and (3) now depend on temperature.

When no heating power is supplied, Eq. (2) is valid with $P = 0$:

$$mc = -Q/T_c', \tag{4}$$

where $T_c' = (dT/dt)_c$ is the cooling rate. Combining Eqs. (2) and (4), we obtain

$$mc = P/(T_h' - T_c'), \tag{5}$$

where c, P, T_h', and T_c' relate to the same temperature of the sample.

Equations (2)–(5) contain P and/or Q values and heating/cooling rates T_h' or T_c' related to various (but the same for all the quantities) temperatures. The heating/cooling rates are time derivatives of the temperature of the sample. In a dynamic experiment, the time and temperature dependences are obtainable in one run. It is possible because the temperature of the sample is measured continuously during the run, and instantaneous values of P and T are stored. Therefore, one can calculate T_h' or T_c' and display them, as well as P, versus the temperature. The temperature dependence of the power of heat losses Q can be measured separately and presented as a polynomial fit. The heat capacity of the sample is thus available (i) from the heating run, by the use of Eq. (2) or Eq. (3); (ii) from the cooling run, by the use of Eq. (4); or (iii) by combining data from both runs, by the use of Eq. (5). Under equilibrium, the power of heat losses equals the supplied power. This statement is valid only for the radiative heat exchange. Additional contributions to the heat losses due to the heat conductance at the ends of the sample or to the surrounding gas depend on the temperature rate. An important question is how to measure the sample temperature, through the electrical resistance of the sample or thermal radiation from it.

Our experiment employs measurements and calculations according to Eq. (2). The tungsten filament of a vacuum light bulb (5 V, 0.11 A) serves as the sample. The sample is connected, through a variable resistor r, to the *Signal generator* of the *750 Interface* (Fig. 1). The resistor r reduces the dependence of the heating current upon the resistance of the sample. The heating current I is stored as the output current of the generator, and the voltage across the sample V

is measured by the *Voltage sensor*. *DataStudio* calculates the electric power P supplied to the sample and the electrical resistance of the sample R. The latter is necessary for calculating the temperature of the sample.

Heat losses and rapid heating. The heat losses from the sample are determined under equilibrium conditions. The *Ramp up waveform* voltage from the *Signal generator* heats the sample, and the run lasts 200 s ($f = 0.005$ Hz). During the run, the heating current and the voltage across the sample are stored. Only data for temperatures above about 700 K are necessary for the calculations.

The resistance R of the sample can be converted to its temperature. For the range 1500–3600 K, Roeser and Wensel (1941) presented the necessary data as the resistance ratio $X = R/R_{273}$ versus temperature. In a handbook (Lide 2008), data on the resistivity are given for temperatures up to 900 K. Using data on thermal expansion of tungsten (White and Minges 1997), the data on resistivity were converted to the resistance ratio X and combined with the data given by Roeser and Wensel (1941). The following relation fits both sets of data over the range 273–3600 K:

$$T = 74 + 202 \times X - 2.91 \times X^2 + 0.042 \times X^3. \quad (6)$$

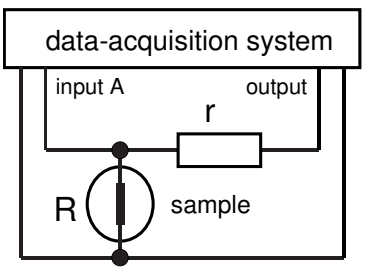

Fig. 1. Schematic of the experiment.

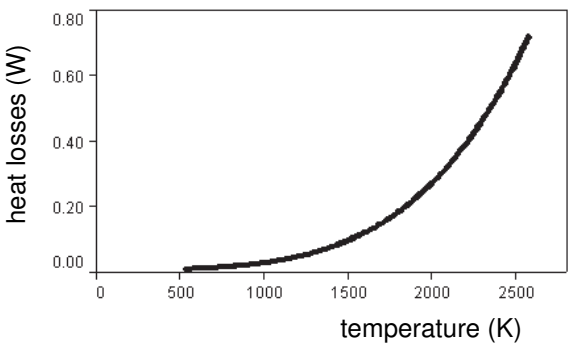

Fig. 2. Temperature dependence of the power of heat losses.

For our sample, $R_{273} = 3.2\ \Omega$. Using the measurement data, *DataStudio* plots a graph $Q(T)$ and calculates a polynomial fit to it. For 2500 K, the power of heat losses exceeds 0.6 W (Fig. 2). Tungsten is not a perfect blackbody, and its emissivity increases with temperature. Therefore, the effective value of the exponent in Stefan–Boltzmann's law is expected to be somewhat larger than 4. In the present experiment, the only requirement is the goodness of the fit, and a four-term polynomial is sufficient to fit the data.

In the second part of the experiment, the sample is rapidly heated. The experiment should be organized in such a way as to maximize the net power consumed for heating the sample. The heating must be ended before the sample achieves its destruction temperature. This means heating by a single electric

pulse of proper duration. The *Signal generator* operates in the *Auto* mode: it starts to produce the signal and to store the measurement data after starting a run, and ends the signal in a time chosen with the *Automatic stop/Time* option. The *Output voltage* is set as a *DC voltage*, so that the voltage applied to the sample is a rectangular 5 V pulse lasting the time chosen. For achieving better measurement conditions, the resistance r and the time of the run can be varied. An increase of the resistance r reduces the heating current, but the current becomes not so strongly dependent on the temperature of the sample. On the other hand, the electric power supplied to the sample decreases, which makes the heat losses more significant.

We use two heating runs; one of them lasts 30 ms, and the second 15 ms. The sample rates are 2 and 4 kHz, respectively, and 60 data points are obtained in both cases. *DataStudio* displays the heating current versus time and calculates the electric power supplied to the sample and the electrical resistance of the sample: $P(t) = V(t)*I(t)$, and $R(t) = V(t)/I(t)$. The $R(t)$ data are converted to the temperature of the sample $T_h(t)$. During the runs, the temperature increases by more than 1000 K. For the two sets of the parameters, the time dependences of the data are very different (Fig. 3). The two very different heating runs are chosen for confirming that the final result, the temperature dependence of the heat capacity, remains the same. This is an important criterion of the correctness of dynamic measurements.

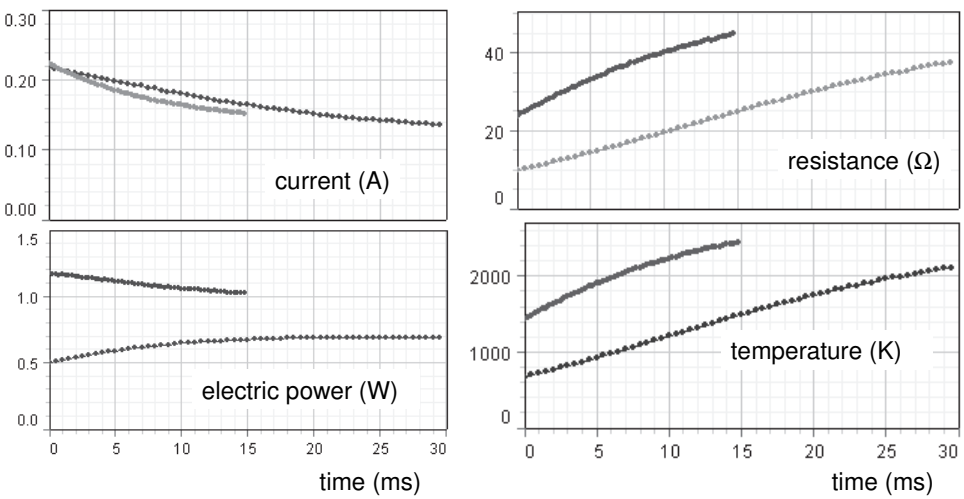

Fig. 3. Data obtained in two runs (15 and 30 ms): heating current, supplied electric power, electrical resistance, and temperature of the sample.

High-temperature specific heat of tungsten. For the evaluation of the heat capacity of the sample, all the quantities entering Eq. (2) should be presented versus temperature. The *Calculate/Special/Derivative* tool calculates the heating rate T_h' and displays it versus temperature. In the 15 ms run, the heating rate

amounts to 10^5 K.s^{-1}. The scatter of these data depends on the time interval, in which the numerical differentiation is done. This interval is chosen by properly settings in the *Derivative* tool. Dynamic calorimetry is applicable when there are no meaningful changes of heat capacity in narrow temperature intervals, which are peculiar to phase transitions. In such cases, calorimetric techniques of better temperature resolution should be used. In our experiment, the differentiation interval includes 10 data points, so that the values of the heat capacity are averaged in wide temperature ranges. This is possible because the specific heat of tungsten at high temperatures increases with temperature by about 2% per 100 K. More accurate determinations of the electrical resistance of the sample during the runs are needed to achieve better temperature resolution.

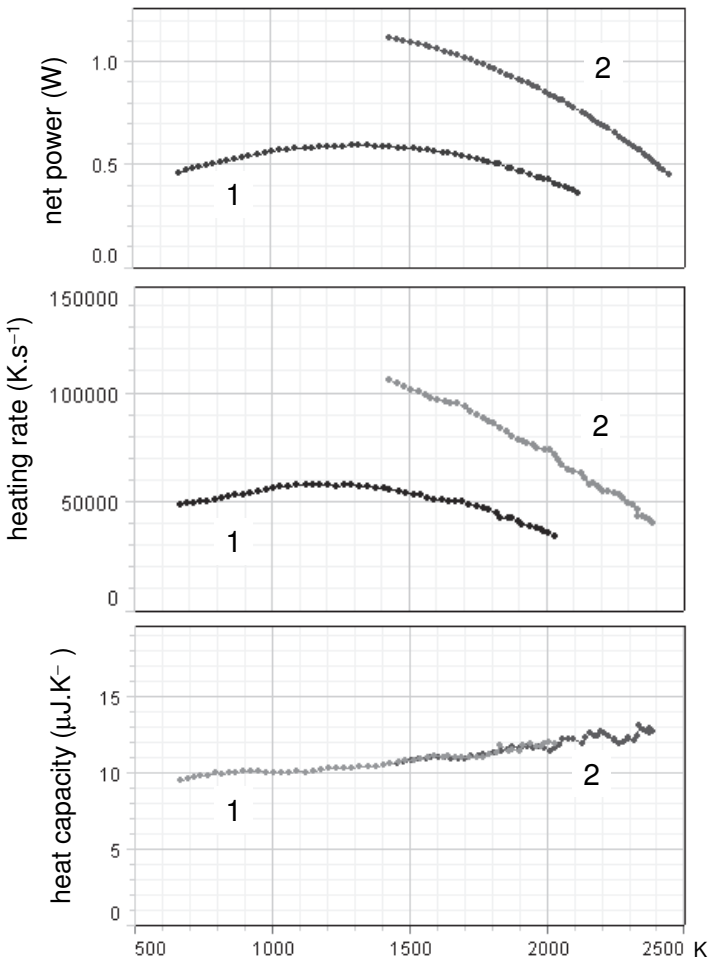

Fig. 4. Net power, heating rate, and heat capacity versus temperature: 1–30 ms run (700–2000 K), 2–15 ms run (1400–2400 K).

Along with the heating rate, *DataStudio* calculates the temperature dependence of the net power consumed for heating the sample, $P - Q$. The data on $P(T)$ are taken from the rapid heating, while the data on $Q(T)$ are introduced by the polynomial obtained in equilibrium measurements. Then Eq. (2) provides data on the heat capacity of the sample over the whole temperature range (Fig. 4).

A weak point of the experiment is the determination of the mass of the sample and thus the evaluation of absolute values of the specific heat. This difficulty is peculiar to all calorimetric measurements with very small samples. To obtain absolute values of specific heat, one can fit the data at a single temperature point to a known value. The specific heat of tungsten at 2000 K is 31.6±0.5 $J.mol^{-1}.K^{-1}$, a value confirmed by all calorimetric methods including dynamic and modulation techniques. Our data were fitted to this value. In the range of the measurements, the specific heat of tungsten exceeds the classical limit for the isochoric specific heat equal to $3R = 24.9$ $J.mol^{-1}.K^{-1}$, and increases with temperature (Fig. 5). The reasons for this increase are the difference between the isobaric and isochoric specific heats and the electronic specific heat. Both contributions are believed to be proportional to temperature. At higher temperatures, a significant nonlinear increase in the specific heat is caused by the formation of equilibrium point defects in the crystal lattice (Kraftmakher 2000a, 2004d).

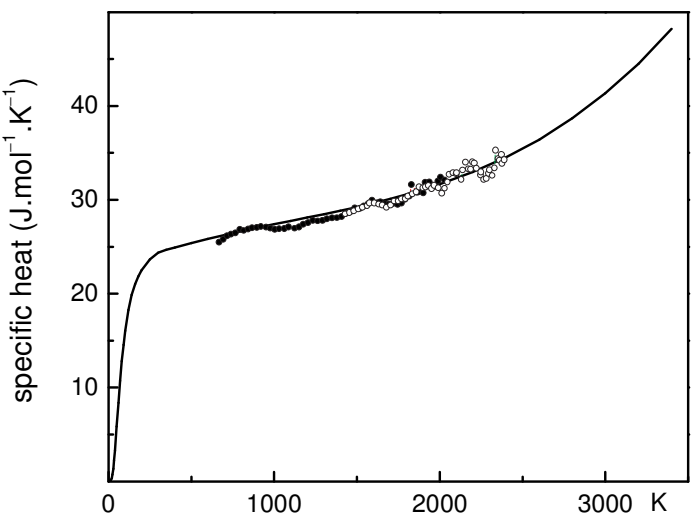

Fig. 5. Specific heat of tungsten determined in two runs and fitted at 2000 K. —— data recommended by White and Minges (1997).

3.4. Principles of modulation calorimetry

The basic relations for the modulation calorimetry are verified. The tungsten filament of a light bulb serves as a sample, a heater, and a thermometer.

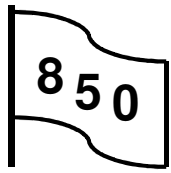

Additional equipment: DC supply, low power light bulb, photodiode, potentiometer, 1.5 V battery, resistors.

Modulation calorimetry (for reviews see Kraftmakher 1973a, 2002a, 2004d) involves periodically modulating the power that heats a sample and creating by this way temperature oscillations in the sample around a mean temperature. Their amplitude depends on the heat capacity of the sample. The use of periodic changes in the temperature provides important advantages. With a sufficiently high modulation frequency, corrections for heat losses become negligible even at extremely high temperatures. The second advantage is that the harmonic temperature oscillations are measured with selective amplifiers and lock-in detectors. This feature is important for achieving good temperature resolution. Modifications of the technique differ by the ways of modulating the heating power (heating by electric current, radiation or electron-bombardment heating, induction heating, use of separate heaters) and of detecting the temperature oscillations (by the resistance of the sample or radiation from it, by means of a thermocouple or a resistance thermometer). In many cases, it is possible to assemble compensation schemes, whose balance does not depend on the amplitude of the power oscillations. In treating the data, the mean temperature and the amplitude of the temperature oscillations are assumed to be constant throughout the sample. Employment of small samples weakly thermally coupled to a bath meets this requirement. Thin wires heated by a current are well suited for modulation measurements. With radiation heating or separate heaters, the thickness of the samples is in the range of 0.1–0.3 mm.

Corbino (1910, 1911) was the first to carry out modulation measurements of specific heat. He developed the theory of the method and used oscillations of the sample's resistance to determine the temperature oscillations. At first, the method was used exclusively at high temperatures. Its most important feature was the small correction for heat losses. The temperature oscillations were determined from the sample's resistance or radiation. With this approach, the high-temperature specific heat of refractory metals has been determined. At the second stage, modulation calorimetry was used at intermediate and low temperatures and for studying nonconducting materials. Due to the excellent temperature resolution, the method is widely used for studying phase transitions (ferro- and antiferromagnets, ferroelectrics, ordering alloys, superconductors, liquid crystals, biological materials). It is applicable also under high pressures.

For a long time, there was no special term for this technique. The term "modulation method for measuring specific heat" appeared in a paper describing

the bridge circuit for measuring specific heat of wire samples (Kraftmakher 1962a). However, for many investigators the acquaintance with this technique began with papers by Sullivan and Seidel (1967, 1968). They considered a system including a sample, a heater, and a thermometer, and performed measurements at low temperatures. The term **"AC calorimetry"** introduced by the authors is now widely accepted.

Theory of modulation calorimetry. When the power heating a sample is modulated by a sine wave, the sample's temperature oscillates around a mean value T_0. For a short interval Δt, during which the quantities involved remain constant, the heat balance equation takes the form

$$(p_0 + p\sin\omega t)\Delta t = mc\Delta T + Q(T)\Delta t, \tag{1}$$

where $p_0 + p\sin\omega t$ is the power applied to the sample, m, c and T are the mass, specific heat and temperature of the sample, $Q(T)$ is the heat loss from the sample, ω is the modulation frequency ($\omega = 2\pi f$), and ΔT is the change of the sample's temperature during the interval Δt.

Assuming $T = T_0 + \Theta$, $\Theta << T_0$, and taking $Q(T) = Q(T_0) + Q'\Theta$ (where $Q' = dQ/dT$ is the heat transfer coefficient), we obtain a differential equation

$$mc\Theta' + Q(T_0) + Q'\Theta = p_0 + p\sin\omega t, \tag{2}$$

where $\Theta' = d\Theta/dt$. The steady-state solution to this equation is

$$Q(T_0) = p_0, \tag{3a}$$

$$\Theta = \Theta_0\sin(\omega t - \varphi), \tag{3b}$$

$$\Theta_0 = (p\sin\varphi)/mc\omega = (p\cos\varphi)/Q', \tag{3c}$$

$$\tan\varphi = mc\omega/Q'. \tag{3d}$$

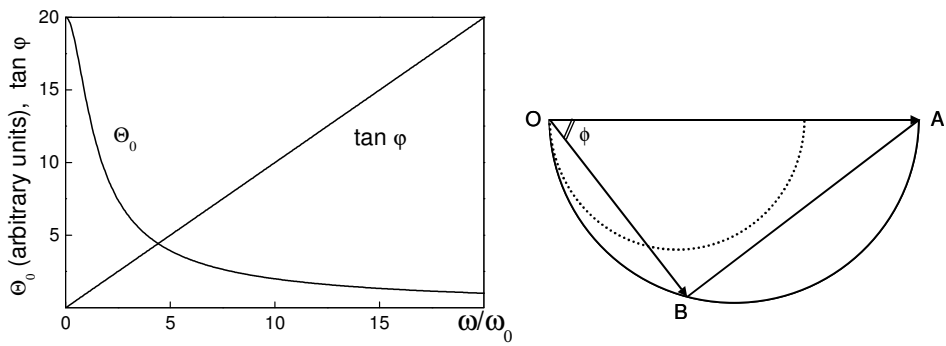

Fig. 1. Θ_0 and $\tan\varphi$ versus frequency, and polar diagram $\Theta_0(\varphi)$. Vector **OA** ($\omega = 0$) equals p/Q'. In adiabatic regime, vector **OB** is nearly perpendicular to **OA**. Dotted circle relates to dense surroundings (Rosenthal 1965).

The frequency dependence of Θ_0 and $\tan\varphi$, and a polar diagram $\Theta_0(\phi)$ (Fig. 1) demonstrate these results. The condition $\tan\phi > 10$ ($\sin\phi \cong 1$) is the criterion of an **adiabatic** regime of the measurements. This means that the oscillations of the heat losses from the sample due to the temperature oscillations are much smaller than the oscillations of the heating power. Measurements under **nonadiabatic** conditions are also possible (Varchenko and Kraftmakher 1973). Under adiabaticity conditions, Eq. (3c) takes the form

$$\Theta_0 = p/mc\omega, \tag{4}$$

which is the basic equation of modulation calorimetry; the quantity $\omega\Theta_0$ does not depend on the modulation frequency.

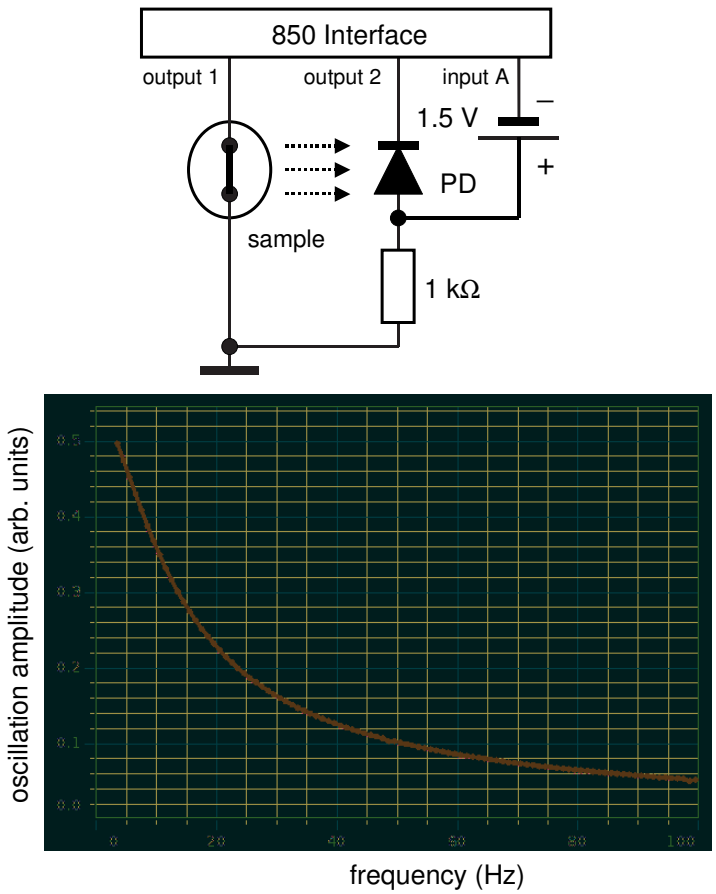

Fig. 2. Diagram of the setup and frequency dependence of the amplitude of temperature oscillations displayed by *Capstone*. PD–photodiode.

Measurements and results. With the *850 Interface*, the setup may be very simple (Fig. 2). The *Output 1* provides a biased sine wave voltage heating the

sample, so the heating current contains independently controlled DC and AC components. The generator operates in the *Sweep* mode: during 200 s, the frequency increases from 3 to 103 Hz. A photodiode views the sample. A DC voltage for the photodiode is taken from the *Output 2*. A 1.5 V battery is put between the 1 kΩ load of the photodiode and the interface (input A). The battery balances the DC component of the signal, which can be adjusted by changing the distance between the sample and the photodiode; however, a strict balance is not needed. For sufficiently small temperature oscillations, the AC signal from the photodiode is proportional to the temperature oscillations of the sample. The *Calculator/Special/peakamp* tool calculates the signal amplitude. *Capstone* displays this amplitude versus the modulation frequency.

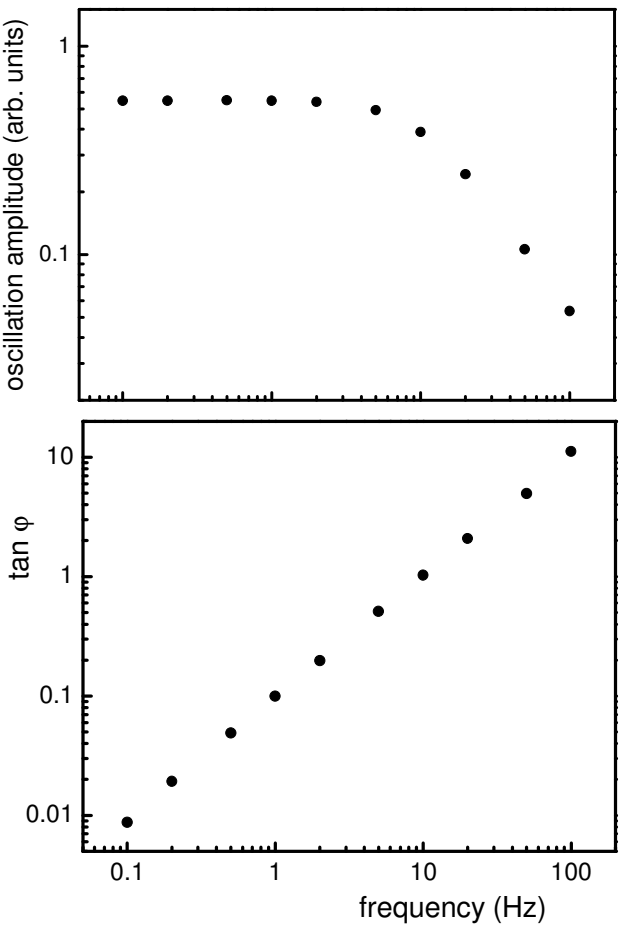

Fig. 3. Results of the measurements: temperature oscillation amplitude and tanφ versus modulation frequency.

For modulation frequencies below 1 Hz, such measurements become inconvenient. For this reason, the amplitude of the temperature oscillations and phase shift φ between the AC component of the heating power and the temperature oscillations was determined for fixed modulation frequencies by using the *Fit/Sine fit* option. The frequencies from 0.1 to 100 Hz were chosen in a 1-2-5-10 sequence appropriate for logarithmic scales (Fig. 3). The frequency dependence of the oscillation amplitude obeys the cosφ dependence. The tanφ values are proportional to the modulation frequency. The oscillation amplitude versus the phase shift φ is also presented as a polar diagram (Fig. 4). The results obtained thus confirm the basic relations of the theory.

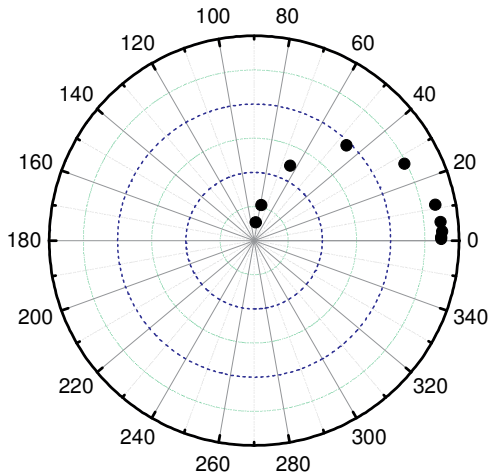

Fig. 4. Polar diagram of oscillation amplitude (arbitrary units) versus phase shift φ.

3.5. Energy stored by capacitor

The energy stored by a capacitor is determined calorimetrically.

Additional equipment: two *Voltage sensors*, capacitor, thermistor, DC supply, multimeter, switches, resistors.

The energy stored by a capacitor is proportional to the square of the voltage across it. A calorimeter with a heater and a thermometer embedded can be used to measure this energy (Weiss 1969; Edgar 1993). The capacitor under test is discharged through the heater, and the energy stored is determined from the temperature rise. Therefore, a calibration is needed for establishing the relation between the two quantities. A disadvantage of this approach is that the thermal inertia of the calorimeter makes the measurements time-consuming. To do the measurements in a short time, it is necessary to minimize the heat capacity of the calorimeter. For instance, a small bead **thermistor** can serve as a calorimeter, a heater, and a thermometer. A data-acquisition system collects the measurement data.

Thermistor is a semiconductor resistor sensitive to temperature changes. The resistivity of semiconductors decreases with increasing temperature; this behavior is quite different from that of metals. In semiconductors, the density n of free carriers strongly increases with increasing temperature:

$$n = A\exp(-B/T), \tag{1}$$

where A and B are constants, and T is the absolute temperature. The behavior of the conductivity of semiconductors is more complicated due to the temperature dependence of the mobility of the carriers. Neglecting this dependence, the resistivity of semiconductors is

$$\rho = C\exp(B/T), \tag{2}$$

where C is a constant. The temperature coefficient of resistivity is

$$(\mathrm{d}\rho/\mathrm{d}T)/\rho = -B/T^2. \tag{3}$$

The resistivity of semiconductors and the sensitivity to temperature changes strongly increase with decreasing temperature. At room temperatures, the temperature coefficient of resistance of the thermistor used (about 6% K^{-1}) is one order of magnitude larger than that of typical metals. At low temperatures, the advantages of the use of semiconductor thermometers become even greater.

The setup for the measurements and calibration is very simple (Fig. 1). With a manually operated switch S1, the capacitor C can be connected to a regulated DC supply of voltage V (up to 30 V) or to a bead thermistor (1 kΩ at 25°C). The voltage across the capacitor is measured with a simple digital voltmeter. The resistance of the thermistor is measured with a Keithley 177 multimeter. The output voltage of the multimeter is acquired by the *Voltage*

sensor and displayed by *DataStudio*, so all the changes in the resistance of the thermistor are seen on the computer screen. Due to the low thermal inertia of the thermistor, one measurement takes less than a minute. Other elements of the setup serve for calibration purposes.

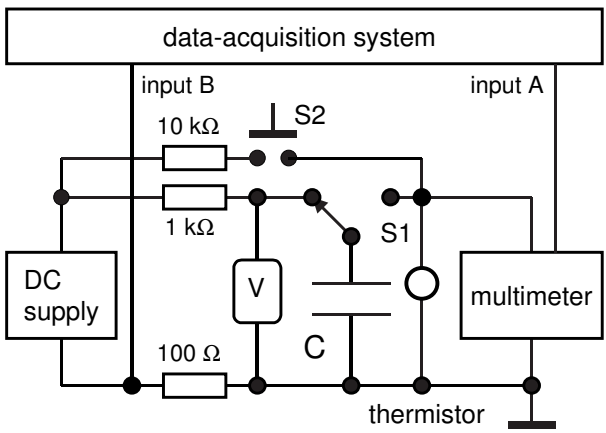

Fig. 1. Diagram of the setup for measurements and calibration.

After the capacitor is discharged, the temperature of the thermistor rapidly increases and then slowly, in a minute, returns to its initial value. The temperature increase ΔT is proportional to the energy E stored in the capacitor. For a short heating period, heat losses from the thermistor are much smaller than the energy E, and the heat balance equation is

$$mc\Delta T = E. \tag{4}$$

The discharging process unavoidably depends on the voltage permanently applied to the thermistor. If this voltage opposes the voltage across the capacitor, the discharge is incomplete, so the energy dissipated in the thermistor becomes smaller than the energy stored in the capacitor, $E = \frac{1}{2}CV^2$. In the opposite case, the energy dissipated becomes greater. The correct value of the energy stored can be taken as a mean of the two values. To ease the problem, the voltage applied to the thermistor for measuring its resistance is decreased. For this aim, the 20 kΩ scale of the multimeter is chosen (the current through the thermistor is 0.1 mA), though the 2 kΩ scale (with a 1 mA current) provides better sensitivity. With this choice, the voltage across the thermistor, nearly 0.1 V, becomes much smaller than across the charged capacitor. Nevertheless, the measurements are done for both polarities of each voltage applied to the capacitor, and mean values of ΔR are used for the calculations.

In all the measurements, the initial temperature of the thermistor is the same, and the temperature jumps after discharging the capacitor are small. Therefore, the energy stored in the capacitor can be considered proportional to the jumps in the resistance of the thermistor. There is no need to exactly know

the temperature characteristic of the thermistor; it is sufficient to determine the resistance jump ΔR versus the square of the voltage applied to the capacitor (Fig. 2). From the measurement data, $\Delta R/V^2 = 0.217\ \Omega.V^{-2}$. From the jumps, it is easy to estimate the temperature changes and the heat capacity of the thermistor. The maximum temperature change corresponding to $\Delta R = 190\ \Omega$ is nearly 4 K, and the heat capacity of the thermistor mc is nearly 1 $mJ.K^{-1}$.

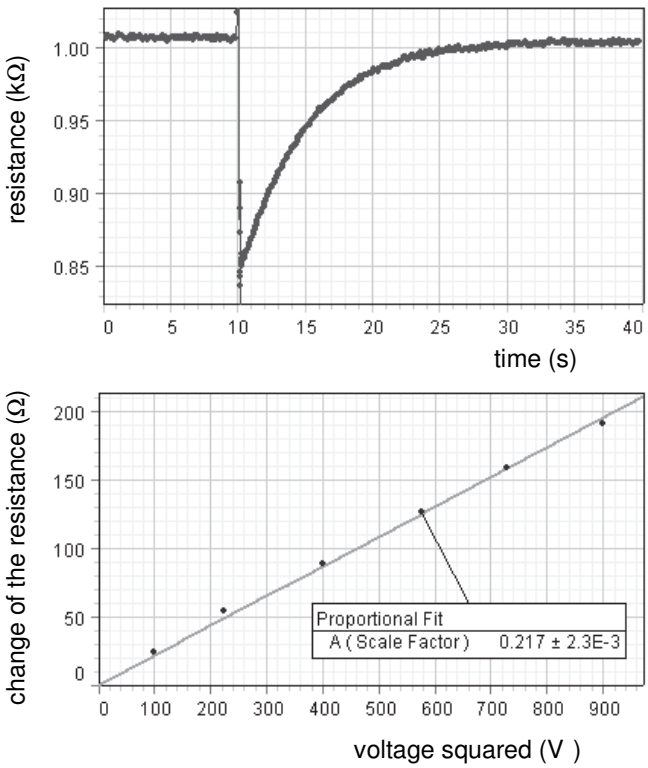

Fig. 2. Example of measurement data and change of resistance of the thermistor versus applied voltage squared.

For the calibration, the same DC supply is connected to the thermistor through a regulated resistor and a manually operated switch S2. The current through the thermistor is measured with the second *Voltage sensor* connected to a 100 Ω resistor put in series with the thermistor. With the *Smart tool*, it is easy to find the heating period and the energy dissipated in the thermistor. Due to the high series resistance, 10 kΩ, the current i passing through the thermistor during the calibration run is constant. The resistance of the thermistor should be taken as the mean of the initial and final values, R_m (Fig. 3). The energy dissipated in the resistor equals $i^2 R_m \Delta t$, where Δt is the heating period determined with the *Smart tool*. The calibration procedure is done for both directions of the current through the thermistor. As expected, the jumps in the resistance of the thermistor

are proportional to the dissipated energy. The *Proportional fit* provides the coefficient of proportionality: $\Delta R/\Delta E = 45.7\ \Omega.\text{mJ}^{-1}$. The energy stored is displayed versus the voltage squared (Fig. 4). From these data, $C = 9.5\ \mu\text{F}$. The capacitance measured with a multimeter appeared to be 9.1 µF.

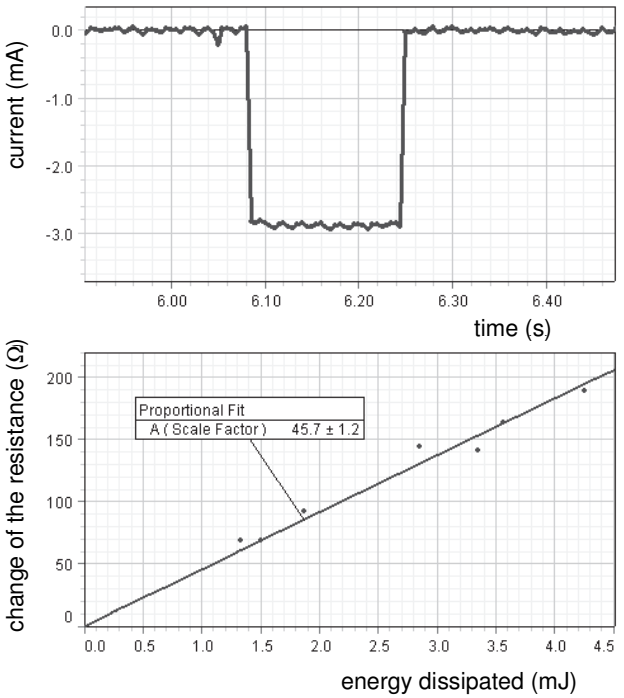

Fig. 3. Example of calibration data and change of the resistance versus energy instantly dissipated in the thermistor.

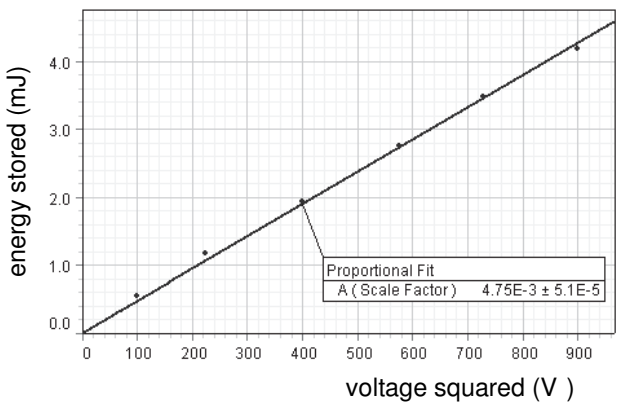

Fig. 4. Energy stored versus voltage squared. From the fit, $C = 9.5\ \mu\text{F}$.

3.6. Rotational viscometer

Rotational viscometers are well suitable for liquids of high viscosity, like glycerol or oils (Kraftmakher 2010g).

Additional equipment: *Rotary motion sensor*, DC motor, DC supply, permanent magnets.

Viscosity of fluids. Viscosity is the internal friction in a fluid (liquid or gas), which opposes the motion of one portion of a fluid relative to another (Hecht 1994; Alonso and Finn 1995; King *et al* 1998; Young and Freedman 2000). Imagine two horizontal plates, separated by a distance z. The region between the plates is filled with a fluid. If the upper plate of area A is brought to a motion in horizontal direction, while the bottom plate is stationary, the fluid starts to move in the same direction. The fluid in contact with each plate has the same velocity as the plate. A constant force F will maintain a constant velocity for the upper plate, and a velocity gradient appears in the fluid. For the case considered, the gradient is constant. Newton has found that the force per unit area, F/A, is proportional to this velocity gradient, v/z:

$$F/A = \eta v/z, \tag{1}$$

where η is a proportionality coefficient called the **viscosity** of the fluid. This is **Newton's law** of viscosity.

The viscosity is a property very important for practical needs (petroleum industry, lubricants, paints, *etc*). Many papers were devoted to teaching the viscosity of fluids (Hibberd 1952; Sandhu 1965; Stajdohar and Towle 1968; Stanley 1972; Bowlt 1975; Mason and Moloney 1977; Wright 1977; Gupta *et al* 1986; Nienart 1994; Agrawal and Menon 1999; Sabaz 2006; Sianoudis and Drakaki 2008; Wadhwa 2008; Even *et al* 2009; Mendoza-Arenas *et al* 2010; Shamim *et al* 2010; Guerra *et al* 2011; Houari 2011). The viscosity of a fluid produces forces on a body moving through it. The body experiences a frictional force, which increases with its velocity relatively to the fluid. At velocities corresponding to conditions of laminar flow (see below), the viscous force is proportional to the velocity v. When a sphere of radius r moves through a fluid of viscosity η, the viscous force F equals

$$F = 6\pi r\eta v. \tag{2}$$

This relation is the **Stokes law**.

When a fluid flows through a cylindrical pipe of inner radius r and length L, the volume flow rate Q is

$$Q = \pi r^4(p_1 - p_2)/8\eta L, \tag{3}$$

where p_1 and p_2 are the pressures at the two ends of the pipe. This expression is the **Poiseuille law**.

Equations (2) and (3) are only valid for the so-called **laminar flow**, in which adjacent layers of fluid slide smoothly past each other, and the flow is steady. Another definition of laminar flow is that no kinetic energy is transferred at right angles to the direction of the flow. Otherwise, the flow is turbulent A criterion of the type of flow is the **Reynolds number** Re:

$$\mathrm{Re} = \rho v l/\eta, \tag{4}$$

where ρ and η are the density and viscosity of the fluid, v is the velocity of the solid relatively to the fluid (the velocity of a sphere moving through the fluid, or the velocity of a fluid relatively to the walls of a pipe), and l is the characteristic size of the system.

Reynolds' number is a qualitative criterion, and the characteristic size is a matter of convention. It can be made a quantitative one only for well-defined conditions. For the simplest cases considered here, the characteristic size in Eqs. (2) and (3) is the diameter of the sphere or pipe. Small characteristic size, low velocities, low density and high viscosity of the fluid are favorable for obtaining laminar flow. The flow through a pipe is laminar for $\mathrm{Re} < 2\times10^3$ and turbulent for $\mathrm{Re} > 4\times10^3$. In a significant transient region between the above numbers, both types of flow are possible.

***Brief review of experimental techniques*.** Four basic techniques for determining the viscosity of liquids (Whittle and Yarwood 1973; King *et al* 1998) are illustrated below (Fig. 1).

The **falling sphere viscometer** rests on Stokes' law. A small ball of radius r falls through the liquid in a cylindrical container. As the velocity of the ball increases, the viscous force also increases. In a short time, the ball reaches a constant velocity v_0, for which the weight of the ball (Archimedes' force must be taken into account) equals the viscous force given by Stokes' law:

$$v_0 = 2(\rho - \rho_0)r^2 g/9\eta, \tag{5}$$

where ρ and ρ_0 are the densities of the ball and the liquid, and g is the acceleration of gravity. All the quantities in this relation, except the viscosity η, are known or can be measured. Millikan used this equation in his famous experiment to determine the electron charge.

In the **capillary viscometer**, the liquid flows through a capillary, and the viscosity is calculated with Poiseuille's law. The capillary can be made sufficiently thin to highly reduce the flow rate, so the laminar flow can be maintained even for liquids of low viscosity, like water or gasoline. The **vibrational viscometer** employs a mechanical resonant system with an oscillating probe immersed into the liquid. Due to the viscosity of the liquid, the decay of the system increases; this increase can be related to the viscosity. In the **rotational viscometer**, a liquid fills a cylinder container of radius r_2. A cylinder of radius r_1 and length l is immersed into the liquid and brought to rotation by an electric motor. The retarding torque produced by the liquid equals (Whittle and Yarwood 1973; Courbin *et al* 2005)

$$T_{\text{ret}} = 4\pi r_1^2 l\eta\omega/(1 - r_1^2/r_2^2), \quad (6)$$

where ω is the angular rotation velocity of the cylinder (rad.s^{-1}).

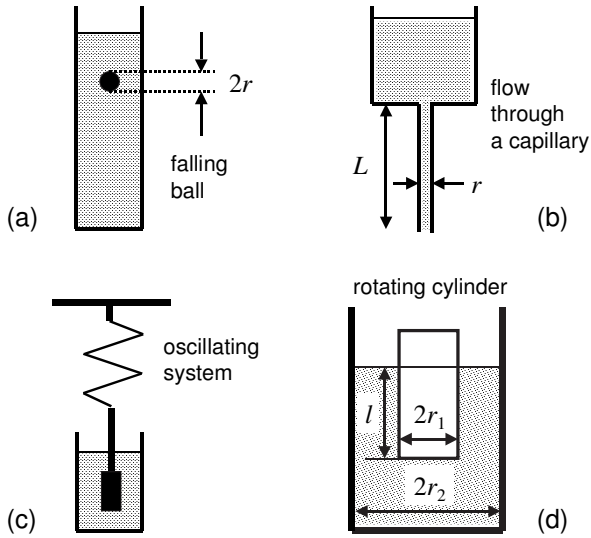

Fig. 1. Methods to measure viscosity of liquids: (a) falling ball; (b) capillary viscometer; (c) vibrational viscometer; (d) rotational viscometer.

Under steady conditions, the motor rotating the inner cylinder produces the same torque. A calculation of the retarding torque is not a simple task. For us, it is only important that the retarding torque is proportional to the viscosity of the liquid. For strict treatment, the end effects and friction losses should be taken into account. Otherwise, the device needs calibration with liquids of known viscosity. Rotational viscometers are very simple to use. Three variants of the rotational viscometer with a DC motor are considered below.

The majority of liquids have viscosity of the order of 1 mPa.s. All these can be considered liquids of low viscosity. Only several liquids have viscosity in the range 10–10^2 mPa.s. On the other hand, glycerol and many oils have viscosity of the order of 10^3 mPa.s. However, it should be remembered that the viscosity of liquids strongly decreases with increasing temperature.

Rotational viscometers. A simple low power DC motor is employed in rotational viscometers considered here. The **stator** is a permanent magnet, and the **rotor** contains a winding connected to a DC source of constant voltage. A commutator and brushes serve for properly operating the motor (Smith 1984; Yap and MacIsaac 2006; Lyna *et al* 2007; Ng *et al* 2009). When a DC current flows through the winding, the interaction between this current and the permanent magnet (Lorentz's force) causes the rotor to rotate. Due to the rotation, an EMF e is created in the winding (Faraday's law). This EMF is proportional to the rotation velocity and opposes the applied voltage (Lenz's

law); it is called the **back EMF**. When a constant DC voltage V is applied to the rotor winding, the steady current i in the winding is governed by Kirchhoff's loop rule:

$$i = (V - e)/R, \qquad \text{so} \qquad e = V - iR, \tag{7}$$

where R is the electrical resistance of the winding. If a heavy load jams the rotor, the back EMF vanishes, so the current in the winding may dramatically increase and overheat the motor. It is easy to demonstrate this phenomenon (Hewitt 2003; Whitaker 2009; Turner 2009).

When the motor is loaded, the rotation velocity and the back EMF unavoidably decrease, so the current in the winding and the input electric power increase. It can be shown that the total mechanical power produced by the motor, including the power of friction losses, equals $P = ie$ (Smith 1984). On the other hand, the mechanical power equals $P = \omega T$, where ω is the angular rotation velocity, and T is the torque generated by the motor. The mechanical and electrical parameters of the motor thus are strictly interrelated.

It is seen from the above considerations that the torque developed by the motor linearly depends on the rotation velocity (Fig. 2). Two basic points define this line: the stall torque T_s (the torque reaches a maximum when $\omega = 0$) and the maximum velocity ω_n when no load is applied to the rotor ($T = 0$). According to this linear model,

$$T = T_s - \omega T_s/\omega_n, \qquad \text{and} \qquad P = \omega T_s - \omega^2 T_s/\omega_n. \tag{8}$$

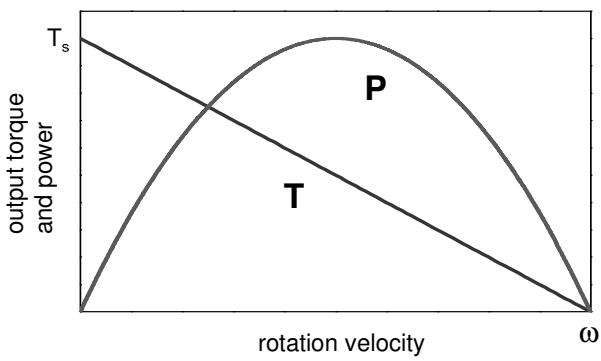

Fig. 2. The torque T and mechanical power P developed by a DC motor versus angular rotation velocity, according to the linear model.

Rotational viscometers considered here are shown in a general scheme (Fig. 3). In the first viscometer, a DC motor (Maxon 2326.939-22.111-006 model) turns a plastic cylinder immersed into a liquid under study. The viscous damping slows down the rotation, so the current in the rotor winding increases. If the linear model is valid, the current and the rotation velocity are strictly interdependent. It was shown that the motor employed in the viscometer follows this model reasonably well (Kraftmakher 2010d). The back EMF e is

proportional to the rotation velocity ω with the coefficient of proportionality only depending on the design of the motor. For our motor, $\omega\,(\mathrm{rad.s^{-1}}) = 38e$ (V). On the other hand, the EMF is available from Eq. (7); however, the resistance of an ammeter put in series with the winding should be taken into account. Either the current or the rotation velocity can be related to the viscosity of the liquid. Varying the DC voltage allows one to find conditions most suitable for liquids of different viscosities. For motor used, heavy loads cause no danger, but when the rotor winding heats up, the increase of its resistance should be taken into account when using Eq. (7).

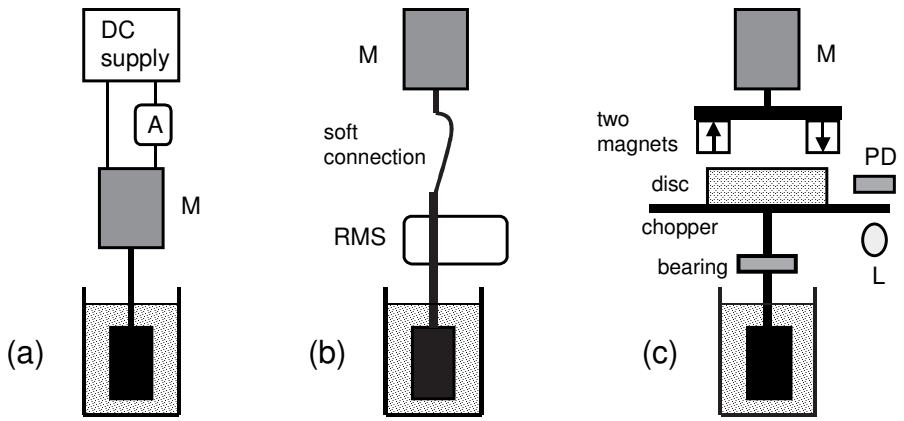

Fig. 3. Variants of the viscometer: (a) current in the rotor winding is measured; (b) rotation velocity is measured; (c) rotating magnetic field rotates the cylinder. M–motor, RMS–rotary motion sensor, L–light source; PD–photodiode.

The second viscometer employs the data-acquisition system. The *Output 1* (DC voltage) feeds the motor. The shaft of the motor is connected to the upper end of the shaft of the *Rotary motion sensor*. Since it is difficult to precisely align the motor and the sensor, a soft connection is made between them. A plastic cylinder attached to the lower end of the shaft is immersed into the liquid. The current in the winding is taken as the *Output current*. *Capstone* records the mean current in the winding and the rotation velocity.

The third variant of the viscometer is more complicated. For clarity, its components are shown separately (Fig. 4). An iron plate is attached to the motor, and two strong ceramic magnets ($12\times12\times12$ mm^3 in size) rest on it. The magnetic field of the magnets penetrates an aluminum disc positioned beneath the magnets on a shaft fixed by a bearing. The magnetic field of the rotating magnets creates eddy currents in the disc (Faraday's law). The interaction between the eddy currents and the rotating magnetic field brings the disc to rotation (Lenz's law). This operation is similar to that of an induction motor, where two- or three-phase currents in stator windings produce the rotating magnetic field. Since the amplitude of the eddy currents is proportional to the difference between the rotation velocities of the magnetic field and of the rotor,

the rotor rotates necessarily slower than the field (Kraftmakher 2001). A plastic cylinder immersed into the liquid under study is attached to the shaft carrying the aluminum disc. Changing the voltage applied to the DC motor or/and the distance between the magnets and the disc changes the rotation velocity of the cylinder. The rotation velocity is measured optically with a light source (light-emitting diode or small light bulb), a chopper pasted to the aluminum disc, and a photodiode. The photodiode operates in the photovoltaic mode, where no voltage source is needed. The chopper pattern contains 18 black areas and is printed on a transparent sheet; it was designed as a graph in polar coordinates. The frequency of the pulses is measured with a simple multimeter set for frequency measurements.

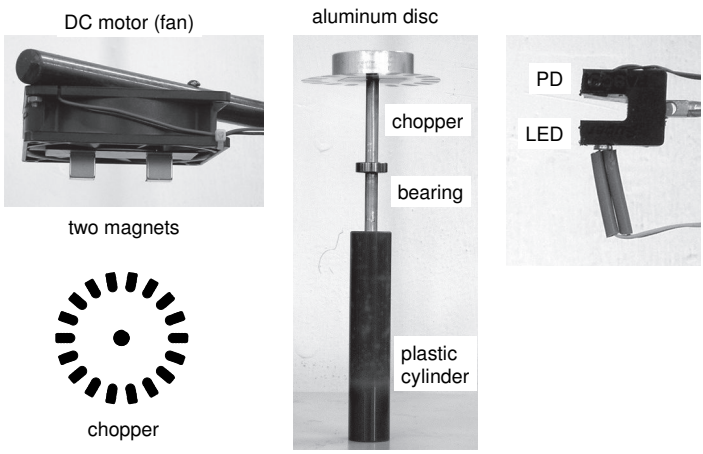

Fig. 4. Parts of the rotational viscometer employing rotating magnetic field are shown separately. LED–light emitting diode.

Viscosity of glycerol. To check the first variant of the viscometer, a plastic cylinder, 1.5 cm in diameter and 9 cm in length, was attached to the shaft of the motor and immersed into a glass filled with glycerol (Fig. 5). Before the measurements, the glycerol was heated up to 75°C. The current in the rotor winding was measured with a moving-coil ammeter, and the temperature of the glycerol with a usual glass thermometer (100°C scale). The voltage applied to the motor, 1 V, was chosen to keep a moderate rotation velocity even at the highest temperature. A serious disadvantage of glycerol is that it is hygroscopic, and that its viscosity is extremely sensitive to water content.

The data were taken during gradually cooling of the glycerol during about 2 hours. The torque generated by the DC motor is proportional to the current in the rotor winding. Therefore, the current was assumed to be proportional to the total torque due to the viscosity of the liquid and the friction forces. The latter were considered proportional to the current with no liquid in the glass. After subtracting this current (7 mA) from the measurement data, the results were considered to be proportional to the viscosity of glycerol.

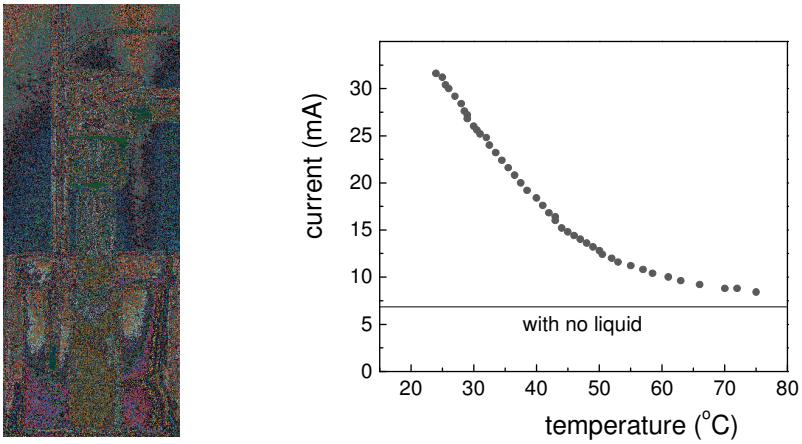

Fig. 5. Simple rotational viscometer with DC motor, and mean current in the rotor winding versus temperature of glycerol.

In a handbook (Lide 2008), the viscosity of glycerol is given for four temperatures, from 25°C to 100°C. In many cases, the viscosity of a liquid follows an exponential function of $1/T$, where T is the absolute temperature:

$$\eta = A\exp(B/T), \tag{9}$$

where A and B are constants. This relation known as **Arrhenius' law** is applicable to glycerol: the logarithm of the viscosity is proportional to $1/T$ (Fig. 6). The results of our measurements reasonably well reproduce the temperature dependence of the viscosity of glycerol. The viscosity strongly depends on temperature: between 25°C and 100°C, the change is about 60 times.

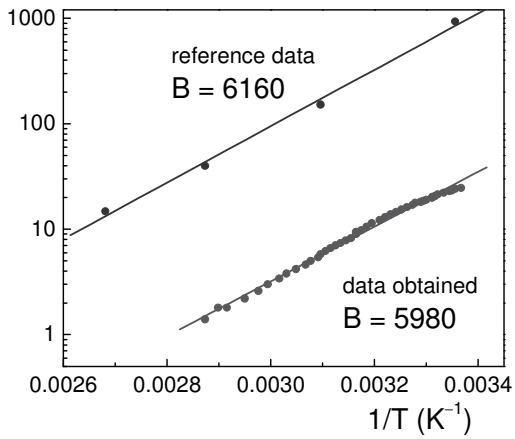

Fig. 6. Current in the rotor winding (mA) and reference data for viscosity of glycerol (mPa.s), versus $1/T$.

3.7. Crookes' radiometer

The experiment follows that described by Arenas *et al* (1996).

Additional equipment: Crookes' radiometer, light bulb, DC supply, photodiode, laser diode, oscilloscope.

The radiometer.

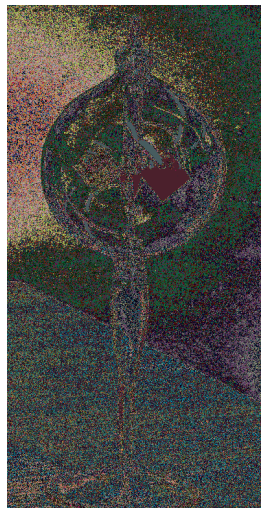

The radiometer consists of four vanes, each of which is blackened on one side and polished or silvered on the other. These are attached to the arms of a rotor, which is balanced on a vertical support in such a way that it can turn with very little friction. The mechanism is encased inside a clear glass bulb, which has been pumped out to a high (but not perfect) vacuum. When electromagnetic radiation falls on the vanes, they turn with the black surfaces apparently being pushed away by the light. When a radiant energy source is directed at the radiometer, the radiant energy from the source warms the black side faster than the silver or white side. The internal air molecules acquire more energy when they touch the black side. The heat loss through the glass keeps the internal bulb temperature steady, so that the two sides of the vanes can develop a temperature difference. The two sides must be thermally insulated to some degree, so that the silver or white side does not immediately reach the temperature of the black side. If the vanes are made of metal, then the black or white paint can be the thermal insulation.

A strong vacuum inside the bulb does not permit motion, because there are not enough molecules to cause air currents to move the vanes and to transfer heat to the outside before both sides of each vane reach thermal equilibrium by heat conduction through the vane material. High pressure also does not permit motion because the temperature differences are not enough to move the higher concentration of air (Hull 1948; Woodruff 1968).

The setup includes a Crookes' radiometer, a light bulb fed by a DC supply, a laser diode, a silicon photodiode, and an oscilloscope, which serves also as an amplifier (Fig. 1). In the experiment, the rotation frequency of the vanes is measured versus the power applied to the light bulb illuminating the radiometer. The laser diode and the photodiode are arranged for obtaining electrical pulses, whose frequency is four times the rotation frequency (four vanes). The electrical pulses from the photodiode are displayed and amplified by the oscilloscope and then fed to the digital input of the *750 Interface* intended for the *Rotary motion sensor*. The rotational frequency is measured through the number of pulses per second measured by the sensor. *DataStudio* displays the rotation frequency during a period including the acceleration of the vanes after switching on the light bulb, the steady rotation, and the deceleration of the vanes after switching off the light bulb (Fig. 2). The rotation frequency is a nearly linear function of **irradiance**.

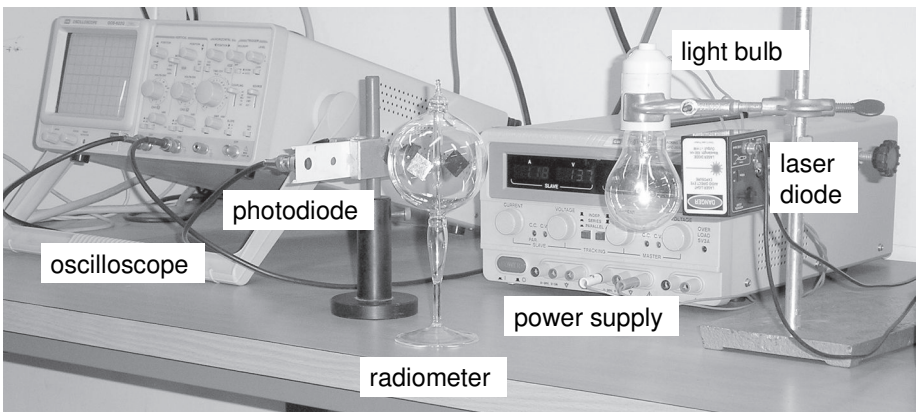

Fig. 1. Setup for the measurements.

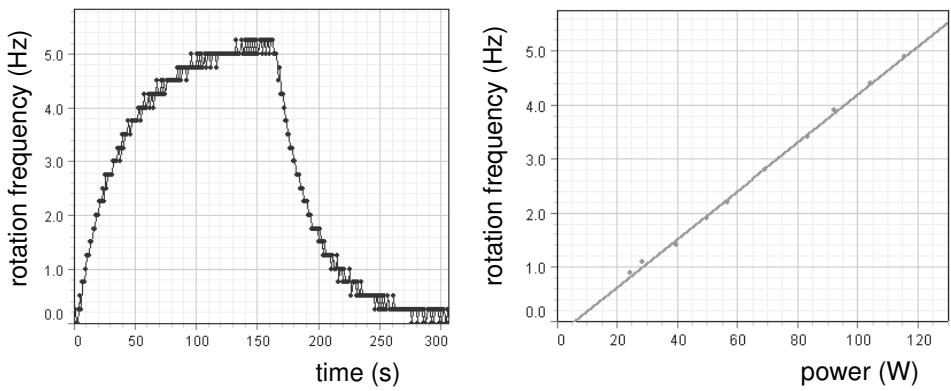

Fig. 2. Rotation frequency during a run and steady rotation frequency versus power of the light bulb irradiating the radiometer.

3.8. Heat of vaporization of nitrogen

The experiment is a computer-assisted version of experiments described earlier: Soloukhin (1975); Tompson and White (1983); Neil and Schulze (1986).

Additional equipment: *Force sensor*, Dewar flask, DC supply, two multimeters, heater.

The **vaporization** of a liquid is a **phase transition** of the **first order**. A definite energy known as the latent heat of vaporization must be supplied to the liquid for accomplishing such a transition. During the transition, the temperature of the liquid remains constant. This means that all the supplied energy is consumed by the phase transition. The **heat of vaporization** of a liquid can be determined by measuring the boiling rate when a known electric power is dissipated in it. In our case, liquid nitrogen is kept in a Dewar flask at a temperature of equilibrium between the liquid and gas phases at normal pressure, which equals 77.35 K. The arrangement for the measurements includes a Dewar flask, a heater, a DC supply, and the *Force sensor* (Fig. 1). The heat balance equation for this process is given by

$$P\Delta t = \lambda \Delta m, \tag{1}$$

where P is the power supplied to the liquid during the time interval Δt, Δm is the mass of the evaporated liquid, and λ is the **latent heat of vaporization**.

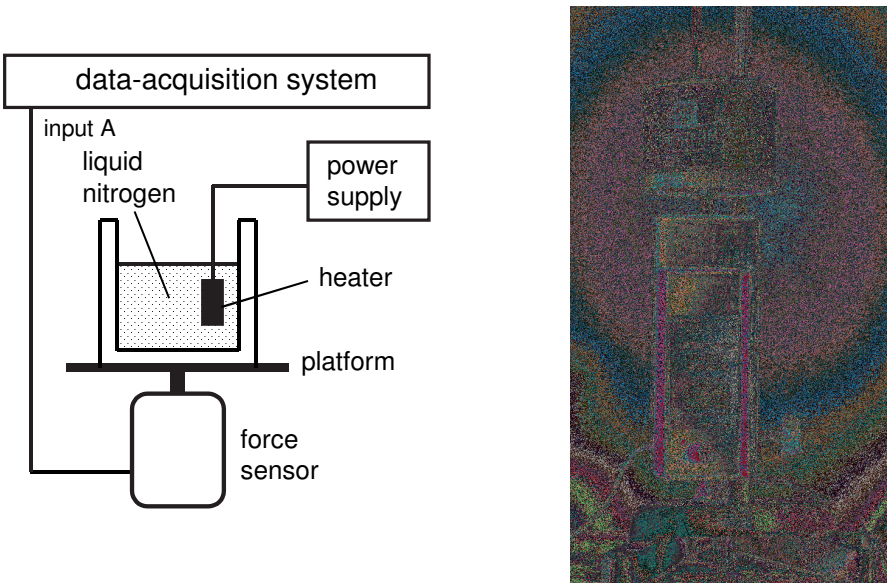

Fig. 1. Setup for the measurements (two multimeters are not shown).

Two multimeters measure the voltage applied to the heater and the heating current. Even with no current in the heater, the mass of the liquid changes. The Dewar flask does not provide full thermal insulation, and evaporation of the nitrogen occurs due to the heat exchange with the environment. On the other hand, the mass of the liquid may increase due to the condensation of oxygen (the normal boiling point of oxygen is 90.19 K) and water vapor from the surrounding air. When an electric power is dissipated in the heater and a stream of gas escapes from the Dewar flask, the above processes are highly suppressed. A glass tube surrounds the heater, so that the evaporation occurs only through this tube.

DataStudio displays the weight of the Dewar flask, measured by the *Force sensor*, versus time (Fig. 2). The *Tare* button cancels the initial weight of the flask. A significant scatter of the data is observed during the intensive boiling of liquid nitrogen. It is easy to improve the graph by the *Smooth* operation. The heat of vaporization is available after making corrections for the background. Generally, the slope of the background before and after the main part of the experiment is different. Therefore, the measurement data are extrapolated to the middle of the heating period. For the example given, the electric power $P = 17.6$ W is applied during 100 s, and the change of the weight of the nitrogen is 0.087 N. From the data, $\lambda = 198$ J.g^{-1}, which is close to the accepted value.

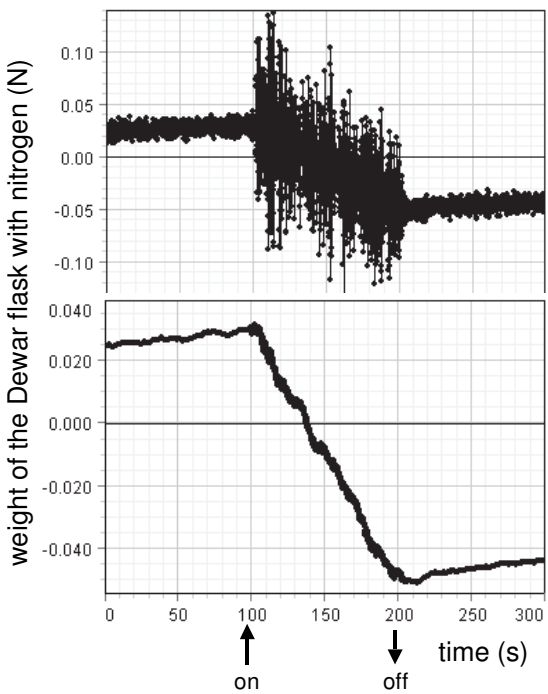

Fig. 2. Data from the *Force sensor* and the data after smoothing.

3.9. Phase diagram of nitrogen

The phase diagram of nitrogen is explored from its triple point (63.18 K) to the normal boiling point (77.35 K), and the heat of vaporization is determined. The experiment follows those described earlier (Iveronova 1962, 1967; Soloukhin 1975; Goldin 1983; Bligh and Haywood 1986; Gesari *et al* 1996).

AIP Emilio Segrè Visual Archives,
E. Scott Barr Collection
Blaise Pascal (1623–1662)

Equipment: bell jar, rotary pump, platinum resistance thermometer, Dewar flask, heater, DC supply, three multimeters.

The states of any material can be represented graphically as a surface in a three-dimensional space with coordinates p, V, and T (pressure, volume, temperature). For a definite volume, each phase of the material is stable only in certain ranges of the temperature and pressure. A transition from one phase to another takes place under conditions of phase equilibrium between the two phases. For a given pressure, the transition occurs at only one specific temperature. A p–T phase diagram shows the regions, in which the various phases exist and where phase transitions occur (Fig. 1). Each point on the phase diagram represents a pair of p and T values. Two phases coexist in equilibrium for points on lines separating the solid, liquid, and vapor regions. All three phases coexist at the **triple point**. The normal boiling point shows the temperature of the equilibrium between liquid and vapor phases at normal pressure. The end point of the vaporization curve is called the **critical point**. At this point, the distinction between liquid and vapor disappears. At a pressure and a temperature above the critical parameters the material does not separate into two phases. In the solid state, several phases can exist differing in crystal or magnetic structure.

In the experiment, the phase diagram of nitrogen is determined during gradually increasing the temperature after cooling the nitrogen by pumping out

the gas. With a rotary pump, liquid nitrogen can be cooled down somewhat below its triple point. The temperature of the triple point of nitrogen is 63.18 K, and the corresponding pressure is 1.25×10^4 Pa.

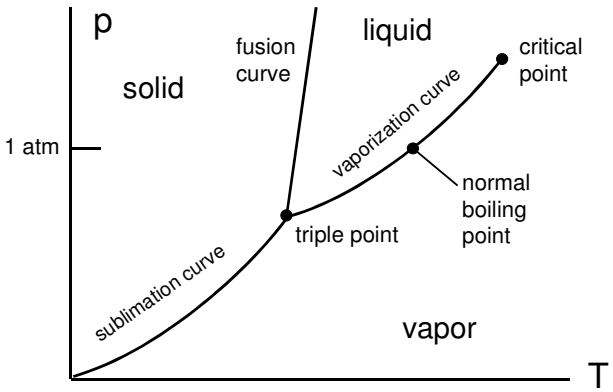

Fig. 1. Typical p–T phase diagram.

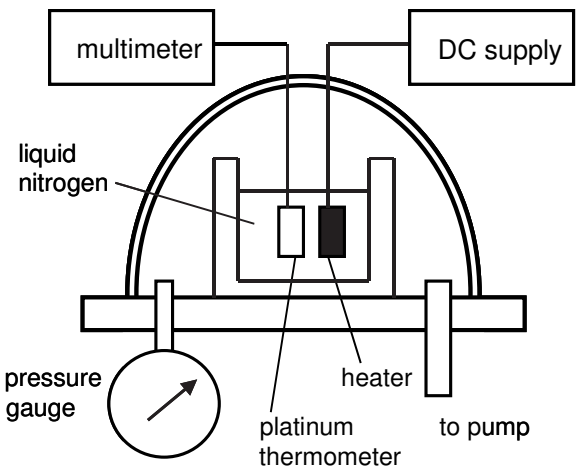

Fig. 2. Schematic of the setup for determining the phase diagram.

A Dewar flask filled with liquid nitrogen is placed under a bell jar connected to a rotary pump (Fig. 2). A pressure gauge measures the pressure. A platinum resistance thermometer and an electrical heater are put into the liquid nitrogen. The power applied to the heater is measured with two multimeters (not shown in Fig. 2). Another multimeter measures the resistance of the thermometer. The absolute temperature is determined from the relation

$$T = 30.9 + 225.4\times X + 16.8\times X^2, \quad (1)$$

where X is the ratio of the resistance to the resistance at 0°C.

When heating the solid/liquid nitrogen, the pressure of the nitrogen gas increases according to the phase diagram (Fig. 3). The measurements are possible at pressures up to 1 atm (≈10^5 Pa). Under equilibrium,

$$p = A\exp(-q/k_B T), \tag{2}$$

where A is a constant, q is the heat of vaporization, and k_B is Boltzmann's constant. Hence,

$$\ln p = \ln A - q/k_B T. \tag{3}$$

The slope of the plot of ln$p$ versus $1/T$ is $-q/k_B$. From the measurements, $q = 207$ J.g^{-1}.

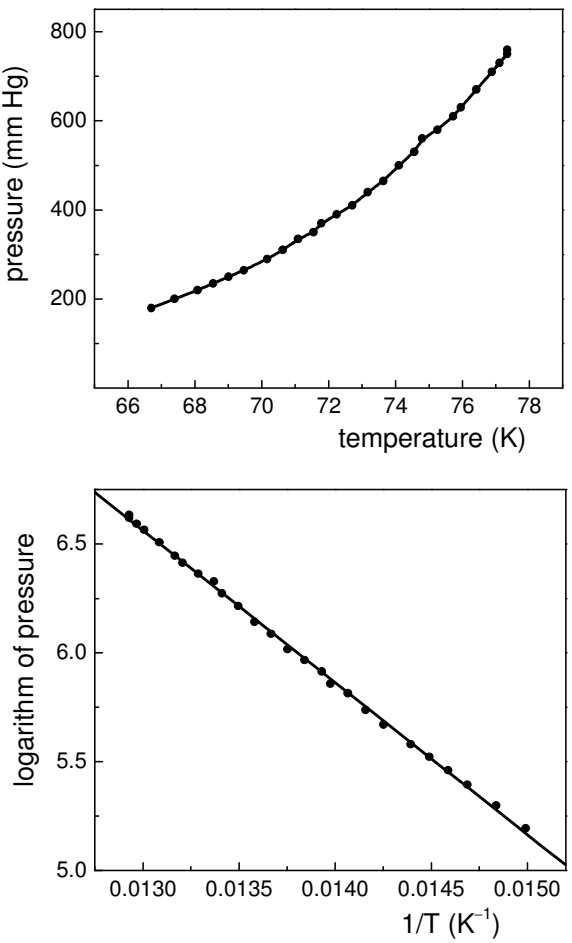

Fig. 3. Vaporization curve of nitrogen and ln$p$ versus $1/T$.

3.10. Thermoelectric phenomena

Different experimental setups (Fig. 1) are used for experiments with a thermoelectric module (Kraftmakher 2005f).

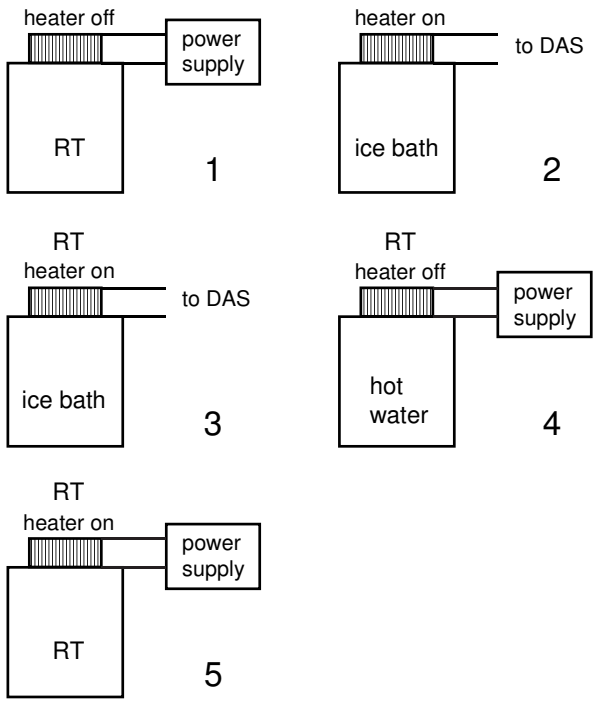

Fig. 1. Schematics of setups: 1–Peltier's effect, 2–Seebeck's effect, 3–thermoelectric generator, 4–maximum temperature difference, 5–Peltier coefficient. RT–room temperature, DAS–data-acquisition system.

Seebeck's and Peltier's effects. Seebeck's effect consists of generation of an EMF between two junctions of dissimilar metals or alloys when the junctions are kept at different temperatures (Fig. 2). For a given mean temperature, the EMF is proportional to the temperature difference ΔT between the junctions:

$$E = S\Delta T, \tag{1}$$

where the coefficient of proportionality S is called **Seebeck's coefficient** or the **thermoelectric power**.

For metals and alloys used for thermocouples, the thermoelectric power is usually in the range 10–60 $\mu V.K^{-1}$. For semiconductors, this figure may be several times larger. Seebeck's effect is used for temperature measurements and for producing electric energy when other sources are inaccessible.

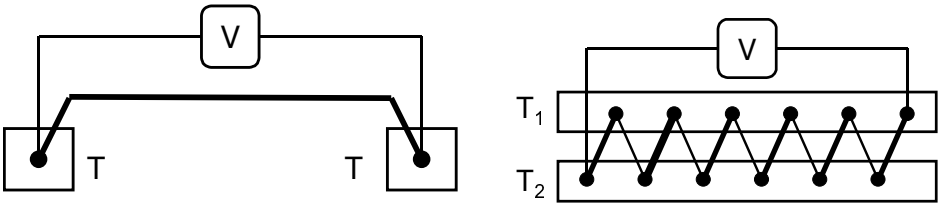

Fig. 2. Thermocouple voltage is proportional to temperature difference between the junctions. A thermopile increases the generated voltage.

Peltier's effect is inverse to Seebeck's effect: when a DC current passes through a junction of two dissimilar materials, a heat additional to that produced by the Joule heating is generated or absorbed in the junction, depending on the direction of the current. The power of the additional heat is proportional to the current: $Q = \Pi I$, where Π is called **Peltier's coefficient**. The effect is used for cooling elements of solid-state electronics, such as lasers and infrared detectors. Using thermodynamic arguments, Kelvin deduced a simple equation that relates Seebeck's and Peltier's coefficients to one another:

$$\Pi = ST, \tag{2}$$

where T is the absolute temperature.

Thermoelectric phenomena constitute a part of theoretical and laboratory university courses. Gross (1961) considered the efficiency of thermoelectric devices and its dependence on the characteristics of thermoelectric materials. Mortlock (1965) determined the coefficient of performance of a thermoelectric device and compared it to that of an ideal heat engine. In measurements at liquid helium temperatures, Guénalt *et al* (1978) achieved a reasonably good agreement with the theory. Gupta *et al* (1984) used a thermoelectric module for verifying the second law of thermodynamics. The reversible and irreversible contributions to the phenomenon were separated, and the results appeared to be in good agreement with theoretical predictions. Cvahte and Strnad (1988) repeated this experiment with better accuracy. With a thermoelectric generator, Gordon (1991) considered the efficiency of heat engines. Garrido *et al* (2013) reported on measurements of Peltier's coefficient.

In the experiments reported (Gupta *et al* 1984; Cvahte and Strnad 1988), the measurements were carried out when temperatures of the sides of a thermoelectric module were kept constant. The cold plate was maintained at a constant temperature by using cooling water. A regulated heater ensured a constant temperature of the hot plate. In the first measurement, the EMF of the unloaded module was determined along with the temperature difference between its sides. Then the module was loaded, and the current and voltage across the load resistor were measured. In the third case, a current was passed through the module from an external DC supply causing an additional heating of the hot side. In all three cases, the heater on the hot plate was adjusted to compensate for changes due to different modes of operation of the module. The changes in the

power supplied to the hot side were determined and used in the calculations. Combining the results of the three measurements, the reversible and irreversible parts of the phenomena were separated. The only disadvantage of the experiment is a long time necessary for establishing a stationary state of the setup. According to Cvahte and Strnad (1988), the experiment takes about 5 h, so in one laboratory session the students carry out only one of its parts.

The quality of a thermoelectric material depends on three properties, namely, the thermoelectric power S, the **conductivity** σ, and the **thermal conductivity** κ. The conductivity defines the internal resistance of a thermoelectric device and the related Joule heating, whereas the thermal conductivity governs the heat flow through the device leading to a decrease of the temperature difference between its sides. The efficiency of a thermoelectric device is given by the so-called thermoelectric **figure of merit** Z, which equals

$$Z = S^2\sigma/\kappa. \tag{3}$$

For metallic systems, **Wiedemann–Franz's** law shows the relationship between σ and κ:

$$\kappa/\sigma = LT, \tag{4}$$

where L is the **Lorenz number** equal to 2.45×10^{-8} $V^2.K^{-2}$.

The efficiency of a thermoelectric device is given by two characteristics. The **thermoelectric efficiency** of a thermoelectric generator is the ratio of the electrical energy produced to the amount of thermal energy absorbed from a heat source. The **coefficient of performance** of a thermoelectric cooler is the ratio of the heat removed from one side of the device to the amount of electric energy consumed. The Joule heating and thermal conductance inside a thermoelectric device cause irreversible energy losses.

An ideal thermoelectric device is considered to have an infinite electrical conductance and zero thermal conductance. For such a device, the second law of thermodynamics governs the thermoelectric efficiency and the coefficient of performance. When the temperature difference between the sides of the device is ΔT, the Seebeck EMF equals $S\Delta T$. If the current through the loaded device is I, the total electric power developed is $IS\Delta T$. On the other hand, the power of the Peltier heat equals ΠI, and the thermoelectric efficiency is $S\Delta T/\Pi$. Taking into account Eq. (2), the efficiency equals $\Delta T/T_h$, that is, the efficiency of an ideal heat engine, where T_h is the temperature of the hot side of the device. When the coefficients S and Π are determined independently, the validity of Eq. (2) can be considered as the verification of the second law of thermodynamics.

For a real thermoelectric device, the thermoelectric efficiency and the coefficient of performance depend on the figure of merit and the temperatures of the two sides of the device (Morelli 1997; Parker 1997). Using mixed crystals and radiation-induced damage, it is possible to reduce the thermal conductivity of the material. These factors also influence the conductivity and thermopower, but the Z value may become more favorable. Nowadays, the most efficient thermoelectric materials are Bi_2Te_3 and PbTe. Typically, many thermocouples

are joined together and sandwiched between two isolating plates of high thermal conductivity. Thermoelectric modules are based on *p*- and *n*-doped Bi_2Te_3 alloys configured to contain many junctions arranged in parallel thermally and in series electrically.

Thermoelectric devices made from even the best available materials have the disadvantages of relatively low efficiencies and concomitant high cost per unit of output. Their use is restricted to situations, in which these disadvantages are outweighed by their small size, low maintenance, quiet performance, and long life. When employing a thermoelectric device, the temperature of the hot side of the device should be as close as possible to that of the heat sink (or source), and the temperature of the cold side as close as possible to that of the cold sink.

Using Peltier's cells, Torzo *et al* (2007) studied the solid–liquid–vapor transitions and supercooling.

Setup with a thermoelectric module. A simple setup is aimed at performing the experiments in a reasonably short time. Reducing the thermal inertia of one side of a thermoelectric device and using a data-acquisition system helps to reach this goal. A thermoelectric module CP1.0-31-08L from Melcor Corporation is sandwiched between a thin electrical heater (upper side) and a massive aluminum block (down side). The module is pressed to the block by a plastic plate and two screws (Fig. 3).

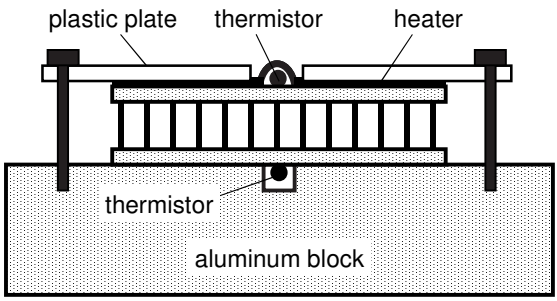

Fig. 3. Arrangement of the thermoelectric module.

The aluminum block is placed in a glass filled with water at room temperature or in an ice bath. The temperatures of the sides of the module are measured by two *Thermistor temperature sensors* pasted to its plates and connected to the inputs of the data-acquisition system. Due to the high thermal inertia of the bottom part of the setup, its temperature changes are small but also measured and taken into account. The first experiment is a demonstration of the thermoelectric heating and cooling. A separate run employing AC currents shows the role of the Joule heating. The goal of the second experiment is the determination of the Seebeck coefficient of the module. From the third experiment, the efficiency of the thermoelectric generator and the figure of merit

are evaluated. Then the maximum temperature difference provided by Peltier's cooler is determined. From these data, the figure of merit is also available. Lastly, Peltier's coefficient of the module is measured and the coefficient of performance of the device is calculated.

The module is connected to a power supply and operates in the regimes of cooling or heating of its upper side. The temperature of the aluminum block is close to room temperature. The *Graph* displays the temperature difference between the sides of the module for different currents passing through it. With AC currents (50 Hz), the role of the Joule heating becomes evident (Fig. 4).

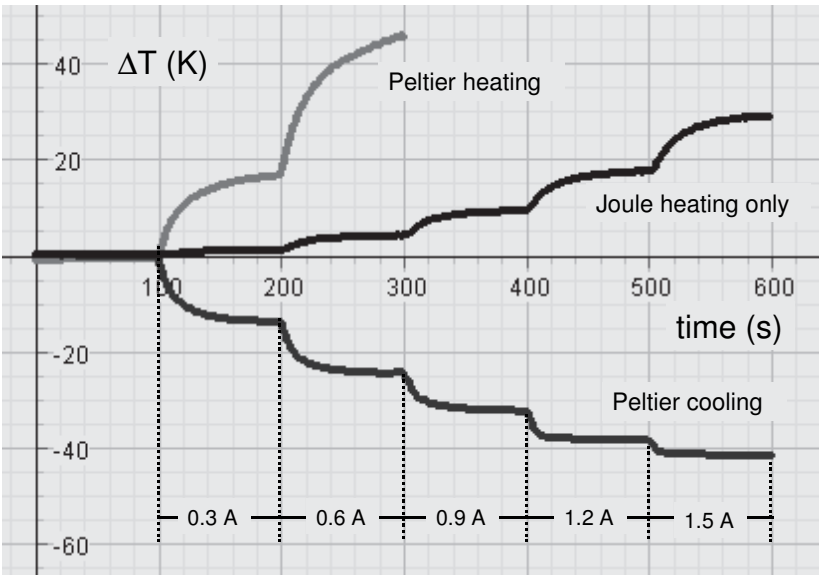

Fig. 4. Temperature difference between two sides of the module for different currents.

1. Seebeck's effect

Seebeck's coefficient and efficiency of a thermoelectric generator are determined.

Additional equipment: two *Thermistor temperature sensors*, DC supply, thermoelectric module, multimeter.

The *Voltage sensor* measures the voltage generated by the thermoelectric module, and *Graph* displays it versus the temperature difference between the sides of the module. The electrical heater attached to the upper side of the module controls its temperature. The measurements are carried out while gradually changing the temperature difference between the sides of the module. From the data obtained (Fig. 5), Seebeck's coefficient of the module equals 8.5 mV.K^{-1}.

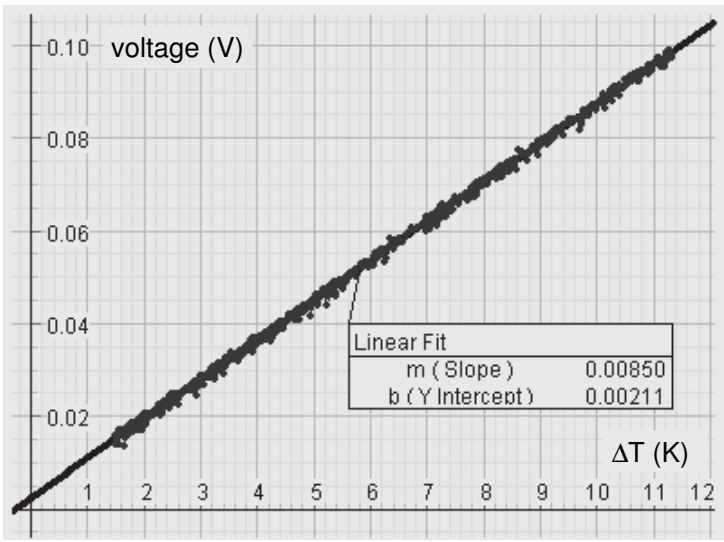

Fig. 5. Voltage generated by the module versus temperature difference between its sides.

Efficiency of a thermoelectric generator cannot exceed the efficiency of an ideal heat engine (Carnot efficiency), $\eta_C = \Delta T/T_h$. The real efficiency is much less than this value. The heat Q_{in} delivered by a heat source to the hot side of the generator is balanced by the heat $K\Delta T$ conducted through the module, and the Peltier heat ΠI developed at the hot junction due to the flow of current. In addition, the Joule heat dissipated in the module is assumed to flow equally to both its sides (Morelli 1997). Hence,

$$Q_{in} = \Pi I + K\Delta T - \tfrac{1}{2}I^2R, \quad (5)$$

where K is the thermal conductance, and R is the electrical resistance.

For determining the maximum electric power delivered by the thermoelectric module, the bottom side of the module is cooled by an ice bath, and the electric power supplied to the heater is adjusted to make the temperature of the upper side equal to room temperature. Under such conditions, the heat exchange between the upper side of the module and the surroundings is excluded. The maximum electric power is delivered to the load of resistance equal to that of the module. In this case, $P_{out} = E^2/4R$, where E is the EMF generated by the module. The efficiency of the generator η equals the ratio of this power to the power Q_{in} supplied to the heater. The resistance of the module is $R = 1.3\ \Omega$. With a load equal to this resistance, $\Delta T = 20.5$ K, $Q_{in} = 1.1$ W, and $P_{out} = 5.8$ mW, so that $\eta = 0.53\%$. The thermal conductance of the module K is available from the measurements when $I = 0$. For the same temperature difference, $Q_{in} = 0.93$ W, and K equals 0.045 W.K^{-1}. The Carnot efficiency is $\eta_C = 5.9\%$. The η_C/η ratio can be used for calculations of the figure of merit of the module. From the general expressions for P_{out} and Q_{in}, it is easy to see that (Morelli 1997)

$$\eta_C/\eta = 2 + 4/ZT_h - \tfrac{1}{2}\eta_C. \quad (6)$$

In our case, $\eta_C/\eta = 13$. With $T_h = 298$ K, the figure of merit from Eq. (6) is $Z = 1.2\times10^{-3}$ K^{-1}, somewhat lower than best present values.

For modulation measurements of Seebeck's coefficient, see Kraftmakher 1973b).

2. Peltier's effect

Peltier's coefficient and coefficient of performance are measured.

Additional equipment: two *Thermistor temperature sensors*, DC supply, thermoelectric module, multimeter.

Temperature difference obtainable with Peltier's cooler. For an ideal Peltier's cooler, the rate of heat removal from its cold side is ΠI. In real thermoelectric coolers, additional heat is delivered to the cold side of the device. The power of this heat equals $\frac{1}{2}I^2R + K\Delta T$, where the term $\frac{1}{2}I^2R$ is due to the Joule heat generated inside the module. The rate of heat removal becomes

$$Q_{\text{rem}} = \Pi I - K\Delta T - \tfrac{1}{2}I^2R. \tag{7}$$

The temperature difference provided by a thermoelectric cooler thus increases with a decrease in the heat, which is to be removed. The maximum temperature difference $\Delta T_{\max}$ is achievable when this heat vanishes. The temperature difference provided by the module is determined when the module operates in the regime of cooling of its upper side, while the bottom side is heated by hot water. The data are taken when the temperature of the upper side becomes equal to that of its surroundings. The heat removal from the upper side thus vanishes, and the term $K\Delta T$ attains its maximum value. The temperature difference depends on the current (Fig. 6).

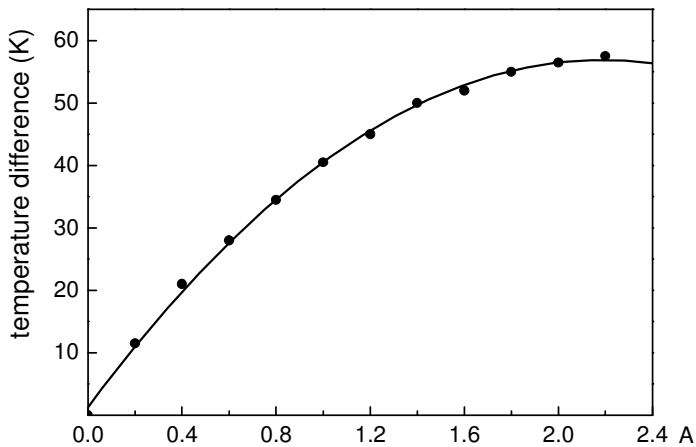

Fig. 6. Temperature difference provided by Peltier cooler, versus electric current.

From a quadratic fit, the maximum temperature difference $\Delta T_{\max}$ is 57 K. This value is valid when the cold side of the module is kept at 25°C. The manufacturer gives two values for $\Delta T_{\max}$,: 67 K when the temperature of the cold side is –42°C and 77 K when it equals –27°C. The value of $\Delta T_{\max}$ can be used for calculations of the figure of merit of a thermoelectric device (Morelli 1997):

$$Z = 2\Delta T_{max}/T_c^2, \tag{8}$$

where T_c is the temperature of the cold side of the device. Using ΔT_{max} = 57 K and T_c = 298 K, the figure of merit appears to be $Z = 1.3\times10^{-3}$ K^{-1}.

Peltier's coefficient. For the determination of Peltier's coefficient, the module operates in the regime of cooling of its upper side, while the bottom side is kept at room temperature. The electrical heater on the upper side serves to compensate for the heat removal by the Peltier cooling. The electric power supplied to the heater is adjusted to nullify the temperature difference between the two sides. After the compensation, the temperatures of both sides of the module become close to room temperature. The term $K\Delta T$ vanishes, and the electric power produced by the heater equals the power of the Peltier cooling minus the Joule term. Therefore, the electric power should be a quadratic function of the current. From the data (Fig. 7), Peltier's coefficient of the module is Π = 2.89 V. According to Eq. (2), it should be 2.53 V.

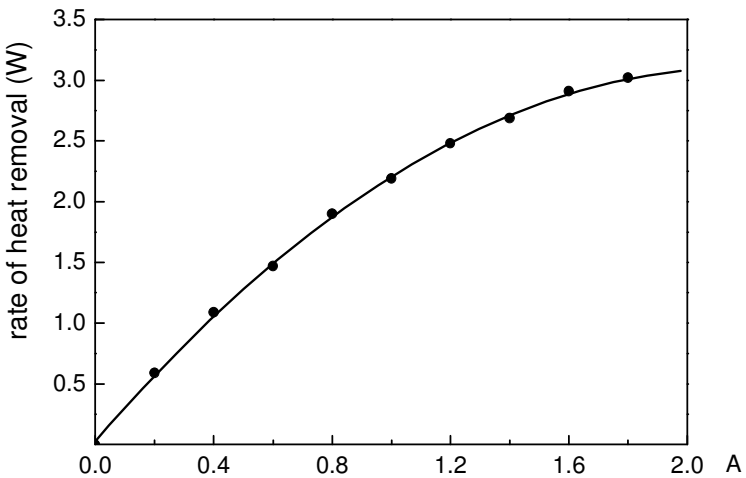

Fig. 7. Rate of heat removal versus current through the module when $\Delta T = 0$. From the fit, Π = 2.89 V.

Coefficient of performance. The cooling ability of a Peltier cooler is given by the coefficient of performance β, which is the ratio of the rate of the heat removal Q_{rem} to the power consumed. The latter is the sum of the Joule term and the power required for overcoming Seebeck's EMF:

$$P = I^2R + SI\Delta T. \tag{9}$$

The coefficient of performance thus equals

$$\beta = \frac{\Pi I - I^2R/2 - K\Delta T}{SI\Delta T + I^2R}. \tag{10}$$

The coefficient of performance depends on the current through the module and the temperature difference. The term $SI\Delta T$, which is of minor importance under normal operational conditions, becomes significant at low currents. When $\Delta T = 0$ and IR is small in comparison with Π and $S\Delta T$, the coefficient of performance equals $\beta = \Pi/S\Delta T$. Under such conditions, it should be equal to that of an ideal heat engine, $T_c/\Delta T$. Using Eq. (10), the coefficient of performance of the module was calculated as a function of the current, for several values of the temperature difference between its sides (Fig. 8). This graph is similar to those given by manufacturers of thermoelectric coolers. The coefficient of performance of thermoelectric coolers is an order of magnitude less than that of refrigerators with the vapor-compression cycle.

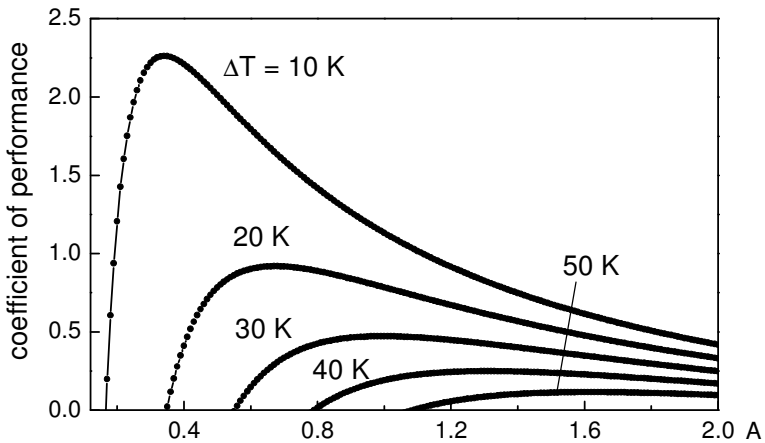

Fig. 8. Coefficient of performance (calculated) versus current, for different values of ΔT.

3.11. Thermal noise

Boltzmann's constant is evaluated from thermal noise measured over a wide temperature range (Kraftmakher 1995).

$S = -k_B \ln W$

$N = N_0 \exp(-E/k_B T)$

$\langle \Delta V^2 \rangle = 4 k_B R T \Delta f$

$k_B = 1.3806 \times 10^{-23}$ J.K^{-1}

AIP Emilio Segrè Visual Archives,
Physics Today Collection
Ludwig Boltzmann (1844–1906)

Additional equipment: two *Voltage sensors*, two high-resistance light bulbs, function generator with VCF input (unnecessary when using the *850 Interface*), DC supply, RMS voltmeter, amplifier, oscilloscope, milliammeter, two resistors.

Electrical fluctuations are an example of **fluctuation phenomena**, which play an important role in physics and technology. Measurements of electrical fluctuations are quite accessible to undergraduate students. The **thermal noise** is quite observable and provides good results for Boltzmann's constant. Such student experiments were described by Earl (1966); Soloukhin (1975); Kittel *et al* (1978); Vetterling and Andelman (1979); Ericson (1988); Dekker *et al* (1991); Melissinos and Napolitano (2003); Rodríguez-Luna and de Urquijo (2010).

The mean square of the sum of two statistically independent noise voltages equals the sum of the mean squares of the voltages. This rule is important for all measurements of electrical fluctuations.

Brief review of measurement techniques. The generation of thermal noise by electrical conductors is a fundamental physical phenomenon. Thermal noise is therefore unavoidable and obeys strict quantitative relations. Johnson (1928) was the first to measure this noise and to show that it is independent of the composition of the resistor and the nature of the charge carriers. Therefore, thermal noise is often called **Johnson's noise**. The noise signals are extremely small, and some ingenuity is required to measure them. Reviews of **noise thermometry** were given by Actis *et al* (1972), Kamper (1972), and by White

et al (1996). Soulen *et al* (1992) reported on noise thermometry for low temperatures developed at the National Institute of Standards and Technology (Gaithersburg).

As was theoretically shown by Nyquist (1928), the mean squared thermal-noise voltage generated by a resistor in a narrow frequency band Δf equals

$$<\Delta V^2> = 4k_B RT\Delta f, \tag{1}$$

where R is the resistance. This equation including Boltzmann's constant k_B and the absolute temperature T confirms the fundamental origin of thermal noise. More generally, **Nyquist's formula** (1) should be written as:

$$<\Delta V^2> = 4hfR\Delta f/[\exp(hf/k_B T) - 1], \tag{2}$$

where h is Planck's constant, and f is the frequency. Usually, $hf << k_B T$, and Eq. (1) remains valid in all cases except of very low temperatures. After amplification by an amplifier, the noise voltage becomes

$$<V^2> = 4k_B RT\int_0^\infty K^2 \mathrm{d}f, \tag{3}$$

where K is the amplifier gain depending on frequency.

These equations offer a method of measuring the **absolute temperature**. An additional expression is important for estimating the attainable precision of noise thermometry. The noise voltage is a fluctuating quantity and must be time-averaged. The statistical uncertainty of such temperature measurements depends on the averaging time τ:

$$\Delta T/T = (2\pi\tau\Delta f)^{-1/2}. \tag{4}$$

When measuring temperature of wire samples through their thermal noise, the noise of low-resistance samples may be comparable with the inherent noise of amplifiers. The **correlation method** of measurements is useful in such cases. In a correlation device, an electric signal V_c (that is, the thermal noise generated by a resistor) is fed to the inputs of two similar amplifiers (Fig. 1).

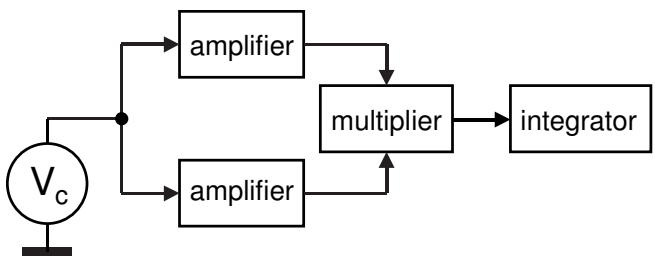

Fig. 1. Block diagram of correlation amplifier. After integration, the output voltage does not depend on inherent noise of the channels.

Their output signals contain the amplified common input voltage V_c (correlated) and inherent noise voltages V_1 and V_2 (uncorrelated). The signals

proceed to a multiplier and then to an integrating circuit. The result of the multiplication is

$$V_{out} = K_1K_2(V_c^2 + V_cV_1 + V_cV_2 + V_1V_2), \quad (5)$$

where K_1 and K_2 are total gains of the two channels. Since the inherent noise voltages of the amplifiers, V_1 and V_2, are uncorrelated with each other and with the common input signal V_c, the corresponding products vanish after averaging. The mean output voltage of the integrator is thus proportional to the square of the correlated input signal V_c:

$$<V_{out}> = K_1K_2<V_c^2>, \quad (6)$$

but it is sensitive to the gains of the channels K_1 and K_2.

A proposed correlation amplifier (Kraftmakher and Cherevko 1972a,b) differs in that it employs a compensation method. The noise voltage to be measured, V_c (correlated), is fed to two amplifiers, and the amplified voltages proceed to a multiplier. For the compensation, two anti-correlated voltages, V_a and $-V_a$, are also fed to the amplifiers. These voltages are taken from an independent noise generator and a phase splitter. After averaging,

$$<V_{out}> = K_1K_2(<V_c^2> - <V_a^2>). \quad (7)$$

When the RMS values of the anti-correlated voltage and of the input voltage are equal, the output voltage becomes zero, regardless of the gains of the channels.

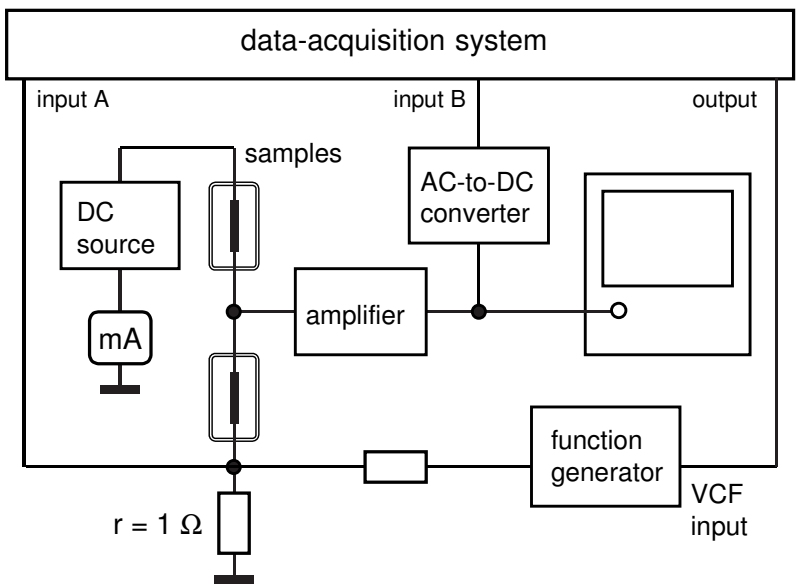

Fig. 2. Setup for the measurements.

The setup. The measurements employ two sources of thermal noise. First, filaments of vacuum incandescent light bulbs (28 V, 40 mA) are utilized. To demonstrate the nature of thermal noise, it is very useful to vary the temperature of the resistor in a wide range. When heating the filaments with a current, there is no equilibrium between the sample and its surroundings, but Nyquist's formula is still valid. To avoid superfluous evaluations, two similar lamps are connected in series relative to a DC source and in parallel relative to the input of an amplifier (Fig. 2). Hence, the noise source is to be considered as a resistor of a quarter of the resistance of two filaments connected in series (Kraftmakher 1973b; Soloukhin 1975). A PAR 124A amplifier operating in the selective mode (the range 10 μV, $f_0 = 50$ kHz, $Q = 2$ or 5) amplifies the noise. The values of Q correspond to the selectivity of the amplifier set by a switch.

The output voltage of the amplifier proceeds to an oscilloscope, Kenwood CS-4025, and to an AC-to-DC converter through a low-pass filter ($R = 1$ kΩ, $C = 2200$ pF). A Hewlett–Packard 400E **true RMS** voltmeter serves as the AC-to-DC converter. Now we have

$$<V^2> = 4k_BRT\int_0^\infty G^2 \mathrm{d}f = 4k_BRTG_0^2\int_0^\infty (G/G_0)^2 \mathrm{d}f = 4k_BRTG_0^2B, \tag{8}$$

where G is the total gain depending on the frequency, G_0 is the maximum total gain, and $B = \int_0^\infty (G/G_0)^2 \mathrm{d}f$ is called the **noise equivalent bandwidth**.

The frequency response of the amplifier is measured using a function generator with a digital frequency indication. From numerical integration, the noise equivalent bandwidth appeared to be 33.3 kHz for $Q = 2$ and 15.2 kHz for $Q = 5$. To determine the maximum total gain, the internal attenuators of the generator are employed (−20 dB and −40 dB). The gain of the oscilloscope may be changed in a wide range, and the total gain is determined with proper steps. In our case, G_0^2 is 4.85×10^9 (the nominal value 10^{10} is reduced by the RC filter). The absolute temperature of the filaments can be deduced from the relation

$$T = 103 + 207X - 1.8X^2, \tag{9}$$

where X is the resistance of the filament to its resistance at 293 K. This expression fits the data by Roeser and Wensel (1941) for the 1500–3600 K range and by Kohl (1962) for the 293–1800 K range; it is valid for temperatures from 400 to 2500 K.

Boltzmann's constant from Johnson's noise. The $<V^2>$ values obtained with both frequency bands are plotted as a function of RT (Fig. 3). The plots are straight lines with slopes $4k_BG_0^2B$. Due to the inherent noise of the amplifier, the lines cross the X-axis at a negative value of RT, nearly 4×10^5 Ω.K. The inherent noise is specified by the so-called **equivalent noise resistance**. This means a resistor generating at room temperature thermal noise equal to the inherent noise of the amplifier. In our case, it is about 1.4 kΩ.

Second, thermal noise of a common resistor (2.4 kΩ) is measured at room and at liquid nitrogen temperatures. The noise and resistance are measured only at the two well-known temperatures. The gain and the frequency band of the

amplifier are the same as when measuring the noise of the incandescent lamps, so the data can be presented together. The results show that employment of an amplifier with relatively high inherent noise causes no trouble when measuring the thermal noise. The experiment requires measurements of many quantities, and the total error includes all the contributions. In the determination of Boltzmann's constant, it is difficult to obtain an error of less than 5%.

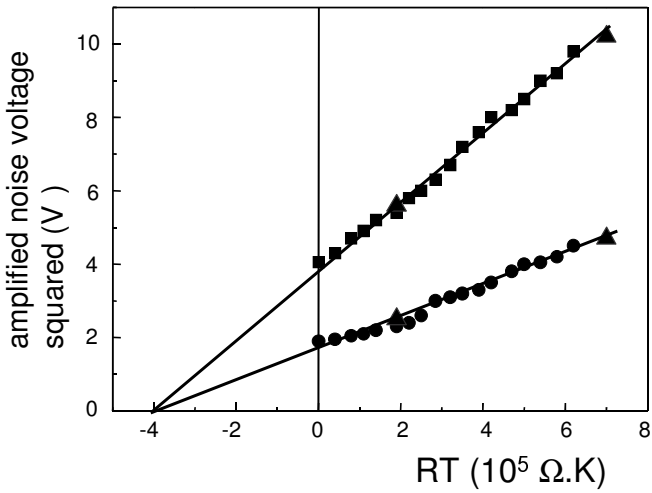

Fig. 3. Thermal noise of incandescent light bulbs: ■ $Q = 2$, ● $Q = 5$; ▲ thermal noise of the 2.4 kΩ resistor, at room and liquid nitrogen temperatures.

Electricity and Magnetism

4. Electricity and Magnetism 201

4.1. Processing of electrical signals

The experiments represent two measurement techniques: (i) the analog-to-digital conversion, and (ii) the noise reduction by the averaging method.

1. Analog-to-digital conversion

Two analog-to-digital conversion (ADC) techniques are demonstrated with a model of a DC voltmeter of 1 V scale and 1 mV resolution. The operations necessary for the conversion are clearly seen, and results obtained coincide with the input voltages to within 1–2% (Kraftmakher 2009d).

Additional equipment: *Voltage sensor*, source of DC voltages up to 1 V.

The **analog-to-digital conversion** is known for more than a half a century. It is quite natural that the first digital meters were pulse counters and frequency meters. This task was the simplest one among others. Special schemes and gas-filled tubes were developed for pulse counting. More advanced technologies are now used for this purpose. **Digital multimeters** (DMMs) are commonly used in student laboratories, and descriptions of the analog-to-digital conversion techniques can be found in many papers and textbooks (Horowitz and Hill 1980, Nicklin and Rafert 1983; Smith 1984, Jones 1986, Millman and Grabel 1987; Donnelly 2004).

Single- and dual-slope integration. Two methods of the analog-to-digital conversion based on voltage-to-time conversion and employing the counting technique can be demonstrated quantitatively. The first method is called the **single-slope integration** (Fig. 1). In this technique, a ramp-up wave generator, such as a current source and a capacitor, is started at point O; at the same time, a counter starts to count pulses from a stable oscillator. When the ramp-up voltage becomes equal to the input voltage V_1 (point A), a comparator stops the counter at time t_1. For a lower input voltage V_2, the counting time is reduced to t_2. The runs are periodically repeated. The number of counts is proportional to the input voltage and the oscillator frequency, and is inversely proportional to the slope of the ramp-up voltage. It is thus easy to arrange necessary scales of the digital voltmeter. The same result is achievable when a gradually increasing step-like voltage is used instead of the ramp up voltage. The steps are equal and sufficiently small, and a counter counts their number necessary to achieve the input voltage.

A significant disadvantage of the single-slope integration technique is its sensitivity to AC components accompanying the DC voltage to be measured. These components are produced by stray electric and magnetic fields; the power line frequency, 50/60 Hz, and its harmonics dominate. The AC components reduce the accuracy of determining the instant, at which the ramp-up voltage

matches the input voltage. The AC components can be suppressed by averaging the input voltage over a long time, but this slows down the speed of operation. The averaging process becomes very effective when it lasts exactly an integer number of periods of the AC component to be eliminated: the average of the AC component becomes zero, regardless of its initial phase. This advantage is realized in the second method considered here, the **dual-slope integration**.

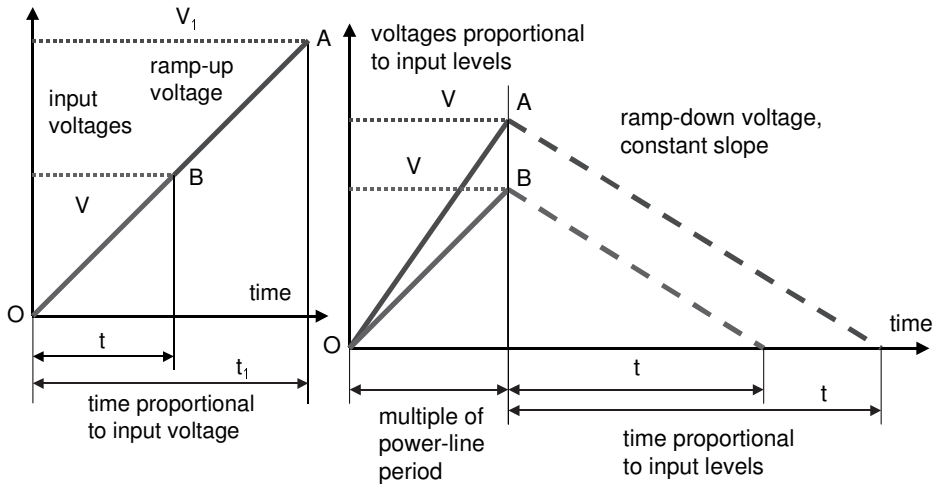

Fig. 1. Diagram of the single- and dual-slope integration techniques.

In the dual-slope integration technique, a current, whose magnitude is proportional to the voltage to be measured, charges a capacitor during a time interval that is a multiple of the power line period. The capacitor is charged to a voltage V_1 (point A) proportional to the input voltage. Due to the proper charging time, the contributions of the power line frequency and its harmonics are eliminated. Then a constant current generated by the meter discharges the capacitor, and the time interval t_1 required for this operation is measured. A smaller input voltage results in a smaller maximum voltage across the capacitor (point B), and thus of the discharge time. The discharge time is strictly proportional to the input voltage. This elegant method is used in many DMMs, including inexpensive battery-operated meters. Since the influence of AC components of the power line frequency and of its harmonics is effectively suppressed, a DMM may have a microvolt resolution. Usually, dual-slope integrators are designed to reject power line interference of two frequencies, 50 and 60 Hz. A charging time of 0.1 s corresponds to 5 periods of the 50 Hz component and 6 periods of the 60 Hz component. The demonstrations described below represent models of a digital DC voltmeter of 1 V scale and 1 mV resolution.

For the first demonstration, the *Voltage sensor* measures a DC input voltage, and the *Graph* tool displays it versus time. The *Positive ramp up wave* voltage of 0.01 Hz frequency and an amplitude of 1 V from the *Signal generator*

is superposed on the same graph. The *Signal generator* operates in the *Auto* mode: it starts to produce the output voltage immediately after a run is started. The run is automatically stopped when this voltage becomes equal to the input voltage. The *Calculate* tool continuously calculates a function *Y* equal to the difference between the *Positive ramp up wave* voltage and the input voltage. The run stops when *Y* crosses zero (*Y rises above* 0). Now it remains to determine the measurement time, which is proportional to the input voltage. Instead of the time, the number of measurements during the run is counted, that is, the time of the run times the *Sample rate*. The *Calculate* tool counts the number of measurements (*Statistical*/*Count*). With this approach, there is no need for an external oscillator, and it is easy to arrange the necessary scale.

In many DMMs, the measurement time does not exceed 0.1 s. However, the time of the demonstration is set to be up to 100 s (full scale). The purpose of this choice is dual: first, it reduces the role of all transients and thus improves the accuracy; second, it is easy to examine the process of the analog-to-digital conversion. In our case, the *Sample rate* is 10 Hz, so that the full-scale count is 1000. One digit thus corresponds to 1 mV. The *Digits* tool displays the counts, along with the input voltages (Fig. 2).

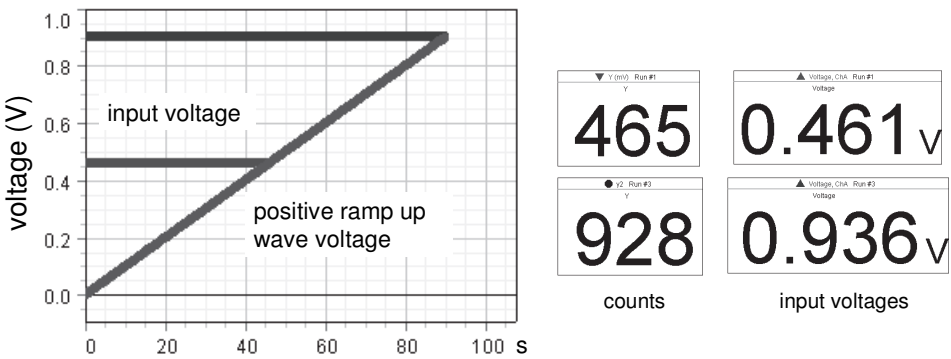

Fig. 2. Single-slope integration: counts and input voltages.

The second experiment demonstrating the dual-slope integration method is not so straightforward as the first one. The *Signal generator* operates in the *Auto* mode. It provides an output *Positive square wave* voltage of 0.01 Hz frequency and 1 V amplitude. The *Calculate* tool multiplies this voltage by the input voltage and thus builds a function, which equals the input voltage during the first 50 s of the period and zero during the next 50 s. Simultaneously, the *Calculate* tool (*Special*/*Integral*) integrates this function. With this procedure, the integral linearly increases during the first 50 s and then remains constant. For a 1 V input voltage, the integral equals 50. The full scale of our model is 1000 mV, so the integral is multiplied by 20. The first 50 s interval represents the integration time that is a multiple of the period of the AC component to be suppressed. Along with the above calculations, the *Calculate* tool calculates a function *F*, which

equals 2000 minus the count number. The latter is the *Sample rate* (20 Hz) times the measurement time (up to 100 s). With the *Automatic stop* tool, the run lasts until this function minus the above integral *falls below* 0. When the run is stopped, the function *F* displayed by the *Digits* tool becomes equal to the input voltage expressed in millivolts (Fig. 3).

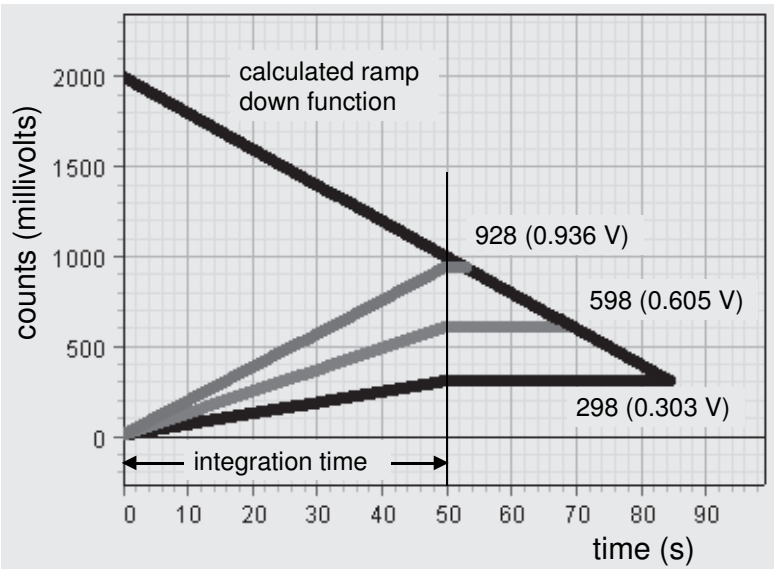

Fig. 3. Dual-slope integration: counts and input voltages.

The operation of our model thus somewhat differs from that of a real DMM, but in essence it is the same: the final count is proportional to the "discharging" time, that is, to the input voltage. The results obtained coincide, within 1–2%, with the input voltages independently measured by *DataStudio*. It is helpful to list the commands used in this experiment:

• *Voltage Ch A* (input voltage) and *Output voltage* (output voltage of the *Signal generator*) are measured and used in the calculations;

• $M = A*B$ (A = *Voltage Ch A*, B = *Output voltage*), necessary for the calculations;

• $I = 20*\text{integral}(M)$, integral of the input voltage normalized for establishing the necessary full scale (1000 mV);

• $N = \text{count}(A)$, the number of measurements during a run;

• $F = 2000 - N$, ramp down function continuously calculated by the *Calculate* tool during a run;

• $S = F - I$, function controlling *Automatic stop* of a run.

An additional experiment confirms the high immunity of the dual-slope integration to AC voltages of a period equal to the time of integration. The AC voltage is taken from a PASCO *Digital function generator-amplifier* (PI-9587C) and added to the DC voltage to be measured. In the example presented (Fig. 4), the input voltage (in volts) equals $0.69+1.39 \sin(2\pi t/50)$, so the amplitude of the AC voltage is twice the DC voltage. The dual-slope integration is performed for different initial phases of the AC voltage, that is, the phase angles at the instant when the measurements are started. Here, the initial phases are nearly 0, 90, 180, and 270°. Despite the four paths to the final point are very different, the results are very close to a mean value, 693 mV. If the integration time differs from the period of the AC voltage, the results strongly depend on the initial phase of the voltage. The integration lasting 25 s may give results ranged from –0.1 to 0.77 V.

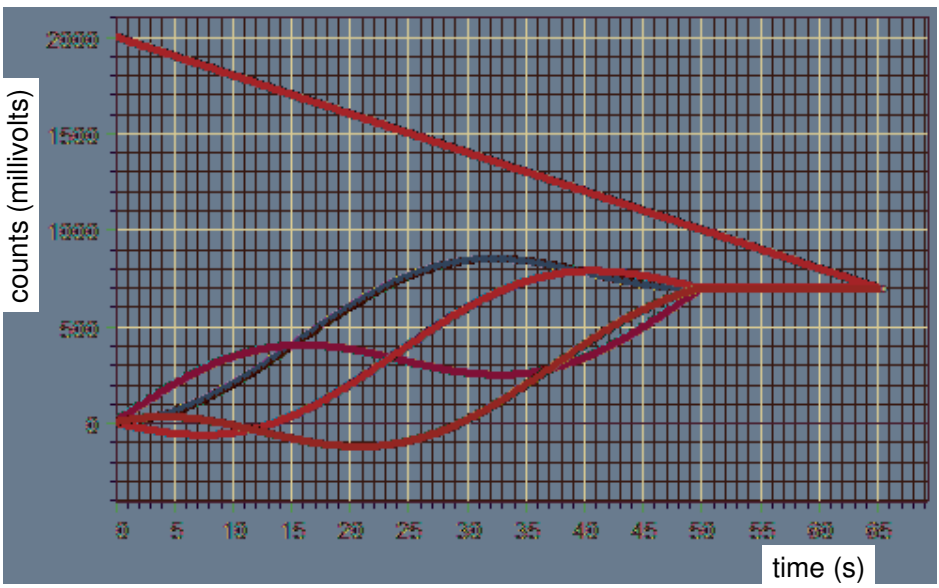

Fig. 4. Measurement of DC voltage accompanied by AC voltage of a period equal to the integration period. The result of integration is independent of the initial phase of the AC voltage.

All the supplementary operations performed here by the *DataStudio* (measurement of the input voltage, generation of various voltages, summation, multiplication, integration, comparing two voltages by a comparator, automatic stop) could be done without using digital techniques. The only digital technique crucial for the analog-to-digital conversion demonstrated here is the counting.

2. Noise reduction by averaging technique

The noise reduction is achieved by signal averaging (Kraftmakher 2006e).

Additional equipment: *Voltage sensor*, light-emitting diode, light dependent resistor, oscilloscope, resistors.

Three main techniques exist for noise reduction. Two of them are based on exactly knowing the period of a signal expected. This is possible when the signal is a response to periodic changes of some external parameters set by the experimenter. For instance, the sample may be subjected to periodic changes of temperature, irradiation, magnetic or electric field, and so on. Therefore, the response of the sample is of exactly the same periodicity as the external influence. A source of this periodic influence provides a reference signal to distinguish the expected signal from noise or signals of other frequencies. The noise-reduction techniques are the following.

● **Averaging technique** permits recovering periodic signals of any waveform (Janssen *et al* 1988; Razak 2009; Hassan and Anwar 2010). The signal is presented as a periodic function of time or of an external parameter. The period of the signal is subdivided to a certain number of equal intervals (channels). During many periods, the instantaneous signal values inside all channels are accumulated separately. The signal does not change during the measurements, so that the accumulation means a summation of definite values of the signal. This sum is thus proportional to the number of the periods. At the same time, the noise or signals of other periods make irregular contributions. The accumulation of noise follows the law of summation of random values: the sum is proportional to the square root of the number of the summations. This means that the signal-to-noise ratio increases proportionally to the square root of the number of periods involved in the accumulation. This simple rule shows the noise reduction achievable with this technique.

● **Lock-in detection** is very suitable for measuring sine wave signals in the presence of noise or signals of other frequencies (Meade 1983). Typical applications of this technique are modulation methods involving relatively small sinusoidal changes of external parameters, such as temperature or magnetic field. For small changes, the response is linear, and the signal to be measured is sinusoidal. Its frequency strictly equals the frequency of the modulation, and the source of the modulation provides the reference. It is very important that the phase shift between the signal to be measured and the reference, under steady experimental conditions, remains constant. At the same time, there is no fixed phase shift between the reference and signals of other frequencies or noise. This makes it possible to determine periodic signals even buried in noise (see Experiment 4.12).

• **Correlation analysis** is based on calculating the auto- and cross-correlation functions. By measuring the autocorrelation function, a periodic component of the signal can be revealed. Its period equals the period of the auto-correlation function. While two signals of the same frequency are correlated, random signals are uncorrelated with a periodic signal (see Experiment 4.13).

When the signal is presented in digital form, the averaging technique becomes extremely simple. However, special software is needed to perform the necessary operations. The way to prepare such software is obvious, and this is a task for students familiar with programming. The measurement data form a set of instantaneous values of x_i (time or an external parameter) and of y_i (the signal plus noise). When the data are obtained as a function of time, the software puts all the x_i values in one period of the signal. The period is divided into a definite number of equal subdivisions (channels) set by the experimenter. Then average values of all x_i belonging to each channel are stored as X_k values. The corresponding y_i values are also averaged and stored as Y_k values. Then software plots a graph of Y_k versus X_k.

In our experiment, the *Square wave* voltage from the *Signal generator* (200 Hz) operating in the *Auto* regime is applied to a light-emitting diode (LED) (Fig. 5). A 50 Ω resistor limits the current through the LED. The rectangular light pulses irradiate a CdS light dependent resistor (LDR) connected in series with a DC source and a 1 kΩ load resistor. The voltage across the load is observed with an oscilloscope serving also as an amplifier; then the *Voltage sensor* measures the amplified voltage.

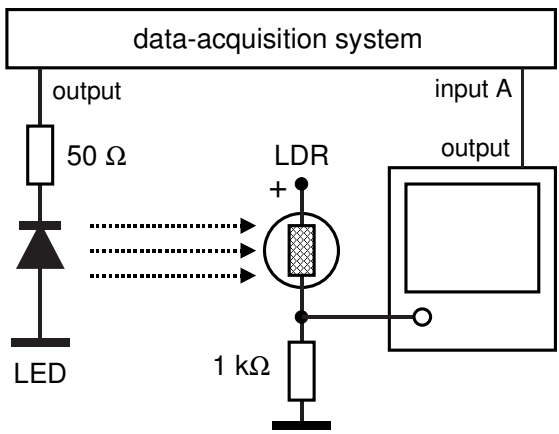

Fig. 5. Schematic of setup for demonstrating the averaging technique.

It is easy to change the signal and thus the signal-to-noise ratio by changing the DC voltage applied to the LDR or the *Square wave* voltage applied to the LED. To maintain good resolution, the number of the channels should be sufficiently large, but this requirement contradicts the necessity to have many data points inside each channel for the averaging. A compromise should be found between the two requirements.

In the example presented, the time of the measurements is 1 s, and the *Sample rate* is 10 kHz. It is impossible to see the shape of the signal from the data accumulated, but the averaging technique solves the problem. The averaging was performed with 50 and 25 subdivisions of the signal period. Therefore, 200 or 400 data points were averaged in each channel, so that the expected improvement of the signal-to-noise ratio is 14 or 20, respectively. The results clearly show the power of the averaging technique (Fig. 6).

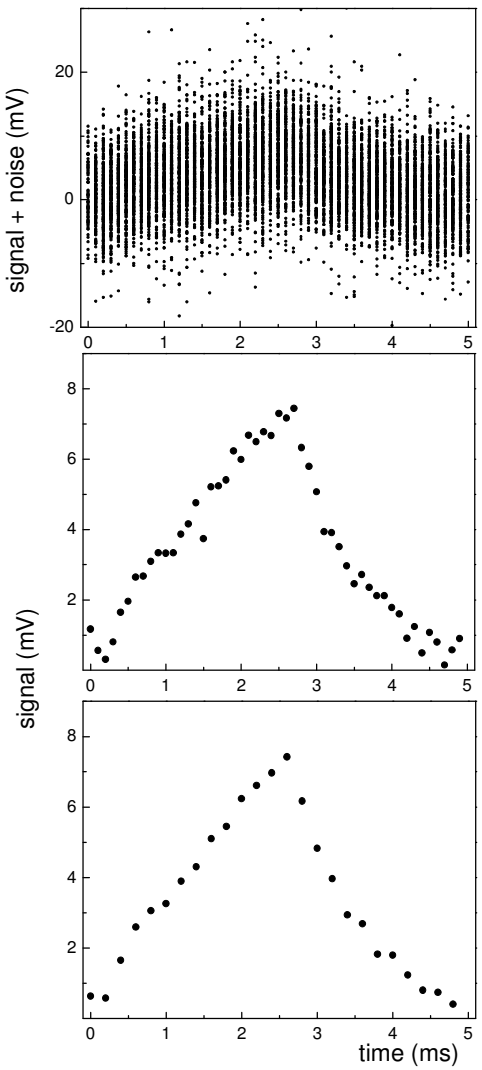

Fig. 6. Data accumulated during 200 periods (10000 experimental points) and signal recovered with 50 and 25 subdivisions of the period.

4.2. Spectra of electrical signals

Spectra of various waveforms and AM and FM signals are demonstrated with the *FFT* option of the data-acquisition system or a DSO.

1. Fourier's great theorem

More than two centuries ago, Jean Baptiste Joseph Fourier (1768–1830) discovered that any function of period T can be represented as a sum of sine waveforms of frequencies equal to an integer times the fundamental frequency $\omega = 2\pi/T$ (Fourier's series):

$$F(t) = \tfrac{1}{2}a_0 + \Sigma(a_k \cos k\omega t + b_k \sin k\omega t), \qquad \text{or} \tag{1}$$

$$F(t) = \tfrac{1}{2}a_0 + \Sigma A_k \cos(k\omega t + \varphi_k), \tag{2}$$

where k are integers, and A_k, a_0, a_k and φ_k depend on the periodic function $F(t)$:

$$a_k = (2/T)\int_{-T/2}^{T/2} F(t)\cos k\omega t\, dt, \qquad b_k = (2/T)\int_{-T/2}^{T/2} F(t)\sin k\omega t\, dt, \tag{3}$$

$$A_k = (a_k^2 + b_k^2)^{1/2}, \qquad \varphi_k = \tan^{-1} b_k/a_k. \tag{4}$$

The term $\frac{1}{2}a_0$ is a mean value of the periodic function. The terms $A_k \cos(k\omega t + \varphi_k)$ are called **harmonics**. The determination of the harmonics of a periodic function is called **Fourier analysis**. To synthesize the function from the set of harmonics, one has to know all the A_k and φ_k. In many cases, however, it is enough to know the frequency band necessary for transferring the signal without significant distortions, so the values of φ_k become not so important. For instance, the human ear is insensitive to the phases of harmonics of sound waves. The set of the harmonics constitutes the **spectrum** of a periodic signal. Spectra of standard waveforms are given in handbooks.

For a square waveform, the amplitudes of odd harmonics are inversely proportional to their numbers, while amplitudes of even harmonics are zero:

$$F(t) = \Sigma(4A/\pi k)\sin k\omega t, \tag{5}$$

where A is the amplitude of $F(t)$, and $k = 1, 3, 5$, and so on. All the initial phases φ_k are equal and can be taken zero, so it is possible to synthesize the square wave function. Due to Fourier's discovery, periodic processes can be presented in the time domain and in the frequency domain; in many cases, the second approach is even preferable. Fourier's theorem is applicable even to non-periodic processes. For those, the period is accepted to be infinity, and the summation is replaced by integration (this is called **Fourier's transform**).

Fourier's analysis constitutes an important part of laboratory courses. Higgins (1976) presented an introduction to this technique. It is very natural to use an LC resonant circuit for separating the harmonics (Lonc 1973; Macomber

1981; Ong and Tang 1985). Matthys and Pedrotti (1982) employed the Fourier transform technique. Pickett *et al* (1984) described the hardware and software for the Fourier transform and its inverse, as well as correlation, convolution, power spectrum, and transfer function. Sandoval and Porta (1985) presented an analysis of the vibration of a string using optical detection. Lambert and O'Driscoll (1985) considered the harmonic analysis and synthesis. Bazin *et al* (1986) demonstrated the properties of Fourier transforms through diffraction phenomena. Kocher (1988) performed the spectrum analysis using a radio receiver. Olejniczak (1989) described the analysis of rectangular pulses with a mechanical resonant system. Whaite and Wolfe (1990) designed an electronic device for demonstrating the Fourier synthesis. Smedley (1998) considered the spectrum analysis for introductory musical acoustics. Bonard (2001) presented spectra of some musical instruments. Now, many computer programs provide options to perform the *Fast Fourier Transform* (*FFT*).

Spectra of some periodic signals calculated by the *FFT* tool are shown here as relative amplitudes of the harmonics versus their frequencies (Fig. 1).

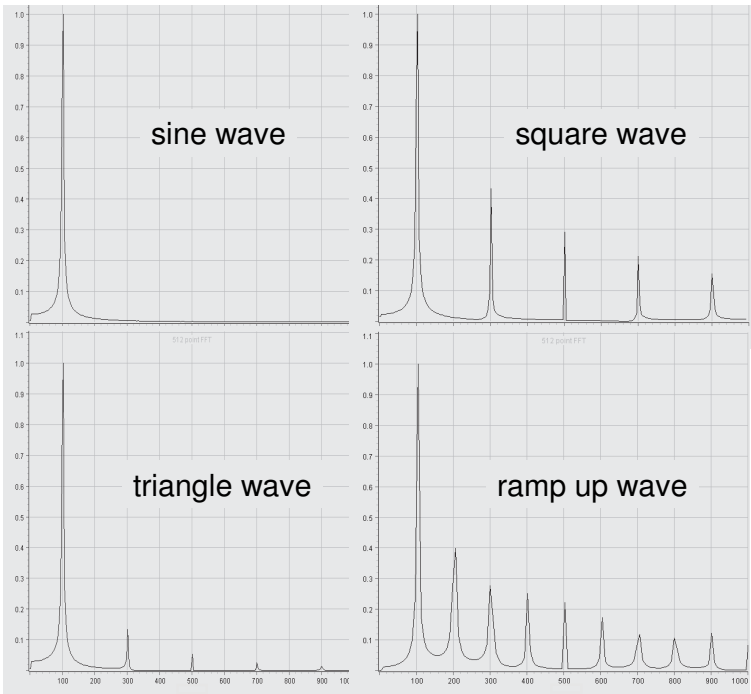

Fig. 1. Spectra of electrical signals from the *Signal generator* displayed by *FFT* tool. The fundamental frequency is 100 Hz, and the spectra are shown for frequencies up to 1000 Hz.

When the quantities a_k and φ_k are known, the original periodic signal can be reconstructed by direct summation of the Fourier series (Fig. 2). A simple

case of such a summation is the rectangular waveform given by Eq. (5). A crucial point here is the same initial phase of all the harmonics. It is easy to show the results of the summation of several harmonics using the *Calculate* tool. The maxima in the reconstructed function somewhat exceed the original waveform. For sufficiently large number of harmonics, this difference does not depend on the number of harmonics involved. This is the so-called **Gibbs phenomenon** (Thompson 1992).

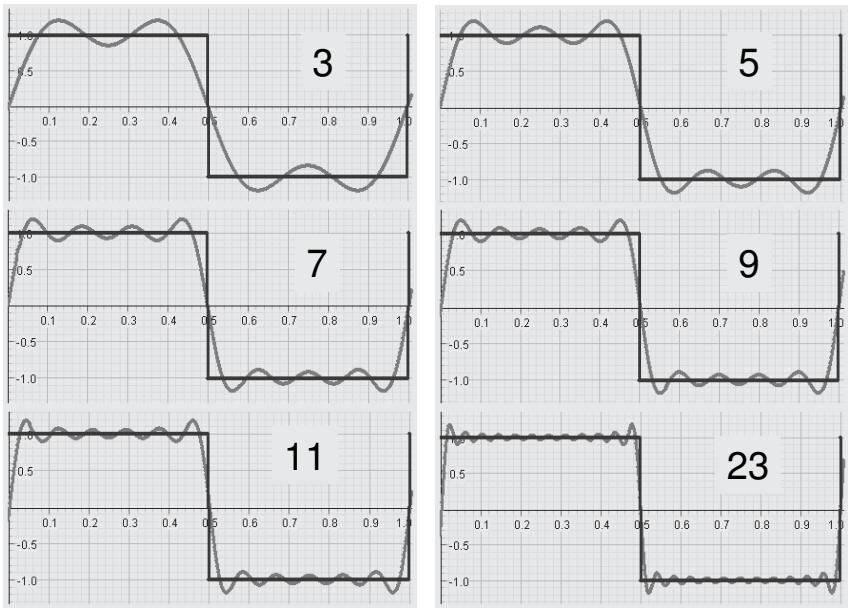

Fig. 2. Rectangular waveform reconstructed by summation of 3 to 23 harmonics. Note the Gibbs phenomenon.

2. Spectra of AM and FM signals

The data-acquisition system displays spectra of AM and FM signals.

Additional equipment: *Voltage sensor***,** function generator with AM and FM option.

With **amplitude modulation** (AM), the amplitude of a high-frequency wave is varied in response to a low-frequency signal (Fig. 3). When a sine wave signal of frequency Ω modulates a sine wave of frequency ω, the resulting oscillation is

$$(1+m\sin\Omega t)\sin\omega t = \sin\omega t+\tfrac{1}{2}m\cos[(\omega-\Omega)t]-\tfrac{1}{2}m\cos[(\omega+\Omega)t], \quad (6)$$

where $m < 1$ is called the modulation index.

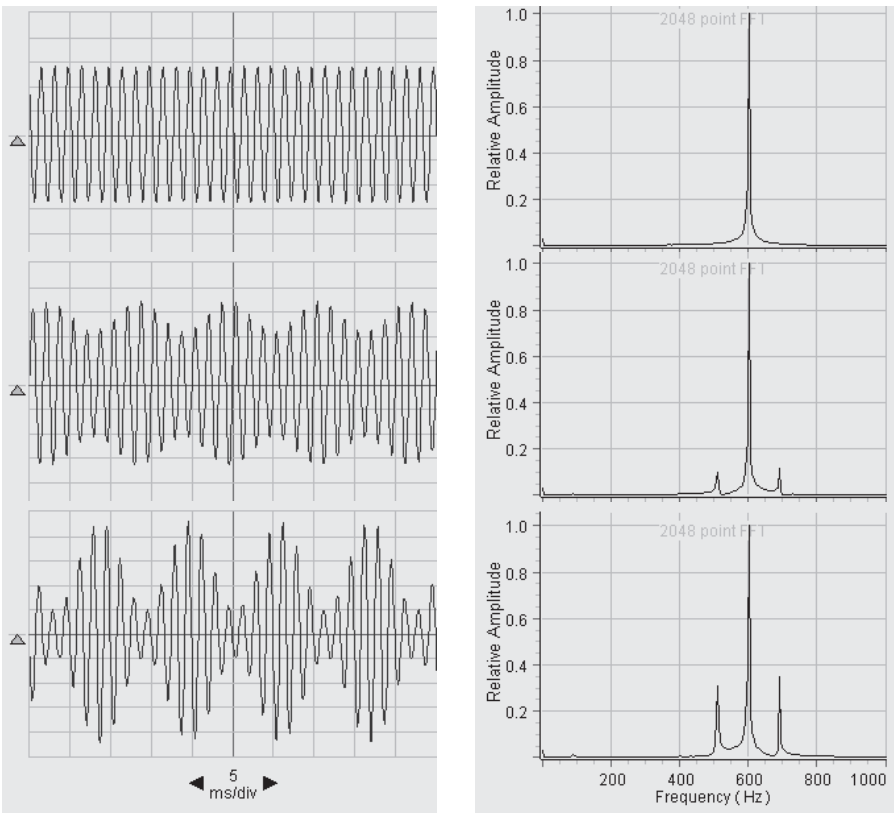

Fig. 3. AM signals modulated with a single sine wave and their spectra. The carrier frequency is 600 Hz, the modulation frequency is 90 Hz.

Equation (6) shows that the amplitude modulation generates new frequencies, called **side frequencies** or **side bands**. AM signals have identical

upper and lower sidebands symmetrically located on each side of the high frequency, often called the carrier. With **frequency modulation** (FM), the frequency of a high-frequency wave is varied in response to a low-frequency signal. To obtain AM and FM signals, a function generator with AM and FM option is needed; the *Signal generator* serves as the source of low-frequency signals. Generally, spectra of FM signals are very complicated, but for slightly modulated signals they are similar to spectra of AM signals (Fig. 4). With frequency modulation, the frequency of the carrier is time dependent. This may cause impression that the spectrum of the signal is continuous. This impression is wrong. Like any periodic waveform, FM signals obey Fourier's theorem.

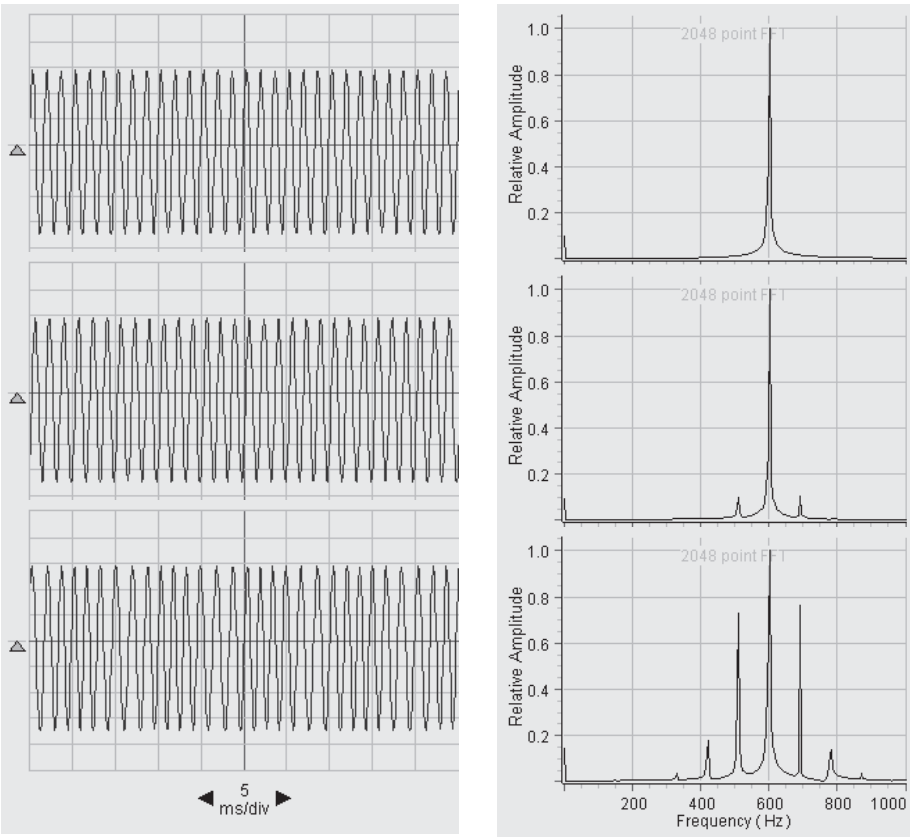

Fig. 4. FM signals modulated with a single sine wave and their spectra. The carrier frequency is 600 Hz, the modulation frequency is 90 Hz.

3. Displaying spectra with DSO

A digital storage oscilloscope providing the *FFT* option displays spectra of electrical signals (Kraftmakher 2012e).

Equipment: DSO, function generator with AM and FM options.

Contemporary DSOs combine features of a data-acquisition system of excellent time resolution and of a usual cathode-ray oscilloscope; nowadays, they are available to undergraduates.

A Tektronix TDS 3012B oscilloscope is set to operate in the single-run mode, with an infinite persistent time of display. All the experiments are performed with no computer involved. While computers are common devices in any teaching laboratory, the software necessary for processing the data may be not readily available. A Hewlett–Packard HP-33120A function generator serves as a source of periodic voltages. However, the experiments are also possible with inexpensive and readily available function generators. The additional components needed for the experiments are commonly available.

Spectra of some standard waveforms. Common function generators provide some standard output voltages including sine-, square- and triangle-wave functions; the duty cycle of the waveforms can be varied. The HP-33120A generator has additional options; in particular, it provides a saw-tooth waveform. In the measurements presented, the period of all the voltages is 1 ms. The voltages and their spectra are seen on the DSO display (Fig. 5).

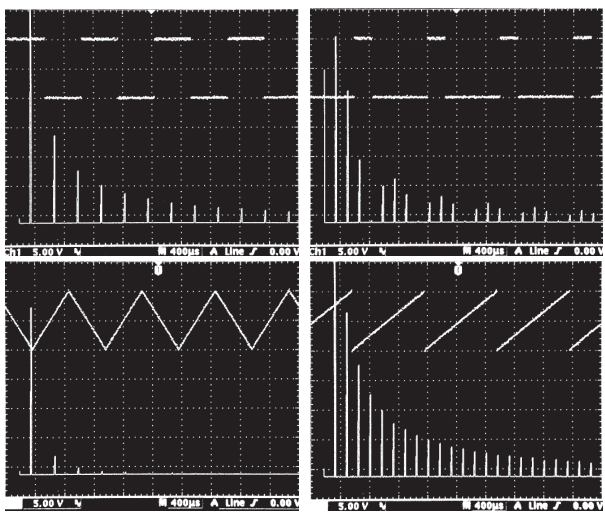

Fig. 5. Some waveforms and their spectra: square, 50% duty cycle; square, 25% duty cycle; triangle; saw-tooth. The time scale is 0.4 ms per division, and the frequency scale for the spectra is 2.5 kHz per division.

For obtaining spectra of good frequency resolution, many periods of the voltage should be involved in the calculations. Therefore, the time scale is 4 ms per division when acquiring the data. Then it is possible to independently change the time scale for the signals and the frequency scale for their spectra. Here, the signals are shown with a time scale of 0.4 ms per division, while the spectra are shown with a frequency scale of 2.5 kHz per division.

For the square waveform, the spectrum confirms the theoretical prediction: only odd harmonics are present, with amplitudes inversely proportional to their numbers. If one changes the duty cycle of the waveform, even harmonics also appear. In the example shown, the duty cycle is reduced to 25%. In this case, the harmonics decay not monotonically, while the harmonics number 4, 8, 12, and so on, disappear. The triangle waveform slightly differs from the sine waveform. For this reason, its first harmonic is much larger than the others. In contrast, the saw-tooth waveform contains many harmonics. All the above features are in full agreement with the theory.

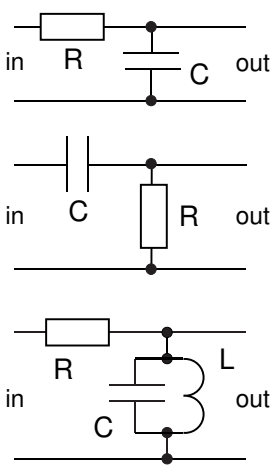

Fig. 6. Frequency-selective circuits: low-pass RC filter, high-pass RC filter, and band-pass filter with LC circuit. $R = 10$ kΩ, $R_1 = 100$ kΩ, $C = 3.8$ nF, and $L = 12$ mH.

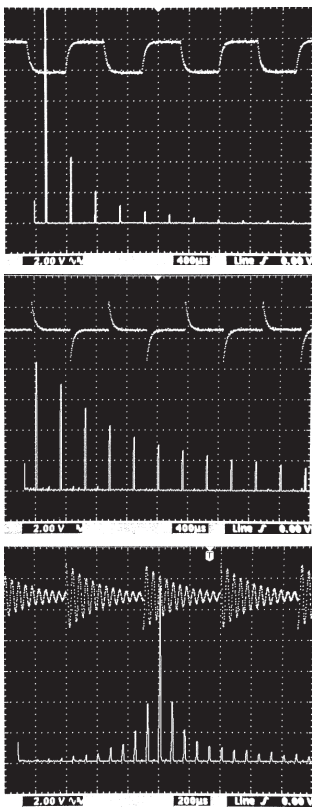

Fig. 7. Output voltages of the circuits shown in Fig. 6, and their spectra. The input voltage is of square waveform, $T = 1$ ms. The frequency scale is 1.25 kHz per division.

Changing spectra by RC and LC circuits. A 1 kHz square waveform voltage from the function generator is applied to inputs of three different circuits: a low-pass RC filter, a high-pass RC filter, and a band-pass filter with a parallel LC circuit (Fig. 6). The band-pass filter contains an 800-turn air-core coil (SF-8611). These frequency-selective circuits change the signals and their spectra. The changes reflect the frequency response of the circuits. The DSO displays the output voltages of the circuits, together with their Fourier spectra (Fig. 7). The low-pass filter suppresses the high-frequency harmonics, while the high-pass filter suppresses the low-frequency ones. With the band-pass filter, the output voltage contains harmonics corresponding to the frequency band of the LC circuit, while other harmonics become much weaker. The frequency-selective circuits change the ratio between the harmonic amplitudes at their inputs and outputs; from these data, the frequency response of the circuits is obtainable.

Spectra of AM and FM signals. The function generator used here provides AM and FM voltages. The 10 kHz carrier is modulated with a 1 kHz sine wave. The spectra of AM signals are shown for various values of the modulation index, up to 100% (Fig. 8). The amplitudes of the sidebands are in agreement with Eq. (6).

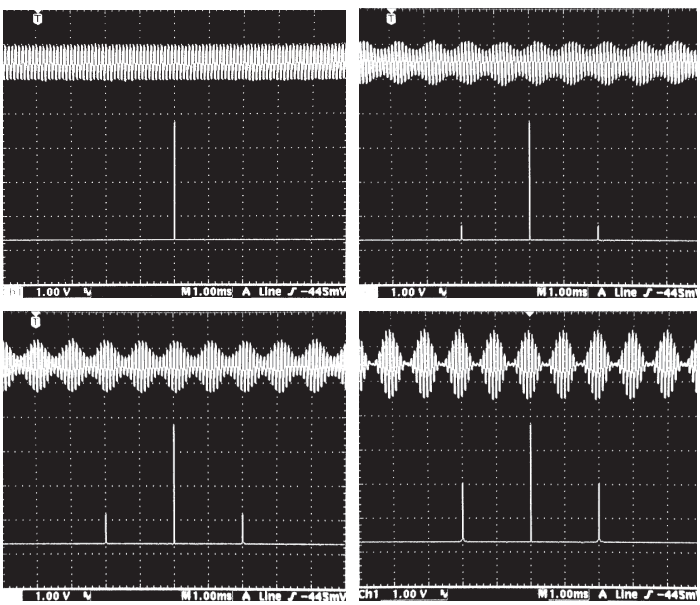

Fig. 8. AM signals and their spectra: the carrier, 10 kHz; 25% modulation; 50% modulation; 100% modulation. The modulation frequency is 1 kHz; the frequency scale is 0.5 kHz per division.

The same pair of frequencies is used for the frequency modulation (FM). The modulation index characterizing the depth of the modulation is the ratio of the maximum frequency deviation in the modulated signal to the modulation

frequency and is not restricted by unity. Examples shown relate to three values of the modulation index (Fig. 9). When increasing the modulation index, the frequency band of the FM signal becomes broader.

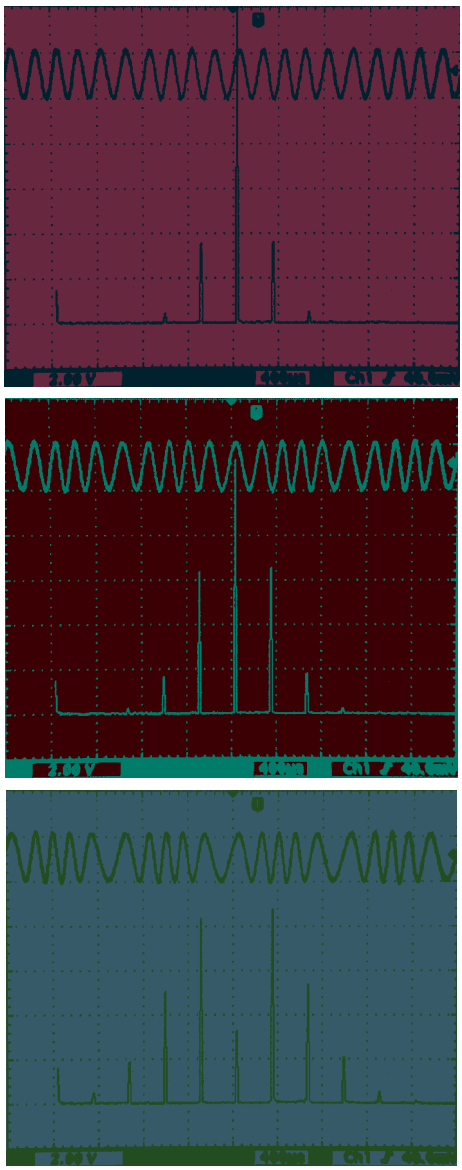

Fig. 9. FM signals and their spectra. The 10 kHz carrier is frequency modulated, the modulation frequency is 1 kHz. The modulation index is set at 0.5, 1, and 2. The frequency scale is 1.25 kHz per division.

4.3. Helmholtz's coils

The magnetic field produced by two coaxial coils is measured.

AIP Emilio Segrè Visual Archives
Hermann von Helmholtz (1821–1894)

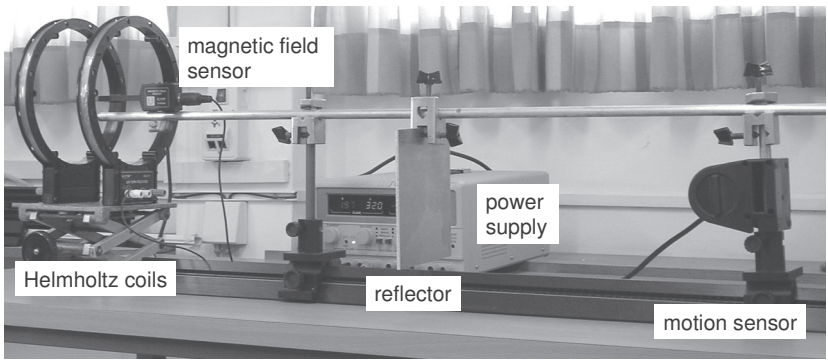

Additional equipment: *Motion sensor*, *Magnetic field sensor*, two coils, DC supply.

Helmholtz's coils are a standard method for producing a uniform magnetic field. For instance, such an arrangement is used in determinations of the *e*/*m* ratio for electrons (see Experiment 9.1). The axial magnetic field generated by a thin coil is

$$B_z(z) = \mu_0 NIa^2/2(a^2 + z^2)^{3/2}, \quad (1)$$

where a is the radius of the coil, z is the distance from its center, N and I are the number of turns and the current in the coil, and μ_0 is the magnetic constant. For two similar coaxial coils positioned with separation equal to the radius (the Helmholtz arrangement), the axial magnetic field at the center of the system is

$$B_z(0) = 8\mu_0 NI/a\sqrt{125}. \quad (2)$$

The Helmholtz coils have been considered by Lucas (1986); Purcell (1989); Murgatroyd (1991); Deacon and Clarke (1993); Calhoun (1996). The Helmholtz arrangement provides a nearly uniform magnetic field in the region between the coils. The field along the axis obeys the approximation

$$B_z(z) = B_z(0)[1 - (144/125)\, z^4/a^4 + \ldots\,], \quad (3)$$

which shows that it is uniform only in a part of the region between the coils. At the coil positions ($z = \pm\frac{1}{2}a$), the field becomes about 7% lower than at the center. The field at the midplane and a distance r from the axis obeys the approximation

$$B_z(r) = B(0)[1 - (54/125)\, r^4/a^4 + \ldots\,], \quad (4)$$

and for $r = \pm\frac{1}{2}a$ the decrease of the field is only 2.7%.

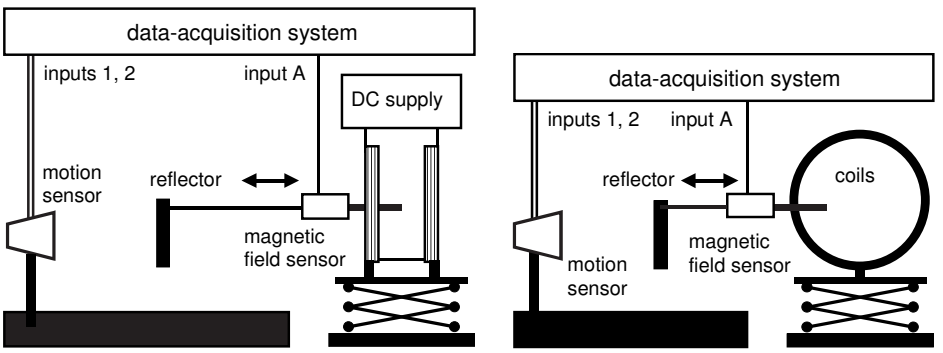

Fig. 1. Schematics of measurements when the probe moves along or perpendicular to the axis of the coils.

When the currents in the two coils are in the opposite direction, the field in the center is zero, and the axial field gradient in the center is nearly constant. This case also has useful applications.

In our setup, a pair of PASCO coils (EM-6711, $N = 200$, $a = 10.5$ cm) is positioned on a laboratory jack, so the magnetic field can be determined along any straight line parallel or perpendicular to the axis of the coils (Fig. 1). The *Motion sensor* measures the horizontal movement of the *Magnetic field sensor* attached to the reflector. The *Magnetic field sensor* includes two selectable Hall's probes measuring either axial or radial magnetic fields. Before the measurements, with no current in the coils, the *Tare* button of the *Magnetic field sensor* zeroes the readout of the sensor. The *Motion sensor* produces 100 ultrasonic pulses per second, and the *Sample rate* is set to be 100 Hz. The results obtained (Figs. 2 and 3) are in agreement with the values given by the above equations.

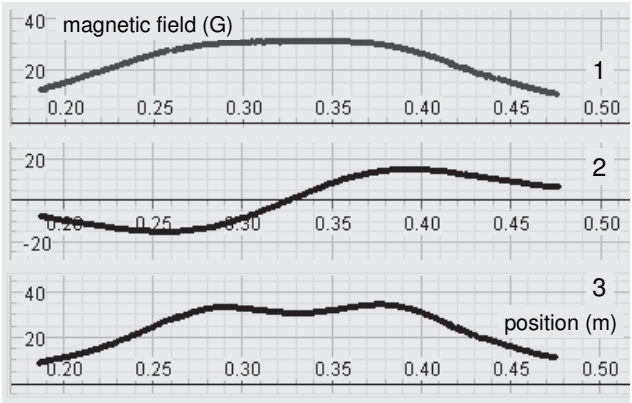

Fig. 2. Axial magnetic field on the axis of the coils when the coils produce fields of (1) the same or (2) opposite directions, and (3) at a distance $\frac{1}{2}a$ from the axis.

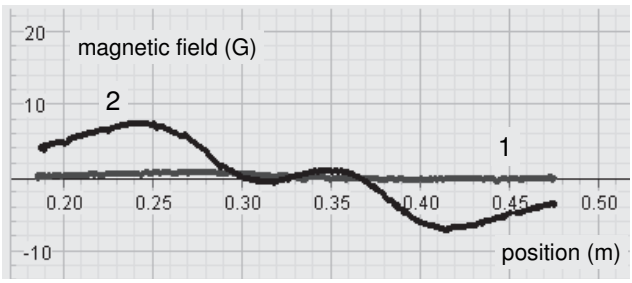

Fig. 3. Transverse magnetic field of the coils (1) on the axis and (2) at a distance $\frac{1}{2}a$ from the axis.

4.4. Ampère's circuital law

A coil with an O-shaped magnetic core serves as a sensor. The demonstration follows that described by Heller (1992).

AIP Emilio Segrè Visual Archives,
Brittle Books Collection
André Marie Ampère (1775–1836)

Additional equipment: *Voltage sensor*, Rogowski's belt, O-shaped magnetic core, coil.

Ampère's circuital law is

$$\oint \boldsymbol{B}\mathrm{d}\boldsymbol{l} = \mu_0 I, \tag{1}$$

where μ_0 is the **magnetic constant**, and I is the net current encircled by a closed loop. The circle on the integral sign means that the scalar product $\boldsymbol{B}\mathrm{d}\boldsymbol{l}$ is to be integrated around the loop. This law makes it possible to find the magnetic field when symmetry allows for solving the integral. For instance, the field at a distance r from a long straight current-carrying wire equals

$$B = \mu_0 I/2\pi r. \tag{2}$$

Rogowski's belt (or Rogowski's coil) is a device based on Ampère's law and serving for contactless measurements of AC currents. It represents a toroidal coil placed around a current-carrying conductor. The AC magnetic field produced by the conductor induces a voltage in the coil. This voltage is proportional to the rate of change of the current. After integration of the voltage from the coil, one obtains a voltage proportional to the current, regardless of the waveform and frequency of the current. Rogowski's coils are wound around either a rigid toroidal core or a flexible belt-like form. For accurate measurements, it is essential that the winding is very uniform. In this case, the output voltage does

not depend on the path the coil takes around the current or on the position of the conductor within the coil. A flexible Rogowski's belt has the following advantages: (i) the good linearity and absence of saturation; (ii) the belt does not load the circuit carrying the current to be measured; and (iii) the belt may be calibrated at any convenient current level, and the calibration will be accurate for all currents.

Demonstrations of the Ampère law have been reported by Klein (1975, 1993); Leclerc (1988); Priest (1990); Heller (1992). Carver and Rajhel (1974) have shown the effect of the displacement current.

Our demonstration follows that described by Heller (1992). A Rogowski belt encircles conductor carrying an AC current. The integrating RC circuit strongly reduces the output voltage of the coil. However, there is no need for the integration. The aim of the demonstration is to show that the output voltage of the Rogowski belt does not depend on the position of the conductor inside it. The belt senses only the net electric current encircled by it. The voltage induced in the belt is seen on the screen of an oscilloscope, and it is easy to demonstrate that the induced voltage does not depend on the position of the conductor inside the belt (Fig. 1).

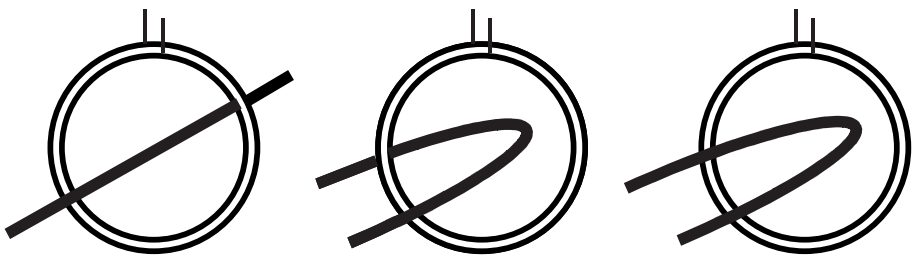

Fig. 1. Demonstration of Ampère's circuital law with Rogowski's belt.

Clamp-on ammeter. For a laboratory experiment (Fig. 2), we use a 3200-turn coil (SE-8613) with an O-shaped magnetic core (SE-8614). The students determine the voltage induced in the coil versus the frequency of the current flowing through the conductor. The *Power amplifier II* serves as the source of this current. The conductor is connected to the amplifier through a 10 Ω resistor. The *Voltage sensor* measures the induced voltage, and the *Fit/Sine fit* option is used to determine it. For constant amplitude of the current, the induced voltage is proportional to the frequency (Fig. 3). The second part of the experiment is a calibration of the device. Generally, the induced voltage is a nonlinear function of the current due to the nonlinear magnetic properties of the core.

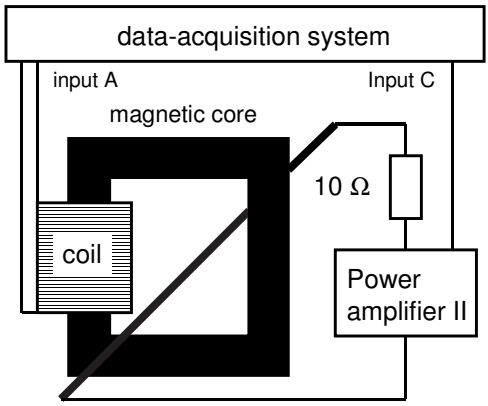

Fig. 2. Schematic of the setup.

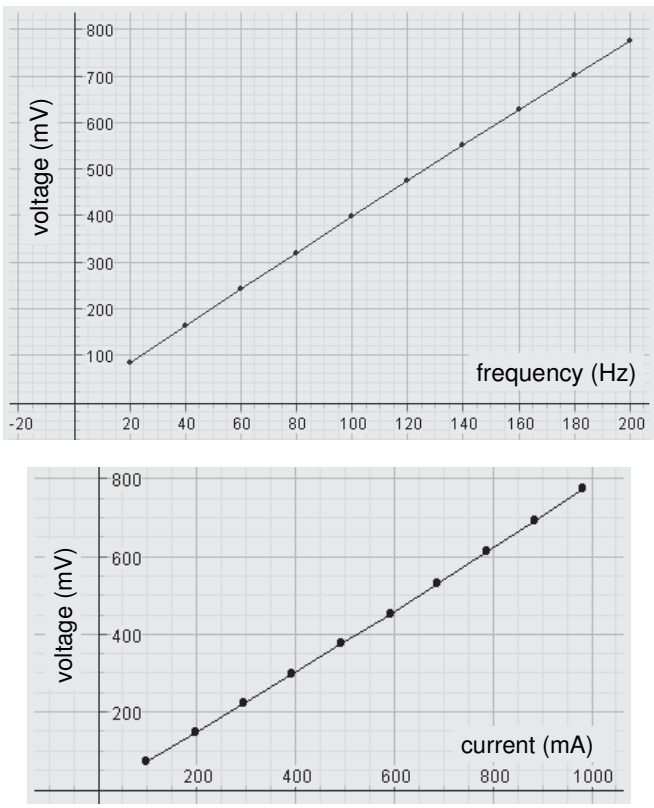

Fig. 3. Induced voltage versus frequency (for constant current amplitude), and versus current amplitude (for constant frequency).

4.5. Magnetic dipole

The experiments show the magnetic field of a magnetic dipole and the interaction between two dipoles.

1. Magnetic field of a dipole

For sufficiently large distances, the measurements confirm the $1/R^3$ law and the angular dependence of the magnetic field (Kraftmakher 2007b).

Additional equipment: *Rotary motion sensor, Magnetic field sensor*, permanent magnet, optics bench.

The magnetic field of a **magnetic dipole** is considered in many papers and textbooks (Cheng 1992, Chabay and Sherwood 1995, Griffiths 1999). Mc Tavish (2000) calculated the field pattern created by a magnetic dipole. At a distance R much larger than the size of the dipole (the so-called dipole approximation), the magnetic field equals

$$\boldsymbol{B} = (\boldsymbol{a}_r 2\cos\theta + \boldsymbol{a}_\theta \sin\theta)\mu_0 m/4\pi R^3, \quad (1)$$

where μ_0 is the **magnetic constant**, m is the **magnetic moment** of the dipole, θ is the angle between the dipole axis and the direction to the point where the field is measured, and $\boldsymbol{a}_r$ and $\boldsymbol{a}_\theta$ are the radial and tangential unit coordinate vectors.

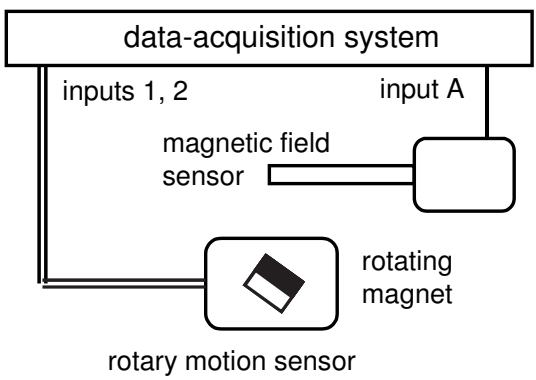

Fig. 1. Setup for measuring magnetic field of permanent magnet.

A strong NdFeB permanent magnet (12×12×12 mm^3 in size) is used. Due to the small dimensions, the dipole approximation becomes valid at relatively short distances. The magnet is attached to the shaft of the *Rotary motion sensor* placed on an optics bench (Fig. 1). The *Magnetic field sensor* measures the field. The radial and tangential components of the field are measured in turn. To exclude possible errors caused by other magnetic fields and by the drift of the

sensor, the data are recorded during one full rotation of the magnet. The magnetic field B is taken as a half of the difference between the maximum and minimum values recorded. When presenting the data as log$B$ versus log$R$, the slope of the graph is close to the theoretical value $n = -3$ (Figs. 2 and 3).

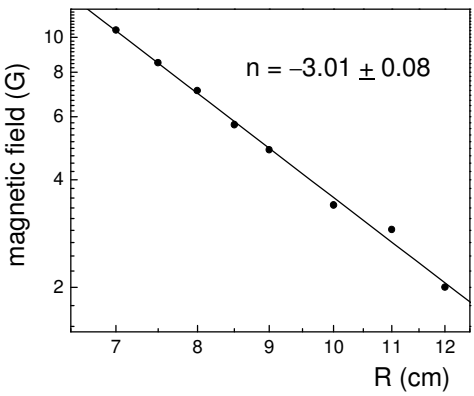

Fig. 2. Log-log plot of the axial magnetic field versus R.

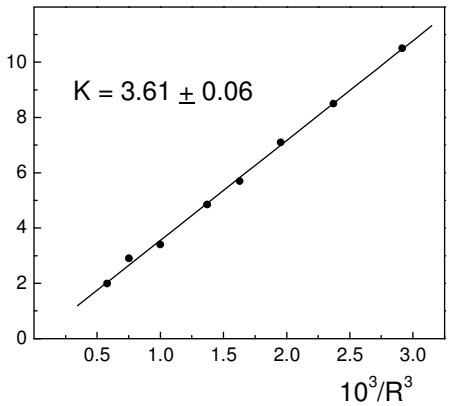

Fig. 3. Axial magnetic field versus $1/R^3$.

The data are in good agreement with Eq. (1): the radial field is twice the tangential field (Fig. 4), and both fields are inversely proportional to R^3. The slope of the graph of B versus $1/R^3$ should equal $K = \mu_0 m/2\pi$. From the slope obtained, the dipole moment of our magnet is 1.80 A.m^2. For a uniformly magnetized magnet, the residual induction B is related to the dipole moment and the volume V of the magnet: $B = \mu_0 m/V$. In our case, $B = 1.3$ T.

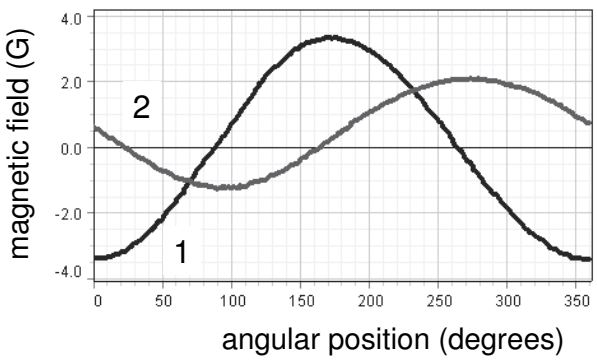

Fig. 4. Angular dependence of (1) axial and (2) tangential components of the magnetic field; $R = 10$ cm.

2. Dipole–dipole interaction

The experiments show the dipole–dipole interaction and its angular dependence for sufficiently large distances (Kraftmakher 2007b).

Additional equipment: *Rotary motion sensor, Force sensor*, two permanent magnets.

The **dipole–dipole interaction** is considered by Dasgupta (1984); Cheng (1992), Chabay and Sherwood (1995), Griffiths (1999); Labinac *et al* (2006); Corbò and Testa (2009); Derby and Olbert (2010); Bonnano *et al* (2011). For a distance R much larger than the size of the dipoles (dipole–dipole approximation), the force between two dipoles having the same magnetic moment m and their axes aligned equals

$$\boldsymbol{F} = \pm \boldsymbol{a}_r 3\mu_0 m^2/2\pi R^4, \tag{2}$$

where μ_0 is the magnetic constant, and $\boldsymbol{a}_r$ is the unit radial coordinate vector.

The interaction force is thus inversely proportional to R^4. On the other hand, when the distance between the poles of two interacting bar magnets is much smaller than their length, the influence of the far poles may be neglected. In this case, the force is inversely proportional to the distance squared.

Lufburrow (1963) measured the interaction between poles of two bar magnets with a balance. Romer (1973) presented a modified version of this apparatus. Defrancesco and Zanetti (1983) determined the magnetic repulsion between two magnets. Levin (1984) measured the magnetic moment of a compass needle. For this purpose, one has to determine the period of free oscillations of the needle in a known magnetic field and its moment of inertia. Shelton and Kettner (1988) measured the interaction force and potential energy for a pair of magnetic pucks. Bisquert *et al* (1990) analyzed small oscillations of a bar magnet along the axis of a circular current-carrying coil. The period of the oscillations depends on the dipole moment of the magnet. Lukefahr (1992) studied the dipole–dipole interaction with an air track. Castañer *et al* (2006) reported on measurements of the magnetic dipole interaction using spring dynamometers. With this very simple technique and a magnetic field meter, the authors measured the magnetic field of the magnet at various distances, the attractive and repulsive forces between two similar magnets, and the torque acting on the magnet in a homogeneous magnetic field. From the data, the magnetic moment and the residual induction of the magnets were evaluated.

Two similar ceramic permanent magnets (12×12×12 mm^3 in size) are used in measurements of the interaction force between them. One of the magnets is fixed to the *Force sensor*, and the second is attached to the shaft of the *Rotary motion sensor* and positioned at a distance R just below the fixed magnet (Fig. 5). The *Force sensor* measures the vertical component of the force acting on the first magnet. This means that the data obtained relate to the axial component of the interaction force. To exclude possible errors caused by other

magnetic fields and by the drift of the sensor, the data are recorded during one full rotation of the lower magnet. The interaction force F is taken as a mean value of the attractive and repulsive forces.

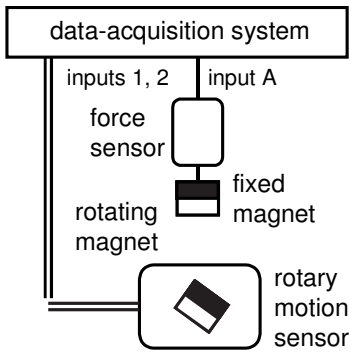

Fig. 5. Setup for measuring the interaction between two magnets.

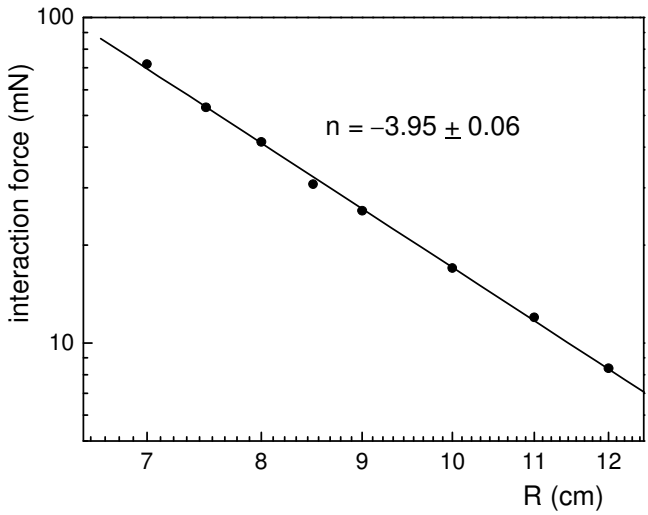

Fig. 6. Log-log plot of interaction force versus R.

When presenting the data as log$F$ versus log$R$, the slope of the graph is close to the theoretical value $n = -4$ (Figs. 6 and 7). According to Eq. (1), the slope of the graph of F versus $1/R^4$ should equal $K = 3\mu_0 m^2/2\pi$. From the slope obtained, the dipole moment of each magnet equals 1.69 A m^2. With this value of the dipole moment, B = 1.2 T. Data obtained during rotation of the second magnet can be presented in polar coordinates. For this purpose, it is necessary to exclude an offset of the data and replace the force by its absolute value. It is easy to measure the interaction for other arrangements of the magnets.

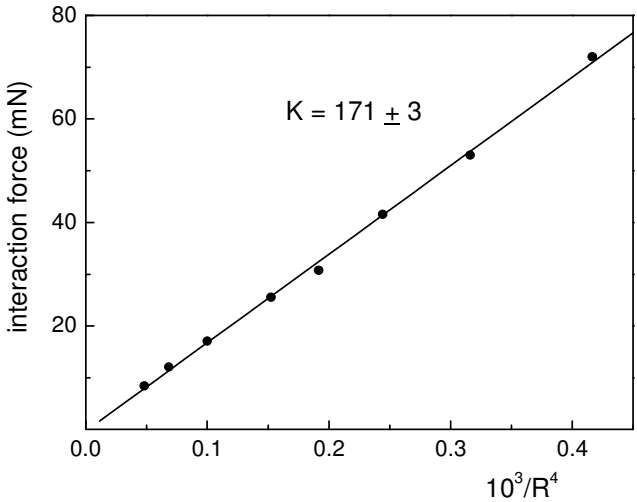

Fig. 7. Interaction force versus $1/R^4$.

The dipole–dipole interaction rapidly decreases with increasing the distance between the dipoles. However, measurements of this interaction become a routine task with a data-acquisition system and sensors now available. The magnetic fields and interaction forces, including their angular dependences, can be measured in a short time.

4.6. Faraday's law of induction II

The magnetic constant is determined by measuring the EMF induced in a coil according to Faraday's law of electromagnetic induction. The experiment is similar to that described by Jones (1987).

Additional equipment: *Voltage sensor*, solenoid, probe coils, resistor.

AIP Emilio Segrè Visual Archives
Michael Faraday (1791–1867)

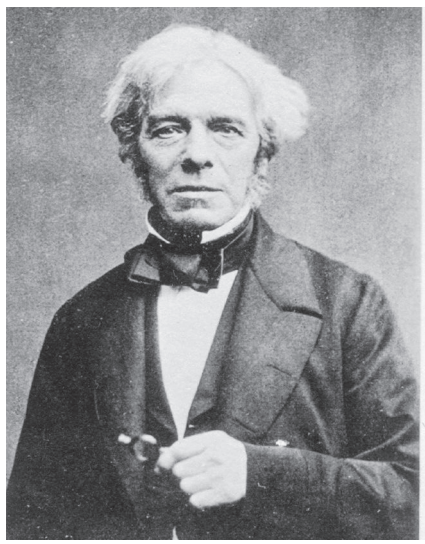

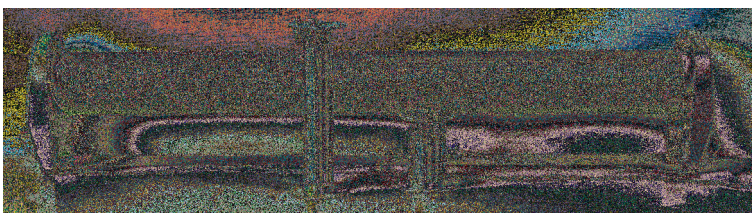

PHYWE coils used in the experiment.

Faraday's great discovery. Michael Faraday discovered the magnetic induction in 1831. Searches for relations between magnetic and electrical phenomena started in 1820 after Oersted observed the influence of electric current in a wire on a magnetic needle. Many researchers unsuccessfully tried to find an inverse effect, generation of an electric current by a magnetic field. However, the magnetic field itself does not generate an electric current. The current (more generally, the electric field) appears only when the magnetic flux is time dependent. It is worth remembering that almost 100% of the electric energy consumed over the world is obtained through the electromagnetic induction.

In the electricity and magnetism course, Faraday's law is one of the central topics and is widely presented in student laboratories. Nicklin (1986) described experiments with a bar magnet dropped through a coil. Measurements of the voltage generated in the coil give quantitative tests of the law of electromagnetic induction. To confirm Faraday's law, Eagleton (1987) used a homopolar generator. Jones (1987) described a simple apparatus consisting of a large coil producing an AC magnetic field and a small probe coil. Saslow (1987) considered theoretical problems related to Faraday's law. Manzanares *et al* (1994) measured the EMF induced by a bar magnet as it moves at constant velocity along the axis of a circular coil. Carpena (1997) and Kingman *et al* (2002) measured the velocity of a magnet flying through a coil. With a PC interface, Singh *et al* (2002) performed experiments on electromagnetic induction and damping. Munley (2004) considered difficulties often encountered when applying Faraday's law to specific situations. Wood *et al* (2004) measured the EMF induced in a coil by an accelerating magnet. Galili *et al* (2006) discussed teaching Faraday's law in an introductory physics course. López-Ramos *et al* (2008) considered conditions for the validity of Faraday's law. Experiments related to Faraday's law were also described by Fredrickson and Moreland (1972); Fox and Reiber (1973); Rochon and Gauthier (1982); Rosen and Schieber (1982).

The EMF e generated in a conductor is proportional to the time derivative of the magnetic flux Φ penetrating the area formed by the conductor (Fig. 1). This statement is known as Faraday's law:

$$e = -\mathrm{d}\Phi/\mathrm{d}t, \tag{1}$$

where the magnetic flux Φ equals

$$\Phi = \int \boldsymbol{B}\mathrm{d}\boldsymbol{A}. \tag{2}$$

The above integral is taken over the area, whose element is $\mathrm{d}\boldsymbol{A}$, and $\boldsymbol{B}\mathrm{d}\boldsymbol{A}$ is a scalar product of the two vectors.

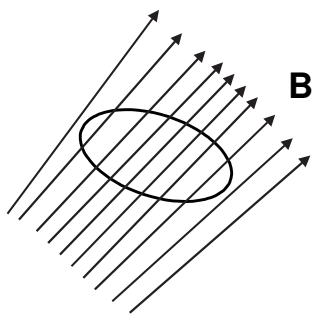

Fig. 1. Magnetic flux penetrating a closed loop depends on its area and orientation.

With SI units, the magnetic field in vacuum is $\boldsymbol{B}_0 = \mu_0\boldsymbol{H}$. The coefficient μ_0 is called the **magnetic constant** or permeability of vacuum. For our aim, the

difference between magnetic fields in vacuum and air is negligible. The field inside a sufficiently long solenoid is

$$B_0 = \mu_0 nI, \tag{3}$$

where n is the number of turns per unit length, and I is the current.

This relation is also valid for an AC current in the solenoid, $I = I_0 \sin\omega t$. If a probe coil containing N turns is placed coaxially inside the solenoid near its center, the EMF induced in this coil equals

$$e = (\mu_0 NAnI_0\omega)\cos\omega t, \tag{4}$$

where A is the cross-sectional area of the probe coil.

Determination of the magnetic constant. Equation (4) offers a way to determine the magnetic constant μ_0. A correct value of this constant would confirm the above equations, from which Eq. (4) is deduced. The setup for the measurements is very simple (Fig. 2).

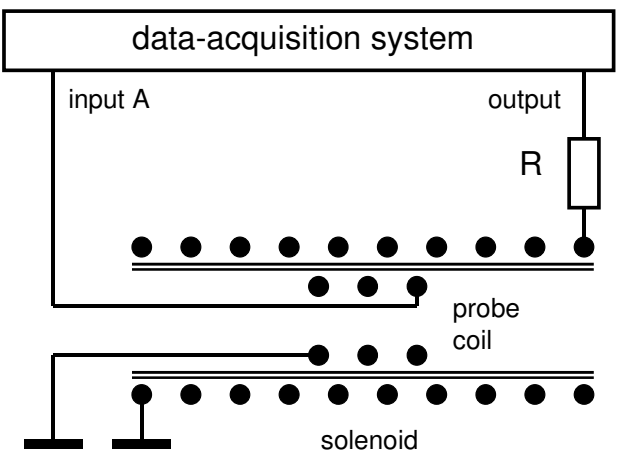

Fig. 2. Schematic of the setup.

A solenoid from PHYWE, 1 m long and containing 485 turns (catalog index 11001.00) is connected to the *Signal generator*. Due to the resistor R, the current does not depend on the frequency. The EMF generated in the probe coil is measured directly (input A). The *Scope* tool displays the EMF versus the *Output current*. The 90^o phase shift between the two signals is seen. Two measurements are possible: (i) the voltage from the probe coil versus the current in the solenoid, for a constant frequency (Fig. 3), and (ii) the voltage from the probe coil versus frequency, for a fixed current (Fig. 4). Two probe coils (PHYWE, 11006.02 and 11006.05) are used: 300 turns, 33 mm in diameter, and 100 turns, 41 mm in diameter. The slopes of the graphs provide data necessary for calculating the μ_0 value.

Without a data-acquisition system, a function generator, two multimeters, and an oscilloscope are sufficient for the experiment.

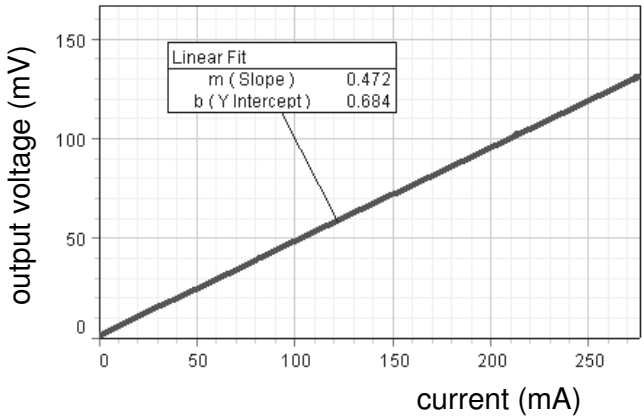

Fig. 3. EMF generated in the probe coil versus current, for $f = 500$ Hz.

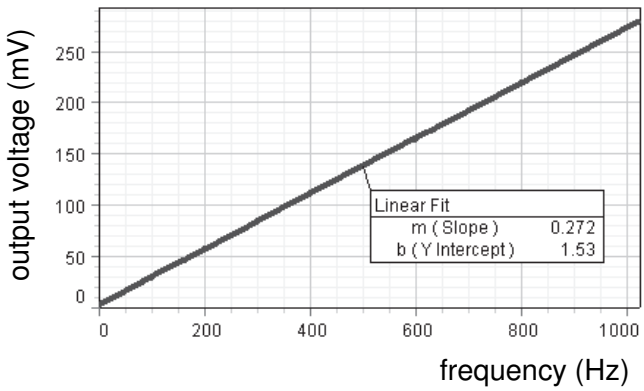

Fig. 4. EMF generated in the probe coil versus frequency, for $I = 290$ mA.

4.7. Iron-core inductance coil

The role of a magnetic core of an inductance coil is shown (Kraftmakher 2011e).

Additional equipment: demountable O-shaped ferromagnetic core, coil.

Most experiments with inductance coils demonstrate the frequency dependence of the coil's impedance and the phase shift between the applied voltage and current through the coil. The measured frequency dependence and phase shift can be used to determine the self-inductance and the intrinsic resistance of the coil (Duffy and Haber-Schaim 1977; Mak and Tao 1988). Measurements with an iron-core inductance coil provide good opportunity to consider properties of ferromagnetic materials (Snider 1971; Meng and Liang 1987; Kiss 1990; Borin and Baffa 1988).

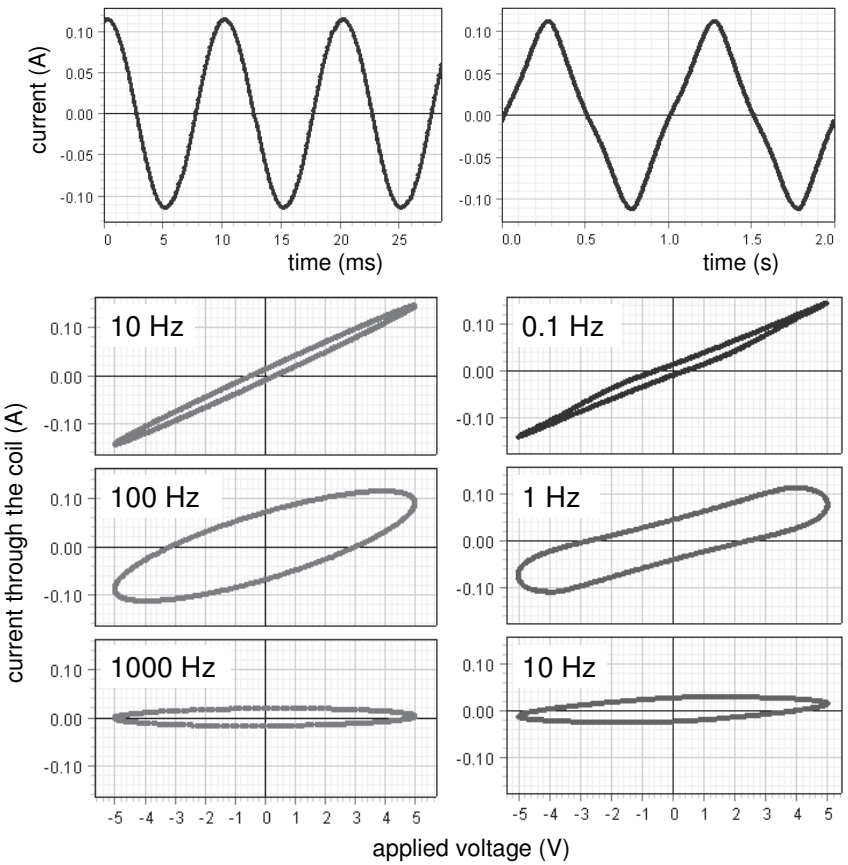

Fig. 1. Current through the coil versus time and versus applied voltage, for the air-core coil (left) and the iron-core coil (right).

For the experiment, we use a 1600-turn coil (SF-8612) and a demountable O-shaped ferromagnetic core (SF-8614). The *Signal generator* feeds the coil, and the current through the coil is the *Output current* (Fig. 1).

Self-inductance and resistance. The **modulus** of the impedance of the coil is

$$Z = V_0/I_0 = (R^2 + \omega^2 L^2)^{1/2}, \quad (1)$$

where V_0 and I_0 are the amplitudes of the voltage and current, $\omega = 2\pi f$, and L and R are the self-inductance and resistance of the coil.

The voltage across the coil is a sine wave of 5 V amplitude. For an iron-core coil, the measured time dependence of the current differs significantly from simple harmonic dependence due to the nonlinear magnetization curve of the core. The current i follows Kirchhoff's loop rule:

$$iR = V_0 \sin\omega t - L\mathrm{d}i/\mathrm{d}t. \quad (2)$$

The term $-L\mathrm{d}i/\mathrm{d}t$ reflects Faraday's and Lenz's laws for electromagnetic induction. For an air-core coil, the **self-inductance** L is constant, and the current remains sinusoidal. The phase shift between the applied voltage and the current through the coil can be determined from the shape of the current–voltage dependence.

The impedance of our **air-core coil** starts to increase significantly at frequencies above 100 Hz. For the **iron-core coil**, this happens at frequencies nearly two orders of magnitude smaller. The self-inductance of the iron-core coil depends on the current and can be called effective self-inductance; it becomes much larger than that for the air-core coil. The self-inductance equals

$$L = (Z^2 - R^2)^{1/2}/2\pi f. \quad (3)$$

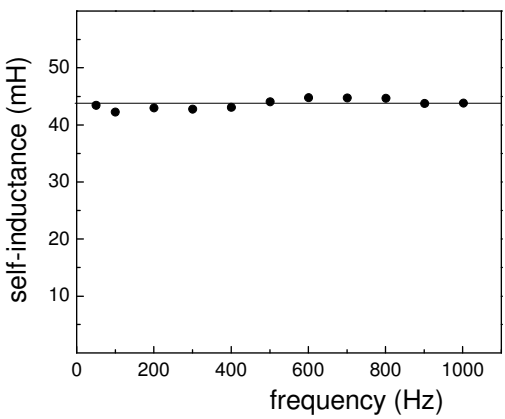

Fig. 2. Self-inductance of the air-core coil versus frequency.

At the moderate frequencies used in our measurements, the resistance R of the air-core coil can be taken from DC measurements. It is found to be $R = 34.4\ \Omega$. The calculated self-inductance of the air-core coil does not depend

on the frequency and amplitude of the current and equals $L = 44$ mH (Fig. 2). The accuracy of the calculated self-inductance depends on the frequency of the current; the frequency should be chosen to provide a significant difference between Z and R.

Properties of magnetic core. Equations (1) and (3) are irrelevant for the analysis of the data with the iron-core coil because its self-inductance and resistance depend on the amplitude and frequency of the magnetizing current. The AC resistance of the coil reflects all power losses, including losses in the core (hysteresis losses, proportional to the frequency, and losses due to eddy currents in the core, proportional to the frequency squared).

With the data-acquisition system, it is easy to calculate the total power loss P in the system and the corresponding effective resistance R_{eff} of the coil. It is sufficient to find the mean value of the product of the voltage applied and the current through the coil (that is, of the *Output voltage* and *Output current*). The total power consumed by the coil equals

$$P = \langle iV \rangle = \langle i^2 \rangle R_{\text{eff}}. \tag{4}$$

DataStudio calculates the above mean values with the *Averaging* tool (*Calculate*/*Statistical*/*Avg*) and displays the results. For the iron-core coil, the measurements are carried out at frequencies between 1 and 5 Hz. In all the measurements, the amplitude of the magnetizing current is kept constant at 0.04 A by adjusting the *Output voltage*. An example of the data and calculations for $f = 5$ Hz is presented here (Fig. 3). The effective resistance is a linear function of the frequency, intercepting the Y-axis at 34.6 Ω. This linear dependence on frequency indicates that the losses in the core are mainly hysteresis losses: at the low frequencies used in these measurements, the effect of eddy currents is insignificant. Routine methods can be used to determine the permeability of the core as a function of the magnetizing current.

The same calculation was carried out for the air-core coil at $f = 50$ Hz; its effective resistance agreed with the value from DC measurements.

Transient processes. After the coil is instantly connected to a source of constant DC voltage V_0, the current i through the coil obeys the equation

$$iR = V_0 - L\mathrm{d}i/\mathrm{d}t. \tag{5}$$

The solution to this equation is

$$i = i_0[1 - \exp(-Rt/L)] = i_0[1 - \exp(-t/\tau)], \tag{6}$$

where $i_0 = V_0/R$ is the steady current, and $\tau = L/R$.

When, after the steady-state current i_0 is established, the DC source is disconnected, while the circuit remains closed, Eq. (5) is still valid but with $V_0 = 0$. The current through the coil decays exponentially:

$$i = i_0\exp(-Rt/L) = i_0\exp(-t/\tau). \tag{7}$$

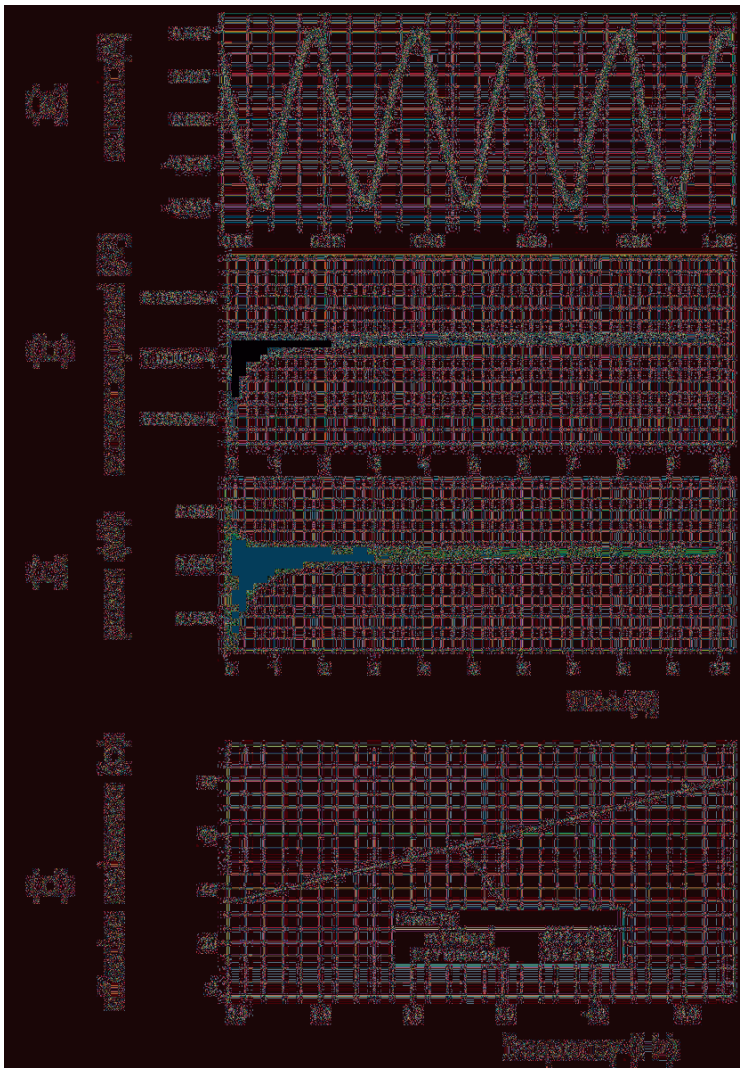

Fig. 3. Results for the iron-core coil at f = 5 Hz: (a) current through the coil; (b) mean value of the current squared; (c) mean power consumed by the coil; and (d) effective resistance versus frequency.

To observe the transient processes in the air-core coil, the *Signal generator* provides a 50 Hz *Positive square wave* voltage of 5 V amplitude. The generator operates in the *Auto* mode: it builds the output voltage after starting a run. The *Automatic stop* option is set to occur 0.02 s after *Start*. The current through the coil is displayed as a function of time (Fig. 4). The transients in the air-core coil follow Eqs. (6) and (7). The time constant can be obtained by displaying the natural logarithm of the decaying current versus time. For this aim, the

measurement data related to this part of the transient process were separated. The *Linear fit* for the logarithm corresponds to $R/L = 817 \pm 2.3\ s^{-1}$. The corresponding time constant of the coil is $\tau = 1.2$ ms. Taking $R = 34.4\ \Omega$, the self-inductance of the coil equals $L = 42$ mH, in agreement with the results of the impedance measurements.

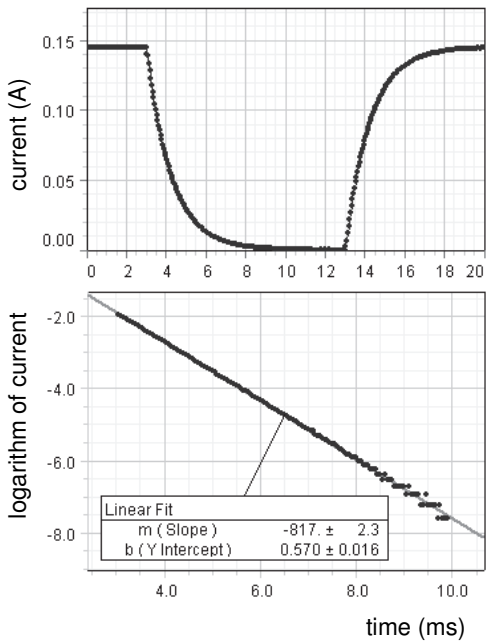

Fig. 4. Transient process and natural logarithm of the decaying current, for the air-core coil.

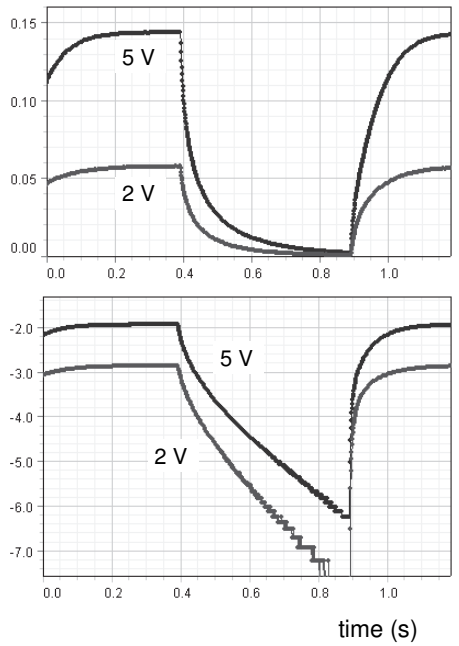

Fig. 5. Transient process and natural logarithm of the current for the iron-core coil, for two applied voltages.

The response of the iron-core coil was studied with a 1 Hz *Positive square wave* voltage. The nonlinear properties of the core make the process dependent on the applied voltage. The data for two DC voltages, 2 and 5 V, demonstrate this dependence (Fig. 5).

4.8. Electrical filters

The data-acquisition system displays the frequency response of simple RC and LC filters.

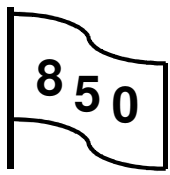

Additional equipment: *Voltage sensors*, resistors, capacitors, coils, AC-to-DC converter.

RC filters. With the new data-acquisition system, the frequency response of any frequency-dependent system is easily available. The *Output 1* operates in the frequency sweep mode (Fig. 1). Input *B* serves for observing the signals after passing the filter.

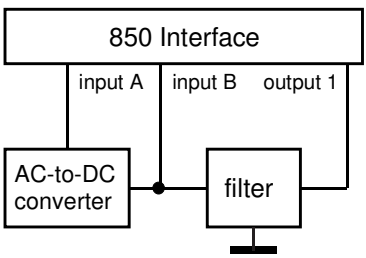

Fig. 1. Diagram of the setup.

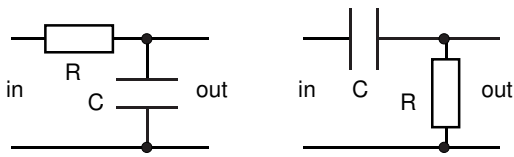

Fig. 2. Low-pass and high-pass RC filters.

In the first experiment, characteristics of a **low-pass** and a **high-pass** RC filters are displayed. For these filters (Fig. 2), it is easy to calculate their frequency response. The output resistance of the source is negligible, while the input resistance of a device connected to the output of the filter is sufficiently high. The phase relations between the input and output voltages are observable with the *Scope* tool. The same arrangement is used for observing changes in the form of the output signals when the input signal differs from the sine waveform. In this case, *Fast Fourier Transform* tool can be employed to analyze the operation of electrical filters (see Experiment 4.2).

To observe the characteristics of the RC filters, the frequency sweeps from 10 to 2000 Hz in 100 s. The input voltage is 1 V. An AC-to-DC converter provides RMS values of the output voltage, and the *Graph* tool displays the frequency response curve (Fig. 3). It is easy to determine the phase shifts between two sinusoidal signals by fitting the simultaneously acquired signals by the *Fit*/*Sine fit* tool. The fits provide the frequency, the amplitude, and the phase of both signals. These data can be used for plotting amplitude and phase characteristics of a circuit.

LC filters. Two band-pass filters (Fig. 4) based on a series and a parallel LC circuits are explored; both filters include an 800-turn coil (SF-8611) and a capacitor $C = 4.7$ nF. In the measurements, the reactance of the inductor is much

greater than its inherent active resistance (not shown in Fig. 4). The input voltage is 1 V. Due to the resonance in the series LC filter, the maximum output voltage is larger than the input voltage.

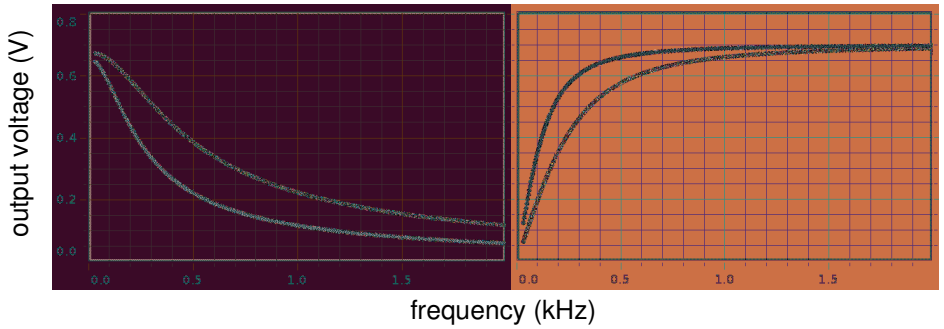

Fig. 3. Frequency response of the RC filters shown in Fig. 2. C = 0.05 µF, R = 10 kΩ and 20 kΩ.

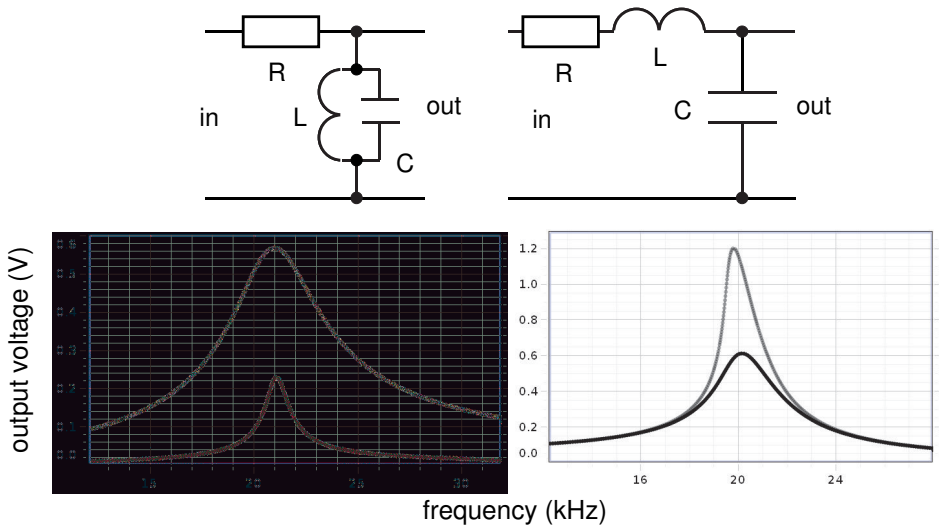

Fig. 4. Band-pass filters with LC circuits, and their characteristics. Left: parallel circuit, R = 100 kΩ and 1 MΩ; right: series circuit, R = 0 and 100 Ω.

4.9. Rotating magnetic field

The experiments include two items: (i) the torque on a conductor versus the rotation frequency of the magnetic field, and (ii) the induction motor.

Not long after Faraday's discovery of the magnetic induction in 1831, Lenz stated a law: when a conducting circuit is moved in a magnetic field, the current induced in it flows in such a direction that the force on the conductor opposes the motion. Many authors considered the interaction of a conductor with a time-dependent magnetic field. Wouch and Lord (1978) calculated the levitation force and heating for a conducting sphere in the magnetic field of a circular AC current. The presence of metal in the vicinity of the loop changes its inductance, and this effect is the basis of metal detectors. Mak and Young (1986) considered the floating metal ring in an AC magnetic field (Elihu Thomson's ring). Perkalskis and Freeman (1997), Schneider and Ertel (1998), and Tanner *et al* (2001) also discussed this phenomenon. Saslow (1987, 1991, 1992) considered many topics related to implications of Faraday's law, including the magnetic braking and induction motor, electromagnetic shielding and levitation. MacLatchy *et al* (1993) described methods of calculating and measuring the terminal velocity and magnetic forces in the popular magnetic breaking experiment, in which a strong button-shaped magnet falls through a long metal tube. Cadwell (1996) proposed a simple theory for analyzing the effect of magnetic damping on an aluminum plate moving on a horizontal air track. Hahn *et al* (1998) measured the motion and damping of a permanent magnet attached to a spring and oscillating inside a conducting tube. The experimental results are in good agreement with the theoretical analysis. Pelesko *et al* (2005) described a version of this experiment. Ponikvar (2010) described some tools and setups for experiments with AC and rotating magnetic fields. Bhattarcharjee (2012) calculated the torque developed in a three-phase squirrel cage motor directly from Maxwell's equation.

The interaction of a conductor with a rotating magnetic field is one of manifestations of Lenz's law and has important applications, first of all, in induction motors. Rotating magnetic field is used for contactless measurements of the resistivity of metals and alloys. For very low resistivities, this technique is advantageous over other contactless methods. The basic question of this topic is the frequency dependence of the torque on a conductor caused by a rotating magnetic field.

1. Torque caused by rotating magnetic field

The experiment shows the dependence of the torque exerted on a conductor upon the rotation frequency of a magnetic field (Kraftmakher 2001).

Equipment: AC voltmeter, *Variable gap magnet* (EM-8618), laser, samples, four similar coils, two variable resistors (100 Ω), two fixed resistors (10 Ω).

Many papers are devoted to teaching the interaction of a conductor with a **rotating magnetic field**. Doyle and Gibson (1979) described a simple classroom demonstration of retarding and repulsive forces acting on a permanent magnet put near a rotating conductor. Wiederick *et al* (1987) proposed an experiment on the magnetic braking of a thin aluminum disc freely rotating between the pole pieces of an electromagnet. Heald (1988) presented an improved theory of this experiment. Marcuso *et al* (1991a,b) computed the torque acting on a moving conductor under the influence of a localized magnetic field and confirmed the calculations by measuring the deceleration of aluminum and copper discs. Aguirregaribia *et al* (1997) studied the braking effect on a thin conducting disc rotating in an external nonuniform magnetic field.

Torque versus frequency. At low frequencies, when the size of the conductor remains smaller than the **skin depth**, the torque is proportional to the frequency of the rotation of the magnetic field. When increasing the frequency, the torque reaches maximum and then decreases because of the skin effect: the eddy currents become smaller, and a phase shift arises between the EMF induced in the conductor and the current in it. Landau and Lifshitz (1984) presented a solution for a spherical sample, and Batygin and Toptygin (1970) considered the case of a cylindrical sample. The torque for a unit length of the cylinder equals

$$M = aH^2 \,\mathrm{Re}[kJ_1(ka)/J_0(ka)]/|k|^2, \qquad (1)$$

where H is the magnetic field, $k^2 = i\omega\mu_0/\rho$, ω is the angular frequency of the field rotation, μ_0 is the magnetic constant, a and ρ are the radius of the cylinder and its resistivity, and J_1 and J_0 are **Bessel functions** of the first kind. The argument of the Bessel functions, ka, is a complex quantity because $\sqrt{i}$ equals to $(1 + i)/\sqrt{2}$. Jahnke and Emde (1945) tabulated these functions, so one can evaluate the theoretical dependence of the torque versus the frequency of rotation of the magnetic field. A more convenient argument for this dependence is $X = |k^2|a^2/2 = \omega\mu_0 a^2/2\rho = (a/\delta)^2$, where $\delta = (2\rho/\omega\mu_0)^{1/2}$ is the skin depth for plane surfaces. The maximum torque M_0 does not depend on the resistivity of the sample and is proportional to a^2H^2, while the **relative torque** $Y = M/M_0$ is a universal function of X. Data for cylindrical samples of various thickness and resistivity can be displayed together and compared with the theoretical $Y(X)$.

In our experiment, two pairs of coils produce magnetic fields in two perpendicular directions (Fig. 1). The currents through the coils are shifted by 90°, which leads to the rotation of the magnetic field. The frequency of the field

rotation equals the frequency of the currents. A Hewlett–Packard 8904A multifrequency synthesizer supplies the currents. The device has two channels, with the frequencies and phases set independently. In our case, the phases are 0 and 90°. A switch (not shown in Fig. 1) changes the direction of the current in one pair of the coils and thus reverses the direction of the torque.

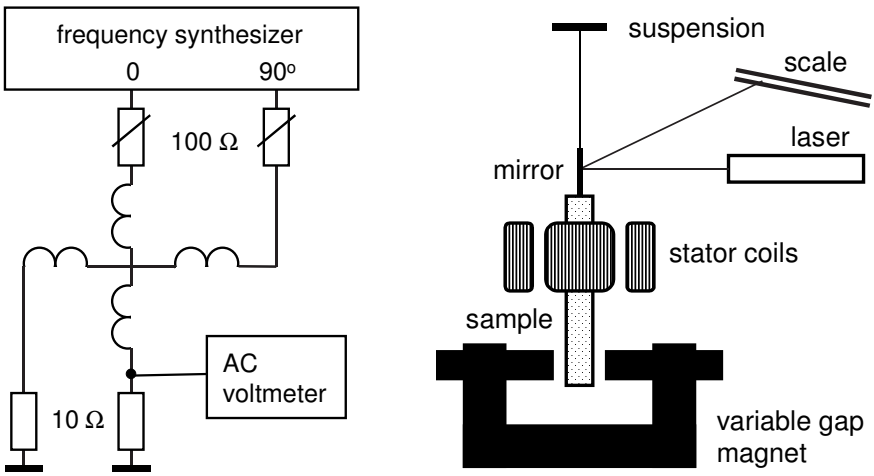

Fig. 1. Setup for measuring the torque on a cylindrical sample.

The sample is suspended on a copper wire 0.1 mm in diameter and 40 cm long. A small flat mirror is pasted to the lower end of the wire. A laser beam reflected from the mirror falls onto a scale 1.5 m apart. The readout is taken as the difference between the deflections corresponding to the two directions of the torque. The samples are cylinders, 1–1.5 cm in diameter and 10 cm long. The lower end of the sample is located in a region of a strong magnetic field produced by the *Variable gap magnet* (EM-8618); this provides magnetic damping of the sample. Two resistors are connected in series with each coil. A variable 100 Ω resistor serves to maintain the same feeding currents for various frequencies. An AC voltmeter measures the voltage drop across the 10 Ω (1%) resistor.

To calculate the argument $X = (a/\delta)^2$, the resistivity of the samples must be known. For the samples employed, the resistivity was previously measured by a contactless method based on determinations of the phase angle of the effective magnetic susceptibility of the samples in an AC magnetic field (Kraftmakher 2000b). The resistivity is 1.73×10^{-8} Ω.m for copper and 4.04×10^{-8} Ω.m for the aluminum alloy. Now the experimental data for both samples can be superimposed on the theoretical curve. The results are in good agreement with the theory (Fig. 2).

Contactless measurement of resistivity. It is possible to employ the previous experiment for contactless measuring the resistivity of metals and alloys. Three

techniques of contactless measurements of resistivity rest on creating eddy currents in a sample (Delaney and Pippard 1972): (i) the effective magnetic susceptibility of cylindrical samples in an axial AC magnetic field; (ii) the decay of eddy currents in a sample after switching off an external DC magnetic field; and (iii) the torque caused by a rotating magnetic field.

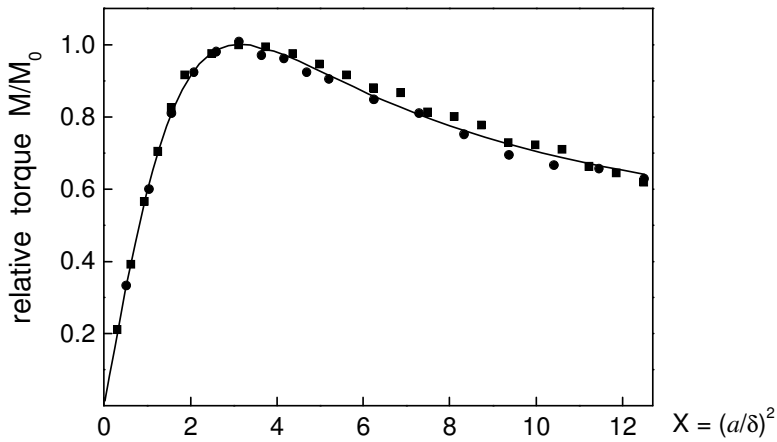

Fig. 2. Relative torque $Y = M/M_0$ versus X: ● copper, ■ aluminum alloy (experimental data); — theoretical curve.

When measuring very low electrical resistivities (pure metals at low temperatures), the use of a rotating magnetic field has definite advantages over other contactless techniques. The maximum torque and the sensitivity of the method, in contrast to other contactless methods, can be kept independent of the resistivity to be measured; for this purpose, it is enough to properly choose the rotation frequency of the magnetic field. The resistivity of a sample can be determined from the frequency of rotation of the magnetic field that provides a maximum torque (Delaney and Pippard 1972). With other contactless techniques, one has to employ very low frequencies of the magnetic field or observe a very long decay of the eddy currents. In both cases, the voltages to be measured become too small.

Zernov and Sharvin (1959) employed the rotating field technique for measuring the resistivity of high-purity tin at liquid helium temperatures. To perform the measurements in the quasi-static limit, the authors used a very low frequency of the field rotation, 2 mHz. Helmholtz coils fed by a DC current and rotating around a vertical axis created the rotating magnetic field. The resistivity of the tin sample was found to be 3.7×10^{-13} Ω.m.

When using the rotating field technique, the broad maximum in the $Y(X)$ dependence makes difficult to find the resistivity. A more accurate method is to determine the quantity $X = (a/\delta)^2$, for which a given relative torque $Y = M/M_0$ is achieved (Zakharov and Kraftmakher 1989).

2. Induction motor

The operation of an induction motor is monitored, and the slip of the rotor versus the load is determined (Kraftmakher 2001, 2005a).

Additional equipment: *Rotary motion sensor*, induction motor, DC generator, DC source, variable AC source, two multimeters, stroboscope, variable resistor.

Single- and three-phase motors. The **induction motor** is the most important application of Lenz's law. In an induction motor, an AC voltage is applied to the **stator** windings (Fig. 3). Two windings are positioned perpendicular to each other. Each winding is a pair of coils. One pair is connected to the AC source directly, and the second via a capacitor. By proper choice of the capacitor, the phase shift between the two currents can be set close to 90°. Calculations of the magnetic field inside the stator are very simple when the windings generate fields $B_y = B_0 \sin\omega t$ and $B_x = B_0 \cos\omega t$. The resulting vector of the field is directed at an angle $\alpha = \omega t$ (Fig. 4). Stator windings may contain four pairs of coils. This makes the frequency of the field rotation half the frequency of the current.

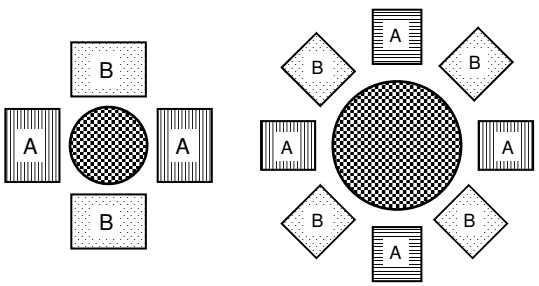

Fig. 3. Stator with two pairs of coils connected to single-phase line.

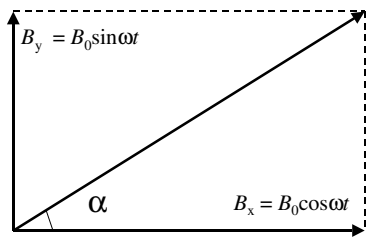

Fig. 4. The sum of $\boldsymbol{B}_x$ and $\boldsymbol{B}_y$ is a vector $\boldsymbol{B}_0$ directed at angle $\alpha = \omega t$, so it rotates with angular frequency ω.

In power motors, a three-phase AC current generates the rotating magnetic field. The 120-degrees shifted currents flow through three coils positioned at 120° angles (Fig. 5). The rotating magnetic field generated by the stator induces eddy currents in the **rotor**. The rotor of a low power induction motor may be simply a metal cylinder. In high power motors, the rotor usually consists of a number of conducting bars running parallel to the axis of the motor, with two conducting rings at the ends. This type of rotor is often called the squirrel-cage rotor. The cage is embedded in steel to enhance the magnetic field (Smith 1984).

It is difficult to calculate the **eddy currents** in the rotor, but Lenz's law unambiguously predicts the result of their interaction with the rotating magnetic field. The eddy currents are proportional to the relative angular velocity of the

magnetic field with respect to the rotor. Therefore, the only way for the rotor to obey Lenz's law is to follow the magnetic field. Arago discovered the interaction between a magnetic needle and a rotating nonmagnetic conductor in 1825. However, the phenomenon remained mysterious until Faraday discovered the electromagnetic induction in 1831.

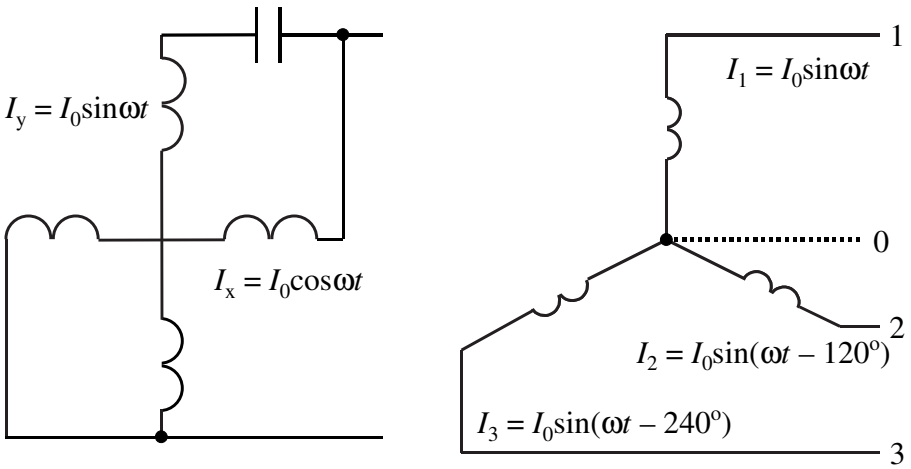

Fig. 5. Electrical circuits for a single- and a three-phase motor.

The rotor of an induction motor rotates somewhat slower than the magnetic field because at equal velocities of rotation the eddy currents vanish. Any increase of the load slows down the rotor and hence increases eddy currents in it and the **driving torque**. At any load, the velocity of the rotor is self-adjusted to produce the necessary torque. The difference between the angular velocity of the magnetic field and that of the rotor depends on the load. Induction motors have very wide applications. Their main advantage is the absence of sliding current-carrying contacts (brushes). Such contacts reduce the efficiency of electrical machines and cause electromagnetic interference. When switched on, the induction motor produces a torque many times larger than that necessary for normal operation and thus rapidly attains its steady velocity. A disadvantage of induction motors is that their velocity is tied to the frequency of the rotating magnetic field.

With a data-acquisition system, it is easy to see how an induction motor reaches its steady velocity and how a DC magnetic field decelerates the rotation after switching off the rotating field. A stator of a low power (3–5 W) induction motor is employed (Fig. 6). One of its windings is connected to a 50 Hz AC source directly, and the second via a capacitor providing the necessary phase shift. Actually, the phase shift differs from 90^o, but the rotating field nevertheless appears. An aluminum or brass cylinder, 30 mm in diameter and 50 mm in length, serves as the rotor. It is attached to the axle of the *Rotary motion sensor* and is positioned inside the stator. The *Graph* tool displays the

angular velocity of the rotor versus time. The *Sample rate* is 1 Hz. The larger the mass of the rotor, the longer is the time for achieving a steady speed of rotation and the decay time. An induction motor with its own rotor may also be used for the demonstration, but in this case the additional friction of the rotor is unavoidable. A switch connects the stator windings to an AC source or to a DC source. If an open stator is employed, the AC source should include an isolating transformer for avoiding a direct connection of the windings to the mains (Fig. 7).

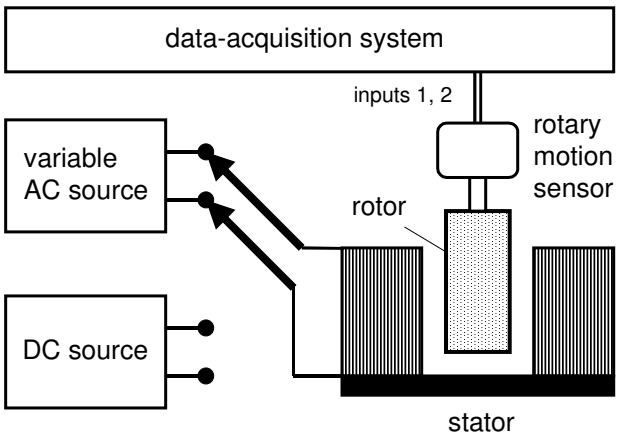

Fig. 6. Diagram of setup for monitoring motor operation. The capacitor providing phase shift between currents in stator coils is not shown.

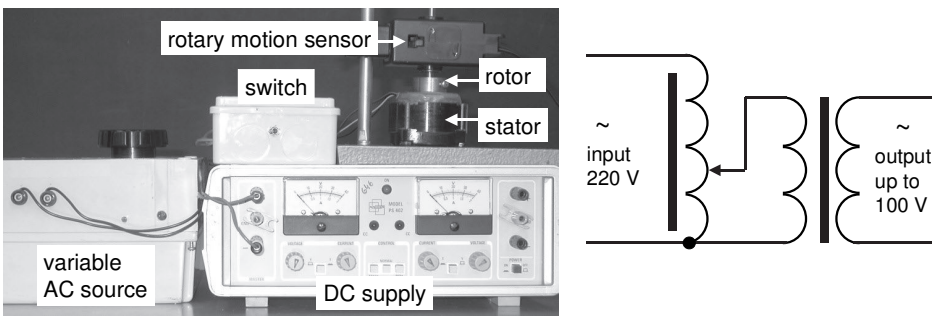

Fig. 7. The setup and diagram of the variable AC source.

The magnetic field rotates at 25 revolutions per second. After reaching a steady velocity of rotation, the windings are switched to the DC source supplying a current to the winding that is directly connected. This current produces a DC magnetic field, which decelerates the rotor, again in accordance with Lenz's law. The measurements are repeated with various DC currents. An ammeter (not shown in Fig. 6) measures the current. The graph obtained clearly

demonstrates the initial period after switching on the motor and the magnetic braking (Fig. 8). The range of angular velocities monitored by the *Rotary motion sensor* is limited to about 20 rotations per second, so it may be necessary to reduce the rotation velocity by decreasing the applied voltage.

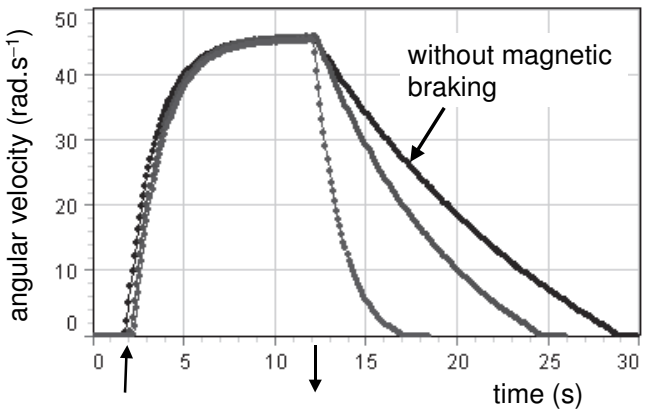

Fig. 8. Decay of rotation without magnetic braking and for two values of the DC current in the winding.

Slip versus load. At any load, the velocity of the rotor is self-matched to provide the necessary torque. The stator's magnetic field rotates at a frequency f_0 determined by the frequency of the current and the number of poles. The rotor rotates at a frequency f somewhat lower than that of the magnetic field. The lag of the rotor relative to the rotating magnetic field, which is necessary for the motor action, is called the slip $s = (f_0 - f)/f_0$. The slip of an induction motor is measured versus its mechanical load (Fig. 9).

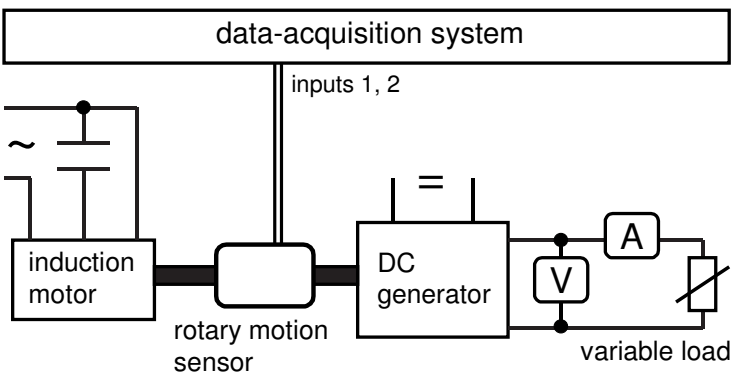

Fig. 9. Schematic of the setup for measuring the rotation frequency versus load.

The rotation frequency of the magnetic field is $f_0 = 25$ revolutions per second. A DC generator with an independent excitation serves as the load. The axle of the motor is connected to the *Rotary motion sensor*, while the second end of the sensor is connected to the axle of the DC generator. Changes in the output current of the generator cause changes in the torque necessary to operate it. Therefore, it is easy to vary the load of the motor: the changes in the load are equal to the changes in the electric power developed by the generator. The *Digits* tool displays the frequency of rotation of the motor. When the current in the stator coils is switched on, large currents are induced in the rotor, causing high initial torque.

The calculations of the electric power produced by the generator should take into account the power dissipated in its winding. The total electric power is $P = IE$, where I is the current, and E is the EMF generated. This EMF is proportional to the frequency of rotation: $E = E_1 f/f_1$, where E_1 and f_1 relate to the unloaded generator. A variable load resistor controls the current, and an ammeter measures it. The steady rotation frequency depends on the load of the generator. The results obtained show a linear dependence of the slip on the load, in agreement with the theory (Fig. 10).

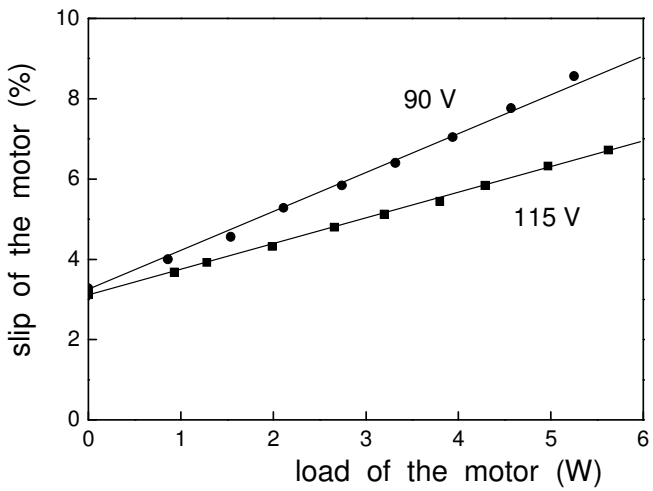

Fig. 10. Slip of the motor versus load, for two feeding voltages.

Without a data-acquisition system, the frequency of rotation of the induction motor can be measured with a stroboscope (Fig. 11). A plastic tube fits the axles of the induction motor and of the generator. A mark on the tube serves to determine the rotational frequency of the rotor by adjusting the frequency of the stroboscope. The resolution of our stroboscope is 0.1 Hz. To reduce the error caused by the insufficient resolution, the stroboscope's frequency is set to be five times higher than the frequency of the rotation; the resolution thus becomes 0.02 Hz. The rotation frequency may be also determined using a small

permanent magnet pasted to the axle of the motor, a coil sensing fast changes of the magnetic flux, and a frequency meter.

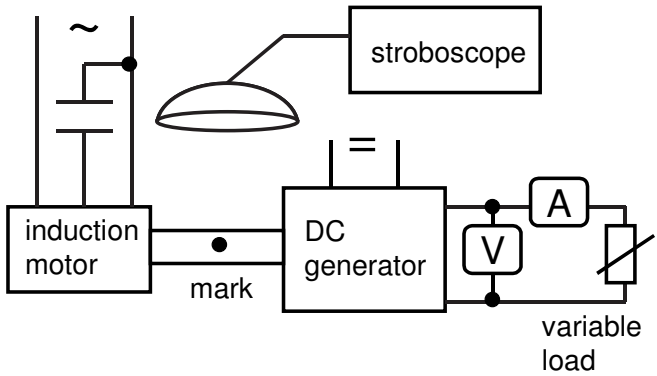

Fig. 11. Schematic of the setup with a stroboscope.

4.10. LCR circuit II

Four experiments are considered: (i) the free oscillations and phase plane plot; (ii) the forced oscillations and transients; (iii) the coupled LCR circuits; and (iv) nonlinear LCR circuits.

The LCR circuit is one of fundamental topics of the electromagnetic theory having many important applications such as radio and television. Many authors have considered free and forced oscillations in an LCR circuit. Luke (1975) and Hurych (1975) observed free and forced oscillations with an oscilloscope. Lewis (1976) used a "negative resistor" to obtain continuous self-oscillations. Jupin (1977) used an LCR circuit for measuring the dielectric constants of liquids. Rodríguez *et al* (1979) described an electronic device for observing resonance curves with an oscilloscope. Clay (1979) demonstrated phase relationships in a series LCR circuit. Janssen *et al* (1984) considered a nonlinear LCR circuit. With a data-acquisition system and a microcomputer, Whiteley and Luke (1989) investigated the time- and frequency-domain behavior of an LCR circuit. Basano *et al* (1996) studied the change in the total energy of an LCR circuit during free oscillations. Moriarty *et al* (2003) used *LabVIEW* software in a laboratory course, in particular, for observing free oscillations in an LCR circuit. Page *et al* (2006) also described an experiment with an LCR circuit. Faleski (2006) considered transient behavior of an LCR circuit. For probing a resonant circuit, Magno *et al* (2007) used a PC sound card. Fernandes *et al* (2010) described computer-assisted experiments with oscillatory circuits. Sokol *et al* (2013) demonstrated phase relationships in LCR circuits.

LCR circuit with feedback. Additional options are offered by the use of **feedback** modifying properties of an LCR circuit. The concept of feedback is very important in physics and in many applications. Combining the two topics, the LCR circuit and feedback, gives better understanding of both items. In electronics, a feedback circuit returns a portion of the output signal of an amplifier to its input. When the signal returned is of the same phase as the input signal, the feedback is called **positive**. When the feedback signal is in opposition to the input signal, the feedback is **negative**. Positive feedback is crucial for some types of generators, including lasers. Negative feedback stabilizes amplifiers and many other technical devices. Two experiments involving this topic were included in the Berkeley laboratory course (Portis and Young 1971). Wolfson (1981) described a simple demonstration of negative feedback, which served to maintain a constant resistance of a photocell regardless of its distance from a light bulb. Stanek *et al* (1993) employed a negative thermal feedback for stabilizing the temperature of a He–Ne laser. The negative feedback strongly suppressed variations in the laser intensity. Skeldon *et al* (1998) described the resonant excitation of a wineglass by positive feedback. The concept of feedback has much wider scope than the above examples.

Usually, one increases the decay of free oscillations in a resonant LCR circuit by means of an additional resistor. Positive feedback makes it possible to decrease the decay and even obtain continuous oscillations. In the case of forced oscillations, feedback modifies the resonance curve, as well as the transient process after changing the applied voltage.

The theory of the LCR circuit with feedback is very simple. The voltage U_C across the capacitor C of the circuit is amplified and then fed, through a variable resistor R_1, to a coil L_1 inductively coupled to the inductor L of the circuit (Fig. 1). Pippard (1989) considered such a circuit in detail. For a circuit without feedback, the basic equation is

$$IR + U_C = -L\mathrm{d}I/\mathrm{d}t, \qquad \text{or} \tag{1}$$

$$\frac{d^2I}{dt^2} + \frac{R}{L}\frac{dI}{dt} + \frac{I}{LC} = 0, \tag{2}$$

where I is the current in the circuit. The solution to this equation is

$$I = I_0 \exp(-\delta_0 t)\sin(\Omega t + \varphi), \tag{3}$$

where $\Omega^2 = \omega_0^2 - \delta_0^2$, $\omega_0^2 = 1/LC$ is the natural frequency of the circuit, $\delta_0 = R/2L$ is the decay constant, and I_0 and φ depend on the initial conditions. Usually, $\omega_0^2 >> \delta_0^2$, and $\Omega \approx \omega_0$.

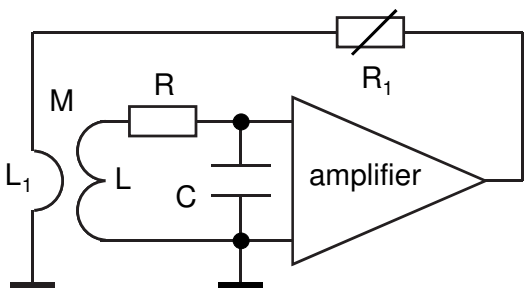

Fig. 1. LCR circuit with feedback.

Due to the feedback, an additional term $\pm M\mathrm{d}i/\mathrm{d}t$ should be added to Eq. (1), where M is the mutual inductance of the coils L and L_1, and i is the current in the feedback circuit. The basic equation for this circuit thus becomes

$$IR + U_C = -L\mathrm{d}I/\mathrm{d}t \pm M\mathrm{d}i/\mathrm{d}t, \qquad \text{or} \tag{4}$$

$$\frac{d^2I}{dt^2} + \frac{R}{L}\frac{dI}{dt} \pm \frac{M}{L}\frac{d^2i}{dt^2} + \frac{I}{LC} = 0. \tag{5}$$

The sign of the additional term is reversible by changing the terminals of the coil L_1. In our case, $R_1 >> \omega L_1$, so the phase of the current i coincides with the phase of the voltage U_C across the capacitor C. The output voltage of the amplifier is proportional to U_C: $U_{out} = KU_C$, where K is the gain of the amplifier. The current through the coil L_1 equals $i = KU_C/R_1$, so that

$$\frac{M}{L}\frac{d^2i}{d^2t} = \frac{KM}{LCR_1}\frac{dI}{dt}, \tag{6}$$

and

$$\frac{d^2I}{dt^2} + \left(\frac{R}{L} \pm \frac{KM}{LCR_1}\right)\frac{dI}{dt} + \frac{I}{LC} = 0. \tag{7}$$

The sign "minus" in the brackets corresponds to positive feedback, which decreases the decay of the oscillations. By comparing Eqs. (2) and (7), the **decay constant** of the LCR circuit with the feedback equals

$$\delta = R/2L \pm KM/2LCR_1 = \delta_0 \pm KM\omega_0^2/2R_1. \tag{8}$$

When the feedback is positive, the decay constant δ becomes zero when $KM/CR_1 = R$. In this case, continuous oscillations occur in the circuit. A question arises about the amplitude of the oscillations when δ becomes negative. From Eq. (3), the amplitude of the oscillations should exponentially increase. Clearly, this is impossible. Every amplifier has a limited range of output voltages. When the input signal increases, the gain of any amplifier inevitably decreases.

We can take the **feedback factor** β as a ratio of the voltage induced in the coil L due to the current in the coil L_1 to the output voltage U_{out} of the amplifier, which equals iR_1:

$$\beta = i\omega_0 M/U_{out} = \omega_0 M/R_1. \tag{9}$$

The phase of the induced voltage differs by 90^o from the voltage across the capacitor C, but coincides or is in opposition to the phase of the current I. Therefore, the feedback modifies the losses in the circuit. The decay constant may be presented as

$$\delta = \delta_0 \pm K\beta\omega_0/2. \tag{10}$$

A simple relation thus exists between the feedback factor and the decay constant of the LCR circuit.

1. Free oscillations

The data-acquisition system displays free oscillations. The feedback modifies the decay constant.

Additional equipment: two *Voltage sensors*, two coils, decade resistance box, oscilloscope, capacitor, resistors.

The LCR circuit contains an inductor L with resistance R, a capacitor C, and two additional resistors, R_1 and R_2 (Fig. 2). An additional coil L_1 is inductively coupled to the coil L. The *Square wave* voltage from the *Signal generator* applied to the resistor R_1 triggers free oscillations in the circuit. The *Graph* tool displays the voltage across the capacitor C. Simultaneously, this signal is amplified and then, through a resistance R_3, fed to the feedback coil L_1.

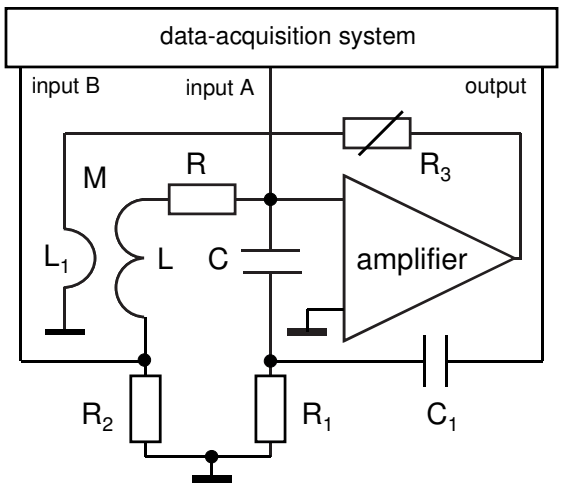

Fig. 2. Schematic of the setup. $R_1 = 20\ \Omega$, $R_2 = 50\ \Omega$.

The coils L and L_1 contain 3200 and 400 turns (SF-8613 and SF-8610). The capacitor C = 0.01 μF is chosen to obtain a sufficiently low resonance frequency of the circuit, about 4 kHz. As the amplifier, we use a Kenwood CS-4025 oscilloscope. To display a fixed number of periods of the free oscillations, it is necessary to choose the frequency of the square wave voltage triggering the free oscillations and to define the conditions of the *Start* and *Stop* of the measurements. The frequency of the square wave voltage is 50 Hz. The measurements start automatically after the voltage from the *Signal generator* exceeds a certain value and last 5 ms (Fig. 3).

To calculate the feedback factor β for all the values of R_3 used in the measurements, it is sufficient, according to Eq. (9), to determine the mutual inductance *M* of the coils L_1 and L. The *Signal generator* supplies an AC current

for these measurements. Equation (10) shows how the feedback modifies the decay constant. After the determination of the amplifier's gain, all the quantities entering the second term of this equation become known.

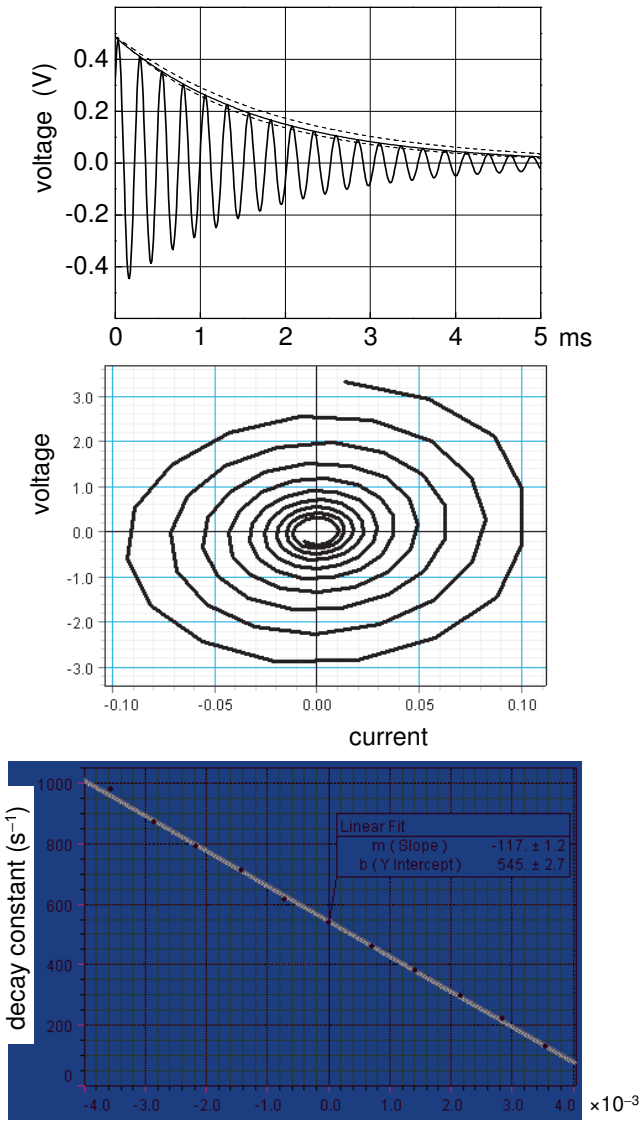

Fig. 3. Free oscillations, phase plane plot, and decay constant versus feedback factor: • experimental data, —— calculations.

Phase plane plot. To build the phase plane plot (phase portrait) of free oscillations, the voltage across the resistor R_2 is displayed versus the voltage across the capacitor C. The plot depends on the feedback factor.

2. Forced oscillations and transients

The experiments include three items: (i) the forced oscillations; (ii) the resonance curves; and (iii) the transient phenomena.

Additional equipment: two *Voltage sensors*, two coils, function generator, decade resistance box, oscilloscope, capacitor, resistors, AC-to-DC converter.

The **resonance curves** of a series LCR circuit are measured using a function generator with FM option (Fig. 4). The output voltage applied to the resistor R_1 drives the oscillations in the circuit. An AC-to-DC converter provides a DC voltage proportional to the AC voltage across the capacitor C, and the *Voltage sensor* measures this DC voltage. The *Graph* tool displays the resonance curve.

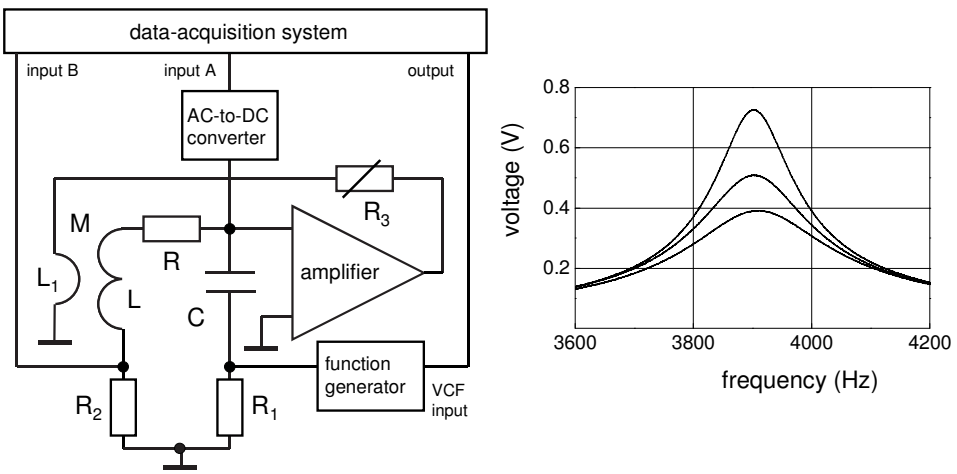

Fig. 4. Schematic of the setup and resonance curves of the LCR circuit with feedback factors 0 and ±0.0014.

Forced oscillations provide data for determining the **quality factor** (*Q*-factor). First, it equals the ratio of the voltage across the capacitor C at the resonance to the driving voltage, which in our case is the voltage across the resistor R_1. Second, the *Q*-factor is available from the width of the resonance curve: $Q = \omega_0/(\omega_2 - \omega_1)$, where ω_1 and ω_2 are frequencies, for which the voltage across the capacitor becomes $\sqrt{2}$ smaller than at the resonance. Supposing $Q >> 1$, it is easy to derive this relation. The difference $\omega_2 - \omega_1 = \Delta\omega$ is called the **bandwidth** of an LCR circuit. This quantity directly relates to the **decay constant** of free oscillations: $\Delta\omega = 2\delta$. The values of the *Q*-factor derived from the free and forced oscillations are in good agreement. From the voltages across the resistor R_2 and across the resistor R_1, one determines the **phase shift** between the driving voltage and the current in the LCR circuit.

The **transient process** that occurs after an external AC voltage is applied to an LCR circuit is caused by the superposition of forced (frequency ω) and free oscillations (frequency Ω). Immediately after an external AC voltage is applied, the amplitudes of the current through the circuit and of the voltage across the capacitor C start to gradually grow. The reason is that free oscillations also arise in the circuit. At the first instant, they have the same initial amplitude as the forced oscillations but an opposite phase. When the frequencies of the two oscillations are equal ($\omega = \Omega$), the amplitude of the resultant oscillation grows monotonically due to the decay of the free oscillations. If these frequencies differ, the resultant oscillation of the current has an amplitude changing within $I_0(1 \pm e^{-\delta t})$, where I_0 is the steady amplitude of the current. The transient process is as long as the decay of the free oscillations. In this experiment, the *Square wave* voltage of the *Signal generator* is used for amplitude modulation of a function generator tuned close to the resonance frequency of the LCR circuit (Fig. 5). The output of the generator is connected to the resistor R_1. The frequency of the *Signal generator* is set at 125 Hz, and the *Sample rate* is 50 kHz. The records clearly show the influence of the frequency of the driving voltage on the transient oscillations.

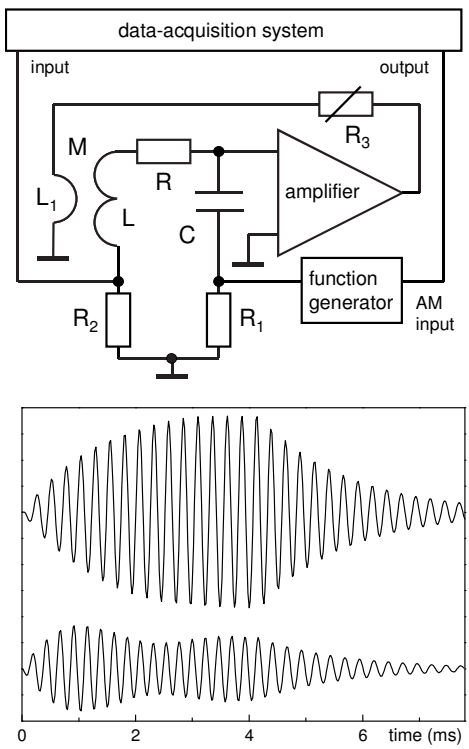

Fig. 5. Schematic of the setup and transients for two frequencies of driving voltage.

3. Experiment with new data-acquisition system

With the new data-acquisition system, the experiments are more convenient and accurate, and the resonance frequency can be enhanced.

Additional equipment: two *Voltage sensors*, two varicaps, coils, AC-to-DC converter, capacitor, resistors.

Free oscillations. The circuit includes an 800-turn coil (SF-8611), a 10 nF capacitor, a decade resistance box R_1 (PI-9588), and a 1 Ω resistor. The resonance frequency of the circuit is nearly 15 kHz. The circuit is connected to the *Output 1* (square waveform voltage, 100 Hz, 5 V) triggering free oscillations in the circuit (Fig. 6). The *Sample rate* is 1 MHz. The start condition is defined as <*Output voltage* rises above 0>, and the run lasts 3 ms. The decay of free oscillations is seen by observing the current in the circuit (input A). *Capstone* fits the data by *Damped sine wave* function, so the decay constant is immediately seen (Fig. 7). For obtaining the phase plane plots, the current is displayed versus the voltage across the capacitor.

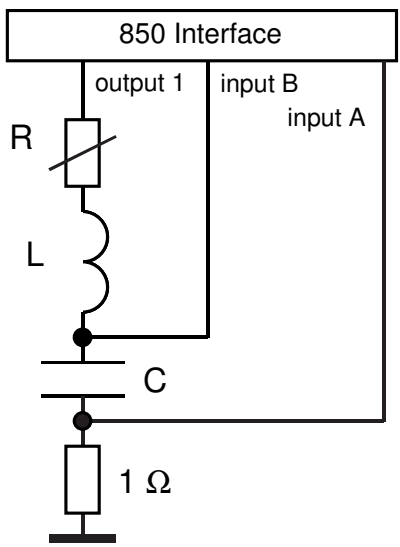

Fig. 6. Schematic of the setup.

LCR circuit with feedback. When observing free oscillations in the circuit, an oscilloscope serves as an amplifier for providing feedback. An additional 400-turns coil (SF-8610) connected to the oscilloscope output through a variable resistor is magnetically coupled to the inductor L of the circuit shown in Fig. 6. The sign of the feedback depends on the polarity of the additional coil, so both

positive and negative feedback can be explored. The time series and phase plane plots are similar to those obtained by changing the resistance in the series LCR circuit shown in Fig. 7.

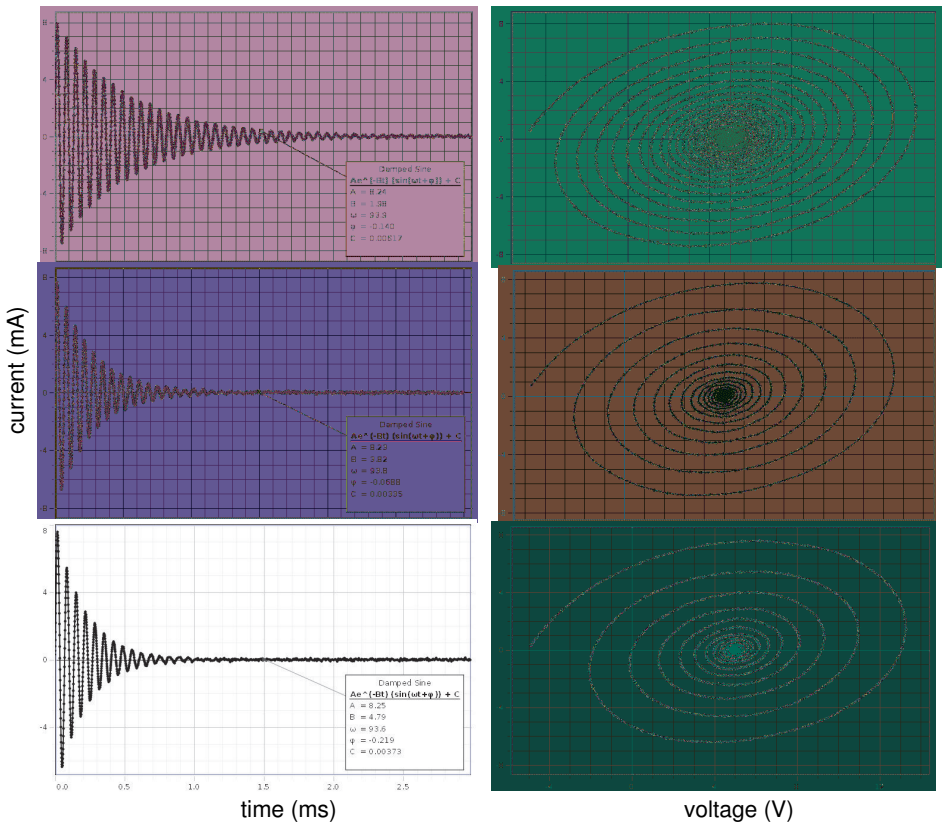

Fig. 7. Free oscillations for R_1 equal to 0, 20, and 80 Ω: time series and phase plane plots.

Resonance curves. The LCR circuit is connected, through a variable resistor, to the *Output 1* operating in the frequency sweep mode (Fig. 8). The frequency sweep between 12 and 18 kHz lasts 100 s; the *Sample rate* is 10 Hz. For displaying resonance curves of the LCR circuit, the voltage across the 1 Ω resistor is fed to an AC-to-DC converter, a Hewlett–Packard 400E voltmeter. The 0.1 V scale of the voltmeter is used, so the amplification of the converter equals 10. *Capstone* displays the resonance curves for different resistances added to the LCR circuit.

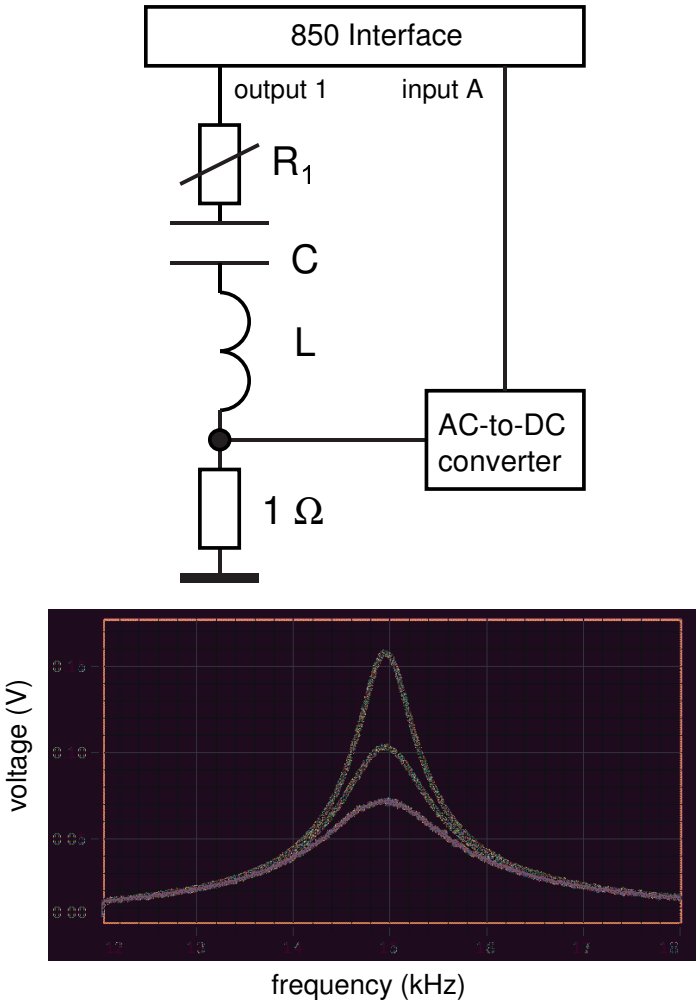

Fig. 8. The setup and resonance curves for R_1 equal to 0, 20, and 40 Ω.

Nonlinear LCR circuit. An LCR circuit becomes nonlinear when varicaps or diodes are put in the circuit. The first circuit is similar to that described by Janssen *et al* (1984). The **varicap** (see Experiment 7.5) is a *p–n* junction having capacitance decreasing with increasing the applied voltage. Two varicaps (BB112 from Philips Electronics) connected in series and in opposition to each other form the capacitor of a series LCR circuit connected to the *Output 1* operating in the frequency sweep mode. The inductor L is an 800-turn coil (SF-8611) (Fig. 9).

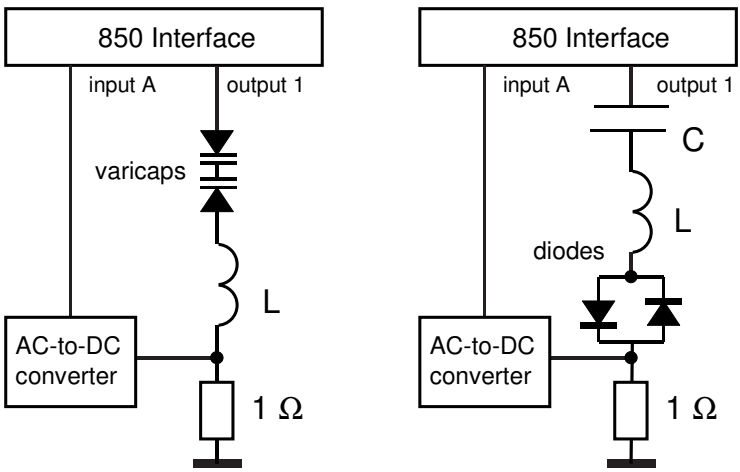

Fig. 9. Nonlinear LCR circuits with varicaps (left) and diodes (right).

The bi-directional frequency sweep between 50 and 90 kHz lasts 400 s; the *Sample rate* is 10 Hz. The current in the circuit is determined through the voltage drop across a 1 Ω resistor measured with an AC-to-DC converter, a Hewlett–Packard 400E voltmeter. The nonlinear behavior of the circuit is seen from its resonance curves when changing the applied voltage. For low voltages, the behavior is quite usual. Under higher voltages, the increase of the resonance frequency is clearly seen.

The second nonlinear circuit reproduces that described by Hellen and Lanctot (2007). Two semiconductor diodes connected in parallel and in opposition to each other are put in series with the inductor and capacitor (800-turn coil, 0.1 μF). Here, we use Schottky's diodes BAT85. The resistance of the diodes strongly depends on the voltage applied to them. In the frequency sweep regime, *Capstone* displays the resonance curves in the range of 2 to 7 kHz (Fig. 10). When increasing the current, the resonance frequency of the circuit increases (Fig. 11). Hellen and Lanctot (2007) explained this phenomenon.

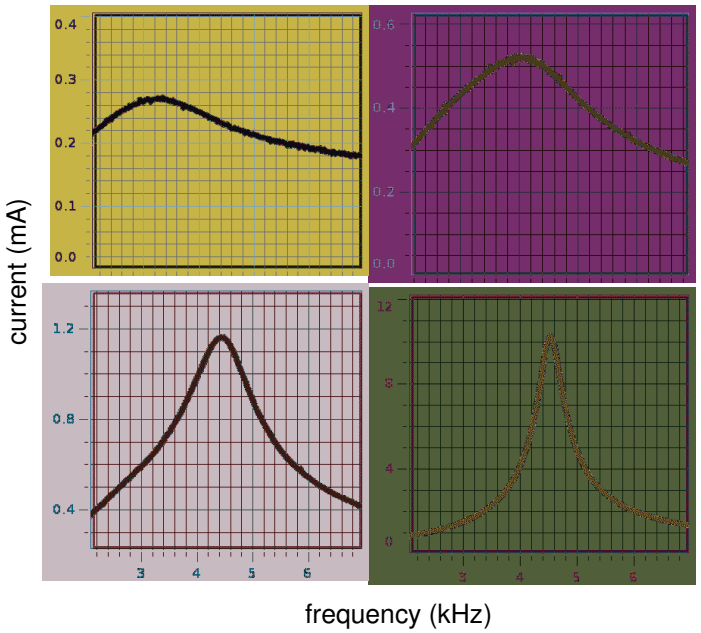

Fig. 10. Resonance curves for different oscillation amplitudes.

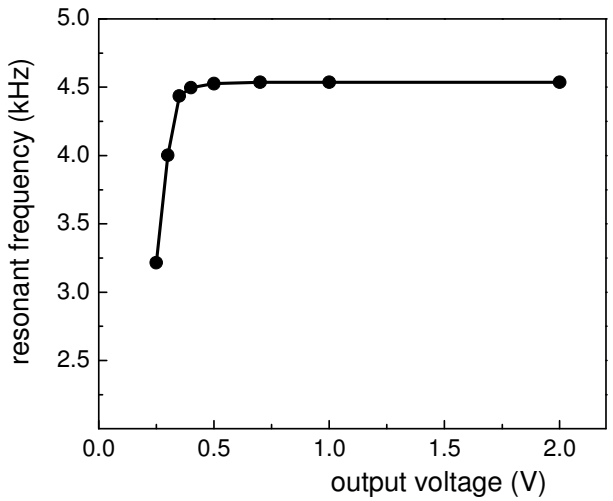

Fig. 11. Resonance frequency versus the voltage applied to the circuit.

4.11. Dielectric constant of gases

The dielectric constant of two gases, nitrogen and carbon dioxide, is determined (Kraftmakher 1996b).

Equipment: oscilloscope, digital frequency meter, vacuum chamber, coil, air capacitor, variable resistor.

The determination of the dielectric constant of gases is based on measuring the resonance frequency of an LC circuit with an air capacitor placed in a vacuum chamber. The capacitor consists of two portions connected in parallel, and the total capacitance amounts to 1030 pF. Continuous oscillations in the circuit arise owing to **positive feedback**. A Kenwood CS-4025 oscilloscope serves as the amplifier. The output voltage of its first channel is fed to the resonance circuit through a variable resistor, 50 kΩ, and to a digital frequency meter of 1 Hz resolution (Fig. 1). In our setup, the oscillation frequency is nearly $f = 270$ kHz. Two hours after switching on the oscilloscope, the drift of the frequency becomes less than 1 ppm per minute. The second channel of the oscilloscope serves for observing the output voltage of the first channel.

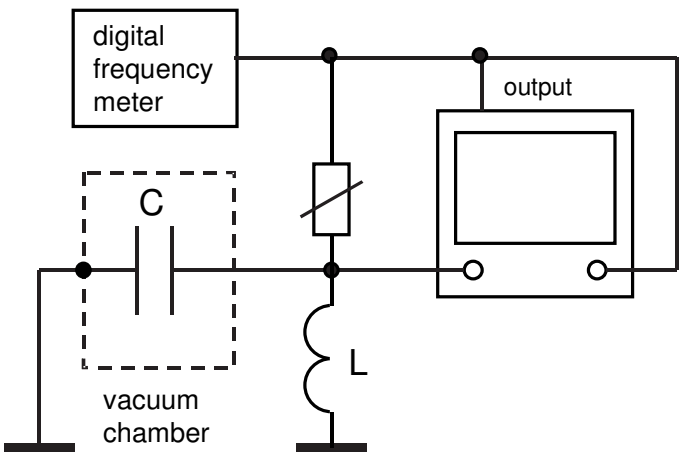

Fig. 1. Schematic of setup for measuring dielectric constant of gases.

Two gases are used, nitrogen and carbon dioxide. A rotary pump pumps out the air in the chamber. After reaching the lowest pressure, the chamber is gradually filled with the gas from a high-pressure vessel. The pressure is measured with a Bourdon gauge with a 0–760 mm Hg scale, 5 mm Hg per division. From the relative change of the frequency (Fig. 2), it is easy to determine the relative change of the capacitance $\Delta C/C$ corresponding to the dielectric constant of the gas at atmospheric pressure:

$$\varepsilon - 1 = \Delta C/C = 2\Delta f/f. \quad (1)$$

For obtaining correct results, it is necessary to take into account the capacitance of the coil itself, of the connecting cables, and of the input of the oscilloscope. This capacitance C_0 is connected in parallel to the main capacitor C. Equation (1) should be modified as follows:

$$\varepsilon - 1 = 2(C + C_0)\Delta f/Cf. \quad (2)$$

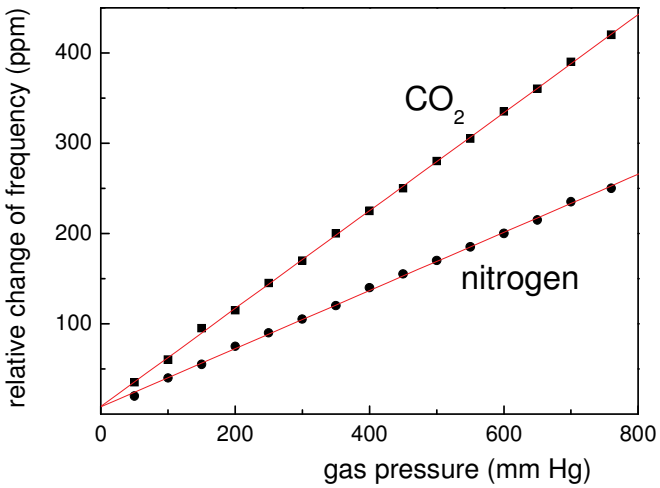

Fig. 2. Relative changes of resonance frequency versus gas pressure for nitrogen and carbon dioxide.

Three methods exist to evaluate the correction factor $(C + C_0)/C$. First, the main capacitance C can be measured beforehand with a capacitance meter. The total capacitance $C + C_0$ is then available from the resonance frequency and the value of L. The inductor has no magnetic core, so that its inductance does not depend on the current or frequency, and any method of measuring the inductance is suitable. The simplest method is the determination of the resonance frequency of a series circuit formed by the inductor and a known capacitor. Second, when a known capacitor is connected in parallel to the circuit, the resonance frequency decreases. The value of $C + C_0$ is available by comparing the two resonance frequencies. Lastly, the ratio of the resonance frequencies measured with and without the main capacitor shows the ratio $(C + C_0)/C_0$. All the methods give close results, and the correction factor for our setup equals 1.20. For nitrogen and carbon dioxide, the results obtained are close to accepted values.

Measurements with air give results definitely higher than the accepted value. This is due to the **humidity** of air. The dielectric constant of saturated water vapor is 1.00022 at 20°C (equilibrium vapor pressure is 17.5 mm Hg) and 1.00037 at 30°C (31.5 mm Hg) (Lide 2008). The sensitivity of the setup is sufficient to determine the air humidity, unless it is very low.

4.12. Lock-in detection

DataStudio demonstrates basic operations of the lock-in detection. Several experiments employing this technique are also described: (i) the determination of the magnetic constant; (ii) the speed of sound in air; and (iii) resonance curves of a single LCR circuit and of coupled LCR circuits.

The lock-in detection is an excellent technique for measuring weak periodic signals in the presence of signals of other frequencies or noise (Horowitz and Hill 1980; Meade 1983; Jones 1986; Dunlap 1988). The signal is measured by a detector controlled by a reference voltage taken from the oscillator governing the process under study. Therefore, the frequency of the expected signal strictly coincides with that of the reference, and the phase shift between them, under steady experimental conditions, remains constant. The output signal of the detector is averaged over a time sufficiently long to suppress irregular pulses caused by signals of other frequencies or noise. The **effective bandwidth** of a lock-in detector is inversely proportional to the averaging time, which is easy to change. Thus, the detector is always tuned to the signal to be measured and has a readily adjustable bandwidth. A lock-in detector contains an electronic switch, which is controlled by the reference voltage and periodically alters the polarity of an incoming signal fed to an integrating RC circuit (Fig. 1). The integration time is much longer than the period of the signal. When measuring a sine wave voltage $V_0\sin(\omega t - \varphi)$, where φ is a phase shift between this voltage and the reference, the average output voltage of the detector equals ($T = 2\pi/\omega$)

$$V_{\text{out}} = \frac{V_0}{T}\left[\int_0^{T/2}\sin(\omega t-\varphi)\,\mathrm{d}t - \int_{T/2}^{T}\sin(\omega t-\varphi)\,\mathrm{d}t\right] = \frac{2V_0}{\pi}\cos\varphi. \qquad (1)$$

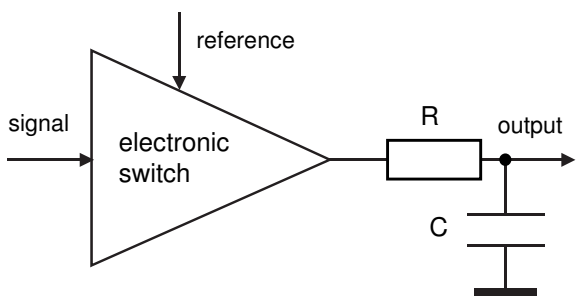

Fig. 1. Basic diagram of lock-in detector. Electronic switch controlled by a reference voltage and integrating RC circuit perform the operations.

A DC voltage at the output appears only when the signal contains a component of the reference frequency. The DC voltage is proportional to the amplitude of this component and to the cosine of the phase shift between it and

the reference (Fig. 2). Lock-in detectors are often called **phase-sensitive detectors**. They incorporate an adjustable phase shifter to achieve maximum output voltages. When the signal contains no components of the reference frequency, the averaged output voltage remains zero. This is because no fixed phase relations exist between the reference and signals of other frequencies or noise.

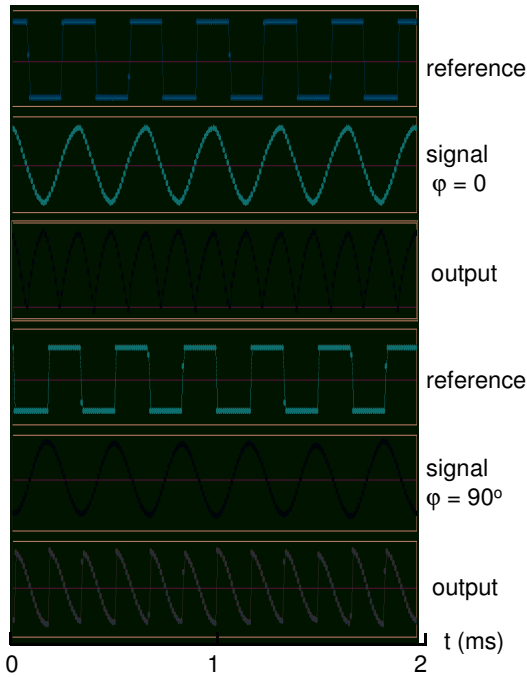

Fig. 2. Diagram showing basic lock-in detection operations for 0 and 90° phase shifts between the signal and the reference.

Amplifiers employing the lock-in detection technique are called lock-in amplifiers. Owing to the narrow effective bandwidth, they provide high noise immunity, so that signals even buried in noise become measurable. Some lock-in amplifiers incorporate two phase-sensitive detectors governed by references with phases shifted by 90°. This makes it possible to measure the signal and its phase shift relative to the reference. Lock-in detectors are also efficient for measuring small phase changes. In this case, the phase shift between the signal and the reference is set to be 90°. Under such conditions, the output voltage of the detector is zero, but the sensitivity to phase changes is the best.

Many student experiments employing the lock-in detection were described. Temple (1975) presented a "student lock-in amplifier" and some experiments with it. Wolfson (1991) reported on an experiment including examining the operation of each section of a lock-in amplifier. Scofield (1994) considered the frequency components of the signal, which are present at various

stages of a lock-in amplifier. Moriarty *et al* (2003) performed lock-in operations with *LabVIEW*. Behringer and Brincat (2004) described a project involving the beam chopping process, which is used for detecting weak optical signals. Spears and Tufillaro (2008) reported on a chaotic lock-in amplifier. Experiments involving lock-in amplifiers were also described by Jewett (1987); Edmondson *et al* (1996); Libbrecht *et al* (2003); Yang (2010).

1. Lock-in detection with *DataStudio*

DataStudio demonstrates the basic lock-in detection operations (Kraftmakher 2006b).

Additional equipment: *Voltage sensor*, photodiode, fluorescent lamp.

For a demonstration of the features of the lock-in detection technique, we use a light-emitting diode fed, through a variable resistor, by a *Square wave* voltage from the *Signal generator*. This 173 Hz voltage serves also as the reference. A photodiode detects the pulses of the light emitted, which strictly follow the feeding current. The output voltage of the photodiode is amplified by an AC amplifier and then measured by the *Voltage sensor*. The *Calculate* tool calculates the product of the reference voltage and the incoming signal, and its average values (*Calculate*/*Statistical*/*Avg*). *DataStudio* thus reproduces the operations of a phase-sensitive detector.

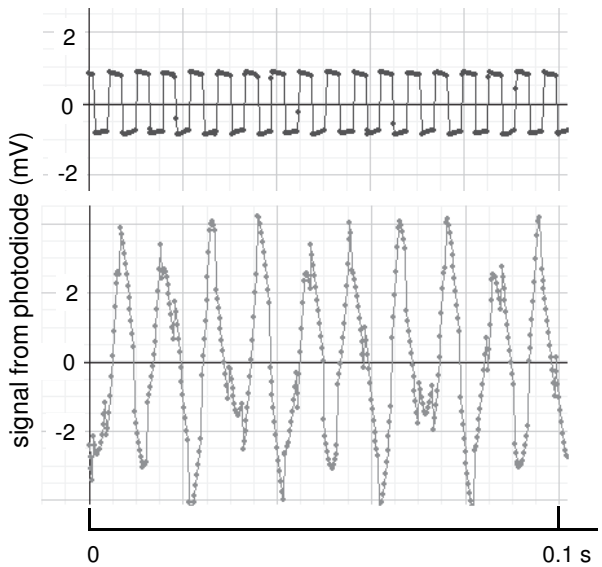

Fig. 3. Signals from the photodiode for a 173 Hz square wave signal and when a five times larger 100 Hz signal is added.

To demonstrate the selectivity of the lock-in detection technique, light from a fluorescent lamp is also directed onto the photodiode. This produces an additional signal containing a 100 Hz component. Results presented here relate to measurements of the locked signal only (173 Hz), and to measurements when an additional unlocked signal (100 Hz) is about five times larger than the locked signal. The *Sample rate* is 4000 Hz, and the averaging of the data lasts 1 s. *DataStudio* displays the signals from the photodiode (Fig. 3) and the results of the lock-in operations (Fig. 4) on the screen of a computer. The importance of the averaging process is clearly seen.

A lock-in detector is capable of measuring a periodic signal even when it is much smaller than signals of other frequencies or noise. The main goal of the demonstration is to show this ability.

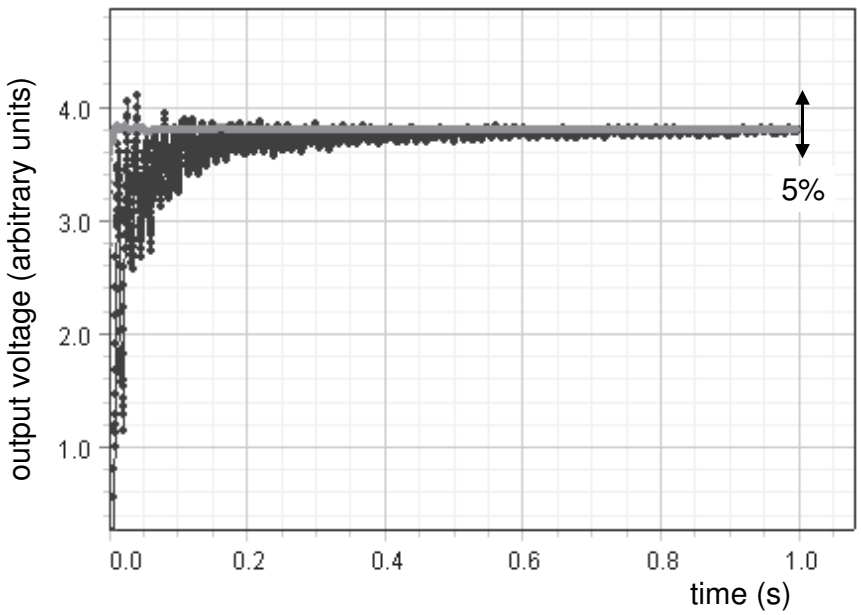

Fig. 4. Averaging process for the 173 Hz locked signal (horizontal line) and when the 100 Hz signal is added.

2. Determination of the magnetic constant

The experiment is based on generating an AC magnetic field and measuring the EMF induced in a probe coil.

Additional equipment: two *Voltage sensors*, four coils.

Equations related to this experiment include the **magnetic constant** μ_0 (the permeability of vacuum). With SI units, the axial magnetic field at the center of Helmholtz's coils is

$$B = 8\mu_0 NI/a\sqrt{125}, \tag{2}$$

where a is the radius of the coil, and I and N are the current in the coils and number of turns in one coil (see Experiment 4.3).

Equation (2) is valid also for an AC current in the coils, $I = I_0 \sin\omega t$. If a small probe coil of cross sectional area A and containing n turns is properly placed between the Helmholtz coils, the amplitude of the EMF induced in this coil, according to Faraday's law, equals

$$V_0 = 8\mu_0 NAnI_0\omega/a\sqrt{125}. \tag{3}$$

An additional coil positioned near the Helmholtz coils supplies the reference voltage, so the signal from the probe is strictly in phase (or opposite to) the reference. Taking Eq. (1) and $f = \omega/2\pi$, we obtain

$$V_{out} = 32\mu_0 NAnI_0 f/a\sqrt{125}. \tag{4}$$

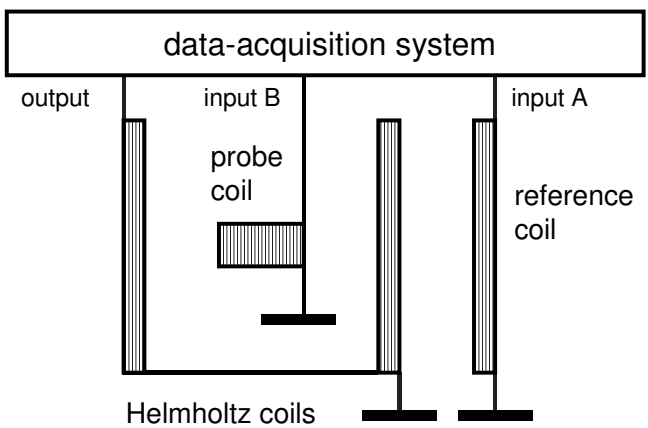

Fig. 5. Setup for determining the magnetic constant.

The setup for the measurements is very simple (Fig. 5). Helmholtz coils (EM-6711, N = 200, a = 10.5 cm) are connected to the *Signal generator*. The current in the coils is taken as the *Output current*. The *Voltage sensor* measuring

the voltage induced in the reference coil is set at *High sensitivity*, so that nearly rectangular pulses of 0.1 V amplitude are stored as the reference. The second *Voltage sensor* measures the AC voltage generated in the probe coil (PHYWE 11006.05, $n = 100$, $a = 2.05$ cm, and $A = 1.32 \times 10^{-3}$ m^2). The *Calculate* tool calculates the product of the reference voltage and the incoming signal and its average values (*Calculate/Statistical/Avg*). The measurements are performed for several frequencies from 0.2 to 1 kHz. Each run lasts 0.05 s, and the *Sample rate* is 20 kHz. The graph of V_{out}/I_0 versus f is a straight line (Fig. 6), and the magnetic constant μ_0 is calculated from its slope.

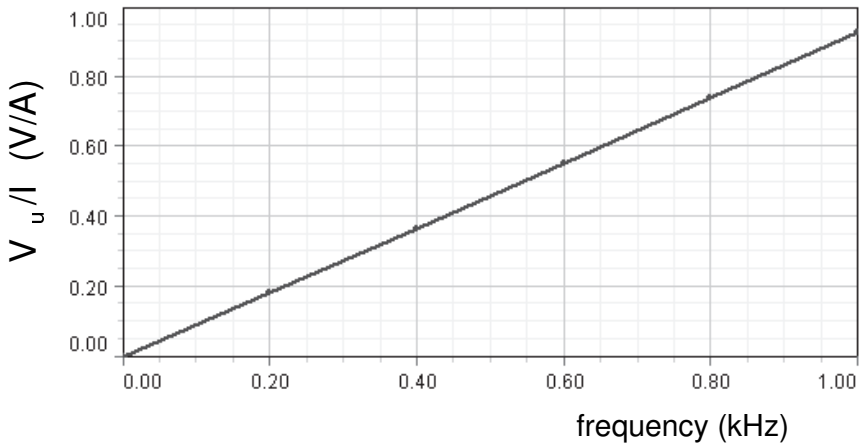

Fig. 6. Dependence of the V_{out}/I_0 ratio on the frequency.

3. Speed of sound in air

The sound wavelength is determined from phase shifts between the voltage driving a loudspeaker and the corresponding signal picked up by the *Sound sensor*.

Additional equipment: *Voltage sensor*, *Sound sensor*, loudspeaker, microphone.

This experiment is well known. The voltage driving a loudspeaker and the corresponding signal picked up by the *Sound sensor* are used to display the Lissajous pattern on the screen of an oscilloscope. Also, the signal from the sensor is measured with a lock-in amplifier, with the loudspeaker driving voltage as the reference (Temple 1975). The sound wavelength is available from the distance between points, for which the output voltage of the lock-in amplifier becomes zero due to 90^o or 270^o phase shifts between the two voltages. A *Sine wave* voltage (5 V) from the *Signal generator* drives the loudspeaker (Fig. 7). The *Voltage sensor* set at *High sensitivity* measures this voltage. When a voltage is measured using this sensitivity range, *DataStudio* restricts the acquired values by 0.1 V. This voltage of nearly rectangular waveform serves as the reference. The *Sound sensor* attached to a slider positioned on a scaled bench provides the acoustic signal. The sound frequency is 3 kHz, and the *Sample rate* is 100 kHz. By using the *Automatic stop* option, each run lasts 2.5 ms thus containing only 7.5 periods of the voltage. This limitation is caused by the insufficient operation rate of the system. For various positions of the *Sound sensor*, the *Calculate* tool calculates the average of the product of the signal and the reference.

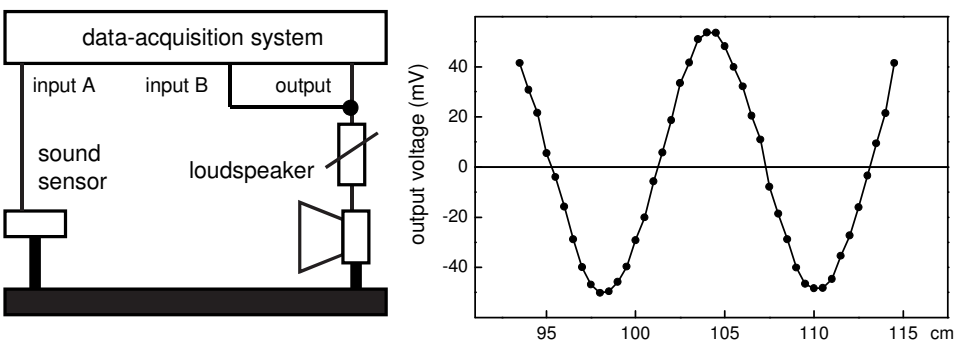

Fig. 7. Schematic of the setup and lock-in detector output voltage versus distance between the loudspeaker and *Sound sensor*.

At the end of each run, the *Digits* tool displays this value, which is then used for plotting it versus the distance between the loudspeaker and the *Sound sensor*. From this graph, the sound wavelength is readily available. In this experiment, absolute values of the signal are of minor importance. With the *Scope*, *DataStudio* displays the Lissajous figures like in experiments with a

common oscilloscope. The advantage of the lock-in detection technique is that the measurements are possible in a noisy environment. From the data, the wavelength is 11.7 cm, so the velocity of sound in air appeared to be 351 m s^{-1}.

With a commercially available lock-in amplifier, determinations of the velocity of sound can be made more convenient and less time-consuming. For this aim, we use an Ithaco 3961 lock-in amplifier. The *Signal generator* feeds a small loudspeaker and provides a reference voltage for the amplifier. The *Motion sensor* is used to continuously measure the position of a small electret microphone, which is mounted on the sensor's reflector (Fig. 8). The reflector rests on the *Dynamics cart* (ME-9430) manually moved toward the loudspeaker on the 120 cm *Dynamics track* (ME-6955). The *Motion sensor* continuously measures the position of the microphone during a run. The signal from the microphone is fed to the lock-in amplifier. The *Voltage sensor* acquires the output voltage of the amplifier, and *DataStudio* displays this voltage versus the distance between the loudspeaker and the microphone (Fig. 9).

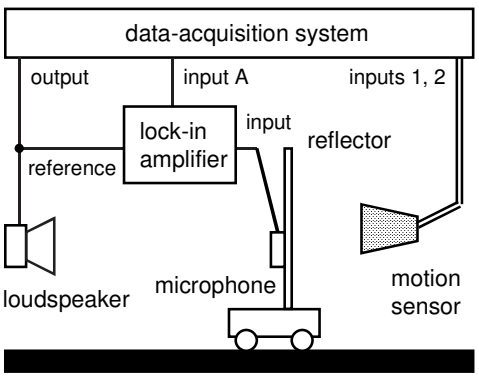

Fig. 8. Schematic of the setup.

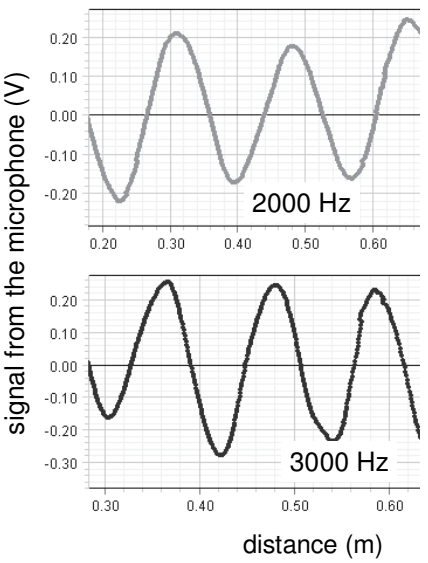

Fig. 9. Lock-in detector output voltage versus the distance.

4. Resonance curves

With a lock-in amplifier, resonance curves are displayed along with the in-phase and out-of-phase components of the input voltage.

Additional equipment: two *Voltage sensors*, lock-in amplifier, coils, resistors, capacitors.

Series LCR circuit. In a series LCR circuit, the current depends on the frequency of an EMF applied to the circuit:

$$I = E/(R^2 + X^2)^{1/2}, \quad (5)$$

where $X = \omega L - 1/\omega C$. At a resonance frequency ω_0, where $X = 0$, the current reaches a maximum value, $I_m = E/R$. The phase shift φ between the EMF and the current obeys the relation:

$$\varphi = \arctan(X/R). \quad (6)$$

At frequencies below the resonance, the current leads the voltage (**capacitive** character of the impedance). Above the resonance, the current lags behind the voltage (**inductive** character of the impedance). With a lock-in amplifier, the **in-phase** and **out-of-phase** parts of the current in the circuit are measured separately.

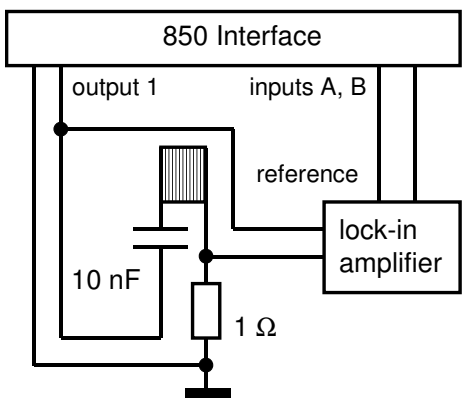

Fig. 10. Schematic of the setup with a series LCR circuit.

The series LCR circuit contains an 800-turn coil (SF-8611), a capacitor $C = 10$ nF, and a 1 Ω resistor (Fig. 10). The *Output 1* operates in the frequency sweep mode: after starting a run, the frequency sweeps from 12 to 18 kHz in 200 s. The voltage across the 1 Ω resistor is fed to the input of an Ithaco 3961 two-phase lock-in amplifier, while the *Output voltage* serves as the reference. The lock-in amplifier provides two output voltages $V_1 = A\cos\varphi$ (in-phase) and

$V_2 = A\sin\varphi$ (out-of-phase), where A is proportional to the voltage amplitude across the 1 Ω resistor, that is, to the current in the LCR circuit. Two *Voltage sensors* acquire the output voltages of the lock-in amplifier during a run, and *Capstone* displays the two voltages versus frequency (Fig. 11). Simultaneously, it calculates the amplitude of the current proportional to $(V_1^2 + V_2^2)^{1/2}$ and the phase shift $\varphi = \arctan(V_2/V_1)$.

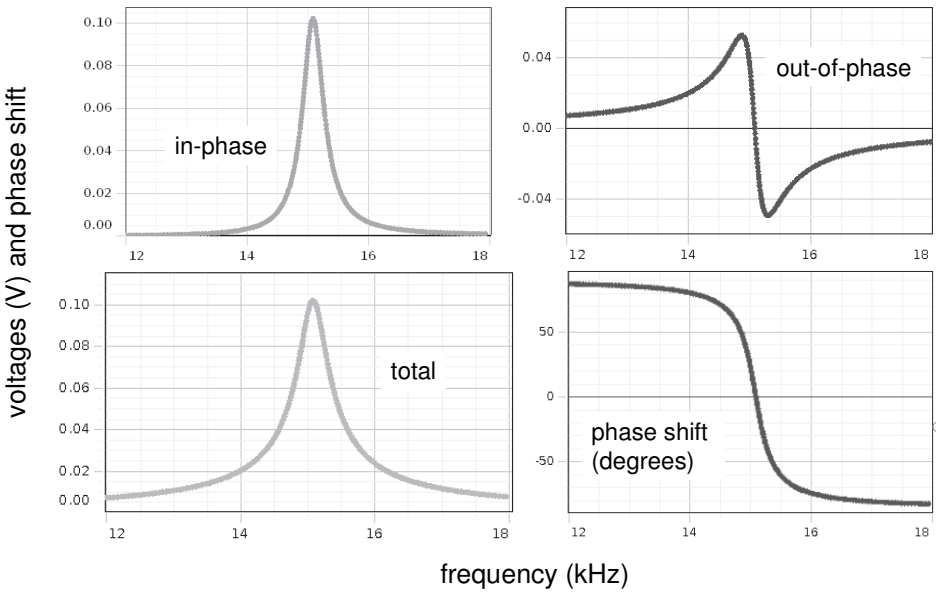

Fig. 11. Output voltages of the lock-in amplifier and phase shift between the input voltage and current, versus frequency.

In a ***parallel LCR circuit***, inductance L and capacitor C are connected in parallel. A variable resistance R_1 is put in series with the inductance (Fig. 12). The current is measured through the voltage across resistor R_2. The resonance occurs when the current through the circuit coincides in phase with the applied voltage. The applied voltage serves also as a reference for the lock-in amplifier.

The experiment with ***coupled LCR circuits*** follows those described by Gamarra et *al* (2007) and Schauber *et al* (2008). Two similar coils, capacitors and resistors connected in series form **magnetically coupled** LCR circuits. The **mutual inductance** of the coils depends on the distance between them. The amplitude and phase of the current in the secondary LCR circuit depend on the frequency and the coupling between the two circuits. The mutual inductances of the coils are given by definitions

$$E_2 = M\mathrm{d}I_1/\mathrm{d}t, \tag{7}$$

$$E_1 = M\mathrm{d}I_2/\mathrm{d}t, \tag{8}$$

where index 1 relates to the primary coil and 2 to the secondary. The mutual inductance M of two coils L_1 and L_2 can be presented as

$$M = k(L_1L_2)^{1/2}, \tag{9}$$

where k is the coefficient of coupling ($0 \le k \le 1$).

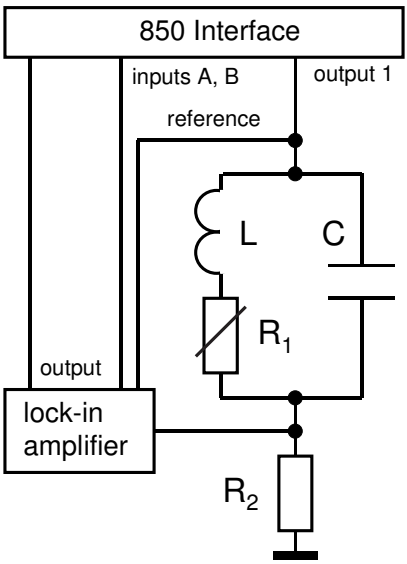

Fig. 12. Schematic of the setup with a parallel LCR circuit.

The setup (Fig. 13) includes two similar 800-turn coils (SF-8611), two capacitors (10 nF), two resistors, and a lock-in amplifier. The *Output 1* of the *850 Interface* operating in the frequency sweep mode feeds the primary circuit. The coupled circuits are positioned on a scaled bench, and the measurements are performed for various distances between the coils.

The current in the secondary circuit is measured through the voltage across a 50 Ω resistor. This voltage proceeds to the input of the oscilloscope (not shown in Fig. 13) and to the dual lock-in amplifier. The voltage applied to the primary circuit serves as a reference for the lock-in amplifier. *Capstone* displays output voltages of the amplifier versus frequency.

For weak coupling, the resonance curves of coupled LCR circuits are similar to that of a single LCR circuit. For strong coupling, however, two maxima arise. The possibility to vary the band-pass frequency range is an advantage of coupled circuits.

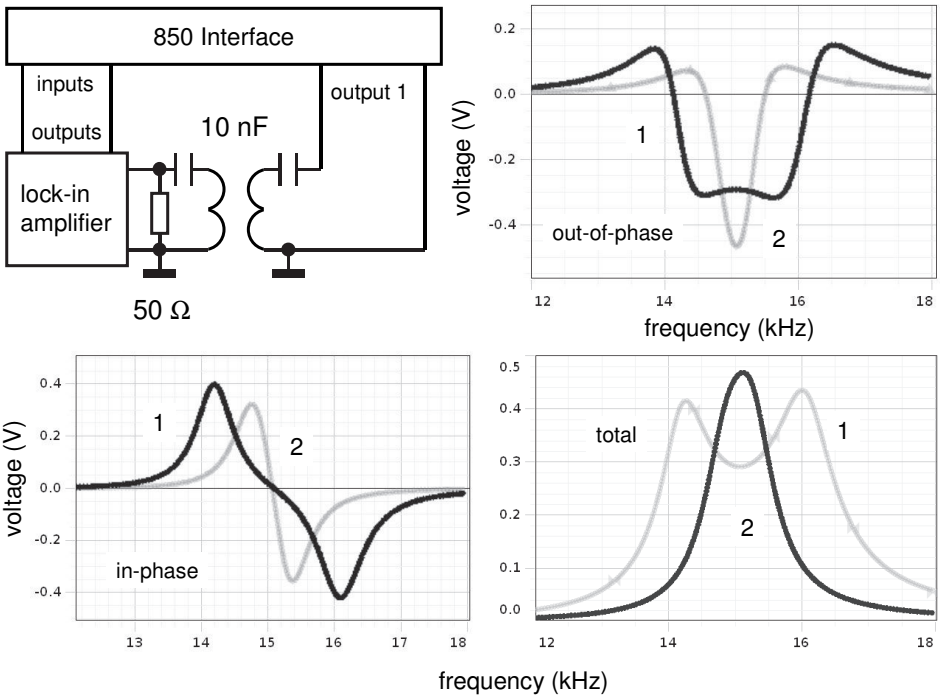

Fig. 13. Schematic of the setup and resonance curves for two distances between the coil edges: 1–no gap, 2–2 cm.

4.13. Correlation analysis

The experiments include four items: (i) the autocorrelation functions for some standard waveforms; (ii) the autocorrelation function for acoustic noise containing minor periodic components; (iii) the correlation functions for acoustic noise and determining the speed of sound in air; and (iv) recovering periodic signals buried in noise.

In contrast to deterministic processes, **random processes** can be described by averaged properties. If all quantities related to a random process are time invariant, the process is called **stationary**. A random process is **ergodic** when its time-averaged properties are equal to the corresponding ensemble-averaged values. Only stationary random processes can be ergodic. In practice, random physical processes are ergodic. The main statistical functions describing random data are the mean and mean square values, **probability density**, **correlation functions**, and **power spectral density**. The correlation analysis is a useful tool in fundamental and applied research (Bendat and Piersol 1971; McPherson 1990).

Because the rate of any physical process is limited, the values of the process at two different times are **correlated**. The autocorrelation function for a random process $X(t)$ defines the statistical influence of the values at one time on the values at another time. An estimate for the **autocorrelation** between the values of X at time t and time $t + \tau$ is given by the product of the two values averaged over the observation time supposed to be sufficiently long:

$$R_x(\tau) = \langle X(t)\, X(t + \tau) \rangle. \quad (1)$$

The quantity $R_x(\tau)$ is a real-valued even function. It has a maximum at $\tau = 0$, which equals the mean square value of $X(t)$. For a periodic function, the autocorrelation function persists over all time displacements τ. For a random process, this function diminishes to zero for large time displacements. The **cross-correlation** function for processes $X(t)$ and $Y(t)$ is

$$R_{xy} = \langle X(t)\, Y(t + \tau) \rangle. \quad (2)$$

This function shows symmetry when $X(t)$ and $Y(t)$ are interchanged:

$$R_{xy}(-\tau) = R_{yx}(\tau). \quad (3)$$

If the means of X and Y are zero and $R_{xy}(\tau)$ is zero for all τ, then the functions $X(t)$ and $Y(t)$ are **uncorrelated**. The autocorrelation function of the sum of two uncorrelated processes is the sum of their autocorrelation functions. This fact provides a way for detecting a periodic signal buried in a random background. The autocorrelation function is measured as follows:

- delay the signal by a time τ.
- multiply the value of the signal at any instant by the value that had occurred at a time τ before.

• average the value of this product over the observation time. As the delay time τ varies, a plot of the autocorrelation function is displayed.

An analog **correlator** accomplishes these operations (Fig. 1). With digital signal processing, the correlation function at the delay time $\tau = r\Delta\tau$ is

$$R_x = (N - r)^{-1} \sum X_n X_{n+r} \qquad (r = 0, 1, 2, ...m), \tag{4}$$

where r is the lag number, and $\Delta\tau$ is the minimum time delay.

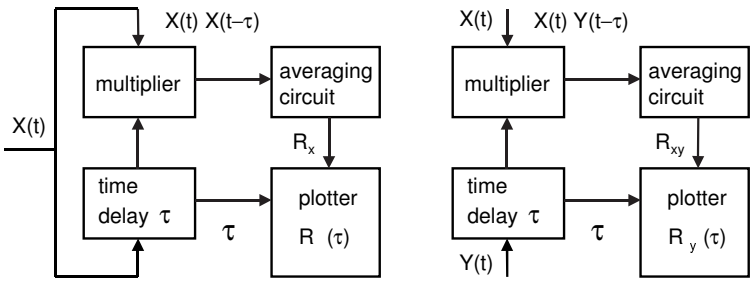

Fig. 1. Block diagram of analog correlators for determining autocorrelation (left) and cross-correlation (right) functions.

For the cross-correlation functions,

$$R_{xy} = (N - r)^{-1} \sum X_n Y_{n+r}, \tag{5}$$

$$R_{yx} = (N - r)^{-1} \sum Y_n Y_{n+r}. \tag{6}$$

The cross-correlation function may be normalized to have values between plus-minus one. This defines the cross-correlation coefficient:

$$\rho_{xy}(\tau) = R_{xy}(\tau)/\sqrt{R_x(0)R_y(0)}. \tag{7}$$

The auto- and cross-correlation functions provide possibility to extract a periodic signal that is even much smaller than the accompanying noise or periodic signals of other frequencies. In this respect, correlation analysis is similar to lock-in detection.

With a microcomputer-based correlator, Miller and Peterson (1982) determined the autocorrelation functions for the intensity of light from a light bulb fed by an AC current, and of laser light scattered by a suspension of small latex spheres. Basano and Ottonello (1986) described demonstrations with a low-cost correlator. The correlation function for the scattered light made it possible to evaluate the mean diameter of the particles. Passmore *et al* (1995) measured the autocorrelation function for the output voltage of a noise generator after it had passed through low-pass filters of various time constants. Tang and Wang (2005) detected weak oscillations of intensity of a fluorescent lamp. Baird (2008) described a magnetometer that uses autocorrelation functions to extract weak signals from background noise.

1. Autocorrelation techniques

The aim of the experiments is to determine autocorrelation functions for some standard waveforms and noise and detect a periodic signal buried in noise (Kraftmakher 2002b).

Additional equipment: *Sound sensor.*

In this experiment, ***autocorrelation functions of some standard signals*** from the *Signal generator* are determined (Fig. 2). The amplitude of all the signals is the same, and their frequency is set to be 40 Hz. The *Output voltage* is measured during 1 s intervals. The *Sample rate* is 5 kHz, so that 5000 measurements are carried out during one run. The results are displayed as the *Graph* of the *Output voltage* versus time and stored in the *Table*. *MATLAB* software evaluates the correlation functions and plots the corresponding graphs. Examples presented here show the main properties of the autocorrelation function for periodic signals: (i) it is a periodic function of the same period; (ii) it persists, without decay, over the entire time of the measurements; and (iii) its maximum equals the mean square value of the signal.

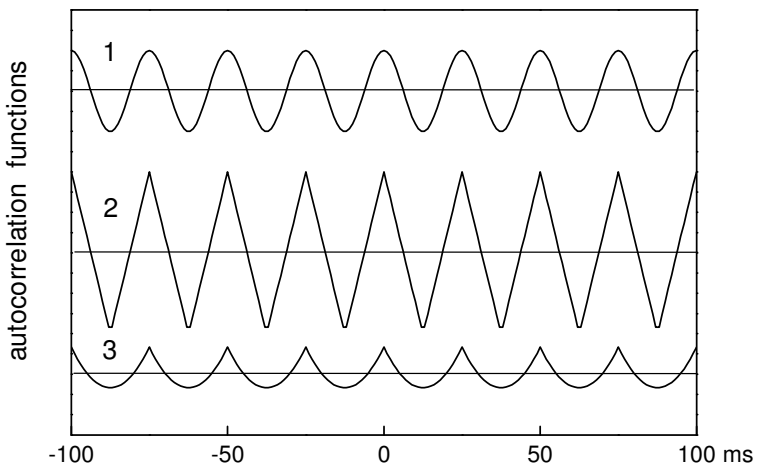

Fig. 2. Autocorrelation functions: 1–sine wave, 2–square wave, and 3–ramp up wave.

Detecting periodic signals. As an example of detecting periodic signals, the autocorrelation function is measured for an acoustic signal produced by an air conditioner and containing noise along with weak periodic components. The *Sound sensor* provides data for the *Graph* and *Table*. The time of the measurements is 1 s, and the *Sample rate* is 10 kHz. The minor periodic components are not seen immediately from the acoustic signal; however, they become evident from the autocorrelation function (Fig. 3).

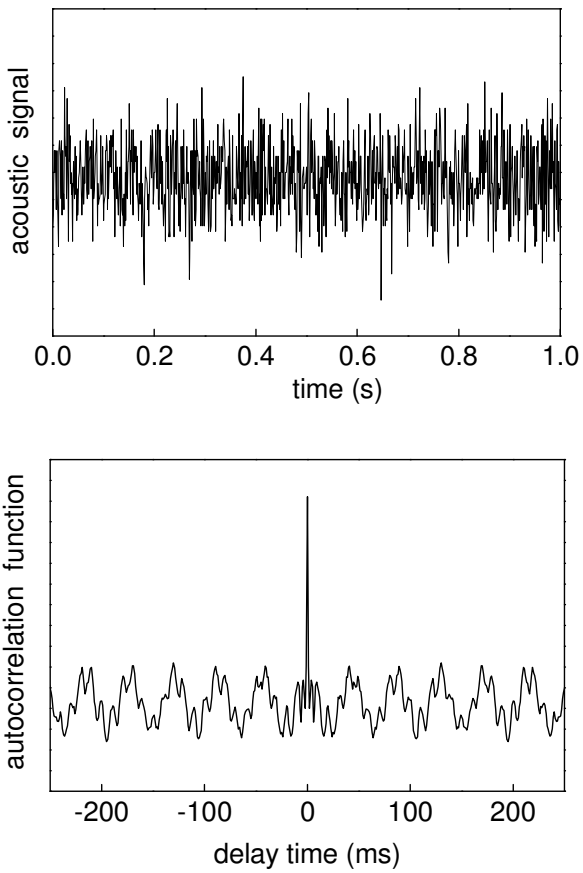

Fig. 3. Acoustic signal produced by the air conditioner and its autocorrelation function.

The autocorrelation function displays a narrow peak at $\tau = 0$ related to the noise and periodic components. The frequency of the main periodic component is nearly 23 Hz, the rotational frequency of the air conditioner's fan. For an induction motor, the rotational speed of its rotor is somewhat lower than that of the magnetic field, 25 Hz. The 23 Hz component is also observable, by means of the *Fast Fourier Transform* tool, in the spectrum of the recorded signal. The second periodic component is caused by a 100 Hz interference in the measuring system. The shape of the noise-related peak provides information about the frequency band of the noise: the narrower the peak, the broader the frequency band.

2. Cross-correlation techniques

The aims of the experiments are to measure the speed of sound in air using acoustic noise and detect periodic signals buried in noise (Kraftmakher 2002b).

Additional equipment: two *Sound sensors*, audio amplifier, noise generator, loudspeaker.

Bendat and Piersol (1971) pointed out three main applications of the cross-correlation technique: (i) the measurement of time delays; (ii) the determination of transmission paths; and (iii) the detection of signals buried in noise.

Speed of sound in air. Measurement of the velocity of sound with acoustic noise demonstrates the determination of time delays with the cross-correlation technique. Two *Sound sensors* are employed, each providing data for the *Graph* and *Table*. A high-gain amplifier (PAR 124A) provides a noise voltage fed to an audio amplifier and then to a loudspeaker (Fig. 4). The frequency band of the noise is 0.5 to 2.5 kHz. The first sensor is located a short distance from the loudspeaker, while the distance between the two sensors is about 1 m.

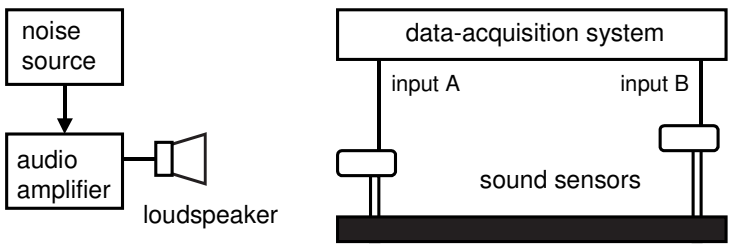

Fig. 4. The setup for measuring velocity of sound with acoustic noise.

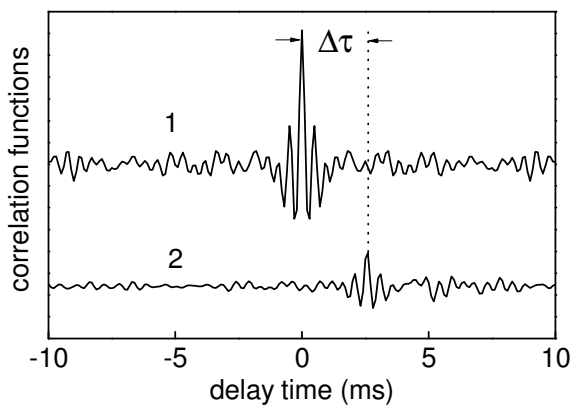

Fig. 5. Autocorrelation function for one signal (1) and cross-correlation function for signals from two sensors (2).

The time of the measurements is 0.2 s, and the *Sample rate* is 10 kHz. Both auto- and cross-correlation functions display narrow peaks related to the noise. The peaks in the autocorrelation functions are seen at $\tau = 0$, but the peak in the cross-correlation function is shifted by $\Delta\tau$ (Fig. 5). The speed of sound in air is available from this shift and the distance between the sensors. This technique often fails in practice because the transmission velocity is frequency dependent. Fortunately, the speed of sound in air is almost independent of frequency.

Recovery of periodic signals buried in noise is demonstrated by means of both autocorrelation and cross-correlation functions. Using a reference signal, the cross-correlation technique becomes similar to the lock-in detection. In the experiment, a 400 Hz sine wave *Output voltage* from the *Signal generator* is added to the noise from a noise generator or a high-gain amplifier. The *Voltage sensor* measures the sum of the noise and the sine signal. Simultaneously, the noise-free output voltage is stored as the reference. The measurement time is 0.1 s, and the *Sample rate* is 10 kHz. For a short measurement time, the cross-correlation technique provides a better signal-to-noise ratio (Fig. 6).

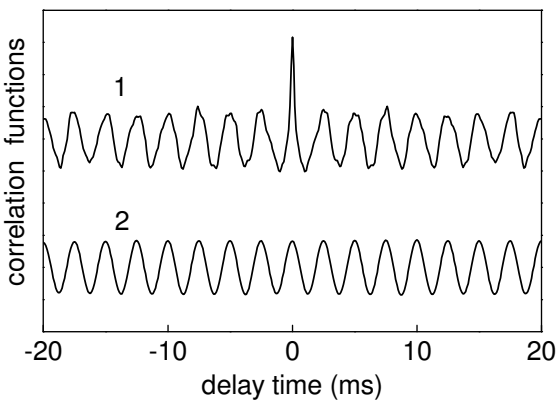

Fig. 6. Recovery of a periodic signal with autocorrelation (1) and cross-correlation (2) techniques.

Detection of weak random signals. An important application of the cross-correlation technique is the detection of a weak random signal masked by extraneous noise, for example, when measuring a noise voltage smaller than the inherent noise of an amplifier employed. In this case, the noise $X(t)$ is amplified by two similar amplifiers. The inherent noises of the amplifiers are uncorrelated, and the cross-correlation function of the two output voltages coincides with the autocorrelation function of the common input noise. At $\tau = 0$, the cross-correlation function equals $\langle X^2 \rangle$, the mean square value of the input noise.

Optics and Atomic Physics

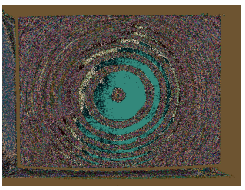

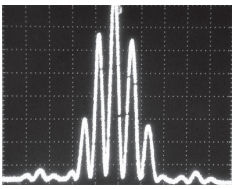

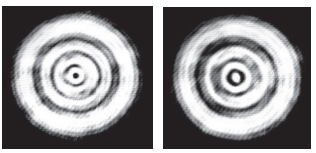

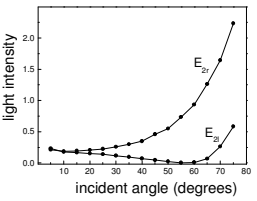

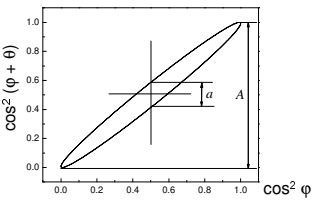

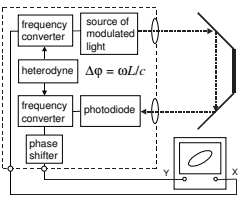

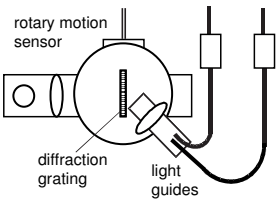

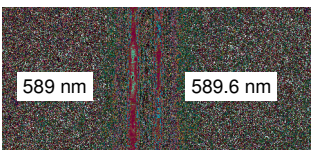

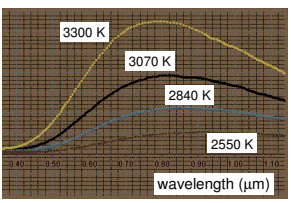

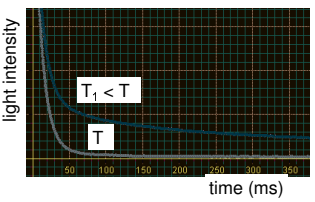

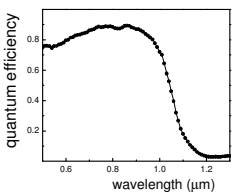

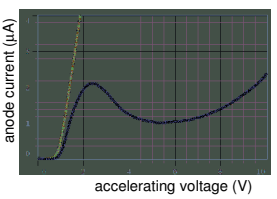

5. Optics and Atomic Physics 285

5.1. Interference of light

Three simple experiments are considered: (i) Newton's rings; (ii) the reflection from a "dusty" mirror; and (iii) the interference filters.

AIP Emilio Segrè Visual Archives
Christiaan Huygens (1629–1695)

AIP Emilio Segrè Visual Archives
Isaac Newton (1643–1727)

Additional equipment: *Radiation sensor*, He–Ne laser, lens, video camera, beam splitter, thin mirror, "dusty" mirror, thin film on a glass.

Only a part of numerous papers devoted to the interference of light is mentioned here. Hilton (1962) designed a Fabry–Perot interferometer. Dutton *et al* (1964) described several demonstrations with a gas laser. De Witte (1967) considered interference in scattered light, a phenomenon observed by Newton and explained by Young and Herschel. Pontiggia and Zefiro (1974) and González *et al* (1999) also carried out similar experiments. Hunt and Karl (1970) performed a demonstration experiment with polarized light beams. Several variants of this experiment were presented by Pontiggia (1971); Pescetti (1972); Mallick (1973); Henry (1981). Brown and Rome (1972) demonstrated the interference and coherence of light. A similar experiment was performed and considered by Laud *et al* (1973). Woolsey (1973) developed experiments with a modified Jamin interferometer. Maddox *et al* (1976) described a demonstration of interference due to the superposition of reflections from the outer and inner surfaces of a cylinder glass. Moloney (1974) and Leung and Lee (1991) demonstrated Newton's rings with a laser and a single lens. With a Fabry–Pérot interferometer, Zajonc (1982) observed the isotope split between hydrogen and deuterium emission lines, and Steinhaus (1983) observed the structure of the red line of a He–Ne laser. To observe interference patterns with an oscilloscope, Bacon and

Varga (1985) employed a rotating mirror and a photodiode. Aghdaie (1988) described an electronic fringe-counting circuit for experiments on interference. Verovnik and Likar (1988) observed interference of light from two independent lasers. With a simple Fabry–Pérot interferometer, Amato *et al* (1991) measured the isotope shift in the hydrogen-deuterium Balmer spectrum. The ratio of the proton mass to the electron mass was determined with better than 1% accuracy. Andrés and Contreras (1992) designed optical fiber interferometers. Louradour *et al* (1993) observed interference fringes between two separate lasers. Two independent lasers synchronously emit picosecond light pulses superimposed at a screen. The fringes are observable directly by eye without a need for additional temporal resolution. Boyd *et al* (1996) reported a series of experiments with a homemade scanning Fabry–Pérot cavity. Perkalskis and Freeman (1996) built Fabry–Pérot etalons suitable for demonstration and laboratory experiments. Derby and Kruglak (1996) performed an interference experiment with a laser or a high-pressure mercury arc and a thin sheet of mica or a thin glass plate. Basano *et al* (1997) observed interference fringes from two independent He–Ne lasers. Later, Basano and Ottonello (2000) used for this experiment independent laser diodes. Catunda *et al* (1998) described a simple experiment to determine the wavelength of light. Rahimi and Baker (1999) reported on a three-dimensional display of interference patterns. Razdan and Van Baak (2002) considered and demonstrated the optical heterodyne detection. Grove (2003) designed a low-cost scanning Fabry–Pérot cavity with a piezoelectric stack. Alanis *et al* (2004) used an interferometer for measuring small displacements. Wheeler *et al* (2004) determined visibility of thin-film interference fringes. Vannoni and Molesini (2004) and Vannoni *et al* (2008) presented experiments on speckle interferometry. Fletcher and Orzel (2005) described a low-cost Fabry–Pérot interferometer. See also Fortin (1970); Collett (1971); Ferguson (1984); Kilty (1997); de Izarra (2001); Hinrichsen (2001); Kanseri *et al* (2008).

Newton's rings. It is easy to demonstrate Newton's rings with a laser. However, the classical arrangement for this aim including a glass plate and a plano-convex lens is not convenient in this case because additional interference patterns arise due to the long coherence length of the laser beam. With a laser, it is better to use a single lens (Moloney 1974; Leung and Lee 1991). Light beam of a laser reflected from the two surfaces of the lens can be superimposed on the screen to produce Newton's rings. The intensity in the center of the rings depends on the thickness of the lens, and it can be changed by slightly tilting the lens. In our setup (Fig. 1), a thin lens rests on a laboratory jack. It is useful to show the two beams not overlapped on the screen and then to adjust the position of the lens to superimpose the beams for observing Newton's rings. The equation for the ring radii includes the refraction index of the lens. The ring number is proportional to the radius squared. Many rings are seen on the screen (Fig. 2). The rings can be demonstrated with a video camera and a monitor.

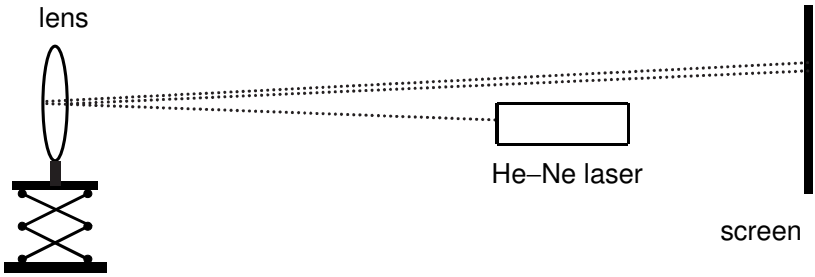

Fig. 1. Setup for demonstrating Newton's rings with a single lens.

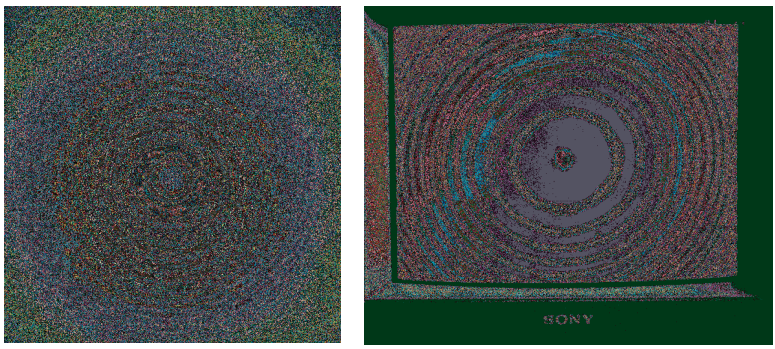

Fig. 2. Newton's rings obtained with He–Ne laser and single lens are seen on a screen and displayed with video camera and monitor.

"Dusty" mirror. This experiment demonstrates the scattered-light interference (Hecht 1998). A laser beam falls onto a back-silvered mirror, whose front side is covered by a thin layer of dust (Fig. 3). De Witte (1967) gave the theory and details of this experiment. At normal incidence, the interference pattern is a series of concentric rings of radii r_n:

$$r_n \cong [nm\lambda a^2 b^2 / d(a^2 - b^2)]^{1/2}, \quad (1)$$

where n is the refraction index of the glass, m is the ring number, λ is the wavelength, a and b are the distances from the mirror to the light source and to the screen, and d is the thickness of the mirror. In our case, the glass is 0.12 mm thick, $a \approx b$, and the interference fringes are seen at a short distance from it.

Other demonstrations of interference include well-known arrangements for obtaining coherent light beams (Fig. 4). Also, it is easy to demonstrate the use of interference filters. The transmittance spectrum of a thin film deposited on a glass plate demonstrates the use of interference filters (Fig. 5). The spectra including the near infrared region were obtained with the *Radiation sensor* (TD-8553).

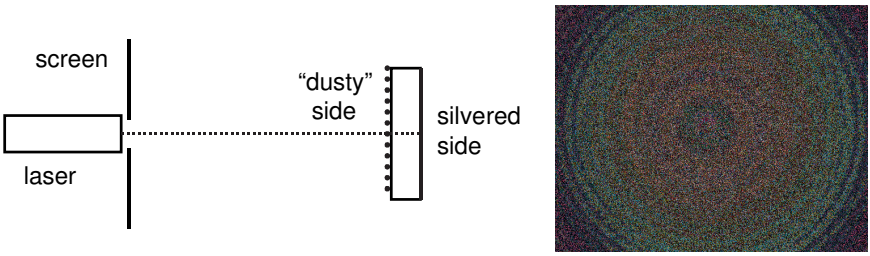

Fig. 3. Schematic of the setup and interference fringes from "dusty" mirror.

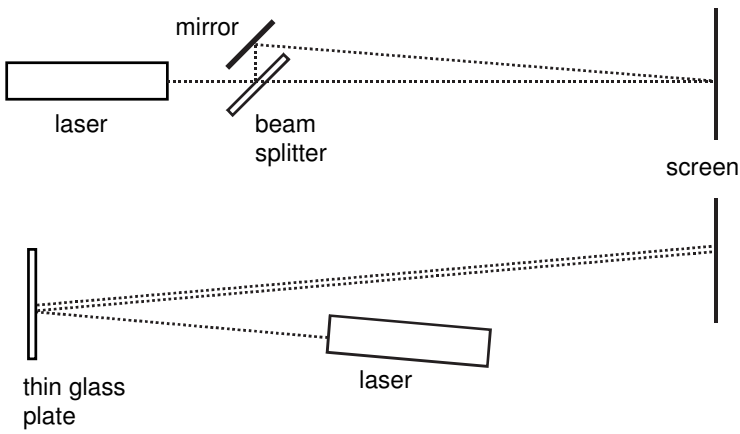

Fig. 4. Schematic of setups for observing interference fringes.

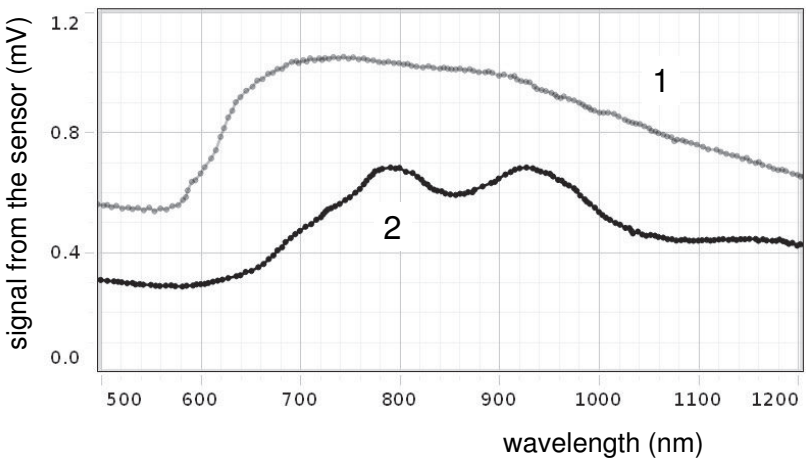

Fig. 5. The maxima in transmittance spectrum of a thin film (2) demonstrate the use of interference filters. The spectrum of incident light is also shown (1).

5.2. Diffraction of light

The experiments include (i) the single- and double-slit diffraction; (ii) the diffraction by narrow obstacles; and (iii) Fresnel's diffraction and Poisson's spot.

AIP Emilio Segrè Visual Archives,
Brittle Books Collection
Thomas Young (1773–1829)

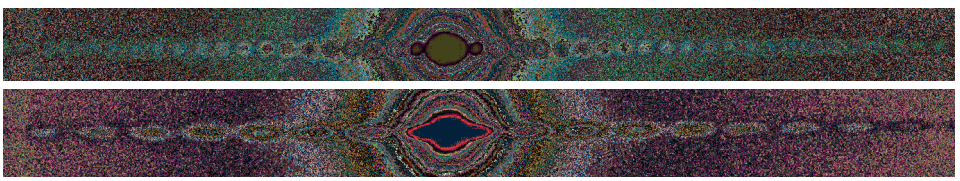

Laboratory experiments and lecture demonstrations on the diffraction of light are described in many papers. Using a He–Ne laser, Whiteside (1965) presented several such experiments. Schawlow (1965) demonstrated measurements of the wavelength of light with a ruler. The beam of a He–Ne laser passes nearly parallel to and just above a ruler. The light reflected by the ruler produces diffraction patterns on a screen. Haskell (1970) observed diffraction patterns of a single slit on the screen of an oscilloscope. For this aim, the slit was swept through the laser beam with a motor. Hunt and Karl (1970) described a double-slit diffraction experiment with polarized light. Moen and Vander Meulen (1970) observed Fresnel's diffraction from a wire. Boyer and Fortin (1972) recorded Fresnel's diffraction patterns from a thin wire with a photoresistor mounted on a traveling microscope. Kang and Young (1972) observed diffraction by ultrasound in liquids. Pescetti (1972) and Mallick (1973) considered a double-slit

experiment with polarized light. From diffraction experiments, Rinard (1974) determined the size of particles. Curry and Schawlow (1974) observed diffraction patterns and measured the diameter of a hair. Pipes and Dutton (1976) and Kang and Yap (1979) recorded diffraction patterns with an X-Y recorder. Rinard (1976) described impressive diffraction experiments with circular objects, an obstacle and an aperture, about 2 cm in diameter. The light source, a He–Ne laser, and the screen were placed 20 m from the objects. Hwu (1977) observed a diffraction pattern produced by a hair. To display diffraction patterns, Lazzeri *et al* (1978) employed a linear array of photodiodes. Using a He–Ne laser, Fortin (1979) demonstrated the effect of the polarization of light on a double-slit diffraction pattern. The patterns strongly depend on the polarization of the incident laser beam. Henry (1981) also described a double-slit experiment with polarized light. To obtain a sufficient separation between two coherent beams, he used a diffraction grating as a beam splitter. Moloney (1983) used punchcard slits for a double-slit experiment. Soundranayagam *et al* (1983) observed diffraction patterns by means of a photoresistor connected to a microcomputer. For the same purpose, Wesley and Behof (1987) used a self-scanning photodiode array. Fischbach and Bond (1984) described an experiment on diffraction of light by opaque particles of 10 to 100 μm size. Racey *et al* (1985) considered the effect of light polarization on the diffraction pattern of thin wires. Burch (1985) considered Fresnel's diffraction by a circular aperture. Klein (1986) displayed diffraction patterns with a small mirror glued to the vibrating part of an electric razor. With the vibrating mirror, the diffraction pattern is swept across the entrance slit of a photodiode connected to an oscilloscope. Using a photodiode and a rotating cubic mirror, Bianchetti and Ganci (1986) displayed diffraction patterns on the screen of an oscilloscope. Leung (1986) determined the wavelength of light in water. A diffraction grating was mounted on the inner surface of a rectangular glass tank and illuminated with a He–Ne laser. After measurements in air, water was added to the tank until the grating was completely submerged. Using a He–Ne laser, Gilliar *et al* (1987) demonstrated the similarities and differences between the diffraction from single slits and fibers. Bennett (1990) reported on a computer-assisted diffraction experiment. Light from a He–Ne laser was modulated with a chopper before illuminating the diffracting aperture. An objective lens was used to form an image of the aperture over a distance to give a magnification of about 100. A photomultiplier attached to a movable base was placed at the image plane. A lock-in amplifier measured its output signal. Dodds (1990) presented some diffraction experiments and related computer simulations. An optical fiber was used to transfer the light to a photometer. Greenler *et al* (1990) considered the diffraction by fine cylindrical fibers. Best agreement with single-slit theory was found for metal wires of diameters larger than a few micrometers, with light polarized parallel to the axis of the wire. Clark and Demkov (1991) presented a program for producing zone plates on laser printers. Murphy and Egan (1993) discussed a new technique for solving Fresnel's diffraction problems. Van der Gracht (1994) described a simple method for demonstrating Fraunhofer's

diffraction. Laser printers were used to create the input and diffraction patterns, which can be viewed without the use of a laser or lenses. Macdonald and O'Leary (1994) measured the wavelength of a He–Ne laser and the diameter of a hair with a steel ruler. De Izarra and Vallee (1994) used a linear coupled charge device photodiode array in optics experiments, in particular, for a quantitative study of Fraunhofer's diffraction. With a 4.90 μm slit, Mayes and Melton (1994) obtained diffraction patterns for angles of incidence between 0 and 45°. Moreno *et al* (1997) considered various kinds of zone plates designed to solve the problem of obtaining a limited number of foci with higher efficiency. Wein (1999) used a video technique for the observation and quantitative analysis of diffraction phenomena. Ganci (2005) considered a case of Fraunhofer's diffraction patterns obtained by a not plane wave, for which the application of Babinet's principle requires caution. Barik *et al* (2005) observed diffraction of light by interfering liquid surface waves. Vollmer (2005) considered the position of diffraction spots upon rotation of a transmission grating. Lucke (2006) presented Rayleigh–Sommerfeld's solution to diffraction problems. Ramil *et al* (2007) used digital images for analysis of diffraction phenomena. Hoover *et al* (2010) demonstrated Poisson's spot with magnetic levitation of a steel ball. Kuhn and Vogt (2012) used infrared remote control as a source of light for diffraction experiments.

1. Single- and double-slit diffraction

DataStudio displays single- and double-slit diffraction patterns.

Additional equipment: *Light sensor*, *Rotary motion sensor* with *Linear translator*, diffraction objects, optics bench, He–Ne laser or laser diode.

Diffraction is a phenomenon peculiar to all wave processes. Diffraction of light, along with interference, made a clear proof of the wave nature of light. This was proved despite Newton's theory that light is a stream of particles. Diffraction is observed when a point source of light illuminates a screen, and an aperture or obstacle is put on the path of the light. If the distances from this object to the source of light and to the screen are very large compared to the dimensions of the object and the light wavelength, **Fraunhofer's diffraction** is concerned. If these distances cannot be regarded as very large, this is **Fresnel's diffraction**.

Here, an example of Fraunhofer's diffraction is considered. The wave front of the light is plane, and after diffraction it is brought to a focus at the receiving screen by a lens (Tenquist *et al* 1969–1970). The intensity of a single-slit diffraction pattern is given by

$$I(\Theta) = I_m(\sin\alpha)^2/\alpha^2, \quad (1)$$

where I_m is the maximum intensity, $\alpha = (\pi a/\lambda)\sin\Theta$, a is the slit width, λ is the wavelength, and Θ is the diffraction angle. Thus the minima of the diffraction pattern are the places where $a\sin\Theta = n\lambda$ ($n = \pm1, \pm2, \ldots$).

The intensity of a double-slit diffraction pattern is

$$I(\Theta) = I_m(\cos\beta)^2(\sin\alpha)^2/\alpha^2, \quad (2)$$

where $\beta = (\pi d/\lambda)\sin\Theta$, and d is the distance between the slits.

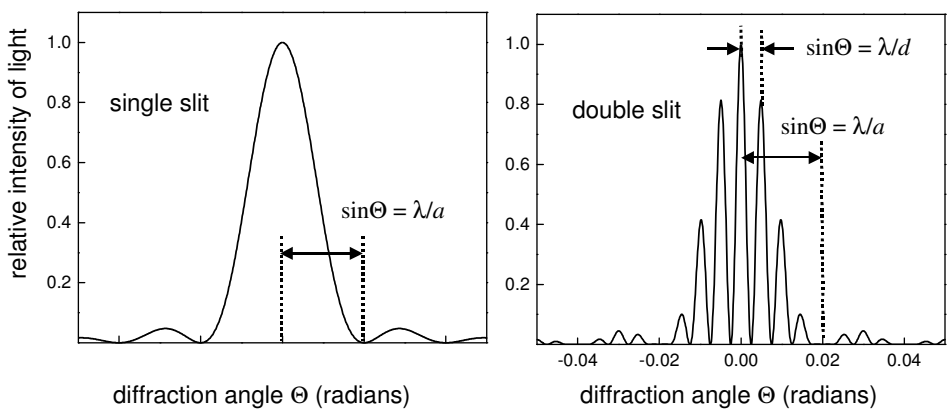

Fig. 1. Diffraction patterns calculated with Eqs. (1) and (2). For the example, $a = 50\lambda$, $d = 200\lambda$.

Taking into account only the term containing cosβ, the maxima of the diffraction pattern should be the places where $d\sin\Theta = m\lambda$ ($m = 0, \pm1, \pm2, \ldots$). The real maxima of the pattern are given by this relation but modulated by the single-slit pattern. Using the above equation, one determines both the width a of the slits and the distance d between the centers of the two slits (Fig. 1).

Diffraction patterns are automatically recorded for some diffraction objects. A He–Ne laser or a laser diode is used as a source of light. The *Light sensor* manually moved along the diffraction pattern measures its intensity versus distance, which is determined by the *Rotary motion sensor* with the *Linear translator* (OS-8535). The width of the entrance slit of the *Light sensor* should be as small as possible. The *Light sensor* is placed 1 m apart the diffraction objects, so that its displacement equals the diffraction angle in radians. The light intensity is displayed versus the diffraction angle (Fig. 2).

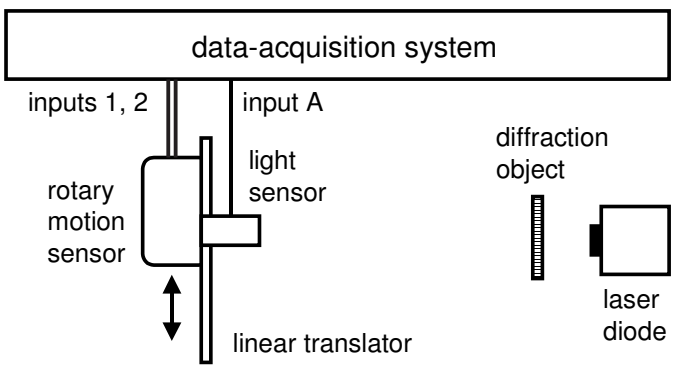

Fig. 2. Schematic of the setup (view from above).

With PASCO diffraction objects (OS-9165), the single- and two-slit diffraction is observed. As predicted by Eq. (1), the width of the diffraction pattern from a single slit is inversely proportional to the width of the slit (Fig. 3). Some measurements were done using a screw mechanism for moving the *Light sensor* along the diffraction pattern. A DC motor operates the mechanism, and the *Rotary motion sensor* measures the rotation angle. The screw parameter is 1.75 mm, so the resolution of the system is nearly 1.2 μm (0.25° resolution of the *Rotary motion sensor*). From the data, the relation between the one-slit and two-slit diffraction patterns is evident. The decrease of intensities in the double-slit diffraction well correspond to the minima in the one-slit diffraction (Fig. 4).

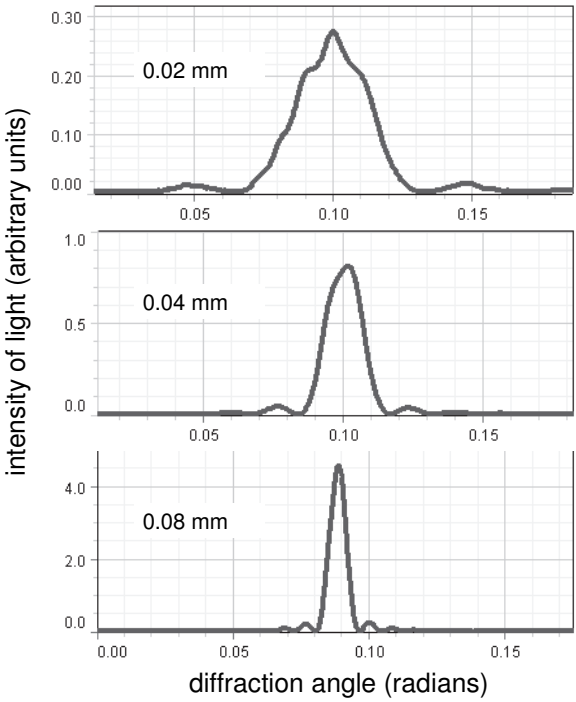

Fig. 3. Patterns of single-slit diffraction for various widths of the slit.

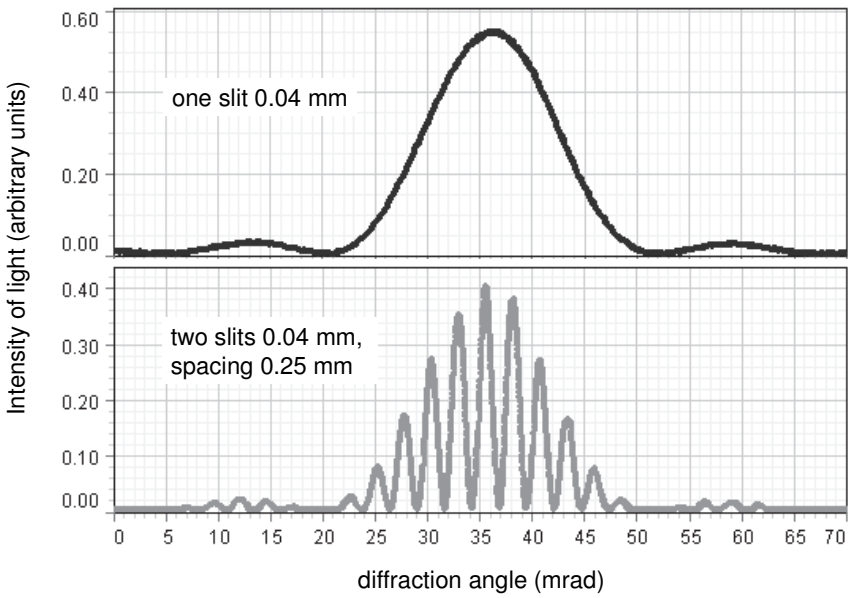

Fig. 4. Patterns of single- and double-slit diffraction.

Experiment with DSO. Quantitative observations of the diffraction of light are usually performed with a data-acquisition system. Displacements of a light sensor are measured with a mechanical device or an ultrasonic ranger. For translating rotations or displacements into electric voltages, some sensors use a potentiometer. For performing the measurements with a DSO (Kraftmakher 2012f), our homemade sensor employs a common 10-turn potentiometer with a wheel on its axle (Fig. 5). The potentiometer is fixed on a plate, together with a photodiode, and is connected to a DC source. The diameter of the potentiometer exceeds that of the wheel, so the wheel relies on the edge of a wooden bar. The voltage applied to the potentiometer is 15 V. The photodiode is a United Detector Technology PIN-10D model. Its sensitive area is a circle of nearly 1 cm in diameter. A mask posed on the photodiode opens a narrow vertical slit, which defines the spatial resolution of the sensor. When manually moving this one-wheeled cart, the output voltage of the potentiometer follows the rotation of the axle of the potentiometer. This voltage is fed to the X-input of a DSO, while the voltage across the load of the photodiode is fed to the Y-input. The distance between the diffraction object and the light sensor is 390 cm. A 5 mW He–Ne laser serves as the light source. Two diffraction objects are used: one slit of width $a = 0.04$ mm and two slits of the same width and distance $d = 0.125$ mm (OS-9165, slides number 1 and 3). For the sensor, the maximum displacement accessible with the 10-turn potentiometer is 80 cm. The data given in the text and Fig. 5 are sufficient to calculate values of a and d.

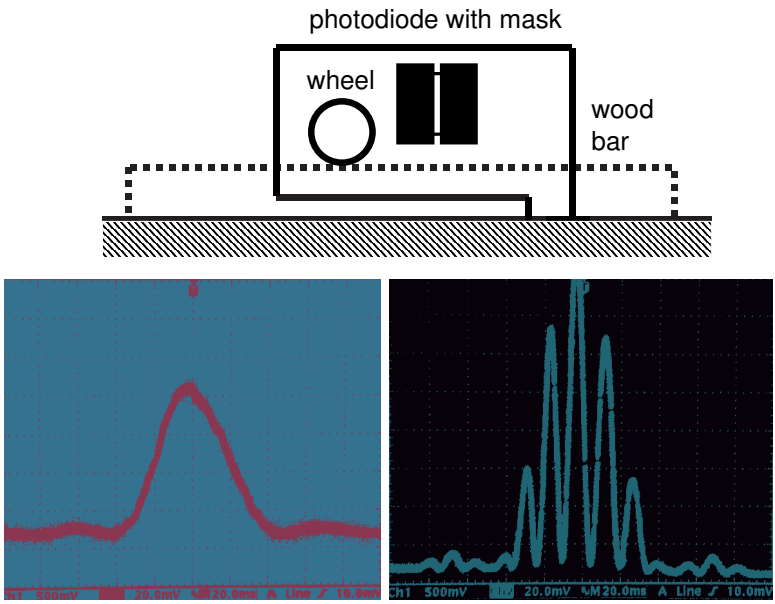

Fig. 5. Schematic of the light sensor and single- and double-slit diffraction patterns on DSO screen.

2. Narrow obstacles

Diffraction patterns produced by wires of different thickness are displayed.

Additional equipment: *Light sensor*, *Rotary motion sensor* with *Linear translator*, He–Ne laser, wires.

Two diffraction screens are said to be complementary when the transparent regions on one exactly correspond to the opaque regions on the other and vice versa (Tenquist *et al* 1969–1970; Hecht 1998). For such diffraction objects, **Babinet's principle** states that the diffraction patterns are identical. This means that the diffraction pattern obtained with a narrow obstacle is the same as the pattern formed by a slit of equal width. Diffraction patterns produced by a 0.2 mm and 0.1 mm wires and a hair obtained with medium and high sensitivity of the *Light sensor* are presented here (Fig. 6).

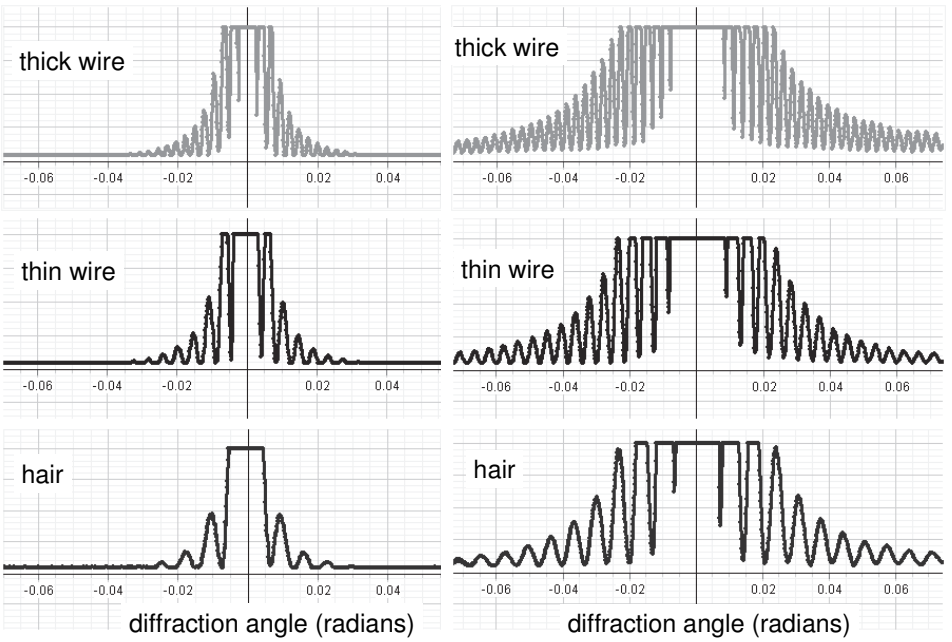

Fig. 6. Diffraction patterns from two wires and a hair obtained with medium (left) and high (right) sensitivity of the *Light sensor*.

3. Fresnel's diffraction

In the classification of diffraction phenomena, one distinguishes Fraunhofer's diffraction and Fresnel's diffraction. Poisson's spot is demonstrated.

Additional equipment: *Light sensor*, optics bench, lens, circular aperture, He–Ne laser, video camera, monitor.

In 1818, the French Academy of Sciences announced a prize competition for an essay on diffraction. Augustin Jean Fresnel (1788–1827) submitted a memoir for the competition. Supporters of Newton's theory that light is a stream of particles dominated the Academy. One of them was a famous mathematician Siméon Denis Poisson (1781–1840). Whittaker (1962) narrated this story as following: "Fresnel had calculated in the memoir the diffraction patterns of a straight edge, of a narrow opaque body bounded by parallel sides, and of a narrow opening bounded by parallel edges, and had shown that the results agreed excellently with his experimental measures. Poisson, when reading the manuscript, happened to notice that the analysis could be extended to other cases, and in particular that it would indicate the existence of a bright spot at the center of the shadow of a circular screen. He suggested to Fresnel that this and some further consequences should be tested experimentally; this was done, and the results were found to confirm the new theory. The concordance of observation and calculation was so admirable in all cases where a comparison was possible that the prize was awarded to Fresnel without further hesitation." Now this bright spot is called **Poisson's spot**.

A convincing verification of the wave theory of light can be seen from Fresnel's diffraction by a circular aperture. In this case, either a bright or dark spot is observable at the center of the diffraction pattern, depending on the radius of the aperture and the distance from it. The theory of this phenomenon is very simple. Let us consider a plane wave front in a circular aperture of radius r (Fig. 7).

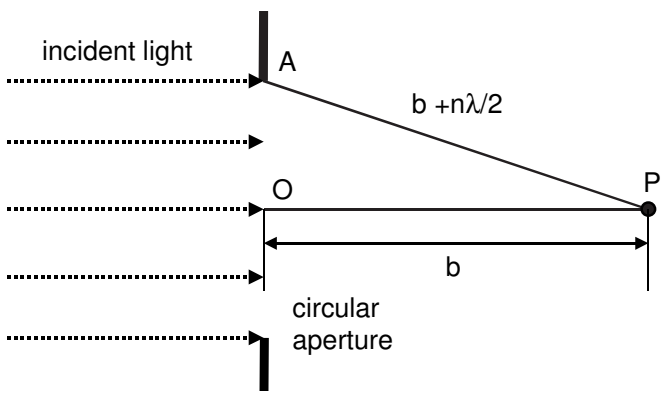

Fig. 7. Plane wavefront in circular aperture.

The path OP to the axial point P is b, while the path AP is somewhat longer. It can be taken in general form as $AP = b + n\lambda/2$. The intensity of light at point P reaches extrema when n is an integer. Namely, maxima of the intensity occur when n is an odd number, and minima correspond to its even values. The result depends on either an odd or even number of the so-called **Fresnel's zones** being opened by the circular aperture when looking from the point P. The number n depends on the radius of the aperture r and the distance b from the aperture: $r^2 = (b + \frac{1}{2}n\lambda)^2 - b^2$. If $n\lambda << b$, $r^2 = nb\lambda$.

In the experiment, a He–Ne laser or a laser diode is a source of light (Fig. 8). Its light beam expanded by a lens falls onto a circular aperture. The diffracted light is observed with a semitransparent screen and a magnifying glass. An observer gradually moves the screen along an optics bench and records its positions corresponding to maxima and minima in the light intensity at the center of the diffraction pattern. These positions should correspond to integers n: $b = r^2/n\lambda$. With a known radius of the aperture, the distances from the aperture corresponding to these maxima and minima can be calculated to estimate the necessary light path. Using the experimental data, one plots the quantity $r^2/b\lambda$ versus b. The experimental points should be close to integers.

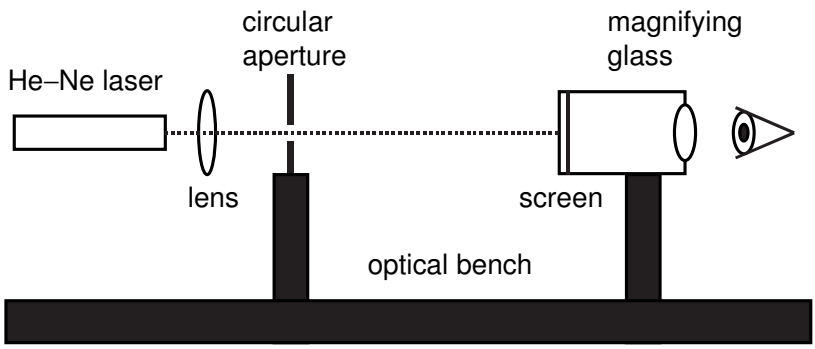

Fig. 8. Observing diffraction patterns from circular aperture.

Poisson's spot. This demonstration reproduces a classical experiment that has clearly shown the wave nature of light. To observe Poisson's spot, one can use as an obstacle a small steel ball hung by fine fibers or glued to a glass plate or mirror (Fig. 9). The larger the ball, the longer the distance to the point where Poisson's spot is observable. With a video camera and a monitor, it is possible to demonstrate Fresnel's diffraction to a large audience (Fig. 10). Even a usual nut can be used as the circular aperture. By moving the camera along an optics bench, one in turn observes dark and bright spots at the center of the diffraction pattern.

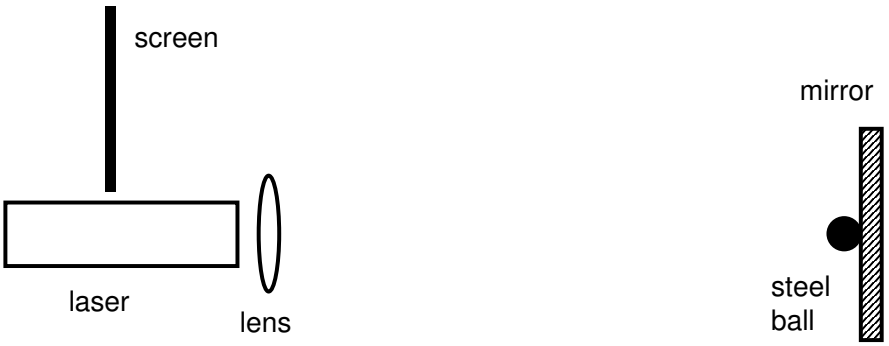

Fig. 9. Arrangement for observing Poisson's spot.

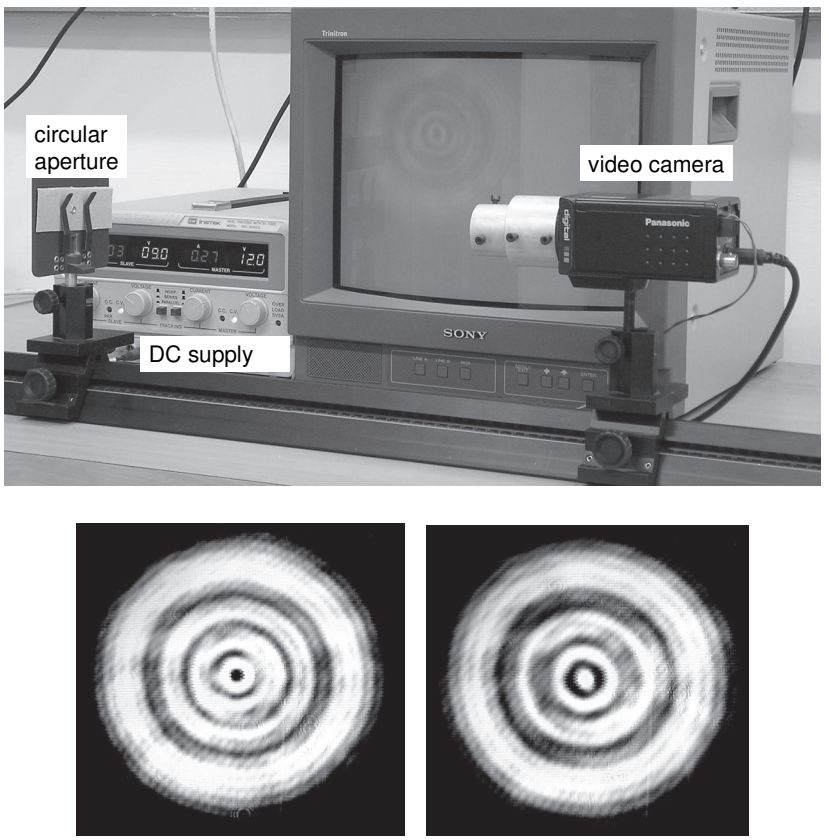

Fig. 10. Setup for observing diffraction patterns with video camera, and patterns with dark or bright central spots.

5.3. Fresnel's formulas

The experiments include (i) the polarization of light by reflection; (ii) Brewster's angle; and (iii) the polarization of light by refraction.

Additional equipment: *Educational spectrophotometer*, *Rotary motion sensor*, *Light sensor*, unpolarized He–Ne laser, optics bench, polarizer, samples, photodiode, multimeter.

Polarization by reflection. The reflection and refraction of light at a boundary is governed by Fresnel's formulas taking into account the polarization of the light beams (Tenquist *et al* 1969–1970):

$$A_{2r} = A_{1r}\frac{\sin(I-R)}{\sin(I+R)}, \tag{1}$$

$$A_{2l} = A_{1l}\frac{\tan(I-R)}{\tan(I+R)}, \tag{2}$$

$$A_{3r} = A_{1r}\frac{2\sin R\cos I}{\sin(I+R)}, \tag{3}$$

$$A_{3l} = 4A_{1l}\frac{\sin R\cos I}{\sin 2I+\sin 2R}, \tag{4}$$

where I and R are the angles of incidence and refraction of light, indices l and r relate to the electric vectors parallel and perpendicular to the plane of incidence, and indices 1, 2, and 3 relate to the incident, reflected, and refracted beams. The relation between angles I and R is given by Snell's law: $\sin I/\sin R = n$.

Equations (1)–(4) give the amplitudes of the parallel components of the electric field vectors of the reflected and refracted light beams in terms of the amplitude of the parallel component in the incident light, and similarly for the perpendicular components. Student experiments concerning Fresnel's formulas were described by Shieh (1968); Driver (1978); Dekker *et al* (1999); Salik (2012).

In the experiment, the light beam from an unpolarized He–Ne laser passes through a polarizer and then falls onto a plane surface of a dielectric. A semicircular acrylic lens serves as the sample (Fig. 1). The experiment is recommended by PASCO (see also Ouseph *et al* 2001). The polarizer can be set at two positions to make the polarization of the incident light to be parallel or perpendicular to the incident plane. A photodiode and a multimeter measure the intensity of the reflected light. At every incident angle, the polarizer is set at two positions, so that both components of the intensity of reflected light, E_{2r} and E_{2l}, are measured in turn (Fig. 2).

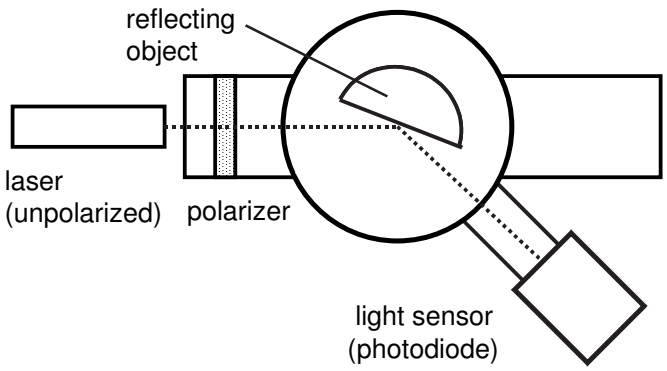

Fig. 1. Schematic of the setup.

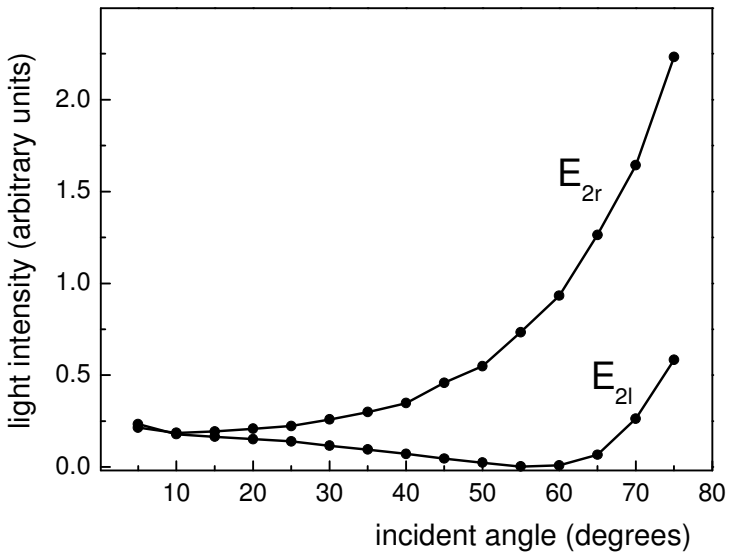

Fig. 2. Example of measurement data.

Brewster's angle. It is seen from Eq. (2) that the vector A_{2l} becomes zero when $I + R = 90^{\circ}$. At this particular angle of incidence, only the perpendicular component A_{2r} remains. This angle of incidence, I_B, is called Brewster's angle. For Brewster's angle, $R = 90^{\circ} - I_B$, and $\tan I_B = n$. With $n = 1.5$, Brewster's angle equals $\arctan(1.5) = 56.3^{\circ}$. Usually, one determines Brewster's angle by gradually changing the angle of incidence and the position of a sensor of the reflected light. Bullen (1963) designed a device for automatically maintaining the equality of angles of incidence of a light beam and the angular position of the sensor. The measurements thus became easier. By measuring Brewster's angle, Bahrim and Hsu (2009) determined the refractive indices of dielectrics.

To demonstrate Brewster's angle, an extended light sensor, a simple solar cell, is positioned to sense the reflected light for a range of incident angles, including Brewster's angle (Fig. 3). The *Rotary motion sensor* measures the incident angle, while the *Voltage sensor* provides the data from the sensor. The intensity of reflected light is displayed versus the incident angle (Fig. 4). The polarizer should be set beforehand to provide light polarized parallel to the incident plane.

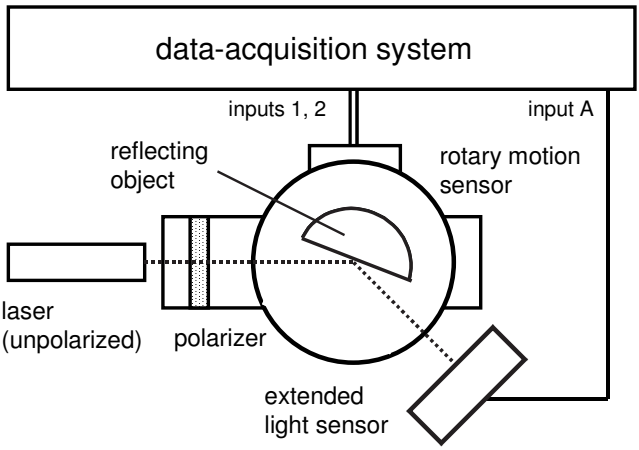

Fig. 3. Setup with extended light sensor.

Fig. 4. Determination of Brewster's angle.

Polarization by refraction. Fresnel's formulas predict the polarization of light when a light beam passes through a dielectric plate. This phenomenon strongly depends on the incident angle. A pile of parallel plates can be used to increase

the polarization. In our experiment, the pile contains 20 plates of 0.13 mm thickness, and the polarization is measured versus the incident angle (Fig. 5). The analyzer is in turn set to achieve a maximum I_{max} and a minimum I_{min} current of a photodiode sensing the intensity of light passing through the pile. The data are taken as the ratio $(I_{max} - I_{min})/(I_{max} + I_{min})$. The results show the efficiency of this method of polarization.

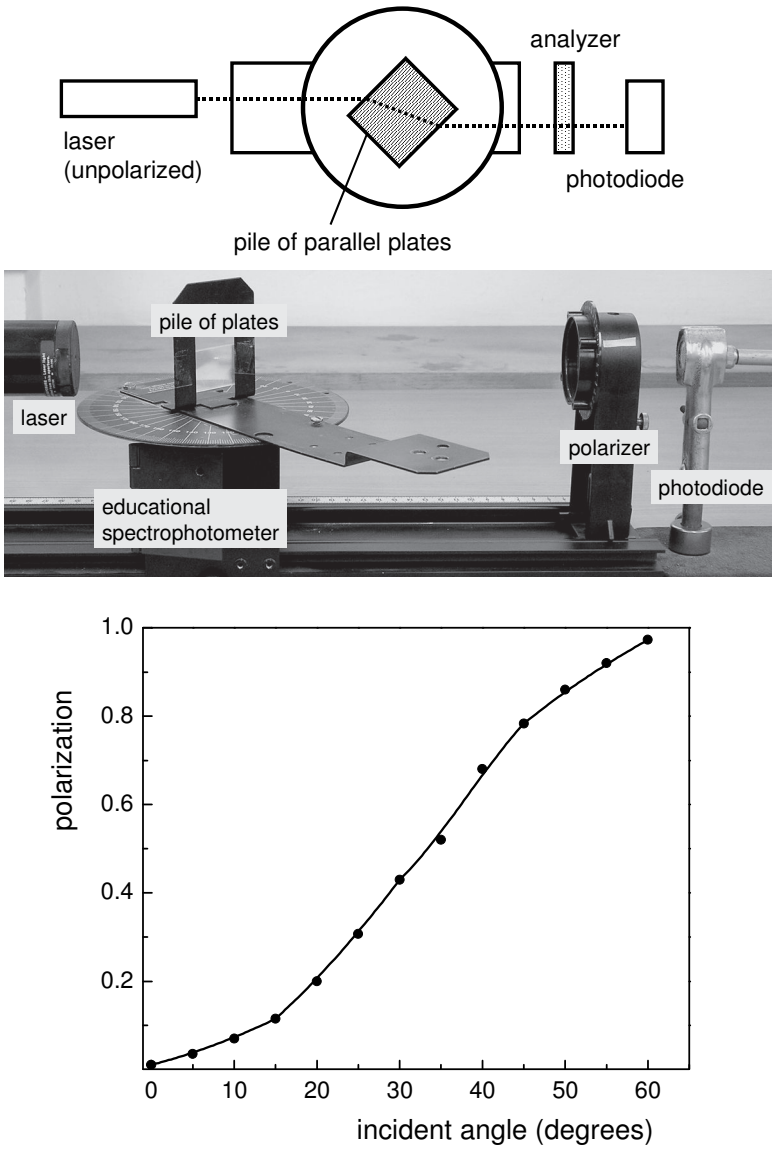

Fig. 5. The setup and measurement data for 20 parallel plates.

5.4. Optical activity

The experiment includes two topics: (i) the optical activity of sucrose, and (ii) Faraday's effect.

The **optical activity** (or **optical rotation**) is the ability of a medium to rotate the plane of polarization of a linearly polarized light. The phenomenon is considered in many textbooks: Jenkins and White (1983); Hecht (1998); Pye (2001); Graham-Smith *et al* (2007). The simplest measurement of the optical rotation is the following. The sample is positioned between a polarizer and analyzer. A light beam passes through the system and is detected visually or by a light sensor. Without a sample, the analyzer is set to obtain a minimum light transmittance. The same operation is done with the sample. The difference in the angular settings of the analyzer equals the optical rotation by the sample. This method commonly used in lecture demonstrations and undergraduate laboratory experiments was considered by Foxcroft (1968); Hill (1973); Freier and Eaton (1975); Hultsch (1982); Mahurin *et al* (1999). Analysis of polarized light was given by Collett (1968) and Cox (1978).

More complicated **polarimeters** are capable of enhancing the resolution of the measurements. In these polarimeters, unfavorable measurements close to the zero intensity are avoided. With visual detection, the operation is based on high sensitivity of the human eye to small differences in intensity or color of two adjacent fields. Polarimeters measuring sugar concentrations in water solutions are called saccharimeters. Descriptions of such devices can be found in textbooks. Automated polarimeters employing rotating analyzers are now available (Griffith 1967; Suits 1971). The devices are based on determinations of the phase shift between the rotation of the analyzer and a signal from a light sensor measuring the light transmittance. In particular, a light beam passing through the polarizer and analyzer but not the sample signals the current position of the analyzer. Though it is possible to assemble a model of a sensitive polarimeter in a student laboratory (Hunte *et al* 2001; Colicchia 2004), the simplest method based on minimizing the transmittance of light passing through the polarizer and analyzer is still widely used.

1. Optical activity of sucrose

A method to improve measurements of optical rotation without using expensive equipment is described (Kraftmakher 2009b).

Additional equipment: two *Light sensors*, laser diode, optics bench, two polarizers, beam splitter, mirror, cuvette.

Simple measurements of optical rotation can be markedly improved. The data with and without a sample are acquired simultaneously, while one manually rotates the analyzer. For this aim, the beam from a light source is split into two beams detected by two light sensors. The first beam passes through a polarizer and analyzer, so the signal from the first sensor is proportional to $\cos^2\varphi$. The second beam passes also through a sample, so the signal from the second sensor is proportional to $\cos^2(\varphi + \theta)$. Here, φ is the angle between the polarizer and analyser (Malus' law), and θ is the optical rotation by the sample. This approach is used in some automated polarimeters, where the phase shift θ between the two signals is measured using a lock-in amplifier or electronic phase meter. Without such expensive devices, the resolution of the measurements can be improved by graphing $\cos^2(\varphi + \theta)$ versus $\cos^2\varphi$. This graph is an ellipse, even if the motion of the analyzer is nonuniform. Since $\cos^2\varphi = (1 + \cos 2\varphi)/2$, the phase shift between the two signals is twice the optical rotation to be determined.

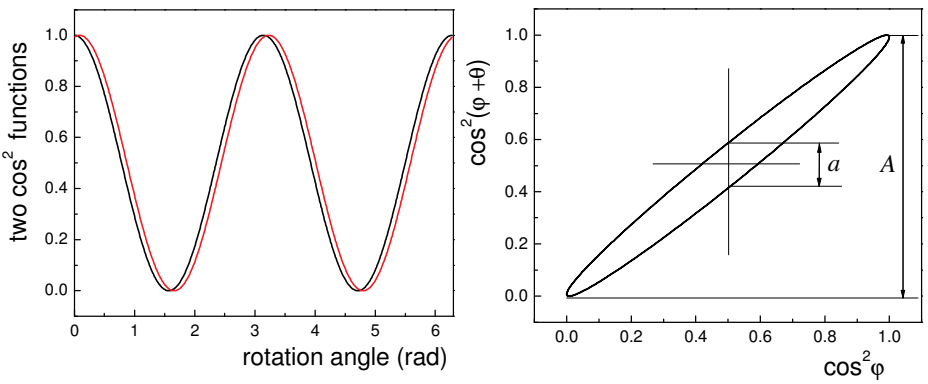

Fig. 1. Functions $\cos^2\varphi$ and $\cos^2(\varphi + \theta)$ versus angle φ (left), and $\cos^2(\varphi + \theta)$ versus $\cos^2\varphi$, for $\theta = 5^o$; $a/A = \sin 2\theta$ (right).

Simple considerations illustrate the proposed approach (Fig. 1). The low resolution of common measurements (left) is improved by graphing $\cos^2(\varphi + \theta)$ versus $\cos^2\varphi$ (right), for $\theta = 5^o$. From the ellipse obtained, $\sin 2\theta = b/B = a/A$, independently of the amplitudes of the two signals. This measurement of phase shifts between two sine voltages of the same frequency is well known. The advantage of using this method is that the optical rotation is obtainable without measuring the rotation of the analyzer, and there is no need to uniformly rotate

it. The information about the current position of the analyzer is available in a form most suitable for our aim. In measurements employing the above method, a beam splitter, two light sensors and a data-acquisition system or an X-Y plotter are needed. Other equipment is the same as in common measurements of optical rotation: a source of monochromatic light, two polarizers, an optically active sample or a cuvette with an optically active solution. The setup is simple and does not include expensive equipment. The optical rotation θ by an optically active solution is

$$\theta = \alpha c l, \quad (1)$$

where α is the specific optical rotation, c is the concentration of the solution, and l is the length of the sample. Usually, values of α are given supposing the concentration in grams per milliliter, and the length in decimeters. Strictly speaking, the optical rotation does not exactly follow a linear dependence on concentration, so that α depends on the concentration of the active material. The specific optical rotation relates to a certain wavelength and temperature, usually, 589 nm sodium line and 20°C. The rotation strongly decreases with increasing the wavelength; this phenomenon is called the **optical rotary dispersion**.

The check of the method was performed by determinations of the optical activity of sugar solutions in water. In water solutions, the cane or beet sugar has the form of sucrose, and its specific optical rotation is well known in a wide wavelength range. The setup is very simple (Fig. 2). A beam splitter and a mirror split the beam of a laser diode (OS-8525A); then the beams pass through a polarizer and analyzer, two similar polaroids (OS-8533). The polarizer is needed because the laser beam may not be completely polarized.

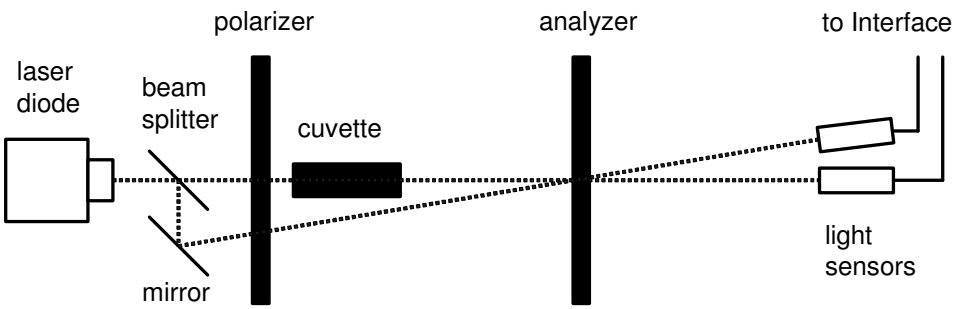

Fig. 2. Arrangement for the measurements (view from above).

The polarizer is set to provide maximum transmittance of the beams. A rectangular cuvette 1 dm long is filled with a solution under study and positioned between the polarizer and analyzer. The first beam does not pass the cuvette and is detected by the first *Light sensor*. The second beam passes the cuvette and the same analyzer; then the second *Light sensor* detects it. Usual silicon photodiodes may serve as well.

Both beams go across the center of the analyzer, so they pass through the same small area when the analyzer is rotated. This was done to avoid ripples in the signals caused by local inhomogeneities in the analyzer. In our case, the second beam crosses the analyzer at normal incidence, but the first beam at nearly 6°. Birefringent prism polarizers have an angular tolerance (angular aperture) for incident beams up to 40°; for polaroids, the situation is even more favorable (Baxter 1956). The slightly oblique incidence of the first beam is quite acceptable. While manually rotating the analyzer, the first signal is proportional to $\cos^2\varphi$. The second signal is proportional to $\cos^2(\varphi + \theta)$, where θ is the optical rotation by the sample. *DataStudio* displays the second signal versus the first. As expected, the graph is an ellipse, whose shape shows the optical rotation. Without a sample, the graph is a straight line.

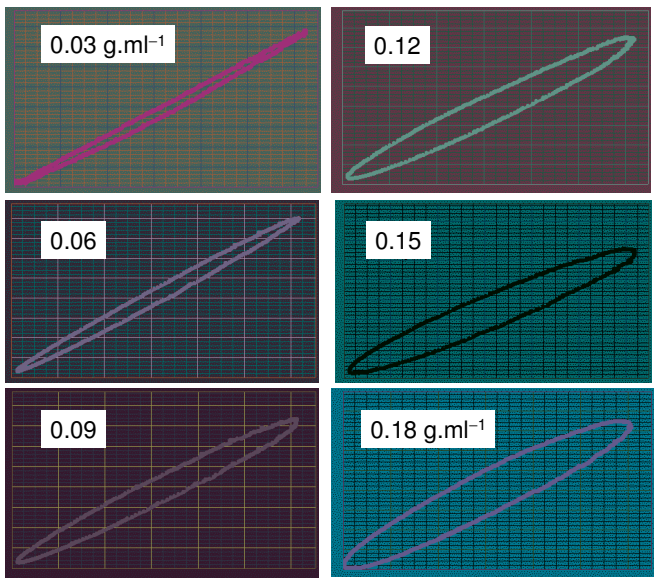

Fig. 3. Examples of graphs for six sucrose concentrations; l = 1 dm.

The measurements were performed for six sucrose concentrations (Fig. 3). The resolution of the measurements is of about 0.2°, that is, better than that with polarizers commonly available in undergraduate laboratories. Six runs were carried out for each sucrose concentration, and mean values obtained were used to determine the optical rotation. From a proportional fit to the data, the specific rotation of sucrose appeared to be 51.7±1.4 deg.ml.g^{-1}.dm^{-1} (Fig. 4). The method used markedly enhances the resolution of the measurements: optical rotations less than 5° are measurable, as well as sucrose concentrations in water with cl values below 0.1 g.dm.ml^{-1}.

The result obtained is in good agreement with optical rotary dispersion data obtained by Mahurin *et a*l (1999) with different lasers (Fig. 5). The authors

used a high sucrose concentration, 0.81 g.ml^{-1}, and a 12 dm long cell (that is, the *cl* value was 10 g.dm.ml^{-1}). The data were fit by equation

$$\alpha = A/(\lambda^2 - \lambda_0{}^2), \tag{2}$$

where $A = 2.17\times10^7$ deg.nm^2.ml.g^{-1}.dm^{-1}, $\lambda_0 = 131$ nm, and λ is the wavelength in nanometers.

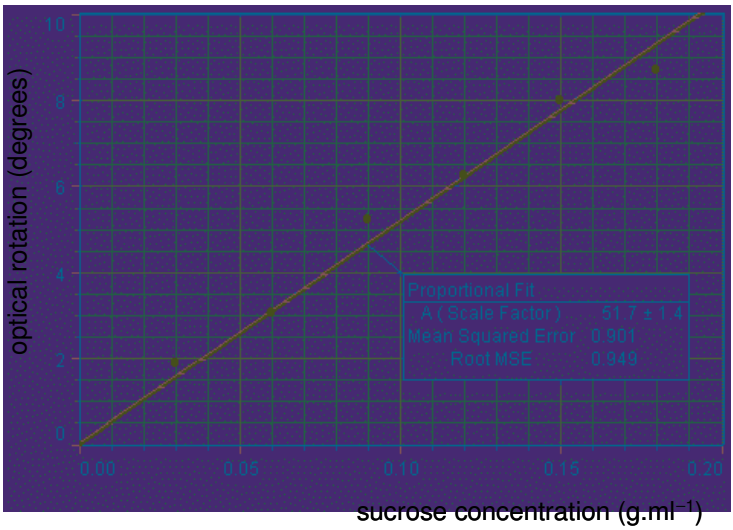

Fig. 4. Optical rotation versus sucrose concentration.

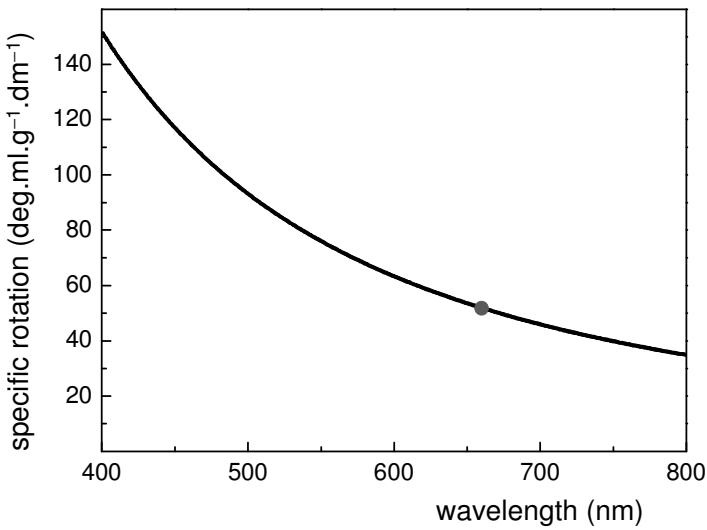

Fig. 5. Specific rotation by sucrose versus wavelength: —— fit by Eq. (2); • present measurements.

2. Faraday's rotation

Verdet's constant for water and NaCl is determined by measuring Faraday's rotation in an AC magnetic field (Kraftmakher 2006b).

Additional equipment: laser diode, Helmholtz's coils, oscilloscope, photodiode, optics bench, AC supply, analyzer, resistors.

In 1845, Michael Faraday discovered the rotation of the plane of polarization of light due to circular birefringence induced in a material by an external magnetic field. This phenomenon is called **Faraday's effect**. When a linearly polarized light passes through such a material along an applied magnetic field, it experiences a rotation of the plane of polarization. The angle of rotation θ depends on the wavelength and is proportional to the thickness of the sample d and the magnetic field B:

$$\theta = K_V B d, \tag{3}$$

where K_V is called **Verdet's constant**.

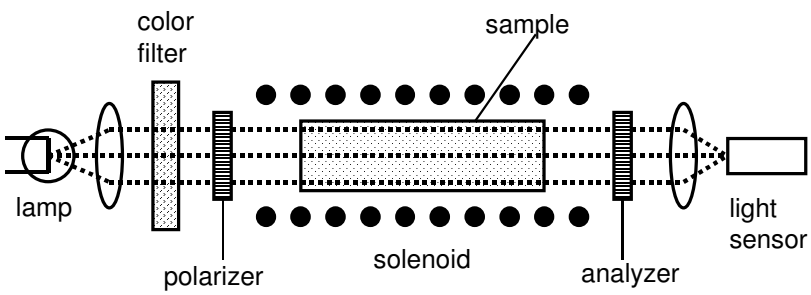

Fig. 6. Classical Faraday's rotation apparatus with a solenoid.

A classical arrangement for observing Faraday's rotation and determining Verdet's constant is very simple (Fig. 6). Light from a lamp is collimated with a lens. The light beam passes through a color filter, a polarizer, and a sample subjected to an external magnetic field parallel to the beam. The sample is positioned inside a solenoid connected to a DC supply. After passing the sample and changing the polarization direction by θ, the beam traverses an analyzer and is focused onto a light sensor. By adjusting the analyzer angle for certain intensity with the magnetic field both on and off, it is possible to determine the rotation angle for the given wavelength. The only objection for such a measurement is the smallness of Verdet's constant. For paramagnetic and diamagnetic materials, it is of the order of 0.1 min.G^{-1}.m^{-1}. High magnetic fields should therefore be applied for obtaining well measurable rotation angles. Magnetic fields up to 0.1 T are achievable with a solenoid (Loeffler 1983). With an electromagnet, magnetic fields of the order of 1 T are possible (Pedrotti and

Bandettini 1990). Another approach is the use of pulsed magnetic fields. Yan and Lonc (1975) measured Faraday's rotation in the microwave range.

Our experiment is based on employing AC magnetic fields and lock-in detection of small AC signals due to the periodic Faraday's rotation. The setup is similar to that described by Jain *et al* (1999) and Valev *et al* (2008), but the lock-in detection operations are performed with *DataStudio* (Fig. 7). Using the AC technique, the measurements are possible with magnetic fields much weaker than those necessary for measurements with DC fields. The laser beam from a laser diode (OS-8525A) passes through a sample subjected to an AC magnetic field produced by Helmholtz coils (EM-6711) connected to an AC supply including a variac and an isolating transformer.

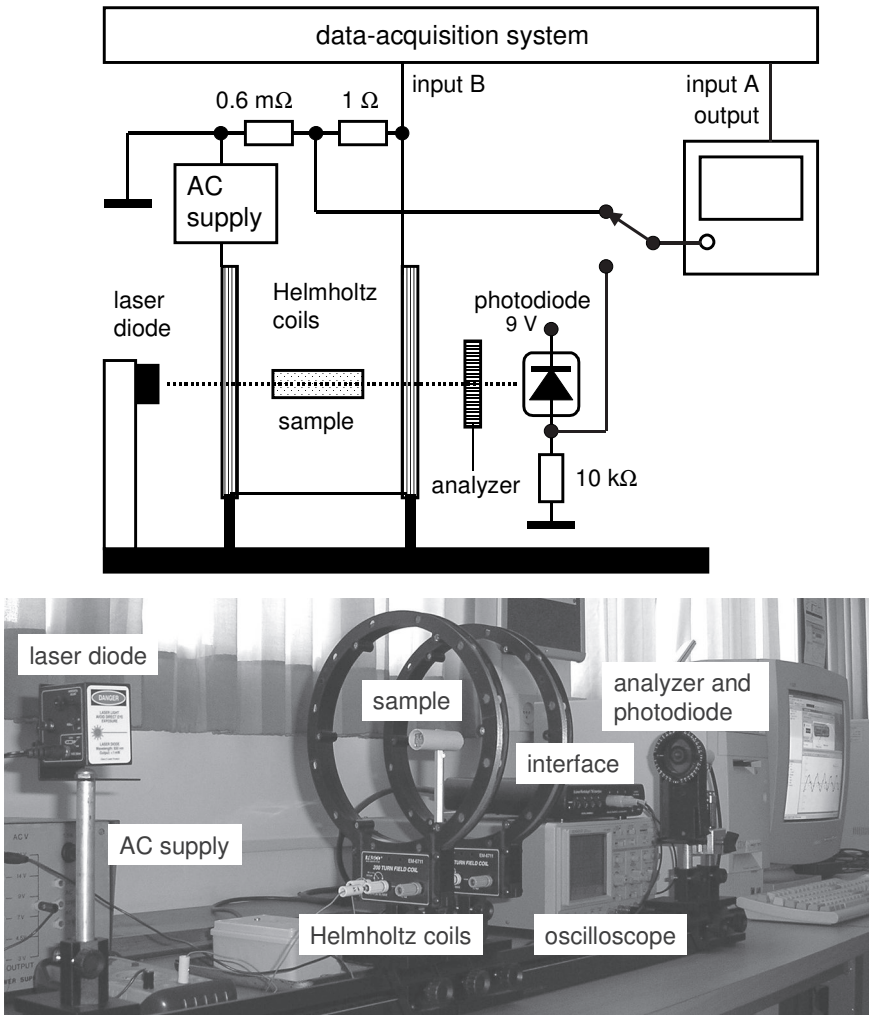

Fig. 7. Setup for the measurements.

The laser beam (λ = 0.67 μm) is polarized, so that only an analyzer is needed. It is set at 45° with respect to the polarization of the laser beam. After the analyzer, the light intensity is measured by a photodiode loaded by a 10 kΩ resistor. A multimeter measures its DC output voltage, while a Kenwood CS-4025 oscilloscope displays the AC component. The oscilloscope serves also as an amplifier providing gain up to G = 100. The *Voltage sensor* measures the amplified voltage, and the second one measures the voltage drop across a 1 Ω resistor connected in series with the Helmholtz coils. This voltage being limited to 0.1 V serves as the reference. The *Sample rate* is 4000 Hz, and each run lasts 0.4 s. Two samples are used for the measurements, water in a quartz cuvette (d = 64 mm) and a NaCl crystal (d = 31 mm). *DataStudio* performs the lock-in detection operations (see Experiment 4.12) and displays the results.

Jain *et al* (1999) gave the theory of the measurements. When the light beam transverses the analyzer set at the angle of $\pi/4$ with respect to the polarizer, the light intensity measured by the detector is

$$I = I_m \cos^2(\pi/4 - \theta), \tag{4}$$

where I_m is the maximum light intensity. The angle θ is very small, and the above relation can be simplified:

$$I = \tfrac{1}{2} I_m (1 + 2\theta). \tag{5}$$

Since the AC magnetic field is $B = B_0 \sin\omega t$, the rotation angle can be presented as $\theta = \theta_0 \sin\omega t$. The light intensity equals

$$I = I_0 + 2I_0\theta_0 \sin\omega t = I_0 + \Delta I \sin\omega t, \tag{6}$$

where ΔI is the amplitude of the AC component of the light intensity. The DC and AC components of the voltage across the load of the photodiode are V_0 and V, respectively. The amplitude of the rotation angle θ_0 relates to them as

$$\theta_0 = V/2V_0, \tag{7}$$

where V is the amplitude value. Verdet's constant is available from Eq. (3) using the amplitude value of the magnetic field.

The magnetic field produced by Helmholtz's coils (N = 200, a = 10.5 cm) is B_0 (G) = 17.1×I (A). The 50 Hz current in the coils equals 2 A (RMS). The setup allows the measurements to be performed in a regime, where the periodic Faraday's rotation is directly compared to the AC magnetic field applied to the sample. A calibrated resistor R (0.6 mΩ, 0.5%) is put in series with Helmholtz's coils. The voltage drop across this resistor is comparable to the AC voltages provided by the photodiode and is measured by the same measuring system. *DataStudio* displays the results of this measurement and of the measurements of the AC voltage from the photodiode (Fig. 8). Verdet's constant equals

$$K_V = \theta_0/B_0 d = AV/2V_R V_0 d. \tag{8}$$

In this relation, B_0 is the amplitude of the AC magnetic field. The voltages V and V_R are the voltages obtained by the lock-in detection operations when measuring

Faraday's rotation and the voltage drop across the resistor R, respectively. The coefficient A takes into account the value of this resistor and the relation between the current and the magnetic field produced by Helmholtz's coils. With this approach, possible errors caused by the amplifier of the oscilloscope and by the data-acquisition system itself are excluded. The rotation angle is given in radians, and it should be translated into angular minutes. After the necessary replacements, Verdet's constant equals

$$K_V = 0.0603 \times V/V_R V_0 d. \quad (9)$$

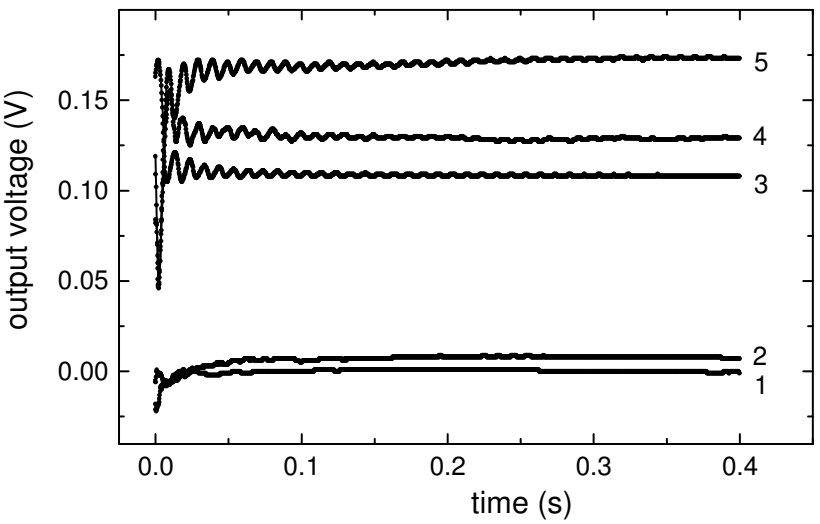

Fig. 8. Output voltages during lock-in operations. 1–no sample, 2–empty cuvette, 3–voltage across resistor R, 4–water, 5–NaCl.

Equation (9) contains the ratio of two voltages, V and V_R, determined by the lock-in detection operations, the DC voltage across the load of the photodiode V_0, and the thickness of the sample d. The total gain of the measuring system is thus excluded. Only the resistance R should be precisely known. A calibrated shunt (100 A, 60 mV) is used for this aim. The contribution of the quartz cuvette is taken into account. If the thickness of the sample is given in meters, Verdet's constant in Eq. (9) is given in $\mathrm{min.G^{-1}.m^{-1}}$. Values of V_0 and d should be introduced for each sample. In the example shown, V_0 equals 1.05 V (water) and 1.10 V (NaCl). Verdet's constants obtained are in good agreement with data from experiments using pulsed magnetic fields.

5.5. Speed of light

A simple addition to the *Lichtgeschwindigkeitsmeβgerät* from PHYWE makes the measurements of the speed of light more accurate (Kraftmakher 1996a).

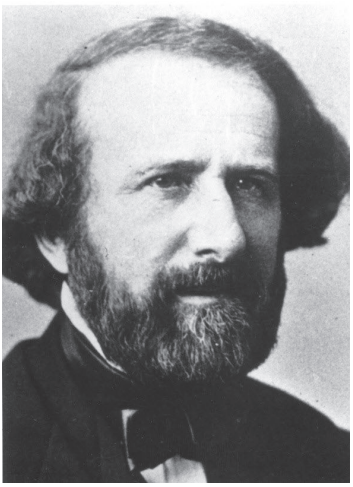

AIP Emilio Segrè Visual Archives,
E. Scott Barr Collection
Armand Hippolyte Louis Fizeau (1819–1896)

AIP Emilio Segrè Visual Archives,
Brittle Books Collection
Jean Bernard Léon Foucault (1819–1868)

Equipment: PHYWE *Lichtgeschwindigkeitsmeβgerät*, oscilloscope, potentiometer, variable resistor, resistors, capacitor.

The speed of light in vacuum is now a fixed quantity and therefore should not be a subject of further measurements. Nevertheless, such measurements by students have great educational value and remain very attractive. The reason for this interest is the high speed of light, six orders of magnitude higher than the speed of sound in air. During many years, it was even believed that the speed of light is infinite. Some textbooks include special chapters devoted to the speed of light: Tenquist *et al* (1969–1970); Jenkins and White (1983).

Brief review of measurement techniques. In 1849, Armand Hippolyte Louis Fizeau was the first to perform terrestrial determinations of the speed of light. His apparatus included a rotating toothed wheel and a remote mirror (Fig. 1). A pulse of light leaving an opening in the wheel struck the mirror and returned. By adjusting the rotational velocity of the wheel, the returning pulse could be made either to pass an opening and be seen or to be obstructed by a tooth. The speed of light appeared to be 315300 $km.s^{-1}$.

In 1850, Jean Bernard Léon Foucault measured the velocity of light using a rotating-mirror arrangement. He found that the velocity of light in water is less than in air. Improving this technique, Albert Abraham Michelson (1852–1931) performed precise determinations of the velocity of light. The precision of further measurements became better than that of the international standard of the meter. Therefore, it was decided to fix the velocity of light in vacuum at 299,792,458 $m.s^{-1}$ (exactly) and to define the meter as the path traveled by light in vacuum during a time interval of 1/299,792,458 of a second.

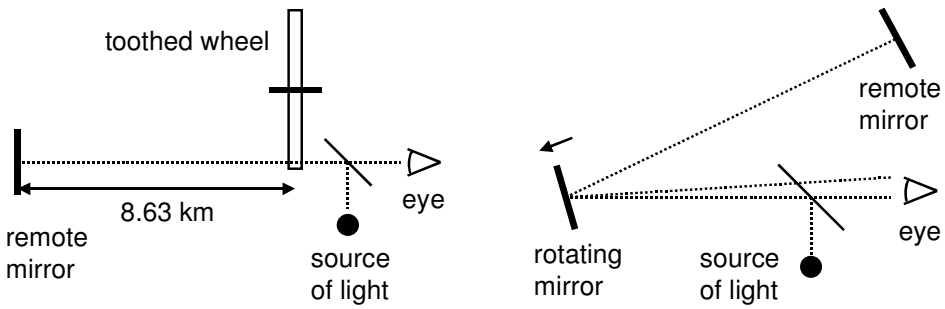

Fig. 1. Simplified diagram of Fizeau's (left) and Foucault's (right) setups.

Alford and Gold (1958) presented an unusual determination of the speed of light. The method is based on the result that Fourier's transform of a pair of identical pulses yields a frequency spectrum with zeroes, which are related to the time separation of the pulses. A free-running spark was viewed by a photomultiplier directly and after reflection from a distant mirror. Maxwell (1961) enhanced the accuracy of the determination of the velocity of the rotating mirror when using a Leybold Company apparatus for determining the speed of light. Dillman (1964) improved the measurements of the displacement of the light beam returning from the rotating mirror. Cooke *et al* (1968) used the pulse technique and a 320 m base. The accuracy of the measurements was of the order of 10%. Rogers *et al* (1969) used the phase-shift method. With a solid-state electro-optical modulator, a laser beam was modulated with a frequency of 510 kHz and detected by a photomultiplier. The signal was mixed in the photomultiplier with a 502 kHz signal to obtain an 8 kHz signal, which then was multiplied by 9. The effective modulation frequency thus became 4.59 MHz. A lock-in amplifier served for the measurements of the phase shifts. With a 2 m change of the distance to the reflecting mirror, the speed of light obtained appeared to be about 2% lower than the accepted value. Proud *et al* (1969) described a commercially available apparatus for measuring the speed of microwaves. With a 3 m base, the accuracy of 1% was possible. Tyler (1969) described an inexpensive and easily constructed apparatus for the determination of the speed of light. A fast light-emitting diode provided light pulses detected by a photomultiplier. An oscilloscope with the horizontal scale of 2 $ns.cm^{-1}$ displayed the output signal of the photomultiplier. With a 3 m base, 2% accuracy

was achieved. Phillips and Thompson (1970) performed a similar experiment using a 337 nm nitrogen laser. Smith and Edmonds (1970) reported on measurements with a 145 m base. Trudeau *et al* (1971) described quite another approach for determining the speed of light. A solid-state light emitter and a photomultiplier coupled to it through a long light path constitute a regenerative feedback loop. By changing the optical path, a frequency change was introduced, from which the speed of light was determined. Blackburn (1980) developed a similar setup for measuring the speed of light in an optical fiber. Electronic delay elements were added to reduce the repetition frequency of the light pulses to about 1 MHz. Edmonds and Smith (1971) described a rotating-mirror apparatus with a He–Ne laser, two photodiodes, and a light path more than 100 m long. A dual-trace oscilloscope with 0.2 $\mu s.cm^{-1}$ sweep time displayed the pulses from the near and far photodiodes. Mulligan (1971) proposed further improvements in the determinations of the speed of the rotating mirror. Page and Geilker (1972) used a Pöckels cell with a KH_2PO_4 (KDP) crystal for a 21.3 MHz modulation of a laser beam. With a 10 m base, the accuracy of the measurements was about 1%. Domkowski *et al* (1972) employed the rotating-mirror method. With a light path length of 38 m and rotation rates up to 500 Hz, the accuracy of the measurements was better than 1%. Vanderkooy and Beccario (1973) described a variant of the time-of-flight method. With a light path of about 220 m, the accuracy of the measurements was about 1%. Thayer (1973) described setup of 1% accuracy with a 50 m base. Bergel and Arnold (1976) used a Doppler shift apparatus to measure the speed of microwaves. Mulligan (1976) reviewed the most accurate determinations of the speed of light involving simultaneous high-precision determinations of the frequency and wavelength of highly monochromatic visible or infrared laser radiation. Due to these determinations, it was suggested to make the speed of light in vacuum a defined constant, and then to use it as the connecting link between the unit of time (the second) and the unit of length (the meter). Biretta and Lang (1978) described a rotating-mirror setup with a 90 m path difference and a 1% accuracy of the speed of light. Feagin (1979) described a similar apparatus. Brickner *et al* (1979) determined the speed of light by measuring the beat frequency of internal laser modes. Ciholas and Wilt (1987) described a pulser circuit for measuring the speed of light. Bates (1988) presented a review of the determinations of the speed of light, from Roemer's discovery of the finite speed of light to measurements that led to the redefinition of the meter. To measure the speed of light, Mak and Yip (2000) used a laser pointer. Aoki and Mitsui (2008) measured the speed of light with a pulsed laser, a fast photodiode, and an oscilloscope with 2 GHz sampling. Ronzani *et al* (2008) measured the speed of light using a modulated laser diode. D'Orazio *et al* (2010) measured the speed of light using beating longitudinal modes in an open-cavity He–Ne laser.

Crandall (1982) considered requirements for speed-of-light measurements in a first-year course lecture:

- The light should be visible.

• The measurements should be of time of flight, so that $c = l/t$.

• The demonstration should take place inside a lecture hall and require one class period for both explanation and execution.

• The apparatus should be simple to set and to use.

Following these recommendations, a bright light-emitting diode (LED) was used as the light source. The LED was modulated at a frequency of 2 MHz. The direct beam and the beam delayed for a time l/c were superimposed on a photodiode with an amplifier loaded by a resonant LC circuit. The speed of light was available by measuring the AC voltages across the load for the first beam only, the second beam only, and for two beams superimposed. The author stressed the possibility of using a light path that makes the phase difference of two beams to be 180^{o}. The beams will cancel each other if they have the same amplitude.

Bates (1983) described independent measurements of the frequency and wavelength of a 9 GHz microwave source. The wavelength was measured using a microwave Michelson interferometer. For determining the frequency, the 9 GHz signal and a signal of about 1 GHz from a variable frequency oscillator were directed to a mixer containing a nonlinear mixing crystal. The oscillator frequency necessary for obtaining the zero beat frequency for the 9th and 10th harmonics was measured. Becchetti *et al* (1987) reported on time-of-flight measurements using a laser and a low voltage Pöckels-cell modulator. With a 90 m base, 0.5% accuracy was achieved.

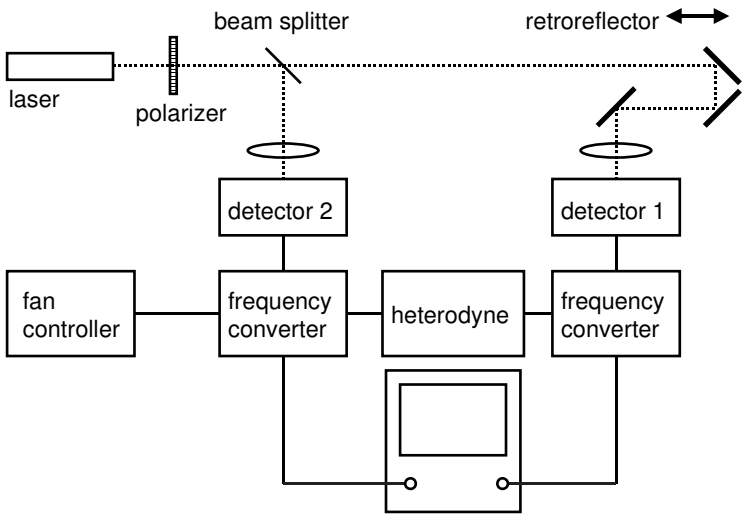

Fig. 2. Schematic of setup used by Barr and Armstrong (1990).

Barr and Armstrong (1990) used the beat frequency of two internal laser modes to produce light modulated at frequencies of about 550 MHz. For the phase-shift measurements, this frequency was converted to 531 kHz (Fig. 2).

The Lissajous figure technique was used to find points of 0 or 180° phase shifts. With a 60 m base, the accuracy of the measurements of the speed of light in air was claimed to be 0.02%. The method was also used for determining the speed of light in transparent media. Deblaquiere *et al* (1991) measured the speed of light using an acousto-optic modulator. Gülmez (1997) determined the time delay for a modulated light pulse from a red LED traveling through optical fibers of different lengths. With a 10 MHz modulation, James *et al* (1999) obtained accuracy better than 1%. Clark (2001) determined the speed of light from dimensions and the resonance frequency of an LCR circuit. An accuracy of about 1% was achieved.

Many years ago, the present author also attempted to develop student experiments on the speed of light. Two such setups were built. At that time, before the laser appeared, a neon lamp served as a source of light for a pulse method, and a modulated thyratron for phase shift measurements. In pulse measurements, an electro-optical transducer equipped with deflecting plates was employed as the receiver (Fig. 3). It thus replaced a photomultiplier and an oscilloscope, and very fast sweeps were possible (Kraftmakher 1962b). To increase the light path to a reflecting mirror, a hole was made in the wall between two laboratory rooms in the new Moscow University building.

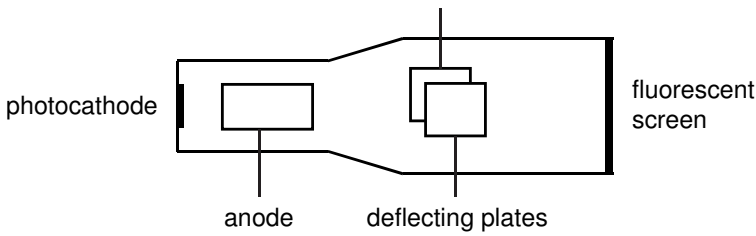

Fig. 3. Electro-optical transducer displays short light pulses.

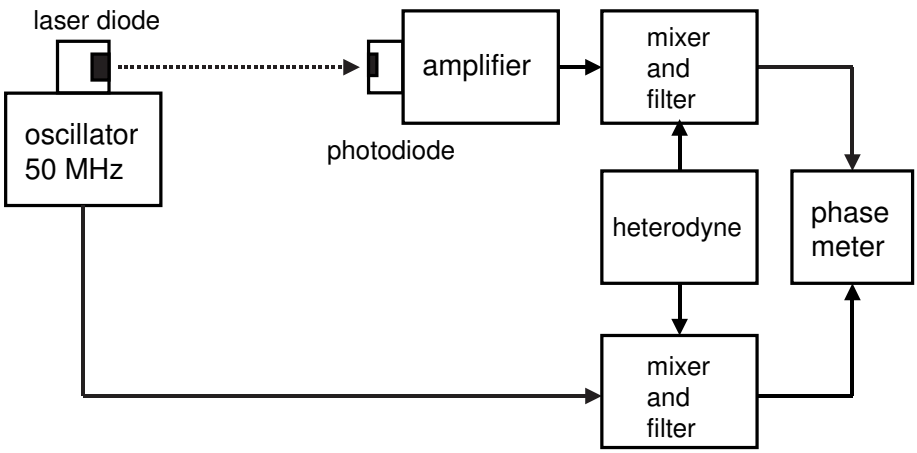

Fig. 4. Schematic of setup with a phase meter (Mitin *et al* 2003).

The apparatus employing the phase shift method appeared to be more convenient and was used also as a classroom demonstration (Kraftmakher 1964). Using the frequency-conversion technique, the phase shifts were measured at moderate frequencies with an electronic phase meter. A much better source of modulated light was found, a gas-discharge lamp designed for phototelegraphy, and the modulation frequency was increased up to 16.5 MHz (Iveronova 1962, 1968). Now the measurements are performed with a laser diode modulated at 50 MHz (Mitin *et al* 2003). The phase of the signal is measured versus the distance between the light source and the receiver (Fig. 4). The speed of light in air, a solid, and two liquids is determined.

Lichtgeschwindigkeitsmeβgerät from PHYWE follows an idée proposed by Barr (1972). The intensity of the light beam is modulated with a high frequency. The intensity of the beam equals $A + a\sin\omega t$. The modulated light travels to a mirror positioned on a calibrated bench and returns back (Fig. 5). The intensity of light coming back is $A + a\sin\omega(t - l/c)$, where ω is the modulation frequency ($\omega = 2\pi f$), l is the path of the light, and c is the speed of light in air. The phase shift between the modulating voltage and the intensity of returned light is

$$\Delta\varphi = \omega l/c. \qquad (1)$$

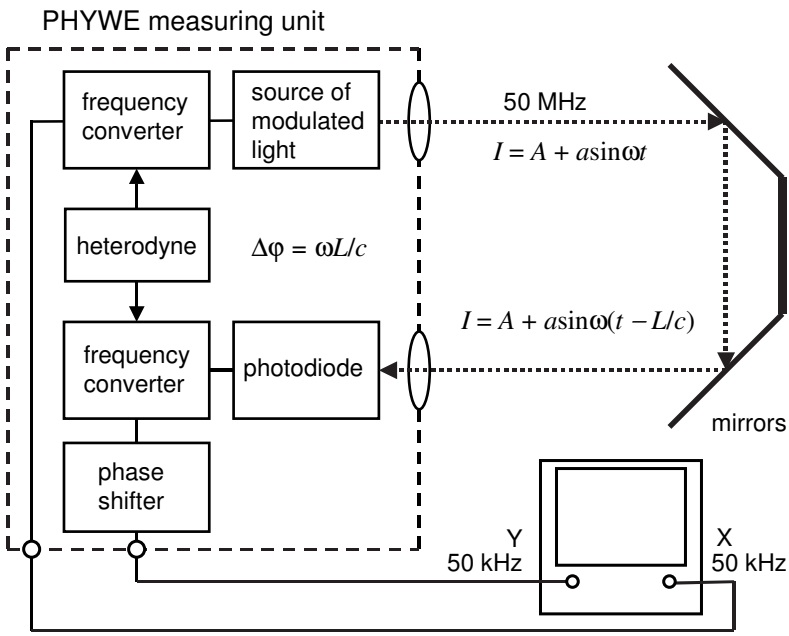

Fig. 5. Block diagram of the *Lichtgeschwindigkeitsmeβgerät*.

The mirror is first positioned close to the measuring unit. With a phase shifter, the phase shift to be measured is adjusted to be zero or 180°. This is seen

from Lissajous pattern on the screen of an oscilloscope. Then the mirror is positioned at such a distance from the measuring unit that an additional phase shift equals 180°, causing the appearance of another straight line on the screen of the oscilloscope. Thus, the measurements are reduced to observations of the 0 and 180° phase shifts. It is very convenient to fix these phase shifts with an oscilloscope. To make the measurements with a short base, the modulation frequency is 50 MHz. The change in the path of the light that causes the 180° phase shift is therefore 3 m, so the distance to the mirror should be changed by 150 cm. The two signals of the 50 MHz frequency are converted into 50 kHz signals and fed to an oscilloscope. With the frequency conversion, the phase shift between the two signals remains the same. Freeman (1997) presented an evaluation of the PHYWE apparatus.

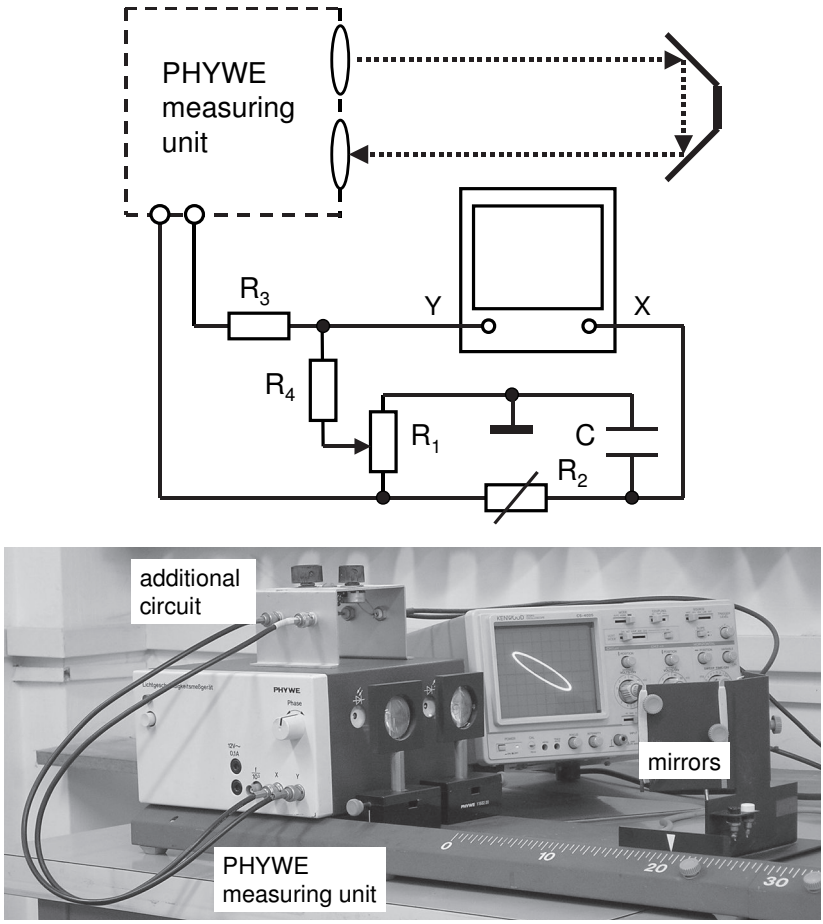

Fig. 6. An addition to the PHYWE apparatus reduces the background signal. $R_1 = R_3 = 10\ \text{k}\Omega$, $R_2 = R_4 = 50\ \text{k}\Omega$, $C = 200$ pF.

Addition to the PHYWE apparatus. A drawback of the PHYWE apparatus arises because the high-frequency oscillator and light receiver are placed in one unit. This causes a significant background in the signal to be measured. In our setup, this background amounts to about 20 mV. A simple addition to the apparatus (Fig. 6) solves this problem.

The 50 kHz voltage intended for the X input of the oscilloscope is used for producing a voltage for compensating the background. An adjustable part of this voltage is added to the background, and the phase shifter incorporated in the PHYWE apparatus controls its phase. An additional circuit R_1R_2C introduces an adjustable phase shift into the voltage fed to the X input of the oscilloscope. Now just this circuit provides the necessary 0 or 180^o phase shift between the signals when the mirror is positioned close to the measuring unit. The additional circuit is mounted in a metal box and connected to the measuring unit and the oscilloscope. With the compensation, the background voltage is reduced to less than 1 mV, so the determination of the speed of light becomes more accurate.

Speed of light in air and in water. Without optical signals, only the background voltage is seen on the screen of the oscilloscope. By adjusting the phase shifter and the potentiometer R_1, the background can be completely balanced. This means that the phase shifter makes the phase of the background equal to that of the voltage intended for the X-input of the oscilloscope, and the potentiometer R_1 equalizes their amplitudes. Then the mirror is positioned close to the measuring unit and the optical signal is observed on the screen. The phase-shifting circuit R_2C is adjusted to make this phase shift equal to 0 or 180^o. Then the mirror is slid to the remote position to change the phase shift by 180^o. To achieve the same phase shift with a water-filled tube of a length l_0, the mirror should be positioned at a distance $l - \Delta l$. It is easy to see that the refraction index of water equals

$$n = 1 + 2\Delta l/l_0. \qquad (2)$$

For determining the speed of light, PASCO scientific offers a measuring system with a laser diode (AP-8586) modulated at 3 MHz. Another PASCO apparatus uses the rotating-mirror technique (OS-9261A, OS-9262).

5.6. Spectrophotometry

Transmission spectra of color filters are displayed.

Additional equipment: *Educational spectrophotometer*, two *Light sensors*, light bulb, monochromator, diffraction grating, color filters, light guides.

When light passes through a medium, the ratio of the transmitted intensity I to the incident intensity I_0 is $I/I_0 = \exp(-\mu l)$, where l is the length of the light path in the medium, and μ is the **absorption coefficient** of the material.

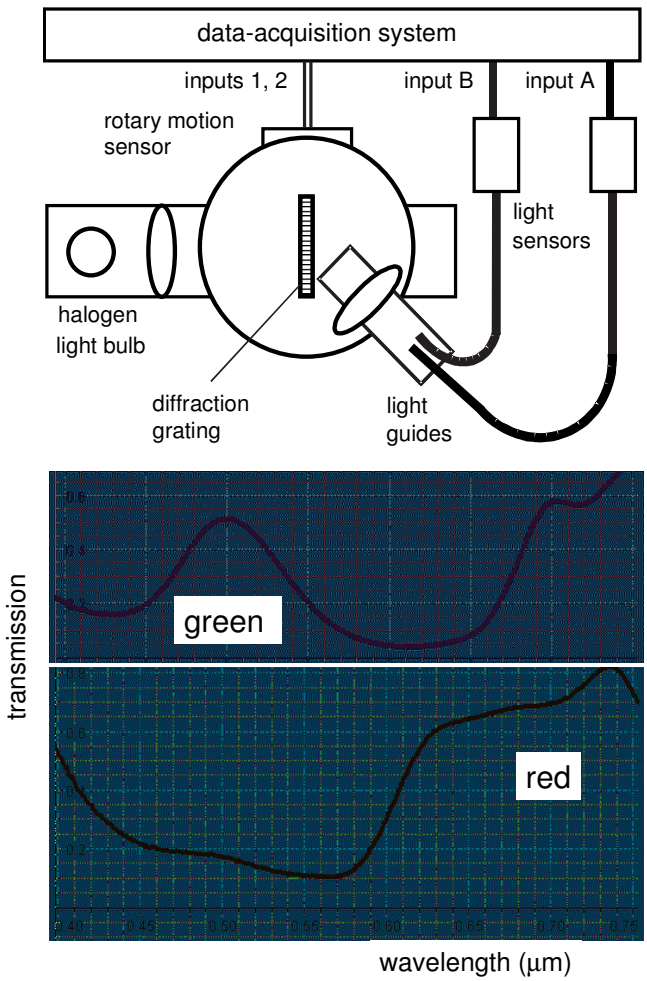

Fig. 1. Schematic of the setup and transmission spectra of two color filters.

For the absorption by a solution, the absorption coefficient is proportional to the solution concentration c: $\mu = Kc$. Usually, two signals are compared: when the radiation is incident directly on the spectrophotometer slit, and when an absorbing sample is put between the radiation source and the slit.

In our experiment, color filters for the measurements are prepared by printing them on pieces of transparent film. The *Educational spectrophotometer* and two *Light sensors* are used (Fig. 1). A diffraction grating displays a spectrum of a light bulb. The spectrum is scanned by a box containing inputs of two light guides positioned in one vertical plane, with a filter placed in front of the input of one of them. *DataStudio* calculates the ratio of the two signals versus the wavelength.

Another version of this experiment employs a monochromator and a photodiode (Fig. 2). For different wavelengths, a multimeter measures the output voltage of the photodiode with and without a color filter placed in front of the entrance of the monochromator. The ratio of the two voltages determines the transmission spectrum.

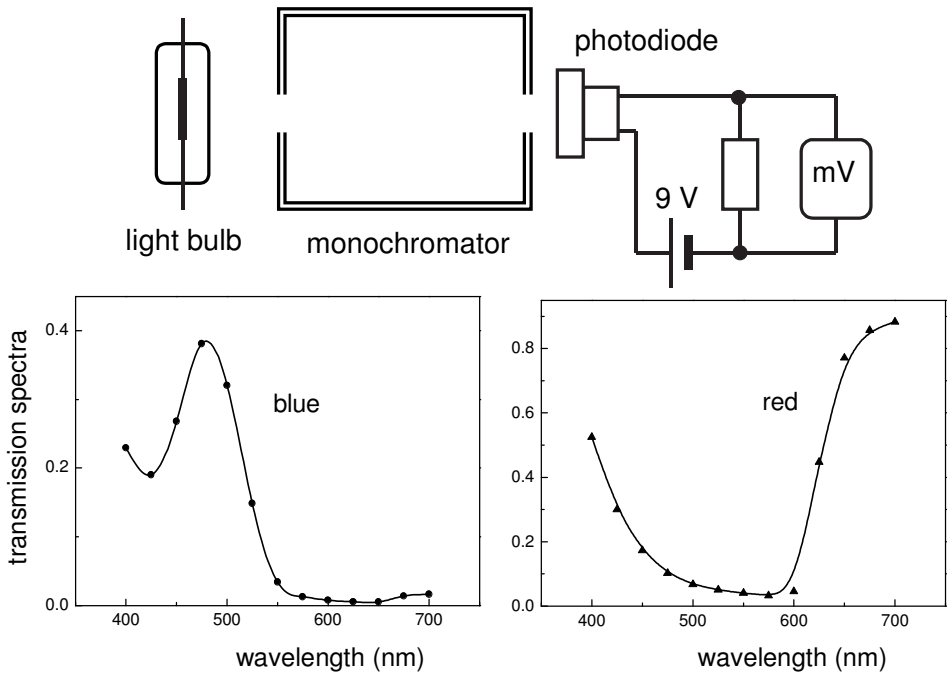

Fig. 2. Setup with a monochromator and transmission spectra obtained.

5.7. Demonstrations of optical spectra

The use of a video camera may improve demonstrations of optical spectra. First, the output electrical signal from the camera can be observed on the screen of a common oscilloscope. Second, increasing the magnification by the camera enhances the resolution of the spectra displayed by a color monitor. In particular, the sodium doublet at 589 nm ($\Delta\lambda$ = 0.6 nm) is resolved (Kraftmakher 2012b).

Equipment: video camera, color monitor, diffraction gratings, oscilloscope, spectral tubes and lamps, compact fluorescent lamps.

Every picture can be presented as a number of small elements (pixels), each being characterized by its coordinates, brightness, and color. A video camera translates the picture into a sequence of electrical signals. Electrical voltages encode the brightness and color of each pixel. The main electrical signal from the camera reflects the changes in the brightness along each horizontal line of a frame. The color of each pixel is encoded by a phase shift between an additional high-frequency voltage and a reference voltage of this frequency sent at the beginning of each line. Two electrical signals are added to this sequence to indicate the starts of each line and of each frame of the picture.

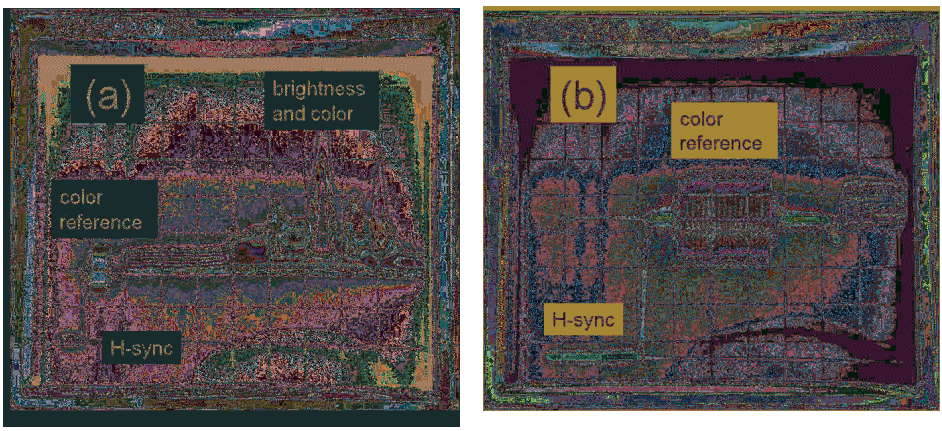

Fig. 1. The signal from the video camera on oscilloscope's screen: (a) the composite signal, and (b) the enlarged initial part of the signal. The H-sync pulse and high-frequency color reference are clearly seen.

At the receiver, these signals called horizontal synchronization pulses (H-sync) and vertical synchronization pulses (V-sync) serve for properly displaying the original picture. To reduce the evident flicker, the camera scans each frame twice, odd and even lines being scanned in turn. Clearly, the receiver must reproduce the same sequence of lines. The composite signal from the camera includes the synchronization pulses, the high-frequency color reference, and the

voltages encoding the brightness and color of all pixels forming the current line of a frame to be transmitted (Fig. 1).

The use of a video camera markedly improves demonstrations of optical spectra. First, the output electrical signal from the camera can be immediately observed on the screen of an oscilloscope. Second, increasing the magnification provided by the camera enhances the resolution of spectra observed with a color monitor. The experiments presented here confirm the above statements. The setups with a video camera are schematically shown below (Fig. 2).

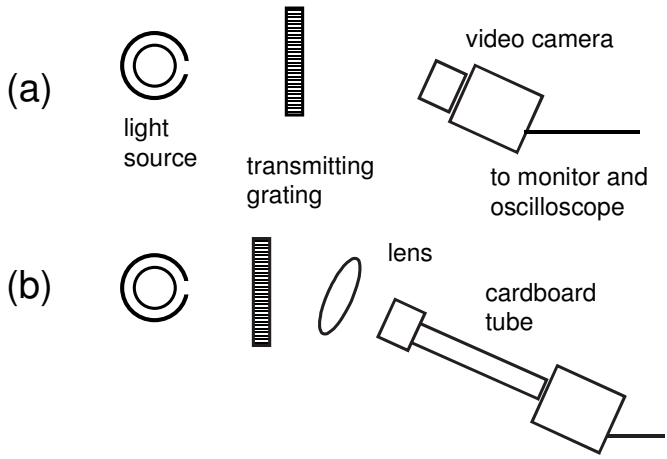

Fig. 2. Scheme of the demonstrations (view from above): (a) observing the whole visible spectrum, and (b) observing narrow parts of the spectrum with enhanced spectral resolution.

Radiant spectra on oscilloscope screen. The first setup is similar to that described by Widiatmoko *et al* (2011), but a digital photo camera is replaced by a color CCD video camera (Panasonic GP-KR222). The camera incorporates a 0.5 inch charge-coupled array (768×494 pixels) and operates in the NTSC format (NTSC means National Television Systems Committee). The camera views spectra obtained with a transmission diffraction grating, 300 lines per millimeter (Fig. 2a). Due to the high sensitivity of the camera, a small aperture of the objective lens can be set, which helps to obtain good focusing. The output of the camera is connected to a color monitor (Sony PVM-14N6U) for observing the visible spectrum and to a common oscilloscope (Kenwood CS-4025) for a simultaneously electrical presentation of the spectrum. At the Y-input of the oscilloscope, the high-frequency component encoding the colors is reduced by a low-pass RC filter (150 Ω, 1 nF). The H-sync pulses synchronize the sweep of the oscilloscope. Signals corresponding to all horizontal lines of the picture are thus superimposed on the oscilloscope's screen. In this case, all the signals repeat each other, so the curve on the screen shows the radiant power spectrum. Really, this curve is only an approximation. First, the spectrum may be distorted

because the efficiency of diffraction gratings depends on wavelength; for the grating used, this dependence is unknown. Second, the signal from the camera does not exactly reproduce real colors.

Capillary spectral tubes from PASCO provide spectra of hydrogen (SE-9461); helium (SE-9462); mercury (SE-9466); and neon (SE-9467). A power supply (SE-9460) operates the tubes. The light from the tube tested is directed onto the diffraction grating positioned 0.7 m apart. The video camera is positioned beyond the grating at such an angle that the monitor displays the first-order visible band. The spectral range corresponding to the width of the monitor screen is nearly 400 nm. Simultaneously, the oscilloscope displays the radiant power spectrum. These pictures (Fig. 3) are obtained with a digital photo camera; the pictures are resized to make clear the relation between the two presentations. The radiant power spectrum displayed by the oscilloscope relates well to the spectrum displayed by the monitor. Except for neon, it is easy to identify the main lines of the atomic spectra observed; the wavelengths indicated are taken from the database of the National Institute of Standards and Technology, Gaithersburg (Ralchenko *et al* 2011).

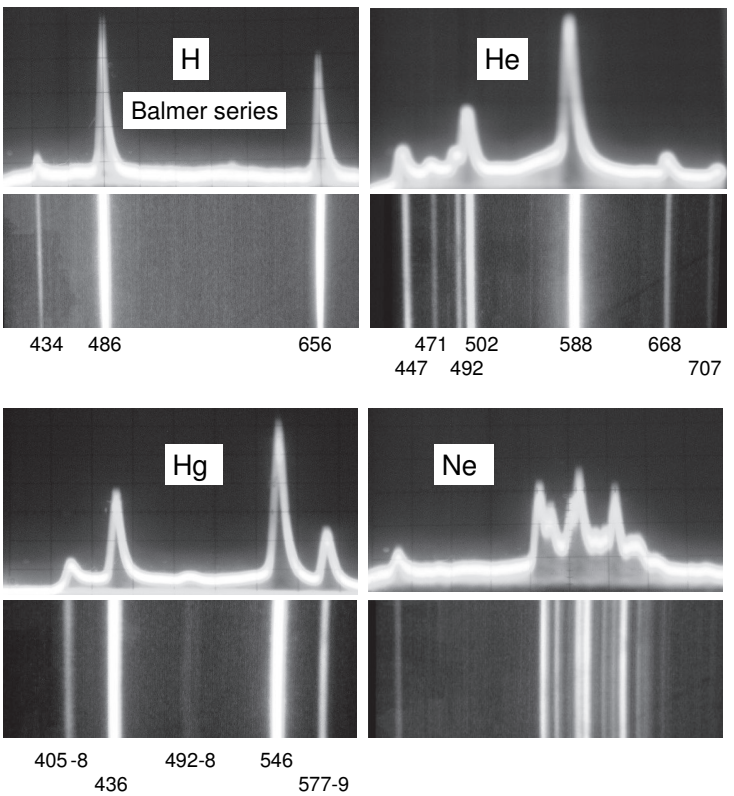

Fig. 3. Spectra of spectral tubes displayed by the oscilloscope and monitor. The wavelengths are given in nanometers.

The same setup, but with a grating of 600 lines per millimeter, is used for comparing spectra of two compact fluorescent lamps (CFL) tested in other experiments (Kraftmakher 2010f). The manufacturers characterize them as a "cool daylight" lamp and a "warm white" lamp. An opaque plastic cylinder with a slot along it, less than 1 mm in width, covers the lamp. For both lamps, the visible spectral lines of mercury are clearly seen (Fig. 4). The violet (405 and 436 nm), green (546 nm), and yellow (577–579 nm doublet) lines of mercury greatly contribute to the total emission of both lamps, thus providing their high efficiency. The phosphorescence excited by the ultraviolet radiation of mercury is different: the "cool daylight" lamp stresses the blue emission, while the "warm white" lamp stresses the red emission. The mercury 546 nm line and the phosphor emission form the intensive green band necessary for obtaining high luminous efficacy of a lighting source (Kraftmakher 2010f, 2011d).

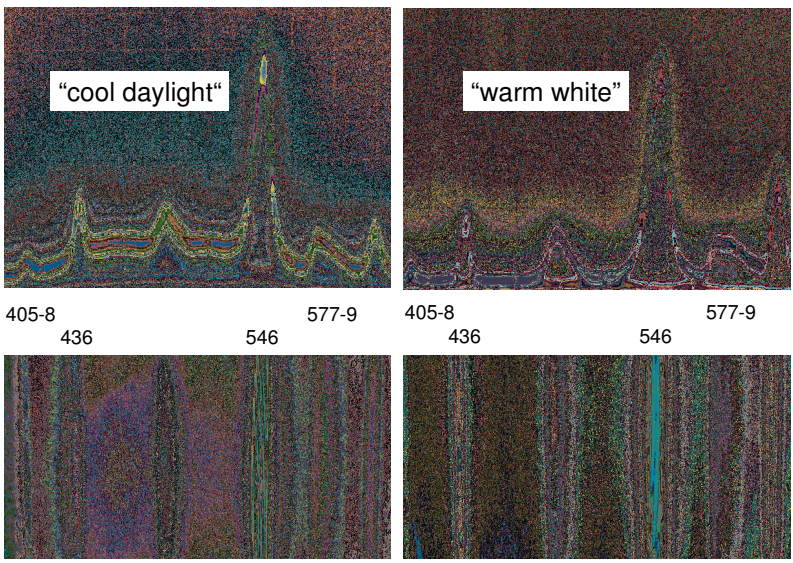

Fig. 4. Spectra of the CFLs displayed by the oscilloscope and monitor. Mercury lines are indicated. The unresolved green line includes the 546 nm mercury line and the phosphor emission.

The demonstrations utilize well-known atomic spectra, so there is no need for an independent determination of wavelengths: the spectra themselves provide the data. An exception is neon, for which the identification of wavelengths is more difficult. If the light source, the diffraction grating, and the video camera are fixed at their positions, the wavelength scale can be established and attached to the monitor screen.

Enhancement of spectral resolution. To achieve good spectral resolution, the light from the source should enter the spectrometric device through a narrow

entrance slit. Second, increasing the magnification by an optical system also enhances the resolution (Ratcliff *et al* 2011). In our setup, the distance between the objective lens and the CCD array of the video camera is increased up to 25 cm (Fig. 2b). A cardboard tube prevents the CCD array from stray light. A diffraction grating has 600 lines per millimeter. The distance between the light source and the grating is nearly 1 m. A focusing lens ($f = 10$ cm) is positioned between the grating and the objective lens of the camera. The monitor and the oscilloscope display the spectra. With this arrangement, the width of the monitor screen corresponds to a spectral range of about 20 nm.

For observing doublets in the spectra of mercury and sodium, we use pectral lamps from PHYWE. The lamps are equipped with an exit slit of about 0.1 mm in width. As examples, parts of the spectra of the "cool daylight" CFL and of the mercury spectral lamp are shown (Fig. 5). The green line in the spectrum, unresolved when observing the whole visible spectrum, is now resolved: one line belongs to mercury (546 nm), and the second to the phosphor. The components of the yellow doublet in the mercury spectrum (577–579 nm, $\Delta\lambda = 2.1$ nm) are now clearly seen. With the same setup, even the sodium doublet at 589 nm ($\Delta\lambda = 0.6$ nm) is resolved. The resolution of this doublet often serves as a criterion of the quality of a spectrometer.

The possibility to immediately observe the radiant power spectra and to enhance the spectral resolution gives a good reason for using a video camera for demonstrating optical spectra.

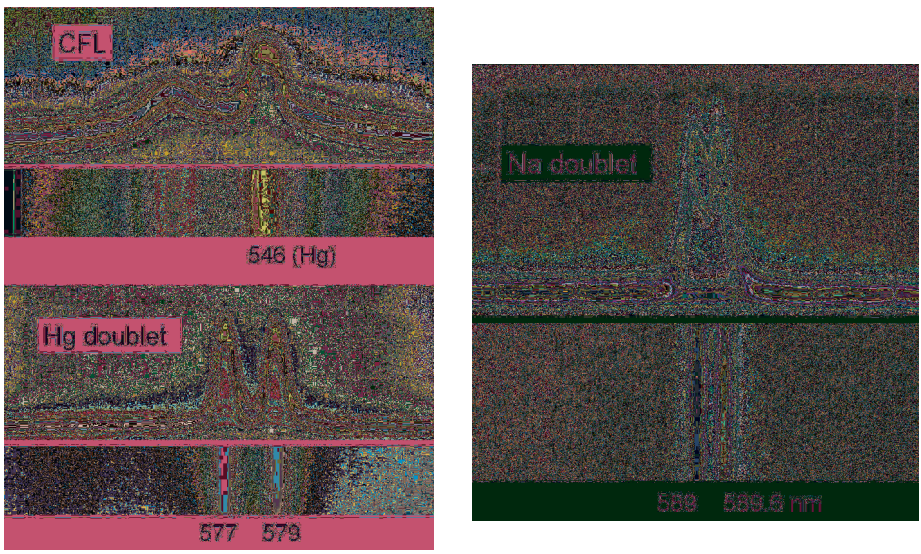

Fig. 5. The 546 nm mercury line and phosphorescence in the CFL spectrum; mercury doublet 577–579 nm; and sodium doublet at 589 nm.

5.8. Thermal radiation

Along with atomic spectra, the thermal radiation strongly required a revision of fundamentals of classical physics.

Wilhelm Wien (1864–1928)

Max Planck (1858–1947)

"…The Stefan–Boltzmann law and the Wien displacement law… do not solve the central problem, i.e. the question as to the distribution of radiation energy over the various wavelengths at different blackbody temperatures. We can however say that Wien's displacement law provides half the answer to the problem."

> E. W. Dahlgren, President of the Royal Swedish Academy of Sciences. Presentation of Wilhelm Wien awarded the Nobel Prize "for his discoveries regarding the laws governing the radiation of heat" (1911).

"…Professor Planck. The Swedish Academy of Sciences has awarded you in recognition of your epoch-making investigations into the quantum theory. This theory, which was originally connected with blackbody radiation, has now demonstrated its validity for other fields and relationships of Nature, and the constant number, named after you… describes a common, but until now unknown, property of matter."

> Å. G. Ekstrand, President of the Royal Swedish Academy of Sciences. Presentation of Max Planck awarded the Nobel Prize "in recognition of the services he rendered to the advancement of Physics by his discovery of energy quanta" (1918).

Additional equipment: *Broad spectrum light sensor*, *Rotary motion sensor*, *Educational spectrophotometer*, optics bench, diffraction grating, lenses, halogen light bulb, DC supply.

Many papers are devoted to experiments on the thermal radiation: Edmonds (1968); George *et al* (1972); Jaecks and Du Bois (1972); Wray (1975); Crandall and Delord (1983); Dryzek and Ruebenbauer (1992); Biermann *et al* (2002); Pesic (2005); Carlà (2013); Navrátil *et al* (2013); Abellán *et al* (2013). Unfortunately, many serious objections exist for quantitatively studying thermal radiation in student laboratories. Our aim is to show results obtainable with inexpensive equipment. It is useful to take into account the following.

• The **radiator** should have a sufficiently high temperature to provide radiation in **visible** and **near infrared** regions. This allows the use of simple and commonly accessible optical equipment. An **incandescent** light bulb with a **tungsten** filament well meets this requirement. The melting point of tungsten is 3695 K, and filaments of gas-filled or halogen lamps may be heated up to 3300–3400 K. A sufficient power of the radiation is also important.

• It is necessary to vary and somehow determine the temperature of the radiator. An incandescent light bulb is quite suitable because the temperature of a tungsten filament is available from its electrical resistance.

• With a **diffraction grating**, it is easy to calculate the wavelengths of the radiation. However, a problem is caused by the contribution of higher-order spectra. Even more important, the transfer of various spectral components varies within the spectrum. The use of a **prism spectrometer** also meets difficulties but this alternative should not be excluded.

• For a comparison with **Planck's formula**, it is useful to employ a body, whose **spectral emittance** ε_λ does not depend on the wavelength ("gray body"). Another possibility is the use of a material, for which the spectral emittance is well known. The spectral emittance of tungsten decreases with increasing wavelength. For producing visible light, a tungsten radiator is thus even more efficient than a blackbody.

• **Radiation sensors** having sensitivity independent of the wavelength are quite available. The *Broad spectrum light sensor* includes a thermopile in argon atmosphere and an amplifier; its response is flat in the range of 0.3 to 10 μm.

• To obtain results in a short time, the use of **data acquisition** is necessary.

Spectra of thermal radiation. Radiation spectra of a halogen light bulb are determined with a diffraction grating and a radiation sensor. The temperature of the filament is available from its electrical resistance. The data obtained are converted into blackbody spectra by using data on the spectral emittance of tungsten. The term **emittance** means the ratio of flux emitted by a sample to that emitted by a blackbody radiator at the same temperature and under the same

spectral and geometric conditions of measurement. Theoretical curves are scaled to the experimental spectra by fit at the point of maximum **spectral exitance**, with the same scaling coefficient for different temperatures. The spectral exitance means the radiant power per unit wavelength per unit area leaving the surface (Richmond 1984). Theoretical radiant spectra of blackbody radiation are given by Planck's formula (Fig. 1).

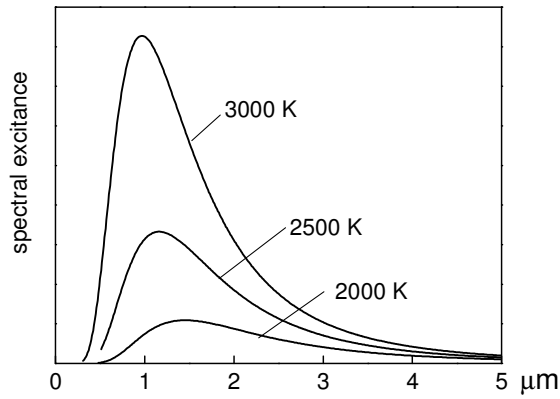

Fig. 1. Spectra of blackbody radiation for several temperatures.

The experimental setup (Fig. 2) is assembled on a 60 cm optics bench (OS-8541). The setup includes a halogen light bulb (12 V, 50 W) fed by a DC power supply, the *Educational spectrophotometer* (OS-8539) with two lenses, a diffraction grating, and the *Broad spectrum light sensor*. Two meters (not shown in Fig. 2) measure the current and voltage applied to the light bulb, so the electrical resistance of the filament and its temperature T are available. For a tungsten filament, a simple relation fits the data by Roeser and Wensel (1941):

$$T = 170 + 184X - 1.8X^2 + 0.02X^3, \quad (1)$$

where $X = R(T)/R_{273}$ is the resistance ratio.

The halogen light bulb is housed in a metal tube with a hole for the outcoming radiation. One lens serves to collimate the light beam falling onto the diffraction grating, and the second to focus the image of the filament on the entrance slit of the *Broad spectrum light sensor*. The size of this image is 2×5 mm (5 mm is the vertical size), whereas the entrance slit is a circle of about 4 mm in diameter. The diffraction grating is fixed at the center of the spectrophotometer, and the second lens and the sensor are placed on the rotating arm. The *Rotary motion sensor* measures the angle of rotation via a friction rim drive. It is useful to check the relation between the rotation of the arm and the rotation measured by the sensor. The simplest way is to rotate the arm to a known angle and to record the data from the sensor. Then the diffraction angles can be translated into wavelengths using the common equation. A laser diode providing radiation at 0.67 μm serves to check the suppression of the second-

order spectrum. From the measurements, the unwanted contribution of a continuous second-order spectrum is estimated to be about 10%. To correctly calculate the diffraction angles and light wavelengths, the starting position of the sensor is at the central maximum of the diffraction pattern. The rotation should be sufficiently slow because of the thermal inertia of the radiation sensor.

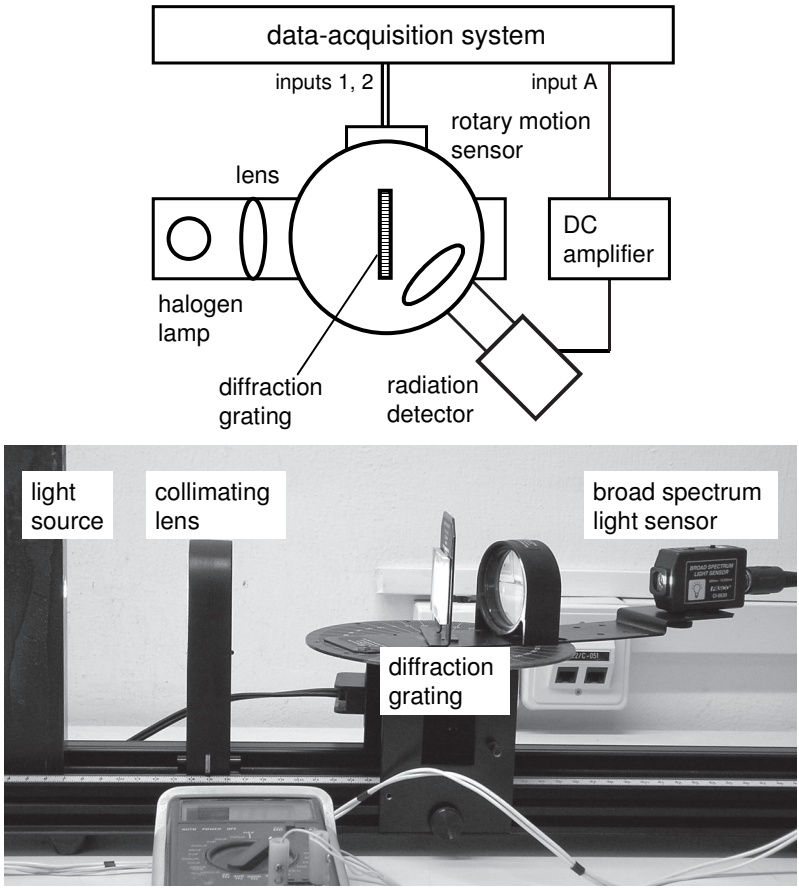

Fig. 2. Setup for recording thermal radiation spectra.

The measurements are carried out for four voltages applied to the light bulb (6, 8, 10, and 12 V). To calculate the temperature of the filament, it is necessary to know its resistance. For low-resistance filaments, this is difficult because of the contribution of the leads inside the bulb. It is useful to remember that the filament of a halogen light bulb normally operates in the range 3100 to 3400 K. The higher the temperature, the more efficient the generation of visible light, but the shorter the lifetime of the filament. Only projection lamps whose lifetime is claimed to be 50 h normally operate at the highest temperature. At 12 V, the temperature of the radiator is supposed to be 3300 K. For this

temperature, the electrical resistance ratio $R(T)/R_{273}$ is 20.08. The resistance of the filament at 273 K thus becomes known, and all the temperatures are available from Eq. (1). To obtain values proportional to the spectral exitance of light, the data from the sensor should be corrected. The radiation power in a narrow wavelength interval from λ to $\lambda + d\lambda$ is

$$dP = M(\lambda, T)d\lambda, \quad (2)$$

where $M(\lambda, T)$ is the spectral exitance.

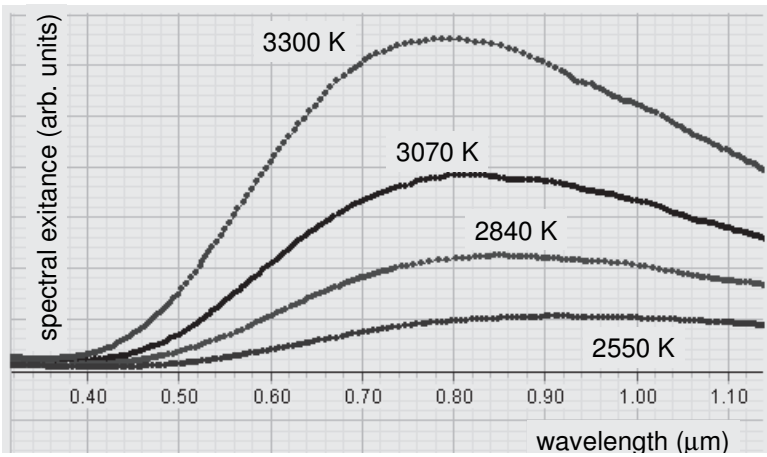

Fig. 3. Radiation spectra of tungsten for four temperatures.

For the first-order spectrum of a diffraction grating, $\lambda = d\sin\varphi$, where λ is the wavelength, d is the constant of the grating, and φ is the diffraction angle. Therefore, $\Delta\lambda = d\cos\varphi\Delta\varphi$, where $\Delta\varphi$ is a constant angle corresponding to the width of the entrance slit of the radiation sensor. From these considerations, the spectral exitance is proportional to the signal from the sensor divided by $\cos\varphi$. *DataStudio* calculates the spectral exitance, and the *Graph* displays it versus the wavelength. The radiation spectra (Fig. 3) show the strong dependence of the total radiation on temperature and displacement of the spectra according to **Wien's displacement law**. Further corrections are necessary to evaluate the blackbody spectra. The spectral emittance of tungsten strongly depends on wavelength and weakly on temperature. For 2800 K, it is given by (Thorn and Winslow 1962)

$$\varepsilon_\lambda = 0.58 - 0.25\lambda + 0.035\lambda^2, \quad (3)$$

where the wavelength λ is in micrometers.

The spectral emittance of tungsten thus varies from 0.46 at 0.5 μm to 0.365 at 1 μm. To calculate the blackbody spectrum, *DataStudio* divides the radiation spectrum of tungsten by its spectral emittance. However, Eq. (3) relates to a polished plane surface, and its applicability to a coiled filament is doubtful.

A solution to this problem might be the use of a standard temperature lamp with a tungsten ribbon. Such lamps serve for calibrating optical pyrometers. Additional advantages of such a lamp are the data on how the temperature of the ribbon depends on the heating current and the possibility to determine the temperature with an optical pyrometer.

With Eq. (3), the spectra obtained are converted into spectra of blackbody radiation (Fig. 4). Planck's radiation law relates the spectral exitance of a blackbody radiator to its temperature and to the frequency or wavelength of the radiation. The frequency presentation is preferable in theoretical studies, but the wavelength presentation is more convenient for practical use. In this case, the spectral exitance of a blackbody radiator equals

$$M(\lambda, T) = C_1/\lambda^5[\exp(C_2/\lambda T) - 1], \quad (4)$$

where $C_1 = 2\pi hc^2 = 3.74\times10^{-16}$ W.m^2, $C_2 = hc/k_B = 1.44\times10^{-2}$ K.m, h is Planck's constant, k_B is Boltzmann's constant, and c is the speed of light in vacuum. The units of $M(\lambda, T)$ are W.m^{-2}.m^{-1}, where the m^{-2} means per area of square meter, and the m^{-1} means per meter of wavelength.

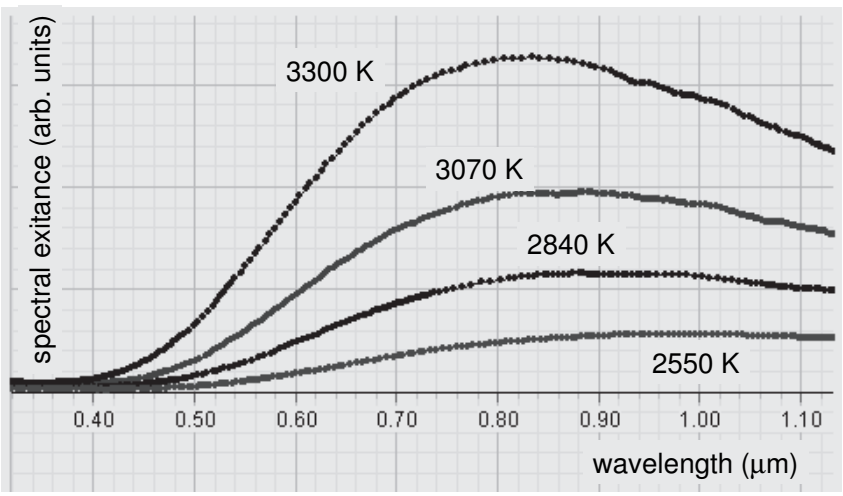

Fig. 4. Radiation spectra corrected for spectral emittance of tungsten.

It is difficult to overcome many objections for obtaining correct radiation spectra. The envelope of the light bulb, the lenses, the diffraction grating, and the window of the radiation sensor partially reflect and absorb the radiation. The losses in the radiation power thus depend on the wavelength. Another important point is the determination of the temperature of the radiator. The resistance data relate to pure tungsten, whereas slightly doped tungsten is used for filaments of incandescent light bulbs. Taking all this into account, the results obtained seem to be reasonable, but further efforts are necessary to improve the experiment.

Wien's displacement law. It can be seen from Eq. (4) that the wavelength λ_m, at which the maximum in the curve occurs, decreases with increasing the temperature. This wavelength can be found by differentiation of Eq. (4) with respect to λ and equating the result to zero. This gives

$$\lambda_m T = 2890\ \mu\text{m.K}. \tag{5}$$

This relation deduced in 1893 and known as Wien's displacement law is strictly correct for the blackbody radiation. For real radiators, the spectra are somewhat shifted because of the temperature dependence of the spectral emittance. Fortunately, the shift is quite moderate. The Wien's law can be verified by comparing temperatures calculated from the position of the maxima in the spectra with values deduced from the electrical resistance of the filament.

Stefan–Boltzmann's law of radiation states that the total radiation power P is proportional to the absolute temperature of the radiator T in the power of four:

$$P = \sigma A(T^4 - T_0^4), \tag{6}$$

where T_0 is the absolute temperature of the surrounding, A is the radiator area, and σ is Stefan–Boltzmann's constant, 5.67×10^{-8} W.m^{-2}.K^{-4}.

Stefan–Boltzmann's law was discovered before Planck derived his formula given by Eq. (4). Equation (6) can be deduced from Planck's formula. For real radiators, the hemispherical total emittance ε, which is specific for a material and depends on the temperature and quality of the sample surface, modifies the above equation:

$$P = \varepsilon\sigma A(T^4 - T_0^4). \tag{7}$$

This law can be confirmed independently of the radiation spectra. Under steady state conditions, the power supplied to a radiator must equal the sum of all heat losses from it. The part related to thermal radiation depends on the design of the radiator and on its temperature. In incandescent light bulbs, the radiation takes most of the supplied power. Measurements of the supplied power versus the temperature of the filament may therefore verify Stefan–Boltzmann's law.

In the experiment, along with the determinations of the power P_{el} supplied to a low voltage light bulb, its radiation is measured with a radiation sensor. The sensor has a constant sensitivity over a wide range of wavelengths. The radiation power from the bulb is taken as $P_{rad} = KT^n$, where the exponent n is expected to be somewhat larger than 4 due to the temperature dependence of the total emittance. The experimental arrangement for the measurements is very simple (Fig. 5). A DC source powers a light bulb. Two *Voltage sensors* measure the heating current and the voltage across the filament. The *Broad spectrum light sensor* is positioned at a definite distance from the radiator. The measurements are carried out during gradually changing the current heating the filament. To keep thermal equilibrium conditions, these changes should not be too fast. The radiation power is determined through the electric power supplied to the light

bulb and from the measurements by the radiation sensor. The data obtained are presented as a log-log graphs of the radiation power versus temperature.

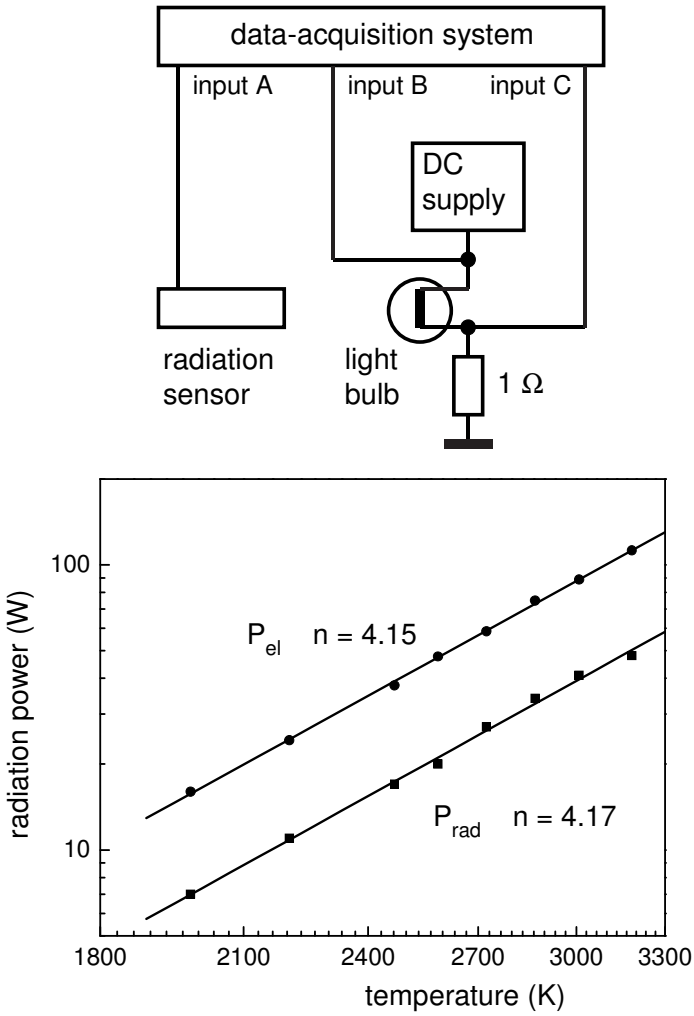

Fig. 5. Schematic of the setup and radiation power versus radiator temperature: P_{el} –power supplied to the light bulb, P_{rad} –measurements by the radiation sensor (arbitrary units).

5.9. Hydrogen atom

Rydberg's constant and energy levels of the hydrogen atom are determined by measuring wavelengths of Balmer's series.

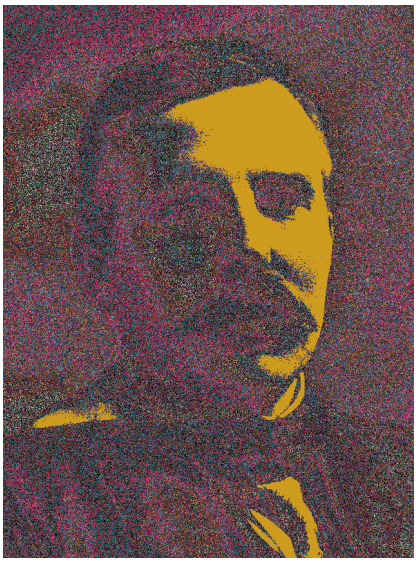

Ernest Rutherford (1871–1937)

Niels Bohr (1885–1962)

"…Though Rutherford's work has been carried out by a physicist and with the aid of physical methods, its importance for chemical investigation is so far-reaching and self-evident, that the Royal Academy of Sciences has not hesitated to award to its progenitor the Nobel Prize…"

> K. B. Hasselberg, President of the Royal Swedish Academy of Sciences. Presentation of Ernest Rutherford awarded the Nobel Prize in Chemistry "for his investigations into the disintegration of the elements and the chemistry of radioactive substances" (1908).

"…Professor Bohr. You have carried to a successful solution the problems that have presented themselves to investigators of spectra… Your great success has shown that you have found the right roads to fundamental truths, and in so doing you have laid down principles which have led to the most splendid advances, and promise abundant fruit for the work of the future."

> S. Arrhenius, Chairman of the Nobel Committee for Physics. Presentation of Niels Bohr awarded the Nobel Prize "for his services in the investigation of the structure of atoms, and of the radiation emanating from them" (1922).

Equipment: hydrogen spectral tube with power supply, spectrometer.

PASCO spectral tube with power supply.

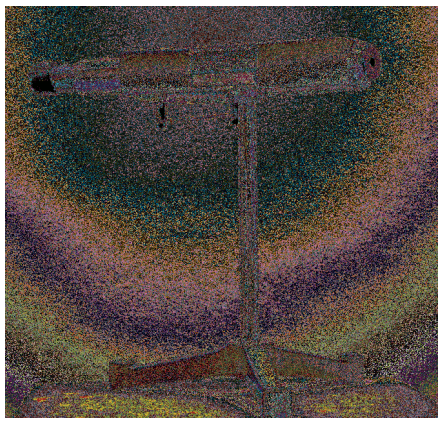

Spectrometer used in the measurements.

Rutherford–Bohr's atom model. In 1910, Rutherford and his co-workers established the nuclear model of the atom by observing the large-angle scattering of α-particles transmitted through a thin foil.

"…The deflection of an α-particle through an angle greater than a right angle was clearly not explicable… and Rutherford in December 1910 came to the conclusion that the phenomenon could be explained only by supposing that an α-particle occasionally (but rarely) passed through a very strong electric field, due to a charged nucleus of very small dimensions in the center of the atom… Thus Rutherford was led to what was perhaps the greatest of all his discoveries, that of the structure of the atom" (Whittaker 1960, p. 22).

Energy levels of hydrogen atom. The hydrogen atom is the simplest one. In **Rutherford's model**, the electron is considered to rotate in a circular orbit around the nucleus. Hydrogen gas is normally in the molecular state, the hydrogen molecule consisting of two atoms bonded together. If an electrical discharge is maintained in hydrogen, the molecular bonds will be split up. The emission spectrum from a hydrogen discharge is thus due primarily to the atoms. The hydrogen atom consists of a single proton (charge $+e$) and a single electron (charge $-e$) bound by the attractive **Coulomb force**. The electron is subjected to an electrostatic force of attraction towards the nucleus, which is balanced against its mass times its radial acceleration away from the nucleus. Bohr alleged that the radiation from an atom (or absorptance of radiation) occurs only due to a

transition of an electron from one stationary orbit to another. The frequency of the emitted or absorbed light f obeys the quantum condition

$$hf = E_n - E_m, \quad (1)$$

where h is Planck's constant, and E_n and E_m, are the energies of the stationary states. The energies of stationary states of a hydrogen atom equal to

$$E_n = -Rch/n^2 \quad (n = 1, 2, 3,\ldots), \quad (2)$$

where c is the velocity of light, and the constant R is called **Rydberg's constant**, which equals 1.098×10^7 m^{-1}. With this relation, one can immediately build the diagram of energy levels of the hydrogen atom (Fig. 1).

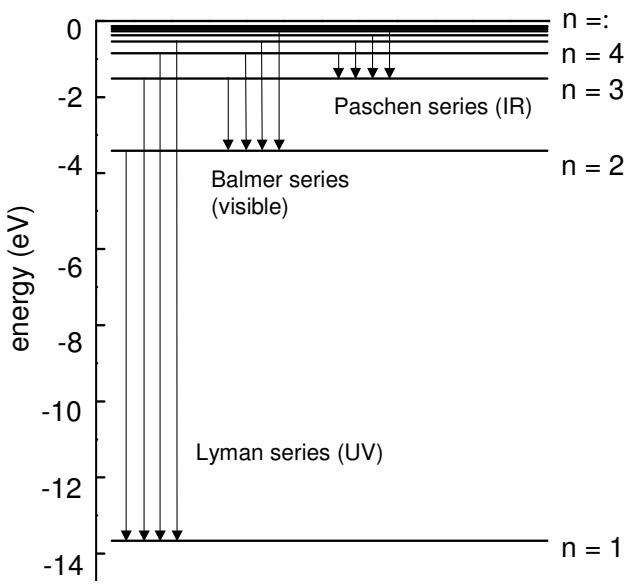

Fig. 1. Diagram of energy levels of hydrogen atom.

Rydberg's constant from Balmer's series. A hydrogen spectral tube (SE-9461) is mounted into the power supply (SE-9460). A spectroscope with a diffraction grating and direct indication of wavelengths is used to observe Balmer's series, and determine Rydberg's constant. Then the diagram of energy levels of the hydrogen atom is built using Eq. (2).

5.10. Photoluminescence

The decay of a fluorescent light bulb and of a phosphor-coated paper is observed.

Additional equipment: *Light sensor*, fluorescent light bulb, phosphor-coated paper.

Photoluminescence is a general term describing any process, in which energy is emitted from a material at a different wavelength from that at which it is absorbed. Such phenomena often occur only in the presence of a trace amount of an activator. **Fluorescence** is a photoluminescence phenomenon, in which electron de-excitation occurs almost spontaneously. In fluorescent materials, the excited state has the same spin as the ground state. Most fluorescence events are fast and follow the exponential decay law. However, for light to be absorbed and emitted at these fast time scales, the energy of the photons involved must be carefully tuned according to the rules of quantum mechanics to match the available energy states and allowed transitions. Electrons arranged in atomic configurations or more complex molecular orbitals group into pairs, which follow the Pauli exclusion principle. Only single electrons can populate a single energy level, or orbital. Each possible orbital is associated with a set of **quantum numbers**, and allowed transitions involve only certain prescribed changes in quantum numbers between states. The allowed energy transitions then determine the preferred **absorptance** and **emission** spectra.

Phosphorescence is similar to fluorescence, but the species are excited to a **metastable state**, from which a transition to the initial state is forbidden. A quasi-stable electron excitation state involves a change of spin state, which decays only slowly. Emission occurs when thermal energy raises the electron to a state, from which it can de-excite, so that the phenomenon is temperature-dependent. The places where we most commonly see phosphors are in a TV screen or computer monitor and in fluorescent lamps. In a TV screen, an electron beam strikes the phosphor to energize it. This process is called **cathodoluminescence**. A color TV screen contains thousands of tiny picture elements that emit three different colors (red, green, and blue). In a fluorescent lamp, there is normally a mixture of **phosphors** that together create light that looks white to us. Phosphors have three main characteristics: (i) the type of energy they require to be energized, (ii) the color of the visible light that they produce, and (iii) the length of time that they glow after being energized.

A fluorescent light bulb is a sealed glass tube containing a small bit of mercury and an inert gas, typically argon, kept under low pressure. A phosphor powder is coated along the inside of the glass. The bulb has two electrodes. As electrons and ions move through the bulb, some of them collide with the gaseous mercury atoms. These collisions excite the atoms. When the electrons return to their original energy level, they emit photons, mostly in the ultraviolet. When such a photon hits a phosphor atom, one of its electrons jumps to a higher energy

level. When the electron returns to its normal level, it emits a photon in the visible region. The photoluminescence in a fluorescent lamp is clearly seen when one observes the intensity of light produced by it (Baker 1966; Ganci 1984; Yuan *et al* 2010; Sulkes and Sulkes 2011). While an AC current feeding the bulb falls down to zero two times per period, the light intensity does not. Various types of phosphors or their combinations are used in fluorescent light bulbs to modify their spectra. The **decay time** for various light bulbs may be quite different (Fig. 1). The shorter the decay time, the larger are the ripples. For comparing the decay times of a fluorescent lamp and a phosphor, the *Light sensor*, the lamp, and a piece of phosphor-coated paper are placed in a closed box (Fig. 2).

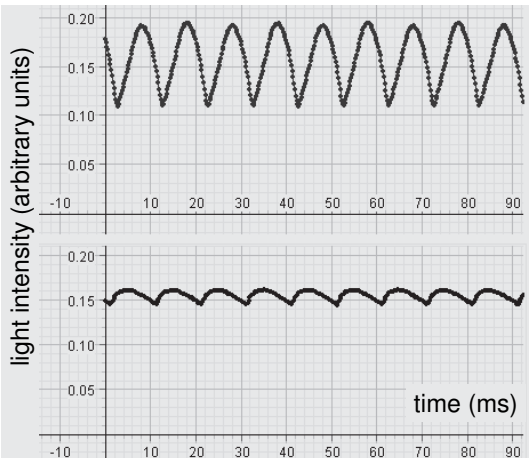

Fig. 1. Light intensity versus time for two fluorescent light bulbs.

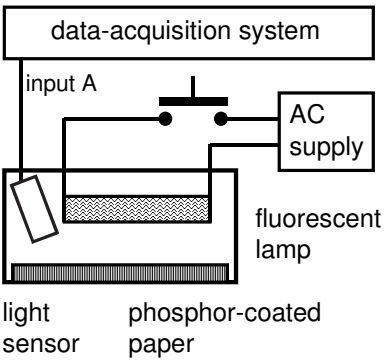

Fig. 2. Schematic of the setup.

When measuring the decay time of the fluorescent light bulb, the phosphor-coated paper is replaced by a piece of white paper. The decay of the light bulb is much faster than that of the phosphor-coated paper (Fig. 3). In the measurements, the *Delayed start* option allows data acquisition to start after switching the light bulb off, when the signal from the sensor becomes below a certain level set by the experimenter. The results obtained show the difference in the decay times for the two cases. The signal from the phosphor-coated paper does not really differ from that including both phenomena. For the fluorescent light bulbs, the decay is fairly exponential, which is typical for fluorescence. For the light bulb manifesting faster decay, the time constant appeared to be 12.5 ms.

An additional experiment confirms the origin of the light emission from the phosphor-coated paper. A typical feature of phosphorescence is its temperature dependence, and even minor temperature changes are sufficient to make this effect observable (Fig. 4). For this experiment, a plane heater is placed under the phosphor-coated paper.

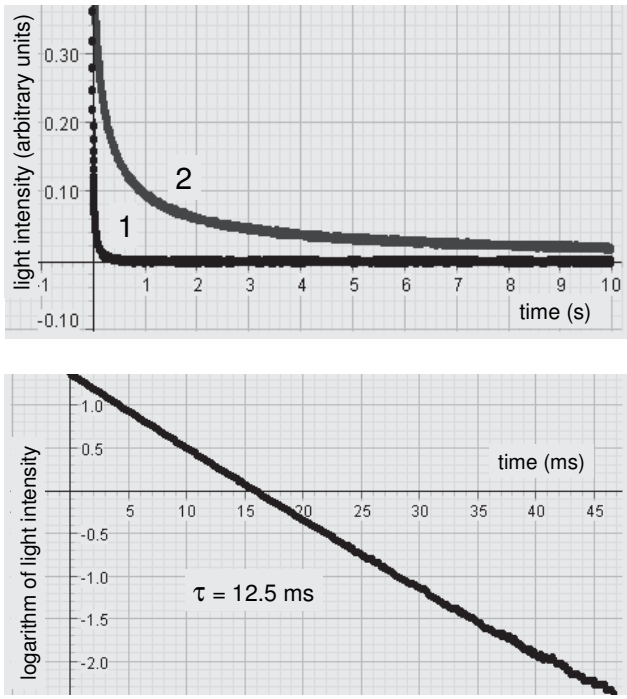

Fig. 3. Fluorescence decay of light bulb (1) and phosphorescence of phosphor-coated paper (2); exponential decay of fluorescent light bulb.

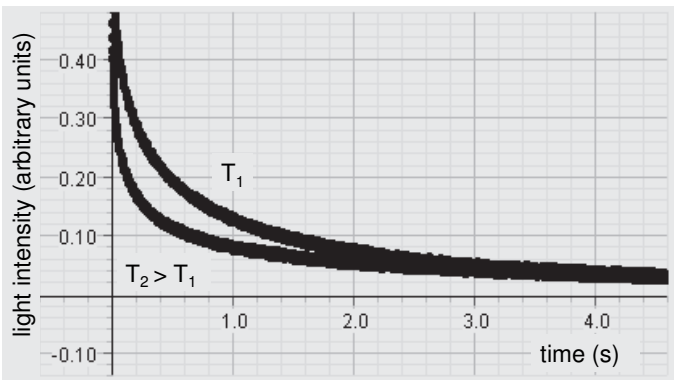

Fig. 4. Decay of the phosphorescence becomes faster at higher temperatures.

5.11. Quantum efficiency of light detector

The external quantum efficiency of a photodiode is determined (Kraftmakher 2008c).

Additional equipment: *Educational spectrophotometer*, *Broad spectrum light sensor*, *Rotary motion sensor*, DC supply, DC amplifier, AC supply, light bulb, two lenses, diffraction grating, silicon photodiode, optics bench, resistors.

The **quantum efficiency** of a light detector is the number of electrons (or electron-hole pairs) released by the photoelectric effect to the number of incident or absorbed photons (Chappell 1978; Marcuse 1980; Jones 1987; Shur 1996). Two types of the quantum efficiency are considered: the **internal efficiency** related to light absorbed by the detector, and the **external efficiency** related to incident light. Here, we deal with the external quantum efficiency η. For a monochromatic light of frequency ν and power P, the number of photons per second is $P/h\nu$, where h is Planck's constant. The electric current I due to the photoelectric effect is

$$I = \eta Pe/h\nu, \tag{1}$$

and the external quantum efficiency equals

$$\eta = Ih\nu/Pe = Ihc/Pe\lambda, \tag{2}$$

where e is the electron charge, c is the velocity of light, and λ is the wavelength. For the I/P ratio in amperes per watt and the wavelength in micrometers,

$$\eta = 1.24 \times I/P\lambda. \tag{3}$$

The sensitivity of a photodiode is usually given as a graph of the I/P ratio versus wavelength or as its values at definite wavelengths. The I/P ratio usually grows with wavelength but rapidly falls down when approaching the photoelectric effect threshold, which depends on the energy bandgap of the semiconductor. For a silicon photodiode used here, the I/P ratio given by the manufacturer is 0.62 $A.W^{-1}$ at $\lambda = 0.9$ μm, so the external quantum efficiency is 0.85. Determinations of the external quantum efficiency of a light detector require measurements of the power of incident light. Such measurements are possible with radiation detectors based on thermal action of totally absorbed light. This approach seems to be preferable, though it is possible to use for this aim photodiodes having the external quantum efficiency very close to 100% (Zalewski and Duda 1983; Larson and Mickelson 1985).

We use the *Educational spectrophotometer*, the *Broad spectrum light sensor*, a gas-filled light bulb (12 V, 45 W), two lenses, a diffraction grating (SE-9358, 600 lines per millimeter), and a silicon photodiode (Edmund Optics J54-520) placed on an optics bench (OS-8541). The radiation detector and the focusing lens are positioned on the rotating arm of the spectrophotometer

(Fig. 1). The light bulb, the collimating lens, and the diffraction grating are fixed. The filament of the light bulb is vertical, and the height of the spectrum focused on the light detector is about twice the size of the detector. A screen prevents the detector from stray light. The *Rotary motion sensor* measures the angular position of the rotating arm. The current of the photodiode is determined through the voltage across a 10 kΩ load. The sensitive area of the photodiode given by the supplier is 5.1 mm^2.

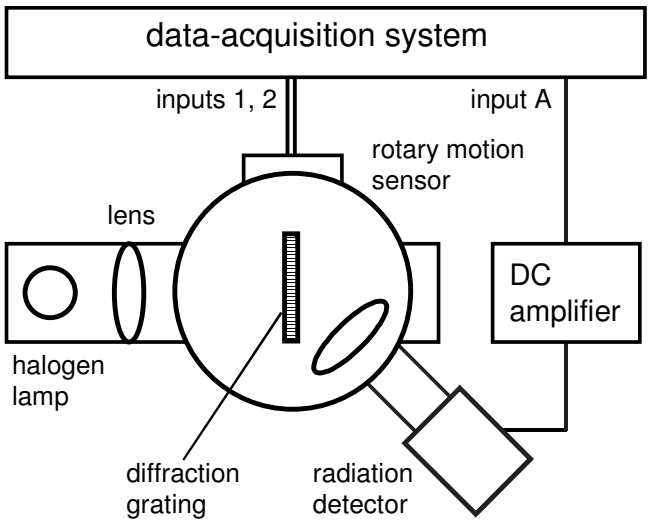

Fig. 1. Diagram of the experimental setup.

Non-selective radiation detector. The *Broad spectrum light sensor* has a flat response from 0.3 to 10 μm. The sensor provides three scales but absolute values of the sensitivity are not given. In our case, the spectral range of interest is 0.5 to 1.3 μm, so that the sensor can be used after properly calibrating it. The sensitive area of the photodiode is known, and the best way is to calibrate the sensor in irradiance units.

A homemade radiation sensor is used for the calibration. The sensor is made of a thin copper foil painted black and equipped with current and potential leads. Its absorptivity is supposed to be 100%. The sensitive area of the sensor restricted by the potential leads is 2.6 cm^2, and its resistance is 12 mΩ. The sensor is fed by a DC supply and a variable AC supply connected in parallel (Fig. 2). The DC current serves for determining the resistance of the sensor. The resistance increases with the temperature of the sensor, by about 0.4% per kelvin. The increment in the temperature is proportional to the power of absorbed radiation. The DC voltage between the potential leads is amplified and then acquired by *DataStudio*. A Keithley 177 multimeter serves as the amplifier. An integrating circuit (50 kΩ, 10 μF) is included at the input of the amplifier to suppress the AC component of the voltage that appears when the AC current

passes through the sensor. This AC current provides an additional easy-to-calculate power dissipated in the sensor. The sensor is a self-calibrated tool, and it is easy to manufacture it.

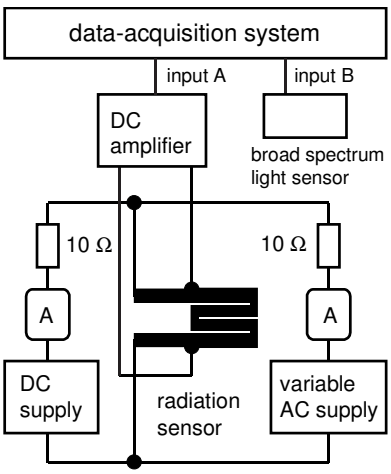

Fig. 2. Setup for calibrating the *Broad spectrum light sensor* with the homemade radiation sensor.

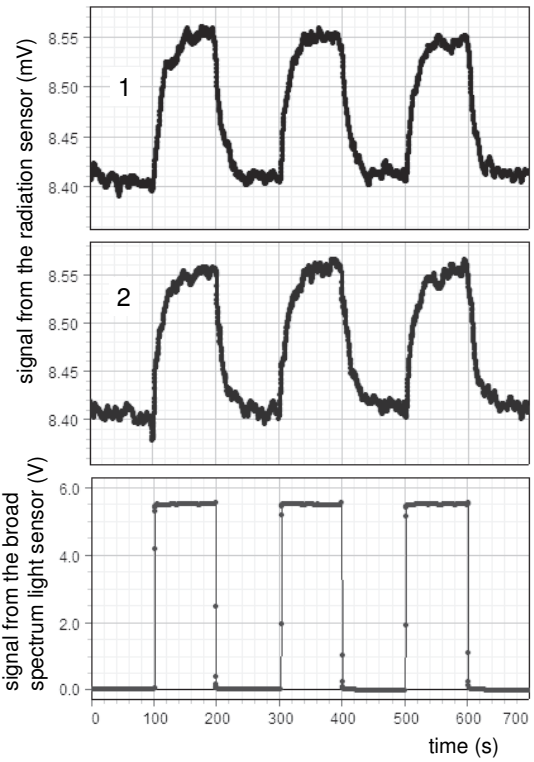

Fig. 3. Signals from the homemade radiation sensor subjected to irradiation from light bulb (1) or to AC heating (2).

For the calibration (Fig. 3), the sensor is placed 20 cm apart a 100 W light bulb. *DataStudio* displays the amplified DC voltage between potential leads of the sensor. After measuring the changes in this voltage due to periodically irradiating the sensor, the irradiation is replaced by periodically AC heating. In both cases, the signals due to the power dissipated in the sensor are of the order of 0.1 mV. There is no need for achieving exactly the same signal in both measurements because the signal is proportional to the dissipated power. The *Smooth* tool is employed for reducing the scatter of the data. The power is calculated from the AC current and the resistance of the sensor. In the example presented, the AC current is 1.75 A. The same irradiation is measured by the *Broad spectrum light sensor*. Its sensitivity, for the unity gain scale, appeared to be 2.5 $mW.cm^{-2}.V^{-1}$, with an uncertainty not exceeding 20%. Clearly, using a certified radiation detector would be preferable.

Quantum efficiency versus wavelength. After the calibration, the experiment becomes very simple. The rotating arm of the spectrophotometer is set at angle zero, and the photodiode is placed at the central maximum of the diffraction pattern. When manually rotating the arm, *DataStudio* acquires the data on the diffraction angle and the current of the photodiode. Simultaneously, it calculates the wavelength of the light. The *Sample rate* is 50 Hz. The procedure is repeated with the *Broad spectrum light sensor*. For converting the voltage from the sensor into the power of radiation falling onto the photodiode, this signal is multiplied by 2.5 $mW.cm^{-2}.V^{-1}$ and 5.1×10^{-2} cm^2.

The data for the longest wavelengths are distorted by a contribution of the second-order spectrum amounting to about 10% of the maximum photoelectric current. This contribution becomes important for the measurements close to the photoelectric threshold. To take it into account, additional measurements are performed with a certified long-pass filter (Thorlabs RG850). The filter eliminates visible light and thus the influence of the second-order spectrum: the background at wavelengths above 1.2 μm is reduced by one order of magnitude (Fig. 4). The calculations of the *I*/*P* ratio are done separately for two wavelength bands: data obtained with no filter are used below λ = 1 μm, and data with the filter for longer wavelengths. With the filter, the wavelength scale can be checked: 50% transmission of the filter corresponds to λ = 0.85 μm.

The data obtained are sufficient for determining the *I*/*P* ratio. However, the wavelengths involved in the different runs do not coincide, so that *DataStudio* cannot simply divide one graph by another. A simple additional program was therefore prepared. The wavelength band is divided on a number of equal subbands, and a middle wavelength is assigned to each subband (see Experiment 4.1). All the photocurrent and incident power data falling into one subband are replaced by their averages. The software thus provides sets of *I* and *P* data related to exactly the same wavelengths, and *DataStudio* computes the *I*/*P* ratio (Fig. 5). This approach is also useful for some other experiments. The software is very simple and can be prepared by students.

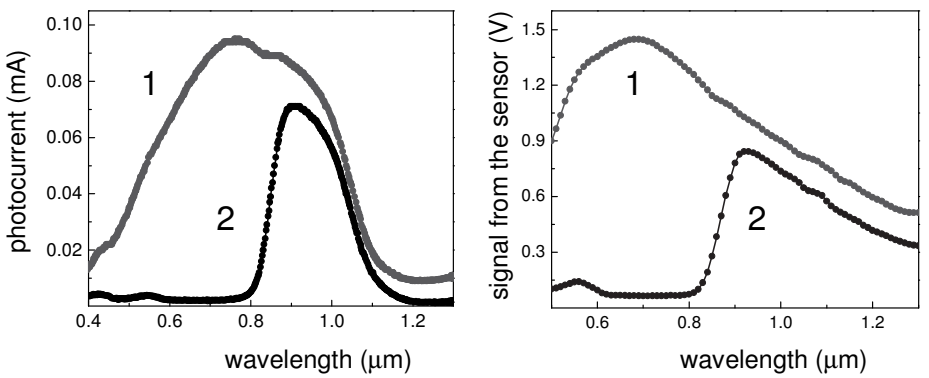

Fig. 4. Normalized spectra of photocurrent and signal from the *Broad spectrum light sensor*: 1–directly, 2–through the filter.

In the example presented, the width of the subbbands is 0.01 μm. The I to P ratio and the quantum efficiency of the silicon photodiode appeared to be in reasonable agreement with expected values. Below the threshold wavelength, the quantum efficiency is nearly constant.

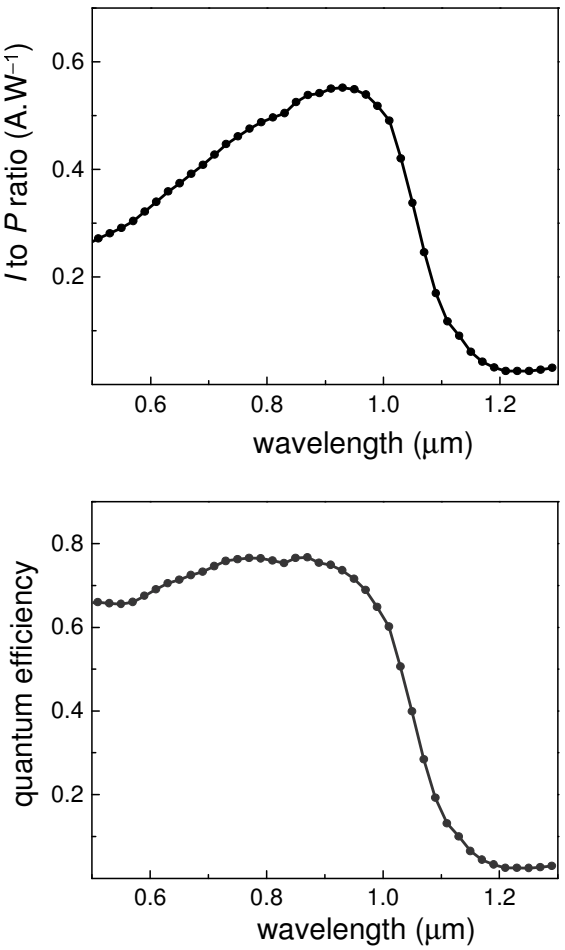

Fig. 5. I to P ratio and external quantum efficiency of the silicon photodiode versus light wavelength. For $\lambda < 1$ μm, the efficiency is nearly constant.

5.12. Electron-atom collisions in gases

Three experiments with a thyratron are presented: (i) Ramsauer–Townsend's effect; (ii) the excitation and ionization potentials of xenon; and (iii) the deionization (ion-electron recombination) process after the electric discharge is interrupted (Kraftmakher 2013f).

The first experiment follows that described by Kukolich (1968) and Woolsey (1971). The second experiment is a computer-assisted modification of a well-known experiment possible with Franck–Hertz's tube or a thyratron (Harnwell and Livingood 1933; Williams 1968; Whittle and Yarwood 1973). In the third experiment, the time resolution is sufficient for observing the ion-electron **recombination** process, and the characteristic **deionization time** is determined.

The *850 Universal Interface* with *Capstone* software is used in the experiments. Some features of the new data-acquisition system—the enhanced output voltage of the internal function generators, the bias option, and the high sample rate—are important for performing the experiments. Measurements of microsecond resolution are needed for observing the deionization process in the thyratron.

The thyratron is a gas-filled triode or tetrode with an electrically heated cathode. A Xe-filled thyratron 2D01 has a cathode, an anode, and two grids (Fig. 1). The first grid is a control electrode. The second one is a screen protecting the tube from external electric fields; usually, it is connected to the cathode. A 6.3 V voltage is needed to heat the cathode.

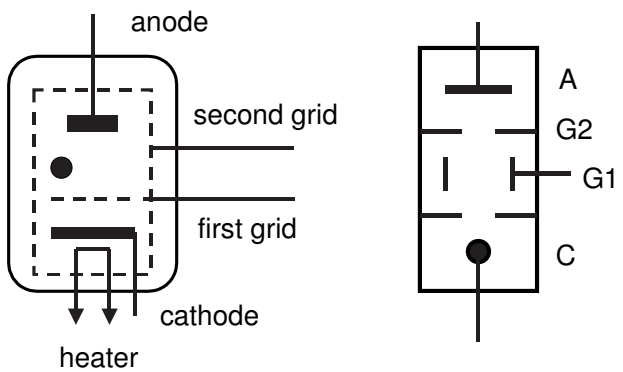

Fig. 1. Schematic of the thyratron.

1. Ramsauer–Townsend's effect

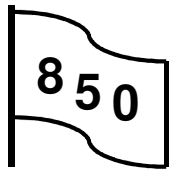

This is a computer-assisted version of an experiment described by Kukolich (1968) and Woolsey (1971).

Additional equipment: *Voltage sensor*, Xe-filled thyratron, power supply for heating the cathode, resistors.

The anode current is measured versus the acceleration voltage provided by the *Output 1*. The output is connected to the cathode, while the grids and anode are kept at a nearly zero potential relative to ground (Fig. 2). At accelerating voltages in the vicinity of 2.5 V, a maximum in the anode current is seen. This means a significant decrease of the scattering cross section for electrons on the gas atoms. The phenomenon is called Ramsauer–Townsend's effect and is explained by quantum mechanics. A virtual characteristic of the vacuum tetrode is seen when the Xe gas inside the thyratron is frozen out using liquid nitrogen.

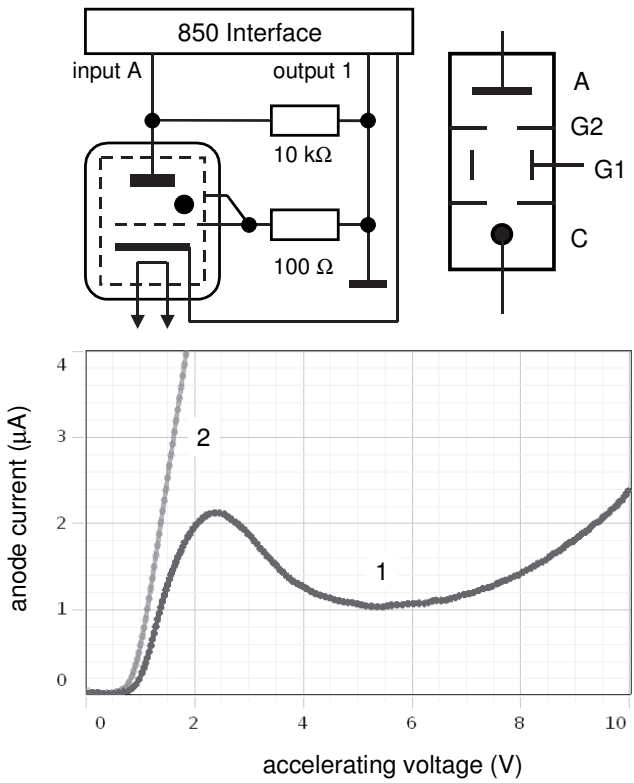

Fig. 2. Diagram of the setup and the anode current of the thyratron versus accelerating voltage. 1–Xe-filled thyratron, 2–Xe gas is frozen out.

2. Excitation and ionization

Excitation and ionization potentials of Xe are determined. The experiment follows those described by Harnwell and Livingood (1933); Kraftmakher (1959a); Iveronova (1962); Williams (1968).

Additional equipment: three *Voltage sensors*, Xe-filled thyratron, power supply, 9 V battery, resistors, capacitor.

Excitation and ionization potentials. A continually varying accelerating voltage from the *Output 1* is applied to the grids connected in parallel (Fig. 3). The maximum of this voltage exceeds the **ionization potential** of xenon. A 100 Ω resistor limits the grid current. The current is determined by measuring the voltage drop across this resistor with the *Voltage sensor*. Another *Voltage sensor* (not shown in Fig. 3) measures the accelerating voltage. With a battery, the potential of the anode is set 9 V lower than that of the cathode. The electrons emitted by the cathode cannot overcome this potential barrier. The term "anode" thus becomes irrelevant but is retained to follow previous papers describing this experiment.

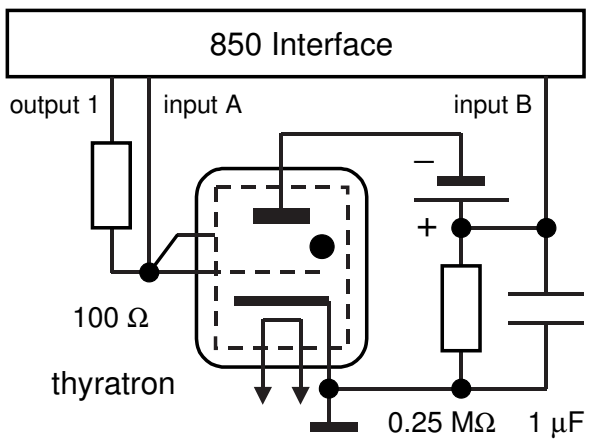

Fig. 3. Diagram of setup for determining the excitation and ionization potentials.

Collisions of the emitted electrons with Xe atoms in the thyratron remain elastic until the energy of the electrons reaches the first **excitation potential** of the atoms. Usually, the excitation potential of a gas is obtained from *I–V* characteristics of the tube operating in an appropriate regime. Our experiment is based on detecting the **photoelectric effect** on the anode after the excitation occurs. The excited atoms immediately return to their initial state. This process is accompanied by emission of photons, which cause photoelectric effect on the

anode. The phenomenon is seen from the voltage across a 0.25 MΩ resistor in the anode circuit measured with the third *Voltage sensor*. A 1 μF capacitor is connected parallel to this resistor for suppressing interference of the 50/60 Hz frequency. The sign of the voltage across the resistor shows that electrons leave the anode. The appearance of the anode current is a sign of the photoelectric effect and thus of the excitation of Xe atoms in the thyratron (Fig. 4).

The ionization potential is obtainable by measuring the grid current, which rises radically when positive ions appear in the tube. The ions move to the cathode and partly neutralize the negative space charge formed by electrons emitted by the cathode; therefore, the grid current increases. The excitation and ionization potentials are seen from the plots of the anode and grid currents versus the accelerating voltage. Both potentials appeared to be somewhat lower than accepted: the correct values are 12.1 V for the ionization potential, and nearly 9 V for the first excitation potential. The low values obtained in our measurements are probably caused by the **contact potential difference** and initial velocities of electrons emitted by the cathode.

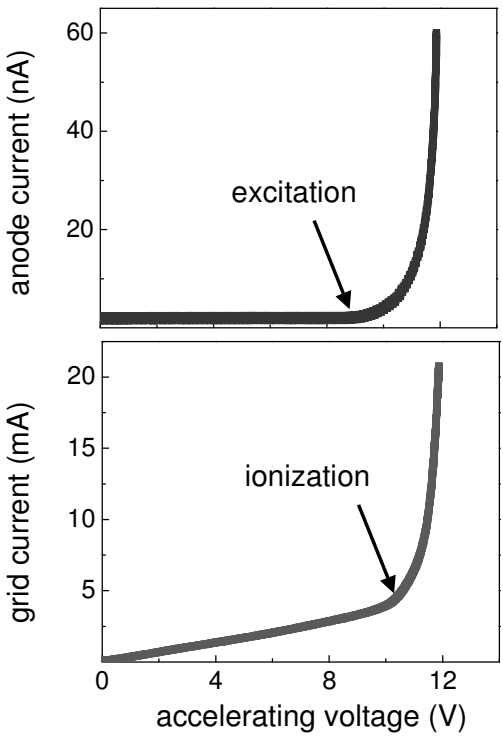

Fig. 4. Anode and grid currents versus accelerating voltage.

Deionization time. The aim of this experiment is to observe the deionization process in the thyratron and determine the characteristic deionization time

(Kraftmakher 2013f). The same thyratron serves for observing the ion-electron recombination after the electric discharge in the tube is interrupted (Fig. 5). A positive voltage exceeding the ionization threshold is applied to the grids for a time sufficient for establishing the discharge in the Xe gas. Then the voltage is rapidly decreased and the discharge interrupted. With a 5 Ω resistor in the grid circuit, a relatively large current and thus a high ion concentration in the tube are created. To decrease the time constant of the load in the anode circuit, the load resistance is reduced to 10 kΩ, and the 1 μF capacitor is excluded. With a battery, the potential of the anode is set 9 V lower than that of the cathode.

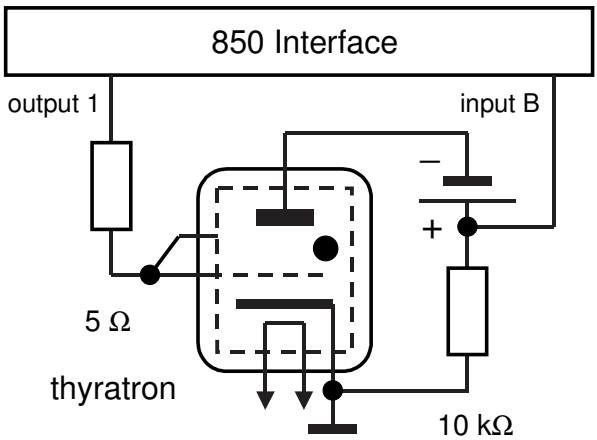

Fig. 5. Diagram of setup for observing the deionization process.

The voltage applied to the grids is a biased 500 Hz square wave voltage from the *Output 1*. The amplitude of this voltage is 6 V, while the DC bias is +9 V. During the positive half of the period, the voltage applied to the grid is 15 V (9 + 6), which exceeds the ionization potential. During the negative half of the period, this voltage becomes +3 V (9 – 6). The discharge is interrupted, while the anode remains under a negative potential due to the battery. The anode current during the deionization process reflects the ion-electron recombination in the tube (Fig. 6). The measurement data are processed with the *Origin* software. The data in the time interval 1.6–1.8 ms related to the deionization process were separated and fitted by an exponential decay:

$$y = y_0 + A\exp[-(t - t_0)/\tau], \tag{1}$$

where τ is the **characteristic time** of deionization. From the fit, τ = 43 μs. This figure falls into a range given by the manufacturers, despite the regime of the thyratron significantly differs from the common regime. From the fit, t_0 coincides with the start of the deionization process, while y_0 is close to zero.

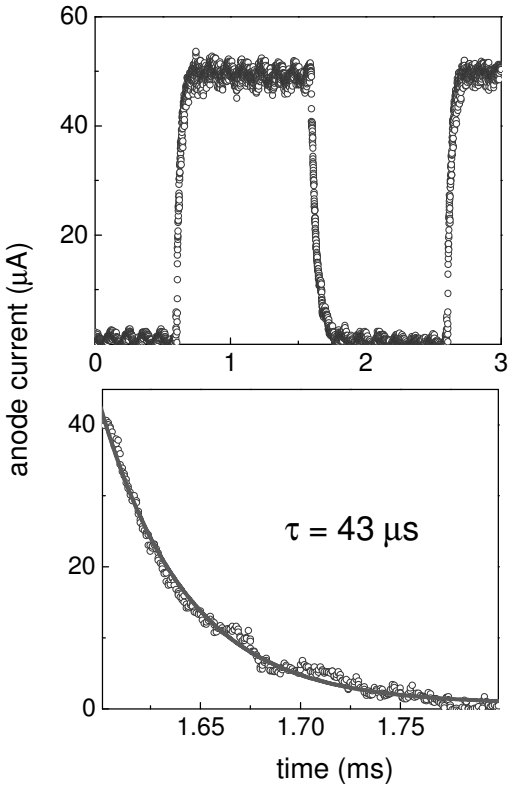

Fig. 6. Anode current versus time and the deionization process; the exponential decay fit is shown.

Condensed Matter Physics

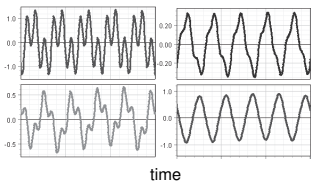

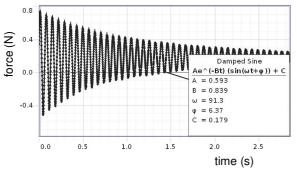

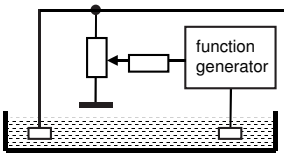

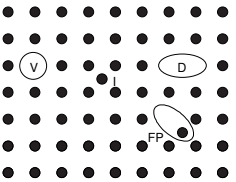

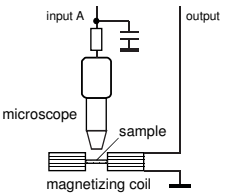

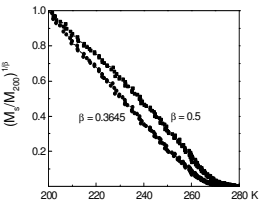

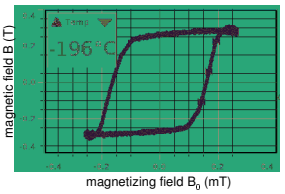

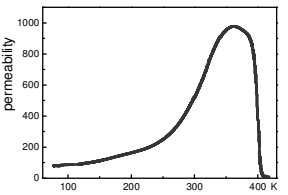

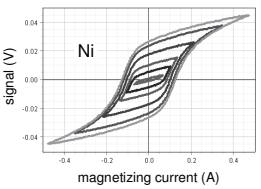

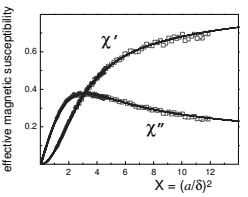

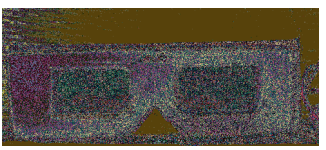

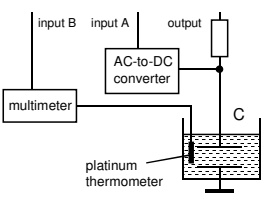

6.1. Speed of sound in solids

Two methods are used to observe longitudinal vibrations of metal rods. The experiment follows those described by Frank and Kluk (1991) and Mak *et al* (2000).

Additional equipment: *Sound sensor*, AC-to-DC converter, microphone, metal rods, coil, permanent magnet.

The frequency f of the fundamental longitudinal vibration of solid rods is related to the length l of the rod and the **longitudinal sound velocity** c:

$$f = c/2l. \quad (1)$$

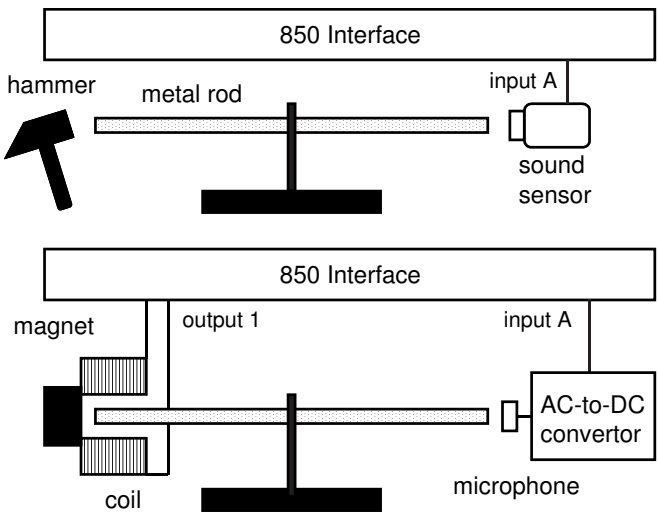

Fig. 1. Setups for observing decay and spectra of standing waves.

The rods must have a suspension that makes possible the creation of a single-frequency standing wave. Striking one of its ends triggers the standing wave and creates many propagating waves with different frequencies. In rods suspended only in the middle, the fundamental frequency standing wave survives longer than others. The complete decay of the standing waves lasts several seconds. With a data-acquisition system, it is possible to record and display different stages of this process.

The first setup employs the *Sound sensor* positioned near one end of the rod clamped at its center. After an impact is given to the other end of the rod, several runs are performed, from which the evolution of the standing waves in the rod is clearly seen. The *Sample rate* is 100 kHz, and one run lasts only 3 ms. The fundamental frequency of the sound wave is obtainable with the *Fit*/*Sine fit*

for the survived standing wave (Fig. 2). For an aluminium-alloy rod (l = 1.468 m), the period is 0.587 ms, so the speed of sound equals 5008 m.s^{-1}. For a brass rod (l = 1.005 m), the period is 0.595 ms, so the speed of sound is 3378 m.s^{-1}.

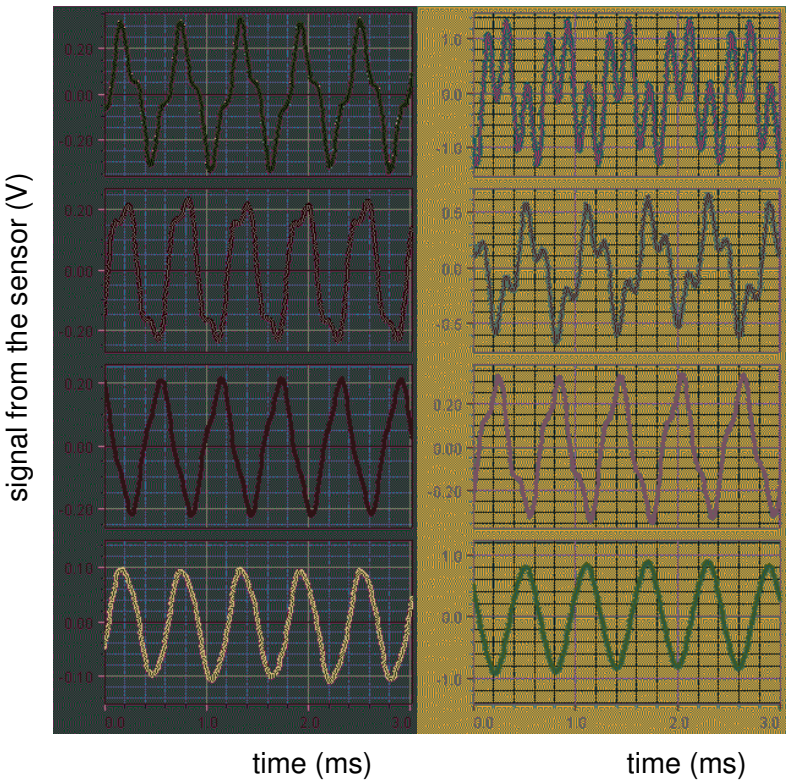

Fig. 2. Measurement data for aluminum alloy (left) and brass (right) rods.

The second method is based on frequency scan of the standing waves in the rod. An AC current from the *Output 1* passes through a coil positioned at one end of the rod. Eddy currents of this frequency are thus created in the rod. The interaction of these currents with a strong permanent magnet causes longitudinal sound oscillations in the rod and thus the standing waves (Simpson and Wolfe 1975). The frequency of the *Output 1* sweeps in the vicinity of the resonance during 400 s. The frequency spectrum of the standing waves is obtained with a common microphone. The signal proceeds to an AC-to-DC converter (Keithley 177 multimeter) and then to the *850 Interface*. *Capstone* displays the signal versus the frequency (Fig. 3). From the data obtained, the longitudinal sound velocities in the rods appeared to be 5010 m.s^{-1} for aluminum alloy and 3540 m.s^{-1} for brass. Handbook values are 5000 m.s^{-1} for pure aluminum and 3480 m.s^{-1} for 70Cu–30Zn brass (Lide 2008).

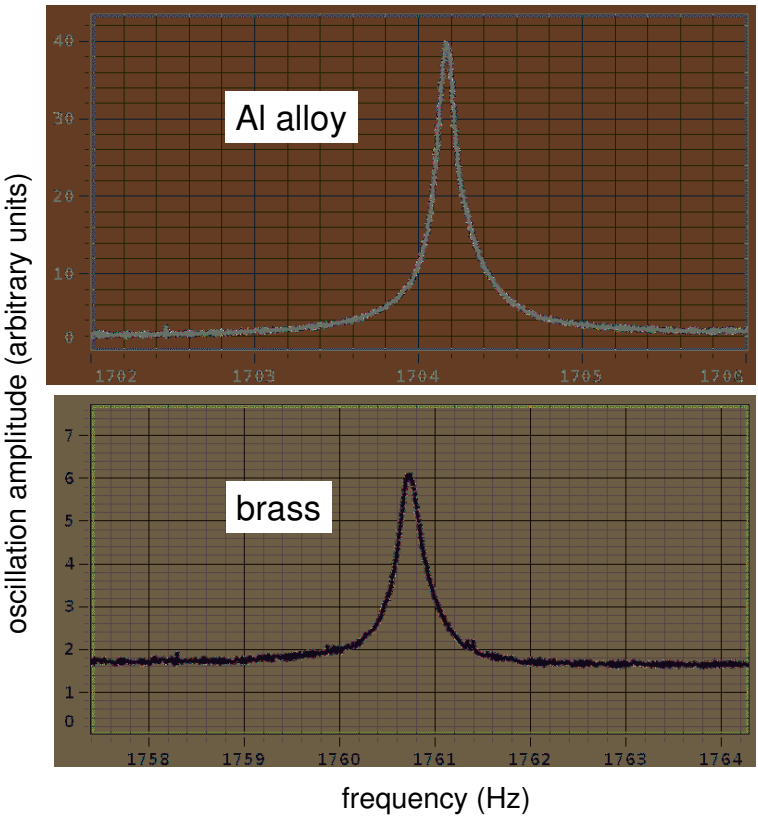

Fig. 3. Spectra of standing waves in aluminum-alloy and brass rods.

6.2. Young's modulus

Young's modulus is determined using dynamic technique based on observations of flexural vibrations of a cantilever.

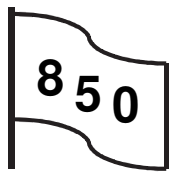

Additional equipment: *Force sensor*, steel ruler, coil, iron core, small magnet.

Young's modulus can be determined using a **static** or a **dynamic** technique as described by many authors: Bullen (1965); Ames (1970); Rhyner (1970); Naba (1972); Nicklin (1973); Wilson and Lord (1973); Britton *et al* (1978); Tyagi and Lord (1980); Hart (1986); Flores-Maldonado *et al* (1987); Bransky (1990); Rossing and Russell (1990); Turvey (1990); Greenslade and Wilcox (1993); Auerbach (1994); Narayanan and Narayanan (1996); Ficker (1999); Key *et al* (2000); Mak *et al* (2000); Potter (2002); Niculescu (2003); Sawicki (2003); Freeman and Freda (2007); Digilov (2008); Waltham and Kotlicki (2009); Velasco *et al* (2010).

For dynamic measurements, a 15 cm steel ruler is rigidly clamped to the *Force sensor* and forms a cantilever beam, whose natural frequency is determined from free and forced oscillations. The *Force sensor* senses the vibrations of the cantilever. The free oscillations are triggered manually. To drive the forced oscillations, we use a small magnet attached to the rule close to the clamp point and a coil (SF-8611) with an U-shaped iron core (SF-8614). The coil is connected to *Output 1* (Fig. 1).

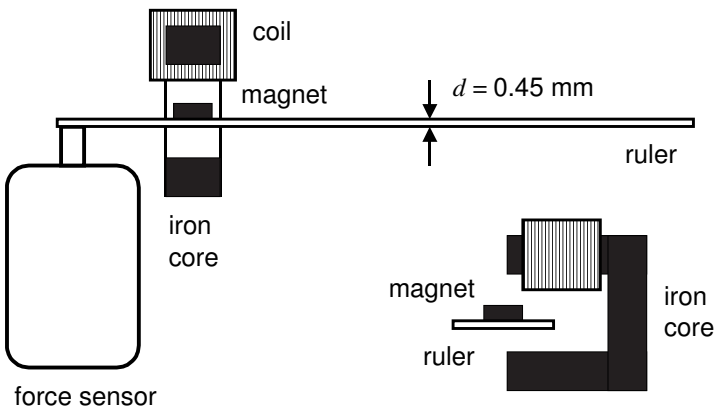

Fig. 1. Schematic of the setup for dynamic measurements of Young's modulus.

For a cantilever beam of rectangular cross section, Young's modulus Y can be found from the resonance frequency f_0, the density ρ, the length l, and the thickness b of the cantilever (Digilov 2008):

$$Y = 38.3 f_0^2 \rho l^4 / d^2. \quad (1)$$

For our sample, l = 158 mm, and d = 0.45 mm. When manually triggering free oscillations of the cantilever, *Capstone* fits the oscillations by the *Damped sine* function (Fig. 2).

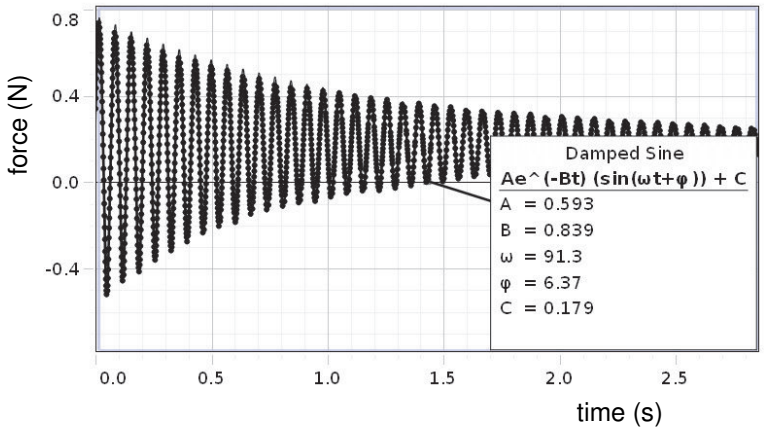

Fig. 2. Free oscillations of the sample.

For observing forced oscillations, the frequency of *Output 1* sweeps from 10 to 20 Hz, and *Capstone* displays the resonance curve (Fig. 3). Close resonance frequencies are derived from the free and forced oscillations of the cantilever. Young's modulus of steel appeared to be nearly 200 GPa, in agreement with the accepted value.

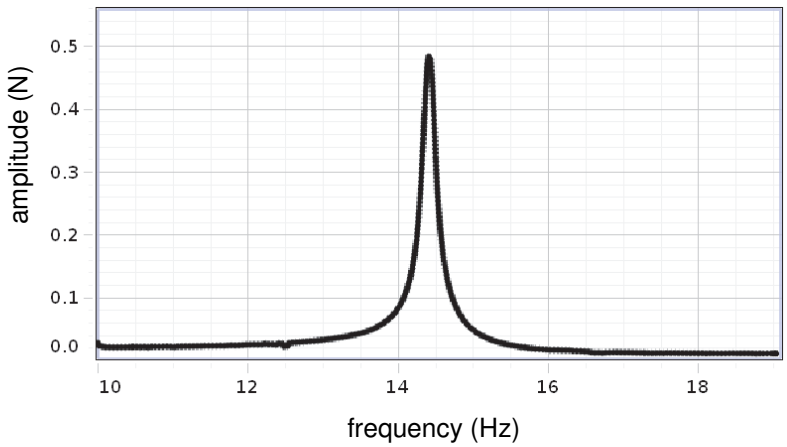

Fig. 3. Resonance curve of the sample.

6.3. Speed of sound in liquids

Speed of ultrasound in water is determined (Kraftmakher 2013e).

Additional equipment: *Motion sensor*, *Rotary motion sensor*, screw mechanism, ultrasonic transmitter and receiver, DC motor, high-frequency function generator, oscilloscope, semiconductor diode, resistors, capacitor, optics bench.

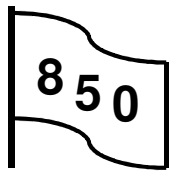

Determination of the **speed of sound** (ultrasound) waves in liquids is a topic of many laboratory courses. The main methods for measuring the speed of sound in liquids are the following:

• **pulse technique**, that is, a direct measurement of the propagation time of pulses of sound (Palmer and Forster 1970; Palmer 1971; Mak and Wu 2000).

• generating **standing waves** in a liquid for determining the wavelength (Ng and Mak 2001);

• **diffraction of light** by a liquid under study, in which standing sound waves form a diffraction grating (Kang and Young 1972; Whittle and Yarwood 1973; Neeson and Austin 1975; Luna *et al* 2002).

A suitable method is generating traveling waves in the liquid and measuring the sound wavelength by phase measurements, which is a popular method of determining the speed of sound in gases. Two ultrasonic transducers, a **transmitter** and a **receiver**, are inserted into a water-filled container (Fig. 1). The receiver is attached to the *Motion sensor* that can be moved along an optics bench. The output of a high-frequency function generator (Hewlett–Packard 33120A) is connected to the transmitter and to the Y1 input of a two-channel oscilloscope (Kenwood CS-4025). The output of the receiver is connected to the Y2 input. It is easy to made the signals on the oscilloscope screen nearly equal by adjusting the sensitivities of the two inputs. The oscilloscope operates in the *Add* mode, so it displays a sum of the voltages from the two inputs. By manually moving the receiver, the signal observed on the screen changes from nearly zero (the signals in opposition) to nearly twice the amplitude. Another possibility is observing Lissajous patterns on the oscilloscope screen. The distance between the nearest positions providing the same signal or phase shift equals the ultrasound wavelength in water. The frequency of the ultrasound waves is 1700 kHz.

The *Keep* mode for recording data with *Capstone* is used: the data are recorded only when commanded. A command for recording data from the *Motion sensor* is given every ten wavelengths. Only these data appear in the *Table*. The corresponding number of wavelengths is added by hand. The total displacement of the receiver is several tens of wavelengths. The *Graph* tool

displays the position of the receiver given in millimeters versus the number of wavelengths. The slope of the straight line obtained equals the mean value of the wavelength, 0.876 mm. The speed of ultrasound waves, which is the wavelength times the ultrasound frequency, equals 1489 m s^{-1}. The handbook values are 1483 m s^{-1} at 20°C and 1497 m s^{-1} at 25°C (Lide 2008).

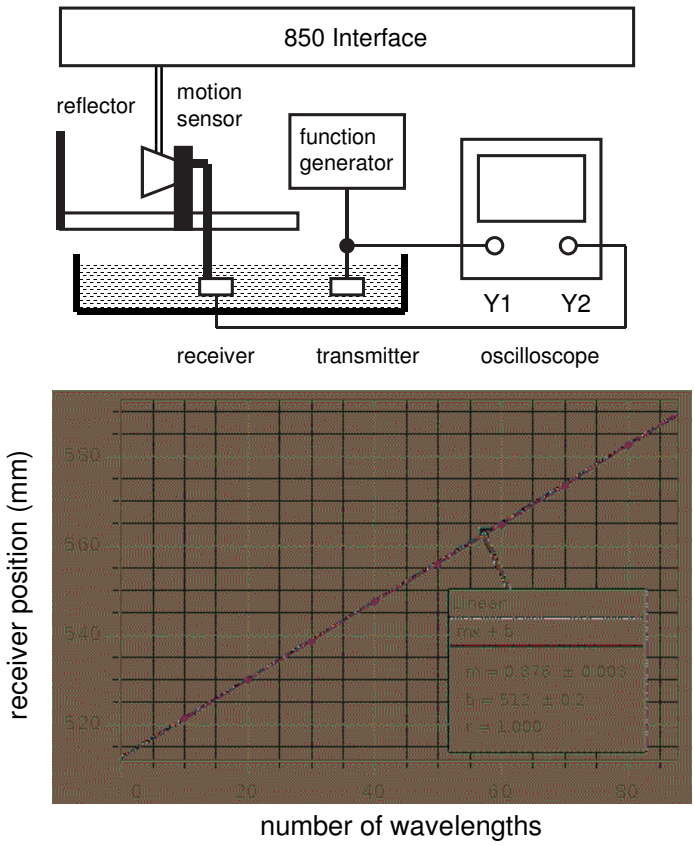

Fig. 1. Schematic of the setup and results obtained.

The resolution of the *Motion sensor* is nearly 0.2 mm. Somewhat better results can be obtained using the *Rotary motion sensor* with the *Linear translator* (OS-8535). With this sensor, the resolution is about 0.1 mm (1440 data points per revolution correspond to a 150 mm distance). In both cases, the resolution is insufficient to measure a distance equal to one wavelength, but is quite acceptable for determining a distance ten times larger. Counting the wavelengths is not a difficult task, and one has to take data only after ten wavelengths. It is impossible to stop the receiver exactly at a desired point, and this causes a scatter of the data. However, the results are quite satisfactory: for a distance of 80 wavelengths (8 experimental points), the error in the sound

wavelength is less than 0.4%. With longer wavelengths, the experiment would become easier.

Automated measurements. The measurements can be made more convenient by automatically recording the number of wavelengths passed by the ultrasound receiver. First, the *Rotary motion sensor* and a screw mechanism are used to smoothly move a carriage with the receiver attached (Fig. 2). The *Rotary motion sensor* is connected to the screw mechanism. One revolution of the screw produces a 1.75 mm shift. This greatly improves the resolution of the measuring system: with 1440 data points per revolution, the resolution becomes 1.2 μm. For f = 1700 kHz, the speed of ultrasound (m.s^{-1}) is 8.264 times the angular shift (degrees) corresponding to one wavelength.

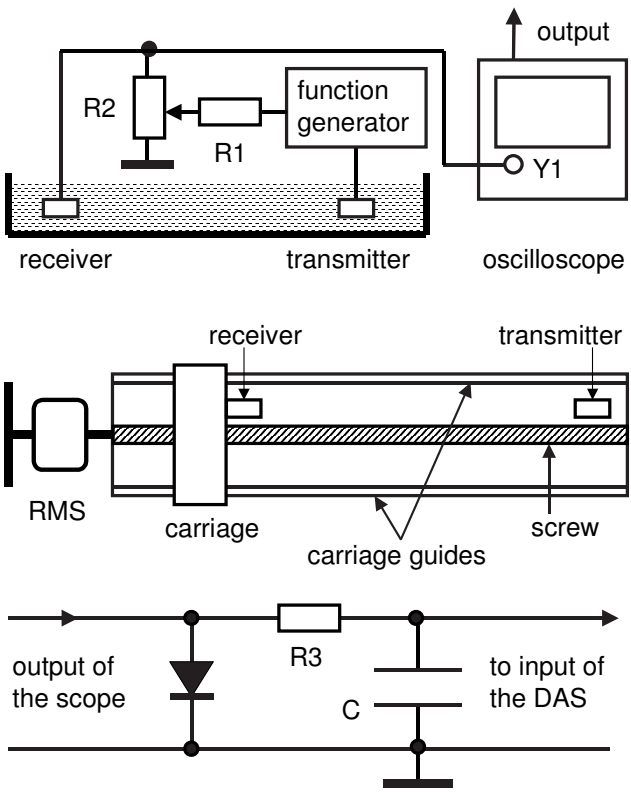

Fig. 2. Schematic of the setup; screw mechanism (view from above); and the detector circuit. RMS–rotary motion sensor, DAS–data-acquisition system.

Second, two simple electrical circuits are added. The signals from the transmitter and receiver are mixed at the Y1 input of an oscilloscope (Kenwood CS-4025). The signal from the receiver proceeds to the input directly. The voltage applied to the transmitter is much larger, and resistors R1 and R2 reduce

this voltage to make it close to the signal from the receiver. By manually moving the receiver, the input voltage will vary from nearly zero (the two signals in opposition) to nearly twice the amplitude. A simple detector circuit connected to the oscilloscope output (a diode, resistor R3, and capacitor C) provides a voltage acquired by the data-acquisition system. The angle position of the *Rotary motion sensor* is displayed versus the number of wavelengths. Accurate data can be obtained even with small displacements of the receiver (Fig. 3).

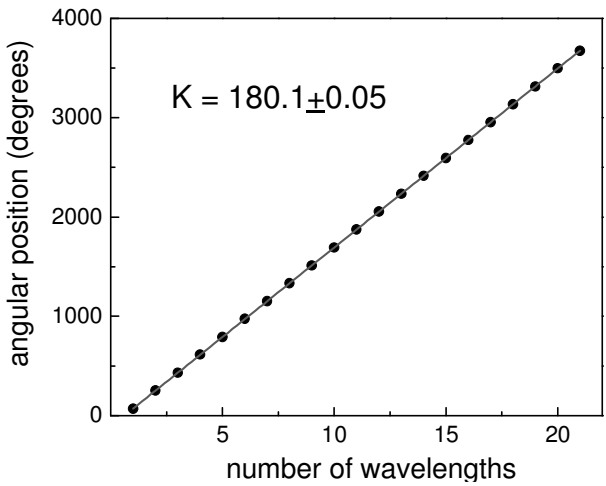

Fig. 3. *Rotary motion sensor* data versus the number of wavelengths. From the data, the speed of sound is $8.264 \times 180.1 = 1488$ m.s^{-1}.

The experiment becomes even more convenient when a DC motor with a gearbox moves the receiver toward the transmitter (Fig. 4).

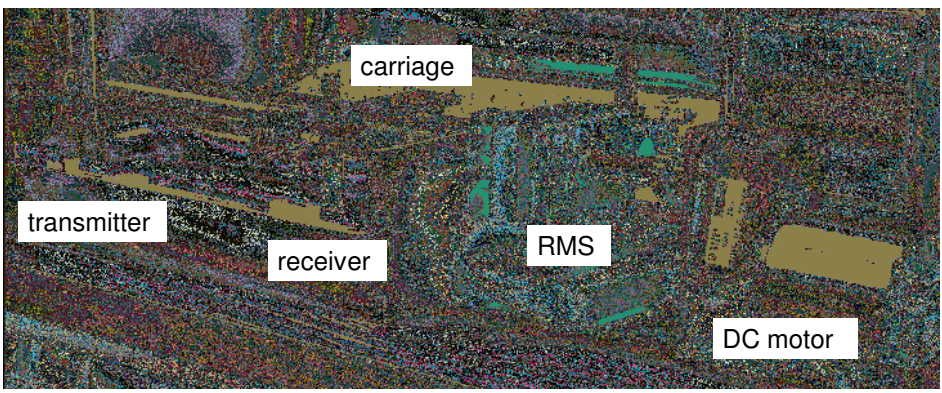

Fig. 4. The setup with a DC motor and *Rotary motion sensor* (RMS) to move the ultrasound receiver.

The shafts of the *Rotary motion sensor* and of the motor are softly connected. The receiver moves smoothly and with a desired velocity. *Capstone* displays the output voltage of the detector circuit versus the position of the receiver. With the *Smart tool*, the data related to definite numbers of wavelength are determined and displayed. The results show good reproducibility and correct values of the speed of sound in water (Fig. 5).

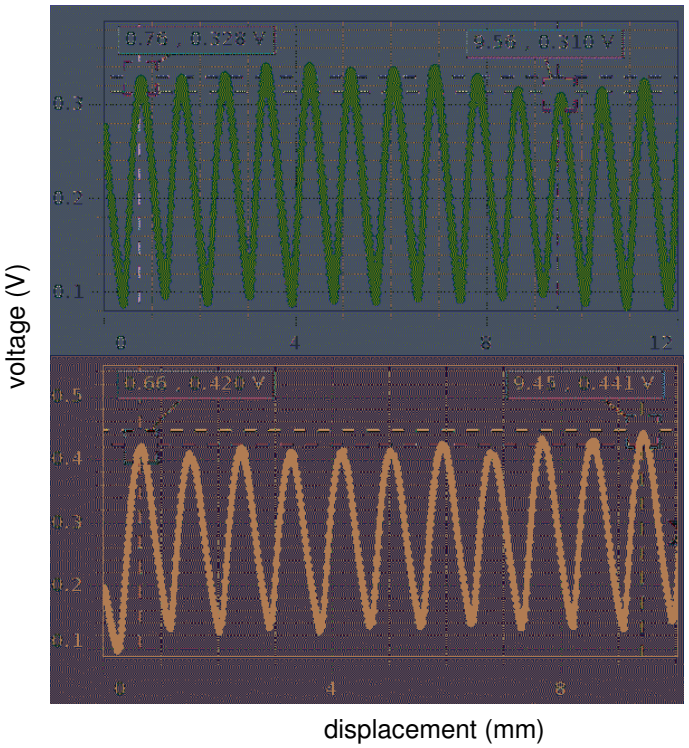

Fig. 5. Examples of data obtained. The distance between the marked points corresponds to 10 wavelengths.

6.4. Equilibrium point defects in metals

A strong nonlinear increase in the high-temperature specific heat of tungsten is probably due to the formation of equilibrium vacancies in the crystal lattice. Accepting this hypothesis, the enthalpy and entropy of the vacancy formation can be determined.

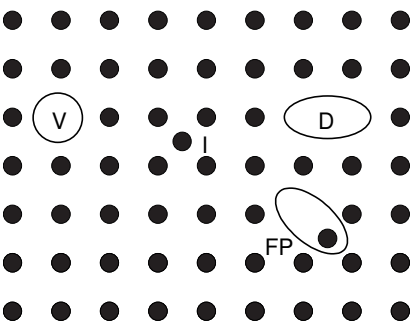

Point defects in crystal lattice: V–vacancy, I–interstitial, FP–Frenkel pair, D–divacancy.

AIP Emilio Segrè Visual Archives, Frenkel Collection

Iakov Frenkel (1894–1952)

Additional equipment: function generator, oscilloscope, low voltage light bulb, DC supply, transformer, decade resistance box, decade capacitance box, resistors.

Equilibrium point defects and specific heat of solids. The **nonlinear increase** in the **specific heat** of metals at high temperatures may be caused by the **point defect formation**. Frenkel (1926) predicted this phenomenon long ago. At high temperatures, some atoms in a crystal lattice acquire energies sufficient for leaving their sites and occupying interstitial positions. In this way a pair of point defects—**vacancy and interstitial**—appears, the so-called **Frenkel's pair**. Wagner and Schottky (1930) have shown how only vacancies may arise: some atoms leave their sites and form new lattice sites at the surface or internal imperfections of the crystal (**Schottky's defects**).

Point defects enhance the **entropy** of a crystal. The Gibbs enthalpy of a crystal has therefore a minimum at a certain concentration of the defects, which grows rapidly with temperature:

$$c_v = \exp(S_F/k_B)\exp(-H_F/k_BT) = A\exp(-H_F/k_BT), \quad (1)$$

where H_F and S_F are the enthalpy and entropy of vacancy formation, k_B is Boltzmann's constant, and T is the absolute temperature.

The entropy S_F relates to changes in the vibration frequencies caused by softening of the atom binding near vacancies. Frenkel believed that melting of solids results from the softening of the lattice by point defects when their equilibrium concentrations become of the order of 1%. Point defects influence many physical properties of metals at high temperatures: mechanical properties, enthalpy, specific heat, thermal expansion, resistivity, and parameters of positron annihilation. The predominant point defects in metals are vacancies. It is commonly recognized now that equilibrium point defects are to be studied at high temperatures. Criteria for the choice of a suitable property sensing point defects are quite clear: the relative value of the defect contribution and the reliability of separating it; the accuracy of the measurements; and the knowledge of parameters entering relations between the defect concentrations and their contributions. The specific heat seems to be the most suitable property because (i) according to theory, the high-temperature specific heat of a hypothetical defect-free crystal weakly depends on temperature; (ii) in many cases, the defect contribution is much larger than the uncertainty of the measurements; and (iii) the concentration of the defects is directly available from their contribution. There exists a temperature range, for which the specific heat increases linearly with temperature. By extrapolating this dependence, the contribution of the point defect formation becomes available (Fig. 1).

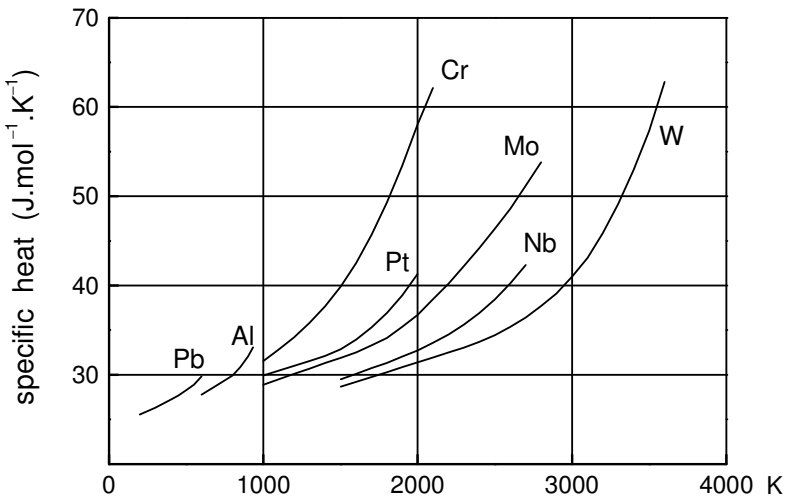

Fig. 1. Specific heat of metals: the difference between low melting point metals (Pb, Al) and high melting point metals (Pt to W) is clearly seen.

The **extra molar enthalpy** due to the equilibrium vacancy formation and the corresponding **extra specific heat** are

$$\Delta H = NH_F c_v = NH_F A \exp(-H_F/k_B T), \tag{2}$$

$$\Delta C_p = (NH_F^2 A/k_B T^2)\exp(-H_F/k_B T), \tag{3}$$

where N is Avogadro's number. A plot of the quantity $\ln T^2 \Delta C_p$ versus $1/T$ is a straight line with a slope $-H_F/k_B$.

After evaluating H_F, the coefficient A and the equilibrium vacancy concentration are obtainable. A more rigorous determination requires a fit of the experimental data by an equation taking into account the vacancy formation:

$$C_p = a + bT + (c/T^2)\exp(-H_F/k_B T). \quad (4)$$

The coefficients in Eq. (4) can be evaluated with the least-squares method. The equation corresponds to the assumption that all the nonlinear increase in the high-temperature specific heat is caused by the vacancy formation. This assumption leads to vacancy concentrations in refractory metals at melting points, c_{mp}, of the order of 1%. Many authors believe that the phenomenon is caused by **anharmonicity**. There are many arguments in favor of the vacancy origin of the nonlinear increase in the specific heat (Kraftmakher 1998a, 2000a).

In the experiment, the high-temperature specific heat of tungsten is measured using modulation calorimetry (see Experiment 3.4). This technique involves periodically modulating the power heating a sample and creating temperature oscillations in the sample around a mean temperature (for reviews, see Kraftmakher 1973a, 1988, 2002a, 2004d). In an adiabatic regime, where oscillations of heat losses from the sample are much smaller than those of the applied power, the amplitude of the temperature oscillations in the sample is

$$\Theta_0 = p/mc\omega, \quad (5)$$

where ω and p are the angular frequency and the amplitude of the oscillations of the heating power, and m and c are the mass and specific heat of the sample.

Equivalent-impedance calorimetric technique. A temperature-sensitive resistor, through which a DC current flows, displays equivalent impedance depending, in particular, on the heat capacity of the resistor (Griesheimer 1947). For simplicity, let us consider an adiabatic regime of the measurements. A long thin wire is heated by a current $I_0 + i\sin\omega t$ ($i << I_0$). In this case, $p = 2I_0 iR$, $\Theta = -\Theta_0 \cos\omega t$. The resistance of the sample is

$$R = R_0 + R'\Theta = R_0 - R'\Theta_0 \cos\omega t, \quad (6)$$

where R_0 is the resistance at the mean temperature, and $R' = dR/dT$ is the temperature derivative of the resistance. It equals $R' = R_{273}\beta$, where R_{273} is the resistance at 273 K, and β is called the temperature coefficient of resistance. Neglecting small terms, the AC voltage across the sample is

$$V = iR_0 \sin\omega t - I_0 R'\Theta_0 \cos\omega t. \quad (7)$$

This voltage contains two components, one is in phase with the AC component of the current, and the other quadrature lagging. The impedance $\boldsymbol{Z}$ of the sample that describes the amplitude and phase relations between the AC components of the current and the voltage across the sample thus contains real and imaginary parts: $\boldsymbol{Z} = R_0 + A - jB$. For an adiabatic regime, $A << B << R_0$

(Fig. 2). The quantity B is obtainable by the use of Eqs. (5) and (6) and dividing the AC voltage across the sample by the AC component of the current. The impedance of the sample equals

$$\boldsymbol{Z} = R_0 - \mathrm{j}(2I_0^2 R_0 R'/mc\omega). \tag{8}$$

The imaginary part of the impedance relates to the heat capacity of the sample. A resistor R and a capacitor C in parallel display similar impedance:

$$\boldsymbol{Z}_1 = (R - \mathrm{i}\omega R^2 C)/(1 + \omega^2 R^2 C^2). \tag{9}$$

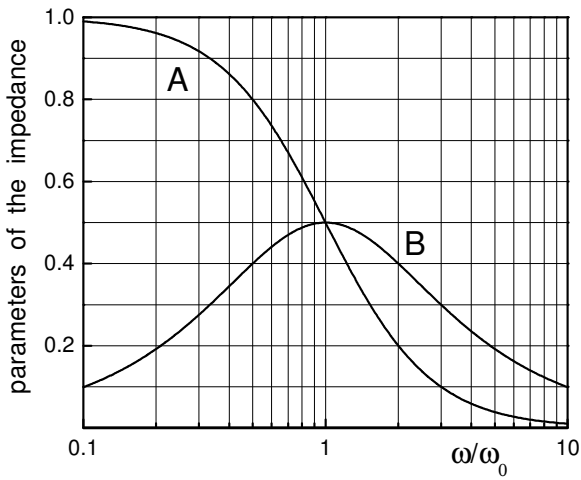

Fig. 2. Parameters of equivalent impedance (arbitrary units) versus frequency; ω_0 is a frequency, for which $A = B$.

In an adiabatic regime, $\omega^2 R^2 C^2 << 1$. Then $B = \omega R^2 C$, and

$$mc = 2I_0^2 R'/\omega^2 RC = 2I_0^2 R_{273}\beta/\omega^2 RC. \tag{10}$$

The heat capacity thus directly relates to the parameters of the equivalent impedance of the sample, R and C. A bridge circuit, in which a variable capacitor shunts one arm, may serve for measuring these parameters. The equivalent-impedance technique (Kraftmakher 1962a) was first used for measuring the high-temperature specific heat of tungsten (Kraftmakher and Strelkov 1962). Tungsten served for a long time for fabrication of filaments for incandescent lamps and cathodes of vacuum tubes. Therefore, the temperature dependence of the resistivity of tungsten is well known. At high temperatures, a strong nonlinear increase of the specific heat was observed and attributed to the vacancy formation in the crystal lattice. The phenomenon was confirmed by other calorimetric techniques.

High-temperature specific heat of tungsten. A gas-filled incandescent light bulb (12 V, 10 W) is included in a bridge circuit (Kraftmakher 1994). A DC

supply feeds the bridge, while a function generator provides the AC component of the heating current (Fig. 3). The *Scope* displays the Lissajous pattern on the screen and serves as a zero indicator of the bridge. Radial temperature differences in the sample are negligible owing to its small thickness and high thermal conductivity. Axial temperature gradients appear only at the ends of the sample. The mean temperature and the amplitude of the temperature oscillations are constant throughout the sample except short portions near its ends. The situation is more favorable at higher temperatures, and the measurements start at 1500 K. At lower temperatures, the influence of the ends of the filament becomes significant.

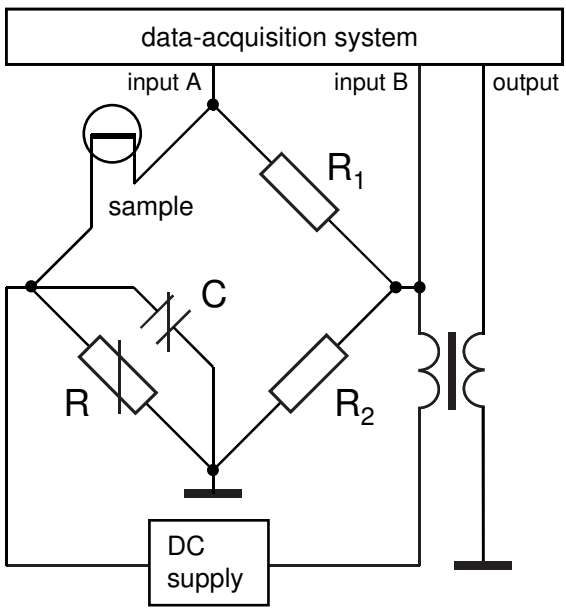

Fig. 3. Bridge circuit for measuring specific heat of wire samples.

When an ammeter (not shown in Fig. 3) measures the total current feeding the bridge, it is necessary to take into account the distribution of the current between the branches of the bridge. In our case, $R_2/R_1 = 100$, so that an additional factor $(100/101)^2$ enters Eq. (10). The modulation frequency of 80 Hz is sufficient to meet the adiabaticity conditions. From the measurements, one obtains values of the mc/β ratio, which equals $2(100/101)^2 I_0^2 R_{273}/\omega^2 RC$. One can present these data as a function of the sample resistance.

The accuracy of the measurements depends on the reliability of the temperature scale and of the values of the temperature coefficient of resistance (for data by Roeser and Wensel (1941) see Experiment 3.2). The temperature coefficient of resistance increases with temperature. However, this increase is less than 1% per 100 K. In our case, $R_{273} = 1.10\ \Omega$. It was determined with the

same bridge when gradually decreasing the heating current. The R_{293}/R_{273} ratio is 1.095. Now it is possible to find points in the graph corresponding to the temperatures 1500 K, 1600 K, and so on, up to 3300 K, and to determine the corresponding mc/β values (Fig. 4). An alternative is to calculate values of the sample's resistance at these temperatures. They are set at the bridge, whose balance is achieved by adjusting the heating current and the capacitance C. Remember that R_{273} in Eq. (10) means the resistance of the sample, while the value of R relates to the resistance set at the bridge, which is 100 times larger.

Absolute values of the specific heat are obtainable by determining the mass of the filament. Light bulbs from one lot have filaments of the same diameter, so it is enough to break only one of them. However, the weighing may cause errors larger than other errors of the measurements. On the other hand, the equivalent-impedance technique was proved by other calorimetric techniques and by measurements on several metals, including tungsten. Therefore, it is possible to fit the data at a point, where results obtained by various methods are in good agreement. At 2000 K, the accepted value is 31.6±0.5 $J.mol^{-1}.K^{-1}$. By the fit, the specific heat of tungsten can be presented over all the temperature range (Fig. 5). With vacuum light bulbs, the measurements are possible up to 2800 K because of significant evaporation of tungsten at higher temperatures. For this temperature range, the nonlinear part in the specific heat remains much smaller than that at 3300 K.

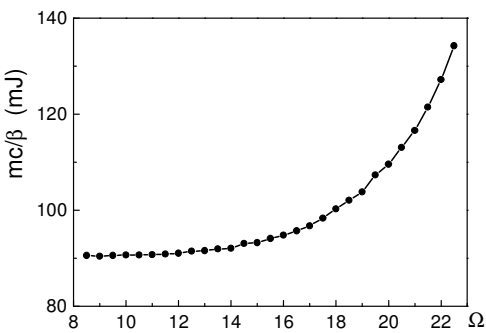

Fig. 4. Values of mc/β versus sample's resistance.

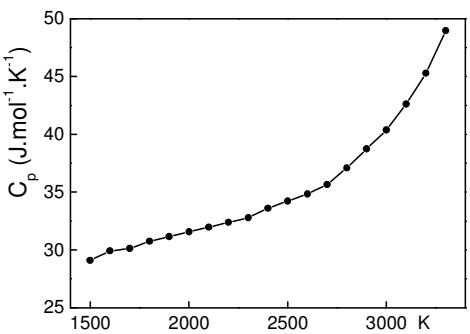

Fig. 5. Specific heat of tungsten after fitting the data at 2000 K.

Equilibrium point defects in tungsten. The vacancy formation enthalpy H_F is obtainable as a parameter providing best fit to the experimental data. After this evaluation, the entropy of vacancy formation S_F is available from the extra specific heat, according to Eqs. (3) and (1). The parameters of vacancy formation in tungsten determined earlier are the following: H_F = 3.15±0.1 eV, A = 670, c_{mp} = 3.4% (Kraftmakher and Strelkov 1962).

6.5. Ferromagnetism

The experiments include (i) the magnetic domains; (ii) the hysteresis loops; (iii) the analogy between magnetic and electric circuits; and (iv) Barkhausen's effect.

1. Magnetic domains

The domain structure seen with a ferrimagnetic sample, is common for ferro- and ferrimagnets. The experiment follows that described by Tanner (1980).

Additional equipment: *Life magnetic domains apparatus*, *Digital function generator-amplifier*, two *Voltage sensors*, microscope, video camera, monitor.

The experiment is based on **Faraday's rotation** and involves the *Life magnetic domains apparatus* consisting of a **ferrimagnetic garnet** slice mounted on a holder incorporating a magnetizing coil (Fig. 1). The slice is positioned between almost crossed polaroids in a transmission optical microscope equipped with a video camera. The *Digital function generator-amplifier* (PI-9587C) provides an AC current of frequency 0.01 Hz for the magnetizing coil. The video camera is connected to a monitor. The voltage across the magnetizing coil is stored by the data-acquisition system, together with the signal from the video camera smoothed by an RC integrating circuit. The camera serves for observing the movement of domain walls during the magnetizing the sample. Also, the camera provides an electrical signal proportional to the net magnetization of the sample. The signal displayed by the *DataStudio* versus a periodic magnetizing current shows the **hysteresis loop** of the sample.

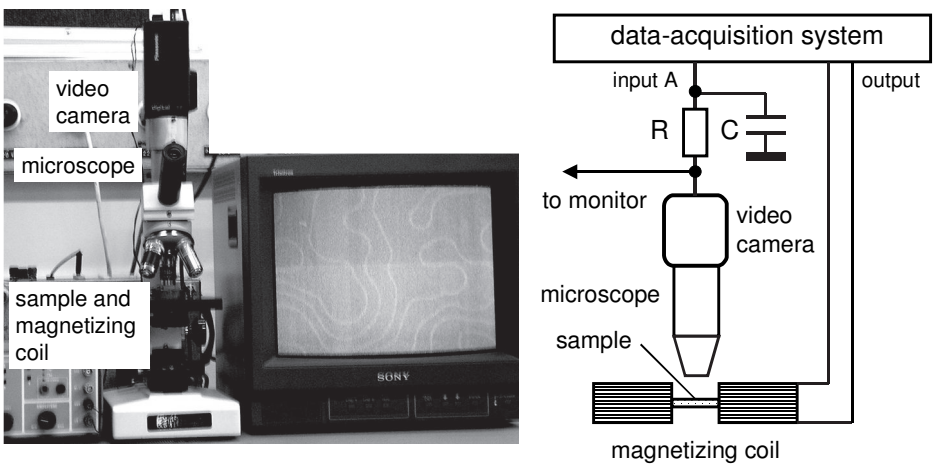

Fig. 1. Setup for observing domain structure in yttrium iron garnet film.

Ferrimagnetic yttrium iron garnet (YIG) films have uniaxial anisotropy perpendicular to the film plane. When a polarized light beam passes normally through the film, Faraday's rotation equals

$$\delta = CMd, \tag{1}$$

where M is the magnetization, d is the thickness of the film, and C is a coefficient of proportionality.

If the analyzer is set at angle β to the crossed position, the intensity of the transmitted light is proportional to $\sin^2(\beta + \delta)$. In the demagnetized state, the sample consists of equal volumes of domains with dipole moments parallel and anti-parallel to the light beam. When, due to the magnetization, the volume fraction of domains oriented parallel is x, the intensity of the light transmitted by the whole sample becomes (Tanner 1980)

$$I = A\,[x\sin^2(\beta + |\delta|) + (1 - x)\,\sin^2(\beta - |\delta|)]. \tag{2}$$

This relation can be written as

$$I = ax + b, \tag{3}$$

where a and b are independent of the magnetic field. The net magnetization of the sample is proportional to the volume difference of the two sets of domains:

$$M = xM_s - (1 - x)M_s = (2x - 1)M_s, \tag{4}$$

where M_s is the **saturation magnetization**. The change in the light intensity ΔI upon the magnetization is thus proportional to the change in the magnetization ΔM. A plot of ΔI versus the magnetizing field shows the hysteresis loop of the sample.

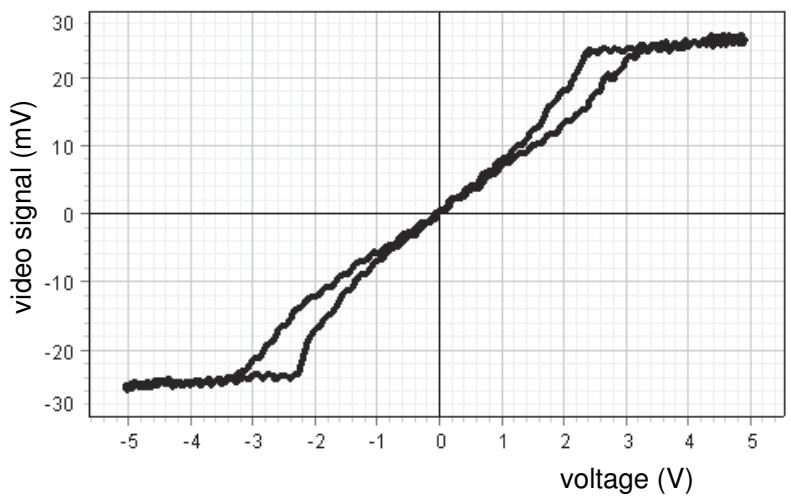

Fig. 2. Hysteresis loop of the sample: integrated video signal versus voltage applied to the magnetizing coil.

A signal proportional to the changes in the light intensity is taken directly from the video camera viewing the sample. After integration with an RC circuit, this signal is used to plot the hysteresis loop of the sample (Fig. 2). The growth of **magnetic domains** oriented up or down is clearly seen using *FlyVideo* software or a TV monitor (Fig. 3).

Fig. 3. Domain structures for magnetizing currents 0, 0.2, and 0.4 A.

2. Hysteresis loops

A common method is used for displaying hysteresis loops (Kraftmakher 2005c).

Additional equipment: two *Voltage sensors*, variable AC supply, DC supply, AC-to-DC converter, LF oscillator, demountable O-shaped magnetic core, coils, capacitor, resistors.

In ferromagnetic materials, the relation between the internal magnetic field B and the external magnetic field B_0 exhibits the phenomenon of **hysteresis**. It is caused by the **domain structure** of a ferromagnet and the **irreversibility** of the **magnetization process**. With a data-acquisition system, it is easy to observe the hysteresis loops. The experiment shows the high permeability of a ferromagnet and the nonlinear and hysteretic behavior of the magnetization.

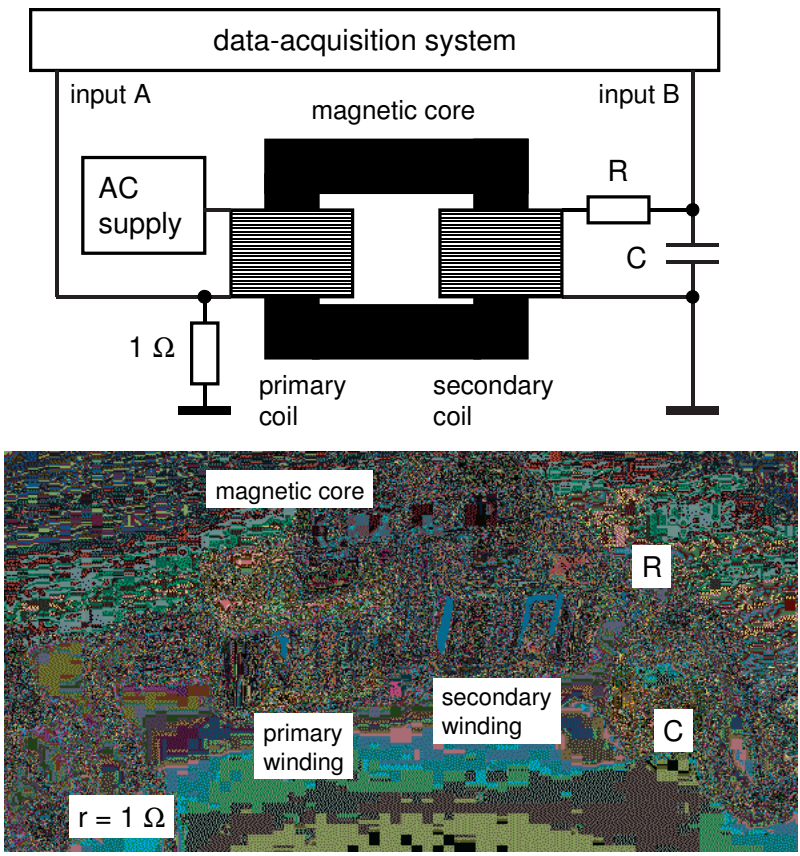

Fig. 4. Setup for observing hysteresis loops.

A common circuit for observing hysteresis loops is used. A demountable magnetic core with two windings forms a transformer fed from the mains. An isolating transformer is obligatory to avoid direct contact of the setup with the mains and exclude damage to the experimenter or the equipment. The primary winding produces the external magnetic field B_0, while the secondary winding senses the field inside the core B (Fig. 4). The field B_0 created by the primary winding is similar to the field inside an infinite solenoid:

$$B_0 = \mu_0 N_1 I_1 / l, \tag{5}$$

where μ_0 is the **magnetic constant**, N_1 is the number of turns of the winding, I_1 is the current flowing through it, and l is the mean circumference of the core.

The magnetic field inside the core equals $B = \mu B_0$, where μ is the **relative permeability**. The **magnetic flux** in the core equals $\Phi = BA$, where A is its cross-sectional area. According to Faraday's law, the EMF induced in the secondary winding equals $E = -N_2 \mathrm{d}\Phi/\mathrm{d}t = -N_2 A \mathrm{d}B/\mathrm{d}t$, where N_2 is the number of turns of the secondary winding. The sign "minus" may be omitted because it is changeable by reversing the terminals of the winding. An integrating RC circuit is connected to the secondary winding. For the mains frequency, the impedance displayed by capacitance C is much smaller than resistance R. This means that the time constant of the integrating circuit $\tau = RC$ is much larger than the period of the AC voltage. The current through the RC circuit thus is $I_2 = E/R$. This current is too small to influence the magnetic field inside the core. The voltage across the capacitor C is proportional to the magnetic field B:

$$V_2 = (1/C)\int I_2 \mathrm{d}t = N_2 BA/RC. \tag{6}$$

The magnetic field to be measured thus equals $B = V_2 RC/N_2 A$. For observing the hysteresis loop, the data-acquisition system displays the voltage V_2 versus the current I_1. The time of the measurements is restricted by one period of the AC current (in our case, 0.02 s). The *Sample rate* should be high to obtain a sufficient number of points for each loop. With the 10 kHz *Sample rate*, each hysteresis loop contains 200 points. To translate the quantities I_1 and V_2 into B_0 and B, the necessary coefficients are obtainable from the above relations. *DataStudio* displays the family of hysteresis loops (Fig. 5) in a minute.

For observing hysteresis loops, see Snider (1971); Goldin (1983); Meiners *et al* (1987); Meng and Liang (1987); Kiss (1990); Francavilla *et al* (2013). Rudowicz and Sung (2003) considered some misconceptions related to hysteresis loops of ferromagnets.

Initial magnetization and permeability. To determine the initial magnetization curve, where the magnetization starts from zero, it is sufficient to connect the ultimate points in the hysteresis loops. The permeability $\mu = B/B_0$ first increases with the external magnetic field, reaches a maximum, and then decreases due to the saturation in the magnetization.

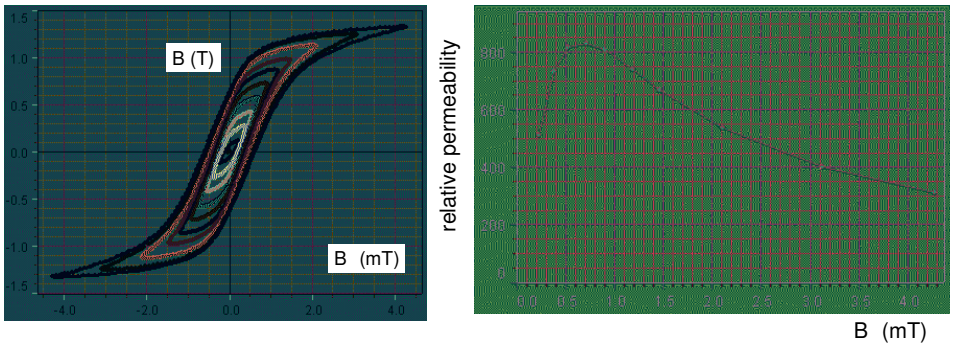

Fig. 5. Hysteresis loops and permeability of the core versus magnetizing field.

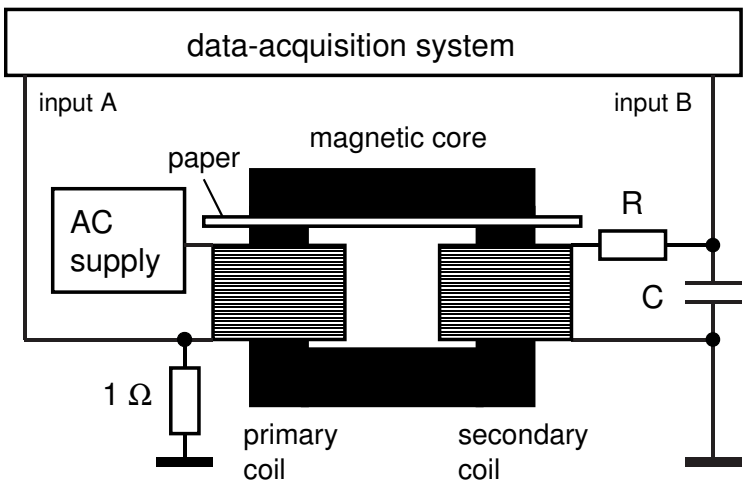

Fig. 6. Magnetic core with two nonmagnetic gaps.

Analogy between magnetic and electric circuits. The O-shaped magnetic core (SF-8614) consists of two parts clamped by a bolt. This makes it possible to check the obtained permeability in a simple way (Fig. 6). The main relations for magnetic circuits resemble those for electrical circuits (Benenson and Raffaele 1986; Parker 1997). The quantity $E_M = NI$ called the magnetomotive is an analog to the electromotive force. The ratio $R_M = l/\mu_0\mu A$ called the reluctance is an analog to the electrical resistance, and the magnetic flux Φ plays a role of the electric current. In a series magnetic circuit, a relation similar to Kirchhoff's loop law is valid: $\Phi = \Sigma E_M/\Sigma R_M$. Here, the magnetomotive force is N_1I_1, and the magnetic flux is $\Phi_1 = \mu_0\mu A N_1 I_1/l$. With a small nonmagnetic gap Δl ($\Delta l << l$), the flux in the core becomes $\Phi_2 = \mu_0 N_1 I_1/(l/\mu A + \Delta l/A) = \mu_0\mu A N_1 I_1/l(1 + \mu\Delta l/l)$. The higher the permeability of the core, the greater the change in the magnetic flux caused by the gap. From the Φ_1/Φ_2 ratio, the permeability of the core equals

$\mu = [(\Phi_1/\Phi_2) - 1]l/\Delta l$. In our case, the gap is introduced by a piece of paper 0.08 mm thick between the two parts of the core, so the total length of the nonmagnetic part of the circuit is 0.16 mm. From the two magnetization curves, the calculated permeability of the core is nearly 10^3 (Fig. 7).

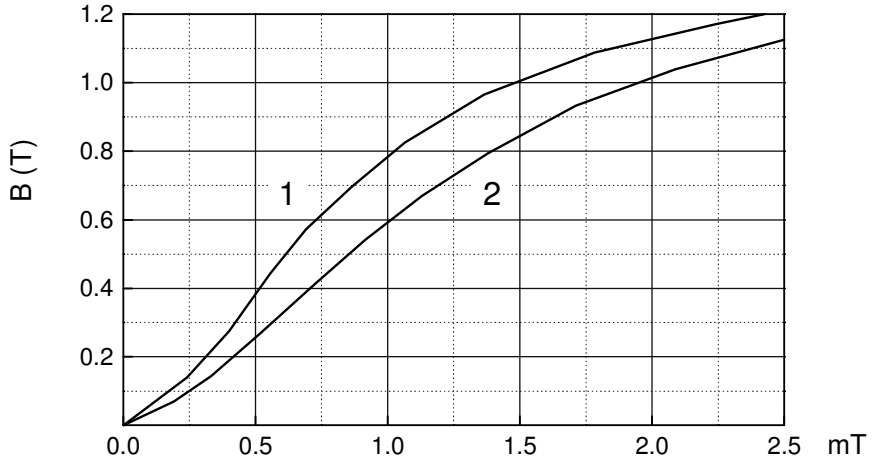

Fig. 7. Initial magnetization curves: 1–no gap, 2–0.16 mm nonmagnetic gap.

Differential permeability. Along with the permeability $\mu = B/B_0$, the differential permeability $\mu_d = dB/dB_0$ is useful for many applications. To measure the differential permeability, Borin and Baffa (1998) measured the inductance of a coil wrapped around a toroidal core, as a function of the applied magnetic field. In our experiment (Fig. 8), the differential permeability is measured versus the mean magnetic field generated by passing a DC current through an 800-turn coil L_1 (SF-8611). A small AC current from the *Signal generator* passes through the modulation coil L_2. A resistor connected in series with this coil makes the current independent of the permeability of the core. The AC magnetic flux induces an AC voltage in a 400-turn pick-up coil L_3 (SF-8610), which is proportional to μ_d. The magnetizing current and the voltage induced in the pick-up coil, after the AC-to-DC conversion, are acquired by the data-acquisition system. A Keithley 177 multimeter serves as the converter. The voltage induced in the pick-up coil is displayed versus the magnetizing current. A large inductance (iron-core coil, not shown in Fig. 8) is put in series with coil L_1 to suppress an AC current due to an EMF induced in this coil.

To measure the differential permeability during the initial magnetization of the magnetic core, the data-acquisition system starts to form the magnetizing current simultaneously with the measurements. Before the measurements, it is necessary to demagnetize the core using a regulated AC supply. Clearly, the differential permeability μ_d changes in a wider range than the common permeability.

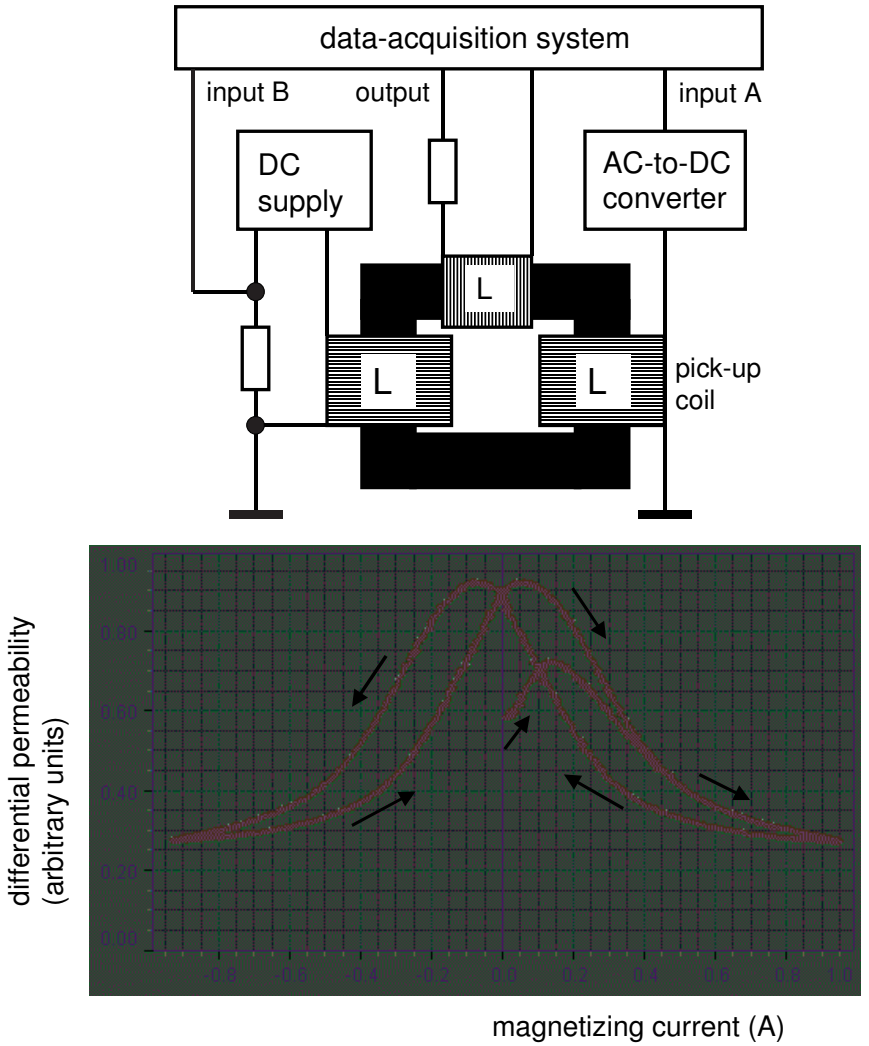

Fig. 8. Schematic of the setup, and differential permeability versus magnetizing current. The initial part of the plot relates to the initial magnetization.

3. Barkhausen's effect

Barkhausen's noise is measured and compared with the field dependence of the differential permeability of the sample (Kraftmakher 2005d).

Additional equipment: two *Voltage sensors*, AC amplifier, function generator, U-shaped magnetic core, coils, AC-to-DC converter, resistor, loudspeaker.

The phenomenon. Barkhausen's effect is a series of sudden changes in the size and/or orientation of ferromagnetic domains during continuous magnetization or demagnetization of a ferromagnet. Therefore, these processes occur not continuously but in minute steps. A coil wound on a sample may detect the sudden **jumps in the magnetization**, which induce voltage pulses in the coil and, after amplification, a series of clicks in a loudspeaker. This noise represents only the audible part of the spectrum of **Barkhausen's noise**, which also includes higher frequencies. The effect discovered in 1919 by Heinrich Georg Barkhausen (1881–1956) confirms the existence of ferromagnetic domains, which were predicted theoretically. Feynman *et al* (1964) gave a clear explanation of the effect, and Lonc (1992) described a qualitative demonstration of it. A simple setup is used here for demonstrating the phenomenon under reproducible conditions (Fig. 9).

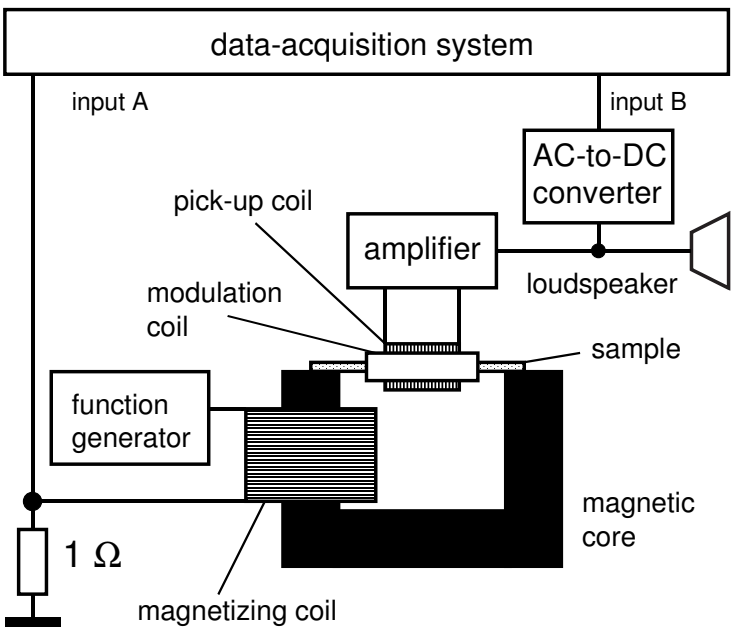

Fig. 9. Setup for demonstrating Barkhausen's effect.

As a sample, we use a straightened out steel paperclip, 0.9 mm in diameter. The sample is 7 cm long and constitutes a part of an O-shaped magnetic circuit. The magnetic core and the magnetizing coil are PASCO SF-8614 and SF-8611. A function generator provides the magnetizing current of an infra low frequency. The circumference of the magnetic circuit including the sample is nearly 30 cm. A pick-up coil wrapped around the sample consists of 1000 turns of 0.06 mm copper wire; it is connected to the input of an audio amplifier. The gain of the amplifier is of the order of 10^5, and its output resistance is matched to the resistance of the loudspeaker.

The magnetizing current should contain no minor steps peculiar to digitally generated waveforms. Such steps induce electric pulses in the pick-up coil, and the phenomenon may be masked or significantly distorted. The same relates to the influence of external AC magnetic fields: AC voltages induced in the pick-up coil increase when the permeability of the sample increases. Therefore, the magnetic core with the sample and the coils is placed inside a box made out of a ferromagnetic material. To suppress ripples in the magnetizing current, an inductor of high inductance is placed in series with the magnetizing coil (not shown in Fig. 9).

An AC-to-DC converter provides a DC voltage proportional to the noise at the output of the amplifier. In our case, a Hewlett–Packard 400E voltmeter serves as the converter, and its output voltage is stored by the data-acquisition system. The magnetizing current is taken as the *Output current*. The Barkhausen's noise is presented as a function of the magnetizing current. The graph clearly manifests a strong magnetic field dependence of the noise and its hysteresis, in agreement with expectations. Along with observing the graph, the students hear the noise produced by the loudspeaker.

Barkhausen's effect and permeability. It is interesting to compare Barkhausen's noise and the differential permeability of the sample. The maximum in the noise is expected in the range, where the magnetization of the sample most strongly depends on the magnetizing field. To verify this expectation, an additional 100-turn coil is wrapped around the sample. This coil serves to slightly modulate the magnetic field applied to the sample. The modulation coil is fed by a low-frequency current from a low voltage transformer through a 500 Ω resistor sufficient to make the current in the coil independent of its inductance (the circuit feeding the modulation coil is not shown in Fig. 9). The AC voltage induced in the pick-up coil is thus proportional to the differential permeability of the sample. This signal is stronger than the Barkhausen noise and is measured by the same amplifier, but with the gain ten-fold reduced. The amplified signal proceeds to the AC-to-DC converter and then to the data-acquisition system and is displayed as a function of the magnetizing current. The graphs presented are obtained with a 0.005 Hz current. The correlation between Barkhausen's noise and the differential permeability of the sample is obvious (Fig. 10).

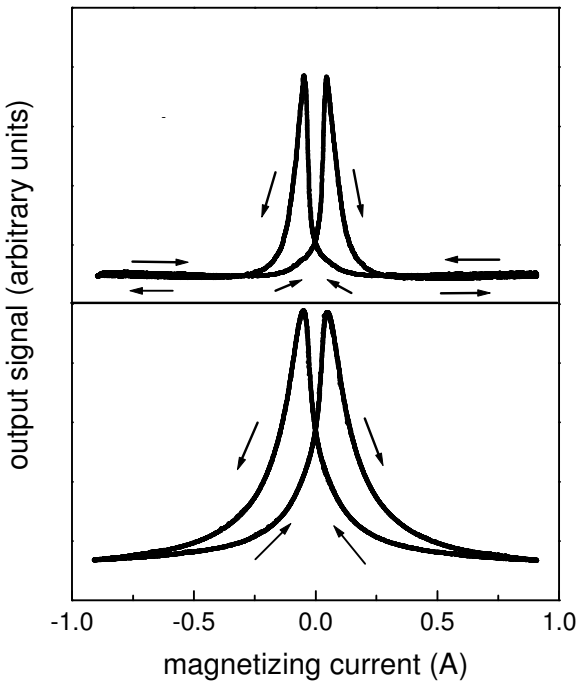

Fig. 10. Barkhausen's noise (top) and differential permeability of the sample (bottom), versus magnetizing current.

6.6. Curie's point II

The experiments include four items: (i) Curie's point and permeability of nickel; (ii) Curie's point of a nickel-based alloy; (iii) the magnetic susceptibility of gadolinium above Curie's point; and (iv) the hysteresis loops and spontaneous magnetization of a ferromagnet over a temperature range including Curie's point.

Pierre Curie (1859–1906)

Theoretical predictions. At temperatures above Curie's point T_c, a ferromagnet loses its spontaneous magnetization. The transition from the ferromagnetic to a nonmagnetic state is a second-order phase transition. Many properties of ferromagnets manifest **singularities** near the **transition point**, usually with power-law dependence (Fig. 1). The exponent in such dependences is called the **critical exponent**, or critical index (Fisher 1965, 1967; Heller 1967; Domb 1996). For instance, the **specific heat** of a ferromagnet obeys the relation

$$C = A + B|T - T_c|^{-\alpha}, \tag{1}$$

where A and B are constants, generally different below and above Curie's point, and α is the critical exponent of the specific heat. Below the transition point, the **spontaneous magnetization** of a ferromagnet equals

$$M = A(T_c - T)^{\beta}, \tag{2}$$

where β is the critical exponent of spontaneous magnetization. Close to Curie's point, the **magnetic susceptibility** is given by

$$\chi = A|T - T_c|^{-\gamma}, \tag{3}$$

where γ is the critical exponent of magnetic susceptibility.

One of the most important objectives of the theory and the experiment is the determination of the critical exponents. The mean-field theory predicted the following values of the critical exponents: $\alpha = 0$, $\beta = 0.5$, $\gamma = 1$. However, observed dependences appeared to be somewhat different. The modern theory of

critical phenomena can be found in many books (Ma 1976; Patashinskii and Pokrovskii 1979; Stanley 1983; Domb 1996). In 1982, Kenneth G. Wilson was awarded the Nobel Prize in Physics "for his theory for critical phenomena in connection with phase transitions." The theory is very complicated, but Maris and Kadanoff (1978) have shown how it could be incorporated into an undergraduate course of statistical physics. Tobochnik (2001) presented a guide to the literature on critical point phenomena and phase transitions.

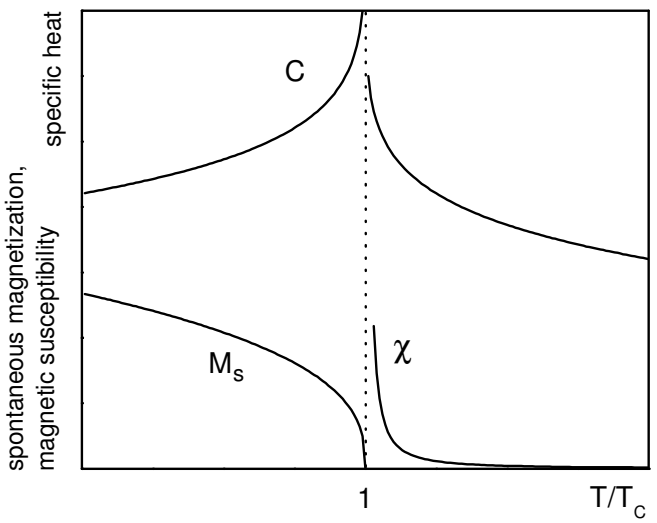

Fig. 1. Singularities in properties of ferromagnets close to Curie's point.

The accepted theoretical values of the critical exponents are the following: $\alpha = -0.115 \pm 0.009$, $\beta = 0.3645 \pm 0.0025$, $\gamma = 1.386 \pm 0.004$ (Domb 1996). The experimentally determined critical exponents are, within experimental errors, in agreement with these theoretical values. The theory predicts also some relations between critical exponents, in particular, a relation fitting the above-mentioned quantities:

$$\alpha + 2\beta + \gamma \geq 2. \tag{4}$$

Both sets of critical exponents given above meet this relation even as equality.

Several student experiments related to Curie's point have been described. Some of these employ the mutual inductance technique (Soloukhin 1975; Edgar and Quilty 1993; Fisher and Franz 1995). Other experiments include measurements of the resistivity (Kamal *et al* 1983; Fox *et al* 1986; Sullivan *et al* 1987) and observations of changes in the resonant frequency of an LC circuit when a sample placed inside the inductor undergoes the transition (Fox *et al* 1986). Lewowski and Woźniak (1997) determined Curie's point of gadolinium by measuring the inductance of a coil with a sample inside.

1. Permeability of nickel

The AC resistivity of nickel depends on the skin depth. By measurements of the resistivity, the permeability of nickel below Curie's point is determined (Kraftmakher 1997).

Additional equipment: three *Voltage sensors*, nickel wire, lock-in amplifier, furnace, DC supply, AC supply, DC amplifier, transformer, oscilloscope, thermocouple.

Close to Curie's point, the resistivity of a ferromagnetic metal manifests specific behavior that becomes more clear when the temperature derivative of resistivity is measured directly (Kraftmakher 1967a; Kraftmakher and Pinegina 1974). The derivative behaves like the specific heat (Kawatra and Budnick 1972).

Many classroom demonstrations and laboratory experiments concerning the skin effect were published. An experiment described by MacDougall (1976) consists of two parts, the electromagnetic shielding by a conducting sheet and distribution of the current flowing through a wire bundle. Young (1980) demonstrated propagation of electromagnetic waves in aluminum. Gosselin *et al* (1982) measured the impedance of a round copper wire. Wiederick and Gauthier (1983) described a simple method for determining the frequency dependence of the **skin depth** in a conductor. Ziólkowska and Szydłowski (1984) measured the amplitude and phase of a voltage induced in a coil placed in a solenoid and screened by conducting tubes of different wall thickness. A similar experiment was described in Soloukhin (1975). Juri *et al* (1986) determined the effective magnetic susceptibility of a conducting rod. Fahy *et al* (1988) calculated the electromagnetic screening for different shapes of the conductor. Rochon and Gauthier (1990) tested these calculations. By studying the screening, Íñiguez *et al* (2005) measured the conductivity of metallic tubes. Magnetic properties of nickel were considered by Barnes (1988).

Skin effect and AC resistance. In the experiment, the temperature dependence of the resistivity of nickel is measured using a DC current and an AC current of enhanced frequency. The transition to the nonmagnetic state becomes evident owing to the change in the skin depth. Moreover, the temperature dependence of the permeability of the sample is available from the ratio of the impedance of the sample to its DC resistance. When an AC current passes through a sample, the skin depth depends on the permeability of the sample μ, its resistivity ρ, and the frequency of the current. With SI units, the skin depth δ for a plane surface is given by $\delta = (2\rho/\omega\mu_0\mu)^{1/2}$, where μ_0 is the magnetic constant, and ω is the angular frequency of the current. The theory of the skin effect is given in many textbooks: Stratton (1941); Scott (1966); Landau and Lifshitz (1984). In the ferromagnetic phase, the skin depth decreases because of the high permeability.

Measurements of the impedance with an AC current of proper frequency provide an additional opportunity to observe the transition to the nonmagnetic state.

Permeability close to Curie's point. A nickel wire, 1 mm in diameter (99.99%, Goodfellow Company), is placed in a furnace and connected to a DC supply and *Signal generator* (Fig. 2). A DC current and an AC current pass through the sample simultaneously. The four-probe technique is used to measure the DC and AC voltages across the central portion of the sample, about 1 cm long. Thin nickel wires welded to the sample serve as the potential probes. The DC voltage is amplified and then fed to the data-acquisition system. The AC component is fed, through a transformer (not shown in Fig. 2), to a PAR 124A lock-in amplifier. The AC voltage to be measured is of the order of 1 mV, and it is very important to reduce the magnetic coupling between the current leads and the potential leads. The areas of both loops should be kept to a minimum. The amplified AC voltage is monitored with an oscilloscope (not shown in Fig. 2).

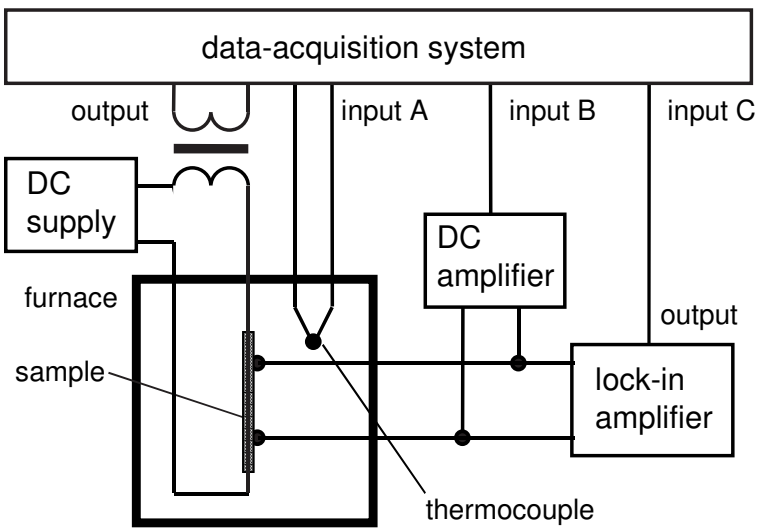

Fig. 2. Schematic of the setup.

The frequency of 10 kHz makes the difference between the modulus of the impedance Z and DC resistance R of the nickel wire significant only in the magnetic phase. Direct measurements of the two quantities are accompanied by unavoidable errors, and the values above Curie's point may appear somewhat different. A good alternative is to fit both quantities to the resistivity of nickel at a selected temperature above Curie's point (for instance, 0.31 $\mu\Omega$.m at 400^{o}C). In this case, one immediately obtains data for the DC resistivity over the whole temperature range, which will be necessary for calculating the permeability of the sample.

The ratio of the impedance **Z** of a round wire to its DC resistance is given through Bessel functions (Irving and Mullineux 1959; Relton 1965):

$$\mathbf{Z}/R = kaI_0(ka)/2I_0'(ka), \tag{5}$$

where $k^2 = i\omega\mu_0\mu/\rho$, and a is the radius of the wire. The ratio Z/R is a function of the parameter $X = (a/\delta)^2$. Numerical data for this plot were taken from Abramowitz and Stegun (1965). Since a, ω and ρ are known, the permeability is available from the determined Z/R ratio. In the range $1 < a/\delta < 3$, the quantity $X = (a/\delta)^2 = a^2\omega\mu_0\mu/2\rho$ can be taken as a function of $Y = Z/R - 1$ (Fig. 3):

$$X = 0.53 + 8.7Y - 5.7Y^2 + 3.2Y^3. \tag{6}$$

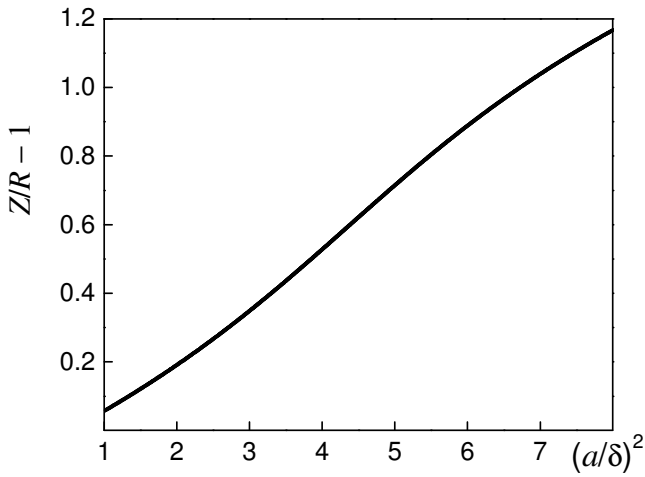

Fig. 3. Theoretical dependence of $Y = Z/R - 1$ versus $X = (a/\delta)^2$.

The permeability of the sample equals

$$\mu = 2X\rho/a^2\omega\mu_0. \tag{7}$$

To increase the thermal inertia and reduce temperature gradients, the sample is placed in an aluminum block inside the furnace. The measurements are carried out when cooling the furnace. After heating up to 400°C, the heating current is reduced to obtain a desired cooling rate near Curie's point, of about 3–5 K.min^{-1}. The temperature is measured with a thermocouple. For the Fe/Cu+43%Ni thermocouple, the temperature relates to the thermal EMF e (in millivolts) as $T = 6.3 + 17.89e + 0.006e^2$; this equation is valid in the range 300–400°C.

The data-acquisition system stores the EMF of the thermocouple, the DC voltage drop across the central portion of the sample, and the DC output voltage of the lock-in amplifier. From the measurements of the impedance, the phase transition is quite evident (Fig. 4). The permeability of nickel evaluated with

Eq. (7) is in reasonable agreement with available data (Herzum *et al* 1974). The increase of the permeability close to Curie's point is also seen (Fig. 5).

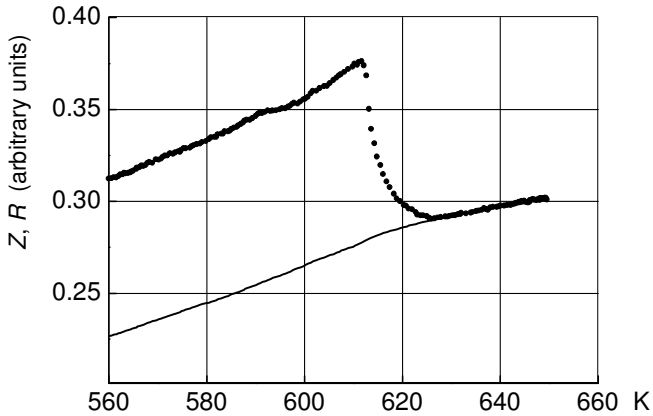

Fig. 4. DC resistance (———) and module of the impedance of the nickel sample at 10 kHz (●) fitted to resistivity at 400°C.

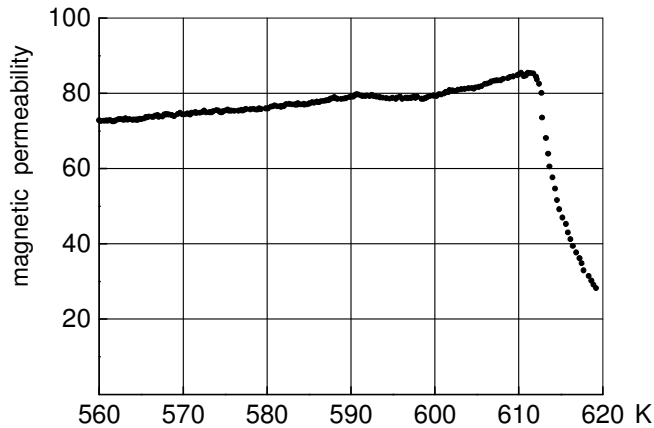

Fig. 5. Permeability of nickel evaluated through the measured Z/R ratio.

2. Curie's point of a nickel-based alloy

The impedance of a nickel-based alloy is measured in the vicinity of Curie's point (Kraftmakher 1997).

Additional equipment: two *Voltage sensors*, monel wire, selective amplifier, furnace, platinum resistance thermometer, transformer, oscilloscope, Dewar flask.

A nickel-based alloy wire, Monel 400 (Ni65/Cu33/Fe2) from the Goodfellow Company, is used; the wire is 1 mm in diameter. The sample is placed in a metallic can provided with an electrical heater and a small platinum thermometer (100 Ω at 0°C). The measurements at 30 kHz are carried out using the four-probe technique (Fig. 6). Thin copper wires soldered to the sample serve as potential probes. A selective amplifier with a DC output (PAR 124A) measures the voltage across the sample. The metallic can is cooled by placing it into a Dewar flask with liquid nitrogen. Then the can is raised above the liquid, and the temperature of the sample starts to increase. The electrical heater heats up the sample above room temperature. Close to the transition, the heating rate should be of about 3–5 K.min^{-1}. The change in the resistance measured at the high frequency clearly shows the phase transition. The permeability of the alloy is smaller than that of pure nickel, so that the frequency necessary to observe the skin effect is higher.

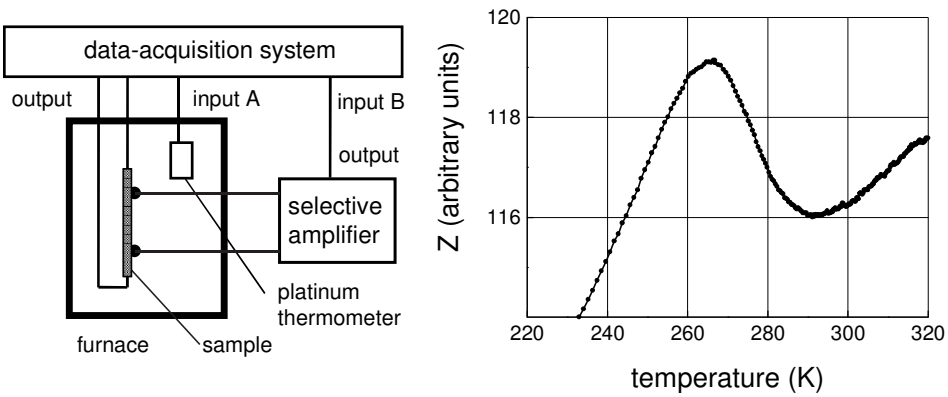

Fig. 6. Schematic of the setup, and impedance of the monel wire at 30 kHz.

3. Magnetic susceptibility of gadolinium

Magnetic susceptibility of gadolinium in the vicinity of Curie's point is determined (Kraftmakher 1997).

Additional equipment: two *Voltage sensors*, *Thermistor temperature sensor*, selective amplifier, gadolinium sample, E-shaped magnetic core, AC-to-DC converter, coils.

In the vicinity of Curie's point, the magnetic susceptibility of a sample depends on the proximity to the transition point, which is limited by values of $|T - T_c|/T_c$ in the range of 10^{-4}–10^{-3}. With such proximity, the magnetic susceptibility χ above Curie's point may become much smaller than that in the ferromagnetic phase (Heller 1967; Herzum *et al* 1974). Gadolinium is rather an exception that possesses high susceptibility above its Curie point. It allows the measurements to be made in a relatively wide temperature range in the nonmagnetic phase, so that it is possible to evaluate the critical exponent of susceptibility.

The differential transformer. For the measurements, E-shaped magnetic core and coils are employed (SF-8615, SF-8610, and SF-8611). The primary winding L_1 ($N_1 = 800$) is connected to the *Signal generator* (Fig. 7).

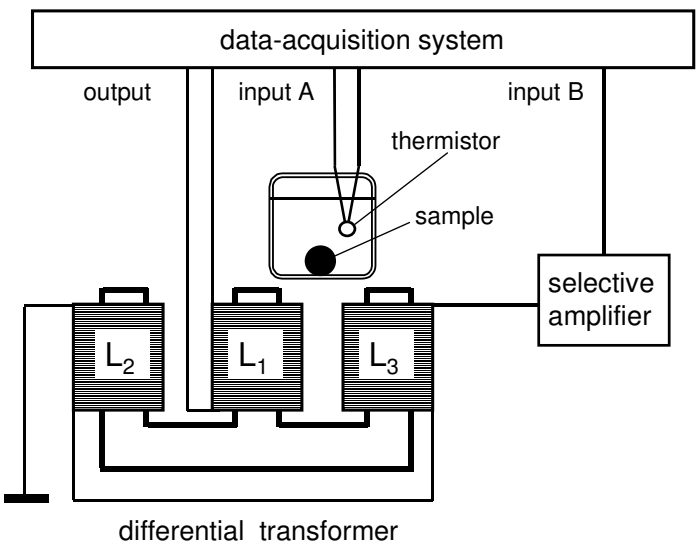

Fig. 7. Setup for measuring magnetic susceptibility of gadolinium. The heater and compensating coil are not shown.

The AC current in L_1 creates a magnetic flux in the magnetic core. Two secondary windings L_2 and L_3 ($N_2 = 400$) are connected in opposition, so that

without a sample the voltage at the transformer output is zero. A small additional coil connected in series with the secondary windings and placed near the core (not shown in Fig. 7) serves to finely balance the transformer. With a magnetic sample in one of the gaps, the magnetic flux through this part of the magnetic circuit increases. This, in turn, causes an increase in the voltage induced in the corresponding secondary winding. To reduce the influence of eddy currents in the sample, the operating frequency is 30 Hz. A spherical gadolinium sample, 5 mm in diameter, is prepared using a rod of 99.9% purity from the Goodfellow Company. It is placed into a small glass filled with glycerol to prevent the sample from oxidation and to reduce temperature gradients. The *Thermistor temperature sensor* is used for the temperature measurements. A nonmagnetic electrical heater is also inserted in the glycerol.

The internal field in the sample H_i is calculated taking into account the demagnetizing factor α. The magnetization is $M = \chi H_i = \chi(H_e - \alpha M)$, where H_e is the external field. Hence, $M = H_e/(\alpha + 1/\chi)$. The output voltage of the differential transformer is proportional to the magnetization and equals $V = KM = KH_e/(\alpha + 1/\chi)$. Below T_c, $1/\chi << \alpha$. This assumption allows for the determination of the external magnetic field: $H_e = \alpha V_0/K$, where V_0 is the output voltage below T_c (Heller 1967). For a sphere, $\alpha = 1/3$, so that

$$\chi = 3V/(V_0 - V). \tag{8}$$

The output voltage of the differential transformer is fed to a PAR 124A amplifier. The amplifier operates in the selective mode and is tuned to the frequency of the current in the primary winding of the transformer. The *Scope* serves to monitor the amplified AC voltage. The amplifier provides also a DC voltage proportional to the input AC signal. For balancing the transformer, it is convenient to observe the Lissajous pattern on the screen. For this purpose, the voltage drop across a resistor connected in series with the primary winding of the transformer is fed to the X input of the *Scope*. The temperature range of the measurements is 285–325 K. Cold water is used to cool the glass with the sample before the measurements. After cooling, the temperature of the sample starts to increase due to the heat exchange with the environment. Close to Curie's point, the heating rate should not exceed 2–3 K.min^{-1}. The low heating rate is necessary to reduce temperature gradients in the sample and thus obtain a sharp transition. The electrical heater inside the glass heats the sample above room temperature.

Magnetic susceptibility and critical exponent. The magnetic susceptibility χ calculated with Eq. (8) is presented as a function of temperature (Fig. 8). The critical exponent is available from the plot of $\ln\chi$ versus $\ln(T - T_c)$. This plot and the value of γ depend on the choice of T_c. In our case, the plot is linear over the broadest temperature range when T_c is taken to be 290.5 K, while the values 290 and 291 K lead to significant curvatures of the plot. A more rigorous treatment should include determinations of both T_c and γ by the least-squares method.

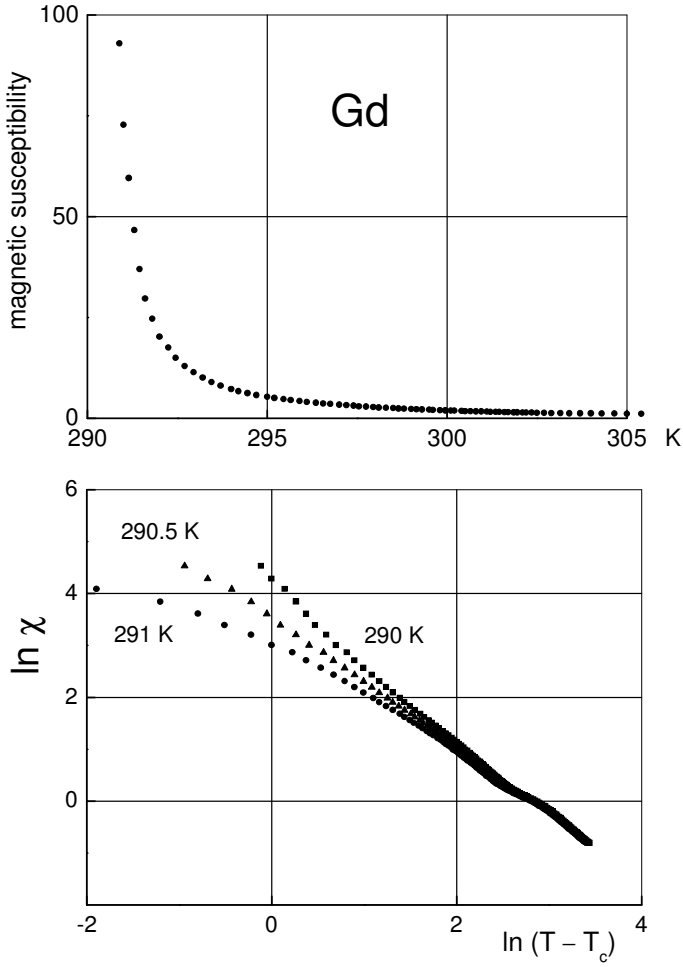

Fig. 8. Magnetic susceptibility χ of gadolinium versus temperature, and $\ln\chi$ versus $\ln(T - T_c)$ for three supposed values of T_c.

4. Spontaneous magnetization

The temperature dependence of the spontaneous magnetization of a monel wire is determined (Kraftmakher 2005e).

Additional equipment: three *Voltage sensors*, monel wire, Dewar flask, AC-to-DC converter, AC supply, platinum resistance thermometer, oscilloscope, coils, resistors, capacitor.

A nickel-based alloy, monel 400 (Ni65/Cu33/Fe2), serves as the sample. The sample is 1 mm in diameter and 10 cm long. The hysteresis loops are observable at temperatures from 77 K up to Curie's point, which is close to 270 K. The determination of the spontaneous magnetization is based on measurements of the magnetic saturation of a polycrystalline sample. The sample contains many domains randomly oriented in the absence of an external magnetic field. Under a sufficiently high external field, the sample reaches saturation and represents a one-domain system oriented along this field. The saturation magnetization can be considered to be equal to the spontaneous magnetization of one domain. In the experiment, nickel and steel samples serve for checking the measurement technique.

Hysteresis loops. The sample is implanted, together with a small platinum resistance thermometer (1×4×5 mm, 1 kΩ at 0°C), into a plasticine (modeling clay) rod, 1 cm in diameter. The rod is put in a glass test tube, which can be cooled by liquid nitrogen. A differential transformer senses the magnetic properties of the sample (Fig. 9). Two 320-turn coils, about 14 cm in diameter, are positioned in the Helmholtz arrangement to form the primary winding of the transformer. The coils are fed by a variable AC supply consisting of a variac and an isolating transformer (the details are not shown in Fig. 9). The isolating transformer is obligatory to avoid direct contact of the setup with the AC mains and thus to prevent harm to the experimenter or equipment. Two 800-turn coils (SF-8611) connected in opposition constitute the secondary winding of the transformer. Without a sample or when its temperature is above Curie's point, the output voltage of the transformer becomes zero. The secondary coils are arranged to nullify the output voltage before the measurements. An additional circuit, consisting of two 0.1 Ω resistors and a variable 100 Ω resistor placed in series with the primary winding, serves to nullify any small imbalance voltage that is in phase with the current in it. With a ferromagnetic sample in one of the secondary coils, a voltage at the output is proportional to the time derivative of the difference between the magnetic fluxes in the two secondary coils.

The output voltage of the transformer is fed to an integrating RC circuit at the Y input of a Kenwood CS-4025 oscilloscope. The output voltage of the integrating circuit is proportional to the magnetization M of the sample. The sensitivity of the oscilloscope should be at least 1 cm.mV^{-1}. One input of the

data-acquisition system and the X input of the oscilloscope are connected to one of the 0.1 Ω resistors. The voltage across the resistor is proportional to the current in the primary coils and thus to the magnetizing field B_0. The oscilloscope displays the output voltage of the RC circuit versus the current in the primary coils. To correctly display the hysteresis loops, the time constant of the integrating RC circuit must be much larger than the period of the AC magnetic field. In our case, $R = 0.13$ MΩ, and $C = 4.7$ μF. The sensitivity of the data-acquisition system is insufficient to display the voltage highly reduced by the integrating circuit. For this reason, the oscilloscope serves also as an amplifier. The maximum gain is 100. The input of the data-acquisition system is connected to the output terminal of the oscilloscope. A Keithley 177 multimeter converts the resistance of the platinum thermometer into a DC output voltage, from which the absolute temperature of the sample is calculated.

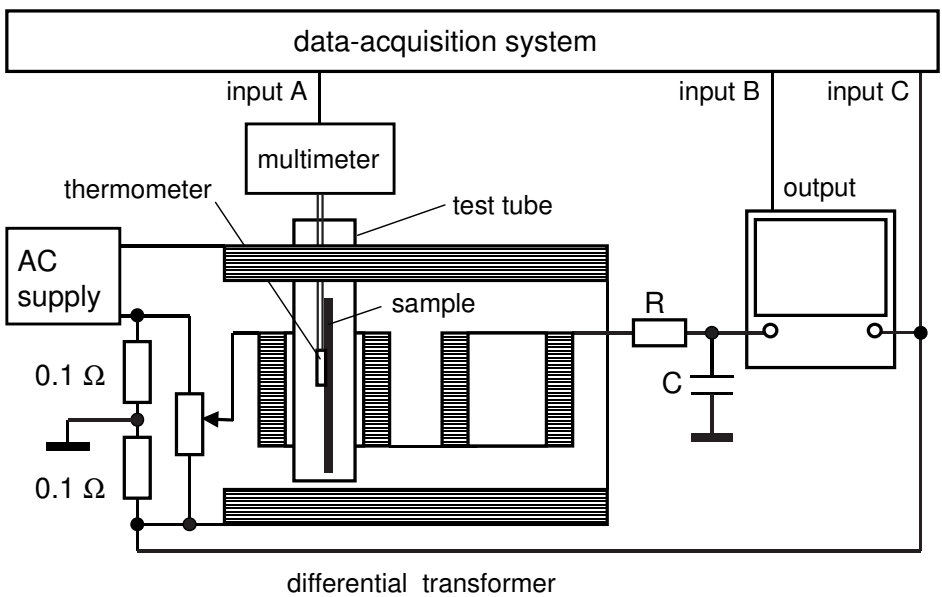

Fig. 9. Setup for recording hysteresis loops at various temperatures.

After cooling in liquid nitrogen, the test tube containing the sample and thermometer is put into one of the secondary coils. The temperature of the sample starts to gradually increase because of the heat exchange with the environment. The heating rate decreases with increasing temperature. For our setup, heating up to Curie's point takes about 20 min. During the run, the hysteresis loops of the sample and the corresponding temperatures are readily available. To calculate the magnetization of the sample, *DataStudio* uses the cross-sectional area of the sample A, the number of turns of the secondary coil N_2, the time constant of the integrating circuit RC, and the voltage at the output of the integrating circuit U:

$M = URC/AN_2$. (9)

This relation is similar to that when observing hysteresis loops of a ferromagnet. The only difference is caused by the differential method of measurements. For our apparatus, M(T) = 0.97×U(mV). The magnetic field produced by the Helmholtz coils equals B_0(mT) = 4.25×I_1(A). The magnetizing field is close to this value. *DataStudio* converts the measurement data into M and B_0 using the above equations and displays the hysteresis loop, M versus B_0. Simultaneously, *Digits* tool displays the temperature of the sample as determined from the resistance of the platinum thermometer. With the *Automatic stop/Time* option, each hysteresis loop is stored during one period of the current. The *Sample rate* is 20 kHz, so each loop contains 400 experimental points (Fig. 10).

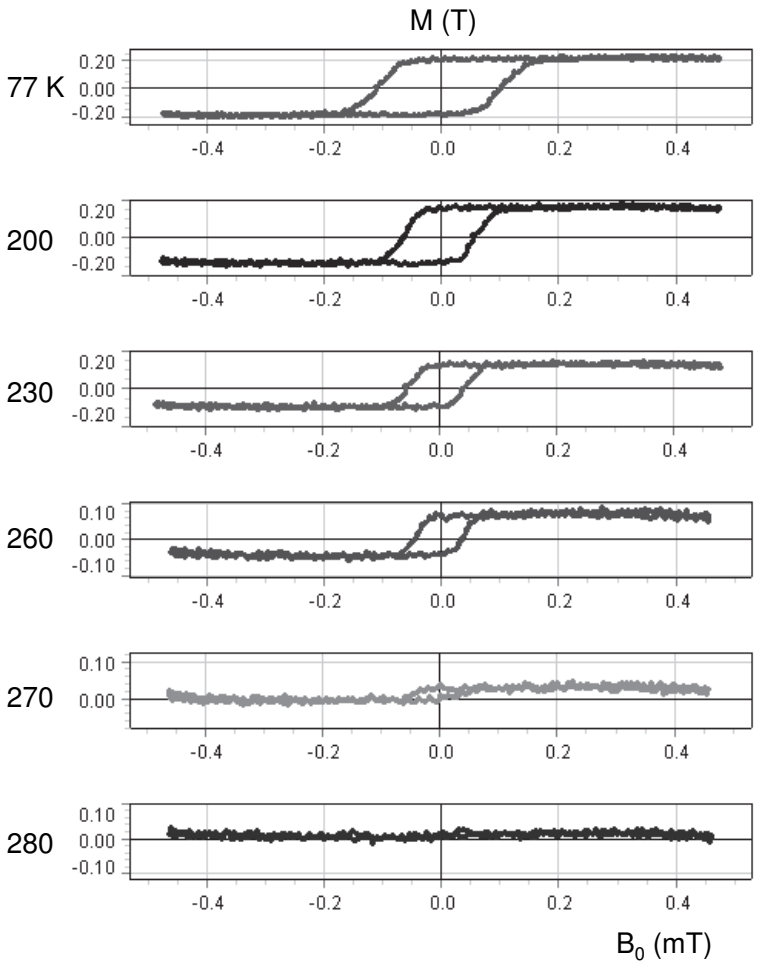

Fig. 10. Hysteresis loops of the monel sample from 77 to 280 K.

The results show dramatic changes in the hysteresis loop with temperature. The **saturation magnetization** and the **coercivity** decrease with increasing temperature. This is quite expectable because the motion of domain walls becomes easier at higher temperatures. At 77 K, the saturation magnetization equals about 0.25 T. Curie's point is close to 270 K, in agreement with that obtained by measurements of the skin effect in the same monel wire. As a test of the setup, similar measurements were carried out with nickel and steel samples of the same geometry. Our magnetizing field is insufficient to achieve saturation of the nickel sample. For the steel sample, the saturation magnetization was found to be about 1.6 T, which falls into the range known for steels.

The spontaneous magnetization of the sample is taken as its saturation magnetization. At sufficiently high external fields, the output voltage of the integrating RC circuit becomes close to a square wave voltage. An AC-to-DC converter, a Hewlett–Packard 400E voltmeter, measures this voltage (Fig. 11). Its DC output voltage directly relates to the saturation magnetization M_s.

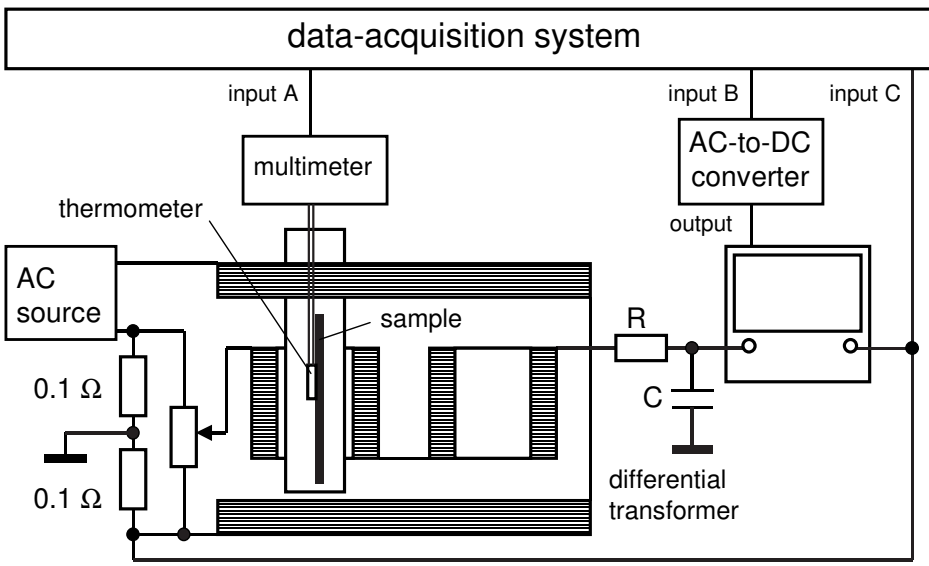

Fig. 11. Diagram of the setup for recording temperature dependence of saturation magnetization.

Along with the expected temperature dependence of the spontaneous magnetization, the data (Fig. 12) indicate the presence of a small magnetization above Curie's point. The reason for this phenomenon is the external magnetic field. The true magnetization is available by gradually decreasing the external field and extrapolating the data to zero fields. The data are obtained with two values of the current in the primary windings, 0.5 and 1 A (RMS). A residual imbalance of the differential transformer also contributes to the signal above

Curie's point. According to Eq. (2), a plot of $M_s^{1/\beta}$ versus temperature should be a straight line intersecting the temperature axis at Curie's point. The ratio M_s/M_{200} (M_{200} is the spontaneous magnetization at 200 K) is used for the comparison. The results obtained with a 0.5 A magnetizing current allow one to distinguish between the $\beta = 0.5$ value of the critical exponent predicted by the mean-field theory, and $\beta = 0.3645$ predicted by the modern theory of critical phenomena. The second value provides a better linear fit to the experimental data (Fig. 13). The magnetization above Curie's point does not markedly influence the fit.

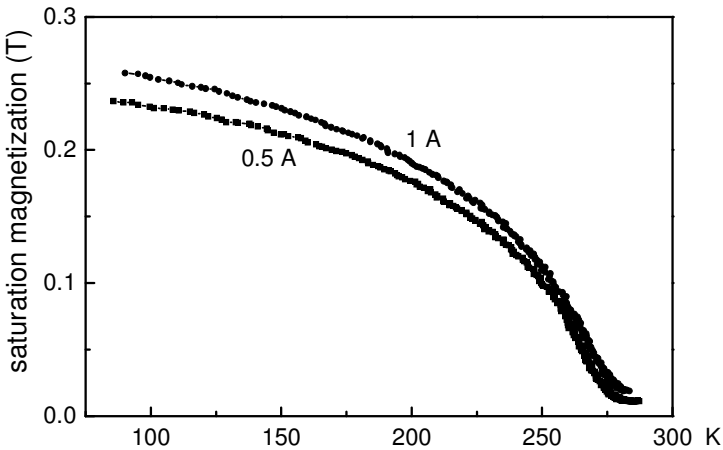

Fig. 12. Temperature dependence of saturation magnetization.

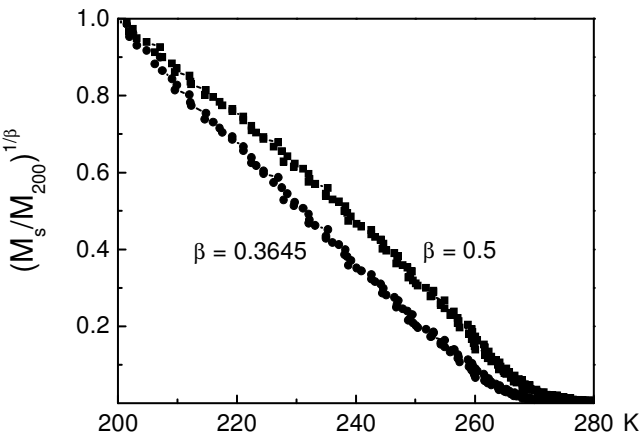

Fig. 13. Plots of $(M_s/M_{200})^{1/\beta}$ versus temperature.

6.7. Ferrimagnetism

The experiments with ferrites include (i) the hysteresis loops; (ii) the differential permeability; (iii) the complex permeability at high frequencies; (iv) the ferrite bead action; and (v) the temperature dependence of magnetic properties.

Néel's discovery. In many modern technologies including television, mobile telephony, and computers, a permanent trend is the increase of frequencies of electrical signals.

Louis Néel (1904 – 2000)

Ferrites maintaining magnetic properties up to very high frequencies play a significant role in these technologies. For a long time, it was believed that according to their magnetic properties, materials fall into three categories: diamagnets, paramagnets, and ferromagnets. Michael Faraday proposed this classification in the middle of the 19th century. About a century later, Louis Néel discovered two new categories of magnetic materials: antiferromagnets and ferrimagnets. The crystal lattice of ferrimagnets forms two sublattices of opposite but different magnetizations (equal magnetizations lead to antiferromagnetism). A net magnetization thus arises (Smit and Wijn 1959; Rogalski and Palmer 2006; Cullity and Graham 2009). It turned out that magnetite Fe_3O_4, believed to be a ferromagnet, is really a ferrimagnet.

In 1970, Louis Néel was awarded Nobel Prize in Physics "for fundamental work and discoveries concerning antiferromagnetism and ferrimagnetism which have led to important applications in solid state physics." In the presentation speech, Professor Torsten Gustafsson, member of the Royal Swedish Academy of Sciences, said: "…In 1948, Néel… generalized his earlier assumption by assuming that the lattices could be of different strengths and could produce external fields. In magnetite, with three atoms of iron and four of oxygen, the effects of two of the iron atoms cancel out while the third gives rise to the magnetic field… Néel could present an accurate description of the behavior of the new synthetic magnetic materials and so explain hitherto puzzling experimental observations. These developments have been of considerable technical importance, *e.g.,* in computer memories and in high-frequency techniques…"

Cubic ferrites forming an important class of ferrimagnets originate from magnetite by replacing one iron atom and have the general formula $MO{\cdot}Fe_2O_3$, where M is a divalent metal ion, like Mn, Ni, Co or Mg. Ferrites can contain two or more different kinds of divalent ion, for instance, $(Mn_xZn_{1-x})O{\cdot}Fe_2O_3$ (mixed

ferrites). Most cubic ferrites commercially available are mixed ferrites. They are manufactured by usual techniques of ceramics including processes of grinding, pressing, and sintering. **Hexagonal ferrites** having garnet structure form another class of ferrites; one of them, the yttrium–iron garnet, $Y_3Fe_5O_{12}$ (YIG), is widely known due to its important applications. Like ferromagnets, ferrimagnets lose their magnetic properties at Curie's point.

Hysteresis loops of "soft" ferrites are very narrow, which means low **coercivity** and small **hysteresis losses**. Ferrites are semiconductors, and their resistivity is much higher than that of metals. This presumes low eddy current losses. As a result, ferrite cores are applicable at high frequencies without significant losses. "Soft" ferrites are widely used as materials for transformer cores, rod antennas, and electromagnetic interference (EMI) suppressors. The last item in this list is a part of modern electronic equipment, including personal computers and related devices. "Hard" ferrites having broad hysteresis loops (that is, high coercivity) serve as permanent magnets.

A narrow hysteresis loop means that the **domain structure** of the material easily follows external magnetic fields, so that the magnetization process occurs without significant energy losses. This is due to the easy movement of domain walls as the external field changes its magnitude or direction. However, at sufficiently high frequencies of the external field, the domain structure cannot follow the fast changes of the field, so the material loses its high permeability. In an intermediate frequency range, the permeability gradually decreases, while the losses increase. For various materials, compositions, and microstructures (grain size and porosity) this transition may occur at very different frequencies, say, from 10^5 to 10^9 Hz. The larger the static permeability, the lower the frequency, at which the transition occurs. To observe this phenomenon in a student laboratory, a material designed for low frequencies is preferred because the measurements at low frequencies are more convenient and accurate, while the necessary equipment is less expensive.

When a ferrite core embraces a wire, the impedance of the wire increases. This increase is proportional to the frequency and the permeability of the ferrite. Due to the significant increase of the losses, high-frequency signals and noise in the wire dissipate in the ferrite core as heat. Such suppressors of electromagnetic interference (ferrite beads) are placed on cables connecting a computer with a mouse, a keyboard, a printer, and so on; they also protect electronic devices from interference through power cords.

Since 1970, the use of ferrites and their importance greatly increased. Ferrimagnetism undoubtedly deserves an appropriate place in undergraduate laboratories, but related student experiments are scarce. Prasad *et al* (1972) determined the permeability of a ferrite rod by measuring resonant frequencies of an LCR circuit with the rod inside the inductor. Mahmood *et al* (2011) measured the heat capacity of magnetite at low temperatures.

In experiments considered below, we use cubic ferrites for measuring their magnetic properties, including the frequency dependence of the **complex permeability**. The measurements at high frequencies follow procedures similar

to those commonly used for this aim in scientific studies (for instance, Dosoudil *et al* 2006). The experiments include five items (Fig. 1): (i) the hysteresis loops and permeability; (ii) the differential permeability versus a DC bias; (iii) the frequency dependence of the complex permeability; (iv) the electromagnetic interference suppression by ferrite chokes and beads; and (v) the temperature dependence of the permeability and hysteresis loops. Two toroidal ferrite cores are used. The first is taken off a "low-frequency" ferrite choke and used in experiments (i)–(iii). The second is a "middle-frequency" ferrite bead taken off a power cord; it is used in experiments (iv) and (v). The materials of both cores are polycrystalline Mn–Zn ferrites.

Important advantages of using ferrites for student experiments are the following: (i) a sufficiently low Curie's temperature of Mn–Zn ferrites; (ii) the high permeability in the ferrimagnetic state; (iii) the low conductivity allowing for applying high-frequency magnetic fields; and (iv) suitable samples are easily available.

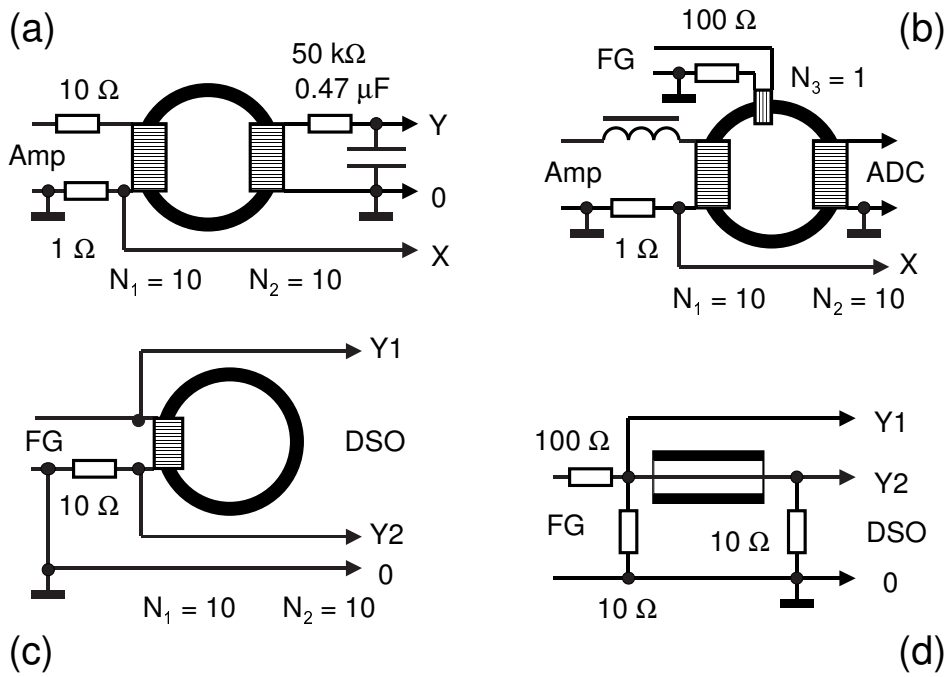

Fig. 1. General scheme of the experiments: (a) hysteresis loops; (b) differential permeability; (c) frequency dependence of complex permeability; (d) ferrite bead in action. Amp–generator-amplifier, FG–function generator, ADC–AC-to-DC converter, DSO–digital storage oscilloscope.

1. Hysteresis loops and permeability

Hysteresis loops are observed, and the permeability B/B_0 and differential permeability dB/dB_0 are determined (Kraftmakher 2013a).

Additional equipment: *Voltage sensors*, *Digital function generator-amplifier*, ferrite sample, DC supply, resistors.

Hysteresis loops are the most informative characteristics of ferromagnets and ferrimagnets. A common setup (Fig. 1a) is used for observing hysteresis loops of a ferrite core. There is no need to wrap many-turn coils on the core; instead, we employ a generator providing a sufficient current of an enhanced frequency. This is necessary for obtaining sufficient voltages across a few-turn coil. The two coils contain ten turns each ($N_1 = N_2 = 10$), while the frequency is $f = 2$ kHz. The primary coil is connected to the *Digital function generator-amplifier* (PI-9587C) through a 10 Ω (10 W) resistor. The primary current is measured through the voltage drop across a 1 Ω resistor put in series with the coil. An integrating RC circuit (50 kΩ, 0.47 μF) is connected to the secondary coil.

The **magnetic field strength** H (or $B_0 = \mu_0 H$) created by the primary coil is available from the number of turns N_1 and current I through the coil:

$$B_0 = \mu_0 N_1 I/l. \tag{1}$$

Here, μ_0 is the **magnetic constant** (permeability of vacuum), and l is

$$l = \pi d_m, \tag{2}$$

where d_m is the mean diameter of the core. This expression is valid when the diameter of the core is much larger than its thickness. A rigorous relation is

$$l = \pi(d_2 - d_1)/\ln(d_2/d_1), \tag{3}$$

where d_2 and d_1 are the outer and inner diameters of the core. For our sample, $d_2 = 28$ mm, $d_1 = 18$ mm, and Eqs. (2) and (3) provide close results. The value $l = 0.071$ m was taken, so B_0 (mT) = $0.177 \times I$ (A).

The **magnetic flux density** in the core (magnetic field B) is available, according to Faraday's law, from the number of turns N_2, cross-sectional area A of the core, and output voltage V of the integrating RC circuit:

$$B = VRC/AN_2. \tag{4}$$

The height of the core h is 15 mm, so $A = 5$ mm×15 mm = 7.5×10^{-5} m^2, and B (T) = $31.3 \times V$ (V). Note the different units for B_0 and B.

Two *Voltage sensors* acquiring the voltages necessary to calculate the quantities B_0 and B operate at a 100 kHz sample rate. *DataStudio* calculates and displays hysteresis loops, from which the dependence $B(B_0)$ and $\mu = B/B_0$ are derived (Fig. 2). The saturation magnetic field is nearly 0.4 T, while the **coercivity** is about 0.01 mT.

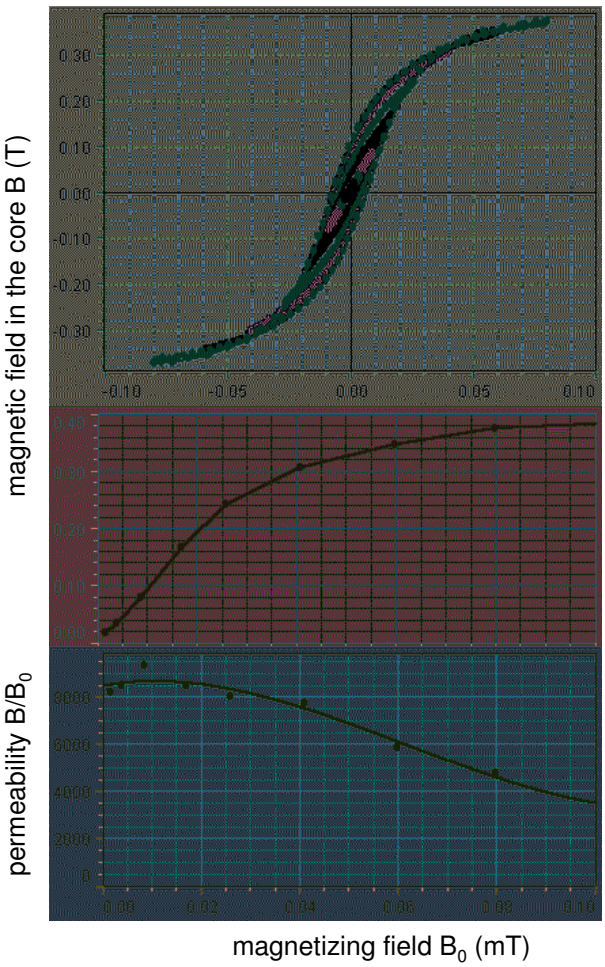

Fig. 2. Properties of the "low-frequency" ferrite versus magnetizing field B_0: family of hysteresis loops, magnetic field B, and permeability $\mu = B/B_0$.

Permeability versus magnetizing field. At low magnetic fields, the permeability of the sample is nearly 8000. Due to the narrow hysteresis loops, it is not easy to find accurately the permeability for various magnetization fields, and direct measurements of the **differential permeability** are highly preferred.

The differential permeability of the sample, that is, $\mu_d = dB/dB_0$, can be measured directly. For this aim, an additional 1-turn coil ($N_3 = 1$) is wrapped on the ferrite core (Fig. 1b). A small current $I_1 \sin\omega t$ from an additional function generator ($f = 2$ kHz) passes through this coil and slightly modulates the magnetic flux in the core. To make the current independent of the permeability of the core, a 100 Ω resistor is put in series with the coil. The current is

determined through the voltage drop across this resistor. The *Digital function generator-amplifier* providing a 0.01 Hz sine waveform current in the first 10-turn coil (N_1) creates a slowly varying bias. An 800-turn coil (SF-8611) with an O-shaped iron core (SF-8614) is put in series with this coil instead of a usual resistor (the coil is shown in Fig. 1b as a choke). The coil suppresses a 2 kHz current in the first 10-turn coil arising due to the modulation of the magnetic flux in the core; otherwise, this current affects the AC magnetic flux and results of the measurements. The slowly varying current in the first 10-turn coil is measured through the voltage drop across a 1 Ω resistor put in series with it. Due to the modulation, an EMF e is generated in the second 10-turn coil (N_2); its amplitude equals

$$e = \mu_0 \omega \mu_d N_3 N_2 A I_1 / l. \quad (5)$$

For our core, $\mu_d = 1.2\times10^7 e/I_1 f$. An AC-to-DC converter (a Keithley 177 multimeter) transforms the EMF e into a DC voltage proceeding to the *750 Interface*. The differential permeability μ_d is displayed versus the DC magnetic field (Fig. 3). If the sample is demagnetized before a run, the graph includes the differential permeability corresponding to the initial magnetization curve and data corresponding to slow periodic changes of the bias. The differential permeability has a maximum at a definite bias, less than 0.01 mT, and then decreases rapidly with increasing the DC field. Data obtained by measuring the inductance of the coil are also shown.

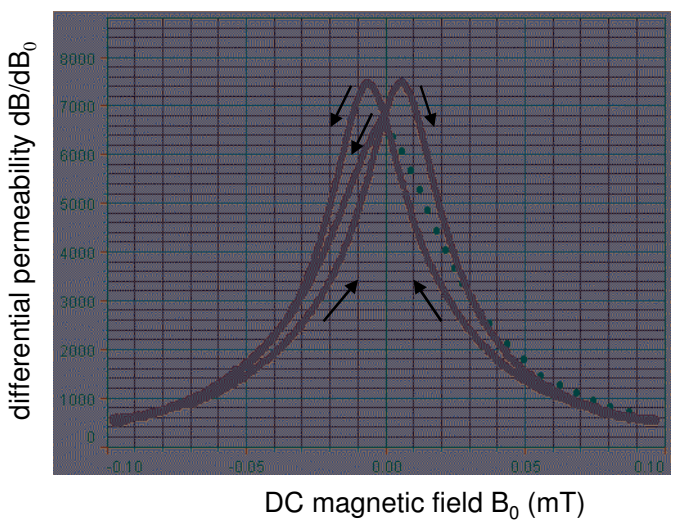

Fig. 3. Differential permeability versus DC bias: ——— measurements started from a demagnetized state, • measurements of inductance of the coil.

2. Frequency dependence of complex permeability

The complex permeability is determined in a wide frequency range, and the action of a ferrite bead is demonstrated (Kraftmakher 2013a).

Additional equipment: ferrite sample, high-frequency function generator, digital storage oscilloscope, resistors.

The AC permeability of a ferrite is a complex quantity containing a real and an imaginary part, μ' and μ'':

$$\mu = \mu' - j\mu''. \tag{6}$$

The impedance $\boldsymbol{Z}$ of a coil wrapped on a toroidal magnetic core equals the impedance of an air-core toroidal coil times the permeability. A generalization of this rule is the use of the complex permeability. Thus,

$$\boldsymbol{Z} = j\omega L + R = j\mu_0\omega A(\mu' - j\mu'')N^2/l, \tag{7}$$

where N is the number of turns of the coil. The inductance L of a ferrite-core coil relates to the real part of the permeability, and the resistance R to the imaginary part. From Eq. (7), both parts of the permeability are available:

$$\mu' = lL/\mu_0 AN^2, \tag{8a}$$

$$\mu'' = lR/\mu_0\omega AN^2. \tag{8b}$$

Complex permeability versus frequency. This experiment relates to topics rarely coming into view in undergraduate laboratories; therefore, many details of the experiment are given. An HP-33120A function generator provides frequencies up to 15 MHz. A sine waveform current from the generator passes through a ferrite-core coil ($N = 10$) and a 10 Ω resistor put in series with the coil at the grounded end of the circuit (Fig. 1c). The voltage applied to this circuit and that across the resistor are fed to the inputs of a DSO, Tektronics TDS 3012B. The function generator and the DSO are used here instead of an expensive impedance analyzer.

The DSO operates in the single run mode. For determining the phase shift between the applied voltage (Y1) and the voltage across the 10 Ω resistor (Y2), we use the *V-bars* (vertical bars) tool of the DSO. The time shift between the voltages is displayed on the screen. Simultaneously, the DSO displays their values. These data are sufficient for calculating the modulus and phase angle of the total impedance of the coil-resistor circuit and its real and imaginary parts. The coil itself has the same inductance, while the resistance is 10 Ω less than that of the total impedance. Above 1 MHz, the time shift between the Y1 and Y2 voltages becomes close to zero and may become negative. Therefore, a zero phase angle was ascribed to all these data. This simplification nullifies the real part of the permeability, while in fact this part is much smaller than the imaginary part.

The μ′ and μ″ values are available from equations (8a) and (8b). The *Origin* software calculates the data and displays them versus frequency of the magnetic field. The modulus and the phase angle of the total impedance (the ferrite-core coil plus the 10 Ω resistor) are measured at frequencies up to 15 MHz (Figs. 4a and 4b). Then the **real** and **imaginary** parts of the ferrite-core coil **impedance** are determined (Fig. 4c). Finally, the real and imaginary parts of the permeability are calculated (Fig. 4d). The current through the coil is sufficiently small, so the results correspond to the initial permeability. These data agree with the observations of the hysteresis loops.

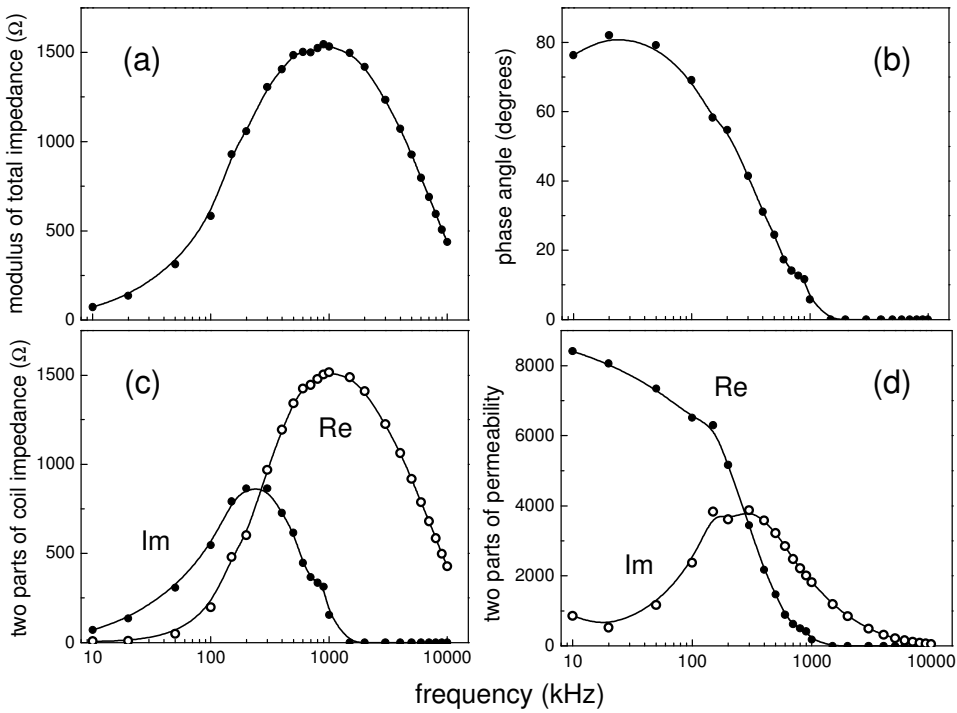

Fig. 4. Properties of the 10-turn ferrite-core coil versus frequency: (a) modulus and (b) phase angle of the total impedance; (c) two parts of the coil impedance and (d) of the complex permeability of the ferrite.

Qualitatively, the frequency dependence of the total impedance of the coil-resistor circuit can be seen from Lissajous patterns (Y2 versus Y1) on the DSO screen (Fig. 5). At low frequencies, a nearly 90° phase shift between the two voltages is seen ($2\pi fL >> R$). Above 100 kHz, the phase angle of the total impedance continuously decreases. Though the phase shift can be determined from the shape of the Lissajous pattern, the use of the *V-bars* tool of the DSO is more convenient and provides results that are more accurate.

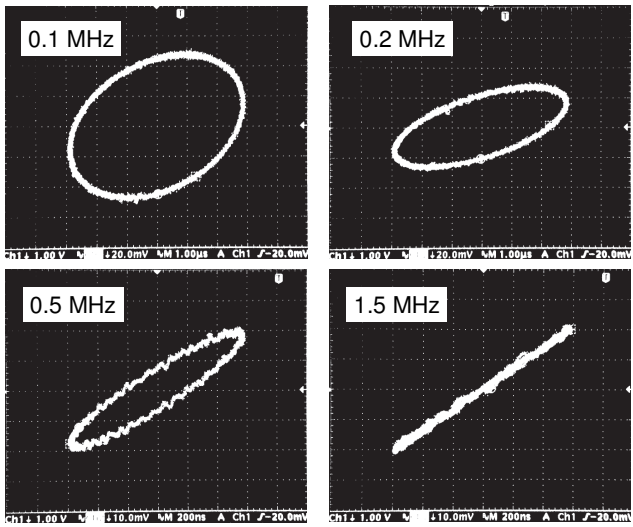

Fig. 5. Voltage across the 10 Ω resistor versus total applied voltage, for various frequencies. Above 100 kHz, the phase angle of the total impedance continuously decreases and becomes nearly zero above 1 MHz.

Relaxation time. The frequency dependence of the complex permeability is similar to data given by the manufacturers. A more accurate comparison is impossible because the composition and microstructure of our sample are unknown. Generally, two phenomena, the domain wall motion and the magnetization rotation, govern the frequency dependence of the complex permeability. The two processes can occur simultaneously, but usually one of them dominates. The magnetization rotation is a **relaxation phenomenon** characterized by a time constant τ. The domain wall motion should manifest a broad resonance, but sometimes the frequency dependence of the permeability also looks as to be of relaxation type (Tsutaoka *et al* 1997; Nakamura 2000; Huang *et al* 2008). From the theory of relaxation phenomena (Smit and Wijn 1959; Hamilton 2011),

$$\mu = \mu_{dc}/(1 + \omega^2\tau^2) + j\mu_{dc}\omega\tau/(1 + \omega^2\tau^2), \qquad (9)$$

where μ_{dc} is the low-field DC permeability. The relaxation time and the low-field DC permeability depend on the composition and microstructure of the core.

Our ferrite core manifests rather relaxation-type behavior of the permeability. The real part monotonically decreases with increasing frequency, while the imaginary part reaches a maximum at a frequency, where $\omega\tau = 1$. At this point, $\mu' = \mu'' = 0.5\mu_{dc}$. The relaxation time can be determined from fits of experimental data by Eq. (9), separately for both parts of the permeability. The data shown in Fig. 4d are used for the fits, but for frequencies only below 1 MHz; they are presented with a linear frequency scale (Fig. 6). The two fits provide close values of μ_{dc} and τ; the mean values of these quantities are 7920

and 0.63 μs. From the point where $\mu' = \mu''$ (f = 256 kHz), these values appeared to be 7820 and 0.62 μs.

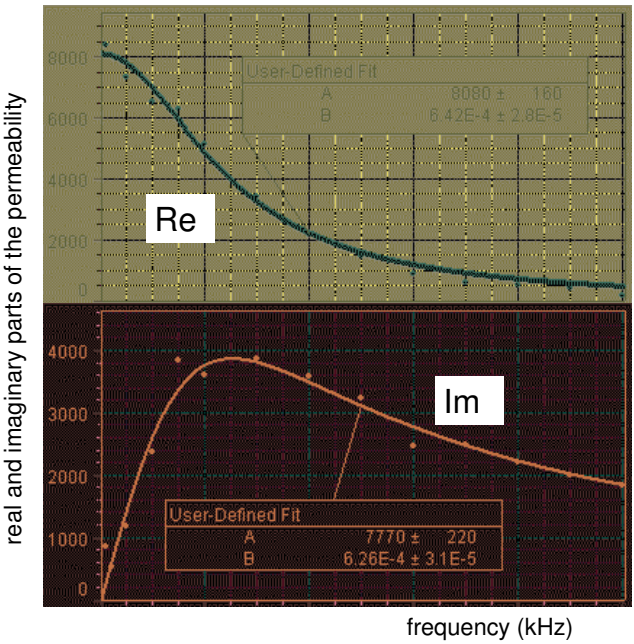

Fig. 6. Two parts of the permeability versus frequency fitted with Eq. (9).

Summarizing, the sequence for the measurements and calculations in this experiment is the following.

● The frequency of the function generator is gradually increased, and four quantities are determined: the frequency f, RMS values of the Y1 and Y2 voltages, and a time shift Δt between the two voltages determined with the *V-bars* of the DSO. Software like *Origin* is needed for processing the measurement data.

● Modulus of the total impedance of the circuit including the ferrite-core coil and the 10 Ω resistor equals $Z_{tot} = 10 \times Y1/Y2$ (Fig. 4a).

● The phase angle of the total impedance of the circuit (in degrees) equals $\varphi = 360 \times f\Delta t$ (Fig. 4b).

● The two parts of the coil impedance equal $R = Z_{tot}\cos\varphi - 10$ and $2\pi fL = Z_{tot}\sin\varphi$ (Fig. 4c).

● The two parts of the complex permeability of the ferrite are calculated using equations (8a) and (8b) (Fig. 4d).

• The data for μ' and μ'' for frequencies below 1 MHz are fitted with Eq. (9), separately for the two quantities, and the DC permeability μ_{dc} and relaxation time τ are determined from the fits (Fig. 6). These parameters are also calculated from the point, where $\mu' = \mu''$.

Ferrite bead action. The impedance of a ferrite-core coil is controlled by properties of the ferrite. The same relates to a wire passing through a ferrite bead: the wire corresponds to a one-turn winding on the core. As expected, a broad maximum arises in the frequency dependence of the impedance of the coil or wire. The maximum occurs at frequencies, where the real part of the impedance becomes much larger than the imaginary part, so the impedance is mainly resistive. Just this phenomenon causes signals of corresponding frequencies to dissipate in the core, and this is the intention when using ferrite beads. The modulus of the impedance of a wire passing through a ferrite bead can be measured directly as a ratio of the applied voltage and the current. Clearly, the efficiency of a bead depends on the total impedance of the circuit.

There exist two ways to employ ferrite beads: (i) only one wire of a two-wire cord passes through the bead (the present experiment), and (ii) both wires pass through the same bead. In the first case, the filtering action of the bead is evident: in a definite frequency range depending on the properties of the ferrite, the wire impedance highly increases and becomes mainly resistive. When both wires pass through the same bead, the two opposite currents produce magnetic fluxes in the core that cancel out, so the bead does not act. In this case, the bead only blocks signals induced in the same way in both wires (the so-called common-mode signals). For instance, such signals are induced in both wires of a cord by electromagnetic induction. Relatively to the bead, the common-mode currents in both wires flow in the same direction, so the two magnetic fluxes in the core are added, and the filtering action occurs.

The filtering action of the "low-frequency" core used in the preceding experiment occurs in a frequency range of nearly 0.2–4 MHz (Fig. 4a). At these frequencies, the wire impedance is insufficient to significantly affect the current in the circuit. For this reason, a "middle-frequency" ferrite bead intended for higher frequencies is used in the experiment. For this bead, $d_2 = 16$ mm, $d_1 = 8$ mm, and $h = 28$ mm; so $l = 0.036$ m, and $A = 1.1\times10^{-4}$ m^2. Two resistors, 100 and 10 Ω, form a voltage divider for reducing the output resistance of the source feeding the wire. The wire is put in series with another 10 Ω resistor (Fig. 1d).

The measurements are similar to those with the "low-frequency" core. First, the modulus and the phase angle of the total impedance (the wire plus the 10 Ω resistor) are determined at frequencies up to 15 MHz (Figs. 7a and 7b). Then the real and imaginary parts of the wire impedance are calculated (Fig. 7c). At frequencies below 1 MHz, the real part of the wire impedance remains nearly zero. The modulus of the impedance reaches a maximum at nearly 10 MHz (Fig. 7d), and the filtering action occurs in a range of nearly 3–20 MHz. The wire impedance is doubled if the wire passes through two similar beads. The

capability of absorbing electromagnetic waves in a definite frequency range demonstrates one of the principles of *Stealth* technology.

The two parts of the permeability can also be calculated. At low frequencies, however, the data are highly scattered due to the scatter in the two parts of the wire impedance. At 1 MHz, the real part of the permeability is nearly 430. This figure was checked by measuring, with the LCR meter, the inductance of a 10-turn coil wrapped on the bead. The inductance at 1 kHz, 0.18 mH, corresponds to $\mu' = 470$.

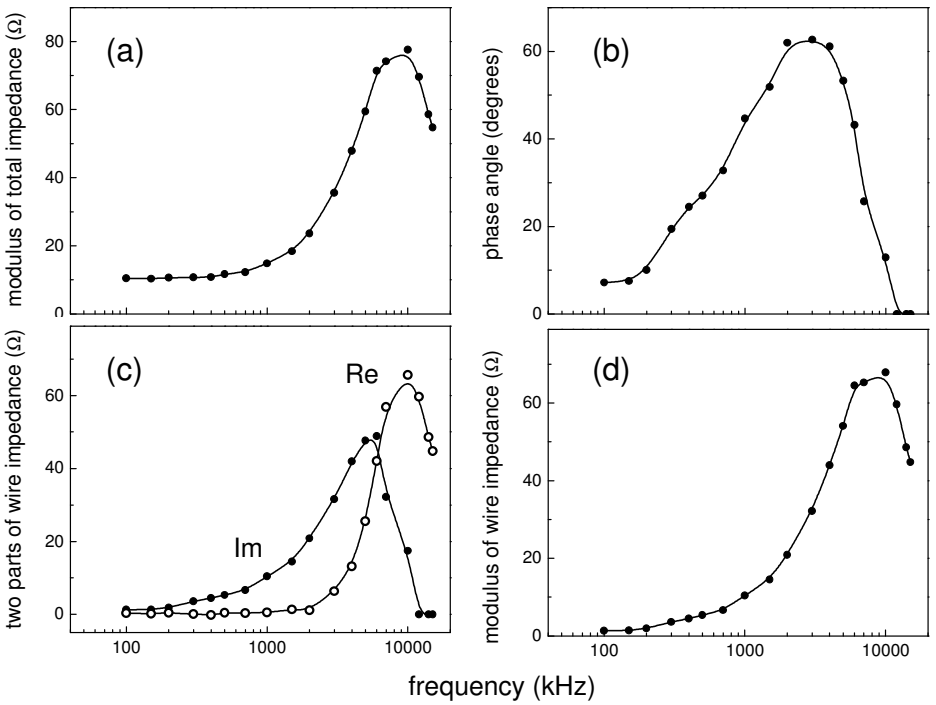

Fig. 7. Properties of a wire passing through the "middle-frequency" ferrite bead: (a) modulus and (b) phase angle of the total impedance; (c) two parts and (d) modulus of the wire impedance.

3. Temperature dependence of magnetic properties

At temperatures from 77 K up to Curie's point, the permeability of a "middle-frequency" ferrite bead is measured, and hysteresis loops are observed.

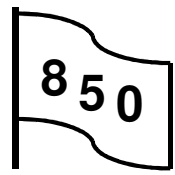

Additional equipment: ferrite sample, electrical oven, Dewar flask, AC-to-DC converter, resistors.

Low-field permeability. The low-field permeability of the sample is determined with two 10-turn windings wrapped on the ferrite bead. The *Output 1* provides a 10 kHz current for the primary winding. The *Output voltage* is 15 V (amplitude value) To make the current independent of the permeability of the core, a 1 kΩ resistor is put in series with the primary winding. The EMF generated in the secondary winding is proportional to the permeability of the core. This EMF is fed to an AC-to-DC converter, a Keithley 177 multimeter, and then to the *850 Interface*. It should be remembered that DC output voltages of the converter correspond to RMS values of input AC voltages.

The inductance L of a winding wrapped on a ferrite toroid equals

$$L = \mu\mu_0 N_1^2 A/l, \tag{10}$$

where μ is the permeability of the ferrite, μ_0 is the magnetic constant, N_1 is the number of turns, A is the cross-sectional area of the core, and l is the average length of the magnetic path in the toroid.

Equation (10) is a consequence of Faraday's law of electromagnetic induction. In our case, the resistance of the winding can be neglected. When a current $I\sin\omega t$ passes through the winding, the voltage drop V_1 (amplitude value) across the winding is

$$V_1 = I\omega L = I\omega\mu\mu_0 N_1^2 A/l. \tag{11}$$

The secondary winding contains N_2 turns. The magnetic flux through both windings is the same, so the EMF e generated in the secondary winding equals $V_1 N_2/N_1$. The permeability of the core equals

$$\mu = el/I\omega\mu_0 N_1 N_2 A. \tag{12}$$

For the sample used, $N_1 = N_2 = 10$, $A = 1.1\times10^{-4}$ m^2, $l = 0.036$ m, and $f = 10$ kHz; thus, $\mu = 41\times e/I$. The current in the primary winding is 15 mA (amplitude value). The magnetic field strength H created by the primary winding obeys Ampère's circuital law, so $B_0 = \mu_0 H$ equals

$$B_0 = \mu_0 N_1 I/l. \tag{13}$$

The amplitude of the magnetizing field B_0 is nearly 0.005 mT. Therefore, the calculated μ values correspond to the low-field permeability of the ferrite. The ferrite bead with two windings is placed in an electrically heated oven

(Fig. 8). The sample embraces the *High-accuracy temperature sensor* (CI-6525), a platinum thermometer suitable for temperatures from –200°C to 200°C. *Capstone* displays the calculated permeability versus the sample temperature.

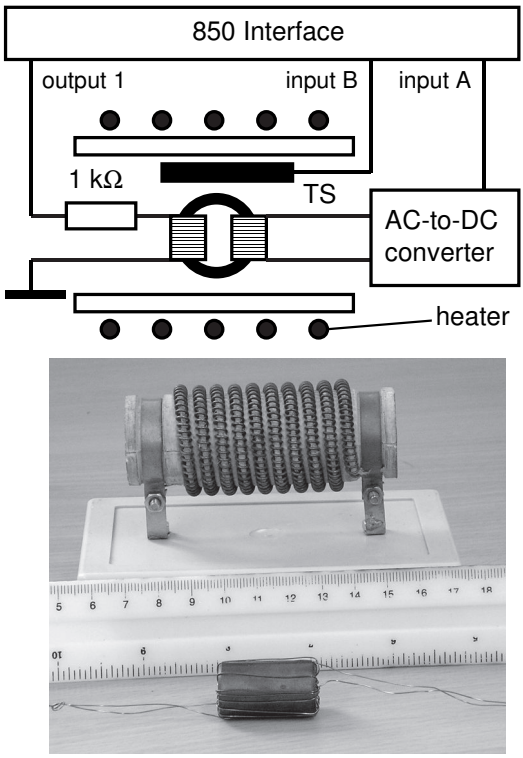

Fig. 8. Diagram of the setup for the measurements above room temperatures, the oven, and the ferrite sample. TS—temperature sensor.

After heating the ferrite above Curie's point T_C, it becomes completely demagnetized. The measurements are performed during the cooling process. To reduce the cooling rate, the heating power is not switched off but step-by-step decreased. After cooling down to room temperatures, the sample with the platinum thermometer is placed into a Dewar flask above the liquid nitrogen level. The data are recorded while the temperature of the sample gradually decreases; for this aim, the Dewar flask is gradually raised. Finally, the sample appears in the liquid, so its temperature becomes equal to 77.35 K (the boiling point of nitrogen at normal pressure). The cooling rate is 2–3 K.min^{-1}, and the entire run lasts about 2 h. All the data are obtained in one run (Fig. 9).

In all the measurement range, up to temperatures close to $0.9T_C$, the permeability increases with temperature. This behavior is typical for ferrites. At room temperatures, the permeability of our sample amounts to about one half the maximum value. It should be remembered that the permeability of ferrites is a

structure-sensitive property depending on purity, heat treatment, deformation, and so on (Cullity and Graham 2009).

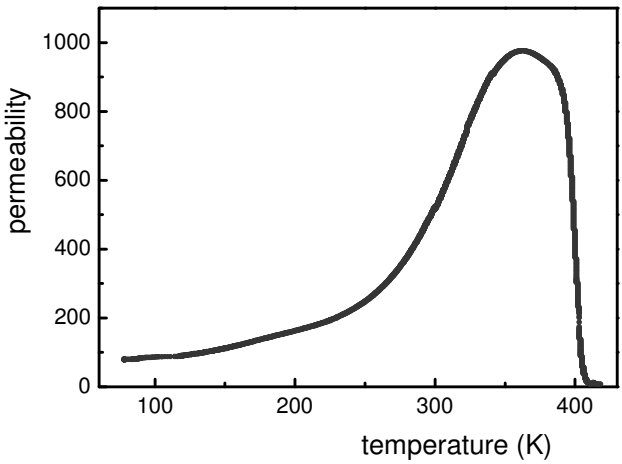

Fig. 9. Low-field permeability of the sample versus temperature.

Hysteresis loops, spontaneous magnetization, and coercivity. The major hysteresis loop provides data on the spontaneous magnetization and coercivity of the sample. The spontaneous magnetization can be taken as the saturation magnetic field B_s in the core. For observing hysteresis loops, we use a common method based on integrating the EMF generated in the secondary winding due to the AC magnetizing current in the primary winding. However, a large current of enhanced frequency is needed for obtaining results with few-turn windings.

In our case, the primary and secondary windings contain 10 turns each, and the frequency of the current is 500 Hz. The large current from the *Output 1* and high sample rate are crucial for the experiment. The *Output 1* is connected to the primary winding through a 10 Ω (10 W) resistor. The magnetizing current is taken as the *Output current*. The *Output voltage* is set to be 10 V, so this current is 1 A (amplitude value). The magnetizing field B_0 is calculated with Eq. (13) and equals B_0 (mT) = 0.35×I (A). The sample rate is 100 kHz.

An integrating RC circuit (50 kΩ, 1 μF) integrates the EMF generated in the secondary winding and provides a voltage V_2, which directly relates to the magnetic field B in the core:

$$B = V_2RC/AN_2. \tag{14}$$

For our sample, B (T) = 45×V (V). Note the different units for B_0 and B.

Capstone displays the hysteresis loops for various temperatures measured by the *Temperature sensor* and displayed by *Digits*. Examples shown (Fig. 10) give good understanding of the temperature dependence of magnetic properties of the sample. *Capstone* calculates the **saturation magnetic field** B_s (that is, the **spontaneous magnetization**) as 0.5*(max[B]–min[B]). The B_s values are shown

by the second *Digits* display and are used to plot the temperature dependence of the spontaneous magnetization. The coercivity of the sample $B_c = \mu_0 H_c$ is determined from the hysteresis loops. Both quantities monotonically decrease with increasing temperature and vanish at Curie's point (Fig. 11).

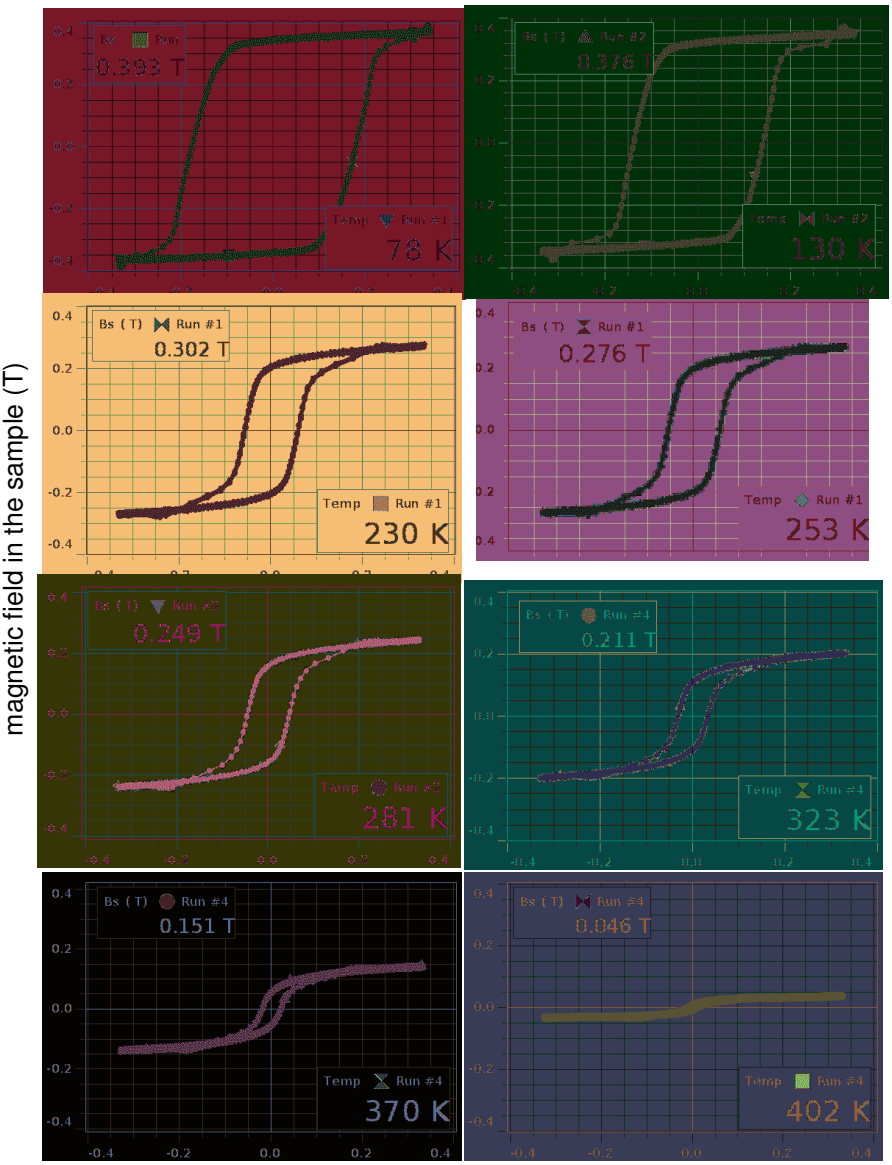

Fig. 10. Examples of hysteresis loops, $B(\mathrm{T})$ versus $B_0(\mathrm{mT})$. All the loops are presented with the same scales, ± 0.4 mT for B_0 and ± 0.4 T for B.

The temperature dependence of the spontaneous magnetization of ferrites significantly differs from that for classical ferromagnets Fe, Co, and Ni (Cullity and Graham 2009). It is possible to perform the above experiments with an older version of the PASCO data-acquisition system, including the *750 Interface* and *DataStudio* software. It is sufficient to increase the number of turns of the windings up to, say, 30 turns. Second, ferrite cores of various dimensions are now commercially available, and it is easy to find a suitable sample. With a small ferrite ring, it would be even easier to achieve constant temperatures over the sample and reduce the time of the measurements.

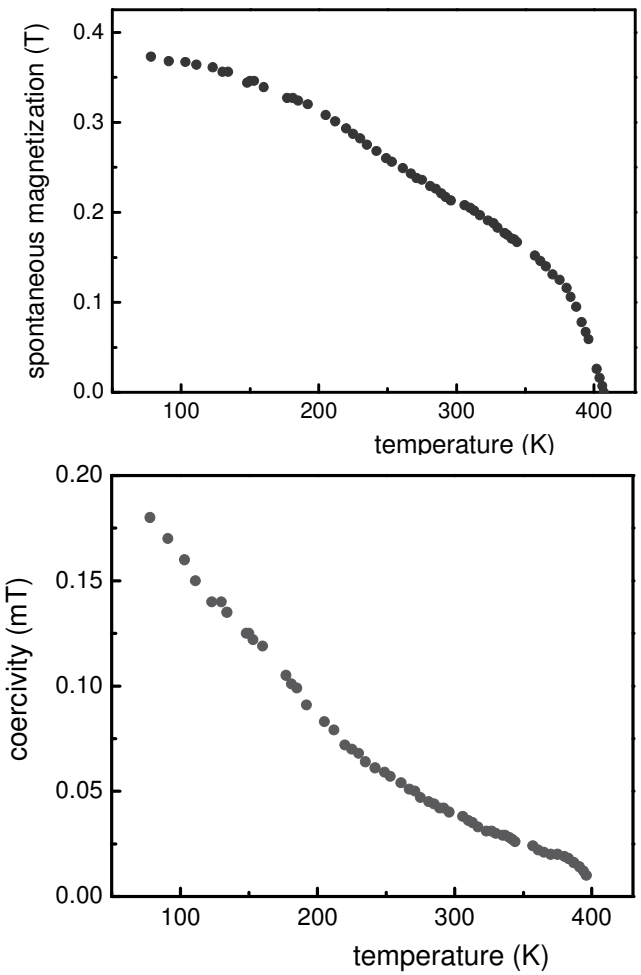

Fig. 11. Spontaneous magnetization and coercivity of the ferrite monotonically decrease with increasing temperature and vanish at Curie's point.

6.8. Magnetic bridge

A differential magnetic circuit (magnetic bridge) is used for observing hysteresis loops of ferromagnets, the superconducting phase transition, and Curie's point of a ferromagnet (Kraftmakher 2010e).

Additional equipment: two *Voltage sensors*, nickel wire, monel wire, AC/DC supply, E-shaped magnetic core, lock-in amplifier, Hall probe, light bulb, platinum resistance thermometer, oscilloscope, coils, resistor, capacitor.

Many physical phenomena are accompanied by changes in the magnetization of the samples and thus in the magnetic fields in their surrounding. One of them is the superconducting-to-normal phase transition. In the superconducting state, the sample completely expels an external magnetic field (**Meissner's effect**), while in the normal state the sample behaves like a usual paramagnet or diamagnet. This phenomenon is commonly used for determining the phase transition point and the temperature dependence of the magnetic susceptibility. Another example is Curie's point of a ferromagnet.

A classical circuit for such measurements is the Hartshorn bridge, a differential transformer consisting of two similar pairs of inductively coupled coils. The primary windings are put in series and fed by an AC source. The secondary windings are connected in opposite, so the output voltage is zero. With a sample in one coil, the output voltage reflects the magnetic susceptibility of the sample; generally, it is a complex quantity. The output voltage can be balanced with a variable mutual inductance and a potentiometer. The circuit is also usable for measuring the effective magnetic susceptibility of nonmagnetic conductors, which depends on the skin effect in the samples. In particular, the resistivity of conductors can be determined with no contacts to them (Kraftmakher 2000b, 2009f).

Another version of the differential transformer employs an E-shaped magnetic core and three coils (Fig. 1a). The coils L_1 and L_2 connected to an AC source form the primary winding and produce opposite magnetic fluxes through the coil L_3, which serves as the secondary winding of the transformer. Without a sample, the output voltage of the transformer is zero. With a sample placed on a side leg of the transformer, the output voltage of the transformer depends on the magnetic susceptibility of the sample.

The magnetic bridge. A differential magnetic circuit is similar to the differential transformer with an E-shaped magnetic core, but employs a Hall probe as a magnetic field sensor (Fig. 1b). Two similar coils magnetize the side legs of the core, and the sensor is positioned on the middle leg. The coils produce magnetic fluxes flowing through the middle leg in opposite directions, so the magnetic flux through the sensor can be reduced to zero. The sensor thus becomes sensitive to changes in the magnetic flux produced by one of the side legs. To

increase the sensitivity, the cross-section of the middle leg is made several times smaller than that of the side legs. Unlike the differential transformer, the circuit operates with magnetic fields of very low frequencies and even DC fields.

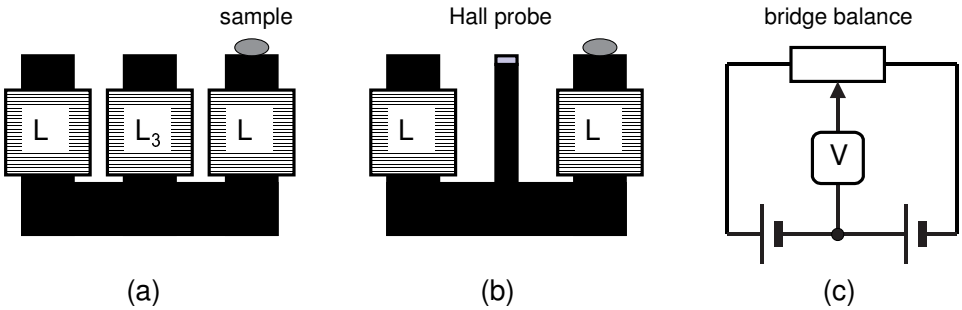

Fig. 1. (a) Differential transformer with three coils; (b) magnetic bridge with a Hall probe; and (c) electrical analog to the magnetic bridge.

Some relations for magnetic circuits resemble those for electrical circuits (Grant and Phillips 1982; Benenson and Raffaele 1986; Parker 1997). The quantity $E_M = NI$, where N is the turn number of a coil, and I is the current through it, is called the **magnetomotive force** and is similar to the electromotive force. The **magnetic flux** Φ is an analog of the electric current. A simple relation for a series magnetic circuit, which is similar to Kirchhoff's loop law, is called **Hopkinson's law**:

$$\Phi = \Sigma E_M / \Sigma R_M \tag{1}$$

The quantity R_M, which is an analog to the electrical resistance, is called the **reluctance** and equals

$$R_M = l/\mu_0 \mu A, \tag{2}$$

where μ_0 is the magnetic constant, μ, l, and A are the relative permeability, length, and cross-sectional area of a part of the circuit.

The above analogy is incomplete because the relative permeability of ferromagnets depends on the magnetic field; however, it is useful for qualitative predictions of the behavior of magnetic circuits. Following this analogy, our magnetic circuit resembles an electrical bridge (Fig. 1c). Generally, an electrical bridge is a circuit, in which two branches (usually in parallel with each other) are "bridged" at some intermediate points along them. A well-known bridge circuit is Wheatstone's bridge developed for measuring electrical resistances. In our case, two batteries represent the magnetomotive forces of the two coils, the reluctance of the magnetic core is considered zero, the potentiometer represents the reluctance of the air gaps, and the voltmeter is an analog to the magnetic sensor on the middle leg. Thus the magnetic circuit is a magnetic bridge.

When the magnetizing coils are connected to an AC supply and a ferromagnetic sample is put between the middle leg and one of the side legs, the

signal from the Hall probe is usable for demonstrating hysteresis loops of the sample. Furthermore, the initial magnetization curve is available if the sample, after being demagnetized in a gradually decreasing AC magnetic field, is subjected to a gradually increasing DC field. When a superconductor sample is placed on one of the side legs, the Hall probe signals that the sample is either in the superconducting or normal state, and the temperature dependence of the magnetic susceptibility of the sample can be recorded. The use of AC magnetic fields highly increases the sensitivity of the bridge because the AC voltage from the Hall probe can be measured with the lock-in detection technique.

The advantages of the magnetic bridge are evident: (i) the temperature of the sensor may differ from that of the sample, which makes experiments more flexible; (ii) the magnetic field applied to the sample can be made much stronger than that to the sensor; (iii) the signal from the sensor can be enhanced by concentrating the magnetic flux; and (iv) magnetic fields of very low frequencies and even DC fields can be used, so the initial magnetization curve of ferro- and ferrimagnets is observable. A Toshiba THS 118 Hall sensor ($1.7\times1.5\times0.6$ mm^3) serves as the probe. With the DC current of 10 mA, the sensitivity of the probe is in the range 1 to 3 V.T^{-1}.

Our magnetic bridge is unsuitable for quantitative measurements. The reason is that the magnetic fluxes in different parts of the bridge cannot be well defined due to unavoidable leakages and very different cross-sectional areas of the circuit parts (the sample, the sensor, and the middle leg). For instance, it is difficult to reliably calculate absolute values of the magnetic field in the samples. Therefore, only those experiments and demonstrations are chosen, for which this point is not crucial.

Hysteresis loops of ferromagnets. The setup for displaying hysteresis loops of a ferromagnet is very simple. An iron rod, 5 mm in diameter, is added to an U-shaped magnetic core (SF-8614) to form the middle leg of the magnetic bridge (Fig. 2). Two 800-turn primary coils (SF-8611) are fed by an AC supply (50 Hz) including a regulated autotransformer (variac) and an isolating step-down transformer, obligatory for the safety reason. The maximum output voltage of the isolating transformer is 35 V (RMS). A 1 Ω resistor is put in series with the coils. The voltage drop across this resistor is measured with the *Voltage sensor*. Current leads of the Hall probe are connected to a 9 V battery through a variable resistor, and the current through the probe is 10 mA. The output voltage of the probe is acquired with another *Voltage sensor*. Using the *Automatic stop* option, each run lasts 0.02 s, one period of the main frequency. The *Sample rate* is 20 kHz, so each hysteresis loop contains 400 data points. Simultaneously, the hysteresis loops can be observed with a common oscilloscope.

The families of hysteresis loops were obtained for wire samples of steel and nickel, 1 mm in diameter. The steel sample was made of a common paperclip. The length of the samples is nearly 30 mm. Before a run, the position of the Hall probe is adjusted to nullify the output voltage. Then a sample is placed to link one of the side legs and the probe. Due to the small diameter of

the samples, the magnetic flux through them is greatly concentrated, and the magnetic field in the samples becomes much stronger than that in the side legs. After each run, a hysteresis loop for definite amplitude of the magnetizing current is displayed (Fig. 3).

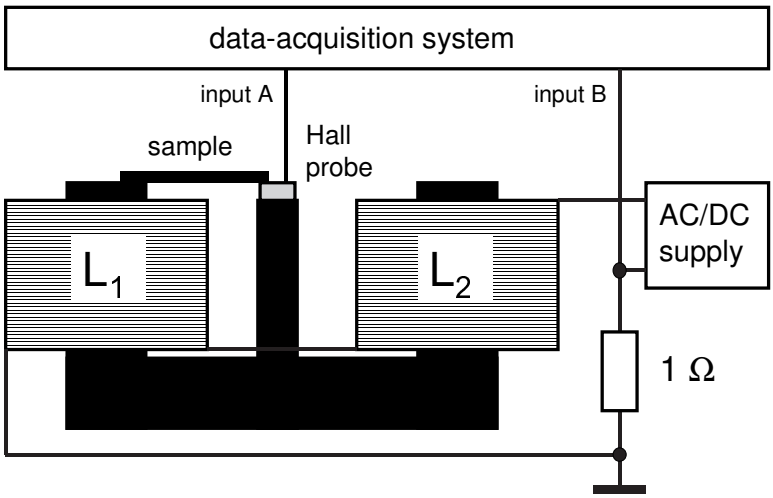

Fig. 2. Setup for displaying hysteresis loops. Details of the AC/DC power supply and the Hall probe circuit are not shown.

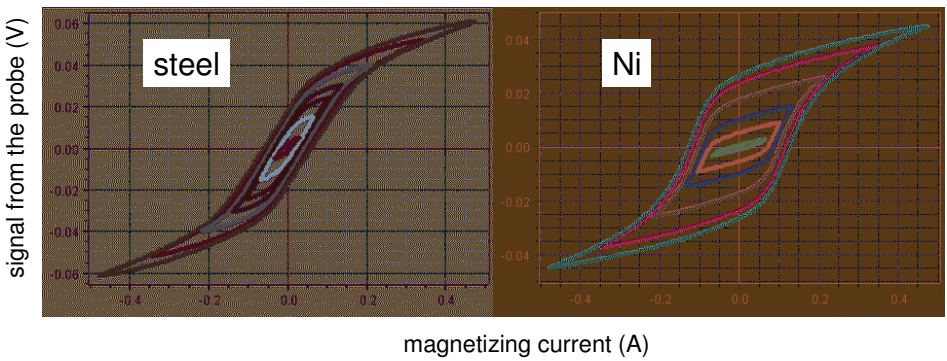

Fig. 3. Families of hysteresis loops for steel and nickel samples.

Initial magnetization, remanence, and coercivity. The hysteresis loops obtained are quite similar to those from measurements with a coil sensing an AC magnetic flux. However, the use of a Hall probe provides an additional option. Since the probe senses DC magnetic fields, it is easy to demonstrate the initial magnetization curve, remanence, and coercivity. For this aim, the magnetizing current provided by a regulated DC power supply is changed manually from

zero to its maximum value and then to zero. Then the direction of the current is changed, and the procedure repeated. The complete hysteresis loop is thus obtainable (Fig. 4).

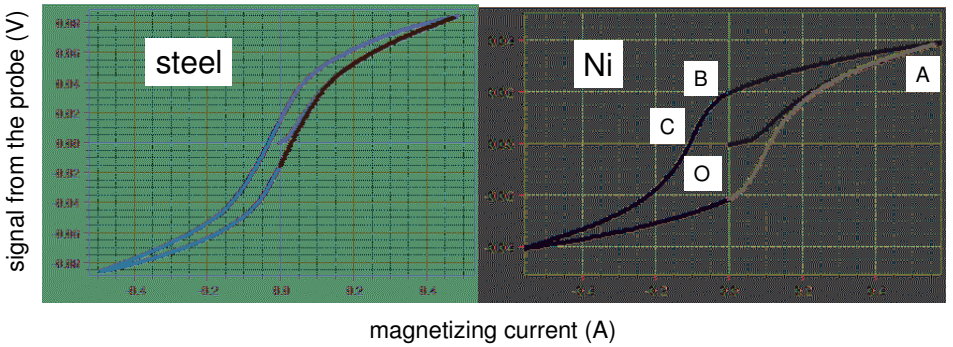

Fig. 4. Hysteresis loops obtained with DC magnetization. The initial curve (OA), remanence (OB), and coercivity (OC) are seen.

The **remanence** is the **residual flux density** in a fully magnetized ferromagnetic material after the external magnetic field is removed. The **coercivity**, or the **coercive field**, is the field intensity necessary to reduce the magnetization of a ferromagnetic material to zero after it was fully magnetized. In these measurements, the *Sample rate* is 100 Hz. Before a run, the magnetic core and sample were demagnetized by the use of the regulated AC supply: the AC current in the magnetizing coil was gradually increased and then decreased to zero.

Phase transition in a superconductor provides a much weaker signal from the Hall probe; therefore, the **lock-in detection technique** is employed (Fig. 5). The magnetizing coils are fed by a function generator (30 Hz). The output of the Hall probe is coupled to the input of a CS-4025 Kenwood oscilloscope, which serves also as an amplifier. An Ithaco 3961 lock-in amplifier measures the amplified voltage. The reference voltage is taken from the function generator. The sample is ten pieces (3 mm in width, 20 mm long) of an Ag-sheathed multifilamentary $Bi_{2-x}Pb_xSr_2Ca_2Cu_3O_{10}$ (BSCCO) tape from the American Superconductor Corporation. The sample is packed together with a flat platinum resistance thermometer (100 Ω at 0^oC) from the Minco Products, Inc. For increasing the thermal inertia, this package is embedded into a piece of plasticine. It is placed in a plastic cup positioned on one of the side legs of the magnetic bridge. The cup is filled with liquid nitrogen. After the nitrogen evaporates, the temperature of the sample starts to increase. A Keithley 177 multimeter measures the resistance of the platinum thermometer. An alternative is to measure the voltage across the thermometer when a definite DC current passes through it. *DataStudio* calculates the temperature of the sample with a common relation:

$T = 30.9 + 225.4X + 16.8X^2$, where X is the ratio of the resistance of the thermometer to the resistance at 0°C. *DataStudio* displays the output voltage of the lock-in amplifier versus the temperature of the sample. The data obtained (Fig. 6) are in agreement with the transition temperature accepted for this superconductor, 110 K (see Experiment 9.9).

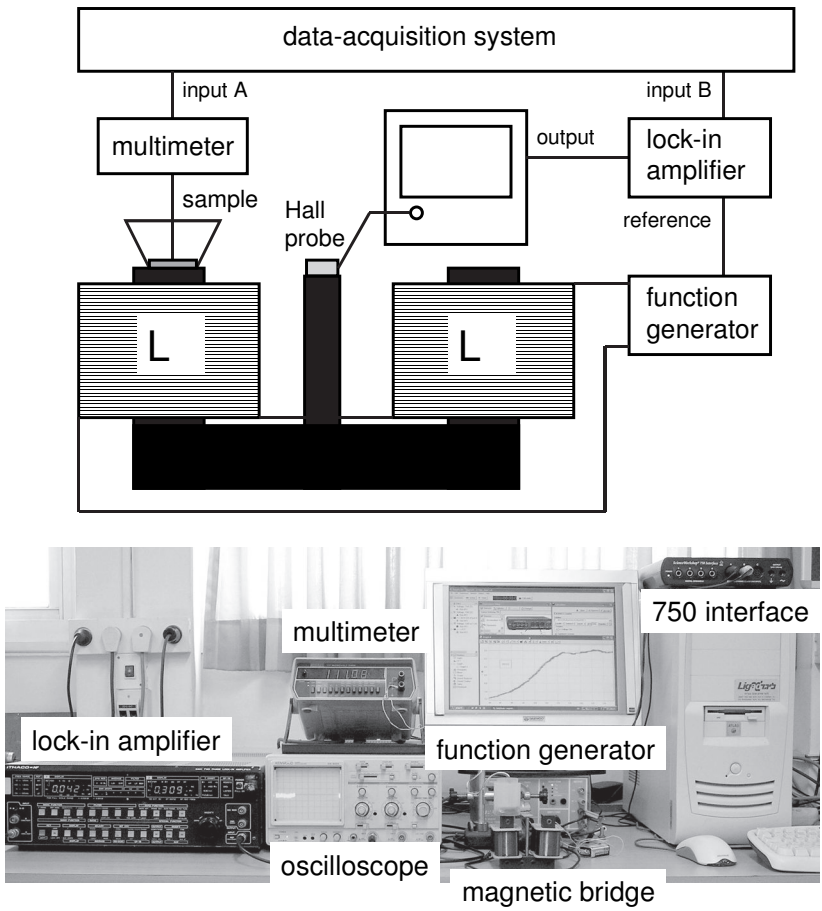

Fig. 5. Setup for observing phase transition in high-temperature superconductors. Details of Hall's probe circuit are not shown.

Curie's point of a nickel-based alloy. The same approach is used for observing Curie's point of a nickel-based alloy from the Goodfellow Company, monel 400 (Ni65/Cu33/Fe2). Earlier, the phase transition in this wire, 1 mm in diameter, was studied by observing the skin effect in the sample (Kraftmakher 1997). Now, eight pieces of the wire, each about 20 mm in length, are packed together with the platinum thermometer. This package embedded into a piece of plasticine is put in a plastic cup placed on one of the side legs of the magnetic

bridge. After cooling the package with liquid nitrogen, the sample temperature starts to increase. When the heating rate becomes insufficient, a 100 W light bulb above the cup provides the necessary heating. In the range 250–320 K, another relation provides better results for the platinum resistance thermometer: $T = 31.3 + 232X + 9.85X^2$. From the data obtained, the phase transition is clearly seen. Curie's point is close to that determined from the skin effect.

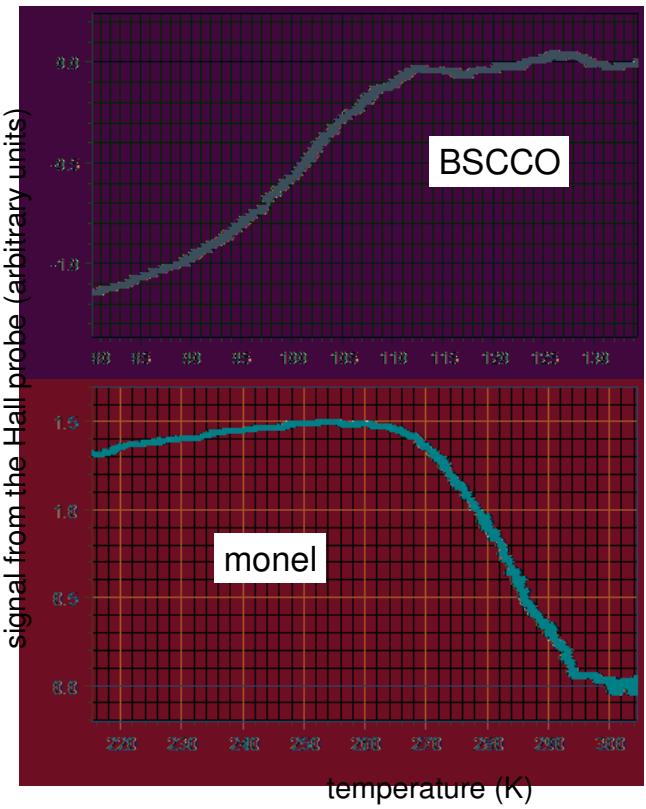

Fig. 6. Signal from Hall's probe versus temperature for the BSCCO and monel samples.

6.9. Eddy currents and skin effect

The experiments include two topics: (i) the effective magnetic susceptibility of a cylindrical conductor in an axial AC magnetic field, and (ii) the contactless measurements of resistivity.

AIP Emilio Segrè Visual Archives
James Clerk Maxwell (1831–1879)

Eddy currents induced in a conductor by an external AC magnetic field have many applications. They produce a torque in induction motors and reveal metallic objects such as weapons or mines. Eddy currents make it possible to levitate a conductor. They are also used for contactless measurements of resistivity. The **effective magnetic susceptibility** of a conductor, $\chi = \chi' + i\chi''$, is very useful in this respect. The susceptibility depends on eddy currents in a sample and has no relation to usual magnetic properties. It depends on the frequency of the AC magnetic field, the resistivity and the shape of the sample. Since a phase shift exists between the electrical field induced by an AC magnetic field and eddy currents in the sample, the effective magnetic susceptibility is a **complex quantity**.

Many demonstrations and laboratory experiments concerning eddy currents were published. Gosselin *et al* (1982) measured the frequency-dependent impedance of a round copper wire. A lock-in amplifier measured the real and the imaginary part of the impedance. A similar experiment is presented in Soloukhin (1975). Wiederick and Gauthier (1983) described a simple method for determining the frequency dependence of the skin depth in a conductor. Juri *et al* (1986) determined the effective magnetic susceptibility of a conducting rod

with a differential transformer. Using a compensation circuit with a lock-in amplifier as the null detector, they measured both parts of the susceptibility versus the frequency of the magnetic field. To fit the experimental data to the theoretical curves, the data were shifted along the X axis by adjusting one parameter, the resistivity of the sample. Wiederick *et al* (1987) presented a simple model of magnetic braking in a metal strip and confirmed it by experimental tests. Hart and Wood (1991) calculated and measured the distribution of eddy currents. Marcuso *et al* (1991a,b) performed an experiment on magnetic drag and compared the data with computer simulations. Saslow (1992) considered the theory of eddy currents in thin conducting sheets. Edgar and Quilty (1993) reported on a mutual inductance apparatus for measuring magnetic susceptibility and resistivity. MacLatchy *et al* (1993) developed a quantitative magnetic braking experiment. Cadwell (1996) presented an analysis of the motion of a conducting plate as it passes through a magnetic field. Hahn *et al* (1998) determined the damping of a magnet oscillating inside a conducting tube. Pellicer-Porres *et al* (2006) measured the interaction force between a solenoid producing an AC magnetic field and eddy currents induced by this field in a conductor. Wagner and Syed (2011) investigated the skin effect in mercury.

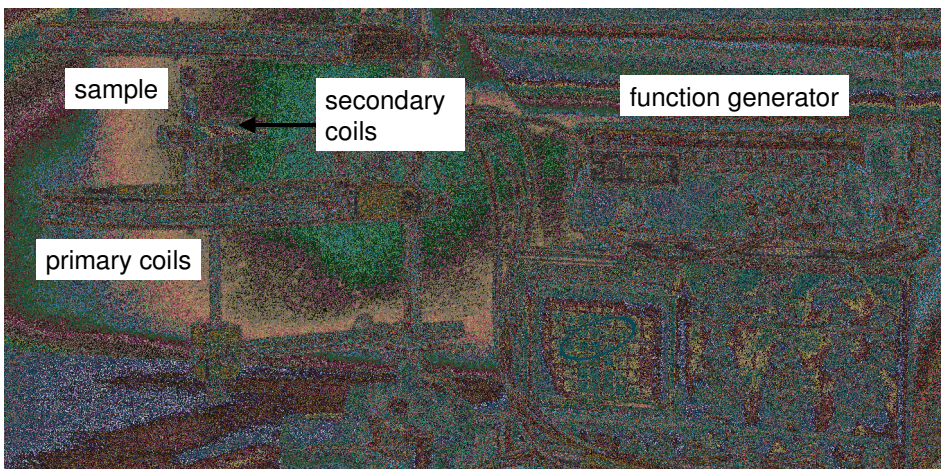

The measurements are also possible without a data-acquisition system.

1. Effective magnetic susceptibility

The effective magnetic susceptibility of a cylindrical conductor in an axial AC magnetic field is determined (Kraftmakher 1991, 2000b).

Additional equipment: *Voltage sensors*, differential transformer, samples, lock-in amplifier, oscilloscope, AC-to-DC converter, samples, coils, resistor.

Predictions of the skin effect theory. In an axial AC magnetic field H, the magnetization M per unit length of a nonmagnetic cylindrical conductor of radius a equals

$$M = \pi a^2 \chi H, \tag{1}$$

where the effective magnetic susceptibility χ of the conductor is

$$\chi = \chi' + i\chi'' = \frac{2J_1(ka)}{kaJ_0(ka)} - 1, \tag{2}$$

and J_0 and J_1 are Bessel functions of the first kind, $k = (1 + i)/\delta$, $\delta = (2\rho/\mu_0\omega)^{1/2}$ is the skin depth for a plane surface, ρ is the resistivity of the conductor, μ_0 is the magnetic constant, and ω is the angular frequency of the magnetic field (Landau and Lifshitz 1984). The susceptibility is a complex quantity depending only on ka, that is, on the a/δ ratio. Our aim is to determine this dependence and to compare it with the theory. It is useful to introduce a new variable, $X = (a/\delta)^2$. From the above definition of the skin depth,

$$X = 4\pi^2 \times 10^{-7} a^2 f/\rho = Aa^2 f/\rho, \qquad \text{and} \qquad \rho = Aa^2 f/X, \tag{3}$$

where $A = 3.95 \times 10^{-6}$. Using numerical values of the Bessel functions, Chambers and Park (1961) tabulated both parts of the susceptibility versus X. The authors expressed the susceptibility through Bessel functions J_2 and J_0, but their relation is equivalent to Eq. (2). In the range $1 < X < 10$, the absolute values of χ' and χ'' can be approximated by polynomials

$$\chi' = -0.088 + 0.15 \times X + 0.0157 \times X^2 - 0.00737 \times X^3 + 7.76 \times 10^{-4} \times X^4 - 2.68 \times 10^{-5} \times X^5, \tag{4a}$$

$$\chi'' = -0.048 + 0.378 \times X - 0.122 \times X^2 + 0.018 \times X^3 - 1.28 \times 10^{-3} \times X^4 + 3.54 \times 10^{-5} \times X^5. \tag{4b}$$

Chambers and Park (1961) measured the effective magnetic susceptibility with the Hartshorn bridge (Fig. 1). An oscillator feeds the primary windings of two mutual inductance coils. The secondary windings are connected in opposition. Without a sample, the variable mutual inductance M is adjusted to balance the voltage induced in the secondary winding. The output voltage thus becomes zero. After a conducting sample is put inside one of the coils, an output

voltage appears due to eddy currents in the sample. Because of the complex nature of the effective magnetic susceptibility of the sample, the variable mutual inductance M and a potentiometer R are to be adjusted for balancing the bridge. The two parts of the effective magnetic susceptibility, χ' and χ'', are proportional to $\omega\Delta M$ and ΔR, respectively.

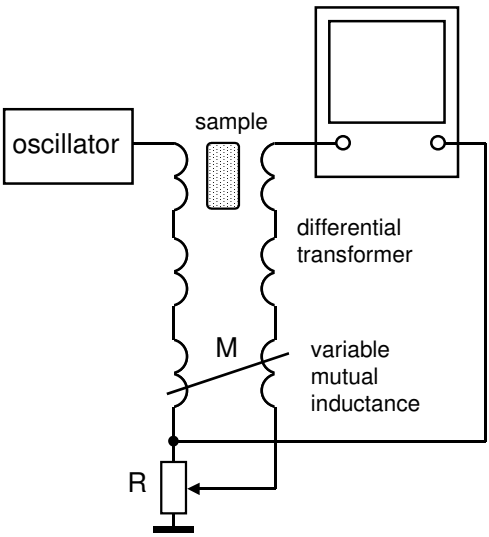

Fig. 1. Hartshorn bridge for determining the effective magnetic susceptibility.

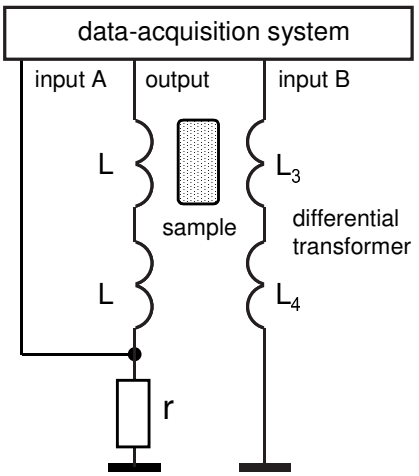

Fig. 2. Setup for determining two parts of magnetic susceptibility.

The effective magnetic susceptibility of a sample can be determined with a differential transformer and a lock-in amplifier. Without a sample, the output voltage of the transformer is zero. The phase of the output voltage, which appears after a conducting sample is put inside one coil, depends on the phase angle of the effective magnetic susceptibility of the sample. With a dual-channel lock-in amplifier, both parts of the susceptibility are available. The phase of a reference voltage for the amplifier must coincide with that of the current passing through the primary windings of the transformer.

Setup and measurements. The Hartshorn bridge and a lock-in amplifier are the best tools for determining the effective magnetic susceptibility. An alternative approach is described below. The Helmholtz coils L_1 and L_2 form the primary windings of a differential transformer (Fig. 2) and produce a homogeneous magnetic field. They are 21 cm in diameter, each containing 200 turns (EM-6711). The *Signal generator* feeds the coils. A resistor $r = 10\ \Omega$ put in series with the Helmholtz coils provides a voltage U_x for the X input of *Scope*, which is proportional to the current passing through the coils, that is, to the AC

magnetic field. Two secondary coils L_3 and L_4 are connected in opposition, so that without a sample the output voltage of the transformer is zero. The secondary coils, each containing 2500 turns, are 2 cm in diameter and 2 cm long. The necessary number of turns depends on the magnetic field and on the radius of the samples. Too many turns are undesirable because of the inherent capacitance of the coils. In our case, a copper sample is 1 cm in diameter and 10 cm long. To obtain a stronger signal, it is better to use thick samples, up to 2 cm in diameter.

The output voltage of the differential transformer is fed to the Y input of the *Scope*. The secondary coils are fixed on a common base, whose position between the Helmholtz coils can be adjusted. Since the magnetic field is somewhat inhomogeneous, such an adjustment serves to finely balance the transformer in the absence of the sample. An additional coil connected in series with the secondary coils (not shown in Fig. 2) and properly placed near the Helmholtz coils provides another possibility for such balancing. A small quadrature component in the output voltage also may appear. This component can be balanced by shunting one of the secondary coils by a variable capacitor.

With a conducting sample inside one of the secondary coils, an output voltage appears due to eddy currents in the sample. Its phase angle α relative to the AC magnetic field is complementary to the phase angle of the magnetic susceptibility φ, which equals $\arctan|\chi''/\chi'|$. It is obtainable from the shape of the Lissajous pattern. The features of the measuring circuit can be explained with a vector diagram (Fig. 3).

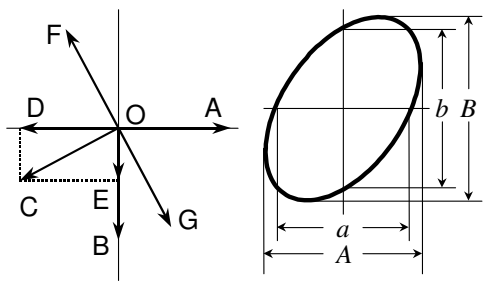

Fig. 3. Vector diagram of the circuit and determination of phase shifts from the Lissajous figure.

The vector **OA** represents the AC current in the primary winding and thus the produced magnetic field. The vector **OB** is the EMF generated in the sample. The vector **OC** shows the eddy currents in the sample and its magnetization. It contains components **OD** and **OE**. The first is opposite to the external magnetic field and relates to χ'. The second relates to χ''. Its phase coincides with that of **OB**, which means that the Joule heating of the sample is due to χ''. The AC magnetization of the sample causes an additional EMF in the corresponding secondary coil (the vector **OF** is perpendicular to **OC**). Since the main EMF is compensated, just this voltage is fed to the Y-input of the *Scope*. With opposite

polarity of the output terminals, the output voltage is represented by the vector **OG** = −**OF**. From the Lissajous pattern, the phase shift between the voltages applied to the oscilloscope inputs obeys the relation

$$\sin\alpha = \pm a/A = \pm b/B. \tag{5}$$

The output voltage of the transformer U_y is proportional to the amplitude and frequency of the current feeding the primary windings. The parts of the effective magnetic susceptibility, in arbitrary units, are thus given by

$$\chi' = (U_y/fU_x)\sin\alpha, \qquad \chi'' = (U_y/fU_x)\cos\alpha, \tag{6}$$

where U_y, U_x, and $\sin\alpha$ are available from the Lissajous pattern.

The resistivity of copper at room temperature, 1.7×10^{-8} Ω.m, is used for calculating the quantity $X = Aa^2f/\rho$. To evaluate absolute values of χ' and χ'', the experimental data are fitted to the theoretical curves at the point of intersection of the two curves. According to Chambers and Park (1961), the theoretical values at the intersection point are $\chi' = \chi'' = 0.377$. An appropriate scaling factor is determined from this fit and then applied to Eqs. (6). Then the experimental data can be superposed on the theoretical curves given by Eqs. (4a) and (4b). The results are in good agreement (Fig. 4).

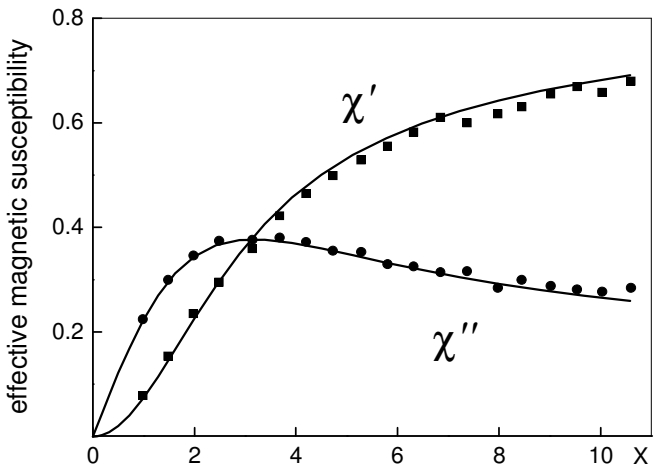

Fig. 4. Two parts of effective magnetic susceptibility versus $X = (a/\delta)^2$: ■ ● experimental data, ——— theory.

Automated experiment. Determinations of the effective magnetic susceptibility of cylindrical samples can be fully automated (Kraftmakher 2009f). Theoretical dependence of χ' and χ'' on X is available from Eq. (2) using *MATLAB* software. The variable X can be presented as a function of the parameter $z = |\chi'/\chi''|$. For $1<X<12$, the necessary relation can be approximated as

$$X = -0.02716 + 3.11332z - 0.14683z^2 + 0.1769z^3. \tag{7}$$

Experimentally determined z values are sufficient for calculating both parts of the effective magnetic susceptibility of the sample. The only parameter to be known beforehand is the radius of the sample. A 500-turn coil L, 21 cm in diameter (EM-6723), forms the primary winding of a differential transformer (Fig. 5). Two secondary coils L_1 and L_2 are connected in opposition, so without a sample the output voltage of the transformer is zero. The 2500 turn secondary coils are 2 cm in diameter and 2 cm long. They are fixed on a common base, whose position inside the primary coil can be adjusted to finely balance the transformer in the absence of a sample. An oscilloscope controls the balance.

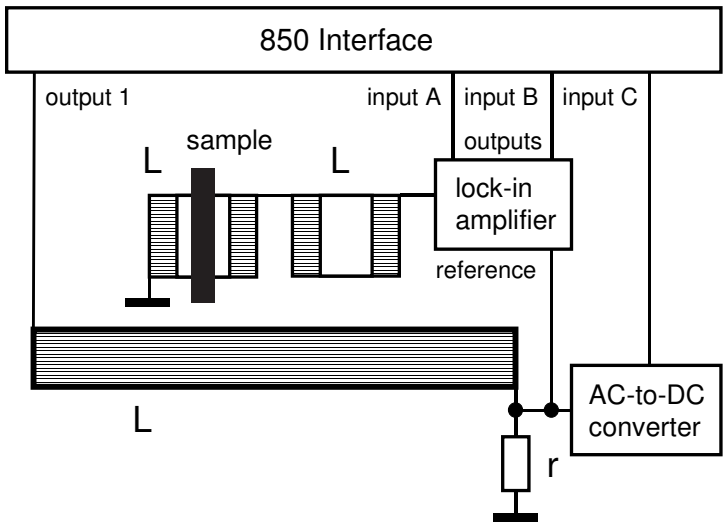

Fig. 5. Schematic of the setup. The secondary coils are shown above the primary coil.

The output voltage of the differential transformer is measured with a dual-channel lock-in amplifier. The reference voltage is the voltage across the resistor $r = 10\ \Omega$. The time constant of the lock-in amplifier is set to be 0.3 s. When a sample is put inside one of the secondary coils, the two DC output voltages of the lock-in amplifier are proportional to χ' and χ'' and to the amplitude and frequency of the current in the primary coil. Two *Voltage sensors* acquire these DC voltages. The demonstration is carried out while sweeping the frequency of the magnetic field. Due to the self-inductance of the primary coil, the current through it depends on the frequency. To take this dependence into account, the voltage on the 10 Ω resistor is measured with a Keithley 177 multimeter, which serves as an AC-to-DC converter. The third *Voltage sensor* acquires the DC output voltage of the converter. For calculating values proportional to χ' and χ'', *DataStudio* divides the output voltages of the lock-in amplifier by the frequency and the voltage measured by the third *Voltage sensor*. The dual-channel lock-in amplifier is needed for determining z values in one run.

The sample is a copper cylinder, 0.96 cm in diameter and 10 cm long. During the run, *DataStudio* displays values proportional to χ' and χ'' and calculates $z = |\chi'/\chi''|$, from which X and ρ are evaluated with Eqs. (2) and (3). The resistivity is displayed versus frequency of the magnetic field (Fig. 6). Ideally, the result should be frequency independent. For frequencies above 450 Hz, $\rho = (1.66\pm0.02)\times10^{-8}\ \Omega.m^{-1}$, close to handbook data. Lower frequencies are unsuitable because the signals to be measured become too small. Similar measurements are performed with an aluminum-alloy rod. The composition of the sample and its resistivity are unknown, so the only criterion of the correctness of the measurement is that the result is independent of the frequency. Above 700 Hz, $\rho = (3.3\pm0.1)\times10^{-8}\ \Omega.m^{-1}$. This value falls into the resistivity range of widely used aluminum alloys (Lide 2008).

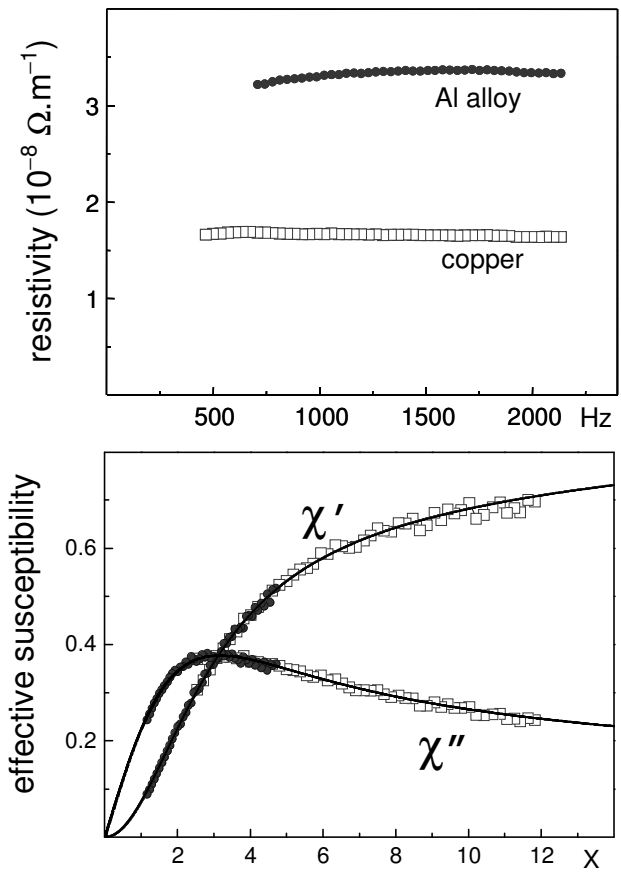

Fig. 6. Top: resistivity versus frequency of the magnetic field, copper (□) and aluminum alloy (●) samples. Bottom: real and imaginary parts of the effective magnetic susceptibility versus $X = (a/\delta)^2$, ——— theoretical curves.

2. Contactless measurement of resistivity

The contactless measurements of resistivity are based on determinations of the phase angle of the effective magnetic susceptibility of a sample in an axial AC magnetic field (Kraftmakher 2000b).

Additional equipment: *Voltage sensors*, differential transformer, cylindrical samples, variable resistor, capacitor, coils, oscilloscope.

In many cases, contactless measurements of resistivity are preferable. With samples in sealed ampoules, the interaction between them and the environment is completely avoided. An example of such measurements is the quality control of metal samples through their low-temperature resistivity. At liquid helium temperatures, scattering of conduction electrons by impurities and physical imperfections of the crystal structure constitutes the main contribution to the resistivity of metals. The **residual resistance ratio** (RRR), the ratio of the resistivities at room and liquid helium temperatures, is a criterion of chemical purity and physical perfection of a metal. For pure metals, this ratio may amount to 10^4–10^5 and even higher. At very low temperatures, contactless measurements on bulk samples are preferable because their diameter can be made larger than the free path of electrons, and correct values of the resistivity are available. Otherwise, one has to perform contact measurements on wire samples of various diameters and then extrapolate the data to an infinite diameter. The resistivity of a cylindrical sample is given by Eq. (3):

$$\rho = 3.95\times10^{-6} a^2 f/X. \tag{8}$$

The simplest way to determine the resistivity is to express X through the phase angle of the effective magnetic susceptibility that equals $\varphi = \arctan|\chi''/\chi'|$. We will use a complementary phase angle $\alpha = \arctan|\chi'/\chi''|$. This angle is determined directly from the Lissajous pattern. The relation between X and $z = \tan\alpha$ can be approximated by a polynomial based on numerical values of χ' and χ''. For $0.1 < z < 2.5$, a sufficient accuracy is achievable with the relation

$$X = -0.01 + 3.06z - 0.105z^2 + 0.167z^3. \tag{9}$$

The measurements are thus reduced to the determination of the phase angle α. To evaluate the resistivity, one measures z and then calculates X from Eq. (9). Then the resistivity is available from Eq. (8). A compensation circuit (Fig. 7) enhances the accuracy of the measurements. The same differential transformer is employed as before, but now a circuit including a potentiometer r, a decade resistance box R, and a capacitor C serves to balance the output voltage. The voltage across the capacitor C is added to the output voltage of the differential transformer, and *Scope* serves as the null detector. The RC circuit provides the necessary phase angle of the compensation voltage, while its amplitude is adjusted by the potentiometer.

To simplify the experiment, only the phase angle α is measured, which is sufficient to evaluate the resistivity of the sample. The phase shift introduced by the RC circuit equals $\arctan(\omega RC)$. Hence, $z = \omega RC$. The resistance of the potentiometer r is much smaller than R, and its contribution is negligible. Only one calibrated variable resistor R is thus necessary, and the potentiometer needs no calibration.

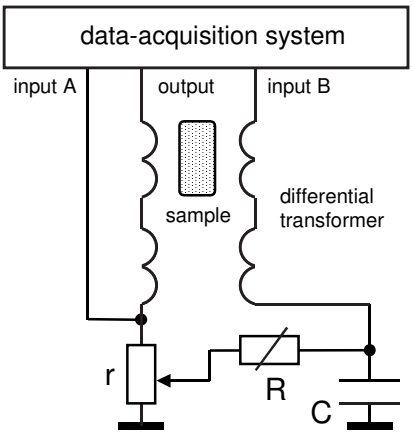

Fig. 7. Compensation circuit for measuring resistivity. R is decade resistance box, $C = 40$ nF.

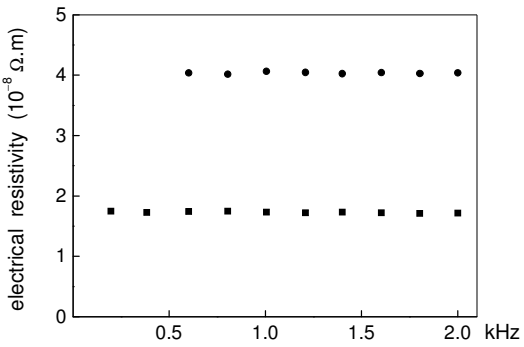

Fig. 8. Resistivity versus magnetic field frequency: ■ copper, ● aluminum alloy.

Contactless measurements are most accurate in a definite frequency range depending upon the radius and resistivity of the sample. Very low frequencies lead to a weak signal, whereas at too high frequencies the phase angle α is close to 90°. In both cases, the error in the resistivity may become unacceptable. Two samples are used, the same copper rod as before, and a cylindrical aluminum-alloy rod. The results are presented versus the frequency of the magnetic field. Using the compensation circuit, the scatter of the data is about 1% (Fig. 8).

The resistivity of the copper sample at room temperature is found to be 1.73×10^{-8} Ω.m. The resistivity of the aluminum alloy is 4.04×10^{-8} Ω.m. The independence of the results on the frequency of the magnetic field confirms the validity of the method. The measurements are performed also at liquid nitrogen temperature. A Dewar flask filled with liquid nitrogen is positioned between the Helmholtz coils. The secondary coils are immersed in the liquid. The frequency range is 0.1–1 kHz. The students can also observe a signal due to a high-temperature superconductor. In this case, the phase angle of the output voltage of the differential transformer cannot be distinguished from 90°, which means a zero resistivity.

Automated measurements of the resistivity are also possible (Kraftmakher 2009f). A 200 turn coil L_1, 21 cm in diameter (EM-6711), forms the primary winding of a differential transformer and produces an AC magnetic field (Fig. 9). An 800-turn coil L_2 (SF-8611) and a variable resistor R (20 Ω) are connected in series with the coil L_1. The *Signal generator* drives the circuit. Coil L_2 and the 1600-turn coil L_3 (SF-8612) form a mutual inductance. The two secondary coils of the differential transformer, L_4 and L_5 with 2500 turns each, are 2 cm in diameter and 2 cm long. They are connected in opposition, and without a sample the output voltage of the transformer is zero.

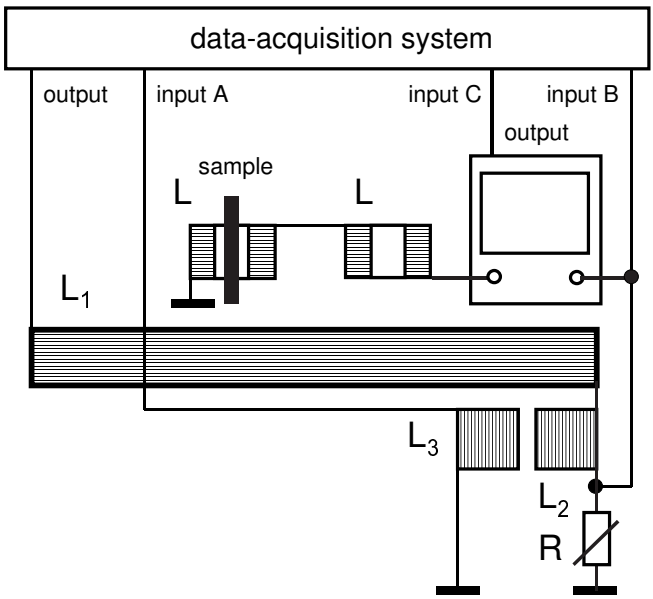

Fig. 9. Schematic of the setup. The secondary coils are shown above the primary coil.

When a cylindrical sample is put inside one of the secondary coils, an output voltage appears, whose phase with respect to the phase of the current through the primary coil of the transformer is defined by the phase angle of the effective magnetic susceptibility of the sample. Coils L_4 and L_5 are fixed on a common base, whose position inside the primary coil can be adjusted to accurately adjust the output voltage to zero when no sample is present. The samples used are cylindrical rods of copper and an aluminum-based alloy. The rods are nearly 1 cm in diameter and 10 cm long. Thicker samples are needed to increase the output voltage of the differential transformer.

The output of the differential transformer is connected to the Y input of a Kenwood CS-4025 oscilloscope. The voltage across resistor R is connected to the X input. The oscilloscope thus shows the phase relation between the current in the primary coil and the output voltage of the differential transformer due to

eddy currents in the sample. The oscilloscope is also used as an amplifier of a gain up to 100. The voltage at its Y input is amplified and then connected to input C of the *Interface*. The coupled coils L_2 and L_3 provide an additional voltage shifted by 90^o to the voltage across resistor R. With the *Voltage sensors*, the *Interface* acquires three voltages: the voltage generated in coil L_3 (input A), the voltage across resistor R (input B), and the amplified output voltage of the differential transformer (input C). Resistor R is adjusted to obtain, for a frequency used, a voltage of amplitude close to that generated by coil L_3; the two voltages are shifted by 90^o. Inputs A and B are set at *High sensitivity*, which restricts the acquired values by 0.1 V. As a result, the sinusoidal waveforms at inputs A and B are converted into nearly square waveforms (Fig. 10), which are used in the calculations. When a sine waveform signal is multiplied by a square waveform of fixed amplitude, the time-average of this product is proportional to the amplitude of the sine waveform signal and to the cosine of the phase shift between the two waveforms; this principle is used in lock-in detectors (see Experiment 4.12).

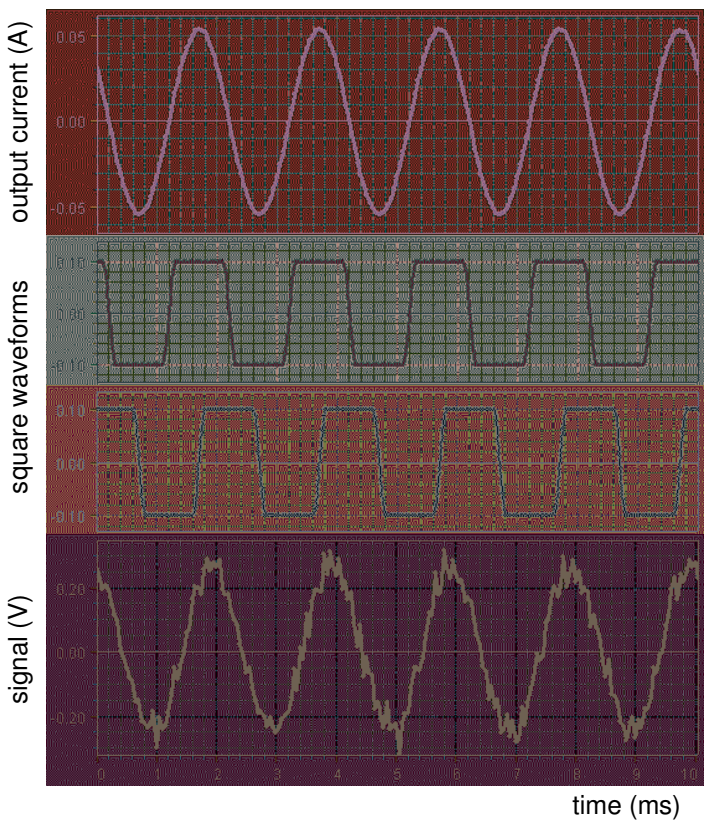

Fig. 10. Output current; two square waveforms shifted by 90^o; and amplified output signal from the differential transformer.

During a run, *DataStudio* acquires three AC voltages; according to the inputs, we call them *A*, *B*, and *C*. For processing the data, the *Calculate* tool computes the following quantities:

- *Y*1 = *A***C*, which after averaging becomes proportional to sinα, where α is an angle complementary to the angle of the effective magnetic susceptibility;
- *Y*2 = *B***C*, which after averaging becomes proportional to cosα;
- *Y*3, averaged values of *Y*1, by the *Calculate*/*Statistical*/*Avg* tool;
- *Y*4, the same for *Y*2;
- *z* = *Y*3/*Y*4;
- the resistivity of the sample, which equals

$$\rho(10^{-8}\ \Omega.\text{m}) = 395*a^2 f/(-0.01+3.06*z-0.105*z\text{^}2+0.167*z\text{^}3), \quad (10)$$

where *a* is the radius of the sample (m), and *f* is the frequency (Hz).

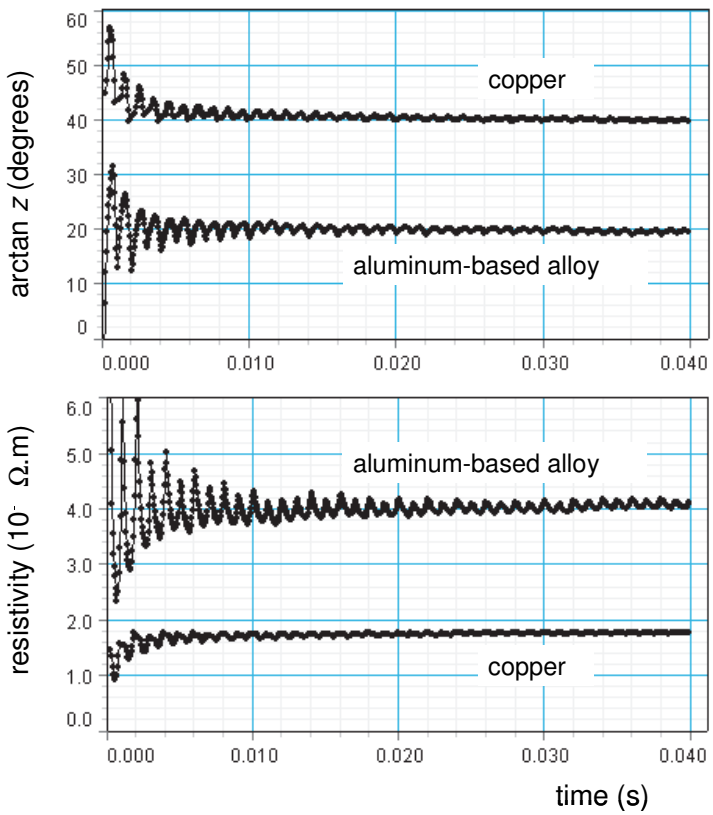

Fig. 11. Calculation process: angle complementary to the phase angle of effective magnetic susceptibility and resistivities at room temperature.

At room temperature, the frequency of the magnetic field is 500 Hz. The *Sample rate* is 20 kHz, and the *Automatic stop* is set at 0.04 s (Fig. 11). The final results of the averaging are displayed in digital form (Fig. 12).

For measurements at liquid nitrogen temperature, a Dewar flask filled with liquid nitrogen is placed inside the primary coil, and the secondary coils are immersed in the liquid. The frequency of the magnetic field is 200 Hz. The *Sample rate* is 10 kHz, and the *Automatic stop* is set at 0.08 s. The resistivity of pure copper is 1.70×10^{-8} Ω.m at 297 K and 0.19×10^{-8} Ω.m at 77 K (White and Minges 1997). The values obtained are somewhat higher, probably due to the contributions of impurities and physical imperfections in the sample. These contributions are weakly dependent on temperature and should be added to the resistivity of a perfect sample. The resistivity of the Al-based alloy significantly exceeds that of pure aluminum and weakly depends on temperature.

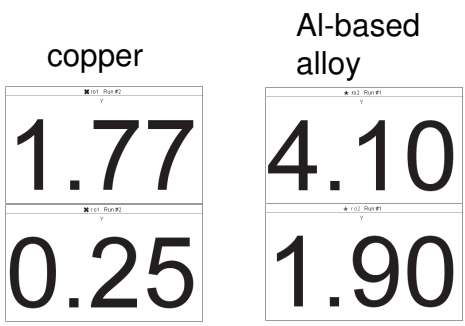

Fig. 12. Resistivity (in 10^{-8} Ω.m) of copper and Al-based alloy at room (top) and liquid nitrogen (bottom) temperatures displayed by *Digits*.

6.10. Liquid crystals

Two characteristics of a liquid crystal shutter are determined: (i) the optical transmission versus applied voltage, and (ii) the time delay of the shutter operations (Kraftmakher 2012d).

Additional equipment: liquid crystal glasses, function generator, oscilloscope, two DC supplies, light-emitting diode, photodiode.

Liquid crystal phase and LC shutters. Many organic substances possess an intermediate state of matter between the solid and liquid phases; this state is called the **liquid crystal phase** (Ball 1980; Ondris-Crawford *et al* 1992, 1995; Pavlin *et al* 2013). Liquid crystals (LCs) find many applications. LC optical shutters are elements of displays of electronic devices, computers, and television sets (Hayn 1981; Bradshaw 1983; Dresser 1984; Becchetti and Dockrill 1984; Crawford and Ondris-Crawford 1994; Collings 1995). For these applications, the main features of the shutters are their electrically controllable transmittance and a relatively fast response to applied voltage. Each element of an LC display contains its own shutter providing the instant light intensity according to the picture to be reproduced. Liquid crystals were used in laboratory experiments and classroom demonstrations described by Nicastro (1983, 1984); Carr and McClymer (1991); Mauron *et al* (1994); Ciferno *et al* (1995).

Most electrically controllable LC shutters employ a **twisted nematic** LC. This LC consists of thread-like molecules arranged nearly parallel to one another. The molecules are electric dipoles and respond to external electric fields. They are also optically active. When a piece of glass has scratches on its surface, molecules of the LC placed in contact with this surface align themselves along the scratches. If a drop of the LC is sandwiched between two such pieces of glass, the array of molecules can be twisted when one glass plate is rotated with respect to the other. In LC shutters, this rotation equals to 90^{o}. The twisted LC rotates the plane of polarization of incident linearly polarized light. For each molecular layer, the rotation is very small, of the order of 0.1^{o}. Thin transparent electrically conductive indium-tin oxide coatings are deposited onto the inner surfaces of the two glasses, and an electric voltage can be applied to the electrodes. The distance between the electrodes is of the order of 10^{-5} m, so it is easy to create in LCs electric fields of the order of 10^{6} V.m^{-1}. The sandwich is placed between two crossed polaroids (Fig. 1). With no voltage applied, the twist structure rotates the polarization plane by 90^{o}, so that the device is transparent. When a DC voltage is applied to the electrodes, the LC molecules tend to align parallel to the electric field. The electric field thus destroys the twist array and the ability of the LC to rotate the polarization plane, so the device becomes opaque.

For the experiments, we employ LC shutter glasses commonly used for obtaining three-dimensional (3-D) images. The **stereoscopic effect** is based on

the fact that when one views a 3-D scene, the visual perception by the left eye somewhat differs from that by the right eye. The two images combined in the brain give the 3-D perception. **Stereoscopy** is a technique for creating or enhancing the illusion of depth by presenting two offset images separately to the left and the right eye of the viewer (Greenslade and Green 1973; Gabrielson 1996; Dukes and Bruton 2008; Schmitzer *et al* 2009; Palmer 2010).

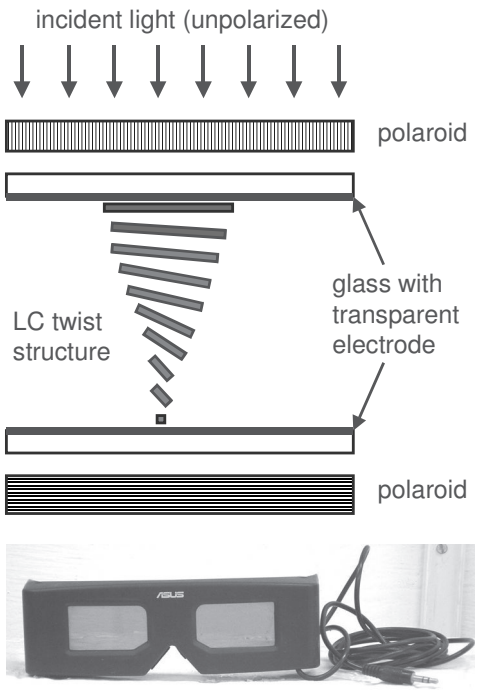

Fig 1. Schematic of a liquid crystal shutter, and ASUS shutter glasses.

One of the methods to attain the stereoscopic effect employs two superimposed offset images, which are differently colored or polarized. Eyeglasses including appropriate color filters or polarizers separate the images intended for the left and right eyes of the viewer. Due to the inertia of human vision, the two images can be viewed in turn. Just this feature is used in the LC shutter glasses technology. Clearly, the switching time of the glasses should be sufficiently short. The transmittance of an LC shutter gradually depends on the controlling voltage, so the brightness of each pixel of an LC display can be varied.

We use ASUS shutter glasses designed for obtaining 3-D illusions in computer games and wired to a personal computer. The computer displays in turn frames intended for the right and left eye. The voltage controlling the glasses is supplied by the computer and is synchronized with the frame rate of the computer's screen. The shutter opens one glass and closes the other, exactly

in the same sequence. High frame rates are required to provide a qualitative 3-D illusion. The LC shutter technology is usually rated by the time it takes to change the optical transmission of the shutter. The synchronizing signal from the computer can be sent to the glasses using radio waves or infrared radiation. The wired glasses used here are more convenient because it is easy to apply to them the controlling voltage. For our experiments, there is no need to break up the glasses, so they remain ready for their usual function.

Optical transmission versus controlling voltage. With a data-acquisition system or a common oscilloscope, the transmittance characteristics of an LC shutter can be displayed in minutes. In addition, it becomes possible to determine the characteristics for various frequencies of the controlling voltage. For the demonstration, one glass of the shutter is positioned between a blue light-emitting diode (LED) and a silicon photodiode (Fig. 2).

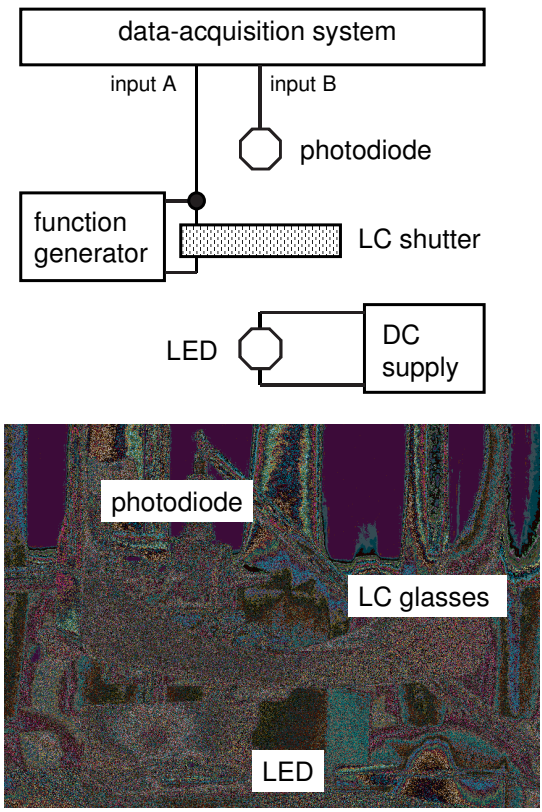

Fig. 2. The signal from the photodiode is measured versus controlling voltage.

Incandescent light bulbs are unsuitable for the measurements because the polaroids of the shutter do not properly operate in the infrared range. The LED is

fed by a DC power supply. A sine wave voltage from the *Digital function generator-amplifier* (PI-9587C) controls the shutter. The generator provides output voltages of amplitudes up to 10 V. The photodiode is connected, in series with a 10 kΩ load resistor, to another DC source. A data-acquisition system or an oscilloscope displays the voltage across the load resistor, which is proportional to the transmittance of the shutter, versus the controlling voltage. The lowest frequency is 0.1 Hz (Fig. 3). With the *Automatic stop* option, each run lasts one period of the controlling voltage. The *Sample rate* is set to obtain a sufficient number of data points during each run. As expected, the operation of the shutter does not depend on the polarity of the controlling voltage. The transmittance of the shutter starts to decrease when the controlling voltage reaches a definite threshold. Above the threshold, the transmittance rapidly decreases. The recovery of the transmittance when decreasing the controlling voltage is much slower. The hysteresis in the characteristic is seen even at low frequencies of the voltage. At 0.1 Hz, the hysteresis becomes insignificant, so this graph shows nearly equilibrium data. The voltage threshold of the operation increases with the frequency of the controlling voltage. The same results are seen with a common oscilloscope.

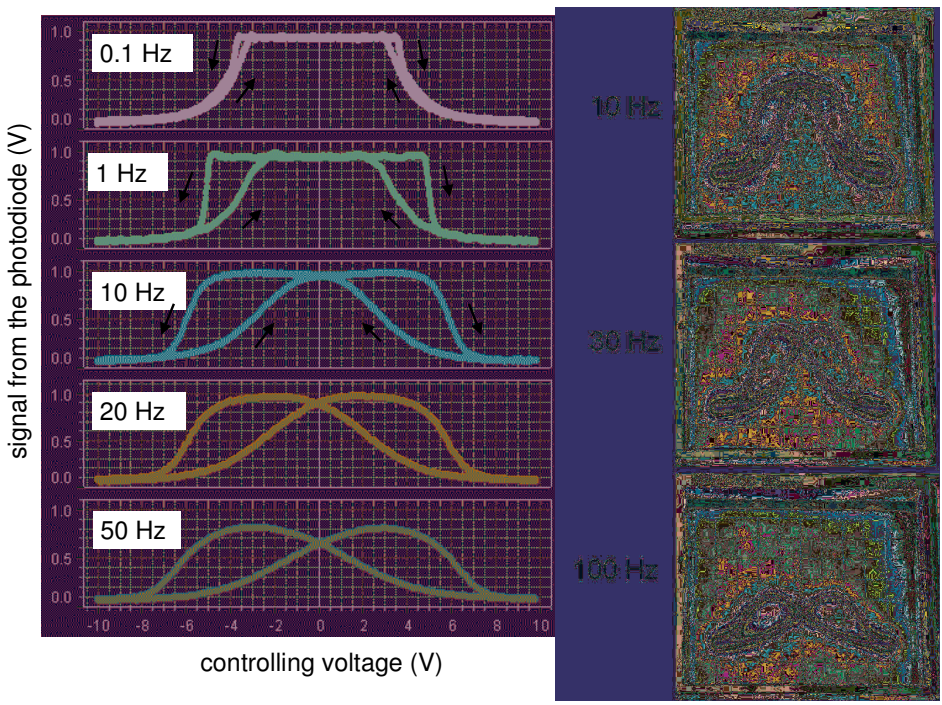

Fig. 3. Transmission versus controlling voltage displayed by *DataStudio* (left) and by oscilloscope (right).

Delay times. The delay in the shutter operations when increasing or decreasing the controlling voltage can be determined directly. To demonstrate this delay, positive square wave voltages of amplitudes up to 10 V from the function generator are applied to the shutter. The frequency of the voltages is 100 Hz, so the shutter should be in turn opened or closed for 5 ms. With the *Automatic stop* option, each run lasts 20 ms. The delay times are clearly seen from the graph (Fig. 4). The delay times when the controlling voltage is turned on or off are very different. The closing time depends on the amplitude of the controlling voltage: the higher the voltage, the faster the operation. For amplitudes above 10 V, the closing time becomes less than 1 ms. A much longer time is needed to return the shutter to the transparent state. Thus, a sufficiently high electric field easily destroys the LC twist structure, while the complete recovery of this structure is a longer process.

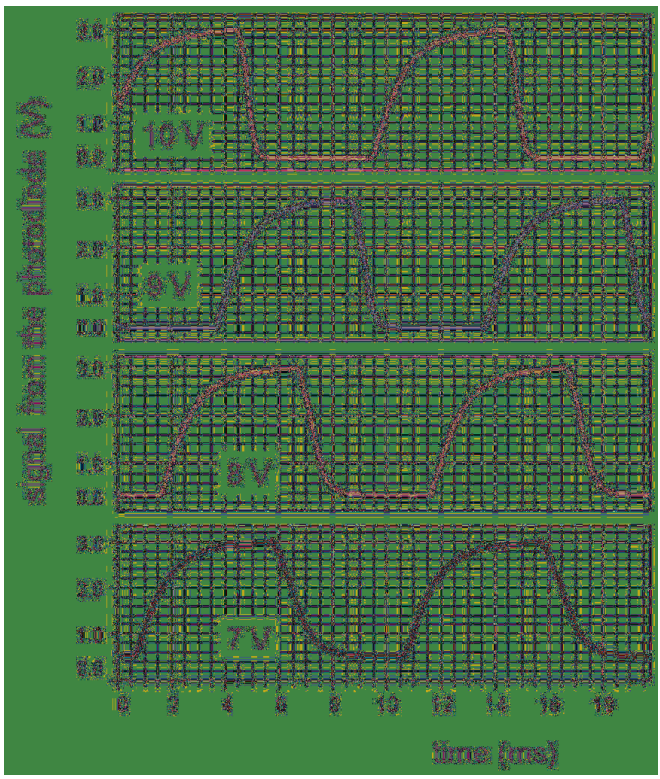

Fig. 4. Response of the shutter to positive square wave voltages of amplitudes from 7 to 10 V.

Modulation characteristic. The LC shutter is capable of modulating the transmitted light. To check this ability, a small sine wave voltage, along with a DC bias, is applied to the shutter. The signal from the photodiode is displayed

versus the controlling voltage. In the example shown (Fig. 5), an AC voltage of various frequencies and of 0.5 V amplitude was added to a 5.9 V bias. The changes in the amplitude and in the phase of the AC component of the transmitted light are caused by the inertia of the shutter.

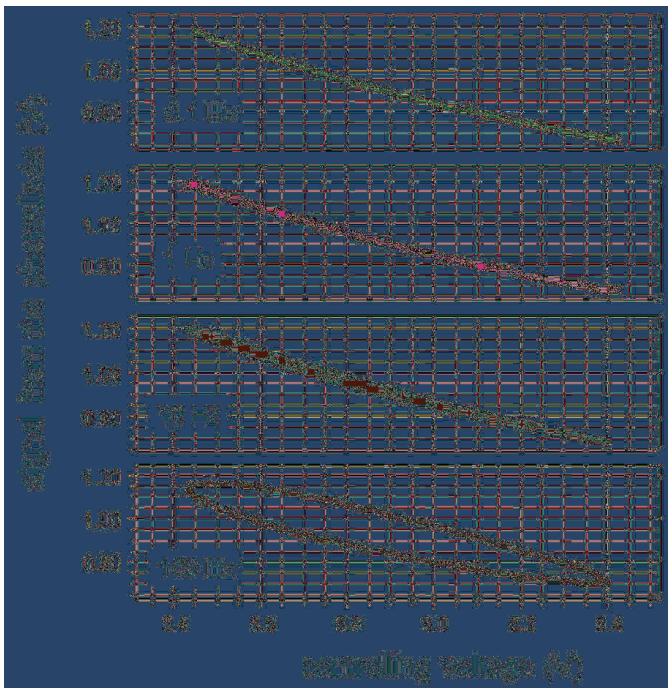

Fig. 5. Signal from the photodiode versus controlling sine wave voltage.

6.11. Dielectric constant of solids and liquids

The dielectric constant of solids and liquids is determined, and methods suitable for such measurements are considered.

Additional equipment: two *Voltage sensors*, function generator, oscilloscope, DC supply, coils, AC-to-DC converter, multimeter, varicap, decade capacitance box, platinum resistance thermometer, resistors, capacitors.

This subject has been considered in many papers. Gingle and Knasel (1975) described measurements of the **real** and **imaginary** parts of the **dielectric constant** of ice as a function of frequency. An AC bridge served for this purpose. Jupin (1977) used a resonant LCR circuit to measure both parts of the dielectric constant of liquids. The imaginary part was deduced from the bandwidth of the resonance curve. Carr and Harmon (1979) measured the dielectric constant of polypropylene glycol at a microwave frequency, 9.6 GHz. Mwanje (1980b) determined the so-called loss angle of mineral rock samples using a simple circuit and an oscilloscope. The data over the range of 1 to 500 Hz were taken from Lissajous patterns. Margulies (1984) calculated the force acting on a dielectric slab partially inserted into a parallel-plate capacitor. The physical origin of the force is shown to arise from the interaction of the fringe field with polarized molecules of the dielectric. Utreras-Díaz (1988) considered the problem of a dielectric slab inside a parallel-plate capacitor. Wilson (1989) described simple experiments with capacitors. Yan and Wong (1993) measured the force between the plates of a parallel-plate capacitor. Meyer and Behof (1994) observed the motion of a dielectric inside a parallel-plate capacitor. Lewowski (1998) determined the electric polarization of water and ice. The impedance of a capacitor containing the sample was measured at 1 MHz. At such a frequency, the impedance becomes much lower than the resistance caused by the ionic conduction of water. Perkalskis and Freeman (1998a) determined the dielectric constant of wood, which is anisotropic. With a bridge, the authors measured the dielectric constant of ice in the range of 10 to 200 kHz (Perkalskis and Freeman 1998b). Grove *et al* (2005) described experiments with a parallel-plate capacitor using a multimeter. Thompson (2005) measured the permittivity of some solids, powders, and liquids.

As an example, a determination of the capacitance of a varicap with the resonance technique is presented here. The capacitance depends on a DC bias. The varicap C_x is included in an LC resonant circuit (Fig. 1). A function generator feeds a 200-turn coil weakly coupled to an 800-turn coil of the LC circuit. An oscilloscope monitors the voltage across the varicap. Two similar varicaps are connected in parallel, but the parasitic capacitance of the connecting cable and the oscilloscope's input causes a problem. To determine the net capacitance of the sample, a decade capacitance box C_0 is connected parallel to the sample. The sample C_x can be disconnected from the circuit by a switch.

First, with C_x disconnected and C_0 set at a definite value (in our case, it is 2000 pF), the function generator is tuned to achieve resonance in the circuit (in our case, it equals 30 kHz). Then the sample is connected to the circuit, and the capacitance C_0 is adjusted to restore the resonance conditions. The parasitic capacitance remains the same, and the change in C_0 equals the capacitance C_x to be measured.

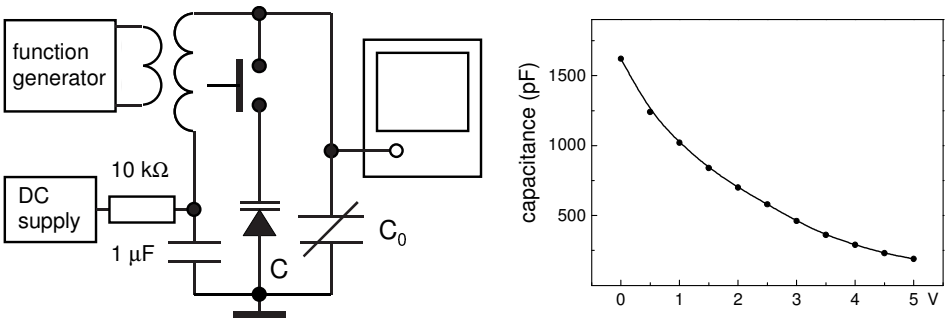

Fig. 1. Schematic of the setup and capacitance of two varicaps connected in parallel, versus bias voltage.

A simple method can be applied for determinations of a relatively large capacitance, where the uncontrollable parasitic capacitance is negligible. In such cases, one measures the voltage drop across a capacitor fed by an AC current through a resistor, whose resistance is much larger than the impedance of the capacitor. The capacitor is connected to the *Signal generator* through a resistor (Fig. 2).

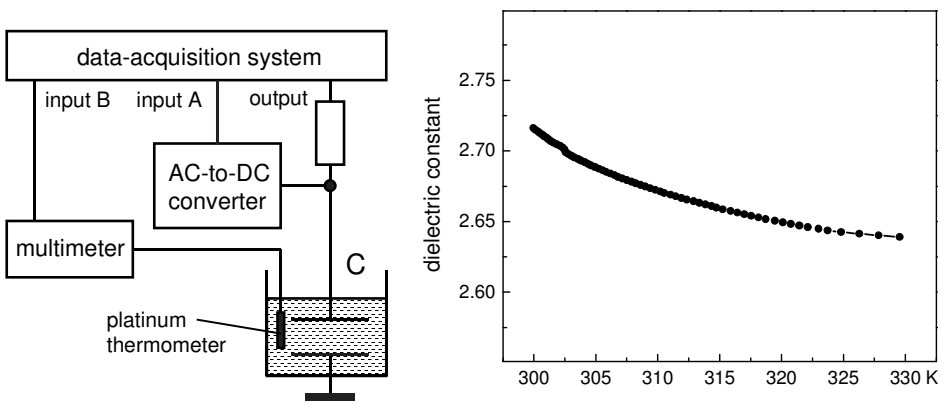

Fig. 2. Schematic of the setup and results for silicone oil.

The frequency is set to make the voltage across the capacitor much smaller than the output voltage of the generator. An AC-to-DC converter measures this

voltage and provides data for the data-acquisition system. As a sample, we use silicone oil. Its dielectric constant weakly depends on temperature. The liquid fills an air capacitor, whose capacitance was determined beforehand. A platinum resistance thermometer connected to a Keithley 177 multimeter measures the temperature of the liquid. Before the measurements, the sample is heated up to about 60°C. Then it cools down, while the data on the voltage across the capacitor and the temperature are stored. *DataStudio* calculates and displays the temperature dependence of the dielectric constant.

With the liquid chosen, there is no need for determinations of the real and imaginary parts of the dielectric constant. On the other hand, the concept of the complex nature of the dielectric constant is very important, and such an experiment is desirable. A simple bridge circuit (Fig. 3) can be used for such measurements.

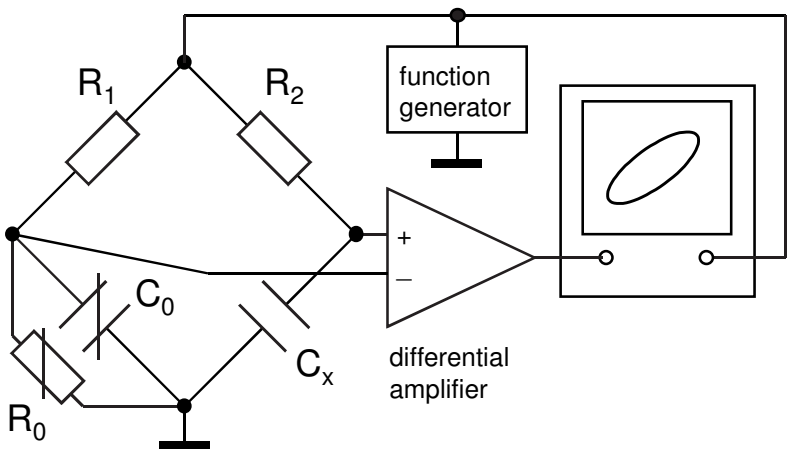

Fig. 3. Bridge circuit for determining real and imaginary parts of the dielectric constant.

Semiconductors

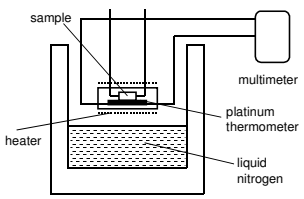

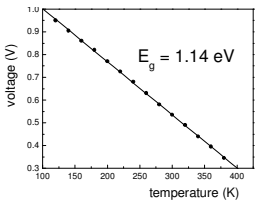

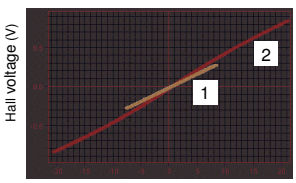

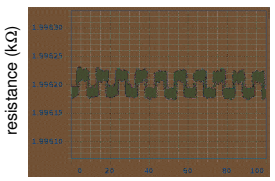

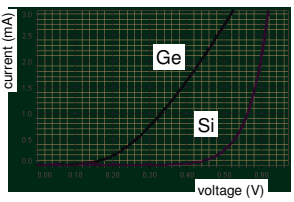

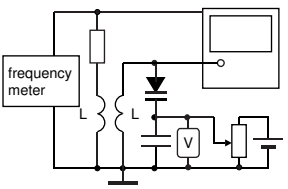

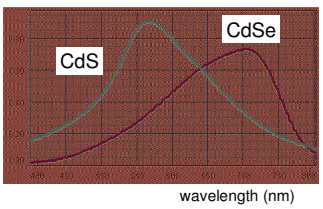

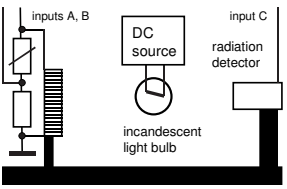

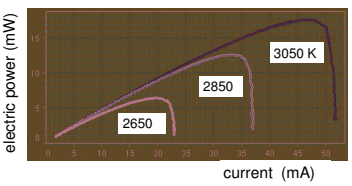

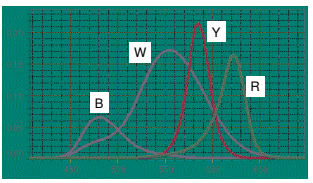

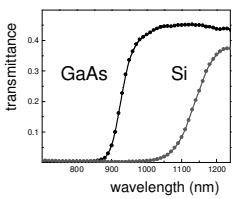

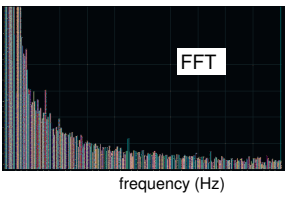

7. Semiconductors 447

7.1. Conductivity of semiconductors

The conductivity of a semiconductor is determined in a temperature range 140 to 290 K. The experiment is similar to that described by Fox and Gaggini (1987).

Additional equipment: two *Voltage sensors*, Dewar flask, heater, platinum resistance thermometer, thermistor, two multimeters.

The nature of the conductivity of metals and semiconductors is very different. This is clearly seen from the temperature dependence of the conductivity (Beeforth and Goldsmid 1970; Li 1993; Balkanski and Wallis 2000). With a data-acquisition system, it is easy to obtain data on conductivity in a wide temperature range.

A thermistor of low resistance (50 Ω at 25°C) serves as a sample. It is placed into a metal cylinder equipped with an electrical heater. A small platinum thermometer is attached to the sample (Fig. 1). The electrical resistances of the sample and of the thermometer are measured with two Keithley 177 multimeters. The sample is first cooled down by liquid nitrogen in a Dewar flask and then positioned above the liquid. The measurements are performed during gradually heating the sample. The resistance of the thermometer is translated into temperature using the common relation: $T = 30.9 + 225.4X + 16.8X^2$, where X is the ratio of the thermometer resistance to its resistance at 0°C.

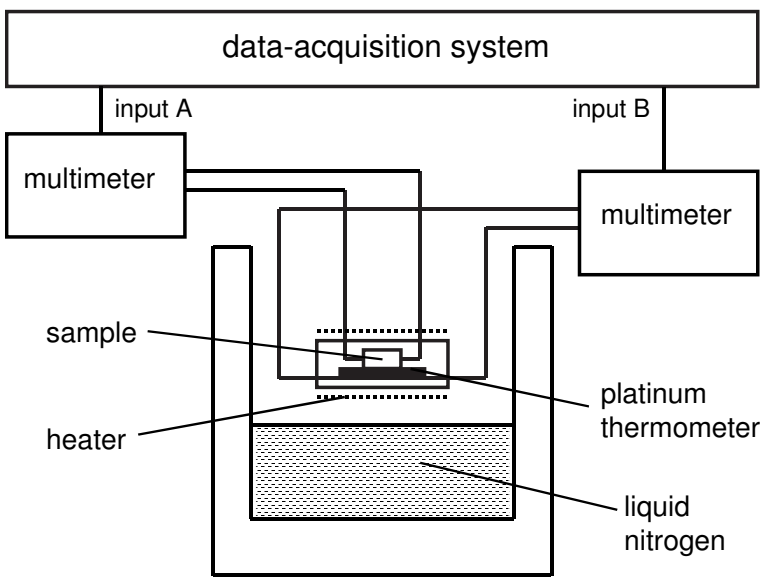

Fig. 1. Schematic of the setup for measuring conductivity.

The multimeter is capable of measuring resistances up to 20 MΩ. To record data in a wide range, one has only to change in time the scale of the multimeter. In the temperature range of 140–290 K, the resistance of platinum manifests a 2.5 times increase, while the resistance of the thermistor encompasses about 5 orders of magnitude (Fig. 2). *DataStudio* displays the resistance of the thermistor, in logarithmic scale, versus the inverse of the temperature.

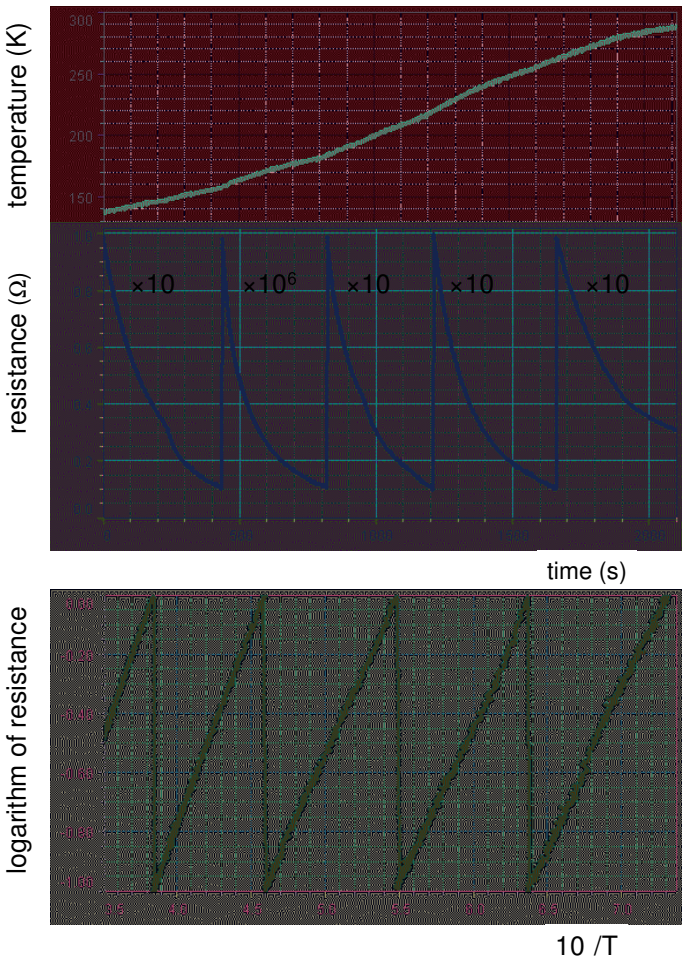

Fig. 2. Temperature and electrical resistance of the thermistor versus time, and logarithm of the resistance versus inverse of the temperature.

The basic relation for the resistivity of a semiconductor is

$$\rho = A\exp(E_g/k_B T), \qquad (1)$$

where A is a constant, E_g is the **energy bandgap** for the semiconductor, k_B is Boltzmann's constant, and T is the absolute temperature. All the measurement data are gathered and presented as the logarithm of resistance versus $1/T$. This graph should be a straight line with a slope E_g/k_B. In our case, $E_g = 0.23$ eV (Fig. 3).

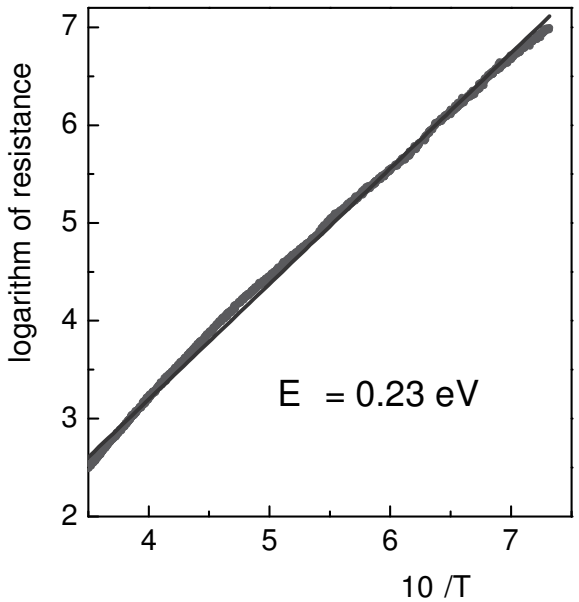

Fig. 3. Logarithm of the resistance versus inverse of temperature.

7.2. Hall's effect

Hall's effect is observed.

Additional equipment: two *Voltage sensors*, Dewar flask, Hall's probe, strong permanent magnet, coil, demountable magnetic core, DC supply, DC amplifier.

Hall's effect is caused by the forces acting on a moving electric charge. Let us consider a bar of rectangular cross section, in which a DC current flows in the presence of a uniform magnetic field $\boldsymbol{B}$ (Fig. 1). The force $\boldsymbol{F}$ on a charge q (Lorentz's force) is given by

$$\boldsymbol{F} = q\boldsymbol{E} + q\boldsymbol{v}\times\boldsymbol{B}, \tag{1}$$

where $\boldsymbol{E}$ is the electric field, and $\boldsymbol{v}$ is the velocity of the charge.

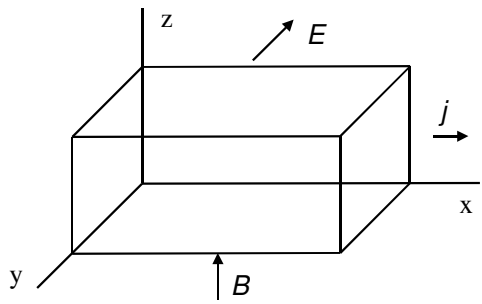

Fig. 1. Schematic for calculating the Hall's effect.

Due to the magnetic field, the carriers are deflected perpendicular to their velocity and the magnetic field. In the case considered, the vector $\boldsymbol{B}$ is perpendicular to the vector $\boldsymbol{v}$. The deflected carriers produce a transverse electric field $\boldsymbol{E}_y$ called the **Hall field**. In the steady state, this field gives rise to an electric force that just cancels the force due to the magnetic field:

$$qE_y = qv_xB_z. \tag{2}$$

The Hall field can be expressed as

$$E_y = j_xB_z/nq = R_Hj_xB_z, \tag{3}$$

where n is the concentration of the carriers, and R_H is called the **Hall coefficient**. In semiconductors, it is given by $R_H = -1/ne$ for electrons and $1/pe$ for holes, where n and p are their concentrations.

From the measurements, the Hall coefficient and thus the concentration of free carriers are available. Furthermore, the sign of the Hall coefficient gives the sign of the carrier charge. From measurements of the conductivity and Hall's effect, basic characteristics of a semiconductor are available, the carrier

concentration and mobility. With Hall's effect, Klein (1987) demonstrated the drift velocity in metals. Armentrout (1990) observed the effect in copper.

In the experiment, we use a commercial Hall's probe. The *Signal generator* feeds the probe, and the *Voltage sensor* measures the Hall voltage generated by the probe (Fig. 2). The feeding DC current is measured as the *Output current*. The *I–V* characteristics of the probe are determined at room temperature and when the probe is immersed in liquid nitrogen. In both cases, the probe is positioned between poles of a permanent magnet providing a field of 0.2 T. The thickness of our probe is less than 1 mm.

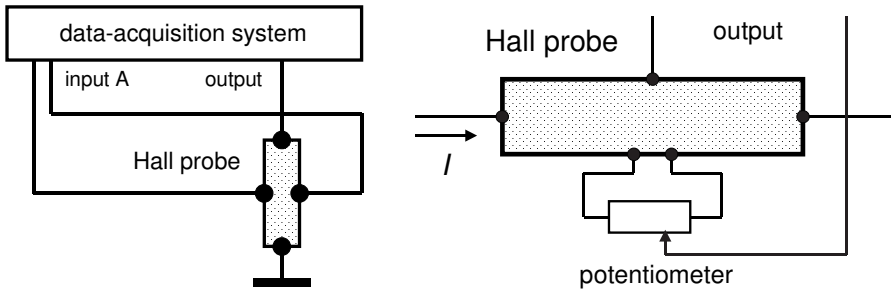

Fig. 2. Electrical circuit for Hall probe and method for zeroing output voltage. Magnetic field is perpendicular to the plane of the figure.

The intention of the designers was to make the sensitivity of the probe independent of temperature. Therefore, the sensitivity of the probe weakly depends on temperature (Fig. 3), but its resistance at 77 K becomes about three times lower than at room temperature. This is seen from the increase of the current through the probe.

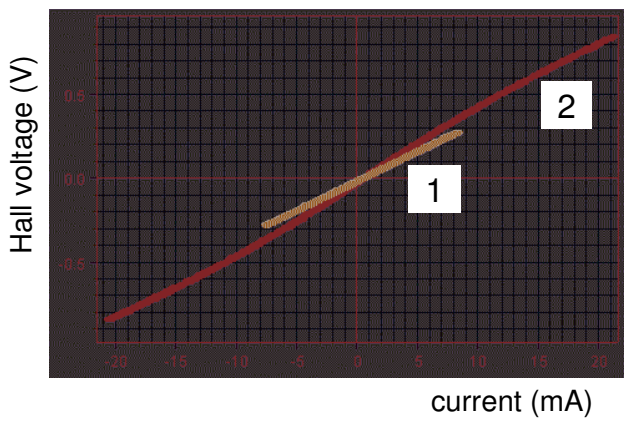

Fig. 3. Hall's voltage versus current through the probe, for magnetic field of 0.2 T. 1–room temperature, 2–77 K.

Second, the Hall probe is placed in a gap in an iron-core coil (SF-8614 and SF-8611) fed by a DC current. From the measurement, the magnetization curve and the hysteresis loop of the core are seen (Fig. 4). It is worth remembering that even a small gap in the core highly reduces the magnetic field (see Experiment 6.5). The same Hall's probe was used as a sensor of a magnetic bridge (see Experiment 6.8).

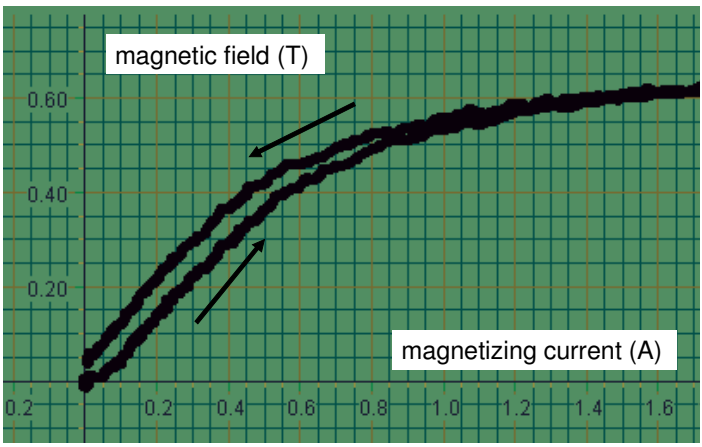

Fig. 4. Magnetic field in a gap of magnetic core versus magnetizing current.

7.3. Thermistors and bolometers

Important characteristics of semiconductor thermistors and bolometers are their sensitivity and thermal inertia; both quantities strongly depend on temperature.

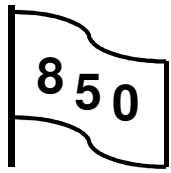

Additional equipment: *High-accuracy temperature sensor*, thermistor, oven, light bulb.

Thermistors are semiconductor devices for determining temperature of media, while **bolometers** sense the incident **thermal radiation** through the absorbed heat. In both applications, the strong temperature dependence of the resistivity is crucial. The basic relation for the resistivity of a semiconductor is

$$\rho = A\exp(E_g/k_B T), \tag{1}$$

where A is a constant, E_g is the energy bandgap for the semiconductor, k_B is Boltzmann's constant, and T is the absolute temperature. From this equation, the temperature coefficient of resistivity equals

$$\beta = (d\rho/dT)/\rho = -E_g/k_B T^2. \tag{2}$$

The **temperature coefficient of resistivity** of semiconductors is negative, and the module of this quantity increases with decreasing the temperature. The thermal inertia of thermistors and bolometers depends on the mass and specific heat of a sample and the rate of heat exchange with the surrounding media (the **heat transfer coefficient**).

The resistance and time constant of a typical thermistor are measured in a 300–350 K temperature range. Second, the same device serves as a bolometer for measuring the power of incident thermal radiation.

Thermistor. The thermistor (5 kΩ at 25°C) and the *High-accuracy temperature sensor* (CI-6525) are put into axial openings in an aluminum cylinder, 20 mm in diameter and 80 mm in height; the cylinder is positioned in an electrically heated oven. After heating up to 80°C, the measurements are performed during the cooling process. The thermistor is connected to *Output 2* through a variable resistor. The measuring current, 0.01 mA, causes a negligible heating effect. The measurements are thus performed under equilibrium conditions. As expected, the resistance of the thermistor follows Eq. (1), and $E_g/k_B = 3840$. According to Eq. (2), the module of the temperature coefficient of resistance at 293 K equals 0.045 K^{-1}, that is, one order of magnitude larger than that for most metals. The energy bandgap equals $E_g = 0.33$ eV (Fig. 1).

To determine the time constant, the thermistor should be instantaneously brought out of the equilibrium. An electrical pulse lasting about 10 s makes the thermistor several degrees warmer than the surrounding air. By monitoring the equilibration process, the time constant of the thermistor is available (Fig. 2). To

increase the sensitivity, the current through the thermistor in the above measurement was 0.1 mA. Due to the increase of the current, the thermistor becomes somewhat warmer than the surrounding air, and the sensitivity to changes of the temperature increases. Under these conditions, the time constant is nearly 10 s.

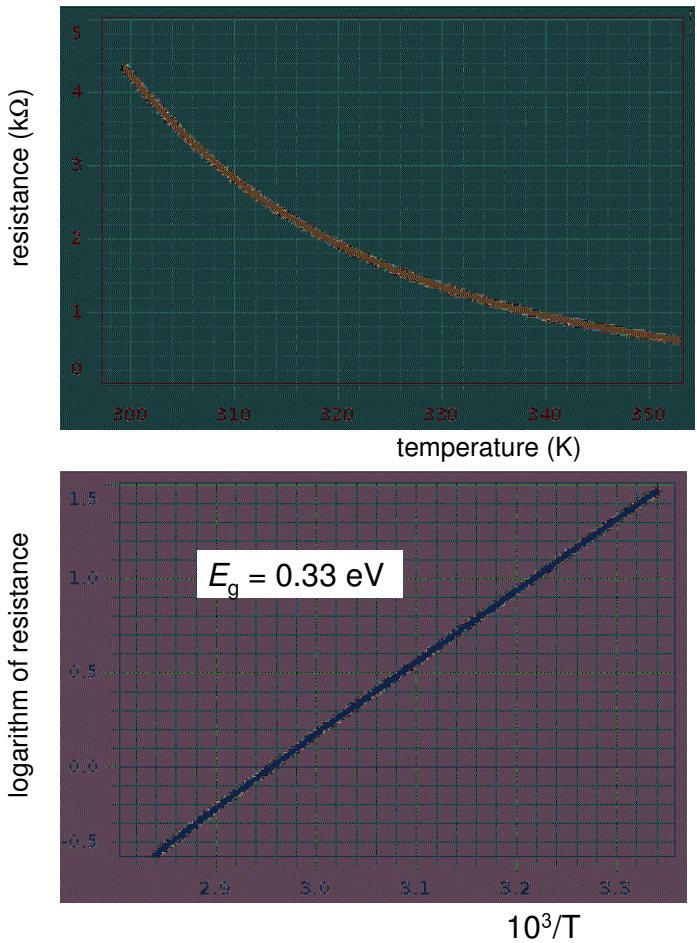

Fig. 1. Resistance versus temperature and graph for calculating the energy bandgap of the semiconductor.

Bolometer. The same device serves for measuring the power of incident thermal radiation. For this experiment, the enhanced sensitivity of the *850 Interface* is crucial. A low power light bulb connected to *Output 1* in series with a 10 Ω (10 W) resistor serves as the source of incident radiation. The output voltage is a 5 V square wave with a 5 V offset. The radiation from the light bulb thus changes from zero to its maximum value. *Output 2* provides a DC current for the

bolometer; a variable resistor R regulates this current. The *Voltage sensor* acquires the voltage across the bolometer. *Capstone* calculates the resistance of the bolometer and displays it versus time (Fig. 3).

The results presented are obtained for a 0.1 Hz modulation of the incident radiation. The feeding current makes the bolometer several degrees warmer than the surrounding air (the resistance becomes nearly 2 kΩ), so the response of the device becomes faster. The oscillations in the resistance of the bolometer under the modulated irradiation are nearly 0.05 Ω (peak-to-peak), and the amplitude of the temperature oscillations is less than 1 mK. An increase of the sensitivity is possible by using the lock-in detection technique.

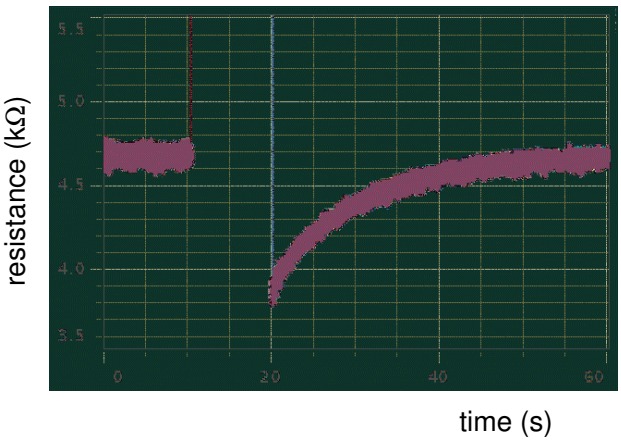

Fig. 2. Recovery of the resistance during thermal equilibration.

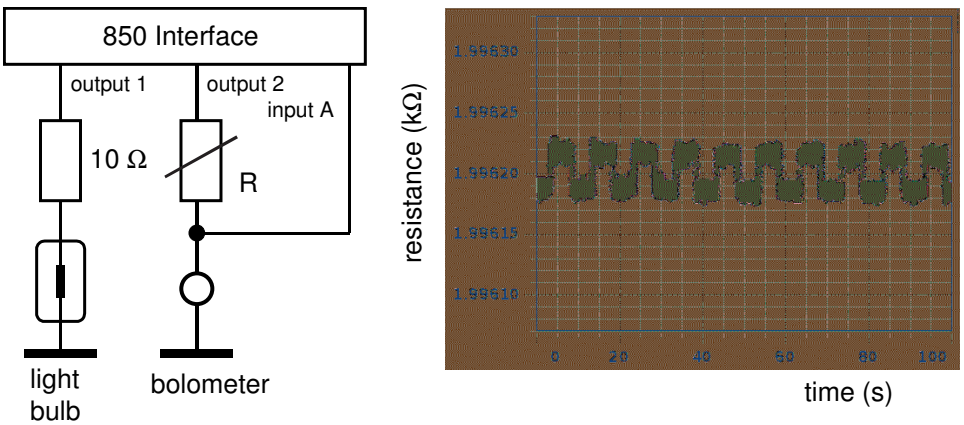

Fig. 3. Diagram of the setup and measurement data. The amplitude of the temperature oscillations is less than 1 mK.

7.4. Semiconductor diode

I–V characteristics of a silicon diode are measured at various temperatures. From the data, the energy bandgap for silicon is available.

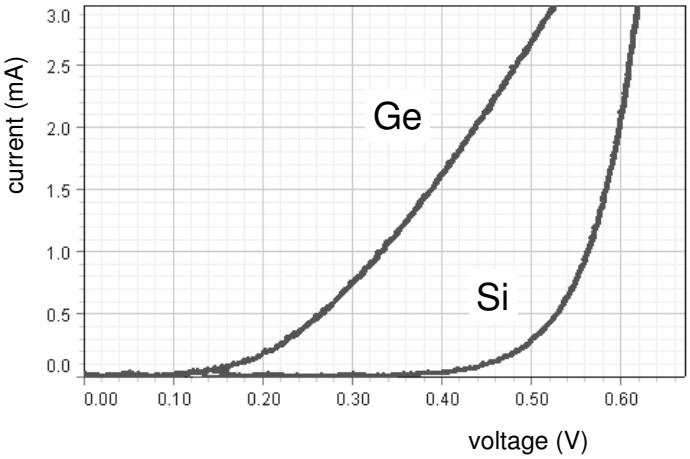

I–V characteristics of two semiconductor diodes.

Additional equipment: *Voltage sensor*, Dewar flask, platinum resistance thermometer, silicon diode.

The semiconductor electronics is an important part of solid-state physics and of many modern technologies (Beeforth and Goldsmid 1970; Li 1993; Balkanski and Wallis 2000). Various items of this subject are included in lecture and laboratory courses and presented in textbooks and journal papers. By measuring the short-circuit collector current versus the emitter-collector voltage of a silicon transistor, Inman and Miller (1973) determined the ratio of the electron charge to Boltzmann's constant. Collings (1980) obtained the energy bandgap in silicon and germanium from measurements of *I–V* characteristics of *p-n* junctions at various temperatures. Experiments with semiconductor diodes were also described by other authors: Canivez (1983); Kirkup and Nicolson (1986); Kirkup and Placido (1986); Sconza and Torzo (1989); Sconza *et al* (1994); Precker and da Silva (2002). Fischer (1982) measured *I–V* characteristics and capacitance of semiconductor diodes. From the data, the energy bandgap and diffusion potential of *p-n* junctions are available. To identify the conduction mechanisms in *p-n* junctions, Mártil and González Díaz (1991) measured *I–V* characteristics of such devices in a very wide range of currents, 10^{-12} to 1 A. Mártil and González Díaz (1992a) determined the energy bandgap through measurements of the complex refractive index of a CdS thin film. Essick and Mather (1993) reported on a similar experiment with silicon and GaAs. Sconza and Torza (1985) described a simple apparatus for measuring minority carrier

lifetime. Sconza and Torza (1987) and Sconza *et al* (2000) reproduced the famous Haynes–Shockley experiment. Rebello *et al* (1997) presented a computer program simulating *p-n* junction devices. Ocaya and Dejene (2007) described a simple method for a characterization of a *p-n* diode.

Data acquisition provides important advantages when it is necessary to display *I–V* characteristics. The measurements are possible in a short time, and the results are displayed immediately, along with results of calculations. In the experiment, *I–V* characteristics of a silicon diode are measured in a wide temperature range. The diode is placed into a metal cylinder equipped with an electrical heater. A small platinum resistance thermometer is attached to the sample (Fig. 1). The electrical resistance of the thermometer R is measured by a multimeter and then translated into temperature using the common relation $T = 30.9 + 225.4X + 16.8X^2$, where X is the ratio of the thermometer resistance to the resistance at 0°C.

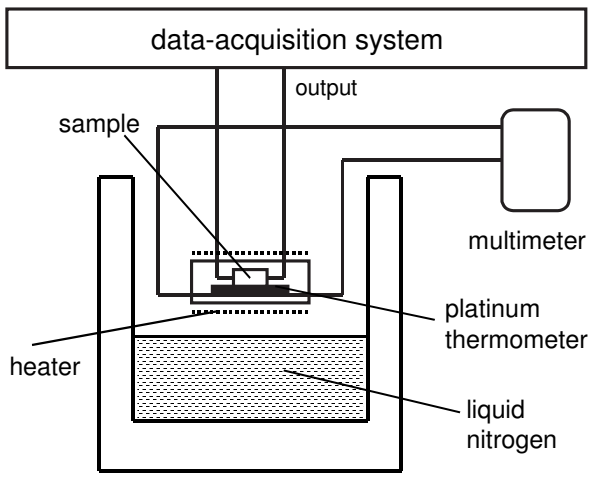

Fig. 1. Setup for recording *I–V* characteristics at various temperatures.

The diode is connected to the *Signal generator*, and the data are taken as the *Output voltage* and *Output current* of the generator. The sample is first cooled down by liquid nitrogen in a Dewar flask and then positioned above the liquid. The measurements are performed during gradually heating the sample with the heater. The characteristic of a semiconductor diode obeys the equation

$$I = I_0[\exp(eV/\eta k_B T) - 1], \tag{1}$$

where I_0 is the reverse saturation current, e is the electron charge, k_B is Boltzmann's constant, η is a constant, normally in the range between 1 and 2, and T is the absolute temperature of the *p-n* junction. On the other hand,

$$I_0 = BT^3\exp(-E_g/\eta k_B T), \tag{2}$$

where B is a constant, and E_g is the energy band gap. Hence,

$$V = E_g/e - (\eta k_B T/e)\ln(BT^3/I). \quad (3)$$

For a definite value of I, the logarithmic term in Eq. (3) can be considered constant, and the voltage V is a linear function of T. From a family of I–V characteristics obtained (Fig. 2), one can find voltages related to a constant current I for different temperatures. According to Eq. (3), the plot of the voltage V versus the temperature T should be a straight line. Extrapolation of this line to a zero temperature gives the bandgap energy E_g. For the example presented (Fig. 3), the energy appeared to be 1.14 eV.

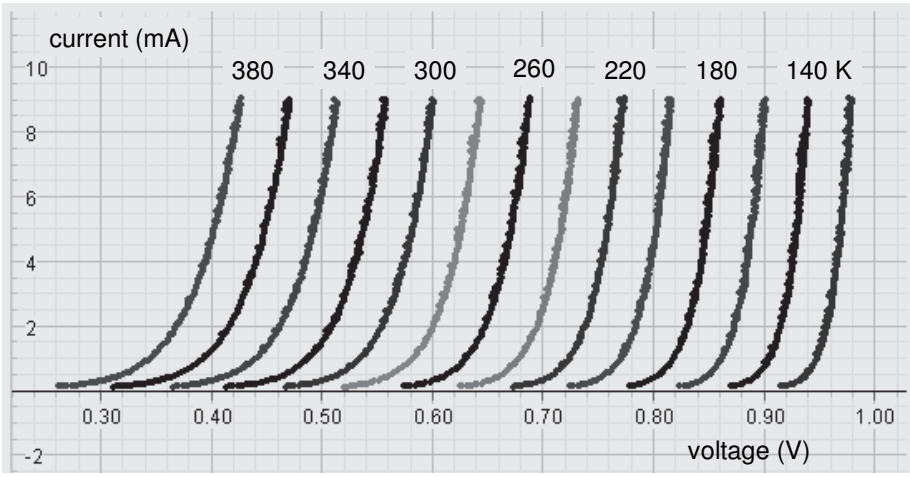

Fig. 2. I–V characteristics of silicon diode at different temperatures.

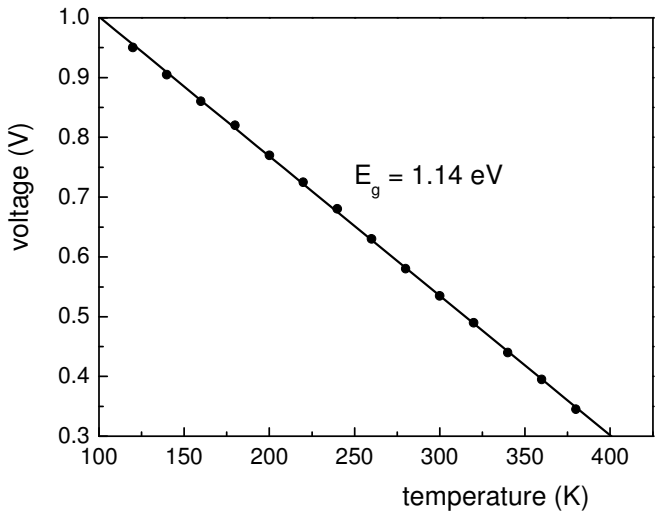

Fig. 3. Determination of the energy bandgap.

7.5. Varicap

Characteristics and applications of a varicap are considered (Kraftmakher 2011a).

Additional equipment: varicap, oscilloscope, multimeter, AC-to-DC converter, 9 V battery, capacitor, resistors, coils, potentiometer.

A **varicap** (variable capacitance diode, or **varactor**) is a semiconductor device with a *p-n* junction, whose capacitance depends on the applied voltage. Varicaps are reverse-biased, so the current flowing through them is very small. The capacitance decreases with increasing the reverse-bias voltage (Sedra and Smith 1998; Sze and Ng 2007).

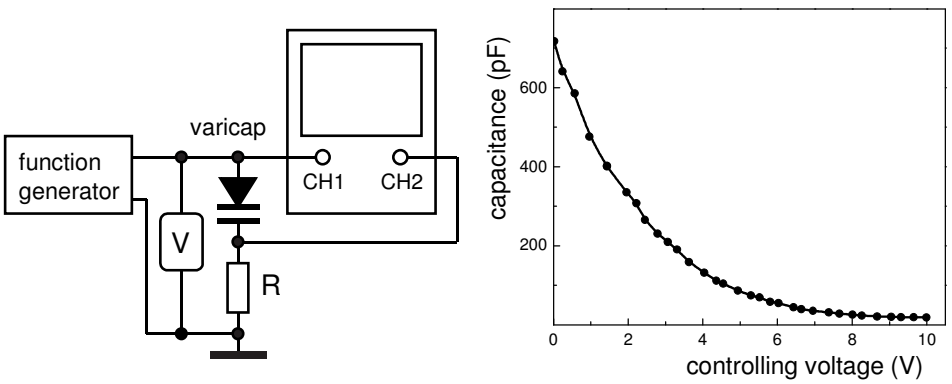

Fig. 1. Diagram of the setup and the *C–V* characteristic.

***The C-V characteristic*.** To determine the dependence of the capacitance of a varicap on the applied DC voltage, a regulated reverse voltage should be applied to the device. The optional DC offset of the output AC voltage, which is common for many types of function generators, serves for this aim. We use a BB112 varicap from Philips Electronics, which was designed for **electronically tuning** radio receivers and **voltage-controlled oscillators**.

The capacitance of the varicap may become comparable to that of standard cables, so one has to use a measurement technique allowing for minimizing the effects of parasitic capacitances. The varicap of capacitance C is connected to the output of a function generator, GFG-8019G, in series with a resistor R = 1 kΩ (Fig. 1). The frequency of the generator is $f = 20$ kHz. At this frequency, the current in the circuit is controlled by the impedance of the varicap, $Z_C = 1/\omega C >> R$. The voltage across resistor R equals $V_R = 2\pi VfRC$, where V is the AC output voltage of the function generator. Therefore, $C = V_R/2\pi VfR$. With the chosen values of f and R, $C(\text{pF}) = 7960V_R/V$. The voltages V and V_R are determined with a two-channel Kenwood CS-4025 oscilloscope. The DC offset V_0 provided by the function generator is measured

with a multimeter. The voltage V is set to be several times smaller than V_0. The capacitance of the varicap is measured as a function of the offset voltage.

An important parameter of any variable capacitor is the ratio of its maximum and minimum capacitances, $C_{max}/C_{min} = k$. The resonant frequency of an LC circuit equals $f_0 = (2\pi\sqrt{LC})^{-1}$, and the frequency range covered with a variable capacitor and a single inductor is defined by $\sqrt{k}$. Due to unavoidable additional capacitances of the inductor and of connecting wires, the real frequency range becomes smaller.

Measurements with a data-acquisition system. The above experiment can be automated and used for a demonstration (Fig. 2).

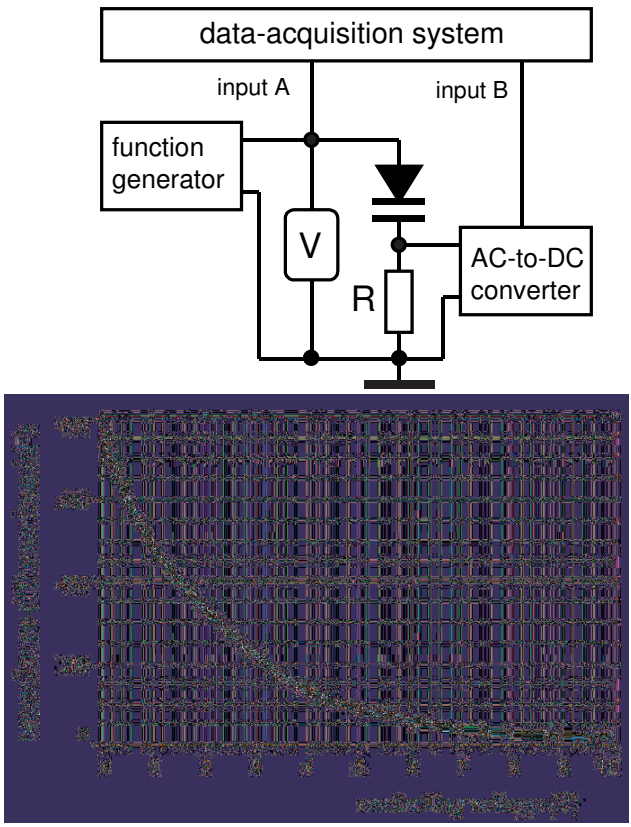

Fig. 2. Schematic of setup with data-acquisition system and example of data obtained.

The variable offset voltage provided by the function generator is acquired with the *Voltage sensor*. It should be remembered that voltages above 10 V are dangerous for the sensor. A Keithley 177 multimeter converts the AC voltage V_R to a DC voltage, which is acquired by the second *Voltage sensor*. The AC output

voltage of the function generator V is determined beforehand using the same AC-to-DC converter. *DataStudio* displays the quantity $C = 7960V_R/V$ versus the controlling voltage.

Electronically tuning of receivers. In the second experiment, the varicap is used as a part of an LC resonant circuit (Fig. 3). The inductor L is a 400-turn coil (SF-8610). Forced oscillations in the circuit are created with the function generator connected, through a 20 kΩ resistor, to a 200-turn coil L_1 (SF-8609) inductively coupled to the inductor L. The two coils thus form a mutual inductance. Any AC current passing through the coil L_1 induces an EMF in the coil L. The forced oscillations are observed with an oscilloscope. The controlling voltage is obtainable with a 9 V battery and a potentiometer. For every controlling voltage, the frequency of the generator is adjusted to obtain the resonance. The resonance frequency is displayed versus the controlling voltage.

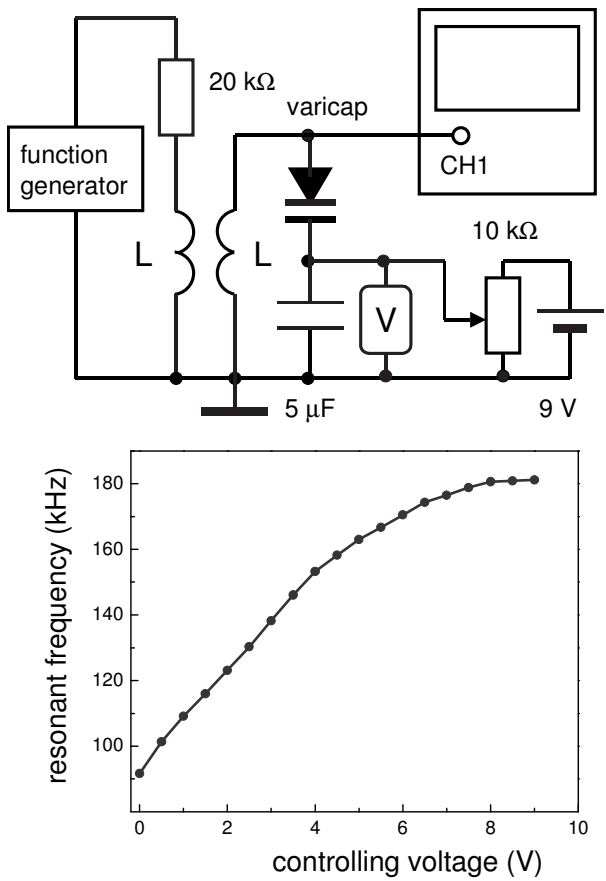

Fig. 3. Setup demonstrating electronically tuning radio receivers and resonance frequency versus controlling voltage.

Due to the capacitance of the connecting cable and of the oscilloscope input, the frequency range covered by the electronic tuning is narrower than that expected from the ratio of the maximum and minimum capacitances of the varicap. The parasitic capacitance C_0 can be calculated from the evident relation:

$$(f_{max}/f_{min})^2 = (C_{max} + C_0)/(C_{min} + C_0). \quad (1)$$

In our case, $f_{max}/f_{min} \cong 2$. For the varicap, $C_{max} \cong 750$ pF, $C_{min} \cong 20$ pF; therefore, $C_0 \cong 220$ pF. A shorter connecting cable reduces the parasitic capacitance. The f_{max}/f_{min} ratio can be increased by setting two varicaps in parallel.

Voltage-controlled oscillator. In the third experiment, the varicap is included in the resonant circuit of an oscillator (Fig. 4). The circuit is very similar to the preceding one, but the oscilloscope serves also as an amplifier, and the self-excited oscillations in the circuit are triggered by positive feedback. The amplification channel CH1 of the Kenwood CS-4025 oscilloscope has an output terminal. The gain of the channel depends on the sensitivity set by the experimenter; the maximum gain is 100. The output of the oscilloscope is connected, through a 20 kΩ resistor, to a 200-turn feedback coil L_1 (SF-8609), which is placed adjacent the coil L. Depending on the polarity of the coils, the feedback is positive (the induced EMF supports oscillations in the circuit) or negative (the induced EMF suppresses the oscillations). The feedback factor depends on the gain of the oscilloscope and the distance between the two coils.

With a definite positive feedback, the oscillations become self-excited. The setup thus becomes a voltage-controlled oscillator. The frequency of the self-excited oscillations is measured with a frequency meter. The GFG-8019G function generator serves as the meter connected to the output of the oscilloscope. The dependence of the oscillation frequency on the controlling voltage is the same as obtained in the preceding experiment.

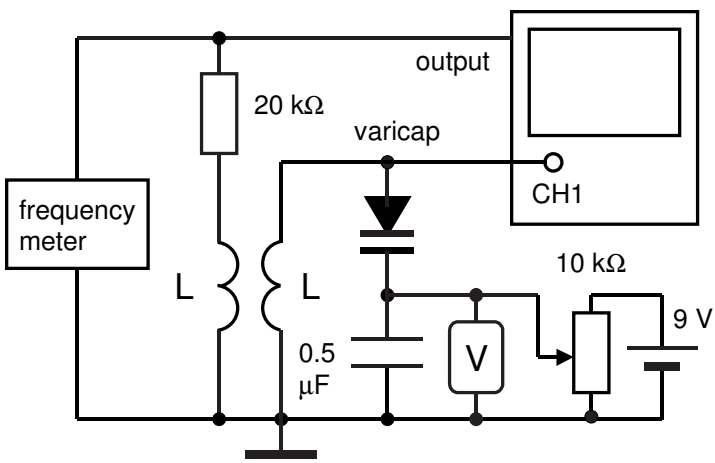

Fig. 4. Schematic of setup demonstrating a voltage-controlled oscillator.

7.6. Photoconductivity

Four topics are included: (i) the spectral response; (ii) the photocurrent versus the incident radiant power; (iii) the rise and decay time constants; and (iv) the frequency response. The photoconductive gain of a photoresistor is estimated (Kraftmakher 2012c).

Additional equipment: *Educational spectrophotometer*, *Rotary motion* sensor, diffraction grating, DC supply, photoresistors, light-emitting diode, photodiode, light bulb, AC-to-DC converter.

Absorption of incident light by a semiconductor may increase the number of free electrons and holes and thus the electrical conductivity of the sample. This phenomenon is called **photoconductivity** (Bube 1960, 1992; Rose 1978; Jones 1987; Sze and Ng 2007). A photoconductor can be either **intrinsic** or **extrinsic**. Intrinsic photoconductors have available electrons only in the valence band, and the incident photons must have enough energy to excite the electrons across the bandgap. For extrinsic photoconductors, photoexcitation occurs between a band edge and an impurity energy level in the forbidden zone, and photons of low energies are sufficient to trigger the device. A semiconductor resistor, whose resistance decreases with increasing the incident radiant power, is called **photoresistor** or **light dependent resistor**.

Photoresistors were already used for teaching purposes. Mullaney (1966) demonstrated photoconductivity of CdS photoresistors. Three regions related to different radiant powers of the incident light were observed. For middle radiant powers, the photocurrent is proportional to the incident power. Chow (1984) reported on a study of the diffusion of charge carriers in homogeneous silicon samples. The decay times of photoconductivity were measured to obtain the necessary information. Peiris and Perera (1987) described a simple photometer with a photoresistor. Kirkup and Cherry (1988) determined the temperature dependence of photoconductive decay in CdS.

Theoretical background. In photoresistors, the concentration of **excess carriers** created by photoexcitation is commonly much larger than the background concentration of free carriers. For intrinsic photoconductors, the concentrations n of electrons and holes are equal. For a rectangular slab of cross-section S and length l, the carrier generation rate F (number of carriers generated per unit volume per second) is

$$F = N/Sl = n/\tau, \tag{1}$$

where N is the total number of carriers generated per second, Sl is the volume of the slab, and τ is the **carrier lifetime**, that is, the length of time that this carrier stays free and able to contribute to the conductivity before it loses energy and returns to its initial state via **recombination** with a carrier of opposite type.

The photoconductivity σ is given by

$$\sigma = en(\mu_n + \mu_p), \tag{2}$$

where e is the electronic charge, and μ_n and μ_p are the mobilities of electrons and holes. The photocurrent through the slab equals

$$i = \sigma ES = enES(\mu_n + \mu_p) = eNV(\mu_n + \mu_p)\tau/l^2, \tag{3}$$

where E is the electric field created in the slab while a voltage V is applied to the electrodes. Equation (3) shows that the current through a photoresistor depends not only on N, but also on the properties of the material given by the quantity $(\mu_n + \mu_p)\tau$ and on the electric field created in the sample. This situation radically differs from that when the same number N of free carriers per second is generated in a photodiode. In the saturation regime, the current i_1 depends only on N:

$$i_1 = eN. \tag{4}$$

It is natural to define the i/i_1 ratio as the **photoconductivity gain**:

$$G = i/i_1 = V\tau(\mu_n + \mu_p)/l^2. \tag{5}$$

The gain may appear to be less than unity. For high photoconductivity gain, the carrier lifetime should be long and mobility of charge carriers high, while the electrode spacing should be short. In most practical photoconductors, the mobility at room temperature is in the range between 10^2 and 10^4 $cm^2.V^{-1}.s^{-1}$. The free carrier lifetime is between 10^{-9} and 10^{-2} s, depending on the density and properties of imperfections present in the material. The photoconductivity gain is a parameter related to a given photoresistor (not to the material) and is proportional to the applied voltage.

The photoconductivity gain is the number of charge carriers that circulate through the circuit for each charge carrier generated by the absorbed light. The carrier lifetime remains undisturbed when a carrier is extracted from the photoresistor by electric field at the same time as an identical carrier is injected from the opposite electrode. One charge carrier generated by the absorbed light causes many carriers supplied by an external source to pass through the sample (Bube 1960; 1992; Rose 1978). With these considerations, it is easier to accept Eq. (5). To determine the photoconductivity gain, one can directly measure the currents i and i_1. Since the quantities V and l are known, and the mobilities μ_n and μ_p are available from other measurements, Eq. (5) allows for estimating the lifetime of free charge carriers.

CdS and CdSe are intrinsic photoconductors, which are sensitive in the visible range. Our unlabelled photoresistors were identified by measuring their **spectral response**. The setups for the experiments are shown in a general scheme (Fig. 1). A common arrangement is used for the first experiment. In the second experiment, a yellow light-emitting diode (LED) irradiates the photoresistors, while the incident radiant power is measured with a silicon photodiode. From these measurements, the photoconductivity gain of the

photoresistors is estimated. To measure the **rise** and **decay** time constants, the LED is fed by the *Positive square wave* voltage from the *Signal generator*. Modulated light from the LED serves for determining the **frequency response** of the photoresistors.

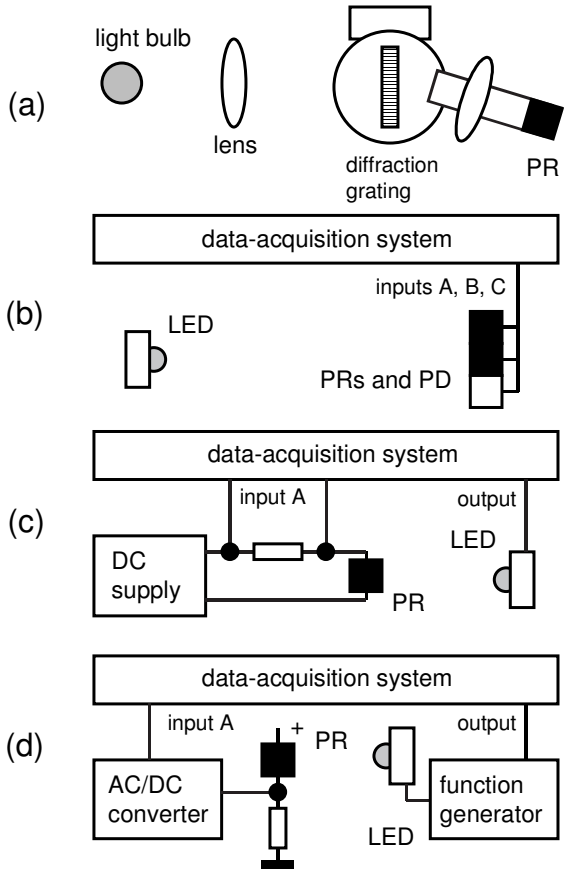

Fig. 1. Schematics of the experiments: (a) spectral response; (b) photocurrent versus incident radiant power; (c) rise and decay time constants; (d) frequency response to modulated light. PD–photodiode, PR–photoresistor.

First of all, the response of the photoresistors to a step-like irradiation was observed. The CdS photoresistor attains its steady response more rapidly and thus is more suitable for quantitative measurements. This observation is in agreement with that by Ross (1995).

Spectral response. The *Educational spectrophotometer* (OS-8537) with a diffraction grating having 600 lines per millimeter, and a 100 W light bulb serve for determining the spectral response of the photoresistors. The photoresistor under test is connected, in series with a load resistor, to a DC supply. The

photocurrent is measured through the voltage drop across the load resistor, whose resistance is much smaller than that of the photoresistor. *DataStudio* displays this voltage versus wavelength. The measurement data (Fig. 2) are shown with no corrections for the spectrum of the incident light. Commonly, photoresistors are characterized by a wavelength of maximum sensitivity. For a given material, this wavelength depends on impurities in the sample and may vary in a relatively wide range. For the photoresistors tested, the maximum sensitivity is achieved at nearly 620 nm (CdS) and 700 nm (CdSe). These values fall into the ranges given by the manufacturers.

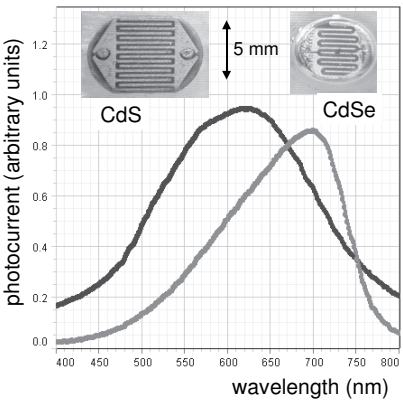

Fig. 2. Spectral response of the photoresistors, with no corrections for the spectrum of incident light.

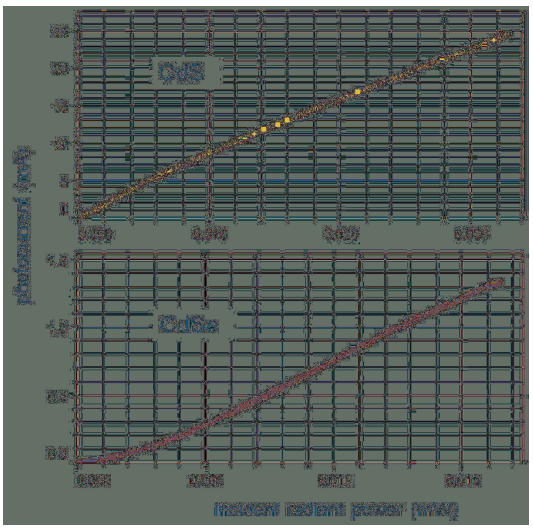

Fig. 3. Current of the photoresistor versus incident radiant power. The applied voltage is 30 V.

Photoconductivity versus incident radiant power. For this measurement, both photoresistors and a silicon photodiode (United Detector Technology PIN-10D model) are placed, in a closed box, at the same distance from the LED. For homogeneous irradiance, the incident radiant power is proportional to the photosensitive areas. The sensitive area of the photodiode is nearly 0.8 cm^2. To determine the sensitive area of the photoresistors, an enlarged image of them was obtained with a video camera and a monitor (the photos are included in Fig. 2). The zigzag shape sensitive areas of the photoresistors appeared to be nearly 0.09 cm^2 (CdS) and 0.045 cm^2 (CdSe).

The photoresistors are connected, in series with load resistors, to a DC supply (30 V). The LED is fed from an adjustable DC source. The currents of the photodiode and of the photoresistors are measured through the voltages across the load resistors using the *Voltage sensors*. The measurements are carried out while gradually changing the current through the LED. In the range

400–800 nm, the spectral response of a silicon photodiode (the current to the incident radiant power ratio) depends on the wavelength λ and can be presented as

$$I/P\ (\mathrm{A.W^{-1}}) = 1.2\times10^{-3}(\lambda - 300), \quad (6)$$

where λ is given in nanometers.

For the LED used, the wavelength of the radiation is 585 nm. The *I*/*P* ratio for the photodiode thus equals 0.34 $\mathrm{A.W^{-1}}$. From this figure and the sensitive areas of the photodiode and the photoresistors, it is easy to determine the incident radiant power for the photoresistors. During a run, the *SataStudio* calculates and displays the photocurrent versus the incident radiant power (Fig. 3). The photocurrent is nearly proportional to the incident radiant power.

Photoconductivity gain. From the measurement data, one can estimate the photoconductivity gain. The **quantum efficiency** of the photoresistors is unknown, and we consider it to be the same as that of the photodiode, that is, nearly 0.8 (Kraftmakher 2008). With this simplification, the photoconductivity gain is simply the relation of the measured *I*/*P* ratio of the photoresistor to that of the photodiode. When the voltage applied to the photoresistors is 30 V, the *I*/*P* ratio for them equals nearly 0.8 $\mathrm{A.mW^{-1}}$ (CdS) and 0.08 $\mathrm{A.mW^{-1}}$ (CdSe). The photoconductivity gain thus exceeds 2×10^3 (CdS) and 2×10^2 (CdSe). Due to the uncertainty in the quantum efficiency of the photoresistors, the above values should be considered as only estimations.

Rise and decay time constants. In this experiment, square waveform light pulses from the LED irradiate the photoresistors. The frequency of the pulses is 200 Hz. The *Automatic stop* is set to occur after two periods of the square wave voltage. The photoresistors are connected, in series with load resistors, to a DC supply, and two *Voltage sensors* acquire the voltages across the load resistors. The time constant of the LED is much shorter than that of the photoresistors, so the measurement data show the processes of generation and recombination of charge carriers in the photoresistors.

We assume that the rise and decay of photoconductivity follow exponential functions, but with time constants generally different. In the absence of traps for the charge carriers, both time constants equal the free carrier lifetime. The traps are formed by defect energy levels in the forbidden zone. In the presence of traps, the **generation-recombination** processes become much more complicated because the trap filling during the rise and the emptying during the decay are involved. For high generation rate and/or low density of traps, the density of free carriers may become much larger than that of trapped carriers. In this case, the decay time constant equals the free carrier lifetime. In the opposite case, the decay time constant may become much longer. The detrapping rate depends on temperature.

After starting the irradiation, the photocurrent and hence the voltage *V* across the load resistor increase:

$$V = V_0[1 - \exp(-t/t_r)], \tag{7}$$

where t_r is the rise time constant, and V_0 is the voltage across the load for $t >> t_r$. After ending the irradiation, the voltage V decays exponentially:

$$V = V_1\exp(-t/t_d), \tag{8}$$

where t_d is the decay time constant, and V_1 is the voltage when the decay starts.

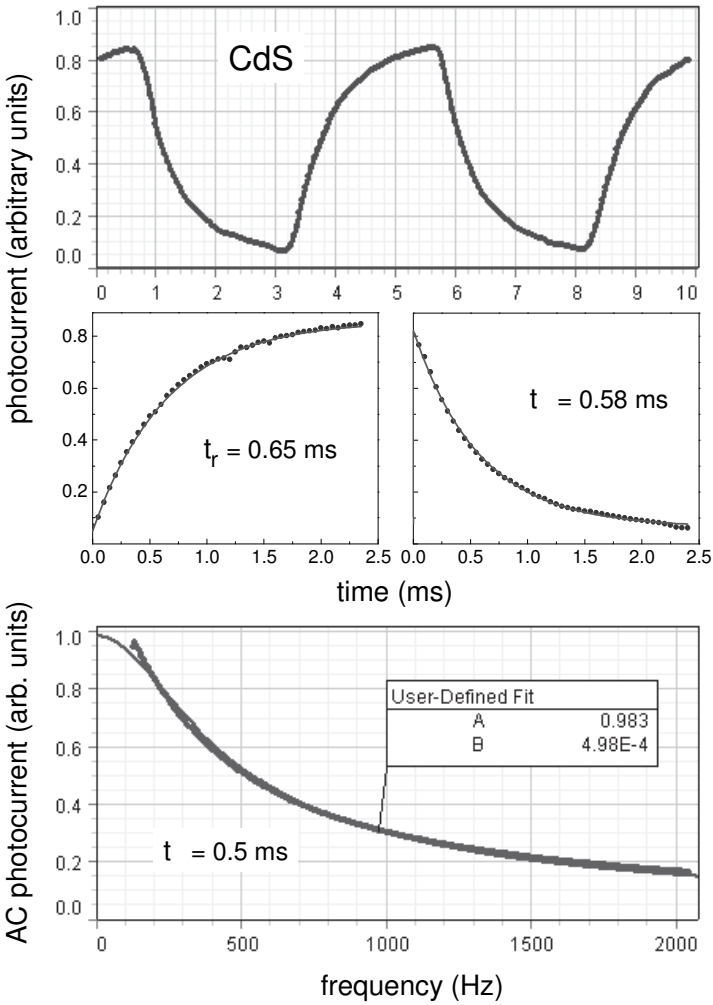

Fig. 4. From the rise and decay data, the two time constants are determined. In the fit for the frequency response data, *A* means i_0, and *B* means t_0.

The data related to the rise and decay of photoconductivity (Fig. 4) are separated and approximated with Eqs. (7) and (8); the necessary time shift is

also introduced. The *Origin* software serves to fit the separated data. For the CdS photoresistor, $t_r = 0.65$ ms, and $t_d = 0.58$ ms. The difference between the two values is insignificant, so it is possible to say that these constants are equal. For the CdSe photoresistor, a significant difference between t_r and t_d values was found, which is rather a rule. In many cases, the manufacturers indicate very different values of these quantities.

Frequency response to modulated light. The frequency response of the photoresistors is determined while automatically scanning the modulation frequency of incident light. A common function generator GFG-8019G feeds the LED. The *Ramp down wave* voltage from the *Signal generator* applied to the VCF input of the generator controls its frequency and provides the desired frequency range. The DC offset of the generator output voltage is set to obtain a sufficient photocurrent, while the AC component of the output voltage is several times smaller. The frequency response is measured in the frequency range from 0.1 to 2 kHz; one run lasts 100 s. The AC component of the voltage across the load resistor is fed to an AC-to-DC converter, a Keithley 177 multimeter. The *Voltage sensor* acquires the DC output voltage of the converter. *DataStudio* displays the frequency response curve of the photoresistor (the results are shown in Fig. 4). The AC component i of the photocurrent was approximated with the common equation:

$$i = i_0/(1 + 4\pi^2 f^2 t_0^2)^{½}, \tag{9}$$

where i_0 is the AC component of the photocurrent at very low frequencies, and t_0 is a characteristic time constant.

This equation is usual for various processes with the same time constant for the rise and decay. In the case of different time constants, Eq. (9) should be considered as only a fit, with t_0 as a parameter. One can expect that t_0 is comparable to t_r and t_d. For the CdS photoresistor, the fit gives $t_0 = 0.5$ ms.

7.7. Photovoltaic effect

The efficiency of energy conversion is determined versus the temperature of the radiator (Kraftmakher 2000c).

Additional equipment: *Radiation sensor*, two *Voltage sensors*, solar cell, gas-filled light bulb (24 V, 100 W), DC supply, optics bench, two multimeters, variable resistor, decade resistance box.

A. Becquerel discovered the photovoltaic effect in 1839, but viable photovoltaic cells were not developed until 1955. The photovoltaic cell is a device that generates an electric voltage by the absorption of radiation (Greaves 1970; Beeforth and Goldsmid 1970; Li 1993; Balkanski and Wallis 2000). Most photovoltaic cells consist of a semiconductor *p-n* junction or Schottky barrier (a contact of a metal to a semiconductor), in which electron-hole pairs produced by absorbed radiation are separated by the internal electric field in the junction. The conversion of incident radiation into electrical energy involves (i) the absorption of the radiation in the semiconductor material; (ii) the generation and separation of free positive and negative charges to different regions of the cell; and (iii) the transfer of these separated charges through electrical terminals to a load.

The main part of a silicon photovoltaic cell (solar cell) is the *p-n* junction (Fig. 1). Pure silicon (a four-column element), to which a trace amount of a fifth-column element such as phosphorus has been added, is an *n*-type semiconductor. Each phosphorus atom contributes one free electron, leaving behind the phosphorus atom bound to the crystal structure with a unit positive charge. Similarly, pure silicon, to which a trace amount of a column-three element such as boron has been added, is a *p*-type semiconductor, where the electric current is carried by free holes. Each boron atom contributes one hole, leaving behind the boron atom with a unit negative charge. The fixed charges at the *p-n* junction create a permanent dipole charge layer with a high electric field.

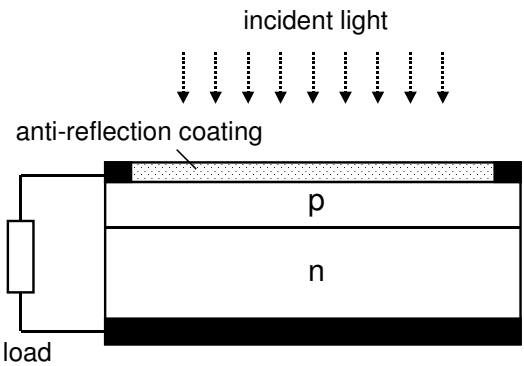

Fig. 1. Schematic of loaded silicon solar cell.

When incident radiation produces electron-hole pairs near the junction, this electric field forces the holes to the *p* side and the electrons to the *n* side. This displacement results in a voltage difference between the two regions of the crystal. When a load is connected to the terminals, an electric power is available at the load. The theory and features of photovoltaic cells are given in many books. Several student experiments with a photovoltaic cell have been reported. Kammer and Ludington (1977) determined the efficiency of a silicon solar cell, that is, the ratio of the electrical power output to the incident solar power. The Sun irradiance above the Earth's atmosphere (AM0 irradiation, where AM denotes the so-called "air mass") is 1.4 $kW.m^{-2}$. To calculate the irradiation at the Earth's surface, one has to take into account the distance in the atmosphere, through which the radiation travels. For a bright, clear day the solar irradiance at sea level is 0.96 $kW.m^{-2}$ for the Sun directly overhead (AM1 irradiation). Chow (1980) employed the solar irradiance and a halogen lamp having a spectrum similar to that of sunlight at sea level with the Sun at 30^{o} above the horizon. In this case, the path through the atmosphere is twice that for the vertical (AM2 irradiation). The author concluded that a determination of the total irradiance is highly desirable because the calibration with sunlight is not entirely reliable unless the turbidity is known or is negligible. Muoy *et al* (1981) described an auxiliary transistorized circuit for recording *I–V* characteristics of solar cells. Kissner (1981) constructed a simple instrument for measuring the instantaneous and integrated values of solar flux. The sensor is a solar cell connected to a resistor located in an insulated water bath. The temperature of the bath is measured by a thermistor. A similar bath is used as a reference. The instrument is calibrated by means of a standard pyranometer and a digital integrator. Mialhe and Charette (1983) used the sunlight to evaluate solar cell parameters that are dependent on the irradiation and the temperature of the cell. Khoury *et al* (1984) measured the open-circuit voltage of a solar cell versus its temperature, up to 100^{o}C. The source of irradiation was a halogen lamp. DuPuy (1989) determined the solar luminosity with a silicon photodiode. The Sun was considered as a blackbody at 5800 K, and necessary corrections were made for the spectral response of the photodiode and absorption of the sunlight in the Earth's atmosphere. Mártil and González Diaz (1992b) employed a halogen lamp to obtain characteristics of a silicon solar cell. Van Sark (2007) considered the solar cell efficiency.

In our experiment, the power of the **incident radiation** is measured directly, and the **energy conversion efficiency** of a photovoltaic cell is determined as a function of the temperature of the radiator. This dependence is caused by the shift of the radiation spectra. The experiment has also practical interest, because the effect of a decrease in the temperature of the radiator is similar to that of an increase in the **energy bandgap** of the semiconductor used.

Ultimate efficiency of energy conversion. Many authors calculated the ultimate efficiency of the energy conversion by a photovoltaic cell. Shockley and Queisser (1961) considered a photovoltaic cell, in which all photons with energy

$E \geq E_0 = hf_0$ produce the same effect, while photons of lower energy do not contribute. Here E_0 is the energy bandgap of the semiconductor, f_0 is the corresponding light frequency, and h is Planck's constant. The first fundamental limitation for the efficiency is caused by photons, whose energy is less than E_0. Each photon having energy $E \geq E_0$ produces one electronic charge at a voltage of $V = E_0/e$. The second limitation for the efficiency is posed by photons of higher energies, because the energy in excess of E_0 is converted into heat inside the cell. It turns out that the efficiency of a photovoltaic cell depends only upon the quantity $X = E_0/k_B T$, where k_B is Boltzmann's constant, and T is the temperature of the source of radiation. The authors presented the results as a graph of the ultimate efficiency versus X. The maximum efficiency is achievable at $X = 2.2$. A silicon photovoltaic cell is thus very suitable to convert solar radiation into electrical power. The evaluated ultimate efficiency appeared to be 44%. However, several factors reduce this figure. Nowadays, the maximum efficiency achieved for silicon solar cells is about 20%.

For the blackbody radiation, the total power of the incident radiation (in arbitrary units) can be written as

$$P_{in} \propto \int_0^\infty f^3 df/[\exp(hf/k_B T) - 1]. \quad (1)$$

To evaluate the ultimate output power from a photovoltaic cell, one has to multiply the number of photons having energy $E \geq E_0$ by $E_0 = hf_0$. Hence,

$$P_{out} \propto \int_0^\infty f_0 f^2 df/[\exp(hf/k_B T) - 1]. \quad (2)$$

The ultimate energy conversion efficiency η^* thus equals

$$\eta^* = \int_0^\infty f_0 f^2 df/[\exp(hf/k_B T) - 1] / \int_0^\infty f^3 df/[\exp(hf/k_B T) - 1]. \quad (3)$$

Necessary calculations were performed for $E_0 = 1.1$ eV and various temperatures of the source of irradiation (Fig. 2).

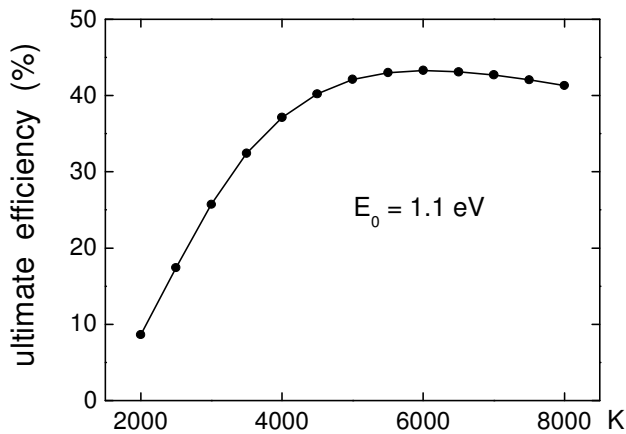

Fig. 2. Calculated ultimate conversion efficiency for $E_0 = 1.1$ eV versus temperature of radiator.

A silicon solar cell was purchased from Edmund Scientific (D37346). The sensitive area of the cell is 6.8 cm^2. A gas-filled incandescent light bulb (24 V, 100 W) fed by a DC supply serves as a source of radiation. The best approach is to measure the power of the incident radiation. The *Radiation sensor* (TD-8553) used for this aim was calibrated with a homemade sensor (see Experiment 5.11). The light bulb is placed at equal distances from the cell and the sensor (Fig. 3).

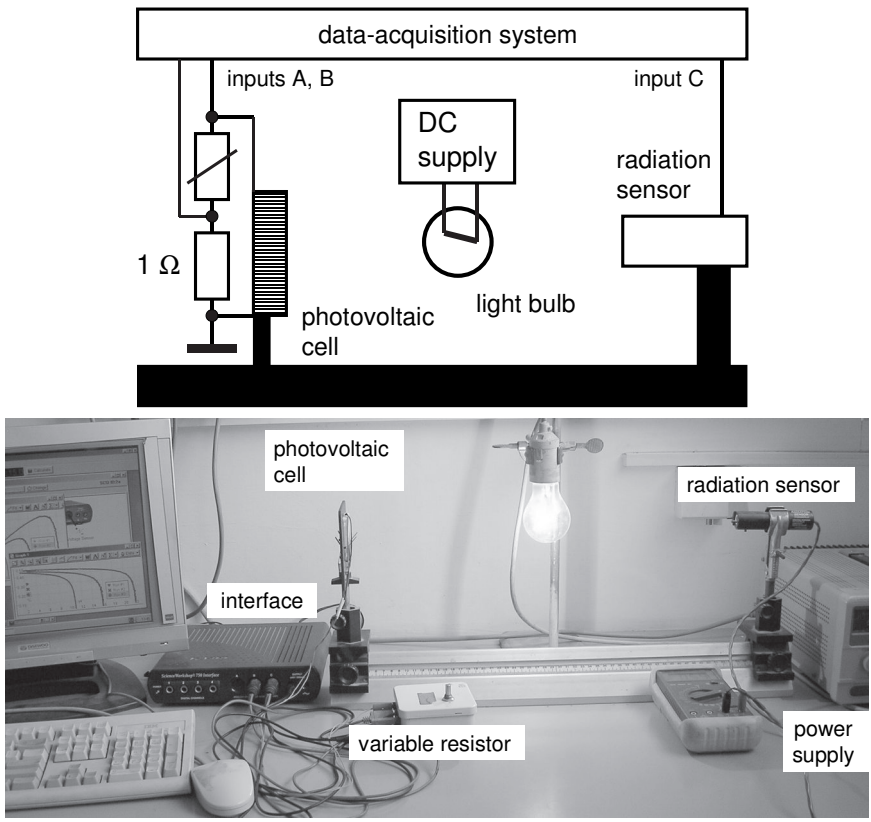

Fig. 3. The experimental setup.

Two *Voltage sensors* measure the voltages across a variable load and a 1 Ω resistor connected in series with the cell. The spectral emissivity of tungsten decreases with increasing wavelength. For producing visible light, tungsten is thus more efficient than a blackbody of the same temperature. Here we consider tungsten as a **"gray body."** This means that its spectral emissivity is less than unity but does not depend on the wavelength. The radiation spectra of a gray body are therefore similar to those of a blackbody of the same temperature and can be calculated from Planck's formula. With a gray body, the efficiency of the energy conversion is the same as that with a blackbody.

The efficiency of the cell is determined for several temperatures of the tungsten filament. In the 2500–3400 K range, the temperature of a tungsten wire follows the relation $T = 261 + 165.5X - 0.76X^2$, where X is the ratio of the resistance of the wire at T to its resistance at 0°C. The above relation fits data by Roeser and Wensel (1941). It is difficult to accurately determine the resistance of a low-resistance filament at room temperature because of a contribution of the electric leads inside the lamp. It is therefore useful to remember that gas-filled incandescent lamps operate in the range of 2700–3000 K. The temperature increases along with the nominal power. For a 100 W gas-filled light bulb, it is about 2850 K (Steeb and Forsythe 1967).

Using a variable resistor as a load, the *V–I* characteristics of the cell are displayed by *DataStudio* (Fig. 4). Simultaneously, *DataStudio* plots a graph of the power generated by the cell versus the current. The temperatures indicated correspond to three voltages applied to the light bulb: 20, 24, and 28 V. Under suitable conditions, the measurements are performed also with solar radiation (Fig. 5). A variable resistor (or a decade resistance box) and two multimeters are necessary for this purpose. The photovoltaic cell should be oriented perpendicular to the Sun radiation. The *Radiation sensor* measures the intensity of radiation.

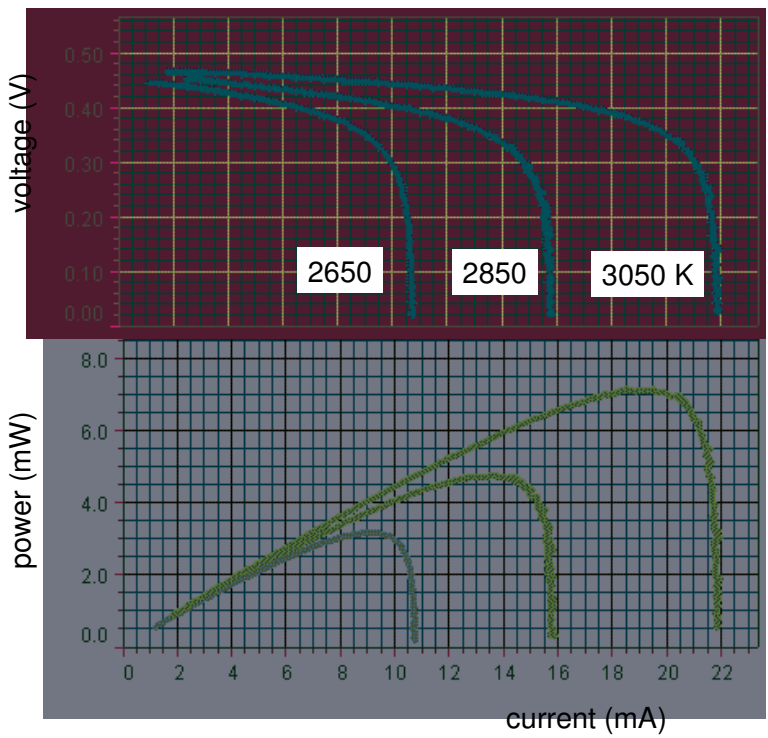

Fig. 4. Output voltage and generated power versus electric current in the load, for three temperatures of radiator.

Efficiency versus temperature of radiator. The maxima of the generated power provide data for calculating the efficiency of energy conversion. For the solar radiation, the efficiency amounts to 12.5%. The energy conversion efficiency can be presented as a function of the temperature of the radiator (Fig. 6). Only a qualitative comparison of the results with the theoretical ultimate efficiency is possible. For photovoltaic devices, see also a review by Loferski (1995) and papers by Kuhn and Postawko (1998); Boitier and Cressault (2011); Dark (2011); Devasia and Kurinec (2011).

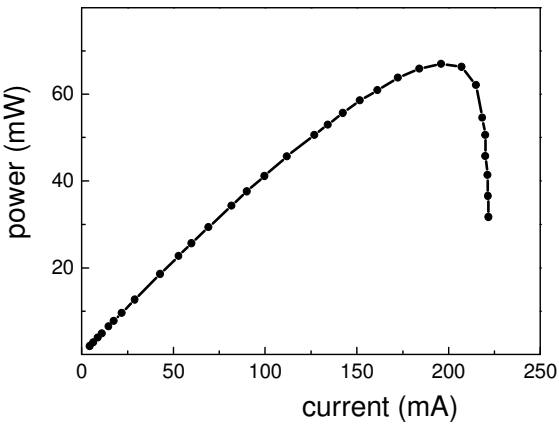

Fig. 5. Generated power versus current for solar irradiation.

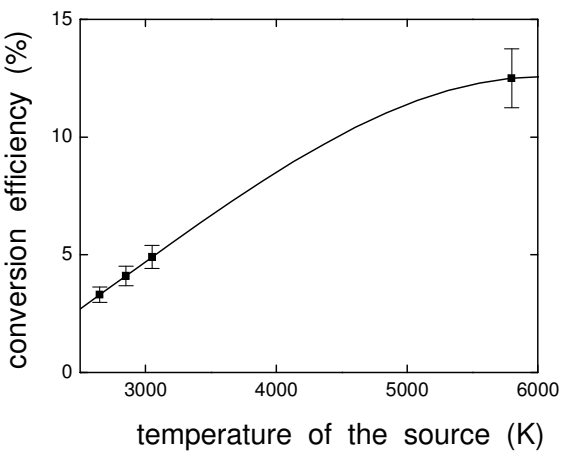

Fig. 6. Energy conversion efficiency versus temperature of the radiator.

7.8. Light-emitting diode

The radiant and luminous power spectra, efficiency, and luminous efficacy of four light-emitting diodes (LEDs) are determined. Their frequency response is determined in the range 10–10^7 Hz. For a white LED, the frequency response is measured separately for the primary blue emission and for the green-yellow phosphorescence (Kraftmakher 2011d).

Additional equipment: *Voltage sensor*, *Educational spectrophotometer*, *Light sensor*, *Aperture bracket*, photodiodes, LEDs, diffraction grating, lenses, DC supply, function generator, resistors.

A light-emitting diode (LED) is a semiconductor device with a *p-n* junction that emits photons when electric current passes through it (Craford and Steranka 1994; Streetman and Banerjee 2000; Sze and Ng 2007). The semiconductor crystal is doped to fabricate an *n*-type region and a *p*-type region, one above the other. Forward electrical bias across the LED causes the holes and electrons to be injected from opposite sides of the *p-n* junction into the active area, where their recombination results in emission of photons. The energy of the emitted photons is approximately the **bandgap energy** of the semiconductor. The bandgap energy of ternary and quaternary semiconductor compounds can be adjusted in a certain range by varying their composition. First LEDs were **homojunction** diodes, in which the material of the core layer and that of the surrounding clad layers are identical. Then **heterostructures** with layers having a varying band gap and refractive index were recognized as advantageous. Contemporary LEDs are more complicated double heterostructure diodes. In 2000, Zhores Alfyorov and Herbert Kroemer shared the Nobel Prize in Physics "for developing semiconductor heterostructures used in high-speed- and optoelectronics."

LEDs are efficient light sources for many applications, including indicators, large-area displays, and opto-couplers. Holonyak (2000) pointed out that the LED is an **ultimate light source**. Mayer (2010) considered the current status and prospective of solid-state lighting, where the LED is an excellent alternative to **incandescent** and **fluorescent** light bulbs. LEDs are easily modulated sources and are used in optical communications with optical fibers (Kogelnik 1995). The possibility to modulate LEDs in a broad frequency band is crucial for simultaneously transmitting many television or audio programs through a single optical fiber. To correctly reproduce the pictures, the amplitude modulation characteristic should be linear.

LEDs were used to demonstrate their basic properties (Kwasnoski 1972; Davis and Mueller 1977; Jewett 1991; Johnson 1995; Lottis and Jaeger 1996; Ojeda *et al* 1997; Redondo *et al* 1997; Escalada *et al* 2004; Precker 2007), and as auxiliary tools for many experiments and demonstrations (Seeley *et al* 1999; DeYoung and Mulder 2002; Mak 2004; Garver 2006).

Three color LEDs and one white LED from HuiYuan Opto-Electronic are used: LB-P200R1C-H3 (red), LB-P200Y1C-H3 (yellow), LB-P200B2C-H3 (blue), and LB-P20WC3-60 (white). The input current of the LEDs indicated by the supplier is 0.75 A. In our experiments, the maximum input current is 0.1 A, and the input power does not exceed 0.3 W. Generally, two types of white LEDs are available. One type combines two or three LEDs of appropriate colors. With such a device, a spectrum similar to that of daylight is achievable. Modifications of the light from "warm white" to "cool daylight" are possible by varying the contributions of the components. In the second type, a suitable phosphor is positioned onto a blue LED, and the output light contains blue light and a **Stokes-shifted phosphorescence band**. The white LED we use is of the second type.

An important characteristic of a lighting source is its **color temperature**. The color temperature does not mean that the spectrum of a light source is similar to that of a blackbody of equal temperature. Fluorescent lamps and many LEDs are designed to emit only visible light. Therefore, their spectra differ radically from those of thermal sources governed by Planck's formula, which unavoidably include intensive infrared emission. The spectrum of a lighting source can be characterized by the **blue-to-red ratio**, which can be equal to that of a blackbody at a certain temperature. This ratio determines the color temperature of the source. The green band in the spectrum is needed for attaining high **luminous efficacy** of lighting sources (see the following). For the white LED, the supplier claims that the color temperature is in the range 6000–7000 K, which is typical for "cool daylight" lamps. For "warm white" sources, the color temperature is in the range 2700–3300 K.

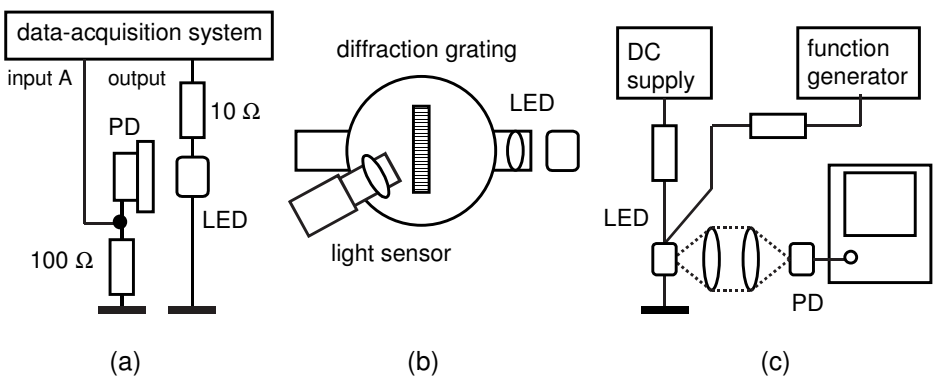

Fig. 1. Scheme of the experiments: (a) radiant power and efficiency; (b) emission spectra; (c) frequency response. PD—photodiode.

The input electric current and power, radiant output power, and efficiency of the LEDs can be measured or calculated, and then displayed versus the voltage applied to the device or versus the current passing through it. The LED

under test is connected, in series with a 10 Ω limiting resistor, to the *Signal generator*. The *Output voltage* is the *Positive ramp up* voltage linearly increasing from zero to a maximum value set to achieve the maximum desired current through the LED. The *Signal generator* operates in *Auto* mode: it begins to generate the *Output voltage* after starting a run. The period of the voltage is 20 s. The option *Automatic stop* is used for automatically ending each run.

The output radiant power of the LEDs is determined with a silicon photodiode by using its typical spectral response. The radiant power spectra are observed with a diffraction grating and converted to the luminous power spectra by using the standard luminosity function. The frequency response of a LED is determined by sine wave modulation of the feeding current. Setups used in the experiments are shown in a general scheme (Fig. 1).

Radiant power and efficiency. The input current of the LEDs is measured as the *Output current* of the *Signal generator*. *DataStudio* calculates the voltage applied to the LED as the *Output voltage* minus the *Output current* times the resistance of the limiting resistor, 10 Ω. The input electric power is calculated from the input current and applied voltage. *DataStudio* displays the input current and power versus the applied voltage (Fig. 2).

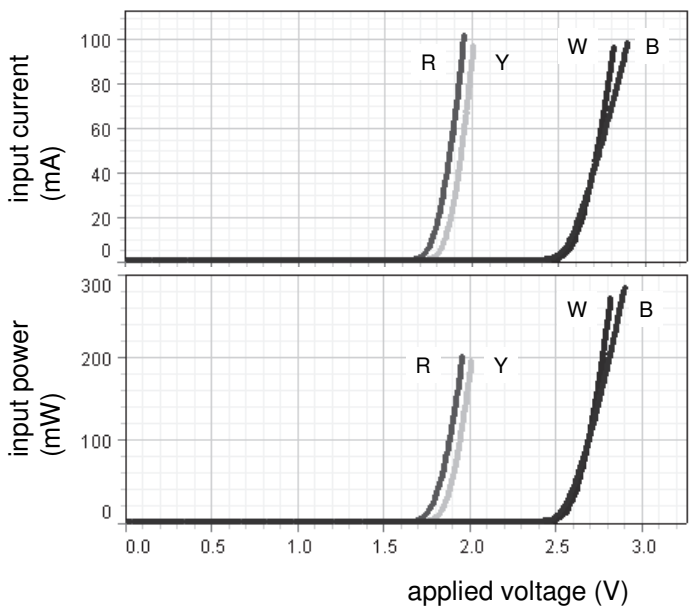

Fig. 2. Input current and power consumed by the LEDs versus the applied voltage. R–red, B–blue, Y–yellow, W–white-light.

To determine the radiant power of a LED, its light is directed onto a silicon photodiode (United Detector Technology, PIN-10D) positioned adjacent

to the LED. The sensitive area of the photodiode is about 1 cm in diameter, so that the light from the LED is almost fully utilized. The *Voltage sensor* acquires the voltage across a 100 Ω load resistor of the photodiode.

The output radiant power (radiant flux) of a LED is calculated from the photoelectric current and the spectral response $R(\lambda)$ of the photodiode, that is, the wavelength dependence of the ratio of the photodiode current I to the incident radiant power P. In the range 400–800 nm, the spectral response of a silicon photodiode can be represented as (λ is in nanometers)

$$I/P\ (\mathrm{A.W^{-1}}) = 1.2\times10^{-3}(\lambda - 300). \quad (1)$$

With minor modifications, Eq. (1) holds for all silicone photodiodes. This approach is not as precise as a measurement with a sensor based on the thermal action of absorbed light. However, it is much simpler and quite satisfactory for our purposes. *DataStudio* displays the output characteristics of a LED versus the input current (Fig. 3).

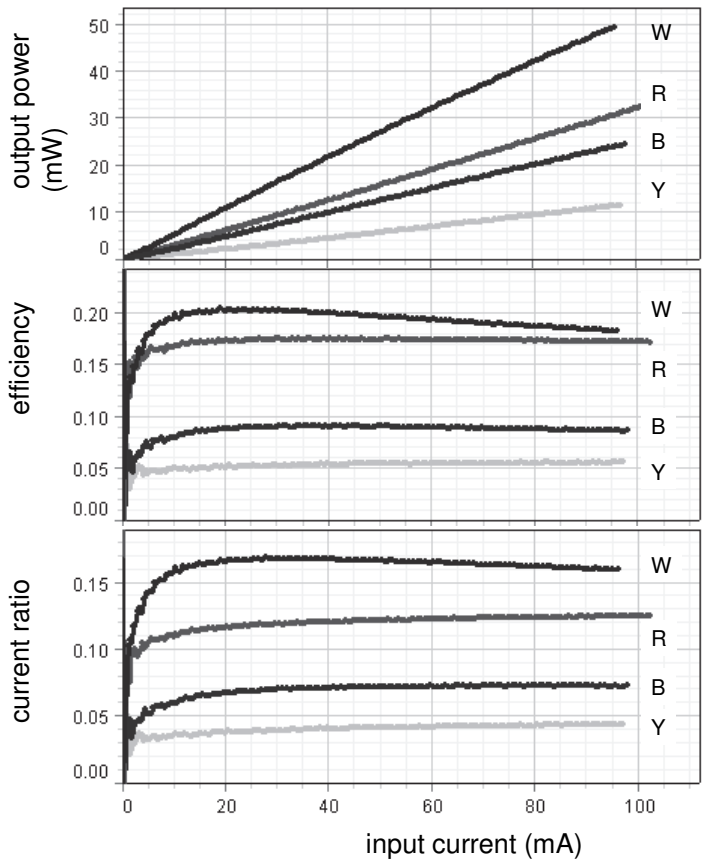

Fig. 3. Radiant output power, electrical efficiency, and current ratio versus input current.

The output radiant power is nearly proportional to the input current, and thus the rapid increase of the input current or power indicates the threshold of the LED emission. For the color LEDs, the wavelengths for Eq. (1) are taken to be at the peaks of the radiant power spectra (see below). For the white LED, the mean wavelength is taken as 550 nm. This simplification introduces an additional uncertainty to the results. For 100 mA input currents, the output radiant power of the LEDs ranges from 13 mW (yellow) to 53 mW (white). The efficiency is the ratio of the output radiant power to the input electric power. This quantity ranges from 0.065 (yellow) to 0.19 (white). For currents in the range of 10–40 mA, the efficiency of the white LED is even somewhat higher.

In an ideal LED, every electron-hole recombination produces one output photon of energy nearly equal to the bandgap energy. The external quantum efficiency of such a device thus equals unity. Similarly, an ideal photodiode produces one electron for every incident photon, and hence its external quantum efficiency also equals unity. For a combination of two such devices, the current produced by the photodiode should be equal to the input current of the LED. For real devices, the current ratio shows how close is the LED–photodiode combination to this ultimate limit. The external quantum efficiency of LEDs is much lower than their internal efficiency because of the difficulty of extracting light from the device. The current ratio for our LEDs ranges from 0.045 (yellow) to 0.16 (white). Because the external quantum efficiency of a silicon photodiode is sufficiently high, the low values of the current ratio are caused mainly by the low external quantum efficiency of the LEDs.

Radiant power spectra. The emission spectra of the LEDs are determined with the *Educational spectrophotometer* (OS-8537) with two lenses and a diffraction grating with 600 lines per millimeter. The *Light sensor* (CI-6504A) and the *Aperture bracket* (OS-8534A) are also used. Initially, the sensor is set at the zero diffraction angle. With the *Delayed start* and *Automatic stop* options, the measurement data are acquired in the wavelength range from 350 to 750 nm. The spectra may be distorted because the efficiency of diffraction gratings depends on wavelength; for the grating we use, this dependence is unknown.

The emission spectra corrected by the use of Eq. 1 are radiant power spectra (in arbitrary units). The spectra of the color LEDs have one peak near the center of the emission band: 465 nm (blue), 585 nm (yellow), and 625 nm (red). The full width of the spectra at half a maximum is nearly 30 nm (Fig. 4).

The radiant power spectrum of the white LED has a peak in the blue band and a wide green-yellow phosphorescence band with a maximum at 555 nm. To make the phosphorescence evident, it is sufficient to illuminate the LED by blue light from outside. This observation confirms that the LEDs can be used for observing phosphorescence spectra. For instance, when we focus the light from the blue LED on the screen of a cathode-ray tube, the spectrum of the phosphorescence is observable by looking at the screen through a diffraction grating. The spectrum can be compared with the cathodoluminescence spectrum of the screen (Kraftmakher 2009a).

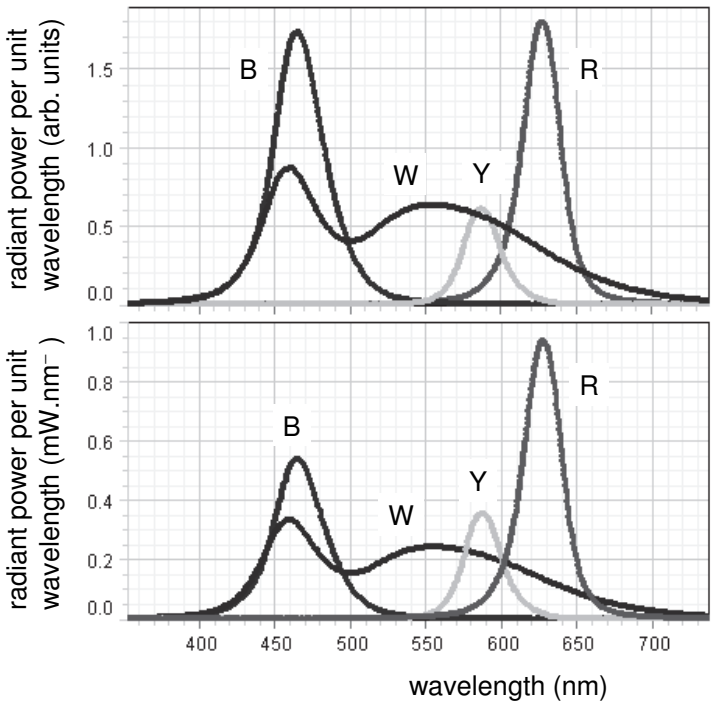

Fig. 4. Radiant power spectra of the LEDs.

To calculate the true radiant power spectra of the LEDs, the radiant power spectrum of each LED (in arbitrary units) is integrated over all wavelengths with *Origin* software. Then each spectrum is normalized to make the integral equal to the output radiant power of the LED determined with the silicon photodiode. This operation provides the true radiant power spectrum, that is, the wavelength dependency of the radiant power per unit wavelength, $P_\lambda(\lambda)$ (mW.nm^{-1}).

LEDs for lighting. The radiant power spectrum is an insufficient characteristic of a lighting source because the human eye is not equally sensitive to the light of different colors. Its typical spectral response is given by the **standard luminosity function** $S(\lambda)$ established by the International Commission on Illumination. For light-adapted vision, this function has a maximum at 555 nm and can be approximated by a simple equation proposed by Agrawal *et al* (1996):

$$S(\lambda) = \exp(-88x^2 + 41x^3), \tag{2}$$

where $x = \lambda/555 - 1$, and λ is the wavelength in nanometers. For our aim, this approximation is satisfactory; however, the original numerical data should be used for precise calculations. The spectral response of the human eye is a crucial factor for providing effective and qualitative (similar to daylight) lighting. The

two requirements are in obvious contradiction: qualitative lighting requires blue and red bands, which are ineffective due to the properties of human vision.

Initially, the base unit of luminous intensity, the **candela** (cd), was based on a "standard candle." The present-day definition of this unit adopted in 1979 says: "The candela is the luminous intensity, in a given direction, of a source that emits monochromatic radiation of frequency 540×10^{12} hertz and that has a radiant intensity in that direction of 1/683 watt per steradian." The above frequency corresponds to $\lambda = 555$ nm, while the factor 1/683 was chosen to match the previous definition of the candela. The lumen (lm) is defined as 1 lm = 1 cd.sr. A light source of one candela provides a total luminous power (luminous flux) of $4\pi \cong 12.57$ lm. By definition, one watt of electromagnetic radiation at $\lambda = 555$ nm produces a luminous power of 683 lm. The ratio of the total luminous power from a light source to the electric power consumed (the lumen-to-watt ratio) is called the **luminous efficacy**. The maximum possible efficacy of a light source thus equals 683 $\mathrm{lm.W^{-1}}$, while much lower values should be expected when the emission includes blue and red optical bands.

The **luminous power spectrum**, that is, the wavelength dependence of the luminous power per unit wavelength, $F_\lambda(\lambda)$ ($\mathrm{lm.nm^{-1}}$), is the radiant power spectrum times the standard luminosity function $S(\lambda)$ and 683 ($\mathrm{lm.W^{-1}}$). This conversion significantly changes the spectra (Fig. 5).

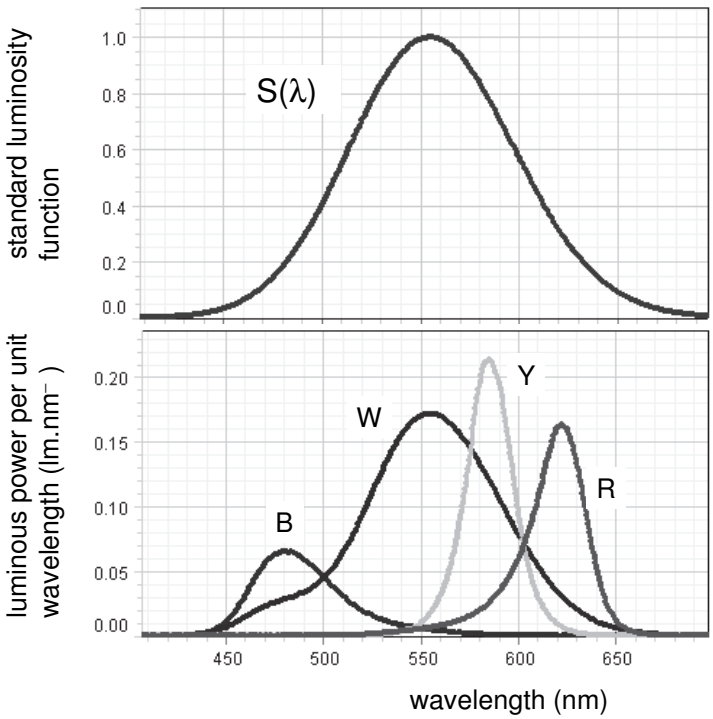

Fig. 5. Standard luminosity function, and luminous power spectra of the LEDs.

The luminous power spectrum of the white LED has only one maximum at 555 nm; however, the blue emission is evidently stressed. The total luminous power F is available by integrating the luminous power spectrum:

$$F\ (\mathrm{lm}) = \int_0^\infty F_\lambda(\lambda)\ \mathrm{d}\lambda. \qquad (3)$$

The integration is performed with *Origin* software. Among our LEDs, the white LED produces the maximum luminous power of nearly 15 lm.

The luminous efficacy of the LEDs appeared to be 33 (red), 33 (yellow), 12 (blue), and 55 $\mathrm{lm.W^{-1}}$ (white). The supplier gives values of the applied voltage and the total luminous power of the LEDs and their tolerances. With mean values of the supplier's data, the efficacy should be 32 (red), 34 (yellow), 11 (blue), and 67 $\mathrm{lm.W^{-1}}$ (white). The agreement between the two sets of data shows that our experiments are free of significant errors. The luminous efficacy is in the range 10–20 $\mathrm{lm.W^{-1}}$ for incandescent lamps and 30–110 $\mathrm{lm.W^{-1}}$ for fluorescent lamps (Mayer 2010).

Modulation characteristic. The frequency response of LEDs is very important for optical communications. Infrared light is commonly used with optical fibers. For teaching purposes, modulated LEDs have been employed in a simple telemetric system (Kraftmakher 2003) and for transmitting video signals through a light guide (Kraftmakher 2008d).

In the setup for measuring the frequency response, a DC supply and a Hewlett–Packard 33120A function generator, each with an additional 100 Ω resistor at the output, are connected in parallel to the LED. The output voltage of the DC supply is set to obtain a 100 mA current through the LED. With two lenses, the light from the LED is focused on the sensitive area of a fast photodiode (United Detector Technology, PIN-5D) operated with a 9 V battery. The signal across a 150 Ω load resistor of the photodiode is observed with a Kenwood CS-4025 oscilloscope. The AC voltage applied to the LED is sufficiently small, and the AC signal from the photodiode is nearly sinusoidal. In the range of 10–10^7 Hz, the characteristics are similar for all the LEDs tested. The frequency response is constant up to 10^3 Hz, slightly decreases up to 10^6 Hz, and then rapidly falls. Because the LEDs have an internal resistance, capacity, and even inductance (Minh *et al* 2008), the actual voltage across the *p-n* junction is unknown and becomes frequency dependent at high frequencies. The data shown relate to the AC voltage at the output of the function generator (Fig. 6).

By measuring the frequency response, it is possible to distinguish the primary blue emission and the green-yellow phosphorescence of the white LED. The two optical bands are separated with color filters, and the frequency response for each band is determined separately. The time constant of the phosphor is very short, and the phosphorescence well follows the primary light up to about 10^6 Hz. From the data obtained, only a rough estimation of the time constant of the phosphor is possible; it is of the order of 10^{-8} s.

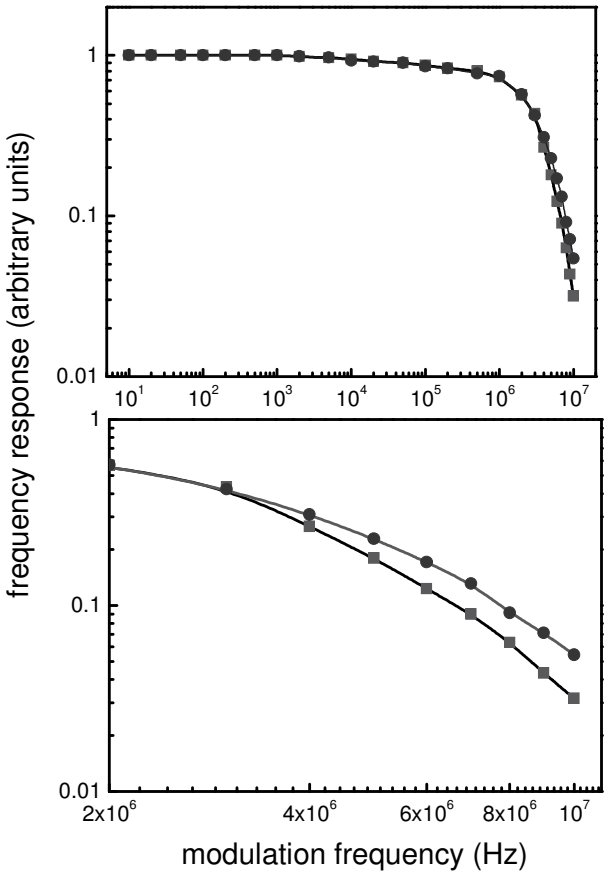

Fig. 6. Frequency response (arbitrary units) of the white-light LED: ● primary blue band, ■ green-yellow phosphorescence.

The h/e ratio. Optical emission from LEDs appears when the applied voltage reaches a definite value V_F, the forward **"turn-on" voltage**. This threshold is assumed to be close to V_g. By taking the energy of emitted photons equal to eV_F or eV_g, it is possible to determine the h/e ratio by a simple experiment. With LEDs of different color, results obtained in such experiments are close to the correct value, usually, within ±10% limits (O'Connor and O'Connor 1974; Nieves *et al* 1997; Zhou and Cloninger 2008). This approach raises doubts (Herrmann and Schätzle 1996; Holcomb 1997; Morehouse 1998) because of the assumptions that are made. It was shown experimentally (Precker 2007) that the energies of photons emitted by four color LEDs were by 7%–20% smaller than the bandgap energies, and the "turn-on" thresholds appeared to be significantly lower than the photon energies. Precise values of the h/e ratio cannot be expected from such measurements, but it is worth looking for LEDs providing

results close to the true value. In any case, students performing this experiment should be familiarized with the problem. An additional decision is the appropriate wavelength to be used in the calculations. Usually, the wavelength relates to the peak in the radiant power spectrum. Because the peaks are 30–50 nm wide, the uncertainty may amount to several percent. Indelicato *et al* (2013) presented an analysis of the measurement of Planck's constant.

We used the relation $h/e = V_F\lambda/c$. The V_F values are found by linearly extrapolating to zero the plots of input current versus applied voltage shown in Fig. 2; the uncertainty of V_F values is nearly 0.05 V. The wavelengths λ were taken at the peaks in the radiant power spectra shown in Fig. 4, and the uncertainty of these values is nearly 10 nm. For the white LED, the wavelength is taken at the peak in the blue part of the spectrum. However, the validity of the relation based on the "turn-on" voltage remains doubtful. For our LEDs, the calculated h/e values appeared to be lower than the true value; the blue and white LEDs provide the best results. All the parameters of the LEDs found in the present experiments are given in Table 1.

Table 1. Parameters of the LEDs for 100 mA input currents. The frequency $f_{0.5}$ corresponds to 50% response; $h/e = V_F\lambda/c$.

LED	red	yellow	blue	white
λ (nm)	625	585	465	460
V_F (V)	1.8	1.85	2.6	2.6
Input power (mW)	185	200	290	280
Output power (mW)	32	13	37	53
Efficiency	0.17	0.065	0.13	0.19
Luminous power (lm)	6.15	6.6	3.6	15.5
Efficacy ($lm.W^{-1}$)	33	33	12	55
$f_{0.5}$ (MHz)		≈ 3		
h/e (10^{-15} J.s.C^{-1})	3.75	3.60	4.05	4.00

7.9. Optical properties of semiconductors

The aim of the optical measurements is to determine the bandgap energy of some semiconductors.

Additional equipment: *Educational spectrophotometer*, *Rotary motion sensor*, *Broad spectrum light sensor*, diffraction grating, lenses, light bulb, samples, polarizer.

Transmittance spectra. A common setup is used for recording transmission spectra of some semiconductors. It includes the *Educational spectrophotometer* and the *Broad spectrum light sensor* (Fig. 1). The samples are placed in front of the light sensor. The arm with a light bulb and diffraction grating is manually rotated, and the rotation angle is determined with the *Rotary motion sensor*. A screen prevents the light sensor from stray light.

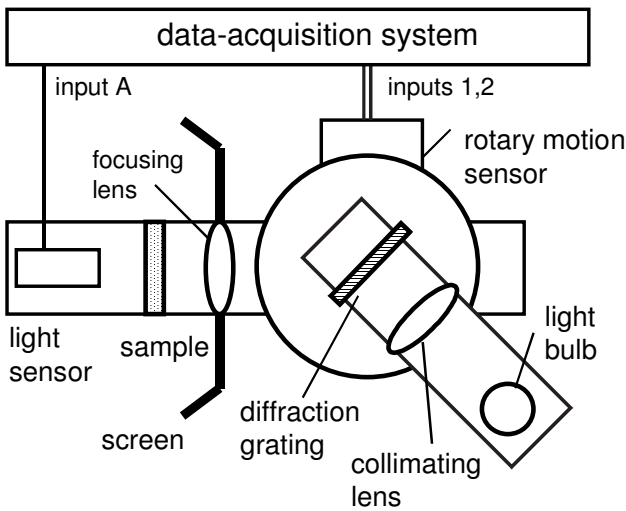

Fig. 1. Schematic of setup for recording transmittance spectra.

Photons with energies equal or more than the bangap energy may cause transitions of electrons to the conductivity band, and they are well absorbed by the material. The optical absorptance rapidly increases with decreasing the wavelength. In contrast, photons with energies less than the bangap energy cannot be absorbed by the material, and pass through the material. Transmittance spectra of semiconductors clearly show the boundary between the two possibilities. An interval of about 100 nm is sufficient for dramatically changing the optical transmittance. *DataStudio* displays the transmittance of the samples, GaAs (0.5 mm thick) and silicon (0.8mm thick), versus the wavelength (Fig. 2).

The boundary wavelength λ_0 can be taken as the wavelength of a transmittance that equals half the maximum transmittance. In our case this wavelength equals nearly 920 nm for GaAs and 1130 nm for silicon. As a first approximation, we can assume the bandgap energy to be equal to energies of photons of wavelength λ_0. With this assumption, the energies appeared to be nearly 1.35 eV for GaAs and 1.1 eV for silicon.

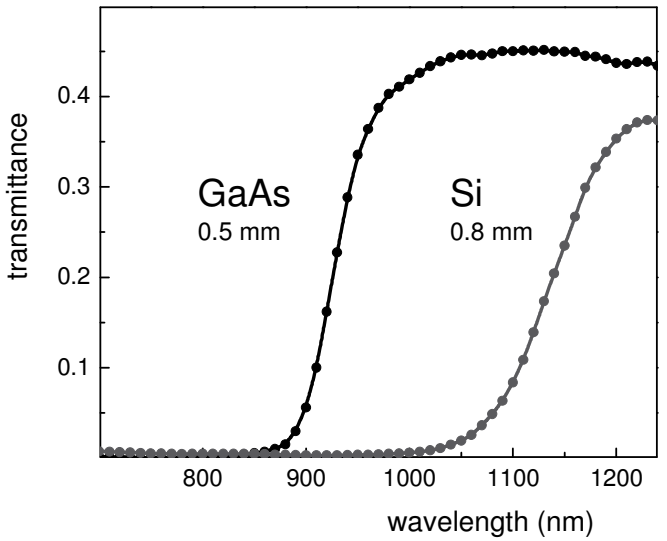

Fig. 2. Transmittance spectra of GaAs and silicon samples.

7.10. Noise in semiconductors

The spectrum of electrical fluctuations in a light dependent resistor (photoresistor) is demonstrated.

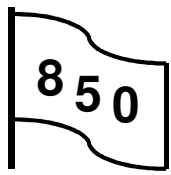

Additional equipment: *Voltage sensor*, photoresistor, DC supplies, light bulb.

Spontaneous fluctuations in current/voltage, which are called **noise**, are common for all electronic devices. In semiconductors, the most important sources of noise are thermal noise, shot noise, generation-recombination noise, and flicker noise (1/*f* noise).

Thermal noise is a fundamental physical phenomenon caused by random thermal motion of charge carriers in a conductor. It is also known as **Johnson's noise**. The spectral density of thermal noise depends only on the resistance R of the conductor and its absolute temperature T; and is constant in a wide frequency band. For this reason, thermal noise is called "white noise." This noise unavoidably presents in any conductor at temperatures above the absolute zero. The mean noise voltage across the conductor is zero, but the mean noise voltage squared, according to **Nyquist's formula**, is a very definite value equal to

$$<\Delta V_{th}^2> = 4k_B TR\Delta f, \quad (1)$$

where Δf is a narrow frequency bandwidth, in which the noise is measured. This is a strict relation allowing for determinations of the absolute temperatures (see Experiment 3.11).

Shot noise is caused by the discrete structure of electricity. When passing a potential barrier, every electron induces in the circuit an electrical pulse. If the interaction between electrons is negligible, these pulses are uncorrelated, which leads to another "white noise" depending on the current I and electron charge e:

$$<\Delta I_{sh}^2> = 2eI\Delta f. \quad (2)$$

This is also a strict relation allowing for determinations of the electron charge (see Experiment 9.1).

Generation-recombination noise is a result of fluctuations in the number of carriers in semiconductors due to the existence of generation-recombination centers. The fluctuations in the carrier density lead to fluctuations in the conductivity of the semiconductor. The spectral density of the noise $S_{g\text{-}r}$ depends on the biasing conditions and frequency:

$$S_{g\text{-}r}(f) = <\Delta N^2>4\tau/(1 + 4\pi^2 f^2 \tau^2), \quad (3)$$

where $<\Delta N^2>$ is the variance of the number of carriers N, and τ is the carrier lifetime.

Flicker noise is associated with defects in the material and is present in all semiconductor devices under biasing. Its spectral density follows a 1/*f* law, so the flicker noise dominates at low frequencies.

In the demonstration, *Capstone* displays the spectral density of the noise of a usual photoresistor (light dependent resistor) by using the *Fast Fourier Transform* tool (*FFT*). The setup for the demonstration is very simple (Fig. 1). The sample with a load resistor is connected to a DC supply (40 V) and illuminated by a light bulb fed by another DC supply (not shown in Fig. 1). The load resistor, 100 Ω, is much smaller than the resistance of the sample under illumination. Therefore, the noise voltage across the load is governed by the current noise in the sample. The voltage across the load is observed with an oscilloscope, which serves also as an amplifier. The *Voltage sensor* acquires the amplified voltage. The run lasts 1 s. The sensitivity of the setup is insufficient for observing the thermal noise.

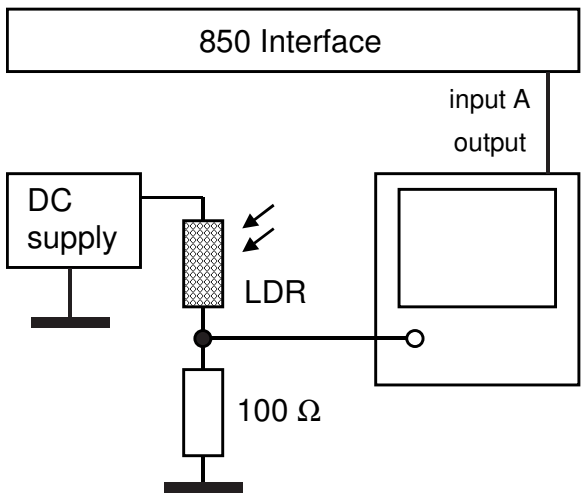

Fig. 1. Schematic of the setup for determining the spectral density of the noise of an LDR.

The results obtained (Fig. 2) are in agreement with the theory. The spectral density of the noise increases with decreasing frequency. However, it is difficult to separate the flicker noise and the generation-recombination noise. Along with regular frequency dependence, single peaks are seen in the spectral density. They relate to the main frequency (50 Hz) and its harmonics.

The demonstration is also a confirmation of the usefulness and power of the Fourier transform technique: single frequency components are seen despite a strong continuous background.

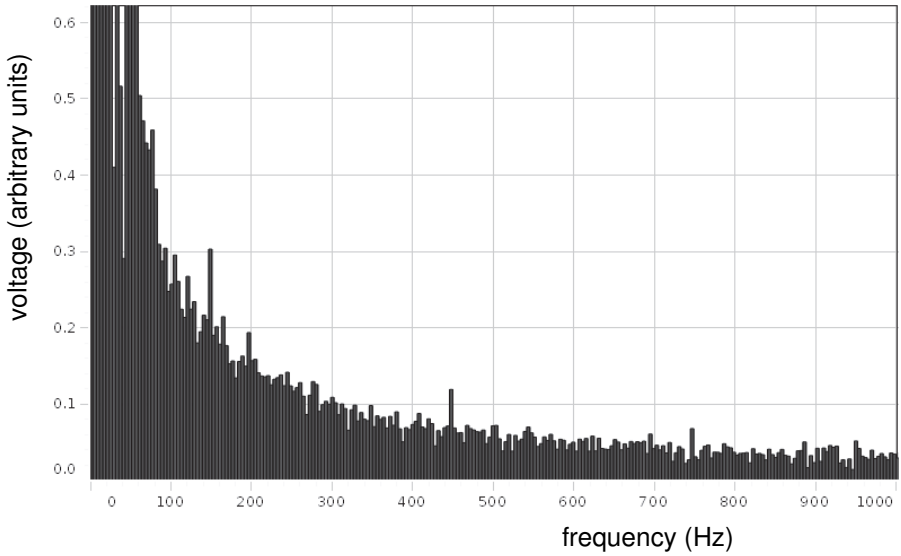

Fig. 2. Spectral density of the noise displayed by *Capstone*.

Applied Physics

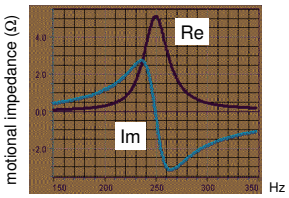

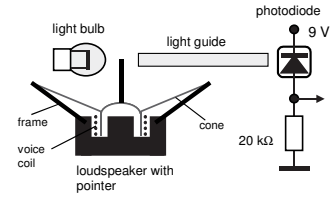

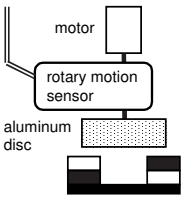

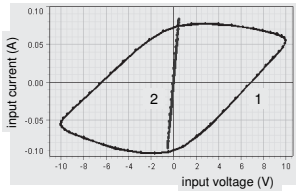

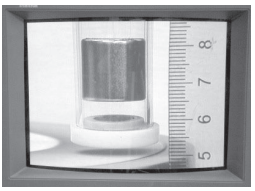

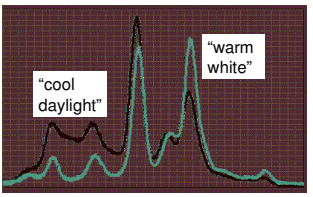

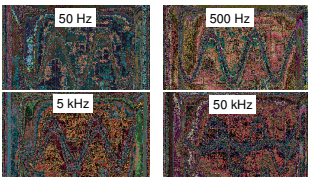

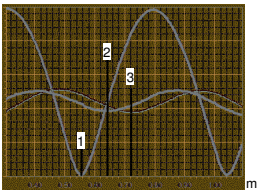

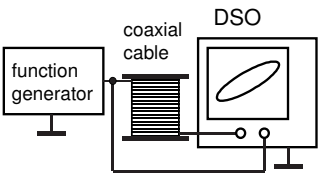

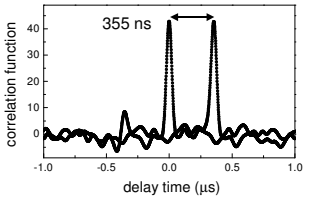

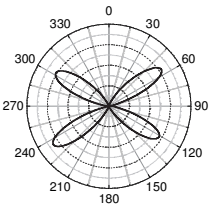

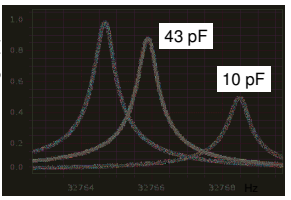

8. Applied Physics 493

8.1. Loudspeaker I

Three items are included: (i) the free oscillations; (ii) the forced oscillations and transients; and (iii) the frequency response and motional impedance. A simple optical device senses oscillations of a loudspeaker (Kraftmakher 2009c).

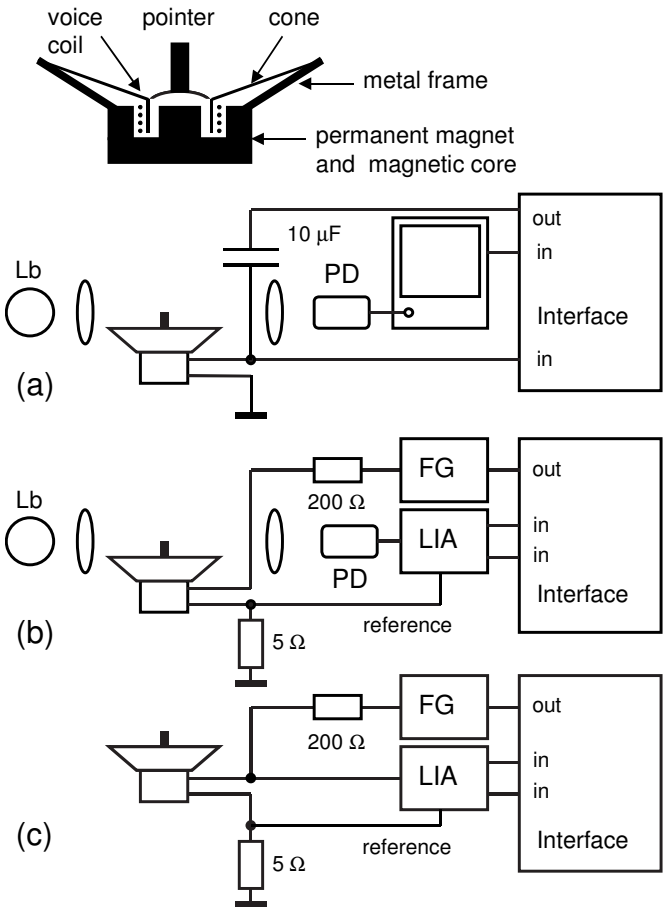

Fig.1. General scheme of the experiments: (a) free oscillations; (b) forced oscillations and frequency response; (c) motional impedance. FG–function generator, PD–photodiode, LIA–lock-in amplifier, Lb–light bulb.

Theoretical background. A moving-coil (dynamic) loudspeaker is a resonant system very suitable for learning harmonic motion. Several papers concerning this topic are mentioned here. Tan (1982) measured the electrical impedance of a loudspeaker in the vicinity of the resonance and under various loading conditions. Fishman (1987) determined the real and imaginary parts of the

loudspeaker impedance. Diamond *et al* (1990) observed the loudspeaker oscillations with a Michelson interferometer. The oscillation amplitude and the phase relationship between the driving force and the displacement were determined. Freschi *et al* (2003) measured the oscillations of a loudspeaker using the Doppler shift technique. From the measurements, electrical and mechanical parameters of the loudspeaker were derived.

A moving-coil loudspeaker consists of a stiff and light diaphragm (a cone) suspended from a rigid metal frame. A **voice coil** is attached to the cone and positioned in a strong magnetic field of a permanent magnet. The magnet and a magnetic core are arranged such a way that the magnetic field B is radial and perpendicular to all parts of the wire in the voice coil (Beranek 1954; Busch-Vishniac and Hixson 1991; Keeney and Hershey 1997; Galeriu 2010). According to Lorentz's force equation, the forces exerting on all parts of the voice coil are directed along the axis of the cone. The total force equals Bli, where i is a current passing through the voice coil, and l is the total length of the wire in the coil. With an AC current $i = i_0\cos\omega t$, the driving force is periodic:

$$F = Bli_0\cos\omega t. \tag{1}$$

When an AC current passes through the voice coil, the cone generates sound waves. At low frequencies, the cone moves as a whole. Oscillations of the voice coil in the magnetic field generate a **back EMF**, whose amplitude and phase should be taken into account when considering the **electrical impedance** of a loudspeaker. When a conductor moves with a velocity $\boldsymbol{v}$ in a magnetic field $\boldsymbol{B}$, the magnetic force $\boldsymbol{F}_\mathrm{m} = q\boldsymbol{v}\times\boldsymbol{B}$ causes the free movable electrons in the conductor to drift toward one end of the conductor. An electric field $\boldsymbol{E}$ appearing along the wire balances the action of the magnetic force: $\boldsymbol{E} = \boldsymbol{v}\times\boldsymbol{B}$. This is a particular case of Faraday's law of electromagnetic induction, which is called the **motional induction** (Saslow 1987, Cheng 1992, Kraus and Fleisch 1999). In a loudspeaker, the voice coil moves perpendicular to the magnetic field, and the wire is perpendicular to the field and to the motion. Therefore, the back EMF in the voice coil is proportional to the total length of the wire in the coil: $\boldsymbol{e} = Bl\boldsymbol{v}$. The oscillations of the cone are considered harmonic: $x = x_0\sin\omega t$, and $v = x' = \omega x_0\cos\omega t$, where x is the displacement of the coil. The back EMF equals

$$\boldsymbol{e} = Bl\boldsymbol{x}' = \mathrm{j}\omega Blx, \tag{2}$$

where j indicates an imaginary part. Generally, the quantities i, F, x, and v are complex. Here, F and i coincide in phase, and their initial phase can be taken zero. The phases of x and v relative to i depend on the frequency. The direction of the driving force along the axis of the cone alters on switching the terminals of the loudspeaker. Setups used in the experiments are shown in a general scheme (Fig. 1). Mechanical parameters of a loudspeaker cone can be taken into account by common equations for a harmonic oscillator (Kibble and Berkshire 1996, Thornton and Marion 2004). For free oscillations,

$$x'' + 2\gamma x' + \omega_0^2 x = 0, \tag{3}$$

where x'' is the acceleration of the cone, $\omega_0 = (k/m)^{1/2}$ is the **natural angular frequency** of the oscillator, m is the mass of the cone, and k and γ are constants. The solution to this equation is

$$x = A\exp(-\gamma t)\cos(\omega_1 t + \varphi), \tag{4}$$

where $\omega_1^2 = \omega_0^2 - \gamma^2$, and A and φ depend on **initial conditions**. It is supposed that $\gamma^2 << \omega_0^2$. For damped oscillations, the phase shift between the displacement and velocity is somewhat smaller than 90^o. The quality factor of an oscillator is $Q = \omega_0/2\gamma$. For forced oscillations, with $F = Bli$,

$$x'' + 2\gamma x' + \omega_0^2 x = Bli/m. \tag{5}$$

The steady-state solution to this equation is the **complex displacement** $\boldsymbol{x}$:

$$\boldsymbol{x} = Bli/[m(\omega_0^2 - \omega^2 + j2\gamma\omega)]. \tag{6}$$

The frequency response $\boldsymbol{x/i}$ of the loudspeaker is a complex quantity:

$$\boldsymbol{x/i} = (Bl/m)a - j(Bl/m)b, \tag{7}$$

where $a = (\omega_0^2 - \omega^2)/[(\omega_0^2 - \omega^2)^2 + 4\gamma^2\omega^2]$, and $b = 2\gamma\omega/[(\omega_0^2 - \omega^2)^2 + 4\gamma^2\omega^2]$. The phase shift θ between the displacement and the driving force is

$$\theta = \arctan[-2\gamma\omega/(\omega_0^2 - \omega^2)]. \tag{8}$$

The negative values of θ correspond to the displacements lagging the force. A 90^o phase lag occurs at $\omega = \omega_0$. At higher frequencies, $\tan\theta$ becomes positive; this means that the lag exceeds 90^o. The **modulus** of the frequency response of the loudspeaker is

$$x/i = Bl/m[(\omega_0^2 - \omega^2)^2 + 4\gamma^2\omega^2]^{1/2}, \tag{9}$$

and the phase angle of the response is θ.

For $\omega^2 << \omega_0^2$, the response contains only a real part, $Bl/m\omega_0^2$. For $\omega^2 >> \omega_0^2$, the response becomes inversely proportional to the frequency squared. The maximum response is achieved at $\omega^2 = \omega_0^2 - 2\gamma^2$. At this frequency, it equals $Bl/2m\gamma\omega_0$, and $\tan\theta$ becomes $-\omega_0/\gamma$. When a voltage V is applied to the voice coil, the current depends also on the back EMF:

$$\boldsymbol{i} = (\boldsymbol{V} - \boldsymbol{e})/\boldsymbol{Z}_E, \tag{10}$$

where $\boldsymbol{Z}_E$ is the usual electrical impedance. The current can be presented as

$$\boldsymbol{i} = \boldsymbol{V}/(\boldsymbol{Z}_E + \boldsymbol{Z}_{mot}), \tag{11}$$

where $\boldsymbol{Z}_{mot} = \boldsymbol{e/i}$ is an additional impedance due to the loudspeaker vibrations; it is called the **motional impedance**. With the same a and b as in Eq. (7), it equals

$$\boldsymbol{Z}_{mot} = j\omega Bl\boldsymbol{x/i} = (B^2l^2\omega/m)b + j(B^2l^2\omega/m)a. \tag{12}$$

The modulus of the motional impedance is

$$Z_{mot} = B^2l^2\omega/m[(\omega_0^2 - \omega^2)^2 + 4\gamma^2\omega^2]^{1/2}. \tag{13}$$

The setup. We use a loudspeaker of 9 cm in diameter. The resistance of its voice coil is 8 Ω, and the nominal power 1 W. An optical method is used for observing oscillations of the loudspeaker cone. A light rectangular pointer made out of a metal foil is pasted to the cone at its center. The pointer is 20 mm in height and 5 mm in width. It is illuminated, with a condenser lens, by a light bulb fed by a DC supply. With a second lens, a magnified image of the pointer edge is focused onto the sensitive area of a photodiode. The photodiode (United Detector Technology, PIN-10D) has a circle sensitive area of about 1 cm in diameter. A shield forms a rectangular window to the sensitive area. The load resistance of the photodiode is 20 kΩ. The photodiode, its load resistor, and a 9 V battery are placed in a metal box. The AC component of the voltage across the load resistor is seen on the screen of a GOS-622G oscilloscope, which serves also as an amplifier. This method is much simpler than those involving interferometric techniques, and the phase of the loudspeaker oscillations is seen. The EMF generated in the voice coil is proportional to the velocity of the oscillations and the quantity *Bl* and is used for measuring free oscillations of the cone triggered by a short electrical pulse applied to the voice coil. For calibration purposes, the loudspeaker rests on a laboratory jack, whose displacement is controlled by a dial indicator of 0.01 mm resolution. The characteristic is linear (Fig. 2).

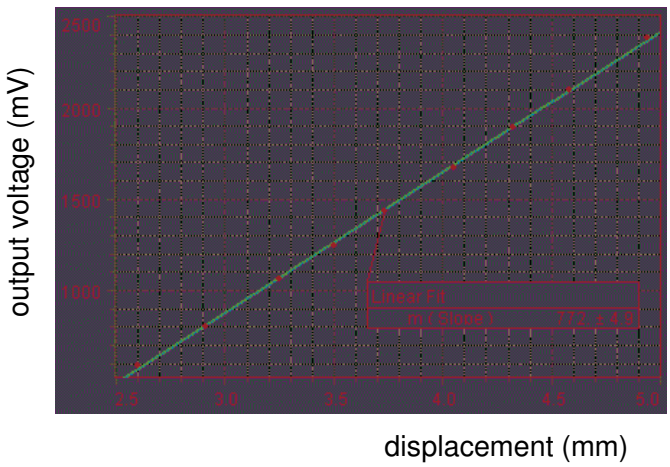

Fig. 2. Results of calibration: the sensitivity is 770 mV.mm^{-1}.

The sensitivity depends on the illumination, so that the calibration should be done under the measurement conditions. In further measurements, one can control the sensitivity by reproducing measurements of the loudspeaker oscillations at a selected frequency. The calibration process causes no doubts, but the main parameters (ω_0, γ, k, m, Q) are obtainable without knowing absolute values of the displacement; these values are necessary only for determining the quantity *Bl*.

1. Free oscillations

Electrical pulses obtained by differentiating a 5 Hz *Square wave* voltage from the *Signal generator* trigger free oscillations.

Additional equipment: two *Voltage sensors*, loudspeaker, two lenses, photodiode, light bulb, resistors, capacitor.

Phase portrait of free oscillations. The AC signal from the photodiode is amplified by the oscilloscope and acquired by *DataStudio*, which provides data on the velocity of the loudspeaker cone (Fig. 1a). A graph of the velocity versus the displacement is the phase portrait of the oscillations (Fig. 3). Shunting the voice coil enhances the damping of the cone. Due to the shunt, a current passes through the voice coil. According to Lenz's law, the interaction of this current with the DC magnetic field slows down the coil. In the example shown, one run is done without a shunt, and two others with a shunt (30 Ω and 10 Ω resistors). The shunting decreases the amplitude of the free oscillations and the decay time.

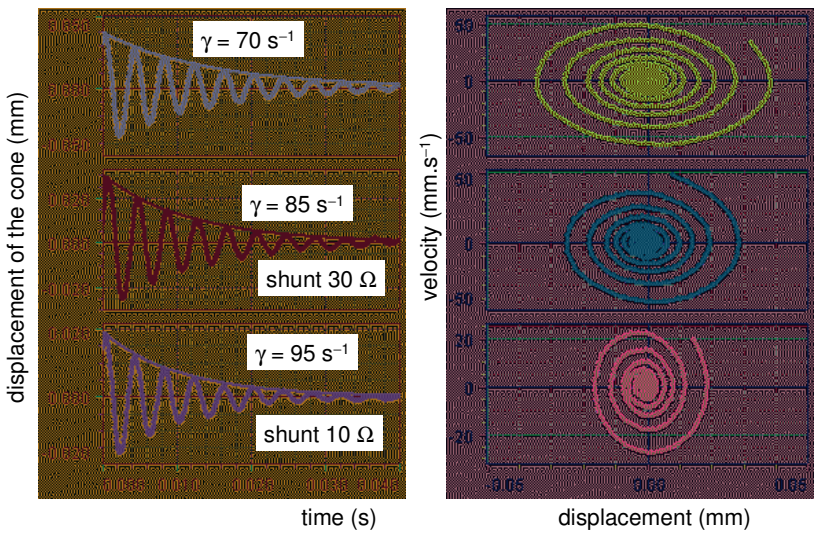

Fig. 3. Free oscillations and their phase portraits, data from the photodiode.

Ripples in the energy decay. Using an oscillator of low quality factor, it is possible to see that its energy does not decay smoothly, but includes considerable ripples (Karlow 1994; Basano *et al* 1996; Thornton and Marion 2004). When the frictional force is proportional to the velocity of the oscillator, the power of losses is proportional to the velocity squared and thus varies during a period. The energy losses are proportional to the integral of the velocity squared. The ripples in the energy decay become obvious for highly damped

systems. To show the ripples in the energy decay of the loudspeaker, *DataStudio* calculates the difference between the initial energy and the losses, both given in arbitrary units (Fig. 4). The initial energy is taken as the total energy decay.

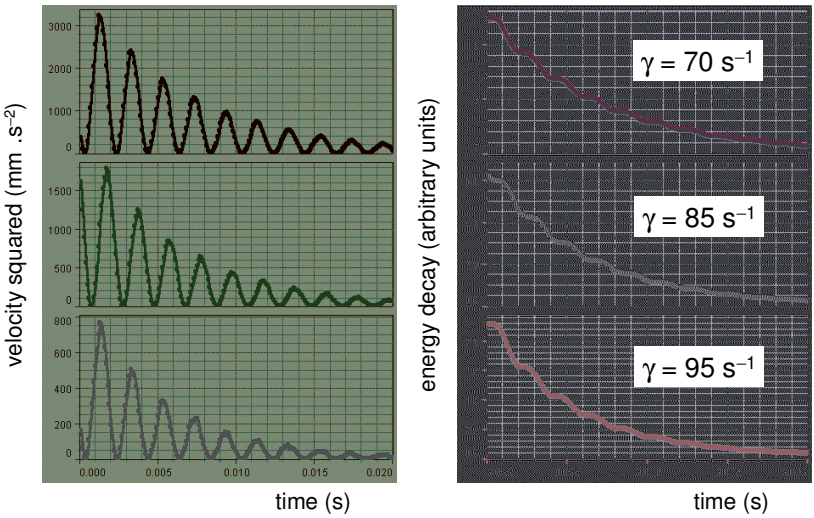

Fig. 4. Ripples in the energy decay are seen by integrating the velocity squared.

The Bl parameter is available by simultaneously measuring the EMF induced in the voice coil and the velocity of the cone. The *Voltage sensor* acquires the EMF, and the velocity is calculated by differentiating the optically determined displacement (Fig. 5). The envelopes to them are approximated by exponential decay functions with the same $\gamma = 70$ s^{-1}. From Eq. (2), $Bl = 1.13$ T.m.

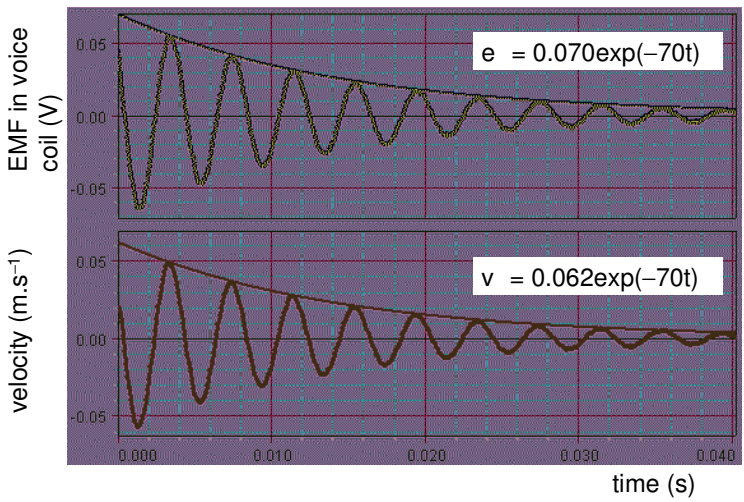

Fig. 5. Free oscillations: EMF in the voice coil and optically detected velocity.

2. Forced oscillations and transients

Forced oscillations and transients of the loudspeaker cone are observed.

Additional equipment: two *Voltage sensors*, loudspeaker, function generator, two lenses, photodiode, light bulb, resistors.

Phase relations between the current in the voice coil and the displacement of the cone are seen from Lissajous patterns displayed by *DataStudio* (Fig. 6). A GFG-8019G function generator connected to the voice coil through a 200 Ω resistor supplies the driving current (Fig. 1b). The photodiode sensing the oscillations of the cone is AC coupled to the oscilloscope, and the *Voltage sensor* acquires the amplified voltage. The second signal needed for graphing the Lissajous pattern is the voltage across a 5 Ω resistor put in series with the voice coil. The phase shift increases from about zero at low frequencies to about 180° at high frequencies; at $\omega = \omega_0$, it should be nearly 90°.

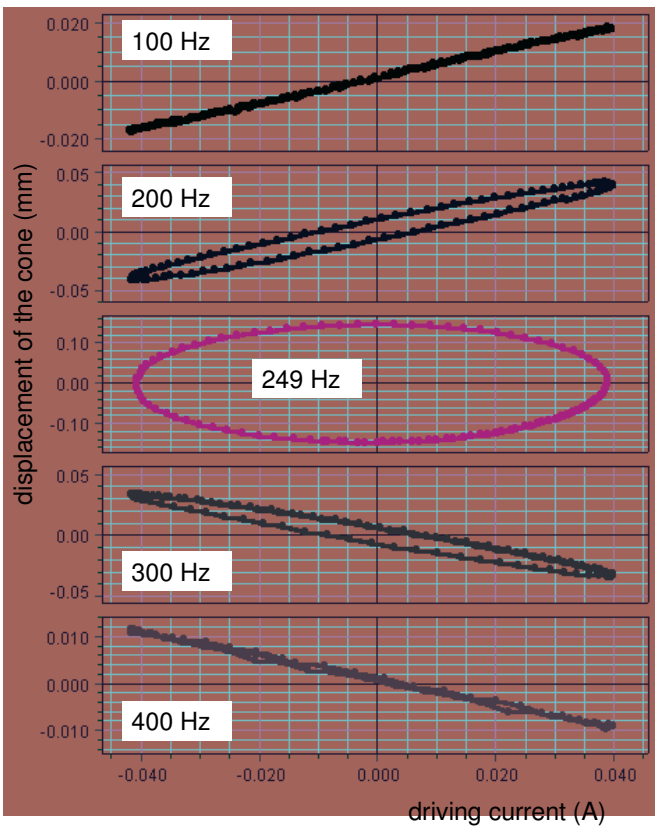

Fig. 6. Displacement versus driving current, for different frequencies.

The transients are seen after an AC driving force is applied to the voice coil. For these observations, the output voltage of the function generator is modulated by square wave voltage from the *Signal generator*. The controlling voltage is adjusted to obtain a 100% amplitude modulation of the function generator. The difference in transients for different frequencies of the driving force is evident (Fig. 7).

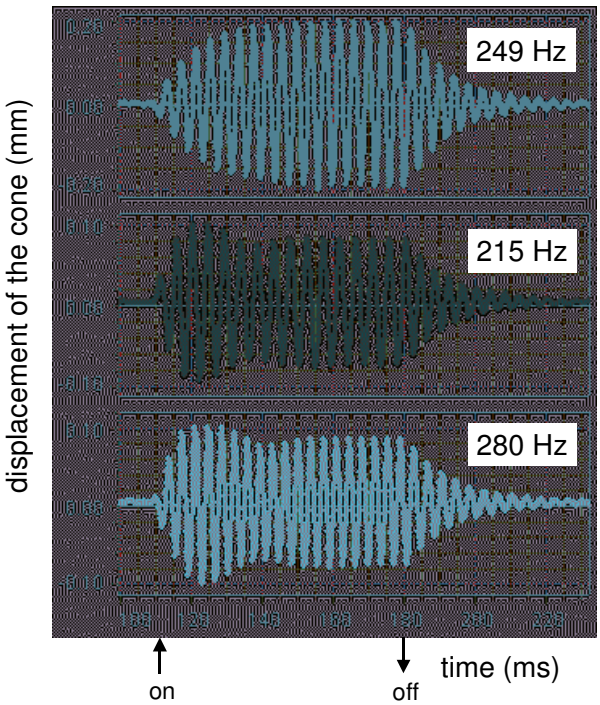

Fig. 7. Transients for different frequencies of the driving force.

Mass of the oscillating system including the cone and the voice coil can be determined by measuring the natural frequency of the cone when a known mass is added to it. For this purpose, a 1.26 g piece of plasticine, in the form of a ring, was pasted to the cone at its center. The additional mass decreases the natural frequency of the cone from 249 to 172 Hz. From the data, the mass of the cone equals m = 1.15 g.

3. Frequency response and motional impedance

The complex motional impedance of the loudspeaker is determined.

Additional equipment: two *Voltage sensors*, loudspeaker, function generator, lock-in amplifier, two lenses, photodiode, light bulb, resistors.

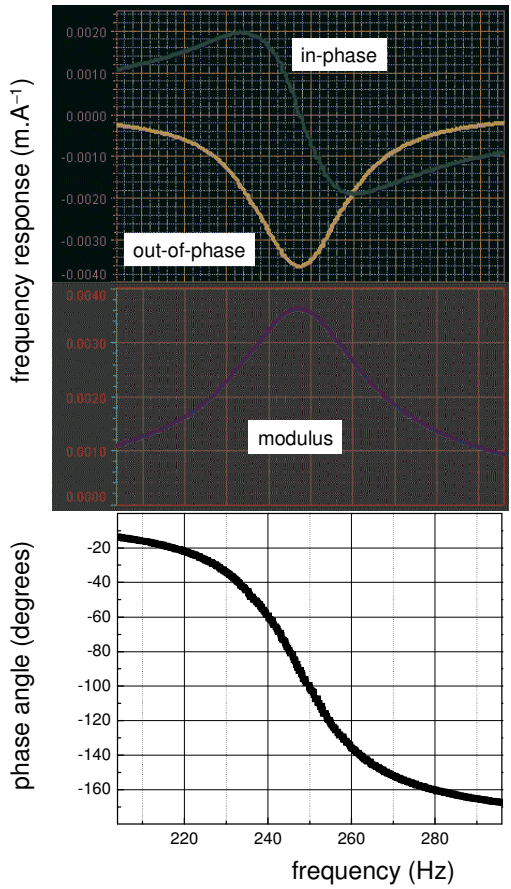

Fig. 8. Frequency response of loudspeaker: in-phase and out-of-phase parts of response, modulus, and phase angle of response.

Frequency response of the loudspeaker (Fig. 8) is recorded by continuously changing the frequency of the driving force (Fig. 1b). A two-phase Ithaco 3961 lock-in amplifier is used for automatically recording the in-phase and out-of-phase parts of the frequency response of the loudspeaker and of the modulus of the response. The loudspeaker is connected in series with a 5 Ω resistor and fed by the GFG-8019G function generator through a 200 Ω resistor, so that the

current in the voice coil weakly depends on the frequency. A voltage V applied to the VCF (voltage controlling frequency) input of the function generator governs its frequency. The *Signal generator* provides this 0.01 Hz ramp down wave voltage of 0.25 V amplitude. The initial frequency of the function generator provides a 90^o phase lag of the oscillations. One run lasts 100 s, and the frequency varies from about 200 to 300 Hz. *DataStudio* calculates the frequency f from the output voltage V of the *Signal generator*; in our case, the appropriate relation is f (Hz) = 249 – 200*V.

The AC voltage from the photodiode is amplified by the oscilloscope and proceeds to the lock-in amplifier. The current through the voice coil is determined from the voltage across the 5 Ω resistor. This voltage also serves as a reference for the lock-in amplifier. Two outputs of the amplifier provide RMS values of the in-phase and out-of-phase parts of the displacement of the cone. Two *Voltage sensors* acquire these voltages, and *DataStudio* calculates the in-phase and out-of-phase parts of the complex frequency response $\boldsymbol{x/i}$ and displays them versus frequency. The modulus and phase angle of the frequency response are also calculated and displayed. The tangent of the phase shift between the displacement and driving current is calculated as the ratio of the out-of-phase and in-phase parts of the displacement. When the phase lag exceeds 90^o, the tangent becomes positive, and *DataStudio* presents positive phase shifts. An intervention is therefore needed for obtaining the correct phase relationship: for frequencies $\omega > \omega_0$, 180^o should be subtracted from the calculated values. The *Origin* software is used for this purpose.

Total impedance. As in the previous measurements, the voice coil is connected in series with a 5 Ω resistor and fed by the GFG-8019G function generator through a 200 Ω resistor (Fig. 1c). The lock-in amplifier measures the RMS values of the real and imaginary parts of the voltage across the voice coil, while the frequency of the driving current gradually increases from 200 to 300 Hz. The two parts of the total electrical impedance are calculated by comparing the output voltages of the lock-in amplifier with the voltage across the 5 Ω resistor. This voltage serves also as the reference for the lock-in amplifier. The total impedance includes the resistance and inductance of the voice coil and the motional impedance of the loudspeaker (Fig. 9).

Motional impedance is determined by performing the measurements twice, when the cone is free to oscillate, and when it is fastened (Beranek 1954). To fasten the cone, a weight was placed on it. Two straight lines show the impedance of the fastened loudspeaker: the resistance of the voice coil is constant, while its inductance makes a contribution proportional to frequency. The motional impedance is the difference between the two results. Close to the resonance, the real part of the motional impedance becomes comparable to the resistance of the voice coil. This means that a significant part of the electrical power dissipated in the voice coil is consumed for generating sound waves. *DataStudio* calculates the modulus of the motional impedance.

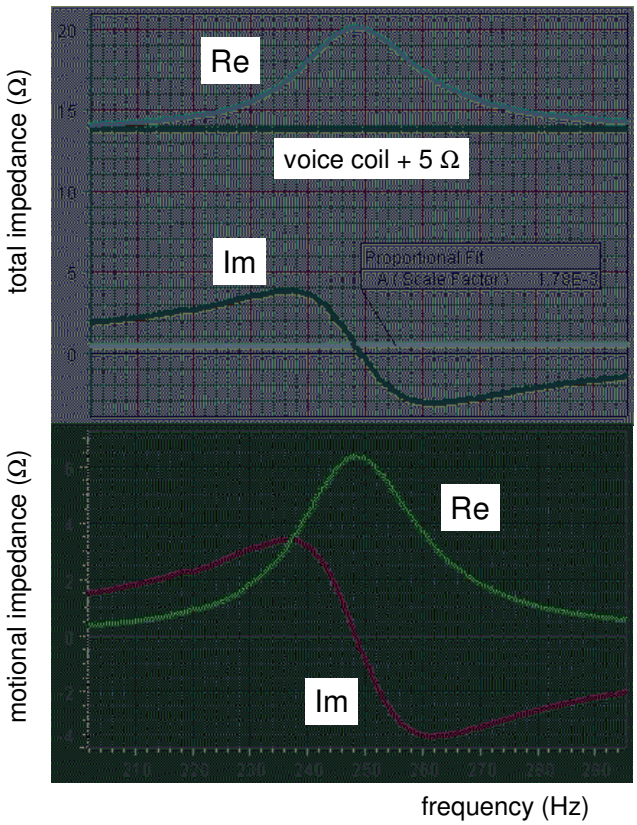

Fig. 9. Real and imaginary parts of the electrical impedance for the free and fastened cone, and of the motional impedance. Two straight lines show the impedance when the cone is fastened.

Parameters of the loudspeaker. The measurement data offer several ways to calculate parameters of the loudspeaker and thus to check the validity of the measurements. The natural frequency ω_0 equals the frequency of the driving force providing a 90^o phase lag of the displacement. In our case, $\omega_0 = 1564\ s^{-1}$. The mass of the cone m was determined from the change of the natural frequency when a known mass is added to the cone; it is $m = 1.15$ g. The coefficient $k = m\omega_0^2$ thus equals 2.8×10^3 N.m^{-1}. The parameter Bl determined from the free oscillations is 1.13 T.m. From the forced oscillations, by comparing the frequency response and the motional impedance of the loudspeaker, the value of Bl appeared to be about 1.1 T.m. The coefficient γ is available from the decay of free oscillations and from the width of the resonance curve. From the free oscillations, $\gamma \cong 70\ s^{-1}$ ($Q \cong 11$). From the fits to Eqs. (9) and (13), $\gamma \cong 75\ s^{-1}$ ($Q \cong 10$). This discrepancy is probably due to the shunting of the voice coil when observing the forced oscillations.

8.2. Loudspeaker II

The experiments include four items: (i) another design of the optical sensor for measuring the cone oscillations; (ii) the positive feedback and self-excited oscillations; (iii) determining the loudspeaker parameters without direct measurements of the cone oscillations; and (iv) the loudspeaker in a vacuum chamber (Kraftmakher 2010b).

The total impedance of the voice coil includes its usual electrical impedance and the **motional impedance**, which reflects the EMF generated in the oscillating voice coil. According to Faraday's law of induction, this EMF is $\boldsymbol{e} = Bl\boldsymbol{x}'$, where $\boldsymbol{x}'$ is the velocity of the cone; the phases of $\boldsymbol{e}$ and $\boldsymbol{x}'$ thus coincide. The motional impedance is a complex quantity $\boldsymbol{Z}_{\text{mot}}$, for which

$$\text{Re } Z_{\text{mot}} = 2B^2l^2\omega^2\gamma/m[(\omega_0{}^2 - \omega^2)^2 + 4\gamma^2\omega^2], \tag{1a}$$

$$\text{Im } Z_{\text{mot}} = B^2l^2\omega(\omega_0{}^2 - \omega^2)/m[(\omega_0{}^2 - \omega^2)^2 + 4\gamma^2\omega^2]. \tag{1b}$$

With a dual-channel lock-in amplifier, it is easy to display both parts of the electrical impedance of the voice coil as functions of frequency. Without such a device, we can display continually the modulus of the total impedance and determine its real and imaginary parts at discrete frequencies (see below). In our case, only the resistance R of the voice coil is significant, so that

$$Z_{\text{total}} = [(R + \text{Re } \boldsymbol{Z}_{\text{mot}})^2 + \text{Im } \boldsymbol{Z}_{\text{mot}}{}^2]^{½}. \tag{2}$$

The **mechanical** and **electrical parameters** of a loudspeaker are tightly connected, and the mechanical parameters are available through measurements of the frequency dependence of Z_{total}. Basic parameters of a loudspeaker are the mass of the cone m, the natural angular frequency ω_0, the decay constant γ, and the quantity Bl. They can be found from different experiments, but the most reliable values are those obtained with a simplest and direct measurement. It will be shown how to determine all the parameters, including Bl, without direct observations of the cone oscillations. We use a small loudspeaker, 9 cm in diameter (8 Ω, 1 W). A light rectangular pointer made out of a metal foil, 20 mm in height and 5 mm in width, is glued to the cone at its center and aligned to the axis of the cone. In all the experiments, the axis is oriented vertically. The loudspeaker rested on a laboratory jack can be gradually moved up and down.

The sensor of displacements of the cone consists of a low power light bulb (12 V, 5 W) and a plastic light guide, 3 mm in diameter (a thicker one would be better). Both are mounted on a frame such a way that the light guide acquires light from the light bulb and transmits it to a photodiode (Fig. 1). The loudspeaker is positioned to put the pointer between the light bulb and light guide. The pointer partly intercepts the light beam from the light bulb, so that the photodiode becomes sensitive to vertical displacements of the cone. To achieve

a linear response to the displacement, a rectangular window is set at the entrance to the light guide. When the cone oscillates, the AC output of the photodiode correctly represents the cone oscillations. The sensor can be arranged without a light guide, but the latter is useful for conveniently positioning the photodiode. The photodiode, its 20 kΩ load resistor, and a 9 V battery are placed in a metal box with an opening for the light guide. The sensitivity can be maintained by adjusting the current through the light bulb. The sensor is more simple and reliable than that employed in the preceding experiment.

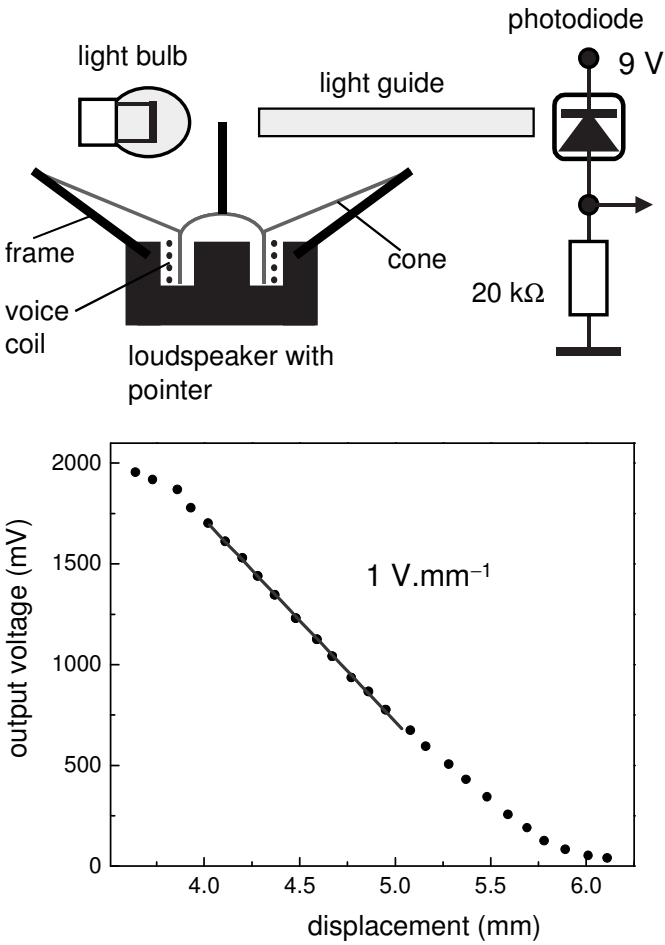

Fig. 1. Design of optical sensor and calibration data.

The sensitivity of the sensor, which is independent of the oscillation frequency, was determined under static conditions with a dial indicator of 0.01 mm resolution. The DC voltage from the photodiode is measured by the *Voltage sensor* and seen with the *Digits* tool. In the measurement range, of about

1 mm, the sensitivity is nearly 1 V.mm^{-1}; that is, 1 mV corresponds to a displacement of 1 μm. One can check the sensitivity by measuring the DC output voltage of the photodiode when the pointer does not intercept the light from the light bulb; in our case, this voltage is 2 V. While measuring the cone oscillations, the loudspeaker is positioned to reduce this voltage to 1 V.

The load resistor of the photodiode can be DC or AC coupled to the data-acquisition system with the *Voltage sensor*. The DC coupling is used for the calibrating and positioning the sensor, and the AC coupling for measuring the cone oscillations. Another *Voltage sensor* acquires the voltage across the voice coil. A common dual-channel oscilloscope serves for observing the voltages from the photodiode and the voice coil. Diagrams of setups for different experiments are shown in a general scheme (Fig. 2). The experiments comprise free oscillations with positive feedback, self-excited oscillations, determination of the motional impedance of the voice coil, and properties of the loudspeaker placed in a vacuum chamber.

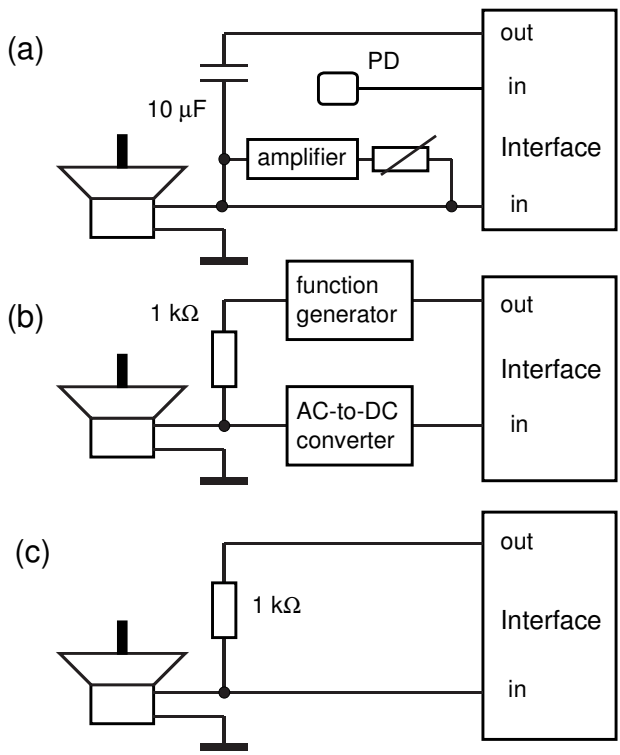

Fig. 2. Setups for the experiments: (a) positive feedback, free and self-excited oscillations; (b) modulus of total impedance; (c) real and imaginary parts of total impedance. PD—photodiode.

1. Loudspeaker with feedback

Positive or negative feedback modifies the properties of the loudspeaker. For this aim, the EMF generated in the voice coil is amplified and returned to the coil.

Additional equipment: two *Voltage sensors*, AC amplifier, AC-to-DC converter, photodiode, resistors, capacitors.

Short electrical pulses obtained by differentiating a square wave voltage (5 Hz, 5 V) from the *Signal generator* trigger free oscillations of the loudspeaker cone (Fig. 2a). The generator output is connected to the voice coil through a 10 μF capacitor. The capacitor and the voice coil form a differentiating RC circuit. The free oscillations of the cone are measured with the optical sensor. The *Voltage sensor* is connected to the load resistor of the photodiode through a 2 μF capacitor (not shown in Fig. 2a). The second *Voltage sensor* measures the EMF generated in the oscillating voice coil.

An amplifier, the PASCO *Digital function generator-amplifier* set for its maximum gain, which equals 2, provides the positive feedback. The amplifier input is connected to the voice coil, while the output to the coil through a 100 Ω variable resistor. By varying the resistor, it is easy to reduce the decay constant of the free oscillations and attain self-excited oscillations. The latter are observed with no triggering pulses. A graph of the velocity versus the displacement represents the phase portrait of the oscillation (Fig. 3). The *Fit*/*User-defined fit* option of *DataStudio* fits the experimental data for the EMF generated in the voice coil. The fit equation is

$$x = A*\exp(-B*x)*\cos(C*x+D)+E, \tag{3}$$

where $B = \gamma$, $C = \Omega \cong \omega_0$ is the angular frequency of the free oscillations, and A and D are the initial amplitude and phase of the oscillations. The offset E may appear due to insufficient precision of the zero adjustment of the *Voltage sensor*; usually, the offset does not exceed 1 mV. To perform the fit, initial guess values of some parameters should be introduced. It is sufficient to provide such values for A, B, and C, which are seen from the measurement data.

The properties of a loudspeaker depend on its environment. For instance, the restoring constant and thus the natural frequency of the cone are sensitive to the position of neighboring objects. The phenomenon is easy to see from free oscillations of the cone for different positions of the loudspeaker over a table.

Self-excited oscillations. With positive feedback, the oscillations of the cone may become self-excited, like those of a pendulum clock or of some toys (Moon 1987, Pippard 1989). The motion equation of the cone becomes

$$x'' + (2\gamma - \beta)x' + \omega_0^2 x = 0, \tag{4}$$

where β depends on the feedback factor; for positive feedback, $\beta > 0$.

Self-excited oscillations arise when an external force applied to the voice coil outweighs the frictional force, that is, $2\gamma - \beta = 0$. For $2\gamma - \beta < 0$, the oscillation amplitude should unlimitedly increase. This is impossible because the coefficient β unavoidably decreases with increasing the oscillation amplitude. The frequency of the oscillations is close to the natural frequency of the loudspeaker, and their steady amplitude depends on the feedback factor.

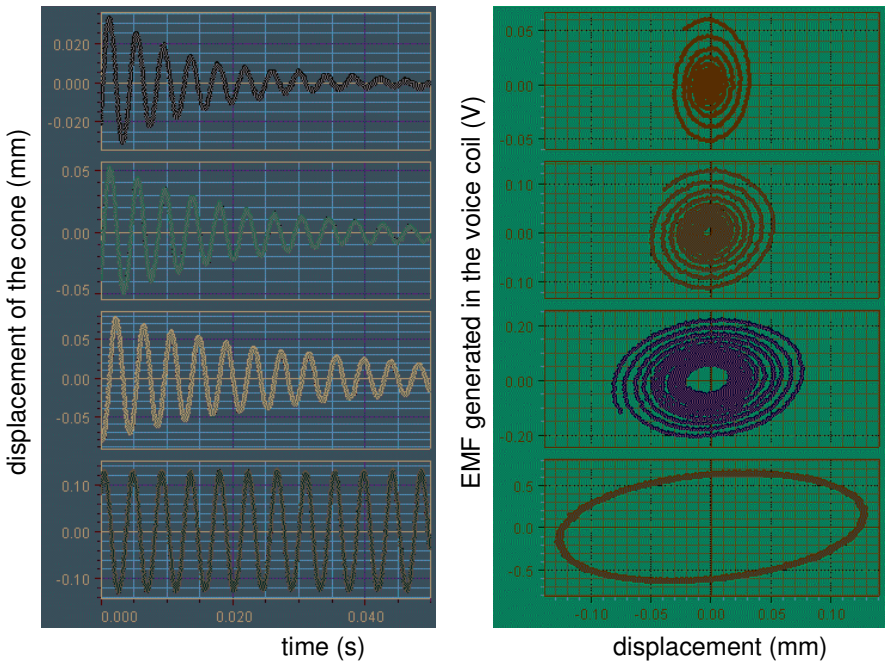

Fig. 3. Time series and phase portraits of free oscillations modified by positive feedback. The last example shows self-excited oscillations.

Loudspeaker impedance. Near the resonant frequency, the motional impedance of the loudspeaker becomes comparable to the usual electrical impedance of the voice coil, and the loudspeaker parameters are available from measurements of the total impedance. The voice coil is connected to the *Signal generator* through a 1 kΩ resistor (Fig. 2b). This regime differs significantly from the usual regime of effectively producing sound waves in a wide frequency range. During a run lasting 200 s, the frequency of the *Signal generator* gradually increases from 150 to 350 Hz. The AC voltage across the voice coil proceeds to an AC-to-DC converter, a Keithley 177 multimeter. Its DC output voltage indicates the RMS values of AC input voltages. During a run, *DataStudio* displays the RMS value of the voltage across the voice coil versus the angular frequency of the driving force. Due to the 1 kΩ resistor, the current through the voice coil is almost independent of frequency. However, the cone oscillations and thus their power

dramatically increase close to the resonant frequency. An evident question arises about the source of the additional power needed for these oscillations. The answer is very simple: the impedance of the voice coil (close to the resonance, it is mainly real) also increases! When a definite AC voltage is applied to the voice coil, the back EMF generated in it reduces the current. This means that the effective impedance of the coil increases. If the cone is fastened, no EMF is generated in the voice coil, and only the usual electrical impedance of the coil is measured.

Mass of the cone and the Bl parameter. The measurement data (Fig. 4) are fitted using the *Fit/User-defined fit* option of *DataStudio*. According to Eq. (2), the fit equation should be

$$Z_{\text{total}} = ((D+2*A*x\text{^}2*C/((B\text{^}2-x\text{^}2)\text{^}2+4*C\text{^}2*x\text{^}2))\text{^}2 + (A*x*(B\text{^}2-x\text{^}2)/((B\text{^}2-x\text{^}2)\text{^}2+4*C\text{^}2*x\text{^}2)\text{^}2))\text{^}0.5, \quad (5)$$

where D is the resistance of the voice coil, $A = B^2l^2/m$, $B = \omega_0$, $x = \omega$, and $C = \gamma$. With an additional AC-to-DC converter, the moduli of the total impedance and of the cone displacement can be recorded simultaneously. For the loudspeaker used, the relation (5) fairly fits the experimental data (the fit parameters are shown in Fig. 4).

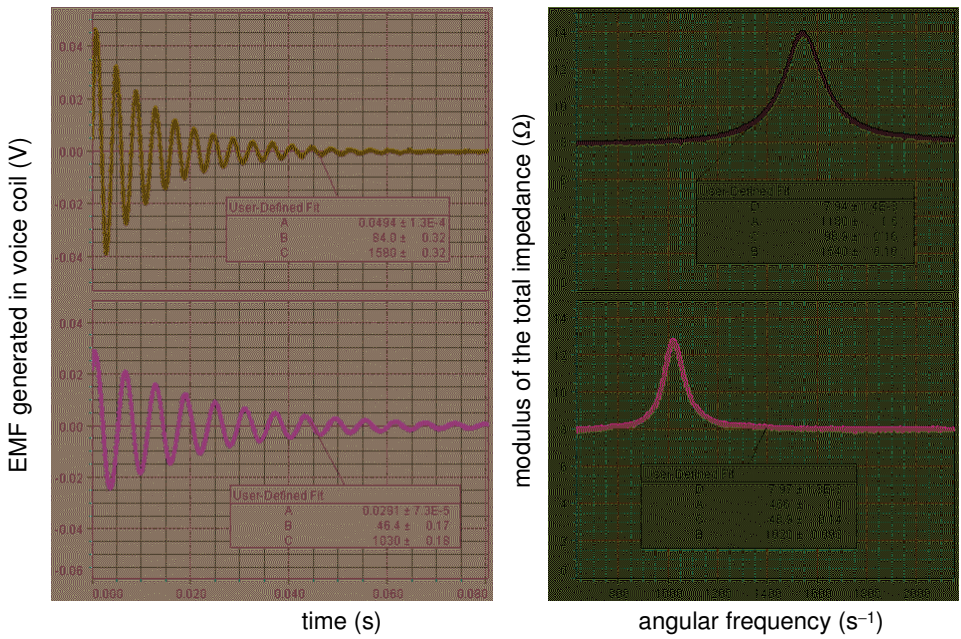

Fig. 4. Determinations of cone mass from changes of natural frequency observed from free oscillations and from the modulus of total impedance.

The mass of the oscillating system, the cone with the voice coil, can be determined by measuring the natural frequency of the system when a known mass is added to it. A 1.41 g piece of plasticine was pasted to the cone, and the natural frequency was found by observing the free oscillations and the frequency dependence of the modulus of the total impedance. From the two measurements, the mass m of the cone, including the air loading mass, appeared to be 1.04 and 1.10 g; a mean value was accepted, 1.07 g. Now the quantity Bl can be calculated from the fit parameter A and the mass. With no mass added, $A = 1180$, and $Bl = 1.12$ T m. With the mass added, $A = 466$, and $Bl = 1.08$ T m. These values are close to those obtained by observing free oscillations of the cone.

Real and imaginary parts of the impedance. The phase angle of the total impedance can be determined at discrete frequencies. For this aim, the *Signal generator* is connected to the voice coil through a 1 kΩ resistor (Fig. 2c). The *Voltage sensor* measures the voltage across the coil. Using the *Sine fit* tool, the initial phases of the current through the voice coil and of the voltage across the coil are measured simultaneously, and the phase shift between the two quantities is known. The *Output current* represents the current through the voice coil. After the phase angle of the total impedance is determined, the real and imaginary parts of the impedance become available. The results obtained with this approach are quite satisfactory (Fig. 5). In this measurement, another example of the same model of loudspeaker was employed; therefore, the change of the natural frequency is quite explainable. At discrete frequencies, both parts of the total impedance are thus obtainable without using a lock-in amplifier.

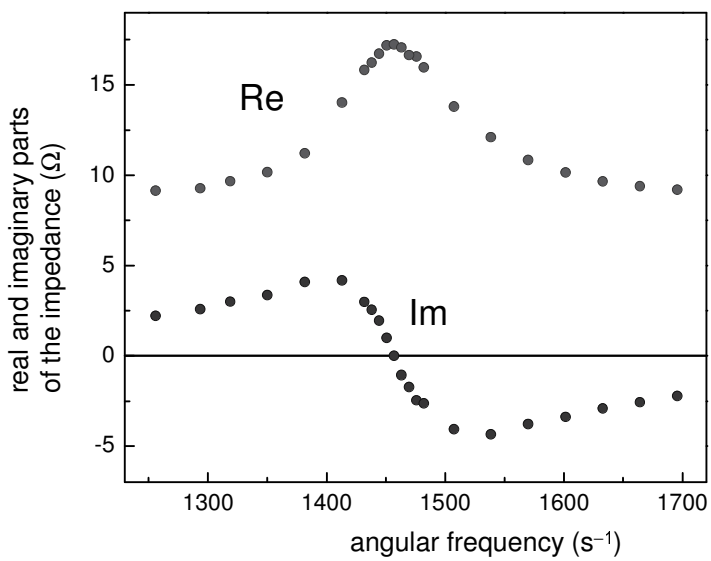

Fig. 5. Real and imaginary parts of total impedance of the voice coil versus angular frequency. The real part includes the usual resistance of the coil.

2. Loudspeaker in a vacuum chamber

Being placed into a vacuum chamber, the loudspeaker does not produce sound waves, but remains an oscillating system.

Additional equipment: *Voltage sensor*, vacuum chamber, vacuum gauges, resistor.

The increase of the natural frequency of the cone after removing the surrounding air clearly shows the contribution of the **air loading mass**, m_A (Tan 1982). This mass is added to the cone mass m_0 when the effective mass of the cone m is measured in air ($m = m_0 + m_A$). In vacuum, the natural frequency of the cone increases. A decrease of the pressure to 1% of the atmospheric pressure is sufficient to exclude m_A. The second result of removing the surrounding air is a decrease of the dissipation constant that equals $2m\gamma$. The energy dissipation is partly caused by the viscous force exerting on the voice coil moving in a narrow gap in the magnetic structure of the loudspeaker.

Resonance frequency versus air pressure. The loudspeaker is placed under a bell jar pumped out by a rotary pump. The vacuum chamber has insulated lead-in terminals. The pressure is measured with a Bourdon gauge (10^5 to 10^3 Pa) and with a Pirani gauge (below 10^3 Pa). The Pirani gauge is a TR 211 model from Oerlikon Leybold Vacuum GmbH. This sensor measures air pressures in the range from 0.05 Pa to 10^5 Pa, but above 10^3 Pa the Bourdon gauge is more reliable. The effect of pumping is clearly seen from the free oscillations of the cone and from the frequency dependence of the modulus of the total impedance (Fig. 6). The data on the natural frequency obtained by the two methods are in good agreement. Significant changes of this parameter occur between 10^5 and 10^3 Pa (Fig. 7). For the decay constant, the data from the two methods somewhat differ, but the general behavior is the same. Significant changes of the decay constant occur between 10^4 and 10^3 Pa.

Air loading mass. According to theory, the air loading mass should be proportional to the density of the gas, that is, to the air pressure under the bell jar. If the restoring constant does not depend on the air pressure, the quantity ω_0^{-2} should be a linear function of the pressure. This guess is confirmed by the data on the pressure dependence of the natural frequency observed from the free oscillations of the cone and from the frequency dependence of the impedance of the voice coil. From the data, $m_0 \cong 0.65$ g, and $m_A \cong 0.45$ g (the total mass is $m = 1.1$ g).

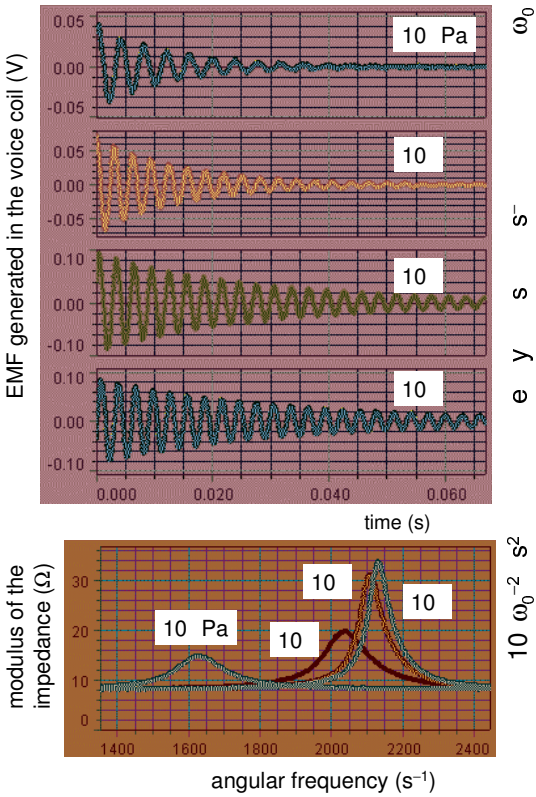

Fig. 6. Free oscillations of the cone and modulus of total impedance for air pressures from 10^2 to 10^5 Pa.

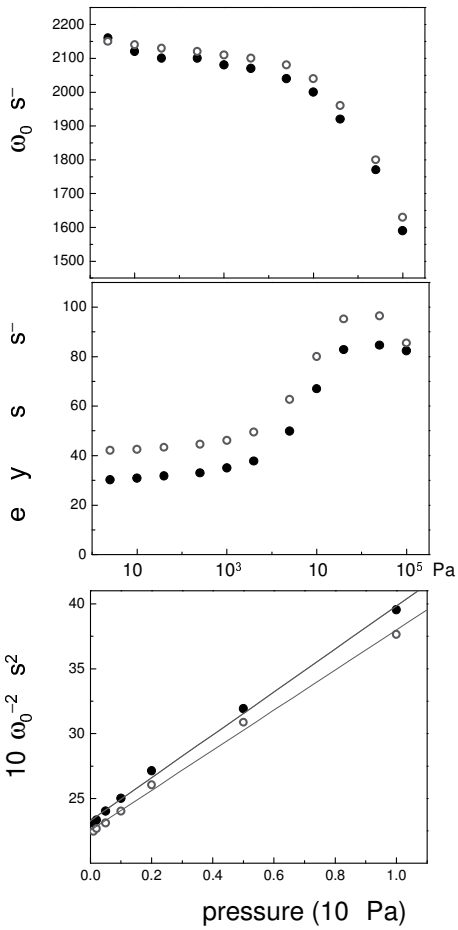

Fig. 7. Natural angular frequency and decay constant from free oscillations (●) and impedance (o), and determination of m_A.

8.3. DC motor

The experiments show how a DC motor approaches its steady rotation, and how its torque, mechanical power, and efficiency depend on the rotation velocity. The tight relationship between the mechanical and electrical parameters is confirmed. Only the current in the rotor winding and the rotation velocity are to be measured (Kraftmakher 2010d).

Additional equipment: *Rotary motion sensor*, DC motor, aluminum disc, two permanent magnets.

Like any electrical machine, a DC motor is a good teaching resource illustrating some fundamental laws of electromagnetism. Only several papers devoted to this issue are listed here (Gluskin 1998; Yap and MacIsaac 2006; Lyna *et al* 2007; Ng *et al* 2009). In a simple DC motor, the stator is a permanent magnet, while the rotor contains a winding connected to a DC source. A commutator and brushes serve for properly operating the motor (Smith 1984; Hecht 1994; Bobrow 1996; Jewett and Serway 2008).

When a DC current flows through the rotor winding, the interaction between this current and the permanent magnet (Lorentz's force) causes the rotor to rotate. Due to the rotation, an EMF is created in the winding (Faraday's law). This EMF e opposes the applied voltage (Lenz's law) and is therefore called the back EMF (or counter EMF). During the acceleration of the rotor, the back EMF gradually increases. When a DC voltage V is applied to the rotor winding, the current i in the winding is governed by Kirchhoff's loop rule:

$$V = L\mathrm{d}i/\mathrm{d}t + iR + e, \tag{1}$$

where L and R relate to the winding. Under steady conditions, the current in the winding is $i = (V - e)/R$, and it decreases with increasing rotation velocity. If a heavy load jams the motor, the current may dramatically increase and overheat the motor (Hewitt 2003; Whitaker 2009; Turner 2009).

Linear model of DC motor. The **mechanical power** P produced by the motor is proportional to the angular rotation velocity $\omega = 2\pi f$ (f is the rotation frequency) and the torque T developed: $P = \omega T$. A good approximation for a DC motor with a permanent magnet is a model assuming a linear dependence of the torque on the rotation velocity (Smith 1984). Two basic points define this dependence: the stall torque T_s (the torque reaches a maximum, but the shaft is not rotating), and the maximum velocity ω_n when no load is applied to the shaft (Fig. 1). Since the mechanical power P is proportional to both the torque and the rotation velocity, the power is zero at both basic points. Accepting the linear model, we have

$$T = T_s - \omega T_s/\omega_n, \qquad \text{and} \tag{2}$$

$$P = \omega T_s - \omega^2 T_s/\omega_n. \tag{3}$$

Thus, the mechanical power, including the power of friction losses, is a quadratic function of the rotation velocity. A maximum of the power achieved at $\omega = \omega_n/2$ equals $\omega_n T_s/4$. The above relations are similar to those for the output voltage and useful electric power of a DC source (T is an analog to the output voltage, T_s to the EMF of the source, ω to the current, and ω_n to the maximum current limited by the internal resistance of the source).

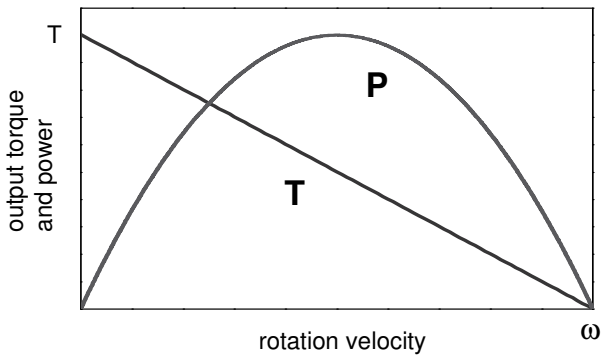

Fig. 1. Torque and mechanical power developed by DC motor versus angular rotation velocity, according to linear model.

When the motor is unloaded and the friction losses can be neglected, the steady rotation is achieved when $e = V$. This relation defines the maximum velocity for a given applied voltage. Since the back EMF is proportional to the rotation velocity, the steady velocity of an unloaded lossless DC motor is proportional to the applied voltage. When the motor is loaded, the rotation velocity and the back EMF unavoidably decrease, so that the current i in the winding and the input electric power P_{el} increase. The input electric power is

$$P_{el} = iV = i(e + iR) = ie + i^2R, \tag{4}$$

where the term i^2R shows the Joule losses in the rotor winding. This equation is only valid in steady-state conditions.

The torque developed by the motor is proportional to the current i, while the back EMF e to the rotation velocity. Equation (4) shows that the mechanical power equals to ie; this term includes the power of friction losses. The equality $P = ie$ can be derived directly from the theory of the DC motor (Smith 1984).

In experiments with a motor, an important question is how to create a controllable load to it. A well-known approach is to use the motor for driving a DC generator and to determine the electric power produced by the generator (Kraftmakher 2001; Ng *et al* 2009). It is easy to change this power in a wide range and determine the friction losses. In the present experiments, the motor rotates a conductor subjected to magnetic braking. The torque provided this way is not determined directly; however, if the linear model of the motor is confirmed, the torque becomes available from the measurement data.

One of the aims of the experiments is the observation of the motor operation immediately after a DC voltage V is applied to the rotor winding (Fig. 2).

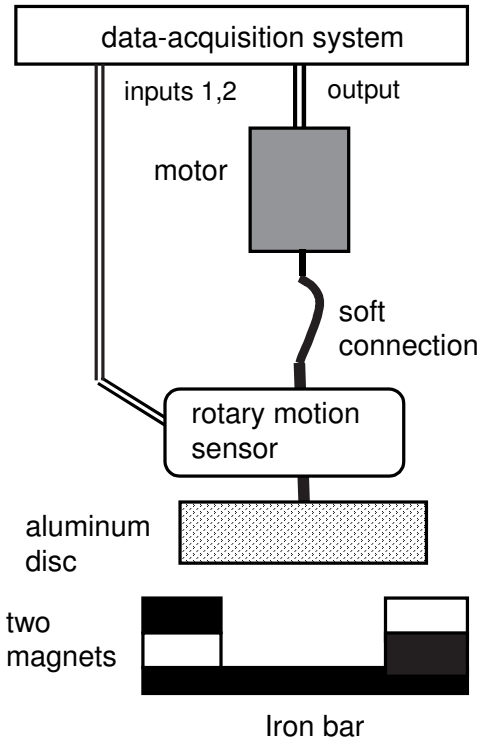

Fig. 2. Setup employing magnetic damping.

The *Signal generator* feeds a low power DC motor (Maxon 2326.939-22.111-006 model). The resistance of the rotor winding is $R = 13.7\ \Omega$. The shaft of the motor is connected to the shaft of the *Rotary motion sensor* measuring the rotation velocity. Since it is difficult to precisely align the motor and the sensor, a soft connection is made between them. An aluminum disc, 1.2 cm thick and 4 cm in diameter, is attached to the other end of the shaft of the sensor and subjected to the magnetic field of two ceramic magnets, each 12×12×12 mm^3 in size. The magnets rest on an iron slab placed on the platform of a laboratory jack, so it is easy to change the distance between the magnets and the disc. With the magnetic braking, the load on the motor can be changed in a sufficiently wide range. The current in the winding i is taken as the *Output current* of the *Signal generator*. *DataStudio* calculates the back EMF, $e = V - iR$, and displays results of the measurements and calculations. In all the experiments, only two parameters are to be measured, the current in the rotor winding and the rotation velocity.

Initial periods of rotation are recorded for different voltages applied to the motor. The *Signal generator* operates in the *Auto* mode: it creates the DC output voltage only after starting a run. The *Sample rate* is 10 Hz, and each run lasts 5 s; the option *Automatic stop* is used for this aim. The measurements are carried out for several DC voltages, from 1 to 4 V. Though the calculations are only valid under the steady-state conditions, the records include data for transient conditions. The data for voltages 2 and 4 V are presented here (Fig. 3). Due to different rotation velocities, the loads for the two cases are not equal. The graphs show how the current in the rotor winding continually decreases until the rotor attains a steady rotation velocity.

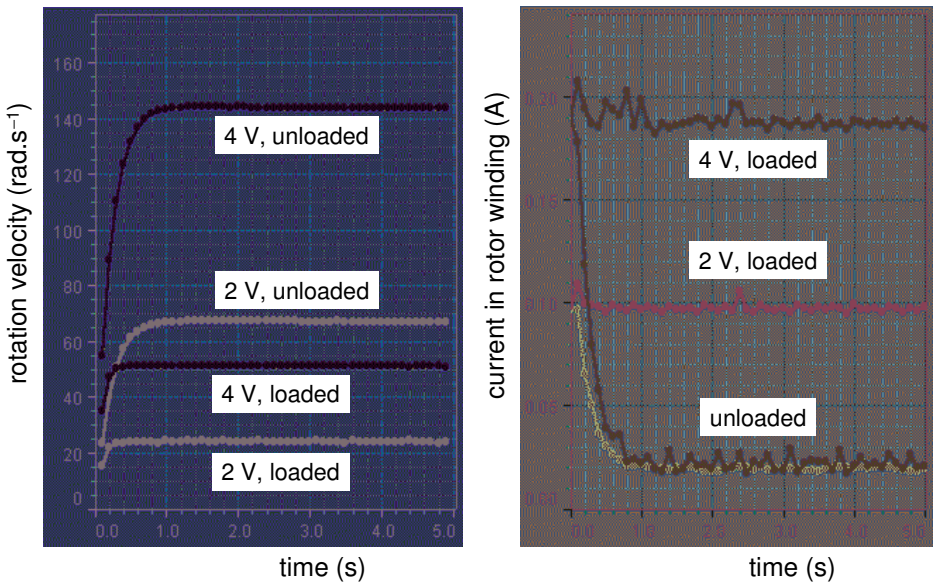

Fig. 3. Records of initial periods of motor operations, for loaded and unloaded motor. The applied voltages are 2 and 4 V.

For the unloaded motor, the steady current is nearly the same for both voltages because the necessary torque should only balance the friction forces. For the loaded motor, the steady rotation becomes slower, and the steady current increases. Second, the transient period needed for establishing the steady state becomes shorter. The rotational inertia of the system is constant, and loading the motor causes the change in transients. When the current in the rotor winding becomes significant, an additional torque brings the rotation velocity to its steady value in a shorter time.

Steady state for different loads. In the next experiment, the initial periods of rotation are recorded for a fixed applied voltage, 4 V, but different loads controlled by the magnetic braking. The latter is varied stepwise (Fig. 4). The

steady-state values of the rotation velocity and of the current in the rotor winding are used for the calculations.

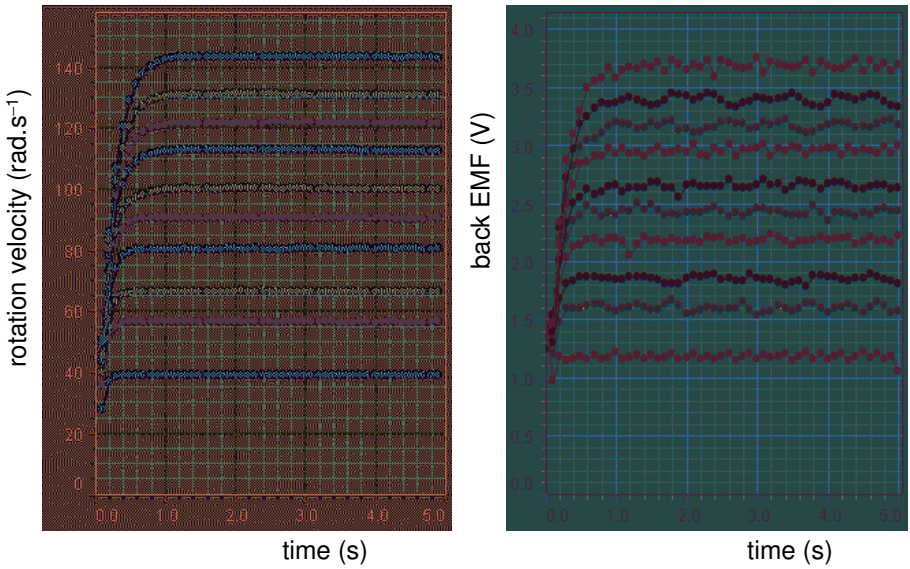

Fig. 4. Records of initial periods for different loads. When the load increases, the rotation velocity and the back EMF decrease.

Torque and mechanical power. The steady-state current in the rotor winding, the back EMF, and the calculated total mechanical power produced by the motor are plotted versus the rotation velocity (Fig. 5). The torque is proportional to the current. Therefore, the linear dependence of the current on the rotation velocity confirms the linear torque–velocity dependence. The proportional fit for the back EMF is used according to the model assuming a constant magnetic field produced by the stator and a constant resistance of the rotor winding. For heavy loads (that is, large currents), these assumptions are doubtful. First, the magnetic field produced by the winding may become significant. Second, the heating of the winding increases its resistance, while the back EMF is calculated assuming a constant resistance. Therefore, the deviations from the proportional fit are quite expectable. If the motor is mechanically caused to rotate, it becomes a DC generator providing an open circuit voltage strictly proportional to the rotation velocity. Such a generator can be used as a speedometer.

The total mechanical power P follows Eq. (3). For fitting purposes, the point of origin ($\omega = 0$, $P = 0$) was added to the measurement data. With this addition, the fit equation is $P(\text{mW}) = 7.6\omega - 0.049\omega^2$ (ω is given in rad.s^{-1}). From the linear term of the fit, $T_s = 7.6\times10^{-3}$ N.m. From the quadratic term, the rotation velocity of the unloaded motor should be $\omega_n = 155$ rad.s^{-1}. Close values of ω_n are seen from the linear fits for the current in the rotor winding and for the back EMF. The torque and the current in the motor winding linearly depend on

the rotation velocity: T (N.m) = $7.6\times10^{-3}(1 - \omega/155)$, i(A) = $0.272(1 - \omega/157)$. Neglecting the difference between the two ω_n values, the torque is proportional to the current: T (N.m) = $0.028i$ (A). The fit parameters are shown in Fig. 5.

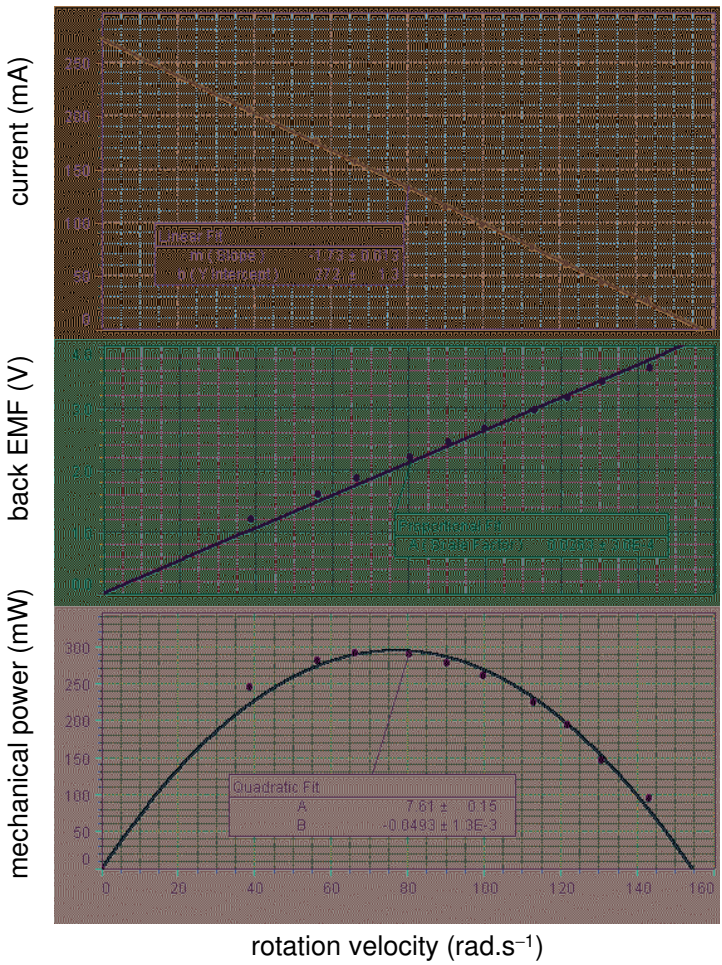

Fig. 5. Current in rotor winding, back EMF, and total mechanical power for different loads, versus steady rotation velocity.

***Friction losses and efficiency*.** To determine the motor efficiency, it is necessary to take into account the friction losses. Their power depends only on the rotation velocity and can be determined by measuring the quantity $P_1 = i_1 e_1$ (the current in the rotor winding times the back EMF for the unloaded motor). Varying the applied voltage changes the rotation velocity. The data (Fig. 6) are fitted with a linear fit, P_1(mW) = $6.6 + 0.4\omega$ (rad.s^{-1}). With this relation, P_1 values are

calculated for the same rotation velocities that are observed for the loaded motor. The efficiency of the motor equals

$$\eta = (P - P_1)/iV, \tag{5}$$

where the P and iV data relate to the loaded motor; for each calculation, all the data are taken for the same rotation velocity. The maximum efficiency is nearly 0.6, a reasonable value for low power motors.

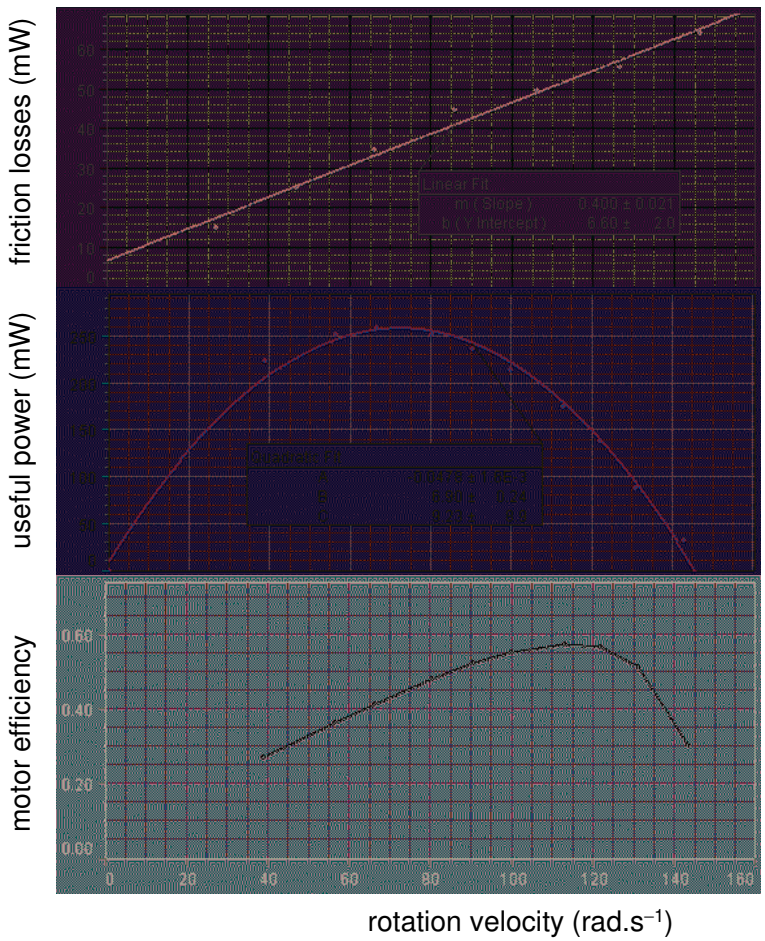

Fig. 6. Power of friction losses, useful mechanical power, and motor efficiency, versus steady-state rotation velocity.

8.4. Transformer

The experiments illustrate (i) the transformer operation; (ii) the properties of the magnetic core; and (iii) the standard tests and efficiency (Kraftmakher 2006c).

Additional equipment: two *Voltage sensors*, *Power amplifier II*, transformer, resistor, capacitor.

The transformer is a key device for the electrical energy transfer. It rests on basic concepts of electromagnetism. With a data-acquisition system, characteristics of a transformer are obtainable in a short time, and exhaustive illustrations are displayed on the screen of a computer. The transformer transfers electrical energy from one circuit to another by means of an AC magnetic field that links both circuits. An ideal transformer has no losses, and the energy transfer from the primary coil to the secondary coil is perfect. A properly designed transformer operates at efficiency higher than 99%, which is an outstanding feature. The theory of the transformer can be found in textbooks by Grant and Phillips (1982); Smith (1984); Bobrow (1996).

The transformer displays a unique collection of physical laws and phenomena and is an invaluable educational resource. Laboratory investigations of the transformer should not be an exclusive privilege of students in electrical engineering. Students in physics also would be grateful for such laboratory experiments, regardless of the attention given to this topic in lecture courses. The use of a data-acquisition system for acquiring, processing, and displaying data allows the students to do the experiments in a short time and immediately see the results of their measurements and calculations. With a data-acquisition system, all the voltages and currents are determined, as well as phase relations between them. The power delivered to the load and that consumed by the primary coil are measured directly.

Some fundamental physical phenomena are involved in the transformer operation. The first is **Faraday's law of induction**, along with **Lenz's law**: $E = -d\Phi/dt$. The second is **Ampère's circuital law** used for calculating the magnetizing field. Lastly, **Kirchhoff's loop rule** must be fulfilled. In our experiments, a low power transformer is used. It has a core of the shell type, in which the iron surrounds the copper. Its two coils are designed for 15 and 5 V (RMS values). Usually, the efficiency of low power transformers is far below the above-mentioned value typical for high power transformers.

Transformer operation. In an ideal transformer, the magnetic core has infinite permeability and does not exhibit saturation. The impedance of the primary coil is therefore infinite. When the secondary coil is opened, no current flows in the primary coil. More rigorously, the current is infinitely small, but it produces an AC magnetic flux, which induces in the primary coil an EMF that exactly balances the input voltage (Kirchhoff's loop rule). Simultaneously, it induces an

EMF in the secondary coil. A current in the primary coil of an ideal transformer appears only due to that in the secondary coil. The two currents produce strictly equal and opposite AC magnetic fluxes in the core. This is a fundamental feature of any transformer.

When an AC voltage is applied to the primary coil of an unloaded real transformer, the input current depends on the impedance of the coil. The voltage drop due to the resistance of the coil is small, and an EMF induced in it approximately equals the applied voltage. This can be verified by measurements of the phase shift between the voltage applied to the coil and the current in it by using the *Fit*/*Sine fit* option provided by *DataStudio*. For nearly sinusoidal currents and voltages, *Sine fit* well fits experimental data. The fits for the current and the voltage measured in one run show their amplitude values and phases. The phase shift between the two sine waves thus becomes available. If the voltage drop due to the resistance of the primary coil is not negligible, it is easy to calculate it.

The magnetic flux must induce in the coil an EMF that, together with the small voltage drop due to the resistance of the coil, balances the input voltage. The magnetic flux through the core thus must be sinusoidal. The current in the primary coil varies in just such a way as to produce a sinusoidal flux. This current, called the magnetization current, will be almost 90° out of phase with the applied voltage, with a small in-phase component due to the losses in the core and in the primary coil. Usually, transformers are designed so that the magnetization current is a small fraction of the input current under a nominal load. Since the flux is accurately sinusoidal, the secondary voltage (and current) will also be sinusoidal (Faraday's law of induction). Therefore, the peculiarities of the magnetization current will not be reflected in the transformer output, and will not cause distortion.

A current drawn from the secondary coil causes a magnetic flux opposite to that produced by the input current (Lenz's law). To balance the input voltage, the current entering the primary coil must therefore increase. The voltage induced in the primary coil by the total magnetic flux always equals the input voltage. The current through the primary coil thus strictly responds to any changes in the current drawn from the secondary coil. In all the experiments presented, the voltages and currents measured with *DataStudio* are given as amplitude values.

Power in AC circuits can be calculated by the summation of energies during short intervals, where the current and the voltage can be considered constant. For arbitrary waveforms of the current and voltage, the mean electric power equals

$$P = (1/T) \int_0^T IU \, \mathrm{d}t, \tag{1}$$

where T is the period of the current. For sine wave currents and voltages,

$$P = (1/T) \int_0^T I_\mathrm{m} U_\mathrm{m} \sin\omega t \sin(\omega t - \varphi) \, \mathrm{d}t, = \tfrac{1}{2} I_\mathrm{m} U_\mathrm{m} \cos\varphi = I_\mathrm{eff} U_\mathrm{eff} \cos\varphi, \tag{2}$$

where I_m and U_m are the amplitude values, $\omega = 2\pi/T$ is the angular frequency, φ is the phase shift between the current and the voltage, and $I_{eff} = I_m/\sqrt{2}$ and $U_{eff} = U_m/\sqrt{2}$ are called effective values.

In a case of complicated waveforms of the current and/or voltage, Eq. (1) is used. This approach is used in modern electronic wattmeters. Here, the data-acquisition system acquires instantaneous values of the current and voltage, and *DataStudio* calculates the products of the data and then the averaged values of the products. The *Calculate*/*Statistical*/*Avg* tool serves for the averaging. All the operations are observable as graphs on the screen of a computer.

The 15 V coil L_1 of the transformer serves as the primary coil (Fig. 1). The *Power amplifier II* (not shown in Figs. 1 and 2) provides voltages up to 10 V at currents up to 1 A, and *DataStudio* stores the *Output voltage* and the *Output current* as the voltage applied to the primary coil and the input current. Two other inputs of the *Interface* are used for measuring the electric power delivered to the load by the secondary coil L_2 of the transformer. In our case, two *Voltage sensors* measure the output voltage of the transformer and the voltage across a 1 Ω resistor placed in series with a variable load resistor. These data, along with those related to the primary coil, are sufficient for determining the input and output powers of the transformer. The phase relations between the voltages and currents are available from *Sine fits* to them.

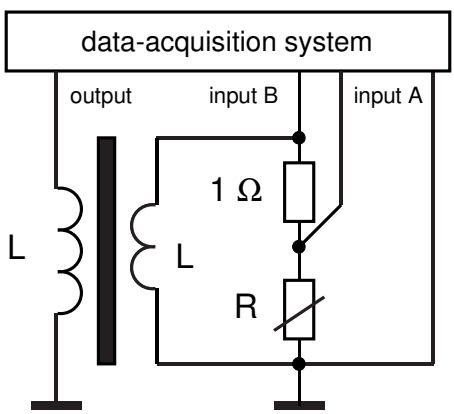

Fig. 1. Setup for measuring input and output voltages and currents.

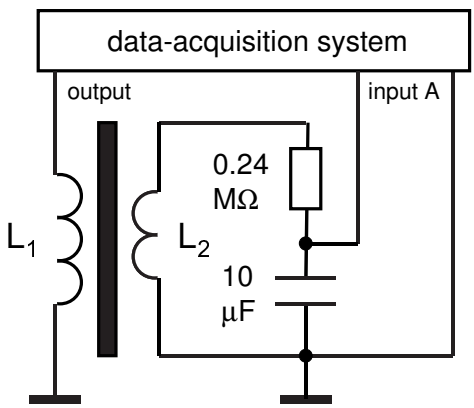

Fig. 2. Setup for observing hysteresis loops.

Magnetic core. Properties of the magnetic core of a transformer are very important for the transformer operations (Redinz 2013). The magnetic field B in a ferromagnet is a nonlinear function of the magnetizing field B_0. This function is given by the magnetization curve. In actual magnetic materials, the flux does not drop to zero when the magnetizing field is removed, but there is a remanent flux. To reduce the flux to zero, a magnetizing field in the reverse direction must be applied. It is called the coercive force. When a ferromagnet is subjected to an

AC magnetizing field, the magnetization curves are moved left and right, displaying hysteresis loops. Since the flux lags the current, there is a component of the voltage in phase with the electric current, which means energy losses called the hysteresis losses. The area inside a hysteresis loop is just equal to the energy lost per cycle per unit of volume of the core. The power of the hysteresis losses in a magnetic core equals the product of this area, the frequency of the magnetizing field, and the volume of the core.

Hysteresis losses. The observation of the hysteresis loops is well known (Goldin 1983; Meiners *et al* 1987; Meng and Liang 1987; Kiss 1990; Kraftmakher 2005c). To extend the range of input currents of our transformer, the frequency of the input current is reduced to 20 Hz. The voltage applied to the primary coil amounts up to 10 V (Fig. 2).

The input current stored as the *Output current* provides X data for a graph. The output voltage of an integrating RC circuit (0.24 MΩ, 10 μF) provides the Y data. The integrating circuit highly reduces the voltage to be measured, but it is necessary to check that it really became less than 10 V. Each measurement lasts 50 ms, one period of the input current, and the *Sample rate* of the data acquisition is 5000 Hz. Before plotting the graph, *DataStudio* converts the voltages to values of B_0 and B:

$$B_0 = \mu_0 N_1 I_1 / l, \tag{3}$$

$$B = U_y RC / A N_2, \tag{4}$$

where N_1 and N_2 are the numbers of turns of the coils L_1 and L_2, I_1 and U_y are the current and the voltages stored, l is the mean length of the core, and A is its cross-sectional area.

In our case, $l = 0.14$ m, and $A = 5.3\times10^{-4}$ m^2. To determine N_1 and N_2, an additional 1-turn coil is wound around the core, and the voltage induced in it is compared with those induced in other coils. From these measurements, $N_1 = 150$, and $N_2 = 50$. The hysteresis loops become observable as values of B versus B_0 (Fig. 3). The current through the secondary coil is small, so that the transformer is nearly unloaded. At highest input voltages, the input current becomes nonsinusoidal. The power of the hysteresis losses is

$$P_h = K_h f B_m^{\,n}, \tag{5}$$

where f and B_m are the frequency and the amplitude of the magnetic field in the core, the constant K_h and exponent n depend on the core material; and n is often assumed to be 1.6 (Smith 1984, Bobrow 1996).

Magnetization curve and permeability. By determining ultimate points in the hysteresis loops, the magnetization curve and the field dependence of the permeability of the core become available (Fig. 4). The magnetic field in the core manifests saturation at relatively small magnetizing fields, which means

high permeability of the core. The permeability first increases with the magnetizing field, reaches a maximum, and than decreases.

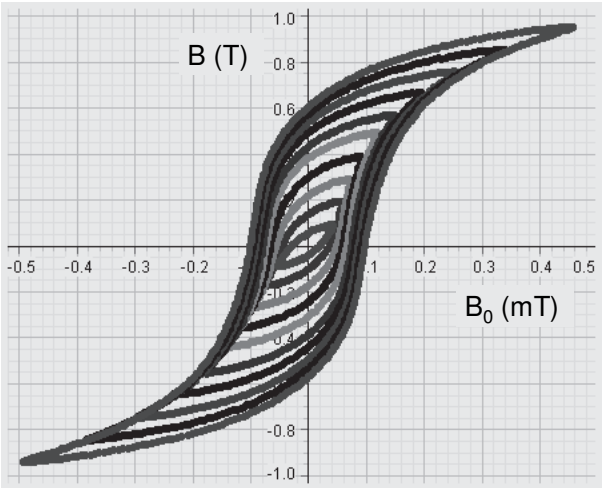

Fig. 3. Family of hysteresis loops of the magnetic core.

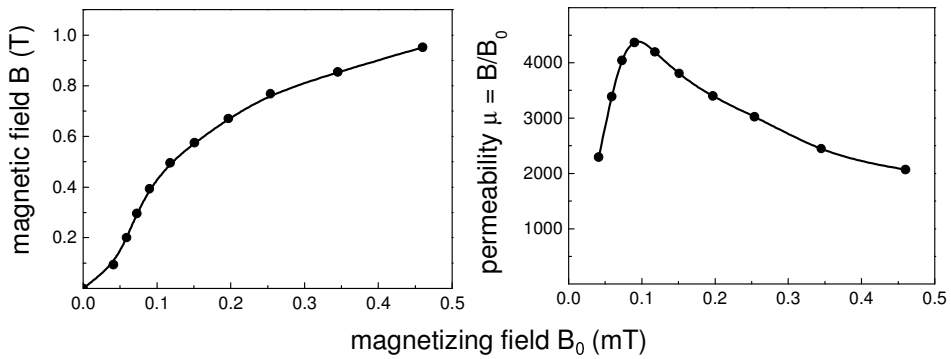

Fig. 4. Magnetization and permeability of the core versus magnetizing field.

Eddy currents in the core cause additional energy losses. They are minimized by making the core from a pile of thin laminations insulated from each other. The eddy current losses are proportional to the square of the thickness of the laminations and to the squares of the frequency and the maximum magnetic field. The power of the eddy current losses equals

$$P_e = K_e f^2 B_m^2, \tag{6}$$

where K_e depends on the core material and thickness of the laminations.

The hysteresis losses and eddy current losses constitute the total **iron losses**. The eddy currents can be highly reduced by high resistivity of silicon

steel and thin laminations. The larger part of the iron losses is the hysteresis losses, which are proportional to the frequency. The eddy current losses and the hysteresis losses can be separated experimentally by tests at different frequencies, because of their distinct frequency dependences.

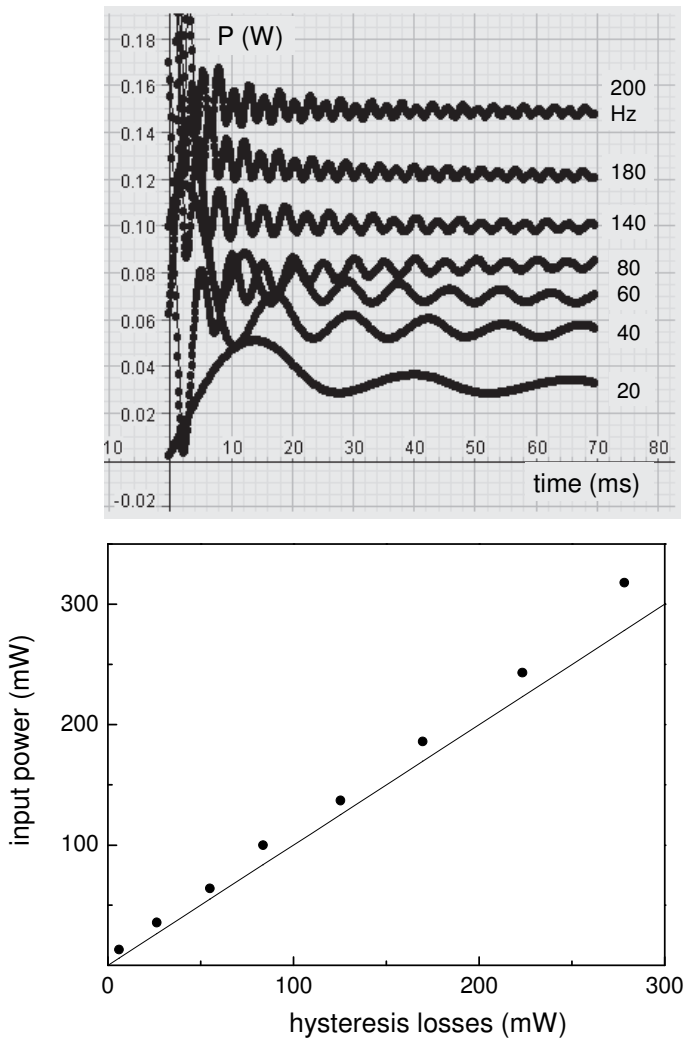

Fig. 5. Top: determination of iron losses for different frequencies of input current; bottom: input power for the unloaded transformer (•), and losses calculated from the areas of hysteresis loops (———).

The iron losses can be measured for different frequencies of the input current (Fig. 5). They are measured at reduced input currents limited by the

impedance of the primary coil for the highest frequency, 200 Hz. To maintain the same input current, the input voltages for lower frequencies should be reduced, from 10 V at 200 Hz to about 2 V at 20 Hz. With negligible resistance of the coil, this voltage should be proportional to the frequency. A linear frequency dependence of the losses means that the iron losses are mainly due to the hysteresis. One can compare the hysteresis losses for different input voltages with the power consumed by the unloaded transformer. The calculation of the areas of the hysteresis loops is performed with *Origin*. The power consumed is determined by averaging products of instantaneous values of the input voltage and current. This power is somewhat larger than the hysteresis losses. This is due to eddy currents in the core and Joule losses in the primary coil.

Open-circuit and short-circuit tests are performed at 50 Hz and consist of measuring the power consumed by the transformer for two regimes, with the secondary coil opened, and when it is short-circuited. The power is determined by averaging products of instantaneous values of the input voltage and current. To make the procedure clear, it is useful to display the input current versus the input voltage (Fig. 6). With the secondary coil L_2 (N_2 = 50) opened, the current in the primary coil L_1 is much less than that under operation conditions. The Joule losses in the coil become therefore negligible. The power consumed is caused by the hysteresis and eddy current losses. Since the iron losses depend on the frequency and the maximum magnetic field, the open-circuit test should be done under nominal frequency and input voltage. In our case, the input voltage is 10 V, and the input current equals 85 mA. The iron losses are 270 mW.

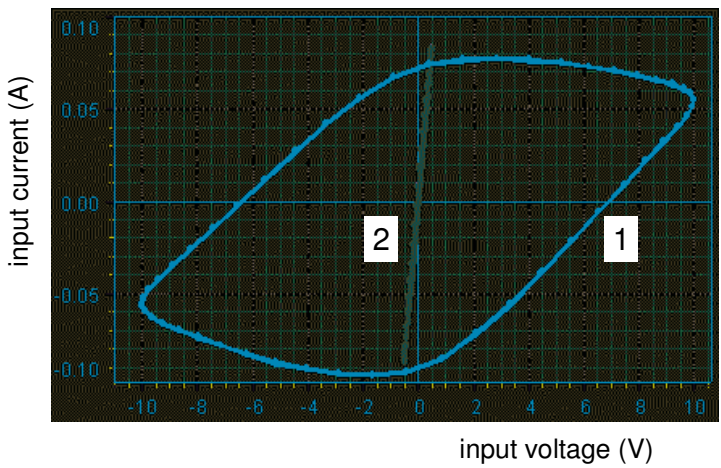

Fig. 6. Input current versus input voltage, the open-circuit (1) and close-circuit (2) tests.

The short-circuit test is done when the secondary coil is short-circuited, and the current in it is limited by the impedance of the coil. To operate at the

same input current (85 mA), the input voltage should be reduced. For this voltage, the magnetic field in the core is small, so that the iron losses become negligible. The power consumed is thus governed only by the Joule losses due to the electrical resistance of both primary and secondary coils. These losses are often called copper losses. To keep the same input current, the input voltage is reduced to 0.5 V. The copper losses are 21 mW. This means that the effective resistance of both windings of the transformer equals $R_{\text{eff}} = 5.8\ \Omega$. From DC measurements, the resistance of the primary coil equals $R_1 = 3.5\ \Omega$, while that of the secondary coil is $R_2 = 0.6\ \Omega$. According to the turn ratio of the transformer (in our case, it equals $n = 15/5 = 3$), the effective resistance R_{eff} should equal to $R_1 + nR_2 = 5.3\ \Omega$.

Coupling between the coils. For an ideal transformer, the magnetic flux penetrating the secondary coil is considered equal to that generated by the primary coil. In fact, some leakage of the flux occurs. The magnetic flux through the secondary coil somewhat decreases, and the secondary voltage becomes less than it should be according to the turn ratio of the transformer. The flux that does not link both windings is called leakage flux. In the transformer used, the leakage flux is insignificant.

Loaded transformer. To perform measurements with a loaded transformer, a variable resistor is connected to the secondary coil. The power P_2 delivered to the load and the power P_1 consumed by the transformer are measured directly by averaging the products of instantaneous values of currents and voltages (Fig. 7).

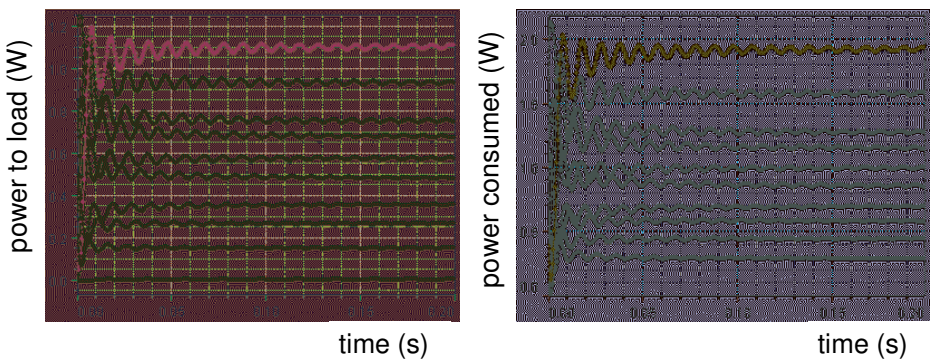

Fig. 7. Mean power delivered by secondary coil to load, and mean power consumed by primary coil.

The power consumed by the transformer strictly follows that delivered to the load (Fig. 8). For small powers, the changes in P_1 just reproduce the changes in P_2. The maximum efficiency of our transformer is only 60%, but this figure is typical for low power transformers. To show how the primary coil senses the

power delivered to the load, it is useful to plot the input current versus input voltage for different loads. The smallest input current relates to the unloaded transformer. When increasing the power delivered to the load, the input current increases, and the phase shift between the input voltage and current decreases.

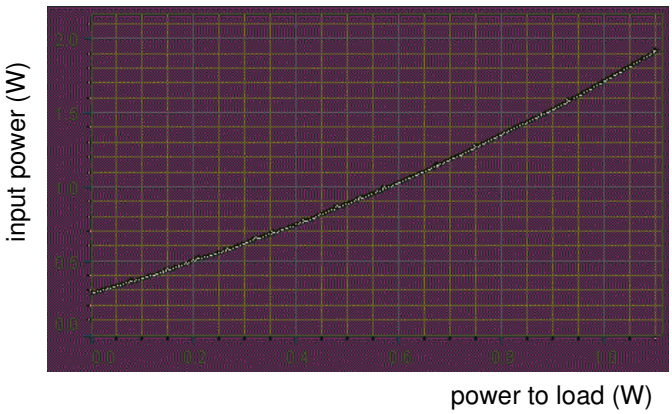

Fig. 8. Electric power consumed by primary coil versus power delivered to load.

For the unloaded transformer, the input current is I_1 = 85 mA. The input current is markedly non-sinusoidal, so that the *Sine fit* by *DataStudio* becomes inaccurate. Therefore, the phase shift between the voltage and current is deduced by measuring the power consumed by the primary coil. This phase shift appeared to be of about 50° (Fig. 9). For the loaded transformer, the input currents are nearly sinusoidal.

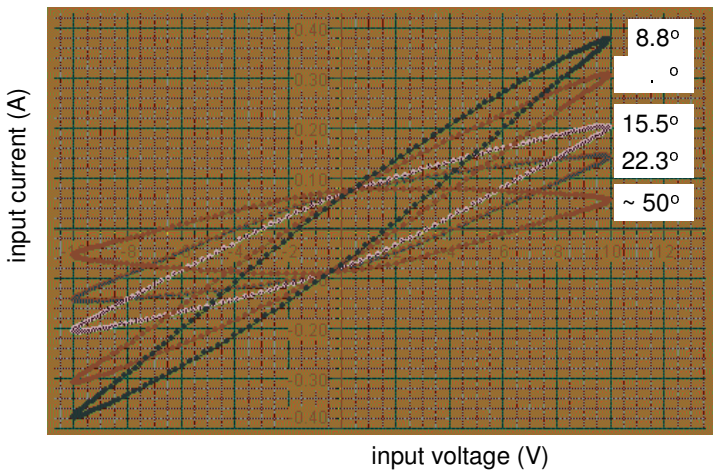

Fig. 9. Input current versus input voltage for different loads. The phase shifts between the currents and voltages are indicated.

8.5. Maglev (magnetic levitation)

The lift, drag, and radial forces on a magnet placed over a rotating conducting disc are measured versus the rotation frequency (Kraftmakher 2008b). The experiment follows that described by Rossing and Hull (1991). The schematics of the setups are shown in a general scheme (Fig. 1).

Additional equipment: *Force sensor*, permanent magnet, conducting disc, induction motor, light bulb, photodiode, video camera, monitor.

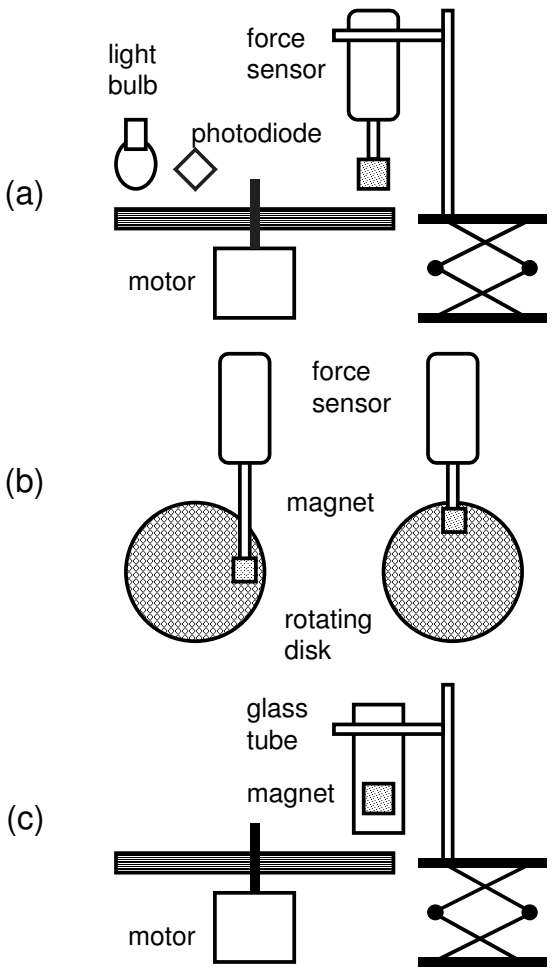

Fig. 1. General scheme of experiments: (a) lift force; (b) drag and radial forces, top view; (c) demonstration of magnetic levitation.

Theoretical background. Maglev (magnetic levitation) is a general term for any transportation system, in which vehicles are suspended and guided by electromagnetic forces (Kolm and Thornton 1973; Danby and Powell 1998). The magnetic field keeps the vehicle above the support structure called guide way; this allows the vehicles to travel at velocities up to 500 $km.h^{-1}$. There are two types of the magnetic suspension:

- **electromagnetic suspension:** electromagnets on the vehicle are drawn toward a steel rail, and their currents are automatically regulated to maintain a fixed gap between the rail and the vehicle;

- **electrodynamic suspension:** electromagnets placed on the vehicle induce in a conducting guide way eddy currents producing a repulsive force as the vehicle moves along the guide way.

The electrodynamic suspension based on Faraday's and Lenz's laws is known for a long time. Superconducting DC magnets on the vehicle are preferable due to their high magnetic fields and low losses, and the linear synchronous motor technology is applicable for electromagnetic forward motion. Nowadays, transportation by magnetic levitation has proven its feasibility and advantages. Under laboratory conditions, the electrodynamic suspension is possible with usual permanent magnets. An experiment and a demonstration described below illustrate the concept of "lift through motion," the basis of one of the techniques for wheel less transportation.

Klauder (1969) calculated the lift and drag forces on a long current-carrying wire moving over a conducting semi-infinite slab. Coffey *et al* (1969) have found that at high velocities the levitation force can be calculated as if the guide way had infinite conductivity. At finite velocities, the resistivity of the guide way reduces the actual lift force and produces a drag force. Reitz (1970) considered a magnetic dipole moving above a thin conducting plate. Davis and Reitz (1971) calculated the eddy-current distribution in a perfectly conducting sheet or disc. Davis (1972) presented a proof of the general relationship between the drag and lift forces. Saslow (1987, 1991, 1992) considered several topics, including magnetic braking, induction motor, electromagnetic shielding, and Maglev.

Many papers were devoted to the interaction of a conductor with a rotating magnetic field. Towler and Beams (1976) reported on a magnetic suspension for lecture and classroom demonstrations. Doyle and Gibson (1979) described a simple classroom demonstration of retarding and repulsive forces on a permanent magnet put near a rotating conductor (Arago's effect). Wiederick *et al* (1987) proposed an experiment on the magnetic braking of a thin aluminum disc freely rotating between the pole pieces of an electromagnet. Heald (1988) presented an improved theory of this experiment. Marcuso *et al* (1991a,b) computed the torque on a moving conductor by a localized magnetic field and confirmed the calculations experimentally. Aguirregaribia *et al* (1997) studied the braking effect on a thin conducting disc rotating in a nonuniform magnetic

field. Íñiguez and Raposo (2009) described a prototype of a low-speed electrodynamic levitation system.

Electrodynamic suspension is caused by repulsive forces between electromagnets on the vehicle and eddy currents induced in a conducting guide way as the vehicle moves along it. The motion is a crucial requirement for obtaining a lift force. The currents in the guide way decay as the vehicle passes, and electrical energy losses in the guide way therefore occur. The vehicle must compensate for these losses. This means that a drag unavoidably accompanies the lift. At high velocities, the electrodynamic drag decreases with increasing velocity, which is a very important feature of these transportation systems. The complete theory of electrodynamic suspension is very complicated, so only a general picture of the phenomenon and formulas important for the present experiment will be given.

A source of magnetic field, a monopole q, which "instantaneously" appears at height z above a conducting plate, induces in it circular eddy currents, which maintain the instantaneous field in the plate. The monopole is the limit of a long thin bar magnet or a solenoid oriented perpendicular to the plate. The pole strength q has the dimensions of magnetic moment per unit length. In the case of a superconductor, the surface currents completely cancel the magnetic field inside the plate (Meissner's effect). The field outside the plate is obtainable by superimposing the source field and the field due to the image of the source (that is, monopole $-q$ at $-z$). On the $z = 0$ plane, this leads to a zero normal component and a doubled transverse component of the resulting magnetic field. Above the plate, the field exerts a repulsive force on the monopole proportional to the normal component of the field. Due to the axial symmetry of the eddy currents, other components of the force are zero. The surface currents in the superconducting plate do not decay, and the repulsive force continues infinitely.

In the case of a normal metal, eddy currents decay in a time, which depends on the conductivity of the plate. To maintain the currents, changes in the external magnetic field must continue, for instance, by moving the monopole parallel to the plate. It is important that the external magnetic field penetrates a normal metal. Due to high conductivity of the metal, the penetration can be slow relative to the changes in the external field. The movement of the monopole breaks the symmetry of the eddy currents: their distribution in front of the monopole and behind it becomes different. This causes a horizontal component of the magnetic field and a horizontal force on the monopole. According to Lenz's law, this force is directed opposite to the movement of the monopole. The phenomenon is well known as magnetic braking. Both lift and drag forces depend on the conductivity and thickness of the plate and on the velocity of the monopole.

Reitz (1970) considered a magnetic dipole (a magnet or a current-carrying coil) moving with velocity v at fixed height h above a plate of conductivity σ and thickness d. The plate was assumed thin compared to the skin depth for the dominant frequencies in the exciting field; therefore, the current density in the

plate does not depend on the z coordinate. The electromagnetic disturbance of a moving dipole has a broad frequency spectrum, but the dominant frequency is of the order of $\omega = v/h$. The penetration of the magnetic field into the plate is characterized by the parameter $w = 2/\mu_0\sigma d$, which has the dimensions of a velocity. The lift force on a monopole was found to be

$$F_L = (\mu_0 q^2/16\pi h^2)[1 - w/(v^2 + w^2)^{1/2}], \quad (1)$$

where μ_0 is the magnetic constant.

A magnetic dipole of moment m oriented vertically was considered constructed of two monopoles. For the dipole, the lift force is

$$F_L = (3\mu_0 m^2/32\pi h^4)[1 - w/(v^2 + w^2)^{1/2}]. \quad (2)$$

The lift-to-drag ratio equals

$$F_L/F_D = (v/w). \quad (3)$$

At high velocities, the lift force asymptotically approaches a constant, while the drag force is inversely proportional to the velocity. This means that the propulsive power to overcome the electrodynamic drag becomes independent of the velocity. For a thick conducting plate, the drag force at high velocities becomes proportional to $v^{-1/2}$.

Saslow (1992) presented a theoretical analysis of two examples considered by Maxwell, a monopole moving above a thin conducting sheet, and a monopole above a rotating thin conducting disc. In the case of a rotating disc, a radial component F_R of the force on the monopole (towards the center of the disc) appears, which is also justified by Lenz's law—the eddy currents push the monopole into the region where the linear velocity of the disc and hence the eddy currents decrease. The components of the force on the monopole are given by formulas:

$$F_L = A\omega^2 r^2, \quad (4)$$

$$F_D = A\omega r w, \quad (5)$$

$$F_R = 2Ah\omega^2 r, \quad (6)$$

where $A = \mu_0 q^2/32\pi h^2 w^2$, ω is the angular rotation frequency, and r is the distance between the monopole and the axis of the disc. The formulas are valid in the low-velocity limit, where $\omega r << w$. The radius of the disc is assumed to be much larger than the distance r.

At very high velocities, the lift force produced by eddy currents in a normal metal approaches that due to persistent currents in a superconductor. Saslow (1992) argued that Maxwell's results "make him the grandfather, if not the father, of eddy current Maglev transportation systems."

Lift, drag, and radial forces on a permanent magnet can be displayed versus the rotation velocity of a conducting disc. We use a cylindrical NdFeB permanent magnet, 18 mm in diameter and 18 mm in height, magnetized along the axis of

the cylinder up to about 1.3 T. An aluminum disc, 20 cm in diameter and 1 cm in thickness, is brought to rotation by an induction motor. The lift, drag, and radial components of the electrodynamic force on the magnet are measured with the *Force sensor* (CI-6537), which can be positioned vertically or horizontally. The magnet is attached to the sensor, and the magnetic dipole is aligned vertically (Fig. 2).

In the induction motor used, the rotation frequency of the magnetic field is 25 Hz. The rotation frequency of the rotor is somewhat less, depending on the load of the motor. The frequency is measured with a photodiode looking at the disc illuminated from above by a light bulb. A piece of paper with black spots properly painted on it is laid on the disc, and electrical pulses from the photodiode provide data on the rotation frequency. These pulses are amplified and then fed to the digital input of the *750 Interface* intended for the *Rotary motion sensor*. With a 1 Hz *Sample rate*, this input is capable of measuring the frequency of incoming pulses. In order to increase the number of the experimental points, the *Sample rate* is set to be 5 Hz.

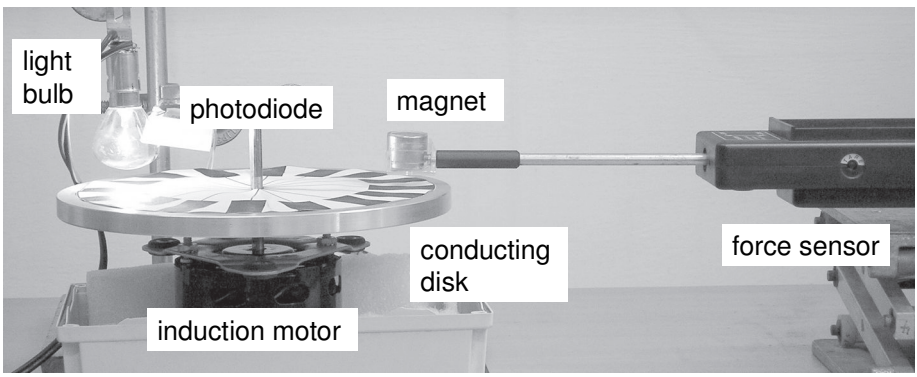

Fig. 2. Setup arranged for measuring radial force.

The aluminum disc is brought to rotation and attains its steady velocity in several seconds, and then the motor is switched off. The force on the magnet and the rotation frequency are measured during a run including periods of acceleration and deceleration of the disc. During each run, *DataStudio* plots a graph of the force versus the rotation frequency. Experimental data from three runs for a given gap are collected in one graph. In the measurements, the gaps h between the magnet and the disc are 10 and 15 mm. The radial force is several times lower than the lift or drag force, and it is measured only for a 10 mm gap. With our motor, the measurements at smaller gaps are impossible since the magnetic braking strongly decreases the rotation frequency.

The conditions of the experiment do not coincide with those used for the theoretical analysis, namely: (i) the dipole approximation is not applicable; (ii)

the thickness of the rotating disc is comparable with the skin depth; (iii) the distance between the magnet and the axis of the disc is close to the disc radius; (iv) neither the low-velocity limit, $v << w$, nor the high-velocity limit, $v >> w$, are fulfilled. Nevertheless, the results obtained (Fig. 3) are in qualitative agreement with calculations (Saslow 1992). The lift-to-drag ratio increases with the rotation frequency. At the edge of the disc, the highest linear velocity is about 50 km.h^{-1}, an order of magnitude lower than that for the magnetically levitated transport. For the latter, the lift-to-drag ratio is much more favorable.

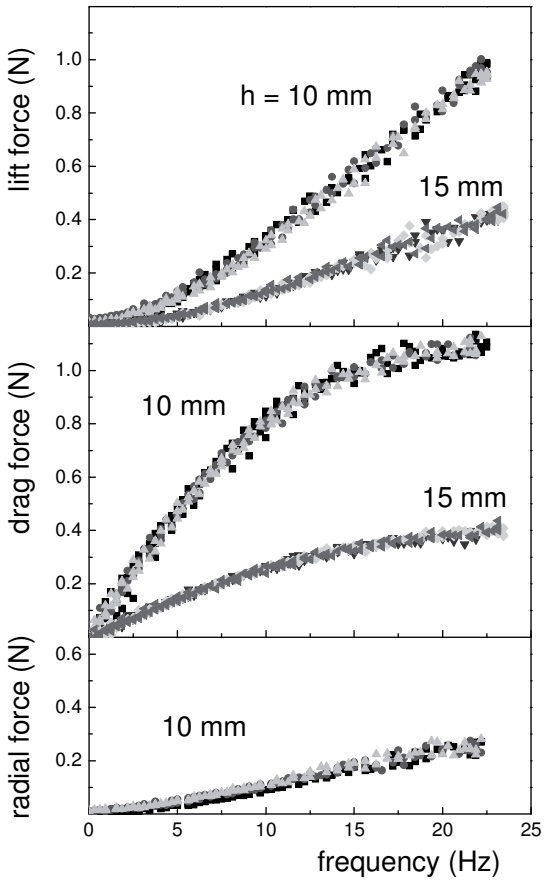

Fig. 3. Lift, drag, and radial forces versus rotation frequency for different gaps between the magnet and the disc.

Electrodynamic levitation. The levitation of a permanent magnet over a rotating disc is an attractive demonstration. The weight of our magnet, about 0.34 N, is less than the maximum lift force for 10 and 15 mm gaps, so that electrodynamic levitation of the magnet is possible. For the demonstration, the magnet is placed into a glass tube positioned vertically over the disc. After switching on the

motor, the magnet gradually moves upwards, according to the increase of the rotation frequency, and reaches an equilibrium position, where the lift force just balances its weight. After switching off the motor, the magnet gradually returns to its lower position. The crucial role of the motion of the disc is clearly seen. The magnet is not free because its position is constrained by the containing tube. This is necessary to oppose the drag force, an unavoidable attribute of the electrodynamic suspension. The levitation is demonstrated with a video camera and a monitor (Fig. 4). The magnet levitates at about $h_0 = 17$ mm above the rotating disc. With a normal metal, the lift force should be smaller than that with a superconductor, which is given by Eq. (2), with $v >> w$:

$$F_L = (3\mu_0 m^2/32\pi h^4). \quad (7)$$

The equilibrium height of a magnet levitated over a superconductor is

$$h_0 = (3\times10^{-7} m^2/8P)^{1/4}, \quad (8)$$

where P is the weight of the magnet. The magnetic moment m determined by measuring the magnetic field of the dipole equals nearly 4.5 A.m^2. With this value, Eq. (2) gives $h_0 \cong 39$ mm.

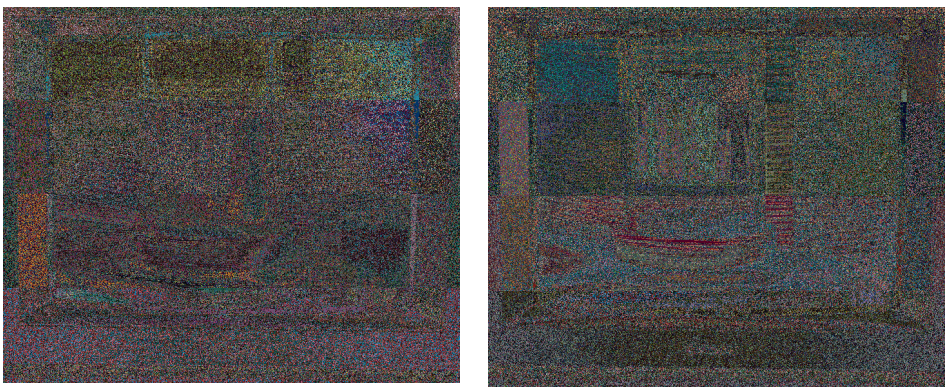

Fig. 4. Demonstration of the electrodynamic levitation with video camera. After the aluminum disc is brought to rotation, the magnet gradually moves upwards.

8.6. Fluorescent lighting

The radiant and luminous spectra of two compact fluorescent lamps are displayed, and their efficacy is compared to that of an incandescent lamp. The electrical signals from a video camera also demonstrate the spectra.

Incandescent and **fluorescent** lamps are based on fundamental physics laws and involve engineering innovations during the last century. This subject is considered in many papers, and only a small number are mentioned here. Manikopoulos and Aquirre (1977) measured spectra of a blackbody cavity in the range 700–1300 K with an infrared spectrometer. Prasad and Mascarenhas (1978) presented a laboratory experiment for the verification of Stefan's law. Dusek *et al* (1980) investigated the validity of Planck's function with derivative spectroscopy. Zanetti (1984) compared the brightness of the Sun and of an incandescent lamp. Leff (1990) and Wagner (1991) considered electrical illumination and the color of incandescent light bulbs. Hodges (1992) compared an incandescent light bulb with a compact fluorescent lamp. Ratcliff *et al* (1992) developed a high-resolution scanning spectrometer for observing the solar spectrum. Agrawal *et al* (1996) calculated properties of incandescent light bulbs. Brizuela and Juan (1996) described a determination of Planck's constant using a light bulb. Soffer and Lynch (1999) and Overduin (2003) discussed some problems of human vision. Gratton *et al* (2004) observed compact fluorescent lamps through a diffraction grating. Escalada *et al* (2004) considered quantum effects in light emitting diodes and fluorescent lamps. Gross *et al* (2005) demonstrated the infrared portion of the spectrum with a standard web camera; this portion becomes observable after removing a filter blocking the infrared. Pesic (2005) estimated the hc/k_B ratio that enters Planck's distribution. Gil *et al* (2006) experimentally determined the luminosity of the Sun.

Thermal radiation of an incandescent lamp cannot exceed that of a perfect blackbody at the same temperature. Planck's distribution shows that only a part of thermal radiation falls into the visible part of the spectrum. The ratio of the power of visible radiation to the total radiation power (or to the power applied to the light source) is called efficiency; for incandescent lamps, it amounts to 10–15%. The temperature of a solid radiator is limited by its melting point. The melting point of tungsten, which is used in incandescent lamps, is 3695 K. The only possible way to improve the efficiency of incandescent lamps is enhancement of their operating temperatures. Gas-filled and halogen lamps allow these temperatures to be increased up to 3200–3300 K, but the cost of this is a reduced lifetime of the lamps. In addition, energy losses arise due to the heat conduction through the gas inside the lamps.

The efficiency is not an exhaustive feature of a light source because the human eye is not equally sensitive to light of different colors. The typical human eye spectral sensitivity is given by the standard luminosity function $S(\lambda)$ established by the International Commission on Illumination. For the light-

adapted vision, this function has a maximum at 555 nm (Fig. 1). Blackbody radiation spectra at 2700 and 6500 K are also shown in the figure because two fluorescent lamps used in our experiments are characterized just by these values. Agrawal *et al* (1996) suggested a simple approximation for the standard luminosity function:

$$S(\lambda) = \exp(-88x^2 + 41x^3), \quad (1)$$

where $x = \lambda/555 - 1$, and λ is the wavelength in nanometers.

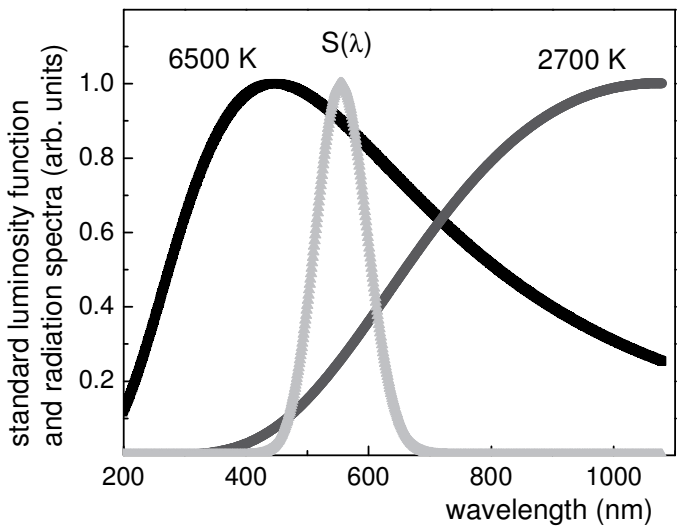

Fig. 1. Standard luminosity function $S(\lambda)$ and normalized blackbody radiation spectra. Really, maximum for 6500 K is about two orders of magnitude higher than that for 2700 K.

Many terms are used in lighting technologies, but we will use mainly two, the irradiance and the illuminance. The irradiance means the power of incident light per unit area ($W.m^{-2}$), while the illuminance is the incident luminous flux per unit area ($lm.m^{-2}$). The total illuminance thus depends on the spectrum of the light. Green light at $\lambda = 555$ nm is most efficient for illumination, and 1 W of electromagnetic radiation of this wavelength provides luminous flux of 683 lm. The modern definition of the candela is based just on this relation: "the candela is the luminous intensity, in a given direction, of a source that emits monochromatic radiation of frequency 540×10^{12} Hz and has a radiant intensity in that direction of 1/683 W per steradian." The lumen is defined in relation to the candela: a light source that uniformly radiates one candela in all directions radiates a total of 4π lumens. The lumen-to-watt ratio characterizing a light source is the luminous efficacy. Green light is most effective in this respect, but other parts of the spectrum are also needed for qualitative illumination.

In fluorescent lamps, the electrical discharge occurs in a gas containing mercury vapor. Mercury atoms ionized in collisions with electrons strongly radiate in the ultraviolet, mainly at 254 nm. This radiation excites phosphors coating the inner wall of the lamps and causes them to emit visible light. The spectrum of this light is governed by properties of the phosphors. Mercury atoms emit also in the visible, mainly at 436, 546, 578, and 612 nm; these spectral lines or narrow bands are also presented in the spectra of fluorescent lamps. The radiation of mercury atoms can be used for effective lighting if the ultraviolet part of radiation were reliably blocked. Phosphors added serve to improve and modify the illumination.

The revolutionary feature of fluorescent lamps is that their radiation spectra and efficiency are not subjected to restrictions posed by Planck's distribution. Many hundreds of phosphors are known, and several of the most effective phosphors were chosen for composing desired spectra and attaining both high efficacy and qualitative lighting.

1. Spectra and color temperatures

Spectra of fluorescent lamps clearly show how their color temperatures can be varied without decreasing the efficacy (Kraftmakher 2010f).

Additional equipment: *Educational spectrophotometer*, *Rotary motion sensor*, *Voltage sensor*, *Light sensor*, *Aperture bracket*, two compact fluorescent lamps, diffraction grating, photodiode, video camera, color monitor, oscilloscope, two lenses.

Two compact fluorescent lamps (CFL) are tested in the experiments (Fig. 2). The manufacturers characterize them as a "warm white" lamp (Osram, 11 W, 600 lm) and a "cool daylight" lamp (Flashlight, 13 W). A more definite characteristic is the color temperature, also given by the manufacturers. The claimed color temperature is 2700 K for the "warm white" lamp and 6500 K for the "cool daylight" lamp. The color temperature of a light source does not mean that its spectrum is similar to that of a blackbody of an equal color temperature. Fluorescent lamps are designed to emit only visible light of desired spectrum. Their color can be qualitatively characterized by the so-called blue-to-red ratio. In optical pyrometry of hot bodies, this ratio is a measure of the color temperature, which equals to the temperature of a blackbody radiator providing the same blue-to-red ratio. For a gray body, the color temperature coincides with its real temperature. For fluorescent lamps, the blue-to-red ratio can be used only for qualitative characterization and comparison of different lamps. The green part in the spectra of fluorescent lamps provides their high efficacy.

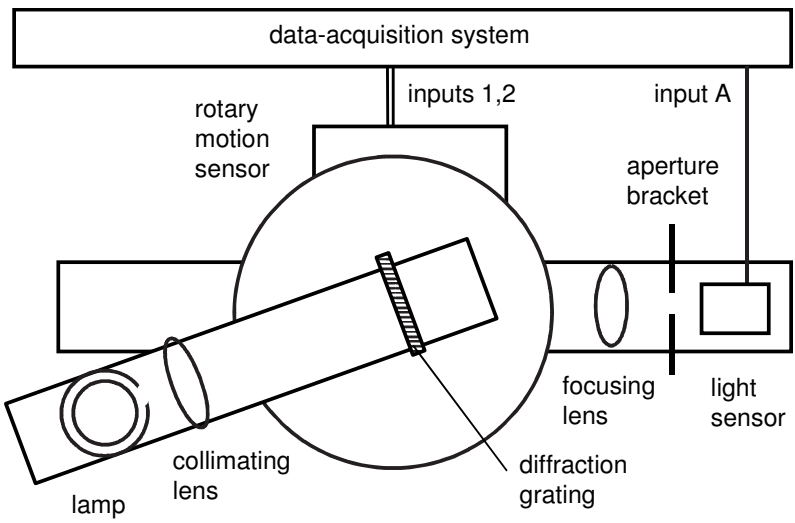

Fig. 2. Schematic of the setup.

The setup includes the *Educational spectrophotometer*, two lenses, the *Rotary motion sensor*, diffraction grating (600 lines per millimeter, SE-9358), and the *Light sensor*. A fluorescent lamp, the grating, and the collimating lens (f = 100 mm) are positioned on the rotating arm of the spectrophotometer, whose angular position is measured by the *Rotary motion sensor*; the positions of the focusing lens (f = 250 mm) and of the *Light sensor* are fixed. The diffracted light is focused onto the *Aperture bracket* (OS-8534) set in front of the sensor.

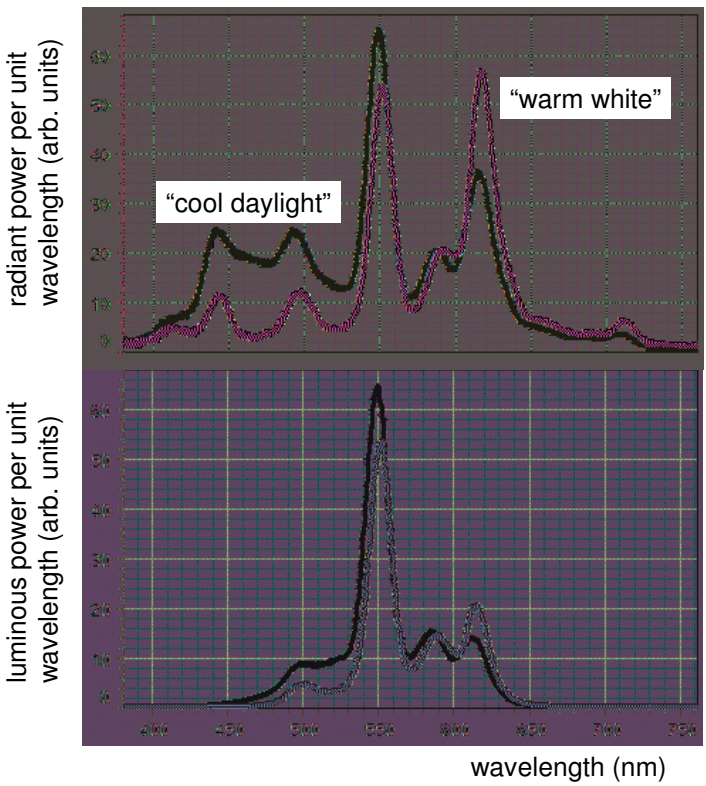

Fig. 3. Radiant and luminous spectra of two fluorescent lamps.

The fluorescent lamp is positioned vertically. An opaque plastic cylinder with a 1 mm slit along it covers the lamp. The light outgoing from the slit is collimated and directed onto the diffraction grating. A very small fraction of the light produced by the lamp is thus utilized for the measurements. The orientation of the lamp and of the slit is adjusted to maximize the signal from the light sensor. The *Sample rate* is 100 Hz. During a run, one rotates the arm of the spectrophotometer. *DataStudio* acquires the data from the sensors, calculates the wavelength, and displays the radiant spectra. The spectra obtained are significantly distorted because the efficiency of a diffraction grating strongly

depends on wavelength. The sensitivity of the light sensor, a silicon photodiode, is assumed to be proportional to the wavelength. The unknown efficiency of the grating cannot be taken into account; nevertheless, the most important features of fluorescent lamps are clearly seen (Fig. 3).

A general feature of fluorescent lamps is a strong green part of the spectrum. The difference in the spectra of the two lamps is due to different contributions of the blue and red parts. The red part is strongly presented by the "warm white" lamp, and the blue by the "cool daylight" lamp. Just this variation makes the color temperatures of the two lamps so different. The spectra obtained are comparable to those given by the manufacturers. However, the resolution of our setup is insufficient to separate sharp spectral lines, and only smoothed spectra are available.

The luminous spectra are obtained by multiplying the radiant spectra by the standard luminosity function $S(\lambda)$. For the present purpose, the accuracy provided by Eq. (1) is quite satisfactory. The luminous power is an integral of this spectrum. It equals (in arbitrary units) 195 for the 11 W "warm white" lamp and 253 for the 13 W "cool daylight" lamp. The difference in the luminous power is mainly due to the different wattage of the lamps. Second, it is difficult to equally illuminate the diffraction grating in the two measurements. The spectra are calculated and displayed by *DataStudio*.

For a demonstration, the spectrum obtained with the diffraction grating is focused on a white screen and viewed by a video camera (Panasonic, GP-KR222) connected to a color monitor (Sony, PVM-14N6U). The difference in the spectra of the two lamps is clearly seen, and the correlation between the color temperatures claimed by the manufacturers and the blue-to-red ratio is evident (Fig. 4). An oscilloscope synchronized by the line frequency of the video camera, 15.734 kHz, also can serve for demonstrating the spectra. The electrical signal from the camera carries all the information about a spectrum; this signal proceeds to the Y-input of a Kenwood CS-4025 oscilloscope. The signal reproduces the sequence of pixels along horizontal lines of the television raster. The signals corresponding to all horizontal lines of the raster are the same for all the horizontal lines and are superimposed on the screen of the oscilloscope. The oscilloscope thus displays the spectrum viewed by the video camera.

The signal from the video camera includes three additional elements needed for correctly displaying any picture. First, a short negative pulse signals the start of each horizontal line. Second, a short radio frequency burst serves as a reference for decoding the color information for a given horizontal line. Third, signals of the same radio frequency are added to the main video signal for creating a color image; the color is encoded by the phase shift between these signals and the reference. All these signals can be seen on the screen of the oscilloscope. In our case, most important are variations in the video signal along the horizontal line, which represent the radiant spectrum. The difference between the spectra of the two lamps is clearly seen, and it is possible to calibrate the horizontal scale of the oscilloscope in wavelengths.

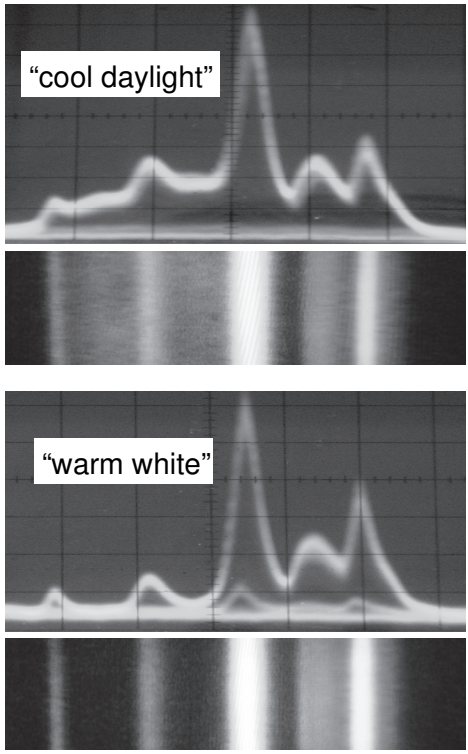

Fig. 4. Spectra of two fluorescent lamps displayed by the oscilloscope and video monitor.

2. Efficacy of fluorescent lamps

The efficacy of a compact fluorescent lamp is several times higher than that of an incandescent lamp (Kraftmakher 2010f).

Equipment: variable AC supply, multimeters, compact fluorescent lamp, incandescent lamp, photodiode, narrow band pass filter (550 nm).

In this experiment, the luminous power produced by a compact fluorescent lamp is compared to that by an incandescent lamp. Both lamps are positioned at a 30 cm distance from a silicon photodiode (United Detector Technology, PIN-10D). The photodiode is chosen for its large sensitive area, 1 cm^2. A narrow band pass filter (Thorlabs, FB-550-10) is set in front of the photodiode. The central wavelength of the filter is 550 nm, and the full width at half maximum is 10 nm. The wavelength band of the filter is thus much narrower than that of the standard luminosity function. Nevertheless, the signal from the photodiode can be assumed proportional to the luminous power produced by the lamps (for this purpose, the FB-550-40 filter would be more suitable). The two lamps in turn illuminate the photodiode, whose output signal is measured with a multimeter.

The incandescent lamp (60 W, 655 lm) is chosen to provide the luminous power close to that by the "warm white" fluorescent lamp (11 W, 600 lm). To determine the efficacy, the total luminous power distributed over all directions should be measured. We cannot perform such measurements, so that the comparison of the two lamps is only estimation. Second, the luminous power is given only in arbitrary units. The manufacturer claims that the efficacy of the fluorescent lamp used is five times the efficacy of an incandescent lamp, and the results obtained are in agreement with this claim.

The luminous power produced by the two lamps is measured as a function of a voltage taken from a regulated AC supply. Due to Wien's displacement law, the luminous power by an incandescent lamp is a stronger function of the operating voltage than that by a fluorescent lamp (Fig. 5).

Unlike large tubular fluorescent lamps, a compact lamp does not manifest ripples in the irradiance whenever the electrical discharge in the lamp interrupts two times per period of the feeding current. This difference is due to the frequency conversion performed by an electronic inverter (electronic ballast) embedded into the compact lamps. For this purpose, the main 50 Hz voltage is converted to a voltage of frequency of about 30 kHz. The interruptions in the feeding current thus become much shorter. The frequency conversion reduces electrical losses in the ballast and thus enhances the efficacy of the lamps. It is easy to reveal the high-frequency current through the lamp with a coil placed near it and connected to an oscilloscope.

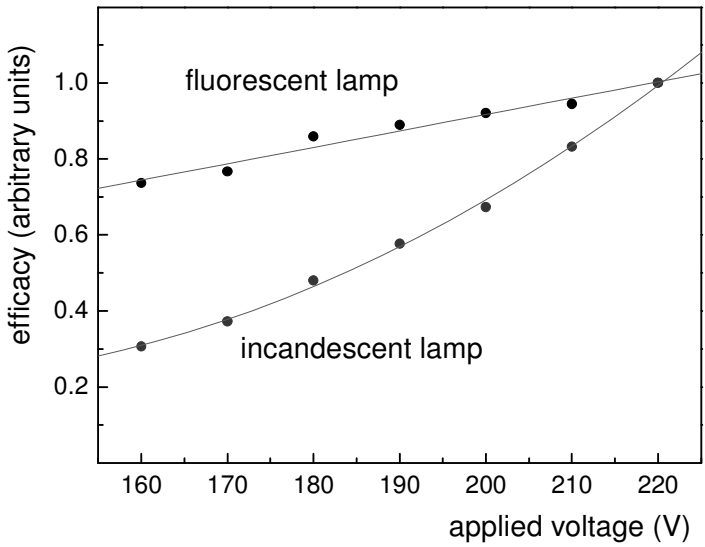

Fig. 5. Efficacy of fluorescent and incandescent lamps versus applied voltage.

8.7. Cathodoluminescence

Cathodoluminescence is a special case of luminescence, the process of light emission, which does not have its cause solely in the temperature of the material (Chappell 1978, Fox 2001).

Cathodoluminescence is the excitation of solids to luminescence by the direct impact of electrons. It involves several processes between the initial excitation and the final emission of light from the phosphor. Cathodoluminescence is used in many cathode-ray devices. The emission from a phosphor continues after the excitation as ceased, and its intensity decreases with time following either an exponential or a power law function. In some cases, it is possible to resolve the decay curve into several exponential functions with different time constants. For cathode-ray tubes, the decay time is stated as the time for the emission to decay to a 10-percent level. The decay times have been classified as very long (longer than 1 s), long (0.1 to 1 s), medium (1 to 100 ms), medium short (0.01 to 1 ms), short (1 to 10 μs), and very short (less than 1 μs).

Many cathode-ray devices, including oscilloscopes, computer monitors, radar displays, and picture tubes, make use of cathodoluminescence. In a color cathode-ray display, three phosphors put on the internal surface of the faceplate of the tube provide the red, green, and blue primary colors. Each of the phosphors forms a thin vertical line on the surface, less than 0.1 mm in width. Three electron guns of the cathode-ray tube produce independent electron beams, each destined for the specific phosphor. To achieve this goal, a precise shadow mask is arranged inside the tube in front of the faceplate. The holes in the mask are arranged in such order that each electron beam can strike only its specific phosphor. Each element of a picture (pixel) contains smallest neighboring spots of the three primary colors presented in an appropriate percentage.

1. Thorough look at computer display

With moderate magnification, the structure of color images on a computer display is seen, and the decay time of phosphors is found (Kraftmakher 2009h).

Equipment: computer, function generator, oscilloscope, photodiode, video camera, monitor, light guide, 9 V battery, resistor.

Structure of color image. To create well-controlled color images, we employ *PowerPoint* software. Horizontal lines of red, green, and blue colors are drawn on a black background using the *Line color*/*More line colors*/*Custom* option. A white line is added for comparison. The image is displayed as *Slide show*. The four adjacent lines, each of about 2 mm in width, are observed with a Panasonic GP-KR222 video camera and a Sony PVM-14N6U color monitor (Fig. 1).

With a suitable objective lens, the distance between the display and the camera is about 10 cm (we use a common objective lens and a 20 mm adapter). The total magnification of the system, of about 25, is sufficient to clearly see the smallest color spots forming any image on the display. According to the orientation of the video camera, the horizontal lines on the computer display are seen as vertical lines on the monitor. Any color line looks as a set of spots of one primary color. The white line contains spots of all the colors. From this observation, it is possible to estimate the ultimate resolution of the display. The color spots forming the image are also observable with a magnifying glass.

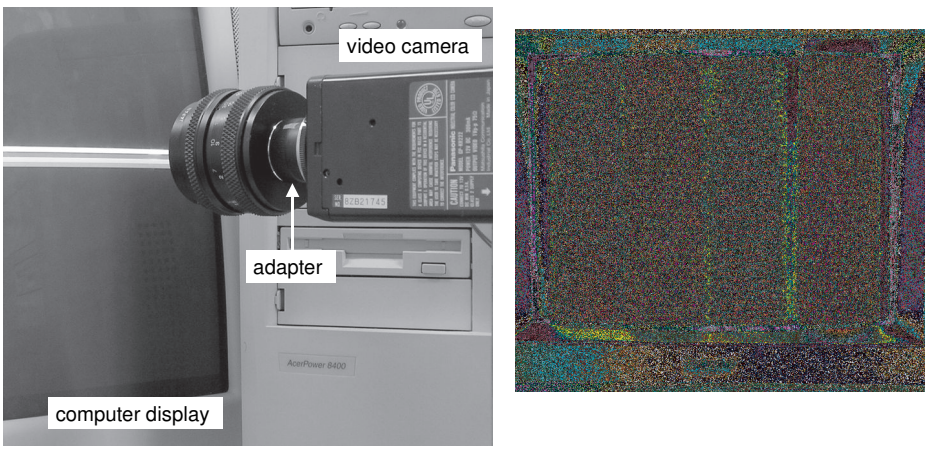

Fig. 1. Video camera views color lines created with *PowerPoint* and displayed as *Slide show*. Enlarged color lines are seen on the monitor.

Decay time of phosphors. The emission from a phosphor continues after the excitation is ceased. Its intensity decreases with time following either an

exponential or a power law function. For observing the decay of different phosphors, thin horizontal lines of the primary colors are drawn on a black background with *PowerPoint* software. A fast photodiode (Edmund Optics, J53-372) views a small fraction of a line with a light guide, 3 mm in diameter. The light guide separates the photodiode from the computer display, where significant disturbances can be caused by AC magnetic fields produced by the deflection coils of the cathode-ray tube. The voltage across the 10 kΩ load resistor of the photodiode proceeds to the Y-input of a GOS-622G oscilloscope (Fig. 2). The photodiode, its load resistor, and a 9 V battery are suited in a metal box positioned near the oscilloscope.

At any point of the color line, the electron beam excites the phosphor repeatedly according to the refresh rate of the computer. In our case, the refresh rate is 60 Hz, so that the excitation repeats every 16.7 ms. The color lines are formed by several neighboring horizontal lines of the raster. Several excitations thus occur being separated by the line period. The raster consists of 768 horizontal lines, and the line period is nearly 0.02 ms. For the red phosphor, the period is much shorter than the decay time, so that several following excitations can be considered one hit. For the green and blue phosphors, this is not the case. For these colors, the horizontal lines are drawn to be as thin as possible. According to the 10% criterion, the red phosphor has a decay time of about 1 ms. For the green and blue phosphors, the decay times appeared to be much shorter, nearly 0.04 and 0.02 ms, respectively.

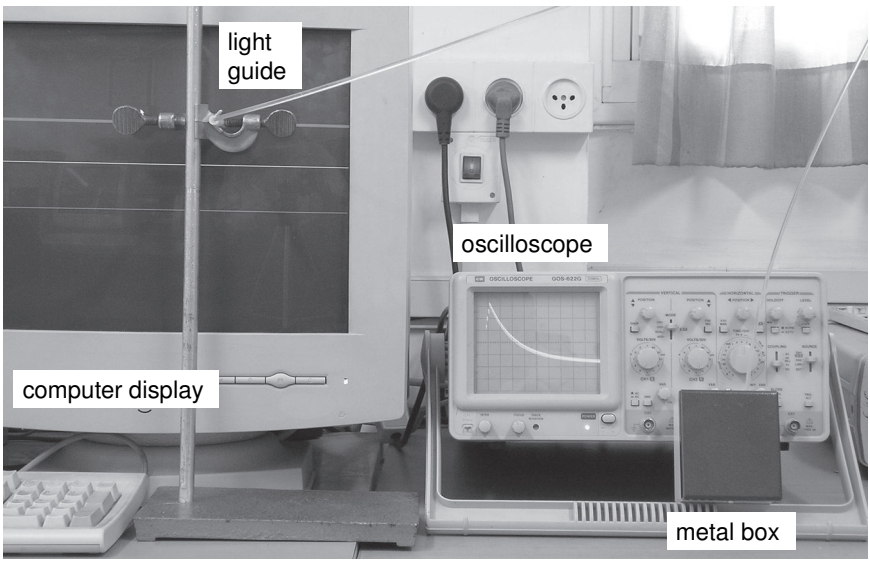

Fig. 2. Observation of decay of phosphors. Decay of the red phosphor is seen with 0.2 ms.div^{-1} scale.

2. Decay time of cathodoluminescence

The aim of the experiment is to determine the decay time of a phosphor covering the inner surface of the screen of a cathode-ray tube (Kraftmakher 2009a).

Equipment: two oscilloscopes, function generator, decade resistance box, capacitor, photodiode, 9 V battery, resistors, capacitor.

The setup for observing the decay of a phosphor includes a function generator (GFG-8020G), two oscilloscopes, a fast photodiode (Edmund Optics J53-372), a 9 V battery, a capacitor, and two resistors (Fig. 3).

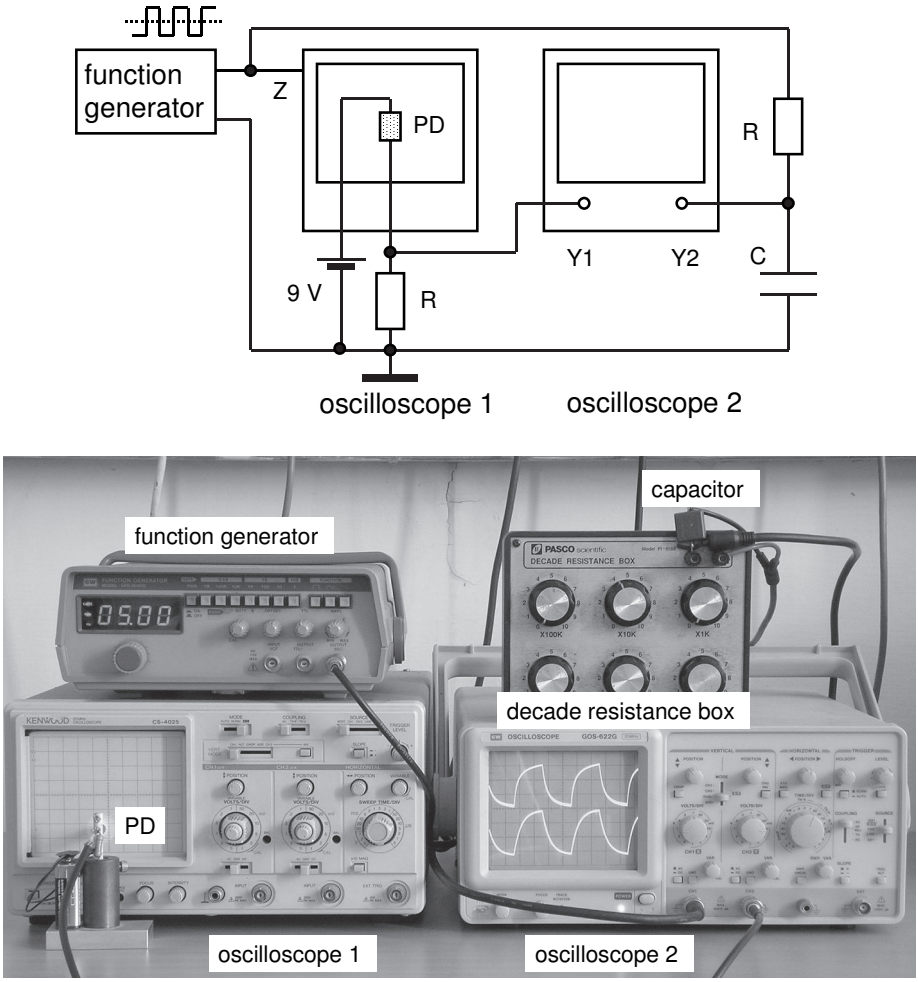

Fig. 3. Schematic of the setup. PD–photodiode.

The first oscilloscope, a Kenwood CS-4025 model, provides a phosphor to be tested. The photodiode views the bright spot on the screen of the oscilloscope, which operates in the X-Y mode with both inputs grounded. To avoid damage of the phosphor, the spot is defocused. A square wave voltage from the function generator is applied to the control grid (modulator) of the cathode-ray tube through the Z input of the oscilloscope. This voltage controls the intensity of the electron beam and thus the excitation of the phosphor and is sufficient for the 100 percent modulation. The voltage on the 10 kΩ load resistor of the photodiode is proportional to the brightness of the spot viewed. The second oscilloscope, GOS-622G model, displays this signal.

Square wave excitation. When using square wave excitation of the phosphor, the voltage displayed by the second oscilloscope resembles the voltage across a capacitor periodically charged and discharged through a resistor. A definite time is needed for the phosphor to attain its full brightness according to the excitation conditions. The brightness does not exactly follow the shape of the rectangular pulses: This becomes clear when gradually increasing the frequency of the function generator.

The square wave voltage from the function generator proceeds also to an integrating RC circuit (C = 500 pF), whose output voltage is displayed by the oscilloscope along with the signal from the photodiode. The time constant of the RC circuit can be adjusted to make its output voltage close to that from the photodiode. For this purpose, the resistor R is adjustable; we use a decade resistance box (PI-9588). Both Y inputs of the oscilloscope are DC coupled. If the decay of the phosphor tested were exactly exponential, the two voltages displayed by the oscilloscope can be made equal. If so, the time constant τ of the phosphor equals that of the integrating circuit, RC. In most cases, however, the decay is not exponential. The phosphor may consist of several compounds, each having its own contribution and decay time. Therefore, one can only determine an apparent decay time according to the 10-percent criterion. From the measurements, it appeared to be about 70 μs. When increasing the modulation frequency, the amplitude of the signal decreases due to the decrease of the excitation time. These data are used for the determination of the time constant of the excitation. In this measurement, we use a criterion similar to the 10-percent criterion for the decay: the excitation time is a time necessary for the phosphor to attain the 90-percent level of its full brightness. From the measurements, this time is about 50 μs. The decay time of the phosphor falls into the "medium short" category.

Sine wave excitation. Another variant of the experiment employs the sine wave modulation of the voltage applied to the Z input of the first oscilloscope. The modulation characteristic can be determined with a regulated DC source. It is seen from the characteristic (Fig. 4) that a definite bias voltage should be applied to the Z input to operate in a nearly linear modulation regime.

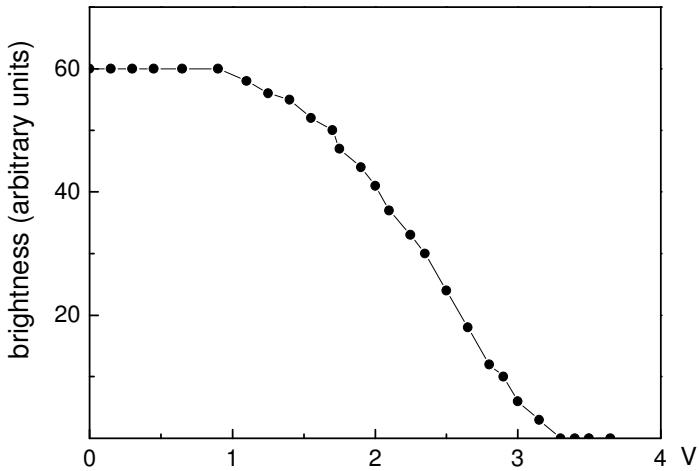

Fig. 4. Brightness versus voltage applied to Z-input.

In the measurements, the output voltage of the function generator contains a DC component added to the sine wave voltage. The DC bias and the amplitude of the AC voltage are chosen to operate within a linear part of the modulation characteristic. The signal from the photodiode is a sine wave voltage, whose amplitude and phase depend on the modulation frequency. The oscilloscope also displays the voltage from the function generator. In these measurements, both Y inputs of the oscilloscope are AC coupled. The signal from the photodiode is measured as a function of the modulation frequency in the range 50 Hz to 50 kHz (Fig. 5). For an exponential decay, this dependence should follow the expression

$$(A_0/A)^2 = 1 + \omega^2\tau^2, \quad (1)$$

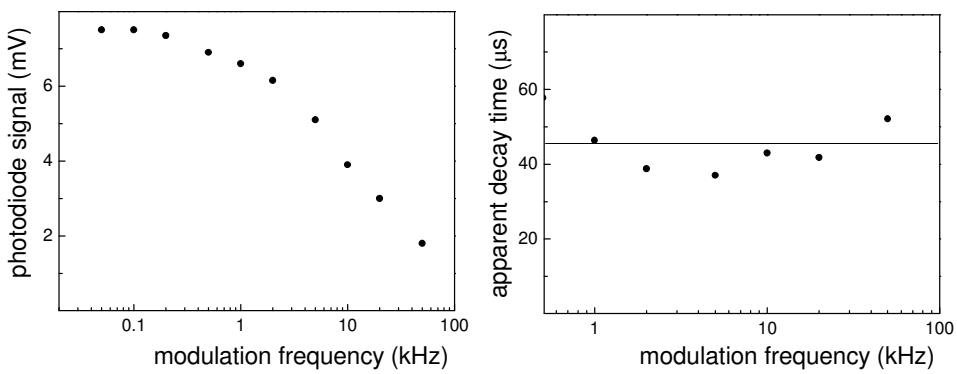

Fig. 5. Signal from the photodiode and apparent decay time versus modulation frequency.

where A and A_0 are the signal amplitudes at the angular frequency ω and at a sufficiently low frequency. Equation (1) can be presented in the form

$$\tau = [(A_0/A)^2 - 1]^{1/2}/\omega, \quad (2)$$

where τ is the apparent decay time. For the calculations, we use the data obtained at frequencies of 1 kHz and above, which provide significant difference between A_0 and A. The apparent decay time is around 45 μs. It is shorter than the time found according to the 10-percent criterion.

The use of the sine wave excitation allows observations of the phase lag between the excitation and the phosphorescence. For this purpose, the second oscilloscope displays both signals, and the gain of its channels is adjusted to equalize the two signals at 50 Hz. At this frequency, the phase shift between the signals is nearly zero, and both graphs coincide. When increasing the modulation frequency, the phase lag increases and is clearly seen, along with the decrease of the signal from the photodiode (Fig. 6).

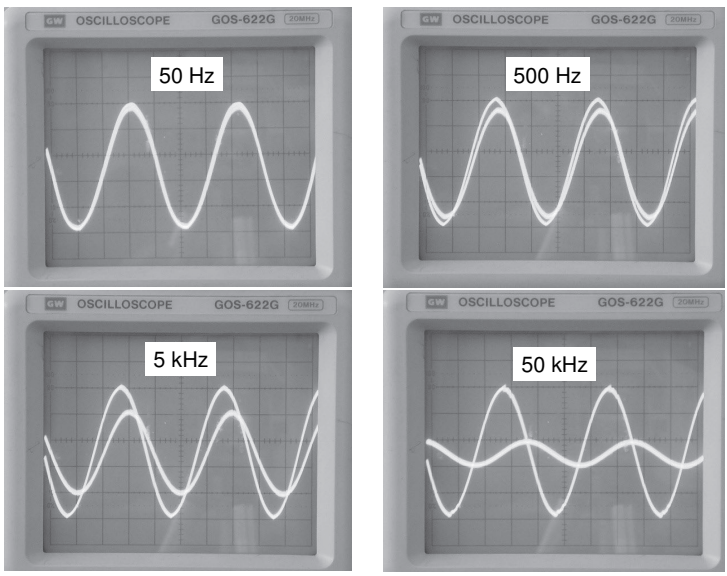

Fig. 6. Modulation voltage and signal from photodiode for different modulation frequencies. At 50 kHz, the phase lag amounts to nearly 90°.

Demonstration with one oscilloscope. The above experiment seems to be simplest ones for observing the decay of a phosphor in a cathode-ray tube. The equipment includes a generator for the modulation, an oscilloscope providing a phosphor for the test, and a photodiode connected to a second oscilloscope to observe the excitation and the decay of the phosphor. However, periodically exciting the phosphor and observing the decay signal are possible with one oscilloscope operating in the dual trace mode (Fig. 7). One of its Y inputs is grounded, and a horizontal straight line appears on the screen. The photodiode

views a small part of this line, where the electron beam periodically excites the phosphor. The phosphor decays after the beam passes this point. The signal from the photodiode proceeds to the second Y input of the oscilloscope, and the decay signal is clearly seen. With this approach, the time resolution depends on the sweep rate of the oscilloscope, which is easy to change, and on the width of the sensitive area of the photodiode. At low sweep rates, the signal from the photodiode is symmetrical: it simply reflects the passage of the electron beam. At high sweep rates, the finite decay time of the phosphor breaks the symmetry: the signal continues after the beam passes the photodiode.

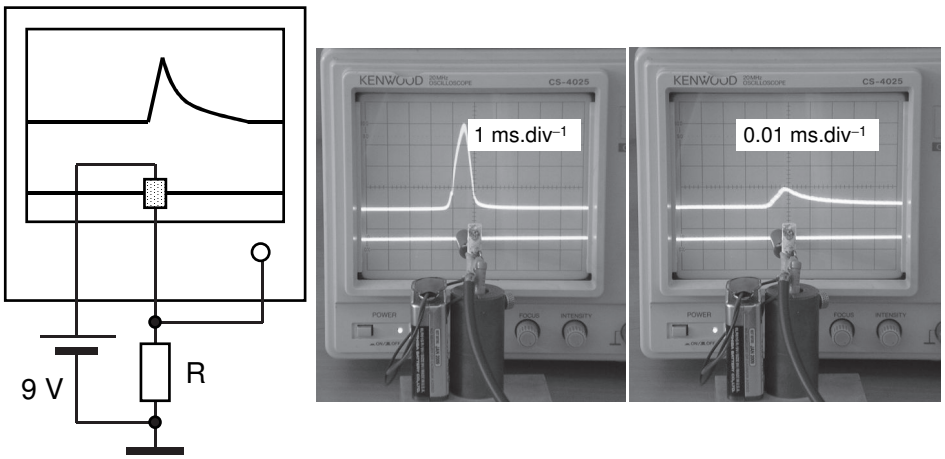

Fig. 7. Demonstration with one oscilloscope. Using different sweep rates, the finite decay time becomes evident.

8.8. Two-wire transmission line

With data acquisition, experiments with a two-wire transmission line become more convenient and less time-consuming, so additional exercises can be added to traditional measurements. The experiments include (i) the wavelengths and propagation velocity of electromagnetic waves; (ii) the characteristic impedance of the line; (iii) the input impedance; and (iv) the determination of unknown load impedances (Kraftmakher 2009e).

Additional equipment: *Voltage sensor*, *Motion sensor*, two-wire transmission line, UHF oscillator, diode.

Using properly designed transmission lines, electromagnetic waves can be carried, without significant losses and distortions, over distances much longer than their wavelength. The most common transmission lines are the coaxial cable, two-wire line, and parallel-strip line. Some papers in this field are listed below. Johnston and Silbernagel (1969) described an experiment with a commercially available strip-type transmission line. A 110 MHz signal was detected with a diode probe and displayed by an oscilloscope. For the transmission line, the characteristic impedance and propagation velocity were determined. Allenson *et al* (1973) reported on experiments with a parallel-wire transmission line using electromagnetic waves of 450 MHz frequency. Howes (1978, 1980) described vacuum tube and transistor oscillator circuits for experiments related to transmission lines and radiation. With relatively low frequencies, less than 10 MHz, Holuj (1982) observed reflections of sinusoidal signals and short electric pulses in a coaxial cable. The propagation velocity of electromagnetic waves, the reflection coefficient, and unknown impedances loading the cable were determined. Blair (1982) described experiments with transmission lines constructed from lumped components. Beers (1983) developed inexpensive sources and detectors for 13 cm electromagnetic waves. Greenslade (1989) described an experiment with a lossy transmission line. To demonstrate the reflection and superposition of electric pulses, Watson (1995) used a 150 m coaxial cable and a 100 ns pulse generator. An inexpensive oscilloscope was sufficient for the demonstrations. Smith and Blackburn (1997) described a design for simulating a lumped element transmission line. With a 10 MHz function generator and a 250 MHz oscilloscope, Mak (2004) measured the propagation velocity of electromagnetic waves along a coaxial line. Kim and Kim (2007) used a video recorder as a source of electromagnetic waves and a computer with a TV card as a receiver. The authors described automated measurements of standing waves in a two-wire transmission line. Starrett (2008) employed a common walkie-talkie device as a source of electromagnetic waves.

Main ***theoretical predictions*** for transmission lines (Cheng 1992; Inan and Inan 1999; Kraus and Fleisch 1999) are the following.

• Each transmission line is characterized by a **capacitance** and **self-inductance** per unit length, C and L. The **propagation velocity** of electromagnetic waves along the line is $(LC)^{-½} = (\varepsilon_0\varepsilon\mu_0\mu)^{-½} = c(\varepsilon\mu)^{-½}$, where ε_0 and μ_0 are the **electric constant** (permittivity of vacuum) and **magnetic constant** (permeability of vacuum), c is the velocity of electromagnetic waves in vacuum, and ε and μ are the **relative permittivity** (dielectric constant) and **permeability of the medium**, in which the line is embedded. This result follows from the differential equations describing electromagnetic waves in a transmission line, often called the telegrapher's equations.

• An important parameter of a transmission line is its **characteristic impedance**, Z_0. For a lossless line, it equals $Z_0 = (L/C)^{½}$ and is purely resistive. When impedance Z_0 terminates the line, the voltage-to-current ratio equals Z_0 at any point along the line. For a two-wire line in vacuum, the characteristic impedance equals $Z_0 = (\mu_0 c/\pi)\cosh^{-1}(D/2a)$, where D and a are the distance between the wires and their radius. For $D^2 >> 4a^2$, $\cosh^{-1}(D/2a) \cong \ln(D/a)$, so

$$Z_0 = 120\ln(D/a); \qquad \text{more precisely,} \tag{1a}$$

$$Z_0 = 120\ln[(D/2a) + (D^2/4a^2 - 1)^{½}]. \tag{1b}$$

• A lossy transmission line has a series resistance per unit length, R, and the shunting conductance per unit length, G. The characteristic impedance equals $Z_0 = [(R + j\omega L)/(G + j\omega C)]^{½}$. For low losses ($R << \omega L$, $G << \omega C$), an additional condition, $R/L = G/C$ (Heaviside's condition), makes the **propagation velocity** and **attenuation** of the electromagnetic waves to be independent of frequency; therefore, this is a distortion less line.

• Generally, electromagnetic waves propagating along a transmission line experience reflections from its end. When an impedance $\boldsymbol{Z}_L$ loads the line, the **reflection coefficient** $\boldsymbol{\Gamma}$ is a **complex quantity**:

$$\boldsymbol{\Gamma} = |\boldsymbol{\Gamma}|\exp(j\theta_\Gamma), \tag{2}$$

where $|\boldsymbol{\Gamma}|$ is the modulus, and θ_Γ is the phase angle. It can be shown that

$$\boldsymbol{\Gamma} = (\boldsymbol{Z}_L - Z_0)/(\boldsymbol{Z}_L + Z_0). \tag{3}$$

• The superposition of the incident and reflected waves creates **standing electromagnetic waves** along the line. No reflection occurs only when $\boldsymbol{Z}_L = Z_0$: the line is matched when the load impedance is equal to the characteristic impedance. Total reflection of electromagnetic waves occurs when the line is open-circuited ($\boldsymbol{Z}_L = \infty$, $\boldsymbol{\Gamma} = 1$), short-circuited ($\boldsymbol{Z}_L = 0$, $\boldsymbol{\Gamma} = -1$), or loaded by a pure reactance ($|\boldsymbol{\Gamma}| = 1$). In all the cases, the amplitudes of the standing wave vary from zero to twice the amplitude of the incident wave.

• The **input impedance** $\boldsymbol{Z}_{in}$ of a loss less transmission line of a length l is a **complex quantity** depending on the l/λ ratio (λ is the wavelength), the load $\boldsymbol{Z}_L$, and the characteristic impedance Z_0:

$$\mathbf{Z}_{in} = Z_0[(\mathbf{Z}_L \cos kl + jZ_0 \sin kl)/(Z_0 \cos kl + j\mathbf{Z}_L \sin kl)], \quad (4)$$

where $k = 2\pi/\lambda$. When $\mathbf{Z}_L = \infty$, $\mathbf{Z}_{in} = -jZ_0 \cot kl$; for $\mathbf{Z}_L = 0$, $\mathbf{Z}_{in} = jZ_0 \tan kl$.

• When a transmission line is loaded by impedance causing partial reflection, the standing wave is superimposed on the traveling wave. The **voltage standing wave ratio** S (**VSWR**) is a ratio of the maximum voltage amplitude of the standing wave to the minimum amplitude. Clearly,

$$S = (1 + |\mathbf{\Gamma}|)/(1 - |\mathbf{\Gamma}|), \quad \text{and} \quad (5a)$$

$$|\mathbf{\Gamma}| = (S - 1)/(S + 1). \quad (5b)$$

When a resistor R loads a transmission line, the reflection and thus the VSWR depend on the ratio of the load resistance to the characteristic impedance. It can be shown that $S = Z_0/R$ for $Z_0 > R$, and $S = R/Z_0$ for $R > Z_0$.

• Any impedance $\mathbf{Z}_L$ loading a transmission line can be determined by observing the standing wave:

$$\mathbf{Z}_L = Z_0(1 - jS \tan kl_m)/(S - j \tan kl_m), \quad (6)$$

where l_m is the distance from the end of the line to the first voltage minimum (Cheng 1992, problem P.9-29). From Eq. (3), the load impedance equals

$$\mathbf{Z}_L = Z_0(1 + \mathbf{\Gamma})/(1 - \mathbf{\Gamma}). \quad (7)$$

The complex reflection coefficient $\mathbf{\Gamma}$ is:

$$\mathbf{\Gamma} = |\mathbf{\Gamma}| \cos\theta_\Gamma + j|\mathbf{\Gamma}| \sin\theta_\Gamma, \quad (8)$$

where the phase angle $\theta_\Gamma = 2kl_m - \pi$ (Cheng 1992, pp 462, 466).

Formulas for load impedance. For determining the **load impedance**, there exist only two parameters of the standing wave, S and l_m; they are used directly with Eq. (6), and indirectly with Eqs. (7) and (8). These equations can be converged into simple relations for the **real** and **imaginary** parts of the load impedance:

$$\mathrm{Re}Z_L = Z_0 x(y^2 + 1)/(x^2 + y^2), \quad (9a)$$

$$\mathrm{Im}Z_L = -Z_0 y(x^2 - 1)/(x^2 + y^2), \quad (9b)$$

where $x = S$, and $y = \tan kl_m$. From the formulas, $\mathrm{Re}Z_L \geq 0$, while the sign of $\mathrm{Im}Z_L$ is opposite to that of y. When $x = 1$, $\mathrm{Re}Z_L = Z_0$, and $\mathrm{Im}Z_L = 0$.

The setup. The line consists of two parallel aluminum-alloy rods, 0.95 cm in diameter and 143 cm long. The distance between the rods is 5 cm. A Wavetek 3005 oscillator provides voltages of frequencies up to 520 MHz. A standard cable connects the output of the oscillator to the input of the line (Fig. 1). The line can be **open-circuited**, **short-circuited**, or **loaded** by any impedance. An electric probe consisting of a 1N23C diode and two short wires is positioned between the rods and oriented perpendicular to the line. The probe detects the AC electric field between the rods with no electrical contact to them. The

Voltage sensor connected to the diode through two RF chokes acquires a DC voltage across the diode. The response of this probe is nonlinear, and a calibration is needed for correcting measurement data if necessary. The data-acquisition system is used to make the measurements less time-consuming.

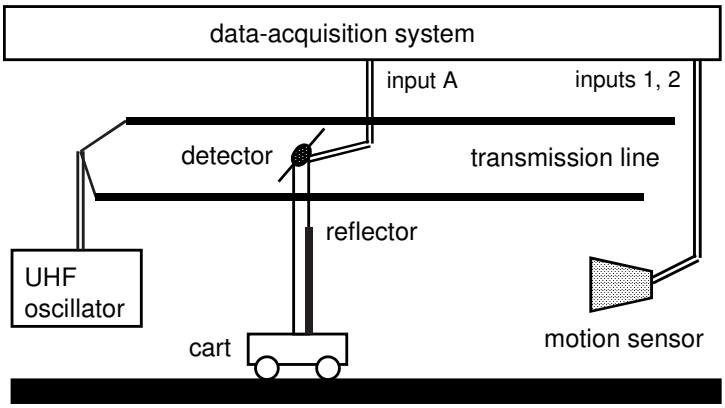

Fig. 1. Schematic of the setup.

The *Motion sensor* measures the position of the probe along the transmission line. The operation of the sensor is based on measuring the time for short ultra sound pulses to reach a reflector and then return back. A plastic reflector rests on the *Dynamics cart* (ME-9430) manually moved on the 120 cm *Dynamics track* (ME-6955) set parallel to the line. The probe is mounted on the reflector. The *Motion sensor* continually measures the position of the probe during a run, and *DataStudio* displays the signal from the probe versus its position. Each run along the line lasts nearly 20 s, so time-consuming measurements are completely excluded.

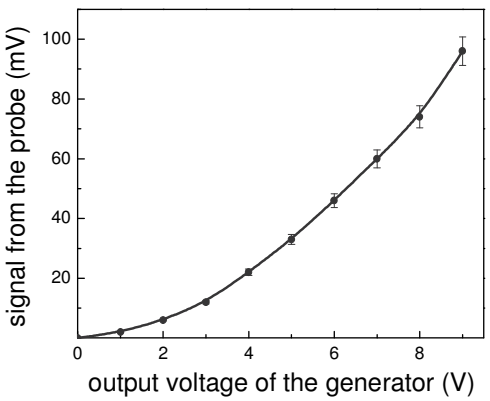

Fig. 2. Calibration curve of the measuring system.

To determine the nonlinear characteristic of the probe, the standing waves were recorded for different voltages set at the output of the oscillator. The graph of the signal from the probe versus the output voltage reflects the nonlinearity of the measuring system (Fig. 2). This characteristic approximated by a polynomial can be used for correcting measurement data. In essence, the corrections are needed only for the VSWR values, so it is sufficient to correct the values of the maximum and minimum voltages in a standing wave.

Wavelengths and propagation velocity. While the probe is moved along the transmission line, *DataStudio* displays a signal proportional to the electric field between the rods versus the distance. The **wavelength** is determined from the spacing between the minima/maxima of the signal, which equals $\lambda/2$. The measurements are carried out for the open-circuited and short-circuited line and for three frequencies of electromagnetic waves, 500, 400, and 300 MHz (Fig. 3).

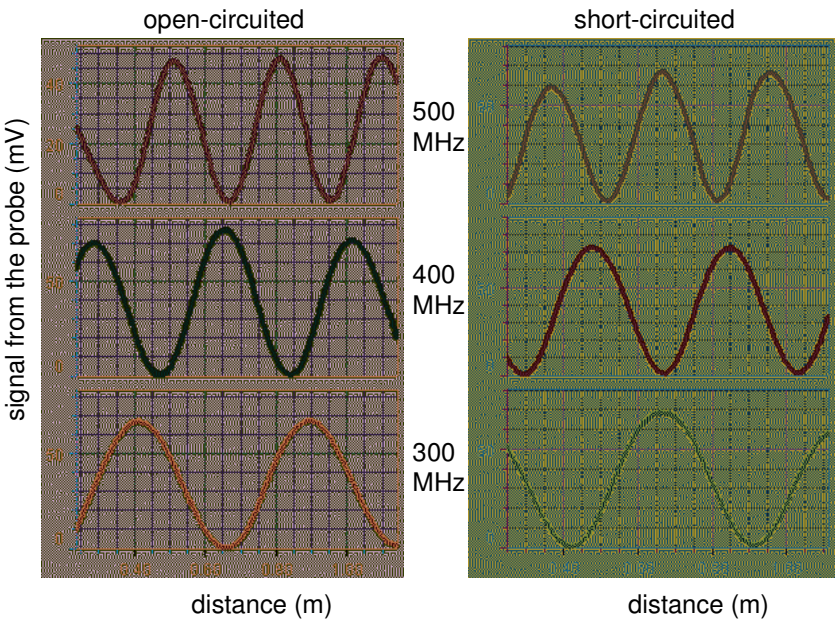

Fig. 3. Standing waves for three frequencies of electromagnetic waves.

The minimum amplitudes in the standing waves are nearly zero, and the points of minima for the open-circuited line coincide with points of maxima for the short-circuited line. This observation is in agreement with the 1 and –1 values of the reflection coefficient. The calculated propagation velocity coincides with the correct value within 1–2%.

Characteristic impedance is determined when the frequency of electromagnetic waves is 400 MHz. The reflection vanishes and the VSWR becomes unity when

the load resistance equals the characteristic impedance; this also means that the load should be purely resistive. The VSWR is measured for various loading resistors. The lowest VSWR values were achievable with small resistors, 1.5–2 mm in diameter and 3 mm long. VSWR values were corrected for the nonlinearity of the measuring system. The characteristic impedance obtained is in agreement with value of 281 Ω from Eq. (1b) (Fig. 4).

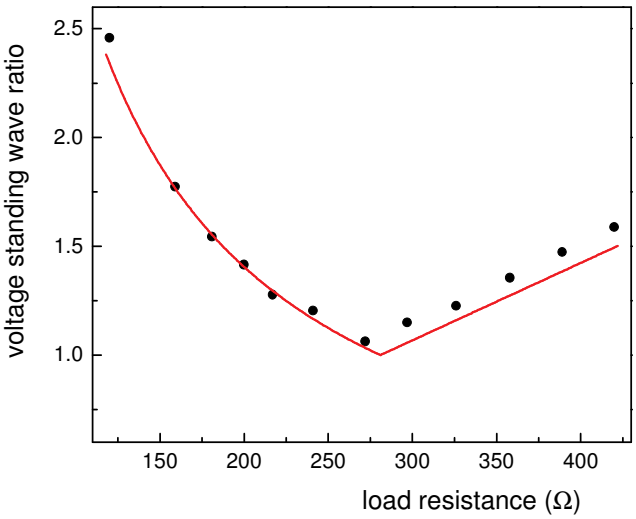

Fig. 4. VSWR versus load resistance: • measurement data, ——— calculations.

Input impedance. Only two particular cases are explored, for which the input impedance, according to Eq. (4), should be zero. For an open-circuited line, this occurs when $l/\lambda = (2n + 1)/4$, where n is an integer, including zero. For a short-circuited line, the condition is $l/\lambda = (n + 1)/2$. The probe is positioned at the input of the line, and *Digits* displays the signal from the probe acquired by the *Voltage sensor*. For $n = 0$ (quarter-wave and half-wave lines), the minima of the signal are seen close to the frequencies matching the above relations (Fig. 5).

Determination of load impedance. The frequency of the electromagnetic waves is 300 MHz. Only two quantities, S and l_m, are needed for the calculations. The S value should be corrected for the nonlinearity of the measuring system. The successive minima in standing waves are separated by $\lambda/2$. Therefore, positions of the minima for the loaded line can be taken relative to the minima for the short-circuited line, which serves as a reference. Data presented (Fig. 6) relate to a 243 Ω or a 299 Ω resistor put in series with a 10 pF capacitor; the reference standing wave is also shown. *DataStudio* uses equations (9a) and (9b) for calculating the impedance parameters and presents the results in digital form with the *Digits* display. Thus tedious calculations of complex numbers are completely excluded.

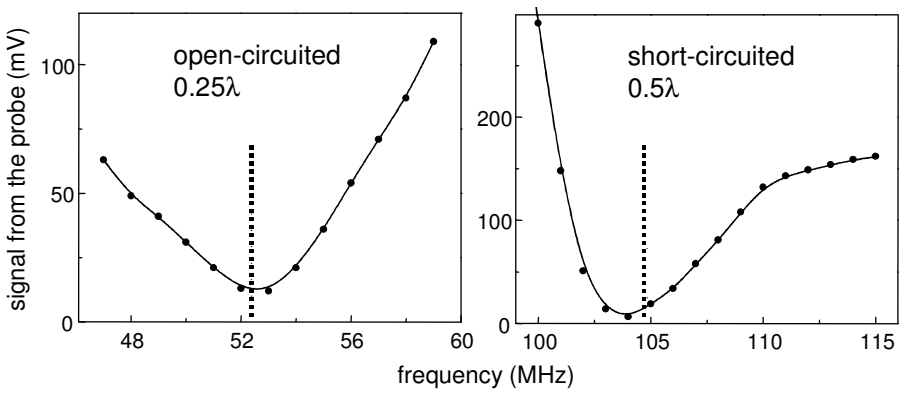

Fig. 5. Signal from the probe in vicinity of frequencies, for which input impedance should be zero (dotted lines).

For the two examples given, the results are in reasonable agreement with the load impedances. For the 243 Ω resistor in series with a 10 pF capacitor, $S = 1.223$, and $l_m = 0.087$ m. From the calculations, $\mathbf{Z}_L = 252 - j45\ \Omega$. At 300 MHz, the imaginary part of this impedance corresponds to a capacitor of 12 pF. For the 299 Ω resistor in series with the same capacitor, $S = 1.255$, and $l_m = 0.168$ m. From the calculations, $\mathbf{Z}_L = 309 - j61\ \Omega$. The imaginary part corresponds to a capacitor of 9 pF. The results are quite satisfactory.

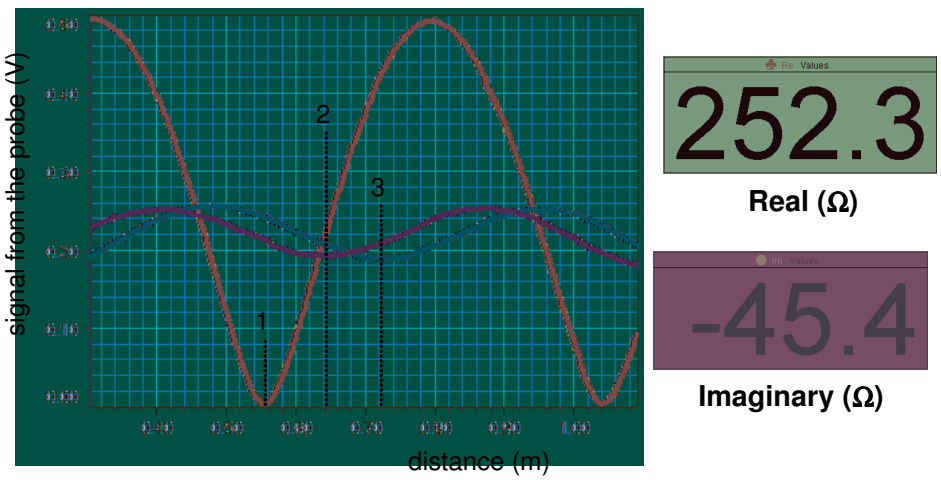

Fig. 6. Left: standing waves for three loads. Dotted lines show points of minima: 1–short-circuited line, 2–243 Ω+10 pF, 3–299 Ω +10 pF. Right: two parts of the load impedance 243 Ω+10 pF displayed by *Digits*.

8.9. Coaxial cable

Three items are included: (i) the speed of electromagnetic waves and dielectric constant of the insulator; (ii) the losses in the cable; and (iii) the speed of electromagnetic waves by using the cross-correlation technique.

Theoretical background. Coaxial cable is a transmission line formed by an inner conductor and a surrounding tubular conducting shield. Usually, an insulating layer is put between the two conductors, and an insulating jacket covers the outer conductor. A great advantage of a coaxial cable is that the electromagnetic field carrying the signal exists only in the space between the inner and outer conductors; therefore, the signal in the cable does not cause electromagnetic interference; at the same time, the outer conductor protects the signal from external interference. Oliver Heaviside (1850–1925), an outstanding English scientist and engineer, patented this device in 1880. The main parameters of a coaxial cable are the following:

- diameters of the inner and outer conductors, d and D;
- **relative permittivity** (dielectric constant) ε of the **insulator** between the inner and outer conductors;
- **relative permeability** μ of the insulator;
- **shunt capacitance** per unit length, $C = 2\pi\varepsilon_0\varepsilon/\ln(D/d)$, where ε_0 is the electric constant;
- **series inductance** per unit length, $L = (\mu_0\mu/2\pi)\ln(D/d)$, where μ_0 is the **magnetic constant**;
- **series resistance** per unit length, R;
- **shunt conductance** per unit length, G.

The speed of electromagnetic waves propagating down the cable equals

$$c^* = (\varepsilon\varepsilon_0\mu\mu_0)^{-½} = c(\varepsilon\mu)^{-½}, \quad (1)$$

where c is the speed of electromagnetic waves in a vacuum (Cheng 1992; Kraus and Fleisch 1999; Santos *et al* 2013).

A simplified expression for the **characteristic impedance** is

$$Z_0 = (L/C)^{½} = (\mu/4\pi^2\varepsilon)^{½}\ln(D/d). \quad (2)$$

Since $\mu = 1$,

$$Z_0\,(\Omega) = (138/\varepsilon^{½})\log_{10}(D/d). \quad (3)$$

Energy losses in the cable are caused by the resistance of the inner and outer conductors and dielectric losses in the insulator. The losses increase with increasing frequency.

1. Speed of electromagnetic waves and losses

Speed of electromagnetic waves and losses in a coaxial cable are determined with a digital storage oscilloscope (DSO) (Kraftmakher 2012f).

Equipment: DSO, 100 m coaxial cable, function generator.

Mak (2003) determined the speed of electromagnetic waves in a coaxial cable 15 m long using 600 kHz square wave voltage and observing signals at the input and output of the cable with a two-channel 20 MHz oscilloscope.

We use a spool of an RG-174/U coaxial cable, 100 m in length (Fig. 1). The **characteristic impedance** of the cable is 50 Ω. A Hewlett–Packard 33120A function generator of 15 MHz frequency range feeds the cable. The ends of the cable are connected to the inputs of a DSO, Tektronix TDS 3012B, and the input resistances are set to be 50 Ω. The DSO displays the voltage at the output of the cable versus that at the input. The experiment is also possible with a common analog oscilloscope, but the broader frequency range of the DSO makes the results more reliable. Also, an inexpensive function generator of narrower frequency band may be used.

Speed of electromagnetic waves. The frequency f of an electromagnetic wave propagating with a speed c^* down a cable of length l can be adjusted to obtain a zero or 180^o phase shift between the input and output voltages, which is easy to see with a Lissajous pattern. The zero phase shift occurs every time when the propagating time l/c^* becomes equal to an integer number n of periods T of the electromagnetic wave, that is, when

$$f = nc^*/l. \tag{4}$$

The dependence of the frequency on n is a straight line with a slope $K = c^*/l$. From the graph obtained, the speed of electromagnetic waves in the cable equals $c^* = (1.973 \pm 0.023) \times 10^8$ m.s^{-1}. The uncertainty in the result thus is nearly 1%. In our case, $\mu = 1$, so the relative dielectric constant ε of the insulator (polyethylene) equals 2.31, in agreement with a handbook value (Lide 2008).

Losses in the cable. To determine losses in the cable, the input and output voltages are measured in the range 10 Hz–10 MHz. The output/input voltage ratio is nearly constant for frequencies up to nearly 0.1 MHz, and then rapidly decreases. The resistance of the inner conductor of the long cable is comparable to the load resistance, so the voltage ratio is less than unity even at low frequencies.

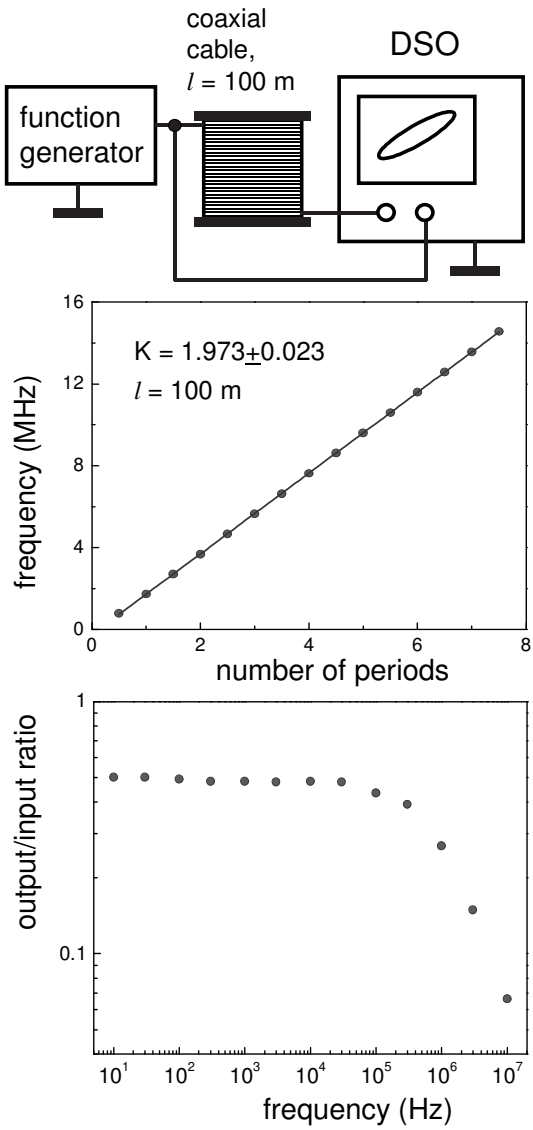

Fig. 1. Schematic of the setup, frequency versus number of periods of the electromagnetic wave, and output/input voltage ratio versus frequency.

2. Speed of waves, cross-correlation technique

The speed of electromagnetic waves in a coaxial cable is determined using a wide-band electrical noise and the cross-correlation technique. The experiment follows that described by Pérez (2011). This technique was used for determining the speed of sound in air (Experiment 4.13).

Equipment: DSO, coaxial cable, wide-band noise generator.

The RG-174/U cable used in the preceding experiment is unsatisfactory for the present measurements because of suppressing high-frequency components of a wide-band noise. For this reason, an RG-58C/U cable was employed. Due to a thicker inner conductor and a better insulator, this cable is more suitable for our aim. The length of the cable appeared to be 70.8 m. For the measurements, we use an Agilent 2022A digital oscilloscope. The oscilloscope has a 200 MHz frequency band. The sample rate is set to be 1 GHz, so the time resolution is 1 ns. The speed of electromagnetic waves in the cable determined using the same method as in the preceding experiment is $c^* = 1.98\times10^8$ m.s^{-1} (Fig. 2).

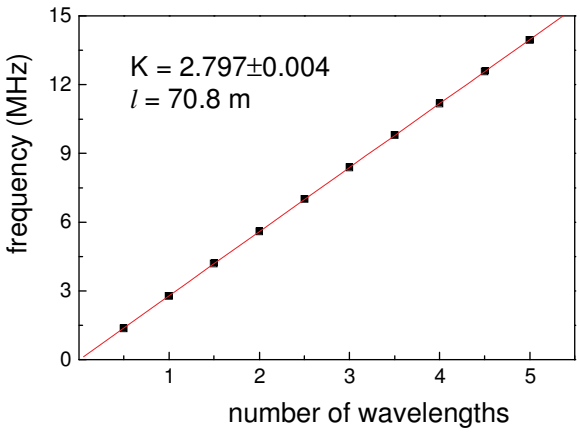

Fig. 2. Frequency versus number of periods of the electromagnetic waves.

The Hewlett–Packard 33120A generator provides a **wide-band noise** voltage. The noise at the output of the cable reproduces that at the input, but with a time delay depending on the speed of the electromagnetic wave and the length of the cable. Both noise voltages are observed with the digital oscilloscope. The data are then transferred to a computer and processed by *MATLAB*. The electromagnetic wave propagates down the cable without remarkable losses. The autocorrelation functions of the noise voltages at the input and output of the cable have sharp maxima at a zero delay time. The sharp maxima show that both signals contain wide-band noise. The cross-correlation function also has a sharp

maximum, but with a delay equal to the propagation time (Fig. 3). The delay time equals 355 ns, so the speed of electromagnetic waves in the cable equals $c^* = 1.99\times10^8$ m.s^{-1}, in agreement with the result obtained with a sine wave signal.

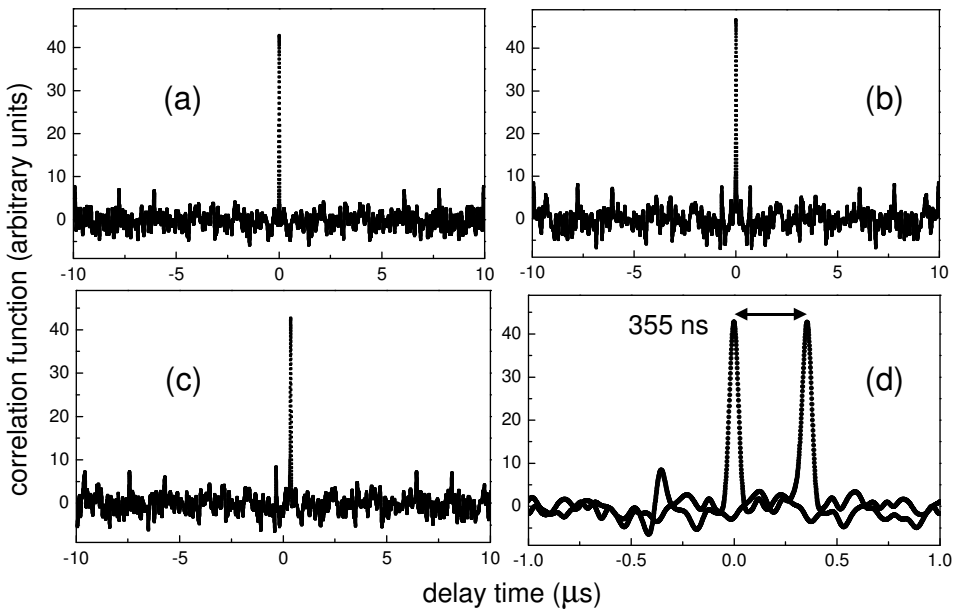

Fig. 3. (a, b) Two autocorrelation functions; (c) cross-correlation function showing the propagation time; (d) with a proper scale, the propagation time can be accurately measured.

8.10. Dipole antennas

The directional patterns of dipole antennas of different lengths are in reasonable agreement with theory. The gain due to a reflector is demonstrated, and a variant of the Yagi–Uda antenna presented (Kraftmakher 2009g).

Additional equipment: *Rotary motion sensor*, *Voltage sensor*, UHF oscillator, telescopic dipole antenna, diode.

Experiments with antennas are rarely used in undergraduate physics laboratories or for classroom demonstrations. Several papers in this field are listed below. Howes (1978) described a VHF vacuum tube oscillator and its use in experiments related to transmission lines and radiation. Half-wave dipole antennas were used for the transmitter and the receiver. Later, the author described an UHF transistor oscillator for transmission line experiments (Howes 1980). Beers (1983) developed inexpensive sources and detectors to demonstrate refraction, diffraction, and interference of 13 cm waves, and used directors to collimate the waves. Benumof (1984) presented the basic theory of a receiving antenna sufficient for calculating the voltage and current induced in the load of an optimally designed TV antenna circuit. Bush (1987) derived an important antenna formula from the results of single-slit diffraction theory (see also Heald 1987). Templin (1996) calculated the radiation resistance of simple radiating systems. To visualize the fields of a 450 MHz electromagnetic wave, Heller (1997) employed homemade probes of the fields and a commercially available high-power UHF transmitter. Smith (2001, 2002) considered the radiation and reception by a simple wire antenna. Derby and Olbert (2008) developed animated computer simulations of the electric field of a radiating antenna. The main purpose of our experiments is the determination of directional patterns of dipole antennas of different length.

Theoretical predictions. The theory of antennas is given in many textbooks. Grant and Phillips (1982) considered a Hertzian dipole, a half-wave and a full-wave dipole, and an antenna consisting of two half-wave dipoles separated by a half-wave length. In more detail, the theory of antennas can be found in Kraus (1984); Cheng (1992); Kraus and Fleisch (1999); Kraus and Marhefka (2002); Stearns (2004); and Orfanidis (2008). The main properties of antennas related to experiments described below are the following.

- Any charge distribution, which changes with time, or any varying current can give rise to electromagnetic waves. An antenna is a **transition device** between a guided electromagnetic wave and a free-space wave. For effectively producing electromagnetic waves, their frequency must be sufficiently high. A simple linear antenna typically consists of a straight wire or metal tube, an integer of half-wavelengths long.

• The **directional pattern** of an antenna shows variations of the electric or magnetic field (or the radiation power) as a function of spherical coordinates. A directional pattern can be presented by plane cuts through the main-lobe axis. Two such cuts at right angles, called the **principal plane patterns**, may be required. If the pattern is symmetrical around one axis, one cut is sufficient.

• According to the reciprocity principle, the directional pattern of an antenna used for **radiation** and **reception** is the same. However, since the output impedance of a generator and the input impedance of a receiver may be different, the antenna impedance may play a very different role in the two cases.

• An important parameter of antennas is the **directivity**. For a radiating antenna, the directivity is equal to the ratio of maximum power density to its average value over a sphere as observed far away from the antenna (the so-called **far-field zone**). Using more than one radiator, the directivity can be significantly increased. The fields produced by several radiators interfere, and the result of the interference depends on the positions of the radiators, the phase shift between the electric currents in them, and the direction of the radiation.

• A **dipole antenna** is a straight conducting wire excited by a voltage source in the middle. At a distance r far away from a radiating dipole ($r >> \lambda$, where λ is the wavelength), the amplitude of electric field E produced at a point A equals

$$E = \frac{60 I_0}{r} \frac{\cos[(\pi L/\lambda)\cos\theta] - \cos(\pi L/\lambda)}{\sin\theta}, \tag{1}$$

where I_0 is the amplitude of the current in the antenna at the maximum current point, L is the total length of the dipole, and θ is the angle between the axis of the antenna and the direction to the point A. Equation (1) is an approximation assuming that the current distribution along the antenna is sinusoidal, and the antenna diameter d is small, say, less than 0.001λ. In the far-field zone, the electric field is inversely proportional to the distance from the radiator. Dipole antennas do not radiate along the axis. Their directional patterns consist of several beams (lobes) depending on the length of the antenna (Fig. 1). All the patterns are presented with the same scale. The **anisotropic patterns** are due to the interference of the waves emitted by various parts of the antennas.

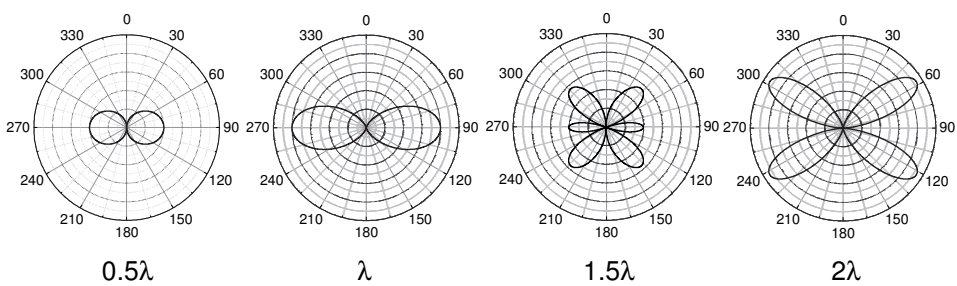

Fig. 1. Calculated directional patterns of dipole antennas of different lengths.

• Equation (1) assumes a definite current in a dipole antenna and tells nothing how to produce the current. An oscillator provides a definite AC voltage to feed the antenna, but the current depends on the **antenna impedance** including a real part called the radiation resistance, and an imaginary part. For a given frequency, both parts strongly and non-monotonically depend on the length of the antenna. Resonance occurs when the imaginary part of the antenna impedance becomes zero; this takes place when the antenna is nearly an integer of half-wavelengths long. The resonant length of a dipole antenna slightly depends on its diameter. For instance, the calculated resonant length of a **half-wave antenna** equals 0.480λ for $d = 0.001\lambda$ and 0.468λ for $d = 0.01\lambda$ (Orfanidis 2008).

• Passive elements, **directors** and **reflectors**, are usually added to antennas to enhance their directivity. A Yagi–Uda antenna, developed by Hidetsugu Yagi and Shintaro Uda in 1926, consists of a half-wave dipole (an active element), a reflector, and several directors. Antennas of this type can be seen on many rooftops. Their important parameters are the half-power beam width and the so-called **front-to-back gain ratio**.

The setup. Many authors described simple sources of short electromagnetic waves (Howes 1978, 1980; Beers 1983; Starrett 2008). We use a low power oscillator available in the laboratory, a Wavetek 3005 model, which provides output voltages up to 10 V at frequencies up to 520 MHz. In the setup (Fig. 2), the oscillator feeds a horizontally positioned half-wave dipole antenna through a coaxial cable. The axis of the dipole is set perpendicular to the direction to the receiver. The operating frequency is 500 MHz ($\lambda = 60$ cm). This arrangement is fixed, so the **radiation field** is the same in all the measurements.

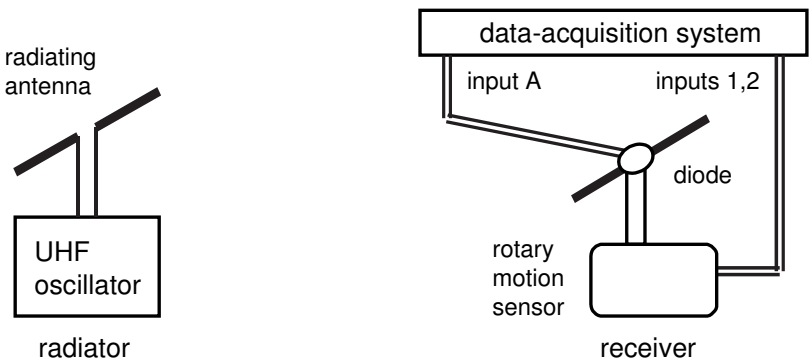

Fig. 2. Schematic of experimental setup.

A telescopic dipole antenna with a diode at its center serves as the receiver. The *Voltage sensor* acquires a DC voltage across the diode. The sensor input is shunted by a capacitor and connected to the diode through two RF chokes (not shown in Fig. 2). The receiving antenna is mounted on the vertically positioned shaft of the *Rotary motion sensor* and distanced nearly 6 m from the

radiator. The *Voltage sensor* measures the signal while manually rotating the antenna. *DataStudio* displays this signal versus the orientation of the antenna, in the 0–360° range. The *Automatic stop* is used to automatically end a run. For graphing the directional patterns in polar coordinates, the measurement data are transferred to *Origin* software. Dipole antennas of several lengths are explored: 0.5λ, λ, 1.5λ, and 2λ. A Yagi–Uda antenna used in the measurements is 1.5λ long. The impedance of a dipole antenna strongly depends on its length, and the matching of the antennas with the receiver would make the experiments too complicated. Therefore, the matching was not pursued. With this simplification, all the experiments are easy to arrange in an undergraduate physics laboratory.

The experiments are performed in a corridor, and electromagnetic waves reflected from the floor, ceiling, and walls unavoidably disturb the results. The response of the receiver is nonlinear, and a calibration is needed for correcting measurement data if necessary. The calibration should be done separately for each length of the antenna. Therefore, only measurement data, with no corrections for the nonlinear response of the receiver, are presented.

Polarization of electromagnetic waves is seen when the *Rotary motion sensor* is set to rotate the receiving dipole in a vertical plane perpendicular to the direction to the radiator. The results (Fig. 3) are quite expectable: the maximum signal is obtained when the dipoles are set parallel. For perpendicular orientations, the signal becomes zero. The horizontal polarization of the electromagnetic waves emitted by the horizontally positioned radiating dipole is evident.

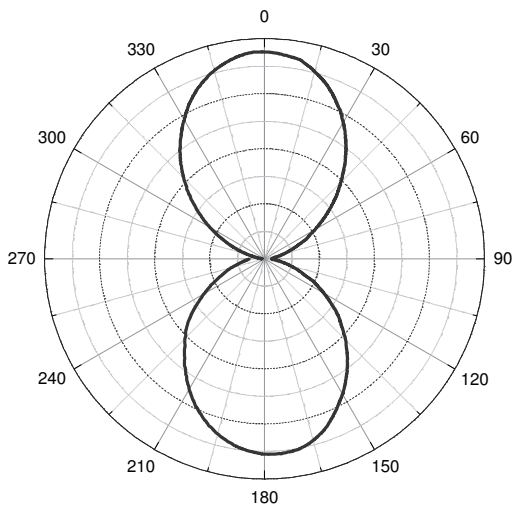

Fig. 3. Polar diagram confirming linear polarization of electromagnetic waves. The polar angle is the angle between the two antennas.

Directional patterns are obtained with a receiving dipole of different lengths, from 0.5λ to 2λ (Fig. 4). With several trials, only patterns similar to those

predicted by Eq. (1) were collected. For this aim, it was necessary to carefully adjust the position of the receiving dipole. Trials are required to find a locality where a plane electromagnetic wave is formed; this difficulty is caused by the reflections of electromagnetic waves from the environment. For the two short antennas, this operation is sufficiently simple. All the patterns are shown with the same scale.

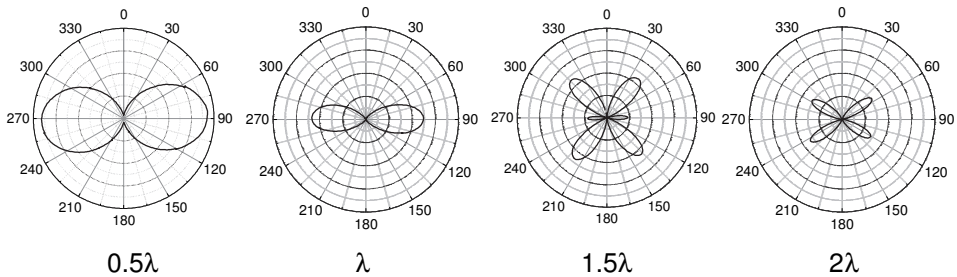

Fig. 4. Directional patterns of dipole antennas of different lengths obtained in the measurements.

The results seem to be satisfactory: in all cases, the directional patterns obtained confirm the main features of the calculated patterns. The discrepancy between the calculated and obtained field amplitudes is an indication of the role of the antenna impedance, which strongly depends on the antenna length and slightly on its diameter. For infinitesimally thin antennas, the real part of the impedance equals 73 Ω for a half-wave antenna, and about 2000 Ω for a full-wave antenna. According to Eq. (1), antennas λ and 2λ long should provide the largest signals. In our measurements, the signal from the half-wave antenna is the largest, due to the role of the antenna impedance.

Improvement with a reflector. Adding a reflector and directors can modify characteristics of a dipole antenna. Their action is based on the re-radiation of incoming electromagnetic waves. To verify this feature, a metal rod, half-wave long, is used as the reflector. It is mounted on a plastic plate attached to a movable cart positioned behind the receiving half-wave dipole and is oriented parallel to the dipole (Fig. 5). The *Motion sensor* measures the position of the reflector, and the plastic plate reflects back the ultrasonic pulses from the sensor. The *Voltage sensor* measures the signal from the antenna while the cart is moved toward the dipole. A maximum signal is achieved when the reflector–antenna distance is nearly 0.25λ, which confirms the 180^{o} phase change when a conductor reflects electromagnetic waves. With the reflector, the signal from the antenna can be doubled or made close to zero, which clearly demonstrates the interference of electromagnetic waves.

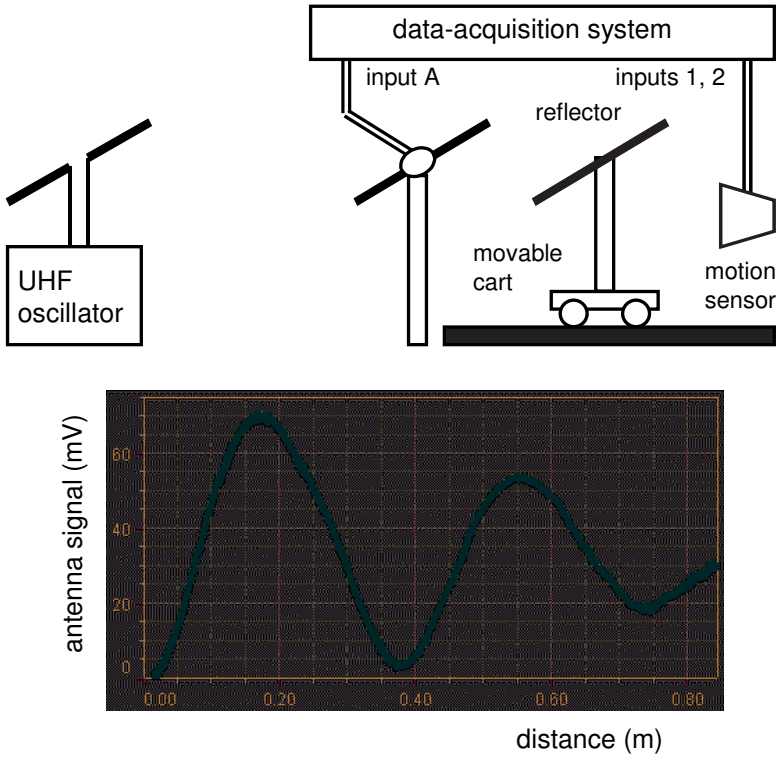

Fig. 5. Schematic of the setup and signal from antenna versus distance between the dipole and reflector.

The Yagi–Uda antenna includes a dipole, four directors positioned nearly equidistantly ahead the dipole, and a reflector. The recommended lengths of the elements and their positions along a boom (Fig. 6) are taken from a textbook (Kraus and Marhefka 2002, p 248). A scaled wooden ruler 1 m long serves as the boom. All the elements are made of a brass rod, 3 mm in diameter. The antenna is mounted on the shaft of the *Rotary motion sensor*, with the center of the dipole just above the shaft. When manually rotating the antenna, *DataStudio* displays the **directional pattern**. The enhanced directivity is clearly seen. However, the back lobe is much larger than it should be. Second, the angular resolution of the setup is insufficient to resolve minor lobes of the pattern.

Arto Lehto and Pertti Vainikainen considered sources of uncertainties of antenna measurements in a special chapter included in the textbook by Kraus and Marhefka (2002). Their main conclusions are the following.

- The distance between the radiator and receiver should be sufficiently long to avoid the influence of the near-field zone and to obtain a plane electromagnetic wave, that is, a wave of uniform phase and amplitude.

• To ensure the correctness of directional patterns, only one signal path should exist between the radiator and receiver. This is achievable in a reflection less environment like in anechoic chambers or in free space.

• The errors of the measuring system, as well as stray electric fields, can severely perturb the data.

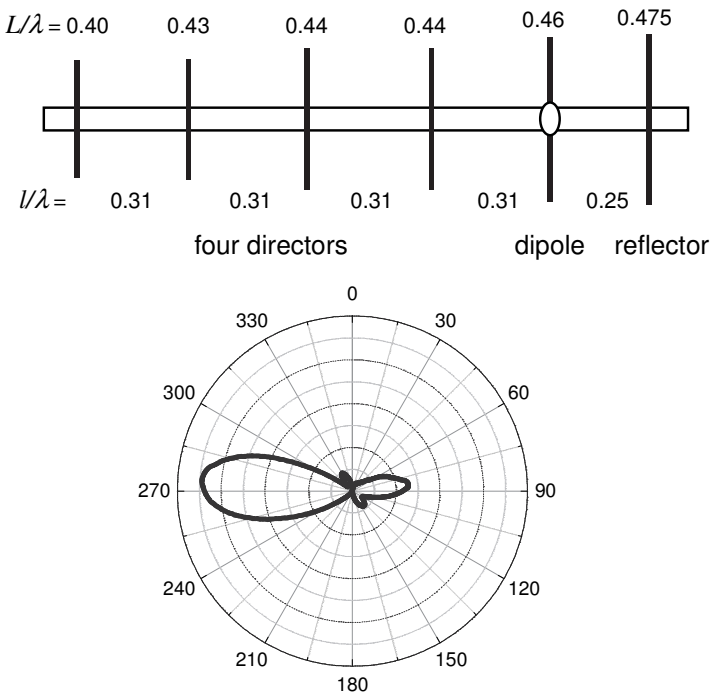

Fig. 6. A 6-element Yagi–Uda antenna and its directional pattern. Lengths of the elements L and distances l between them are shown.

In our measurements, the distance between the radiating and receiving antennas seems to be insufficiently long, especially for the dipole antennas 1.5λ and 2λ long and for the Yagi–Uda antenna. An inexpensive UHF amplifier could be employed to increase the distance between the antennas. The second requirement seems to be most difficult to satisfy because even an experimenter himself influences the electric field to be measured. Next, the simple measuring system is unsuitable for accurate measurements. Nevertheless, the main features of the directional patterns of all the antennas explored are observable using reasonably priced equipment.

8.11. Quartz resonator

Three items are considered: (i) the frequency response and transient processes; (ii) the temperature dependence of the resonance frequency; and (iii) the equivalent impedance. A quartz resonator designed for generating oscillations of frequency 32768 Hz (=2^{15}) is used (Kraftmakher 2013d).

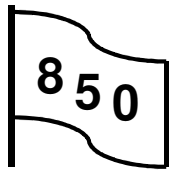

Additional equipment: quartz resonator, AC-to-DC converter.

Quartz resonators are based on the phenomenon of **piezoelectricity** discovered by brothers Jacques and Pierre Curie in 1880 (Redwood 1980; Brice 1981; Hook and Hall 1991; Kittel 2005). The **direct piezoelectric effect** is the generation of electricity in dielectric crystals subjected to pressure or strain. The **converse effect** is the generation of stress in such crystals by an electric field. The phenomena are due to **electric dipoles** created in a crystal by pressure or strain; conversely, electric fields produce deformations of the crystal. A quartz resonator is a **quartz plate** or a **tuning fork** with two electrodes, which has definite resonance frequencies (Ballato and Vig 1996; Meeker 1996). The mechanical and electrical oscillations in the resonator are strictly **interrelated** and occur with **low losses**. With such a device, oscillations of very **stable frequency** can be generated. The quartz resonator has many important applications, where generation of precise time intervals or frequencies is crucial: quartz clocks and watches, computers, radio transmitters, *etc*. The resonance frequency depends on the shape and size of the resonator, the crystal plane, how the quartz is cut, and the mode of vibration. Student experiments with quartz resonators are rare and addressed mainly to advanced laboratories (Friedt and Carry 2007; Sandoz *et al* 2009; Greczyło *et al* 2010). Here, simple experiments are described, which are well suited for undergraduate laboratories. The experiments presented include topics not considered earlier for student works.

A 32768 Hz (= 2^{15}) tuning fork resonator oscillating in the flexural mode is used. The resonator is encapsulated in a metal cylinder, 3 mm in diameter and 8 mm in height. Such resonators are commonly used in computers and quartz clocks and watches (Crane 1993, 1994). A train of 15 divide-by-two stages provides 1 s time intervals. Intentionally, the resonance frequency of such resonators is somewhat lower, but a simple method exists to generate the desired frequency. Friedt and Carry (2007) described some experiments using this popular resonator. Rossing *et al* (1992) considered the vibration modes of tuning forks. The resonator used here was taken out of an out-of-use computer. Its resonance frequency appeared to be about 3 Hz lower than the oscillation frequency necessary for quartz clocks.

The *850 Interface* includes three independent function generators. *Outputs 2* and *3* provide frequencies up to 500 kHz of high resolution and stability. An additional device needed for the measurements, an AC-to-DC converter (or an

AC voltmeter providing the AC-to-DC conversion), is available in many undergraduate laboratories.

The **equivalent circuit** of a quartz resonator includes an inductance L, a capacitance C, and a resistance R connected in series (Fig. 1). An unavoidable capacitance C_0 shunts the series LCR circuit. The **equivalent impedance** of the resonator is called the **motional impedance**. It forms when a voltage applied to the resonator causes deformation of the crystal, and the deformation, in turn, creates charges on the crystal surfaces. In the vicinity of the resonance, the net voltage across the resonator changes dramatically, and this causes changes in the electrical impedance. Resistance *R* reflects both mechanical and electrical losses. The resonance in the series LCR circuit occurring when $\omega L = 1/\omega C$ is very sharp. Another resonance arises at a somewhat higher frequency, where the impedance of the series circuit becomes inductive and forms a parallel LC circuit with the capacitor C_0. The capacitance *C* is usually in the range 10^{-15}–10^{-14} F. This small value means that the equivalent inductance *L* is very large. The capacitance C_0 is of the order of 10^{-11} F.

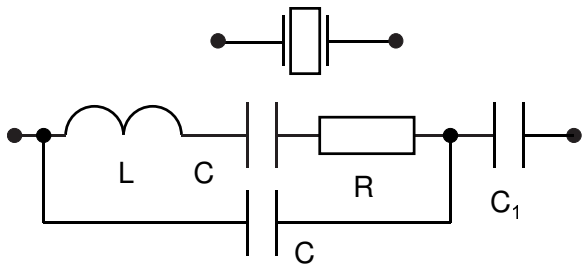

Fig. 1. Equivalent circuit of a quartz resonator. An additional capacitor C_1 for tuning the oscillation frequency is also shown.

Energy losses in a quartz resonator are so small that the **quality factor** *Q* is in the range of 10^4–10^6. For normal LC circuits, this figure does not exceed 10^2 (with the exception of superconducting circuits). To maintain the high stability of the resonance frequency and low losses, quartz resonators are usually sealed in metal containers filled with an inert gas.

Frequency response and transients. The frequency response of the quartz resonator is determined with an AC-to-DC converter (Fig. 2). The resonator is connected to *Output 2* of the *850 Interface* in series with a load resistor $R_1 = 1$ kΩ. To avoid damage of the resonator, the output voltage is set to be 1 V, and this value is also set as the limit of output voltage. A Hewlett–Packard 400E voltmeter serves as the AC-to-DC converter and measures the voltage across the load. The DC output voltage of the voltmeter is acquired by the *850 Interface*. The AC voltage across the load is also observed with a dual-channel Kenwood CS-4025 oscilloscope (not shown in Fig. 2).

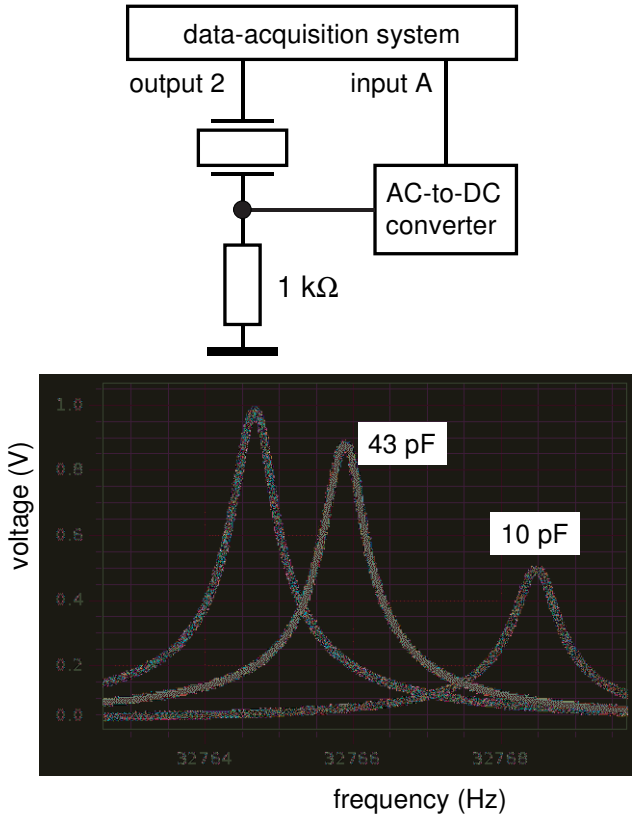

Fig. 2. Schematic of the setup and resonance curves of the resonator itself and when capacitors of 43 pF or 10 pF are added.

The sweep frequency option of *Output 2* is used for automatically recording the frequency response of the resonator. The generator operates in the *Auto* mode: it begins to change the output frequency after starting a run. Over 200 s, the frequency increases from 32760 to 32770 Hz. *Capstone* displays the output voltage of the AC-to-DC converter versus the frequency stored as *Output frequency*. The measurements are thus simple and straightforward. The oscilloscope allows observation of changes in the phase shift between the applied voltage and the current through the resonator. The dramatic change in the phase shift when passing through the resonance frequency f_0 is clearly seen.

Minor changes in the resonance frequency are possible by adding a capacitor C_1 in series with the resonator. In the example shown, the resonance frequency is somewhat less than 32765 Hz, but it exceeds the desired 32768 Hz value when a 10 pF capacitor is put in series with the resonator. Thus, frequencies higher than the original resonance frequency of the resonator can be generated in quartz clocks; however, only minor corrections are possible.

Variable capacitors in quartz clocks bring the oscillation frequency closer to the desired value. A 1 Hz lower frequency makes the clock 2.6 s slower per day.

The quality factor of the resonator is $Q = f_0/\Delta f$, where Δf is a frequency bandwidth, in which the oscillation amplitude exceeds $1/\sqrt{2}$ of its resonance value. For our resonator, $\Delta f \approx 0.32$ Hz, so $Q \approx 10^5$. These data relate to the resonator put in series with the load resistor R_1.

For observing the transient processes, the amplitude of the output voltage of *Output 2* is 100% modulated by a square wave voltage from *Output 1*. This option is provided by the new data-acquisition system. The frequency of *Output 1* is 0.15 Hz, and the amplitude of the square wave voltage is 0.5 V. By using the *Calculate* tool, the amplitude of *Output 2*'s voltage is set to be 0.5+[Output Voltage, Ch 01(V)]. The transients are recorded with the AC-to-DC converter. When the frequency of the applied voltage equals the resonance frequency, the oscillation amplitude grows monotonically. For somewhat different frequencies, beats arise between the forced and free oscillations (Fig. 3).

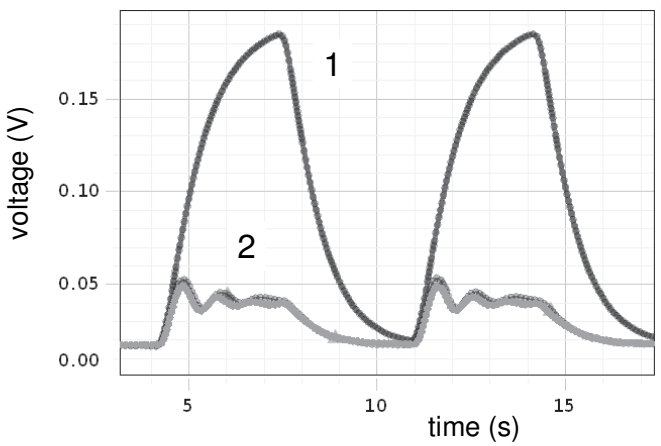

Fig. 3. The transients recorded with the AC-to-DC converter for the resonance frequency (1) and for frequencies 1 Hz above and below the resonance (2).

After interrupting the applied voltage, free oscillations occur in the resonator. Such a behavior is typical for all oscillators, and only the large ratio of the oscillation frequency to the decay constant is unusual. The quality factor equals $Q = \pi f_0 \tau$, where τ is the time, in which the oscillation amplitude becomes e times smaller. For the sample, $\tau \approx 1.25$ s, and $Q = \approx 1.3 \times 10^5$. Under our conditions, this determination of the quality factor is less accurate than that from the frequency response of the resonator.

Temperature dependence of resonance frequency is caused by variations in the elastic properties and the shape of the resonator. This dependence is different for different crystallographic axes, and even changes its sign. Resonators for quartz

clocks are designed to make the resonance frequency weakly dependent of temperature just at room temperature. Simultaneously, the frequency reaches its maximum and becomes lower above and below this temperature. For quantitatively studying the temperature dependence of the resonance frequency, the resonator and the *High-accuracy temperature sensor* (CI-6525) are put into axial openings in an aluminum cylinder, 20 mm in diameter and 80 mm in height. The cylinder is positioned in a cup filled with hot water. After heating up to 70–80°C, a number of resonance curves are recorded during the cooling process. Similar measurements are performed at low temperatures, accessible using a Dewar flask with liquid nitrogen. The *Digits* display shows the temperature (Fig. 4).

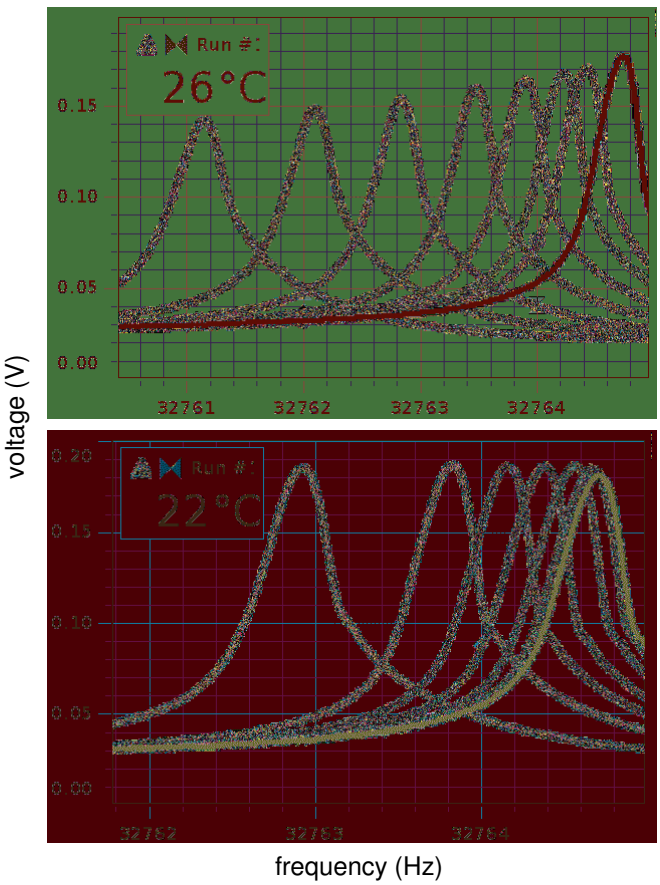

Fig. 4. Resonance curves of the resonator for various temperatures, left to right: from 76°C to 26°C (top) and from –23°C to 22°C (bottom).

The resonance frequency obtained from the resonance curves is displayed versus the temperature of the resonator (Fig. 5). The data obtained are in

agreement with the expectations and demonstrate the high repeatability of the resonance frequency.

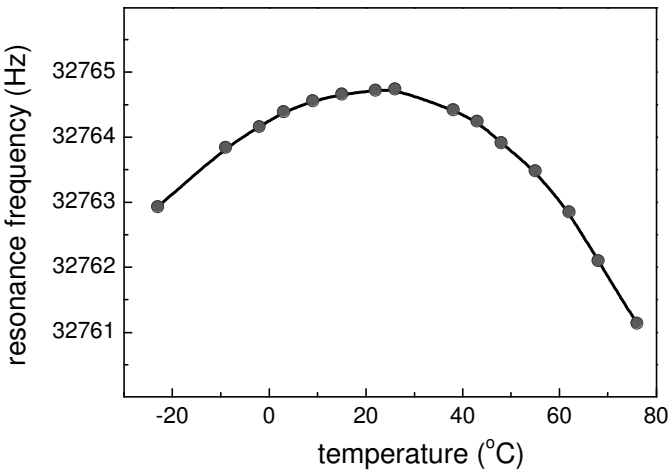

Fig. 5. Temperature dependence of the resonance frequency. The weakest temperature dependence occurs just at room temperature.

Parameters of equivalent impedance. From the measurement data, it is possible to calculate the parameters of the equivalent impedance of the resonator. First, the equivalent resistance R is available from the current at the resonance. In our case, $R \approx 22.3$ kΩ. This value includes the 1 kΩ load resistor; thus, the error due to the load is quite acceptable. Then the parameters L and C become available from one of the definitions of the quality factor: $Q = \omega_0 L/R = 1/\omega_0 CR$. From the ω_0 and R values, $L \approx 1.1\times10^{4}$ H, and $C \approx 2.2\times10^{-15}$ F. The values of L and C are very unusual, but it is easy to check their correctness. The frequency response of the derived equivalent impedance of the resonator can be calculated and compared with the experimental curve. The module of the equivalent impedance of the resonator including the load resistor equals

$$Z = [(R^2 + (\omega L - 1/\omega C)^2]^{1/2} = [R^2 + (\omega^2/\omega_0^2 - 1)^2/\omega^2 C^2]^{1/2}. \quad (1)$$

Due to measurement errors, the resonance frequency ω_0 cannot be precisely found from the calculated values of L and C, and must be taken from the measurement data. To calculate the current through the resonator, do not forget that the output voltages of *Output 2* are given as amplitudes, while the output voltages of the AC-to-DC converter as RMS values. Second, for matching the two curves, it was necessary to shift up the calculated response by 0.04 V (that is, 4% of the maximum value) to compensate for the background in the experimental data. After this correction, the calculated frequency response is sufficiently close to the experimental curve (Fig. 6). Thus, the "very unusual" parameters of the equivalent impedance of the resonator are quite reasonable.

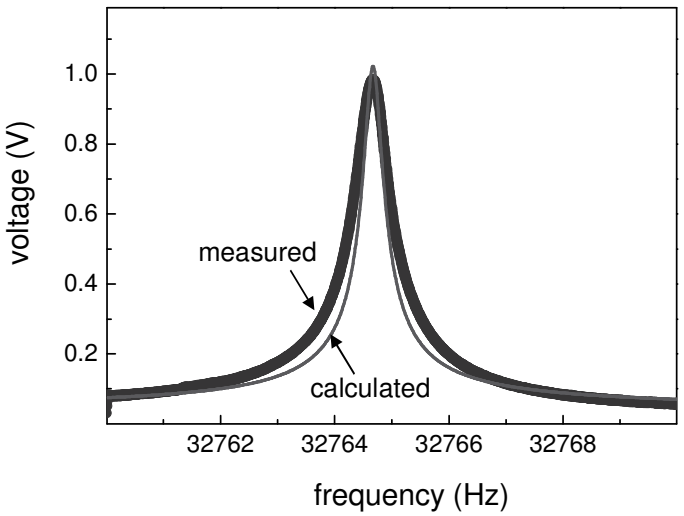

Fig. 6. Frequency response of the resonator and curve calculated from the "very unusual" parameters of the equivalent impedance.

If a lock-in amplifier is available, the real and imaginary parts of the current through the resonator can be displayed versus frequency. We use a dual-phase Ithaco 3961 lock-in amplifier. The voltage from *Output 2* applied to the resonator serves as a reference for the amplifier. The input of the amplifier is connected to the 1 kΩ load resistor. The amplifier provides RMS values of the in-phase and out-of-phase voltages across the load and the phase shift between the applied voltage and the current through the resonator. The frequency of the *Output 2* sweeps from 32760 to 32770 Hz in 400 s. During one scan, output voltages of the lock-in amplifier are recorded versus frequency (Fig. 7).

The complex current $\boldsymbol{i}$ through the resonator is inversely proportional to the complex impedance $\boldsymbol{Z}$:

$$\boldsymbol{i} = V/\boldsymbol{Z} = V/[R + \mathrm{j}(\omega L - 1/\omega C)], \tag{2}$$

where V is the voltage applied to the resonator.

The out-of-phase component of the current equals

$$-V(\omega L - 1/\omega C)/[R^2 + (\omega L - 1/\omega C)^2]. \tag{3}$$

It is easy to see that the maximum and minimum in the frequency dependence of this component occur at frequencies, where the oscillation amplitude becomes $1/\sqrt{2}$ of the maximum. The difference Δf between these frequencies can be used for calculating the quality factor $Q = f_0/\Delta f$. The phase shift between the applied voltage and the current changes gradually from nearly 90° (capacitive impedance) to -90° (inductive impedance), but the main change occurs within a 1 Hz interval.

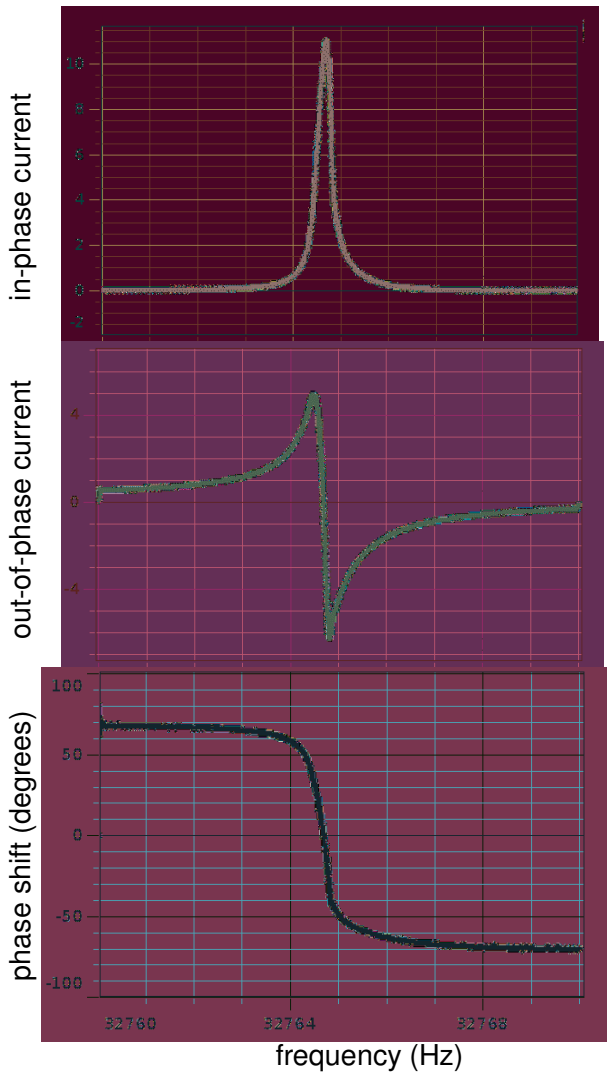

Fig. 7. Real and imaginary parts of the current through the resonator (arbitrary units), and phase shift between the applied voltage and current.

Quartz oscillator. To build a quartz oscillator, the resonator should be included in the positive feedback loop of an amplifier. Like in many other cases, we use a Kenwood CS-4025 oscilloscope having an output from one of the amplification channels. The resonator used in the experiments is very small, and a high voltage of the resonance frequency may damage it. Therefore, measures should be taken to limit the voltages that can be applied to the resonator.

Nobel Prize Experiments

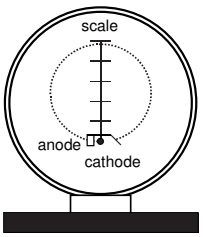

1906

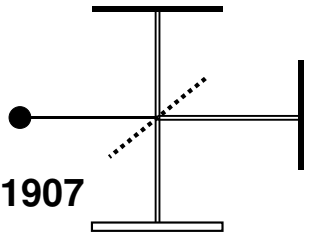

1907

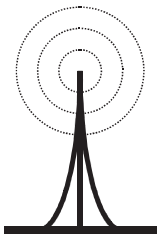

1909

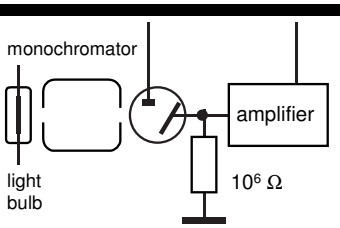

1923

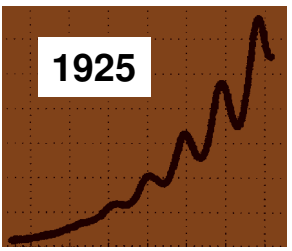

1925

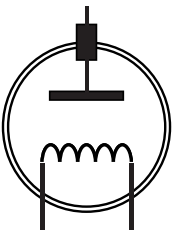

1928

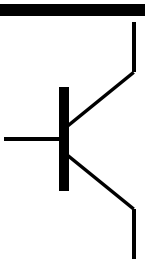

1956

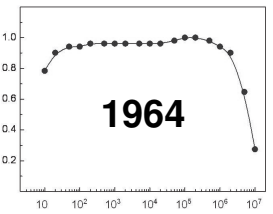

1964

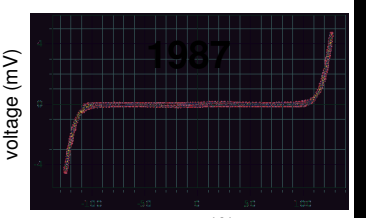

1987

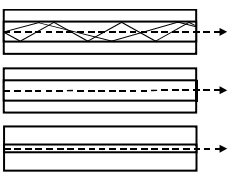

2009

9. Nobel Prize Experiments 583

9.1. Electron

The e/m ratio is calculated from the electron trajectory in a transverse magnetic field, while the electron charge is determined from shot-noise measurements. The charge and mass of the electron are thus obtained.

Joseph John Thomson (1856–1940)

"…You have thus been worthily treading in the footsteps of your great and renowned compatriots, Faraday and Maxwell, men who set to the world of science the highest and noblest examples."

> J. P. Klason, President of the Royal Swedish Academy of Sciences. Presentation of Joseph John Thomson awarded the Nobel Prize "in recognition of the great merit of his theoretical and experimental investigations on the conduction of electricity in gases" (1906).

Thomson's great discovery. Joseph John Thomson discovered the electron in 1897. In his cathode tube, electrons were accelerated and then subjected to electric and magnetic fields, $\boldsymbol{E}$ and $\boldsymbol{B}$. Lorentz's force $\boldsymbol{F}$ applied to a moving electron is

$$\boldsymbol{F} = e\boldsymbol{E} + e\boldsymbol{v}\times\boldsymbol{B}, \tag{1}$$

where e is the electron charge, and $\boldsymbol{v}$ is its velocity.

The fields $\boldsymbol{E}$ and $\boldsymbol{B}$ were set to be perpendicular to each other and to the vector $\boldsymbol{v}$. The forces $e\boldsymbol{E}$ and $e\boldsymbol{v}\times\boldsymbol{B}$ were directed in opposition, and it was possible to balance their actions. Under compensation,

$$v = E/B. \tag{2}$$

On the other hand, the velocity of the electrons equals

$$v = (2eV/m)^{1/2}, \quad (3)$$

where m is the mass of the electron, and V is the accelerating voltage.

$$e/m = E^2/2VB^2. \quad (4)$$

With the velocity known from Eq. (2), the e/m ratio for the electrons can also be found from measurements of their deflection by an electric field. Such a process occurs in a cathode-ray tube of an oscilloscope. In experiments involving the movement of electrons in electric and magnetic fields, the forces acting on the electron are proportional to its charge e, while the acceleration is inversely proportional to its mass m. This is the reason why only the e/m ratio is available from such measurements. Many methods, including very ingenious ones, exist for determining the e/m ratio. At the same time, the number of techniques for the determination of the electron charge is very limited. The main methods remain the famous Millikan's experiment with small oil drops and measurements of the shot noise.

Glascock and Sparlin (1972) described an e/m experiment with a cathode-ray tube. Huggins and Lelek (1979) presented a series of laboratory experiments and computer simulations of the motion of electrons in electric and magnetic fields. Peterson (1983) designed various accessories for a commercially available e/m apparatus, the Bainbridge tube (K. Bainbridge, 1938). Thompson (1990) proposed taking into account the Earth's magnetic field for more accurate determinations of the e/m ratio with this tube. To determine the e/m ratio, Yang (1998) used the magnetic focusing method. Rechenberg (1997) presented a 100-year chronology of discoveries related to the electron. Howell (2006) considered correction for the radii of curvature for electron beam trajectories in CENCO e/m apparatus. Callegaro (2006) presented a unified derivation of Johnson's and shot noise expressions.

1. The *e/m* ratio

The Bainbridge tube is a standard apparatus for determining the *e/m* ratio in teaching laboratories.

Equipment: *e/m* apparatus, power supplies, multimeter.

The Bainbridge tube for determining the *e/m* ratio (Fig. 1) is a more convenient apparatus than that used by Thomson. In a sealed chamber, a hot cathode emits electrons, which are accelerated by an electric field and focused into a beam. The electrons move in a region of uniform magnetic field produced by Helmholtz's coils and directed perpendicular to the electron velocities. The Lorentz's force $e\boldsymbol{v}\times\boldsymbol{B}$ continually deflects the electrons, causing them to follow a circular path. The path becomes visible because atoms of a gas at low pressure in the chamber emit light when some of the electrons collide with them. Clearly,

$$F = evB = mv^2/r, \qquad \text{so that} \tag{5}$$

$$e/m = v/Br, \tag{6}$$

where r is the radius of the electron trajectory. The velocity of the electrons depends on the accelerating voltage V:

$$v^2 = 2eV/m. \tag{7}$$

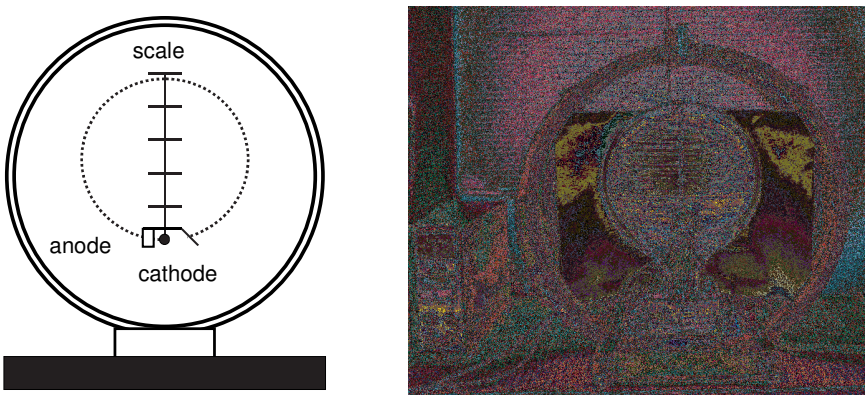

Fig. 1. Apparatus for determining the *e/m* ratio.

From the above equations,

$$e/m = 2V/B^2r^2. \tag{8}$$

A scale arranged inside the chamber is very useful for accurately determining the radius of the electron trajectory. The distance between two neighbouring marks equals 2 cm, and the maximum diameter of the trajectory is 10 cm. A power supply provides voltages for heating the cathode (5–6 V) and

accelerating the emitted electrons (150 or 200 V). Since the first voltage amounts to several per cent of the accelerating voltage, it becomes important, to which side of the cathode the anode circuit is connected. The best way is to connect it to a middle point between two similar resistors shunting the cathode (Fig. 2).

Measurements and results. The radius of Helmholtz's coils equals 0.15 m, and the number of turns is $N = 124$, so $B\,(\mathrm{T}) = 7.43\times10^{-4}\times I\,(\mathrm{A})$. Another power supply provides a DC current for the coils. The e/m ratio is taken as the slope of a graph of $1/B^2$ versus $r^2/2V$ (Fig. 3). The horizontal component of the Earth's magnetic field can be determined and taken into account. The simplest way of doing so is to observe the curvature of the electron trajectory with no current in Helmholtz's coils. Then one adjusts the current in the coils to straighten out the trajectory. This current should be added to (or subtracted from) all the currents necessary to achieve circular trajectories of definite radii. The total error of the measurements does not exceed 5%.

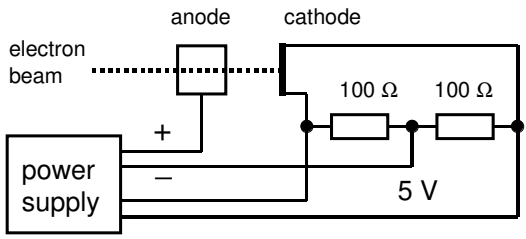

Fig. 2. Connection of the anode circuit to the cathode.

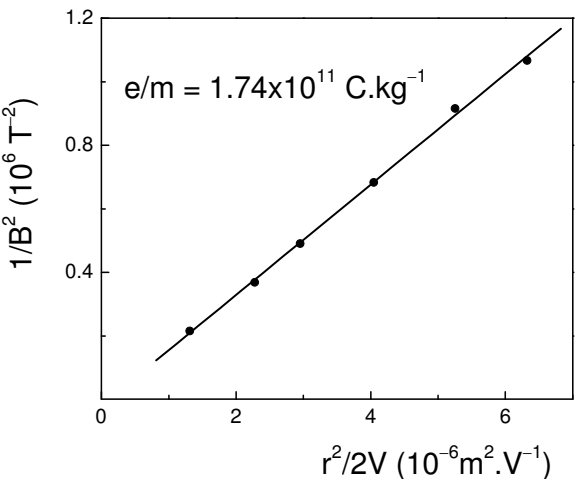

Fig. 3. Plot of the quantity $1/B^2$ versus $r^2/2V$ provides the e/m ratio.

2. Shot-noise measurements of electron charge

Shot-noise measurements are quite accessible to undergraduates (Earl 1966; Livesey and McLeod 1973; Spiegel and Helmer 1995; Kraftmakher 1961, 1995, 2005g).

Additional equipment: *Voltage sensor*, coil, vacuum phototube, AC-to-DC converter, DC supply, light bulb, resistors, capacitor.

Setup with vacuum phototube. A vacuum phototube is used like in some other experiments (Portis 1964; Portis and Young 1971; Spiegel and Helmer 1995). The mean square of the current fluctuations in a narrow frequency band Δf is (Bleaney and Bleaney 1968)

$$<\Delta I^2> = 2eI\Delta f, \tag{9}$$

where e is the electron charge, and I is the mean phototube current. When the current flows through a load of impedance $\boldsymbol{Z}$, the mean square of the noise voltage across the load equals

$$<V^2> = 2eI\int_0^\infty Z^2(f)\mathrm{d}f. \tag{10}$$

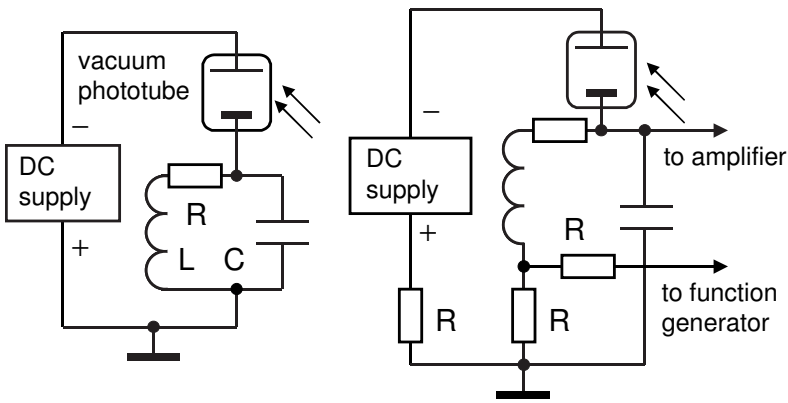

Fig. 4. Vacuum phototube loaded by parallel LCR circuit, and the circuit with additional resistors for measuring the phototube current and Q-factor.

In our setup, a parallel LCR circuit forms a load of a vacuum phototube (Fig. 4). An advantage of this circuit is that it has low impedance for DC current and high impedance for fluctuations of the current at frequencies close to the resonance. As a source of the current, the phototube is connected in series with the LCR circuit. At the same time, the phototube is connected parallel to it, through a DC supply. The internal resistance of the phototube shunts the LCR circuit and should be taken into account. The impedance of an LCR circuit can be expressed through its resonance frequency and the quality factor $Q = \omega_0 L/R$.

Assuming $Q >> 1$, the integration in Eq. (10) leads to a simple relation (Stigmark 1952; Soloukhin 1975; Goldin 1983; Pippard 1989):

$$\langle V^2 \rangle = eIQ/2\omega_0 C^2. \tag{11}$$

With Eq. (11), there is no need for determining the frequency dependence of the impedance. Stigmark (1952) used this method for a precise determination of the electron charge. In our setup, three resistors are added to the basic circuit. Resistor R_1 serves for the determination of the mean photoelectric current. Resistor R_2 is connected, through resistor R_3, to a function generator. The AC voltage across the resistor R_2 drives forced oscillations in the series LCR circuit, which serve to determine the Q-factor of the circuit. The output terminals of a DC supply providing a voltage for the phototube should not be grounded.

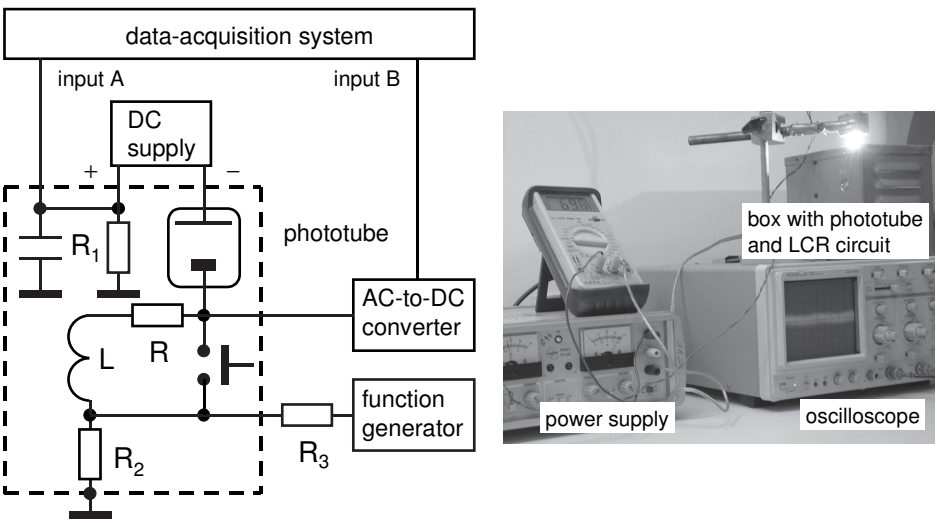

Fig. 5. The setup. $R_1 = 10$ kΩ (1%), $R_2 = 1$ Ω, $R_3 = 1$ kΩ.

The phototube and the circuit are housed in a metal box. The phototube is irradiated by an incandescent light bulb (6 V, 5 W) through a hole in the box. The light bulb is powered by a regulated DC supply. A sensitive AC-to-DC converter, a Hewlett–Packard 400E voltmeter, measures the noise voltage across the LCR circuit and produces a DC voltage for the data-acquisition system (Fig. 5). A full-scale AC input voltage produces a 1 V DC output voltage. With the 1 mV scale, the gain of the voltmeter is $G = 10^3$. The intrinsic noise at the input of the converter does not exceed 50 μV. The noise voltages amount to 20% of the 1 mV range, and this is quite satisfactory. The shot noise can be observed directly with an oscilloscope. However, its connection may cause additional interference to the converter, so it would be better to disconnect the oscilloscope when measuring the shot noise. The phototube current is measured through the voltage drop across the resistor R_1 (10 kΩ, 1%) shunted by a 5 μF capacitor. The

DC voltage applied to the phototube is 150 V, and the maximum current under irradiation is 0.1 mA.

Measurements and results. In the first part of the experiment, the *Q*-factor of the LCR circuit is determined for several values of the phototube current *I*. When measuring the *Q*-factor, the elements of the LCR circuit are connected in series with the source of the driving voltage. The latter is the voltage across the resistor $R_2 = 1\ \Omega$ connected to the function generator in series with the resistor $R_3 = 1\ k\Omega$ positioned outside the metal box. The measurements are based on the well-known fact that at resonance the voltage across the capacitor of a series LCR circuit becomes *Q* times larger than the driving voltage. An additional complication arises because the resonance frequency also depends on the phototube current. Therefore, the measurements of the voltage across the capacitor should be made in the vicinity of the resonance using frequency variations. *DataStudio* measures the phototube current through the voltage across the resistor R_1. The driving voltage is set to be one order of magnitude larger than the noise. It is measured when shortening the inductor L by a switch. The main change of the *Q*-factor occurs at currents below 20 μA (Fig. 6). This part may be excluded when the dependence of the *Q*-factor on the phototube current is fitted by a polynomial. The change in the resonance frequency with the current can be neglected.

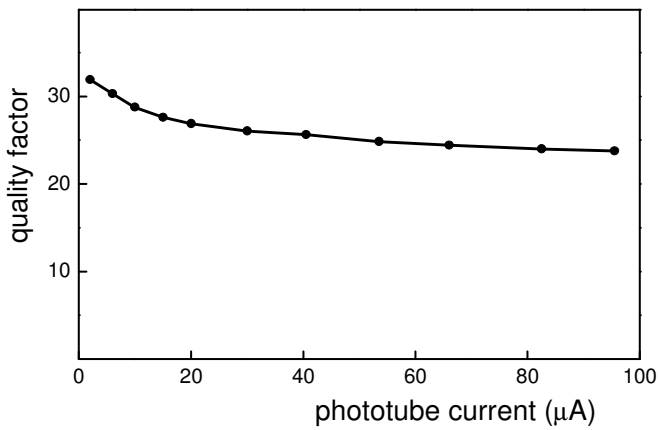

Fig. 6. *Q*-factor of the LCR circuit versus phototube current.

The capacitance of the LCR circuit includes the capacitance of the wiring, of the cable connecting the circuit to the AC-to-DC converter, and of the converter's input. The smaller the capacitance, the larger the shot-noise voltage. Therefore, no special capacitor is included in the LCR circuit. The capacitance can be calculated from the resonance frequency ω_0 and the inductance *L*. The inductor has no magnetic core, so the inductance does not depend on the current or frequency. Any method of measuring the inductance is thus appropriate. The

simplest way is to determine the resonance frequency of a series circuit formed by the inductor and a known capacitor.

In the second part of the experiment, one gradually increases the current passing through the light bulb. *DataStudio* calculates and displays the mean square of the amplified noise voltage versus IQ (Fig. 7). According to Eq. (11), the slope of the straight line is $K = eG^2/2\omega_0 C^2$, where G is the gain of the AC-to-DC converter. The dependence of Q on I is taken from the polynomial previously evaluated.

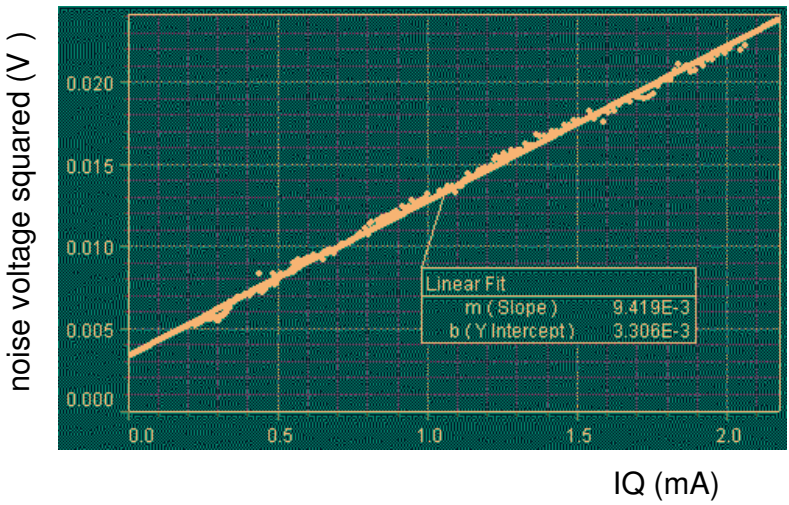

Fig. 7. Mean square of amplified noise voltage versus IQ.

All the quantities necessary for determining the electron charge are known from the measurements. Usually, values obtained differ by not more than 5% from the accepted value. For the data presented, $K = 9.42\ \mathrm{V^2.A^{-1}}$, $G = 1000$, $\omega_0 = 8.17\times10^5\ \mathrm{s^{-1}}$, $L = 14.8$ mH, $C = 101$ pF, and $e = 1.57\times10^{-19}$ C. For a demonstration, one may use, with little loss of accuracy, a constant value of the Q-factor.

9.2. Michelson's interferometer

The experiments employ Michelson's interferometer from PASCO.

Albert Abraham Michelson (1852–1931)

"… The foregoing will suffice not only to explain… the comprehensive and fundamental nature of Michelson's research in one of the most difficult fields of precision physics, but also to demonstrate how fully justified is the decision of this Academy to reward it with the Nobel Prize in Physics."

> K. B. Hasselberg, member of the Royal Swedish Academy of Sciences. Presentation of Albert Abraham Michelson awarded the Nobel Prize "for his optical precision instruments and the spectroscopic and metrological investigations carried out with their aid" (1907).

Additional equipment: PASCO interferometer, *Light sensor*, *Rotary motion sensor*, *Mechanical wave driver,* He–Ne laser, light guide.

The interferometer. Michelson's interferometer is an instrument that widely separates two beams from a single source and then brings them to one point for observing their interference. The way of obtaining the two beams is to use a semi-transparent mirror set at 45^{o} to the axis of the incident light. It is even possible to prepare a mirror providing two beams of the same amplitude. This achievement is due to Albert Abraham Michelson (1852–1931). The operation of the interferometer is very clear. The light beam is incident upon a plane-parallel plate of homogeneous glass set at 45^{o} to it (Fig. 1). The back surface of the plate is coated with a semi-transparent film of aluminum. After refraction in the plate, the incident beam is equally divided into two beams perpendicular to one another. The plate thus serves as a beam splitter. One of the two beams is

reflected from a fixed mirror, and the second from a movable mirror. Then the reflected beams are brought together and continue towards an observer. An additional glass plate parallel to the beam splitter makes the paths of both beams identical. If the two mirrors are accurately perpendicular to one another, a set of concentric circular interference fringes of equal inclination is seen on a screen. When one of the mirrors is slightly tilted from the perpendicular position, fringes of equal thickness appear.

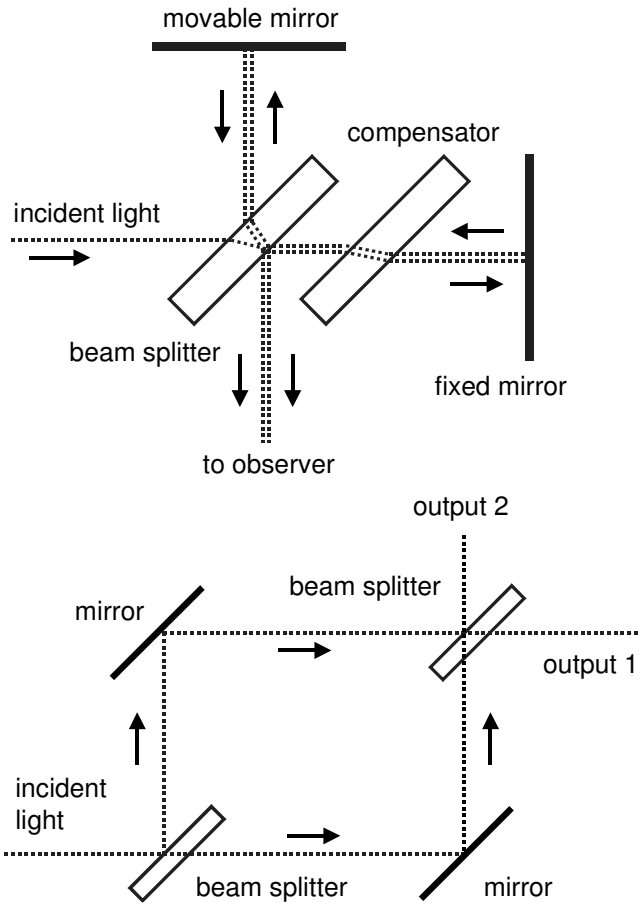

Fig. 1. Michelson interferometer (top) and Mach–Zehnder interferometer (bottom).

Applications of Michelson's interferometer include measurements of the light wavelength or of a geometrical length, determinations of refractive indices, or studies of the fine structure of spectral lines. In 1892–1893, Michelson and Benoît performed a comparison of the standard meter with the wavelength of light of a cadmium lamp. For a long time, the basic unit of length, the meter, was

defined through a certain wavelength. Now it is defined as the length (in vacuum) necessary for light to pass in a definite time.

Many authors considered the use of Michelson's interferometer in student laboratories. Dutton *et al* (1964) described some demonstrations using a gas laser, including a demonstration of Doppler's effect. Whiteside (1965) modified the interferometer for long-path difference and for combining beams emitted from opposite ends of a 0.1 mW He–Ne laser. The 12 m path difference served to show the long coherence length of the laser beam. Shamir and Fox (1967) used an interferometer of Mach–Zehnder type for demonstrating the square relation between the electric vector and the intensity of the light beam, and energy conservation in interference phenomena. Yap (1971) measured the refractive index of a gas by placing an air-tight transparent cylinder in one arm of Michelson's interferometer (such an experiment is now offered by PASCO). Berkey and King (1972) used an interferometer as a Fourier-transform spectrometer. They demonstrated interferograms of white light and of light from a He–Ne laser and a mercury lamp. With Michelson's interferometer, D'Iorio *et al* (1975) determined the coherence length of the 546 nm line of a mercury lamp as a function of the voltage applied to it. The coherence length varied from about 1 to 2.5 mm. Da Costa *et al* (1988) employed an interferometer with an optoelectronic sensor for recording small mechanical oscillations. Mellen (1990) described experiments with circularly polarized light. Rudmin *et al* (1980) used Michelson's interferometer for producing holograms. Diamond *et al* (1990) measured small vibrations of a loudspeaker cone. Belansky and Wanser (1993) reported on a student experiment on laser Doppler velocimetry. A spectrum analyzer was used to determine the frequency shift produced by the motion of a moving mirror. Nachman (1995) considered the Mach–Zehnder interferometer. The students set up such an interferometer from ready components. Nachman *et al* (1997) employed an interferometer for detecting mechanical resonance of a piezoelectric element. With a photodiode and an oscilloscope, the amplitude and phase characteristics of the element were determined. Kovács *et al* (1998) used a diffraction grating when observing white-light interference fringes at the output of Michelson's interferometer. The spectrally resolved fringes were observed with a charge-coupled device chip. Fox *et al* (1999) described a low-cost Michelson wavemeter of picometer accuracy. By recording white-light fringes, Cormack *et al* (2000) measured the group velocity dispersion of a crystal and of the reflectivity of a silver-coated mirror. Freschi *et al* (2003) presented an experiment that combines opto-mechanical and electrical measurements to characterize a loudspeaker. With Michelson's interferometer, Alanis *et al* (2004) measured microscopic displacements. Scholl and Liby (2009) measured the thermal expansion of copper. Lloyd and Paetkau (2010) used Michelson's interferometer for characterization of a piezoelectric buzzer.

The basic interferometer from PASCO, OS-9255A (Fig. 2), operates in either the Michelson or Fabry–Pérot mode. For observations of fringe patterns of equal inclination, one needs to adjust the positions of the two mirrors and to make them accurately perpendicular to one another. In this case, one sees

concentric fringes of equal inclination on the screen. Then by slightly tilting the movable mirror equipped with adjusting screws one observes fringes of equal thickness (Fig. 3). Since the interfering light beams are widely separated, it is easy to add polarizers in the paths of the light. Then one observes the change in the interference fringes when changing the orientation of the polarizers.

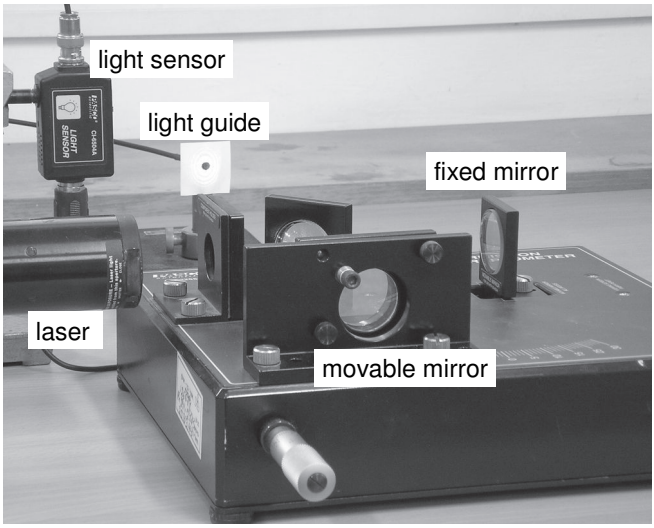

Fig. 2. Michelson's interferometer from PASCO with *Light sensor* and light guide added.

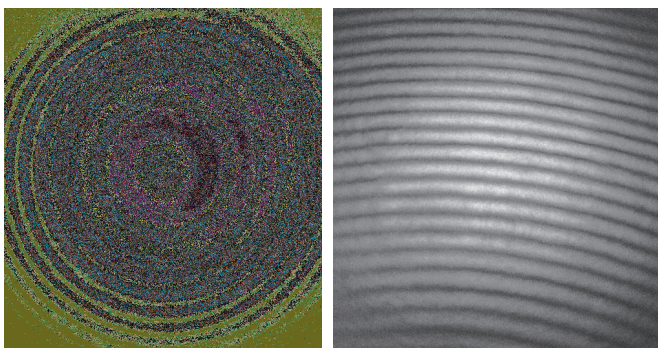

Fig. 3. Fringe patterns of equal inclination and of equal thickness.

Determination of light wavelength. This experiment requires slowly moving the movable mirror using a special micrometer head and simultaneously counting the disappearance of circular dark fringes at the center of the pattern. To make the measurements easier, we use the *Light sensor* and a light guide, whose entrance is positioned at the center of the interference fringes. *DataStudio*

displays electrical pulses from the sensor (Fig. 4), and then it becomes easier to count them. The measurements are carried out with a 25 μm displacement of the moving mirror, so that the change in the optical path is 50 μm. The next step in this experiment should be an automated count of interference fringes (Aghdaie 1988).

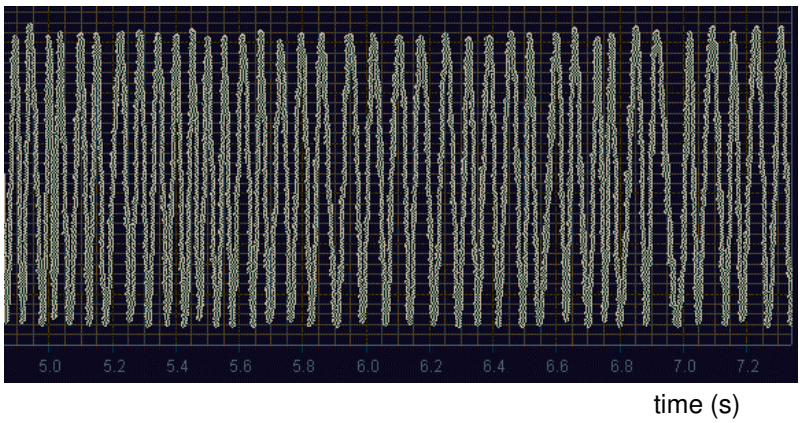

Fig. 4. Example of records by *DataStudio* when measuring wavelength.

Refraction index of glass. The experiment is an additional demonstration of the interference of light and of the interferometer (Fig. 5).

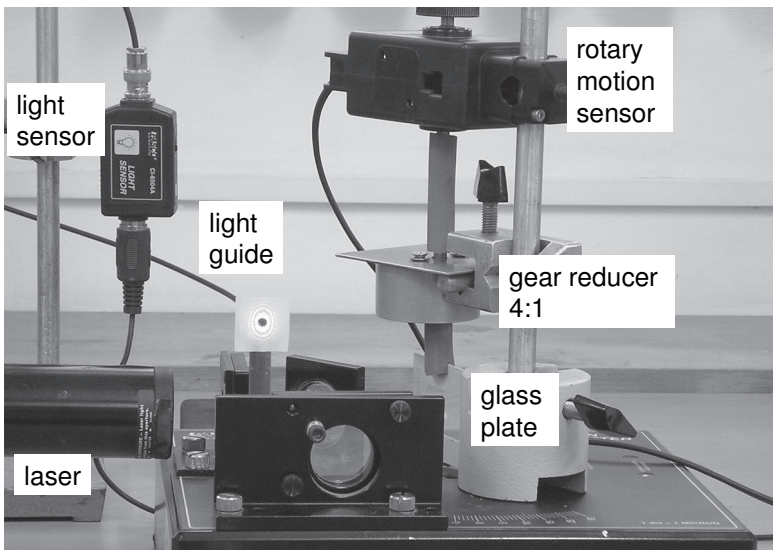

Fig. 5. Arrangement for determining refractive index of glass.

For the measurements, a plane-parallel glass plate is put in one arm of the interferometer. The plate is positioned perpendicular to the light beam. Then one slightly rotates the plate and observes the disappearance of circular dark fringes in the center of the pattern. To make the measurements easier, the *Rotary motion sensor* measures the angle position of the plate. Simultaneously, the *Light sensor* measures the intensity of light at the center of the interference pattern. The angular resolution of the *Rotary motion sensor* (0.25^{o}) is sufficient only when the incident angles are close to zero. For large incident angles, a gear reducer is used. Also, *DataStudio* displays the signal from the sensor versus $1/\cos\beta - 1$, where β is the refraction angle. The refraction index was assumed to be 1.5. Now the peaks of light intensity become equidistant (Fig. 6). For determining the refraction index of air, the measurements involve slow evacuation of the gas from a special gas cell provided by PASCO. The dependence of the refraction index of air on its temperature can be seen from distortions in fringes of equal thickness when a small heater is placed under the light path in one arm of the interferometer.

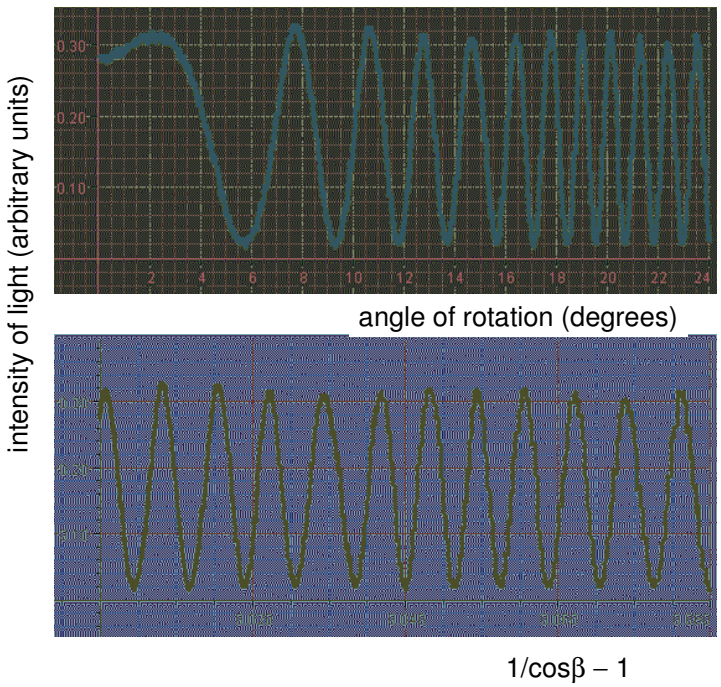

Fig. 6. With $1/\cos\beta - 1$ scale, peaks of light intensity become equidistant.

9.3. Principles of radio

The amplitude modulation and demodulation, the selectivity of a radio receiver, and the directivity of a ferrite-rod antenna are demonstrated (Kraftmakher 2002c).

Guglielmo Marconi
(1874–1937)

Carl Ferdinand Braun
(1850–1918)

"…Research workers and engineers toil unceasingly on the development of wireless telegraphy. Where this development can lead, we do not know. However, with the results already achieved, telegraphy over wires has been extended by this invention in the most fortunate way... This is the magnificent practical invention which has flowered upon one of the most brilliant scientific discovery of our time!"

> H. Hildebrand, President of the Royal Swedish Academy of Sciences. Presentation of Guglielmo Marconi and Carl Ferdinand Braun awarded "in recognition of their contributions to the development of wireless telegraphy" (1909).

Additional equipment: *Rotary motion sensor*, *Voltage sensor*, oscilloscope, ferrite-rod antenna, varicap, function generator, AC-to-DC converter, audio amplifier with loudspeaker, semiconductor diode, resistors, capacitors.

In 1895, Marconi succeeded in sending wireless signals over a distance of one and a half miles, thus becoming the inventor of the first practical system of

wireless telegraphy. In 1899, he established wireless communication between France and England. In 1897, Braun invented a cathode-ray tube. In 1898, he attempted to transmit Morse signals through water. Braun was one of the first to send electromagnetic waves in a definite direction.

Only few technical achievements play in our life a role comparable to that of radio and television. Regrettably, only few physics textbooks pay attention to this subject. The textbook by Hecht (1994) that tells somewhat about radio communications and describes a simple radio receiver is rather an exception. Hill *et al* (1993) described a classroom demonstration of radio interferometry. Davids *et al* (2010) considered the fundamentals of cell phones and wireless communications. Hare (2010) presented a demonstration for exploring the radio waves generated by a mobile phone. With a simple radio receiver, Straulino and Orlando (2012) also demonstrated principles of wireless communication. The *McGraw–Hill Encyclopedia* (Parker 1997) may serve as a handbook.

Theoretical background. For radio communications, the information to be transmitted must cause amplitude or frequency modulation of a high-frequency carrier (Fig. 1). **Amplitude modulation** (AM) is the oldest form of modulation. The amplitude of the high-frequency wave is varied in response to a low-frequency signal. This technique is used in AM broadcasting, television picture transmission, radiotelephony and radiotelegraphy, and navigational aids. Each radio transmitter operates within a specific radio-frequency channel. The minimum usable channel widths depend upon the amount of information the channel must transmit. With amplitude modulation, when a sine wave of frequency Ω modulates a sine wave of frequency ω, the resulting oscillation is

$$(1 + m\sin\Omega t)\,\sin\omega t = \sin\omega t + \tfrac{1}{2}m\cos[(\omega - \Omega)t] - \tfrac{1}{2}m\cos[(\omega + \Omega)t], \qquad (1)$$

where $m < 1$ is called the modulation index.

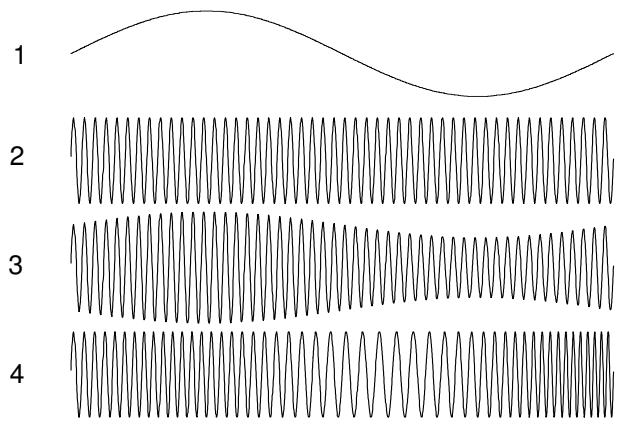

Fig. 1. Signal waveforms: 1–low-frequency signal, 2–high-frequency carrier, 3–amplitude modulation, 4–frequency modulation.

This equation shows that the amplitude-modulation process generates new frequencies, called side frequencies or side bands (Fig. 2). AM signals have identical **upper and lower sidebands** symmetrically located on each side of the carrier. The necessary channel width depends on the upper frequency of the signal used for the modulation. In AM broadcasting, the channel width is 10 kHz. In television, it is 6 MHz because of a large amount of essential video information. **Frequency modulation** is used in FM broadcasting, television sound transmission, and microwave relaying. In FM broadcasting, the channel width is 200 kHz. The insufficient bandwidth in AM broadcasting limits the quality of musical transmissions. The FM broadcasting improves the situation but needs to use higher carrier frequencies.

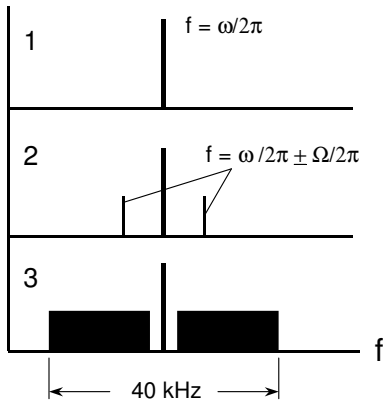

Fig. 2. Spectra of radio signals: 1–the carrier; 2–AM by single frequency; 3–AM by 20 Hz–20 kHz audio band.

At a broadcasting station, a low-frequency signal modulates a high-frequency carrier, and the corresponding modulated current is sent to an antenna. The antenna creates high-frequency electromagnetic waves, which induce a voltage in an antenna of a radio receiver. This signal is selected by tuning the antenna circuit, and then amplified and demodulated. The low-frequency signal obtained by the demodulation reproduces the signal used for the modulation at the broadcasting station (Fig. 3).

The simplest AM-broadcasting receiver consists of an antenna, a tuneable band-pass filter, a high-frequency amplifier, a demodulator, a low-pass filter, and an audio amplifier with a loudspeaker (Fig. 4). Such a receiver is called the tuned-radio-frequency receiver. A simple demodulator employs a semiconductor diode. More complex methods of demodulation are now in use. They consist of creating a sine wave voltage of the same frequency and phase that the broadcast carrier has. This can be done, for instance, by means of a limiting amplifier. The amplifier provides a voltage of the same sign as the input voltage, but of constant magnitude. To obtain the audio signal, it is enough to multiply the broadcast signal by the created voltage and to smooth the product.

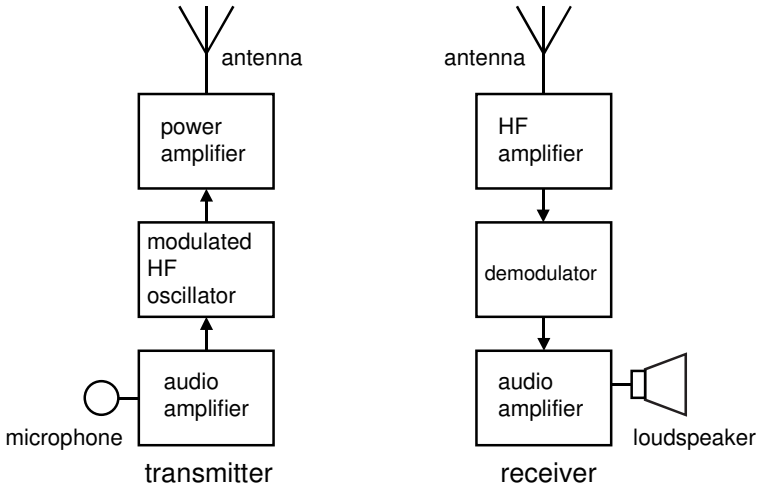

Fig. 3. Scheme of radio broadcasting.

Tuned-radio-frequency receivers do not provide the necessary selectivity. Modern radio receivers, so-called **superheterodynes**, employ the **frequency-conversion** technique. In such a receiver, the high-frequency (HF) signal passes to a frequency converter. The converter includes a local oscillator and a mixer, which translates the high-frequency signal to a signal of an intermediate frequency (IF). This frequency does not depend on the frequency of the original signal, so that there is no need for tuning the IF amplifier. The amplitude modulation of the intermediate-frequency voltage exactly reproduces the original modulation. A high-performance fixed-frequency filter follows the frequency converter and ensures the necessary selectivity.

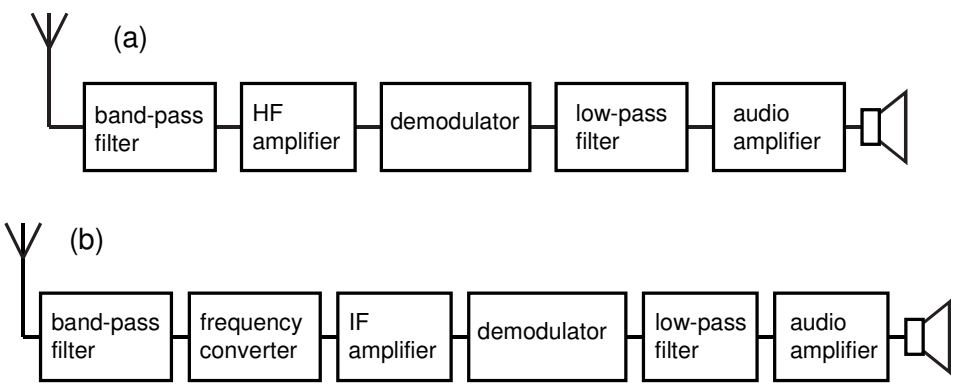

Fig. 4. Structures of radio receivers: (a) tuned-radio-frequency receiver, and (b) superheterodyne receiver.

Setup and calibration of the AM receiver. The experiment illustrates the main principles of radio: **modulation** and **demodulation**, the **selectivity** of a radio receiver, and the **directivity of antenna**. A simple radio setup serves for this purpose (Fig. 5). It includes a **ferrite-rod antenna** with a variable capacitor, a high-frequency amplifier, a semiconductor diode serving as a demodulator, and an audio amplifier with a loudspeaker. The ferrite-rod antenna is a coil wrapped on a ferrite rod. The setup thus is a simple tuned-radio-frequency receiver.

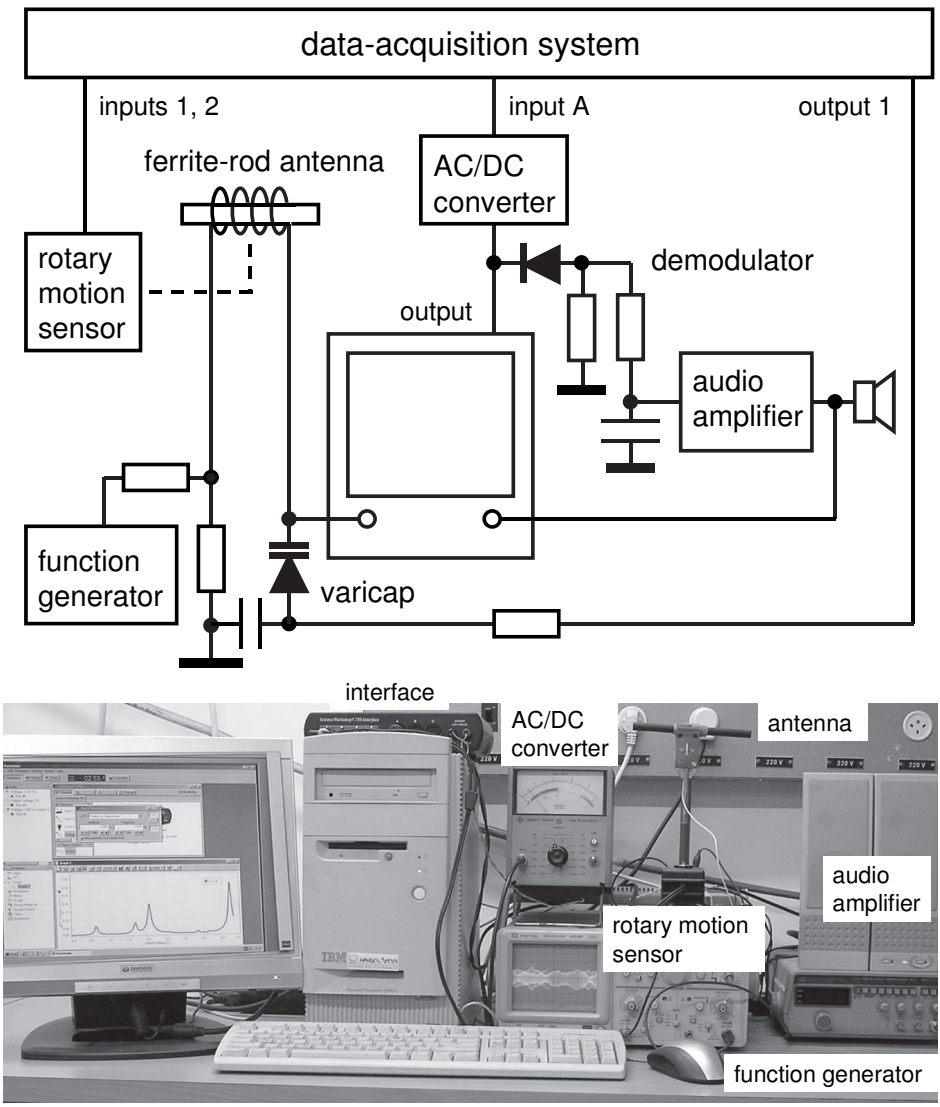

Fig. 5. The setup. The oscilloscope amplifies and displays antenna signals.

A dual-channel Kenwood CS-4025 oscilloscope amplifies the antenna signals and displays modulated high-frequency signals and audio signals. The oscilloscope has an output terminal from one of the channels, with the usable gain up to 100. An integrating RC circuit follows the demodulator. It suppresses high-frequency voltages, but retains low-frequency oscillations for the audio amplifier. Two sensors are used, the *Rotary motion sensor* and the *Voltage sensor*. A **varicap** (Philips Electronics BB112) is a variable capacitor governed by an external DC voltage. The varicap (variable capacitor), also known as **varactor**, uses a reverse-biased *p–n* junction; its capacitance decreases with increasing the applied voltage. The *Output 1* provides the controlling voltage, up to 10 V. A Hewlett–Packard 400E voltmeter is connected to the output of the oscilloscope and serves as an AC-to-DC converter. The *Voltage sensor* acquires its DC output voltage, which is proportional to the high-frequency voltage induced in the antenna circuit. The audio-frequency signal proceeds to the audio amplifier.

Changing the voltage applied to the varicap does the tuning of the antenna circuit. A function generator GoodWill GFG-8019G with digital frequency indication serves for the calibration. With a voltage divider, a small part of the generator output voltage is applied to the antenna circuit. The students calibrate the circuit by stepwise changing the voltage applied to the varicap and tuning the function generator. From the data, a graph and a polynomial fit are available (Fig. 6). At voltages above 8 V, the electronic tuning is ineffectual because the capacitance of the varicap becomes a small part of that of the antenna circuit.

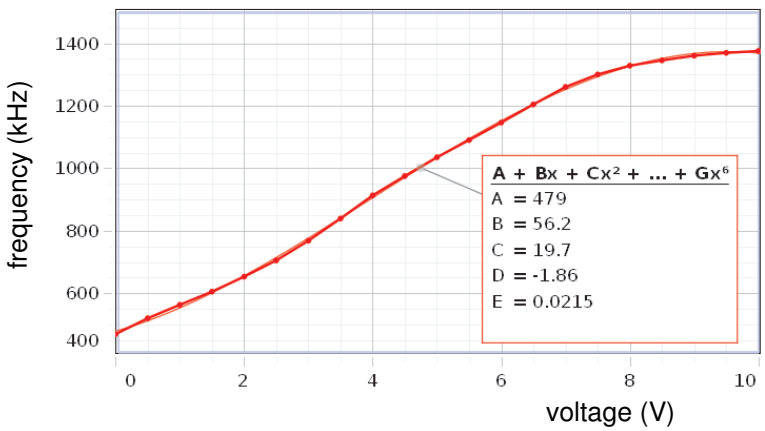

Fig. 6. Resonance frequency versus voltage applied to the varicap.

Selectivity of antenna circuit. The resonance curve of the antenna circuit is measured by means of a weak frequency modulation of the *Output 1*. The *Voltage sensor* measures the output voltage of the AC-to-DC converter. The resonance curve is a graph of the AC-to-DC converter output voltage versus frequency (Fig. 7). For the frequency of 1 MHz, the bandwidth of the antenna

circuit well matches the channel width used in AM broadcasting. For a carrier frequency of 10 MHz, the resonance curve of a circuit of the same quality is ten times broader and does not provide the necessary selectivity. Superheterodyne receivers must be used at such frequencies.

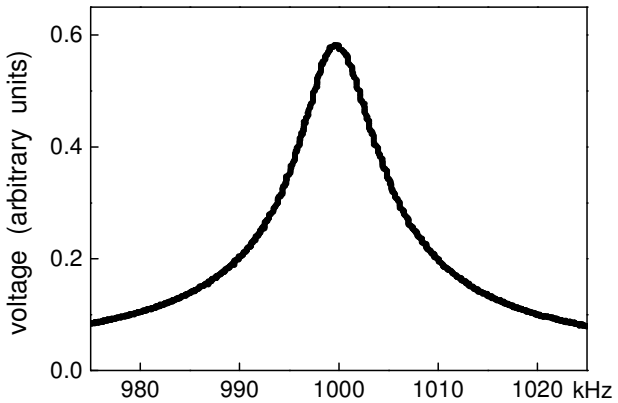

Fig. 7. Resonance curve of antenna circuit tuned to 1 MHz.

Panorama of accessible broadcasting stations. To determine frequencies and relative amplitudes of the electromagnetic fields of accessible broadcasting stations, the *Positive ramp up* voltage from the *Output 1* feeds the varicap. The frequency of this voltage is 0.001 Hz, but only a half of the period is used (output voltages from zero to 10 V). The voltage is translated into frequency with the polynomial fit obtained by the calibration. Two perpendicular orientations of the ferrite-rod antenna are necessary for determining correct amplitudes of the electromagnetic fields (Fig. 8). The two runs (A and B) provide correct amplitudes $C = (A^2 + B^2)^{½}$. In our case, only three broadcast stations are observable; other peaks are caused by technical devices.

The two-channel oscilloscope displays modulated high-frequency signals from AM broadcasting stations and signals obtained by demodulation, so the relation between the two signals is clearly seen.

Directivity of antenna. For this measurement, one should use a sufficiently strong broadcasting station. The directivity diagram of the ferrite-rod antenna is measured with the *Rotary motion sensor*. The angle range from 0 to 360° limits the measurements by properly setting the *Automatic stop*. The directivity diagram (Fig. 9) is obtainable with the *Origin* software. The diagram is in reasonable agreement with the theory: the signal should be proportional to the sine of the angle between the axis of the antenna and the direction to the transmitting station. The diagram confirms that electromagnetic waves are transverse. To convert the data to polar coordinates with *Capstone*, one has to create functions $y = r\sin\varphi$ and $x = r\cos\varphi$ and then plot a graph $y(x)$.

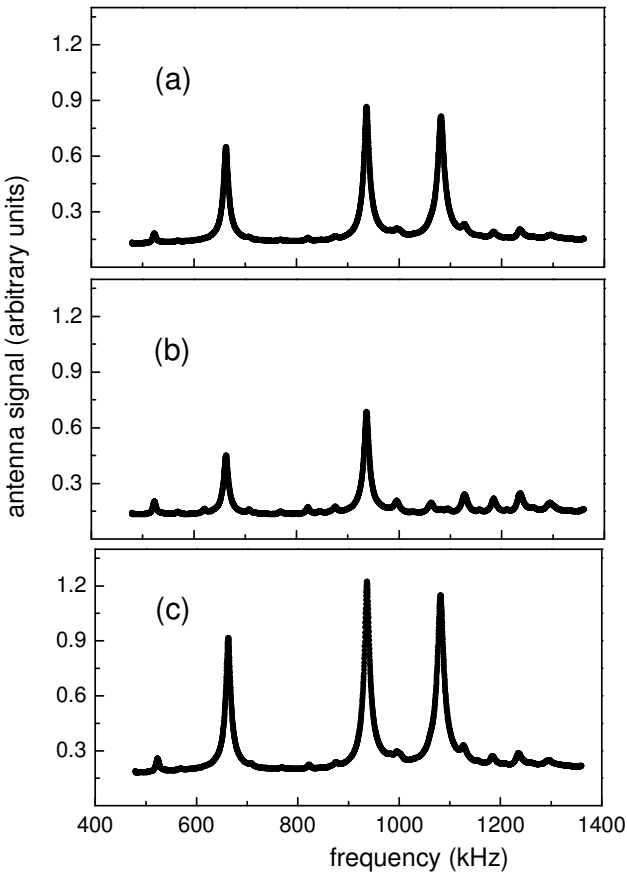

Fig. 8. (a, b) Data for two perpendicular orientations of antenna; (c) correct amplitudes of electromagnetic fields.

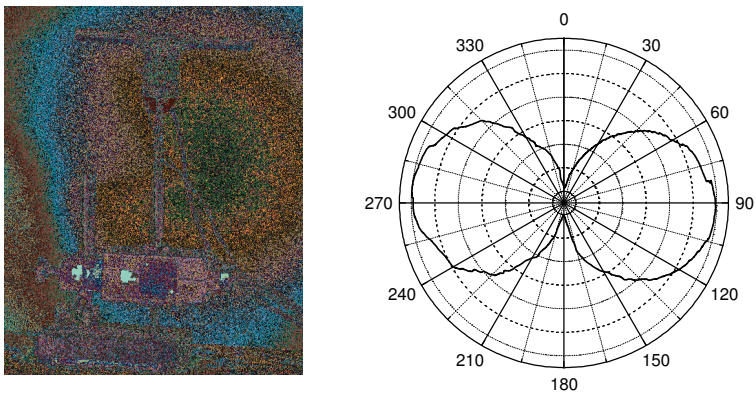

Fig. 9. Ferrite-rod antenna mounted on the axle of the *Rotary motion sensor* and its directivity diagram.

Without the *Rotary motion sensor*, it is possible measure the directivity pattern by mounting the antenna on the axle of a many-turn potentiometer (Fig. 10). The DC voltage applied to the potentiometer is adjusted to obtain 360 mV readout per turn. A digital multimeter measures the output voltage of the potentiometer.

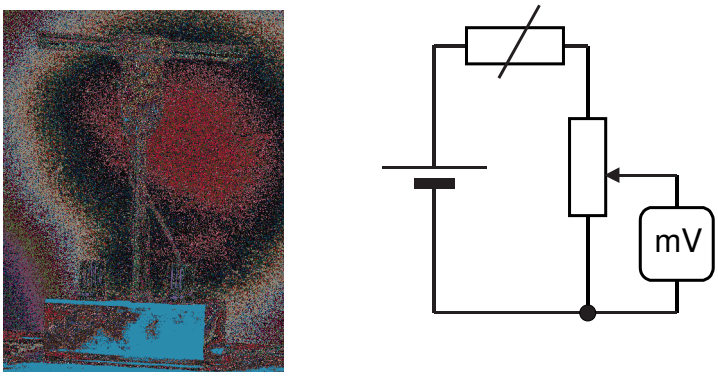

Fig. 10. Ferrite-rod antenna mounted on the axle of a potentiometer.

Polarization of electromagnetic waves. It is easy to check the polarization of electromagnetic waves from a broadcasting station. For this purpose, the axle of the *Rotary motion sensor* with the ferrite-rod antenna is positioned horizontally and aimed at the selected station. To obtain the polar diagram of the incoming signal, the antenna is manually rotated in the vertical plane.

Examples of AM broadcasts and their spectra. The high sensitivity and broad frequency band of a digital storage oscilloscope (DSO) make it possible to observe spectra of AM broadcasting stations (Kraftmakher 2012e). We use a Tektronix TDS 3012B oscilloscope. The examples of the signals and their spectra presented here were taken during a broadcast from an AM station operating at 660 kHz (Fig. 11). The scale is 2 ms per division for the signals and 1.25 kHz per division for the spectra. To make the narrow frequency band around the carrier observable, one should use a large frequency scale (for instance, 125 kHz per division) and bring the spectrum to the center of the DSO display. When reducing the scale, the carrier frequency remains at the center, while the sidebands become well observable. To reduce distortions, the modulation index in AM broadcasting usually does not exceed 30%. To arrange more broadcasting channels, the frequency band allowed for one AM channel is only 10 kHz (5 kHz for each sideband). This is the reason of the unsatisfactory quality of AM musical broadcasts. The FM broadcasting operates at frequencies of the order of 100 MHz, and a broad frequency band is allowed for each FM channel.

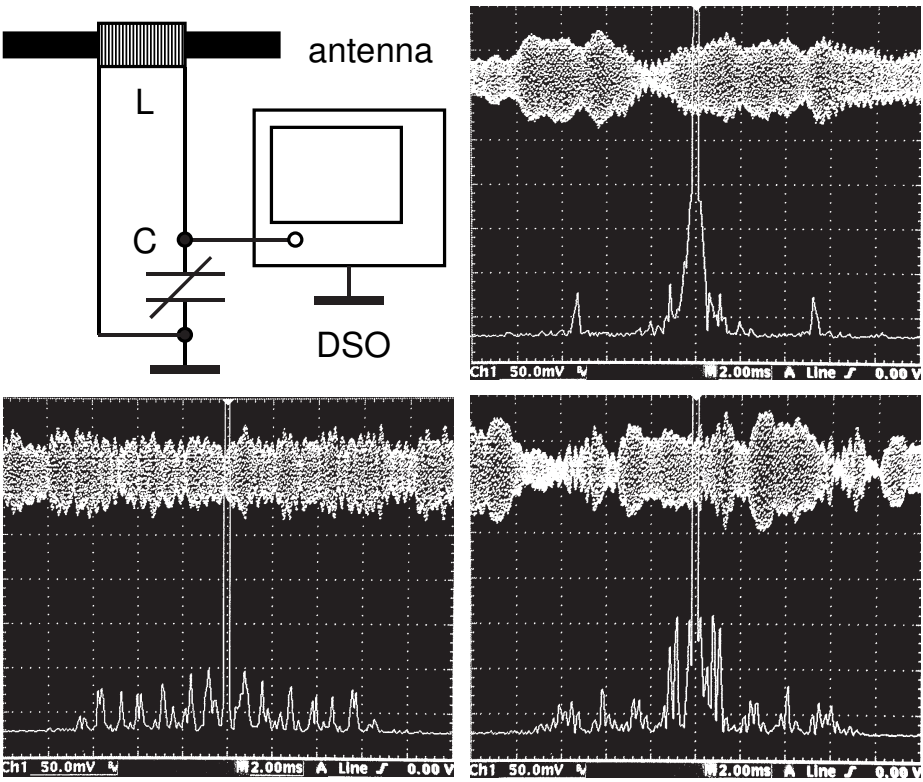

Fig. 11. Schematic of the setup with DSO, 20 ms fragments of AM broadcasts, and their spectra. Frequency scale is 1.25 kHz per division. Each sideband does not exceed 5 kHz.

9.4. Photoelectric effect

This phenomenon introduces students to quantum physics.

Robert Andrews Millikan (1868–1953)

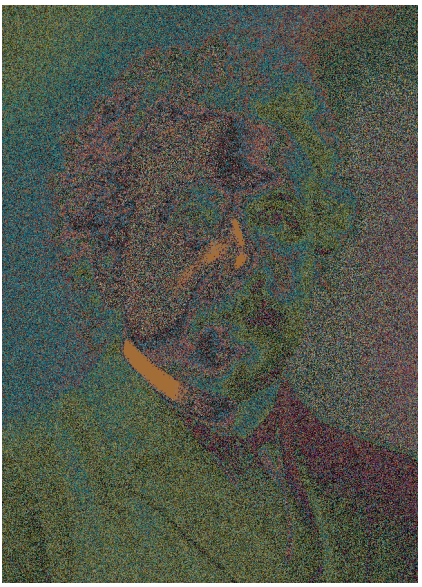

Albert Einstein (1879–1955)

"…There is probably no physicist living today whose name has become so widely known as that of Albert Einstein… Einstein's law has become the basis of quantitative photochemistry in the same way as Faraday's law is the basis of electrochemistry."

> S. Arrhenius, Chairman of the Nobel Committee for Physics. Presentation of Albert Einstein awarded the Nobel Prize "for his services to Theoretical Physics, and especially for his discovery of the law of the photoelectric effect" (1921).

"…Millikan's aim was to prove that electricity really has the atomic structure… It was necessary to measure the charge of a single ion with such a degree of accuracy as would enable him to ascertain that this charge is always the same, and it was necessary to furnish the same proofs in the case of free electrons. By a brilliant method of investigation and by extraordinarily exact experimental technique Millikan reached his goal."

> A. Gullstrand, Chairman of the Nobel Committee for Physics. Presentation of Robert Andrews Millikan awarded the Nobel Prize "for his work on the elementary charge of electricity and on the photoelectric effect" (1923).

Many papers were published on this experiment, and only a fraction of them is mentioned here. Hanson and Clotfelter (1966) presented an evaluation of equipment commercially available for determining the *h*/*e* ratio in student laboratories. The authors stressed that certain practical problems encountered in this experiment make good results difficult to obtain. In particular, a serious problem is caused by the emission of electrons from the anode. The Leybold's apparatus includes a vacuum phototube with an anode in the form of a platinum wire loop that can be heated shortly before taking data. The purpose of the heating is to vaporize any material that has condensed on the anode from the photocathode. It turned out that the results obtained strongly depend on this procedure. Hall and Tuttle (1971) used an AC amplifier for measuring the photocurrent caused by an AC-powered mercury arc. Hall (1971) developed an efficient amplifier for AC photoelectric measurements. Carver and Crawford (1975) described a demonstration of the photoelectric threshold. Powell (1978) justified a procedure of determining the stopping potential from a plot of photocurrent root squared versus applied bias voltage. Steinberg *et al* (1996) developed a computer-based tutorial on the photoelectric effect.

Einstein's famous equation and Millikan's outstanding experiment. Under normal conditions, free electrons that move inside a metal cannot leave it and escape outwards. This means that a potential barrier exists at the surface of the metal that prevents electrons from leaving it. The energy necessary for an electron to leave the metal at the absolute zero temperature is called the **work function** φ. Several sources are known to deliver to the electron the necessary energy: the thermal motion (thermionic emission), quanta of light (photoelectric effect), and bombardment by electrons or other particles (secondary electron emission).

The photoelectric effect manifests peculiarities that cannot be explained by the wave theory of light. The energy of electrons leaving the cathode is independent of the intensity of incident light, but depends on the wavelength. However, it is easy to explain the phenomenon accepting the quantum theory. Einstein has shown in 1905 that the energy conservation law fairly explains the effect. He supposed that Planck's formula $E = hf$, where h is Planck's constant and f is the frequency of light, is valid not only for atomic energy levels. Einstein's revolutionary idea was that the light is formed by particles having this energy, and these particles are elemental portions of light. At that time, Planck did not accept this concept, but soon he became one of the adepts of the new theory. When light falls onto a metal, a free electron acquires the full energy of a photon. This energy is utilized to overcome the potential barrier φ, and the rest is partly consumed in interactions inside the metal. For electrons leaving the cathode of a vacuum phototube,

$$hf = \varphi + \tfrac{1}{2}mv_{\mathrm{m}}^2, \tag{1}$$

where m is the electron mass, and v_{m} is the maximum velocity of electrons leaving the cathode.

This extremely simple and now evident relation is Einstein's famous equation confirmed by Millikan's outstanding experiment. For the determination of the maximum energy of electrons leaving the cathode (emitter) of a vacuum phototube, a negative potential that slows down the electrons is applied to the anode (collector). For the stopping potential V_0,

$$eV_0 = \tfrac{1}{2}mv_m^2, \quad \text{and} \tag{2}$$

$$hf/e = \varphi/e + V_0. \tag{3}$$

The energy of the electrons is in the range from zero to a maximum because their energy is reduced during the escape from the emitter. In Eq. (3), the contact potential between the electrodes of the phototube was not taken into account. Many authors considered the validity of Eq. (3): James (1973); Hodgson and Lambert (1975); Rudnick and Tannhauser (1976); McClellan *et al* (1978); Wong *et al* (2011). It seems to be simple to make use of Eq. (3) to determine the h/e ratio. For this aim, one needs to determine the threshold energies for several frequencies of incident light. However, complicating effects may cause the thresholds to be difficult to observe (Keesing 1981): (i) the point to point variation of the work function; (ii) the energy dependent electron reflection at the collector; (iii) the geometrical effects, which cause an electron to have sufficient energy, but insufficient momentum to reach the collector; (iv) the reverse photoelectric and leakage currents; and (v) the thermal effects.

Two distinct methods are used to determine the threshold energy. The first method employs an open circuit phototube and allows the collector to charge negatively in response to the photocurrent from the emitter until no more electrons can reach it. This self-induced bias is measured as a function of the frequency of incident light. However, it was shown (Keesing 1981) that increasing the light intensity causes the bias to increase. Nevertheless, this method was used in some student experiments (Boys *et al* 1978; Bobst and Karlow 1985; Barnett and Stokes 1988).

The second method repeats Millikan's observations of I–V characteristics of a vacuum phototube. The experiment is included in many laboratory manuals. Among the complicating effects listed above, the thermal effects are of fundamental nature. Einstein's equation is strictly correct when the emitter is at the absolute zero temperature. At any finite temperature, the thermal motion of electrons contributes to their initial velocities when leaving the emitter. Therefore, the Eq. (3) becomes inapplicable (Keesing 1981). Knudsen (1983) has shown that the problem can be solved by applying Fowler's theory taking into account the emitter's temperature, and using a plane-parallel geometry of the electrodes. With these improvements, the results obtained were within 1% of the correct value.

1. The *h*/*e* ratio

With the *850 Interface*, determinations of the *h*/*e* ratio become more accurate.

Additional equipment: *Voltage sensor*, vacuum phototube, monochromator, light bulb, DC amplifier.

The setup and results. Results obtainable by using simple commercial apparatus may differ significantly from the correct *h*/*e* value. One of the reasons for this disagreement is the reverse current of electrons emitted by the collector, also due to the photoelectric effect. For these electrons, the potential applied to the phototube is an accelerating voltage. To suppress this effect, the collector should be screened from the direct incident light. The second possible drawback is the insufficient isolation of the photocell. When the isolation resistance is of the order of 10^{10} Ω, this causes a reverse leakage current, which is proportional to the applied voltage. To reduce the influence of the insufficient isolation, it is worth employing more intense light sources. Another possibility is to determine the leakage current as a function of the applied voltage and to introduce the necessary corrections (Kraftmakher 2006d). In our setup, the vacuum phototube is irradiated by means of a halogen light bulb and a grating monochromator (Bausch and Lomb, 1200 grooves per millimeter) (Fig. 1).

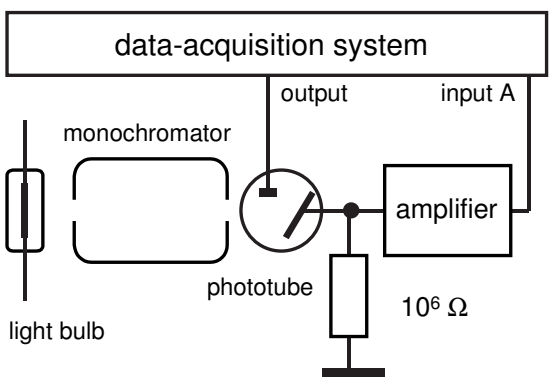

Fig. 1. Schematic of the setup.

The load resistor of the phototube is 10^6 Ω. The voltage across the resistor is amplified by a Keithley 177 multimeter and then fed to the input of the data-acquisition system. With the 20 mV scale, the multimeter provides 100-fold amplification. A 0.001 Hz *Sine wave* voltage from the *Output 1* is applied to the phototube. After starting the measurements, the generator starts to reproduce the negative part of this waveform, and one run lasts 250 s. For the results presented (Fig. 2), the leakage current (dark current) can be neglected. The current contains only two contributions: the photoelectric current from the emitter, and

that from the collector. The latter is sufficiently small and reaches saturation at low voltages. The h/e ratio is close to the correct value (Fig. 3).

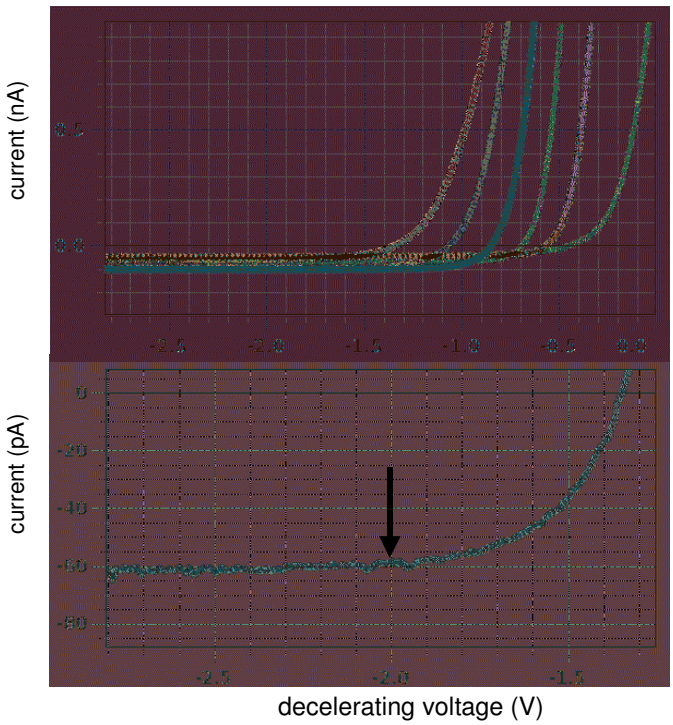

Fig. 2. I–V characteristic for six wavelengths, from 400 to 650 nm, and determination of the stopping potential for $\lambda = 400$ nm.

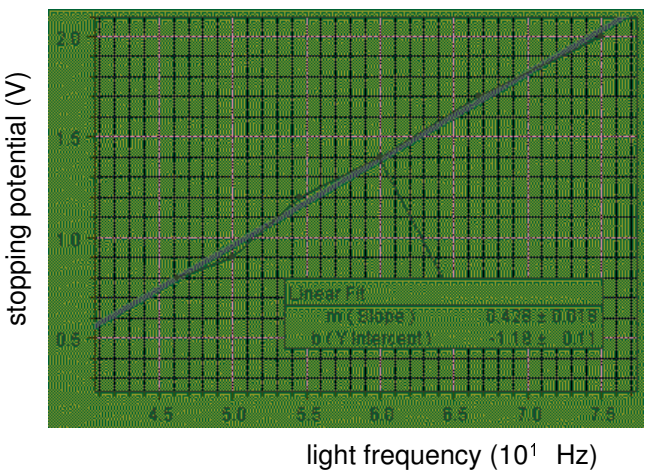

Fig. 3. Stopping potential versus frequency of light; $h/e = 4.28\times10^{-15}$ J.s.C^{-1}.

Demonstration with DSO. With a digital storage oscilloscope, it is easy to demonstrate the dependence of the stopping potential on the wavelength of the light (Fig. 4). A Keithley 177 multimeter amplifies the voltage across the $10^6\ \Omega$ load of the phototube. With the 20 mV range, 1 mV of the amplified voltage corresponds to a photoelectric current of 10^{-11} A. The amplified voltage is fed to the Y input of the DSO. The negative anode voltage is provided by a 100 μF capacitor, which is charged to about 3 V and then disconnected from the source. To control the discharge time of the capacitor, an appropriate resistor (not shown in Fig. 5) shunts the capacitor; in our case, the resistance is 100 kΩ. The X input of the DSO is connected to the anode of the phototube.

Measurements for several wavelengths are performed during one run. The sensitivities of the DSO channels are set to display only parts of the *I–V* characteristics that include the stopping potentials. Before a run, the capacitor is charged, and the voltage applied to the phototube appears out of the X range of the DSO. Then the capacitor is disconnected from the source, and the run started. The bright dot on the display moves from left to right and shows the rise of the photoelectric current. After the dot leaves the display, the wavelength is changed and the capacitor charged again. During one run, this procedure can be repeated several times. In the example presented, the characteristics are shown for three wavelengths: 400, 500, and 600 nm. Because of the limited accuracy, the experiment with a DSO is suitable as a classroom demonstration rather than as a laboratory work (Kraftmakher 2012f).

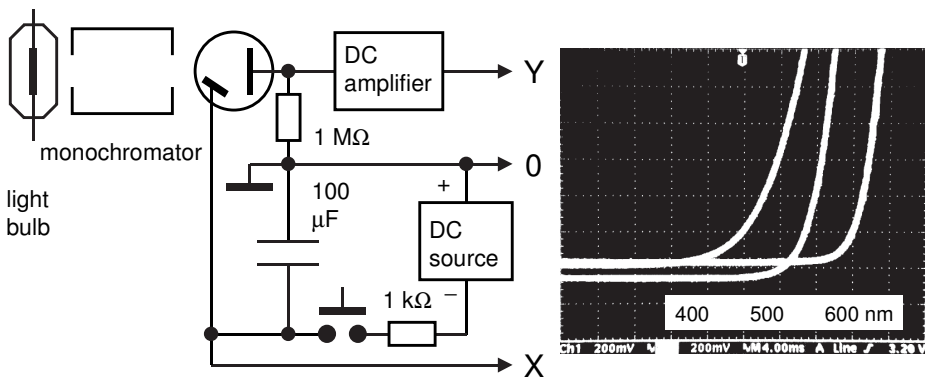

Fig. 4. Schematic of the setup with a DSO and characteristics of the vacuum phototube for three light wavelengths.

2. The work function

The work function is determined from the photoemission threshold.

Equipment: vacuum phototube, light bulb, monochromator, DC supply, multimeter.

The simplest method to determine the work function φ is the measurement of the photoemission threshold λ_0, the longest wavelength of light, for which the photoelectric effect is still possible (Fig. 5). The energy of quanta related to the photoemission threshold equals the work function:

$$hc/\lambda_0 = \varphi. \quad (4)$$

The above expression is a case of a general relation between a wavelength of light λ (μm) and the corresponding energy E (eV) of light quanta:

$$E = 1.24/\lambda. \quad (5)$$

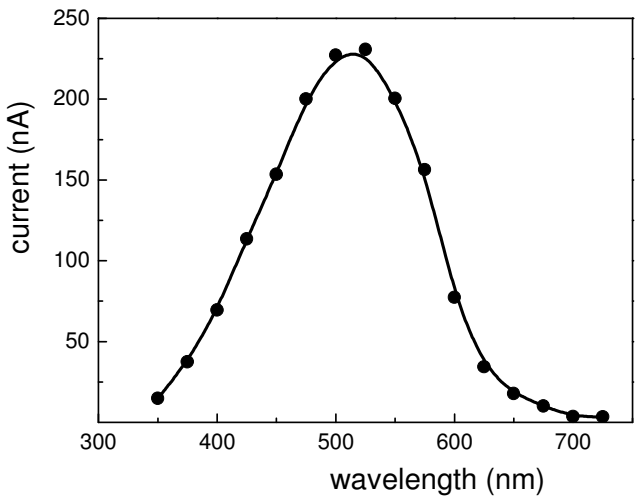

Fig. 5. Photoelectric current versus light wavelength. Photoemission threshold is about 0.7 μm, so the work function is nearly 1.8 eV.

9.5. Franck–Hertz's discovery

Franck–Hertz's experiment with the PHYWE apparatus can be performed with a data-acquisition system or a digital storage oscilloscope.

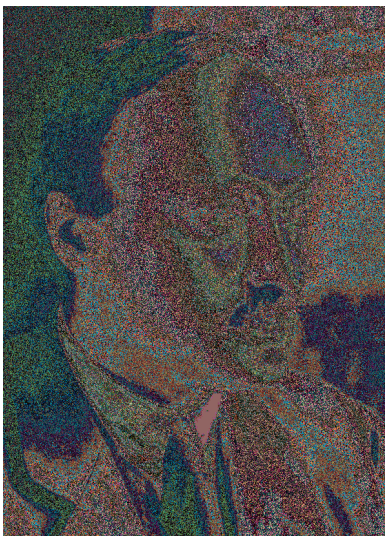

James Franck 1882–1964)

Gustav Hertz (1887–1975)

"…Professor Franck. Professor Hertz. Through clear thinking and painstaking experimental work in a field which is continuously being flooded by different hypotheses, you have provided a firm footing for future research."

> C. W. Oseen, member of the Nobel Committee for Physics. Presentation of James Franck and Gustav Hertz awarded "for their discovery of the laws governing the impact of an electron upon an atom" (1925).

Additional equipment: two *Voltage sensors*, DSO, Franck–Hertz's tube from PHYWE, DC supply, DC amplifier, capacitor, resistors, switch, 1.5 V battery.

In 1914, James Franck and Gustav Hertz reported on an experimental work concerning collisions between electrons and mercury atoms. A hot cathode emits electrons, which are accelerated by a potential applied to a grid (Fig. 1). The electrons undergo collisions with mercury atoms in the space between the cathode and the grid. After the grid, the electrons arrive at a metallic plate, and the current is measured by a galvanometer. The potential of the plate is kept somewhat lower than that of the grid. Therefore, if the electrons lose their

energies in the collisions, their kinetic energy may become smaller than necessary to overcome the potential barrier between the grid and the plate.

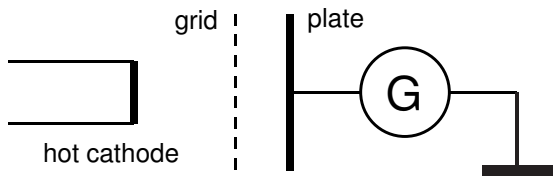

Fig. 1. Scheme of Franck–Hertz's experiment for studying collisions between electrons and mercury atoms. G—galvanometer.

When measuring the plate current versus the accelerating voltage, periodic maxima and minima are observed. If the kinetic energy of electrons is less than 4.9 eV, the collisions are elastic, that is, the electron can change the direction but not the velocity. When the energy reaches 4.9 eV, many collisions become completely inelastic, the electron gives up its entire kinetic energy to an atom. A bit above 4.9 eV many electrons still give 4.9 eV to the atoms, then continue with an energy that is lower by that amount. According to Bohr's theory, this energy corresponds to the first discrete excited state. The *I–V* characteristic shows a minimum in the vicinity of the accelerating voltage equal to the energy level of the mercury atom. The electrons can undergo such collisions several times, so that several minima are observable when the accelerating voltage is changed over a wide range. The excited atom drops back to its original state and emits a photon of energy *hf* determined by the relation

$$hf = E_2 - E_1, \tag{1}$$

where E_2 and E_1 are the energy levels of the atom.

Variants of Franck–Hertz's experiment are described in many papers. Adelberger and Kinsey (1972), Caley (1972), and Huebner and Humphries (1974) described an experiment employing an oscilloscope. Carpenter (1975) used an X-Y recorder for displaying the electron current versus the accelerating voltage. Huebner (1976) observed light-emitting zones appeared inside the Franck–Hertz tube. With a photomultiplier, Buhr *et al* (1983) observed UV emission in Franck–Hertz's experiment. McMahon (1983) considered elastic electron-atom collisions. Martin and Quinn (1984) used a two-grid tube to determine electron energy-loss spectra. With such a tube, Liu (1987) observed higher excitation levels of the mercury atom. Hanne (1988) considered some phenomena involved in the electron collisions with mercury atoms. Nornes and Tu (1989) developed a computer-assisted experiment. By upgrading the experiment, Nicoletopoulos (2002) obtained more accurate values of critical potentials of mercury. Fedak *et al* (2003) employed the *LabVIEW* software. Rapior *et al* (2006) have shown that the spacings between the minima in Franck–Hertz's curves are not exactly equidistant. The experiment is included in many laboratory courses (Portis 1972; Goldin 1983; Melissinos and Napolitano 2003).

Experiment with data-acquisition system. The PHYWE apparatus includes a tube with a cathode and two additional electrodes, a grid and an anode. After pumping out, the tube is filled with a small amount of mercury, and then sealed. It is positioned in an electrically heated furnace. The appropriate density of the mercury vapor is achievable by changing the temperature, which is measured with a thermocouple. The electrons emitted by the cathode are accelerated by a DC voltage between the cathode and the grid and undergo collisions with the mercury atoms. With a battery, the potential of the anode is set to be 1.5 V lower than that of the grid (Fig. 2). Therefore, electrons that lose their energy due to inelastic collisions cannot arrive at the anode.

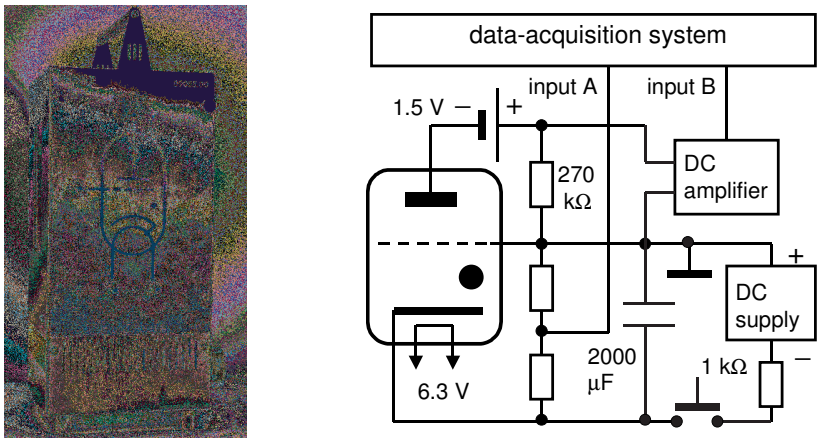

Fig. 2. PHYWE apparatus and diagram of the setup.

The accelerating voltage is provided by a capacitor that can be connected to a DC supply. Before a run, the capacitor is charged to the maximum DC voltage. After the run is started, the capacitor is disconnected from the supply, and its discharge lasts nearly 1 min. The anode current is measured through the voltage drop across a 270 kΩ resistor in the anode circuit. A DC amplifier amplifies this voltage, which is then acquired by the data-acquisition system. Simultaneously, the system measures a definite part of the accelerating voltage (voltages more than 10 V are dangerous for the inputs of the *750 Interface*). *DataStudio* displays the anode current versus the accelerating voltage (Fig. 3).

The pressure of the mercury vapor inside the Franck–Hertz tube plays a crucial role in obtaining convincing experimental data. Too low pressures provide favorable conditions for the ionization of mercury atoms when the accelerating voltage exceeds the ionization potential of mercury, 10.4 V. At too high pressures, this effect is suppressed, but the current in the tube decreases. At 100°C, the equilibrium mercury vapor pressure is 0.037 kPa; it becomes 0.38 kPa at 150°C and 2.3 kPa at 200°C (Lide 2008). Therefore, some efforts should be applied to find a proper temperature regime of the oven. The data presented were obtained when the temperature inside the oven was nearly 150°C.

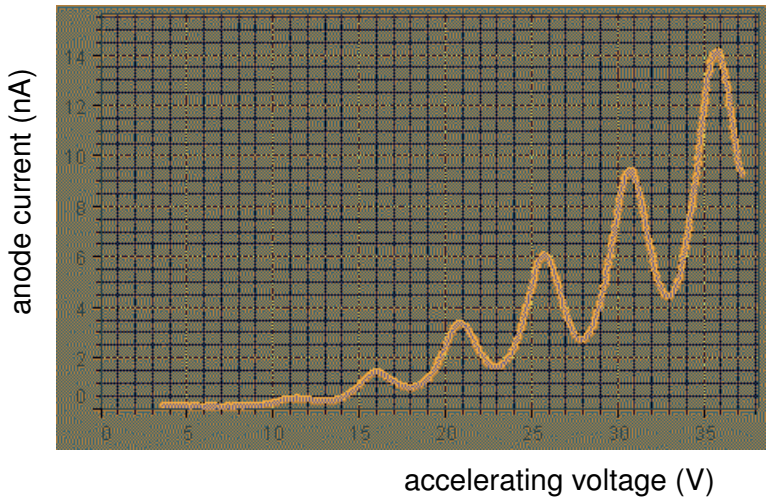

Fig. 3. The distance between neighboring maxima or minima is nearly 4.9 V, the energy of the first excited state of mercury atoms.

Experiment with DSO. Similar results are obtainable with a digital storage oscilloscope (Kraftmakher 2012f). The accelerating voltage is fed to the X input of the oscilloscope, while a voltage proportional to the anode current to the Y input (Fig. 4). A 100 kΩ variable resistor shunting the capacitor (not shown in Fig. 4) controls the discharge time. The anode current is measured through the voltage drop across a 1 MΩ load (this is a resistance of the DSO inputs). For suppressing AC voltages due to the interference, the load is shunted by a 0.1 μF capacitor. The characteristic is quite similar to that obtainable with a data-acquisition system or an X–Y recorder.

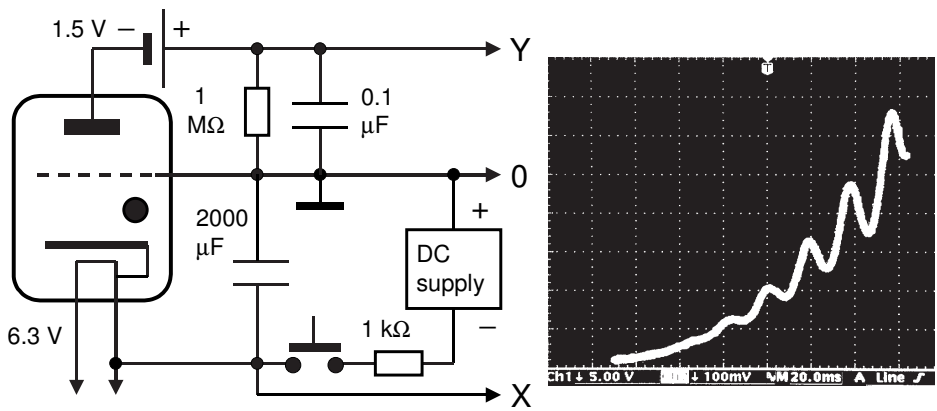

Fig. 4. Schematic of the setup and results displayed on the DSO screen.

9.6. Thermionic emission

The experiments include (i) Richardson's law and the work function; (ii) the temperature of emitted electrons; and (iii) the calorimetric determination of the work function.

Owen Willans Richardson (1879–1959)

"…Professor Richardson. You are a happy man. You possess the very thing that gives life its chief value. You can devote yourself with all your strength to the activity that you love. We constantly see the results of this activity come to light. Besides this, you are fortunate enough to see the harvest ripen to the benefit of mankind in the fields you tilled in your youth."

> O. W. Oseen, member of the Nobel Committee for Physics. Presentation of Owen Willans Richardson awarded the Nobel Prize "for his work on the thermionic phenomenon and especially for the discovery of the law named after him" (1928).

The above formula "for the discovery of the law named after him" offers an excellent idea how to get a Nobel Prize laureate. It is worth remembering, in this connection, discoveries bearing the names of the laureates: Röntgen rays (1901), Zeeman effect (1902), Wien law (1911), Planck formula (1918), Bohr theory (1922), Compton effect (1927), Wilson chamber (1927), Raman effect (1930), Heisenberg principle (1932), Dirac equation (1933), Pauli principle (1945), Cherenkov effect (1958), Mössbauer effect (1961), Néel point (1970), BCS theory (1972), Josephson effect (1973), Abrikosov vortices (2003), Higgs boson (2013)… to be continued.

Da liegt der Hund begraben!

Thermionic emission is of primary importance with vacuum tubes, electron microscopes, and other devices depending on a continuous supply of electrons. The discovery and studies of this phenomenon played an important role in the development of modern physics. Thomas Alva Edison (1847–1931) was probably the first to discover that negative electricity escapes from a hot filament (1883). In 1897, Joseph John Thomson established that the charge carriers are very small compared to the hydrogen ion. This was the electron. In 1900, Paul Drude (1863–1906) suggested that electrons are the carriers of current in metals, and Thomson proposed that they are also the negative charges emitted by hot metals. Owen Willans Richardson made a study on this basis (1901) and derived equations relating the current density to the absolute temperature. In 1925, Richardson used the new Drude's theory for explaining the emission in terms of the work function φ. The work function is the basic concept related to thermionic emission and the photoelectric effect. This quantity is defined as the energy difference between the Fermi level and the energy at a point in a field-free space outside the conductor (Fig. 1). Four basic methods exist for the determination of the work function: Richardson's method, the photoemission threshold, the contact potential difference, and the calorimetric technique (Herring and Nichols 1949; Craig 1975; Swanson and Davis 1985).

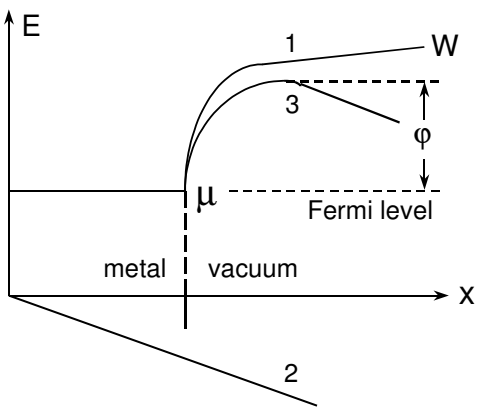

Fig. 1. Work function and Schottky's effect: 1–energy barrier for zero external field, 2–potential of electric field, 3–resulting energy barrier.

Work function and Schottky's effect. To be emitted, the electrons must have sufficient energy, directed in the positive x direction, to overcome the barrier $W = \mu + \varphi$. Assuming that all of the electron's energy is kinetic, this condition may be stated as

$$mv_x^2/2 > \mu + \varphi, \tag{1}$$

where m is the mass of the electron, v_x is the velocity component along the positive x direction, and μ is the Fermi level, the maximum electron energy in

a metal at the absolute zero temperature. It was shown by Schottky that an external electric field E reduces the work function by

$$\Delta\varphi = -e^{3/2}E^{1/2}, \tag{2}$$

where e is the electron charge.

The problem is calculating the number of electrons that have the required velocities. The result is the Richardson–Dushman law for the thermionic current density:

$$j = (4\pi emk_B^2/h^3)T^2\exp(-\varphi/k_BT) = AT^2\exp(-\varphi/k_BT), \tag{3}$$

where k_B is Boltzmann's constant, T is the absolute temperature, and h is Planck's constant. From this formula, the constant A is 120 $A.cm^{-2}.K^{-2}$. Experimental values of φ and A for a number of metals and monomolecular films on tungsten are given in Table 1.

Table 1. Parameters of thermionic emission φ (eV) and A ($A.cm^{-2}.K^{-2}$).

Metal	φ	A	Film	φ	A
Cs	1.81	162	Cs on W	1.36	3.2
Ba	2.11	60	Cs on O on W	0.72	0.003
Mo	4.15	55	Ba on W	1.56	1.5
W	4.54	60–100	Ba on O on W	1.34	0.18
Pt	5.40	170			

Vacuum diode. The simplest vacuum tube is a diode comprising a cathode and an anode. Three ranges of the I–V characteristic can be distinguished according to the potential V, at which the anode is held with respect to the cathode. The saturation current is obtained if a sufficient positive potential is applied to the anode, so that all the emitted electrons are collected. At voltages below that are required for saturation, the repulsion between the electrons tends to limit the current. In this region, the current is proportional to $V^{3/2}$ (the Child–Langmuir law, or the so-called "$^3/_2$ law"). For a coaxial cathode and anode, the anode current is given by

$$I_a = 4A(e/m)^{1/2}\varepsilon_0 U^{3/2}/(3r\beta)^2 = KV^{3/2}, \tag{4}$$

where A is the area of the cathode surface, ε_0 is the electric constant, r is the anode radius, and β is a geometrical correction constant (for the case of parallel-plane electrodes see Umstattd *et al* 2005).

When the applied voltage is reversed so as to become retarding for electrons, the current is limited by the number of electrons with energy sufficient to overcome the retarding potential:

$$I = I_0\exp(-eV/k_BT). \tag{5}$$

This expression is valid for the plane geometry of the electrodes. The temperature relates to the gas of electrons emitted by the cathode.

Vacuum tubes have now a limited practical use, but they provide an excellent opportunity to teach some fundamental physical phenomena such as thermionic emission, the velocity distribution of electrons emitted, the Child–Langmuir law, and the Schottky effect. Corresponding experiments are included in many laboratory manuals. Brody and Singer (1970) determined the *e*/*m* ratio for the electron and the work function of tungsten. Dodd (1971) reported on an experiment, in which the cathode temperature was deduced from the energy distribution of the emitted electrons. Luke (1974) described an experiment including several aspects of thermionic emission. Knudsen (1985) compared the temperature of the emitted electrons with the cathode temperature measured with an optical pyrometer. Using a commercially available vacuum diode with a tungsten cathode, Greenslade (1991) determined the work function of tungsten. Wagner and Soonpaa (1994) developed a picoammeter for measurements over a wide range of thermionic currents. Angiolillo (2009) considered the thermionic emission and the use of vacuum tubes in the advanced physics laboratory (see also Polley 2010). Battaglia *et al* (2010) described an experiment on the velocity distribution of thermionic electrons.

Leybold–Heraeus vacuum diode and other vacuum tubes used in the experiments.

1. Richardson's law

A vacuum diode with a tungsten cathode of direct heating (Leybold–Heraeus, catalog index 55507) is used for the measurement (Fig. 2).

Additional equipment: three *Voltage sensors*, vacuum diode with a tungsten cathode, DC supplies, DC amplifier, decade resistance box, resistors.

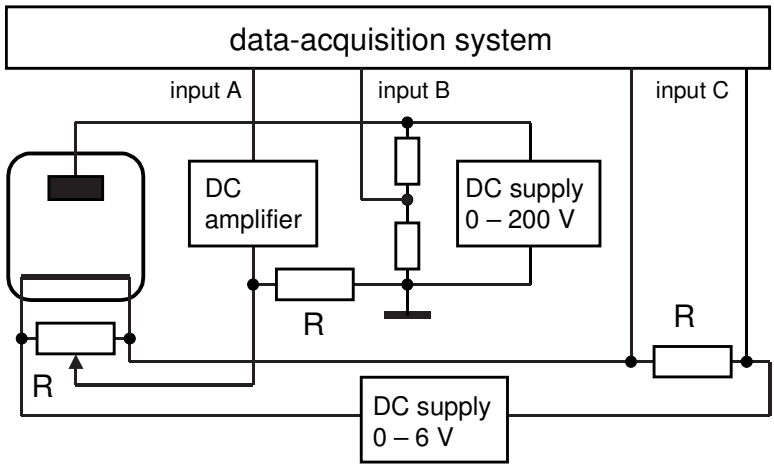

Fig. 2. Schematic of setup for measuring thermionic current.

To reduce the influence of the voltage drop across the cathode, the anode circuit is connected to the middle point of a resistor R_1 shunting the cathode. Since a voltage at the inputs of the data-acquisition system must be below 10 V, the voltage applied to the anode is measured using a voltage divider. The anode current is determined through the voltage across a resistor R_2. This voltage is amplified by a DC amplifier and then fed to the input of the data-acquisition system. The current heating the cathode is determined through the voltage drop across a resistor $R_3 = 0.1\ \Omega$. When a current I_h passes through a wire of length l and diameter d, the electric power dissipated in it equals

$$P = 4I_h^2 \rho l/\pi d^2, \tag{6}$$

where ρ is the resistivity of the wire. In vacuum, this power is balanced by thermal radiation given by Stefan–Boltzmann's law:

$$P = \varepsilon\sigma\pi l d T^4, \tag{7}$$

where ε is the hemispherical total emittance of the sample, and σ is Stefan–Boltzmann's constant. From the above relations,

$$T^4 = 4I_h^2 \rho/\pi^2 \varepsilon\sigma d^3. \tag{8}$$

The parameters ρ and ε and their temperature dependences are specific for different metals. For any given temperature, Eq. (8) contains only one variable parameter, the I_h^2/d^3 ratio. The steady temperature of a tungsten wire is a known function of this ratio, or of the ratio $X = I_h/d^{3/2}$. From the data in Table 2, it is easy to calculate the temperature of a tungsten cathode from its diameter (cm) and the heating current (A). The polynomial fit to the dependence $T(X)$ is

$$T = 790 + 1.3X - 1.2\times10^{-4}X^2. \quad (9)$$

Table 2. Temperature of long tungsten wire in vacuum versus $X = I_h/d^{3/2}$.

$I/d^{-3/2}$ (A.cm$^{-3/2}$)	T (K)	$I/d^{-3/2}$ (A.cm$^{-3/2}$)	T (K)
581	1500	1217	2200
662	1600	1319	2300
747	1700	1422	2400
836	1800	1526	2500
927	1900	1632	2600
1022	2000	1741	2700
1119	2100	1849	2800

In the first experiment, the anode current is measured, for several temperatures of the cathode, as a function of the anode voltage (Fig. 3). Then the saturation current is determined as a function of the heating current (Fig. 4).

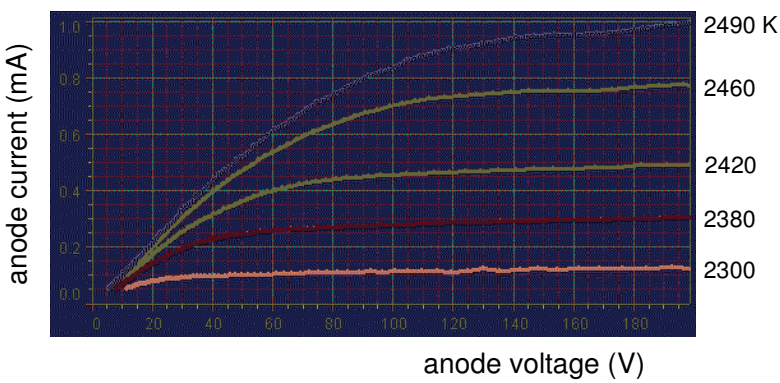

Fig. 3. *I–V* characteristics for various cathode temperatures.

According to Eq. (3), a plot of $\log(I_a/T^2)$ versus $1/T$ should be a linear graph ("Richardson's line"), from which the work function of tungsten is available (Fig. 5). Due to the large diameter of the cathode, temperatures of its end parts are markedly lower than those of the center. There exist two ways to avoid or greatly reduce the influence of this effect. First, diodes with thinner

cathodes should be used. Second, the currents from the ends of the cathode can be excluded with a special design of the diode. The diode contains three cylinder anodes, which are kept at the same potential, but the current through the central anode is only measured. Also, one has to somehow determine the diameter of the cathode. The knowledge of real temperatures of tungsten cathodes is also useful for the estimation of the diameter. Here, the diameter was taken as 0.15 mm.

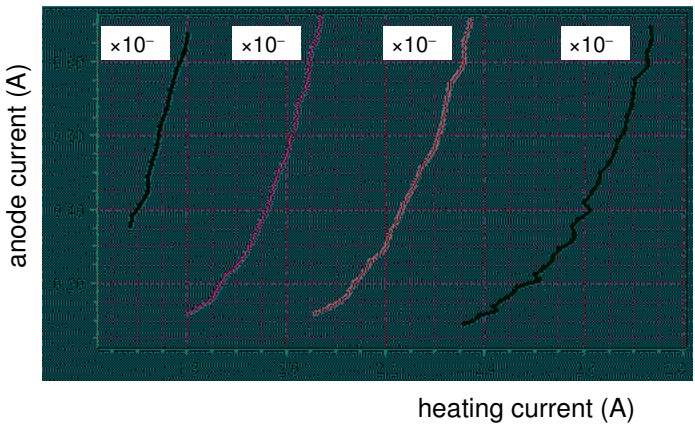

Fig. 4. Saturation current versus current heating the cathode.

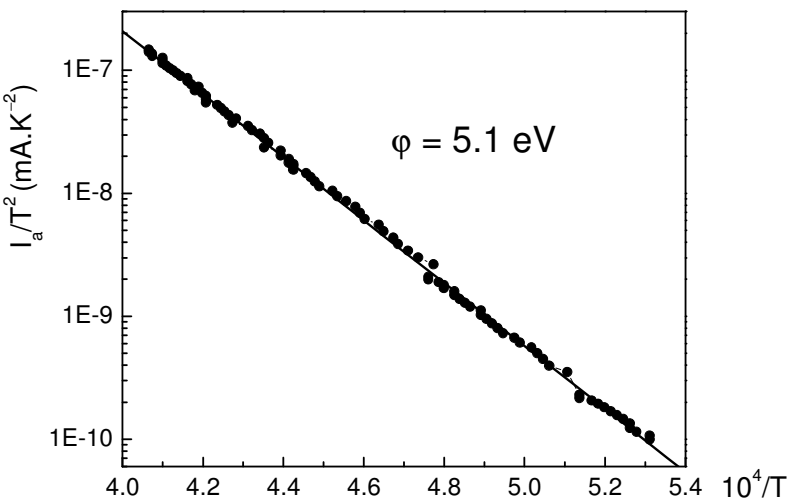

Fig. 5. "Richardson's line" combining all the measurement data. The work function appeared to be about 10% higher than the correct value.

2. Temperature of emitted electrons

The temperature of the emitted electrons coincides with that of the cathode.

Additional equipment: *Voltage sensor*, vacuum diode with an oxide-coated cathode of indirect heating, DC supply, DC amplifier, decade resistance box.

A vacuum diode with an oxide-coated cathode of indirect heating is employed for this experiment (Fig. 6).

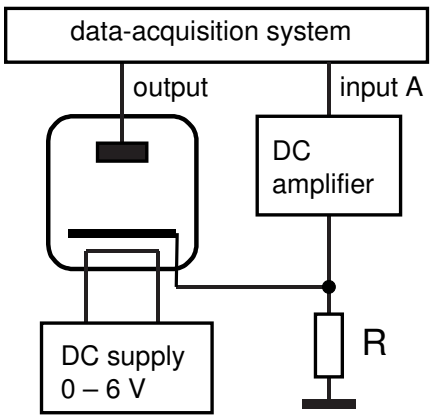

Fig. 6. Schematic of setup for determining temperature of emitted electrons.

The load resistor R of the diode can be set to be 10^2, 10^3, 10^4, or 10^5 Ω. We use a decade resistance box (PI-9588). The voltage across it is amplified by a Keithley 177 multimeter and then fed to the input of the data-acquisition system. With the 20 mV scale, the multimeter provides 100-fold amplification. A 0.001 Hz sine voltage from the *Signal generator* is applied to the diode. After switching the generator on, it starts to reproduce the negative part of the waveform. Then one observes the readout of the multimeter and starts the measurements when the voltage measured falls below 10 mV. When this voltage achieves 1 mV, one changes the load resistor. These measurements repeated for all the load resistors provide data in the range from 10^{-8} to 10^{-4} A (Fig. 7). The low-current part of the *I*–*V* characteristic obeys Eq. (5), so the dependence of $\log I_a$ versus V is a straight line. The decrease of the slope at higher currents means the transition to the space-charge-limited region. The transition point differs from the zero voltage because of the contact potential difference between the cathode and anode. The measurements of the characteristics are done for two regimes of heating the cathode: 6 V (0.6 A) and 4 V (0.46 A). From the graphs combining all the data (Fig. 8), the temperatures of the electrons emitted by the cathode are available.

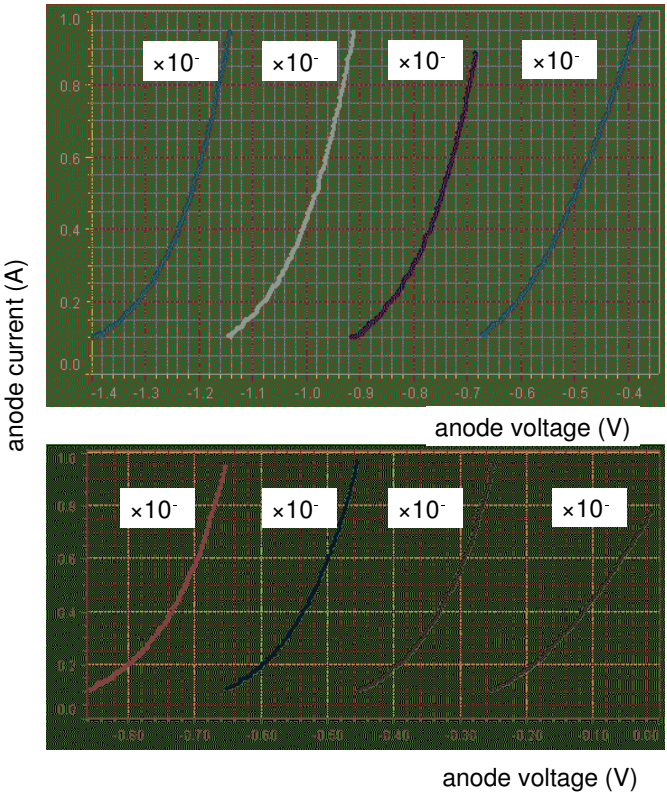

Fig. 7. *I–V* characteristics of vacuum diode for negative anode voltages and two voltages for the cathode heater, 6 V (top) and 4 V (bottom).

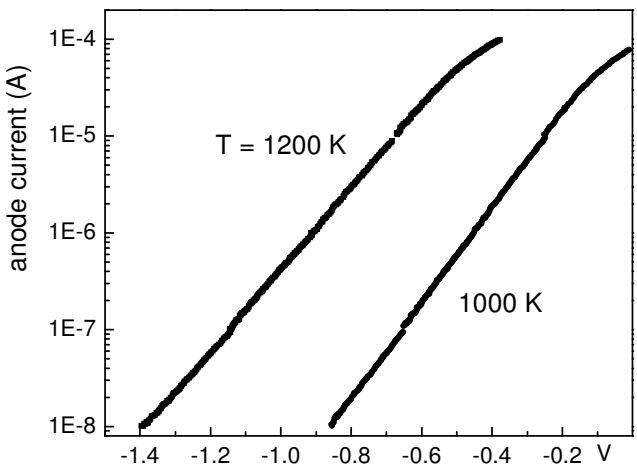

Fig. 8. *I–V* characteristics for two voltages applied to cathode heater. The calculated temperatures are reasonable values for oxide-coated cathodes.

3. Calorimetric determination of work function

The experiment demonstrates the energy transfer by electrons emitted by the cathode of a vacuum tube. Oxide-coated cathodes are more suitable for such measurements than tungsten cathodes (Kraftmakher 1959a, 1998b).

Additional equipment: *Voltage sensor*, vacuum diodes, DC supply, decade resistance box, DC amplifier, 9 V battery, multimeters, resistors.

Theoretical background. The calorimetric technique of determining the work function was used very rarely and is not even mentioned in many textbooks. One of the last such measurements was probably reported by Fleming and Henderson (1940). However, a direct determination of the work function according to its definition deserves attention. The calorimetric method makes use of the cooling of the cathode due to the emission of electrons. The theory of this phenomenon is very simple. Every electron leaving the cathode takes away energy $\varphi + 2k_B(T - T_0)$, where the second term is due to initial velocities of the emitted electrons, which leave the cathode at a high temperature T and return to it at room temperature T_0. The term $2k_BT$ differs from the mean thermal energy because the energy transfer depends also on the velocity of the emitted electrons in a given direction. This term is an order of magnitude smaller than the work function, so there is no need for precisely determining the temperature of the cathode. When a current I_a flows through a vacuum tube, the number of electrons leaving the cathode per second is I_a/e. When the anode circuit is disconnected, the emitted electrons form a space charge around the cathode and equilibrium is set up between the emitted electrons and those returning to the cathode. After closing the anode circuit, a steady current flows through the tube, causing cooling of the cathode (Fig. 9). The additional heat loss is given by

$$\Delta P = [\varphi + 2k_B(T - T_0)]I_a/e. \tag{10}$$

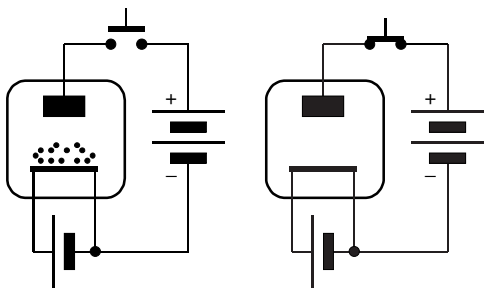

Fig. 9. Vacuum tube with open and closed anode circuit.

This power amounts to only a small part of the total heat losses from the cathode, which is mainly due to thermal radiation. To estimate the expected results, it is useful to consider the ratio of the thermionic current to the power heating the cathode. Since both quantities are proportional to the cathode's area,

this ratio depends only on the temperature and the parameters of the thermionic emission and can be considered as the efficiency of a cathode. The thermionic current grows with temperature more rapidly than the heating power. The efficiency thus increases with temperature, being 10–100 $mA.W^{-1}$ for oxide-coated cathodes and 0.1–1 $mA.W^{-1}$ for tungsten cathodes. The main part of the energy transfer by emitted electrons per second equals the anode current times the work function expressed in electron volts. The expected contributions to the heat loss thus range from 1.5% to 15% for oxide-coated cathodes ($\varphi = 1.5$ eV) and from 0.05% to 0.5% for tungsten cathodes (4.5 eV).

A compensation technique is applicable in the measurements: the energy transfer by emitted electrons can be balanced by properly changing the current heating the cathode. There is no need for measuring the temperature drop caused by the energy transfer, but it is easy to estimate this drop. With the radiation heat transfer, the power necessary to heat the cathode is proportional to T^4, so that $\Delta P/P = 4\Delta T/T$. From this relation, the temperature drop is expected to be 6 to 60 K for an oxide-coated cathode and 0.3 to 3 K for a tungsten cathode. Oxide-coated cathodes are thus more favorable for calorimetric determinations of the work function.

Oxide-coated cathode. Any vacuum tube with an oxide-coated cathode of direct heating is suitable for the measurements. Thin cathode filaments, that is, of low heating current, are preferable. We use a vacuum tube CV 1758/1L4 (a pentode), with its control and screen grids connected to the anode. The cathode is included in a bridge circuit (Fig. 10) fed by a DC supply operating in the constant-current mode, that is, the current is independent of the load. The output voltage of the bridge is amplified by a Keithley 177 multimeter (not shown in Fig. 10) and then fed to the data-acquisition system. The anode of the vacuum tube is connected to a 9 V battery through a switch. The second terminal of the battery is connected to a middle point of a potentiometer shunting the cathode. This is done to reduce the influence of the additional voltage drop across the cathode caused by the current through the tube. The resistance of the potentiometer is two orders of magnitude larger than that of the cathode. A variable resistor R_3 and a milliammeter form an auxiliary circuit for producing adjustable and readily measurable changes in the current heating the cathode. This circuit is connected in parallel to the bridge through the second pair of contacts of the switch. These contacts are closed when the first pair is broken and vice versa. Therefore, when the anode circuit is disconnected and the temperature of the cathode is increased, the auxiliary circuit takes away part of the heating power. Since the DC supply operates in the constant-current mode, the decrease in the current feeding the bridge is exactly equal to the current through the auxiliary circuit. The power heating the cathode decreases by $2RI_h\Delta I_h$, where R is the resistance of the cathode, I_h is the heating current, and ΔI_h is its small decrease. The current through the parallel circuit is adjusted to restore the initial resistance (that is, the initial temperature) of the cathode. Hence,

$$\varphi = 2eRI_h\Delta I_h/I_a - 2k_B(T - T_0). \tag{11}$$

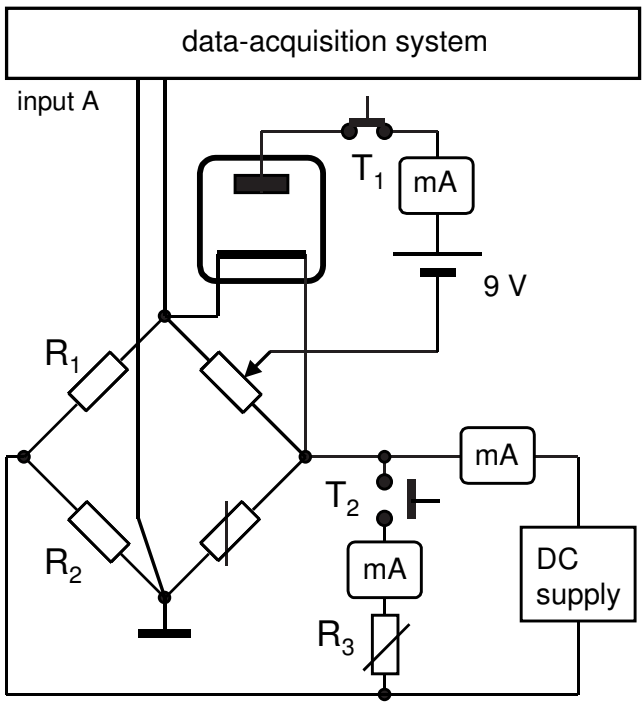

Fig. 10. Circuit for calorimetric determinations of work function.

In the bridge, $R_1 = 10\ \Omega$, $R_2 = 1\ \mathrm{k}\Omega$, and there is no need to take into account the distribution of the feeding current in the arms of the bridge. The measurements are performed with anode currents from 1 to 5 mA. The work function is calculated as an average of the results obtained for both directions of the heating current. The position of the slide of the potentiometer shunting the cathode should be set to obtain a minimum difference between the two results. The energy transfer by emitted electrons can be easily seen when the current through the tube is periodically interrupted, and the output voltage of the bridge is recorded (Fig. 11).

The temperature of oxide-coated cathodes is in the range 1200–1800 K. The quantity $2k_B(T - T_0)$ thus is 0.2±0.05 eV. The temperature dependence of the work function of an oxide-coated cathode may be expressed as $\varphi = \varphi_0 + \alpha T$. For a mixture of BaO and SrO, values of $\varphi_0 \cong 1$ eV and $\alpha \cong 6{\times}10^{-4} T\ \mathrm{eV.K^{-1}}$ were recommended by Craig (1975). The results obtained are in reasonable agreement with this fit (Fig. 12). Richardson's method is hardly applicable to oxide-coated cathodes: due to the strong dependence of the work function on the electric field on the cathode surface, they manifest no saturation current.

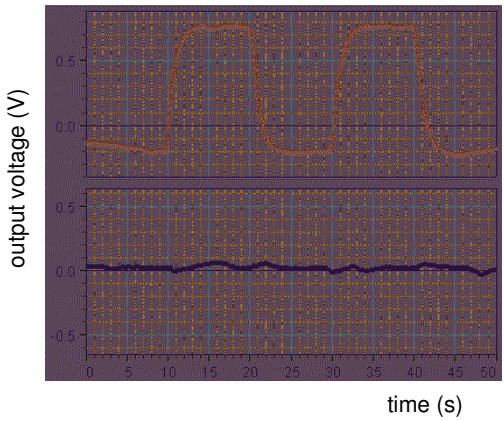

Fig. 11. Output voltage, after 100-fold amplification, when switching on and off 1 mA anode current, before and after compensation.

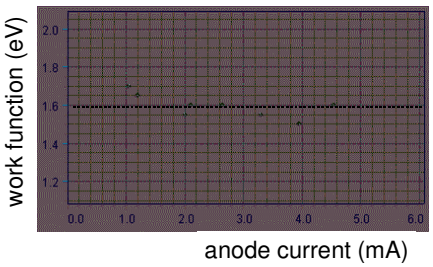

Fig. 12. Work function measured with various anode currents.

Tungsten cathode. The only vacuum tube with a tungsten cathode available to us is the diode from Leybold–Heraeus, catalog index 55507. The same bridge circuit was employed for the measurements, but with $R_1 = 1\ \Omega$ (25 W), $R_2 = 100\ \Omega$, and $R_3 = 200\ \Omega$. For tungsten cathodes, the quantity $2k_B(T - T_0)$ can be taken as 0.4 ± 0.05 eV. The determined value of the work function, 5.3±0.3 eV, is markedly above the expected one, 4.5 eV. Greenslade (1991) reported a similarly high value from Richardson's plot. He explained the increase in the work function by a surface contamination. In our case, it may be partly caused by the resistance of long current leads inside the tube and by the influence of the cold portions of the cathode adjacent to the leads. The length of these portions amounts to about 10% of the total length of the cathode. Thin cathodes should be used to reduce this effect. To check the above assumption, the measurements were carried out with a thin tungsten filament from a light bulb (12 V, 10 W). After removing the glass envelope, it was placed in a vacuum chamber providing pressure of about 10^{-4} Pa. An additional electrode mounted close to the filament served as the anode. The same bridge was used as in the measurements with the oxide-coated cathode. For this filament, the work function appeared to be close to the correct value.

Experiments on the thermionic emission are included in many laboratory manuals: Iveronova (1962, 1968); Portis (1964, 1972); Whittle and Yarwood (1973); Soloukhin (1975); Goldin (1983). Some of the experiments were described by the author (Kraftmakher 1959a, 1959b, 1961, 1998b).

9.7. Transistor

I–V characteristics of a bipolar junction transistor and of a junction field-effect transistor are displayed.

William Shockley (1910–1989)

John Bardeen (1908–1991)

Walter Houser Brattain (1902–1987)

"…The summit of Everest was reached by a small party of ardent climbers. Working from an advance base, they succeeded. More than a generation of mountaineers had toiled to establish that base. Your assault on the semiconductor problem was likewise launched from a high-altitude camp, contributed by many scientists. Yours, too, was a supreme effort—of foresight, ingenuity and perseverance, exercised individually and as a team. Surely, supreme joy befalls the man to whom those breathtaking vistas from the summit unfold."

> E. G. Rudberg, member of the Nobel Committee for Physics. Presentation of William Shockley, John Bardeen, and Walter Houser Brattain awarded the Nobel Prize "for their researches on semiconductors and their discovery of the transistor effect" (1956).

1. Bipolar junction transistor

The 8*50 Interface* serves as a source of necessary voltages, and *Capstone* displays characteristics of a bipolar junction transistor 2N2222A.

Additional equipment: *Voltage sensors,* transistor, resistors.

Bipolar junction transistors are three-layer devices, basically either *p-n-p* or *n-p-n* sandwiches (Fig. 1). Both types function in the same manner, although potentials and charges will have opposite polarities in the two cases. Several operating modes of a transistor may be considered (Beeforth and Goldsmid 1970; Li 1993; Balkanski and Wallis 2000). Suppose the base-emitter voltage V_{BE} applied to the base of an *n-p-n* transistor to be negative. The collector-base and base-emitter junctions will be reverse-biased, and only the usual diode leakage current will flow through them. The transistor is said to be "off". Biasing the base positive with respect to the emitter will turn the transistor "on". The emitter junction will be forward-biased, whereas the collector junction will still be reverse-biased. Usually, the emitter doping is made substantially heavier than the base doping, so that forward currents across the emitter-base junction are almost entirely due to carrier injection from emitter to base rather than from base to emitter. By having very narrow base widths, almost all the emitter-to-base current will arrive at the collector junction and cross into the collector. The base current I_B equals to the net recombination rate of excess minority carriers within the base. The ratio of the collector and base currents, I_C/I_B (the gain), is usually denoted by β.

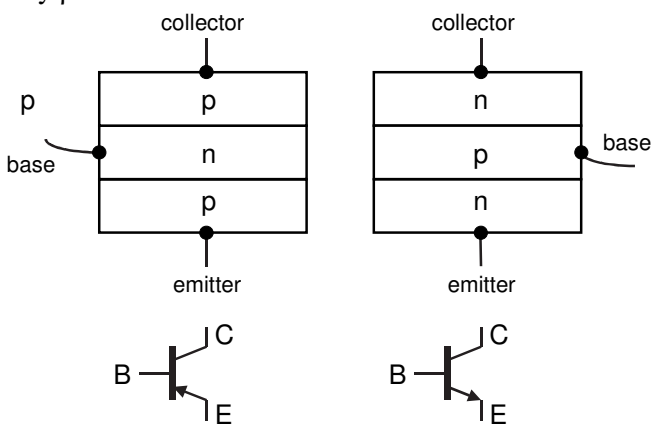

Fig. 1. Schematics of *p-n-p* and *n-p-n* transistors.

The input of the transistor may be considered either as a base-emitter voltage V_{BE} or as a base current I_B. With the data-acquisition system, it is easy to observe *I–V* characteristics of the transistor (Fig. 2).

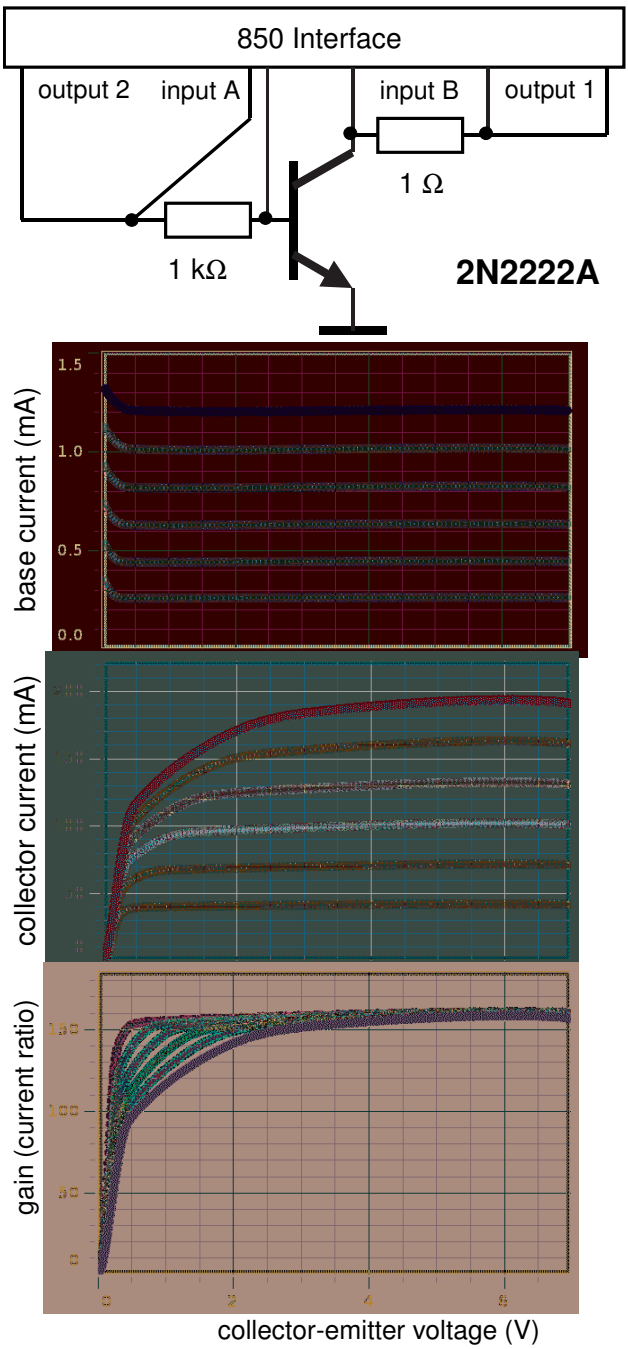

Fig. 2. Setup for the measurements and characteristics of the bipolar transistor 2N2222A for base-emitter voltages from 1 to 2 V.

The *Output 1* provides the collector-emitter voltage, while the base is connected to the *Output 2* through a 1 kΩ resistor. The base current is measured through the voltage drop across this resistor, and the collector current through the voltage across a 1 Ω resistor. Both currents are stored and displayed versus the collector-emitter voltage. The characteristics show the narrow range of the controlling voltage, the need for a bias, and the current gain.

With the same setup, the collector current is displayed, for a constant collector–emitter voltage (10 V) and various resistors in the base circuit (from 1 to 5 kΩ), versus the base-emitter voltage (Fig. 3).

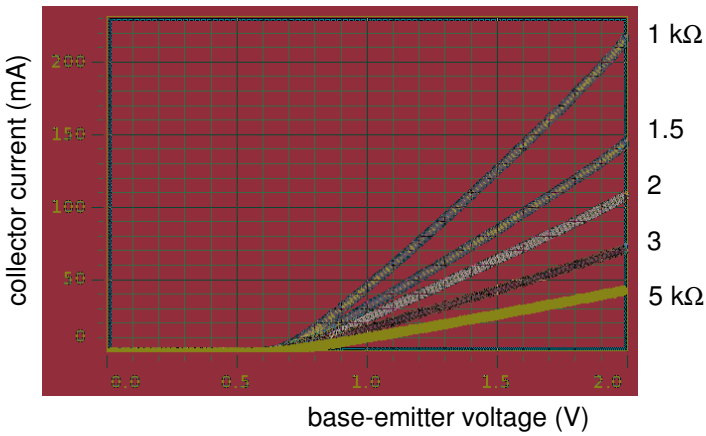

Fig. 3. Collector current versus base–emitter voltage, for various resistors in the base circuit.

Demonstration with DSO. Displaying the *I–V* characteristics of a simple electronic device, such as photodiode or a transistor, is a routine function of a common oscilloscope. Additional electronic circuits are used for observing families of characteristics depending on an extra parameter (Barnes 1974a; Ramachandran 1993). It is quite expectable that a DSO in conjunction with a computer equipped with appropriate software is also suitable for this purpose (de Buyl 2010). In some cases, however, a DSO can display families of *I–V* characteristics without involving a computer or additional software.

The DSO operates in the X–Y mode and is triggered by the line frequency. The key point in this approach is that the changes of the extra parameter are made while the voltage applied to the transistor is zero. Another possibility is to position the points of the maximum voltage out of the DSO display, so the changes of the parameter can be made at both minimum and maximum voltages. During one run, the DSO displays a family of *I–V* characteristics. The real *V* and *I* values are available from the sensitivities of the DSO channels, which are seen on the display. When necessary, the DSO is capable of inverting input voltages.

Two families of characteristics of the bipolar junction transistor 2N2222A are obtained in turn (Fig. 4). First, the emitter current is determined through the

voltage drop across a 20 Ω resistor and displayed versus the voltage between the collector and emitter (Y versus X1). The voltage drop across this resistor is small in comparison with that between the emitter and collector. Also, the difference between the emitter and collector currents can be neglected. The extra parameter is a DC voltage from a regulated supply connected to the base of the transistor through a resistor R = 1 kΩ. This voltage is varied from 1 to 4 V.

Second, the emitter current is displayed versus a DC voltage applied to the base (Y versus X2), for several values of resistance R, from 1 to 100 kΩ. Such a regime is used for the amplification of small signals. The collector voltage is 10 V. The graphs obtained show linear dependence of the current on the base voltage, but a definite bias should be set up for operating in the linear regime. The slope of the linear part decreases with increasing the resistance R.

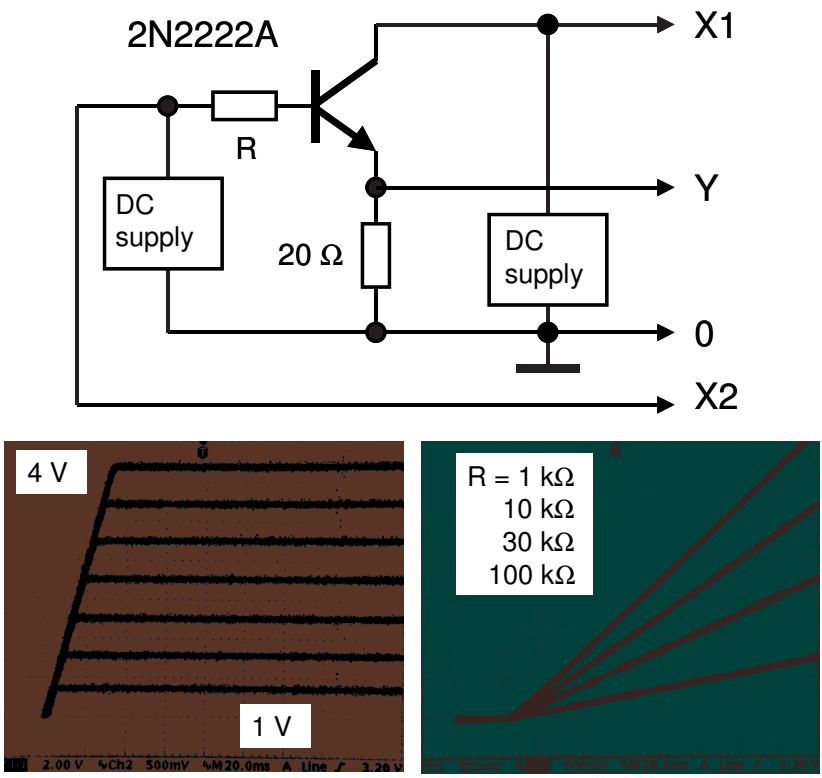

Fig. 4. Schematic of the setup and characteristics of the transistor. Left: emitter current versus collector voltage (Y versus X1), for base voltages from 1 to 4 V and R = 1 kΩ. Right: emitter current versus base voltage (Y versus X2), for various R and a constant collector voltage (10 V).

2. Junction field-effect transistor

Capstone displays characteristics of a junction field-effect transistor.

Additional equipment: *Voltage sensor,* transistor, resistor.

The **junction field-effect transistor** (JFET) is a three-terminal device consisting of a source, a gate, and a drain electrode (Fig. 5). The current flow through a channel between the source and drain electrodes is controlled by a voltage applied to the gate. The channel is formed between the gate and the substrate. If the current flow is due to electrons, we have an *n*-channel. The main feature of a JFET is that a reverse-bias gate voltage controls the width of the depletion layer in the *p*-gate and *n*-channel space-charge region and thus its conductance.

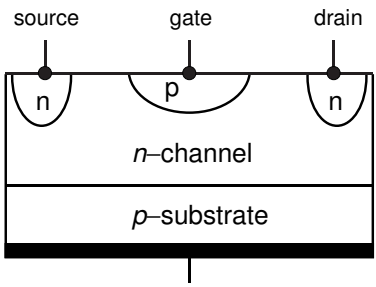

Fig. 5. Schematic of *n*-channel junction field-effect transistor.

In the experiment, the *Output 1* provides a voltage applied between the source and the drain of a JFET (Fig. 6). The voltage is stored as the *Output voltage*.

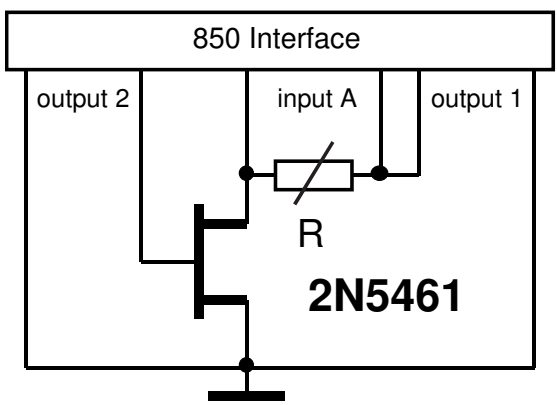

Fig. 6. Schematic of the setup.

The *Output 2* provides a voltage applied to the gate. The current is measured through the voltage across a 100 Ω resistor. For various gate-source voltages, the drain current is plotted versus the drain-source voltage (Fig. 7).

Characteristics of the transistor can be observed with a DSO.

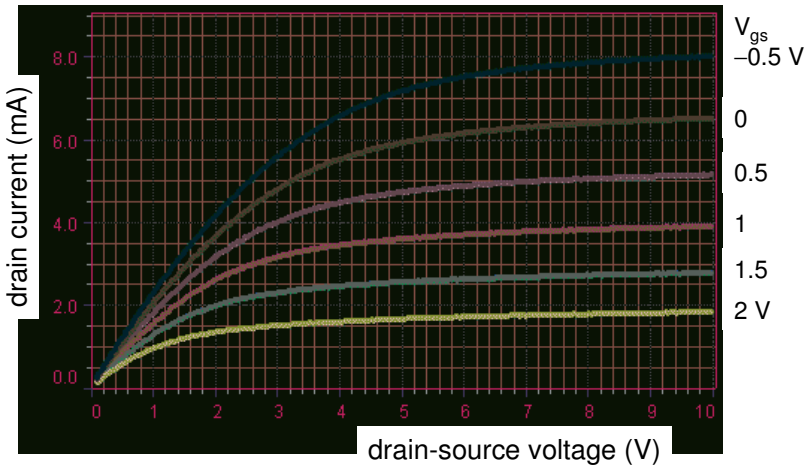

Fig. 7. Characteristics of the field-effect transistor 2N5461.

3. Transistor amplifier

A simple circuit with an oscilloscope demonstrates the operation of a transistor amplifier.

Additional equipment: *Voltage sensor***,** transistor, oscilloscope, decade resistor box.

The load of the transistor 2N5461 is a decade resistor box R (Fig. 8). An AC voltage from a function generator is applied between the source and gate of the transistor and monitored with an oscilloscope. The second input of the oscilloscope shows the voltage across the load, and it is easy to see the relation between the input and output voltages for different load resistors.

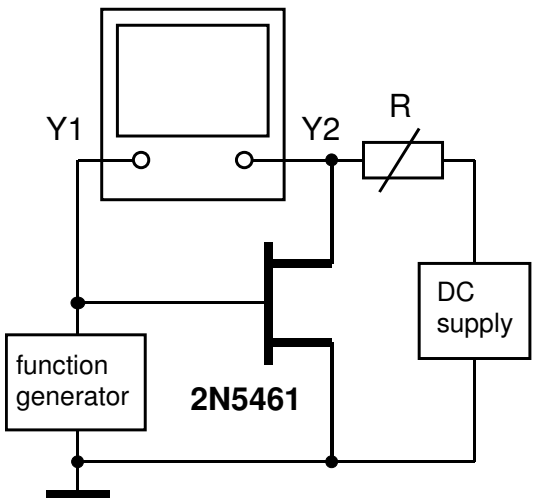

Fig. 8. Schematic of single-stage amplifier with a field-effect transistor.

9.8. Quantum electronics

Experiments with a laser diode include four items: (i) the radiant output power and efficiency; (ii) the polarization of the light beam; (iii) the *h*/*e* ratio; and (iv) the modulation characteristics (Kraftmakher 2011c).

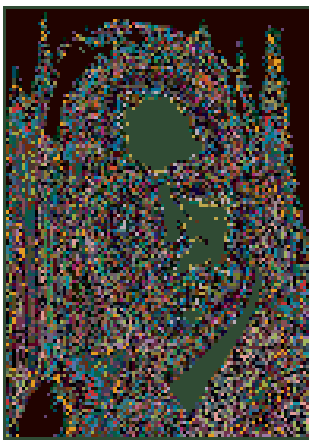

Charles H. Townes (b. 1915)

Nikolai G. Basov (1922–2001)

Alexandr M. Prokhorov (1916–2002)

"…By your ingenious studies of fundamental aspects of the interaction between matter and radiation you have made the atom works for us in a new and most remarkable way. These magic devices called maser and laser have opened up vast new fields for research and applications, which are being exploited with increasing intensity in many laboratories all over the world."

> Professor B. Edlén, member of the Nobel Committee for Physics. Presentation of Charles H. Townes, Nilolai G. Basov, and Alexandr M. Prokhorov awarded the Nobel Prize "for fundamental work in the field of quantum electronics, which has led to the construction of oscillators and amplifiers based on the maser–laser principle" (1964).

The contributions by the Nobel Laureates can be understood by reading their Nobel lectures: "Production of coherent radiation by atoms and molecules" (Charles H. Townes), "Semiconductor lasers" (N. G. Basov), and "Quantum electronics" (A. M. Prokhorov). Experiments presented here relate to only one of these topics, the laser diode.

Additional equipment: *Voltage sensor*, *Light sensor*, *Aperture bracket*; *Rotary motion sensor*, *Linear translator*, laser diode, silicon photodiodes, oscilloscope, function generator, polarizer, DC supply.

***Laser diode for beginners*.** The laser (light amplification by stimulated emission of radiation) is one of outstanding achievements in physics of 20th century (Jenkins and White 1983; Hecht 1994; Jackson *et al* 2001; Henningsen 2011). The first **laser** appeared in 1960, after all the principles of such a device were already realized in similar **microwave devices** (**masers**). The basic principles of lasers are the following.

• **Population inversion** is needed for continuously emitting photons: the number of particles n_2 in an excited state of energy E_2 should exceed the number of particles n_1 in a lower-energy state of energy E_1. Under thermal equilibrium,

$$n_2/n_1 = \exp(-\Delta E/k_B T), \tag{1}$$

where $\Delta E = E_2 - E_1$, T is the absolute temperature, and k_B is Boltzmann's constant. Thus, the population inversion, where $n_2 > n_1$, is a **nonequilibrium** state. The process of supplying the energy required for **inverting** the population is called **pumping**; the necessary energy is supplied as an electric current or as light at a different wavelength.

• **Stimulated emission.** Electromagnetic emission can be **spontaneous** or **stimulated**. The presence of photons of energy ΔE can stimulate the transition from the upper energy level to the lower level. Photons generated by stimulated emission are strictly similar to primary photons in direction, wavelength, phase, and polarization. Albert Einstein introduced the concept of stimulated emission in 1917, long before the masers and lasers were developed. Together with the optical feedback, this gives the laser output light its characteristic **coherence** and **directionality**, as well as uniform **polarization** and **monochromaticity**. To maintain constant populations n_2 and n_1, the rate of pumping must balance the spontaneous and stimulated emission. The stimulated emission triggered by light passing through the laser medium can overcome the losses, so the light will be amplified.

• **Optical feedback** with an **optical cavity**, together with the stimulated emission, forms a highly directed light beam. Two mirrors confining the laser medium produce in it standing wave patterns called modes. Light bounces back and forth between the mirrors, each time passing through the medium. One of the two mirrors is partially transparent, and the output beam is emitted through it. The laser medium amplifies any passing photons, but only photons in a mode supported by the optical cavity will pass more than once through the medium and receive substantial amplification. If the gain in the laser medium is larger than the losses, then the power of the light inside the cavity can rise exponentially. However, each stimulated emission event returns an atom from its excited state to the ground state, thus reducing the gain of the medium. The minimum pump power needed to begin the laser action is called the **lasing threshold**; the term originates from "laser."

Gas lasers, as well as semiconductor ones, are invaluable tools in student laboratories (Benumof 1965; Abella *et al* 1966; Lengyel 1966; Yu and Wang 1973; Camparo and Klimcak 1983; Boruah 2009).

The most common type of **laser diode** is formed from a ***p-n* junction** (Jones 1987; Ogasawara 1994; Streetman and Banerjee 2000; Sze and Ng 2007). The crystal is doped to produce an *n*-type region and a *p*-type region, one above the other. Forward electrical bias across the diode causes the holes and electrons to be injected from opposite sides of the junction into the active region. The **recombination** of electrons and holes results in **emission of photons**. The emission wavelength is basically determined by the bandgap energy of the active-region material. The bandgap energy of ternary and quaternary semiconductor compounds can be adjusted in a certain range by varying their composition. The devices are sometimes referred to as **injection laser diodes** to distinguish them from optically pumped laser diodes. A photon of energy equal to the recombination energy can cause stimulated emission. This process generates another photon of the same frequency, traveling in the same direction, with the same polarization and phase as the first photon. The **optical gain** in the injection region increases with the number of electrons and holes injected into the active region. The optical bandwidth of output light amounts to a few nanometers.

Laser diodes differ from other lasers in several important respects (Sze and Ng 2007): (i) the transitions are associated with the band properties of semiconductors; (ii) because the active region is very narrow, the divergence of the laser beam is larger; (iii) the spatial and spectral characteristics are strongly influenced by the variations of the bandgap energy and refractive index; (iv) the laser action is triggered simply by passing a forward current, so a high efficiency and modulation at high frequencies are achievable.

The first laser diodes were **homojunction** diodes, where the material of the core layer and that of the surrounding clad layers were identical. Then **heterostructures** employing layers of varying bandgap and refractive index were recognized as advantageous. Contemporary laser diodes, first demonstrated in 1970, are more complicated double heterostructure diodes.

A laser diode from a laser pen (laser pointer) is used in the experiments. Its emission wavelength appeared to be 660 nm. The batteries operating the laser pen were removed, and two wires were used to connect the device to an external DC supply. One of the wires (minus) is fixed inside the pen. The second connection (plus) is on the metal case of the pen (Fig. 1). The laser switch is fixed in the "on" position. Usually, a laser diode includes an electronic driver preventing the device from damage. In the driver, a photodiode sensing the output light governs a transistor put in series with the laser diode. Such a driver is not included in an inexpensive laser pen. Instead, a limiting resistor is positioned inside the case and connected in series with the laser diode; in the laser pen used, the limiting resistance is 67 Ω.

The input electric current and power, radiant output power, and efficiency of the laser can be measured or calculated and displayed as functions of the

voltage applied to the device or of the current through it. The *Signal generator* feeds the laser diode. The *Positive ramp up* voltage linearly increases from zero to a maximum value set to be safe for the laser. The period of the *Output voltage* is 20 s, and the *Sample rate* is 100 Hz. The input current is taken as the *Output current* of the *Signal generator*, and the voltage applied to the laser diode as the *Output voltage* minus the *Output current* times the limiting resistance. The *Signal generator* operates in *the Auto* mode. The option *Automatic stop* is used for automatically ending each run.

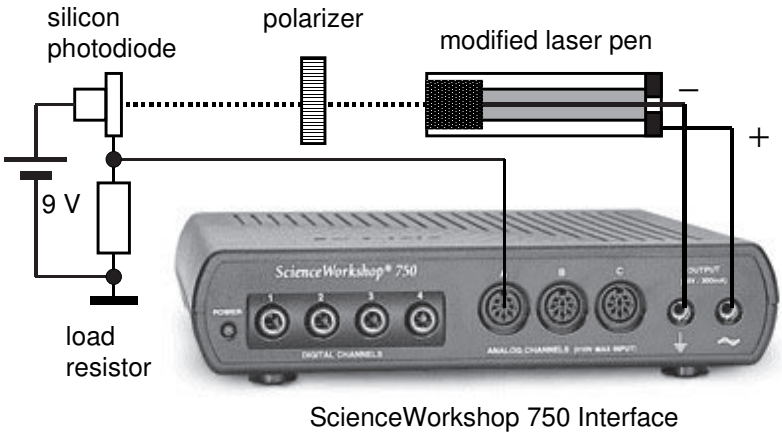

Fig. 1. Setup with modified laser pen, polarizer, and silicon photodiode.

Radiant power and efficiency. This experiment is similar to that described by Ojeda *et al* (1997). For determining the radiant output power, the laser beam is directed onto a silicon photodiode (United Detector Technology, PIN-10D) operated with a 9 V battery. The *Voltage sensor* acquires the voltage across a 1 kΩ load of the photodiode. The radiant power P of the laser diode is calculated from the photoelectric current and the spectral response of the photodiode, $R(\lambda)$, the ratio of the photodiode current I to the incident light power P. In the range 400–800 nm, the spectral response of the photodiode can be approximated as

$$R(\lambda) = I/P\ (\mathrm{A.W^{-1}}) = 1.2\times10^{-3}(\lambda - 300), \qquad (2)$$

where λ is the wavelength in nanometers. With minor variations, this relation holds for all silicon photodiodes. For $\lambda = 660$ nm, the I/P ratio is 0.43 $\mathrm{A.W^{-1}}$. With this value, *DataStudio* calculates the radiant output power and efficiency of the laser diode. This approach is not as precise as the use of a proper sensor, but is much simpler and quite sufficient for our aim.

During a run, the *Output voltage* of the *Signal generator* increases linearly from zero to 3.5 V, while the voltage applied to the laser diode to nearly 2.3 V. The data are displayed versus the applied voltage (Fig. 2). Two threshold points are seen on the plots: rise of the input current and power near 1.8 V, and rise of the output radiant power and efficiency near 2.1 V. The first point shows the

threshold of spontaneous emission, and the second the lasing threshold. For the maximum applied voltage, the radiant output power amounts to 2 mW.

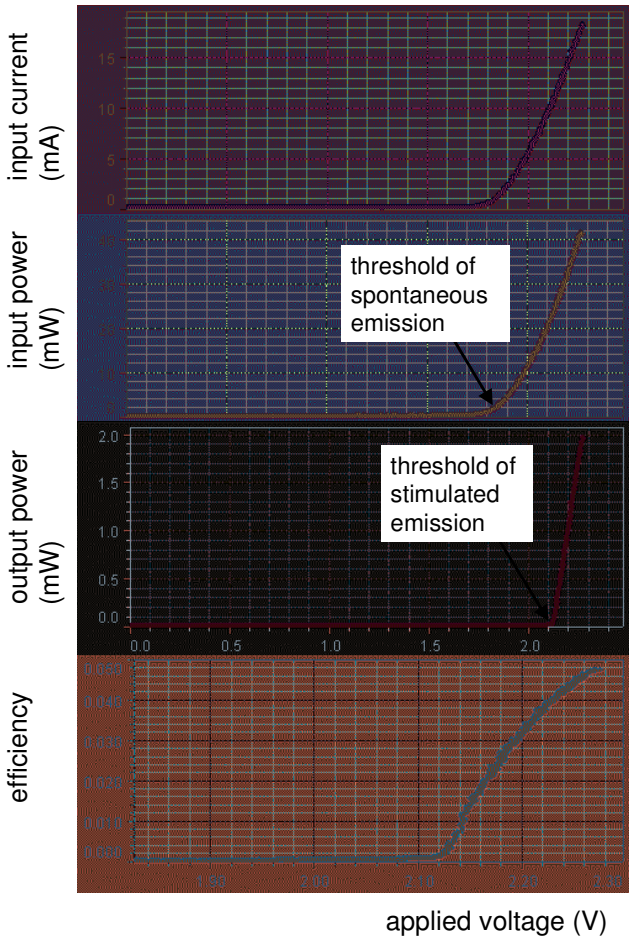

Fig. 2. Characteristics of the laser diode versus applied voltage.

The laser efficiency increases with the applied voltage and reaches nearly 0.05, but further increase of the voltage may destroy the laser. The measurement data are well reproducible. This experiment can be used as a laboratory work and as a classroom demonstration of two thresholds in the laser action and of the efficiency of a laser diode.

Spontaneous emission and h/e ratio. Spontaneous emission from a laser diode arises when the applied voltage reaches a definite value V_F, the forward "turn-on" voltage. The energy of photons emitted is close to eV_F. Therefore, $h/e \cong \lambda V_F/c$, where h is Planck's constant, e is the electron charge, c is the speed

of light, and λ is the emission wavelength. Since the values of V_F and λ are easy to measure, this possibility of determining the *h*/*e* ratio is very attractive. Many such measurements were done with light-emitting diodes (LEDs). Precise values of the *h*/*e* ratio could not be expected from such measurements, but it is worth looking for an LED (or a laser diode) providing a more or less correct result.

In our measurements, the "turn-on" voltage is determined from the rapid rise of the input current and of the radiant output power; the spontaneous emission starts at 1.85±0.05 V (Fig. 3). From these data, the *h*/*e* ratio is $(4.07\pm0.1)\times10^{-15}$ J.s.C^{-1}, close to the correct value. The students can calculate the *h*/*e* ratio in the course of demonstrating the "turn-on" voltage.

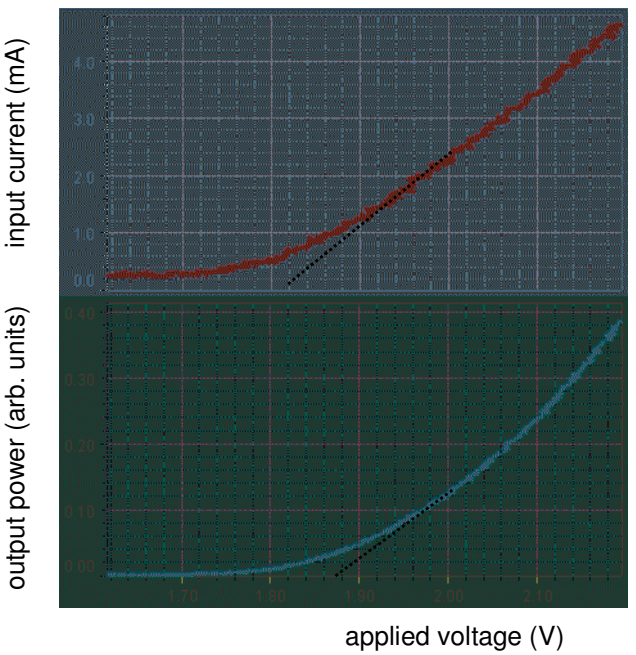

Fig. 3. Input current and radiant output power close to the threshold of spontaneous emission.

Lasing threshold. Within the cavity, the optical gain *g* due to stimulated emission is compensated by optical loss α due to absorption. The net gain as a function of the distance *z* is given by (Sze and Ng 2007)

$$\exp[(g - \alpha)z]. \tag{3}$$

Taking into account the reflections R_1 and R_2 of the two mirrors confining the cavity, the total optical gain will be positive when

$$R_1R_2 \exp[(g - \alpha)2L] > 1, \tag{4}$$

where *L* the length of the laser cavity. The threshold gain for lasing thus equals

$$g_{th} = \alpha + (1/2L)\ln(1/R_1R_2). \quad (5)$$

Therefore, the lasing threshold depends on the laser design. The injected electron concentration is proportional to the input current, so the optical gain linearly depends on the current. Two methods are used here for determining the lasing threshold: (i) the output radiant power and efficiency rapidly increase above the threshold, and (ii) for the stimulated emission, the emission line becomes much narrower (Fig. 4).

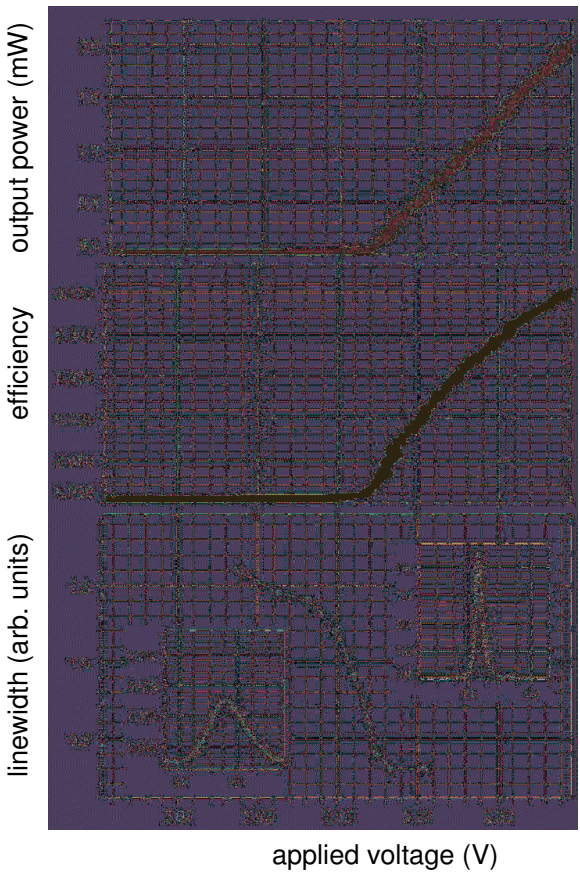

Fig. 4. Characteristics close to the lasing threshold: the output power, efficiency, and emission line width. In the inserts, the horizontal scale is nearly the same, while the vertical scales differ by a factor of 100.

Polarization of output light. The polarization is measured with a usual polarizer placed in front of the laser diode. One run is performed with the polarizer set for a maximum signal from the photodiode, I_{max}, and the second for a minimum, I_{min}. The ratio $(I_{max}–I_{min})/(I_{max}+I_{min})$ is a measure of the polarization; from the data obtained (Fig. 5), it equals nearly 100.

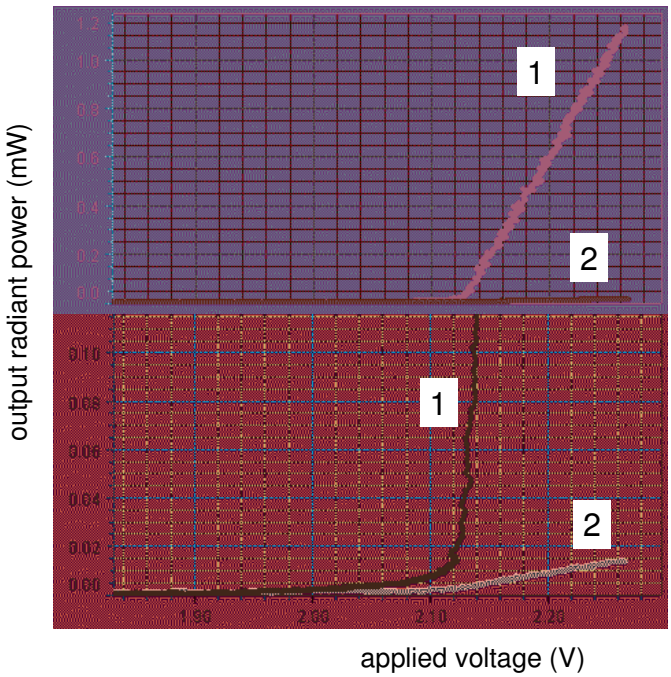

Fig. 5. Output power versus applied voltage with polarizer set for (1) maximum and (2) minimum transmission. Note the difference in the vertical scales.

Modulation characteristics. Laser diodes are easily modulated sources and find wide use in **optical communications** (Kogelnik 1995). **Optical fibers** are commonly used with infrared light due to less attenuation and dispersion. The signal encoding is typically simple intensity modulation. Free space optics systems can function over distances of several kilometers when there is a clear line of sight between the transmitter and receiver. A broad frequency band is necessary for simultaneously transmitting many programs, and a linear amplitude characteristic is also important.

When a current step above the threshold value is applied to a laser diode, a delay of a few nanoseconds occurs before the stimulated emission begins. When the input current, above the lasing threshold, is modulated with a small AC signal, the output power follows the modulation waveform but only to a certain frequency limit. For laser diodes intended for optical communications, this limit lies in the gigahertz range. The frequency limit depends on the average photon lifetime in the cavity before the photons are lost by absorption or emission through the two mirrors. High doping levels are needed for increasing the frequency limit. Laser diodes were already employed in student experiments on optical communications (Kraftmakher 2003, 2008d; Lee *et al* 2006).

The modulation characteristics of the laser diode are determined with a Hewlett–Packard 33120A function generator. A DC supply and the function

generator, each with a 100 Ω resistor added at the output, are connected to the laser in parallel. The output voltage of the DC supply is adjusted to obtain a sufficient radiant output from the laser. The AC output voltage of the function generator is set several times smaller than this DC voltage. The laser beam is directed onto a fast photodiode (United Detector Technology, PIN-5D) operated with a 9 V battery. The signal across a 100 Ω load of this photodiode is observed with a Kenwood CS-4025 oscilloscope. The same oscilloscope serves for monitoring the voltage applied to the laser diode. The frequency response is determined in the 10–10^7 Hz range (Fig. 6). The amplitude characteristic measured at 100 kHz is fairly linear. Since the laser diode has inherent capacity, the real voltage across the *p-n* junction becomes frequency dependent at high frequencies. The frequency response presented here relates to the AC voltage at the output of the function generator.

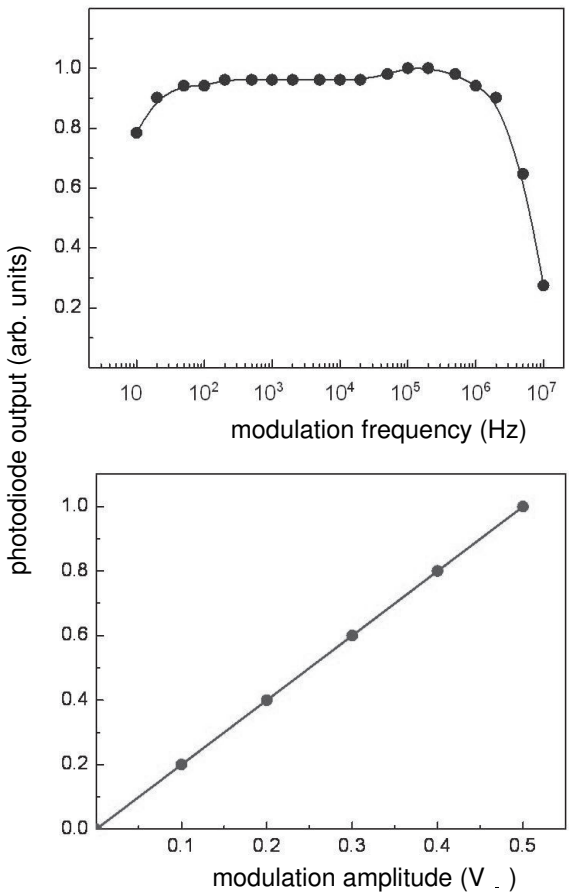

Fig. 6. Modulation characteristics of the laser diode.

9.9. High-temperature superconductivity

The experiments include (i) the zero resistivity; (ii) the *V–I* characteristic and critical current; (iii) the transition to the superconducting state; and (iv) the diamagnetism of superconductors.

J. Georg Bednorz

K. Alexander Müller

"…This discovery is quite recent—less than two years old—but it has already stimulated research and development throughout the world to an unprecedented extent. The discovery made by this year's laureates concerns the transport of electricity without any resistance whatsoever and also the expulsion of magnetic flux from superconductors."

> Gösta Ekspong, the Royal Academy of Sciences. Presentation of J. Georg Bednorz and K. Alexander Müller awarded the Nobel Prize "for their important breakthrough in the discovery of superconductivity in ceramic materials" (1987).

High-temperature superconductors provide an excellent opportunity for including superconductivity in student laboratory courses. This seems not to have been fully exploited until now, although many classroom demonstrations and laboratory experiments on superconductivity have been reported. First such student experiments were described even before the discovery of high-temperature superconductors. In most of the demonstrations, the interaction between a permanent magnet and a superconducting sample was shown (Early *et*

al 1988; Reich 1988; Oseguera *et al* 1989; Ouseph 1989; Valenzuela *et al* 1999). The temperature dependence of the resistivity of superconductors was also measured (Smith and Tinkham 1980; Kirkup 1988; Brown *et al* 1989; Pechan and Horvath 1990; Vandervoort *et al* 1995; León-Rossano 1997). Critical currents (Oldenburg *et al* 1993) and the diamagnetic screening (Lukefahr *et al* 1997) were demonstrated. In other experiments, superconductivity was observed through changes in the resonance frequency of an LC circuit with a sample inside the inductor (Fox *et al* 1988), by measurements of the persistent currents (Rowland 1975; Liu *et al* 1990; Tiernan 1997), and of the AC magnetic susceptibility (Behroozi and King 1976; Behroozi 1983; Nicolo 1995; Nanda 1998). Ewert (1987) demonstrated the phase transition of a tantalum sample calorimetrically. Gabrys *et al* (1992) reported on a high-speed demonstration motor with superconducting bearings. Hegman *et al* (1998) considered a superconducting pendulum as a thermodynamic machine. Badía-Majós (2006) considered conditions of stable levitation of superconductors in a nonuniform magnetic field. Iqbal *et al* (2009) demonstrate the persistence of field/current with time in a superconductor.

The main techniques for contactless detection of superconductivity are the following: (i) samples in DC magnetic fields (susceptibility, magnetization, field shielding, and forces in nonuniform magnetic fields); (ii) samples in AC magnetic fields (magnetic susceptibility, field shielding, and torque caused by rotating field); and (iii) persistent currents and remanent magnetization of a sample.

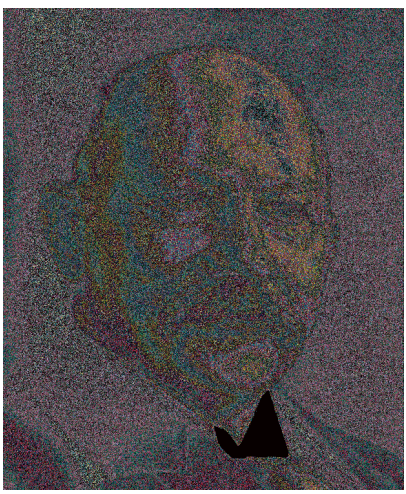

"…Thus the mercury at 4.2 K has entered a new state, which, owing to its particular electric properties, can be called the state of superconductivity."

H. Kammerlingh-Onnes, Nobel lecture.

Heike Kammerlingh-Onnes (1853–1926)

The discovery of superconductivity became possible after liquefying helium, the last "true" gas at low temperatures. For this achievement, Heike Kammerlingh-Onnes was awarded the Nobel Prize (1913). In his Nobel lecture, the laureate drew also attention to a recently discovered (1911) phenomenon consisting of abruptly dropping the resistivity of mercury to zero at 4.1 K. The decrease of

the resistivity of metals with decreasing temperature was well known, and Kammerlingh-Onnes planned to confirm this behavior at very low temperatures. Unexpectedly, he observed a sharp transition to a state with exactly zero resistivity (Fig. 1).

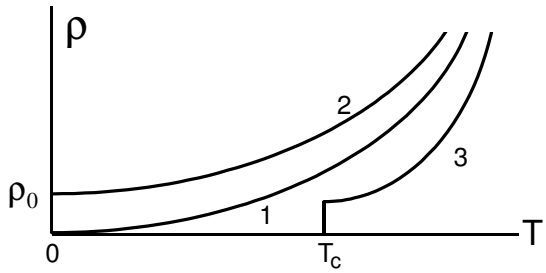

Fig. 1. Resistivity at low temperatures. 1–ideal metal; 2–metal with impurities and structure defects manifests residual resistivity ρ_0; 3–resistivity of a superconductor vanishes at T_C.

Meissner's effect. In 1933, Meissner and Ochsenfeld discovered the second fundamental feature of superconductors: they appeared to be **ideal diamagnets** because persistent currents in a sample are sufficient to entirely compensate for any external magnetic field inside the sample. This means that the magnetic field inside a superconductor always equals zero. However, there exists the so-called **critical external field** B_c, which destroys superconductivity; this field depends on temperature. The next important point is the existence of superconductors of type I and of type II, manifesting very different magnetic properties (Fig. 2).

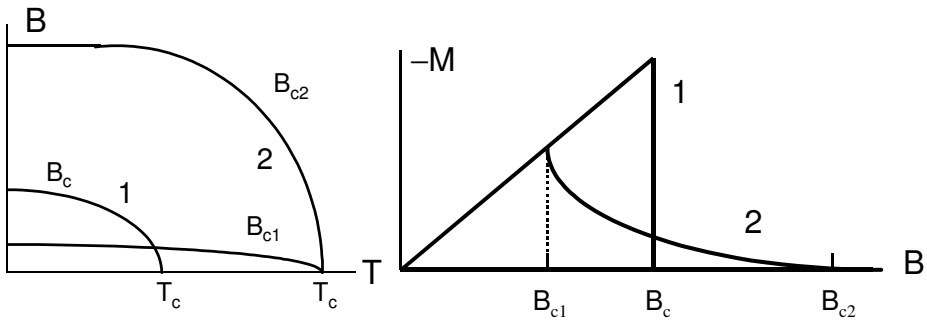

Fig. 2. Left: phase diagram of superconductors of type I (1) and type II (2). Right: magnetization of superconductors in external magnetic field. Superconductors of type II have two critical fields, B_{c1} and B_{c2}.

In 1957, Bardeen, Cooper, and Schrieffer (BCS) developed a theory of superconductivity, the BCS theory (Nobel Prize, 1972). The phenomenon has great potential for applications (Gabovich and Kuznetsov 2013) in various fields (transformers, power transmission cables, electrical generators and motors,

magnetically levitated transport). It is not surprising that great efforts were applied to synthesize superconductors having higher critical temperatures. During many years, the critical temperature was enhanced up to about 23 K. At that time, the majority of the scientific community believed that high-temperature superconductivity is impossible. Therefore, the ***Bednorz–Müller's amazing discovery*** (1986) of a new class of superconductors possessing high critical temperatures was immediately recognized as one of the most important discoveries of the century. Many physicists, even those who never dealt with superconductivity, began to intensively work in this field. In a short time after the discovery, new superconductors of the same type (oxide cuprates) were found, and now the highest critical temperature under normal pressure is about 134 K. Even higher critical temperatures were achieved under high pressures (Fig. 3). It is worth mentioning that the boiling point of nitrogen (77.4 K at normal pressure) is a crucial temperature point, above which a superconductor can be called a high-temperature superconductor from a practical point of view. This is due to the low cost and other advantages of using liquid nitrogen compared to liquid helium or other coolants providing lower temperatures.

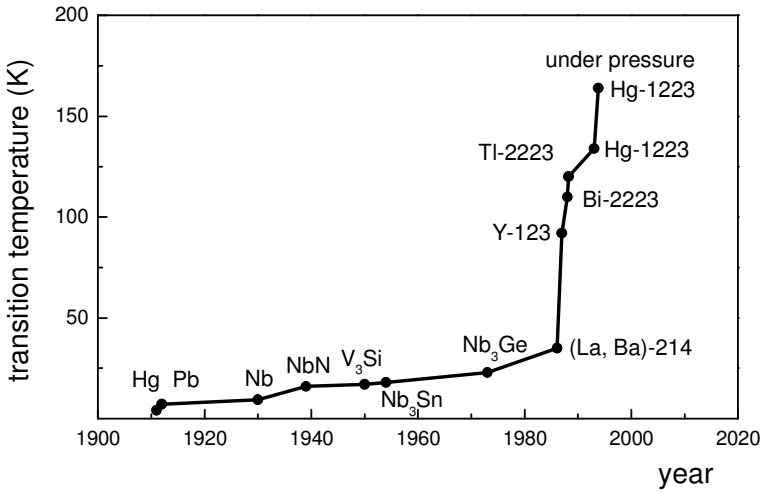

Fig. 3. Diagram clearly showing the importance of Bednorz–Müller's discovery.

Nowadays, superconducting tapes containing filaments embedded in a metal matrix became available. Such tapes allow one to prepare stable superconducting samples. An YBCO tape ($YBa_2Cu_2O_3$) and an Ag-sheathed multifilamentary $Bi_{2-x}Pb_xSr_2Ca_2Cu_3O_{10}$ (BSCCO-2223/Ag) tape were purchased from the American Superconductor Corporation. The transition temperature is nearly 92 K for YBCO compound, and nearly 110 K for BSCCO.

1. Resistance versus temperature

Capstone displays the resistance of superconductor tapes versus temperature.

Additional equipment: two *Voltage sensors*, YBCO and BSCCO-2223/Ag tapes, Dewar flask, DC supply, platinum resistance thermometer.

Pieces of a BSCCO-2223/Ag and an YBCO tapes equipped with potential probes are sandwiched, together with a small platinum thermometer (100 Ω at 0°C), between two aluminum plates. A 3 A DC current passes through the sample (Fig. 4). The resistance of the thermometer is measured by passing through the thermometer a DC current taken from the *Output 1*. The *Output voltage* is set 10 V, and a resistor put in series with the thermometer is adjusted to provide a 1 mA current. With this current, *Capstone* calculates the temperature as

$$T = 30.9 + 2254V_B + 1680V_B^2, \quad (1)$$

where V_B is the voltage drop across the thermometer in volts.

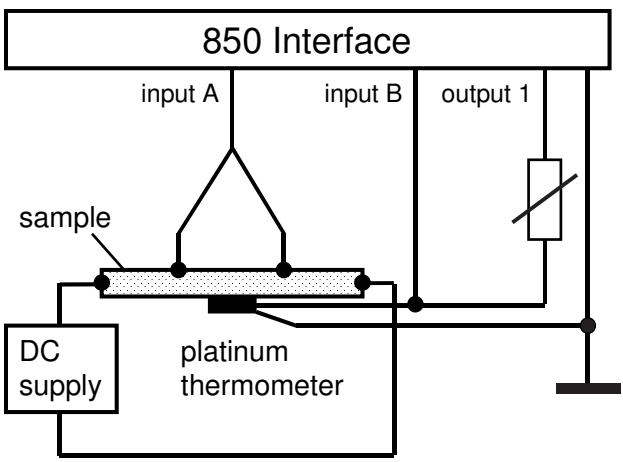

Fig. 4. Schematic of the setup.

After cooling in liquid nitrogen, the sandwich is raised above the liquid and starts to warm up with a rate of about 4 K.min^{-1}. The voltage between the potential probes and the resistance of the platinum thermometer are measured during the warming process. *Capstone* performs the necessary calculations and displays the resistance of the sample versus temperature (Fig. 5). The transition points are close to the claimed values, 92 K (YBCO) and 110 K (BSCCO).

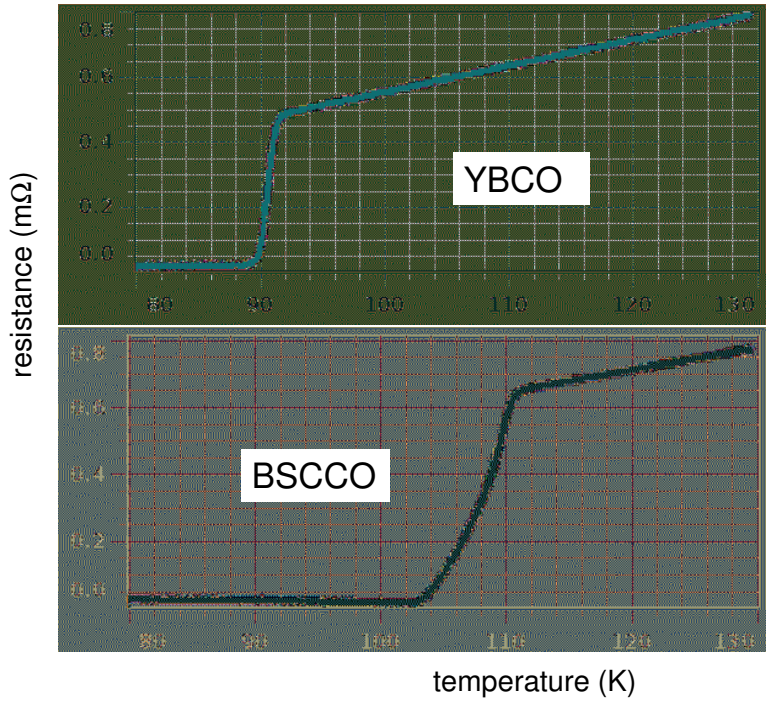

Fig. 5. Measurement data for the YBCO and BSCCO tapes.

2. *V–I* characteristic and critical current

The *V–I* characteristics of superconductors are determined with a contactless technique (Kraftmakher 2004e).

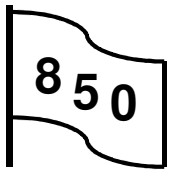

Additional equipment: two *Voltage sensors*, YBCO and BSCCO-2223/Ag tapes, demountable O-shaped magnetic core, coil, clamp-on ammeter.

A superconducting ring was prepared by soldering two ends of a piece of a BSCCO-2223/Ag (or YBCO) tape, 35 cm long. The soldering introduces contact resistance of the order of 10^{-6} Ω. It is easy to determine and take into account this resistance. The use of a short-circuited sample provides very important advantages because currents of the order of 10^2 A are obtainable with a low power AC source. The well-known transformer method (González-Jorge *et al* 2004) is used for obtaining the *V–I* curve of the ring. This technique is sufficiently simple to be reproduced in any student laboratory (Fig. 6).

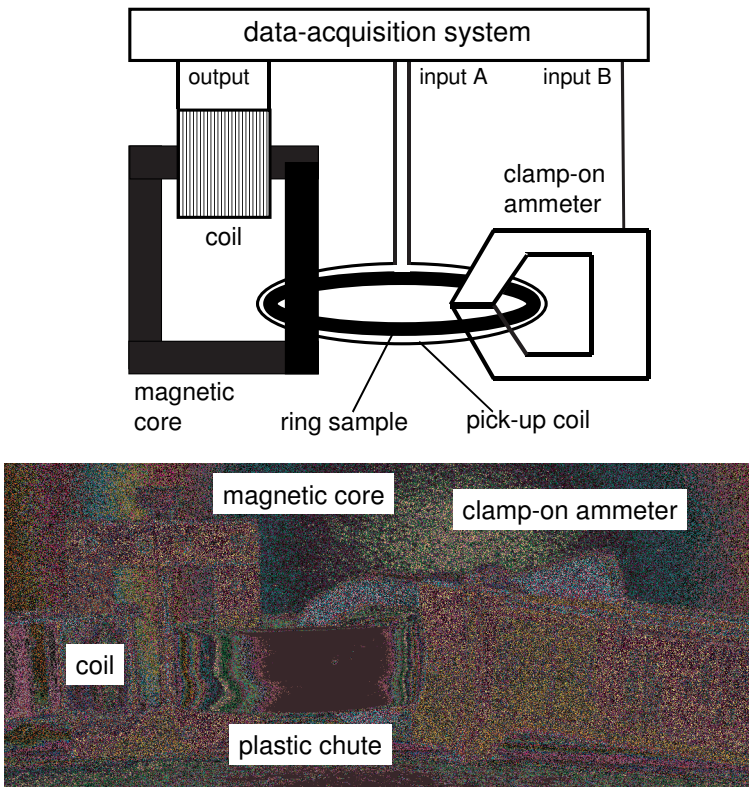

Fig. 6. Setup for the measurements. Transformer generates EMF in the superconducting ring, and clamp-on ammeter measures the current.

The ring sample is placed in a plastic chute embracing the magnetic core of a demountable transformer and filled with liquid nitrogen. The chute retains liquid nitrogen for a short time, but quite sufficient for the measurements. The time of collecting the data is restricted by one period of the AC voltage generated in the ring. The sample rate is set to obtain several hundred experimental points during one period of the voltage. When the frequency of the current is sufficiently low, the *V–I* characteristic is very similar to that obtainable by usual contact measurements.

An 800-turn coil (SF-8611) fed by the *Output 1* constitutes the primary winding of an O-shaped demountable iron-core transformer (SF-8614). The ring sample forms the short-circuited secondary winding. A pick-up coil wrapped around the ring serves for measuring the voltage generated in the ring. When the same AC magnetic flux penetrates areas within the ring and the pick-up coil, the voltage generated in the coil strictly relates to that in the ring, according to the number of turns in the coil. Only a minor magnetic flux through an unavoidable small gap between the ring and the pick-up coil makes a contribution that is difficult to take into account. In our case, the pick-up coil contains ten turns and provides a voltage ten times larger than that generated in the ring. This voltage proceeds to the input of the data-acquisition system. A clamp-on ammeter measures the current flowing in the ring and provides data for the second input of the data-acquisition system. The sensitivity of our meter is 1 $mV.A^{-1}$.

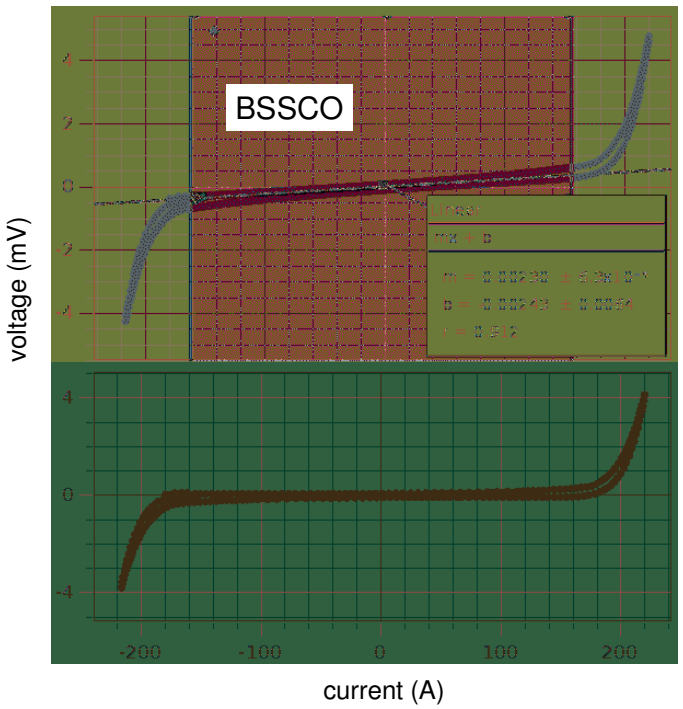

Fig. 7. *V–I* characteristic of the BSCCO sample, raw and corrected data.

The *V–I* characteristic (Fig. 7) was obtained with a 1 Hz current in the primary winding. The characteristic clearly shows a sharp increase in the voltage necessary to be generated in the ring when the current exceeds a definite critical value. According to a widely accepted criterion, the critical current obtained when the electric field in a sample amounts to 1 $\mu V.cm^{-1}$. A small constant slope of the *V–I* characteristic at currents lower than the critical current is due to the resistance of the joint point. This resistance is taken into account by separating and fitting the linear part of the characteristic. The critical current is nearly 150 A for the BSCCO sample and nearly 100 A for the YBCO sample (Fig. 8).

In the vicinity of the critical value, the characteristic follows a power-law dependence, $V = AI^n$ (Carr 2001). The better the homogeneity of the sample, the larger the power index *n*, and the sharper the *V–I* dependence.

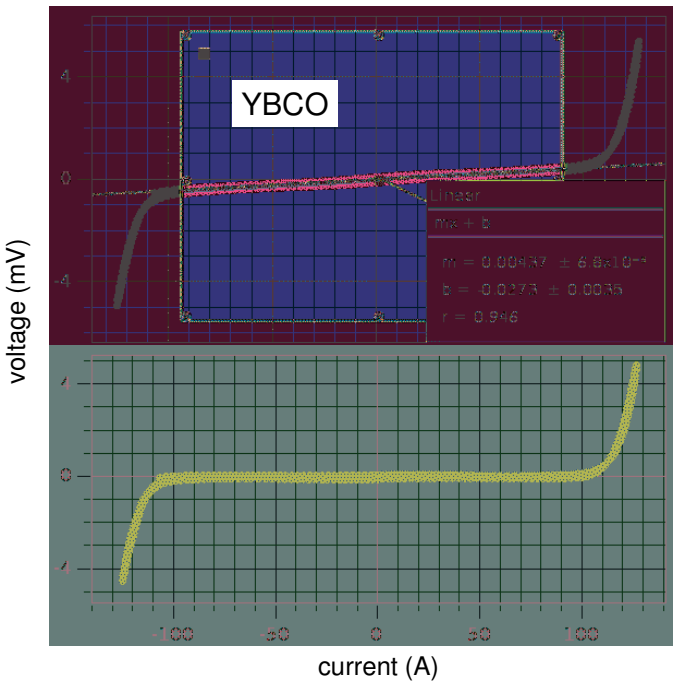

Fig. 8. *V–I* characteristic of the YBCO sample, raw and corrected data.

The *V–I* characteristic of a superconducting ring can also be demonstrated with a DSO (Kraftmakher 2012f).

3. Transition curves

The superconducting-to-normal state transition is demonstrated by measuring the magnetic susceptibility of a sample.

Additional equipment: two *Voltage sensors*, BSCCO-2223/Ag tape, Dewar flask, oscilloscope, multimeter, platinum resistance thermometer, coils, lock-in amplifier, resistor, laboratory jack.

In this experiment, a number of pieces of the same superconducting tape, 0.5 to 1 cm long, are placed into a glass container, 1 cm in diameter and 2 cm in height, together with a small platinum resistance thermometer (100 Ω at 0°C). A differential transformer serves for measuring the magnetic susceptibility of the sample (Fig. 9). A 200-turn coil, 21 cm in diameter (EM-6711), forms the primary winding of the transformer fed by the *Signal generator*. The frequency of the current may be chosen in a wide range, from several tens to several hundreds of hertz. As a rule, we perform the measurements at 90 Hz, and the amplitude of the AC magnetic field is 0.2 mT. A second similar coil (not shown in Fig. 9) allows for studying the influence of external DC magnetic fields on the transition curve. A glass Dewar flask with liquid nitrogen rests on a laboratory jack inside the coils and can be raised and lowered (Fig. 10). Two similar secondary coils positioned inside the flask are connected in opposition, so that in the absence of a sample the output voltage of the differential transformer is zero. Each secondary coil, 2 cm in diameter and 2 cm in height, contains 500 turns.

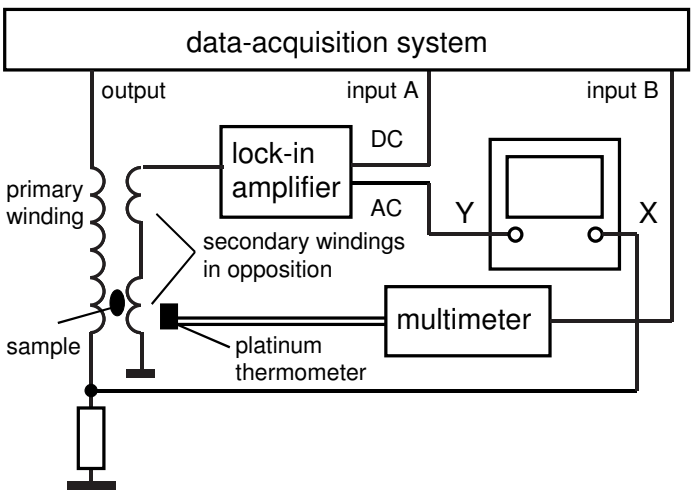

Fig. 9. Schematic of setup with differential transformer.

With a superconducting sample inside one of the secondary coils, the magnetic flux through it decreases. A voltage therefore appears at the output of

the differential transformer. This voltage is proportional to the magnetic susceptibility of the sample and serves for recording the phase transition from the superconducting to the normal state. A PAR 124A lock-in amplifier measures this voltage and provides a DC output voltage for the data-acquisition system and an amplified AC voltage for the Y input of an oscilloscope. A voltage proportional to the current in the primary coil serves as the reference for the lock-in amplifier and the signal for the X input.

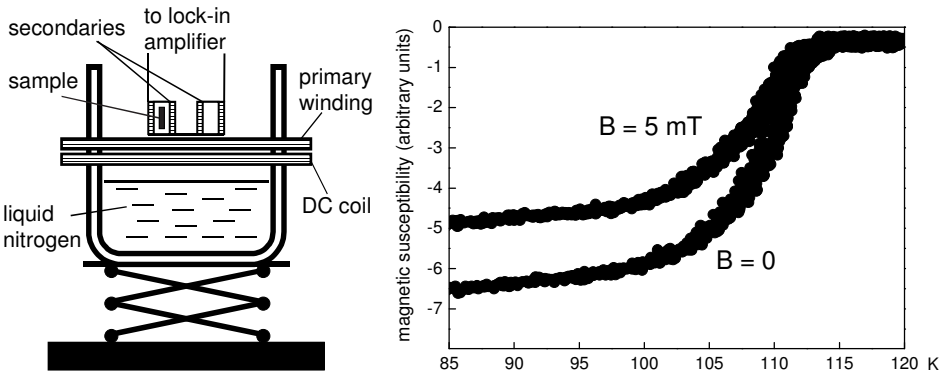

Fig. 10. Arrangement for measuring magnetic susceptibility and transition curves.

A Keithley 177 multimeter measures the resistance of the platinum thermometer. The output voltage of the multimeter proceeds to the second input of the data-acquisition system and then is translated into temperature. After cooling the secondary coils and the sample in the liquid nitrogen, the Dewar flask is lowered, so that the sample appears above the liquid. Without a sample, the secondary coils are positioned to minimize the output voltage of the differential transformer. Then the sample is put into one of the secondary coils. The DC output voltage of the lock-in amplifier is displayed versus temperature when the sample starts to warm up.

To ensure good thermal equilibration between the sample and the thermometer, the heating rate should not exceed 2 $K.min^{-1}$. The *Sample rate* is 1 or 2 Hz. The temperature dependence of the magnetic susceptibility of the sample clearly shows the phase transition from the superconducting to the normal state. Above the critical temperature, the output voltage of the differential transformer becomes zero. Due to the low frequency of the magnetic field and small dimensions of the conducting pieces of the sample, eddy currents in them are too small to influence the results. In an external DC magnetic field, the magnetic susceptibility of the sample decreases. In the experiment, a DC current in the second large coil produces this field. The maximum current allowed for the coil is 2 A, and the corresponding magnetic field is about 5 mT.

4. Diamagnetism of superconductors

The diamagnetism of a superconductor is demonstrated with a differential transformer (Kraftmakher 2004e).

Additional equipment: two *Voltage sensors*, coils, YBCO sample, resistor, E-shaped magnetic core.

A superconducting sample is placed into a plastic cup, which can be filled with liquid nitrogen. A differential transformer with an E-shaped core (SF-8615) senses the magnetic susceptibility of the sample (Fig. 11). Two 800-turn coils L_1 and L_2 (SF-8611) form the primary winding of the transformer fed by *Output 1*. A 3200-turn coil L_3 (SF-8613) constitutes the secondary winding of the transformer. The coils L_1 and L_2 generate opposite magnetic fluxes through the coil L_3. Without a sample or above its critical temperature, the output voltage of the transformer is zero.

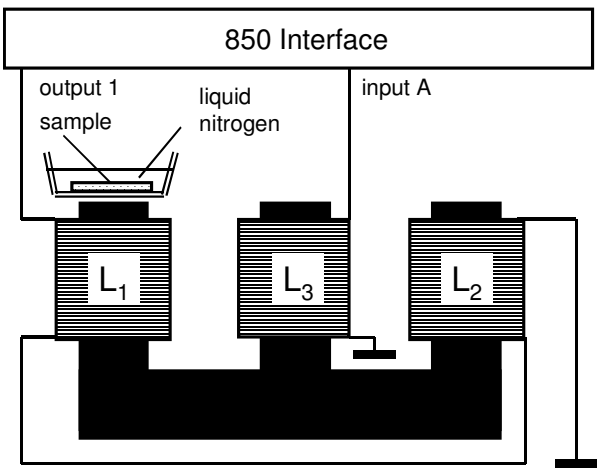

Fig. 11. Schematic of setup for demonstrating diamagnetism of superconductors.

The *Scope* displays the output voltage of the differential transformer versus *Output current*. An ellipse is seen on the screen. The *Scope* serves also for adjusting the transformer before the measurements. Arranging the primary coils does the adjusting. The frequency of the current in the primary windings is 30 Hz. When a superconducting sample is placed in one arm of the magnetic core, the magnetic flux through this arm decreases, and a voltage appears at the output of the differential transformer. This voltage is proportional to the magnetic susceptibility of the sample. The students observe the phase transition from the superconducting to the normal state after evaporation of the liquid nitrogen from the plastic cup. A small piece of a ferromagnet is used to show

that the superconducting sample is diamagnetic. The demonstration is possible without a data-acquisition system (Fig. 12).

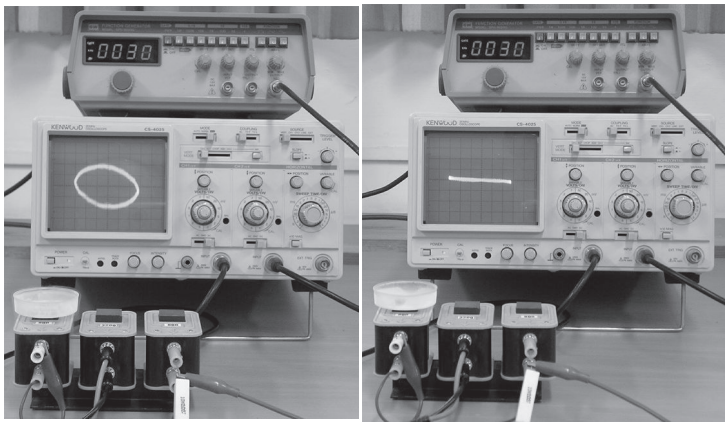

Fig. 12. A function generator and an oscilloscope are sufficient for the demonstration.

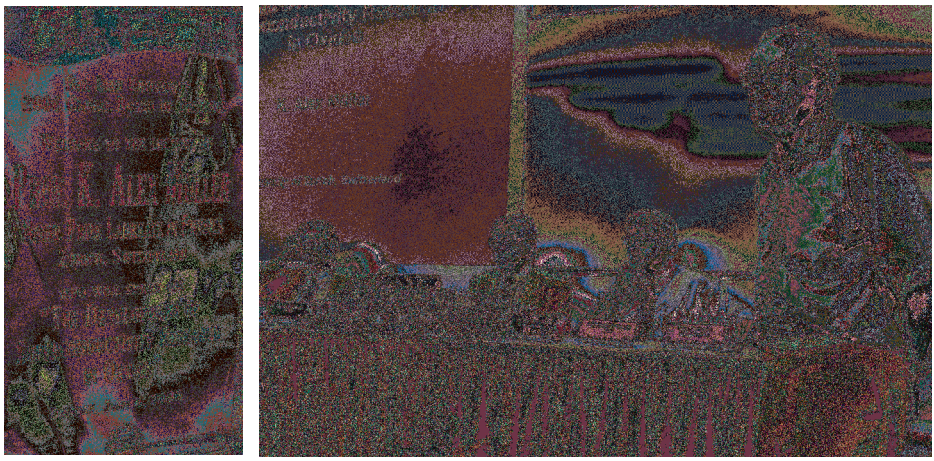

It remains to say that Professor Müller is *Doctor honoris causa* of Bar-Ilan University. From left to right: Professor Moshe Kaveh, President; Professor K. Alex Müller; Professor Yosef Yeshurun, Rector; Professor Moshe Gitterman introducing the Nobel laureate. June 6, 2006.

9.10. Fiber optics communication

The experiments include (i) the speed of light in an optical fiber; (ii) the optical telemetry with a light guide; and (iii) transmitting a video signal through a light guide.

Charles Kuen Kao
(b. 1933)

"...In 1966, Charles K. Kao made a discovery that led to a breakthrough in fiber optics. He carefully calculated how to transmit light over long distances via optical glass fibers. With a fiber of purest glass it would be possible to transmit light signals over 100 kilometers, compared to only 20 meters for the fibers available in the 1960s. ...Today optical fibers make up the circulatory system that nourishes our communication society. These low-loss glass fibers facilitate global broadband communication such as the Internet. Light flows in thin threads of glass, and it carries almost all of the telephony and data traffic in each and every direction. Text, music, images and video can be transferred around the globe in a split second."

> Joseph Nordgren, Chairman of the Nobel Committee for Physics. Presentation of Charles K. Kao awarded the Nobel Prize "for groundbreaking achievements concerning the transmission of light in fibers for optical communication" (2009).

The theoretical background for the experiments may be found in articles in *McGraw–Hill Encyclopedia of Science and Technology* (Parker 1997) and in Bergstein and Van Slyke (1997). **Telecommunication** means communication at a distance and includes radio and television, mobile telephony, telemetry, *etc*. The information to be transmitted must cause modulation of a high-frequency carrier. Amplitude modulation (AM) is the oldest and simplest form of modulation. The amplitude of a high-frequency carrier is varied in response to a low-frequency signal. This technique is used in AM broadcasting,

television picture transmission, radiotelephony, and navigational aids. Frequency modulation (FM) is used in broadcasting, television sound transmission, and microwave relaying.

Frequency band and information. Each radio transmitter operates within a specific radio-frequency channel. The minimum usable channel width depends upon the amount of information a channel must transmit per second. When a sine wave of frequency Ω modulates a sine wave of frequency ω, the resulting AM oscillation is

$$(1 + m\sin\Omega t)\sin\omega t = \sin\omega t + \tfrac{1}{2}m\cos[(\omega - \Omega)t] - \tfrac{1}{2}m\cos[(\omega + \Omega)t], \quad (1)$$

where $m < 1$ is called the modulation index. This equation shows that the necessary channel width is governed by the upper frequency of the signal used for the amplitude modulation.

Clearly, the frequency of the carrier must be at least several times higher than the highest modulation frequency. Optical waves corresponding to frequencies of the order of 10^{14} Hz thus provide an excellent opportunity for transmitting information containing extremely high modulation frequencies or providing many separate channels of modest frequency bands. One of the methods to create many separate channels consists of modulating the light wave by very high frequencies, for instance, of the order of 10^{10} Hz. The sidebands obtained serve as carriers for separate channels, so-called **subcarriers**. When transmitting information, the subcarriers are modulated, so that new sidebands appear around each subcarrier (Fig. 1).

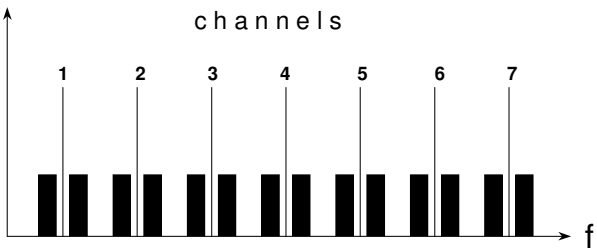

Fig. 1. Spectra of an optical signal modulated by high frequencies. Many subcarriers for separate communication channels are formed.

Optical fibers are now the preferred means for communications over long distances. The fibers for light wave transmission are made of fused silica (SiO_2) glass. A fiber consists of a central core and a surrounding cladding. The core is doped to a higher refraction index than the cladding to confine the light in the core by total internal reflection. Three basic types of optical fibers are the following (Fig. 2). **Step-index** fibers are limited to short distances because the high-angle modes have a longer distance to travel relative to the low-angle modes. This causes broadening of the transmitted light pulses and thus limits the applicable frequency of the signals. In **graded-index** fibers, the core refractive

index varies across the core diameter, so that light travels slower in the central high-index region of the core. Therefore, significant equalization of the transit time for various modes is possible. **Single-mode** fibers have a core diameter and refractive index distribution such that only one fundamental mode is guided. These fibers are best suited for transmissions over long distances. Optical-fiber systems are not the only optical systems that are now in use. Other systems include light beams in free space and through the atmosphere. In all the cases, a **semiconductor laser** is the best source for transmitting the information. A semiconductor photodiode converts the incoming optical signal into an electrical signal. The highest **transparency** for electromagnetic radiation in a solid material is that of silica glass in the range of 1 to 1.5 μm.

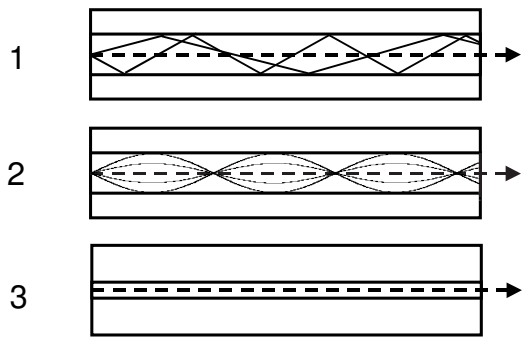

Fig. 2. Structures of optical fibers: 1–step-index fiber, 2–graded-index fiber, and 3–single-mode fiber.

Advantages of optical communications are the following:

- the extremely high frequency of the optical carrier provides a very **wide bandwidth** and permits much more information to be transmitted over a single optical channel than is possible with one radio channel;
- the short light wavelength permits the realization of very compact components;
- optical transmission is **immune** to any **electromagnetic interference** (EMI) and does not generate its own electrical noise.

Many authors considered the fabrication and applications of optical fibers for teaching purposes. Bunch (1990) described several student experiments. Cornwall (1992) simulated light propagation in an optical fiber by using a laser beam and interdiffusing liquid layers. Lau *et al* (1992) described experiments with fiber-optics sensors. Barton (1994) considered types of optical fibers and experiments with a displacement sensor and a fiber-optic Michelson's interferometer. Lavers (1996) reported on processes necessary for the fabrication of optical fibers for optoelectronics needs. Chaudhry and Morris (2000) described the composition, manufacturing, and properties of optical fibers. Conklin *et al* (2007) constructed a sensor applicable to some experiments.

1. Speed of light in optical fiber

The speed of light in an optical fiber is determined.

Equipment: optical fiber, *Lichtgeschwindigkeitsmeβgerät* apparatus from PHYWE with an auxiliary circuit, oscilloscope.

The experiment is similar to the determination of the speed of light in air using the *Lichtgeschwindigkeitsmeβgerät* apparatus with an auxiliary circuit (Fig. 3). An auxiliary circuit serves to reduce unavoidable background and make the measurements more accurate. Two pieces of optical fiber are needed. With a short fiber, the phase shift between the outgoing and incoming light modulated at 50 MHz is adjusted to be 0 or 180°, so that a straight light is seen on the oscilloscope screen. Then the measurements are repeated with a long fiber. An ellipse appeared on the screen shows the difference in the propagation times in the two fibers. It is easy to calculate the corresponding phase shift $\Delta\varphi$ from the shape of the ellipse.

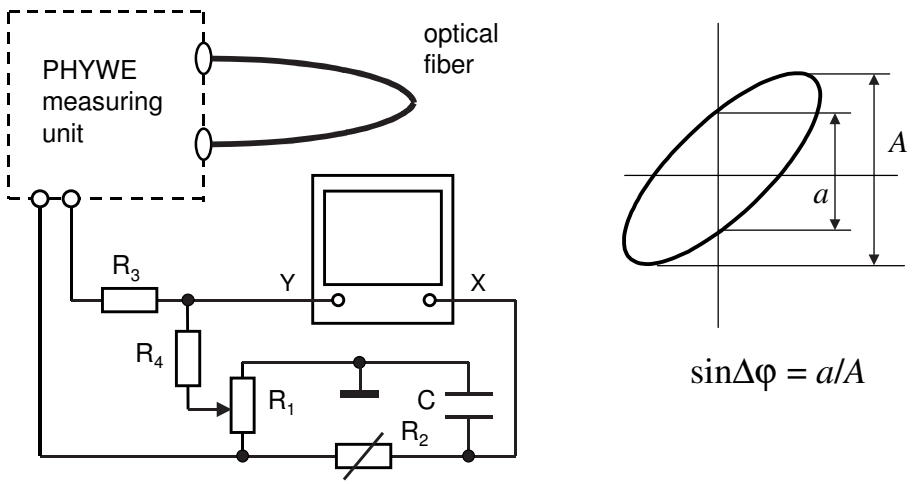

Fig. 3. Schematic of the setup and method to calculate the phase shift from the Lissajous pattern.

2. Optical telemetry

An optical fiber transmits measurement data to a remote receiver (Kraftmakher 2003).

Additional equipment: LED, photodiode, thermistor, function generator, DC supply, light guide, decade resistance box, resistors, oscilloscope.

The setup is designed for remote temperature measurements. For simplicity, the so-called baseband transmission is used: the information is transmitted by direct pulse modulation of the intensity of light transmitted to an optical detector (Fig. 4).

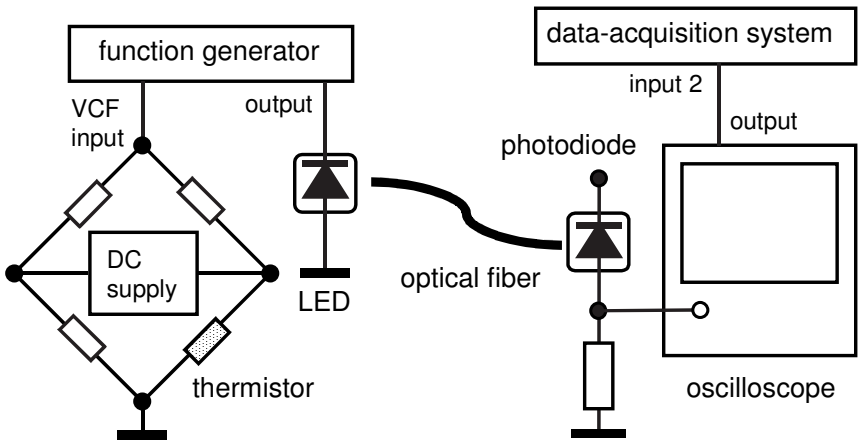

Fig. 4. Schematic of the setup for optical telemetry with LED and light guide.

A simple function generator provides square wave pulses feeding a light-emitting diode (LED). The LED generates light pulses, which are transmitted to a remote photodiode in the laboratory through a light guide. The VCF (voltage controlling frequency) input of the function generator serves for encoding the data to be transmitted. The frequency of the light pulses represents temperature measurement data.

The voltage applied to the VCF input of the function generator is the output voltage of a Wheatstone bridge containing three fixed resistors and a **thermistor**, that is, a temperature-sensitive semiconductor resistor. A 4.5 V DC supply feeds the bridge. The frequency of the light pulses created by the LED thus depends on the temperature of the thermistor. The calibration data for the thermistor, the resistance versus temperature, must be known or determined beforehand. The light pulses are detected by a photodiode and then observed and amplified with an oscilloscope. After the amplification, the amplitude of the pulses becomes of the order of 1 V. The pulses proceed to the data-acquisition

system. Their frequency is measured by employing the digital input intended for the *Rotary motion sensor*. With a 1 Hz *Sample rate*, this input measures the frequency of pulses (*Rotation counts/Counts/Sample*). For the measurements, an additional plug is necessary. With a thermistor from PASCO scientific (100 kΩ at 25°C), it is easy to obtain data on the temperature dependence of its electrical resistance. It is sufficient to connect a variable resistor to the input of the *Thermistor temperature sensor* (CI-6527A) and gradually change the resistance. *DataStudio* measures the resistance R and converts it to the temperature according to the relation accepted for the thermistor. The graph provides the necessary polynomial fit. For the range 20–100°C,

$$R = A\exp(B/T), \quad \text{and} \quad T = B/\ln(R/A), \tag{2}$$

where T is the absolute temperature.

The dependence of the frequency of the light pulses on the temperature of the thermistor is nonlinear and must be determined experimentally. For this aim, the resistance of the thermistor at various temperatures given by Eq. (2) is set at the decade resistance box, and the frequency of the light pulses is measured. These data are fitted by a polynomial. The remote temperature measurements are carried out when the thermistor is put into a furnace resistively heated up to 90–100°C and then allowed to freely cool down. The *Graph* tool displays the data converted to temperature (Fig. 5).

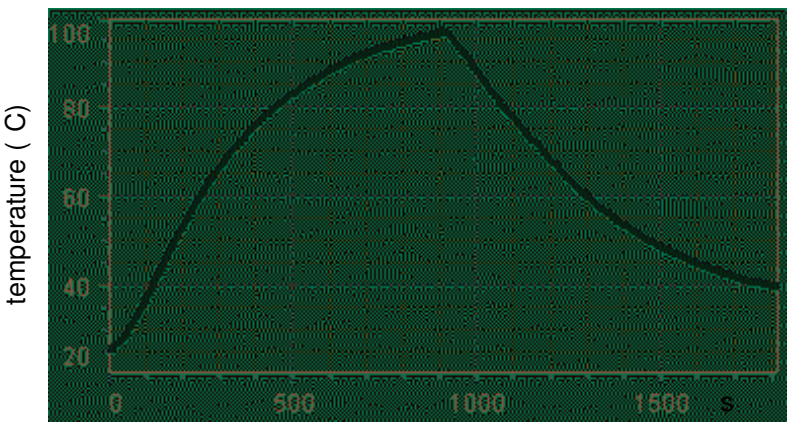

Fig. 5. Temperature data obtained by remote measurements.

With the *850 Interface* and *Capstone* software, the calibration procedure can be completely avoided. For this aim, the resistance of the thermistor is measured during a run, and the frequency of the pulses is set to be equal to the temperature using Eq. (2). With this approach, the frequency of the incoming pulses simply equals to the temperature in the furnace.

3. Video through light guide

The experiment gives understanding of how a picture is converted into an electrical signal, sent to a remote receiver, and correctly reproduced there. A light guide transmits a video signal (Kraftmakher 2008d).

Equipment: LED, photodiode, function generator, light guide, DC supply, resistors, 9 V battery, two oscilloscopes, video camera, video monitor.

Basic principles of television. Television involves the electrical transmission and reception of visual images. At a **transmitter**, small elements of a scene, sampled for brightness and color, are presented as electrical signals and transmitted consecutively. At a **receiver**, the electrical signals are converted back into brightness and color, and properly displayed on a screen to reproduce the original scene. Television thus requires the following basic operations:

- at the transmitter, a camera samples a scene in a pre-defined order, as a sequence of small pixels;
- the information about **brightness** and **color** of each **pixel** is converted into an electrical signal;
- the sequence of electrical signals obtained modulates a high-frequency carrier specific for a particular television channel;
- the modulated signal is transmitted to a receiver by means of radio waves, an electric cable, a light guide, or a laser beam;
- at the receiver, the desired channel is selected, and the incoming signal is detected and used to arrange a sequence of pixels on a visual display in exactly the same order as that used to sample the original scene.

Clearly, television is a much more complicated technique than radio. However, a demonstration of key principles of TV is possible with relatively simple equipment. Every scene can be viewed as a number of small pixels, each being characterized by its brightness and color. An electrical voltage, determined through the photoelectric effect, represents the brightness. The scene is sampled many times per second in order to create a sequence of images (**frames**). Within each frame, sampling is done along many horizontal scan lines, from the left edge of the picture to the right. The visual information is thus converted into a definite sequence of electrical signals. Two additional signals, called **horizontal synchronization pulses** (H-sync) and **vertical synchronization pulses** (V-sync), are added to this sequence to indicate the ends of each scan line and frame. The receiver uses these signals to properly display the original scene. A small period of time, called blanking or retrace, is allocated to return the scanning beam to the left edge of the next scan line. Each frame is scanned twice, odd and even lines in turn. This is called interlaced scanning. The receiver must reproduce exactly the same sequence of lines.

The frequency bandwidth required for a TV channel depends on the number of bits to be transmitted per second. The NTSC (National Television Systems Committee) standard assumes 30 frames per second (29.97 frames for color television) and 525 horizontal lines per frame. The width-to-height ratio of the picture is 4:3. Therefore, the maximum frequency bandwidth required for the video signal is about 5.5 MHz. In reality, only a 4.2 MHz band is allowed, which is a compromise between the quality of the image and the need to provide separate frequency bands for other TV channels. For the addition of sound, the total width of bands assigned to each channel is 6 MHz.

To simultaneously transmit many TV channels, the video signal modulates a high-frequency carrier wave, whose frequency is unique for each TV channel. The carrier frequency should be at least one order higher than the upper limit of the modulation frequency. In the United States, TV channels are assigned to 6 MHz wide frequency bands, starting at 54 MHz. The video signals are sent with amplitude modulation (AM), and the accompanying audio signals with frequency modulation (FM). For AM, the frequency bandwidth is twice the upper modulation frequency. Amplitude-modulated signals have identical upper and lower sidebands, symmetrically located on each side of the carrier frequency. For video signals, the single sideband technique is used to reduce the frequency band requirements. The video carrier is positioned 1.25 MHz above the lower end of the band, and the audio carrier 0.25 MHz below the upper edge of the band (Fig. 6). Huebner and Porter (1977) and Ellington *et al* (1980) considered the physics of television broadcasting.

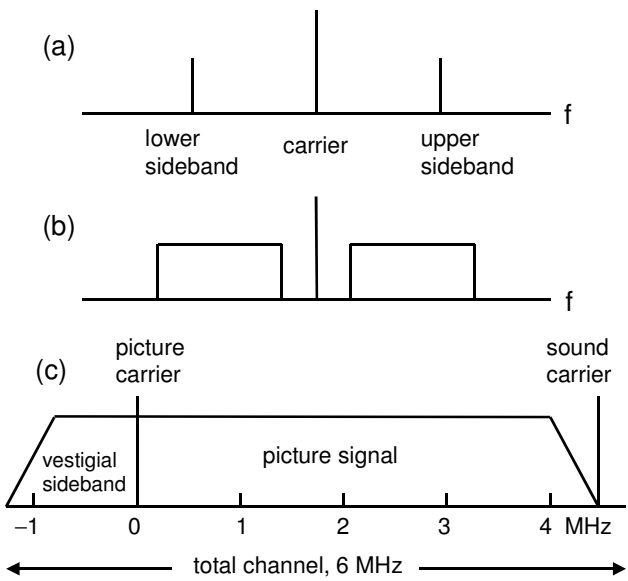

Fig. 6. Spectra of AM signals: sine wave modulated by (a) single frequency and (b) frequency band; (c) standard TV spectrum.

Contemporary TV receivers use solid-state technologies with many functions integrated on a few chips. The **picture tube**, also called a **kinescope**, is a vacuum **cathode-ray tube** with magnetic deflection of the electron beam and capable of obtaining large deflection angles. The electron gun produces a stream of high-velocity electrons, which is focused on a small spot of the **fluorescent screen** of the tube. The beam scans the screen in a systematic **raster** of horizontal lines, strictly following the scanning process of the camera. The video signal, applied between the cathode and the control grid of the tube, controls the intensity of the beam. Nowadays, LCD screens are used instead of cathode-ray tubes for TV receivers, as well as for computers.

The setup. The transmission of visual information by modulating a high-frequency carrier wave requires expensive equipment. As an alternative, we use an optical fiber to directly transmit the video signals; for this approach, a 4 MHz frequency band is sufficient. This approach is simple and inexpensive to use in student laboratories and for demonstrating some basic principles of TV. An obvious disadvantage is that only one video signal is transmitted.

The demonstration setup (Fig. 7) is arranged by using equipment available in the laboratory. The transmitter includes a Panasonic GP-KR222 color video camera, a Kenwood CS-4025 oscilloscope, and a Hewlett–Packard HMLP-8100 red LED. Electrical signals from the camera modulate the LED. The modulated light propagates through a plastic light guide, 3 mm in diameter. The receiver consists of a fast silicon photodiode (United Detector Technology PIN-5D), and a Sony PVM-14N6U color video monitor. Additional elements required are a DC supply for the video camera and the LED, a 9 V battery for the photodiode, and three resistors. The monitor displays images received by the optical transmitting or with a common electric cable.

The LED is connected to the DC supply through a 300 Ω resistor. The signal from the video camera is fed to it through another 300 Ω resistor, so that the feeding current becomes modulated following the video signal. The LED and the light guide are brought in contact using a Perspex slab. The light guide enters the slab on one its side, and the LED on the other. The first oscilloscope displays the electrical signals produced by the video camera. Its sweep is synchronized by the negative H-sync signals at the beginning of each horizontal scan line.

At the receiver, the incoming modulated light falls onto the photodiode loaded by a 1 kΩ resistor. The photodiode, the resistor, and the 9 V battery are mounted in a metal box positioned close to the Y-input of the second oscilloscope. This avoids an additional cable, whose capacitance put in parallel to the 1 kΩ resistor reduces the frequency band of the transmitting system. The light guide enters the box and contacts the photodiode. The signal from the photodiode is seen on the screen of the oscilloscope. The oscilloscope serves also as a wide-band amplifier; its maximum gain is 100. The output signal that proceeds to the video monitor contains synchronization pulses necessary for its proper action.

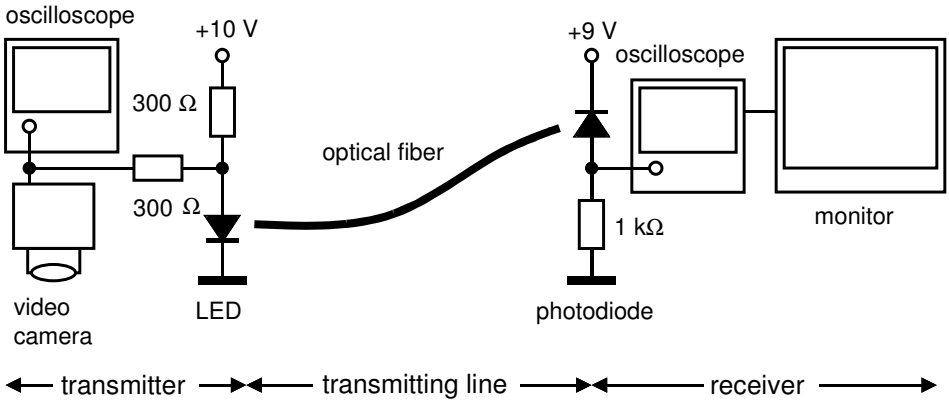

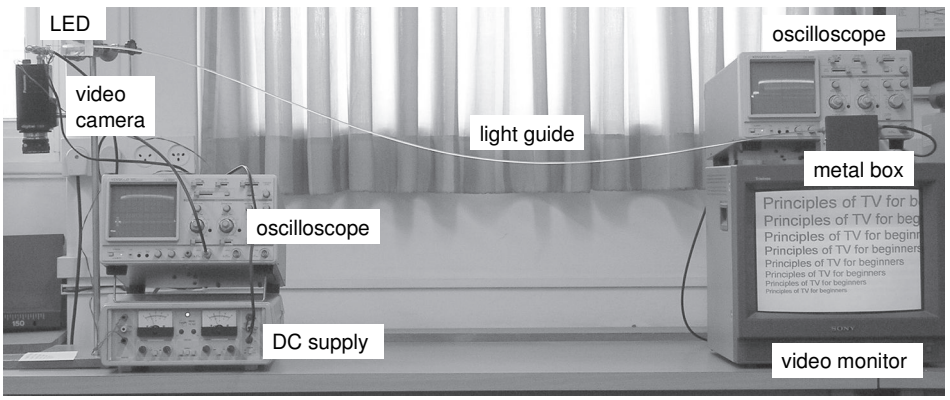

Fig. 7. Setup for optically transmitting video signals. Text transmitted is typed with fonts from 8 to 22 points.

Video signal. The video camera incorporates a 0.5-inch charge-coupled device (CCD) containing about 380000 pixels. With the frame rate of 29.97 Hz and 525 scan lines, the line frequency is 15.734 kHz. The scan of one line thus lasts nearly 64 μs. Only 485 of the 525 scan lines are used for the display; the rest are used for the V-sync signal. Similarly, about 17% of the horizontal lines are used for the H-sync and some other auxiliary signals. To show the relation between the video signal and the image, a piece of white paper with a black rectangle printed on it is used (Fig. 8). When the image is moved to the right, in the direction of the scan lines, the corresponding dip of the electrical pulse moves to the right on the oscilloscope screen. A positive electrical pulse appears when the camera views a white rectangle on a black background, also aligned perpendicular to the scan lines. If the rectangle is aligned parallel to the scan lines, the electrical signals contain two levels: the lower level represents all

black lines, and the upper all white lines. When the oscilloscope is properly synchronized, the negative H-sync pulses are seen at the beginning of the sweep. A high-frequency burst following these pulses relates to the reproduction of color pictures. The monitor is connected to the video camera by a standard cable.

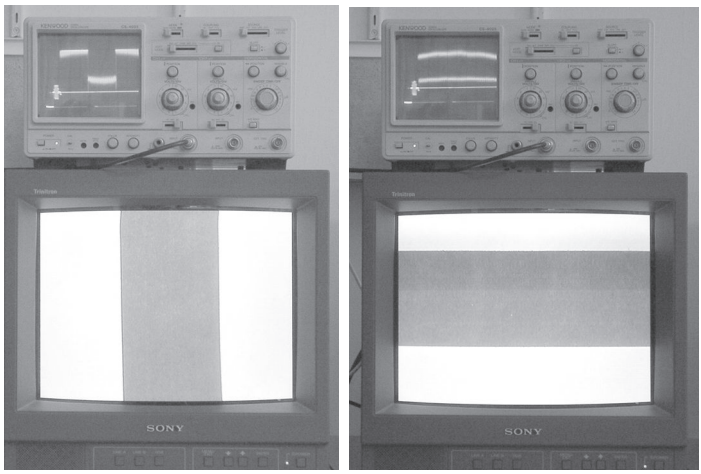

Fig. 8. Electrical signals observed with oscilloscope and images displayed by video monitor.

The above experiments show that it is possible to create any image by generating the proper electrical signal. This process occurs every time when one is viewing the output of a computer program on a video monitor. In this case, the information necessary to create the electrical signals was prepared and stored beforehand; our action reduces to positioning them in a due place. The process of creating a picture is observable by means of the *Paint* program (Fig. 9).

Fig. 9. Elements of a text or a picture (pixels) can be seen.

Demonstration with DSO. With a DSO, the demonstration of the structure of a video signal becomes more informative than with a common cathode-ray oscilloscope (Kraftmakher 2012f). The DSO operates in the regime of single run triggered by the H-sync pulses. With a proper choice of the time scale, the DSO displays a signal corresponding to one or several scan lines. Simultaneously, the DSO displays a spectrum of the signal using the built-in *Fast Fourier Transform* (*FFT*) software (Fig. 10). The picture viewed by the video camera is a rectangular strip of white paper placed on a black background. The strip is perpendicular to the horizontal scan lines. Therefore, all the lines contain the same signal, a positive rectangular pulse at the center of the scan line. Negative

H-sync pulses 64 μs apart are seen at the beginning of the scans. A high-frequency burst following this pulse provides the information needed for reproducing the sequence of colors along each scan line. The color of each pixel is encoded by a phase shift between the reference (the burst) and a signal of the same frequency superimposed on the voltage governing the brightness of the pixels along the scan line. The frequency of the reference is nearly 4 MHz. The reference contains only several periods, so it is not surprising that its spectrum is about 0.5 MHz in width.

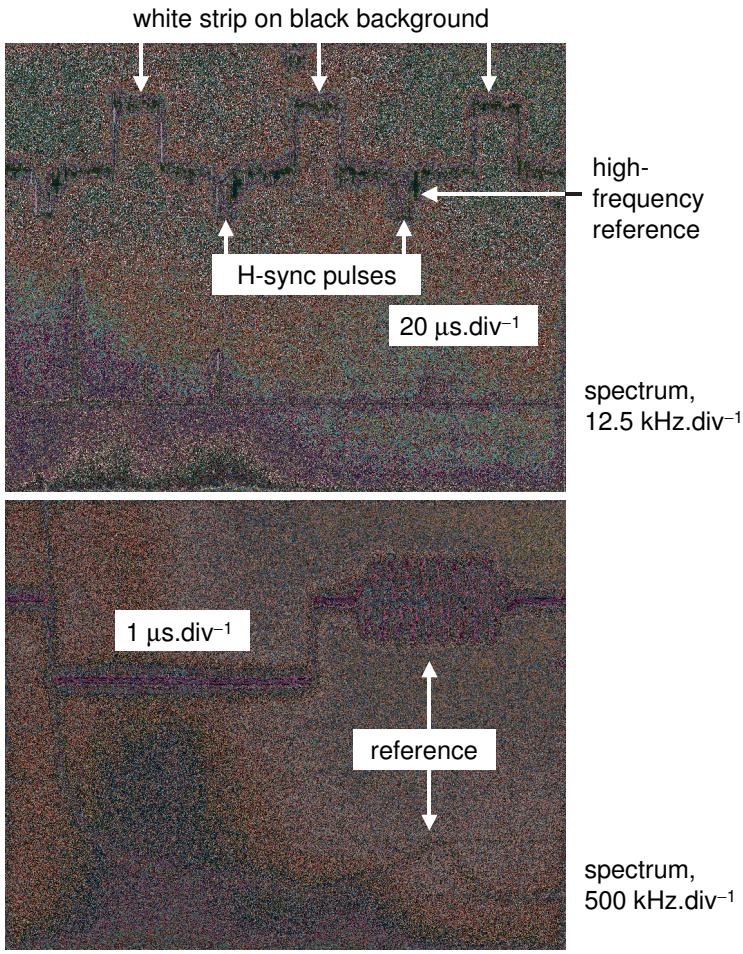

Fig. 10. Elements of video signal shown with different time scales, 20 and 1 μs.div^{-1}, and their spectra.

For obtaining sharp spectra, many periods of the signal should be accumulated. After the acquisition, the time base can be rescaled and details of the signal examined. In the example presented, the signal is shown with the

scales 20 and 1 μs per division. When accumulating the data for the *FFT* operation, the time scales are 400 and 20 μs per division, and the spectra are displayed with scales of 12.5 kHz.div^{-1} and 500 kHz.div^{-1}.

Modulation characteristics. The LED and the photodiode are critical elements of the transmitting system. The LED should possess a high brightness, a narrow directivity diagram (in this respect, the models HMLP-8102 or 8103 are better than HMLP-8100), and a short time constant. The important characteristics of the photodiode are its **sensitivity**, **spectral response**, and **time constant**. Photodiodes with nanosecond rise times are now reasonably priced. The desired broadening of the frequency band is limited by the time constant of the LED used (for the LEDs mentioned, the time constant is 45 ns).

The suitability of the LED and the photodiode used can be verified by measurements of their characteristics. Here, the characteristics are measured for the whole system, that is, for the LED–photodiode combination (distortions brought in by a short light guide are negligible). For this measurement, an oscillator is used to modulate the LED. The voltage seen on the screen of the second oscilloscope is measured as a function of the amplitude and frequency of the modulation voltage (Fig. 11). The frequency response drops at high frequencies and at very low frequencies. The AC coupling at the output of the second oscilloscope and the low input impedance of the video monitor causes the drop at low frequencies. The picture obtained with the optical transmission system can be compared with that with a standard cable. Color pictures can be transmitted as well because the frequency band used for color television is the same as that for monochrome television.

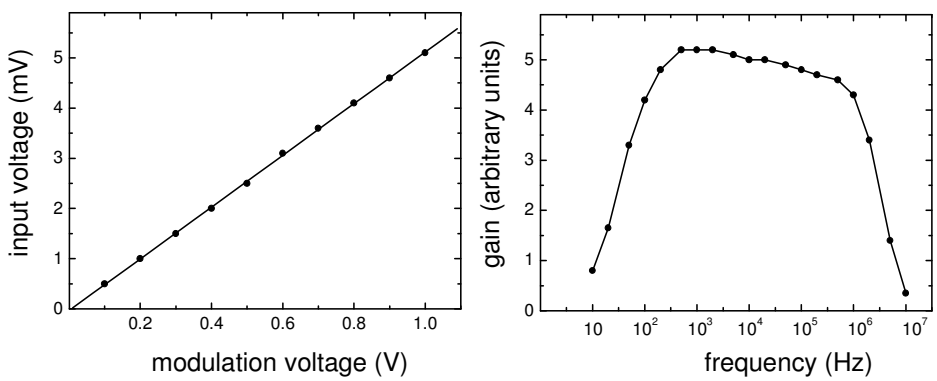

Fig. 11. Modulation characteristics of the transmitting system. The input voltage is that at the input of second oscilloscope.

Student Projects

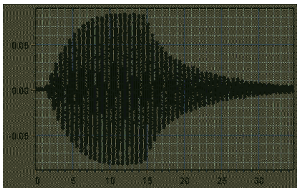

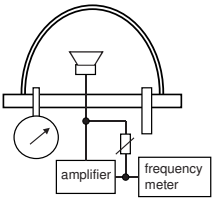

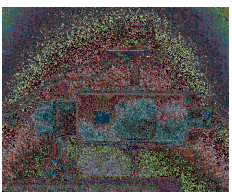

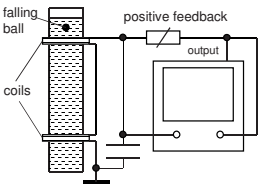

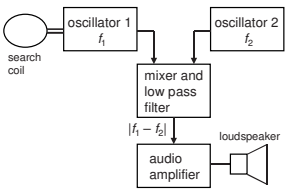

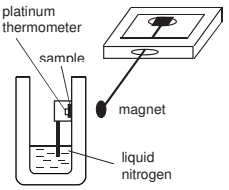

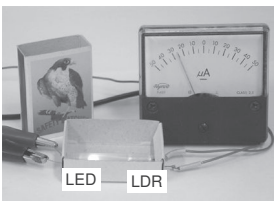

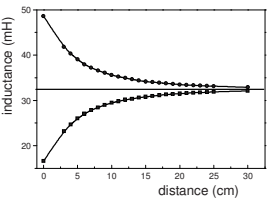

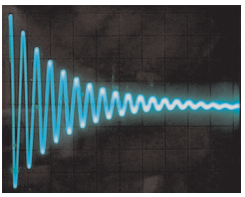

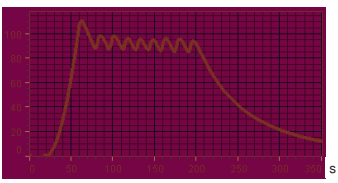

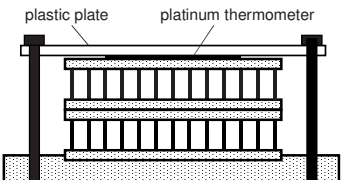

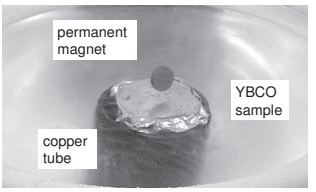

10. Student Projects 677

10.1. Moving-coil meter as a pendulum

A moving-coil meter used as a pendulum demonstrates free and forced oscillations.

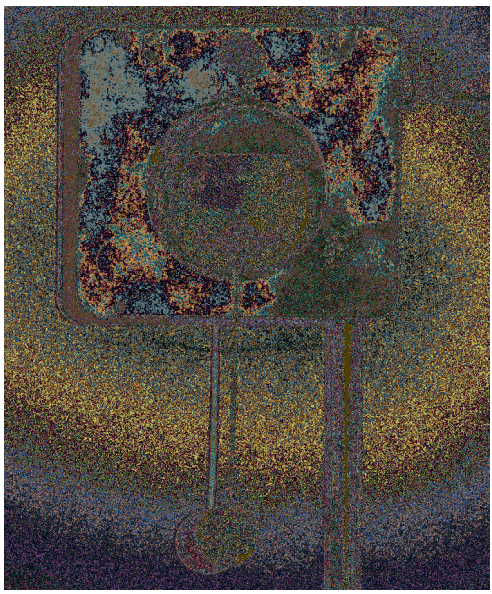

Moving-coil meter as a pendulum.

The use of a moving-coil meter as a pendulum is well known. Gruber and Baart (1975) observed oscillations of a wall-mounted galvanometer driven by an AC source. Eagle and Jackson (1977) used a galvanometer as a harmonic oscillator with recording facilities. Main (1988) used an inverted long-period moving-coil galvanometer for demonstrating free and forced oscillations. A resistor shunting the coil controlled the damping of the galvanometer. An optical lever served to demonstrate the oscillations of the coil. A closed circuit television enabled comparison of the displacement and applied force. Moore (1994) employed a similar meter for obtaining an electric signal proportional to the velocity of the oscillations. With a simple electronic circuit, the coil of the meter acts as the driver and sensor of the oscillations.

A simplified circuit for this purpose is used here. The coil of an inverted moving-coil microammeter constitutes one arm of a bridge fed by the *Signal generator* (Fig. 1). The pointer of the meter is extended and loaded by a nonmagnetic conducting disc. For observing forced oscillations, the bridge is balanced when the movable part of the meter is fixed. After this adjustment, the output voltage of the bridge reflects the velocity of the forced oscillations (Fig. 2).

To demonstrate free oscillations, there is no need for the bridge and a data-acquisition system. The EMF generated in the coil is observable with a plotter or an oscilloscope.

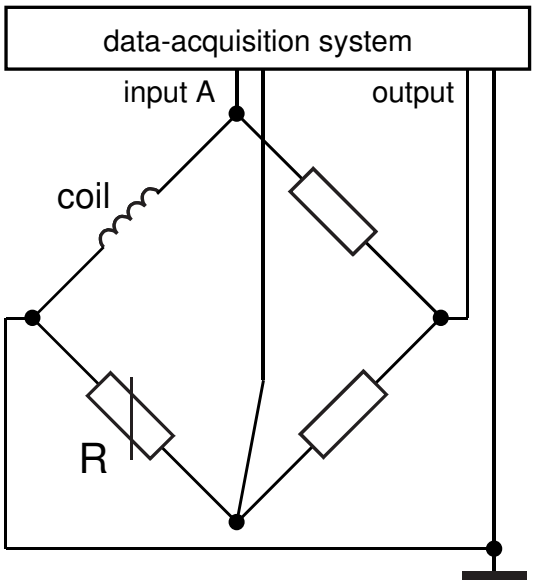

Fig. 1. Diagram of bridge circuit including moving-coil meter.

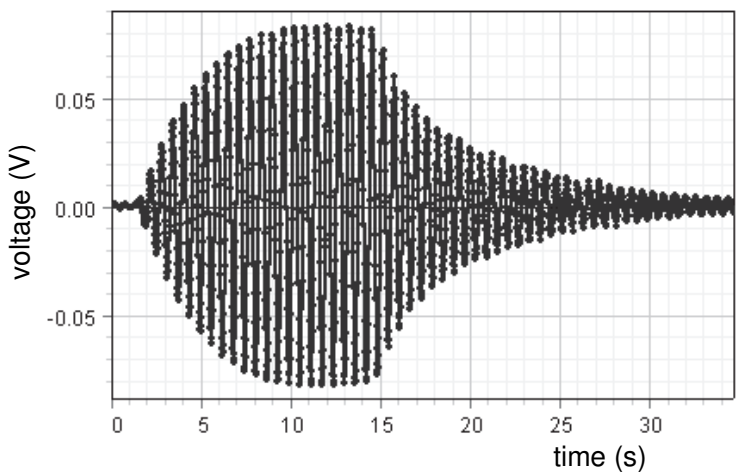

Fig. 2. Forced and free oscillations of the movable part of the meter.

10.2. Magnetically coupled pendulums

When two similar pendulums are coupled by some means, their oscillations become interdependent. Due to the coupling, energy exchange occurs between the pendulums, and the oscillation amplitude of each pendulum periodically reaches maxima and minima (Kraftmakher 2008a).

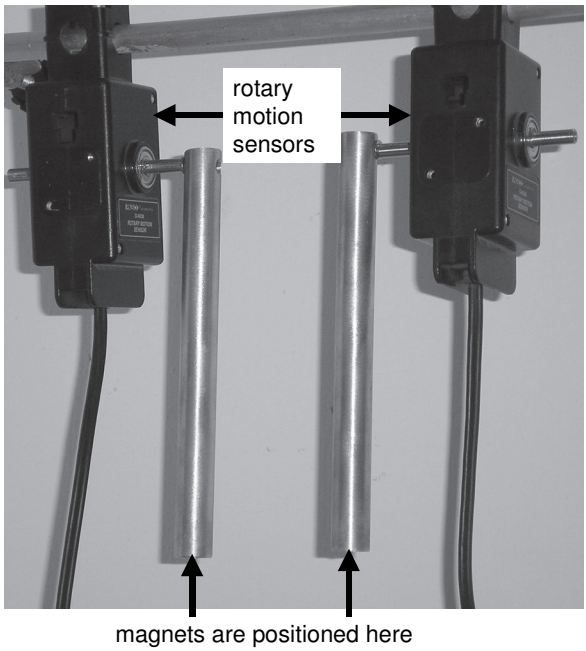

Magnetically coupled pendulums. Permanent magnets are positioned inside the tubes at their lower ends.

The magnetically coupled pendulums represent a case of coupled pendulums (Fig. 1). The pendulums are two similar non-magnetic tubes with small permanent magnets positioned inside them at the lower ends of the tubes. The axes of the magnetic dipoles are oriented along one line to cause attraction between the magnets. When one of the pendulums is removed from its equilibrium position and then released, its free oscillations gradually decay, while the second pendulum becomes active. The process of the energy exchange repeats until both pendulums stop due to unavoidable energy losses.

The magnets are arranged so that the audience does not see them, which provides an opportunity to discuss the origin of the coupling between the pendulums. The pendulums should be very similar. For instance, the periods of our pendulums are equal to within 0.2%. To finely adjust the period, one of the magnets can be slightly moved up or down inside the tube.

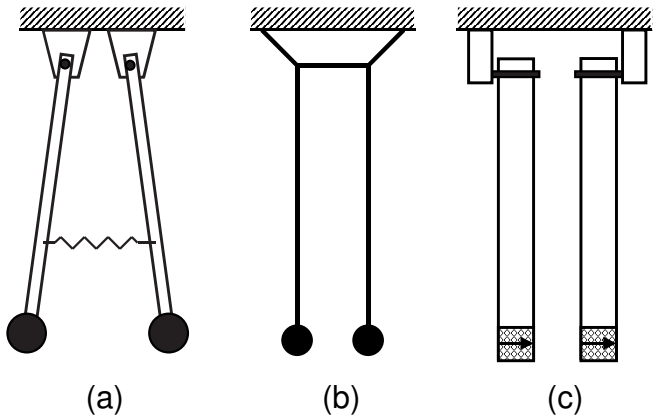

Fig. 1. Variants of coupled pendulums: (a) coupling with a spring, (b) coupling with horizontal thread, (c) magnetic coupling.

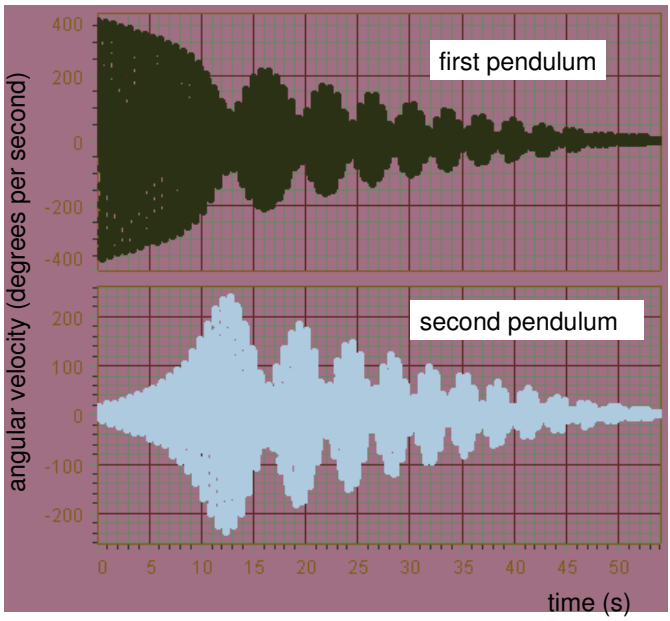

Fig. 2. Free oscillations of coupled pendulums at a distance of 7 cm.

The properties of the pendulums are very different from those of pendulums coupled with a spring or a thread. The interaction force between two magnetic dipoles follows the $1/R^4$ law (see Experiment 4.5), so the magnetic coupling strongly depends on the distance between the pendulums. Also, the interaction between the pendulums can be considered to occur only for close angular positions. It is easy to demonstrate the magnetically coupled pendulums

with no additional tools. However, the demonstration becomes more informative with *DataStudio* and two *Rotary motion sensors* (Fig. 2).

The magnetic interaction between the two pendulums is seen from measurements of the angular position of one pendulum versus that of the other under equilibrium conditions. *DataStudio* takes as a zero position the point where the measurement starts. Therefore, the measurements have to be started when both pendulums are in their equilibrium positions. The angular position of one pendulum is gradually changed, and *DataStudio* stores the positions of both pendulums and builds the corresponding graph (Fig. 3). The results presented here were obtained with 5 s intervals between the measurements.

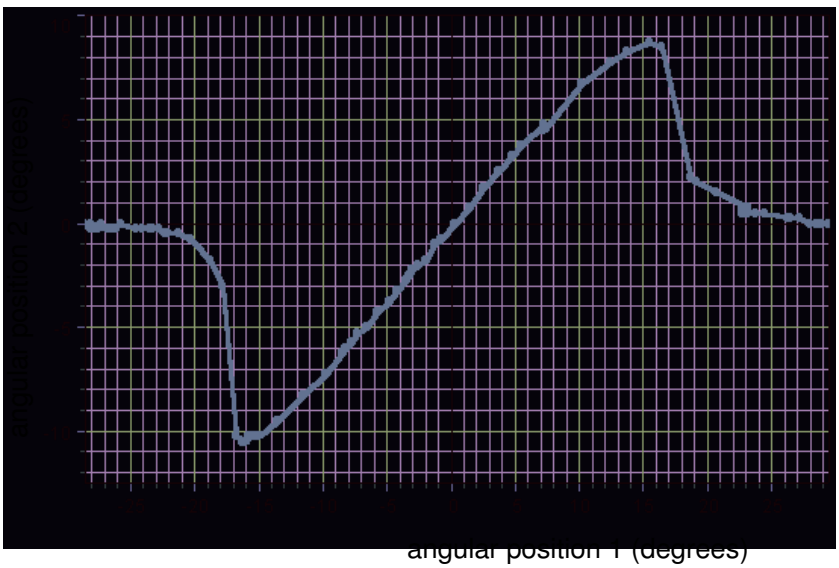

Fig. 3. Equilibrium angular position of one pendulum versus that of the other. Distance between the pendulums is 5 cm.

The kinetic energy of each pendulum is proportional to its angular velocity squared. The *Rotary motion sensors* measure the angular velocities of the pendulums along with their angular positions, and the *Calculate* tool calculates the angular velocities squared. The kinetic energy is presented in arbitrary units (Fig. 4). An unusual feature of the magnetic coupling is that the energy exchange between the pendulums becomes faster with decreasing oscillation amplitudes. This is quite understandable because the time of the interaction between the pendulums increases with decreasing their velocities.

The interaction between two permanent magnets is considered by Castañer *et al* (2006); Gayetsky and Caylor (2007); Kraftmakher (2007b). For coupled oscillations, see Blair (1971); Monsoriu *et al* (2005); Moloney (2008); Donoso *et al* (2010).

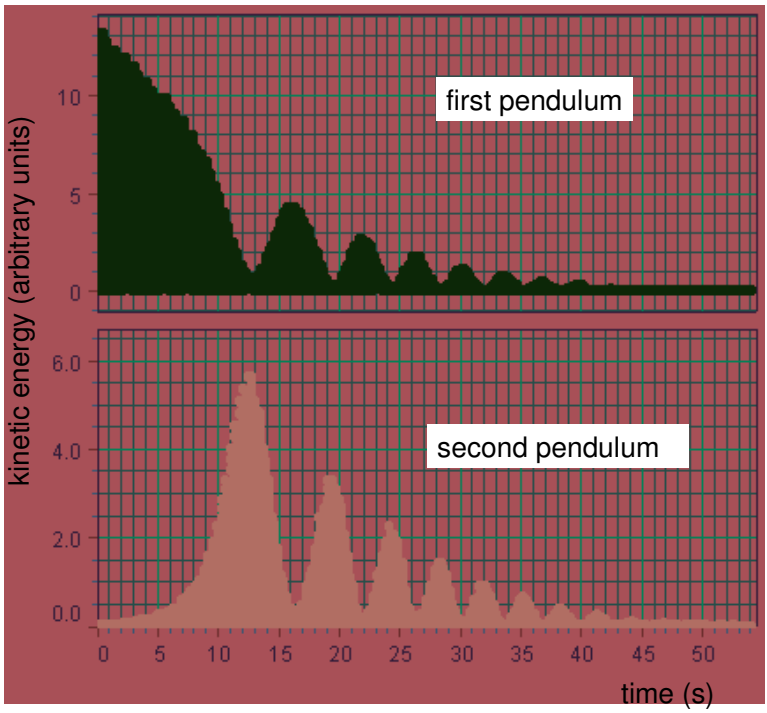

Fig. 4. Energy exchange between the pendulums. Data of Fig. 2 were used for the calculations.

10.3. Speed of sound versus temperature

The experiment is similar to those described by Ouseph and Link (1984) and Worland and Wilson (1999).

The *Motion sensor* determines the distance to a reflector positioned inside a cardboard box (see Experiments 1.8 and 2.3). An electrical heater heats the box. The sensor provides data on the distance to the reflector and on the time needed for the ultrasonic pulses to return to the sensor. For the *Motion sensor*, the position-to-time ratio is 172 $m.s^{-1}$ (the speed of sound was taken 344 $m.s^{-1}$). A platinum thermometer or a thermistor measures the temperature inside the box (Fig. 1).

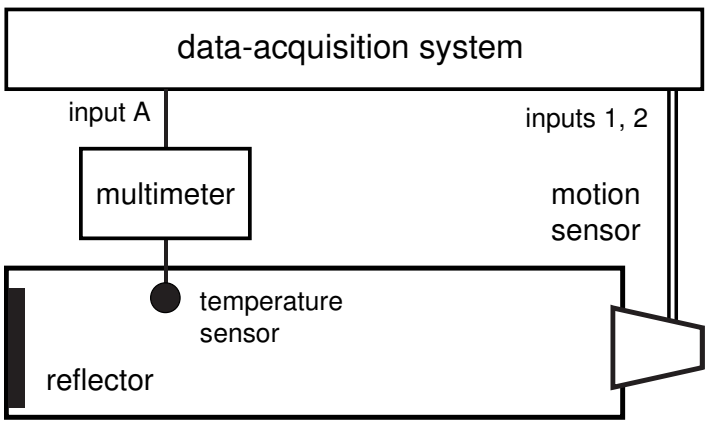

Fig. 1. Setup for the measurements.

When heating the air, the apparent distance to the reflector decreases, and this decrease can be taken as a measure of the changes in the sound velocity. The temperature variation of the velocity of sound obeys the relation

$$c = c_0(T/T_0)^{½}, \quad (1)$$

where c relates to temperature T, and c_0 to temperature T_0.

For the demonstration, the air in the box is heated by a fan. The results of the measurements are recorded during gradually cooling of the air. *DataStudio* displays data from the *Motion sensor* and from the temperature sensor. From the data and the distance between the *Motion sensor* and the reflector, the velocity of sound at various temperatures becomes available.

10.4. Loudspeaker senses air pressure

A common loudspeaker senses air pressure (Kraftmakher 2010b).

Due to the contribution of the air loading mass, the natural frequency of a loudspeaker depends on the air pressure (see Experiment 8.2). The natural frequency is available by observing free oscillations of the loudspeaker cone or from the frequency dependence of the modulus of the total impedance of the voice coil. For the present purpose, it is better to employ positive feedback and generate continuous oscillations of the loudspeaker cone. The frequency of the continuous oscillations depends on the air pressure.

The loudspeaker is placed under a bell jar pumped out by a rotary pump. The air pressure is measured with a Bourdon gauge. An amplifier is needed to provide the positive feedback. An oscilloscope with output from one of the channels serves for this aim, and a digital frequency meter measures the oscillation frequency (Fig. 1). Many function generators are also capable of measuring frequencies of external signals. Significant changes in the natural frequency of the loudspeaker cone occur in the pressure range between 10^5 and 10^4 Pa. In this range, the natural frequency of a small loudspeaker changes by about 30%. After determining the calibration curve (the oscillation frequency versus air pressure), the system is ready for the measurements.

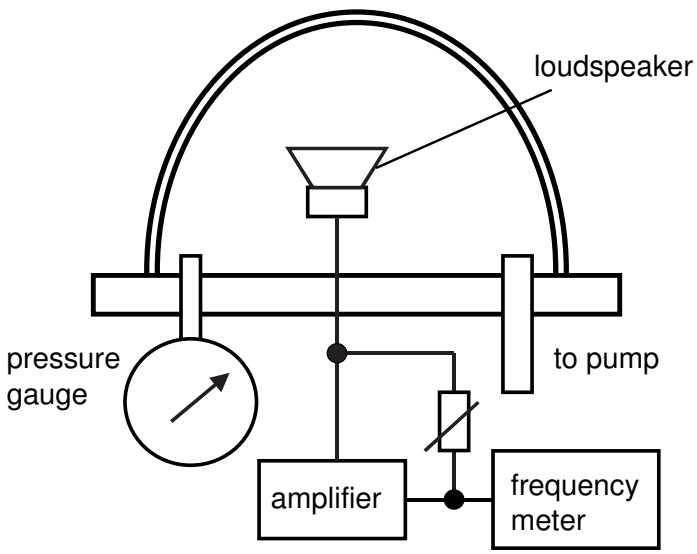

Fig. 1. Schematic of the setup.

10.5. Hot-wire anemometry

Hot-wire anemometry is a technique for measuring the velocity of air based on sensing the temperature of an electrically heated thin hot wire; the temperature depends on the air motion.

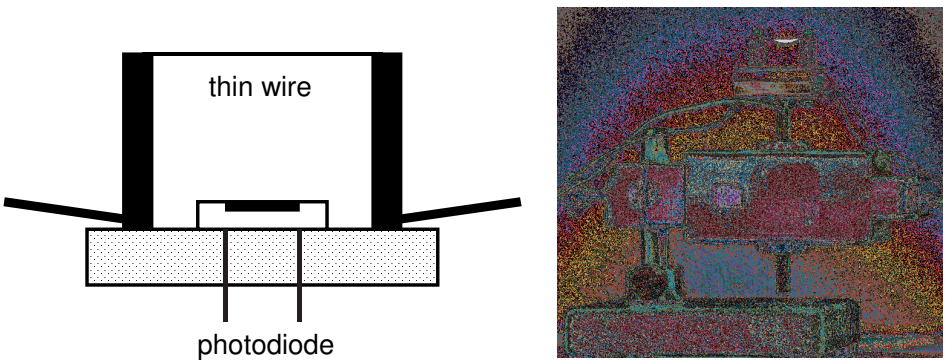

Fig. 1. Hot-wire anemometer mounted on the axle of the *Rotary motion sensor*.

The hot-wire anemometer is very simple (Fig. 1). A thin wire is mounted on two current leads. A photodiode positioned on a plastic plate beneath the wire is shielded from the outside light. The wire is connected to a DC supply operating in the constant-current mode. The wire of the anemometer must withstand relatively high temperatures, of about 1000°C. A thin platinum wire, 0.05 or 0.1 mm in diameter and 2 cm long may serve for this aim. For a 0.1 mm platinum wire, the heating current is about 5.5 A. In professional hot-wire anemometers, the wire is much thinner and shorter. The voltage across the load of the photodiode is measured by the *Voltage sensor*. For determining the angle dependence of the signal, the anemometer is mounted on the axle of the *Rotary motion sensor*. The cooling effect of the air motion reaches a maximum when the air moves perpendicular to the wire.

Advantages of hot-wire anemometry are the fast response of a thin wire and capability of local measurements. A homogeneous air motion, which can be measured with other tools, serves for the calibration. The aim of the project is to build a hot-wire anemometer and to find the best operation conditions for it. In fact, there are only three parameters to vary: the diameter and length of the wire, and the heating current. It would be useful to compare the sensitivity of the device when measuring the resistance of the wire and when using a photodiode.

10.6. Demonstrations with a microscope

Several demonstrations can be arranged with a microscope equipped with a video camera and a monitor. For student experiments involving a microscope, see Peidle *et al* (2009).

Hooke's law. For this demonstration a wire, 0.1–0.2 mm in diameter, is needed. One of its ends is fixed, while the other is loaded by a weight. The wire passes beneath the objective of a microscope (Fig. 1). The elongation of the wire when changing its load is seen on the screen of a monitor. A necessary mark on the wire can be made by dust. Young's modulus of the material is available from the data.

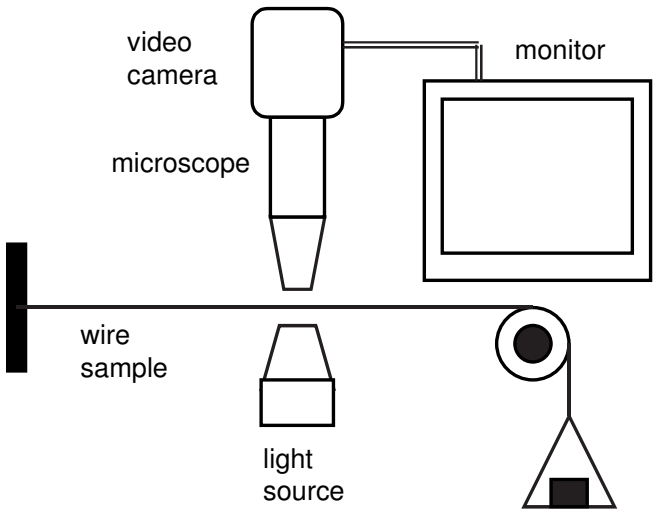

Fig. 1. Schematic of the setup with a microscope and a video camera.

Thermal expansion. A DC current heats a thin wire. The current and the voltage drop across the wire provide data on its electrical resistance. The temperature coefficient of the electrical resistance of copper at room temperatures equals nearly 0.4% per degree. By changing the heating current, one observes the elongation of the wire. The coefficient of thermal expansion of copper at room temperature is 1.65×10^{-5} K^{-1}. To observe thermal expansion of a wire 1 m long, it is sufficient to increase its temperature by 10–20 K.

10.7. Stokes' viscometer

Two variants of a viscometer based on Stokes' law and applicable to opaque liquids are proposed.

Oscillator technique. This viscometer was designed long ago for measurements with opaque liquids or under high pressures, where optical sensors are difficult to use (Kraftmakher 1957). Two coils are wrapped, at a definite distance, on a glass tube, which is filled with a liquid to be studied. The coils connected in series and a capacitor in parallel to them constitute a resonant LC circuit, continuous oscillations in which are generated due to the positive feedback (Fig. 1). A metal ball, preferably ferromagnetic, falls in the liquid. When passing through the coils, the ball slightly modifies the frequency of the oscillations and the *Q*-factor of the LC circuit. You have to choose a method for sensing the ball (see Experiments 10.9 and 10.17) and determining the time interval of the fall between the two coils.

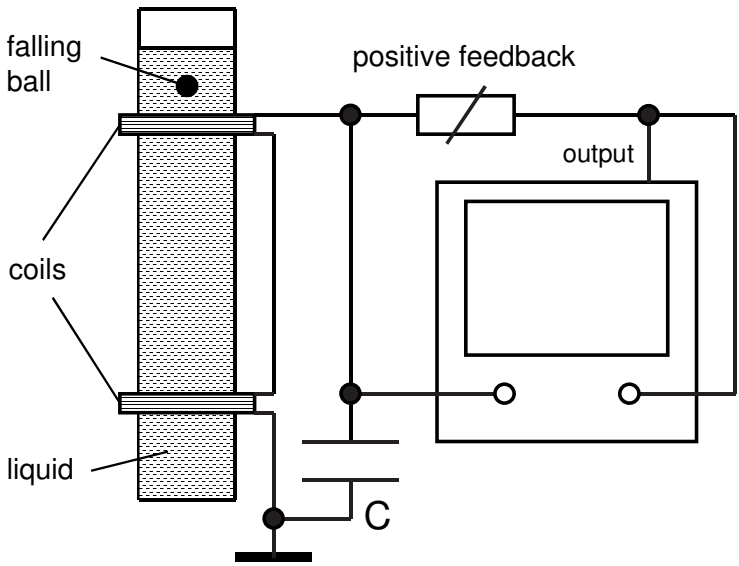

Fig. 1. Schematic of a viscometer with an oscillator sensing metal ball.

Viscometer with a differential transformer utilizes a differential transformer (see Experiment 6.9). Two primary coils L_1 and L_2 connected in series are fed by the *Signal generator*. Two secondary coils L_3 and L_4 are connected in series, but in opposition to each other (Fig. 2). The transformer is adjusted to nullify its output voltage. When a metal ball passes through a coil, an output voltage appears. This voltage is observed and amplified by an oscilloscope, converted

into a DC voltage and acquired by *DataStudio*. The *Graph* tool displays two peaks spaced by the time necessary to travel between the two coils.

With the viscometer, the strong temperature dependence of the viscosity of glycerol can be demonstrated. The liquid is heated up to about 60°C. Many runs can be done during the cooling period. Each run provides data for a certain temperature, which is measured with a thermistor or a usual glass thermometer. For transparent liquids, two photogates can be used.

For experiments on Stokes' law, see Mason and Moloney (1977); Dowd (1978); Greenwood *et al* (1986); Auerbach (1988); Lindgren (1988).

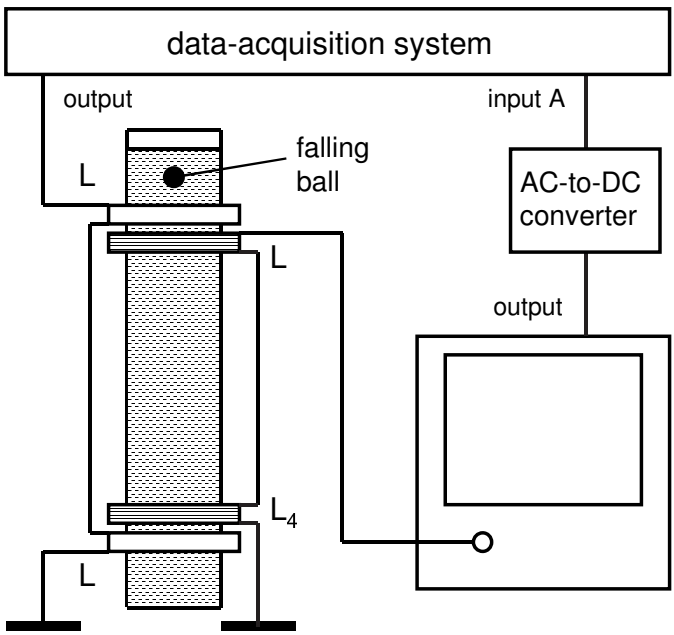

Fig. 2. Schematic of viscometer with a differential transformer.

10.8. Contactless measurement of resistivity

Contactless determinations of resistivity are based on applying an AC magnetic field to a sample and observing manifestations of eddy currents induced in it.

One variant of contactless measurements of resistivity of nonmagnetic metals and alloys is used. A sample, in the form of a cylinder, is placed inside a coil included in a resonant LC circuit. For not very high frequencies, the main effect of eddy currents is a decrease of the magnetic field inside the sample. The inductance of the coil thus decreases, and the resonance frequency of the circuit increases. A simple method for detecting this increase is creating continuous oscillations in the LC circuit. This can be done with an amplifier and positive feedback (see Experiment 10.17).

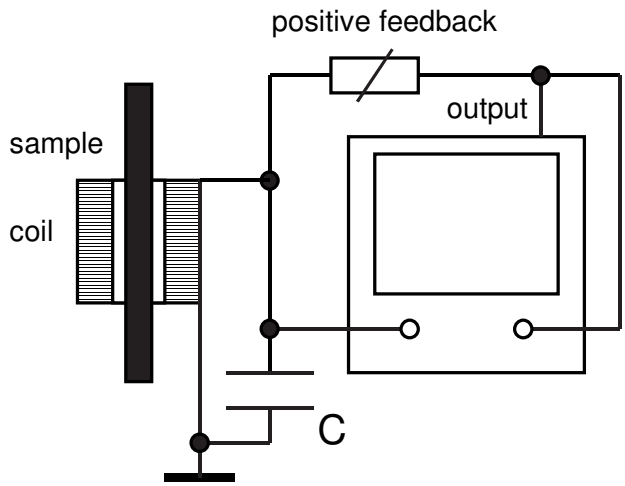

Fig. 1. Diagram of setup employing the oscillator technique.

The setup includes an LC circuit, an amplifier, and a variable resistor in the feedback circuit. An oscilloscope may serve as the amplifier (Fig. 1). With a fixed resistor in the feedback circuit, the generation threshold is achieved by adjusting the gain of the oscilloscope. To obtain significant changes of the frequency due to a conducting sample, its diameter should be close to the inner diameter of the coil. The frequency of the oscillations is of the order of 10^4 Hz and is measured with a frequency meter (not shown in Fig. 1). The aim of the project is to build the setup and calibrate it with samples of known resistivity. Another subject of interest may be the dependence of the results on the sample diameter.

10.9. Metal detection and the Theremin

This demonstration shows a sensitive method for detecting metals (Kraftmakher 2005h). The setup uses the beat oscillations technique and equipment usually available in student laboratories. The setup serves also as the Theremin, a famous electronic musical instrument.

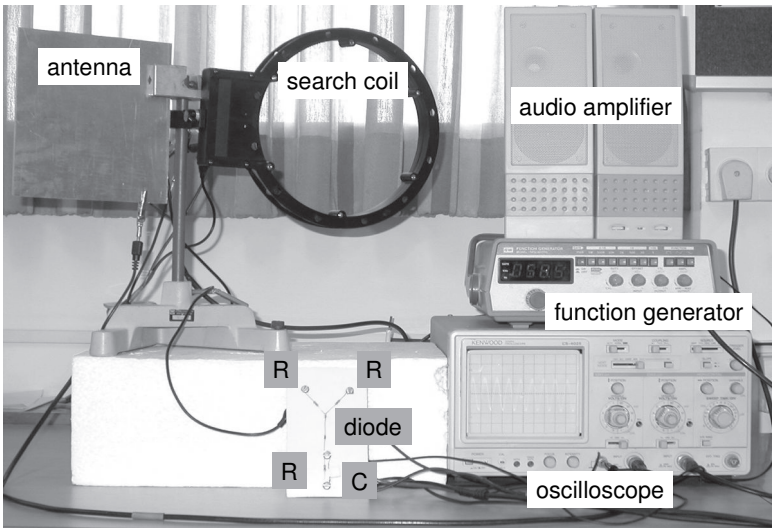

Setup for metal detection and playing melodies. $R = 1$ kΩ, $C = 0.1$ μF.

Nowadays, the detection of metals has become more important than ever before. Everyone may be subjected to such detecting, for example at airports. The aim of the demonstration is to show the metal detection technique appropriate for both magnetic and nonmagnetic metals. The detection of nonmagnetic metals is based on positioning a conducting sample in an AC magnetic field. According to Faraday's law, the AC field induces an EMF and eddy currents in the sample. The eddy currents modify the magnetic field in the sample. For samples of simple geometry, the changes in the magnetic field can be used for contactless determinations of the resistivity of metals and semiconductors (see Experiment 6.9). Several techniques are known for detecting eddy currents in a sample. Of these, the beat oscillations technique is simple and very sensitive.

About a century ago, the same principle was used to design the first electronic musical instrument, the famous Theremin. The design of this instrument has been considered in many sources. In particular, Skeldon *et al* (1998) described two versions of this device. The present apparatus is much simpler because it employs usually available off-the-shelf equipment. The setup for demonstrating metal detection and melody playing may be assembled in minutes. For the demonstration, one needs an oscilloscope, a high frequency

oscillator, an audio amplifier with a loudspeaker, a search coil, a semiconductor diode, four resistors, and one capacitor.

Beat oscillations. The beat oscillations technique involves two high frequency oscillators (Fig. 1). One of them contains a search coil, whose inductance, along with the capacitance, governs the resonance frequency according to Thomson's formula, $\omega_1 = 1/\sqrt{LC}$. An AC current flowing through the search coil creates a magnetic field around it. When the coil is placed near a metal sample, eddy currents in the sample affect the magnetic field and thus the inductance of the coil and the oscillator frequency. The change in the frequency depends on the geometry of the sample and the resistivity of the metal. The second oscillator has a constant but adjustable frequency ω_2.

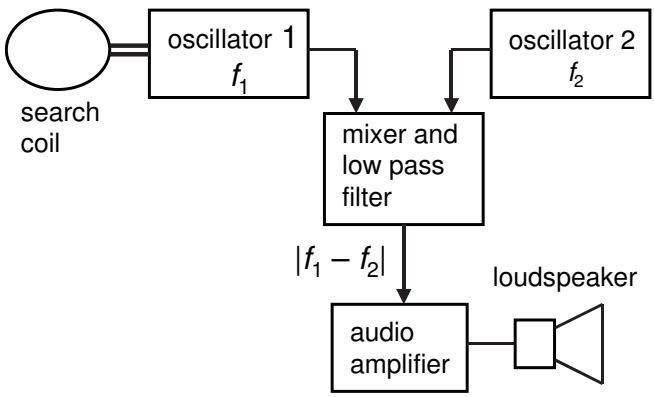

Fig. 1. Diagram of beat frequency apparatus for detecting metals.

A difference frequency, $|\omega_1 \pm \omega_2|$, appears when the two high-frequency voltages are fed to a semiconductor diode. Due to the nonlinearity of *I–V* characteristic of the diode, the output current contains, along with components of the main frequencies ω_1 and ω_2, components of additional frequencies, generally given by $|n_1\omega_1 \pm n_2\omega_2|$, where n_1 and n_2 are integers. The amplitudes of these components may be very different, according to the characteristic of the nonlinear device. For a quadratic *I–V* characteristic, the diode current is proportional to

$$(A_1\sin\omega_1 t + A_2\sin\omega_2 t)^2 = A_1^2\sin^2\omega_1 t + 2A_1\sin\omega_1 t\, A_2\sin\omega_2 t + A_2^2\sin^2\omega_2 t. \quad (1)$$

The second term on the right-hand side of this equality contains $\omega_1 + \omega_2$ and $\omega_1 - \omega_2$ components. The low-frequency signal is amplified and then fed to a loudspeaker. A low-pass filter suppresses signals of high frequencies. The frequency of the audio signal obtained is very sensitive to a piece of metal close to the search coil. Now it will be more convenient to deal with usual frequencies, $f = \omega/2\pi$. Let us suppose, for instance, that the frequencies of the two oscillators are of the order of 10^6 Hz, while the beat frequency is in the range 10^2 to 10^3 Hz.

In this case, the human ear can detect changes in the frequency of the order of 10 Hz, which equals 0.001% of the high frequency governed by the inductance of the search coil. With an electronic meter, the sensitivity is limited only by the stability of the high-frequency oscillators.

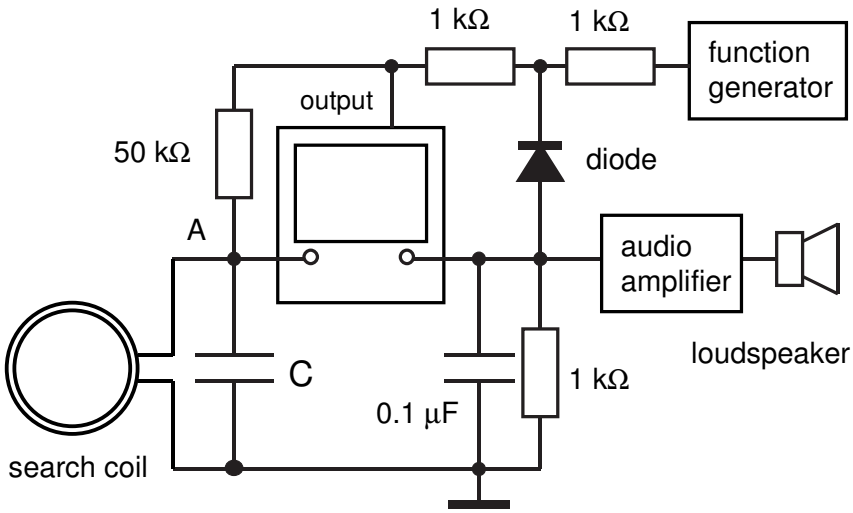

Fig. 2. Schematic of setup for detecting metals.

The setup and metal detection. The search coil is a 200-turn coil, 21 cm in diameter (EM-6711). The coil is connected to the input of an amplifier (Fig. 2). The capacitance C of the amplifier's input and of the connecting cable forms the capacitance of the LC circuit. As the amplifier, we use a Kenwood CS-4025 oscilloscope. One of its channels has an output terminal and provides gain up to 10^2. The output of the oscilloscope is connected to the coil through a 50 kΩ resistor. This positive feedback compensates for losses in the LC circuit and causes continuous oscillations in it.

The signal of frequency f_1 taken from the output of the oscilloscope is fed to a semiconductor diode. A GoodWill GFG-8020G function generator provides the signal of frequency f_2. Any other high-frequency oscillator can be used. A parallel RC circuit, placed as the load of the diode, reduces all high-frequency components of the output voltage and retains the audio component, which proceeds to an audio amplifier and then to a loudspeaker. It is also fed to the second channel of the oscilloscope and is seen on its screen. The output resistances of the oscilloscope and of the function generator should be taken into account. In our case, they equal 50 Ω. The audio signal may appear even without a special nonlinear device, when the two high-frequency signals are fed to the audio amplifier: the nonlinearity of the amplifier itself provides the necessary nonlinear operation.

It is necessary to set the gain of the oscilloscope for triggering continuous oscillations in the LC circuit and to tune the function generator to obtain an

audible beat frequency. The frequency f_2 may be higher or lower than f_1. A nonmagnetic sample causes a decrease in the inductance of the search coil, in accordance with Lenz's law. The frequency f_1 thus increases. In our case, this frequency is nearly 58 kHz. The audio signals appear when the frequency f_2 is set near 29 kHz ($2f_2 \approx f_1$), 58 kHz ($f_2 \approx f_1$), or 116 kHz ($f_2 \approx 2f_1$). The additional signals are produced due to the interactions of harmonics of the basic frequencies. As the sample, we use an aluminum alloy plate 2 mm thick. This plate, when brought close to the search coil, produces significant changes in the beat frequency. It is useful to demonstrate that the effect of the sample is maximum when the plate is parallel to the plane of the coil. This configuration allows the production of the largest eddy currents in the plate and thus the greatest influence on the inductance of the search coil. In our case, the maximum change in the beat frequency amounts to about 1 kHz. When the plate is placed perpendicular to the plane of the coil, its small thickness does not allow for high eddy currents. This demonstration shows why magnetic cores of common transformers contain many thin sheets made of ferromagnetic materials of high resistivity. To increase the sensitivity of the device, the high frequency of the oscillators should be increased. A search coil of smaller number of turns is needed for this aim.

Dead zone. If two oscillators of close frequencies are coupled, a specific phenomenon occurs, the synchronization (locking) of the oscillators. When the two frequencies fall into a narrow frequency range, they converge into one frequency. For beat frequency oscillators, this means the appearance of a dead zone, in which the beat frequency remains zero regardless of the tuning of the oscillators (Fig. 3). To decrease the zone, the coupling between the oscillators must be reduced.

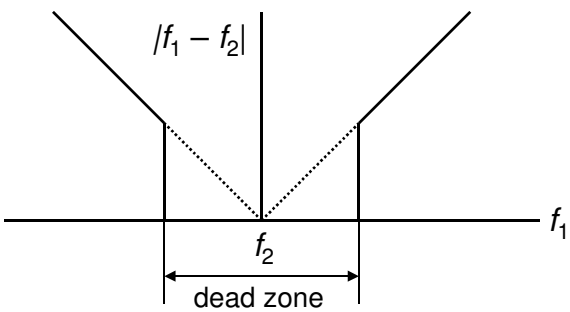

Fig. 3. Due to synchronization (locking) effect, a dead zone appears.

When detecting magnetic materials, the magnetic field in the sample and thus the inductance of the search coil increase. Usually, this effect is stronger than that due to the eddy currents in the sample, and the change in the beat frequency is opposite to that caused by a piece of a nonmagnetic metal.

The Theremin. In 1920, a Russian radio engineer Lev Termen (1896–1993) designed a beat frequency device as an electronic musical instrument. The instrument was named Termenvox, that is, the voice of Termen. Beginning in 1925, Lev Termen (known also as Léon Théremin) took his instrument on tour around Europe and the USA. At that time, it was indeed amazing to see a mysterious instrument playing without any physical contact with the performer. The pitch of the instrument was controlled by the proximity of the player's hand to an antenna. The other hand controlled the sound volume, also without physical contact. Termen spent about ten years in New York developing electrical musical instruments, the Theremins, until he suddenly vanished without a trace in 1938. Termen was thought to be dead, but after many years he was found in Moscow. His unbelievable story, with the crucial role of the KGB, may be found elsewhere (see Holonyak 1999, and references therein).

After considering the beat oscillation technique and metal detection, it is easy to explain the operation of the Theremin. The beat frequency depends also on the capacitance of the LC circuit of one of the high-frequency oscillators. For this purpose, an antenna, a metal plate or a rod well isolated from the ground, should be electrically connected to the LC circuit and positioned conveniently for the player. The player's hand can be considered as a grounded conductor. Its position near the antenna affects the capacitance of the LC circuit and thus the frequency of the audio signal. The other hand controls the sound volume by changing the frequency of an additional beat frequency oscillator. This beat frequency is translated into voltage, which governs the gain of the audio amplifier. After a short period of training, a musician becomes capable of playing simple melodies with this instrument. The synchronization (locking) of the high frequency oscillators of the Theremin is very undesirable. For reproducing low frequencies, the dead zone should not exceed 100 Hz.

To play melodies with the above apparatus, it is sufficient to arrange an antenna, a metal plate connected to point A in Fig. 2. Our demonstration setup provides two possibilities for governing the audio frequency: either by a piece of metal close to the search coil or by a hand close to the antenna plate. Theremins, as well as beat frequency oscillators and metal-detecting tools, are commercially available. A beat frequency oscillator can immediately be adapted to play melodies: it is sufficient to add an antenna to the LC circuit of one of the high-frequency oscillators.

Returning to metal detection, it is worth mentioning that there are some additional options for detecting ferromagnets. Ferromagnets display a variety of distinctive properties, which are more informative than the resistivity of nonmagnetic metals. The magnetization curve of a ferromagnet, that is, the dependence of the magnetization on the external magnetic field, is very individual. This provides a way to distinguish between keys in a customer's bag and thin ferromagnetic labels fixed to goods in a shop. An intriguing question is how to disable the label at the cash desk after a purchase and how to restore the label if necessary. Rich information about metal detection and the Theremin can be found on the Internet.

10.10. Recording magnetometer

A recording magnetometer is made out of a microammeter (Kraftmakher 1999).

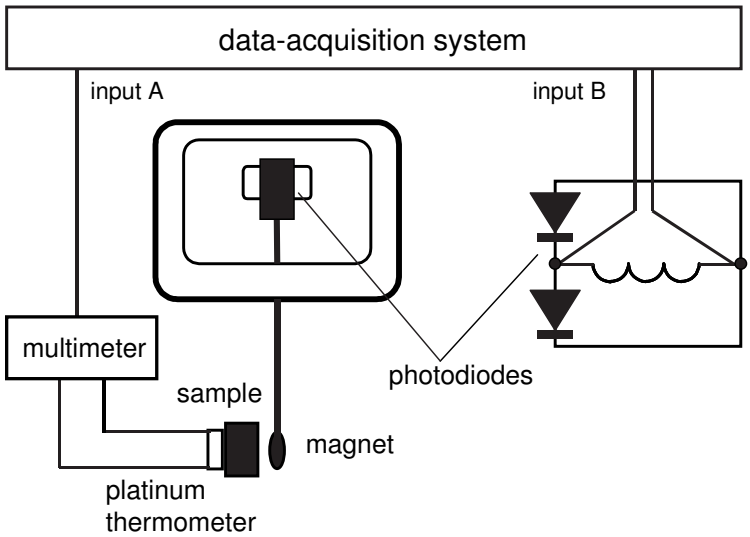

Fig. 1. Principle of operation of the recording magnetometer.

A rectangular paper screen is pasted to the pointer of a moving-coil meter, and two photodiodes are mounted beneath the screen (Fig. 1). The photodiodes are connected to the coil of the meter in opposition. A piece of copper wire 0.5 mm thick and 15 cm long is soldered to the movable part of the meter on the side opposite to the pointer. A small NdFeB permanent magnet, 5 mm in diameter and 1 mm thick, is glued to the end of this wire. The photodiodes beneath the screen are illuminated by a light bulb. In the absence of a sample, their currents are nearly equal, so that the current passing through the coil of the meter is about zero. With a superconducting sample near the magnet, a repulsing force arises between the sample and the magnet. The displacement of the movable part of the meter causes a redistribution of the light flux falling onto the photodiodes, and a current passes through the coil of the meter. This current produces a torque opposite to that caused by the interaction between the sample and the magnet. Owing to this negative feedback, the displacement of the magnet is small, whereas the current passing through the coil is nearly proportional to the interaction force. The voltage drop across the coil is fed to a plotter or to a data-acquisition system.

The magnetometer is similar to those developed by Lin and Berger (1989) and Weeks (1990), but provides an electrical signal corresponding to the torque to be measured. Valenzuela *et al* (1999) also measured the interaction force between a high temperature superconductor and a permanent magnet. Adhikari

et al (2012) developed a sensitive cantilever beam magnetometer to measure the magnetization and magnetostriction of ferromagnets.

For recording the transition curve of a superconductor, a ceramic sample of YBCO was prepared as a tablet, 12 mm in diameter and 3 mm thick. After preparation, it was sealed with epoxy resin for avoiding any interaction between the sample and the environment. The sample is attached to the inner side of an aluminum box thermally linked to the liquid nitrogen in a Dewar flask. The magnet of the magnetometer is positioned opposite to the sample (Fig. 2).

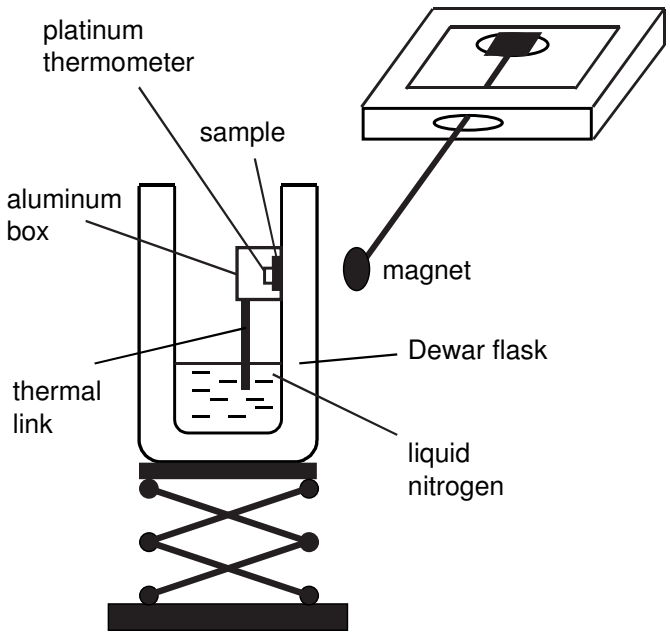

Fig. 2. Arrangement for recording phase transition from superconducting to normal state.

The Dewar flask containing liquid nitrogen rests on a laboratory jack. The sample is cooled in the liquid nitrogen far from the magnet (zero-field cooling) and then brought near it to obtain an electrical signal from the magnetometer. The second possibility is to place the sample near the magnet and cool it by lifting the Dewar flask (field cooling). After lowering the Dewar flask, the sample appears above the liquid nitrogen, so the temperature of the sample starts to increase. A resistive heater inside the Dewar flask can be used to evaporate the nitrogen and thus enhance the heating rate that should be of the order of 1 $K.min^{-1}$. A small platinum thermometer is pasted to the sample; its resistance is measured with a Keithley 177 multimeter. *DataStudio* displays the transition curve from the superconducting to the normal state.

10.11. Lock-in detector in a matchbox

An LED–LDR combination demonstrates the lock-in detection technique.

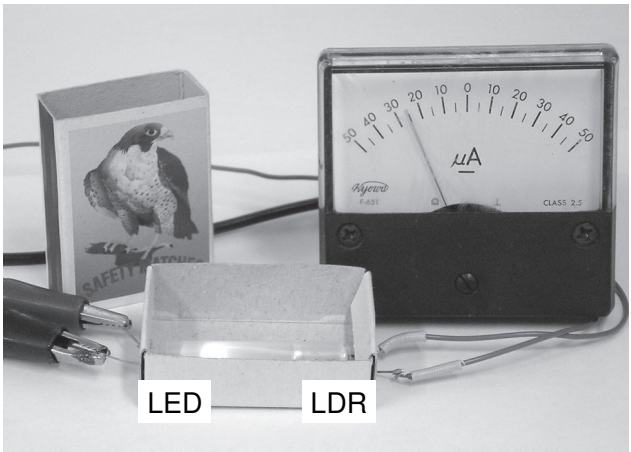

The lock-in detector in a matchbox is a LED–LDR combination.

The circuit. A simple circuit is capable of demonstrating the lock-in detection technique (see Experiment 4.12). A square wave reference voltage is fed to a light-emitting diode (LED). A light dependent resistor (LDR) senses the incoming rectangular light pulses. The LDR is connected in series with the source of the expected signal and a zero-centered DC microammeter (Fig. 1).

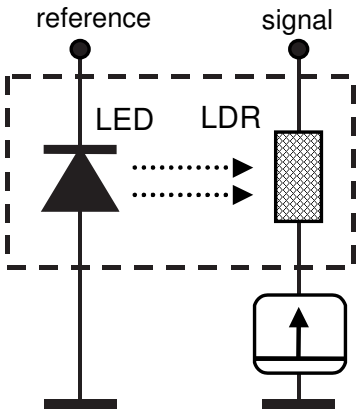

Fig. 1. LED–LDR circuit performs lock-in detection operations.

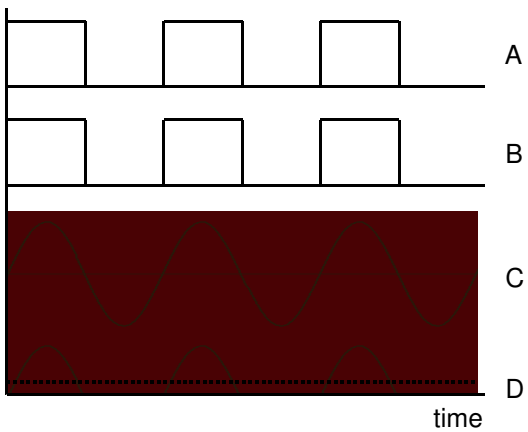

Fig. 2. Diagram of operation of the circuit. Dotted line is averaged output voltage.

This simple circuit is not equipped with a phase shifter, and we suppose the expected signal to be in phase (or in opposite) to the reference. The operation of the circuit is clear from a diagram shown (Fig. 2). The square wave voltage applied to the LED (reference) produces light pulses (A). For low frequencies, the electrical conductance of the LDR (B) follows these pulses. The signal (C) meets a very low resistance during light pulses and a very high resistance between them. The current through the microammeter thus represents positive half-periods of the sine wave (D). The microammeter, due to its inertia, serves also as an averaging stage. Its steady deflection occurs only when the signal contains a component of the reference frequency. A disadvantage of the circuit is that the negative half-periods of the signal are not detected at all. However, simply changing the polarity of the signal or of the reference voltage shows their presence. It remains to say that the LED and LDR are put inside a matchbox, and the device needs no additional power supply. The operations of the lock-in detector can be monitored with an oscilloscope or a data-acquisition system.

Spectrum analyzer. The device can operate as a spectrum analyzer. For this purpose, a square wave voltage of adjustable frequency from a function generator serves as the reference. When its frequency approaches the frequency of a component present in the signal, the moving part of the meter starts to oscillate around its zero point. The frequency of the oscillations, which equals the difference between the frequencies of the two voltages, should be decreased to obtain the ultimate amplitude of the oscillations. In this case, the amplitude becomes proportional to the amplitude of the related frequency component in the signal. For instance, the device may serve for harmonic analysis (Fig. 3).

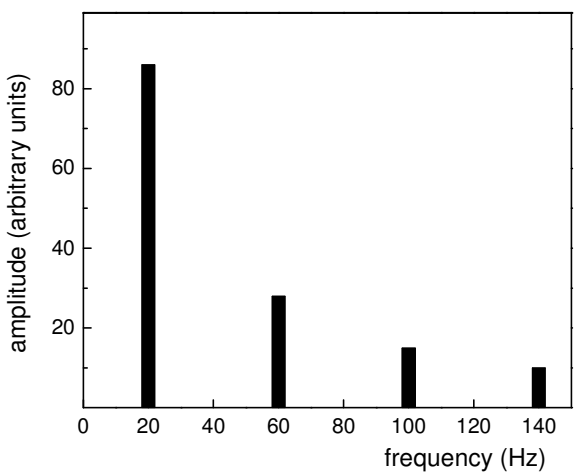

Fig. 3. Spectrum of a square wave voltage determined with the lock-in detector.

The LDR employed is very sensitive to illumination, but has a relatively large time constant. The device thus operates only at low frequencies. To

overcome this drawback, an electronic switch controlled by the reference voltage can be used instead of the LED–LDR combination (Fig. 4).

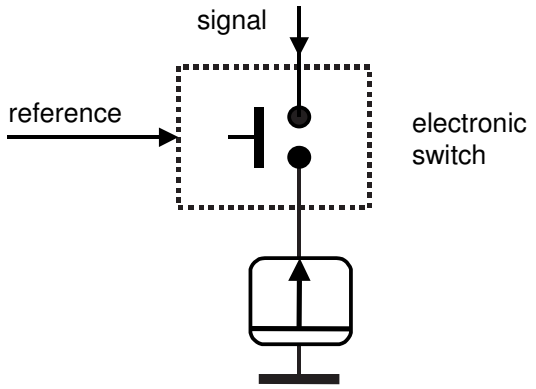

Fig. 4. Schematic of lock-in detector with electronic switch.

Phase shifter for the detector. The next step recommended for this project is adding a phase shifter. The amplitude of its output signal should not depend on the signal frequency. A well-known circuit (Fig. 5) is suitable for this aim. Clearly, the vectors **AD** and **DB** are perpendicular to each other. When changing the variable resistor R, the point D moves along the circle, and the phase shift between the vectors **AB** (input) and **CD** (output) changes nearly from 0 to 180°. The output voltage is half the input signal, regardless of the frequency. An input transformer is necessary when one point of the output should be grounded.

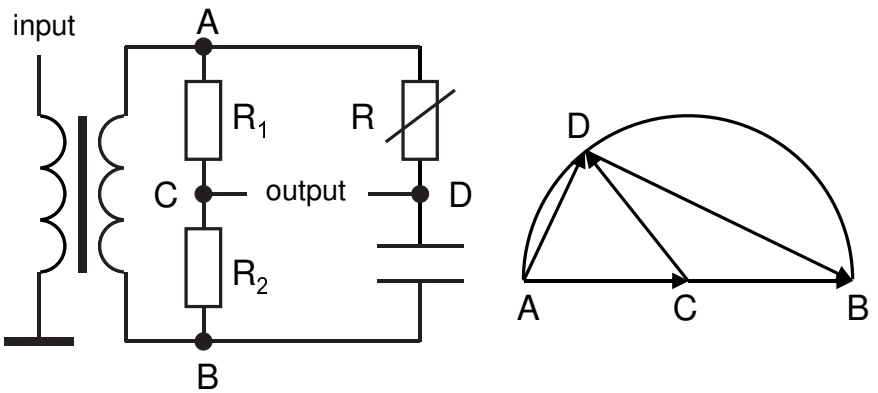

Fig. 5. Phase shifter, for which the amplitude of output voltage does not depend on frequency. $R_1 = R_2$.

10.12. Measurement of thermal radiation

A simple setup senses the incident thermal radiation (Kraftmakher 2008c). Earlier, Hager (1965) and Wieder and Jaoudi (1978) described devices for this purpose.

Design and calibration of the sensor. Two simple tools may serve for determining the power of incident thermal radiation (see Experiment 5.11). The first sensor is made out of a thin copper foil, painted black and provided with current and potential leads. Its absorptivity is supposed to be 100%. The sensitive area of the sensor is 2.6 cm^2, and its resistance, between the potential leads, is 12 mΩ. The sensor is fed by a DC supply operating in the constant-current mode and by a variable AC supply (Fig. 1). The AC supply consists of a variac and an insulating low-voltage transformer. The DC and AC currents are measured by multimeters. The DC current is used to determine the resistance of the sensor, which is a measure of the increment in its temperature and thus of the incident power. This current, 1 A, heats the sensor above the ambient temperature by about 1.5 K. The AC current serves to change the power dissipated in the sensor. The employment of the AC heating makes the calibration of the sensor much easier.

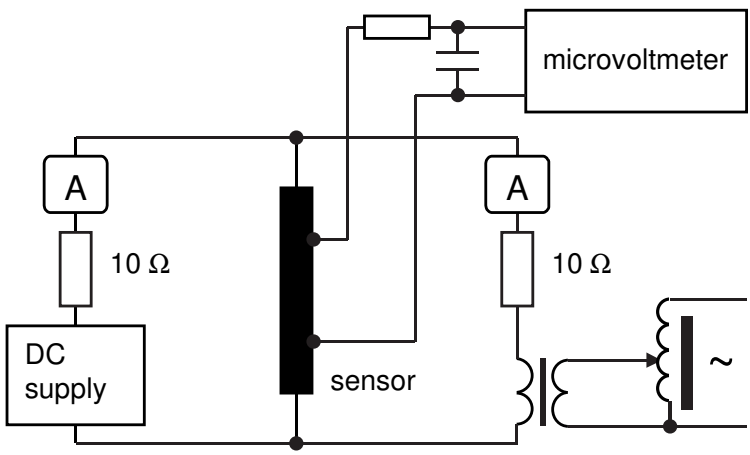

Fig. 1. Schematic of the circuit for measuring power of incident radiation.

With this sensor, a simple method can be used to compensate for changes in the ambient temperature during the measurements. A thin copper wire (not shown in Fig. 1) with potential leads is fed by a DC current from an additional source. The voltage between the potential leads is added to the voltage from the sensor. The DC current through the compensation wire is adjusted to balance the voltage from the sensor. In the absence of the irradiation and of the AC heating,

the output voltage is zero. Since the sensor and the compensation wire have the same temperature coefficient of resistance, this balance does not depend on the ambient temperature. The compensation wire is placed near the sensor, but is shielded from the irradiation. The output voltage is measured by a Keithley 197A multimeter of 1 μV resolution. An integrating circuit (R = 50 kΩ, C = 10 μF) is included at the input of the meter to suppress an AC component of the voltage that appears when an AC current passes through the sensor.

When the sensor is exposed to radiation, its resistance becomes higher: it increases by about 0.4% per kelvin. This increase is seen from the increase in the voltage from the sensor. For small temperature increments, the increase is proportional to the absorbed power. Only the coefficient of proportionality has to be known. It is available from measurements of the resistance of the sensor versus the AC electrical power dissipated in it. The calibration should be made with the same position of the sensor as when performing the measurements. Otherwise, changes in the heat losses from the sensor may cause significant errors. The increase in the resistance of the sensor is proportional to the dissipated electrical power (Fig. 2). In our case, the sensitivity of the sensor is about 6 $\mu\Omega.mW^{-1}$.

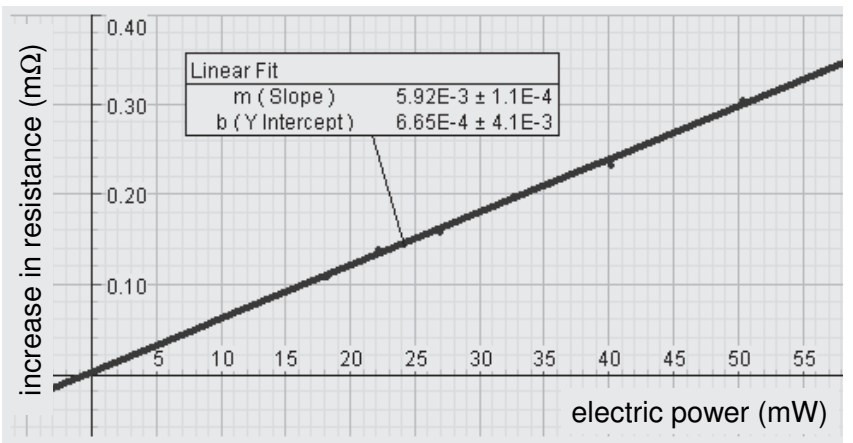

Fig. 2. Increase in resistance of the sensor versus electric power dissipated in it.

The incident power is measurable if it heats up the sensor by 1 K or more. When measuring the incident radiation, the AC current is zero. With the known sensitivity of the sensor, the incident power is readily available. Another method of measurement involves replacing the radiation heating by the AC heating. In this case, one observes the increase in the sensor's resistance caused by the irradiation, and then the same result is achieved with the AC heating. This procedure is more simple and more reliable than using a calibration graph. The advantages of the sensor are quite evident: (i) it is a self-calibrated tool; (ii) it is easy and not expensive to manufacture such a sensor.

The second sensor differs in that its temperature is measured through the resistance of a miniature thermistor pasted to the back of the sensor. The high sensitivity of the thermistor, about 4.5% per kelvin, allows one to employ a simple multimeter to measure its resistance. The sensitive area of this sensor is about 1 cm^2. The sensor is also provided with potential leads, so that both methods of measurement, through the resistance of the sensor and through the resistance of the thermistor, are possible. To compare the results obtained by the two sensors and using both methods of measurement, the irradiation from an incandescent light bulb was measured by both tools versus the electrical power applied to the bulb. The incident power per unit area was evaluated and used for the calculations. The results obtained are in good agreement. The scatter of the experimental points is less than 10% (Fig. 3). For measuring the solar radiation, the sensor with a thermistor is most appropriate because its resistance is measurable with a simple multimeter.

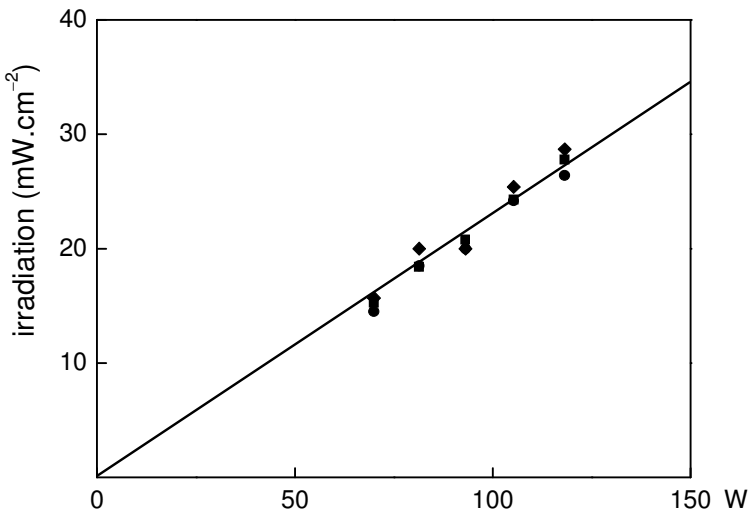

Fig. 3. Irradiation versus power applied to the lamp: ■ first sensor, ● second sensor, by its resistance, ♦ second sensor, by means of the thermistor.

10.13. Percolation board

The aim of the project is to build a "percolation board" and perform experiments with it.

Percolation is involved in a broad range of physical phenomena. One of the simplest such phenomena is the electrical behavior of a system of conducting particles dispersed in an insulating matrix. When the volume fraction of the conducting material p is lower than a critical value p_c, the composite remains in the insulating phase. When this fraction exceeds the critical value, the system becomes electrically conducting. Near the transition, the conductivity σ of the composite obeys the relations

$$\sigma = 0 \quad \text{if} \quad p < p_c, \tag{1}$$

$$\sigma = \sigma_0 (p - p_c)^t \quad \text{when} \quad p \geq p_c, \tag{2}$$

where t is the critical exponent.

Many papers and several books on percolation have been published. Scott (1972) presented a description of the phenomenon for beginners. The critical behavior of percolation has not been solved exactly, but it can be studied experimentally or with simulations. Stauffer (1977) described Monte Carlo simulations of percolation. Mehr *et al* (1986) developed an experiment to demonstrate the phenomenon. The electrical resistance of a 20×20 cm^2 sheet of conducting silver paper was measured between its opposite sides by a digital ohmmeter. Small squares, 0.5×0.5 cm^2, were then randomly cut out of this sheet. During the cutting, the resistance of the remaining paper was measured at concentration intervals of 1%, that is, every 16 sites. It was assumed that this system is an experimental realization of a percolation model. The critical concentration appeared to be $p_c \cong 0.59$. To overcome the problem of statistical fluctuations, it is possible to average the results of many measurements. Basta *et al* (1994) presented an introduction to percolation phenomena. An experiment for studying two-dimensional percolation was described by Schwartz and Ludueña (2004). The authors developed a computer program to draw small black particles over a white background. For different concentrations p, the particles were randomly placed on a 64×64 lattice. Then the layout was printed on an ink jet printer with conducting ink. The values of $p_c = 0.58$ (±0.005) and $t = 1.28$ (±0.07) were found.

The aim of the project is to build a "percolation board"—a device capable of unlimited realizations of the percolation process (Fig. 1). Electrical switches randomly switched on provide the necessary connections between individual cells of the board. Each connection includes a 100 Ω resistor. A multimeter measures the total resistance of the board. An important part of the project is the choice of the type of switches to be used. The switches should be as simple and cheap as possible. A board containing 30×30 cells seems to be quite realistic.

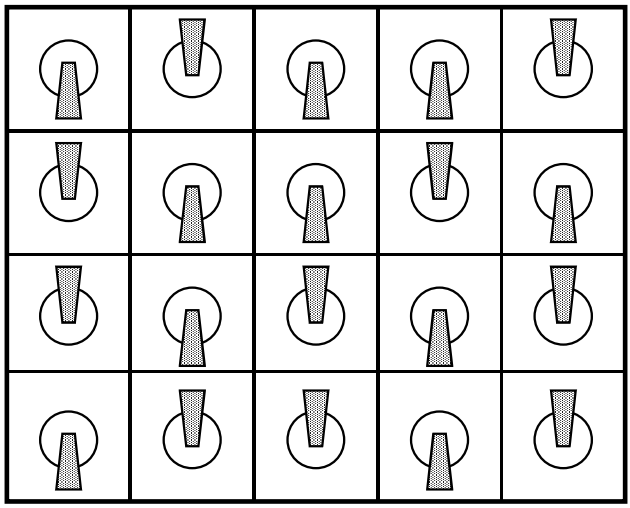

Fig. 1. Electric switches serve for connecting cells of the board. Only a part of the board is shown.

10.14. Clamp-on ammeter

Two models of the clamp-on ammeter employ a demountable O-shaped magnetic core (for instance, SF-8614).

The clamp-on ammeter is a tool commonly used by professional electricians (see Experiments 4.4 and 9.9). A basic advantage of this tool is that it allows measurements of electric currents without breaking the electrical circuit. The closed magnetic core forms a magnetic circuit with a coil wrapped around it (Fig. 1). The core embraces an AC current-carrying wire. The lines of the magnetic field produced by the current are concentrated in the magnetic core. The voltage induced in the coil is a measure of the current flowing through the wire. Hence, the clamp-on ammeter is based on Ampère's circuital law. Such a tool was already used in student laboratories (Henry 2001; Kamata *et al* 2002). In essence, it is a transformer with the current-carrying wire as the primary and the coil wrapped around the magnetic core as the secondary.

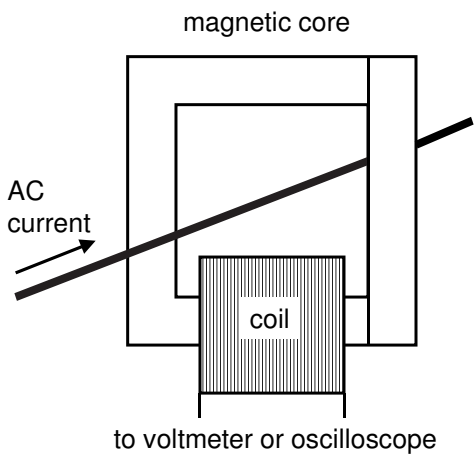

Fig. 1. Clamp-on ammeter for measuring AC currents.

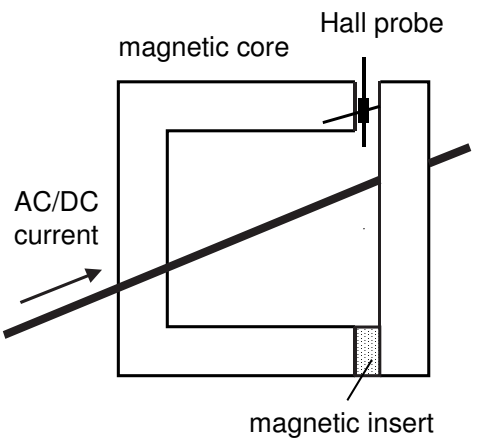

Fig. 2. Clamp-on ammeter for measuring both AC and DC currents.

A Hall probe is very suitable for contactless measurements of DC currents. In this case, a small gap is made for it in the closed magnetic circuit (Fig. 2). Clearly, this device is suitable for measurements of both AC and DC currents. The goal of the project is to build the two models of the clamp-on ammeter and perform the necessary calibration. It should be remembered that a gap in the magnetic core strongly reduces the sensitivity of the tool (see Experiment 6.5).

10.15. Variable inductor

Three methods to build a variable inductor can be considered.

Simple methods to build a variable inductor are the following (Fig. 1): (i) a coil with a ferro- or ferrimagnetic rod inside, which can be slid or screwed in and out of the coil; (ii) a coil with a magnetic core, permeability of which is controlled by a DC bias; and (iii) two connected in series magnetically coupled coils, where the coupling can be varied by changing the distance between the coils or the angle between their axes. The inductance of an inductor can be determined with a simple multimeter capable of measuring inductances. Also, the inductance is available by measuring the voltage drop across the inductor when an AC current passes through it. The frequency of the current should be chosen to make the impedance of the inductor much larger than its DC resistance.

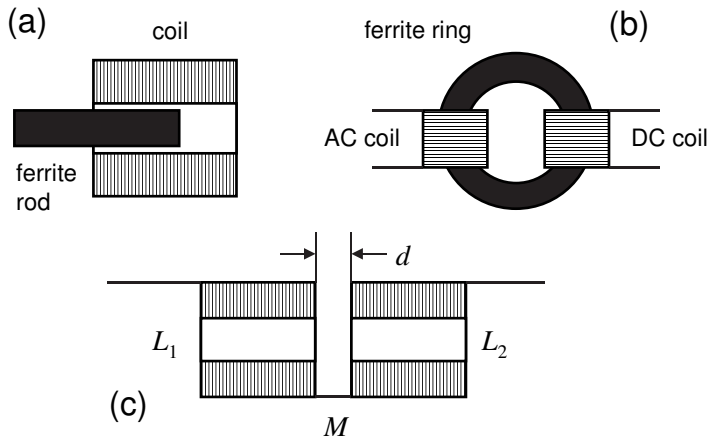

Fig. 1. Variable inductors: (a) coil with movable core; (b) core with controllable permeability; and (c) two magnetically coupled coils.

The items (i) and (ii) are obvious. With a ferrite rod, the inductance of a coil can be changed in a wide range. Also, a bias DC magnetic field effectively controls the inductance of a coil with a ferromagnetic or a ferrimagnetic core. To avoid AC currents in the bias coil, it should be connected to a DC supply through a resistor of sufficiently high resistance or a choke (see Experiment 6.7).

The inductance of a two-coil inductor is determined as a function of the distance between the coils, for two polarities of one of the coils. The inductance L of two coils connected in series equals

$$L = L_1 + L_2 \pm 2M, \tag{1}$$

where L_1 and L_2 are inductances of the coils with no coupling between the coils, and M is the mutual inductance between them. The mutual inductance is defined

through the EMF induced in one coil due to changes of the current in the second one (see Experiment 1.21). The mutual inductance is a function of L_1 and L_2 and of the coefficient of magnetic coupling between the coils, k:

$$M = k(L_1L_2)^{1/2}, \tag{2}$$

where $0 < k < 1$; the limits 0 and 1 cannot be achieved. When $L_1 = L_2$, the total inductance equals

$$L = 2L_1 \pm 2M = 2L_1(1 \pm k). \tag{3}$$

To achieve a maximum change in the variable inductor L, the coupling should be of changeable sign, and the coefficient k should be close to unity. A variable inductor based on changing the angle between the axes of the two coils is called variometer.

For the measurements, it is possible to use two similar coils from PASCO (EM-6711, 200 turns, or SF-8611, 800 turns). The coils connected in series are positioned on an optical bench. The inductance of the two-coil inductor is displayed versus the distance between the two coils, for both signs of the coupling between them (Fig. 2). The upper branch of the plot relates to the sign "plus" (due to the coupling, the inductance increases). At sufficiently large distances between the coils, both branches converge to one value (no coupling between the coils). An extension of the project could be manufacturing a variometer.

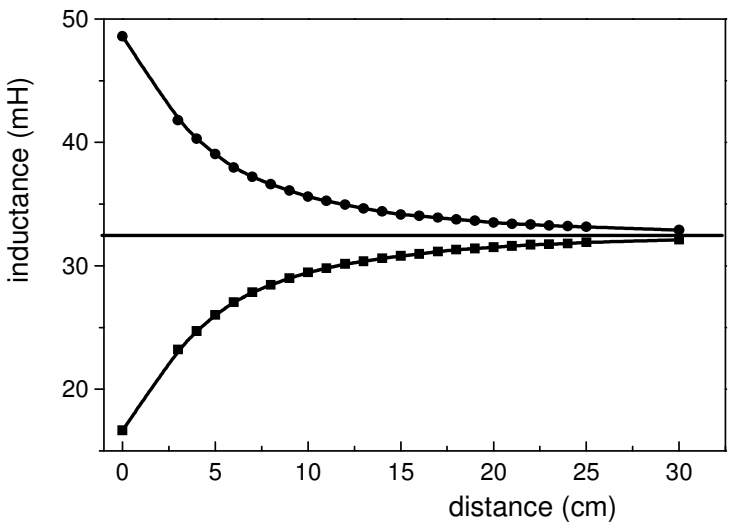

Fig. 2. The inductance versus distance d between edges of the EM-6711 coils, for two polarities of one coil.

10.16. Linear variable differential transformer

The aim of the project is to build and explore a model of a linear variable differential transformer (LVDT), a device for measuring small linear displacements.

The device contains a primary winding and a secondary winding consisting of two similar coils. These coils are connected in opposition, so the output voltage of the transformer is normally zero. Therefore, the windings form a differential transformer. A movable ferrite rod controls the magnetic coupling between the primary and secondary coils. The output voltage of the transformer strongly depends on the position of the rod, so the device becomes sensitive to small displacements (Fig. 1).

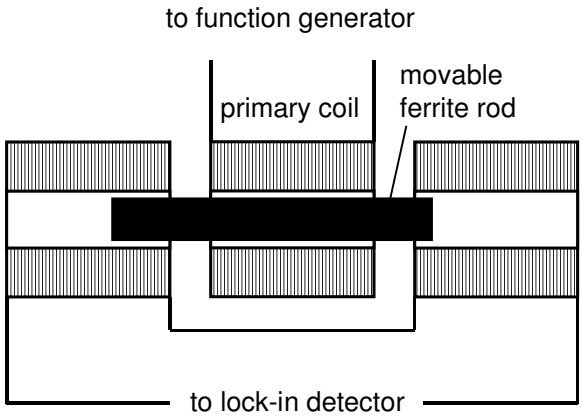

Fig. 1. Schematic of the model of linear variable differential transformer.

To model an LVDT, coils from PASCO (for instance, SF-8611, 800 turns) are usable. The primary coil is connected to a function generator through a 1 Ω resistor. The voltage across this resistor is fed to the X input of an oscilloscope, while the output voltage of the differential transformer to the Y input. A ferrimagnetic rod is attached to a mechanical device, whose displacements are measurable with a dial gauge. When the transformer is balanced, a horizontal straight line is seen on the screen of the oscilloscope. When the position of the rod relatively to the transformer changes, an output voltage arises, so that an ellipse is seen on the screen of the oscilloscope. This pattern does not tell us the direction of the displacement of the rod. To immediately clarify this point, the voltage for the X-input of the oscilloscope should be taken from an additional coil magnetically coupled to the primary coil of the differential transformer. This coil provides a voltage coinciding in phase with the output voltage of the differential transformer. In this case, a tilted straight line appears on the screen when the transformer is unbalanced; the direction of the line depends on the

phase shift between the voltages at the inputs of the oscilloscope (0 or 180^o), that is, on the sign of the displacement of the ferrite rod from the neutral position. After the device is built and its operation confirmed, the aim of the project becomes obtaining high real sensitivity.

Also, the lock-in detection technique can be employed to provide data including the direction of the displacement. The time constant of the lock-in detector should be sufficient to suppress an unavoidable noise and signals of other frequencies. It is possible to perform the lock-in detection operation with *DataStudio* (see Experiment 4.12). A screw mechanism with the *Rotary motion sensor* (see Experiment 6.3) provides small and controllable displacements of the ferrimagnetic rod.

10.17. Demonstrations with LCR circuits

Free and self-excited oscillations are demonstrated (Kraftmakher 2011b).

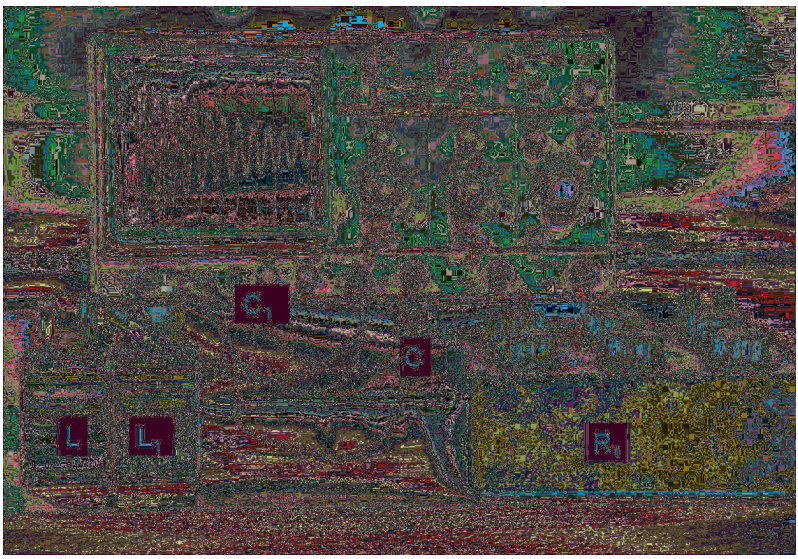

The demonstration setup.

The LCR circuit is an important topic in the course of electricity and magnetism (Chadha 1986; Ramachandran 1991; Mak 1994; Backman *et al* 1999; Morse 2005).

With a Kenwood CS-4025 oscilloscope, it is easy to demonstrate free oscillations in a series LCR circuit (Fig. 1). The circuit consists of an 800-turn coil (SF-8611), a 0.1 μF capacitor, and a variable 100 Ω resistor; instead of the latter, several fixed resistors can be used. The inductance of the coil is 12 mH. The capacitor C is connected to the Y input of the oscilloscope. Rectangular electric pulses from the oscilloscope (100/120 Hz, 1 V peak-to-peak), intended for calibration purposes, trigger the free oscillations. The source of the pulses is connected to the LCR circuit through a capacitor $C_1 = 1$ nF. The capacitor C_1 and the LCR circuit form a differentiating circuit, so short positive and negative electric pulses are periodically applied to the capacitor C (Fig. 1a).

Free oscillations. The first demonstration shows changes in the frequency and decay of the free oscillations caused by changing the parameters *C* and *R*. The frequency of undamped oscillations in an LC circuit is $\omega_0 = (LC)^{-½}$. Due to energy losses in the circuit, the frequency of free oscillations ω becomes lower: $\omega^2 = \omega_0^2 - \delta^2$, where $\delta = R/2L$ is called the decay constant. The resistance *R* reflects all sources of energy losses in the circuit: the resistance of the coil and of

the resistor added, losses in the capacitor, resistance of the source of rectangular pulses, input resistance of the oscilloscope input, and losses for radiation of electromagnetic waves (the resistance R is not shown in Fig. 1). In our case, $\delta^2 << \omega_0^2$, and ω is close to ω_0. The oscillations decay exponentially, so the amplitudes of the voltage across the capacitor C and of the current in the circuit are proportional to $\exp(-\delta t)$. The free oscillations are observed on the oscilloscope screen for several values of C and of the variable 100 Ω resistor.

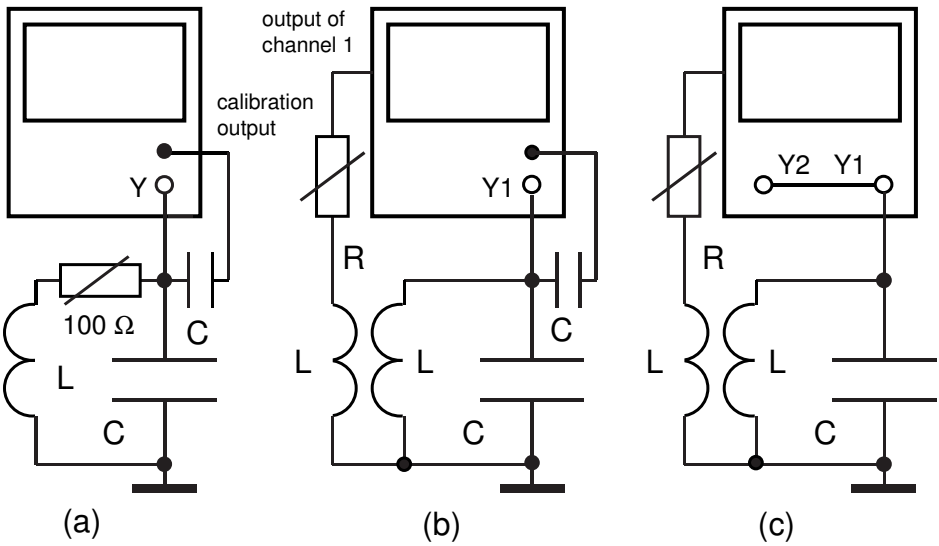

Fig. 1. The setups: (a) basic LCR circuit; (b) LCR circuit with feedback; (c) circuit for observing self-excited oscillations.

Magnetic or conducting core. In the second demonstration, a ferrite or an aluminum rod is put inside the inductor L. With the ferrite rod, the frequency of free oscillations decreases, while the decay of the oscillations becomes slower (Fig. 2). Due to the high permeability of the ferrite, the magnetic flux through the coil and its inductance also increase. With the aluminum rod, the frequency of free oscillations increases. When a conductor is subjected to an external AC magnetic field, eddy currents arise in it (Faraday's law). These currents tend to reduce the magnetic field inside the coil (Lenz's law). Therefore, the magnetic flux through the coil and its inductance also decrease. The magnetic field inside the conductor depends on the frequency of the magnetic field and the resistivity of the conductor. This phenomenon is called the skin effect and may serve for contactless measurements of resistivity of nonmagnetic conductors and for metal detection (see Experiment 6.9). With the aluminum rod inside the coil, the decay constant increases. An additional energy loss arises due to the eddy currents in the rod. For the ferrite rod, this effect is negligible due to the high resistivity of the ferrite.

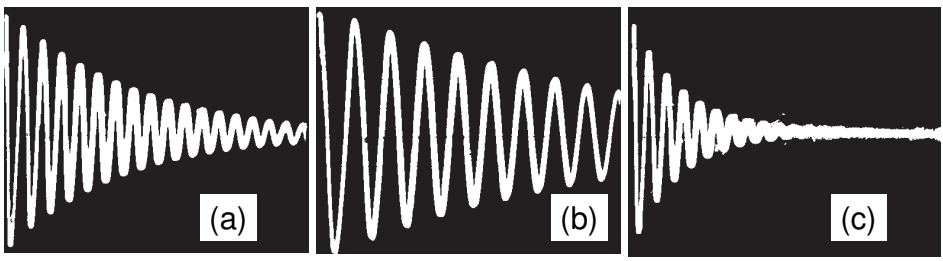

Fig. 2. Examples of free oscillations: (a) basic LCR circuit; (b) ferrite rod inside inductor; (c) aluminum rod inside inductor.

Circuit with feedback. The next experiment demonstrates positive or negative feedback (Fig. 1b). The Kenwood CS-4025 oscilloscope has an output terminal from the amplification channel 1 and serves also as an amplifier. The gain depends on the arranged sensitivity. The maximum gain achieved with the sensitivity of 1 $mV.div^{-1}$ is 100; for 0.1 $V.div^{-1}$, the gain becomes unity. The voltage across the capacitor C is amplified and then fed, through a variable resistor $R_1 = 5\ k\Omega$, to a coil L_1 (feedback coil) inductively coupled to the coil L. As the variable resistor, we use a decade resistance box (PI-9588). A 400-turn coil (SF-8610) serves as the feedback coil and is positioned adjacent to the coil L. The current in the feedback coil L_1 induces an EMF in the coil L. It is easy to see that this EMF is in phase with or opposite to the current in the LCR circuit, thus providing positive or negative feedback. The sign of the feedback depends on the polarity of the two coils. The feedback enhances or reduces the decay constant of the free oscillations, while the oscillation frequency remains the same (Fig. 3). Therefore, it is easy to distinguish the changes in the decay caused by the feedback and those due to the ferrite or aluminum rod inside the coil.

Self-excited oscillations. The strength of the feedback depends on the distance between the coils L and L_1, the amplification of the oscilloscope, and the resistance R_1. With positive feedback, continuous self-excited oscillations are achievable. For this demonstration, the calibration output is disconnected from the LCR circuit (Fig. 1c). For triggering self-excited oscillations, the energy supplied to the LCR circuit by the feedback should outweigh the energy losses. The decay constant δ becomes negative, so the oscillation amplitude should exponentially and unlimitedly increase. Clearly, this is impossible. When the oscillation amplitude increases, the amplification in the feedback circuit unavoidably decreases because the output signal of the circuit is evidently limited.

When self-excited oscillations are achieved, their amplitude becomes out of scale of the oscilloscope. To see the oscillations nevertheless, channel 2 of the oscilloscope is used. The capacitor C is connected to both channels: channel 1 provides the feedback, while channel 2 serves for observing the voltage across the capacitor. Intentionally, the inductor L and capacitor C were chosen to obtain

the resonance frequency of the LCR circuit in the audio range. To hear the oscillations, an audio amplifier with a loudspeaker is connected to the output of the channel 1. With the 800-turn coil and C = 0.1 μF, the resonance frequency is nearly 4.5 kHz. With the ferrite inside the coil, it becomes nearly 2.5 kHz, and with the aluminum rod nearly 5 kHz. The changes in the frequency thus become audible for the audience. Since the rods inside the coil L lead to changes in the decay constant, parameters of the feedback circuit should be readjusted for maintaining the self-excited oscillations. Instead of the variable resistor R_1, a suitable light dependent resistor (LDR) can be put in the feedback circuit, so that the continuous oscillations are initiated by illuminating the LDR.

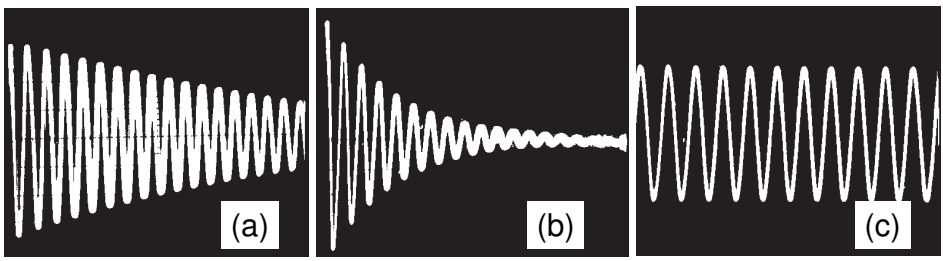

Fig. 3. Examples of oscillations with feedback: (a) positive feedback; (b) negative feedback; (c) self-excited oscillations.

The experiments provide good opportunity to consider some additional topics (permeability, skin effect, light dependent resistor). The self-oscillation amplitude strongly depends on the distance between the coils L and L_1 (or on the position of a magnetic core inside the coils) or on the resistance of the LDR in the feedback circuit. This feature can be used for designing sensors of position or illuminance.

10.18. Curie's point III

Curie's point T_C is a temperature, above which the spontaneous magnetization of a ferromagnet or a ferrimagnet vanishes (see Experiments 6.6 and 6.7).

Rotary magnetic engine. An impressive experiment by Toftlund (1987) shows Curie's point of gadolinium (Fig. 1).

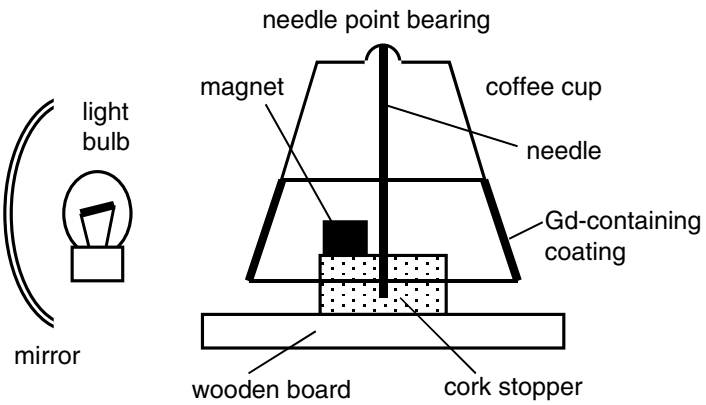

Fig. 1. Demonstration model of rotary magnetic engine (Toftlund 1987).

"The engine is mounted on a wooden board. A cork stopper is glued to the board, and a large needle is inserted into a vertical position with the point upward. A small powerful magnet is placed on the cork stopper with the poles a few centimetres from the needle shaft. A paste consisting of 99.9% pure gadolinium filings (20 g) and carbon black (2 g) stirred into cement (5 ml) is fastened to the outer surface of a small plastic cup in a 4–6-cm broad ribbon… A frictionless needlepoint bearing is made by gluing the bottom of a small test tube to the midpoint of the inner bottom of the cup. The whole cup can then balance on the needlepoint… The light source is placed at a distance of about 30 cm from the apparatus on the same side as the magnet, but in direction about 20° away from the shaft magnetic pole line. In this engine, radiant energy serves as the heat source, and the surrounding air as the heat reservoir. When sunlight or light from an electric lamp is irradiated perpendicularly onto the black surface of the gadolinium wheel, the surface temperature will quickly exceed the transition temperature T_C. The wheel will then rotate with a frequency determined by the rate of heat loss from the non-irradiated parts of the wheel" (Toftlund 1987).

Sample inside inductor. Lewowski and Woźniak (1997) put a gadolinium rod inside a small coil. The inductance of the coil was measured with a multimeter. By heating and cooling the sample around the transition point, the changes in the inductance demonstrate the phase transition.

Differential transformer. For this demonstration (Fig. 2), it is sufficient to heat up the gadolinium sample above Curie's point by hand.

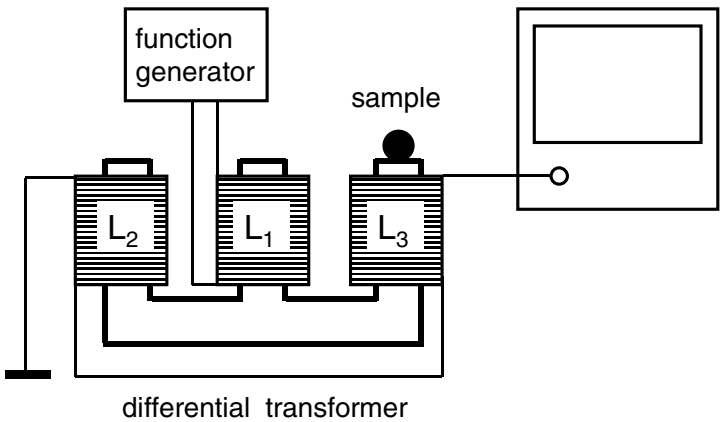

Fig. 2. Setup with a differential transformer.

Smart soldering iron. Magnetic control used in some types of soldering irons offers a good opportunity to demonstrate Curie's point. In such tools, the heating current passes through a magnetically controlled switch. The switch breaks out the circuit when the temperature exceeds Curie's point of the material used. When the temperature falls below Curie's point, the heating continues (Fig. 3). The necessary temperature is achieved in one minute and then starts to oscillate around a certain value. Various alloys provide choice for Curie's points. For the demonstration, the signal from the *Broad spectrum light sensor* viewing the soldering iron is displayed by *DataStudio*.

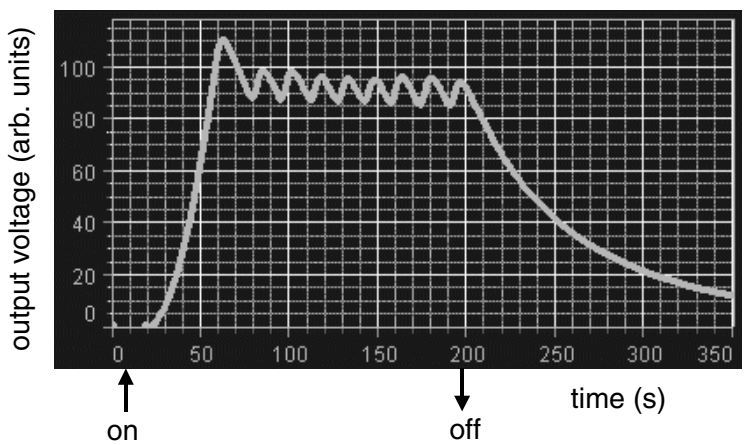

Fig. 3. Signal from *Broad spectrum light sensor* viewing the soldering iron.

10.19. Simple electro-musical instruments

Two variants of a simple electro-musical instrument employ a function generator, whose audio frequency is governed by a DC voltage applied to its VCF (voltage controlling frequency) or FM (frequency modulation) input.

The device proposed by Lev Termen is based on manually changing the light flux falling onto a light sensor like a light dependent resistor (see Experiment 7.6). A resistor R loads the LDR, and the player controls the voltage drop across it. This voltage being applied to the VCF or FM input of a function generator governs the frequency of its output voltage. A loudspeaker is connected to the output of the generator (Fig. 1). The same principle is applicable for manual control of the sound volume. A light dependent resistor and a fixed resistor constitute a voltage divider inserted between the output of the generator and the loudspeaker. The instrument can be arranged in a short time, but playing melodies with it is not a simple task.

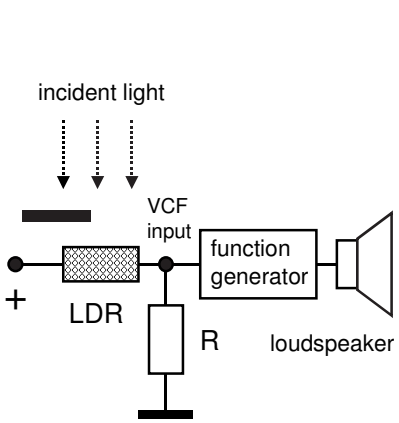

Fig. 1. Schematic of setup with LDR for playing melodies.

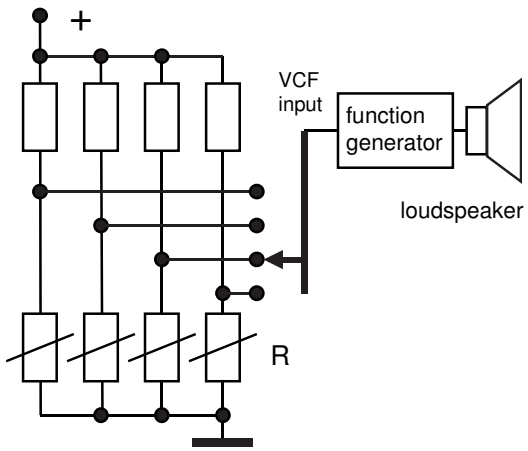

Fig. 2. Schematic of model of keybord musical instruments.

The second device employs the same principle of controlling the pitch of the function generator, but the controlling voltages are set beforehand for obtaining a set of definite output frequencies. In this case, the device is a keyboard instrument. A number of voltage dividers can be prepared to obtain controlling voltages for producing desired frequencies (Fig. 2).

10.20. Cavendish's great experiment

A simple addition to the popular Cavendish torsion balance is proposed for automatically recording the balance deflection.

AIP Emilio Segrè Visual Archives
Henry Cavendish (1731–1810)

The Cavendish experiment is one of the greatest experiments in physics. Even today, when the apparatus for this experiment became commercially available and very popular, it seems to be a *Mission Impossible*. Many papers have been devoted to this experiment and the design of Cavendish's torsion balance. Block *et al* (1965) described a homemade Cavendish balance. Crandall (1983) developed an electronic servomechanism to maintain rotational equilibrium as an external mass is introduced. To increase the rotation, Shaw (1983) used a periodic movement of the external mass to drive the balance into resonance and employed a position-sensitive photodiode for recording the balance angular displacement. Karim and Toohey (1986) developed a balance, in which eddy currents generated in the small lead spheres served for producing the required compensating torque. Clotfelter (1987) pointed out that Cavendish thought that he had measured the mean density of the Earth because the system of units at that time did not include a unit for force, so that a measurement of the gravitational constant was not a recognized problem. As a torsion spring for the balance, Dunlap (1987) used a Cu–Zr amorphous metallic ribbon, 16 μm thick and 0.89 mm wide. This makes the balance more stable and accurate. With significant improvements of the common gravitational apparatus, Dousse and

Rhême (1987) reported on 0.1% accuracy in the determinations of the gravitational constant. An optical tracking system with a servomechanism was developed, and a microcomputer served for driving the apparatus and controlling the data acquisition. Fischer *et al* (1987) reported on an automatic recording of the angular displacement of the balance with a two-element photodiode mounted on the pen carriage of a chart recorder. For the same purpose, D'Anci and Armentrout (1988) used a phototransistor and a recorder. Saulnier and Frish (1989) modified the balance by suspending it by a tungsten wire of about 12 μm in diameter and 1.9 m long. The restoring torque thus was very small, and the linear accelerations of the test masses were measured directly. Fitch *et al* (2007) automated the data acquisition for the Cavendish balance. The Cavendish torsion balance with automatic recording is now available from PHYWE.

The aim of the project is a simple addition to the original balance allowing for automatic recording the angular displacement of the balance. Two options considered below are applicable to any torsion balance and do not demand an invasion into it. An inexpensive position-sensitive photocell may be built using an extended photosensor, such as a solar cell. It should be positioned close to the gravitational balance, so that the reflected light beam always falls onto the sensor. A filter covering the sensor and having a position-dependent absorption makes the current delivered by the cell to be sensitive on the displacement of the balance. One can prepare the filter by printing it with a printer. The desired result is a linear dependence of the output current on the position of the light spot. With a data-acquisition system, a nonlinear dependence is also acceptable because it is easy to translate the signal obtained to the angular displacement of the balance. Second, a profiled screen may be used instead of the filter. In this case, the task becomes even simpler.

10.21. Optics communication

An optics communication line employs a laser diode and a photodiode.

Optics communication is one of very important modern technologies, and it is useful to learn it (see Experiment 9.10). Selvarajan and Ramakrishna (1979) described a laser communication system using an ultrasonic light modulator. Their transmitter included a He–Ne laser, a source of audio signals, a 10 MHz oscillator, an amplitude modulator, an amplifier, and an ultrasonic light modulator. The receiver included a photodiode and an audio amplifier with a loudspeaker. The 10 MHz subcarrier is modulated by the audio signals. Leung *et al* (1980) and Lee *et al* (2006) also described communication systems. With a laser diode or a light-emitting diode, a direct modulation of the light intensity is achievable by changing the applied voltage (Kraftmakher 2003; Mak 2004b).

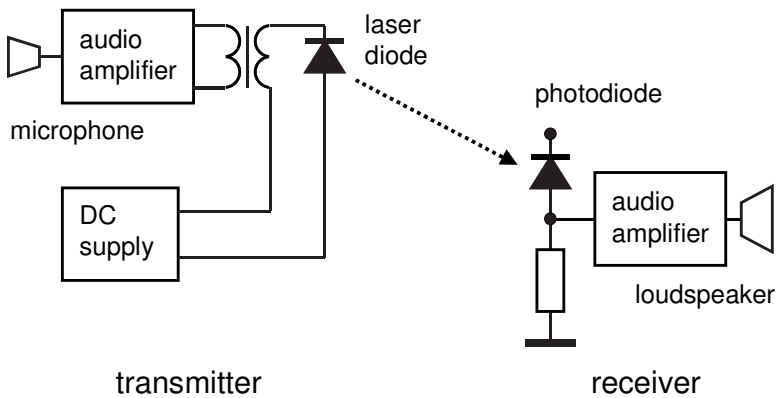

Fig. 1. Diagram of simple system for optics communication.

The amplified signal from a microphone is added, with an audio transformer, to the DC voltage feeding the laser diode (Fig. 1). Due to the modulaton of the feeding voltage, the intensity of the laser beam becomes modulated. One has to adjust the DC voltage for obtaining an effective modulation without significant distortions. The laser beam drives a photodiode of the receiver. Since the divergence of the laser beam is very small, the receiver can be placed at any reasonable distance from the transmitter. The audio voltage produced by the photodiode is amplified and then fed to a loudspeaker. The aim of the project is to build the communication system and find parameters of the transmitter providing good conditions for the communications. An oscilloscope may serve for checking the operations of the transmitter and receiver.

PASCO scientific offers a communication kit for transmitting audio and video signals with a laser (SE-8793); another kit includes some experiments with optical fibers (SE-8794).

10.22. Two-stage Peltier's cooler

A two-stage Peltier's cooler provides a deeper cooling.

In this demonstration, two Peltier modules (see Experiment 3.10) are arranged as a two-stage cooler (Fig. 1). The DC current through both modules flows in such a direction as to cool their upper sides. A platinum thermometer measures the temperature of the upper side of the two-stage cooler. Its electrical resistance is measured with a common digital multimeter. Instead of a platinum thermometer, a thermistor or a homemade copper thermometer can be used. For the latter, it is important to make the resistance sufficiently high, of the order of 10 Ω. A very thin copper wire is necessary for this purpose. Good thermal contacts should be made between all the contact surfaces. The aluminum block is placed in a vessel filled with water.

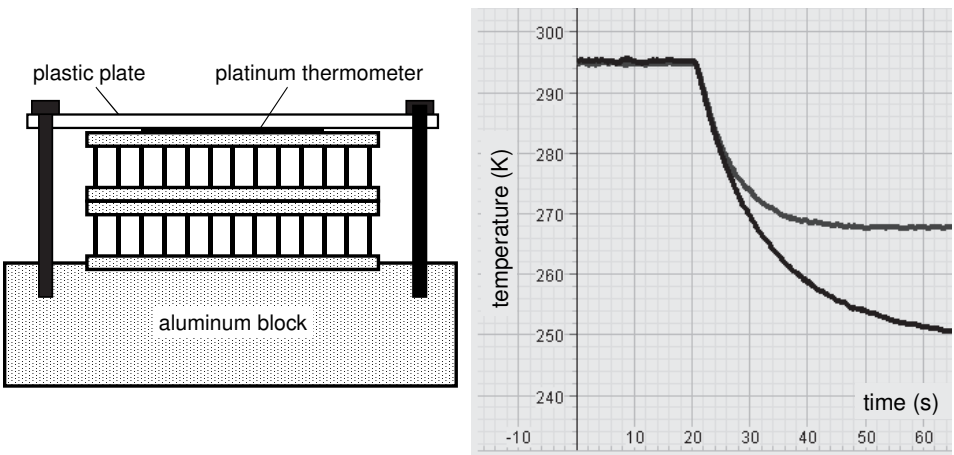

Fig. 1. Arrangement of two-stage Peltier's cooler and cooling curves obtained with a single and a two-stage cooler.

The demonstration is performed as follows. First, only the upper module operates, while the current through the bottom module is switched off. In this case, the cooler operates nearly as a single-stage cooler (the difference is caused by the thermal resistance of the lower module). The temperature of the upper side of the cooler is monitored after switching on the current. Second, the cooling process is observed with both modules.

10.23. Absolute temperature scale

The absolute temperature scale can be established by measuring thermal noise.

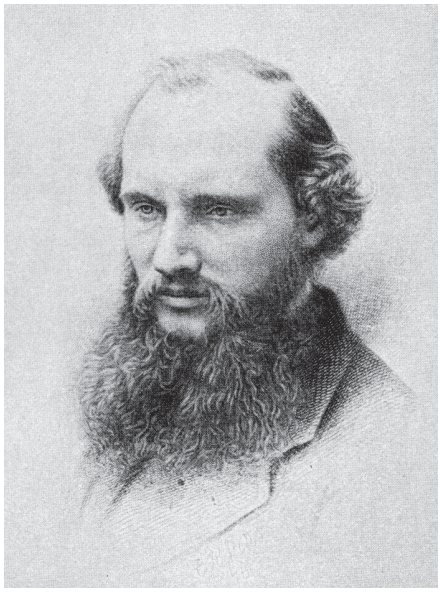

AIP Emilio Segrè Visual Archives,
Brittle Books Collection
William Thomson (Lord Kelvin)
(1824–1907)

The absolute temperature scale (that is, the thermodynamic temperature scale) was proposed by William Thomson (Lord Kelvin). The scale was established with the intention of retaining the temperature unit of the centigrade scale. This meant that the difference between the absolute temperatures of the normal boiling point of water and of its freezing point had to be 100 K (exactly). The absolute temperature scale is based on one fixed point, the triple point of water, which is accepted as 273.16 K (exactly). All other temperatures, including the freezing and boiling points of water, are to be determined experimentally (see Experiment 1.13). The freezing point of water is 273.15 K, while the boiling point (under normal pressure) appeared to be somewhat lower than 373.15 K.

The project aims at the determination of the absolute temperature of the freezing point of water. Measurements of thermal noise (see Experiment 3.11) are used for this purpose. In the present experiment, there is no need to know the bandwidth of the amplifier. It is sufficient that the bandwidth is the same in all the measurements. The amplified noise is observed with an oscilloscope and measured with an RMS (root mean square) voltmeter (Fig. 1). The influence of the inherent noise of the amplifier can be excluded by using a correlation amplifier (Kraftmakher and Cherevko 1972a,b).

For reviews of noise thermometry, see Actis *et al* (1972), Kamper (1972), and White *et al* (1996). Soulen *et al* (1992) reported on noise thermometry for low temperatures that was developed at the National Institute of Standards and

Technology (Gaithersburg). Denoting the absolute temperature of the freezing point as T_0, and of the boiling point as $T_0 + 100$, one obtains

$$R_{100}(T_0 + 100)/R_0T_0 = \langle V_{100}^2 \rangle / \langle V_0^2 \rangle, \quad (1)$$

where $\langle V_0^2 \rangle$ and $\langle V_{100}^2 \rangle$ are the corresponding values of thermal noise, and R_0 and R_{100} are the resistances of the probe that generates the thermal noise.

All the quantities, except T_0, are measurable. The success of the project depends on the availability of a suitable amplifier. The probe (a resistor generating the thermal noise) should be placed inside a properly shielded box and connected to the amplifier with a cable.

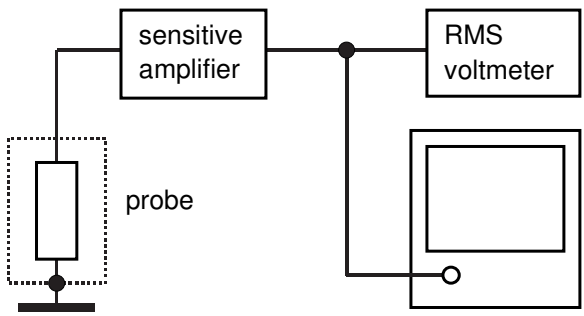

Fig. 1. Schematic of the setup for determining absolute temperatures by measuring thermal noise of a resistor.

10.24. Diamagnetism of superconductors

It is easy to demonstrate the diamagnetism of high-temperature superconductors (see Experiment 9.9).

Superconductor in nonuniform magnetic field. The simplest proof of the diamagnetism of superconductors is the behavior of a sample in a nonuniform magnetic field. An YBCO tablet is hung on a thread inside a plastic cup filled with liquid nitrogen. The tablet deflects from the initial position when a permanent magnet is placed close to it (Fig. 1). The magnet repels the tablet like any diamagnetic sample, but for a superconductor the effect is much stronger.

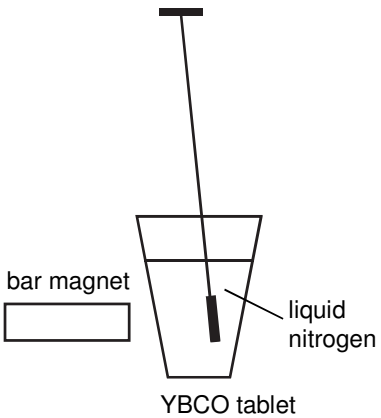

Fig. 1. Superconducting tablet deflects when a permanent magnet is placed close to it.

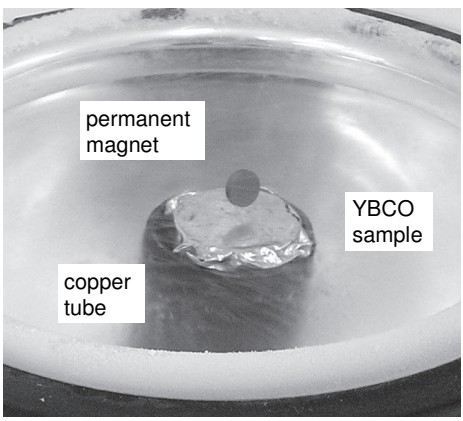

Fig. 2. Small magnet levitates above YBCO sample put in liquid nitrogen.

Magnet levitation. It is easy to show the levitation of a small permanent magnet above a superconducting sample. An YBCO tablet 10 to 20 mm in diameter and 2 to 5 mm thick is wrapped by a metal foil and cooled by a copper tube inside a Dewar flask filled with liquid nitrogen. After cooling the sample, the magnet is shifted towards the sample and then released. The air gap between the magnet and the sample is seen from the separation between the magnet and its reflection from the foil (Fig. 2). Our magnet is 1 mm thick and 4 mm in diameter. With a video camera and a monitor, the levitation is demonstrated to a large audience.

For the magnet levitation, see Byer *et al* (1974); Brandt (1990); Ouseph (1990); Edge (1995); Simon *et al* (1997, 2001); Schreiner and Palmy (2004); Strehlow and Sullivan (2009); French (2010); Becker *et al* (2010); Gough *et al* (2013).

10.25. Impedance meter

The aim of this project is to design and explore a device capable of determining the modulus and phase angle of the impedance of an unknown electric circuit put into a "black box."

Any electric impedance $\boldsymbol{Z}$ can be presented in two forms:

$$\boldsymbol{Z} = A + \mathrm{j}B, \qquad \text{or} \qquad (1)$$

$$\boldsymbol{Z} = Z(\cos\varphi + \mathrm{j}\sin\varphi) = Z\exp(\mathrm{j}\varphi). \qquad (2)$$

In the above relations, Z, A, and B are the modulus and the real and imaginary parts of the impedance, and φ is the so-called phase angle of the impedance. It is possible to determine quantities Z and φ using a function generator and a dual-channel oscilloscope (Fig. 1).

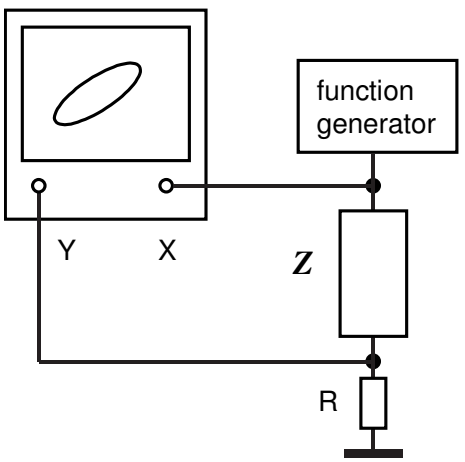

Fig. 1. Schematic of setup for measuring impedances.

The resistance R is much smaller than the modulus of the unknown impedance, so it does not have an effect on the current in the circuit. The modulus of the impedance thus is the ratio of the voltage applied to the circuit (input X of the oscilloscope) to the voltage across the resistor R (input Y). The phase shift φ is available from the shape of the Lissajous pattern on the screen (see Experiment 1.9). The sign of the phase shift can be found by displaying the two voltages on the time scale.

The unknown impedance is determined in a range of frequencies.

References

Abella I D, Bass M, Dutton D, Faust W L, Mintz E, Moos H W 1966 Laser experiments and apparatus for teaching purposes *Am. J. Phys*. **34** 98–103

Abellán F J, Ibáñez J, Valerdi R P, García J A 2013 The Stefan–Boltzmann constant obtained from the *I–V* curve of a bulb *Eur. J. Phys*. **34** 1221–1226

Abramowitz M, Stegun I A 1965 *Handbook of Mathematical Functions* (New York: Dover)

Actis A, Cibrario A, Crovini L 1972 Methods of noise thermometry above 400°C *Temperature, Its Measurement and Control in Science and Industry* vol 4 (Pittsburgh: Instrument Society of America) pp 355–364

Adelberger R E, Kinsey K F 1972 An automated Franck–Hertz experiment *Am. J. Phys*. **40** 349–350

Adhikari R, Kaundal R, Sarkar A, Rana P, Das A K 2012 The cantilever beam magnetometer: A simple teaching tool for magnetic characterization *Am. J. Phys*. **80** 225–231

Adler L, Breazeale M A 1971 Parametric phenomena in physics *Am. J. Phys*. **39** 1522–1527

Aghdaie B 1988 A fringe-counting circuit for use with the Michelson interferometer *Am. J. Phys*. **56** 664–665

Agrawal D C, Leff H S, Menon V J 1996 Efficiency and efficacy of incandescent lamps *Am. J. Phys*. **64** 649–654

Agrawal D C, Menon V J 1999 Thanks to the three viscous formulae *Phys. Educ*. **34** 149–152

Aguirregabiria J M, Hernández A, Rivas M 1997 Magnetic braking revisited *Am. J. Phys*. **65** 851–856

Alanis E, Romero G, Martínez C, Álvarez L, Salazar G 2004 An inexpensive interferometric setup for measuring microscopic displacements *Phys. Teach*. **42** 223–225

Albergotti J C 1981 Speed of sound by a time-of-flight method *Am. J. Phys*. **49** 595–596

Alessi N, Fischer C W, Gray C G 1992 Measurement of amplitude jumps and hysteresis in a driven inverted pendulum *Am. J. Phys*. **60** 755–756

Alford W P, Gold A 1958 Laboratory measurement of the velocity of light *Am. J. Phys*. **26** 481–484

Allen L C, Wallace J, Deutscher G, Lindenfeld P 1988 Measurement of optical absorption by calorimetry and analysis of a solar collector *Am. J. Phys*. **56** 53–57

Allenson M B, Piercy A R, Taylor K N R 1973 An improved Lecher wire experiment *Phys. Educ*. **8** 47–49
Alonso M, Finn E J 1995 *Physics* (Wokingham: Addison–Wesley)
Amato J C, Williams R E, Helm H 1991 An inexpensive, easy to build Fabry–Pérot interferometer and its use in the introductory laboratory *Am. J. Phys*. **59** 992–994
Ames O 1970 A direct measurement of the speed of sound in rods *Am. J. Phys*. **38** 1151–1152
Andrés M V, Contreras O 1992 Experiments on optical fiber interferometers and laser modes *Am. J. Phys*. **60** 540–545
Angiolillo P J 2009 On thermionic emission and the use of vacuum tubes in the advanced physics laboratory *Am. J. Phys*. **77** 1102–1106
Aoki K, Mitsui T 2008 A tabletop experiment for the direct measurement of the speed of light *Am. J. Phys*. **76** 812–815
Arenas A, Victoria L, Abellán F J, Ibáñez J A 1996 Dynamic characterization of a windmill radiometer *Eur. J. Phys*. **17** 331–336
Armentrout C E 1990 The Hall effect in copper: An undergraduate experiment *Am. J. Phys*. **58** 758–762
Arnold T W, Case W 1982 Nonlinear effects in a simple mechanical system *Am. J. Phys*. **50** 220–224
Arvind, Chandi P S, Singh R C, Indumathi D, Shankar R 2004 Random sampling of an alternating current source: A tool for teaching probabilistic observations *Am. J. Phys*. **72** 76–82
Ashkenazi S, Polturak E 1988 An acoustic laboratory experiment to determine the coefficient of mutual diffusion of gases *Am. J. Phys*. **56** 836–839
Auerbach D 1988 Some limits to Stokes' law *Am. J. Phys*. **56** 850–851
Auerbach D 1994 Colliding rods: Dynamics and relevance to colliding balls *Am. J. Phys*. **62** 522–525
Backman P, Murley C, Williams P J 1999 The driven RLC circuit experiment *Phys. Teach*. **37** 424–425
Bacon M E 2012 Speed of sound versus temperature using PVC pipes open at both ends *Phys. Teach*. **50** 351–353
Bacon M E, Varga M 1985 Apparatus for intensity measurements of interference patterns *Am. J. Phys*. **53** 599–600
Badía-Majós A 2006 Understanding stable levitation of superconductors from intermediate electromagnetics *Am. J. Phys*. **74** 1136–1142
Bahrim C, Hsu W-T 2009 Precise measurements of the refractive indices for dielectrics using an improved Brewster angle method *Am. J. Phys*. **77** 337–343
Baird W H 2008 Magnetometer construction and applications for introductory physics *Am. J. Phys*. **76** 807–811
Baker D J 1966 Time dependence of fluorescent lamp emission—a simple demonstration *Am. J. Phys*. **34** 627–628
Baker G L 2006 Probability, pendulums, and pedagogy *Am. J. Phys*. **74** 482–489
Baker G L, Gollub J P 1996 *Chaotic Dynamics: An Introduction* 2nd ed (Cambridge: Cambridge University Press)

Balkanski M, Wallis R F 2000 *Semiconductor Physics and Applications* (New York: Oxford University Press)
Ball J E 1980 Liquid crystals *Phys. Educ*. **15** 108–109
Ballato A, Vig J R 1996 Piezoelectric devices *Encyclopedia of Applied Physics* vol 14, ed G L Trigg (VCH Publishers, Inc) pp 129–145
Ballico M J, Sawley M L, Skiff F 1990 The bipolar motor: A simple demonstration of deterministic chaos *Am. J. Phys*. **58** 58–61
Barik T K, Roy A, Kar S 2005 A simple experiment on diffraction of light by interfering liquid surface waves *Am. J. Phys*. **73** 725–729
Barnes G 1974a Families of transistor characteristics on an oscilloscope *Phys. Teach*. **12** 239–241
Barnes G 1974b A Doppler experiment *Am. J. Phys*. **42** 905–909
Barnes G 1988 The three-dimensional hysteresis surface for nickel *Am. J. Phys*. **56** 45–48
Barnett J D, Stokes H T 1988 Improved student laboratory on the measurement of Planck's constant using the photoelectric effect *Am. J. Phys*. **56** 86–87
Barr R 1972 An inexpensive apparatus for the measurement of the velocity of light in transparent media *J. Phys. E: Sci. Instrum*. **5** 1142–1146
Barr R, Armstrong T R 1990 An inexpensive apparatus for the measurement of the group velocity of light in transparent media using a modified helium-neon laser *Am. J. Phys*. **58** 1059–1064
Barton J S 1994 Making measurements with optical fibres *Phys. Educ*. **29** 151–154
Basano L, Chittofrati R, Crivello S, Piano E, Pontiggia C 1997 Simple setup for detecting interference fringes produced by independent lasers *Am. J. Phys*. **65** 996–1000
Basano L, Ottonello P 1975 Thermal noise as a source of Poisson distribution *Am. J. Phys*. **43** 452–453
Basano L, Ottonello P 1986 Laboratory demonstrations through the use of a general purpose correlator *Am. J. Phys*. **54** 1039–1043
Basano L, Ottonello P 1991 Digital pendulum damping: The single oscillation approach *Am. J. Phys*. **59** 1018–1023
Basano L, Ottonello P 2000 Interference fringes from stabilized diode lasers *Am. J. Phys*. **68** 245–247
Basano L, Ottonello P, Palestini V 1996 Ripples in the energy of a damped oscillator: The experimental point of view *Am. J. Phys*. **64** 1326–1329
Basano L, Ottonello P, Pontiggia C 1988 The magnet-solenoid equivalence: A modern experiment using a personal computer *Am. J. Phys*. **56** 517–521
Basta M, Picciarelli V, Stella R 1994 An introduction to percolation *Eur. J. Phys*. **15** 97–101
Bates H E 1983 Measuring the speed of light by independent frequency and wavelength determination *Am. J. Phys*. **51** 1003–1008
Bates H E 1988 Resource Letter RMSL-1: Recent measurements of the speed of light and the redefinition of the meter *Am. J. Phys*. **56** 682–687
Battaglia O R, Fazio C, Guastella I, Sperandeo-Mineo R M 2010 An experiment on the velocity distribution of thermoionic electrons *Am. J. Phys*. **78** 1302–1308

Batygin V V, Toptygin I N 1970 *Сборник задач по электродинамике* (Москва: Наука) 96–97, 313–314
Baxter L 1956 On the properties of polarization elements as used in optical instruments. III. Angular aperture functions of a positive dichroic film polarizer *J. Opt. Soc. Am.* **46** 435–442
Bazin M J, Lucie P H, de Oliveira S M 1986 Experimental demonstrations of the mathematical properties of Fourier transforms using diffraction phenomena *Eur. J. Phys.* **7** 183–188
Becchetti F D, Dockrill A G 1984 LCD devices for overhead projectors *Am. J. Phys.* **52** 467
Becchetti F D, Harvey K C, Schwartz B J, Shapiro M L 1987 Time-of-flight measurement of the speed of light using a laser and a low-voltage Pöckels-cell modulator *Am. J. Phys.* **55** 632–634
Becker M, Koblischka M R, Hartmann U 2010 Measurement of levitation forces of high-T_C superconductors *Phys. Educ.* **45** 42–49
Beeforth T H, Goldsmid H J 1970 *Physics of Solid State Devices* (London: Pion)
Beers Y 1983 Inexpensive sources and detectors for microwave demonstrations *Am. J. Phys.* **51** 925–929
Behringer E R, Brincat J A 2004 A beam chopping experiment to help students develop research skills *Am. J. Phys.* **72** 695–698
Behroozi F 1983 Magnetic behavior of superconductors: An experiment for the advanced laboratory *Am. J. Phys.* **51** 28–32
Behroozi F, King K R 1976 Superconductivity in the advanced laboratory *Am. J. Phys.* **44** 1187–1191
Belansky R H, Wanser K H 1993 Laser Doppler velocimetry using a bulk optic Michelson interferometer: A student laboratory experiment *Am. J. Phys.* **61** 1014–1019
Bendat J S, Piersol A G 1971 *Random Data: Analysis and Measurement Procedures* (New York: Wiley–Interscience)
Benenson R E, Raffaele R 1986 Magnetic forces and circuits *Am. J. Phys.* **54** 525–527
Bennett C A 1990 A computer-assisted experiment in single-slit diffraction and spatial filtering *Am. J. Phys.* **58** 75–78
Bennett S J 1977 An absolute interferometric dilatometer *J. Phys. E* **10** 525–530
Bensky T J, Frey S E 2001 Computer sound card assisted measurements of the acoustic Doppler effect for accelerated and unaccelerated sound sources *Am. J. Phys.* **69** 1231–1236
Benumof R 1965 Optical pumping theory and experiments *Am. J. Phys.* **33** 151–160
Benumof R 1984 The receiving antenna *Am. J. Phys.* **52** 535–538
Beranek L L 1954 *Acoustics* (New York: McGraw–Hill); 1996 (Acoustical Society of America and American Institute of Physics)
Berdahl J P, Vander Lugt K 2001 Magnetically driven chaotic pendulum *Am. J. Phys.* **69** 1016–1019
Berg R E, Brill D R 2005 Speed of sound using Lissajous figures *Phys. Teach.* **43** 36–39
Bergel L, Arnold S 1976 Speed of light determined by microwave interference *Am. J. Phys.* **44** 546–547

Berger J E, Nunes G 1997 A mechanical Duffing oscillator for the undergraduate laboratory *Am. J. Phys*. **65** 841–846
Bergstein L, Van Slyke R 1997 Telecommunications *Encyclopedia of Applied Physics* vol 20, ed G L Trigg (VCH Publishers, Inc) pp 511–538
Berkey D K, King A L 1972 An undergraduate experiment in Fourier-transform spectrometry *Am. J. Phys*. **40** 267–270
Bhathal R, Sharma M D, Mendez A 2010 Educational analysis of a first year engineering physics experiment on standing waves: based on the ACELL approach *Eur. J. Phys*. **31** 23–35
Bhattarcharjee S 2012 Analysis of a three phase induction motor directly from Maxwell's equations *Am. J. Phys*. **80** 43–46
Bianchetti G B, Ganci S 1986 A demonstration experiment to display diffraction patterns on an oscilloscope *Am. J. Phys*. **54** 283–284
Bianchetti G B, Ganci S 1994 A quantitative acoustical Doppler-shift experiment *Eur. J. Phys*. **15** 157–161
Biehl G 1989 Measuring the speed of sound *Phys. Teach*. **27** 172
Biermann M L, Katz D M, Aho R, Diaz Barriga J, Petron J 2002 Wien's law and the temperature of the Sun *Phys. Teach*. **40** 398–400
Biretta J A, Lang J E 1978 A simple velocity of light experiment *Am. J. Phys*. **46** 1189–1190
Bisquert J, Hurtado E, Mafé S, Pina J 1990 Oscillations of a dipole in a magnetic field: An experiment *Am. J. Phys*. **58** 838–843; **59** 567 (Erratum)
Blackburn J A 1980 Fiber optic wink-around speed of light experiment *Am. J. Phys*. **48** 523–525
Blackburn J A, Baker G L 1998 A comparison of commercial chaotic pendulums *Am. J. Phys*. **66** 821–830
Blackburn J A, Koenig R 1976 Precision falling body experiment *Am. J. Phys*. **44** 855–857
Blair J M 1971 Laboratory experiments involving the two-mode analysis of coupled oscillators *Am. J. Phys*. **39** 555–557
Blair J M 1982 Standing and traveling waves on lumped component lines *Am. J. Phys*. **50** 753–756
Bleaney B I, Bleaney B 1968 *Electricity and Magnetism* 2nd ed (London: Oxford University Press)
Bligh P H, Haywood R 1986 Latent heat—its meaning and measurement *Eur. J. Phys*. **7** 245–251
Bligh P H, Haywood R, Johnson J J 1987 Heat capacity of solids—by courtesy of the computer *Phys. Educ*. **22** 310–315
Block B, Moore R D, Roos P 1965 Do-it-yourself Cavendish balance *Am. J. Phys*. **33** 963–965
Blum H 1974 Acoustic interference demonstration *Am. J. Phys*. **42** 413–414
Bobrow L S 1996 *Fundamentals of Electrical Engineering* 2nd ed (New York: Oxford University Press)
Bobst R L, Karlow E A 1985 A direct potential measurement in the photoelectric effect measurement *Am. J. Phys*. **53** 911–912

Boitier V, Cressault Y 2011 Characterization of photovoltaic generators *Eur. J. Phys*. **32** 657–674
Bonard J-M 2001 The physicist's guide to the orchestra *Eur. J. Phys*. **22** 89–101
Bonanno A, Camarca M, Sapia P 2011 Magnetic interactions and the method of images: a wealth of educational suggestions *Eur. J. Phys*. **32** 849–866
Borin J F, Baffa O 1998 Measuring magnetic properties of ferromagnetic materials *Am. J. Phys*. **66** 449–452
Boruah B R 2009 Dynamic manipulation of a laser beam using a liquid crystal spatial light modulator *Am. J. Phys*. **77** 331–336
Bowlt C 1975 A simple capillary viscometer *Phys. Educ*. **10** 102–103
Boyd R A, Bliss J L, Libbrecht K G 1996 Teaching physics with 670-nm lasers—experiments with Fabry–Perot cavities *Am. J. Phys*. **64** 1109–1116
Boyer R, Fortin E 1972 Intensity measurement in a Fresnel diffraction pattern *Am. J. Phys*. **40** 74–76
Boyer T H 1988 The force on a magnetic dipole *Am. J. Phys*. **56** 688–692
Boys D W, Cox M E, Mykolajenko W 1978 Photoelectric effect revisited (or an inexpensive device to determine *h*/*e*) *Am. J. Phys*. **46** 133–135
Bradshaw M J 1983 Liquid crystal devices *Phys. Educ*. **18** 20–26
Brandt E H 1990 Rigid levitation and suspension of high-temperature superconductors by magnets *Am. J. Phys*. **58** 43–49
Bransky J 1990 Measurement of sound velocity by means of PZT *Phys. Teach*. **28** 125–127
Brice J C 1981 Quartz resonators *Phys. Educ*. **16** 162–166
Brickner R G, Kappers L A, Lipschultz F P 1979 Determination of the speed of light by measurement of the beat frequency of internal laser modes *Am. J. Phys*. **47** 1086–1087
Briggs E, Netterfield B, Barber J, Peterson R 1993 Resonance display apparatus *Am. J. Phys*. **61** 279–281
Briggs K 1987 Simple experiments in chaotic dynamics *Am. J. Phys*. **55** 1083–1089
Britton W G B, Fendley J J, Michael M E 1978 Longitudinal impact of rods: A continuing experiment *Am. J. Phys*. **46** 1124–1130
Brizuela G, Juan A 1996 Planck's constant determination using a light bulb *Am. J. Phys*. **64** 819–821
Brody S B, Singer S R 1970 Experiment on thermionic emission of electrons *Am. J. Phys*. **38** 1044
Brown D C, Rome T L 1972 A simple demonstration of the interference and coherence of light *Am. J. Phys*. **40** 470–471
Brown G C, Rasure J O, Morrison W A 1989 Simple demonstration of superconductivity in $YBa_2Cu_3O_7$ *Am. J. Phys*. **57** 1142–1144
Brownstein K R 1993 Force exerted on a magnetic dipole *Am. J. Phys*. **61** 940–941
Bube R H 1960 *Photoconductivity of Solids* (New York: Wiley)
Bube R H 1992 *Photoelectronic Properties of Semiconductors* (Cambridge: Cambridge University Press)
Buhr W, Klein W, Pressler S 1983 Electron impact excitation and uv emission in the Franck–Hertz experiment *Am. J. Phys*. **51** 810–814
Bullen T G 1963 Apparatus for determining Brewster's angle *Am. J. Phys*. **31** 302

Bullen T G 1965 Determination of Young's modulus in the freshman laboratory *Am. J. Phys*. **33** 855
Bunch R M 1990 Optical fiber sensor experiments for the undergraduate physics laboratory *Am. J. Phys*. **58** 870–874
Bunker K 1991 A new free-fall experiment to determine the acceleration due to gravity *Phys. Educ*. **26** 386–390
Burch D S 1985 Fresnel diffraction by a circular aperture *Am. J. Phys*. **53** 255–260
Busch-Vishniac I, Hixson E 1991 Acoustical instrumentation *Encyclopedia of Applied Physics* vol 1, ed G L Trigg (New York: VCH Publishers, Inc) pp 63–88
Bush R T 1987 The antenna formula: An application of single-slit diffraction theory *Am. J. Phys*. **55** 350–351
Byer R L, Begley R F, Stewart G R 1974 Superconducting, magnetically levitated merry-go-round *Am. J. Phys*. **42** 111–125
Cadwell L H 1996 Magnetic damping: Analysis of an eddy current brake using an airtrack *Am. J. Phys*. **64** 917–923
Caley W J 1972 Suggestions on "An automated Franck–Hertz experiment" *Am. J. Phys*. **40** 1877–1878
Calhoun R C 1996 An elementary derivation of the midplane magnetic field inside a pair of Helmholtz coils *Am. J. Phys*. **64** 1399–1404
Callegaro L 2006 Unified derivation of Johnson and shot noise expressions *Am. J. Phys*. **74** 438–440
Camp P R 1997 Inexpensive optics for polarized light demonstrations *Am. J. Phys*. **65** 449–450
Camparo J C, Klimcak C M 1983 Laser spectroscopy on a "shoestring" *Am. J. Phys*. **51** 1077–1081
Canivez Y 1983 Quick and easy measurement of the band gap in semiconductors *Eur. J. Phys*. **4** 42–44
Carlà M 2013 Stefan–Boltzmann law for the tungsten filament of a light bulb: Revisiting the experiment *Am. J. Phys*. **81** 512–517
Carpena P 1997 Velocity measurements through magnetic induction *Am. J. Phys*. **65** 135–140
Carpenter K H 1975 An automated Franck–Hertz experiment using an X-Y recorder *Am. J. Phys*. **43** 190–191
Carr E F, Harmon G S 1979 Measurement of the dielectric constant of a liquid at a microwave frequency *Am. J. Phys*. **47** 281–282
Carr E F, McClymer J P 1991 A laboratory experiment on interference of polarized light using a liquid crystal *Am. J. Phys*. **59** 366–367
Carr W J 2001 *AC Loss and Macroscopic Theory of Superconductors* (London: Taylor and Francis)
Carvalho C C, Lopes dos Santos J M B, Marques M B 2008 A time-of-flight method to measure the speed of sound using a stereo sound card *Phys. Teach*. **46** 428–431
Carvalho P S, Sampaio e Sousa A 2008 Helping students understand real capacitors: measuring efficiencies in a school laboratory *Phys. Educ*. **43** 400–406
Carver T R, Crawford J O 1975 Useful lecture demonstration of photoelectric wavelength threshold *Am. J. Phys*. **43** 370–371

Carver T R, Rajhel J 1974 Direct "literal" demonstration of the effect of a displacement current *Am. J. Phys.* **42** 246–249
Case W 1980 Parametric instability: An elementary demonstration and discussion *Am. J. Phys.* **48** 218–221
Castañer R, Medina J M, Cuesta-Bolao M J 2006 The magnetic dipole interaction as measured by spring dynamometers *Am. J. Phys.* **74** 510–513
Catunda T, Sartori J, Nunes L A O 1998 Plane wave interference: A didactic experiment to measure the wavelength of light *Am. J. Phys.* **66** 548–549
Cezairliyan A 1984 Pulse calorimetry *Compendium of Thermophysical Property Measurement Methods* vol. 1, eds K D Maglić, A Cezairliyan, V E Peletsky (New York: Plenum) pp 643–668
Cezairliyan A 1988 Pulse calorimetry *Specific Heat of Solids*, ed C Y Ho (New York: Hemisphere) pp 323–353
Cezairliyan A, McClure J L 1971 High-speed (subsecond) measurement of heat capacity, electrical resistivity, and thermal radiation properties of tungsten in the range 2000 to 3600 K *J. Natl. Bur. Stand. A* **75** 283–290
Chabay R, Sherwood B 1995 *Electric and Magnetic Interactions* (New York: Wiley)
Chadha G 1986 Using an *X-Y* plotter to illustrate electrical resonance in an *LCR* series circuit *Phys. Educ.* **21** 187–188
Chambers R G, Park J G 1961 Measurement of electrical resistivity by a mutual inductance method *Brit. J. Appl. Phys.* **12** 507–510
Chappell A (ed) 1978 *Optoelectronics: Theory and Practice* (New York: McGraw–Hill)
Chaudhry S, Morris P 2000 Optical fibres: have you seen the light? *Phys. Educ.* **35** 226–231
Cheng D K 1992 *Field and Wave Electromagnetics* 2nd ed (Reading, MA: Addison–Wesley)
Childs P R N, Greenwood J R, Long A C 2000 Review of temperature measurement *Rev. Sci Instrum.* **71** 2959–2978
Chow R H 1980 Photovoltaic experiment using light from a solar simulation lamp *Am. J. Phys.* **48** 48–50
Chow R H 1984 Study on diffusion and recombination of minority carriers by the method of photoconductive decay *Am. J. Phys.* **52** 842–844
Ciferno T M, Ondris-Crawford R J, Crawford G P 1995 Inexpensive electrooptic experiments on liquid crystal displays *Phys. Teach.* **33** 104–110
Ciholas M E, Wilt P M 1987 A pulser circuit for measuring the speed of light *Am. J. Phys.* **55** 853–854
Clark C, Demkov Y 1991 Making zone plates with a laser printer *Am. J. Phys.* **59** 158-162
Clark G W 2001 An electrical measurement of the speed of light *Am. J. Phys.* **69** 110–112
Clauss D A, Ralich R M, Ramsier R D 2001 Hysteresis in a light bulb: connecting electricity and thermodynamics with simple experiments and simulations *Eur. J. Phys.* **22** 385–394
Clay F P 1979 Demonstration of phase relationships in a series *RLC* circuit using a four-channel multiplexer and a single-channel oscilloscope *Am. J. Phys.* **47** 337–340

Clay F P, Kernell R L 1982 Standing waves in a string driven by loudspeakers and signal generators *Am. J. Phys*. **50** 910–912
Clayhold J, Priest J 2007 Automated heat capacity apparatus on a circuit board *Am. J. Phys*. **75** 379–381
Clotfelter B E 1987 The Cavendish experiment as Cavendish knew it *Am. J. Phys*. **55** 210–213
Coffey H T, Chilton F, Barbee T W 1969 Suspension and guidance of vehicles by superconducting magnets *J. Appl. Phys*. **40** 2161
Colicchia G 2004 A simple device for exploring optical activity *Phys. Teach*. **42** 478–480
Collett E 1968 The description of polarization in classical physics *Am. J. Phys*. **36** 713–725
Collett E 1971 Mathematical formulation of the interference laws of Fresnel and Arago *Am. J. Phys*. **39** 1483–1495
Collings P J 1980 Simple measurement of the band gap in silicon and germanium *Am. J. Phys*. **48** 197–199
Collings P J 1995 Liquid crystal displays *Am. J. Phys*. **63** 1044–1048
Conklin J A, Ouseph P J, Cox H L 2007 A modular, fiber-optic sensor for micro-optical mechanical sensor education *Am. J. Phys*. **75** 760–763
Cooke J, Martin M, McCartney H, Wilf B 1968 Direct determination of the speed of light as a general physics laboratory experiment *Am. J. Phys*. **36** 847
Corbino O M 1910 Thermische Oszillationen wechselstromdurchflossener Lampen mit dünnem Faden und daraus sich ergebende Gleichrichterwirkung infolge der Anwesenheit geradzahliger Oberschwingungen *Phys. Z.* **11** 413–417
Corbino O M 1911 Periodische Widerstandsänderungen feiner Metallfäden, die durch Wechselstrome zum Gluhen gebracht werden, sowie Ableitung ihrer thermischen Eigenschaften bei hoher Temperatur *Phys. Z.* **12** 292–295
Corbò G, Testa M 2009 Magnetic dipoles and electric currents *Am. J. Phys*. **77** 818–820
Cormack I G, Baumann F, Reid D T 2000 Measurement of group velocity dispersion using white light interferometry: A teaching laboratory experiment *Am. J. Phys*. **68** 1146–1150
Cornwall M G 1992 Light travels in straight lines?—a physical simulation of light propagation in a graded index optical fibre *Phys. Educ*. **27** 273–279
Coullet P, Gilli J M, Monticelli M, Vandenberghe N 2005 A damped pendulum forced with a constant torque *Am. J. Phys*. **73** 1122–1128
Courbin L, Cristobal G, Winckert M, Panizza P 2005 Design of a low cost Zimm–Crothers viscometer: From theory to experiment *Am. J. Phys*. **73** 851–855
Cox A J 1978 Quantitative analysis of elliptically polarized light *Am. J. Phys*. **46** 302–303
Cox A J, Peavy J J 1998 Quantitative measurements of the acoustic Doppler effect using a walking speed source *Am. J. Phys*. **66** 1123–1125
Craford M G, Steranka F M 1994 Light-emitting diodes *Encyclopedia of Applied Physics* vol 8, ed G L Trigg (VCH Publishers, Inc) pp 485–514
Craig E J 1975 Vacuum tubes *Methods of Experimental Physics* vol 2A (New York: Academic Press) pp 147–164

Crandall R E 1982 Minimal apparatus for the speed-of-light measurement *Am. J. Phys.* **50** 1157–1159
Crandall R E 1983 Electronic Cavendish device *Am. J. Phys.* **51** 367–368
Crandall R E, Delord J F 1983 Minimal apparatus for determination of Planck's constant *Am. J. Phys.* **51** 90–91
Crane H R 1993 The quartz analog watch: A wonder machine *Phys. Teach.* **31** 501–503
Crane H R 1994 The quartz watch with digital readout *Phys. Teach.* **32** 298–299
Crawford G P, Ondris-Crawford R J 1994 Liquid crystal displays: molecules at work *Phys. Educ.* **29** 307–312
Cullity B D, Graham C D 2009 *Introduction to Magnetic Materials* 2nd ed (IEEE, Inc)
Curry S M, Schawlow A L 1974 Measuring the diameter of a hair by diffraction *Am. J. Phys.* **42** 412–413
Curzon F L, Loke A L H, Lefrançois M E, Novik K E 1995 Parametric instability of a pendulum *Am. J. Phys.* **63** 132–136
Cvahte M, Strnad J 1988 A thermoelectric experiment in support of the second law *Eur. J. Phys.* **9** 11–17
D'Anci A M, Armentrout C E 1988 A light-beam data recorder for determination of the gravitational constant: Anomalous driven oscillations of a gravitation torsion balance *Am. J. Phys.* **56** 348–351
D'Iorio M, Fortin E, Piché M 1975 A simple source for a direct measurement of coherence length *Am. J. Phys.* **43** 927–928
D'Orazio D J, Pearson M J, Schultz J T, Sidor D, Best M W, Goodfellow K M, Scholten R E, White J D 2010 Measuring the speed of light using beating longitudinal modes in an open-cavity HeNe laser *Am. J. Phys.* **78** 524–528
Da Costa G, Kiedansky G, Siri R 1988 Optoelectronic seismograph using a Michelson interferometer with a sliding mirror *Am. J. Phys.* **56** 993–997
Danby G T, Powell J R 1998 Transport by magnetic levitation *Encyclopedia of Applied Physics* vol 22, ed G L Trigg (New York: Wiley–VCH) pp 233–261
Dark M L 2011 A photovoltaic module for incoming science, technology, engineering and mathematics undergraduates *Phys. Educ.* **46** 303–308
Dasgupta B B 1984 Magnetic field due to a solenoid *Am. J. Phys.* **52** 258
Davids M, Forrest R, Pata D 2010 Teaching the fundamentals of cell phones and wireless communications *Phys. Teach.* **48** 217–221
Davis J A, Mueller M W 1977 Temperature dependence of the emission from red and green light emitting diodes *Am. J. Phys.* **45** 770–771
Davis L C 1972 Drag force on a magnet moving near a thin conductor *J. Appl. Phys.* **43** 4256–4257
Davis L C, Reitz J R 1971 Eddy currents in finite conducting sheets *J. Appl. Phys.* **42** 4119–4127
de Buyl P 2010 A digital oscilloscope setup for the measurement of a transistor's characteristic curves *Am. J. Phys.* **78** 1425–1429
de Izarra C 2001 The Ashby and Jephcott interferometer *Eur. J. Phys.* **22** 429–432
de Izarra C, Vallee O 1994 On the use of linear CCD image sensors in optics experiments *Am. J. Phys.* **62** 357–361

de Souza Lima F M, Venceslau G M, dos Reis Nunes E 2002 A new Hooke's law experiment *Phys. Teach*. **40** 35–36
De Witte A J 1967 Interference in scattered light *Am. J. Phys*. **35** 301–313
Deacon C G, Clarke H C 1993 Use of a linear offset Hall effect transducer in student laboratory experiments to measure magnetic fields *Am. J. Phys*. **61** 947–948
Deblaquiere J A, Harvey K C, Hemann A K 1991 Time-of-flight measurement of the speed of light using an acousto-optic modulator *Am. J. Phys*. **59** 443–447
Defrancesco S, Zanetti V 1983 Experiments on magnetic repulsion *Am. J. Phys*. **51** 1023–1025
Dekker A J, Hickman H, Chen T M 1991 A tutorial approach to the thermal noise in metals *Am. J. Phys*. **59** 609–614
Dekker M, Kromminga A J, Van Baak D A, Pilskalns O J, Jacobs J P 1999 Quantitative investigation of Fresnel reflection in the electromagnetism laboratory *Am. J. Phys*. **67** 606–612
Delaney J A, Pippard A B 1972 Electrodeless methods for conductivity measurement in metals *Rep. Prog. Phys*. **35** 677–715
Denardo B, Earwood J, Sazonova V 1999 Parametric instability of two coupled nonlinear oscillators *Am. J. Phys*. **67** 187–195
Derby N, Olbert S 2008 Electromagnetic field of a linear antenna *Am. J. Phys*. **76** 1048–1053
Derby N, Olbert S 2010 Cylindrical magnets and ideal solenoids *Am. J. Phys*. **78** 229–235
Derby S K, Kruglak H 1996 Interference fringes with a laser *Am. J. Phys*. **64** 508
DeSerio R 2003 Chaotic pendulum: The complete attractor *Am. J. Phys*. **71** 250–257
Devasia A, Kurinec S K 2011 Teaching solar cell *I–V* characteristics using SPICE *Am. J. Phys*. **79** 1232–1239
DeYoung P A, Mulder B 2002 Studying collisions in the general physics laboratory with quadrature light emitting diode sensors *Am. J. Phys*. **70** 1226–1230
Diamond J B, Donnelly D P, Breault J D, McCarthy M E 1990 Measuring small vibrations with interferometry *Am. J. Phys*. **58** 919–922
Digilov R M 2008 Flexural vibration test of a cantilever beam with a force sensor: fast determination of Young's modulus *Eur. J. Phys.* **29** 589–597
Dillman L T 1964 Improvements in measurement of the speed of light *Am. J. Phys*. **32** 567
Dittrich W, Minkin L, Shapovalov A S 2013 Mechanical parametric oscillations and waves *Phys. Teach*. **51** 163–165
Dixon M, Lowell J, Lyon S 1985 Amplitude jumps of a nonlinear oscillator *Eur. J. Phys.* **6** 72–79
Dodd J G 1971 An experiment on electron emission *Am. J. Phys*. **39** 1159–1163
Dodds S A 1990 An optical diffraction experiment for the advanced laboratory *Am. J. Phys*. **58** 663–668
Domb C 1996 *The Critical Point* (London: Taylor and Francis)
Domkowski A J, Richardson C B, Rowbotham N 1972 Measurement of the speed of light *Am. J. Phys*. **40** 910–912
Donnelly D 2004 Nibbling at A/D in introductory electronics *Am. J. Phys*. **72** 1342–1344

Donnelly D P, Bechard M 1986 Wind velocity from audio phase shift measurements *Am. J. Phys*. **54** 379
Donoso G, Ladera C L, Martín P 2011 Damped fall of magnets inside a conducting pipe *Am. J. Phys*. **79** 193–200
Dosoudil R, Ušak E, Olah V 2006 Computer controlled system for complex permeability measurement in the frequency range of 5 Hz–1 GHz *J. Electrical Engineering* **57** 105–109
Dounas-Frazer D R, Gandhi P R, Iwata G Z 2013 Uncertainty analysis for a simple thermal expansion experiment *Am. J. Phys*. **81** 338–342
Dousse J-C, Rhême C 1987 A student experiment for accurate measurements of the Newtonian gravitational constant *Am. J. Phys*. **55** 706–711
Dowd J 1978 An interactive computer experiment for the introductory laboratory *Am. J. Phys*. **46** 63–64
Doyle W T, Gibson R 1979 Demonstration of eddy current forces *Am. J. Phys*. **47** 470–471
Dresser M J 1984 Digital displays for the overhead projector *Am. J. Phys*. **52** 379
Drish W F, Wild W J 1983 Numerical solutions of Van der Pol's equation *Am. J. Phys*. **51** 439–445
Driver H S T 1978 An undergraduate experiment to measure the reflectances of a dielectric surface *Am. J. Phys*. **46** 696–699
Dryzek J, Ruebenbauer K 1992 Planck's constant determination from black-body radiation *Am. J. Phys*. **60** 251–253
Duffy R J, Haber-Schaim U 1977 Establishing $V = L(\mathrm{d}I/\mathrm{d}t)$ directly from experiment *Am. J. Phys*. **45** 170–172
Dukes P, Bruton D 2008 A GeoWall with physics and astronomy applications *Phys. Teach*. **46** 180–183
Dunlap R A 1987 The use of amorphous metallic ribbon as a torsion spring for the measurement of the gravitational constant *Am. J. Phys*. **55** 380
Dunlap R A 1988 *Experimental Physics* (New York: Oxford University Press)
DuPuy D L 1989 Measuring solar luminosity with a photodiode *Am. J. Phys*. **57** 826–828
Dusek J, Kearney R J, Baldini G 1980 Analysis of blackbody radiation with derivative spectroscopy *Am. J. Phys*. **48** 232–236
Dutton D, Givens M P, Hopkins R E 1964 Some demonstration experiments in optics using a gas laser *Am. J. Phys*. **32** 355–361
Eagle B A, Jackson P J 1977 The reflecting galvanometer as a damped, driven simple harmonic oscillator with recording facilities *Am. J. Phys*. **45** 1113–1115
Eagleton R D 1987 Two laboratory experiments involving the homopolar generator *Am. J. Phys*. **55** 621–623
Earl J A 1966 Undergraduate experiment on thermal and shot noise *Am. J. Phys*. **34** 575–579
Early E A, Seaman C L, Yang K N, Maple M B 1988 Demonstrating superconductivity at liquid nitrogen temperatures *Am. J. Phys*. **56** 617–620
Easton D 1987 Hooke's law and deformation *Phys. Teach*. **25** 494–495
Ebert R, Harvey J 1992 RLC phase measurements *Phys. Teach*. **30** 135

Eckstein S G 1993 The computerized student laboratory: Motion in a potential well *Am. J. Phys*. **61** 363–366
Eckstein S G, Fekete D 1991 Investigation of driven harmonic oscillations in the computerized student laboratory *Am. J. Phys*. **59** 398–402
Eddy J K, Fox J N, Gaggini N W, Ramsey D, Kirkpatrick T 1987 The velocity of sound in a closed tube *Am. J. Phys*. **55** 1136–1138
Edgar A 1993 Calorimetric measurements of capacitance and inductance using an integrated circuit temperature sensor *Am. J. Phys*. **61** 949–951
Edgar A, Quilty J W 1993 A mutual inductance apparatus for measuring magnetic susceptibility and electrical conductivity *Am. J. Phys*. **61** 943–946
Edmonds D S, Smith R V 1971 A velocity of light measurement using a laser beam *Am. J. Phys*. **39** 1145–1148
Edmonds I R 1968 Stephan–Boltzmann law in the laboratory *Am. J. Phys*. **36** 845–846
Edmondson K, Agoston S, Ranganathan R 1996 Impurity level lifetime measurements using a lock-in amplifier *Am. J. Phys*. **64** 787–791
El Hakeem A S 1965 A refined-tube method for measuring the sound wavelength in gases *Am. J. Phys*. **33** 263–265
Ellington H I, Addinall E, Hately M C 1980 The physics of television broadcasting *Phys. Educ*. **15** 222–228
Ericson T J 1988 Electrical noise and the measurement of absolute temperature, Boltznann's constant and Avogadro's number *Phys. Educ*. **23** 112–116
Escalada L T, Rabello N S, Zollman D A 2004 Student explorations of quantum effects in LEDs and luminescent devices *Phys. Teach*. **42** 173–179
Essick J M, Mather R T 1993 Characterization of a bulk semiconductor's band gap via a near-absorption edge optical transmission experiment *Am. J. Phys*. **61** 646–649
Euler M 2008 Hooke's law and material science projects: exploring energy and entropy springs *Phys. Educ*. **43** 57–61
Even C, Bouquet F, Rémond J, Deloche B 2009 Measuring viscosity with a levitating magnet: application to complex fluids *Eur. J. Phys*. **30** 13–22
Ewert S 1987 A demonstration experiment on the phase transition of a superconductor in a magnetic field *Eur. J. Phys*. **8** 161–163
Fahy S, Kittel C, Louie S G 1988 Electromagnetic screening by metals *Am. J. Phys*. **56** 989–992
Fakhruddin H 2006 Quantitative investigation of thermal expansion using single-slit diffraction *Phys. Teach*. **44** 82–84
Faleski M C 2006 Transient behavior of the driven RLC circuit *Am. J. Phys*. **74** 429–437
Falk L 1978 Recurrence effects in the parametric spring pendulum *Am. J. Phys*. **46** 1120–1123
Falk L 1979 Student experiments on parametric resonance *Am. J. Phys*. **47** 325–328
Fameli N, Curzon F L, Mikoshiba S 1999 Floquet's theorem and matrices for parametric oscillators: Theory and demonstrations *Am. J. Phys*. **67** 127–132
Feagin J M 1979 Another modification of Foucault's method of determining the speed of light *Am. J. Phys*. **47** 288–289

Fedak W, Bord D, Smith C, Gawrych D, Lindeman K 2003 Automation of the Franck–Hertz experiment and the Tel-X-Ometer x-ray machine using LABVIEW *Am. J. Phys*. **71** 501–506
Fendley J, Hutchins M 1984 A selective-surface solar radiometer *Am. J. Phys*. **52** 550–555
Ferguson J L 1984 A simple, bright demonstration of the interference of polarized light *Am. J. Phys*. **52** 1141–1142
Ferlen R P 1974 A simple release mechanism for the free fall experiment *Am. J. Phys*. **42** 255–256
Fernandes J C, Ferraz A, Rogalski M S 2010 Computer-assisted experiments with oscillatory circuits *Eur. J. Phys*. **31** 299–306
Feynman R P, Leighton R B, Sands M 1964 *The Feynman Lectures on Physics* (Reading: Addison–Wesley)
Ficker T 1999Young's modulus of elasticity in student laboratories *Phys. Educ*. **34** 376–383
Fischbach F A, Bond J S 1984 Fraunhofer diffraction patterns of microparticles *Am. J. Phys*. **52** 519–521
Fischer C W 1982 Elementary technique to measure the energy band gap and diffusion potential of *pn* junctions *Am. J. Phys*. **50** 1103–1105
Fischer C W, Hunt J L, Sawatzky P 1987 Automatic recording for the Cavendish balance *Am. J. Phys*. **55** 855–856
Fisher D G, Franz W T 1995 Undergraduate laboratory demonstration of aspects of phase transitions using Curie temperature determination in amorphous ferromagnetic materials *Am. J. Phys*. **63** 248–251
Fisher M E 1965 *The Nature of Critical Points* (Boulder: University of Colorado Press)
Fisher M E 1967 The theory of equilibrium critical phenomena *Rep. Prog. Phys*. **30** 615–730
Fishman F J 1987 Computer-based impedance meter *Am. J. Phys*. **55** 1047–1050
Fitch N, Bliven W, Mitchell T 2007 Automating data acquisition for the Cavendish balance to improve the measurement of G *Am. J. Phys*. **75** 309–312
Fleming G M, Henderson J E 1940 The energy losses attending field current and thermionic emission of electrons from metals *Phys. Rev*. **58** 887–894
Fletcher C D, Orzel C 2005 Construction and calibration of a low cost Fabry–Perot interferometer for spectroscopy experiment *Am. J. Phys*. **73** 1135–1138
Flores-Maldonado J, Galindo S, Jiménez-Domínguez H 1987 Note on an apparatus for Young's modulus measurement *Am. J. Phys*. **55** 664–665; **56** 856 (Erratum)
Flynn C, Wilson N 1998 A simple method for controlling chaos *Am. J. Phys*. **6**6 730–735
Fortin E 1970 Direct demonstration of the Fresnel–Arago law *Am. J. Phys*. **38** 917–918
Fortin E 1979 Fraunhofer diffraction and polarization *Am. J. Phys*. **47** 239–240
Fox G T 1971 Three experiments in friction for the introductory laboratory *Am. J. Phys*. **39** 947–951
Fox J N 1990 Measurement of thermal expansion coefficients using a strain gauge *Am. J. Phys*. **58** 875–877

Fox J N, Gaggini N W 1987 A computer-interfaced experiment to measure the electrical resistivity of a semiconductor *Eur. J. Phys*. **8** 273–275
Fox J N, Gaggini N, Eddy J K 1986 A study of the phase transition of a ferromagnetic material *Am. J. Phys*. **54** 723–726
Fox J N, McMaster R H 1975 Measurement of the thermal properties of a metal using a relaxation method *Am. J. Phys*. **43** 1083–1086
Fox J N, Reiber D G 1973 Magnetic induction and the linear air track *Am. J. Phys*. **41** 73–77
Fox J N, Rustad F A, Smith R W 1988 Measurement of the transition temperature of a high T_c superconductor *Am. J. Phys*. **56** 980–982
Fox M 2001 *Optical Properties of Solids* (New York: Oxford University Press)
Fox P J, Scholten R E, Walkiewicz M R, Drullinger R E 1999 A reliable, compact, and low-cost Michelson wavemeter for laser wavelength measurement *Am. J. Phys*. **67** 624–630
Foxcroft G E 1968 Optical activity *Phys. Educ*. **3** 233–237
Francavilla T L, Claassen J H, Willard M A 2013 A digital hysteresis loop experiment *Am. J. Phys*. **81** 745–749
Frank M T, Kluk E 1991 Velocity of sound in solids *Phys. Teach*. **29** 246–251
Fredrickson J E, Moreland L 1972 Electromagnetic induction: A computer-assisted experiment *Am. J. Phys*. **40** 1202–1205
Freeman W L 1997 The velocity-of-light apparatus by PHYWE—an evaluation *Phys. Teach*. **35** 295–297
Freeman W L, Freda R F 2007 A simple experiment for determining the elastic constant of a fine wire *Phys. Teach*. **45** 224–227
Freier G, Eaton B G 1975 Optical activity demonstration *Am. J. Phys*. **43** 939
French M M J 2010 The wonders of levitation *Phys. Educ*. **45** 37–41
Frenkel J I 1926 Über die Wärmebewegung in festen und flüssigen Körpern *Z. Physik* **35** 652–669
Freschi A A, Caetano N R, Santarine G A, Hessel R 2003 Laser interferometric characterization of a vibrating speaker system *Am. J. Phys*. **71** 1121–1126
Friedt J-M, Carry É 2007 Introduction to the quartz tuning fork *Am. J. Phys*. **75** 415–422
Froehle P 1999 Reminder about Hooke's law and metal springs *Phys. Teach*. **37** 368
Fulcher L P, Davis B F 1976 Theoretical and experimental study of the motion of the simple pendulum *Am. J. Phys*. **44** 51–55
Fundaun I, Reese C, Soonpaa H H 1992 Charging a capacitor *Am. J. Phys*. **60** 1047–1048
Gabovich A M, Kuznetsov V I 2013 What do we mean when using the acronym 'BCS'? The Bardeen–Cooper–Schrieffer theory of superconductivity *Eur. J. Phys*. **34** 371–382
Gabrielson C 1996 One brain, two eyes, three-D *Phys. Teach*. **34** 10–15
Gabrys C, Hull J R, Mulcahy T M 1992 A high-speed demonstration motor with superconducting bearings *Am. J. Phys*. **60** 1153–1154
Gabuzda D C 1987 Magnetic force due to a current-carrying wire: A paradox and its resolution *Am. J. Phys*. **55** 420–422
Gagne R 1996 Determining the speed of sound using the Doppler effect *Phys. Teach*. **34** 126–127

Galeriu C 2010 Magnetostatics analysis, design, and construction of a loudspeaker *Phys. Teach*. **48** 537–540
Galili I, Kaplan D, Lehavi Y 2006 Teaching Faraday's law of electromagnetic induction in an introductory physics course *Am. J. Phys*. **74** 337–343
Gamarra R F, Josebachuili M, Zurita P, Gil S 2007 Experimental study of the frequency repulsion effect *Am. J. Phys*. **75** 1073–1077
Ganci S 1984 The standing wave pattern of a string in fluorescent light *Am. J. Phys*. **52** 250–251
Ganci S 2005 Fraunhofer diffraction by a thin wire and Babinet's principle *Am. J. Phys*. **73** 83–84
Garg M, Kalimullah, Arun P, Lima F M S 2007 Accurate measurement of the position and velocity of a falling object *Am. J. Phys*. **75** 254–258
Garrido J, Casanovas A, Chimeno J M 2013 Peltier coefficient measurement in a thermoelectric module *Eur. J. Phys*. **34** 1255–1262
Garver W P 2006 The photoelectric effect using LEDs as light sources *Phys. Teach*. **44** 272–275
Gathers R G 1986 Dynamic methods for investigating thermophysical properties of matter at very high temperatures and pressures *Rep. Prog. Phys*. **49** 341-396
Gatland I R 1991 Theory of a nonharmonic oscillator *Am. J. Phys*. **59** 155–158
Gatland I R, Kahlscheuer R, Menkara H 1992 Experiments utilizing an ultrasonic range finder *Am. J. Phys*. **60** 451–454
Gayetsky L E, Caylor C L 2007 Measuring the forces between magnetic dipoles *Phys. Teach*. **45** 348–351
George S, Fredrickson J E, Sankaranarayanan A 1972 Planck's constant from Wien's displacement law *Am. J. Phys*. **40** 621–622
Gesari S, Irigoyen B, Juan A 1996 An experiment on the liquid-vapor equilibrium for water *Am. J. Phys*. **64** 1165–1168
Gil S, Mayochi M, Pellizza L J 2006 Experimental estimation of the luminosity of the Sun *Am. J. Phys*. **74** 728–733
Gilliar W, Bickel W S, Videen G, Hoar D 1987 Light scattering from fibers: An extension of a single-slit diffraction experiment *Am. J. Phys*. **55** 555–558
Gingle A, Knasel T M 1975 Undergraduate laboratory investigation of the dielectric constant of ice *Am. J. Phys*. **43** 161–167
Gintautas V, Hübler A 2009 A simple, low-cost, data-logging pendulum built from a computer mouse *Phys. Educ*. **44** 488–491
Glascock M, Sparlin D M 1972 Thomson's experiment revisited *Am. J. Phys*. **40** 1663–1668
Glaser J 1991 A Jolly project for teaching Hooke's law *Phys. Teach.* **29** 164–165
Glazkov S Y, Kraftmakher Y A 1983 High-temperature modulation dilatometer with interferometric recording *High Temperature* **21** 591–594
Glukhikh L K, Efremova R I, Kuskova N V, Matizen E V 1966 *Исследования при высоких температурах*, ред И И Новиков, П Г Стрелков (Новосибирск: Наука) с 75–88
Gluskin E 1998 A possible way to measure the mechanical torque developed by an electric motor *Eur. J. Phys*. **19** 93–95

Gnanatilaka H G, Fernando P C B 1987 An investigation of the magnetic field in the plane of a circular current loop *Am. J. Phys*. **55** 341–344
Golden L B, Klein J R, Tongston L 1988 An introductory low-cost magnetic field experiment *Am. J. Phys*. **56** 846–848
Goldin L L (ed) 1983 *Лабораторные занятия по физике* (Москва: Наука)
González J, Bravo A, Juárez K 1999 Interference of laser light scattered from a "dusty" plane mirror *Am. J. Phys*. **67** 839–840
González-Jorge H, González-Salgado D, Peleteiro J, Carballo E, Domarco G 2004 Ability of a contactless inductive device for the characterization of the critical current versus temperature in superconducting rings at temperatures close to T_c *Cryogenics* **44** 115–119
Gordon J M 1991 Generalized power versus efficiency characteristics of heat engines: The thermoelectric generator as an instructive illustration *Am. J. Phys*. **59** 551–555
Gosselin J R, Rochon P, Gauthier N 1982 Study of eddy currents in a cylindrical wire: An undergraduate laboratory experiment *Am. J. Phys*. **50** 440–443
Gough W, Hunt M O, Summerskill W S H 2013 Levitation of a magnet by an alternating magnetic field *Eur. J. Phys*. **34** 181–187
Graf E H 2012 A demonstration apparatus for linear thermal expansion *Phys. Teach*. **50** 181
Graham-Smith F, King T A, Wilkins D 2007 *Optics and Photonics: An Introduction* 2nd ed (Chichester: Wiley)
Grant I S, Phillips W R 1982 *Electromagnetism* (New York: Wiley)
Gratton L M, Perini M, Zanetti V 2004 Compact fluorescent lamp observed through a diffraction grating *Phys. Teach*. **42** 270–271
Greaves C 1970 The direct conversion of solar light energy into electricity *Phys. Educ*. **5** 100–105
Greczyło T, Mazur P, Dębowska E, Wieczorek P 2010 Determination of mass sensitivity of crystal quartz resonators at student's laboratory *Eur. J. Phys*. **31** 257–265
Greenler R G, Hable J W, Slane P O 1990 Diffraction around a fine wire: How good is the single-slit approximation? *Am. J. Phys*. **58** 330–331
Greenslade T B 1989 An intermediate experiment with a lossy transmission line *Am. J. Phys*. **57** 275–276
Greenslade T B 1991 A new tube for Richardson–Dushman experiments *Am. J. Phys*. **59** 957–958
Greenslade T B, Green M W 1973 Experiments with stereoscopic images *Phys. Teach*. **11** 215–221
Greenslade T B, Wilcox R 1993 An inexpensive Young's modulus apparatus *Phys. Teach*. **31** 116–117
Greenwood M S, Fazio F, Russotto M, Wilkosz A 1986 Using the Atwood machine to study Stokes' law *Am. J. Phys*. **54** 904–906
Griesheimer R N 1947 Microwave power measurements *Technique of Microwave Measurements*, ed C G Montgomery (New York: McGraw-Hill) pp 79–220
Griffith R C 1967 A rotating polarizer for Faraday rotation measurements *Applied Optics* **6** 772

Griffiths D J 1999 *Introduction to Electrodynamics* 3rd ed (Upper Saddle River, NJ: Prentice–Hall)
Gross E T B 1961 Efficiency of thermoelectric devices *Am. J. Phys.* **29** 729–731
Gross N A, Hersek M, Bansil A 2005 Visualizing infrared phenomena with a webcam *Am. J. Phys.* **73** 988–990
Grosu I, Ursu D 1986 Linear and nonlinear oscillations: an experiment for students *Eur. J. Phys.* **7** 91–94
Grove T T 2003 A low-cost scanning Fabry–Perot cavity for laser experiments *Am. J. Phys.* **71** 184–185
Grove T T, Masters M F, Miers R E 2005 Determining dielectric constants using a parallel plate capacitor *Am. J. Phys.* **73** 52–56
Gruber G M, Baart E E 1975 Laboratory experiment on forced linear oscillations *Am. J. Phys.* **43** 926–927
Guénault A M, Lawson N S, Veazey S D 1978 Measurement of thermoelectric effects at low temperature *Am. J. Phys.* **46** 399–401
Guercio G, Zanetti V 1987 Determination of gravitational acceleration using a rubber ball *Am. J. Phys.* **55** 59–63
Guerra D, Corley K, Giacometti P, Holland E, Humphreys M, Nicotera M 2011 An introduction to dimensionless parameters in the study of viscous fluid flows *Phys. Teach.* **49** 175–179
Gülmez E 1997 Measuring the speed of light with a fiber optic kit: An undergraduate experiment *Am. J. Phys.* **65** 614–618
Gupta P D 1988 Coloration on a string vibrating in a standing wave pattern *Phys. Teach.* **25** 371–372
Gupta V K, Shanker G, Saraf B, Sharma N K 1984 Experiment to verify the second law of thermodynamics using a thermoelectric device *Am. J. Phys.* **52** 625–628
Gupta V K, Shanker G, Sharma N K 1986 Experiment on fluid drag and viscosity with an oscillating sphere *Am. J. Phys.* **54** 619–622
Hager N E 1965 A student radiometer *Am. J. Phys.* **33** 92–96
Hahn K D, Johnson E M, Brokken A, Baldwin S 1998 Eddy current damping of a magnet moving through a pipe *Am. J. Phys.* **66** 1066–1076
Hall D E 1981 Comments on Fourier analysis of the simple pendulum *Am. J. Phys.* **49** 792
Hall D E 1987a Wind velocity and temperature from audio phase shift *Am. J. Phys.* **55** 761
Hall D E 1987b Optical measurement of string motion *Am. J. Phys.* **55** 573
Hall D E, Shea M J 1977 Large-amplitude pendulum experiment: Another approach *Am. J. Phys.* **45** 355–357
Hall H H 1971 A new amplifier for the photoelectric effect and Planck's constant experiment *Am. J. Phys.* **39** 1542–1543
Hall H H, Tuttle R P 1971 Photoelectric effect and Planck's constant in the introductory laboratory *Am. J. Phys.* **39** 50–54
Hamilton N 2011 The small-signal frequency response of ferrites *High Freq. Electron.* (June 2011) 36–52

Hanne G F 1988 What really happens in the Franck–Hertz experiment with mercury? *Am. J. Phys*. **56** 696–700
Hansen O P 1972 Classical skin effect for the undergraduate laboratory *Phys. Educ*. **7** 100–103
Hanson R J, Clotfelter B E 1966 Evaluation of commercial apparatus for measuring h/e *Am. J. Phys*. **34** 75–78
Hare J 2010 A simple demonstration for exploring the radio waves generated by a mobile phone *Phys. Educ*. **45** 481–486
Harnwell G P, Livingood J J 1933 *Experimental Atomic Physics* (New York: McGraw–Hill)
Hart F X 2000 Computer-based experiments to measure RC *Phys. Teach*. **38** 176–177
Hart F X, Wood K W 1991 Eddy current distributions: Their calculation with a spreadsheet and their measurement with a dual dipole antenna probe *Am. J. Phys*. **59** 461–467
Hart G P 1986 Measurement of the speed of sound in metal rods using the microcomputer *Phys. Teach*. **24** 89
Haskell R E 1970 A simple experiment on Fresnel diffraction *Am. J. Phys*. **38** 1039–1042
Hassan U, Anwar M S 2010 Reducing noise by repetition: introduction to signal averaging *Eur. J. Phys*. **31** 453–465
Hastings R B 1969 Thermistor explorations in a Kundt tube *Am. J. Phys*. **37** 709–712
Hayn C H 1981 Liquid crystal displays *Phys. Teach*. **19** 256–257
Heald M A 1987 Antenna formulas *Am. J. Phys*. **55** 873–874
Heald M A 1988 Magnetic braking: Improved theory *Am. J. Phys*. **56** 521–522
Hecht E 1994 *Physics* (Pacific Grove: Brooks/Cole)
Hecht E 1998 *Optics* 3rd ed (Reading, MA: Addison–Wesley)
Hegman N, Vad K, Mészáros S, Lindenmájer J 1998 A superconducting pendulum as a thermodynamic machine *Eur. J. Phys*. **19** 259–264
Heinrich F 1986 Entropy change when charging a capacitor: A demonstration experiment *Am. J. Phys*. **54** 742–744
Hellen E H, Lanctot M J 2007 Nonlinear damping of the LC circuit using antiparallel diodes *Am. J. Phys*. **75** 326–330
Heller P 1967 Experimental investigation of critical phenomena *Rep. Prog. Phys*. **30** 731–826
Heller P 1992 Analog demonstrations of Ampère's law and magnetic flux *Am. J. Phys*. **60** 17–25; **60** 274 (Erratum)
Heller P 1997 Electromagnetic waves in space: Visualization of E and B, and pedagogical approaches using superposition *Am. J. Phys*. **65** 22–25
Henningsen J 2011 Teaching laser physics by experiments *Am. J. Phys*. **79** 85–93
Henry D C 2001 Enhancing electromagnetism experiments with clamp-on ammeters *Am. J. Phys*. **69** 76–78
Henry M 1981 Fresnel–Arago laws for interference in polarized light: A demonstration experiment *Am. J. Phys*. **49** 690–691
Herring C, Nichols M H 1949 Thermionic emission *Rev. Mod. Phys*. **21** 185–270

Herrmann F, Schätzle D 1996 Question #53. Measuring Planck's constant by means of an LED *Am. J. Phys*. **64** 1448
Herzum N, Stierstadt K, Wunsch L 1974 Critical behaviour of magnetic losses *Phys. Status Solidi A* **21** 529–541
Hewitt P 2003 Overheating motor *Phys. Teach*. **41** 266–267
Hibberd F H 1952 A simple arrangement for a rotating cylinder viscometer *Am. J. Phys.* **20** 134–135
Higgins R J 1976 Fast Fourier transform: An introduction with some minicomputer experiments *Am. J. Phys*. **44** 766–773
Hilborn R C 1994 *Chaos and Nonlinear Dynamics* (New York: Oxford University Press)
Hill J W 1973 An overhead projection demonstration of optical activity *J. Chem. Educ*. **50** 574
Hill T, Lawson P, Everitt W 1993 Radio interferometry *Phys. Educ*. **28** 243–247
Hilton E 1991 RLC phases *Phys. Teach*. **29** 550
Hilton W A 1962 Construction and use of a Fabry–Perot interferometer *Am. J. Phys*. **30** 724–726
Hinrichsen P F 2001 A simple interference scanner *Am. J. Phys*. **69** 917–919
Hmurcik L V, Micinilio J P 1986 Contrasts between maximum power transfer and maximum efficiency *Phys. Teach*. **24** 492–493
Ho C Y (ed) 1988 *Specific Heat of Solids* (New York: Hemisphere)
Hodges L 1992 Compact fluorescent light bulbs *Phys. Teach*. **30** 90–91
Hodgson E R, Lambert R K 1975 Photoelectric effect *Phys. Educ*. **10** 123–124
Holcomb D F 1997 LEDs: their charm and pitfalls *Phys. Teach*. **35** 198
Holonyak N 1999 Theremin oscillators and oscillations *Am. J. Phys*. **67** 369
Holonyak N 2000 Is the light emitting diode (LED) an ultimate lamp? *Am. J. Phys*. **68** 864–866
Holuj F 1982 Simple measurements involving transmission lines *Am. J. Phys*. **50** 282–283
Hook J R, Hall H E 1991 *Solid State Physics* 2nd ed (Chichester: Wiley)
Hoover M, Everhart M, D'Arruda J 2010 Poisson spot with magnetic levitation *Phys. Teach*. **48** 135–136
Horowitz P, Hill W 1980 *The Art of Electronics* (Cambridge: Cambridge University Press)
Houari A 2011 Determining the viscosity of liquids using an extended falling ball method *Phys. Educ*. **46** 688–691
Howell J 2006 Correction for the radii of curvature for electron beam trajectories in CENCO's e/m apparatus *Am. J. Phys*. **74** 1061–1065
Howes R 1978 A simple v.h.f. oscillator and its uses *Phys. Educ*. **13** 50–53
Howes R W 1980 U.h.f. power transistors and Lecher line oscillators *Phys. Educ*. **15** 49–51
Huang R, Zhang D, Tseng K-J 2008 Determination of dimension-independent magnetic and dielectric properties for Mn-Zn ferrite cores and its EMI applications *IEEE Trans. Electromagn. Compat.* **50** 597–602
Huebner J S 1976 Comment on the Franck–Hertz experiment *Am. J. Phys*. **44** 302–303

Huebner J S, Humphries J T 1974 Storage oscilloscopes in the modern physics laboratory *Am. J. Phys.* **42** 870–876
Huebner J S, Porter D S 1977 Pictures of television *Phys. Teach.* **15** 175–177
Huggins E R, Lelek J J 1979 Motion of electrons in electric and magnetic fields; introductory laboratory and computer studies *Am. J. Phys.* **47** 992–999
Hull G F 1948 Concerning the action of the Crookes radiometer *Am. J. Phys.* **16** 185–186
Hultsch R A 1982 A demonstration of optical activity *Phys. Teach.* **20** 476
Hunt J L, Karl G 1970 Interference with polarized light beams *Am. J. Phys.* **38** 1249–1250
Hunte C, Gibbs P, Singh U 2001 An optical technique for studying phase transitions *Am. J. Phys.* **69** 91–92
Hurych Z 1975 Study of the phase relationships in resonant *RCL* circuits using a dual-trace oscilloscope *Am. J. Phys.* **43** 1011–1012
Hwu Y P 1977 Diffraction pattern of a hair *Am. J. Phys.* **45** 404
Inan U S, Inan A S 1999 *Engineering Electromagnetics* (Menlo Park, CA: Addison-Wesley)
Inbanathan S S R, Moorthy K, Balasubramanian G 2007 Measurement and demonstration of thermal expansion coefficient *Phys. Teach.* **45** 566–567
Indelicato V, La Rocca P, Riggi F, Santagati G, Zappalà G 2013 Analysis of LED data for the measurement of Planck's constant in the undergraduate laboratory *Eur. J. Phys.* **34** 819–830
Íñiguez J, Raposo V 2009 Laboratory scale prototype of a low-speed electrodynamic levitation system based on a Halbach magnet array *Eur. J. Phys.* **30** 367–379
Íñiguez J, Raposo V, Flores A G, Zazo M, Hernández-López A 2005 Measurement of the electrical conductivity of metallic tubes by studying magnetic screening at low frequency *Am. J. Phys.* **73** 206–210
Inman F W 2006 A standing-wave experiment with a guitar *Phys. Teach.* **44** 465–468
Inman F W, Miller C E 1973 The measurement of *e/k* in the introductory physics laboratory *Am. J. Phys.* **41** 349–351
Iqbal I, Ireson G, Moss K 2009 Demonstrating the persistence of field/current with time in a superconductor *Phys. Educ.* **44** 573–575
Irving J, Mullineux N 1959 *Mathematics in Physics and Engineering* (New York: Academic Press)
Iveronova V I (ed) 1962 *Физический практикум* (Москва: Государственное издательство физико-математической литературы)
Iveronova V I (ed) 1967 *Физический практикум. Механика и молекулярная физика* (Москва: Наука)
Iveronova V I (ed) 1968 *Физический практикум. Электричество и оптика (Москва: Наука)*
Jackson M, Bauen D, Hasbun J E 2001 Investigation of laser fundamentals using a helium–neon laser *Eur. J. Phys.* **22** 211–218
Jaecks D H, Du Bois R 1972 Stefan–Boltzmann and radiation distribution laws in the laboratory *Am. J. Phys.* **40** 1179–1180
Jahnke E, Emde F 1945 *Tables of Functions* (New York: Dover)

Jai C, Boisgard R 2007 On the interactions of a harmonic oscillator *Eur. J. Phys*. **28** 1207–1218
Jain A, Kumar J, Zhou F, Li L, Tripathy S 1999 A simple experiment for determining Verdet constants using alternating current magnetic fields *Am. J. Phys.* **67** 714–717
James A N 1973 Photoelectric effect, a common fundamental error *Phys. Educ*. **8** 382–384
James M B, Ormond R B, Stasch A J 1999 Speed of light measurement for the myriad *Am. J. Phys*. **67** 681–684
Janssen H J, Beerden L, Flerackers E L M 1984 An experimental look at the resonant behaviour of a nonlinear *LC* circuit *Eur. J. Phys*. **5** 94–100
Janssen H J, Serneels R, Beerden L, Flerackers E L M 1983 Experimental demonstration of the resonance effect of an anharmonic oscillator *Am. J. Phys*. **51** 655–658
Janssen P, Heremans G, Witters J 1988 Signal averaging in the undergraduate laboratory *Eur. J. Phys*. **9** 131–134
Jenkins F A, White H E 1981 *Fundamentals of Optics* 4th ed (Auckland: McGraw–Hll)
Jewett J W 1980 Air column resonance spectra using basic laboratory equipment *Am. J. Phys*. **48** 24–27
Jewett J W 1987 Demonstrating phase detection technique using ultrasonic transducers *Am. J. Phys*. **55** 665–666
Jewett J W 1991 Get the LED out *Phys. Teach*. **29** 530–534
Jewett J W, Serway R A 2008 *Physics for Scientists and Engineers with Modern Physics* 7th ed (London: Brooks/Cole)
Jiang D, Xiao J, Li H, Dal Q 2007 New approaches to data acquisition in a torsion pendulum experiment *Eur. J. Phys*. **28** 977–982
Johansen T H 1987 An AC-dilatometer for thermal expansivity measurements *High Temperatures – High Pressures* **19** 77–87
Johnson D A 1995 Demonstrating the light-emitting diode *Am. J. Phys*. **63** 761–762
Johnson J B 1928 Thermal agitation of electricity in conductors *Phys. Rev*. **32** 97–109
Johnston D C, Silbernagel B G 1969 A quantitative transmission line experiment *Am. J. Phys*. **37** 1207–1211
Jones B K 1986 *Electronics for Experimentation and Research* (Englewood Cliffs: Prentice–Hall International)
Jones C C 1987 Faraday's law apparatus for the freshman laboratory *Am. J. Phys*. **55** 1148–1150
Jones K A 1987 *Introduction to Optical Electronics* (New York, Wiley)
Jones R 2000 The rail gun: A popular demonstration of the Lorentz force *Am. J. Phys*. **68** 773–774
José J V, Saletan E J 1998 *Classical Dynamics: A Contemporary Approach* (Cambridge: Cambridge University Press)
Jupin W R 1977 Measurement of dielectric constants and capacitor dissipation using resonant circuit *Am. J. Phys*. **45** 663–666
Juri L O, Bekeris V I, Steinmann R G 1986 Skin depth and complex magnetic susceptibility: An experimental alternative approach *Am. J. Phys*. **54** 836–838
Kamal R, Sikri S, Sood B R 1983 An experiment for studying the electrical conductivity and its critical behavior in ferromagnets *Am. J. Phys*. **51** 631–633

Kamata M, Takeuchi N, Akahane H, Shoji R 2002 Practical research using a new ammeter with a clamp-on probe in science classes in junior high school *Phys. Educ*. **37** 521–525
Kammer D W, Ludington M A 1977 Laboratory experiments with silicon solar cells *Am. J. Phys*. **45** 602–605
Kamper R A 1972 Survey of noise thermometry *Temperature, Its Measurement and Control in Science and Industry* vol 4 (Pittsburgh: Instrument Society of America) pp 349–354
Kang C S, Yap B C 1979 Modified Young's double slit experiment *Am. J. Phys*. **47** 1103–1104
Kang P, Young F C 1972 Diffraction of laser light by ultrasound in liquid *Am. J. Phys*. **40** 697–704
Kanseri B, Bisht N S, Kandpal H C, Rath S 2008 Observation of the Fresnel and Arago laws using the Mach-Zehnder interferometer *Am. J. Phys*. **76** 39–42
Karim M, Toohey W J 1986 Compensated Cavendish balance *Am. J. Phys*. **54** 1043–1045
Karlow E A 1994 Ripples in the energy of a damped harmonic oscillator *Am. J. Phys*. **62** 634–636
Karshner G B 1989 Direct method for measuring the speed of sound *Am. J. Phys*. **57** 920–922
Kashy E, Johnson D A, McIntyre J, Wolfe S L 1997 Transverse standing waves in a string with free ends *Am. J. Phys*. **65** 310–313
Kautz R L 1993 Chaos in a computer-animated pendulum *Am. J. Phys*. **61** 407–415
Kawatra M P, Budnick J I 1972 Transport properties of ferromagnetic systems near the critical point: electrical resistivity *Dynamical Aspects of Critical Phenomena*, eds M P Kawatra, J I Budnick (New York: Gordon and Breach) pp 257–291
Keeney A, Hershey B 1997 Making your own dynamic loudspeaker *Phys. Teach*. **35** 297–299
Keesing R G 1981 The measurement of Planck's constant using the visible photoelectric effect *Eur. J. Phys*. **2** 139–149
Kernohan J C 1998 Another use for the sonic ranger *Phys. Teach*. **36** 126–127
Kettler J E 1997 Whistlin' Dixie and the speed of sound *Phys. Teach*. **35** 469
Key T, Smidrovskis R, From M 2000 Measuring the speed of sound in a solid *Phys. Teach*. **38** 76–77
Khosropour R, Millet P 1992 Demonstrating the bent tuning curve *Am. J. Phys*. **60** 429–432
Khoury A, Charles J-P, Charette J, Fieux M, Mialhe P 1984 Solar cells: A laboratory experiment on the temperature dependence of the open-circuit voltage *Am. J. Phys*. **52** 449–451
Kibble T W B, Berkshire F H 1996 *Classical Mechanics* 4th ed (Harlow: Prentice–Hall)
Kiers K, Schmidt D, Sprott J C 2004 Precision measurements of a simple chaotic circuit *Am. J. Phys*. **72** 503–509
Kilty K T 1997 A simple interferometer *Phys. Teach*. **35** 507–508
Kim S M, Kim J B 2007 Visualizing standing waves along the two parallel conducting pipes using household electronic appliances *Am. J. Phys*. **75** 602–607

Kinchin J 2001 Standing waves on strings *Phys. Educ*. **36** 255
King H E, Segrè P N, Appel M 1998 Viscosity and diffusion *Encyclopedia of Applied Physics* vol 23, ed G L Trigg (Weinheim: Wiley–VCH Verlag) pp 239–270
Kingman R, Rowland S C, Popescu S 2002 An experimental observation of Faraday's law of induction *Am. J. Phys*. **70** 595–598
Kirkup L 1988 Resistance measurements as a function of temperature on the high-T_C superconductor $YBa_2Cu_3O_{7\square\square}$ *Eur. J. Phys*. **9** 1–4
Kirkup L, Cherry I 1988 Temperature dependence of photoconductive decay in sintered cadmium sulphide *Eur. J. Phys*. **9** 64–68
Kirkup L, Nicolson M 1986 Band-gap measurements based upon the behaviour of a p-n junction *Eur. J. Phys*. **7** 49–51
Kirkup L, Placido F 1986 Undergraduate experiment: Determination of the band gap in germanium and silicon *Am. J. Phys*. **54** 918–920
Kiss E M 1990 Circuit for displaying hysteresis loop of two-terminal inductors *Am. J. Phys*. **58** 794–795
Kissner F 1981 Inexpensive photovoltaic solar radiometer *Am. J. Phys*. **49** 439–442
Kittel C 2005 *Introduction to Solid State Physics* 8th ed (Wiley, Inc)
Kittel C, Kroemer H 1980 *Thermal Physics* 2nd ed (San Francisco: Freeman)
Kittel P, Hackleman W R, Donnelly R J 1978 Undergraduate experiment on noise thermometry *Am. J. Phys*. **46** 94–100
Klauder L T 1969 A magnetic field diffusion problem *Am. J. Phys*. **37** 323–325
Klein A G 1975 Demonstrations of Ampère's circuital law using a Rogowski coil *Am. J. Phys*. **43** 368–370
Klein A G 1993 On demonstrations of Ampère's law *Am. J. Phys*. **61** 1045
Klein W 1986 The direct display of diffraction patterns using an electric razor *Am. J. Phys*. **54** 956–958
Klein W 1987 In memoriam J. Jaumann: A direct demonstration of the drift velocity in metals *Am. J. Phys*. **55** 22–23
Knudsen A W 1983 The photoelectric determination of *h*/*e*: A new approach to an old problem *Am. J. Phys*. **51** 725–729
Knudsen A W 1985 Boltzmann temperature: An instructional experiment for the advanced laboratory *Am. J. Phys*. **53** 409–415
Kocher C A 1988 Experiments with Fourier transforms at radio frequencies *Am. J. Phys*. **56** 524–530
Kogelnik H 1995 Optical communications *Encyclopedia of Applied Physics* vol 12, ed G L Trigg (VCH Publishers, Inc) pp 119–155
Kohl W H 1962 *Materials and Techniques for Electron Tubes* (London: Chapman and Hall)
Kollie T G 1967 Specific heat determination by pulse calorimetry utilizing a digital voltmeter for data acquisition *Rev. Sci. Instrum*. **38** 1452–1463
Kolm H H, Thornton R D 1973 Electromagnetic flight *Sci. Amer*. **229** (4) 17–25
Kosiewicz R M 1971 The Doppler effect and Lissajous figures using a linear air track *Am. J. Phys*. **39** 229
Kovács A P, Varjú K, Osvay K, Bor Z 1998 On the formation of white-light interference fringes *Am. J. Phys*. **66** 985–989

Kraftmakher Y 1957 Вискозиметр с индуктивными датчиками *Измерительная техника* (5) 78–79
Kraftmakher Y 1959a Две лабораторные работы по электронике *Известия высших учебных заведений – Физика* (4) 95–97
Kraftmakher Y 1959b Определение заряда электрона по эффекту Шоттки *Известия высших учебных заведений – Физика* (3) 172–173
Kraftmakher Y 1961 Три лабораторные работы по определению заряда электрона *Известия высших учебных заведений – Физика* (2) 138–142
Kraftmakher Y 1962a Модуляционный метод измерения теплоёмкости *Журнал прикладной механики и технической физики* (5) 176–180
Kraftmakher Y 1962b Определение скорости света в физическом практикуме *Известия высших учебных заведений – Физика* (5) 65–70
Kraftmakher Y 1964 Демонстрационные измерения скорости света *Методика и техника лекционных демонстраций по физике* (Москва: Издательство Московского университета)
Kraftmakher Y 1967a Electrical conductivity of nickel close to the Curie point *Sov. Phys. Solid State* **9** 1199–1200
Kraftmakher Y 1967b Compensation scheme for measuring thermal expansivity *Zh. Prikl. Mekhan. Tekhn. Fiz.* N 4 143–144
Kraftmakher Y 1967c Vacancy formation and thermal expansion of platinum *Sov. Phys. Solid State* **9** 1197–1198
Kraftmakher Y 1972 Equilibrium vacancies and thermal expansion of tungsten at high temperatures *Sov. Phys. Solid State* **14** 325–327
Kraftmakher Y 1973a Modulation method for measuring specific heat *High Temperatures – High Pressures* **5** 433-454
Kraftmakher Y 1973b Modulation methods for studying thermal expansion, electrical resistivity, and the Seebeck coefficient *High Temperatures – High Pressures* **5** 645-656
Kraftmakher Y 1984 Modulation calorimetry *Compendium of Thermophysical Property Measurement Methods* vol 1, eds K D Maglić, A Cezairliyan, V E Peletsky (New York: Plenum) pp 591–641
Kraftmakher Y 1988 Modulation calorimetry *Specific Heat of Solids*, ed C Y Ho (New York: Hemisphere) pp 299–321
Kraftmakher Y 1991 Measurement of electrical resistivity via the effective magnetic susceptibility *Meas. Sci. Technol.* **2** 253–256
Kraftmakher Y 1992 Practical modulation calorimetry *Compendium of Thermophysical Property Measurement Methods* vol 2, eds K D Maglić, A Cezairliyan, V E Peletsky (New York: Plenum) pp 409–436
Kraftmakher Y 1994 High-temperature specific heat of metals *Eur. J. Phys.* **15** 329–334
Kraftmakher Y 1995 Two student experiments on electrical fluctuations *Am. J. Phys.* **63** 932–935
Kraftmakher Y 1996a On the measurements of the velocity of light *Am. J. Phys.* **64** 183–184
Kraftmakher Y 1996b Measurement of dielectric constant of gases *Am. J. Phys.* **64** 1209–1210
Kraftmakher Y 1997 Curie point of ferromagnets *Eur. J. Phys.* **18** 448–452

Kraftmakher Y 1998a Equilibrium vacancies and thermophysical properties of metals *Physics Reports* **299** 79–188
Kraftmakher Y 1998b Calorimetric determination of the work function *Am. J. Phys*. **66** 225–227
Kraftmakher Y 1999 Student experiments on superconductivity *Eur. J. Phys*. **20** 161–166
Kraftmakher Y 2000a *Lecture Notes on Equilibrium Point Defects and Thermophysical Properties of Metals* (Singapore: World Scientific)
Kraftmakher Y 2000b Eddy currents: Contactless measurement of electrical resistivity *Am. J. Phys*. **68** 375–379
Kraftmakher Y 2000c Photovoltaic cell: efficiency of energy conversion *Eur. J. Phys*. **21** 159–166
Kraftmakher Y 2001 Two experiments with rotating magnetic field *Eur. J. Phys.* **22** 477–482
Kraftmakher Y 2002a Modulation calorimetry and related techniques *Physics Reports* **356** 1–117
Kraftmakher Y 2002b Correlation analysis with ScienceWorkshop *Am. J. Phys*. **70** 694–697
Kraftmakher Y 2002c Principles of radio: a laboratory experiment *Phys. Educ.* **37** 417–421
Kraftmakher Y 2003 Telemetry in the classroom *Phys. Teach.* **41** 544–545
Kraftmakher Y 2004a Classroom demonstration of the magnetic force *Phys. Teach.* **42** 500–501
Kraftmakher Y 2004b Computerized experiments with a tuning fork *Eur. J. Phys.* **25** 869–875
Kraftmakher Y 2004c Pulse calorimetry with a light bulb *Eur. J. Phys.* **25** 707–715
Kraftmakher Y 2004d *Modulation Calorimetry: Theory and Applications* (Berlin: Springer)
Kraftmakher Y 2004e Two demonstrations on superconductivity *Eur. J. Phys.* **25** 689–694
Kraftmakher Y 2005a Demonstration of Lenz's law with an induction motor *Phys. Educ*. **40** 281–284
Kraftmakher Y 2005b Computerized physical pendulum for classroom demonstrations *Phys. Teach.* **43** 244–246
Kraftmakher Y 2005c Hysteresis loops of a ferromagnet *Phys. Teach*. **43** 439–441
Kraftmakher Y 2005d Demonstration of the Barkhausen effect *Am. J. Phys*. **73** 367–369
Kraftmakher Y 2005e Spontaneous magnetization of ferromagnets *Am. J. Phys*. **73** 1191–1194
Kraftmakher Y 2005f Simple experiments with a thermoelectric module *Eur. J. Phys*. **26** 959–967
Kraftmakher Y 2005g A shot-noise experiment with computer control and data acquisition. *Am. J. Phys*. **73** 985–986
Kraftmakher Y 2005h Metal detection and the Theremin in the classroom *Phys. Educ.* **40** 167–171

Kraftmakher Y 2006a Determination of electric power in ac circuits *Eur. J. Phys*. **27** 621–624
Kraftmakher Y 2006b Lock-in detection with DataStudio *Am. J. Phys*. **74** 207–210
Kraftmakher Y 2006c Computer-controlled experiments with a transformer *Eur. J. Phys*. **27** 769–778
Kraftmakher Y 2006d The photoelectric effect experiment with computer control and data acquisition *Am. J. Phys*. **74** 941–943
Kraftmakher Y 2006e Noise reduction by signal accumulation *Phys. Teach*. **44** 528–530
Kraftmakher Y 2007a Dynamic calorimetry for students *Eur. J. Phys*. **28** 351–358
Kraftmakher Y 2007b Magnetic field of a dipole and the dipole–dipole interaction *Eur. J. Phys*. **28** 409–414
Kraftmakher Y 2007c Experiments with a magnetically controlled pendulum *Eur. J. Phys*. **28** 1007–1020
Kraftmakher Y 2008a Pendulums are magnetically coupled *Phys. Educ*. **43** 248–251
Kraftmakher Y 2008b Maglev for students *Eur. J. Phys*. **29** 663–669
Kraftmakher Y 2008c Determination of the quantum efficiency of a light detector *Eur. J. Phys*. **29** 681–687
Kraftmakher Y 2008d Video through a light guide *Am. J. Phys*. **76** 788–791
Kraftmakher Y 2009a Decay time of cathodoluminescence *Phys. Educ*. **44** 43–47
Kraftmakher Y 2009b Measurement of small optical polarization rotations *Eur. J. Phys*. **30** 271–276
Kraftmakher Y 2009c Experiments with a loudspeaker *Eur. J. Phys*. **30** 567–579
Kraftmakher Y 2009d Demonstrations of analog-to-digital conversion techniques *Am. J. Phys*. **77** 851–854
Kraftmakher Y 2009e Computer-assisted experiments with a two-wire transmission line *Eur. J. Phys*. **30** 1163–1171
Kraftmakher Y 2009f Contactless measurement of resistivity with DataStudio *Am. J. Phys*. **77** 953–955
Kraftmakher Y 2009g Experiments with dipole antennas *Eur. J. Phys*. **30** 1391–1399
Kraftmakher Y 2009h It is worth thoroughly looking at the computer display *Phys. Teach*. **47** 499–501
Kraftmakher Y 2010a Standing sound waves in air with DataStudio *Phys. Teach*. **48** 122–123
Kraftmakher Y 2010b Further experiments with a loudspeaker *Eur. J. Phys*. **31** 579–589
Kraftmakher Y 2010c Demonstrations with a magnetically controlled pendulum *Am. J. Phys*. **78** 532–535
Kraftmakher Y 2010d Experiments with a dc motor *Eur. J. Phys*. **31** 863–870
Kraftmakher Y 2010e A differential magnetic circuit for teaching purposes *Eur. J. Phys*. **31** 1239–1247
Kraftmakher Y 2010f Experiments with fluorescent lamps *Phys. Teach*. **48** 461–464
Kraftmakher Y 2010g Rotational viscometers—a subject for student projects *Phys. Educ*. **45** 622–628
Kraftmakher Y 2011a Experiments with a varicap *Phys. Educ*. **46** 29–32
Kraftmakher Y 2011b Demonstrations with an LCR circuit *Phys. Teach*. **49** 168–170

Kraftmakher Y 2011c Computer-assisted experiments with a laser diode *Eur. J. Phys*. **32** 793–802
Kraftmakher Y 2011d Experiments with light-emitting diodes *Am. J. Phys*. **79** 825–830
Kraftmakher Y 2011e Computer-assisted experiments with an inductance coil *Am. J. Phys*. **79** 1180–1182
Kraftmakher Y 2012a Charge and energy stored by a capacitor *Phys. Teach*. **50** 73–74
Kraftmakher Y 2012b Demonstrations of optical spectra with a video camera *Phys. Educ*. **47** 184–188
Kraftmakher Y 2012c Experiments on photoconductivity *Eur. J. Phys*. **33** 503–511
Kraftmakher Y 2012d Demonstrations with a liquid crystal shutter *Phys. Educ*. **47** 329–333
Kraftmakher Y 2012e Some applications of Fourier's great discovery for beginners *Eur. J. Phys*. **33** 1249–1258
Kraftmakher Y 2012f Digital storage oscilloscopes in the undergraduate laboratory *Eur. J. Phys*. **33** 1565–1577
Kraftmakher Y 2013a Experiments on ferrimagnetism *Eur. J. Phys*. **34** 213–224
Kraftmakher Y 2013b Spectra of standing waves in an elastic cord *Phys. Educ*. **48** 281–282
Kraftmakher Y 2013c Data-acquisition system provides new possibilities *Phys. Educ*. **48** 401–406
Kraftmakher Y 2013d Experiments with a quartz resonator *Eur. J. Phys*. **34** 1299–1306
Kraftmakher Y 2013e Two computer-assisted experiments *Phys. Educ*. **48** 636–639
Kraftmakher Y 2013f Electron-atom collisions in gases *Phys. Educ*. **48** 746–749
Kraftmakher Y 2014a Two demonstrations with a new data-acquisition system *Phys. Teach*. **52** 164–166
Kraftmakher Y A, Cheremisina I M 1965 Modulation method for studying thermal expansion *Zh. Prikl. Mekhan. Tekhn. Fiz.* (2) 114–115
Kraftmakher Y A, Cherevko A G 1972a Noise correlation thermometer *Phys. Status Solidi A* **14** K35–38
Kraftmakher Y A, Cherevko A G 1972b Корреляционный усилитель для изучения флуктуационных явлений *Приборы и техника эксперимента* (4) 150–151
Kraftmakher Y A, Krylov S D 1980 Temperature fluctuations and specific heat of tungsten at constant volume *Sov. Phys. Solid State* **22** 1845–1846
Kraftmakher Y A, Pinegina T Y 1974 Anomaly in the electrical resistivity of iron at the Curie point *Sov. Phys. Solid State* **16** 78–81
Kraftmakher Y A, Strelkov P G 1962 Energy of formation and concentration of vacancies in tungsten *Sov. Phys. Solid State* **4** 1662–1664
Kraus J D 1984 *Electromagnetics* 3rd ed (Auckland: McGraw–Hill)
Kraus J D, Fleisch D A 1999 *Electromagnetics with Applications* 5th ed (New York: WCB/McGraw–Hill)
Kraus J D, Marhefka R J 2002 *Antennas for All Applications* 3rd ed (New York: McGraw–Hill)
Kruglak H 1975 Laboratory exercise on the inverse square law *Am. J. Phys*. **43** 449–451
Kuhn J, Vogt P 2012 Diffraction experiments with infrared remote controls *Phys. Teach*. **50** 118–119

Kuhn W R, Postawko S E 1998 Solar radiation and the earth's atmosphere *Phys. Teach*. **26** 266–273
Kukolich S G 1968 Demonstration of the Ramsauer–Townsend effect in a xenon thyratron *Am. J. Phys*. **36** 701–703
Kwasnoski J B 1972 A laboratory investigation of light-emitting diodes *Am. J. Phys*. **40** 588–591
Labinac V, Erceg N, Kotnik-Faruza D 2006 Magnetic field of a cylindrical coil *Am. J. Phys*. **74** 621–627
Lambert R K, O'Driscoll R C 1985 Fourier series experiment for the undergraduate physics laboratory *Am. J. Phys*. **53** 874–880
Landau L D, Lifshitz E M 1980 *Statistical Physics* (London: Pergamon)
Landau L D, Lifshitz E M 1982 *Mechanics* 3rd ed (Oxford: Pergamon)
Landau L D, Lifshitz E M 1984 *Electrodynamics of Continuous Media* (Oxford: Pergamon)
Laperre J, Thys W 1992 About standing waves in an air column: transient regime and transfer function *Eur. J. Phys*. **13** 236–244
Lapidus I R 1970 Motion of a harmonic oscillator with sliding friction *Am. J. Phys*. **38** 1360–1361
Larson L E, Mickelson M E 1985 A super optical radiation power meter *Am. J. Phys.* **53** 1108–1110
Lau K S, Wong K H, Yeung S K 1992 Fibre optic sensors for laboratory measurements *Eur. J. Phys*. **13** 227–235
Laud B B, Sandersai P L, Behere S H 1973 On a demonstration of the interference and coherence of light *Am. J. Phys*. **41** 720–722
Lavers C R 1996 The fabrication of integrated optical glass waveguide sensors—towards 2000 *Phys. Educ*. **31** 24–27
Laws P W 2004 A unit on oscillations, determinism and chaos for introductory physics students *Am. J. Phys*. **72** 446–452
Lazzeri F, Legitimo I, Minguzzi P 1978 New method to display diffraction patterns *Am. J. Phys*. **46** 945–947
Leclerc M 1988 Hall effect probe and Ampere's law *Am. J. Phys*. **56** 954–955
Lee S K, Kim D I, Kim G-N, Cho D 2006 Voice transmission via frequency-modulated diode laser light *Am. J. Phys*. **74** 1037–1039
Leff H S 1990 Illuminating physics with light bulbs *Phys. Teach*. **28** 30–35
Lengyel B A 1966 Evolution of masers and lasers *Am. J. Phys*. **34** 903–913
León-Rossano L M 1997 An inexpensive and easy experiment to measure the electrical resistance of high-T_C superconductors as a function of temperature *Am. J. Phys*. **65** 1024–1026
Lestz S S 1963 A method for measuring the sound wavelength in gases *Am. J. Phys*. **31** 96–98
Leung A F 1986 Wavelength of light in water *Am. J. Phys*. **54** 956
Leung A F, Lee J E 1991 Newton's rings: A classroom demonstration with a He–Ne laser *Am. J. Phys*. **59** 662–664
Leung W P, Ho K H, Ng M B 1980 Laser communication—an ideal student project *Phys. Educ*. **15** 288–290

Levien R B, Tan S M 1993 Double pendulum: An experiment in chaos *Am. J. Phys*. **61** 1038–1044
Levin E 1984 Magnetic dipole moment measurement *Am. J. Phys*. **52** 248–250
Lewis E A S 1976 Negative resistor to provide self-oscillation in *RLC* circuits *Am. J. Phys*. **44** 1217–1219
Lewowski T 1998 Dipole and induced electric polarization of water in liquid and solid phase: A laboratory experiment *Am. J. Phys*. **66** 833–835
Lewowski T, Woźniak K 1997 Measurement of Curie temperature for gadolinium: a laboratory experiment for students *Eur. J. Phys*. **18** 453–455
Lewowski T, Woźniak K 2002 The period of a pendulum at large amplitudes: a laboratory experiment *Eur. J. Phys*. **23** 461–464
Li S S 1993 *Semiconductor Physical Electronics* (New York: Plenum)
Libbrecht K G, Black E D, Hirata C M 2003 A basic lock-in amplifier experiment for the undergraduate laboratory *Am. J. Phys*. **71** 1208–1213
Lide D R (ed) 2008 *CRC Handbook of Chemistry and Physics* 87th ed (Boca Raton: CRC Press)
Lin S W, Berger L I 1989 New method for recording the onset temperature of superconductivity of high-temperature superconductors *Rev. Sci. Instrum*. **60** 507–508
Lindemuth J 1971 The effect of air resistance on falling balls *Am. J. Phys*. **39** 757–759
Lindgren E R 1988 Comments on "Using the Atwood machine to study Stokes' law" *Am. J. Phys*. **56** 940
Liu F H 1987 Franck–Hertz experiment with higher excitation level measurements *Am. J. Phys*. **55** 366–369
Liu F, Tucker R R, Heller P 1990 Nitrogen temperature superconducting ring experiment *Am. J. Phys*. **58** 211–218
Livesey D L, McLeod D L 1973 An experiment on electronic noise in the freshman laboratory *Am. J. Phys*. **41** 1364–1367
Lloyd S, Paetkau M 2010 Characterization of a piezoelectric buzzer using a Michelson interferometer *Phys. Teach*. **48** 610–611
Loeffler F J 1983 A Faraday rotation experiment for the undergraduate physics laboratory *Am. J. Phys*. **51** 661–663
Loferski J J 1995 Photovoltaic devices *Encyclopedia of Applied Physics* vol 13, ed G L Trigg (VCH, Inc) pp 533–557
Lonc W 1992 A simple demonstration of the Barkhausen effect *Am. J. Phys*. **60** 860
Lonc W P 1973 Experiment in Fourier analysis *Am. J. Phys*. **41** 401–404
López-Ramos A, Menéndez J R, Piqué C 2008 Conditions for the validity of Faraday's law of induction and their experimental confirmation *Eur. J. Phys.* **29** 1069–1076
LoPresto M C 2005 Measuring end correction for a quarter-wave tube *Phys. Teach*. **43** 380
LoPresto M C, Holody P R 2003 Measuring the damping constant for under-damped harmonic motion *Phys. Teach.* **41** 22–24
Lottis D, Jaeger H 1996 LEDs in physics demos: a handful of examples *Phys. Teach*. **34** 144–146
Louradour F, Reynaud F, Colombeau B, Froehly C 1993 Interference fringes between two separate lasers *Am. J. Phys*. **61** 242–245

Lucas P A 1986 Modifying Helmholtz coils to magnetically drive a small dipole *Am. J. Phys*. **54** 666–667
Lucke R L 2006 Rayleigh–Sommerfeld diffraction and Poisson's spot *Eur. J. Phys*. **27** 193–204
Lufburrow R A 1963 Inverse-square law experiment *Am. J. Phys*. **31** 60–62
Lührs O 2004 Gases reveal standing waves in tubes *Phys. Educ*. **39** 333–334
Luke K L 1974 An experiment on thermionic emission using a nuvistor triode *Am. J. Phys*. **42** 847–856
Luke K L 1975 Laboratory investigation of free and driven oscillations using a *RLC* circuit *Am. J. Phys*. **43** 610–614
Lukefahr H G 1992 Magnetic dipole interactions on an air track *Am. J. Phys*. **60** 1134–1136
Lukefahr H G, Priest V, St.Jean K B, Worley J S R, Yeager C S, Gajewski D A, Maple M B 1997 A very simple and inexpensive apparatus for detecting superconducting transitions via magnetic screening *Am. J. Phys*. **65** 132–135
Luna D A, Real M A, Durán D V 2002 Undergraduate experiment to measure the speed of sound in liquid by diffraction of light *Am. J. Phys*. **70** 874–875
Lyna, Chia T C, Chia L S, and Goh N K 2007 Demonstrating direct current through a DC motor with Pasco interface datalogger *Phys. Educ*. **42** 20–21
Ma Shang-keng 1976 *Modern Theory of Critical Phenomena* (London: W A Benjamin)
Macdonald J, O'Leary S V 1994 Measuring the diameter of a hair with a steel rule *Am. J. Phys*. **62** 763–764
MacDougall J W 1976 An experiment on skin effect *Am. J. Phys*. **44** 978–980
MacIsaac D, Hämäläinen A 2002 Physics and technical characteristics of ultrasonic sonar systems *Phys. Teach*. **40** 39–46
MacLatchy C S, Backman P, Bogan L 1993 A quantitative braking experiment *Am. J. Phys*. **61** 1096–1101
Macomber H K 1981 Experiment on impulsive excitation, resonance, and Fourier analysis of a harmonic oscillator *Am. J. Phys*. **49** 31–33
Maddox W C, Koehn B W, Stout F H, Ball D A, Chaplin R L 1976 Interference pattern of a cylindrical glass tube *Am. J. Phys*. **44** 387–388
Maglić K D, Cezairliyan A, Peletsky V E (eds) 1984, 1992 *Compendium of Thermophysical Property Measurement Methods* vols 1, 2 (New York: Plenum)
Magno W C, de Araújo A E P, Lucena M A, Montarroyos E, Chesman C 2007 Probing a resonant circuit with a PC sound card *Am. J. Phys*. **75** 161–162
Mahmood W, Anwar M S, Zia W 2011 Experimental determination of heat capacities and their correlation with theoretical predictions *Am. J. Phys*. **79** 1099–1103
Mahurin S M, Compton R N, Zare R N 1999 Demonstration of optical rotatory dispersion of sucrose *J. Chem. Educ*. **76** 1234–1236
Main I G 1988 The use of a moving-coil galvanometer to demonstrate free and forced vibrations *Am. J. Phys*. **56** 839–841
Mak S 2004a Speed of radio waves along a coaxial transmission line *Am. J. Phys*. **72** 671–675b
Mak S-y 2004b A multipurpose LED light source for optics experiments *Phys. Teach*. **42** 550–552

Mak S Y, Tao P K 1988 Measurement of self-inductance *Phys. Teach*. **26** 378–381
Mak S Y, Young K 1986 Floating metal ring in an alternating magnetic field *Am. J. Phys*. **54** 808–811
Mak S, Yip D 2000 The measurement of the speed of light using a laser pointer *Phys. Educ.* **35** 95–100
Mak S-y 2003 Speed of electromagnetic signal along a coaxial cable *Phys. Teach*. **41** 46–49
Mak S-y 1994 The *RLC* circuit and the determination of inductance *Phys. Educ*. **29** 94–97
Mak S-y, Ng Y-k, Wu K-w 2000 Measurement of the speed of sound in a metal rod *Phys. Educ*. **35** 439–445
Mak S-y, Wu A K-W 2002 Speed of sound in a liquid *Phys. Educ*. **37** 530–532
Mallick S 1973 Interference with polarized light *Am. J. Phys*. **41** 583–584
Manche E P 1979 A rapid, convenient, and precise method for the absolute determination of the acceleration of gravity *Am. J. Phys*. **47** 542–544
Manikopoulos C N, Aquirre J F 1977 Determination of the blackbody radiation constant *hc*/*k* in the modern physics laboratory *Am. J. Phys*. **45** 576–578
Manzanares J A, Bisquert J, Garcia-Belmonte G, Fernández-Alonso M 1994 An experiment on magnetic induction pulses *Am. J. Phys*. **62** 702–706
Marcuse D 1980 *Principles of Quantum Electronics* (Orlando, FL: Academic Press, Inc)
Marcuso M, Gass R, Jones D, Rowlett C 1991a Magnetic drag in the quasi-static limit: A computational method *Am. J. Phys.* **59** 1118–1123
Marcuso M, Gass R, Jones D, Rowlett C 1991b Magnetic drag in the quasi-static limit: Experimental data and analysis *Am. J. Phys*. **59** 1123–1129
Marega E, Ioriatti L, Zilio S C 1991 Harmonic generation and chaos in an electromechanical pendulum *Am. J. Phys*. **59** 858–859
Marega E, Zilio S C, Ioriatti L 1990 Electromechanical analog for Landau's theory of second-order symmetry-breaking transitions *Am. J. Phys*. **58** 655–659
Margulies S 1984 Force on a dielectric slab inserted into a parallel-plate capacitor *Am. J. Phys*. **52** 515–518
Maris H J, Kadanoff L P 1978 Teaching the renormalization group *Am. J. Phys*. **46** 652–657
Martin B E 2001 Measuring the speed of sound—Variation on a familiar theme *Phys. Teach*. **39** 424–426
Mártil I, González Díaz G 1991 A laboratory experiment for DC characterization of p-n devices *Eur. J. Phys*. **12** 149–152
Mártil I, González Díaz G 1992a Undergraduate laboratory experiment: Measurement of the complex refractive index and the band gap of a thin film semiconductor *Am. J. Phys*. **60** 83–86
Mártil I, González Diaz G 1992b Determination of the dark and illuminated characteristic parameters of a solar cell from *I–V* characteristics *Eur. J. Phys*. **13** 193–197
Martin A D, Quinn P J 1984 Electron spectroscopy using a Franck–Hertz tube *Am. J. Phys*. **52** 1114–1116

Martínez Ricci M L, Mazzaferri J, Bragas A V, Martínez O E 2007 Photon counting statistics using a digital oscilloscope *Am. J. Phys*. **75** 707–712
Mason P R, Moloney M J 1977 Stokes's law correction *Am. J. Phys*. **45** 305–306
Masters M F, Miers R E 1997 Use of a digital oscilloscope as a spectrum analyzer in the undergraduate laboratory *Am. J. Phys*. **65** 254–255
Matthys D R, Pedrotti F L 1982 Fourier transforms and the use of a microcomputer in the advanced undergraduate laboratory *Am. J. Phys*. **50** 990–995
Mauron F, Vaquer P, Mason J, Higgs D, Augousti A T 1994 A low cost computer-controlled system for the rapid evaluation of liquid crystal test samples *Eur. J. Phys*. **15** 149–153
Maxwell H N 1961 Determination of the angular speed of the Leybold rotating mirror for the velocity of light experiment *Am. J. Phys*. **29** 711
May J 1980 A standing sound wave demonstration *Phys. Teach*. **18** 145–146
Mayer S K 2010 Bringing science policy into the optics classroom: Solid state lighting and United States lighting standards *Am. J. Phys*. **78** 1258–1264
Mayes T W, Melton B F 1994 Fraunhofer diffraction of visible light by a narrow slit *Am. J. Phys*. **62** 397–403
Mc Tavish J P 2000 Field pattern of a magnetic dipole *Am. J. Phys*. **68** 577–578; **69** 1112 (Erratum)
McClellan G, Didwall E M, Rigby C J 1978 Experiments on the photoelectric effect and on the diffusion of electrons in gases *Am. J. Phys*. **46** 832–839
McMahon D R A 1983 Elastic electron-atom collision effects in the Franck–Hertz experiment *Am. J. Phys*. **51** 1086–1091
McPherson G 1990 *Statistics in Scientific Investigation: Its Basis, Application, and Interpretation* (New York: Springer)
Meade M L 1983 *Lock-in Amplifiers: Principles and Applications* (London: Peregrinus)
Meeker T R 1996 Piezoelectric resonators and applications *Encyclopedia of Applied Physics* vol 14, ed G L Trigg (VCH Publishers, Inc) pp 147–169
Mehr R, Grossman T, Kristianpoller N, Gefen Y 1986 Simple percolation experiment in two dimensions *Am. J. Phys*. **54** 271–273
Meiners H F, Eppenstein W, Oliva R A, Shannon T 1987 *Laboratory Physics* (New York: Wiley)
Meissner H, Schmidt G 1986 A simple experiment for studying the transition from order to chaos *Am. J. Phys*. **54** 800–804
Melissinos A C, Napolitano J 2003 *Experiments in Modern Physics* 2nd ed (New York: Academic Press)
Mellen W R 1990 Interference patterns from circularly polarized light using a Michelson interferometer *Am. J. Phys*. **58** 580–581
Mendoza-Arenas J J, Perico E L D, Fajardo F 2010 Motion of a damped oscillating sphere as a function of the medium viscosity *Eur. J. Phys*. **31** 129–141
Meng Y, Liang Z 1987 Improvements in the demonstration of the hysteresis loops of ferromagnetic materials *Am. J. Phys*. **55** 933–937
Meyer J J, Behof A F 1994 Experiment on the motion of a dielectric in a parallel-plate capacitor *Am. J. Phys*. **62** 931–934

Mialhe P, Charette J 1983 Experimental analysis of I–U characteristics of solar cells *Am. J. Phys*. **51** 68–70
Miiller A P 1988 Theory of specific heat of solids *Specific Heat of Solids*, ed C Y Ho (New York: Hemisphere) pp 1–89
Miiller A P, Cezairliyan A 1982 Thansient interferometric technique for measuring thermal expansion at high temperatures: Thermal expansion of tantalum in the range 1500–3200 K *Intern. J. Thermophys*. **3** 259–288
Miller S R, Peterson M A 1982 Microcomputer as a real-time autocorrelator *Am. J. Phys*. **50** 1129–1133
Millman J, Grabel A 1987 *Microelectronics* 2nd ed (New York: McGraw–Hill)
Minh Hoa Le, O'Brien D, Faulkner G, Lubin Zeng, Kyungwoo Lee, Daekwang Jung, YunJe Oh 2008 High-speed visible light communications using multiple-resonant equalization *IEEE Photonics Technology Letters* **20** 1243–1245
Mita K, Boufaida M 1999 Ideal capacitor circuits and energy conservation *Am. J. Phys*. **67** 737–739
Mitin I V, Saletskii A M, Chervyakov A V 2003 *Новые задачи по оптике. Лабораторный практикум* (Москва: Физический факультет Московского университета)
Moen A L, Vander Meulen D L 1970 Fresnel diffraction using a He–Ne gas laser *Am. J. Phys*. **38** 1095–1097
Moloney M J 1974 Laser-lens demonstration of interference rings *Am. J. Phys*. **42** 411–412
Moloney M J 1983 Laser interference experiment using punchcard slits *Am. J. Phys*. **51** 468
Moloney M J 2008 Coupled oscillations in suspended magnets *Am. J. Phys*. **76** 125–128
Monsoriu J A, Giménez M H, Riera J, Vidaurre A 2005 Measuring coupled oscillations using an automated video analysis technique based on image recognition *Eur. J. Phys*. **26** 1149–1155
Moon F C 1987 *Chaotic Vibrations* (New York: Wiley)
Moore G I 1994 Simple mechanical forced damped oscillator with electronic output *Am. J. Phys*. **62** 140–143
Morehouse R 1998 Answer to Question #53. Measuring Planck's constant by means of an LED *Am. J. Phys*. **66** 12
Morelli D T 1997 Thermoelectric devices *Encyclopedia of Applied Physics* vol 21, ed G L Trigg (Weinheim: Wiley–VCH) pp 339–354
Moreno V, Román J F, Salgueiro J R 1997 High efficiency diffractive lenses: Deduction of kinoform profile *Am. J. Phys*. **65** 556–562
Moriarty P J, Gallagher B L, Mellor C J, Baines R R 2003
Graphical computing in the undergraduate laboratory: Teaching and interfacing with *LabVIEW Am. J. Phys*. **71** 1062–1074
Morse R A 2005 Conceptualizing ideal circuit elements in the AP Physics C syllabus *Phys. Teach*. **43** 540–543
Mortlock A J 1965 Experiments with a thermoelectric heat pump *Am. J. Phys*. **33** 813–815
Muldawer L, Meiners H F 1967 New acoustic Doppler-shift experiments

Am. J. Phys. **35** 1136–1142
Mullaney P F 1966 Simple demonstration of photoconductivity in CdS *Am. J. Phys*. **34** 812–814
Mulligan J F 1971 A note on the rotating-mirror method for determining the velocity of light *Am. J. Phys*. **39** 1537–1538
Mulligan J F 1976 Some recent determinations of the velocity of light *Am. J. Phys*. **44** 960–969
Mungan C E, Lipscombe T C 2013 Oscillations of a quadratically damped pendulum *Eur. J. Phys*. **34** 1243–1253
Munley F 2004 Challenges to Faraday's flux rule *Am. J. Phys*. **72** 1478–1483
Muoy Y H, Charles J P, Adbelkrim M 1981 Reliable and economical circuit for characterization of solar cells *Am. J. Phys*. **49** 508–509
Murgatroyd P N 1991 The radial field of the Helmholtz pair *Am. J. Phys*. **59** 949–950
Murphy J A, Egan A 1993 Examples of Fresnel diffraction using Gaussian modes *Eur. J. Phys*. **14** 121–127
Mwanje J 1980a An approach to Hooke's law *Phys. Educ*. **15** 104–105
Mwanje J 1980b Dielectric loss measurements on raw materials *Am. J. Phys*. **48** 837–839
Naba N 1972 Observation of longitudinal vibration of metal rods *Am. J. Phys*. **40** 1339–1340
Nachman P 1995 Mach–Zehnder interferometer as an instructional tool *Am. J. Phys*. **63** 39–43
Nachman P, Pellegrino P M, Bernstein A C 1997 Mechanical resonance detected with a Michelson interferometer *Am. J. Phys*. **65** 441–443
Nakamura T 2000 Snoek's limit in high-frequency permeability of polycrystalline Ni-Zn, Mg-Zn, and Ni-Zn-Cu spinel ferrites *J. Appl. Phys*. **88** 348–353
Nanda K K 1998 An extremely simple and inexpensive apparatus for detecting the superconducting transition *Eur. J. Phys*. **19** 351–354
Narayanan V A, Narayanan R 1996 Speed of sound in tuning fork metal *Phys. Educ*. **31** 389–392
Navrátil Z, Dosoudilová L, Jurmanová J 2013 Study of Planck's law with a small USB grating spectrometer *Phys. Educ*. **48** 289–297
Neeson J F, Austin S 1975 Sound velocity and diffraction intensity measurements based on Raman–Nath theory of the interaction of light and ultrasound *Am. J. Phys*. **43** 984–986
Neil T E, Schulze P D 1986 Mechanical equivalent of heat: Electrical method by vaporization of liquid nitrogen *Am. J. Phys*. **54** 474–475
Nelson R A 1981 Determination of the acceleration due to gravity with the Cenco–Behr free-fall apparatus *Am. J. Phys*. **49** 829–833
Nelson R A, Olsson M G 1986 The pendulum—rich physics from a simple system *Am. J. Phys*. **54** 112–121
Nerbun R C, Leskovec R A 1976 Quantitative measurement of the Doppler shift at an ultrasonic frequency *Am. J. Phys*. **44** 879–881

Neuhoff J G, McBeath M K 1997 Overcoming naïve mental models in explaining the Doppler shift: An illusion creates confusion *Am. J. Phys*. **65** 618–621
Newburgh R 2005 Two theorems on dissipative energy losses in capacitor systems *Phys. Educ*. **40** 370–372
Ng P-h, Wong S-l, Mak S-y 2009 Efficiency measurement using a motor–dynamo module *Phys. Educ*. **44** 639–643
Ng T W, Ang K T 2005 The optical mouse for harmonic oscillator experimentation *Am. J. Phys*. **73** 793–795
Ng Y-k, Mak S-y 2001 Measurement of the speed of sound in water *Phys. Educ*. **36** 65–70
Nicastro A J 1983 Demonstrations of some optical properties of liquid crystals *Phys. Teach*. **21** 181–182
Nicastro A J 1984 Experiment in critical phenomena at phase transitions in liquid crystals *Am. J. Phys*. **52** 912–915
Nicklin R C 1973 Measuring the velocity of sound in a metal rod *Am. J. Phys*. **41** 734–735
Nicklin R C 1986 Faraday's law—Quantitative experiments *Am. J. Phys*. **54** 422–428
Nicklin R C, Rafert B 1983 The computer in lab—A/D and D/A conversion *Am. J. Phys*. **51** 434–439
Nicklin R C, Rafert J B 1984 The digital pendulum *Am. J. Phys*. **52** 632–639
Nicoletopoulos P 2002 Critical potentials of mercury with a Franck–Hertz tube *Eur. J. Phys*. **23** 533–548
Nicolo M 1995 Superconductivity: A guide to alternating current susceptibility measurements and alternating current susceptometer design *Am. J. Phys*. **63** 57–65
Niculescu A, Shumaker R 2003 Apparatus for measuring Young's modulus *Phys. Teach*. **41** 364–367
Nienart L 1994 Measuring the viscosity of gases *Am. J. Phys.* **62** 566–568
Nieves L, Spavieri G, Fernandez B, Guevara R A 1997 Measuring the Planck constant with LEDs *Phys. Teach*. **35** 108–109
Nornes S, Tu Y Z 1989 Augmenting traditional undergraduate advanced laboratory experiments by automation using IEEE-488 and RS-232 interfaces *Am. J. Phys*. **57** 937–940
Nyquist H 1928 Thermal agitation of electric charge in conductors *Phys. Rev*. **32** 110–113
O'Connell J 2002 Tension in a pendulum string *Phys. Teach*. **40** 24–25
O'Connor P J, O'Connor L R 1974 Measuring Planck's constant using a light emitting diode *Phys. Teach*. **12** 423–425
Ocaya R O, Dejene F B 2007 Estimating p–n diode bulk parameters, bandgap energy and absolute zero by a simple experiment *Eur. J. Phys*. **28** 85–91
Ochoa O R, Kolp F 1998 Quantitative demonstration of Lenz's law *Phys. Teach*. **36** 50–51
Ochoa O R, Kolp N F 1997 The computer mouse as a data acquisition interface: Application to harmonic oscillators *Am. J. Phys*. **65** 1115–1118
Ogasawara N 1994 Lasers, semiconductor *Encyclopedia of Applied Physics* vol 8, ed G L Trigg (VCH Publishers, Inc) pp 425–442

Ojeda A M, Redondo E, González Díaz G, Mártil I 1997 Analysis of light-emission processes in light-emitting diodes and semiconductor lasers *Eur. J. Phys.* **18** 63–67
Ojha A, Moon S, Hoeling B, Siegel P B 1991 Measurements of the transient motion of a simple nonlinear system *Am. J. Phys.* **59** 614–619
Oldenburg K E, Morrison W A, Brown G C 1993 Critical current density of $YBa_2Cu_3O_{7-x}$ *Am. J. Phys.* **61** 832–834
Olejniczak J 1989 Fourier analysis of the mechanical rectangular signal *Eur. J. Phys.* **10** 42–44
Oliver W R, Pirie J 1969 Measurement of *g* by free fall *Phys. Educ.* **4** 49–51
Ondris-Crawford R J, Crawford G P, Doane J W 1995 Resource letter: LC-1: Liquid crystals: Physics and applications *Am. J. Phys.* **63** 781–788
Ondris-Crawford R, Crawford G P, Doane J W 1992 Liquid crystals: The phase of the future *Phys. Teach.* **30** 332–339
Ong P P 2002 Little known facts about the common tuning fork *Phys. Educ.* **37** 540–542
Ong P P, Tang S H 1985 Fourier analysis with Lissajous figures *Am. J. Phys.* **53** 252–254
Onorato P, De Ambrosis A 2012 Magnetic damping: Integrating experimental and theoretical analysis *Am. J. Phys.* **80** 27–35
Orfanidis S J 2008 *Electromagnetic Waves and Antennas* http://www.ece.rutgers.edu/~orfanidi/ewa
Oseguera U, Perez R, Cruz J 1989 Demonstration of possible applications of the Meissner effect using the new high-T_C superconductors *Eur. J. Phys.* **10** 19–21
Ouseph P J 1989 Meissner oscillator *Am. J. Phys.* **57** 955–956
Ouseph P J 1990 Levitation of a magnet over a superconductor *Phys. Teach.* **28** 205–209
Ouseph P J, Driver K, Conklin J 2001 Polarization of light by reflection and the Brewster angle *Am. J. Phys.* **69** 1166–1168
Ouseph P J, Link J J 1984 Variation of speed of sound in air with temperature *Am. J. Phys.* **52** 661
Overduin J M 2003 Eyesight and the solar Wien peak *Am. J. Phys.* **71** 216–219
Page A, Candelas P, Belmar F 2006 On the use of local fitting techniques for the analysis of physical dynamic systems *Eur. J. Phys.* **27** 273–279
Page D N, Geilker C D 1972 Measuring the speed of light with a laser and Pockels cell *Am. J. Phys.* **40** 86–88
Palmer L 2010 Physics of projecting and perceiving 3-D movies: Depth perception, stereoscopic images, and polarized light *Phys. Teach.* **48** 207
Palmer S B 1971 Measurement of the velocity of sound in liquids *Am. J. Phys.* **39** 340–342
Palmer S B, Forster G A 1970 Experiments in pulsed ultrasonics *Am. J. Phys.* **38** 814–821
Parker S P (ed) 1997 *McGraw–Hill Encyclopedia of Science and Technology* (New York: McGraw–Hill) **1** 603–606 (amplitude-modulation detector), 606–609 (amplitude-modulation radio), 738–748 (antenna); **3**, 333–343 (cathode-ray tube), 519–522 (charge-coupled devices); **6** 254–260 (electronic display); **7** 37–39 (feedback circuit); **10** 305–307 (magnetic circuits); **11** 347–350 (modulation); **12** 425–429 (optical communications), 431–433 (optical fibers); **13** 590–592 (picture tube); **15** 58–60 (radio),

65–72 (radio broadcasting), 84–89 (radio receiver), 296–300 (refrigeration), 300–303 (refrigeration cycle); **16** 485–487 (single sideband); **18** 179–183 (telemetering), 207–212 (television), 212–216 (television camera), 216–221 (television camera tube), 221–226 (television networks), 226–232 (television receiver), 232–233 (television scanning), 234–235 (television standards), 238–241 (television transmitter), 347–349 (thermoelectric power generator), 349–359 (thermoelectricity)
Parwani R R 2004 An approximate expression for the large angle period of a simple pendulum *Eur. J. Phys.* **25** 37–39
Passmore J L, Collings B C, Collings P J 1995 Autocorrelation of electrical noise: An undergraduate experiment *Am. J. Phys.* **63** 592–595
Patashinskii A Z, Pokrovskii V L 1979 *Fluctuation Theory of Phase Transitions* (New York: Pergamon)
Pavlin J, Vaupotič N, Čepič M 2013 Liquid crystals: a new topic in physics for undergraduates *Eur. J. Phys.* **34** 745–761
Pechan M J, Horvath J A 1990 Quasiequilibrium determination of high-T_C superconductor transition temperatures *Am. J. Phys.* **58** 642–644
Pecori B, Torzo G, Sconza A 1999 Harmonic and anharmonic oscillations investigated by using a microcomputer-based Atwood's machine *Am. J. Phys.* **67** 228–235
Pedrotti F L, Bandettini P 1990 Faraday rotation in the undergraduate advanced laboratory *Am. J. Phys.* **58** 542–545
Peidle J, Stokes C, Hart R, Franklin M, Newburgh R, Pahk J, Rueckner W, Samuel A 2009 Inexpensive microscopy for introductory laboratory courses *Am. J. Phys.* **77** 931–938
Peiris M G, Perera I K 1987 A simple photometer using light-dependent resistors *Am. J. Phys.* **55** 1147
Pelesko J A, Cesky M, Huertas S 2005 Lenz's law and dimensional analysis *Am. J. Phys.* **73** 37–39
Pellicer-Porres J, Lacomba-Perales R, Ruiz-Fuertes J, Martínez-García D, Andrés M V 2006 Force characterization of eddy currents *Am. J. Phys.* **74** 267–271
Pérez A T 2011 Measuring the speed of electromagnetic waves using the cross correlation function of broadband noise at the ends of a transmission line *Am. J. Phys.* **79** 1042–1045
Perkalskis B S, Freeman J R 1996 Fabry–Perot interferometers for lecture demonstrations and laboratories *Am. J. Phys.* **64** 1210–1212
Perkalskis B S, Freeman J R 1997 Extending Elihu Thomson's demonstration and Lenz's law *Am. J. Phys.* **65** 1022–1024
Perkalskis B S, Freeman J R 1998a Examining tensors in the lab: The dielectric permittivity and electrical resistivity of wood *Am. J. Phys.* **66** 816–820
Perkalskis B S, Freeman J R 1998b Showing dispersion for the dielectric permittivity of ice *Am. J. Phys.* **66** 931–932
Pescetti D 1972 Interference between elliptically polarized light beams *Am. J. Phys.* **39** 735–740
Pesic P 2005 Estimating *hc*/*k* from sunlight *Am. J. Phys.* **73** 457–458; **73** 979 (Erratum)
Peters R D 1995 Chaotic pendulum based on torsion and gravity in opposition *Am. J. Phys.* **63** 1128–1136

Peters R D 1996 Resonance response of a moderately driven rigid planar pendulum *Am. J. Phys.* **64** 170–173
Peters R D 1999 Student-friendly precision pendulum *Phys. Teach.* **37** 390–393
Peterson F C 1983 Instrumenting an *e/m* experiment for use in large enrollment courses *Am. J. Phys.* **51** 320–322
Pettersen I H A 2002 Speed of sound in gases using an ultrasonic motion detector *Phys. Teach.* **40** 284–286
Phillips D T, Thompson R 1970 Speed of light with N_2 laser *Am. J. Phys.* **38** 1353
Pickett R C, Lindgren G E, Anderson R K 1984 An FFT-based signal processor for 6502 microcomputers *Am. J. Phys.* **52** 713–719
Pinkston E R 1981 The use of demonstrations in teaching introductory physics *Phys. Teach.* **19** 387–388
Pipes P B, Dutton T F 1976 Simple recording photometer for diffraction experiments *Am. J. Phys.* **44** 399
Pippard A B 1989 *The Physics of Vibration* (Cambridge: Cambridge University Press)
Pohl R O 1987 Lattice vibrations of solids *Am. J. Phys.* **55** 240–246
Polley P 2010 Comment on "On thermionic emission and the use of vacuum tubes in the advanced physics laboratory" by Paul J. Angiolillo *Am. J. Phys.* **78** 878
Ponikvar D 2010 Tools and setups for experiments with AC and rotating magnetic fields *Eur. J. Phys.* **31** 1255–1266
Pontiggia C 1971 Interference with polarized light *Am. J. Phys.* **39** 679
Pontiggia C, Zefiro L 1974 An experiment on interference in scattered light *Am. J. Phys.* **42** 692–694
Portis A M 1964 The Berkeley Physics Laboratory *Am. J. Phys.* **32** 458–464
Portis A M 1972 *Физическая лаборатория* (Москва: Наука)
Portis A M, Young H D 1971 *Berkeley Physics Laboratory* 2nd ed (New York: McGraw–Hill)
Potter D 2002 The speed of sound in an iron rod *Phys. Teach.* **40** 56–57
Potter D 2003 Phase changes in reflected sound waves *Phys. Teach.* **41** 12–13
Powell R A 1978 Photoelectric effect: Back to basics *Am. J. Phys.* **46** 1046–1051
Prasad B S N, Mascarenhas R 1978 A laboratory experiment on the application of Stefan's law to tungsten filament electric lamps *Am. J. Phys.* **46** 420–423
Prasad B S N, Shastry S V, Hebrar K M 1972 An experiment to determine the relative permeability of ferrites *Am. J. Phys.* **40** 907–910
Precker J W 2007 Simple experimental verification of the relation between the band-gap energy and the energy of photons emitted by LEDs *Eur. J. Phys.* **28** 493–500
Precker J W, da Silva M A 2002 Experimental estimation of the band gap in silicon and germanium from the temperature-voltage curve of diode thermometers *Am. J. Phys.* **70** 1150–1153
Priest J 1990 Verifying Ampere's law *Am. J. Phys.* **58** 600–601
Prosperetti A 1976 Subharmonics and ultraharmonics in the forced oscillations of weakly nonlinear systems *Am. J. Phys.* **44** 548–554
Proud J, Cronson H, Huber H, Weinstein R 1969 Apparatus for direct measurement of the velocity of light *Am. J. Phys.* **37** 939–940
Purcell E M 1989 Helmholtz coils revisited *Am. J. Phys.* **57** 18–22

Pye D 2001 *Polarised Light in Science and Nature* (Bristol: Institute of Physics Publishing)
Quist G M 1983 The PET and pendulum: An application of microcomputers to the undergraduate laboratory *Am. J. Phys.* **51** 145–149
Racey T J, Rochon P, Gauthier N 1985 Effect of light polarization on the diffraction pattern of small wires *Am. J. Phys.* **53** 783–786
Rahimi S, Baker R A 1999 Three-dimensional display of light interference patterns *Am. J. Phys.* **67** 453–455
Ralchenko Yu, Kramida A E, Reader J 2011 *NIST Atomic Spectra Database* http://physics.nist.gov/PhysRefData/ASD/lines_form.html
Ramachandran V 1991 Revisiting the *LCR* circuit *Phys. Educ.* **26** 318–321
Ramachandran V 1993 Investigating the active region of transistor characteristics *Phys. Educ.* **28** 252–254
Ramil A, López A J, Vincitorio F 2007 Improvements in the analysis of diffraction phenomena by means of digital images *Am. J. Phys.* **75** 999–1002
Rapior G, Sengstock K, Baev V 2006 New features of the Franck–Hertz experiment *Am. J. Phys.* **74** 423–428
Rasor N S, McClelland J D 1960 Thermal properties of graphite, molybdenum and tantalum to their destruction temperatures *J. Phys. Chem. Solids* **15** 17–26
Ratcliff S J, Martin B T, Ambuske A A, Rong Lu, Blair E, Randall S W, Shion Kono 2011 Modular spectrographs for undergraduate laboratories *Am. J. Phys.* **79** 716–722
Razak A M A 2009 Detection and extraction of weak signals buried in noise *Am. J. Phys.* **77** 1061–1065
Razdan K, Van Baak D A 2002 Demonstrating optical beat notes through heterodyne experiments *Am. J. Phys.* **70** 1061–1067
Rebello N S, Ravipati C, Zollman D A, Escalada L T 1997 Computer simulation of p–n junction devices *Am. J. Phys.* **65** 765–773
Rechenberg H 1997 The electron in physics—selection from a chronology of the last 100 years *Eur. J. Phys.* **18** 145–149
Redinz J A 2011 Forces and work on a wire in a magnetic field *Am. J. Phys.* **79** 774–776
Redinz J A 2013 The role of the magnetic core in transformers *Eur. J. Phys.* **34** 519–526
Redondo E, Ojeda A, González Díaz G, Mártil I 1997 A laboratory experiment with blue light-emitting diodes *Am. J. Phys.* **65** 371–376
Redwood M 1980 Piezoelectric devices in electronics *Phys. Educ.* **15** 9–14
Reed L J 1975 Magnetic induction and the linear air track *Am. J. Phys.* **43** 555–556
Reich S 1988 Zero permeability of a high T_C superconductor demonstrated with a piece of cork and some salty water *Am. J. Phys.* **56** 1039–1040
Reitz J R 1970 Forces on moving magnets due to eddy currents *J. Appl. Phys.* **41** 2067–2071
Relton F E 1965 *Applied Bessel Functions* (New York: Dover)
Rhyner C R 1970 Measurement of the speed of sound in metal rods *Am. J. Phys.* **38** 1152–1153
Richards D A 1981 Extension–load curves for materials under tension *Phys. Educ.* **16** 44–46

Richmond J C 1984 Measurement of thermal radiative properties of materials *Compendium of Thermophysical Property Measurement Methods* vol 1, eds K D Maglić, A Cezairliyan, V E Peletsky (New York: Plenum) pp 709–768
Righini F, Bussolino G C, Spišiak J 2000 Pulse calorimetry at high temperatures *Thermochim. Acta* **347** 93-102
Righini F, Roberts R B, Rosso A, Cresto P C 1986 Thermal expansion by a pulse-heating method: theory and experimental apparatus *High Temperatures – High Pressures* **18** 561–571
Rinard P M 1974 Determination of particle size by diffraction of light *Am. J. Phys*. **42** 320–325
Rinard P M 1976 Large-scale diffraction patterns from circular objects *Am. J. Phys*. **44** 70–76
Rochon P, Gauthier N 1982 Induction transducer for recording the velocity of a glider on an air track *Am. J. Phys*. **50** 84–85
Rochon P, Gauthier N 1990 Strong shielding due to an electromagnetically thin metal sheet *Am. J. Phys*. **58** 276–277
Rodríguez A L P, Bernal J J P, Balsera B M 1979 Electronic device of didactic and electrometric interest for the study of *RLC* circuits *Am. J. Phys*. **47** 178–181
Rodríguez-Luna J C, de Urquijo J 2010 A simple, sensitive circuit to measure Boltzmann's constant from Johnson's noise *Eur. J. Phys*. **31** 675–679
Roemer I C, Koentop P E 1965 Tube method for measuring the velocity of sound in gases *Am. J. Phys*. **33** 803–806
Roeser W F, Wensel H T 1941 Appendix *Temperature, Its Measurement and Control in Science and Industry* (New York: Reinhold) pp 1293–1323
Rogalski M S, Palmer S B 2006 *Advanced University Physics* 2nd ed (Boca Raton, FL: Chapman and Hall)
Rogers J, McMillan R, Pickett R, Anderson R 1969 A determination of the speed of light by the phase-shift method *Am. J. Phys*. **37** 816–822; 1163 (Erratum)
Romer A 1973 Magnetic repulsion: An introductory experiment *Am. J. Phys*. **41** 1332–1336
Ronzani A, Maccarrone F, Di Lieto A 2008 Measuring light speed with a modulated laser diode *Eur. J. Phys.* **29** 857–965
Rose A 1978 *Concepts in Photoconductivity and Allied Problems* (New York: Krieger)
Rosen N, Schieber D 1982 Some remarks on Faraday's law *Am. J. Phys*. **50** 974–975
Rosenthal L A 1965 Nonlinear bridge for electrothermal measurements *Rev. Sci. Instrum*. **36** 1179–1182
Ross J N 1995 Thick-film photoresistors *Meas. Sci. Technol*. **6** 405–409
Rossing T D, Hull J R 1991 Magnetic levitation *Phys. Teach*. **29** 552–562
Rossing T D, Russell D A 1990 Laboratory observation of elastic waves in solids *Am. J. Phys*. **58** 1153–1162
Rossing T D, Russell D A, Brown D E 1992 On the acoustics of tuning forks *Am. J. Phys*. **60** 620–626
Rovers W, Skarsgard H M 1967 Demonstration of the Doppler effect for acoustic waves *Am. J. Phys*. **35** 530–533

Rowland J J 1975 A simple direct demonstration of persistent current in a superconducting circuit *Am. J. Phys.* **43** 1105–1106
Roy M K, Harbola M K, Verma H C 2007 Demonstration of Lenz's law: Analysis of a magnet falling through a conducting tube *Am. J. Phys.* **75** 728–730
Ruby L 1996 Applications of the Mathieu equation *Am. J. Phys.* **64** 39–44
Rudmin J W, Taylor G R, Hand P M, Ashworth J N, Wehr P H 1980 Simple ultra-low-cost undergraduate holography using a modified Michelson interferometer *Am. J. Phys.* **48** 746–748
Rudnick J, Tannhauser D S 1976 Concerning a widespread error in the description of the photoelectric effect *Am. J. Phys.* **44** 796–798
Rudowicz C, Sung H W F 2003 Textbook treatments of the hysteresis loop for ferromagnets—Survey of misconceptions and misinterpretations *Am. J. Phys.* **71** 1080–1083
Rueckner W, Titcomb P 1987 An accurate determination of the acceleration of gravity for lecture hall demonstration *Am. J. Phys.* **55** 324–330
Russell D A 2000 On the sound field radiated by a tuning fork *Am. J. Phys.* **68** 1139–1145
Saba M M F, da Rosa R A S 2003 The Doppler effect of a sound source moving in a circle *Phys. Teach.* **41** 89–91
Sabaz L 2006 Can bubbles explain viscosity? *Phys. Educ.* **41** 112–114
Salik E 2012 Quantitative investigation of Fresnel reflection coefficients by polarimetry *Am. J. Phys.* **80** 216–224
Sandhu H S 1965 Apparatus for the measurement of viscosity of water *Am. J. Phys.* **33** 508–509
Sandoval J L, Porta A V 1985 Fourier analysis for vibrating string's profile using optical detection *Am. J. Phys.* **53** 1195–1203
Sandoz P, Carry É, Friedt J-M, Trolard B, Reyes J G 2009 Frequency domain characterization of the vibrations of a tuning fork by vision and digital image processing *Am. J. Phys.* **77** 20–26
Sankovich R 1985 Faraday's law demonstration *Am. J. Phys.* **53** 89
Santarelli V, Carolla J, Ferner M 1993 Standing waves in a mailing tube *Phys. Teach.* **31** 557–558
Santos A C F, Santos W S, Aguilar C E 2013 Electromagnetic wave velocities: an experimental approach *Eur. J. Phys.* **34** 591–597
Saslow W M 1987 Electromechanical implications of Faraday's law: A problem collection *Am. J. Phys.* **55** 986–993
Saslow W M 1991 How a superconductor supports a magnet, how magnetically "soft" iron attracts a magnet, and eddy currents for the uninitiated *Am. J. Phys.* **59** 16–25
Saslow W M 1992 Maxwell's theory of eddy currents in thin conducting sheets, and application to electromagnetic shielding and MAGLEV *Am. J. Phys.* **60** 693–711
Saulnier M S, Frisch D 1989 Measurement of the gravitational constant without torsion *Am. J. Phys.* **57** 417–420
Sawicki C A 2003 Induced current measurement of rod vibrations *Phys. Teach.* **41** 42–44

Scanlon P J, Henriksen R N, Allen J R 1969 Approaches to electromagnetic induction *Am. J. Phys*. **37** 698–708
Schauber M J, Newman S A, Goodman L R, Suzuki I S, Suzuki M 2008 Measurement of mutual inductance from the frequency dependence of impedance of AC coupled circuits using a digital dual-phase lock-in amplifier *Am. J. Phys*. **76** 129–132
Schawlow A L 1965 Measuring the wavelength of light with a ruler *Am. J. Phys*. **33** 922–923
Schery S D 1976 Design of an inexpensive pendulum for study of large-angle motion *Am. J. Phys*. **44** 666–670
Schiel D, Slaets J, Mascarenhas S 1978 Measurement of acoustical second-order Doppler effect as an introductory experiment to special relativity *Am. J. Phys*. **46** 211–213
Schmidt V H, Childers B R 1984 Magnetic pendulum apparatus for analog demonstration of first-order and second-order phase transitions and tricritical points *Am. J. Phys*. **52** 39–43
Schmitzer H, Tierney D, Toepker T 2009 Real 3-D: How does it work? *Phys. Teach*. **47** 456–459
Schneider C S, Ertel J P 1998 A classroom jumping ring *Am. J. Phys*. **66** 686–693
Scholl R, Liby B W 2009 Using a Michelson interferometer to measure coefficient of thermal expansion of copper *Phys. Teach*. **47** 306–308
Schottky W 1918 Über spontane Stromschwankungen in verschiedenen Elektrizitätsleitern *Ann. Physik* **57** 541–567
Schreiner M, Palmy C 2004 Why does a cylindrical permanent magnet rotate when levitated above a superconducting plate? *Am. J. Phys*. **72** 243–248
Schwartz G A, Ludueña S J 2004 An experimental method for studying two-dimensional percolation *Am. J. Phys*. **72** 364–366
Scofield J H 1994 Frequency-domain description of a lock-in amplifier *Am. J. Phys*. **62** 129–133
Sconza A, Galet G, Torzo G 2000 An improved version of the Haynes–Shockley experiment with electrical or optical injection of the excess carriers *Am. J. Phys*. **68** 80–87
Sconza A, Torzo G 1985 A simple apparatus for the measurement of minority carrier lifetime in semiconductors *Eur. J. Phys*. **6** 295–298
Sconza A, Torzo G 1987 A simple and instructive version of the Haynes–Shockley experiment *Eur. J. Phys*. **8** 34–40
Sconza A, Torzo G 1989 An undergraduate laboratory experiment for measuring the energy gap in semiconductors *Eur. J. Phys*. **10** 123–126
Sconza A, Torzo G, Viola G 1994 Experiment on the physics of the PN junction *Am. J. Phys*. **62** 66–70
Scott H L 1972 Percolation processes and cooperative phenomena *Am. J. Phys*. **40** 1134–1139
Scott W T 1966 *The Physics of Electricity and Magnetism* (New York: Wiley)
Sedra A S, Smith K C 1998 *Microelectronic circuits* 4th ed (New York: Oxford University Press)

Seeley F B, Bandas A, Fowler M, Gibson R 1999 An inexpensive light-emitting diode strobe system for measuring the radius of a single sonoluminescing bubble *Am. J. Phys.* **67** 162–164
Selvarajan A, Ramakrishna B S 1979 Laser communication system using the ultrasonic light modulator *Am. J. Phys.* **47** 282–283
Shamim S, Zia W, Anwar M S 2010 Investigating viscous damping using a webcam *Am. J. Phys.* **78** 433–436
Shamir J, Fox R 1967 Classroom demonstration of interference phenomena using a He–Ne gas laser *Am. J. Phys.* **35** 161–162
Shanker G, Gupta V K, Saraf B, Sharma N K 1985 Temperature variation of modulus of rigidity and internal friction: An experiment with torsional oscillator *Am. J. Phys.* **53** 1192–1195
Sharpe J P, Sungar N 2010 Supercritical bifurcation in a simple mechanical system: An undergraduate experiment *Am. J. Phys.* **78** 520–523
Shaw G E 1983 Harmonically forced Cavendish balance *Am. J. Phys.* **51** 913–916
Shelton D P, Kettner M E 1988 Potential energy of interaction for two magnetic pucks *Am. J. Phys.* **56** 51–52
Shieh S-Y 1968 Unified derivation of Fresnel's formulas for both polarizations parallel and perpendicular to the plane of incidence *Am. J. Phys.* **36** 273–274
Shinbrot T, Grebogi C, Wisdom J, Yorke J A 1992 Chaos in a double pendulum *Am. J. Phys.* **60** 491–499
Shockley W, Queisser H J 1961 Detailed balance limit of efficiency of p-n junction solar cells *J. Appl. Phys.* **32** 510–519
Shur M 1996 *Introduction to Electronic Devices* (New York: Wiley)
Siahmakoun A, French V A, Patterson J 1997 Nonlinear dynamics of a sinusoidally driven pendulum in a repulsive magnetic field *Am. J. Phys.* **65** 393–400
Sianoudis I A, Drakaki E 2008 An approach to Poiseuille's law in an undergraduate laboratory experiment *Eur. J. Phys.* **29** 489–495
Silva N 2011 Studying Hooke's law by using a pogo stick *Phys. Teach.* **49** 300–301
Simon M D, Heflinger L O, Geim A K 2001 Diamagnetically stabilized magnet levitation *Am. J. Phys.* **69** 702–713
Simon M D, Heflinger L O, Ridgway S L 1997 Spin stabilized magnetic levitation *Am. J. Phys.* **65** 286–292
Simon R, Riesz R P 1979 Large amplitude simple pendulum: A Fourier analysis *Am. J. Phys.* **47** 898–899
Simpson H M, Wolfe P J 1975 Young's modulus and internal damping in a vibrating rod *Am. J. Phys.* **43** 506–508
Singh A, Mohapatra Y N, Kumar S 2002 Electromagnetic induction and damping: Quantitative experiments using a PC interface *Am. J. Phys.* **70** 424–427
Singh N P, Gupta S C, Sood B R 2002 An experiment to determine the skin depth and Fermi velocity in metals *Am. J. Phys.* **70** 845–846
Skeldon K D, Nadeau V J, Adams C 1998a The resonant excitation of a wineglass using positive feedback with optical sensing *Am. J. Phys.* **66** 851–860
Skeldon K D, Reid L M, McInally V, Dougan B, Fulton C 1998b Physics of the Theremin *Am. J. Phys.* **66** 945–955

Smedley J E 1998 Spectrum analysis for introductory musical acoustics *Am. J. Phys*. **66** 144–147
Smit J, Wijn H P J 1959 *Ferrites* (Eindhoven: Philips' Technical Library)
Smith A D, Tinkham M 1980 Superconductivity demonstration *Am. J. Phys.* **48** 940–941
Smith G S 2001 Teaching antenna radiation from a time-domain perspective *Am. J. Phys*. **69** 288–300
Smith G S 2002 Teaching antenna reception and scattering from a time-domain perspective *Am. J. Phys*. **70** 829–844
Smith H J T, Blackburn J A 1997 Experimental measurements on a simulated lumped transmission line *Am. J. Phys*. **65** 716–725
Smith R J 1984 *Circuits, Devices, and Systems* 4th ed (New York: Wiley)
Smith R V, Edmonds D S 1970 A simple velocity of light measurement for the undergraduate laboratory *Am. J. Phys*. **38** 1481–1483
Snider J W 1971 Magnetic hysteresis measurements with an integrating magnetometer *Am. J. Phys*. **39** 964–965
Sobel M 2007 The standing wave on a string as an oscillator *Phys. Teach*. **45** 137–139
Soffer B H, Lynch D K 1999 Some paradoxes, errors, and resolutions concerning the spectral optimization of human vision *Am. J. Phys*. **67** 946–953
Sokol P E, Warren G, Zheng B, Smith P 2013 A circuit to demonstrate phase relationships in *RLC* circuits *Phys. Educ*. **48** 312–316
Soloukhin R I (ed) 1975 *Методы физических измерений* (Новосибирск: Наука)
Soloukhin R I (ed) 1983 *Оптика и атомная физика* (Новосибирск: Наука)
Soulen R J, Fogle W E, Colwell J H 1992 A decade of absolute noise thermometry at NIST using a resistive SQUID *Temperature, Its Measurement and Control in Science and Industry* vol 6 (New York: AIP) pp 983–988
Soundranayagam R, Ramayya A V, Cleeman L, Riecken M, Fuson N, Springer J 1983 Diffraction pattern intensity measurements in the introductory college physics laboratory using microcomputers *Am. J. Phys*. **51** 906–909
Spears B K, Tufillaro N B 2008 A chaotic lock-in amplifier *Am. J. Phys*. **76** 213–217
Spiegel D R, Helmer R J 1995 Shot-noise measurements of the electron charge: An undergraduate experiment *Am. J. Phys*. **63** 554–560
Sprott J C 2000 Simple chaotic systems and circuits *Am. J. Phys*. **68** 758–763
Squire P T 1986 Pendulum damping *Am. J. Phys*. **54** 984–991
Stajdohar R E, Towle L C 1968 High-pressure viscosity experiment for the undergraduate laboratory *Am. J. Phys.* **36** 340–343
Stanek F, Tobin R G, Foiles C L 1993 Stabilization of a multimode He–Ne laser: A vivid demonstration of thermal feedback *Am. J. Phys*. **61** 932–934
Stanley H E 1983 *Introduction to Phase Transitions and Critical Phenomena* (London: Oxford University Press)
Stanley R C 1972 Non newtonian viscosity and some aspects of lubrication *Phys. Educ*. **7** 193–198
Starrett M J 2008 Resonance and radio *Phys. Educ*. **43** 515–518
Stauffer D 1977 Percolation clusters as teaching aid for Monte Carlo simulation and critical exponents *Am. J. Phys*. **45** 1001–1002

Stavrou D, Assimopoulos S, Skordoulis C 2013 A unit on deterministic chaos for student teachers *Phys. Educ*. **48** 355–359
Stearns S D 2004 *Antenna Impedance Models—Old and New* www.fars.k6ya.org/docs/antenna-impedance-model.pdf
Steeb E S, Forsythe W E 1967 Photometry and Illumination *Handbook of Physics*, eds E U Condon, H Odishaw (New York: McGraw–Hill) pp 6-48–6-64
Steinberg R N, Oberem G E, McDermott L C 1996 Development of a computer-based tutorial on the photoelectric effect *Am. J. Phys*. **64** 1370–1379
Steinhaus D W 1983 Measurements on the He–Ne laser lines near 633 nm *Am. J. Phys*. **51** 824–825
Stigmark L 1952 A precise determination of the charge of the electron from shot noise *Ark. Fys*. **5** 399–426
Stockard D P, Johnson T L, Sears F W 1967 Study of amplitude jumps *Am. J. Phys*. **35** 961–963
Stockman H E 1962 Demonstration of the Doppler effect *Am. J. Phys*. **30** 307–308
Stratton J A 1941 *Electromagnetic Theory* (New York: McGraw–Hill)
Straulino S, Orlando A 2012 A simple radio receiver aids understanding of wireless communication *Phys. Educ*. **47** 211–219
Streetman B G, Banerjee S 2000 *Solid State Electronic Devices* 5th ed (Upper Saddle River, NJ: Prentice Hall)
Strehlow C P, Sullivan M C 2009 A classroom demonstration of levitation and suspension of a superconductor over a magnetic track *Am. J. Phys*. **77** 847–851
Struganova I 2005 A spring, Hooke's law, and Archimedes' principle *Phys. Teach.* **43** 516–518
Suits J C 1971 Magneto-optical rotation and ellipticity measurements with a spinning analyzer *Rev. Sci. Instrum*. **42** 19–22
Sulkes M, Sulkes Z 2011 Measurement of luminescence decays: High performance at low cost *Am. J. Phys*. **79** 1104–1111
Sullivan P, Seidel G 1967 AC temperature measurement of changes in heat capacity of beryllium in a magnetic field *Phys. Lett. A* **25** 229–230
Sullivan P, Seidel G 1968 Steady-state, AC-temperature calorimetry *Phys. Rev*. **173** 679–685
Sullivan R A L, Dunk A, Ford P J, Hampton R N, Hopkins J C 1987 Undergraduate laboratory experiment to determine the Curie temperature of nickel using a resistance technique *Eur. J. Phys*. **8** 300–305
Sungar N 1996 Teaching the superposition of waves *Phys. Teach*. **34** 236–237
Sungar N, Sharpe J P, Moelter M J, Fleishon N, Morrison K, McDill J, Schoonover R 2001 A laboratory-based nonlinear dynamics course for science and engineering students *Am. J. Phys*. **69** 591–597
Swanson L W, Davis P R 1985 Work function measurements *Methods of Experimental Physics* vol 22 (Orlando: Academic Press) pp 1–22
Sze S M, Ng K K 2007 *Physics of Semiconductor Devices* 3rd ed (Hoboken, NJ: Wiley)
Tan B T G 1982 Fundamental resonant frequency of a loudspeaker *Am. J. Phys*. **50** 348–351

Tang G-H, Wang J-C 2005 Correlation detection of fluorescent lamp flicker using a sound card *Am. J. Phys*. **73** 1189–1191
Tanner B K 1980 Magneto-optical experiments on rare earth garnet films *Am. J. Phys*. **48** 59–63
Tanner P, Loebach J, Cook J, Hallen H D 2001 A pulsed jumping ring apparatus for demonstration of Lenz's law *Am. J. Phys*. **69** 911–916
Temple P A 1975 An introduction to phase-sensitive amplifiers: An inexpensive student instrument *Am. J. Phys*. **43** 801–807
Templin J D 1996 Direct calculation of radiation resistance in simple radiating systems *Am. J. Phys*. **64** 1379–1383
Tenquist D W, Whittle R M, Yarwood J 1969–1970 *University Optics* vols 1–2 (London: Iliffe Books)
Terzella T, Sundermier J, Sinacore J, Owen C, Takai H 2008 Measurement of *g* using a flashing LED *Phys. Teach*. **46** 395–397
Thayer D 1973 Another speed of light apparatus *Am. J. Phys*. **41** 722–724
Thompson F 2005 Permittivity measurements in solids, powders, and liquids *Am. J. Phys*. **73** 787–789
Thompson W J 1990 Determining *e/m* with a Bainbridge tube: Less data, more physics *Am. J. Phys*. **58** 1019–1020
Thompson W J 1992 Fourier series and the Gibbs phenomenon *Am. J. Phys*. **60** 425–429
Thorn R J, Winslow G H 1962 Radiation of thermal energy from real bodies *Temperature, Its Measurement and Control in Science and Industry* vol 3 (New York: Reinhold) pp 421–447
Thornton S T, Marion J B 2004 *Classical Dynamics of Particles and Systems* 5th ed (Belmont, CA: Brooks/Cole)
Tiernan W M 1997 A superconducting persistent current experiment for an undergraduate laboratory *Am. J. Phys*. **65** 778–784
Tobochnik J 2001 Resource letter CPPPT-1: Critical point phenomena and phase transitions *Am. J. Phys*. **69** 255–263
Toftlund H 1987 A rotary Curie point magnetic engine: A simple demonstration of a Carnot-cycle device *Am. J. Phys*. **55** 48–49
Tompson C W, White H W 1983 Latent heat and low-temperature heat capacity experiment for general physics laboratory *Am. J. Phys*. **51** 362–364
Torzo G, Soletta I, Branca M 2007 Using Peltier cells to study solid–liquid–vapour transitions and supercooling *Eur. J. Phys*. **28** S13–S27
Towler W R, Beams J W 1976 Magnetic suspension for lecture and classroom demonstrations *Am. J. Phys*. **44** 478–480
Trudeau J, Loh E C, Hartman P L 1971 Another method for the determination of *c* *Am. J. Phys*. **39** 877–881
Tsutaoka T, Kasagi T, Nakamura T, Hatakeyama K 1997 High frequency permeability of Mn-Zn ferrite and its composite materials *J. Phys. IV France* **7** C1-557–558
Tucholski E J 2009 Tabletop demonstration of multiple source interference using ultrasonic transducers *Am. J. Phys*. **77** 938–942
Turner L 2009 A simple demonstration of back emf *Phys. Teach*. **47** 513–515

Turvey K 1990 An undergraduate experiment on the vibration of a cantilever and its application to the determination of Young's modulus *Am. J. Phys*. **58** 483–487
Tyagi S, Lord A E 1980 Simple and inexpensive apparatus for Young's modulus measurement *Am. J. Phys*. **48** 205–206
Tyler C E 1969 A pedagogical measurement of the velocity of light *Am. J. Phys*. **37** 1154–1156
Umstattd R J, Carr C G, Frenzen C L, Luginsland J W, Lau Y Y 2005 A simple physical derivation of Child–Langmuir space-charge-limited emission using vacuum capacitance *Am. J. Phys*. **73** 160–163
Utreras-Díaz C A 1988 Dielectric slab in a parallel-plate condenser *Am. J. Phys*. **56** 700–701
Vaidman L 1990 Torque and force on a magnetic dipole *Am. J. Phys*. **58** 978–983
Valenzuela S O, Jorge G A, Rodríguez E 1999 Measuring the interaction force between a high temperature superconductor and a permanent magnet *Am. J. Phys.* **67** 1001–1006
Valev V K, Wouters J, Verbiest T 2008 Precise measurements of Faraday rotation using ac magnetic fields *Am. J. Phys*. **76** 626–629
Van der Gracht J 1994 Simple method for demonstrating Fraunhofer diffraction *Am. J. Phys*. **62** 934–937
van Sark W G J H M 2007 Teaching the relation between solar cell efficiency and annual energy yield *Eur. J. Phys*. **28** 415–427
Vanderkooy J, Beccario M J 1973 An inexpensive, accurate laboratory determination of the velocity of light *Am. J. Phys*. **41** 272–275
Vandervoort K G, Willingham J M, Morris C H 1995 Simple, inexpensive probe for resistivity measurements above 77 K on metals and superconductors *Am. J. Phys*. **63** 759–760
Vannoni M, Molesini G 2004 Speckle interferometry experiments with a digital photocamera *Am. J. Phys*. **72** 906–909
Vannoni M, Trivi M, Arizaga R, Rabal H, Molesini G 2008 Dynamic speckle imaging with low-cost devices *Eur. J. Phys.* **29** 967–975
Varchenko A A, Kraftmakher Y A 1973 Nonadiabatic regime in modulation calorimetry *Phys. Status Solidi A* **20** 387–393
Velasco S, Román F L, González A, White J A 2004 A computer-assisted experiment for measurement of the temperature dependence of the speed of sound in air *Am. J. Phys*. **72** 276–279
Velasco S, Román F L, White J A 2010 A simple experiment for measuring bar longitudinal and flexural vibration frequencies *Am. J. Phys*. **78** 1429–1432
Verovnik I, Likar A 1988 A fluctuation interferometer *Am. J. Phys*. **53** 231–234
Vetterling W T, Andelman M 1979 Comments on: Undergraduate experiment on noise thermometry *Am. J. Phys*. **47** 382–384
Vollmer M 2005 Diffraction revisited: position of diffraction spots upon rotation of a transmission grating *Phys. Educ*. **40** 562–565
Wadhwa A 2008 An innovative method to study Stokes' law in the laboratory *Phys. Educ*. **43** 301–304
Wadhwa A 2009 Measuring the coefficient of restitution using a digital oscilloscope *Phys. Educ*. **44** 517–521

Wagner C, Schottky W 1930 Theorie der geordneten Mischphasen *Z. phys. Chemie* **11** 163–210
Wagner C, Soonpaa H H 1994 A simple picoammeter for thermionic emission measurements *Am. J. Phys*. **62** 473–474
Wagner J, Syed M 2011 Investigation of skin effect in mercury using a simple solenoid setup *Am. J. Phys*. **79** 850–855
Wagner W S 1991 Temperature and color of incandescent lamps *Phys. Teach*. **29** 176–177
Waltham C, Kotlicki A 2009 Construction and calibration of an impact hammer *Am. J. Phys*. **77** 945–949
Walton D S 1974 A simple apparatus for the determination of *g* by free fall *Phys. Educ*. **9** 80–81
Wang X, Schmitt C, Payne M 2002 Oscillations with three damping effects *Eur. J. Phys*. **23** 155–164
Warden J A 1970 Demonstration of amplitude jumps *Am. J. Phys*. **38** 773–774
Watson G H 1995 Transmission line exercises for the introductory physics laboratory *Am. J. Phys*. **63** 423–425
Weeks D E 1990 A torsion balance to measure hysteretic levitation forces in high T_C superconductors *Rev. Sci. Instrum*. **61** 197–200
Wein G R 1999 A video technique for the quantitative analysis of the Poisson spot and other diffraction patterns *Am. J. Phys*. **67** 236–240
Weiss R 1969 A quantitative demonstration of the energy stored in a capacitor or an inductor *Am. J. Phys*. **37** 566
Weltin H 1961 Demonstration of the Doppler effect *Am. J. Phys*. **29** 713–714
Wesley J T, Behof A F 1987 Optical diffraction pattern measurements using a self-scanning photodiode array interfaced to a microcomputer *Am. J. Phys*. **55** 835–844
Whaite G, Wolfe J 1990 Harmonic or Fourier synthesis in the teaching laboratory *Am. J. Phys*. **58** 481–483
Wheeler C R, Henriksen P N, Ramsier R D 2004 Visibility of thin-film interference fringes *Am. J. Phys*. **72** 279–281
Whitaker R J 2009 Motors and bulbs in series *Phys. Teach*. **47** 353–354
White D R, Galleano R, Actis A, Brixy H, DeGroot M, Dubbeldam J, Reesink A L, Edler F, Sakurai H, Shepard R L, Gallop J C 1996 The status of Johnson noise thermometry *Metrologia* **33** 325–335
White G K, Minges M L 1997 Thermophysical properties of some key solids: An update *Int. J. Thermophys.* **18** 1269–1327
Whiteley R V, Luke K L 1989 An inexpensive, versatile experiment for teaching computer-aided experimentation *Am. J. Phys*. **57** 741–746
Whiteside H 1965 Laser optics experiments and demonstrations *Am. J. Phys*. **33** 487–492
Whittaker E 1960 *A History of the Theories of Aether and Electricity* vol 2 (New York: Harper and Brothers)
Whittaker E 1962 *A History of the Theories of Aether and Electricity* vol 1 (London: Nelson and Sons)

Whittle R M, Yarwood J 1973 *Experimental Physics for Students* (London: Chapman and Hall)
Wick K, Ruddick K 1999 An accurate measurement of *g* using falling balls *Am. J. Phys.* **67** 962–965
Widiatmoko E, Widayani M, Budiman M, Abdullah M, Khairurrijal 2011 A simple spectrophotometer using common materials and a digital camera *Phys. Educ.* **46** 332–339
Wieder S, Jaoudi E 1978 Autobalancing radiometer *Am. J. Phys.* **46** 935–937
Wiederick H D, Gauthier N 1983 Frequency dependence of the skin depth in a metal cylinder *Am. J. Phys.* **51** 175–176
Wiederick H D, Gauthier N, Campbell D A, Rochon P 1987 Magnetic braking: Simple theory and experiment *Am. J. Phys.* **55** 500–503
Wilkening G, Hesse J 1981 Electrical pendulum for educational purpose *Am. J. Phys.* **49** 90–91
Williams B L 1968 The Franck–Hertz experiment using a thyratron *Phys. Teach.* **6** 322–323
Wilson D E 1989 A direct laboratory approach to the study of capacitors *Am. J. Phys.* **57** 630–632
Wilson F, Lord A E 1973 Young's modulus determination via simple, inexpensive static and dynamic measurements *Am. J. Phys.* **41** 653–656
Winters L M 1993 A visual measurement of the speed of sound *Phys. Teach.* **31** 284–285
Wintle H J 1963 Measurement of the velocity of sound in gases *Am. J. Phys.* **31** 942–943
Wolfson R 1991 The lock-in amplifier: A student experiment *Am. J. Phys.* **59** 569–572
Wolfson R L T 1981 Intelligent light bulb: A negative feedback demonstration *Am. J. Phys.* **49** 374–375
Wong D, Lee P, Shenghan G, Xuezhou W, Qi H Y, Kit F S 2011 The photoelectric effect: experimental confirmation concerning a widespread misconception in the theory *Eur. J. Phys.* **32** 1059–1064
Wood L T, Rottmann R M, Barrera R 2004 Faraday's law, Lenz's law, and conservation of energy *Am. J. Phys.* **72** 376–380
Woodruff A E 1968 The radiometer and how it does not work *Phys. Teach.* **6** 358–363
Woolsey G A 1971 An extension of the Ramsauer–Townsend experiment in a xenon thyratron *Am. J. Phys.* **39** 558–560
Woolsey G A 1973 Laser optics experiments with glass plates and a modified Jamin interferometer *Am. J. Phys.* **41** 255–259
Worland R S, Wilson D D 1999 The speed of sound in air as a function of temperature *Phys. Teach.* **37** 53–57
Wouch G, Lord A E 1978 Eddy currents: Levitation, metal detectors, and induction heating *Am. J. Phys.* **46** 464–466
Wray E M 1975 A simple test of Stefan's law *Phys. Educ.* **10** 25–27
Wright P G 1977 The variation of viscosity with temperature *Phys. Educ.* **12** 323–325
Yan F N, Wong H K 1993 Force between the plates of a parallel-plate capacitor *Am. J. Phys.* **61** 1153
Yan K L, Lonc W P 1975 Microwave Faraday rotation *Am. J. Phys.* **43** 718–720

Yang W 2010 Teaching phase-sensitive demodulation for signal conditioning to undergraduate students *Am. J. Phys.* **78** 909–915
Yang Y-K 1998 Determining the ratio of charge to mass *e*/*m* for electrons by magnetic focusing *Am. J. Phys.* **66** 157–162
Yap F Y 1971 Laser measurement of refractive index of a gas *Am. J. Phys.* **39** 224
Yap J and MacIsaac D 2006 Analysing simple electric motors in the classroom *Phys. Educ.* **41** 427–431
Young C T 1980 Electromagnetic wave propagation in aluminum *Am. J. Phys.* **48** 417–418
Young H D, Freedman R A 2000 *Sears and Zemansky's University Physics* 10th ed (San Francisco: Addison–Wesley)
Yu F T S, Wang E Y 1973 Undergraduate coherent optics laboratory *Am. J. Phys.* **41** 1160–1169
Yuan B, McClellan S R, Al-Mifgai B F, Growney E A, Komolafe O A 2010 A cost-efficient frequency domain fluorescence lifetime measurement system *Am. J. Phys.* **78** 28–34
Yurke B 1984 Conservative model for the damped harmonic oscillator *Am. J. Phys.* **52** 1099–1102
Zajonc A G 1982 Measurement of spectral line splitting with a scanning, student-grade, Fabry–Perot interferometer *Am. J. Phys.* **50** 404–406
Zakharov I L, Kraftmakher Y A 1989 Обращённый метод измерения электропроводности с помощью вращающегося магнитного поля *Журнал прикладной механики и технической физики* (4) 22–26
Zalewski E F, Duda C R 1983 Silicon photodiode device with 100% external quantum efficiency *Appl. Optics* **22** 2867–2873
Zanetti V 1984 Sun and lamps *Am. J. Phys.* **52** 1127–1130
Zernov V B, Sharvin Y V 1959 Measurement of the resistance of high purity tin at helium temperatures *Sov. Phys. JETP* **36** 737–741
Zhong A 1989 An acoustic Doppler shift experiment with the signal-receiving relay *Am. J. Phys.* **57** 49–50
Zhou F, Cloninger T 2008 Computer-based experiment for determining Planck's constant using LEDs *Phys. Teach.* **46** 413–415
Zilio S C 1982 Measurement and analysis of large-angle pendulum motion *Am. J. Phys.* **50** 450–452
Ziólkowska E A, Szydlowski H 1984 Remarks on the skin effect experiment in an undergraduate laboratory *Am. J. Phys.* **52** 857

This page intentionally left blank

Index